Yoshiaki Oka
Seiichi Koshizuka
Yuki Ishiwatari
Akifumi Yamaji

Super Light Water Reactors and Super Fast Reactors

Supercritical-Pressure Light Water Cooled Reactors

Springer

Super Light Water Reactors and Super Fast Reactors

Yoshiaki Oka • Seiichi Koshizuka •
Yuki Ishiwatari • Akifumi Yamaji

Super Light Water Reactors and Super Fast Reactors

Supercritical-Pressure Light Water Cooled Reactors

Springer

Yoshiaki Oka
Department of Nuclear Energy
Graduate School of Advanced Science
and Engineering
Waseda University
Nishi-Waseda campus Building 51
11F, room 09B
3-4-1 Ohkubo
Shinjuku-ku
Tokyo 169-8555
Japan
okay@waseda.jp

Seiichi Koshizuka
Department of Systems Innovation
Graduate School of Engineering
Building 8, 3FL room 317
Hongo-campus, University of Tokyo
7-3-1 Hongo
Bunkyo-ku, Tokyo 113-8656
Japan
koshizuka@sys.t.u-tokyo.ac.jp

Yuki Ishiwatari
Department of Nuclear Engineering
and Management
Graduate School of Engineering
University of Tokyo
7-3-1 Hongo, Bunkyo-ku,
Tokyo, 113-8656,
Japan
ishi@nuclear.jp

Akifumi Yamaji
Department of Nuclear Engineering
and Management
University of Tokyo
Hongo 7-3-1, 113-8656, Tokyo,
Japan
yamaji.akifumi@jaea.go.jp

ISBN 978-1-4419-6034-4 e-ISBN 978-1-4419-6035-1
DOI 10.1007/978-1-4419-6035-1
Springer New York Dordrecht Heidelberg London

Library of Congress Control Number: 2010929945

© Springer Science+Business Media, LLC 2010
All rights reserved. This work may not be translated or copied in whole or in part without the written permission of the publisher (Springer Science+Business Media, LLC, 233 Spring Street, New York, NY 10013, USA), except for brief excerpts in connection with reviews or scholarly analysis. Use in connection with any form of information storage and retrieval, electronic adaptation, computer software, or by similar or dissimilar methodology now known or hereafter developed is forbidden.
The use in this publication of trade names, trademarks, service marks, and similar terms, even if they are not identified as such, is not to be taken as an expression of opinion as to whether or not they are subject to proprietary rights.

Printed on acid-free paper

Springer is part of Springer Science+Business Media (www.springer.com)

To our wives, Keiko, Yukari, Mayumi, and Satomi, who have continually provided us with the inspiration and support necessary for carrying out the research and writing of this book.

Preface

The emerging importance of ground-breaking technologies for nuclear power plants has been widely recognized. The supercritical pressure light water cooled reactor (SCWR), a generation IV reactor, has been presented as a reactor concept for innovative nuclear power plants that have reduced capital expenditures and increased thermal efficiency. The SCWR concepts that were developed at the University of Tokyo are referred to as the super light water reactor (Super LWR) and super fast reactor (Super FR) concepts. This book describes the major design features of the Super LWR and Super FR concepts and the methods for their design and analysis.

The foremost objective of this book is to provide a much needed integrated textbook on design and analysis of water cooled reactors by describing the conceptual development of the Super LWR and Super FR. The book is intended for students at a graduate or an advanced undergraduate level. It is assumed that the reader is provided with an introduction to the understanding of reactor theory, heat transfer, fluid flows, and fundamental structural mechanics. This book can be used in a one-semester course on reactor design in conjunction with textbooks on BWR and PWR design and safety. In addition, the book can serve as a textbook on reactor thermal-hydraulic and neutronic analysis.

The defining feature of this textbook is its coverage of major elements of reactor design and analysis in a single book. These elements include the fuel (rods and assemblies), the core and structural components, plant control systems, startup schemes, stability, plant heat balance, safety systems, and safety analyses. The information is presented in a way that enhances its usefulness to understand the relationships between various fields in reactor design. The book also provides the reader with an understanding of the differences in design and analysis of the Super LWR and the Super FR which distinguish them from LWRs. Though the differences are slight, the reader needs to grasp them to better understand the fundamental and essential features of the design and analysis. This knowledge will enhance in-depth understanding of the design and safety of LWRs and other reactor types.

The second objective of this book is to serve as a reference for researchers and engineers working or interested in the research and development of the SCWR. This book is the first comprehensive summary of the reactor conceptual studies of the SCWR, which were begun initially by researchers at the University of Tokyo and are continuing to be led by them.

Methodology in SCWR design and analysis, together with physical descriptions of systems, is emphasized more in the text rather than numerical results. Analytical and design results will continue to change with the ongoing evolution of the SCWR design, while many design methods will remain fundamentally unchanged for a considerable time. The book's topics are divided into six areas: Overview; Core and fuel; Plant systems, plant control, startup, and stability; Safety; Fast reactors; and Research and development.

The first chapter provides an overview of the Super LWR and Super FR reactor studies. It includes elements of design and analysis that are further described in each chapter. The reader will also be interested in what ways the new reactor concepts have been developed and how the analyses have been improved.

Chapter 2 covers design and analysis of the core and fuel. It includes core and fuel design, coupled neutronic and thermal hydraulic core calculations, subchannel analysis, statistical thermal design methods, fuel rod design, and fuel rod behavior and integrity during transients.

Chapters 3–5 treat the plant system and behaviors. They include system components and configuration, plant heat balance, the methods of plant control system design, plant dynamics, plant startup schemes, methods of stability analysis, thermal-hydraulic analyses, and coupled neutronic and thermal-hydraulic stability analyses.

Chapter 6 covers safety topics. It includes fundamental safety principles of the Super LWR and Super FR in comparison with that of LWRs, safety features, safety system design, abnormal transient and accident analyses at supercritical pressure, analyses of loss of coolant accidents (LOCAs) and anticipated transients without scram (ATWSs) and simplified probabilistic safety assessment (PSA).

Chapter 7 covers the design and analysis of fast reactors. The features of the Super LWR and Super FR are that the plant system configuration does not need to be changed from the thermal reactor to the fast reactor. The analysis of plant control, stability, and safety of the Super FR as well as core design are provided.

Chapter 8 presents a brief summary worldwide on research and development of the SCWR.

Reviews of supercritical fossil-fuel fired power plant technologies and high temperature water and steam cooled reactor concepts in the past are described in the Appendix.

Tokyo, Japan

Yoshiaki Oka
Seiichi Koshizuka
Yuki Ishiwatari
Akifumi Yamaji

Acknowledgements

Numerous people have contributed to the development of the Super LWR and Super FR concepts. Among the most notable are Yasushi Okano and Satoshi Ikejiri who collaborated with us as research assistants. Important technical contributions were provided by graduate students of the University of Tokyo who prepared the computer codes and carried out the analyses. They are Kazuyoshi Kataoka, Tatjana Jevremovic, Jong Ho Lee, Kazuaki Kito, Kazuo Dobashi, Toru Nakatsuka, Tami Mukohara, Tin Tin Yi, Jee Woon Yoo, Tomoko Murakami (Yamasaki), Naoki Takano, Tadasuke Tanabe, Mikio Tokashiki, Suhan Ji, Kazuhiro Kamei, Yohei Yasoda, Mitsunori Kadowaki, Isao Hongo, and Shunsuke Sekita. Post doctoral researchers, Jue Yang, Liangzhi Cao, Jiejin Cai, Haitao Ju, Junli Gou, Haoliang Lu, and Chi Young Han took part in the study and contributed to its progress.

Helpful information and advice were given by Osamu Yokomizo, Kotaro Inoue, Michio Yokomi, Takashi Kiguchi, Kumiaki Moriya, Junichi Yamashita, Masanori Yamakawa, Shinichi Morooka, Takehiko Saito, Shigeaki Tsunoyama, Katsumi Yamada, Shungo Sakurai, Masakazu Jinbo, Shoji Goto, Takashi Sawada, Hideo Mori, Yosuke Katsumura, Yusa Muroya, Takayuki Terai, Shinya Nagasaki, Hiroaki Abe, Yoshio Murao, Keiichiro Tsuchihashi, Keisuke Okumura, Hajime Akimoto, Masato Akiba, Naoaki Akasaka, and Motoe Suzuki. Discussions with researchers in the European HPLWR project and researchers in the SCWR project on the Generation Four International Forum (GIF) were useful.

The text was assembled by Wenxi Tian in collaboration with post doctoral researchers, Misako Watanabe, and Yuki Munemoto. They also prepared figures, tables, and indexes. An incalculable debt of gratitude is due them. The authors are grateful for the editing assistance of Carol Kikuchi.

The most recent part of the work on the Super FR includes the results of the project “Research and Development of the Super Fast Reactor” entrusted to the University of Tokyo by the Ministry of Education, Culture, Sports, Science and Technology of Japan (MEXT).

The Super LWR research and the publication of this book were financially supported by the Global Center of Excellence Program “Nuclear Education and Research Initiative” entrusted to the University of Tokyo by MEXT.

In the final analysis, however, it was the willing sacrifice and loving support of four individuals, Keiko Oka, Yukari Koshizuka, Mayumi Ishiwatari, and Satomi Yamaji, who enabled four over-committed husbands to devote the time and energy necessary to allow this book to become a reality.

Contents

1 Introduction and Overview 1
1.1 Industrial Innovation 1
1.2 Evolution of Boilers 1
1.3 Overview of the Super LWR and Super FR 6
1.3.1 Concept and Features 6
1.3.2 Improvement of Thermal Design Criterion 10
1.3.3 Core Design Criteria 12
1.3.4 Improvement of Core Design and Analysis 13
1.3.5 Fuel Design 16
1.3.6 Plant Control 19
1.3.7 Startup Schemes 22
1.3.8 Stability 28
1.3.9 Safety 37
1.3.10 Super FR 54
1.3.11 Computer Codes and Database 61
1.4 Past Concepts of High Temperature Water and Steam Cooled Reactors 62
1.5 Research and Development 63
1.5.1 Japan 63
1.5.2 Europe 68
1.5.3 GIF and SCWR 68
1.5.4 Korea, China, US, Russia and IAEA 68
References 69

2 Core Design 79
2.1 Introduction 79
2.1.1 Supercritical Water Thermophysical Properties 80
2.1.2 Heat Transfer Deterioration in Supercritical Water 82
2.1.3 Design Considerations with Heat Transfer Deterioration 90
2.2 Core Design Scope 92
2.2.1 Design Margins 92

2.2.2 Design Criteria 96
2.2.3 Design Boundary Conditions 98
2.2.4 Design Targets 100
2.3 Core Calculations 102
2.3.1 Neutronic Calculations 102
2.3.2 Thermal-Hydraulic Calculations 112
2.3.3 Equilibrium Core Calculations 120
2.4 Core Designs 122
2.4.1 Fuel Rod Designs 122
2.4.2 Fuel Assembly Designs 128
2.4.3 Coolant Flow Scheme 137
2.4.4 Low Temperature Core Design with R-Z Two-Dimensional Core Calculations 140
2.4.5 High Temperature Core Design with Three-Dimensional Core Calculations 145
2.4.6 Design Improvements 161
2.4.7 Summary 170
2.5 Subchannel Analysis 173
2.5.1 Subchannel Analysis Code 173
2.5.2 Subchannel Analysis of the Super LWR 177
2.6 Statistical Thermal Design 181
2.6.1 Comparison of Thermal Design Methods 182
2.6.2 Description of MCSTDP 184
2.6.3 Application of MCSTDP 190
2.6.4 Comparison with RTDP 198
2.6.5 Summary 200
2.7 Fuel Rod Behaviors During Normal Operations 200
2.7.1 Evaluation of the Maximum Peak Cladding Temperature 200
2.7.2 Fuel Rod Analysis 201
2.7.3 Fuel Rod Design 205
2.8 Development of Transient Criteria 208
2.8.1 Selection of Fuel Rods for Analyses 209
2.8.2 Principle of Rationalizing the Criteria for Abnormal Transients 210
2.9 Summary 217
References 218

3 Plant System Design 221
3.1 Introduction 221
3.2 System Components and Configuration 222
3.3 Main Components Characteristics 223
3.3.1 Containment 224
3.3.2 Reactor Pressure Vessel 226

3.3.3 Internals 227
3.3.4 Turbine 228
3.3.5 Steam Lines and Candidate Materials 230
3.4 Plant Heat Balance 230
3.4.1 Super LWR Steam Cycle Characteristics 230
3.4.2 Thermal Efficiency Evaluation 232
3.4.3 Factors Influencing Thermal Efficiency 235
3.5 Summary 238
References 239

4 Plant Dynamics and Control 241
4.1 Introduction 241
4.2 Analysis Method for Plant Dynamics 241
4.3 Plant Dynamics Without a Control System 246
4.3.1 Withdrawal of a Control Rod Cluster 248
4.3.2 Decrease in Feedwater Flow Rate 248
4.3.3 Decrease in Turbine Control Valve Opening 250
4.4 Control System Design 252
4.4.1 Pressure Control System 253
4.4.2 Main Steam Temperature Control System 255
4.4.3 Reactor Power Control System 256
4.5 Plant Dynamics with Control System 258
4.5.1 Stepwise Increase in Pressure Setpoint 259
4.5.2 Stepwise Increase in Temperature Setpoint 261
4.5.3 Stepwise Decrease in Power Setpoint 262
4.5.4 Impulsive Decrease in Feedwater Flow Rate 262
4.5.5 Decrease in Feedwater Temperature 264
4.5.6 Discussion 265
4.6 Summary 266
References 266

5 Plant Startup and Stability 269
5.1 Introduction 269
5.2 Design of Startup Systems 270
5.2.1 Introduction to Startup Schemes of FPPs 270
5.2.2 Constant Pressure Startup System of the Super LWR 273
5.2.3 Sliding Pressure Startup System of the Super LWR 279
5.3 Thermal Considerations 282
5.3.1 Startup Thermal Analysis Code 282
5.3.2 Thermal Criteria for Plant Startup 288
5.3.3 Thermal Analyses 289
5.4 Thermal-Hydraulic Stability Considerations 295
5.4.1 Mechanism of Thermal-Hydraulic Instability 295
5.4.2 Selection of Analysis Method 297

5.4.3 Thermal-Hydraulic Stability Analysis Method 298
5.4.4 Thermal-Hydraulic Stability Analyses 304
5.5 Coupled Neutronic Thermal-Hydraulic Stability Considerations 316
5.5.1 Mechanism of Coupled Neutronic Thermal-Hydraulic Instability 316
5.5.2 Coupled Neutronic Thermal-Hydraulic Stability Analysis Method 318
5.5.3 Coupled Neutronic Thermal-Hydraulic Stability Analyses 324
5.6 Design of Startup Procedures with Both Thermal and Stability Considerations 335
5.7 Design and Analysis of Procedures for System Pressurization and Line Switching in Sliding Pressure Startup Scheme 338
5.7.1 Motivation and Purpose 338
5.7.2 Redesign of Sliding Pressure Startup System 339
5.7.3 Redesign of Sliding Pressure Startup Procedures 340
5.7.4 System Transient Analysis 343
5.8 Summary 345
References 347

6 Safety 349
6.1 Introduction 349
6.2 Safety Principle 349
6.3 Safety System Design 350
6.3.1 Equipment 350
6.3.2 Actuation Conditions of the Safety System 355
6.4 Selection and Classification of Abnormal Events 357
6.4.1 Reactor Coolant Flow Abnormality 358
6.4.2 Other Abnormalities 360
6.4.3 Event Selection for Safety Analysis 361
6.4.4 Uniqueness in the LOCA of the Super LWR 362
6.5 Safety Criteria 363
6.5.1 Criteria for Fuel Rod Integrity 364
6.5.2 Criteria for Pressure Boundary Integrity 365
6.5.3 Criteria for ATWS 365
6.6 Safety Analysis Methods 366
6.6.1 Safety Analysis Code for Supercritical Pressure Condition 366
6.6.2 Safety Analysis Code for Subcritical Pressure Condition 371
6.6.3 Blowdown Analysis Code 372
6.6.4 Reflooding Analysis Code 377

6.7 Safety Analyses 380
6.7.1 Abnormal Transient Analyses at Supercritical Pressure 382
6.7.2 Accident Analyses at Supercritical Pressure 391
6.7.3 Loss of Coolant Accident Analyses 395
6.7.4 ATWS Analysis 401
6.7.5 Abnormal Transient and Accident Analyses at Subcritical Pressure 412
6.8 Development of a Transient Subchannel Analysis Code and Application to Flow Decreasing Events 415
6.8.1 A Transient Subchannel Analysis Code 415
6.8.2 Analyses of Flow Decreasing Events 417
6.8.3 Summary 423
6.9 Simplified Level-1 Probabilistic Safety Assessment 423
6.9.1 Preparation of Event Trees 423
6.9.2 Initiating Event Frequency and Mitigation System Unavailability 431
6.9.3 Results and Considerations 432
6.9.4 Summary 435
6.10 Summary 436
References 437

7 Fast Reactor Design 441
7.1 Introduction 441
7.2 Design Goals, Criteria, and Overall Procedure 441
7.2.1 Design Goals and Criteria 441
7.2.2 Overall Design Procedure 443
7.3 Concept of Blanket Assembly with Zirconium Hydride Layer 445
7.3.1 Effect of Zirconium Hydride Layer on Void Reactivity 445
7.3.2 Effect of Zirconium Hydride Layer on Breeding Capability 450
7.3.3 Effect of Hydrogen Loss from Zirconium Hydride Layers on Void Reactivity 451
7.4 Fuel Rod Design 453
7.4.1 Introduction 453
7.4.2 Failure Modes of Fuel Cladding 454
7.4.3 Fuel Rod Design Criteria 456
7.4.4 Fuel Rod Design Method 459
7.4.5 Fuel Rod Design and Analysis 462
7.4.6 Summary of Fuel Rod Design 465
7.5 Core Design Method and 1,000 MWe Class Core Design 467
7.5.1 Discussion of Neutronic Calculation Methods 467
7.5.2 Core Design Method 468
7.5.3 Materials Used in Core Design 479

7.5.4 Fuel Assembly Design 480
7.5.5 Core Arrangement 481
7.5.6 Design of 1,000 MWe Class Core 483
7.6 Subchannel Analysis 491
7.6.1 Introduction 491
7.6.2 Temperature Difference Arising from Subchannel Heterogeneity 493
7.6.3 Evaluation of MCST over Equilibrium Cycle 495
7.7 Evaluation of Maximum Cladding Surface Temperature with Engineering Uncertainties 499
7.7.1 Treatment of Downward Flow 499
7.7.2 Nominal Conditions and Uncertainties 501
7.7.3 Statistical Thermal Design of the Super FR 505
7.7.4 Comprehensive Evaluation of Maximum Cladding Surface Temperature at Normal Operation 506
7.8 Design and Improvements of 700 MWe Class Core 508
7.8.1 Design of Reference Fuel Rod and Core 509
7.8.2 Core Design Improvement for Negative Local Void Reactivity 509
7.8.3 Core Design Improvement for Higher Power Density 518
7.9 Plant Control 522
7.9.1 Plant Transient Analysis Code for the Super FR 523
7.9.2 Basic Plant Dynamics of the Super FR 523
7.9.3 Design of Reference Control System 525
7.9.4 Improvement of Feedwater Controller 527
7.9.5 Plant Stability Analyses 530
7.9.6 Comparison of Improved Feedwater Controllers 534
7.9.7 Summary of Improvement of Feedwater Controller 535
7.10 Thermal and Stability Considerations During Power Raising Phase of Plant Startup 536
7.10.1 Introduction 536
7.10.2 Calculation of Flow Distribution 537
7.10.3 Thermal and Thermal-Hydraulic Stability Considerations 539
7.10.4 Sensitivity Analyses 547
7.11 Safety 550
7.11.1 Introduction 550
7.11.2 Analyses of Abnormal Transients and Accidents at Supercritical Pressure 551
7.11.3 Analyses of Loss of Coolant Accidents 556
7.11.4 Analyses of Anticipated Transient Without Scram Events 563
7.12 Summary 564
References 567

8 Research and Development 571
8.1 Japan 571
8.1.1 Concept Development 571
8.1.2 Thermal Hydraulics 575
8.1.3 Materials and Water Chemistry 577
8.2 Other Countries 581
8.2.1 Europe 581
8.2.2 Canada 583
8.2.3 Korea 584
8.2.4 China 584
8.2.5 USA 585
8.3 International Activities 587
8.3.1 Generation-IV International Forum 587
8.3.2 IAEA-Coordinated Research Program 587
8.3.3 International Symposiums 588
References 590

Appendix A: Supercritical Fossil Fired Power Plants – Design and Developments 599

Appendix B: Review of High Temperature Water and Steam Cooled Reactor Concepts 619

Index 645

Chapter 1
Introduction and Overview

1.1 Industrial Innovation

A model for the dynamics of industrial innovation is described in the book, *Mastering the Dynamics of Innovation* [1]. In brief, the model states that product design innovation dominates at first. After the dominant product design, holding the largest market share is established, production process innovation follows. Today, LWRs are the dominant product design of nuclear power plants. Their design is characterized mainly by a reactor pressure vessel, control rods, a containment vessel, steam turbines, feedwater pumps, an emergency core cooling system, etc. These design features were established in the 1950s and 1960s. LWRs have reached the era of production process innovation. Standardization is one type of production process innovation.

The modular construction of the Kashiwazaki–Kariwa ABWR is shown in Fig. 1.1. Modules of base mat, control room, containment shell, etc. are prefabricated either at their factories or at the construction site. They are erected and put in place at the construction site. This is another type of production process innovation and it shortened the construction period.

In the 1980s, computer aided design (CAD) of nuclear power plants was extensively developed in Japan. It replaced handwritten drawings and the scaled plastic models of the plants. Handling and modification of the drawings became much easier than before. Connection of piping and maintenance spaces for equipment could be easily checked on the computer. Presently, design information in the computer is used not only for construction but also for maintenance of the plants. This is a third type of production process innovation.

1.2 Evolution of Boilers

Evolution of boilers is shown in Fig. 1.2. Boilers have evolved from primitive boilers to circular boilers and once-through boilers. Primitive boilers are like a large tea kettle. They have a transfer surface at the bottom. The coolant can be circulated

Y. Oka et al., *Super Light Water Reactors and Super Fast Reactors*,
DOI 10.1007/978-1-4419-6035-1_1, © Springer Science+Business Media, LLC 2010

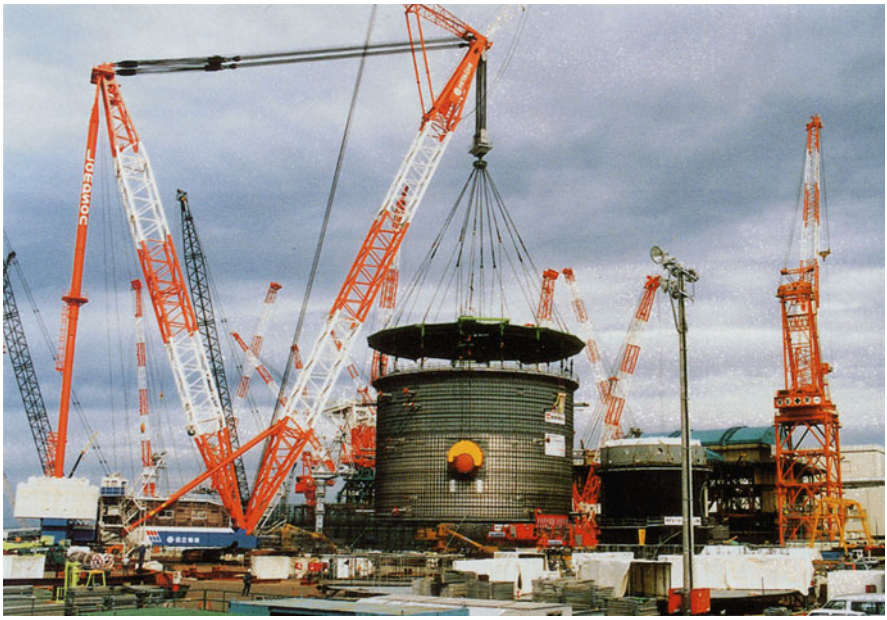


Fig. 1.1 Modular construction of the Kashiwazaki–Kariwa ABWR (courtesy of Tokyo Electric Power Co.)

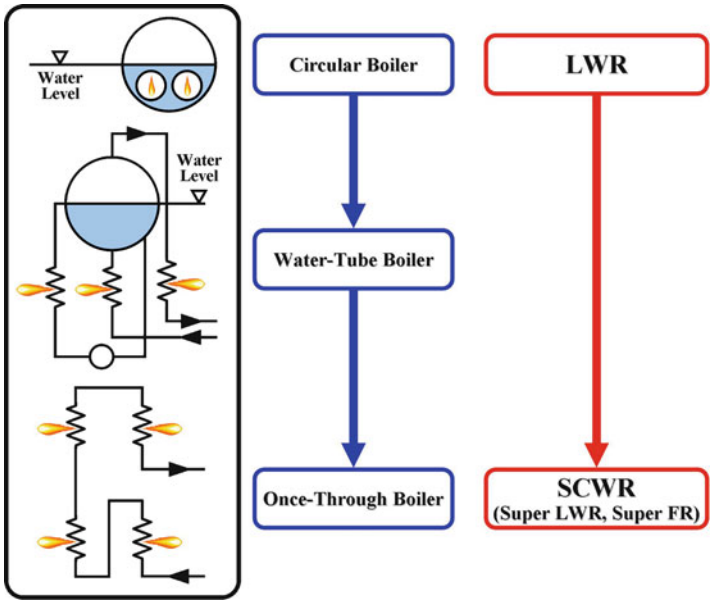


Fig. 1.2 Evolution of boilers

naturally in the boilers. Primitive boilers operate at atmospheric pressure. They take a long time to start up when their capacity is large. A primitive boiler was adopted as Newcomen's thermal engine in 1715. Circular boilers have an inside heat transfer surface. This heat transfer surface was increased in water tube boilers. Coolant circulation has been enhanced with its evolution from boilers without circulation to those with natural circulation and forced circulation. The capacity was increased with the evolution. Once-through boilers are considered as the newest type of boilers. They operate at supercritical pressure where the boiling phenomenon does not exist. The water level disappears. All the feedwater is converted to steam. BWRs are a type of circular boiler that adopts an immersion principle of the heat transfer surface. PWRs are a type of circular boiler with forced circulation. Judging the boilers from the history of evolution, the once-through supercritical pressure light water cooled reactors will be the natural evolution of current LWRs.

The milestone parameters of the supercritical fossil-fuel fired power plants (FPPs) in the USA and in Japan are shown in Table 1.1. The plants were developed in the USA in the late 1940s and 1950s. The first plant Philo No.6 started operation in 1957 and the second, Eddystone No.1, in 1959. Both plants used higher pressures and steam temperatures than today's plants. But Breed No. 1, also started in 1959, used 24.1 MPa and 566°C for operating pressure and steam temperature; later plants also used similar pressure and temperature. Due to the low fossil fuel prices in the USA and constantly increasing power demands, it was not economically attractive to pursue high thermal efficiency and use of expensive austenitic steels with large thermal expansion coefficients for the boiler units. The steam conditions of supercritical pressure FPPs in the USA stayed the same as those of Breed No.1 for a long time.

In Japan, the first supercritical FPP, Anegasaki No.1 started operation in 1967 with a rated power of 600 MWe. The supercritical FPP technologies have been improved constantly in Japan because of the high fossil fuel prices. Since fuel cost is the major part of the power generation cost in FPPs, improvement of the thermal efficiency would reduce the power cost. The sliding pressure plant Hirono No. 1 was deployed in 1980. It operates at subcritical pressure at partial load. Japanese

Table 1.1 Supercritical fossil-fuel fired power plants in USA and Japan

USA; Developed in 1950s
Philo #6 (125 MWe, 31 MPa, 621°C, 1957)
Eddystone #1 (325 MWe, 34.5 MPa, 649°C, 1959)
Breed #1 (450 MWe, 24.1 Mpa, 566°C, 1959)
Largest unit operated: 1,300 MWe
Japan; Deployed in 1960s and constantly improved
Anegasak I #1(600 MWe, 24.1 MPa, 538°C, 1967)
Hirono #1 (600 MWe, Sliding-pressure, 1980)
Kawagoe #2 (700 MWe, 31.0 MPa, 566°C, 1989)
Hekinan #3 (700 MWe, 24.1 MPa, 593°C, 1993)
Tachibanawan #1 (1,050 MWe, 25 MPa, 610°C, 2001)
28 units (600–1,050 MWe) started operation in 1990–2000

FPPs need to be operated in the daily load-follow mode. Frequent startups and shutdowns are necessary. Sliding pressure plants meet these needs.

Since sliding pressure plants are operated at subcritical pressure at partial load, they achieve higher thermal efficiency than constant pressure operation at supercritical pressure. To improve the thermal efficiency at rated power, the high pressure plant, Kawagoe No. 2 started operation with conditions of 31 MPa and 566°C in 1989. This was followed by the high temperature plant, Tachibanawan No. 1, with conditions of 25 MPa and 610°C.

The technology of supercritical steam turbines has also been improved. Compact 700 MWe turbines without an intermediate pressure turbine were used for Kawagoe No. 2. The design and development of supercritical FPPs is described in Appendix A.

Supercritical boilers and power plants were also developed in Russia and Western Europe. The number of FPPs worldwide is larger than that of LWRs.

The research and development of ultra high temperature and high pressure plants was started in Japan, Europe, and the USA to achieve higher thermal efficiency and reduce greenhouse gas emissions. Examples for goals of steam temperatures and pressure are (650°C/30 MPa), (650°C/35.4 MPa), (700°C/37.5 MPa), and (760°C/38 MPa).

The steam conditions of FPPs and nuclear power plants are shown in Fig. 1.3. The steam condition of current LWRs has remained low. The superheat test reactors that were studied in the USA in the 1960s tried to increase the coolant temperature at subcritical pressure.

Competition among uses of thermal engines has been strong as shown in Table 1.2. Steam engines are used for central power stations, internal combustion

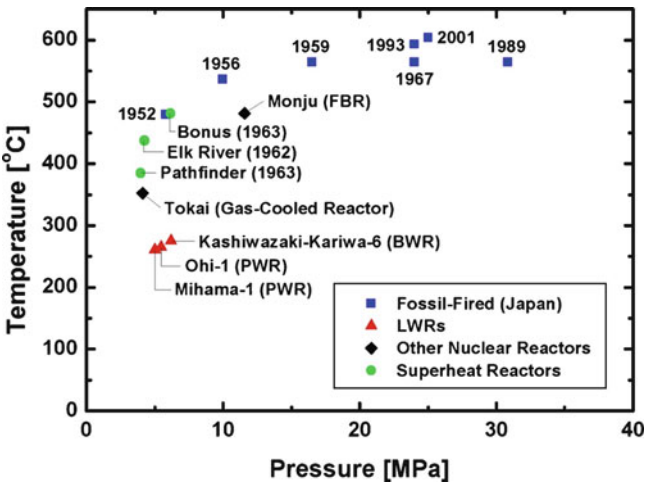


Fig. 1.3 Steam conditions of nuclear and fossil-fuel fired power plants

Table 1.2 Competition among uses of thermal engines

Present
Steam engines (steam turbines): large central power plants
Internal combustion engines: automobiles, ships etc.
Jet engines (gas turbines): aircraft and modular power plants
Rocket engines: rockets
Past steam engine applications
Nineteenth century: automobiles
Before 1960: ships
Before 1970: locomotives
Jet engines entered use in central power plants as natural gas combined cycle gas turbine power plants from the 1980s.

engines for automobiles and ships, jet engines for aircraft, and rocket engines for rockets. Steam power was used for automobiles in the nineteenth century, ships before 1960, and locomotives before 1970. Use of jet engines in central power plants was introduced into combined cycle gas turbine power plants in the 1980s. These plants consist of one or more gas turbine generators equipped with heat recovery steam generators to capture heat from the gas turbine exhaust. Steam produced in the heat recovery steam generators powers a steam turbine generator to produce additional electric power. Use of the otherwise exhausted wasted heat in the turbine exhaust gas results in high thermal efficiency compared to other combustion-based technologies. These plants use natural gas as the fuel. The power rating of gas turbines is not as large as that of steam turbines of nuclear power plants. But modules of the combined cycle power plants are used for large central power stations.

Nuclear power plants are expected to play an important role for meeting the challenges of protecting the global environment, reducing greenhouse gas emissions, and securing stable energy supplies. When total power cost is considered, nuclear power generation has advantages over fossil-fuel fired power in its lower fraction of production cost. The production cost consists of the costs of fuel and plant operation. The cost of nuclear fuel including fabrication and enrichment is approximately 15–20% of the total power generation cost, while it is 60–70% for FPPs. The capital cost of nuclear power plants is very high; while it is low for FPPs, in particular combined cycle power plants. The construction of a nuclear power plant requires a large investment. Reducing investment volume and financial risk is important in a deregulated market economy. Capital cost reduction of nuclear power plants through innovative technologies is a very important goal; increasing thermal efficiency is effective in reducing capital cost and the volume of spent fuel and radioactive waste per generated watt of electricity.

Pursuing innovation of nuclear power plant technologies in making plants more compact and raising their thermal efficiency is important for the competitiveness of nuclear power plants in the twenty-first century.

1.3 Overview of the Super LWR and Super FR

1.3.1 Concept and Features

The critical pressure of water is 22.1 MPa. The changes in specific heat and water density at 25 MPa are depicted in Fig. 1.4. Supercritical water does not exhibit a change of phase. The water density decreases continuously with temperature. The concept of boiling does not exist. The specific heat exhibits a peak at the pseudo-critical temperature. This corresponds to the boiling point at the subcritical water cooling. No abrupt change of coolant density, however, is observed at supercritical water cooling. The heat is efficiently removed at the pseudo-critical temperature, which is approximately 385°C at 25 MPa. The low density fluid above this temperature is often called "steam" and high density fluid below it is called "water." The enthalpy difference between water and steam is so large that much heat can be removed with low coolant flow rates.

The design concept of a light water cooled reactor operating at supercritical pressure was devised by one of this book's authors, Y. Oka [2, 3]. The reactor concept has been actively developed within his research group at the University of Tokyo [4–8]. It adopts a once-though coolant cycle without recirculation and a reactor pressure vessel (RPV) as shown in Fig. 1.5.

The water coolant is pressurized to the supercritical pressure by the main coolant pumps. They drive the coolant through the core to the turbines. A comparison of plant systems of BWRs, PWRs, and supercritical FPPs is made in Fig. 1.6. The coolant cycle of the Super Light Water Reactor (Super LWR) and Super Fast Reactor (Super FR) is a once-through direct cycle as the supercritical FPPs. The steam-water separators, dryers, and recirculation system of BWRs and the

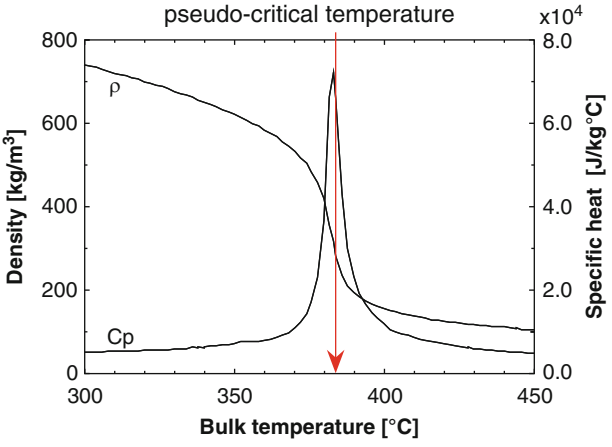


Fig. 1.4 Changes in specific heat and density of water at 25 MPa

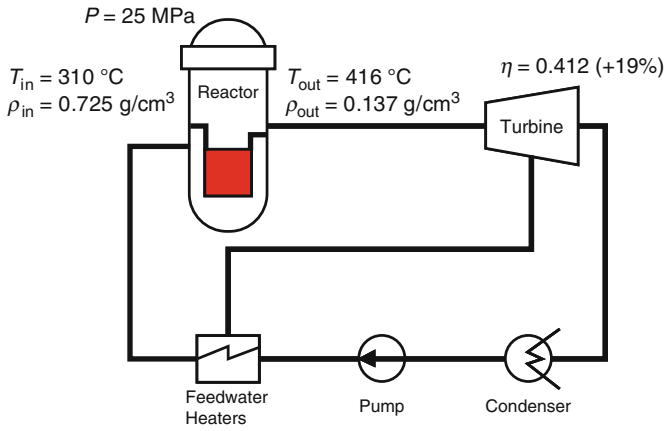


Fig. 1.5 Once-through coolant cycle reactor plant system (original plant parameters)

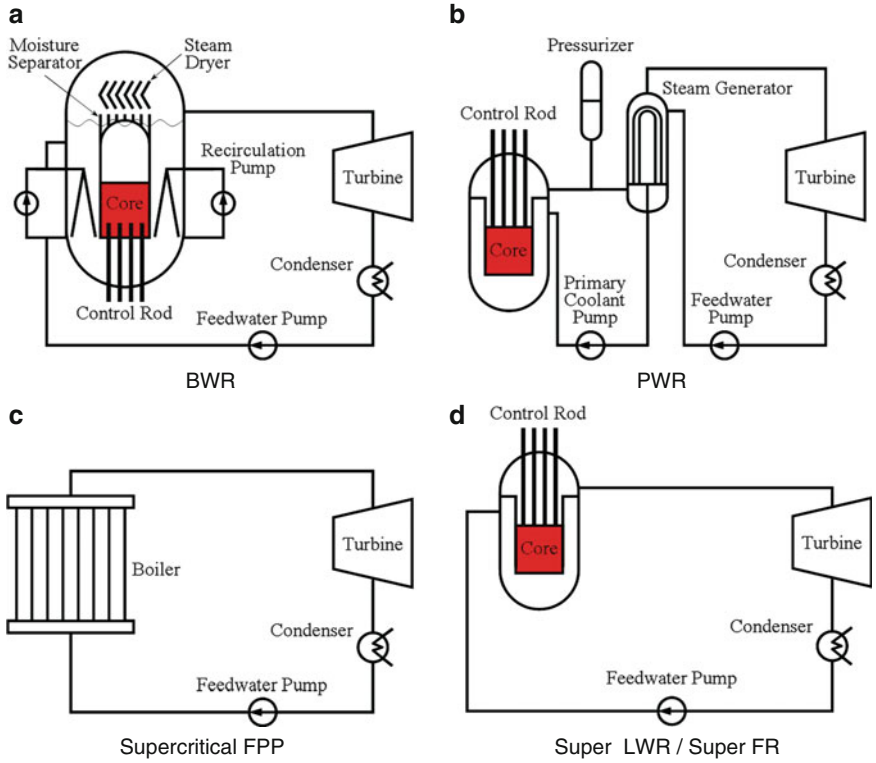


Fig. 1.6 Comparison of plant systems of BWR, PWR, supercritical fossil-fuel fired power plants and the Super LWR and Super FR

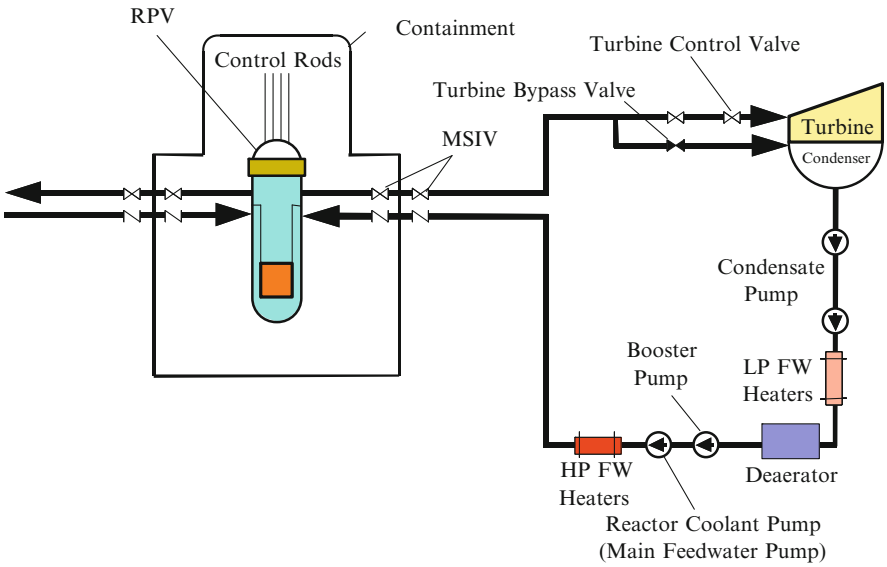


Fig. 1.7 Plant system of the Super LWR and Super FR

pressurizer, steam generators, and primary coolant loops of PWRs are not necessary. The control rod drives are mounted on the top of the RPV.

Some more details of the plant system of the Super LWR and Super FR are shown in Fig. 1.7. The RPV and control rods are similar to those of PWRs, the containment and safety systems are similar to those of BWRs and the balance of plant (BOP) is like that of supercritical FPPs. All RPV walls are cooled by inlet coolant as in PWRs. The operating temperatures of major components such as the RPV, control rods, steam turbines, pipings and pumps are within the experiences of those of LWRs and supercritical FPPs.

There are several advantages to the plant system of the Super LWR and Super FR. The first two advantages are the compactness of the plant system due to the high specific enthalpy of supercritical water and the simplicity of the plant system without the recirculation system and dryers of BWRs and steam generators of PWRs.

The RPV is as small as that of PWRs. The enthalpy difference in the core is so large that much heat is removed with low coolant flow rates. The rates are from one-fifth to one-tenth of BWRs and PWRs. The number of main coolant pipings is two for a 1,000 MWe reactor.

The control rod drives are mounted on the top of the RPV since there is no need for the steam-water separators and dryers. The position of the RPV in the containment vessel (CV) is lowered due to the top-mounted control rod drives. No space below RPV is necessary for the withdrawal and maintenance of the control blades.

Adopting the RPV rather than pressure tubes simplifies the plant system by eliminating not only many pressure tubes but calandria tanks and the auxiliary systems of pressure tube reactors.

The coolant enthalpy inside the primary coolant loops and the RPV in the CV is substantially smaller than that of LWRs. This makes the CV more compact and lower in height. The construction period will be shortened due to the decrease in the number of reactor building floors.

The third advantage is the high temperature of the coolant. Boiling phenomenon does not exist at supercritical pressure. The temperature of the coolant can be raised without the limit of boiling point. The high thermal efficiency is good not only for producing electricity but also for reducing the amount of spent fuel per generated watt of electricity.

The fourth advantage is the good compatibility of the once-through plant with a tight fuel lattice fast reactor core. The plant system configuration can be identical for both fast and thermal reactors. The water-cooled fast reactor needs to adopt a tight fuel lattice. But increases in the core pressure drop and pumping power due to the tight lattice are not problems as they are in LWRs. The reactor coolant flow rates are substantially lower than those of BWRs and PWRs. The slight increase in the core pressure drop does not impose a problem for required power of the feedwater pump that drives coolant up to 25 MPa.

Both thermal and fast reactors have been studied. Here, they are called the Super LWR and Super FR. Early designs carried different names such as SCLWR and SCLWR-H for the thermal reactors and SCFBR, SCFBR-H, SCFR-H, and SWFR for fast reactors.

LWRs were developed 50 years ago. Their successful implementation was based in part on experiences with subcritical fossil-fuel fired power technologies at that time. The number of supercritical FPPs worldwide is larger than that of nuclear power plants. Considering the evolutionary history of boilers and the abundant experiences with supercritical FPP technologies, the supercritical pressure light water cooled reactor is the natural evolution of LWRs.

The guidelines of the Super LWR and Super FR concept development are the following:

1. Utilize supercritical FPP and LWR technologies as much as possible.
2. Minimize large-scale development of major components.
3. Pursue simplicity in design.

The maximum temperature of the major components such as turbines, RPV, main steam piping, reactor coolant pumps, and control rod drives has been kept within the experiences of supercritical FPPs and LWRs. The concept development started from the simplest design. If a design did not meet a goal, for example, a reactor outlet temperature of 500°C, then an alternative design was studied.

It should be pointed out that the advantages of the Super LWR and Super FR remain valid even if the outlet temperature is 400°C. The general corrosion of fuel cladding at the high temperature will be reduced substantially than that of the

reactor of 500°C outlet coolant temperature. Starting from the low temperature test reactor will be the one way of the development.

1.3.2 Improvement of Thermal Design Criterion

The plant parameters of the original supercritical pressure light water cooled reactors were shown in Fig. 1.5. The outlet coolant temperature is low, 416°C. In the early designs before 1996, the core was designed to satisfy the limits of the critical heat flux that was determined from the empirical correlation proposed by Yamagata et al. [9] to avoid deteriorated heat transfer which occurs at high heat flux and low flow conditions at supercritical pressure. The criterion was called the minimum deteriorated heat flux ratio (MDHFR) criterion. But the critical heat flux increases greatly with coolant mass flux by reducing the fuel pitch to diameter ratio. The heat transfer deterioration is milder than the dryout and cladding temperature does not increase sharply even if the deterioration does occur as shown in Fig. 1.8.

The mechanisms of heat transfer deterioration were not clearly understood by experiments. But the numerical simulation based on the k–ε model by Jones–Lander successfully explained them [10]. Heat transfer deterioration occurs via two mechanisms depending on the flow rate. When the flow rate is high, viscosity increases locally near the wall by heating. This makes the viscous sublayer thicker and the Prandtl number smaller. Both effects reduce the heat transfer. When the flow rate is low, buoyancy force accelerates the flow velocity distribution, flattening it, and generation of turbulence energy is reduced. This heat transfer deterioration mechanism appears at the boundary between forced and natural convection. The heat transfer coefficient and deterioration heat flux that was calculated by the numerical simulation [10] agreed with the experimental data obtained by Yamagata et al. [9].

Taking critical heat flux as the core design criterion is not necessary at the supercritical pressure where no dryout and burnout phenomena occur. Supercritical water is a single-phase fluid. No critical heat flux criterion is used for the design of gas cooled reactors and liquid metal cooled fast reactors. The maximum cladding surface temperature (MCST) is taken as the design criterion and it is limited accordingly so that the fuel cladding integrity is maintained at abnormal transients.

To evaluate the cladding temperatures directly during abnormal transients, it was necessary to develop a database of heat transfer coefficients at various conditions of heat flux, flow rate, and coolant enthalpy. The database of heat transfer coefficients was prepared by numerical simulations that successfully analyzed the deterioration phenomenon itself. The database, Oka–Koshizuka correlation, has been used for safety analysis.

The concept for refining the transient criteria, without using the MDHFR criterion, was reported in 1997 [11]. Higher temperature cores for thermal reactors and the fast reactor SCFR-H were designed using the new transient criterion of the

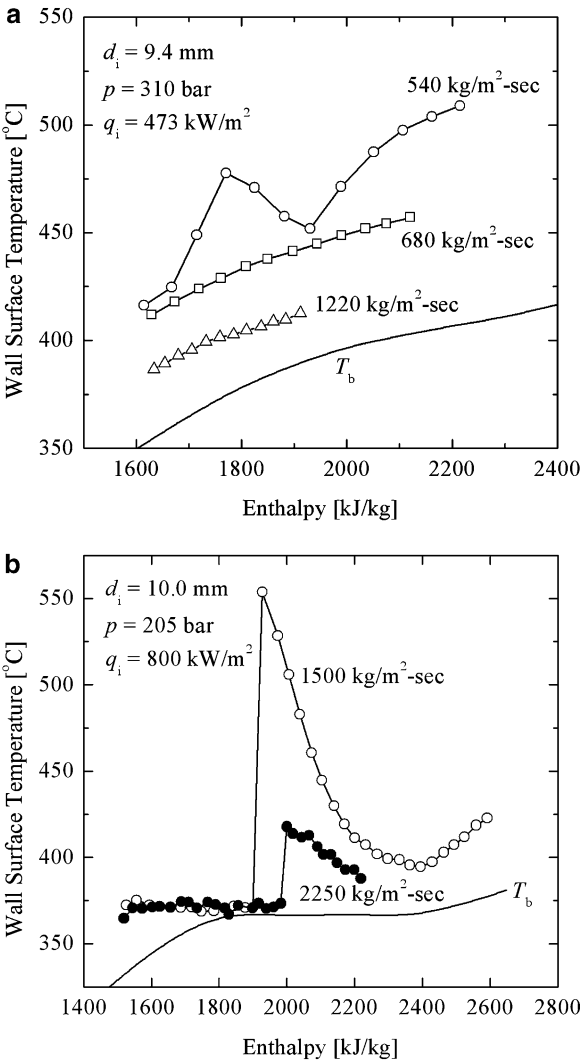


Fig. 1.8 Comparison of heat transfer deterioration at supercritical pressure and dryout at subcritical pressure

MCST [12, 13]. For high temperature reactors, the coolant enthalpy rise in the core is high and coolant flow rate is inevitably low. The gap between fuel rods is kept small to increase the coolant velocity in the core.

Removing the critical heat flux criterion (i.e., the MDHFR) from the core design and taking the MCST criterion makes it possible to raise the outlet coolant temperature of the Super LWR and Super FR to that of the supercritical FPP. The high enthalpy rise and low coolant flow rate are advantages of the once-through coolant cycle.

1.3.3 Core Design Criteria

The core design criteria are summarized in Table 1.3. The maximum linear heat generation rate (MLHGR) at rated power is 39 kW/m. It is slightly lower than those of PWRs (42.6 kW/m) and BWRs (44 kW/m) due to the high average coolant temperature. The fuel centerline temperature stays nearly the same as that of LWRs. The fission gas release rate from the fuel pellets is similar to that of LWRs. The fuel design of the Super LWR follows that of LWRs.

The maximum cladding temperature criterion is determined considering the strength of cladding material. Stainless steel is used for the design of the Super LWR and Super FR. Nickel-base alloys are an alternative. Cladding material development is an important R&D issue and requires extensive experiments and testing. Both general corrosion at high temperatures and stress cracking corrosion at low temperatures need to be considered. Supercritical water shows "gas-like" properties above the pseudo-critical temperature. General corrosion by oxidation occurs at high temperature and it is primarily reduced by lowering oxygen content in the coolant. Stress corrosion cracking must be avoided during the service life of the fuel cladding. Joint R&D into material science and water chemistry is necessary.

The MCST is taken as another criterion. The surface temperature is taken from the viewpoint of corrosion, but the cladding centerline temperature is taken from the viewpoint of the cladding material strength. By adding the temperature difference between the surface and the centerline of the cladding, which is approximately 12°C for austenitic stainless steel cladding, the MCST can be used as the criterion for the strength of fuel cladding of Super LWR and Super FR.

All the reactor coolant is purified after condensation in the once-through coolant cycle of the Super LWR and Super FR. This differs from BWRs and PWRs in which reactor coolant is circulated in a closed loop as recirculating coolant and primary loop coolant, respectively. The purity of reactor coolant is therefore different from that of LWRs.

The moderator temperature in the water rods should be below the pseudo-critical temperature to keep the moderator density high. Thin layer of zirconia (ZrO_2) is used for thermal insulation on the water rods. The thermal insulation also reduces the stress of stainless steel plates of water rods below allowable stress level.

Table 1.3 Core design criteria

Thermal design criteria
Maximum linear heat generation rate (MLHGR) at rated power $\leqq$ 39 kW/m
Maximum cladding surface temperature at rated power $\leqq$ 650°C for Stainless Steel cladding
Moderator temperature in water rods $\leqq$ 384°C (pseudo critical temperature at 25 MPa)
Neutronic design criteria
Positive water density reactivity coefficient (negative void reactivity coefficient)
Core shutdown margin $\geqq$ 1.0%Δk/k

The positive reactivity coefficient or negative coolant void reactivity coefficient is necessary for the inherent negative feedback of the Super LWR and Super FR at the loss of coolant accident. The reactor power should decrease automatically at the loss of coolant accident.

The core shutdown margin should be above 1.0%Δk/k with one-rod stuck condition. It is the same criterion as in LWRs.

1.3.4 Improvement of Core Design and Analysis

The first design of the supercritical pressure light water cooled reactor (SCLWR) in 1992 adopted zirconium hydride rods as moderator for flattening axial power distribution [2]. The next core design in 1994 adopted water rods [14]. Heat transfer between core coolant and water rods was considered by single channel models of a fuel rod and a water rod. The core design was carried out in the two-dimensional R-Z model with the cell burn-up calculation [15]. It was used for the designs of early version of the Super LWR and the Super FR. The neutronic–thermal hydraulic coupling was considered in the two-dimensional core calculation [16, 17]. Plant heat balance and thermal efficiency were also analyzed in 1997 [17].

The high temperature core without the critical heat flux criterion (i.e. the MDHFR) was designed in 1998 [12]. The two-dimensional R-Z model of the core cannot accurately predict burn-up of fuel rods. The three-dimensional coupled neutronic–thermal-hydraulic core calculation was developed in 2003 [18]. It is shown in Fig. 1.9. This calculation considered the control rod pattern and fuel loading pattern [19, 20] and was similar to the core calculation for BWRs. But the finite difference code SRAC [21] was used for the three-dimensional neutronic calculation instead of a nodal code. The core design of the Super FR also adopted the three dimensional neutronic and thermal hydraulic coupled core burn-up calculation.

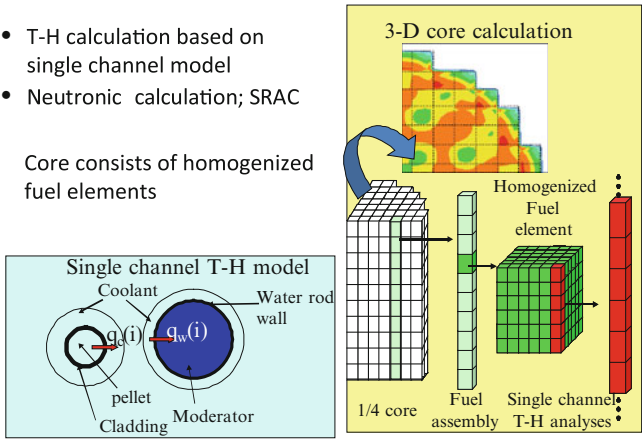


Fig. 1.9 Three-dimensional neutronic and thermal-hydraulic coupled core calculation

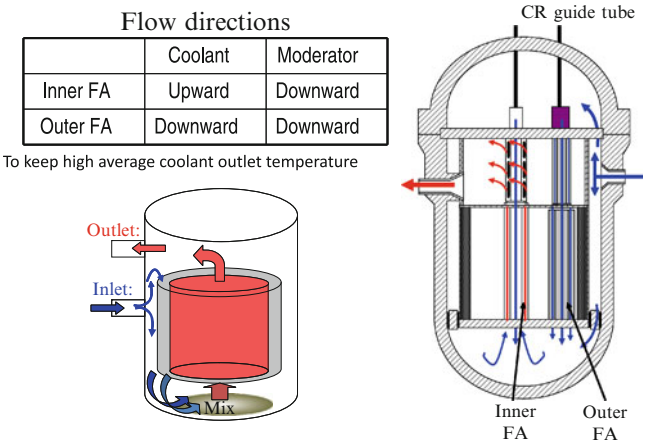


Fig. 1.10 Coolant flow scheme of two-pass core

A new coolant flow scheme was proposed in which the fuel assemblies loaded on the core periphery are cooled by a descending flow. The coolant mixes with the rest of the coolant from the downcomer at the lower plenum and then rises up the fuel channels in the fuel assemblies loaded in the inner region of the core. It is called a two-pass core and shown in Fig. 1.10. The average reactor outlet coolant temperature is increased in this core [22, 23]. The two-pass core is compatible with the low leakage fuel loading pattern (LLLP) that the burnt (third cycle) fuel assemblies are loaded in the core periphery [24]. The average fuel enrichment is decreased using the LLLP. The one-pass core where whole coolant is upward flow needs fresh fuel assemblies in the core periphery not to decrease the outlet coolant temperature. But the fuel enrichment of the out-in fuel loading becomes inevitably higher than that of the LLLP.

The Super FR also adopted the two-pass core where all blanket fuel assemblies and part of seed fuel assemblies are cooled by a descending flow so as to keep average reactor outlet coolant temperature high. By adopting the two-pass core, the conventional concepts of the hot channel factors of PWR and the peaking factors of BWR are not applicable to the Super LWR and the Super FR.

The cladding temperature that was obtained by the three-dimensional coupled core calculation is the average temperature over the assembly. The peak cladding temperature of a fuel rod is necessary for the evaluation of the fuel cladding integrity. The subchannel analysis code of the Super LWR is coupled with the fuel assembly burn-up calculation code for this purpose [25]. Fuel pin-wise power distributions are produced for various burn-ups, coolant densities, and control rod positions. The pin-wise power distributions are combined with the homogenized fuel assembly power distribution to reconstruct the pin-wise power distribution of the core fuel assembly. The power distribution over the fuel assembly is taken into account as shown in Fig. 1.11. The reconstructed pin-wise power distribution is used in the evaluation of peak cladding temperature with the subchannel analysis.

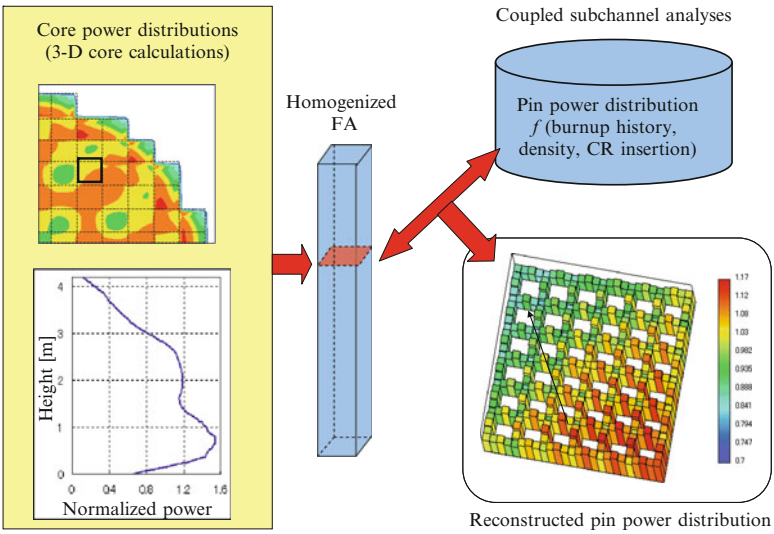


Fig. 1.11 Coupling of subchannel analysis with three-dimensional core calculation (Reconstruction of pin-wise power distribution for the subchannel analysis)

The maximum cladding temperature predicted by the subchannel analysis is higher than that predicted by single channel analysis which is used for the three-dimensional core calculation.

The thermal performance of a nuclear reactor core contains various engineering uncertainties which arise from calculation, measurement, instrumentation, fabrication, and data processing. A statistical method is developed and employed in the thermal design of the Super LWR to compensate for such uncertainties [26, 27].

The evaluation of peak cladding temperature is summarized in Fig. 1.12. The radial and local flux factors are evaluated separately, but further improvement was made. Incorporating subchannel analysis into the three-dimensional core coupled calculation, iterating the subchannel analysis with the core calculation rationalizes the evaluation of radial and local flux factors [28]. The nominal peak steady state temperature decreases 25°C from the value of the separate evaluation of Fig. 1.12.

Increasing the fuel rod spacing decreases the coolant velocity in the fuel channel, but the sensitivity of the maximum cladding temperature to the engineering uncertainties of the spacing decreases. The core with a 2-mm fuel rod spacing was designed for the two-pass core. It was 1 mm in the first two-pass core. The improved core design with the 2-mm fuel rod spacing was studied with rationalization of the core design method. The subchannel analysis was iterated with the three-dimensional core design. The local flux factor effect on cladding temperature was incorporated in the core design. The cladding temperature at the nominal peak steady state condition of the new core with 2-mm fuel rod spacing decreased 12°C, even if the average coolant flow rate in the fuel channel decreased 27%. The core

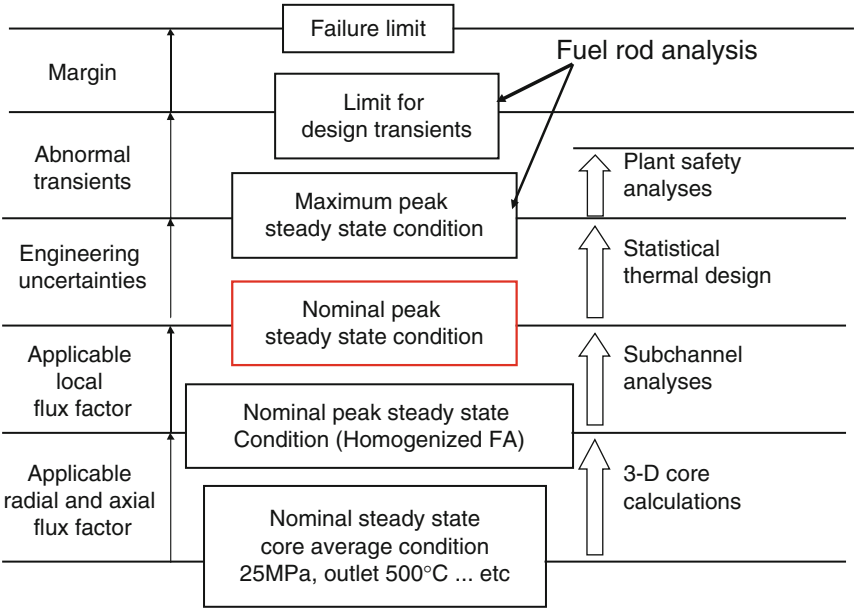


Fig. 1.12 Evaluation of peak cladding temperature

height was increased slightly from 4.2 m to 5 m not to decrease the coolant flow rare in the fuel channel substantially [28].

A correlation of the heat transfer coefficient of supercritical water is needed for the design work. The Oka–Koshizuka correlation was used for the early designs. But it is applicable to upward flow only. Watts–Chou correlation includes both upward flow and downward flow correlations. It was used for the core designs of the Super LWR and Super FR. But present correlations are based on experiments using smooth tubes. These experiments did not include the effect of fuel rod spacers on the heat transfer coefficient. Since supercritical fluid exhibits gas-like properties at high temperatures, nitrogen gas was used as the fluid and the effect of spacers was evaluated by measuring the turbulence due to the grid spacers at Kyushu University. The experiments were analyzed by a computational fluid dynamics (CFD) code. The effect of various geometries of grid spacers on the heat transfer coefficient in the downstream was derived. The cladding temperature was expected to decrease 20–30°C due to the effect of grid spacers [29].

1.3.5 Fuel Design

The fuel design of the Super LWR follows that of LWRs [30]. UO_2 is used for fuel pellets. Stainless steel and Ni-base alloy are the candidate cladding materials.

Its fuel rod design also follows that of LWRs. The failure modes of fuel rods considered are over-heating, pellet cladding mechanical interaction (PCMI), buckling collapse, and creep rupture at both normal and abnormal transients.

The four basic design criteria in the fuel rod design are as follows, for both normal and abnormal transients:

(a) Fuel rod failure by any of the four failure modes does not occur.
(b) Fuel rod centerline melting does not occur.
(c) The stress and pressure difference on the cladding are less than the maximum allowable values defined in the fuel rod failure modes.
(d) Internal pressure of the fuel rod does not exceed the normal operating coolant pressure (25 MPa).

PCMI is the limiting failure mode in LWRs, because the thermal expansion rate coefficient of the Zircaloy cladding is smaller than that of the UO_2 pellets. The criterion in LWRs is that the plastic deformation of the fuel rod is less than 1.0%. This criterion should be applied to the Super LWR fuel too. However, it is not likely to be limiting because the thermal expansion rate coefficients of the candidate cladding materials are likely to be greater than, or close to, that of UO_2 pellets. The MLHGR of 39 kW/m in the core design is determined from the rates of 44 kW/m of BWRs and 43.1 kW/m of PWRs so that the fuel centerline temperature and the fission gas release rate are about the same as in LWRs considering the high average reactor coolant temperature.

In LWRs, buckling collapse and creep rupture are not included in the design failure modes, because experimental verifications have shown that these failure modes are not limiting as long as the plastic deformation of the fuel rod is less than 1.0%. The core pressure and temperature of the Super LWR are much higher than those in LWRs, so these failure modes need to be included in the design failure modes. The evaluations of stresses on the cladding are based on ASME Boiler and Pressure Vessel Code Section III as adopted in BWRs for simplified evaluations.

In BWRs, all stresses (pressure difference, hydraulic vibrations, contact pressure of spacers, etc.) are first evaluated and categorized into primary membrane stress, primary bending stress, and secondary stress. The maximum allowable stresses are set for each of these categorized stresses at both normal and abnormal transients. The maximum allowable stresses in the Super LWR fuel rod design are determined similarly.

For the evaluation of stress rupture, the limiting criterion is to maintain the stress below one half of the tensile strength at abnormal transients. In LWRs, this is the limiting criterion in evaluating the maximum allowable stress on the cladding. In the Super LWR, the buckling collapse or creep rupture of the cladding can also be limiting depending on the cladding materials and its temperature.

The ratio of the gas plenum volume to the pellet volume is roughly the same as that in BWR fuel rods, 01. The gas plenum temperature is determined assuming it is placed at the top of the fuel rod and the temperature is equal to that of the outlet coolant.

The maximum allowable cladding temperature at abnormal transients is determined for the fuel rod design purpose. The relevant material properties of the cladding are used to determine the cladding thickness in the design. Exceeding the maximum cladding temperature does not mean that the cladding fails above the maximum design temperature.

The fuel rods are to be internally pressurized with helium gas as in BWRs and PWRs. The initial internal pressure of the fuel rods should be optimized to minimize the stresses and especially the pressure difference on the cladding. However, the internal pressure should not exceed the normal operating coolant pressure (25 MPa) to prevent any creep deformations that causes the gap between the pellet and cladding to increase. The four basic design criteria were determined to ensure the fuel integrity at all anticipated transients based on simple, but conservative evaluations [30].

However, such conservative criteria severely limited the plant operability during anticipated transients. In order to maximize the economical potential of the Super LWR and Super FR, and minimize the R & D efforts, the criteria were rationalized based on detailed fuel analyses. The FEMAXI-6 code [31] for LWR fuel analyses was used for the study. The principle of rationalization of the criteria for anticipated transients of Super LWR was developed [32, 33]. The design and integrity analysis of the Super LWR fuel rods is summarized in ref. [34].

An example of fuel assembly design of the Super LWR is shown in Fig. 1.13 [35]. An example Super LWR core and fuel characteristics are given in Table 1.4 [24]. The core coolant flow rate of the Super LWR is substantially lower than that of LWRs due to the high enthalpy rise in the core. The gap between fuel

Design requirements →	Solution
Low flow rate per unit power (< 1/8 of LWR) due to large ⊿T of once-through system	Narrow gap between fuel rods to keep high mass flux
Thermal spectrum core	Many/Large water rods
Moderator temperature below pseudo-critical	Insulation of water rod wall
Reduction of thermal stress in water rod wall	
Uniform moderation	Uniform fuel rod arrangement

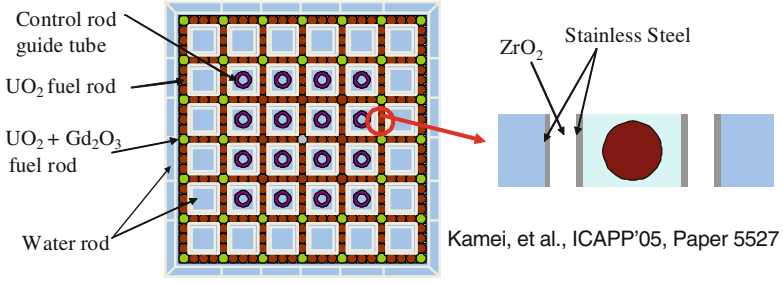


Fig. 1.13 Example of fuel assembly design of Super LWR

Table 1.4 Example of Super LWR core and fuel characteristics

Core pressure (MPa)	25
Thermal/Electrical power (MW)	2,744/1,200
Coolant inlet/outlet temperature (°C)	280/500
Thermal efficiency (%)	43.8
Core flow rate (kg/s)	1,418
Number of all fuel assemblies/fuel assemblies with descending-flow cooling	121/48
Fuel enrichment bottom/top/average (wt%)	6.2/5.9/6.11
Active height/equivalent diameter (m)	4.2/3.73
Fuel assembly average discharge burn-up (GWd/t)	45
MLHGR/ALHGR	38.9/18.0
Average power density (kW/l)	59.9
Fuel rod diameter/Cladding thickness [material] (mm)	10.2/0.63 [Stainless Steel]
Fuel assembly structure thickness [material] (mm)	0.2 [Stainless Steel]
Thermal insulation thickness [material] (mm)	2.0 [ZrO_2]

Taken from ref. [24] and used with permission from Atomic Energy Society of Japan

rods should be small to keep the high mass flux. The coolant density in the upper part of the core is low. Moderation is provided by introducing large square water rods. Single-array fuel rods are surrounded by the water rods for achieving uniform moderation. There are two fuel enrichments, 5.9% and 6.2%. Further flattening of pin power distribution will be possible by increasing the number of enrichments.

A thin thermal insulation of Zirconia is provided between the water rods and fuel coolant channels. Gadolinia is used for compensating burn-up reactivity and axial power flattening. The control rods are the cluster rod type. The control elements are inserted in the guide tubes that are located in the central water rods.

The water rods are supplied with the water from the top dome of the RPV through the control guide tubes. Descending flow in the water rods is employed. The moderator is mixed with the reactor coolant through the downcomer in the lower plenum of the RPV. This design concept is good for keeping the average reactor outlet coolant temperature high and the axial power distribution uniform.

1.3.6 Plant Control

The plant control system has been designed in a similar way to that of BWRs [36–39]. It is shown in Fig. 1.14. The plant transient analysis code SPRAT-DOWN was developed and used in the design work. The node-junction model, shown in Fig. 1.15, contains the RPV, the control rods (CRs), the main feedwater pumps, the turbine control valves, the main feedwater lines, and the main steam lines. The characteristics of the turbine control valves and the changes of the feedwater flow rate according to the core pressure are given in the calculation.

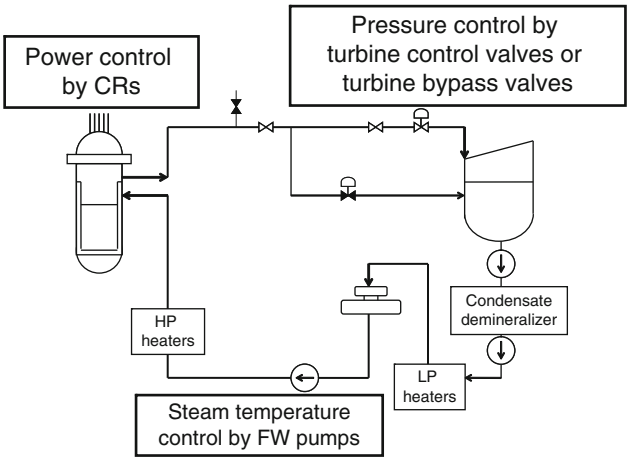


Fig. 1.14 Plant control system of the Super LWR

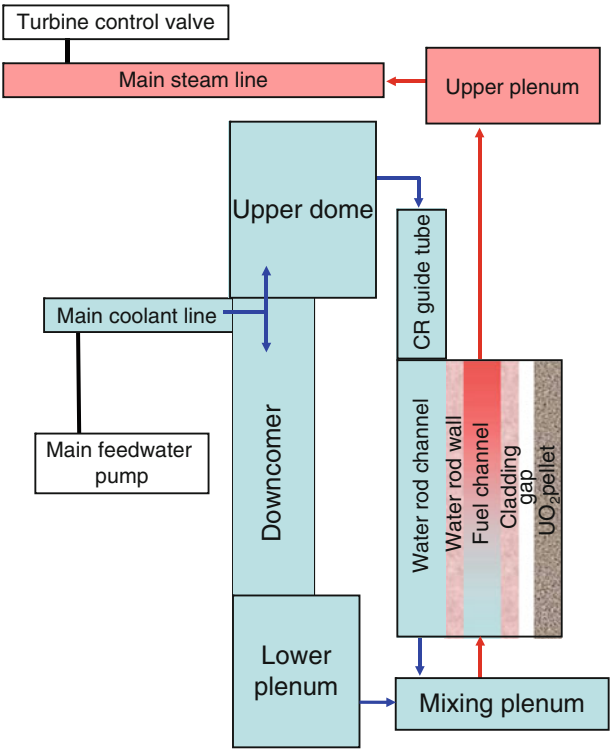


Fig. 1.15 Node junction model of transient analysis code SPRAT-DOWN

First, the step responses without the plant control system are analyzed. The major perturbations are:

1. Increase in the reactivity by \$0.1 resulting from withdrawal of a control rod cluster.
2. Decrease in the feedwater flow rate by 5%.
3. Decrease in the main steam flow rate by 5% resulting from closure of the turbine control valves.

The core power of the Super LWR was found not to be sensitive to the feedwater flow rate due to the existence of many water rods.

According to the calculated step responses, the pressure is sensitive to the turbine control valve opening and the feedwater flow rate. The main steam temperature is sensitive to the control rod position and the feedwater flow rate. Therefore the turbine inlet pressure is controlled by the turbine control valves. The main steam temperature is controlled by the feedwater pumps. The core power is controlled by the control rods.

The plant control system should be designed so that it does not generate divergent or continuous oscillations that exceed the permissible range. The criteria are as follows:

1. Damping ratio is less than 0.25. This is most generally used as the criterion for control quality and is applied to existing FPPs.
2. Over shoot is less than 15%.

The plant control system is designed based on the proportional, integral, and differential (PID) control principle (see Sect. 4.4). The reactor behavior has been analyzed against various perturbations with the designed and optimized plant control system.

BWRs have an inverse response of reactor power to the turbine load. When the electricity demand and the turbine load increase, the turbines consume more steam. This decreases the reactor pressure and increases the average void fraction of the core. The reactor power decreases due to the negative void reactivity effect. Then BWRs are operated as turbine-following-reactor control strategy. PWRs have normal response of reactor power to the turbine load. When the electricity demand and consumption of steam increase in the turbine, more heat is removed in the steam generators. The coolant temperature of the primary loop and the reactor inlet coolant temperature decrease. This increases reactor power due to the negative coolant temperature coefficient. Then PWRs are operated as reactor-following-turbine control. The Super LWR is like BWRs because of the direct cycle and it is operated as the turbine-following-reactor control strategy.

FPPs adopt turbine-boiler-coordination control. The ratio of the boiler (fuel) input and the feedwater flow rate is used for the control parameter of the feedwater pumps. The plant control strategies of BWRs, PWRs, FPPs, and the Super LWR are compared in Table 1.5.

Table 1.5 Comparison of plant control strategies

	Control strategy	Control method		
		Electric power	Steam pressure	Reactor or boiler power
Super LWR	Turbine following reactor	Reactor power	Turbine control valves	Control rods
BWR	Turbine following reactor	Reactor power	Turbine control valves	Control rods, recirculation pumps
PWR	Reactor following turbine	Turbine control valves	Reactor power	Control rods
FPP	Boiler turbine coordinated	Turbine control valves, boiler input		

The turbine-boiler coordination control using the power to feedwater flow rate ratio was studied for the control of the Super FR and good performance was predicted to be obtained [40].

1.3.7 Startup Schemes

There are two types of supercritical FPPs. One is the constant pressure FPP that starts heating and operates at partial load at the supercritical pressure. The other is the sliding pressure FPP that starts heating at a subcritical pressure, and operates at subcritical pressure at partial load. A steam-water separator and a drain tank are needed for the startup of the sliding pressure FPP. The sliding pressure FPP operates with better thermal efficiency at subcritical pressure at partial load than the constant pressure FPP. In Japan, nuclear power plants are used for base load, and the FPPs are used for daily load following. Minimum partial load is 30% for the constant pressure FPP and 25% for the sliding pressure one [41, 42].

Startup schemes of the Super LWR are considered by referring to those of supercritical FPPs [43–45]. The constant pressure startup systems of the Super LWR and a supercritical FPP are shown in Fig. 1.16 [41]. The register tube and flash tank are installed on the bypass line. The supercritical steam is depressurized at the register tube and used for heating up the turbine during the startup (Table 1.6).

The sliding pressure startup systems of the Super LWR and a supercritical FPP are shown in Fig. 1.17 [41]. A steam-water separator is installed on the bypass line for the Super LWR, while it is installed on the main steam line for the supercritical FPP. The Super LWR has an additional heater installed to recover heat from the drain of the steam-water separator. When the enthalpy is low, the drain is dumped into the condenser directly. A boiler circulation pump can be used instead of the additional heater the same as in the sliding pressure FPP.

The thermal criteria for startup of the Super LWR are summarized in Table 1.9. The maximum cladding temperature during the power raising phase is limited below the same value as the rated power. The moisture content of steam sent to

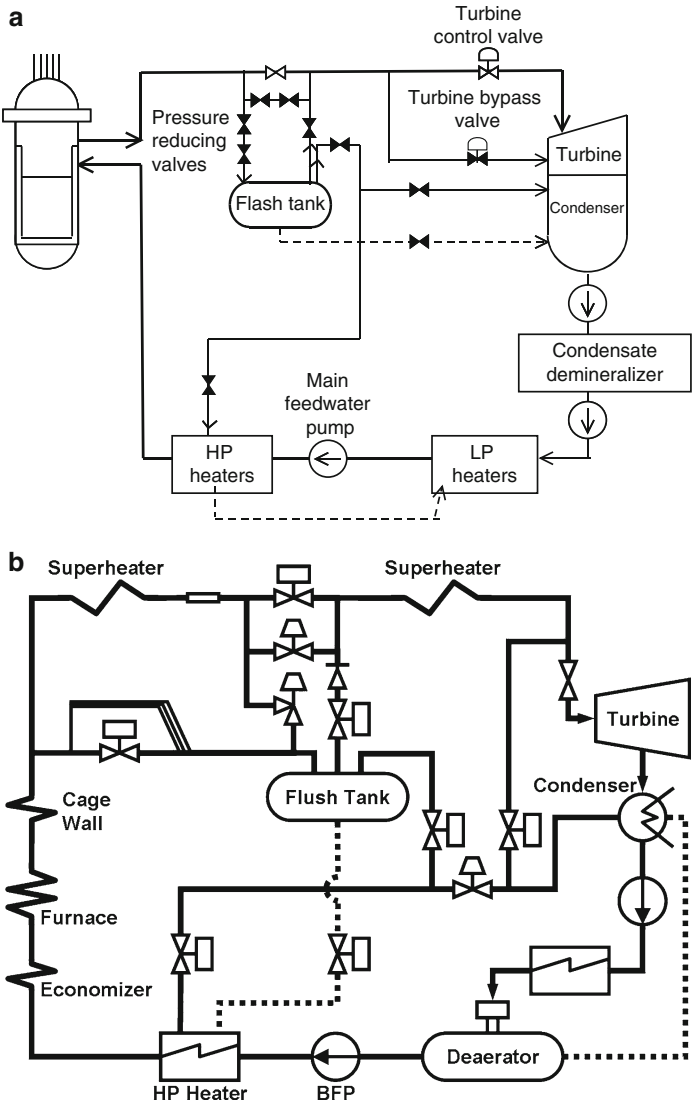


Fig. 1.16 Constant pressure startup systems of the Super LWR and supercritical FPP. (a) Super LWR (b) Supercritical FPP

Table 1.6 Thermal criteria for startup of Super LWR

Maximum cladding surface temperature must be the same as the rated power limit.
Moisture content in the turbine inlet must be less that 0.1% (the same criterion as BWR)
The enthalpy of the core outlet coolant must be high enough to provide the required turbine inlet steam enthalpy.
Boiling (and dryout) must be prevented in the water rods at subcritical pressures (in sliding pressure startup scheme).

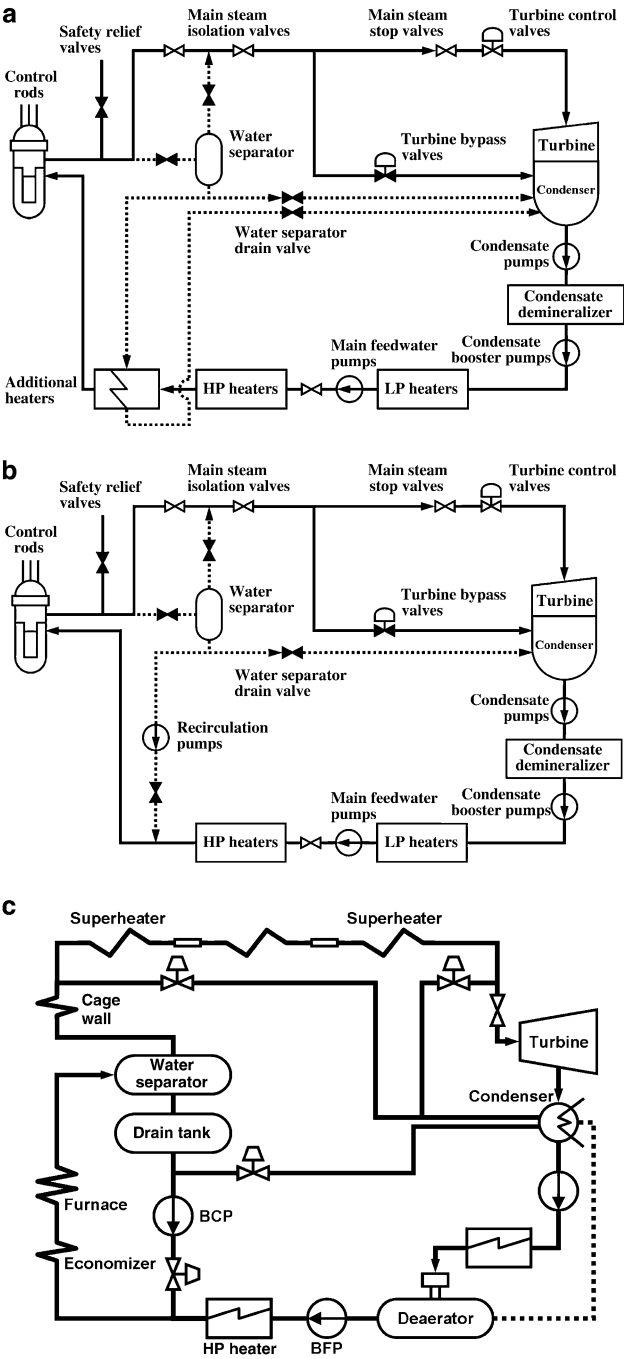


Fig. 1.17 Sliding pressure startup systems of the Super LWR and supercritical FPP. (a) Super LWR with additional heaters [41] (b) Super LWR with recirculation pumps [41]. (c) Supercritical FPP. (Taken from ref. [41] and used with permission from American Nuclear Society)

the turbine should be low enough not to damage the turbine blades at startup. The wetness in steam should be less than 0.1% at turbine startup, which is consistent with that of BWRs.

The third criterion states the enthalpy of the core outlet coolant must be high enough to provide the required turbine inlet steam enthalpy. Boiling must be prevented in the water rods at subcritical pressure of the sliding pressure startup scheme.

The calculation model for sliding pressure startup of the Super LWR is shown in Fig. 1.18 [43]. Examples of the sliding pressure startup curves based on the thermal considerations are shown in Fig. 1.19 [43].

With sliding pressure startup, the reactor starts up at a subcritical pressure and the pressure increases with the load. A steam-water separator and a drain tank are needed for two-phase flow. The heat loss is less than that of the constant pressure operation. At the reactor outlet, coolant evaporation is almost completed. Dryout inevitably occurs in the core at subcritical pressure in the once-through plant. The strategy for protection of furnaces in the once-through boilers is to keep the wall temperature in the post-dryout region below an adequate value by having a sufficient feedwater flow rate. To reduce the volume of the separator, it is also desirable for the core to be pressurized to a supercritical pressure with a low flow rate and a low power. The minimum feedwater flow rate is determined from the viewpoints of stability, core cooling, and pump performance. The cladding temperature can be calculated for a certain feedwater flow rate with various core powers. The reactor is pressurized to supercritical at 35% feedwater flow rate and 20% core power.

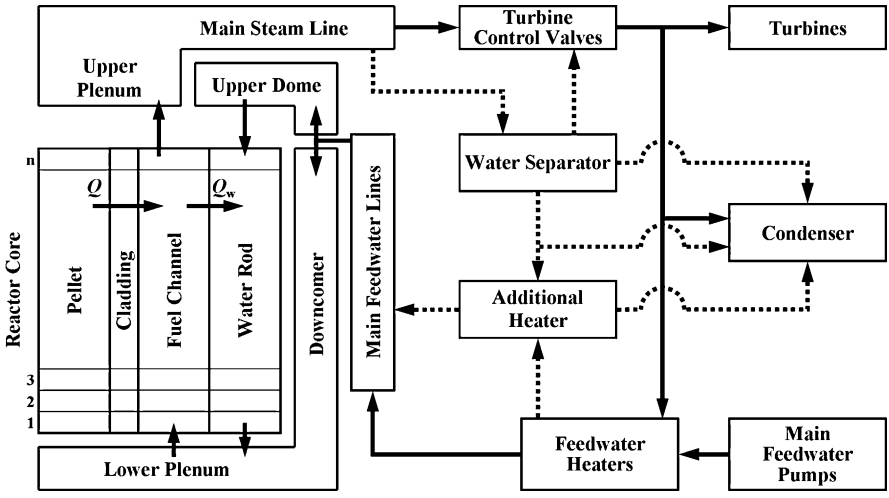


Fig. 1.18 Calculation model for sliding pressure startup scheme. (Taken from ref. [43] and used with permission from Atomic Energy Society of Japan)

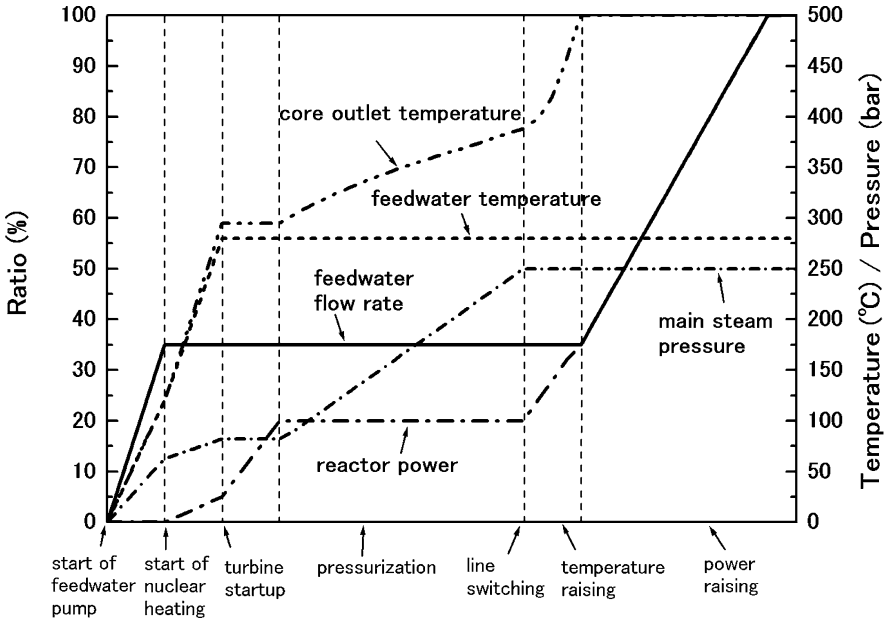


Fig. 1.19 Sliding pressure startup curves based on thermal considerations. (Taken from ref. [43] and used with permission from Atomic Energy Society of Japan)

After setting the feedwater flow rate at 35%, nuclear heating starts at a subcritical pressure. When the pressure of the core reaches an adequate value, saturated steam from the separator flows to the turbines. After startup of the turbines, the core is pressurized to a supercritical pressure with a core power at 20%. Startup operation ends and the plant is switched to the normal operation mode. The reactor power increases with the feedwater flow rate.

The sizes of the components required for the startup schemes are assessed. The sliding pressure startup with a steam separator in a bypass line is the best from the viewpoint of weight of the components. A study of the times needed for the startup schemes remains as future work. There is a limitation on the rate due to thermal stresses on thick-walled components such as the RPV. In BWRs, the temperature rise rate of the RPV wall is limited to below 55°C per hour.

The minimum allowable power and the minimum required power during the pressurization phase in the sliding pressure startup scheme are depicted in Fig. 1.20. The reactor power should be kept within narrow ranges at the pressure range between 20 and 22 MPa where boiling transition occurs. The MCST becomes high in this pressure range due to dryout as shown in Fig. 1.21 [43, 44]. But it is maintained below the limit of the rated value of the cladding temperature.

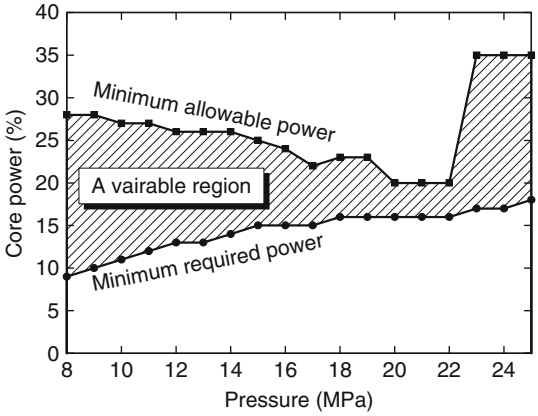


Fig. 1.20 Maximum allowable power and minimum required power during pressurization phase with feedwater flow rate of 35% and feedwater temperature of 280°C

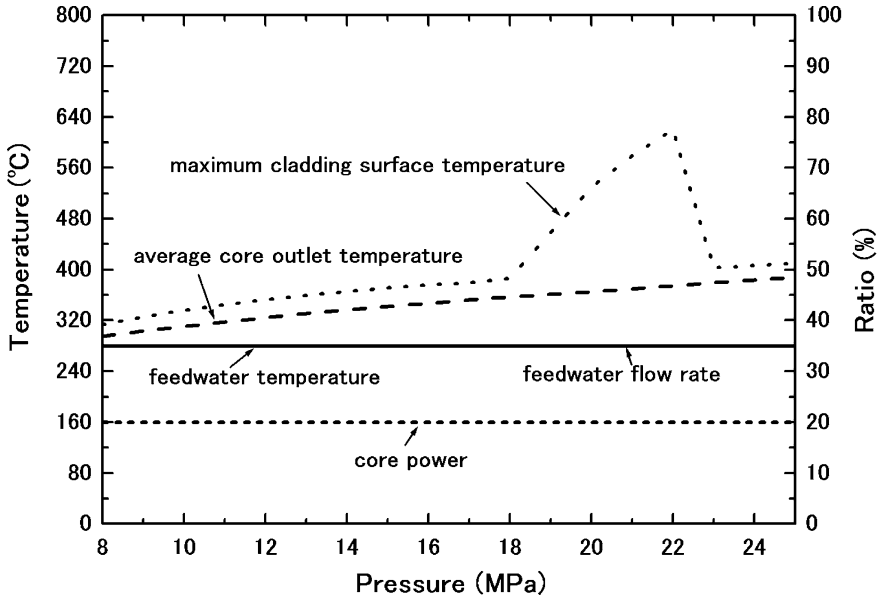


Fig. 1.21 Plant parameters in pressurization phase. (Taken from ref. [43] and used with permission from Atomic Energy Society of Japan)

The present analysis is based on the heat transfer correlations for smooth tubes. When turbulence is promoted, the cladding temperature rise at dryout will be suppressed. The maximum allowable power between 20 and 22 MPa will increase. Ribbed or rifled tubes and spiral tapes are used in supercritical FPPs to suppress the boiling transition during the sliding pressure operation and the sliding pressure

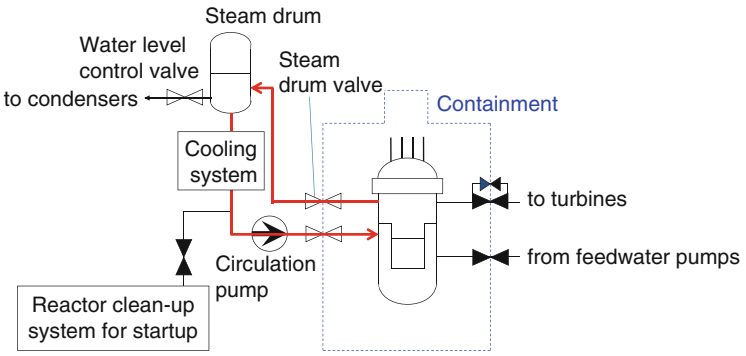


Fig. 1.22 Revised sliding pressure startup system of the Super LWR and the Super FR

startup. The critical heat flux correlations should be improved, including the effect of grid-spacers on the boiling transition.

Further elaboration of the startup considerations was made [46]. The turbines of the Super LWR and the Super FR and their startup will be similar to or the same as for of FPPs where the turbines are warmed and started using subcritical pressure superheated steam generated by superheaters. However, the Super LWR and the Super FR have no superheater and it is difficult to generate superheated steam in the core due to concern about fuel damage by dryout. A startup loop with a pump and a steam drum is used instead of the additional heater. This revised startup system is shown in Fig. 1.22. The Super LWR and Super FR adopt the once-through coolant cycle like FPPs without a circulation loop. Since it is difficult to raise the pressure and temperature in the once-through cycle, however, a circulation loop, just for startup, is added to the Super LWR and the Super FR plant (cf. the FPP shown as Fig. 1.17). Since the Super LWR and Super FR have no pressurizer heater, nuclear heating is chosen for raising the pressure and temperature in the loop. The circulation loop for startup consists of the reactor, the steam drum, the heat exchanger ("cooling system"), the circulation pump, and the piping. The roles of each component are described in Sect. 5.7. Startup of the Super FR is analyzed and the startup curves are shown in Fig. 1.23. The startup curves of the Super LWR will be obtained in the same way as that of the Super FR.

1.3.8 Stability

Instability is a nonlinear phenomenon. However, the dynamic behavior of nuclear reactors can be assumed to be linear for small perturbations around steady-state conditions. This allows the reactor stability to be studied and the threshold of instability in nuclear reactors to be predicted by using a linear model and solving linearized equations. Linear stability analyses in the frequency domain have been

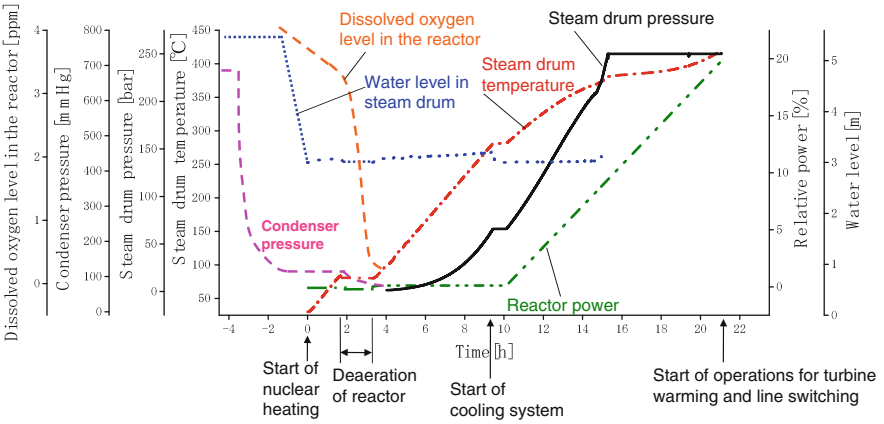


Fig. 1.23 Redesigned curves of sliding pressure startup before the power raising phase

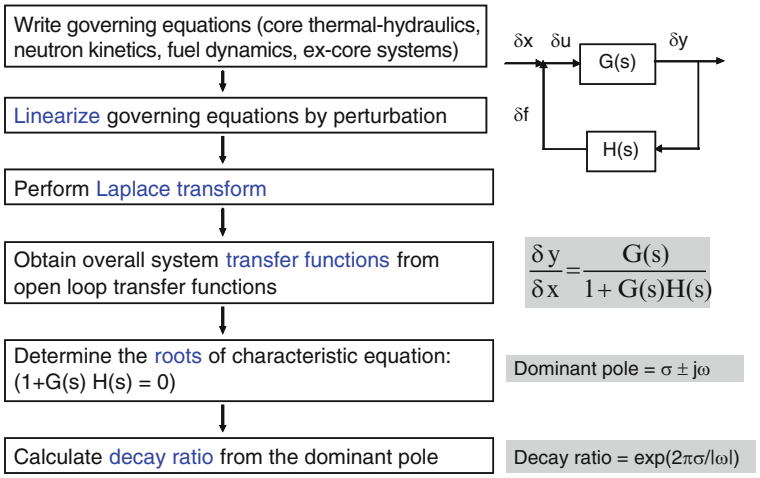


Fig. 1.24 Procedure for frequency domain linear stability analysis

made [44, 47–51]. Thermal-hydraulic stability, coupled neutronic and thermal-hydraulic stability and the stabilities during sliding pressure startup at subcritical pressure of Super LWR were analyzed [44, 47–50]. The thermal-hydraulic stability of the Super FR was also analyzed [51]. The present stability analysis code was developed by using a linearized one-dimensional, single-channel, and single-phase model. It is known from the parallel channel stability analysis of BWRs that the single-channel stability analysis is sufficient if the upper plenum and lower plenum are large [52, 53].

The procedure for the linear stability analysis is shown in Fig. 1.24. In the linear stability analysis, the governing equations are first perturbed around the steady-state

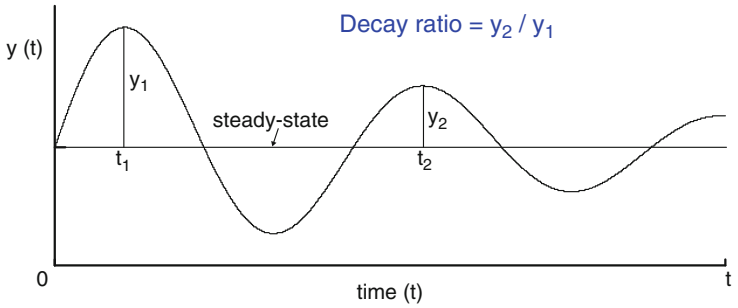
parameters. The perturbed equations are then linearized and Laplace transformed from the time domain to the frequency domain. The resulting equations are used to evaluate various system transfer functions by applying proper boundary conditions. After all the required transfer functions are derived, the individual transfer functions are combined to provide the overall system transfer functions. The frequency response and stability characteristics of the Super LWR are studied with respect to small perturbations in system parameters such as inlet flow velocity, inlet coolant pressure, etc.

The linearized and Laplace-transformed equations of the models are used to evaluate the various system transfer functions as functions of the Laplace variables $s = \sigma + j\omega$, where σ is the real part and ω is the imaginary part of the complex variable s. σ refers to the damping constant (or damped exponential frequency) and ω refers to the resonant oscillation frequency of the system. The forward transfer function and feedback transfer function of the system are represented by $G(s)$ and $H(s)$, respectively. The closed loop transfer function or system transfer function is obtained from $G(s)$ and $H(s)$. The poles of the closed loop transfer function are determined by solving the characteristic equation: $1+ G(s)\, H(s) = 0$. The poles may be real and/or complex conjugate pairs. For systems with more than one pole, the pole which has the slowest response is dominant over other poles after some time. For stable systems, the dominant pole is the pole nearest to the imaginary axis (the pole with the largest value of σ/ω) and it is used to determine the stability of the system. The stability of the system depends on the value of σ. For the system to be stable, all the poles of the closed loop transfer function must have negative real parts ($\sigma < 0$). The system becomes unstable if a pole crosses the imaginary axis and enters into the right half of the s-plane ($\sigma > 0$). The system will be on the margin of stability and will sustain an oscillation without damping if the pole lies on the imaginary axis ($\sigma = 0$).

The system stability is described by the decay ratio, which is defined as the ratio of two consecutive peaks of the impulse response of the oscillating variable as shown as Fig. 1.25. For the complex pole $s = \sigma + j\omega$, the impulse response of the system is represented by $Ke^{\sigma t}(\cos\omega t + j\ \sin\omega t)$ where K is a constant. Hence, if the positions of the complex poles of the closed loop transfer function are known, the decay ratio DR can be calculated by using the following equation:

$$\text{Decay ratio} = \text{DR} = \frac{y_2}{y_1} = \frac{\left|Ke^{\sigma t_2}(\cos\omega t_2 + j\sin\omega t_2)\right|}{\left|Ke^{\sigma t_1}(\cos\omega t_1 + j\sin\omega t_1)\right|} = e^{\sigma(t_2 - t_1)} = e^{2\pi\sigma/\omega} \quad (1.1)$$

The axial mesh size has a significant effect on the decay ratio and the frequency response just as it does for LWR stability analysis. The decay ratio generally increases as the axial mesh size decreases. The decay ratio is determined by extrapolation to zero mesh size using the method of least squares.



Stability Criteria

	Normal operating conditions	All operating conditions
Thermal-hydraulic stability	Decay ratio ≤ 0.5 (damping ratio ≥ 0.11)	Decay ratio <1.0 (damping ratio > 0)
Coupled neutronic thermal-hydraulic stability	Decay ratio ≤ 0.25 (damping ratio ≥ 0.22)	Decay ratio < 1.0 (damping ratio > 0)

The same stability criteria as BWR

Fig. 1.25 Definitions of the decay ratio and stability criteria

The stability criteria of the decay ratio are taken to be the same as those of BWRs as shown in Fig. 1.25.

(a) The decay ratio of thermal-hydraulic stability should be less than 0.5 for normal operating conditions and that of coupled stability should be less than 0.25.
(b) The decay ratio must be less than 1.0 for all operating conditions.

The decay ratios of the thermal-hydraulic stability of the hottest channel and the average channel are obtained as shown in Fig. 1.26.

The relation between the decay ratios and orifice pressure drop coefficients is shown in Fig. 1.27. The reactor becomes more stable when the orifice pressure drop coefficient increases as is also known for BWRs. It can be seen that the thermal-hydraulic stability criterion is satisfied in the Super LWR at full power normal operation for the average power channel. The maximum power channel can be stabilized by applying a proper orifice pressure drop coefficient. The minimum orifice pressure drop coefficient required for thermal-hydraulic stability at full power operation is found to be 6.18 (a pressure drop of 0.0054 MPa). The total core pressure drop at 100% maximum power operation is 0.133 MPa. The required orifice pressure drop is small compared with the total core pressure drop.

The block diagram used for coupled neutronic and thermal-hydraulic stability of the Super LWR is shown in Fig. 1.28. The neutronic model is used to find the forward transfer function $G(s)$ and the thermal-hydraulic heat transfer and ex-core models are used to determine the backward transfer function $H(s)$. The frequency

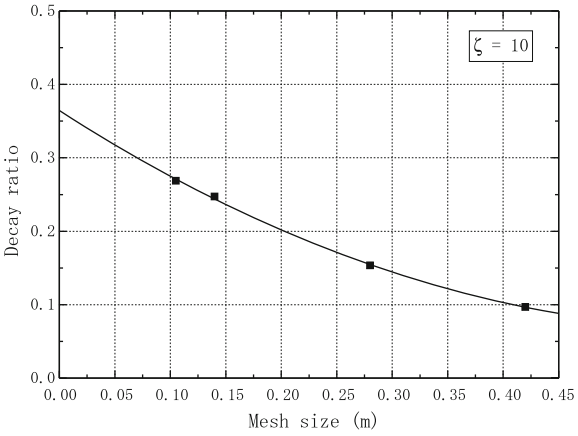


Fig. 1.26 Effect of axial mesh size on decay ratio. (Taken from ref. [49] and used with permission from Atomic Energy Society of Japan)

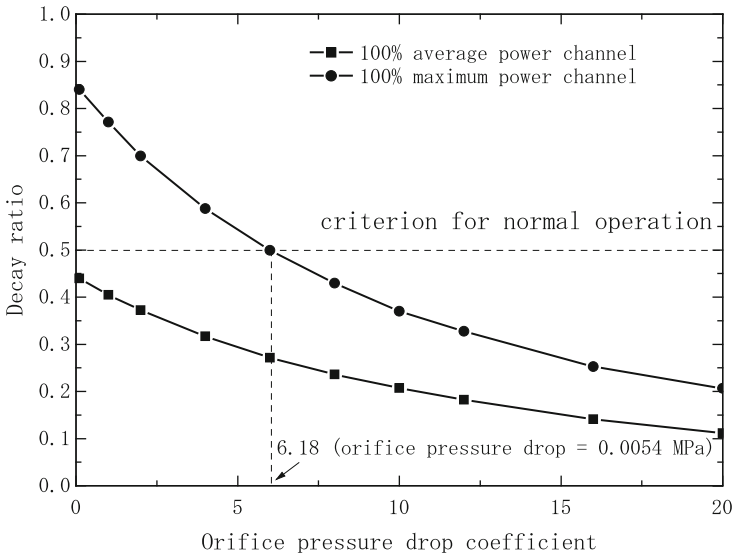


Fig. 1.27 Orifice pressure drop coefficient versus decay ratio of thermal-hydraulic stability at full power operation. (Taken from ref. [49] and used with permission from Atomic Energy Society of Japan)

response of the closed loop transfer function for coupled neutronic and thermal-hydraulic stability of the Super LWR for the 100% average power channel is shown in Figs. 1.29 and 1.30. The presence of water rods clearly increases the resonant peak and the phase lag of the closed loop transfer function due to the destabilizing effects of neutronic feedback.

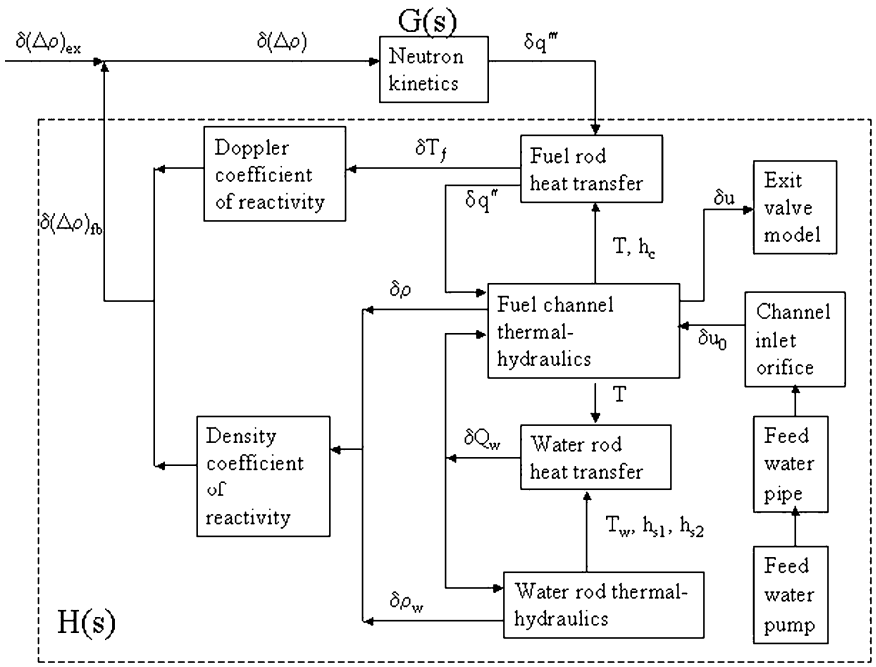


Fig. 1.28 Block diagram for coupled neutronic thermal-hydraulic stability of the Super LWR. (Taken from ref. [50] and used with permission from Atomic Energy Society of Japan)

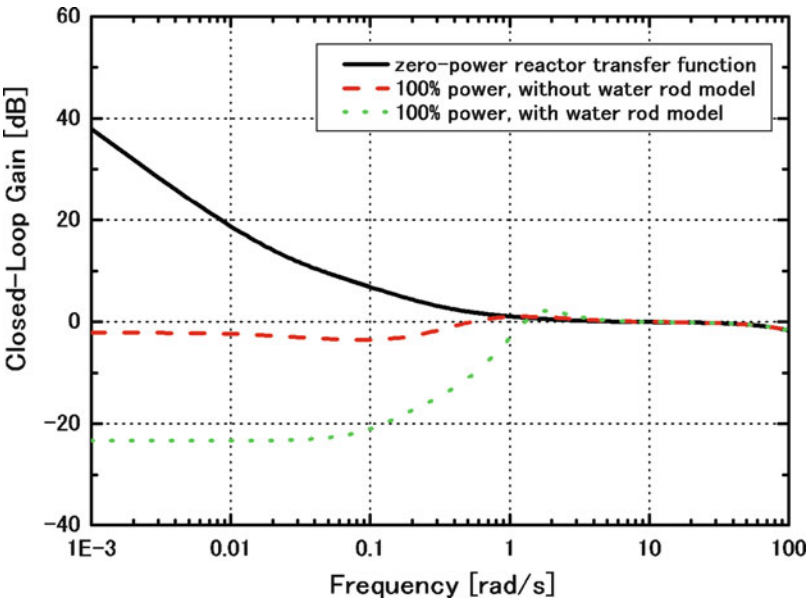


Fig. 1.29 Gain response of closed loop transfer function of coupled neutronic thermal-hydraulic stability

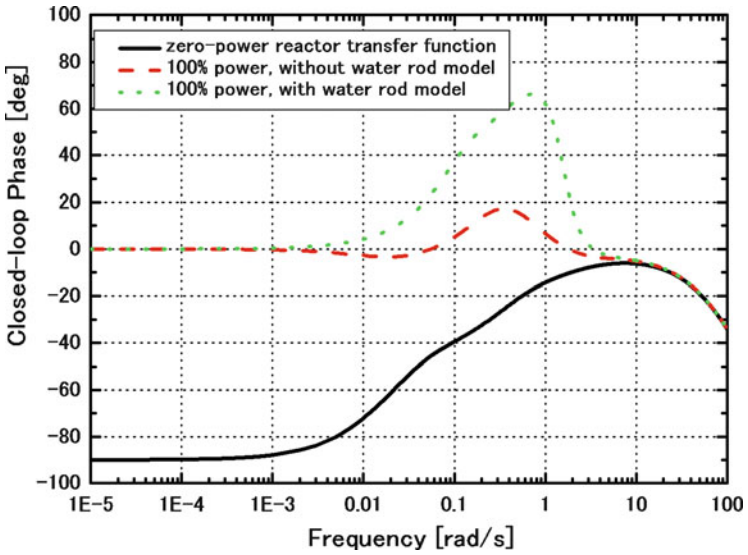


Fig. 1.30 Phase response of closed loop transfer function of coupled neutronic thermal-hydraulic stability

The time delay of the heat transfer to the coolant and moderator water is an important factor in the mechanism of coupled neutronic and thermal-hydraulic instability. The Super LWR is a reactor system with a positive density coefficient of reactivity and a large time delay constant. If there is no time delay, a decrease in density would cause a decrease in power generation, which suppresses any further decrease in density, stabilizing the system. However, if there is a large time delay, it causes a decrease in the gain of the density reactivity transfer function, and reduces the effect of density reactivity feedback, making the system less stable. The time delay of the heat transfer to the water rods is much larger than that to the coolant. Thus the reactor system becomes less stable when the water rod model is included than the case without it.

Figure 1.31 shows the decay ratio contour map for coupled neutronic and thermal-hydraulic stability of the Super LWR. The decay ratio contour line of DR = 1.0 indicates the stability boundary on the power versus flow rate map of the Super LWR. At the high power low flow rate region, the reactor becomes unstable. At low power operation and during startup, it is necessary to take care to satisfy the stability criteria. At the low power low flow rate region, the unstable conditions should be avoided by carefully adjusting the flow rate.

In summary, the following points are obtained regarding stability of the Super LWR.

1. In spite of the low flow rate and large coolant density change, the thermal-hydraulic stability of the Super LWR can be maintained by a sufficient orifice pressure drop coefficient.

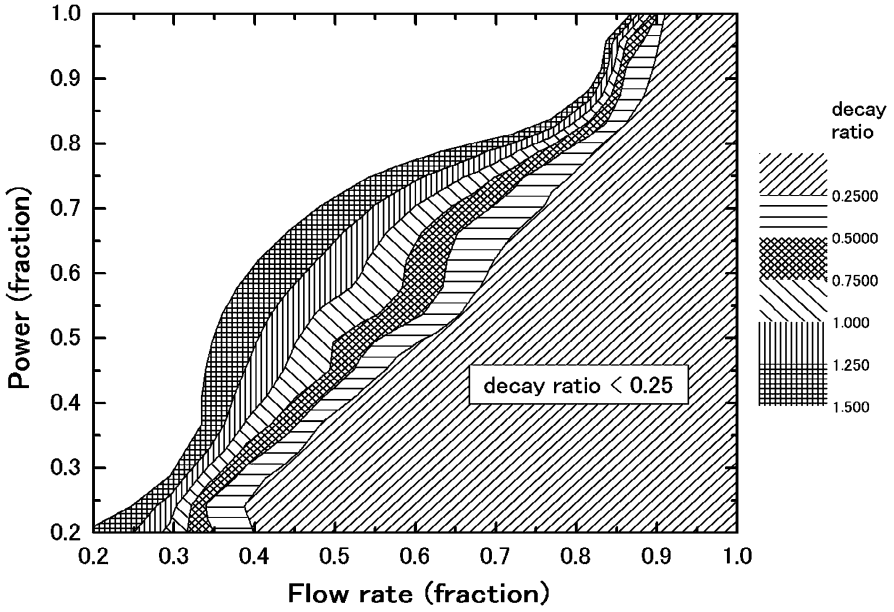


Fig. 1.31 Decay ratio map for coupled neutronic and thermal-hydraulic stability of the Super LWR

2. The presence of water rods reduces the density reactivity feedback effect due to the large time delay in the heat transfer to the water rods, and this affects the coupled neutronic and thermal-hydraulic stability.
3. The coupled neutronic and thermal-hydraulic stability of the Super LWR can be maintained by controlling the power to flow rate ratio.

Stability during sliding pressure startup was analyzed [44]. The changes of decay ratio and flow rate with core power during the power raising phase are shown in Fig. 1.32. A high flow rate is necessary at low core power. Figure 1.33 shows the sliding pressure startup curves with the stability criteria. High flow rate is required after line switching compared with the startup curves without the stability criteria.

In summary, at the subcritical pressure operation during the pressurization phase, thermal criteria are more limiting due to dryout. The startup scheme prior to line switching is mainly determined by thermal criteria. The thermal-hydraulic stability criterion is satisfied by applying a sufficient orifice pressure drop coefficient. The coupled neutronic and thermal-hydraulic stability is also satisfied, since the power to flow rate ratio is low during this phase.

In the power raising phase, the thermal criteria are not as limiting as stability criteria, because the coolant flow is a single phase one at supercritical pressure operation. If only thermal criteria are considered, the power to flow rate ratio in the power raising phase can be kept as one, and the MCST can be maintained so it does not exceed the rated value. However, if stability considerations are also taken into

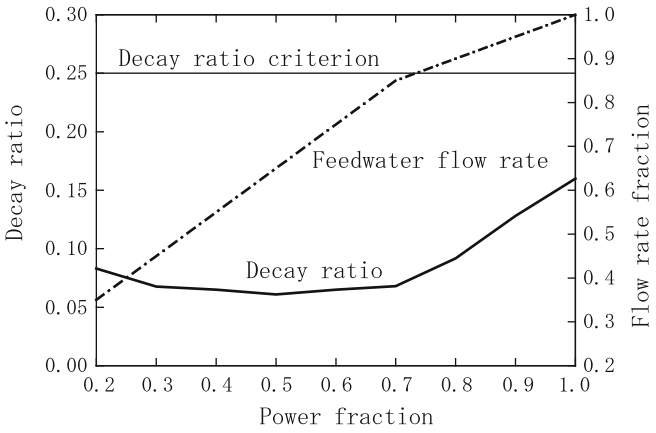


Fig. 1.32 Coupled neutronic thermal-hydraulic stability analysis result at power increase phase

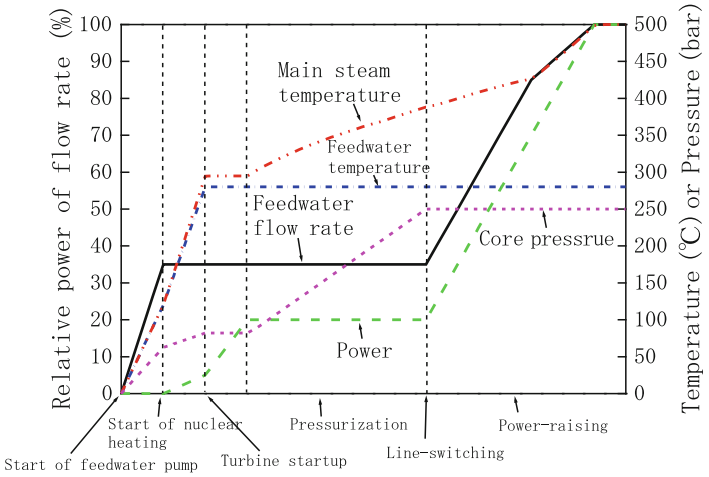


Fig. 1.33 Sliding pressure startup curve with thermal and stability considerations

account, while the thermal-hydraulic stability criterion can be satisfied with an orifice pressure drop coefficient, the power to flow rate ratio needs to be reduced at low-power operations to satisfy the coupled neutronic and thermal-hydraulic stability criterion. The power and flow rate are to be controlled as required during this phase. Thus, the startup procedure after line switching is determined and limited by stability criteria, more than it is by thermal criteria.

Stability is maintained by increasing orifice pressure drop in the design. The pumping power increases with the total pressure drop, but it is not a problem in the once-through cycle reactor. The pump is powerful and pumping power is not excessive because of the small reactor coolant flow rate.

1.3.9 Safety

1.3.9.1 Safety Principle

The unique advantage of the once-through cooling system is that depressurization cools the core effectively [54–56]. The coolant flow during depressurization is shown in Fig. 1.34 [56]. Actuating the automatic depressurization system (ADS) induces core coolant flow. The downward flow water rod system enhances this effect because low temperature water in the top dome and in the water rods flows through the core to the ADS. An example of depressurization behavior is shown in Fig. 1.35 [56]. The core coolant flow rate is maintained during depressurization even though the feedwater flow is lost. Due to the downward-flow water rod system, the coolant flowing to the core during depressurization is not only from the bottom dome and the downcomer but also from the top dome and the water rods. The top dome serves as an "in-vessel accumulator". The core coolant flow rate changes with the ADS flow rate, which oscillates due to the change of the pressure, temperature, and the steam quality. The reactor power increases immediately after the ADS actuation due to the increased flow rate and then decreases due to boiling and the reactor scram. The hottest cladding temperature does not increase from the initial value because the power to flow rate ratio is kept above unity. After the depressurization, the decay heat is removed by the low pressure core injection system (LPCI).

LWRs have a coolant circulation system such as the recirculation system of BWRs and the primary coolant system of PWRs. The fundamental safety requirement for LWRs is keeping the coolant inventory so as to maintain core cooling by

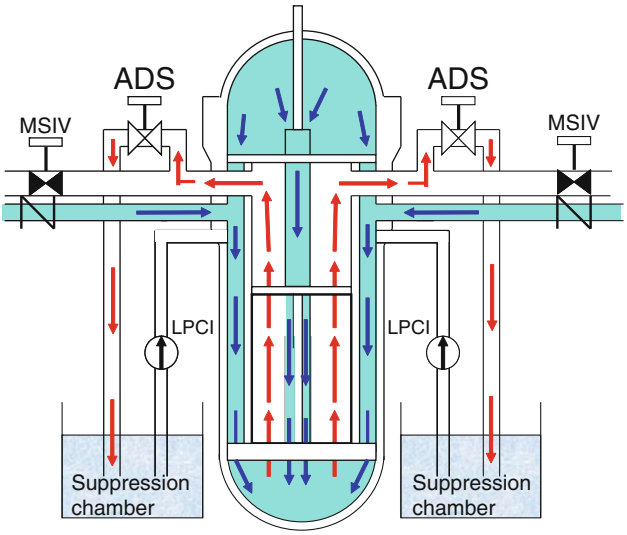


Fig. 1.34 Coolant flow during reactor depressurization. (Taken from ref. [56] and used with permission from Korean Nuclear Society)

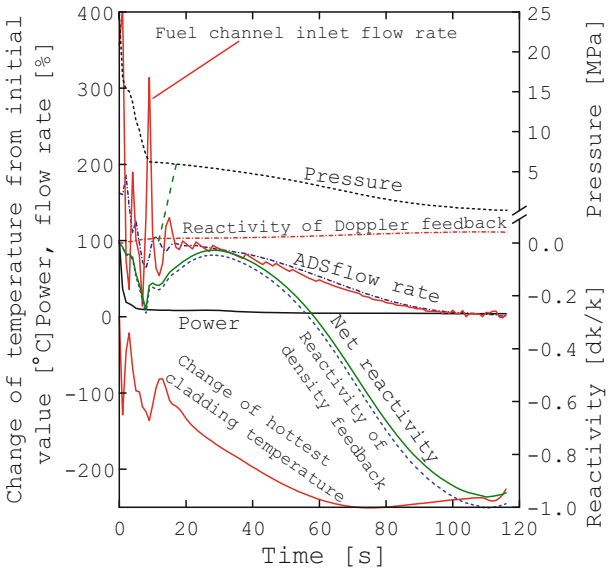


Fig. 1.35 Behavior during reactor depressurization. (Taken from ref. [56] and used with permission from Korean Nuclear Society)

either forced circulation or natural circulation. Coolant inventory is kept by maintaining the water level in the RPV of a BWR and the pressurizer of a PWR. It is monitored and used for the fundamental safety signal of LWRs.

The once-through cooling system has no coolant circulation system and there is no water level during supercritical pressure operation. The depressurization behavior described above indicates that a decrease in the coolant inventory does not threaten the safety of the once-through cooling system as long as the core coolant flow rate is maintained. Inventory control is not necessary for the Super LWR and Super FR. The fundamental safety requirement of the Super LWR is maintaining the core coolant flow rate. Since the once-through cooling system has both coolant inlet and outlet, the core coolant flow rate is kept by "keeping the coolant supply from the cold-leg" and "keeping the coolant outlet open at the hot-leg" [54–64].

"Loss of feedwater flow" is the same as "loss of reactor coolant flow" for the once-through cooling Super LWR and Super FR. BWRs have a recirculation system and there is large coolant inventory in the RPV. PWRs have the secondary system as well as the primary system and there is a large coolant inventory in the steam generators. Therefore, the feedwater is more important for the Super LWR than for LWRs. "Feedwater flow," "feedwater system," and "feedwater pump" of the Super LWR are described as "main coolant flow," "main coolant system," and "reactor coolant pump (RCP)," respectively, in the safety analysis, to be distinguished from those of LWRs. The main coolant flow rate is equal to the core coolant flow rate and the main steam flow rate at the steady state due to once-through cooling system.

The safety principle of the Super LWR and Super FR is compared with those of PWRs and BWRs in Table 1.7. The main coolant flow rate and turbine inlet pressure are monitored and used for the emergency signal, instead of the "water level" of LWRs.

1.3.9.2 Plant and Safety Systems

The plant and safety systems of the Super LWR and Super FR are shown in Fig. 1.36 [56]. The safety system design is summarized in Sect. 6.3.2.

The relation between the levels of abnormalities and the safety system actuations are shown in Table 1.8 [54]. A decrease in the coolant supply is detected as low levels of the main coolant flow rate. The reactor scram, the AFS and the ADS/LPCI are actuated sequentially depending on the levels of abnormality. The reactor is scrammed at level 1 (90%) and then the AFS is actuated at level 2 (20%). Level 3 (6%) means that the decay heat cannot be removed at supercritical pressure, so the reactor is depressurized.

Table 1.7 Comparison of safety principles

	PWR	BWR	Super LWR, Super FR
Requirement	Primary coolant inventory	Coolant inventory in the reactor vessel	Coolant flow rate in the core
Monitored parameter	Water level in the pressurizer	Water level in the reactor vessel	Main coolant flow rate, turbine inlet pressure

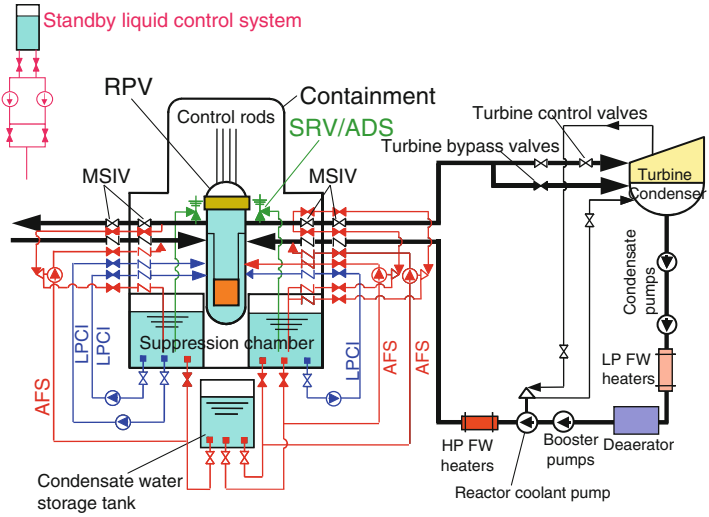


Fig. 1.36 Plant and safety systems of Super LWR and Super FR. (Taken from ref. [56] and used with permission from Korean Nuclear Society)

Table 1.8 Principle of safety system actuation

Flow rate low (feedwater or main steam)	
Level 1 (90%)[a]	Reactor scram
Level 2 (20%)[a]	AFS
Level 3 (6%)[a]	ADS/LPCI system
Pressure high	
Level 1 (26.0 MPa)	Reactor scram
Level 2 (26.2 MPa)	SRV
Pressure low	
Level 1 (24.0 MPa)	Reactor scram
Level 2 (23.5 MPa)	ADS/LPCI system

Taken from ref. [54] and used with permission from Atomic Energy Society of Japan
AFS auxiliary feedwater system, *ADS* automatic depressurization system, *LPCI* low pressure core injection system
[a]100% corresponds to normal operation

Closure of the coolant outlet is detected as pressure high levels. The reactor is scrammed at level 1 (26.0 MPa) and then the SRVs are actuated at level 2 (26.2 MPa). The ratio of the SRV set point and the normal operating pressure is smaller than that of an ABWR because the relative change of the core pressure is smaller in the Super LWR due to higher operating pressure of the latter.

Abnormal valve opening and pipe break are detected as pressure low levels. If the pressure decreases from supercritical to subcritical, dryout occurs on the fuel rod surface, which will lead to a rapid increase in the cladding temperature. Therefore, it is better to avoid keeping the core pressure near the critical pressure. In the present design, the ADS is actuated at level 2 (23.5 MPa), which is about 106% of the critical pressure (22.1 MPa). During rapid depressurization, an increase in the cladding temperature is prevented due to the large core flow rate even though dryout occurs.

Generally, the scram signal should be released before the emergency core cooling system (ECCS) signal. In consideration of this relationship, the low pressure scram set point, which is 24.0 MPa, is above the ADS/LPCI set point (one of the ECCS set points), which is 23.5 MPa.

1.3.9.3 Safety Criteria

Safety criteria need to be defined for the same abnormal transients and accidents as those of LWRs. Abnormal transients are defined as abnormal incidents that are expected to occur one or two times during the reactor service life. The requirements are the same as those of LWRs: no systematic fuel rod damage, no fuel pellet damage, and no pressure boundary damage. Abnormal incidents with expected frequency below 10^{-3} per year are further categorized as accidents as in LWRs. They are required not to result in excessive core damage.

Table 1.9 Principle of safety criteria for fuel rod integrity

Category	Requirement	Mechanical failure			Heat-up
		Buckling	Burst	PCMI	
Accident	No excessive damage			Enthalpy < Limit (RIA)	Oxidation<Limit MSCT<Limit
Transient	No systematic damage	ΔP on clad. <Limit	Plastic strain < Limit	Pellet temp.<Limit Plastic strain<Limit Enthalpy<Limit	

The principle of fuel rod integrity is summarized in Table 1.9. Four damage modes of the fuel cladding are expected at transients: (a) buckling collapse, (b) stress rupture, (c) PCMI, and (d) thermal damage [65].

The criterion for buckling collapse is simple: the pressure difference on the cladding does not exceed one-third of the buckling collapse pressure.

Removing the MDHFR criterion (analogous to the critical heat flux criterion of LWRs) and taking the MCST criterion were described in Sect. 1.3.2 and in ref. [66]. But the fuel rod integrity criteria for the stress rupture were further improved in two steps. The old criteria were derived from the mechanical strength requirement of the cladding based on ASME Boiler and Pressure Vessel Code Section III in which the requirement assumed an infinite period for the transients. The MCST criterion was set at 800°C for Ni-base alloy cladding and the fuel rods were designed to withstand that temperature [66].

But in reality, the period of transients is short. The improvement of fuel rod integrity assessment considering the period of transients was studied in Japanese liquid metal cooled fast breeder reactors (LMFBRs) R&D programs. Based on obtained results, it was proposed to raise the limit of the MCST from 830°C to over 900°C for future LMFBRs. It is possible to analyze the fuel rod integrity of the Super LWR and Super FR at transients using the FEMAXI-6 code. The improved criteria of fuel rod integrity for abnormal transients for Super LWRs were developed using the code [32]. The new criteria raised the limit of MCST to 850°C for stainless steel cladding. Experimental validation of the criteria remains for future study. Old and new criteria are compared in Table 1.10. The improved criteria for abnormal transients are further summarized in Table 1.11.

The criterion related to PCMI is that the plastic deformation of the cladding should be below 1.0%, which is the same as for LWRs. The relation between plastic deformation and damage of the candidate materials needs to be assessed by experiments.

The thermal damage criterion is limited by the cladding temperature. It is the same value derived from stress rupture. The criterion of MCST for accidents is 1,260°C for stainless steel cladding. It is the same value as the early USNRC criterion for LWRs using stainless steel cladding [67].

Table 1.10 Comparison of fuel rod integrity criteria for abnormal transients

Requirements	Old criteria	New criteria
No buckling collapse of cladding	Pressure difference $<1/3 \times$ collapse pressure	Pressure difference $<1/3 \times$ collapse pressure
No mechanical failure of cladding	ASME B&PV code III	No plastic strain
No melting of fuel pellet	Centerline temperature $<$ melting point	Centerline temperature $<$ melting point

Table 1.11 New criteria for fuel rod integrity for abnormal transients

	Old criteria	New criteria				
Maximum cladding surface temperature (°C)	800 (Ni-base alloy)	850 (Stainless steel)				
Maximum allowable power (%P_0)	none	Power rise rate [%P_0/s]	<0.1	0.1–1	1–10	>10
		Scram set point	120	124	136	182
Maximum system pressure (MPa)	28.9	28.9				

P_0 initial power

The initial conditions and criteria for MCST in abnormal transients and accidents are shown in Fig. 1.37. The maximum peak temperature at the steady state condition, 740°C, has changed with improvement of the core design method and data as already described in Sect. 1.3.4. But when 740°C is taken, the temperature difference between the limits, 110°C for abnormal transients and 520°C for accidents are the margins.

For reactivity insertion accidents (RIAs), the pellet enthalpy criterion of 230 cal/g UO_2 is taken. It is the same as for LWRs. For abnormal transients with reactivity insert over \$1, the criterion is set as 170 cal/g, again taken from that of LWRs. However, this criterion has not been applied to the safety analysis of the Super LWR and Super FR because no transient is followed by reactivity insertion over \$1. It should be considered in the future study whether the pellet enthalpy criterion for transients is necessary, as in LWRs, or not, as in sodium cooled reactors.

The concept of keeping pressure boundary integrity is the same as that of LWRs. The maximum allowable pressures are 28.9 MPa at a transient, which is 105% of the maximum pressure of normal operation, and 30.3 MPa at an accident, which is 110% of the maximum pressure of normal operation while they are 110% at a transient and 120% at an accident in LWRs. However, the Super LWR still has a sufficient margin to the criteria because its pressure change is milder than that of LWRs.

The criterion for anticipated transients without scream (ATWS) is the same as that of accidents. Experimental validation of the criteria remains for future study.

1.3.9.4 Safety Analysis at Supercritical Pressure

The abnormalities of the Super LWR and Super FR are considered with reference to those of LWRs (see Sect. 6.4). The initiating events for safety analysis are summarized in Table 1.12.

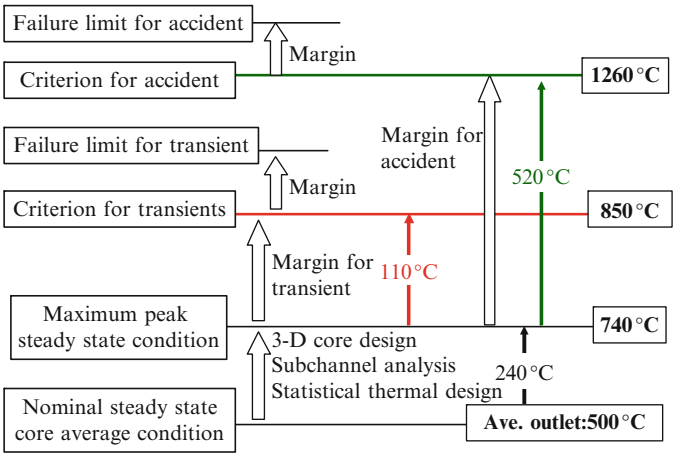


Fig. 1.37 Maximum cladding surface temperature criteria and margins for abnormal transients and accidents

Table 1.12 Abnormal events in safety analysis

Abnormal transients
Decrease in core coolant flow rate
Partial loss of reactor coolant flow
Loss of offsite power
Abnormality in reactor pressure
Loss of turbine load
Isolation of main steam line
Pressure control system failure
Abnormality in reactivity
Loss of feedwater heating
Inadvertent startup of AFS
Reactor coolant flow control system failure
Uncontrolled CR withdrawal at normal operation
Uncontrolled CR withdrawal at startup
Accidents
Decrease in core coolant flow rate
Total loss of reactor coolant flow
Reactor coolant pump seizure
Abnormality in reactivity
CR ejection at full power
CR ejection at hot standby
LOCA
Large LOCA
Small LOCA

The "reactor coolant flow abnormality" is important for the Super LWR because maintaining the core coolant flow rate is the fundamental safety requirement. It should be noted that there are two types of reactor coolant flow abnormalities with and without reactor scram before events; the former are abnormal transient types

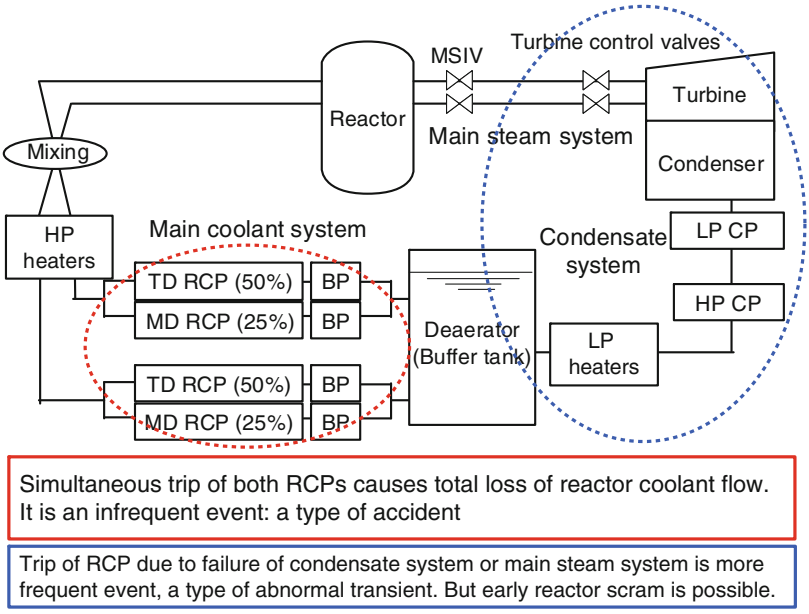


Fig. 1.38 Two types of "loss of flow" events

and the latter are accident types [55, 56, 64, 65]. This point is summarized in Fig. 1.38 and described in detail in Sect. 6.4.

The node-junction model of the safety analysis code at supercritical pressure is shown in Fig. 1.39. Mass, energy, and momentum conservation equations are solved. The heat transfer between fuel coolant channels and water rods is taken into account. The hot and average channels are analyzed. The Oka–Koshizuka heat transfer correlation is used for the analysis. It covers the flow and power conditions of the safety analysis. It gives smaller heat transfer coefficients at low mass flux condition compared with experiments and other existing correlations such as the Watts–Chou correlation and Bishop correlation. It predicts higher cladding temperature than other correlations. Location of the hottest cladding temperature tends to be at the high temperature "gas-like" coolant region above 500°C where the heat transfer coefficient should agree with the Dittus–Boelter correlation. The Oka–Koshizuka correlation agrees relatively well with the Dittus–Boelter correlation at this region compared with the other correlations.

The results of the "total loss of reactor coolant flow" accident are explained in Fig. 1.40. The heat conduction to the water rods increases and the water rods serve as a "heat sink". This heat conduction also thermally expands the water in the water rods and temporarily supplies water to the fuel channels. Thus, water rods serve as a "water source" also and enable the backup pumps (AFSs) to have a realistic delay time. The results of "loss of turbine load without turbine bypass" transient are shown in Fig. 1.41. This is a type of pressurization event and an important one for

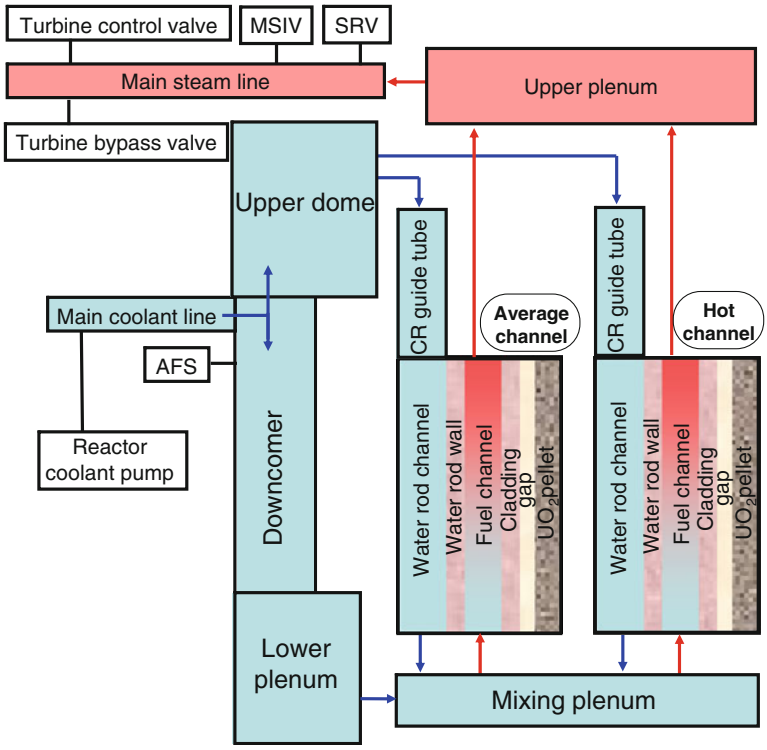


Fig. 1.39 Calculation model of SPRAT-DOWN for safety analyses

BWR safety design. But the power rise is mild for the Super LWR because of the smaller water density change than that of BWRs due to the high pressure. Flow stagnation occurs and increases density feedback. It also mitigates the power rise. The pressure change itself is also small at the supercritical pressure [65]. The abnormal transient and accident analyses are summarized in Sects. 6.7.1 and 6.7.2, respectively.

The anticipated transients without scram (ATWSs) of the Super LWR were analyzed to clarify its safety characteristics [68, 69]. An ATWS is defined as an abnormal transient followed by the failure of reactor scram. The results of "loss of offsite power" are shown in Fig. 1.42. An alternative action is not needed either to satisfy the safety criteria or to achieve a high temperature stable condition for all ATWS events. Initiating the automatic depressurization system is a good alternative action that induces a strong core coolant flow and inserts a negative reactivity. It provides an additional safety margin for the ATWS events. The Super LWR has excellent ATWS characteristics, providing a key reactor design advantage. The ATWS analyses are summarized in Sect. 6.7.4.

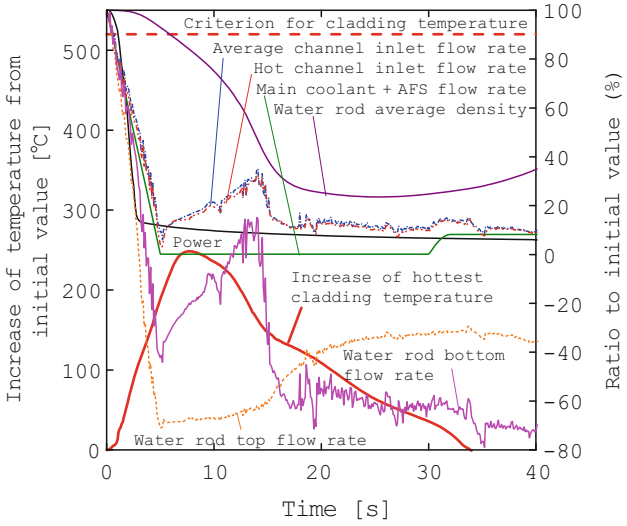


Fig. 1.40 Calculated results for "total loss of reactor coolant flow"

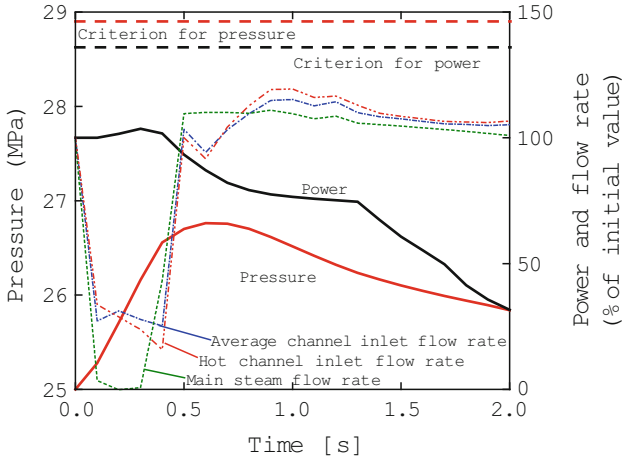


Fig. 1.41 Calculated results for "loss of turbine load without turbine bypass"

The change of cross flow within a subassembly may occur during transients. The MCST may change from the result of the single-channel calculation. A transient subchannel analysis code was developed and the safety analysis of a Super LWR was carried out [70]. The temperature rises from the steady state value are about 20°C at the abnormal transients and about 130°C at accidents. The maximum values still stay below the MCST criteria for transients and accidents. The development and application of the transient subchannel analysis code are summarized in Sect. 6.8.

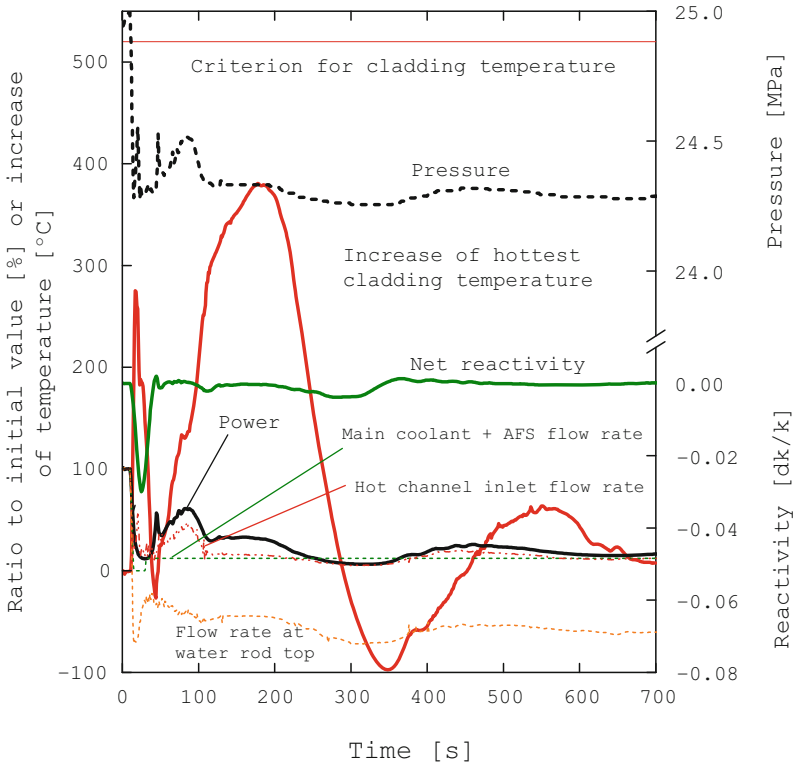


Fig. 1.42 Calculation results for "loss of offsite power" (ATWS) without alternative action

1.3.9.5 LOCA Analysis

Loss of coolant accidents (LOCAs) of the Super LWR and Super FR are treated as design basis accidents as in current LWRs. There are mainly two differences in the LOCA phenomena between the Super LWR/Super FR and LWRs. One is that a "double-ended break" does not occur in the Super LWR and Super FR. Figure 1.43 [71] compares blowdown phenomena among PWRs, BWRs and the Super LWR. Since PWRs and BWRs have circulation loops in the primary cooling system (i.e. the primary system of PWRs and the recirculation system of BWRs), two flow paths are generated on both sides of the break. In the Super LWR, only one break flow path is generated because the once-through cooling system has both the coolant inlet and outlet. It is a "single-ended break". Therefore, a 100% break is the largest break to be considered in the Super LWR LOCA analysis, while a 200% break should be considered in LWRs.

The reflooding phase of the Super LWR is similar to that of PWRs rather than that of BWRs. Figure 1.44 [71] compares the reflooding phenomena of PWRs and the Super LWR. When the Super LWR adopts the pressure suppression type

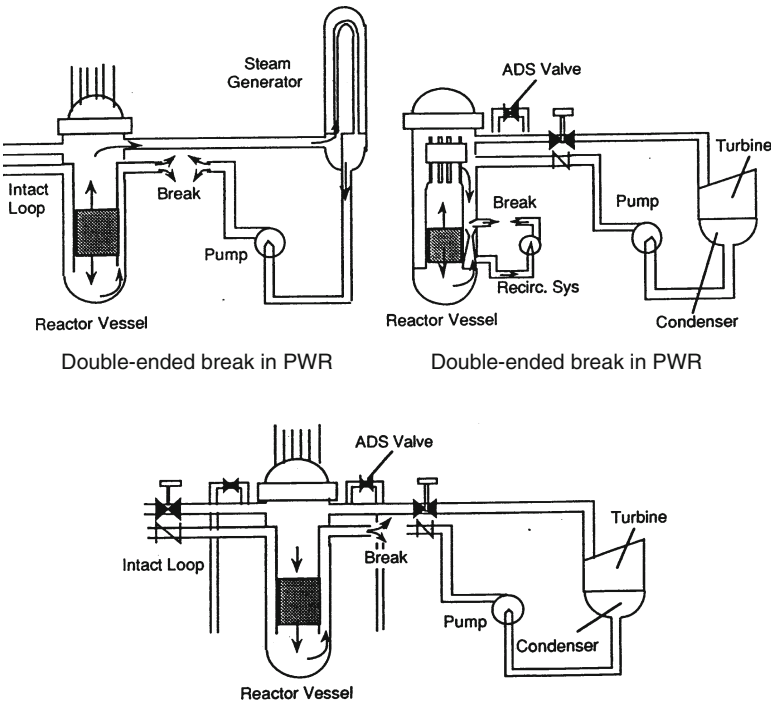


Fig. 1.43 Comparison of blowdown phenomena. (Taken from ref. [71] and used with permission from Atomic Energy Society of Japan)

containment as the BWRs, the steam generated in the core is released through the ADS lines to the suppression chamber while it is released through the steam generator and the break point to the dry type containment in PWRs. The submergence of the ADS line needs to be considered during reflooding. This is the second difference in LOCA phenomena. Whether the Super LWR and Super FR adopt the dry containment remains for future study. But the LOCA analyses have been performed with the pressure suppression containment [55, 56, 71–74].

The SCRELA code was developed for large LOCA analyses for the SCFR, an early version of the Super FR [72, 73]. The SPRAT-DOWN, including the downward flow water rod model for the Super LWR, was extended to the SPRAT-DPWN-DP code for the large LOCA analyses [71]. The critical flow at supercritical pressure is not known. Then, the correlation at the subcritical pressure has also been used in the supercritical pressure for the LOCA analyses since the duration of supercritical pressure is very short. Both codes were verified in comparison with the REFLA-TRAC code. The SPRAT-DOWN code was applied to the small LOCAs of the Super LWR because the system pressure stays in supercritical region at the small LOCAs [71].

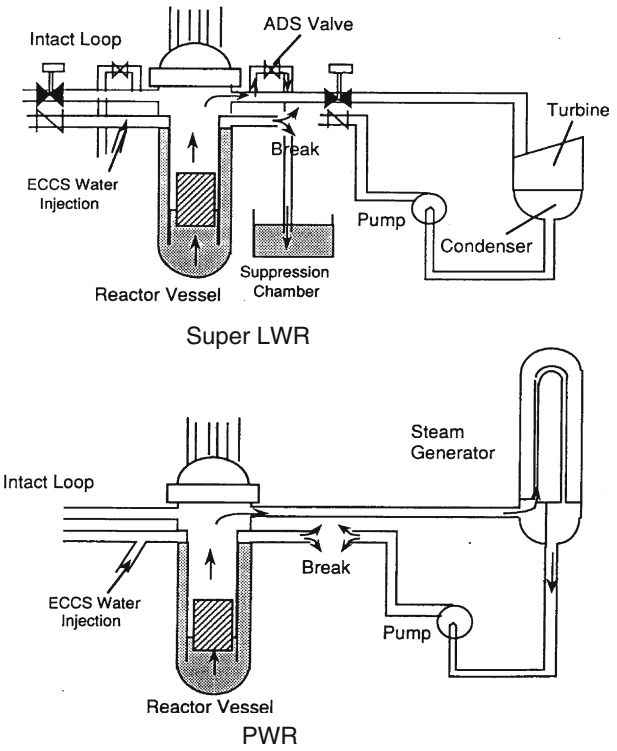


Fig. 1.44 Comparison of reflooding phenomena. (Taken from ref. [71] and used with permission from Atomic Energy Society of Japan)

Analysis results of 1–100% hot-leg/cold-leg breaks of the Super LWR are reported in ref. [71]. At the cold-leg large break, excessive core heat-up is mitigated by the ADS during blowdown because reactor depressurization induces core coolant flow. This is explained in Fig. 1.45. The coolant inventory in the top dome and the water rods is effectively used for core cooling. After blowdown, the core is slowly reflooded by the low pressure ECCS as in PWRs. The reflooding phase is influenced by submergence of ADS pipes in a suppression pool as seen in Fig. 1.46. The highest cladding temperature of the large LOCA is lower than the criterion (1,260°C) by about 430°C which appears during the reflooding phase. A small cold-leg break gives higher cladding temperatures than that of the large break because the ADS is not actuated in the analysis. The boundary of the large and small breaks that gives the highest cladding temperature is lower than the criterion by about 260°C. The analysis results of the cold-leg break small LOCAs are shown in Fig. 1.47. If the ADS actuation is assumed by the "drywell pressure high" signal, the cladding temperature is lower. The hot-leg break is less severe than the cold-leg break because it increases the core coolant flow rate and forced flooding is expected after blowdown.

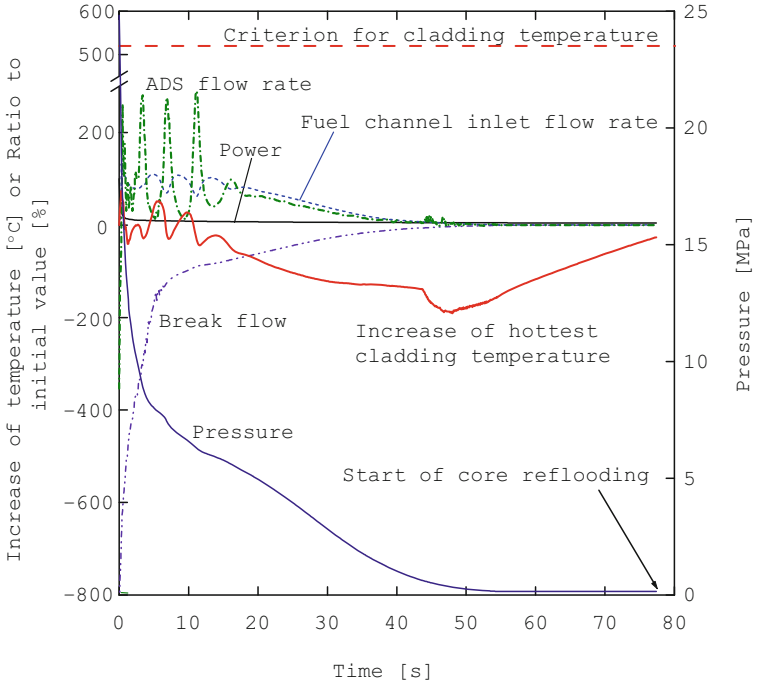


Fig. 1.45 Blowdown phase of 100% cold-leg break LOCA

The LOCA analyses are summarized in Sect. 6.7.3.

1.3.9.6 Summary of Safety Analysis

The results of safety analyses of the Super LWR are summarized in Fig. 1.48 [56]. The temperature rises of the fuel cladding of Super LWR are illustrated in comparison with the criteria and margins in Fig. 1.49. Safety characteristics of the Super LWR are summarized in Table 1.13.

1.3.9.7 Simplified Probabilistic Safety Assessment

No natural circulation coolant path exists in the once-through cycle reactor when the main feedwater pumps stop. The effect of the feature on core damage frequency was assessed by the simplified probabilistic safety assessment (PSA) method. Two analysis were performed; one was for the SCFR based on the early safety system design [73, 75]. In order to carry out the PSA of the SCFR, the potential significant events that can lead to severe core damage were identified as initiating events. Five initiating events, large LOCA, intermediate LOCA, two categories of small break

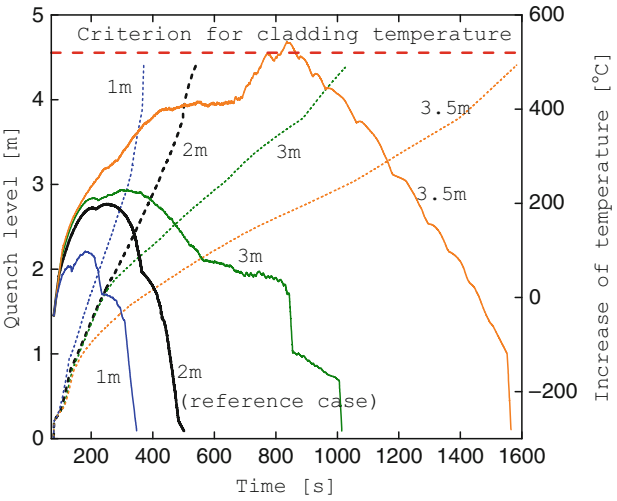


Fig. 1.46 Influence of submergence of quencher in suppression pool on reflooding phase of 100% cold-leg break LOCA

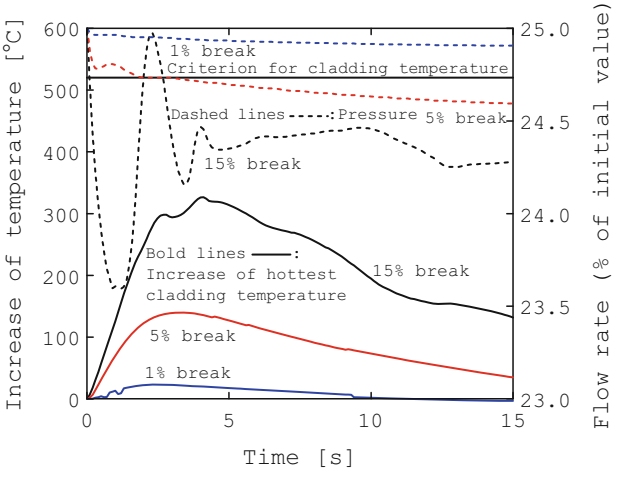


Fig. 1.47 Cold-leg small break LOCAs

LOCAs, and loss of offsite power (LOSP) were selected by considering SCFR characteristics and by acknowledging the results of NUREG 1150. Mitigation sequence for each initiating event was established with the required safety system. Event trees were constructed based on the mitigating sequences for each initiating event and referring to the current PSA results.

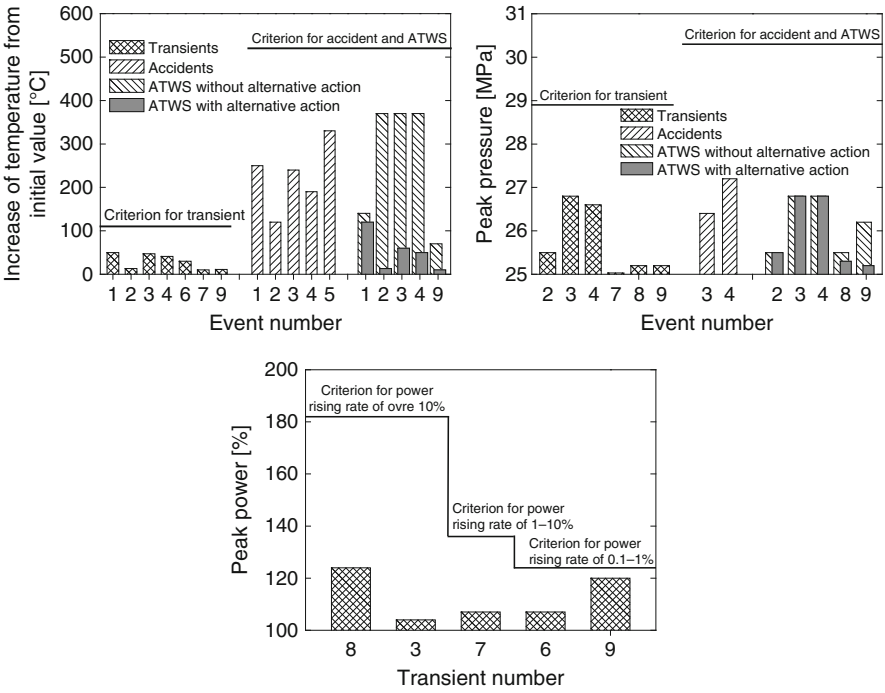


Fig. 1.48 Summary of safety analyses of the Super LWR. (Event numbers are taken from Table 1.12). (Taken from ref. [56] and used with permission from Korean Nuclear Society)

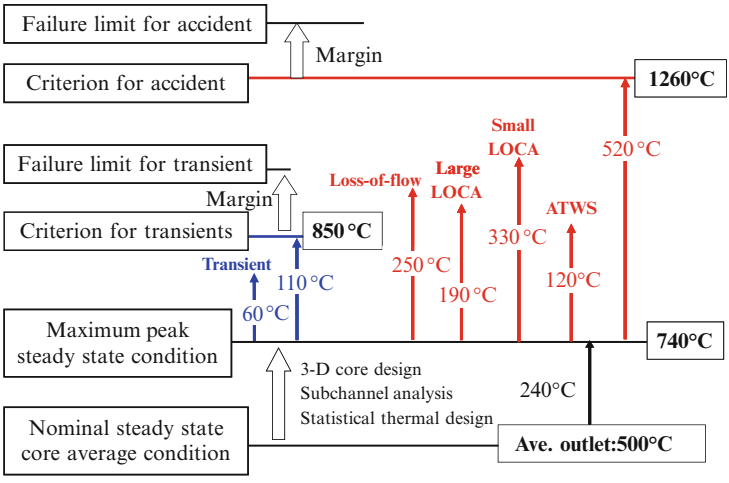


Fig. 1.49 Summary of temperature rises of the fuel cladding.

Table 1.13 Summary of safety characteristics of the Super LWR

Core cooling by depressurization
Top dome and water rods serve as an "in-vessel accumulator"
Loss of flow mitigated by water rods
Short period of high cladding temperature at transients
Mild behavior at transients, accidents and ATWS
Simple safety principle (keeping flow rate) due to once-through cooling cycle

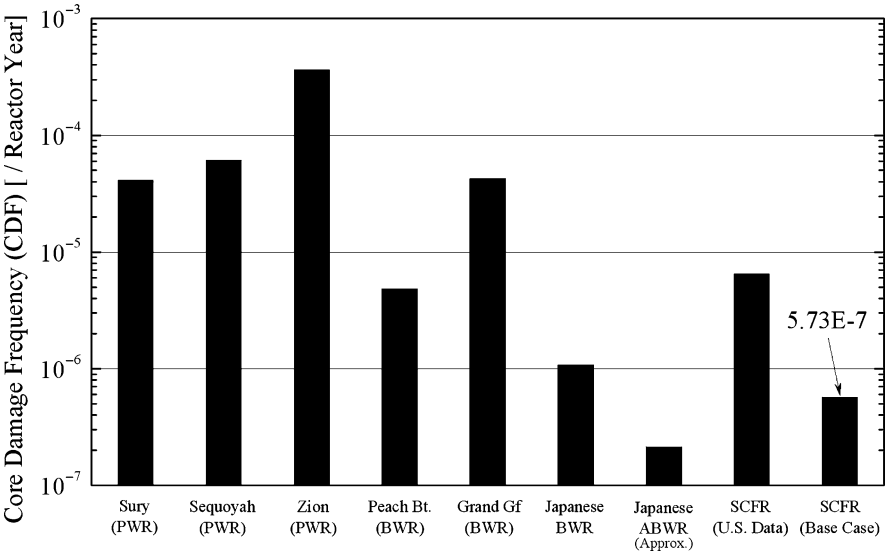


Fig. 1.50 Comparison of total core damage frequencies of SCFR (early design of the Super FR)

The total core damage frequency (CDF) of the SCFR was compared with the PSA results of current LWRs in Fig. 1.50. The estimated CDF is smaller than those of the US BWR plants considering the characteristics of the reactor system and referring to the Japanese PSA data. Accordingly, for the relative comparison between the two results, the case is calculated which imposes the same initiating event frequencies as in the US BWR plants. The estimated CDF of this case shows the similar trend to the results of US BWR plants. It is concluded that the CDF is not high. Although no natural circulation is established at total loss of feedwater flow in the once-through coolant system, the core damage frequency is maintained as the same level as the conventional Japanese BWR because of the diversity of feedwater systems in the direct cycle reactors.

The Super LWR was also studied using simplified PSA methodology in an event tree analysis. As shown in Fig. 1.51, it was found that the contribution of the large LOCA event was approximately 50% of the CDF. As shown in Fig. 1.52, it was found that the failures of coolant supply to the core and automatic depressurization caused most of the CDF. The PSA study on the Super LWR is summarized in Sect. 6.9.

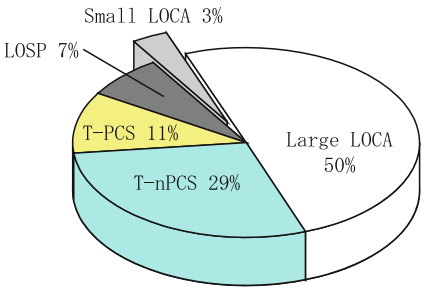


Fig. 1.51 Contributions of initiating events to total CDF in the Super LWR

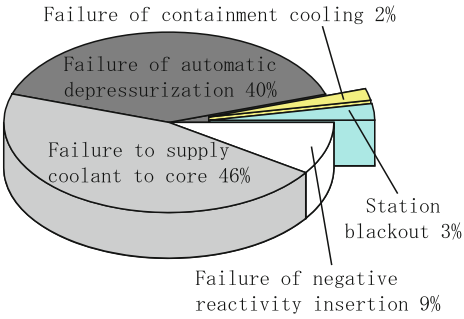


Fig. 1.52 Contributions of each function to total CDF in the Super LWR

1.3.10 Super FR

1.3.10.1 Fuel, Core and Plant System

Water cooled fast reactors require a tight fuel lattice. The once-through coolant cycle is compatible with the tight lattice core of water cooled fast reactors [76–78]. The increase in the core pressure drop due to the tight lattice does not cause problems with pumping power and stability because of the low coolant flow rate of the once-through cycle. Increasing orifice pressure drop for improving stability is also not a problem.

The plant system of the Super FR is the same as that of the Super LWR, a thermal reactor. Fast reactors do not need a moderator. Their power density is inevitably higher than that of thermal reactors. High power density is an advantage in economy. The Super FR has higher power density than the Super LWR. The Super LWR is expected to show better economy than LWRs due to the compactness, simplicity of the plant systems, and high thermal efficiency. Improving economy of the fast reactor over that of LWRs is an important goal of fast reactor development. The Super FR has good potential in this regard [79].

The supercritical pressure light water cooled fast reactors with MOX fuel have been studied at the University of Tokyo from the beginning (1989). But early designs adopted approximate two-dimensional core calculations and a linear

burn-up model. The core performances cannot be predicted accurately and cannot be used for the present Super FR design and analysis. Three-dimensional coupled neutronic and thermal-hydraulic calculations as made in the Super LWR core design are necessary for predicting the Super FR core performances accurately. The core design method of the Super FR is the same as that of the Super LWR. But a three-dimensional tri-z geometry was developed for the design [80–82]. A sub-channel analysis code for the Super FR was developed and used for evaluating the nominal MCST [83]. The principle of MOX fuel rod design of the Super FR is the same as that of UO_2 fuel of the Super LWR, but high Pu content needs to be accommodated. The fission gas release rate is high. The FEMAXI-6 code has been used for the design [84–87]. Care should be taken for meeting the requirement at both local and whole-core voiding in the core design. A core with negative void reactivities for both local and whole voiding conditions was designed [88, 89]. The core of the Super FR consists of hexagonal fuel assemblies with wrapper tubes (channel boxes). An example of core layout, seed and blanket assemblies are shown in Fig. 1.53. The zirconium hydride layer is placed in the blanket assembly for the negative coolant void reactivity. Examples of fuel and core characteristics are shown in Table 1.14 [87]. The two-pass flow scheme in the RPV is illustrated Fig. 1.54. The blanket fuel assemblies are cooled by downward flow to increase the average reactor outlet temperature. Part of the seed assemblies can also be cooled by downward flow.

Supercritical water is single-phase fluid. A CFD code is useful for predicting the behavior [90–92]. The radial distribution of cladding temperature was evaluated by a CFD code [93, 94]. Cladding temperatures, especially their circumferential

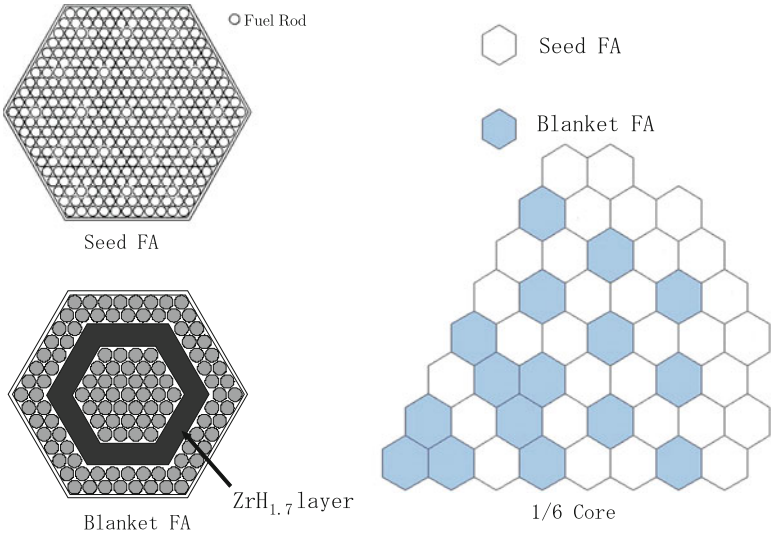


Fig. 1.53 Example of seed and blanket fuel assemblies and core layout

Table 1.14 Examples of fuel and core design characteristics of Super FR

Fuel rod diameter (mm)	5.5
P/D	1.19
Gap clearance (mm)	1.045
Cladding thickness (mm)	0.4
Pellet cladding gap (mm)	0.03
Heated length (cm)	200
Assembly pitch (cm)	11.561
Number of rods in a seed assembly (total/fuel/CR tube)	271/252/19
Core thermal power (MWt)	1,602
Equivalent diameter (cm)	186
Number of seed assemblies	162
Number of blanket assemblies	73
Coolant outlet temperature (°C)	504.6
MCST calculated by subchannel analysis (°C)	628.5
Average power density (W/cm^3)	294.8
Coolant void reactivity (%Δk/k) at BOEC/EOEC	−0.839/−1.712

Taken from ref. [87] and used with permission from Atomic Energy Society of Japan

distribution, are difficult to measure accurately by experiments because of the narrow spacing between the fuel rods. The radical temperature distribution of a uniform channel is approximately 12°C, when heat conduction of fuel cladding is considered as seen in Fig. 1.55 [93]. It is also seen from the figure that the temperature difference between inner and outer claddings is approximately 24°C. The MCST criterion is converted to that of the maximum cladding centerline temperature by adding 12°C for the evaluation of cladding stress. The temperature of supercritical "steam" is sensitive to the enthalpy change. The pressure drop increases when heating is in the narrow channel. This reduces the coolant flow in the channel and increases the temperature. The effect was analyzed in detail by the CFD code for unsymmetrical geometric and heating conditions. Adjusting the spacing between the fuel rods and unheated surface toward the heated perimeters is effective for making the temperature distribution uniform [93, 94].

A large-scale CFD calculation is useful for the design of the Super FR and Super LWR. For example, the ACE-3D code for supercritical water calculation was developed for analysis of the 37-fuel rod bundle geometry. Validation of the code with 7-rod bundle experiments can be expected to reduce future R&D work on fuel assemblies. The flow characterization within the RPV will also be made by CFD calculation.

The neutron spectrum of the Super FR is compared with those of LWRs and the sodium cooled fast reactor in Fig. 1.56. The blanket assemblies of the Super FR are equipped with zirconium hydride layer for the negative coolant void reactivity. The spectrum near the layer is similar to that of LWRs. Both fast and thermal neutron spectra are available in the Super FR. Availability of both will be suitable for the transmutation of long-lived fission products as well as minor actinides [95, 96]. The improved core design for the high power density was reported [87].

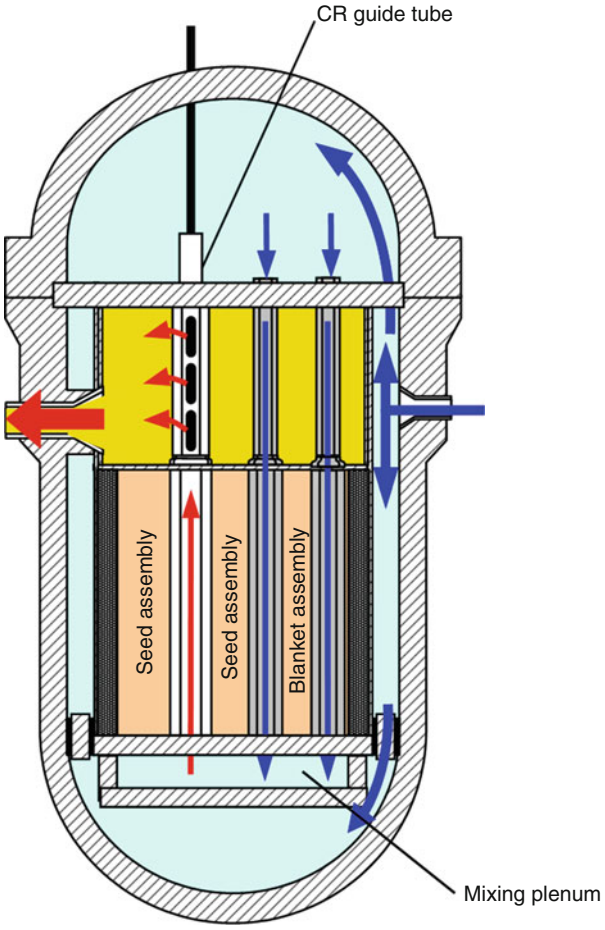


Fig. 1.54 Two-pass flow scheme with downward flow in blanket assemblies and part of the seed assemblies

The plant and safety systems of the Super FR are the same as that of the Super LWR. The safety and stability analyses of the Super FR have been reported [97–100]. Improvement of the plant control system was studied for the Super FR. The power to flow rate ratio was taken for the control parameter of the feedwater pumps in order to suppress a fluctuation of the main steam temperature. This is the same as in supercritical FPPs. It showed better convergence than taking only the feedwater flow rate as the control parameter [101].

A cut-away view of the RPV is shown in Fig. 1.57 [102]. The outlet nozzles are exposed to the high temperature outlet coolant. The structural considerations were made on the reactor vessel and internals. A seal pipe is provided at the main steam nozzle as seen in the Fig. 1.57 [102].

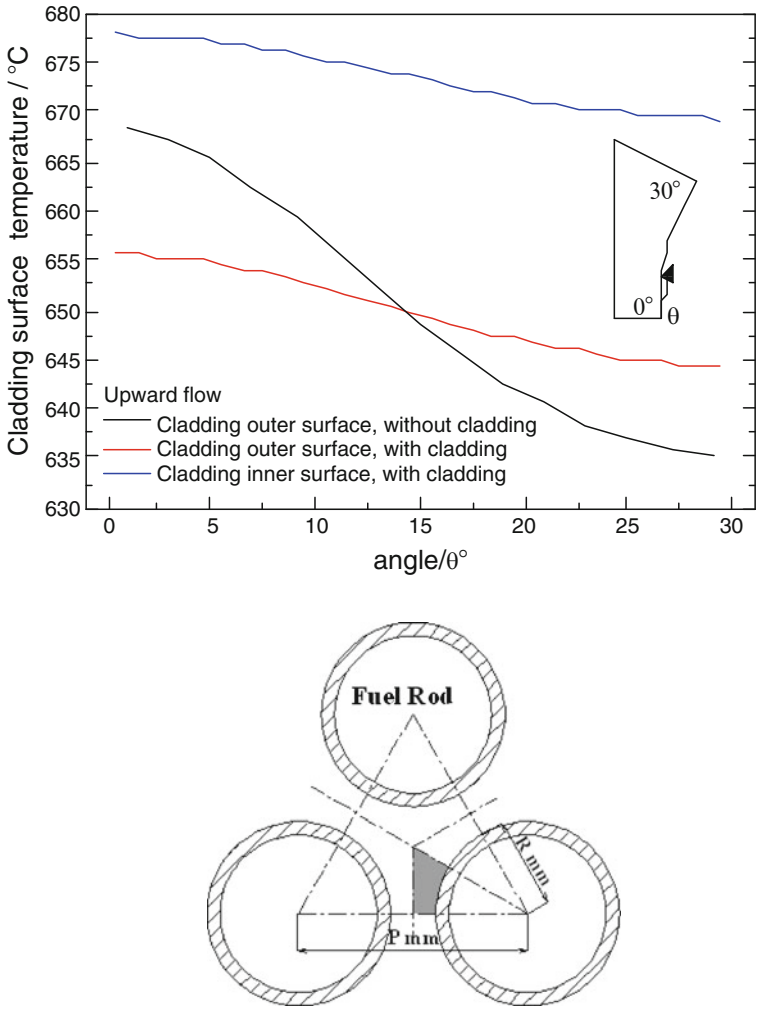


Fig. 1.55 Examples of radial temperature distributions on fuel cladding surface. (Taken from ref. [93] and used with permission from Atomic Energy Society of Japan)

1.3.10.2 Zirconium Hydride Layer Concept for Negative Void Reactivity

The reactivity increases at the LOCA in large-sized fast reactors due to the neutron spectrum hardening. In the design of water cooled fast reactors, negative reactivity addition is necessary for inherent decrease of reactor power at the LOCA. Increasing the leakage by flattening the core shape is not suitable for the Super FR because that would make the RPV wall thick. Softening the spectrum of the core by using graphite is the alternative, but it is not effective for water cooled fast reactors.

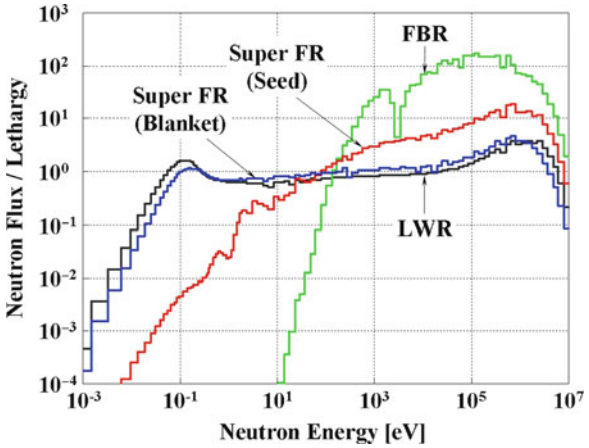


Fig. 1.56 Comparison of neutron spectra of the Super FR, a LWR and a sodium cooled fast breeder reactor

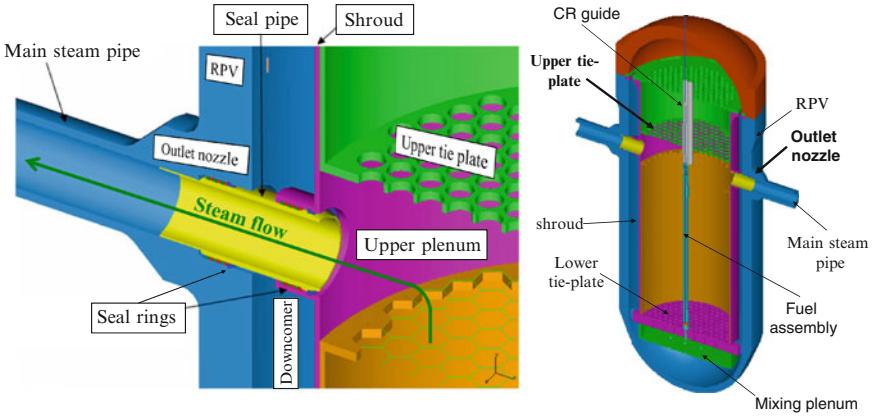


Fig. 1.57 Example of in-core structure of Super FR. (Taken from ref. [102] and used with permission from Atomic Energy Society of Japan)

Placing a thin zirconium hydride layer between the seed and blanket fuel assemblies was found effective in changing the reactivity with steam density in the study of a steam cooled fast reactor [103, 104]. The typical geometry and calculation result are shown in Figs. 1.58 and 1.59, respectively. The effectiveness was explained in the subsequent studies [105, 106]. The mechanism is described in Sect. 7.3. The fast neutrons are generated in the seed assemblies. They are moderated by the thin zirconium hydride layer between the seed and blanket. The layer is installed in the blanket assemblies in the present Super FR design. The moderated neutrons are effectively absorbed in the blanket fuel by the capture of U-238. The

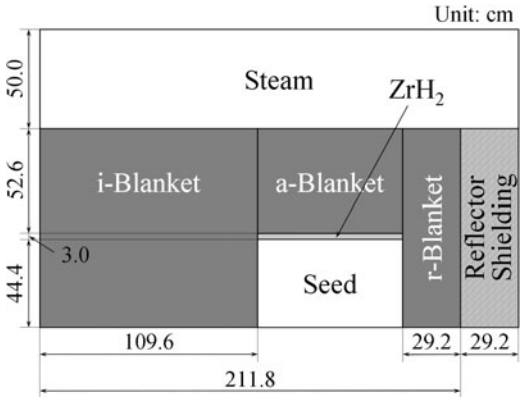


Fig. 1.58 Original zirconium hydride layer concept of indirect cycle supercritical steam cooled fast reactor in two-dimensional core calculation model

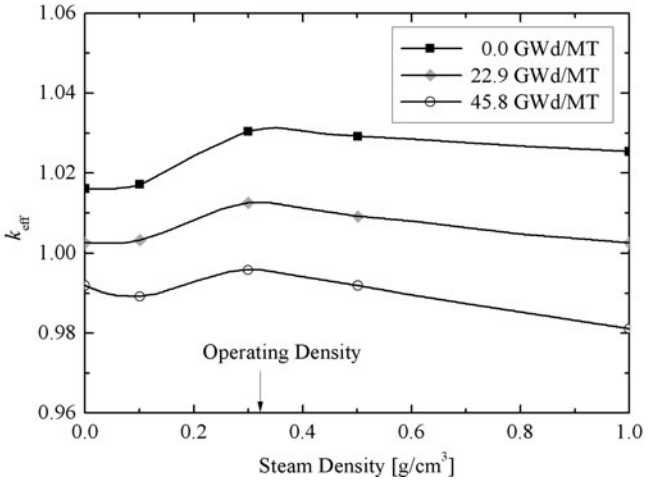


Fig. 1.59 Change of effective multiplication factor with steam density for the indirect cycle supercritical steam cooled fast reactor

whole-core neutron balance becomes negative due to the effective absorption of moderated neutrons. Without placing the zirconium hydride layer, the fast neutrons from the seed fuel assemblies cause fast fissions in the blanket fuel. This gives rise to the positive reactivity at voiding.

The mechanism of achieving negative reactivity is not whole-core spectrum softening by the moderator, but moderation through the zirconium hydride layer and absorption in the blanket. The breeding capability is not deteriorated much because the neutron spectrum of the remaining part of the core does not change much.

The zirconium hydride layer concept is suitable for the Super FR, because the core shape stays normal, and is not flattened. The thickness of the RPV stays within

the fabrication capability. The thickness will be comparable with that of the PWR RPV, when high tensile strength steel is used. Such steel has already been developed for a large-sized PWR.

It should be pointed out that making the effective multiplication factor the maximum at the operating steam density (Fig. 1.59) is not desirable. The reactivity coefficient becomes positive during the startup from the flooded core. The effective multiplication factor should be increased when the core is flooded.

But getting an operating steam density of 0.3 g/cm^3 (Fig. 1.59) requires supercritical pressure. This was the start of Super FR and Super LWR studies at the University of Tokyo. The plant system of the supercritical steam cooled fast reactor was an indirect cycle at first [104], but the advantage of the once-through cycle was soon recognized and a report on this was made in 1992 [2, 107].

1.3.11 Computer Codes and Database

The scope of studies and computer codes are summarized in Table 1.15. SRAC is a neutronic core calculation code developed by Japan Atomic Energy Agency (JAEA) [21]. FEMAXI-6 is a light water reactor fuel analysis code also developed by JAEA [31]. All other codes in the table were developed mostly by graduate students at the University of Tokyo during their thesis studies. Some codes did not have names.

One-dimensional burn-up and two-dimensional R-Z core calculation procedures for the fast reactor are found in refs. [108, 109]. The LOCA analysis code, SCRELA was described in ref. [110]. The procedure for a simplified PSA is also described there. The single channel thermal-hydraulic calculation code SPROD, the two-dimensional coupled core calculation scheme of the thermal spectrum reactor with water rods and transient and accident analysis code at supercritical-pressure, SPRAT are described in ref. [111].

Table 1.15 Scope of studies and computer codes

Fuel and core
Single channel thermal hydraulics (SPROD), 3D coupled core neutronic/thermal-hydraulic (SRAC-SPROD), Coupled subchannel analysis, Statistical thermal design method, Fuel rod behavior (FEMAXI-6), Data base of heat transfer coefficients of supercritical water (Oka–Koshizuka correlation)
Plant system; Plant heat balance and thermal efficiency
Plant control
Safety; Transient and accident analysis at supercritical-and subcritrical pressure (SPRAT-F, SPRAT-DOWN), ATWS analysis (SPRAT-DOWN), LOCA analysis (SCRELA,SPRAT-DOWN-DP), Time-dependent subchannel analysis
Start-up (sliding pressure and constant pressure)
Stability (TH and core stabilities at supercritical and subcritical-pressure)
Probabilistic safety assessment

Analysis of the heat transfer deterioration mechanism by numerical simulation using the k–ε turbulence model is in ref. [112]. Transient and accident analysis code for fast reactors, SPRAT-F, and calculation of the Oka–Koshizuka heat transfer correlation for the safety analysis at supercritical pressure are described in ref. [113].

Plant heat balance and the thermal efficiency calculation are in ref. [114]. This reference also includes the two-dimensional coupled core calculation procedure for the thermal reactor.

The plant dynamics code for the analysis of plant control and startup thermal considerations are described in ref. [115]. The subchannel analysis code and the analysis are found in refs. [116, 117]. Thermal-hydraulic and coupled stability calculations at supercritical and at subcritical pressure as well as startup considerations are described in ref. [118].

Three-dimensional, coupled core calculation scheme using SRAC, ASMBURN, COREBN, and the JENDL3.3 nuclear data of JAEA and SPROD and the core design method are described in ref. [119]. It also includes fuel rod design and rationalization of fuel integrity criteria during transients at high temperature using FEMAXI-6. Three dimensional coupled core design calculation of the Super FR is described in ref. [120]. The statistical thermal design procedure is described in refs. [26, 27].

Safety analysis of the Super LWR is described in ref. [121]. The SPRAT-DOWN code for the analysis of downward flowing water rods and the SPRAT-DOWN-DP code for depressurization in an LOCA were prepared. The LOCA analysis of the Super LWR was performed in combination with SPRAT-DOWN-DP and the reflooding module of SCRELA. ATWS analysis is also described in ref. [121]. The momentum equation is included in the SPRAT-DOWN code from the ATWS analysis. The design of the two-pass core of the Super LWR and the safety analysis at subcritical pressure during startup are described in ref. [122].

An improved core design procedure of the Super LWR that coupled the subchannel analysis with three-dimensional coupled core calculations is described in ref. [28]. The time-dependent subchannel analysis code for safety analysis of the Super LWR is described in ref. [123].

Watts–Chou correlation was employed as the heat transfer correlation for the core design of the Super LWR and Super FR, because of the accuracy and applicability to both upward and downward flow cooling. For safety analysis, the Oka–Koshizuka correlation is used. CFD analysis of the effect of grid spacers on heat transfer correlation is found in ref. [124].

1.4 Past Concepts of High Temperature Water and Steam Cooled Reactors

Reviews of high temperature water and steam cooled fast reactor concepts from the 1950s to the mid 1990s are described in Appendix B grouped as: supercritical pressure water cooled reactors; nuclear super heaters; and steam cooled fast reactors.

A steam cooled fast reactor is defined as one in which the core inlet coolant is "steam", not water. Blowers are required for steam cooled reactors instead of reactor coolant pumps. The pumping power of blowers is huge. Some supercritical pressure water cooled reactors have adopted pressure tubes instead of the RPV and have separate moderator and coolant. Indirect cycle reactors with a RPV are also found.

What is the closest to the Super LWR and Super FR is the high pressure FBR of B&W (Fig. B.22 in Appendix B) operating at 3,700 psia (25.52 MPa). It adopts a RPV, but the inlet temperature of the reactor coolant is 750°F (399°C). This is above the pseudo-critical temperature and so it is a type of steam cooled reactors. In addition to the required blowers to drive the large volume of steam as coolant and the large pumping power consumption in steam cooled reactors, a large fraction of the reactor outlet coolant is consumed for heating the feedwater up to "steam". This is also a disadvantage.

No detailed calculations and analyses have been given in the reports on the past concepts, including their safety systems and safety analysis.

The Super LWR and Super FR are new concepts based on the experiences with LWRs and fast reactors as well as supercritical FPPs. The concepts have been developed with full numerical analyses.

1.5 Research and Development

1.5.1 Japan

The conceptual design study made at the University of Tokyo for the Super LWR and Super FR was described in Sect. 1.3. The early designs carried other names such as SCLWR, SCLWR-H, SCFR, SCFR-H, SCFBR-H, SWFR etc. Publications are found on the home page [125].

Heat transfer experiments and material research studies have been carried out at Kyushu University, JAEA, the University of Tokyo and elsewhere. Comparison of heat transfer coefficients predicted by different correlations is shown in Fig. 1.60. Accuracy above 500°C is important for the calculation of MCST. Calculated MCSTs with different correlations are compared in Table 1.16 [122]. The largest difference is 44°C. Current heat transfer correlations were developed based on experiments using smooth circular tubes. Experiments on fuel bundle geometry are necessary. The effect of grid spacers on the heat transfer correlation should be included in the prediction of MCST. The correlation of downward flow is necessary for the design. Downward flow is adopted in the low temperature region below the pseudo-critical temperature.

Dryout or boiling transition may occur during the sliding-pressure startup of the once-through reactor as seen in Fig. 1.21 [43, 44]. Ribbed tubes and spiral tapes have been used for the supercritical boilers to improve the critical heat flux. The

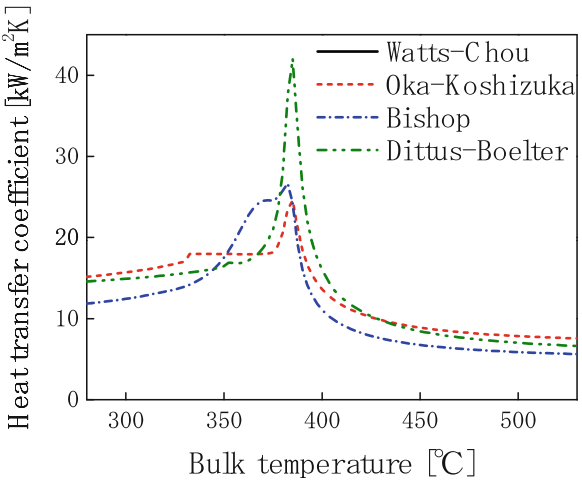


Fig. 1.60 Comparison of heat transfer correlations

Table 1.16 Maximum cladding surface temperatures predictions by different heat transfer correlations (in °C)

	BOEC	MOEC	EOEC
Watts–Chou	637	638	647
Oka–Koshizuka	604	606	603
Bishop	627	629	635
Dittus–Boelter	617	618	616

Taken from ref. [122]

photo of one ribbed tube, a so-called rifled tube is seen in Fig. 1.61. Critical heat flux may also be increased by use of the grid spacers.

There are no correlations of critical flow in supercritical fluid. The condensation of supercritical steam in water also needs to be tested by experiments. A list of thermal-hydraulic experiments done by researchers of Kyushu University using HCFC22 as surrogate fluid is given in Fig. 1.62. Single-tube and 7-rod bundle tests were done. A photo of the test loop installed at Kyushu University along with the test sections is seen in Fig. 1.63 [126]. Single-tube and 7-rod bundle heat transfer testing were carried out at JAEA using supercritical water as working fluid [127, 128].

Experiments on some austenitic stainless steels as cladding materials were performed at JAEA and the University of Tokyo. Creep rapture strength of austenitic stainless steel PNC316 and PNC1520 that had been developed for the sodium cooled fast reactor and that of PNC316 are shown in Fig. 1.64 [119] as well as the result of fuel rod analysis. The upper part of the fuel rod is exposed to high temperatures and general corrosion is important at them. Stress



Fig. 1.61 Rifled tube of a supercritical boiler

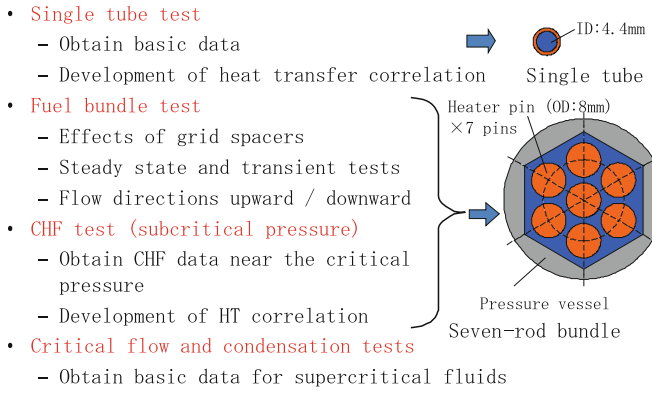


Fig. 1.62 Thermal-hydraulic experiments done by researchers of Kyushu University

corrosion cracking needs to be tested at low temperature. The cladding material development should be made in close collaboration with considerations on water chemistry. The difference from LWRs is that all the reactor coolant goes to the turbine and is purified after condensation. The Super LWR and Super FR are like the supercritical FPPs.

The temperature difference between the moderator in the water rods and the coolant in the fuel channels is large, approximately 250°C. Without thermal insulator, thermal stress exceeds the tensile strength of typical stainless steel as shown in Fig. 1.65 [122]. Yittria-stabilized zirconia was developed for the thermal insulator [129].

Supercritical water exhibits unique properties. Supercritical water chemistry and dissolution of corrosion products in supercritical water have been studied [130–132].

Researchers and engineers in the Japanese nuclear industry have also been studying reactor plants, thermal hydraulics of supercritical fluid and materials [133–138].

The symposium on supercritical water cooled reactors started in 2000. The first and second ones were held at the University of Tokyo in November 2000 and September 2003. The third one was held at Shanghai Jiao Tong University, China in March 2007. The fourth one was held is Heidelberg, Germany in March 2009. The proceedings were published.



Test loop

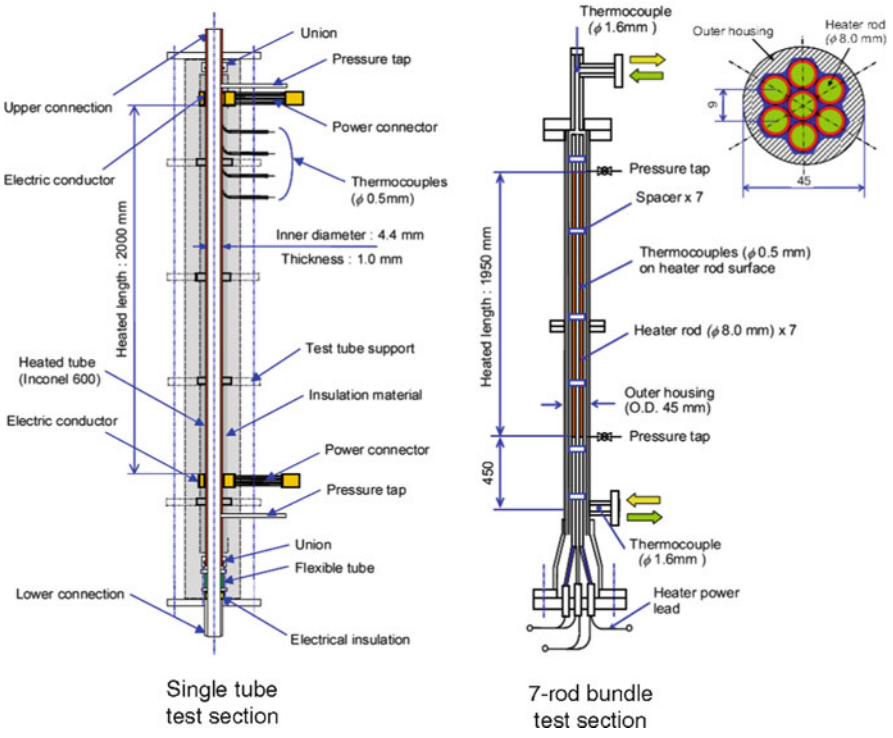


Fig. 1.63 Thermal-hydraulic test loop installed at Kyusyu University. (Taken from ref. [126] and used with permission from Atomic Energy Society of Japan)

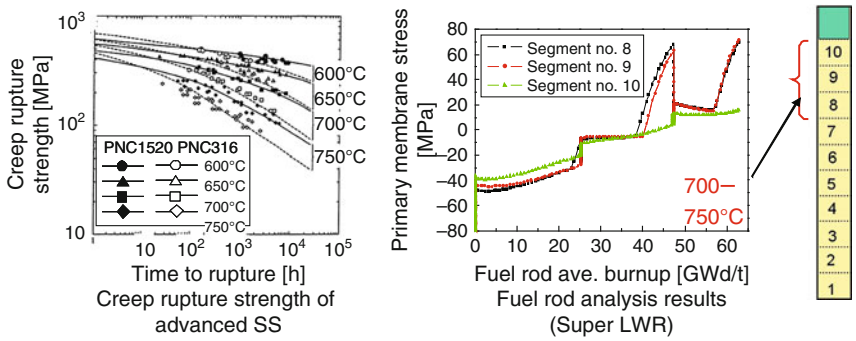


Fig. 1.64 Creep rupture strength of austenitic stainless steel and primary membrane stress on a fuel rod cladding. (Taken from ref. [119])

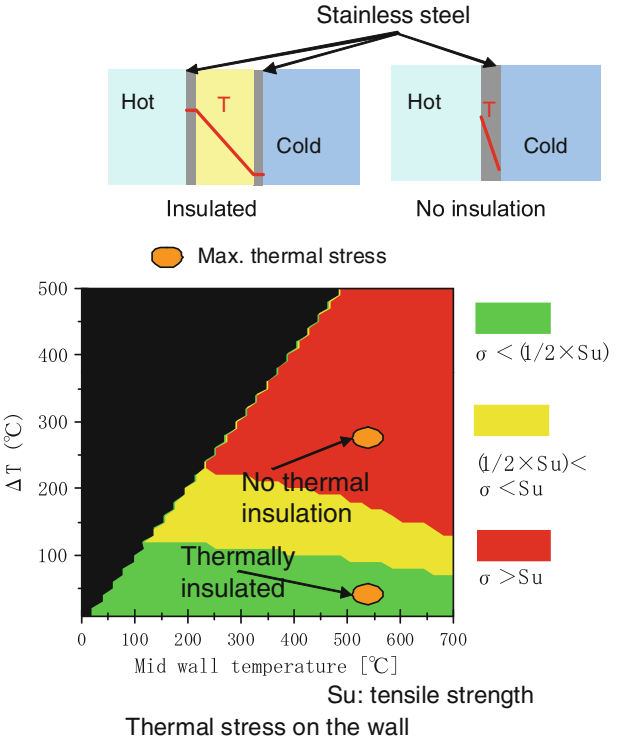


Fig. 1.65 Thermal stresses with and without thermal insulator layer. (Taken from ref. [122])

1.5.2 Europe

Research and development of the supercritical water cooled reactor are being done in Europe as the High Performance Light Water Reactor (HPLWR) with funding by the European Union. The first phase work for the HPLWR was conducted in 2000–2002. Forschungs Zentrum Karlsruhe (FZK) was the coordinator. The University of Tokyo was invited to participate and its design was taken as the reference. The results of the first phase were reported in refs. [139–142]. The second phase started in September 2006 again with FZK as the coordinator. Design and integration, core design, safety, materials, and heat transfer are being studied by ten European partners [143–145]. The HPLWR activities are found in the FZK homepage [146].

1.5.3 GIF and SCWR

The Generation Four International Forum (GIF) was started in 2002. The supercritical water cooled reactor (SCWR) was taken as one of the six generation 4 reactors. Canada serves as the lead country. The activities are seen in the GIF home page [147]. Canadian researchers are also carrying out studies of a pressure tube type SCWR [148–151].

1.5.4 Korea, China, US, Russia and IAEA

SCWR research in Korea has been mainly promoted by the Korea Atomic Energy Research Institute (KAERI) and Korea Electric Power Research Institute (KEPRI) [152–156]. Funding for research and development of the SCWR was begun in 2007 in China. Eight organizations take part in it. Shanghai Jiao Tong University is the lead organization [157]. R&D, conceptual design, and construction of an experimental SCWR (ESCWR) was announced in 2009. In the US, SCWR had also been researched in the early 2000s [158–160]. Russian research has a long history and many experiences have been obtained with supercritical FPPs. There are thermal-hydraulic test loops at IPPE in Obninsk. A workshop on supercritical water cooled reactors was held at NIKIET in Moscow in October 2008. The Coordinated Research Program (CPP) on heat transfer of supercritical fluid has been organized by the International Atomic Energy Agency (IAEA) [161].

Glossary

ABWR	advanced boiling water reactor
ADS	automatic depressurization system
ATWS	anticipated transients without scream

BOP	balance of plant
CAD	computer aided design
CDF	core damage frequency
CFD	computational fluid dynamics
CPP	Coordinated Research Program
CR	control rod
CV	containment vessel
ECCS	emergency core cooling system
FPP	fossil-fuel fired power plant
FR	fast reactor
FZK	Forschungs Zentrum Karlsruhe
GIF	Generation Four International Forum
HPLWR	High Performance Light Water Reactor
IAEA	International Atomic Energy Agency
JAEA	Japan Atomic Energy Agency
KAERI	Korea Atomic Energy Research Institute
KEPRI	Korea Electric Power Research Institute
LLLP	low leakage fuel loading pattern
LMFBR	liquid metal cooled fast breeder reactors
LOCA	loss of coolant accidents
LOSP	loss of offsite power
LPCI	low pressure core injection system
LWR	light water reactor
MCST	maximum cladding surface temperature
MDHFR	minimum deteriorated heat flux ratio
MLHGR	maximum linear heat generation rate
PCMI	pellet cladding mechanical interaction
PID	proportional, integral and differential
PSA	probabilistic safety assessment
RCP	reactor coolant pump
RPV	reactor pressure vessel
SCLWR	supercritical pressure light water cooled reactor
SCWR	supercritical water cooled reactor

References

1. J. M. Utterback, Mastering the Dynamics of Innovation, Harvard Business School Press, Boston MA, USA (1994)
2. Y. Oka, S. Koshizuka and T. Yamasaki, "Direct Cycle Light Water Reactor Operating at Supercritical Pressure," *Journal of Nuclear Science and Technology*, Vol. 29(6), 585–588 (1992)
3. Y. Oka and S. Koshizuka, "Concept and Design of a Supercritical-Pressure, Direct-Cycle Light Water Reactor," *Nuclear Technology*, Vol. 103, 295–302 (1993)
4. Y. Oka, S. Koshizuka, T. Jevremovic and Y. Okano, "Systems Design of Direct-Cycle, Supercritical-Water-Cooled Reactors," *Transactions of ENC'94, International Nuclear Congress*, Vol. 2, 473–477 (1994)

5. Y. Oka, S. Koshizuka, T. Jevremovic and Y. Okano, "Systems Design of Direct-Cycle Supercritical-Water-Cooled Fast Reactors," *Nuclear Technology*, Vol. 109, 1–10 (1995)
6. Y. Oka, S. Koshizuka, T. Jevremovic, Y. Ohno and K. Kitoh, "Direct-Cycle Supercritical-Pressure, Light-Water-Cooled Reactors for Improving Economy and Plutonium Utilization," *Proc. Global95, International Conference on Evaluation of Emerging Nuclear Fuel Cycle Systems*, Versailles, France, September 11–14, 1995, 930–937 (1995)
7. Y. Oka and S. Koshizuka, "General Features of Direct-Cycle, Supercritical-Pressure, Light-Water-Cooled Reactors," *Proc. ICONE-4*, New Orleans, LA, April, March 10–14, 1996, Vol. 2, 191–198 (1996)
8. Y. Okano, S. Koshizuka and Y. Oka, "Core Design of a Direct-Cycle, Supercritical-pressure, Light Water Reactor with Double Tube Water Rods," *Journal of Nuclear Science and Technology*, Vol. 33, 365–373 (1996)
9. K. Yamagata, K. Nishikawa, S. Hasegawa, T. Fujii and S. Yoshida, "Forced Convective Heat Transfer to Supercritical Water Flowing in Tubes," *International Journal of Heat and Mass Transfer*, Vol. 15, 2575 (1972)
10. S. Koshizuka, N. Takano and Y. Oka, "Numerical Analysis of Deterioration Phenomena in Heat Transfer to Supercritical Water," *International Journal of Heat and Mass Transfer*, Vol. 38, 3077–3084 (1995)
11. K. Kitoh, S. Koshizuka and Y. Oka, "Improvement of Transient Criteria of a Supercritical Water Cooled Reactor Based on Numerical Simulation," *Proc. ICONE-5*, Nice, France, May 26–30, 1997, ICONE5-2341 (1997)
12. K. Dobashi, A. Kimura, Y. Oka and S. Koshizuka, "Conceptual Design of a High Temperature Power Reactor Cooled and Moderated by Supercritical Light Water," *Annals of Nuclear Energy*, Vol. 25(8), 487–505 (1998)
13. T. Mukohara, S. Koshizuka and Y. Oka, "Core Design of a High-Temperature Fast Reactor Cooled by Supercritical Light Water," *Proc. ICONE-6*, San Diego, CA, May 10–15, 1998, ICONE-6229 (1998)
14. Y. Okano, S. Koshizuka and Y. Oka, "Design of Water Rod Cores of a Direct Cycle, Super-Critical-Pressure Light Water Reactor," *Annals of Nuclear Energy*, Vol. 21, 601–611 (1994)
15. Y. Okano, S. Koshizuka and Y. Oka, "Core Design of a Direct-Cycle, Supercritical-Pressure, Light Water Reactor with Double Tube Water Rods," *Journal of Nuclear Science and Technology*, Vol. 33, 365–373 (1996)
16. Y. Okano, S. Koshizuka and Y. Oka, "Direct-Cycle, Supercritical-Pressure, Light-Water-Cooled Thermal Spectrum Reactor with Double Tube Water Rods," *Proc. PHYSOR 96*, Vol. 2, 11–20 (1996)
17. K. Dobashi, Y. Oka and S. Koshizuka, "Core and Plant Design of the Power Reactor Cooled and Moderated by Supercritical Light Water with Single Tube Water Rods," *Annals of Nuclear Energy*, Vol. 24(16), 1281–1300 (1997)
18. A. Yamaji, Y. Oka and S. Koshizuka, "Core Design of a High Temperature Reactor Cooled and Moderated by Supercritical Light Water," *Proc. GENES4/ANP2003*, Kyoto, Japan, September 15–19, 2003, Paper 1041 (2003)
19. A. Yamaji, Y. Oka and S. Koshizuka "Three-dimensional Core Design of SCLWR-H with Neutronics and Thermal-Hydraulic Coupling," *Proc. Global2003*, New Orleans, November 16–20, 2003, 1763–1771 (2003)
20. A. Yamaji, Y. Oka and S. Koshizuka, "Three-dimensional Core Design of High Temperature Supercritical-Pressure Light Water Reactor with Neutronic and Thermal-Hydraulic Coupling," *Journal of Nuclear Science and Technology*, Vol. 42(1), 8–19 (2005)
21. K. Okumura, K. Kaneko and K. Tsuchihashi, "SRAC95; General Purpose Neutronics Code System," JAERI-Data/Code 96-015, Japan Atomic Energy Research Institute (JAERI) (1996) (in Japanese)
22. A. Yamaji, K. Kamei, Y. Oka and S. Koshizuka, "Improved Core Design of High Temperature Supercritical-Pressure Light Water Reactor," *Proc. ICAPP'04*, Pittsburgh, PA, June 13–17, 2004, Paper 4331 (2004)

23. A. Yamaji, K. Kamai, Y. Oka and S. Koshizuka, "Improved Core Design of the High Temperature Supercritical-Pressure Light Water Reactor," *Annals of Nuclear Energy*, Vol. 32, 651–670 (2005)
24. K. Kamei, A. Yamaji, Y. Ishiwatari, Y. Oka and J. Liu, "Fuel and Core Design of Super Light Water Reactor with Low Leakage Fuel Loading Pattern," *Journal of Nuclear Science and Technology*, Vol. 43(2), 129–139 (2006)
25. A. Yamaji, T. Tanabe, Y. Oka, J. Yang, J. Liu, Y. Ishiwatari and S. Koshizuka, "Evaluation of the Nominal Peak Cladding Surface Temperature of the Super LWR with Subchannel Analyses," *Proc. Global 2005*, Tsukuba, Japan, October 9–13, 2005, Paper 556, (2005)
26. J. Yang, Y. Oka, J. Liu, Y. Ishiwatari and A. Yamaji, "Development on Statistical Thermal Design Procedure for Super LWR," *Proc. Global 2005*, Tsukuba, Japan, October 9–13, 2005 Paper 555 (2005)
27. J. Yang, Y. Oka, J. Liu, Y. Ishiwatari and A. Yamaji, "Development of Statistical Thermal Design Procedure to Engineering Uncertainty of Super LWR," *Journal of Nuclear Science and Technology*, Vol. 43(1), 32–42 (2006)
28. M. Kadowaki, "Rationalization of Core Design Method and Improved Core Design of Super LWR," Master's thesis, University of Tokyo (2009) (in Japanese)
29. Y. Ishiwatari, I. Hongo, Y. Oka, et al., "Numerical Analysis of Heat Transfer Enhancement by Grid Spacers in Supercritical Water," *Proc. NURETH-13*, Kanazawa, Japan, September 27–October 2, 2009, N13P1436 (2009)
30. A. Yamaji, Y. Oka and S. Koshizuka, "Fuel Design of High Temperature Reactors Cooled and Moderated by Supercritical Light Water," *Proc. GENES4/ANP2003*, Kyoto, Japan, September 15–19, 2003, Paper 1040 (2003)
31. M. Suzuki and H. Saitou, "Light Water Reactor Fuel Analysis Code FEMAXI-6 (Ver.1); Detailed Structure and User's Manual," Department of Reactor Safety Research, Nuclear Safety Research Center, Tokai Research Establishment, Japan Atomic Energy Research Institute (JAERI)
32. A. Yamaji, Y. Oka, Y. Ishiwatari, J. Liu and S. Koshizuka, "Rationalization of the Fuel Integrity and Transient Criteria for the Super LWR," *Proc. ICAPP'05*, Seoul, Korea, May 15–19, 2005, Paper 5538 (2005)
33. A. Yamaji, Y. Oka, Y. Ishiwatari, J. Liu, S. Koshizuka and M. Suzuki, "Principle of Rationalizing the Criteria for Abnormal Transients of the Super LWR with Fuel Rod Analyses," *Annals of Nuclear Energy*, Vol. 33(11–12), 984–993 (2006)
34. A. Yamaji, Y. Oka, J. Yang, J. Liu, Y. Ishiwatari and S. Koshizuka, "Design and Integrity Analyses of the Super LWR Fuel Rod", *Proc. Global 2005*, Tsukuba, Japan, October 9–13, 2005 Paper 556 (2005)
35. K. Kamei, A. Yamaji, Y. Ishiwatari, J. Liu and Y. Oka, "Fuel and Core Design of Super LWR with Stainless Steel cladding," *Proc. ICAPP'05*, Seoul, Korea, May 15–19, 2005, Paper 5428 (2005)
36. T. Nakatsuka, Y. Oka and S. Koshizuka, "Control of a Fast Reactor Cooled by Supercritical Light Water," *Nuclear Technology*, Vol. 121, 81–92 (1998)
37. T. Nakatsuka, Y. Oka and S. Koshizuka, "Plant Control of a Fast Breeder Reactor Cooled by Supercritical Light Water," *Proc. 1997 International Meeting on Advanced Reactors Safety (ARS '97)*, Orlando, FL, June 1–5 1997, 1165–1172 (1997)
38. T. Nakatsuka, Y. Oka and S. Koshizuka, "Plant Control of the Fast Reactor Cooled by Supercritical Light Water", *Proc. ICONE-6*, San Diego, CA, May 10–15, 1998, ICONE-6224 (1998)
39. Y. Ishiwatari, Y. Oka and S. Koshizuka, "Control of a High Temperature Supercritical Pressure Light Water Cooled and Moderated Reactor with Water Rods," *Journal of Nuclear Science and Technology*, Vol. 40(5), 298–306 (2003)

40. Y. Ishiwatari, C. Peng, T. Sawada, S. Ikejiri and Y. Oka, "Design and Improvement of Plant Control System for a Super Fast Reactor," *Proc. ICAPP'09*, Tokyo, Japan, May 10–14 2009, Paper 9261 (2009)
41. T. Nakatsuka, Y. Oka and S. Koshizuka, "Startup Thermal Considerations for Supercritical-Pressure Light Water-Cooled Reactors," *Nuclear Technology*, Vol. 134(3), 221–230 (2001)
42. T. Nakatsuka, Y. Oka and S. Koshizuka, "Start-up of Supersritical-pressure Light Wtater Cooled Reactors," *Proc. ICONE-8*, Baltimore, MD., April 2–6, 2000, ICONE-8304 (2000)
43. T. T. Yi, Y. Ishiwatari, S. Koshizuka and Y. Oka, "Startup Thermal Analysis of a High-Temperature Supercritical-Pressure Light Water Reactor," *Journal of Nuclear Science and Technology*, Vol. 41(8), 790–801 (2004)
44. T. T. Yi, Y. Ishiwatari, J. Liu, S. Koshizuka and Y. Oka, "Thermal and Stability Considerations of Super LWR during Sliding Pressure Startup," *Journal of Nuclear Science and Technology*, Vol. 42(6), 537–548 (2005)
45. T. T. Yi, Y. Ishiwatari, S. Koshizuka and Y. Oka, "Startup of a High-Temperature Reactor Cooled and Moderated by Supercritical-Pressure Light Water", *Proc. GENES4/ANP2003*, Kyoto, Japan, September 15–19, 2003, Paper 1036 (2003)
46. S. Yamada, Y. Ishiwatari, S. Ikejiri, et al., "Design and Analysis of Procedures for System Pressurization and Line-Switching to One-through Mode in Plant Startup of SCWR," *Proc. NURETH-13*, Kanazawa, Japan, September 27–October 2, 2009, N13P1435 (2009)
47. S. Ji, H. Shirahama, S. Koshizuka and Y. Oka, "Stability Analysis of Supercritical-Pressure Light Water-Cooled Reactor in Constant Pressure Operation," *Proc. ICONE-9*, Nice, France, April 8–12, 2001, ICONE-9306 (2001)
48. Tin Tin Yi, S. Koshizuka and Y. Oka, "Linear Stability Analysis of a High-temperature Supercritical-pressure Light Water Reactor", *Proc. Global 2003*, New Orleans, LA, November 16–20, 2003, 1781–1790 (2003)
49. T. T. Yi, S. Koshizuka and Y. Oka, "A Linear Stability Analysis of Supercritical Water Reactors, (I) Thermal-Hydraulic Stability," *Journal of Nuclear Science and Technology*, Vol. 41(12), 1166–1175 (2004)
50. T. T. Yi, S. Koshizuka, Y. Oka, "A Linear Stability Analysis of Supercritical Water Reactors, (II) Coupled Neutronic Thermal-Hydraulic Stability," *Journal of Nuclear Science and Technology*, Vol. 41(12), 1176–1186 (2004)
51. J. Cai, Y. Ishiwatari, S. Ikejiri and Y. Oka, "Thermal and Stability Considerations for a Supercritical Water-Cooled Fast Reactor with Downward-Flow Channels During Power-Raising Phase of Plant Startup," *Nuclear Engineering and Design*, Vol. 239, 665–679 (2009)
52. A. Hotta, et al., "BWR Regional Instability Analysis by TRAC0BF1-ENTRÉE-I: Application to Density-wave Oscillation," *Nuclear Technology*, Vol. 135(1), 1–6 (2001)
53. A. Hotta, et al., "BWR Regional Instability Analysis by TRAC0BF1-ENTRÉE-II: Application to Righals Unit-1 Stability Test," *Nuclear Technology*, Vol. 135(1), 17–38 (2001)
54. Y. Ishiwatari, Y. Oka, S. Koshizuka, A. Yamaji and J. Liu, "Safety of Super LWR, (I) Safety System Design," *Journal of Nuclear Science and Technology*, Vol. 42(11), 927–934 (2005)
55. Y. Ishiwatari, Y. Oka, S. Koshizuka and J. Liu, "Safety Characteristics of the Super LWR Design Concept," *Proc. ICAPP'07, Nice*, France, May 13–18, 2007, Paper 7309 (2007)
56. Y. Ishiwatari, Y. Oka and S. Koshizuka, "Safety of the Super LWR," *Nuclear Engineering and Technology*, Vol. 39(4), 257–272 (2007)
57. Y. Okano, S. Koshizuka, et al., "Flow Induced Transient Analysis of a Supercritical Pressure, Light-Water-Cooled Fast Breeder Reactor," *Proc. 3 rd JSME/ASME Joint International Conf. on Nuclear Engineering*, Kyoto, Japan, April 23–27, 1995, 891–895 (1995)
58. K. Kitoh, S. Koshizuka and Y. Oka, "Control Rod, Pressure and Flow-Induced Accident and Transient Analyses of a Direct-Cycle, Supercritical Pressure, Light-Water-Cooled Fast Breeder Reactor," *Proc. ICONE-4*, New Orleans, LA, April, March 10–14, 1996, Vol. 2, 537–545 (1996)

59. Y. Okano, S. Koshizuka and Y. Oka, "Flow and Pressure-Induced Transient Analysis of the Supercritical-Pressure, Light-Water-Cooled and Moderated Reactor," *Proc. ICONE-4*, New Orleans, LA, April, March 10–14, 1996, Vol. 1, 771–780 (1996)
60. Y. Okano, S. Koshizuka, K. Kitoh and Y. Oka, "Flow-Induced Accident and Transient Analyses of a Direct-Cycle, Light-Water Cooled, Fast Breeder Reactor Operating at Supercritical Pressure," *Journal of Nuclear Science and Technology*, Vol. 33(4), 307–315 (1996)
61. K. Kitoh, S. Koshizuka and Y. Oka, "Pressure and Flow-Induced Accident and Transient Analysis of a Direct-Cycle, Supercritical-Pressure, Light-Water-Cooled Fast Reactor," *Nuclear Technology*, Vol. 123, 233–244 (1998)
62. Y. Ishiwatari, Y. Oka and S. Koshizuka, "Safety Analysis of a High Temperature Supercritical Pressure Light Water Cooled and Moderated Reactor," *Proc. ICAPP*, Hollywood, FL, June 9–13, 2002, Paper 1045 (2002)
63. Y. Ishiwatari, Y. Oka and S. Koshizuka, "Safety Analysis of High Temperature Reactor Cooled and Moderated by Supercritical Water," *Proc. GENES4/ANP2003*, Kyoto, Japan, September 15–19, 2003, Paper 1059 (2003)
64. Y. Ishiwatari, Y. Oka and S. Koshizuka, "Safety Design Principle of Supercritical Water Cooled Reactors," *Proc. ICAPP'04*, Pittsburg, PA, June 13–17, 2004, Paper 4319 (2004)
65. Y. Ishiwatari, Y. Oka, S. Koshizuka, A. Yamaji and J. Liu, "Safety of Super LWR, (II) Safety Analysis at Supercritical Pressure," *Journal of Nuclear Science and Technology*, Vol. 42 (11), 935–948 (2005)
66. K. Kitoh, S. Koshizuka and Y. Oka, "Refinement of Transient Criteria and Safety Analysis for a High-Temperature Reactor Cooled by Supercritical Water," *Nuclear Technology*, Vol. 135, 252–264 (2001)
67. F. D. Coffman, Jr., LOCA Temperature Criterion for Stainless Steel Clad Fuel, NUREG-0065, (1976)
68. Y. Ishiwatari, Y. Oka, S. Koshizuka and J. Liu, "ATWS Characteristics of Super LWR With/Without Alternative Action," *Journal of Nuclear Science and Technology*, Vol. 44(4), 572–580 (2007)
69. Y. Ishiwatari, Y. Oka and S. Koshizuka, "ATWS Analysis of Supercritical Pressure Light Water Cooled Reactor," *Proc. Global 2003*, New Orleans, LA, November 16–20, 2003, 2335–2341 (2003)
70. K. Yoshimura, Y. Ishiwatari, et al., "Development of Transient Subchannel Analysis Code of Super LWR and Application to Flow Decreasing Events," *Proc. NURETH-13*, Kanazawa, Japan, September17–October 2, 2009, N13P1434 (2009)
71. Y. Ishiwatari, Y. Oka, S. Koshizuka and J. Liu, "LOCA Analysis of Super LWR," *Journal of Nuclear Science and Technology*, Vol. 43(3), 231–241 (2006)
72. J.H. Lee, S. Koshizuka and Y. Oka, "Development of a LOCA Analysis Code for the Supercritical-Pressure Light Water Cooled Reactors," *Annals of Nuclear Energy*, Vol. 25 (16), 1341–1361 (1998)
73. J.H. Lee, "LOCA Analysis and Safety System Consideration for the Supercritical-Water Cooled Reactor," Doctoral Thesis, the University of Tokyo (1996)
74. Y. Ishiwatari, Y. Oka and S. Koshizuka, "LOCA Analysis of High Temperature Reactor Cooled and Moderated by Supercritical Water," *Proc. GENES4/ANP2003*, Kyoto, Japan, September 15–19, 2003, Paper 1060 (2003)
75. J.H. Lee, Y. Oka and S. Koshizuka, "Safety System Consideration of a Supercritical-Water Cooled Fast Breeder Reactor with Simplified PSA," *Reliability Engineering & System Safety*, Vol. 64, 327–338 (1999)
76. Y. Oka and S. Koshizuka "Supercritical-Pressure, Once-Through Cycle Light Water Cooled Reactor Concept," *Journal of Nuclear Science and Technology*, Vol. 38(12), 1081–1089 (2001)

77. Y. Oka and S. Koshizuka "Once-Through Cycle, Supercritical-Pressure Light Water Cooled Reactor Concept," *Proc. Global 2001*, Paris, France, September 9–13, 2001, FP-172 (2001)
78. Y. Oka, S. Koshizuka, Y. Ishiwatari and A. Yamaji "Elements of Design Consideration of Once-Through Cycle, Supercritical-Pressure Light Water Cooled Reactor," Proc. ICAPP, Hollywood, FL, June 9–13, 2002, Paper 1005 (2002)
79. Y. Oka, Y. Ishiwatari, et al., "Research Program of a Super Fast Reactor," *Proc. ICAPP'06*, Reno, NV, June 4–8, 2006, Paper 6353 (2006)
80. J. Yoo, Y. Ishiwatari, Y. Oka and J. Liu, "Composite Core Design of High Power Density Supercritical Water Cooled Fast Reactor," *Proc. Global 2005*, Tsukuba, Japan, October 9–13, 2005, Paper 248 (2005)
81. J. Yoo, Y. Ishiwatari, Y. Oka and J. Liu, "Conceptual Design of Compact Supercritical Water-cooled Fast Reactor with Thermal Hydraulic Coupling," *Annals of Nuclear Energy*, Vol. 33(11–12), 945–956 (2006)
82. J. Yoo, Y. Oka, J. Yang and J. Liu, "Static Thermal Design Analyses of Supercritical Water-Cooled Fast Reactor," *Proc. ICAPP'06*, Reno, NV, June 4–8, 2006, Paper 6224 (2006)
83. J. Yoo, Y. Ishiwatari, Y. Oka and J. Liu, "Subchannel Analysis of Supercritical Light Water-Cooled Fast Reactor Fuel Assembly," *Nuclear Engineering and Design*, Vol. 237, 1096–1105 (2007)
84. L. Cao, Y. Oka, Y. Ishiwatari and Z. Shang, "Fuel, Core Design and Subchannel Analysis of a Super Fast Reactor," *Journal of Nuclear Science and Technology*, Vol. 45(2), 138–148 (2008)
85. J. Yoo, Y. Oka, Y. Ishiwatari and J. Liu, "Thermo-Mechanical Analysis of Supercritical Pressure Light Water-Cooled Fast Reactor Fuel Rod by FEMAXI-6 Code", *Annals of Nuclear Energy*, Vol. 33(17), 1379–1390 (2006)
86. H. Ju, L. Cao, Y. Ishiwatari, Y. Oka and S. Ikejiri, "Research and Development of a Super Fast Reactor (3) Fuel Rod Analyses under Normal Operating Condition," *Proc. 16PBNC*, Aomori, Japan, October 13–18, 2008, P16P1292 (2008)
87. H. Ju, L. Cao, et al., "Core Design and Fuel Rod Analyses of a Super Fast Reactor with High Power Density," *Proc. ICAPP'09*, Tokyo, Japan, May 10–14, 2009, Paper 9264 (2009)
88. L. Cao, H. Ju, Y. Ishiwatari, et al., "Research and Development of a Super Fast Reactor (2) Core Design Improvement on Local Void Reactivity," *Proc. 16th PBNC*, Aomori, Japan, October 13–18, 2008, P16P1291 (2008)
89. L. Cao, Y. Oka, Y. Ishiwatari and S. Ikejiri, "Three-Dimensional Core Analysis on a Super Fast Reactor with Negative Local Void Reactivity," *Nuclear Engineering and Design*, Vol. 239, 408–417 (2009)
90. X. Cheng, E. Laurien and Y.H. Yang, "CFD Analysis of Heat Transfer in Supercritical Water in Different Flow Channels," *Proc. Global 2005*, Tsukuba, Japan, October 9–13, 2005, Paper 369 (205)
91. J. Yang, Y. Oka, Y. Ishiwatari, J. Liu and J. Yoo, "Numerical Study on Heat Transfer in Supercritical Pressure Water in Tight Fuel Rod Channels," *Proc. ICAPP'06*, Reno, NV, June 4–8 2006, Paper 6334 (2006)
92. J. Yang, Y. Oka, Y. Ishiwatari, J. Liu and J. Yoo, "Numerical Investigation of Heat Transfer in Upward Flows of Supercritical Water in Circular Tubes and Tight Fuel Rod Bundles," *Nuclear Engineering and Design*, Vol. 237, 420–430 (2007)
93. J. Gou, Y. Ishiwatari, Y. Oka, M. Yamakawa and S. Ikejiri, "Research and Development of Super Fast Reactor (5) Thermal Hydraulic Analysis of Tight-laiice Subchannels," *Proc. 16th PBNC*, Aomori, Japan, October 13–18, 2008, P16P1294 (2008)
94. J. Gou, Y. Ishiwatari, Y. Oka, M. Yamakawa, "CFD Analyses in Tight-Lattice Subchannels and Seven-Rods Bundle Geometries of a Super Fast Reactor," *Proc. ICAPP09*, Tokyo, Japan, May 10–15, 2009, Paper 9262 (2009)

95. L. Cao, H. Lu, Y. Ishiwatari, Y. Oka and S. Ikejiri, "Research and Development of a Super Fast Reactor (4) Transmutation Analyses of Minor Actinides and Transuranium Elements," *Proc. 16th PBNC*, Aomori, Japan, October 13–18, 2008, P16P1293 (2008)
96. H. Lu, Y. Ishiwatari, C. Han, Y. Oka, S. Ikejiri, "Evaluation of Transmutation Performance of Long-Lived Fission Products with a Super Fast Reactor," *Proc. ICAPP09*, Tokyo, Japan, May 10–15, 2009, Paper 9263 (2009)
97. S. Ikejiri, Y. Guo, Y. Ishiwatari, Y. Oka and T. Sawada, "Research and Development of a Super Fast Reactor (6) Analyses of Abnormal Transients," *Proc. 16th PBNC*, Aomori, Japan, October 13–18, 2008, P16P1295 (2008)
98. S. Ikejiri, Y. Ishiwatari, Y. Oka, "Loss of Coolant Accident Analysis of a Supercritical-Pressure Water-Cooled Fast Reactor with Downward Flow Channels," *Proc. ICAPP09*, Tokyo, Japan, May 10–15, 2009, Paper 9257 (2009)
99. J. Cai, Y. Ishiwatari, S. Ikejiri and Y. Oka, "Thermal and Stability Considerations for a Supercritical Water-cooled Fast Reactor During Power-Raising Phase of Plant Startup," *Proc. ICAPP09*, Tokyo, Japan, May 10–15, 2009, Paper 9265 (2009)
100. J. Cai, Y. Ishiwatari, S. Ikejiri and Y. Oka, "Thermal and Stability Considerations for a Supercritical Water-Cooled Fast Reactor with Downward-Flow Channels During Power-Raising Phase of Plant Startup," *Nuclear Engineering and Design*, Vol. 239, 665–679 (2009)
101. Y. Ishiwatari, C. Peng, T. Sawada, S. Ikejiri and Y. Oka, "Design and Improvement of Plant Control System for a Super Fast Reactor," *Proc. ICAPP09*, Tokyo, Japan, May 10–15, 2009, Paper 9261 (2009)
102. Y. Ishiwatari, M. Yamakawa, Y. Oka and S. Ikejiri, "Research and Development of a Super Fast Reactor (1) Overview and High-Temperature Structural Design," *Proc. 16th PBNC*, Aomori, Japan, October 13–18, 2008, P16P1290 (2008)
103. K. Kataoka and Y. Oka, "Neutronic Feasibility of Supercritical Steam Cooled Fast Breeder Reactor," *Journal of Nuclear Science and Technology*, Vol. 28, 585–58 (1991)
104. Y. Oka and K. Kataoka "Conceptual Design of a Fast Breeder Reactor Cooled by Supercritical Steam," *Annals of Nuclear Energy*, Vol. 19, 243–247 (1992)
105. Y. Oka, T. Jevremovic and S. Koshizuka, "Negative Void Reactivity in Large FBRs with a Hydrogeneous Moderator," *Transactions of American Nuclear Society*, Vol. 68, Part A, 301–303 (1993)
106. Y. Oka and T. Jevremovic, "Negative Void Reactivity in Large Fast Breeder Reactors with Hydrogeneous Moderator Layer," *Annals of Nuclear Energy*, Vol. 23, 1105–1115 (1996)
107. Y. Oka and S. Koshizuka, "Conceptual Design of a Supercritical-Pressure Direct-Cycle Light Water Reactor," *Proc. ANP'92*, Tokyo, Japan, October 25–29, 1992, Vol. 1, Session 4.1, 1–7 (1992)
108. K. Kataoka, "A Supercritical Steam Cooled Fast Breeder Reactor," Doctoral thesis, the University of Tokyo (1990) (in Japanese)
109. T. Jeveremovic, "Conceptual Design of Fast Breeder Reactors Cooled by Supercritical Steam," Doctoral thesis, the University of Tokyo (1993)
110. J.H. Lee, "LOCA Analysis and Safety System Consideration for the Supercritical-Water Cooled Reactor," Doctoral thesis, the University of Tokyo (1996)
111. Y. Okano, "Systems Design of Direct-Cycle Supercritical-Water-Cooled Fast Reactors," Doctoral thesis, the University of Tokyo (1997) (in Japanese)
112. N. Takano, "A Numerical Investigation of Heat Transfer Deterioration Mechanism at Supercritical Water Cooling," Master's thesis, the University of Tokyo (1994) (in Japanese)
113. K. Kitoh, "Safety Analysis of a Supercritical Water Cooled Reactor," Doctoral thesis, the University of Tokyo (1997) (in Japanese)
114. K. Dobashi, "Conceptual Design of Supercritical-pressure Light Water Cooled and Moderated Reactor," Doctoral thesis, the University of Tokyo (1998) (in Japanese)
115. T. Nakatsuka, "Control and Startup of Supercritical Pressure Light Water Cooled Reactor," Doctoral thesis, the University of Tokyo (1998) (in Japanese)

116. T. Mukohara, "Design of Supercritical-Pressure Light Water Cooled Fast Reactor and the Subchannel Analysis," Doctoral thesis, the University of Tokyo, (2001) (in Japanese)
117. Y. Tanabe, "Subchannel Analysis of Super LWR," Master's thesis, the University of Tokyo, (2005) (in Japanese)
118. T. T. Yi, "Startup and Stability of a High-Temperature Supercritical-Pressure Light Water Reactor," Doctoral thesis, the University of Tokyo (2004)
119. A. Yamaji, "Core and Fuel Design of Super LWR," Doctoral thesis, the University of Tokyo (2005) (in Japanese)
120. J. Yoo, "Three-dimensional Core Design of Large Scale Supercritical Light Water Cooled Fast Reactor", Doctoral thesis, the University of Tokyo (2006) (in Japanese)
121. Y. Ishiwatari, "Safety of Super LWR", Doctoral thesis, the University of Tokyo (2006) (in Japanese)
122. K. Kamei, "Core Design of Super LWR and the Safety Analysis at Subcritical-Pressure", Master's thesis, the University of Tokyo (2006) (in Japanese)
123. K. Yoshimura, "Development of a Transient Subchannel analysis code and safety analysis for the Super LWR," Graduate thesis, the University of Tokyo (2009) (in Japanese)
124. I. Hongo, "Numerical Analysis of Heat Transfer Enhancement by Grid Spacers on High Temperature Supercritical Fluid", Master's thesis, the University of Tokyo (2009) (in Japanese)
125. http://www.nuclear.jp/~rohonbu/lab/paper/paper.htm, //www.f.waseda.jp/okay/UTpaper/paper.htm
126. H. Mori, M. Ohno, et al., "Research and Development of a Super Fast Reactor (7) Heat Transfer to a Supercritical Pressure Fluid Flowing in a Sub-bundle Channel," *Proc. 16th PBNC*, Aomori, Japan, October 13–18, 2008, P16P1297 (2008)
127. K. Ezato, M. Akiba, et al., "Research and Development of a Super Fast Reactor (8) Heat Transfer Experiments Around a Simulated Fuel Rod with Supercritical Pressure Water," *Proc. 16th PBNC*, Aomori, Japan, October 13–18, 2008, P16P1240 (2008)
128. K. Ezato, Y. Seki, et al., "Heat Transfer in a Seven-Rod Test Bundle with Supercritical Pressure Water (1) Experiments," *Proc ICAPP'09,* Tokyo, Japan, May 10–14, 2009 Paper 9464 (2009)
129. K. Sasaki, T. Kubo, et al., "Research and Development of a Super Fast Reactor (10) Fabrication and Characterization of Durable Thermal Shielding Material," *Proc. 16th PBNC*, Aomori, Japan, Oct. 13–18, 2008, P16P1427 (2008)
130. Z. Han, Y. Katsumura, et al., "Effect of Temperature On the Absorption Spectra of the Solvated Electron in 1-Propanol and 2-Propanol: Pulse Radiolysis and Laser Photolysis Studies at Temperatures Up to Supercritical Condition," *Radiation Physics and Chemistry*, Vol. 77, 409–415 (2008)
131. Z. Han and Y. Muroya, "Research and Development of a Super Fast Reactor (11) An Approach to Evaluate the Elution Characteristic of Stainless Materials in Subcritical and Supercritical Water," *Proc. 16th PBNC*, Aomori, Japan, October 13–18, 2008, P16P1315 (2008)
132. Z. Han and Y. Muroya, "Development of a New Method to Study Elution Properties of Stainless Materials in Subcritical and Supercritical Water," *Proc. 4th Int. Symp. on SCWR*, Heidelberg, Germany, March 8–11, 2009, Paper No. 75 (2009)
133. S. Tanaka, Y. Shirai, et al., "Plant Concept of Supercritical Pressure Light Water Reactor," *Proc. ICONE-5*, Nice, France, May 26–30, 1997, ICONE-5-2346 (1997)
134. S. Shiga, K. Moriya, Y. Oka, S. Yoshida, H. Takahashi, "Progress of Development Project of Supercritical Water Cooled Power Reactor, 2003," *Proc. ICAPP'03*, Cordoba, Spain, May 4–7, 2003, Paper 3258 (2003)
135. A. Shioiri, K. Moriya, et al., "Development of Supercritical-Water Cooled Power Reactor Conducted by a Japanese Joint Team," *Proc. GENES4/ANP2003*, Kyoto, Japan, September 15–19, 2003, Paper 1121 (2003)
136. Y. Oka and K. Yamada, "Research and Development of High Temperature Light Water Cooled Reactor Operating at Supercritical-Pressure in Japan," *Proc. ICAPP'04*, Pittsburgh, PA, June 13–17, 2004, Paper 4233 (2004)

137. K. Yamada, S. Sakurai, et al., "Recent Activities and Future Plan of Thermal-Spectrum SCWR Development in Japan," *Proc. 3 rd Int. Symp. on SCWR*, Shanghai, China, March 12–15, 2007, Paper No. SCWR2007-P054 (2007)
138. Y. Ishiwatari, Y. Oka and K. Yamada, "Japanese R&D Projects on Pressure-Vessel Type SCWR," *Proc. 4th Int. Symp. on SCWR*, Heidelberg, Germany, March 8–11, 2009, Paper No. 73 (2009)
139. G. Heusener, U. Muller, T. Schulenberg and D. Square, "A European Development Program for a High Performance Light Water Reactor (HPLWR)," *Proc. 1st Int. Symp. on Supercritical Water-cooled Reactors*, Tokyo, Japan, November 6–9, 2000, Paper 102 (2000)
140. D. Squarer, D. Bittermann, et al., "Overview of the HPLWR Project and Future Direction," *Proc. ICAPP'03*, Cordoba, Spain, May 4–7, 2003, Paper 3137 (2003)
141. D. Squarer, T. Schulenberg, et al., "High Performance Light Water Reactor," *Nuclear Engineering and Design*, Vol. 221, 167–180 (2003)
142. J. Starflinger, N. Aksan, et al., "Roadmap for Supercritical Water-Cooled Reactor R&D in Europe," *Proc. GLOBAL 2003*, New Orleans, LA, November 16–20, 2003, 1137–1142 (2003)
143. J. Starflinger, T. Schulenberg, et al., "European Research Activities within the Project: High Performance Light Water Reactor Phase 2," *Proc. ICAPP'07*, Nice, France, May 13–18, 2007, Paper 7416 (2007)
144. T. Schulenberg and J. Starflinger, "European Research Project on the High Performance Light Water Reactor," *Proc. 4th Int. Symp. on SCWR*, Heidelberg, Germany, March 8–11, 2009, Paper No. 54 (2009)
145. J. Starflinger, T. Schulenberg, et al., "Results of the Mid-Term Assessment of the High Performance Light Water Reactor 2 Project," *Proc. ICAPP'09*, Tokyo, Japan, May 10–14, 2009, Paper 9268 (2009)
146. //www.iket.fzk.de/hplwr/
147. //www.gen-4.org/Technology/systems/scwr.htm
148. D. Brady, D. Duttey, et al., "Generation IV Reactor Development in Canada," *Proc. 3 rd Int. Symp. on SCWR*, Shanghai, China, March 12–15, 2007, SCR2007-P057 (2007)
149. D. Boyle, D. Brady, et al., "Canada's Generation IV National Program – Overview," *Proc. 4th Int. Symp. on SCWR*, Heidelberg, Germany, March 8–11, 2009, Paper No. 74 (2009)
150. C.K. Chow and H.F. Khartabil, "Conceptual Fuel Channel Designs for CANDU-SCWR," *Nuclear Engineering and Technology*, Vol. 40(2), 139–146 (2008)
151. H.F. Khartabil, "Review and Status of the Gen-IV CANDU-SCWR Passive Moderator Core Cooling System," *Proc. ICONE-16*, Orlando, FL, May 11–15, 2008, ICONE16-48741 (2008)
152. Y.Y. Bae, K.M. Bae, et al., "R&D on a Supercritical Pressure Water Cooled Reactor in Korea," *Proc. ICAPP'06*, Reno, NV, June 4–8, 2006, Paper 6022 (2006)
153. Y.Y. Bae, K.M. Bae, et al., "SCWR Research in Korea," *Proc. 3 rd Int. Symp. on SCWR*, Shanghai, China, March 12–15, 2007, SCR2007-P006 (2007)
154. Y.Y. Bae, G. Jang, et al., "Research Activities on a Supercritical Pressure Water Reactor in Korea," *Nuclear Engineering and Technology*, Vol. 39(4), 273–286 (2007)
155. Y.Y. Bae, H.Y. Kim, et al., "Update on the SCWR Research in Korea," *Proc. 4th Int. Symp. on SCWR*, Heidelberg, Germany, March 8–11, 2009, Paper No. 52 (2009)
156. S.Y. Hong, K. Lee, et al., "Interim Results of SCWR Development Feasibility Study in Korea," *Proc. 4th Int. Symp. on SCWR*, Heidelberg, Germany, March 8–11, 2009, Paper No. 50 (2009)
157. X. Cheng, "R&D Activities on SCWR in China," *Proc. 4th Int. Symp. on SCWR*, Heidelberg, Germany, March 8–11, 2009, Paper No. 53 (2009)
158. J. Buongiorno, "The Supercritical Water Cooled Reactor: Ongoing Research and Development in the U.S.," *Proc. ICAPP'04*, Pittsburgh, PA, June 13–17, 2004, Paper 4229 (2004)

159. S.M. Modro, "The Supercritical Water Cooled Reactor Research and Development in the U.S.," *Proc. ICAPP'05*, Seoul, Korea, May 15–19, 2005, Paper 5694 (2005)
160. J. Buongiorno and P. Macdonald, "Supercritical Water Reactor (SCWR), Progress Report for the FY03 Generation-IV R&D Activities for the Development of the SCWR in the U.S.," INEEL/EXT03-03-01210, Idaho National Engineering and Environmental Laboratory (2003)
161. S. León and N. Aksan, "IAEA Coordinated Research Programme on Heat Transfer Behavior and Thermo-Hydraulics Code Testing for Super Critical Water Cooled Reactors," *Proc. ICAPP'09*, Tokyo, Japan, May 10–14, 2009, Paper 9482 (2009)

Chapter 2
Core Design

2.1 Introduction

The fuel and core design is the central issue for a nuclear power plant (NPP). This chapter describes the design concepts of the Super LWR core including the fuel rod and fuel assembly designs. The core characteristics are explained together with the design method, criteria, and the research and development subjects to comprehensively develop these concepts.

The core design should be considered to match the concepts of the Super LWR. As is described in Chap. 1, one of the main objectives of developing the Super LWR is to achieve high performance and economy in generating electricity. This development target is far beyond the scope considered by simply modifying or improving LWRs, which are currently commercially operating worldwide. The general methodologies in the development of the Super LWR for achieving such a system are, first, to develop a simple and compact plant system with a once-through direct cycle and then to move the steam cycle into the supercritical region, which dramatically improves the plant thermal efficiency from about 34% of the current LWRs to around 44% or more, depending essentially on the enthalpy rise of the coolant in the core. The general guideline for this development is pursuing simplicity in the design and fully utilizing the current technology and experience to minimize the research and development efforts.

The general role of a reactor core is to generate heat energy by controlled nuclear fissions and transfer the energy safely and efficiently to the coolant. The term "safely" in this context primarily implies that all nuclear fuel and fission products are securely isolated from the coolant and contained in the fuel element (e.g., fuel rod, fuel plate, coated fuel particle). This is usually considered as ensuring the fuel integrity during normal operations as well as in abnormal transient events, which may occur during the plant lifetime. The term "efficiently" in this context primarily implies that the core average outlet enthalpy is raised to a design value without excessive heat up of the fuel elements. Obviously, the efficient cooling of the core is directly related to ensuring the fuel integrity. The process of a core design may be

Y. Oka et al., *Super Light Water Reactors and Super Fast Reactors*,
DOI 10.1007/978-1-4419-6035-1_2, © Springer Science+Business Media, LLC 2010

generalized to finding a set of solutions to meet such requirements under the guideline of the system development.

The supercritical water cooled reactor concept allows both thermal and fast spectrum cores to be designed with the same plant system. Although the specific designs differ between the two types of cores, the basic design principles are the same. This chapter describes the core design of the thermal spectrum core (the Super LWR), in which the supercritical water serves as both the reactor coolant and the neutron moderator. The fast spectrum core (Super Fast Reactor) concept is described in Chap. 7.

2.1.1 Supercritical Water Thermophysical Properties

In the phase diagram of a liquid, as shown in Fig. 2.1, the region above the critical point is called the "supercritical region." In the case of water, the critical point is at 374.2°C and 22.1 MPa. Above this temperature and pressure, the water is called "supercritical water." Pressures below the critical point are referred to as subcritical pressures. Due to the relatively low viscosity of supercritical water with respect to its density and high specific heat enthalpy, it has a good ability as a coolant.

Figure 2.2 shows the changes of water density with respect to its temperature at pressures of 7 MPa (subcritical pressure) and 24 MPa (supercritical pressure). At this subcritical pressure, the fluid phase change takes place at the saturation temperature discontinuously. The boiling phenomenon takes place at the boiling point (saturation temperature) and the water boils to steam. On the other hand, the property changes of the supercritical fluid are continuous. Unlike the sudden large density drop of a subcritical fluid with boiling, the density change of the supercritical fluid around the pseudocritical temperature is small and its density is kept

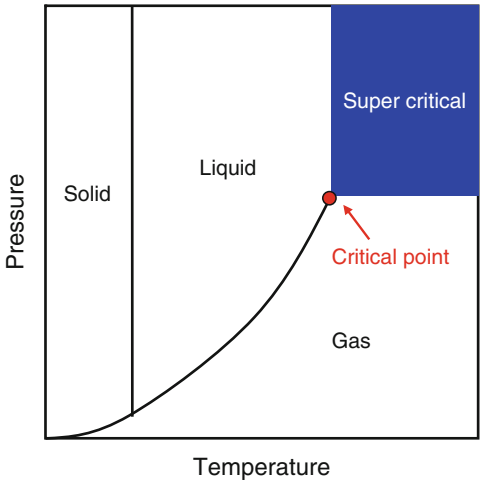


Fig. 2.1 Phase diagram of water

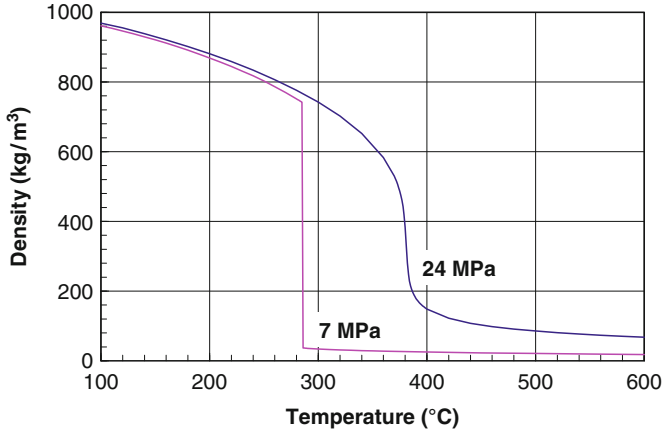


Fig. 2.2 Changes of water density with respect to its temperature

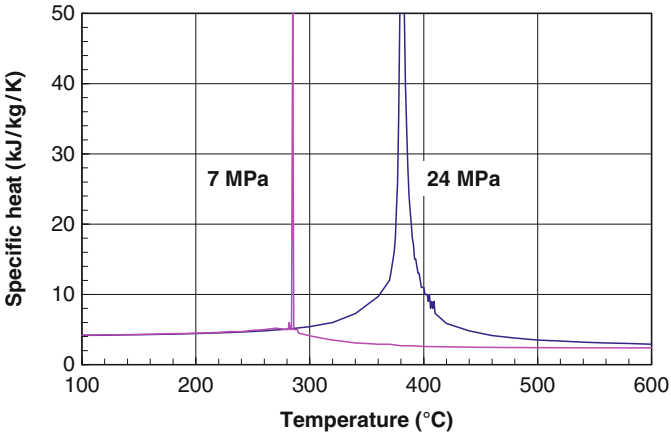


Fig. 2.3 Changes of specific heat capacity of water with respect to temperature

relatively high even above the pseudocritical temperature. The changes of specific heat capacities of water with respect to temperature are shown in Fig. 2.3. For the subcritical pressure condition, the specific heat capacity has a peak value at the saturation temperature. The temperature at which a supercritical fluid has a peak in its specific heat capacity is called the pseudocritical temperature. Similar to the heat transfer by boiling, the supercritical fluid exhibits a large cooling capability around the pseudocritical temperature.

A phenomenon similar to the boiling transition of a subcritical fluid is recognized to occur during heat removal by a supercritical fluid. It is known as the heat transfer deterioration phenomenon and occurs when the fluid flow rate is relatively low for the high heat flux [1–4]. However, unlike the boiling transition of a subcritical fluid,

the deterioration in the heat transfer rate is continuous and mild and does not lead to burnout of the heated surface wall.

As far as the Super LWR core design is concerned, the core is cooled by the "normal" heat transfer of supercritical water for all normal operating modes. So the main thermal-hydraulic concern of the core design is associated with the normal heat transfer to the supercritical water. Some deterioration in heat transfer may be observed during abnormal transients or accidents. Since the heat transfer deterioration does not lead to the immediate burnout of the heated surface, the heat transfer deterioration during abnormal transients may be permissible as long as the fuel integrity is maintained. (The fuel integrities and abnormal transients are discussed in Sect. 2.8.)

2.1.2 Heat Transfer Deterioration in Supercritical Water

2.1.2.1 Background

The "boiling crisis" is a general term used to describe the deterioration in the heat transfer rate due to the sudden change in the boiling mode. The heat flux at which this boiling crisis occurs is called the critical heat flux (CHF). There are two types of boiling crises. The first type is the boiling crisis due to the boiling transition from nucleate boiling to film boiling. This transition is called "departure from nucleate boiling" (DNB) and it often occurs in pool boiling, in subcooled boiling, or in a low quality region of forced convective boiling. The DNB usually results in a sudden temperature rise of the heated surface wall or "burnout" of the heated surface wall. Hence, the CHF for DNB is usually called the "burnout heat flux." The second type is the boiling crisis due to fractures of liquid films in the annular flow. This phenomenon occurs in a high quality region of the forced convective boiling and it is usually called "dryout" since the heated surface wall is exposed to the steam and not covered by any liquid. Compared with the DNB, the postdryout temperature rise of the heated surface wall is small and does not immediately lead to burnout.

In BWRs or PWRs, the occurrence of a boiling crisis (DNB or dryout) may lead to burnout of the fuel rod cladding and fuel rod failures. Therefore, these reactors are designed to operate with sufficient margins to the boiling crises so that they are prevented even under abnormal transients. For assuring the operational margins, a design criterion is determined for both BWRs and PWRs. In normal BWR operation, the minimum critical heat flux ratio (MCHFR) or the minimum critical power ratio (MCPR) must be greater than a certain value (e.g., MCHFR > 1.9, or MCPR > 1.2 for normal operation). The MCHFR is the ratio of the CHF to the operating heat flux of the fuel rod, while the MCPR is the ratio of the critical power of the fuel assembly to the operating power of the fuel assembly. Similarly, in normal PWR operation, the minimum departure from nucleate boiling ratio (MDNBR) must be greater than a certain value (e.g., MDNBR > 1.72 for normal operation).

In the Super LWR operating at the supercritical pressure, there is no boiling transition. However, the specific heat capacity of the coolant has a peak at the pseudocritical temperature, which corresponds to the boiling temperature of subcritical pressure water. Around the pseudocritical temperature, the coolant undergoes large changes in its thermophysical properties and changes from a high density liquid-like state to a low density gas-like state. Under a high heat flux and low flow rate condition, the phenomenon known as "heat transfer deterioration" occurs. This phenomenon is similar to, but differs slightly from, the boiling crises of subcritical pressure. The heat transfer deterioration may occur during the plant startup or abnormal transitions of the Super LWR.

Correlations of the heat transfer coefficient and criteria for the deterioration have been developed on the basis of experiments. These correlations and criteria are used, for example, in the design of supercritical pressure fossil fuel fired power plants (FPPs). However, correlations that were obtained by specific experiments are not suitable when the flow conditions are much changed from those of a fossil fuel fired boiler to the super LWR. Furthermore, though more correlations of the heat transfer coefficient have been developed recently for supercritical water cooling, most of them include wall temperature as an input parameter, and some correlations show discontinuity. Correlations including wall temperature need many iterations to evaluate the heat transfer coefficient, so it is more difficult to use them in design work. Oka's group has carried out numerical computations on heat transfer to supercritical water based on a *k-e* model by Jones-Launder [5, 6]. A new Oka–Koshizuka heat transfer correlation has been proposed for supercritical water cooling, which has a form similar to the Dittus–Boelter' correlation [7]. This new correlation is relatively simple and easy to use in reactor design.

$$\begin{aligned} Nu &= 0.015 \times Re^{0.85} \times Pr^{0.69-81{,}000/qs+fc\times q}, \\ qs &= 200 \times G^{1.2} \end{aligned} \tag{2.1}$$

$$fc = \begin{cases} 2.9 \times 10^{-8} + \dfrac{0.11}{qs} \\ h < 1.5 \text{ MJ/kg} \\ -8.7 \times 10^{-8} - \dfrac{0.65}{qs} \\ 1.5 \text{ MJ/kg} \leqslant h \leqslant 3.3 \text{ MJ/kg} \\ -9.7 \times 10^{-7} + \dfrac{1.30}{qs} \\ 3.3 \text{ MJ/kg} \leqslant h \leqslant 4.0 \text{ MJ/kg} \end{cases},$$

where G is the mass flux (kg/m^2 s), h is the bulk enthalpy (MJ/kg), and q is the heat flux (kW/m^2).

2.1.2.2 Numerical Computations

The unusual phenomena of supercritical fluids have been explained by many theories, which are roughly categorized into two types: single-phase and two-phase fluid dynamics. In theories based on single-phase fluid dynamics, unusual behaviors are attributed to single-phase turbulent flow with excessive change of thermophysical properties by heating. On the other hand, pseudoboiling is assumed in theories based on two-phase fluid dynamics. Deterioration of heat transfer is explained by transition from pseudonucleate to pseudofilm boiling.

For analytical studies assuming single-phase fluid dynamics, mixing length models are employed for turbulence. Since this type of model requires the distribution of turbulent viscosity in advance, a special assumption is used to incorporate effects of excessive change of thermophysical properties. In this case, validity of the special assumption is somewhat contentious even if the calculation results agree with the experimental values. In addition, change of density is not considered in the continuity and momentum equations, which implies that buoyancy force and fluid expansion are not incorporated. Therefore, these studies are applicable only to limited flow conditions.

As mentioned above, numerical computations were carried out [5, 6] based on a *k-e* model by Jones-Launder. This model has a more general description for turbulence than the mixing length models. Effects of buoyancy force and fluid expansion on the heat transfer to normal fluids are successfully analyzed by the *k-e* model. Thermophysical properties are treated as variables in the governing equations and evaluated from a steam table library. Thus, extremely nonlinear thermophysical properties of supercritical water are evaluated directly and correctly. This approach is applicable to a wide range of flow conditions of supercritical water. Many cases of different inlet temperatures can be calculated and the relation between the heat transfer coefficient and the bulk enthalpy can be obtained in a wide range.

Calculated results are compared with experimental data of Yamagata et al. [8] in Fig. 2.4. The heat transfer coefficient shows a maximum peak near the pseudocritical temperature. The peak decreases and moves to the lower bulk enthalpy as the heat flux increases. These behaviors agree with the experimental data. These results show better agreement than those obtained by the mixing length model. This is mainly attributed to the formulation of extreme changes of thermophysical properties in the governing equations. In the calculation, changes of thermophysical properties affect many terms in the governing equations, while most of them are neglected or approximated when the mixing length model is used. Heat transfer coefficients calculated by the Dittus–Boelter correlation are drawn in Fig. 2.4 as well. The Dittus–Boelter correlation gives the ideal coefficient α_0 when the heat flux is zero because it assumes constant thermophysical properties at the bulk temperature. Though the Dittus–Boelter correlation gives smaller coefficients than those at the smallest heat flux, 2.33×10^5 W m^{-2}, it should not be concluded that the heat transfer coefficient is enhanced at low heat fluxes. It is known that the Dittus–Boelter correlation predicts relatively small heat transfer coefficients at high

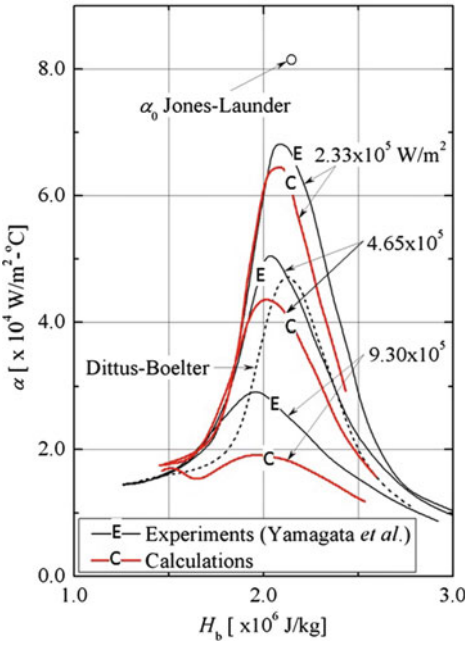


Fig. 2.4 Heat transfer coefficient near the pseudocritical temperature; comparison with the calculated results, experimental results of Yamagata et al. [8] and results from the Dittus–Boelter correlation

Prandtl numbers. Thus, the coefficient near the pseudocritical temperature, where the Prandtl number becomes large, may be smaller. The ideal coefficient calculated by the Jones-Launder *k-e* model at the pseudocritical temperature is plotted in Fig. 2.4. It is calculated by fixing the thermophysical properties at the pseudocritical temperature. This value is higher than that shown by the curve of 2.33×10^5 W m^{-2}. When the Jones-Launder *k-e* model is used, it is known that the wall shear stress is relatively large and the heat transfer coefficient is also large with a constant turbulent Prandtl number. As indicated by Jackson and Hall [4], the heat transfer coefficient is the maximum when the heat flux is zero and it monotonically decreases as the heat flux increases. The calculation supports their assertion.

2.1.2.3 Determination of Deteriorated Heat Flux

To obtain the deteriorated heat flux, calculations have been carried out with various combinations of flow rate G and heat flux q″. Deterioration is assessed where the bulk temperature reaches the pseudocritical temperature. The deterioration ratio α/α_0 is defined where α_0 is the ideal heat transfer coefficient. Some calculation results are shown in Fig. 2.5. The heat transfer coefficient monotonically decreases when the flow rate is large. On the other hand, it abruptly drops at a certain heat flux and maintains a constant value or increases with larger heat fluxes when the flow rate is small. The boundary is around 200 kg m^{-2} s^{-1} under the analyzed flow

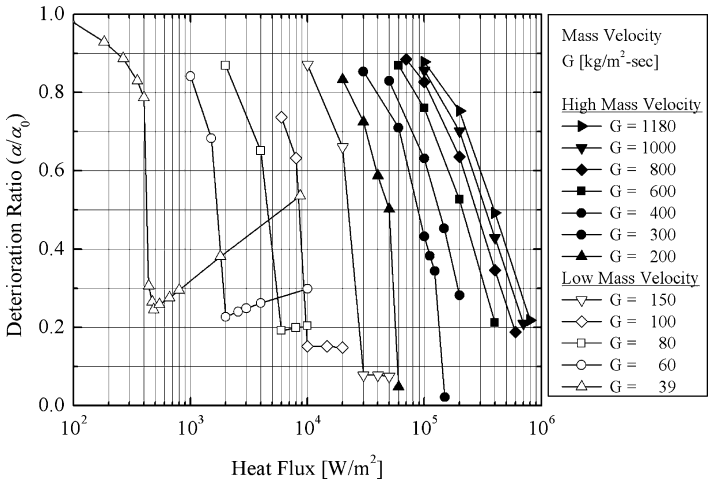


Fig. 2.5 Heat transfer deterioration ratio at various flow rates, α heat transfer coefficient; α_0: ideal heat transfer coefficient at $q'' = 0$.

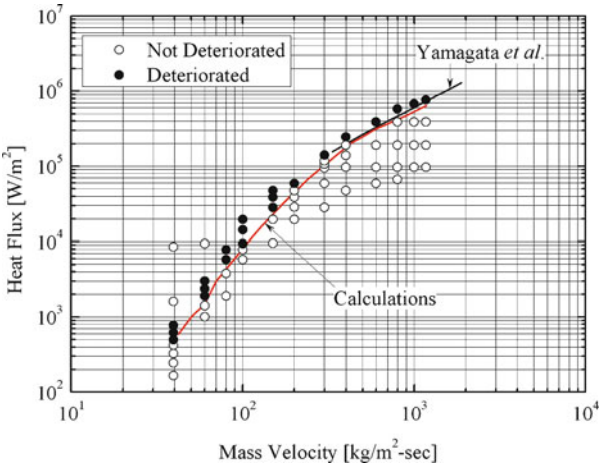


Fig. 2.6 Map of heat transfer deterioration. (**a**) Temperature and (**b**) Prandtl number

conditions. These behaviors suggest that there exist different mechanisms of deterioration depending on the flow rate.

A map of deterioration is presented in Fig. 2.6. Occurrence of deterioration is judged when the deterioration ratio is smaller than 0.3 in the present analysis. A line obtained with the correlation of Yamagata et al. [8] is also provided in Fig. 2.6. This correlation was obtained when the heat transfer coefficient was deteriorated to about 1/3 to 1/2 of normal heat transfer predicted by their own correlation. The present calculation results agree with the correlation results by Yamagata et al.

when the flow rate is high. The slope of the curve becomes steep when the flow rate is small. Deterioration occurs at a relatively small heat flux in this region. There is an arbitrary choice in the present criterion of deterioration, $\alpha/\alpha_0 < 0.3$, but the above discussion will not be much affected by changing this.

2.1.2.4 Heat Transfer Deterioration at High Flow Rates

Radial profiles of temperature and Prandtl number near the wall ($y = 0$–2.0×10^{-5} m) at $G = 1{,}180$ kg m^{-2} s^{-1} and $T_b = T_m$ are shown in Fig. 2.7. When the heat flux increases, the flow velocity and the turbulence energy decrease near the wall.

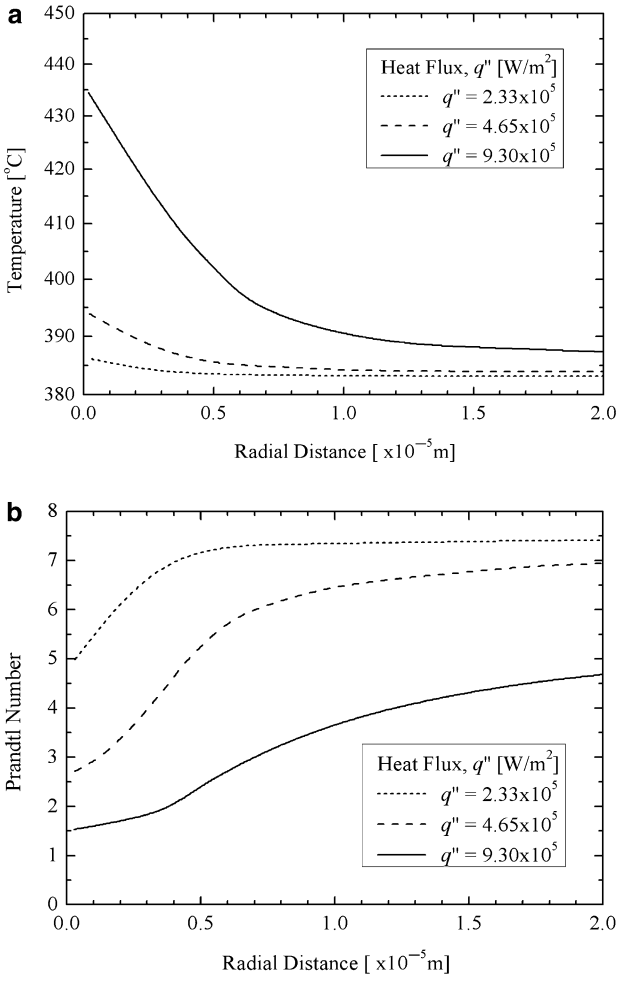


Fig. 2.7 Radial distributions near the wall at $G = 1{,}180$ kg m^2 s^{-1}

The viscosity increases and the Prandtl number decreases locally because the temperature is enhanced by heating. Higher viscosity leads to a thicker viscous sublayer, which reduces turbulence near the wall and heat transfer is deteriorated. Smaller Prandtl numbers reduce the heat transfer as well. This explanation is consistent with the monotonic behavior of deterioration at high flow rates.

2.1.2.5 Heat Transfer Deterioration at Low Flow Rates

Figures 2.5 and 2.6 reveal that deterioration is caused by a different mechanism at low flow rates. The calculation results at $G = 39$ kg m^{-2} s^{-1} and $T_b = T_m$, which gives the Reynolds number 10,000, are rearranged in terms of the Grashof number and the Nusselt number in Fig. 2.8. Nu has a minimum value at $Gr = 2 \times 10^7$. Nu is constant when Gr is lower than it, which means forced convection is dominant. On the other hand, Nu increases linearly when Gr is larger than the minimum point, which implies that natural convection is dominant. The minimum point emerges at the boundary between the two convection modes. Flow velocity and turbulence energy profiles are depicted in Fig. 2.9. When the heat flux is enhanced, the flow velocity increases near the wall and the profile becomes flat. Since turbulence energy is produced by the derivative of flow velocity, it is reduced. Hence, heat transfer is deteriorated. When the heat flux is enhanced above the minimum point, the flow velocity profile is more distorted and turbulent heat transfer is then enhanced. This type of heat transfer deterioration is attributed to acceleration as well as buoyancy. In the present analysis, buoyancy force is dominant. The computational results without the buoyancy force term in the Navier–Stokes equations are

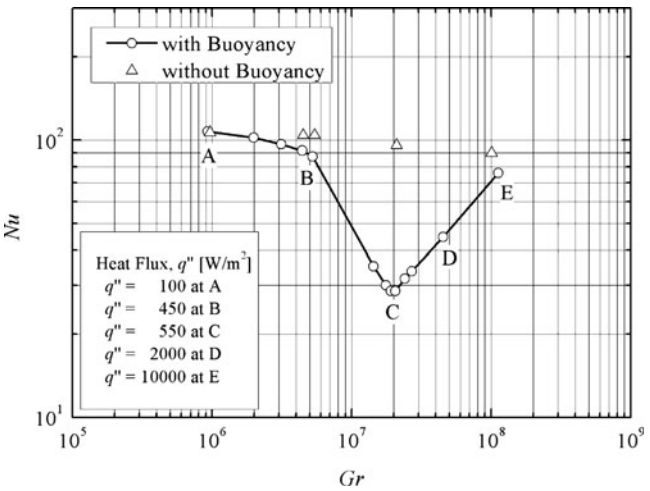


Fig. 2.8 Relation between Gr and Nu at $G = 39$ kg m^2 s^{-1}. (**a**) Flow velocity and (**b**) turbulence energy

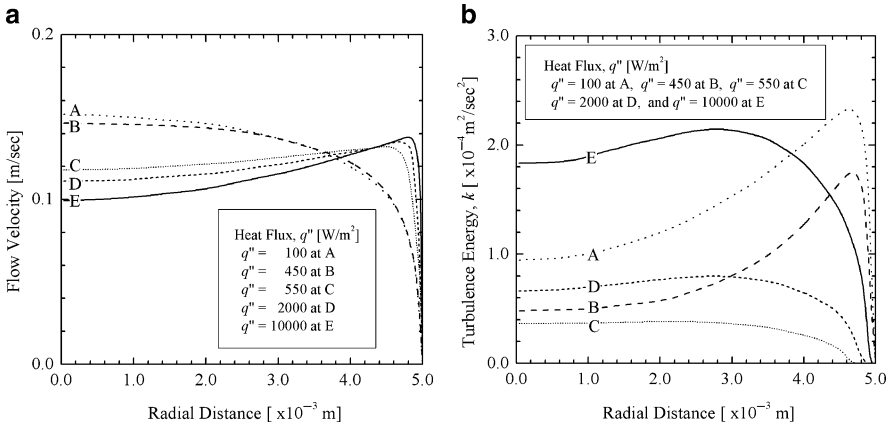


Fig. 2.9 Radial distributions at $G = 39$ kg m^2 s^{-1}

also plotted in Fig. 2.9. Without the buoyancy force term, the minimum point completely disappears.

Generally speaking, the conventional numerical analysis with a *k-e* turbulence model and accurate treatment of thermophysical properties can successfully explain the unusual heat transfer phenomena of supercritical water. Heat transfer deterioration occurs due to two mechanisms depending on the flow rate. When the flow rate is large, viscosity increases locally near the wall by heating. This makes the viscous sublayer thicker and the Prandtl number smaller. Both effects reduce the heat transfer. When the flow rate is small, buoyancy force accelerates the flow velocity near the wall. This makes the flow velocity distribution flat and generation of turbulence energy is reduced. This type of heat transfer deterioration appears at the boundary between forced and natural convection. As the heat flux increases above the deterioration heat flux, a violent oscillation of wall temperature is observed. It is explained by the unstable characteristics of the steep boundary layer of temperature.

More recent research studies on the heat transfer deterioration have revealed the following characteristics. Generally, the heat transfer deterioration phenomenon occurs only around the critical point (for water, the critical point is at 374.2°C and 22.1 MPa) or the pseudocritical temperature. The mechanisms of the heat transfer deterioration differ from those of the boiling crises of the subcritical pressure. Compared with the boiling crisis, the temperature rise of the heated surface wall is milder. The post deterioration heat transfer rate can be predicted by numerical analyses based on turbulence models and the occurrence of the heat transfer deterioration can be suppressed by promoting the turbulence.

Therefore, in the core design of the Super LWR, it is possible to eliminate the CHF from the core design criteria. In this case, the occurrence of the heat transfer deterioration may be permitted as long as the fuel cladding temperature is kept below its limit. If the core design of the Super LWR were limited by the CHF to prevent the heat transfer deterioration, the core outlet average coolant temperature

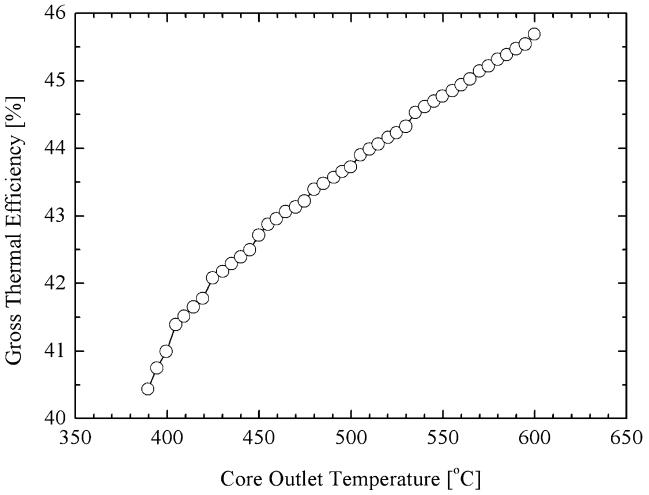


Fig. 2.10 Relation between plant thermal efficiency and core outlet temperature at 25 MPa and inlet temperature of 295°C

would be limited to around the pseudocritical temperature. The rationalization in the design criteria allows a core design with an average outlet temperature much higher than the pseudocritical temperature. By increasing the average outlet temperature, the plant thermal efficiency can be dramatically improved as shown in Fig. 2.10 and the balance of plant (BOP) component weight can be reduced with a lower flow rate.

2.1.3 Design Considerations with Heat Transfer Deterioration

In conventional subcritical pressure LWRs, such as BWRs or PWRs, the core is effectively cooled by the boiling heat transfer. Therefore, the coolant inlet temperature is set below its saturation temperature and the saturated steam is sent to the turbine. (In BWRs, the core inlet and outlet temperatures are 216 and 286°C, respectively. In PWRs, the inlet and outlet temperatures are 289 and 325°C, respectively.) The boiling phenomenon starts as the coolant becomes heated close to its saturated temperature. The coolant starts its phase change from liquid to gas with large discontinuous property changes. The coolant flow becomes a two-phase flow and the bulk coolant temperature is kept below its saturation temperature. There have been very few reactors that could produce superheated steam; one example was the American Boiling Nuclear Super heater Power Station (BONUS): an integral boiler-super heater, which was shut down permanently in 1968 and decommissioned by 1970.

The operating temperatures of other types of reactors, such as gas cooled reactors or liquid metal fast breeder reactors (LMFBRs), are also limited by the phase change of the coolant. These reactors can operate only in the temperature range where the coolant is either in the gas phase or liquid phase. Since supercritical water does not exhibit a phase change, the core inlet coolant temperature of the Super LWR can be below the pseudocritical temperature and the outlet temperature can be above it. The high specific heat capacity of the coolant around the pseudocritical temperature allows efficient cooling of the core with a large flexibility in designing the core inlet and outlet temperatures.

Gaining a large enthalpy rise in the core (by raising the core outlet temperature) has two major impacts on the system design of the Super LWR. Firstly, it improves the plant thermal efficiency. Figure 2.10 shows the relationship between the plant thermal efficiency and the core outlet temperature (for the coolant pressure and inlet temperature of 25 MPa and 295°C respectively). For the same coolant pressure and inlet temperature, raising the core outlet temperature from 450 to 500°C improves the plant thermal efficiency from about 42.8 to 43.8%. This improvement is significant for the commercial power plant use. The second impact is the reduction in the BOP component weight. There is a simple relationship between the thermal output of the core Q, the core flow rate W, and the enthalpy change of the coolant in the core ΔH: $Q = W \cdot \Delta H$. For a given core thermal output, a higher enthalpy rise in the core can reduce the core flow rate. The reduction in the core flow rate leads to the reduction of the required number and weight of the BOP components.

Considering the above points and by referring to experiences with supercritical FPPs, researchers are developing the concepts of the Super LWR with a system pressure of 25 MPa, core coolant inlet temperature of 280°C, and outlet temperature of about or higher than 500°C.

Figure 2.11 shows the temperature and density changes of supercritical water at a pressure of 25 MPa. From the core inlet to the outlet, the coolant undergoes continuous large changes of temperature and density. The specific heat of the supercritical water (i.e., the change in temperature with respect to the change in specific enthalpy) is low around the pseudocritical temperature, but becomes large in the higher enthalpy region. This implies that when designing a core with a core outlet average coolant temperature of around 500°C or higher, the local coolant

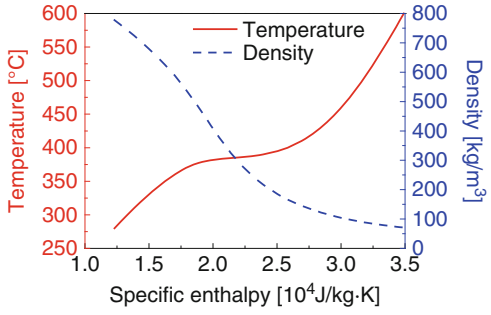


Fig. 2.11 Temperature and density vs. specific enthalpy of water at 25 MPa

temperature becomes sensitive to the local enthalpy rise and may locally become significantly higher than the core average. For effective core cooling, the coolant temperature across the core outlet should be as uniform as possible so that there is no excess heat up locally. The large density change of the coolant affects the coolant flow as well as the neutron moderations and therefore the core power distribution. Hence, coupling the thermal-hydraulic and neutronic calculations is especially important in designing the Super LWR core.

2.2 Core Design Scope

The core design scope of the Super LWR can be roughly defined by the considerations of the design margins, criteria, boundary conditions, and targets. How these four items affect the Super LWR core design is explained in this section.

2.2.1 Design Margins

Generally, the following three points are considered to be the fundamental requirements of all kinds of reactors:

1. A sufficient design margin is kept from the fuel failure limit during normal operation
2. The reactor can be brought to a cold shutdown state with a sufficient margin (shutdown margin)
3. The reactor retains inherent safety features (e.g., negative feedbacks to reactivity insertions)

The design criteria are determined more specifically for each reactor type, taking into account the reactor characteristics, to satisfy the above basic requirements.

In developing the concepts for a new reactor, establishing the concept of design criteria for assuring sufficient design margins is especially important. While the criteria are directly related to the fuel integrity, they are also related to the upper limits of the core performances such as the average power density and the outlet temperature.

Figure 2.12 [9] describes the design margins in current LWRs. The reactor core, which is operating at its nominal steady state core average condition, contains a "hot spot" which is at a higher state relative to the core average condition. The nominal peak denotes a hot spot at the peak state when all core parameters are at their nominal design values. The nominal peak depends on spatial fluctuations of the core parameters. The maximum peak further takes into account various engineering uncertainties. The maximum peak state is determined such that the probability of any hot spot exceeding this state is low enough to be excluded from the design considerations. The fuel failure should be prevented under abnormal

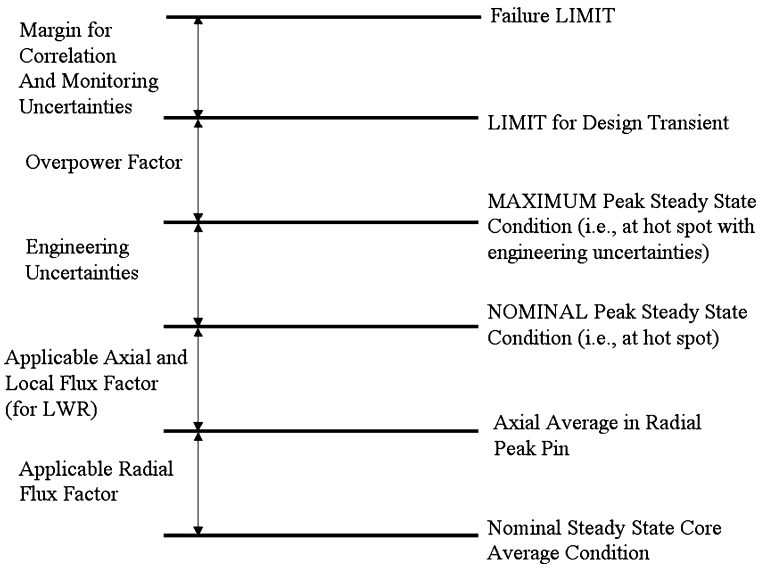


Fig. 2.12 Design margins in BWRs and PWRs. (Taken from doctoral thesis of A. Yamaji, the University of Tokyo (2005) [9])

transient conditions. Hence, in current LWRs, the design limit of the normal operating condition is determined by taking appropriate margins from the failure limit. The failure limit is usually determined by experiments for each fuel and core design. In order to determine the failure limit, the failure modes of the fuel need to be identified. For current LWRs, the failure modes of the fuel rods can be roughly divided into failure due to the excess heat up of the cladding and failure due to excess strain of the cladding as a result of a pellet-cladding mechanical interaction (PCMI). The former failure mode is prevented by the design criterion of the MCPR or MDNBR, while the latter failure mode is prevented by limiting the maximum linear heat generation rate (MLHGR). The fuel integrity and its failure modes are discussed in more detail in Sects. 2.7 and 2.8.

The basic design concepts of the Super LWR for assuring sufficient design margins follow those of the current LWRs. However, two distinctive differences need to be carefully considered. One of them is the difference between the boiling transition of the subcritical water and the heat transfer deterioration of the supercritical water. To consider the design margin from excess heat up of the fuel rod cladding, the occurrence of the heat transfer deterioration may be regarded as not permissible. By preventing the heat transfer deterioration, the cladding temperature can be kept close to the coolant temperature and its excess heat up can be prevented as long as the operating coolant temperature is close to or below the pseudocritical temperature. This is effectively equivalent to regarding the supercritical water cooling as a two-phase flow cooling and the Super LWR concept under this restriction may be called the “critical heat flux-based design concept” (for the

purpose of distinguishing the different Super LWR design concepts in this chapter), or it may alternatively be called the "low temperature design concept," since the CHF criterion limits the core outlet temperature to a relatively low value around the pseudocritical temperature. In the low temperature design concept, a design criterion for the minimum deterioration heat flux ratio (MDHFR) needs to be determined. The MDHFR corresponds to the MCPR or MDNBR of current LWRs and it is defined as the ratio of the deterioration heat flux (the heat flux at which the heat transfer deterioration occurs) to the maximum heat flux of the core. The failure limit of the MDHFR is 1.0 (i.e., the occurrence of the heat transfer deterioration). To maintain a sufficient design margin, the MDHFR at the normal operating condition needs to be sufficiently larger than 1.0.

The alternative and more advanced approach is to prevent the excess heat up of the fuel rod cladding by directly limiting the cladding temperature. The Super LWR concept under this restriction may be called the "temperature-based design concept," or it may be alternatively called the "high temperature design concept," since the elimination of the CHF design criterion enables the core outlet temperature to be significantly higher than the pseudocritical temperature. In the high temperature design concept, the occurrence of heat transfer deterioration may be permitted as long as the temperature of the cladding is kept below its failure limit. This idea is similar to the concept of the LMFBR core design. The prediction of the heat transfer rate after the onset of the heat transfer deterioration (deteriorated heat transfer rate) is more difficult compared with the prediction of the critical heat flux of the heat transfer deterioration. However, recent advances in this field have enabled reasonably accurate predictions of deteriorated heat transfer rates [10, 11]. Therefore, development of the high temperature design concept has become possible. In this case, the failure limit of the excess heat up largely depends on the cladding material. The core outlet temperature can be raised significantly higher than the pseudocritical temperature as long as a sufficient design margin is maintained from the failure limit.

The second distinctive difference between the core designs of the Super LWR and current LWRs is that the failure limit cannot be determined for the Super LWR from the viewpoint of the fuel integrity considerations, while it is clearly determined for the current LWRs through experiments and operational experiences. This difference needs to be highlighted especially when the high temperature design concept is considered. Regarding the failure limit, the development of the Super LWR core may be based on either of two different strategies. One of the strategies is to develop the concept under tentative design criteria. The developed concept under this guideline may be called the "criteria-dependent design concept." If this strategy is adopted, the core performance parameters, such as the average outlet temperature and power density, will depend on the tentatively determined criteria of the permissible maximum temperature and power density. The advantage of this strategy is that research and development targets for in-core materials, especially the fuel cladding material, can be easily identified and efficiently accomplished. This strategy seems to match well with the general guideline of the Super LWR development, which is to make the best use of current technologies, because the

in-core material development is expected to be one of the largest development requirements for the Super LWR. The disadvantage of the criteria-dependent design concept is that it is difficult to anticipate the basic design concept until the concept is established. For example, until the basic design concept is established, it is difficult to estimate the core average outlet temperature or average power density. The operating level may vary through the process of the development as new findings are discovered. The large uncertainties in these basic parameters may discourage research and development of the new concept itself.

The other strategy is to develop the concept under tentative design targets. The concept under this guideline may be called the "target-dependent design concept." If this strategy is adopted, the operating level of the reactor can be roughly fixed from the initial stage of the conceptual development. Therefore, the basic design concept and its advantages over other concepts can be clearly stated from the early stage of development. This may be one of the most important points when a number of different concepts are in a competition to be selected for the final development under a limited budget. The disadvantage of the target dependent design concept is that it is difficult to anticipate the research and development targets for the in-core materials until the basic design concept is established. For example, until the basic design concept is established, it is difficult to estimate the maximum temperature that the fuel cladding has to withstand. The material requirements may vary through the process of the development as new findings are discovered. This may delay the material developments and raise the material development cost.

To summarize, there are roughly three different core design concepts for the Super LWR depending on how the design margin is treated.

1. The low temperature design concept (critical heat flux criterion-dependent design concept)
2. The high temperature design concept with tentative design criteria
3. The high temperature design concept with tentative design targets

As is described in the previous section, the flexibility in selecting the inlet and outlet temperatures is a unique characteristic of the Super LWR core. It is also expected that raising the core outlet temperature above the pseudocritical temperature will make the Super LWR a more attractive concept. Hereafter, this chapter focuses on the core design of the average temperature target-dependent concept, but the other two concepts are also briefly introduced.

Figure 2.13 [9] describes the design margins and evaluating methods for the average temperature target-dependent Super LWR core design concept. The basic core design concepts (e.g., in-core coolant flow scheme) can be designed by three-dimensional core calculations and the basic characteristics during the normal operations can be evaluated; details of the core calculations are explained in Sect. 2.3. However, it is difficult and inefficient to model each fuel rod or fuel channel by such core calculations, and therefore, the peak cladding temperature cannot be accurately determined by the core calculations. For accurate evaluation of the peak cladding temperature, subchannel analyses are required with considerations of engineering uncertainties; these are included in Sects. 2.5 and 2.6.

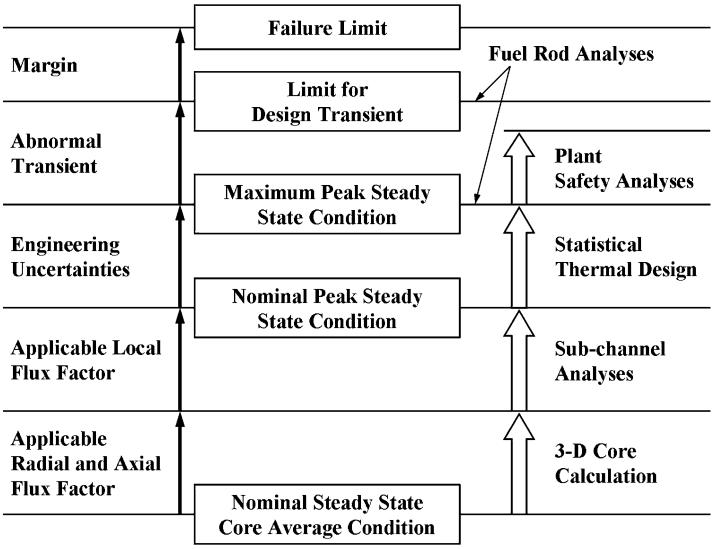


Fig. 2.13 Design margins in the Super LWR. (Taken from doctoral thesis of A. Yamaji, the University of Tokyo (2005) [9])

Section 2.7 explains the basic fuel rod behavior under the maximum peak normal operating condition and evaluates the mechanical strength required for the cladding to withstand the operation. Section 2.8 describes the concept for rationalizing the criteria for abnormal transients by referring to the plant safety analyses and by analyzing the fuel rod behaviors under the abnormal transient conditions. By combining these designs and analyses, the design methods and the core concept of the Super LWR core are comprehensively presented.

2.2.2 Design Criteria

The neutronic and thermal-hydraulic design criteria (limits for normal operations) of the Super LWR core are described next.

2.2.2.1 Neutronic Design Criteria

1. Core shutdown margin greater than or equal to 1%dk/k.
   The control rods are used for the normal shutdown of the Super LWR core. The shutdown margin is the negative reactivity of the core when all control rods are inserted into the core and the core is at the shutdown state. This is an important index for the core ability to be shut down. Usually, the core shutdown margin is evaluated with the assumption that the insertion of the control rod with the

maximum worth is failed. This shutdown margin is sometimes called the "one rod stuck margin." The same criterion should be satisfied by the Super LWR. Furthermore, as is the case in current LWRs, the core should be equipped with an alternative shutdown mechanism such as the injection of borated water.

2. Retention of inherent reactor safety features.
   The inherent safety feature is the tendency of the system to fall to the safer side when a positive reactivity is inserted. The main contributions to the inherent safety features of the Super LWR are the positive coolant (and moderator) density reactivity coefficient (which is equivalent to the negative void reactivity coefficient of the BWR) and the negative Doppler reactivity coefficient. These inherent safeties should be maintained throughout the operation.

2.2.2.2 Thermal Design Criteria (Thermal Limit for Normal Operations)

1. Design limit for preventing excess heat up of the fuel rod cladding.
   As is already discussed, a design criterion is necessary to prevent the excess heat up of the fuel rod cladding and the criterion itself depends on the type of the concept to be developed. For the critical heat flux criterion-dependent design concept, the criterion may be to limit the MDHFR to be greater than or equal to 1.30 during the normal operation to prevent the heat transfer deterioration at abnormal transients. For the maximum temperature criterion-dependent concept, the allowable maximum cladding surface temperature (MCST) for normal operations may tentatively be set below or equal to 650°C for a high temperature alloy such as nickel alloy cladding. In this case, the primal design issue is to maximize and accurately determine the average core outlet temperature under the MCST constraint. In the average temperature target-dependent concept, the primal design issue is to minimize and accurately determine the peak cladding temperature under the average outlet temperature constraint.
2. Design limit for the MLHGR.
   The design limit for the MLHGR has been widely adopted by different types of reactors. In current LWRs, it is primarily determined to prevent failure of the fuel cladding due to excess strain on the cladding caused by PCMI. In BWRs, the MLHGR design limit during the normal operation is 44 kW/m. It has been experimentally verified that this upper limit assures the fuel integrity during abnormal transients. In PWRs, the MLHGR limit for the design transient is determined to be 59.1 kW/m. This heat flux corresponds to the fuel centerline temperature of about 2,300°C, which is low enough to prevent fuel melting. It is known that the fuel centerline melting causes a volumetric expansion of the fuel pellets, which may lead to strong PCMI. By taking an appropriate margin, the design limit of the MLHGR for the normal operation of the PWRs is determined to be 43.1 kW/m (which is equivalent to the fuel centerline temperature of about 1,870°C). In BWRs and PWRs, the PCMI is one of the main causes of fuel failures. The PCMI occurs as the burnup proceeds mainly due to pellet swelling and cladding creep down. Especially large PCMI may occur during overpower

transients, because the thermal expansion rate of the pellets is larger than that of the Zircaloy cladding. In the case of LMFBRs, the FCMI (fuel cladding mechanical interaction is the term usually used among LMFBR designers and it is analogous to PCMI of LWRs) is not expected to be a big issue because of the relatively low density pellet (around 85% of the theoretical density), low coolant pressure (almost atmospheric pressure), and the high thermal expansion rate of the stainless steel cladding (higher than that of MOX pellets).
The fuel rod design of the Super LWR follows those of BWRs and PWRs. It is designed for a high density UO_2 pellet. The coolant pressure of 25 MPa is significantly higher than the 7.0 MPa of BWRs or the 15.4 MPa PWRs. Therefore, PCMI needs to be considered as one of the major fuel rod failure mechanisms.

2.2.3 Design Boundary Conditions

The main design boundary conditions used to develop the core concepts of the Super LWR are described next. Many of the following parameters define the basic characteristics of the core represented by the nominal steady state core average condition shown in Fig. 2.13.

2.2.3.1 Core Pressure, Inlet Temperature and Average Outlet Temperature

These basic thermal-hydraulic parameters have been roughly determined from the considerations of reducing the BOP weight and improving the plant thermal efficiency (this is described in Chap. 3). The core design explained below is based on the core pressure of 25 MPa, inlet temperature of 280°C, and the average outlet temperature of 500°C. When these conditions are selected, the plant thermal efficiency becomes about 43.8%. These are the reference core characteristics.

2.2.3.2 Determination of the Core Size

The core size is determined by first deciding the core thermal output (power scale) and the power density. The power scale of the reactor is an important factor in nuclear power generation, because of the high capital cost in building the power station. Large reactors have scale merits. However, the power scale should essentially be determined from the power demands or the limitations from the power grids. It is expected that in many countries, where demands for replacing old reactors with the next generation reactors are present, the total power demands will not increase significantly. Therefore, the target power scale (electric) of the Super LWR has been provisionally determined as around 1,000 MWe (it is not a big technical issue to change the power scale target later on). Assuming the plant

efficiency of 43.8%, the power scale corresponds to a thermal output of about 2,280 MWt.

The fuel rod design of the Super LWR is expected to be similar to designs of current LWRs and the average linear heat generation rate (ALHGR) of the core is determined to be 18 kW/m. This implies that the level of the core power density will be close to that of current LWRs (from about 50 W/cm^3 for BWRs to about 100 W/cm^3 for PWRs).

For the pressure vessel of the Super LWR, a similar design to that of PWRs is expected to be possible with the power scale similar to that of current LWRs [12, 13]. From the viewpoint of neutron economy, the core height to the equivalent diameter ratio of around 1.0 is desirable. However, from the viewpoint of thermal-hydraulic stability, a greater ratio is favorable. From these arguments, the core active height is determined to be 4.2 m.

From the viewpoint of plant economy, increasing the number of fuel assemblies is disadvantageous, because of the longer time required for fuel replacement work. The number of different types of fuel assemblies should also be small, as it affects standardization in the fuel fabrication. The upper core structures can be simplified by using fewer fuel assemblies because of the smaller number of penetrations to the top dome. On the other hand, reducing the number of fuel assemblies would cause difficulties in flattening the radial core power distributions. The flattening of the core radial power distribution is especially important for raising the average outlet temperature of the Super LWR (this is explained later in this section). From these arguments, the size and number of fuel assemblies are determined to be similar to those of PWRs. The core is to be composed from three cycle fuels, namely, the fresh fuel assemblies (first cycle fuel assemblies), the second cycle fuel assemblies, and the third cycle fuel assemblies. The number of fuel assemblies is to be based on (1) a multiple of four from the viewpoint of the core symmetry, (2) a multiple of three from the viewpoint of composing a three-batch fuel core, and (3) one fuel assembly loaded at the center of the core to flatten the core radial power distribution. Thus, the number of fuel assemblies should be given by $12N + 1$. The flow in determining the core size is described in Fig. 2.14 [9].

2.2.3.3 Fuel Discharge Burnup and Enrichment

For a typical LWR, the capital cost is about 50–60% of the total cost for generating electricity. On the other hand, the fuel cycle cost is only about 20% of the total cost. Within this fuel cycle cost, more than half of the cost is the cost for recycling and treating the spent fuel. Due to such a high capital cost relative to the fuel cycle cost, raising the capacity factor is an effective way to improve the economy. However, the power plant must be shut down for maintenance. Therefore, shortening the maintenance period and extending the operational cycle is necessary to raise the capacity factor.

The operational cycle can be extended by raising the fuel enrichment and the discharge burnup of the fuel. The fuel cycle cost may also be reduced by

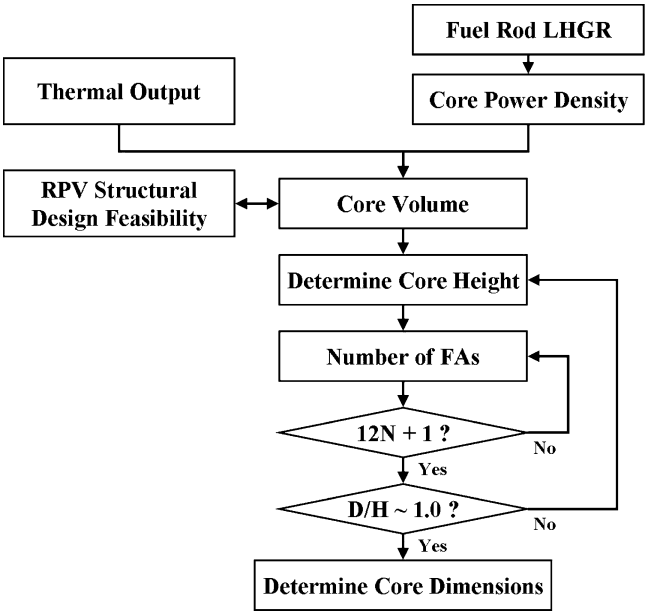


Fig. 2.14 Flow in determining the core size. (Taken from doctoral thesis of A. Yamaji, the University of Tokyo (2005) [9])

using high burnup fuel because the amount of energy output per given fuel mass can be increased, and therefore, the amount of spent fuel per given energy output can be reduced. On the other hand, development of new pellets or claddings may be required for such a high performance fuel, raising the fuel cycle cost.

From these considerations, the target average discharge burnup of the Super LWR is provisionally determined as about 45,000 MWd/t, which is expected to be easily attainable with the current LWR fuel experiences.

2.2.4 Design Targets

2.2.4.1 Flat Coolant Outlet Temperature Distribution

As the coolant temperature exceeds the pseudocritical temperature, the specific heat capacity decreases. This implies that for an average core outlet temperature of 500°C, the local coolant temperature may be significantly higher than that. The local increase of the coolant temperature may cause an excess heat up of the fuel rod cladding and may cause fuel failures. Therefore, the coolant outlet temperature distribution should be as uniform as possible to achieve a high average outlet temperature.

The coolant temperature depends on its flow rate and the heat flux from the fuel rods. Therefore, flattening the core radial power distribution is effective in flattening the coolant outlet temperature distribution. The outlet temperature distribution can also be flattened by adjusting the coolant flow rate to each fuel assembly, so that the power to flow rate ratio is kept the same for all fuel assemblies. The flow rate can be adjusted by designing appropriate pressure drops at the entrance of each fuel assembly using an inlet orifice.

The orifices in BWRs are mainly used for improving the core thermal-hydraulic stabilities. Generally, the BWR channel stability improves when the pressure drops and inertia in the single-phase flow region are increased. This is why inlet orifices are used in BWRs. For LMFBRs, inlet orifices are used to control the coolant flow rate to the fuel assemblies to effectively cool the fuel.

The primal reason of orifices use for the Super LWR is for effectively cooling the fuel. This is the same as the role of the orifices in LMFBRs. However, the former orifices are also important for attaining thermal-hydraulic stabilities, especially during the plant startup (see Chap. 5 for more details).

2.2.4.2 Flat Core Power Distribution

As is described above, the flattening of the core radial power distribution is important for effectively cooling the fuel (i.e., flattening the core outlet temperature distribution). The radial power distribution should also be kept constant throughout the operation, because the change in the power distributions would change the local power to flow rate ratio. For effectively cooling the fuel rods, the large temperature rise of the coolant from the core inlet to the outlet needs to be considered. Large power peaks near the outlet of the core should be prevented to stop excess heat up of the fuel rod cladding.

The power distributions should also be kept flat for reducing the MLHGR. The MLHGR needs to be kept as low as possible to reduce the fuel temperature. From the viewpoint of reducing the fuel temperature, large power peaks near the outlet of the core should also be prevented.

The radial core power distribution can be flattened by designing a heterogeneous core with different cycles of fuel assemblies and designing appropriate fuel loading patterns. For the fuel loading patterns of the Super LWR, similar patterns to those of PWRs are considered. The axial fuel designs largely depend on the axial moderator density distributions. In a PWR core, there is no bulk boiling and the moderator (coolant) density distribution is almost uniform. Hence, the axial design of the PWR fuel is basically uniform. In a BWR core, there is bulk boiling and the void fraction changes axially. The core average moderator density near the outlet is about half of that near the inlet. Hence, the BWR fuel is axially divided into two or more regions with different enrichments to flatten the axial power distribution. Although there is no boiling of water in the Super LWR core, the coolant (moderator) density continuously changes from the inlet to the outlet of the core. Therefore, the axial

design of the Super LWR needs to be considered in relation to this density distribution.

2.2.4.3 Burnup Reactivity Compensation

In the fast reactor, the production rate of the fissile material (predominantly the conversion of U-238 to Pu-239 via two-step β decays) is high relative to the consumption rate of the fissile material. This is why the reactivity change of a fast reactor is small. In the case of a fast breeder reactor, the production rate of the fissile material exceeds its consumption rate.

In contrast, the Super LWR is a thermal spectrum reactor (basically the same as BWRs or PWRs) and the fission chain reactions are maintained predominantly by the thermal neutrons. The conversion rate is low (about 0.5–0.6) and the core reactivity gradually decreases with the burnup. Therefore, a large excess reactivity is required at the beginning of each cycle. Compensating the large burnup reactivity change by control rods is undesirable as the insertions and withdrawals of control rods cause distortions of the core power distribution. Also, for such large reactivity compensation, the reactivity worth of the control rods would have to be large, but this would make a reactivity insertion accident severe. In PWRs, the chemical shim (controlling the concentration of boron in the primary coolant) is used for the burnup reactivity compensation, but this is not applicable to the Super LWR with a once-through direct cycle plant system. In BWRs, the burnable gadolinia (Gd_2O_3) poison is mixed in the fuel pellets for the burnup reactivity compensation. The burnup reactivity compensation of the Super LWR will be predominantly done by gadolinia, the same as in BWRs.

2.3 Core Calculations

The core calculations consist of neutronic and thermal-hydraulic parts. These parts are coupled to evaluate the core characteristics such as the core power or coolant temperatures.

2.3.1 Neutronic Calculations

2.3.1.1 Calculation Codes and Data Libraries

All calculations used for the development of the Super LWR are done by open source codes. For the neutronic calculations, SRAC2002 developed by the Japan Atomic Energy Agency (JAEA) is used. It is a general-purpose neutronics code system applicable to core analyses of various types of reactors [14]. The system

consists of: seven kinds of nuclear data libraries (ENDF/B-IV, -V, -VI, JENDL-2, -3.1, -3.2, -3.3); five modular codes integrated into SRAC2002 (collision probability calculation module (PIJ) for 16 types of lattice geometries, two Sn transport calculation modules (ANISN, TWOTRAN), and two diffusion calculation modules (TUD, CITATION)); and two optional codes for fuel assembly and core burnup calculations (ASMBURN, COREBN).

In the following, the Super LWR core is designed with the SRAC2002 using the JENDL3.3 nuclear data library. JENDL3.3 is a general-purpose nuclear data library applicable to the designs and analyses of both fast reactors and thermal reactors [15].

2.3.1.2 Cell Burnup Calculations of Normal Fuel Rods

The core neutronic calculation code used here is the COREBN code in SRAC2002. COREBN is a multidimensional core burnup calculation code based on macro-cross section interpolations by burnups and the finite difference diffusion method. The macro-cross section sets required by the core burnup calculations can be prepared by numerous cell burnup calculations and assembly burnup calculations.

An example horizontal cross section of a Super LWR fuel assembly is shown in Fig. 2.15 [9]. This fuel assembly consists of 300 fuel rods, 36 square water rods (inner water rods), 24 rectangular water rods, 16 control rod guide tubes, and an instrumentation guide tube. The details of their design are explained in Sect. 2.3.2. In the BWR and PWR fuel assemblies, most of the fuel rods are regularly aligned in a square lattice and the neutrons are moderated by the surrounding coolant. Some BWR fuel assemblies are equipped with water rods (or water channels) at the center of the fuel assemblies to provide additional neutron moderations. In such fuel assembly designs, the unit "fuel cell" for representing the fuel rods and the coolant

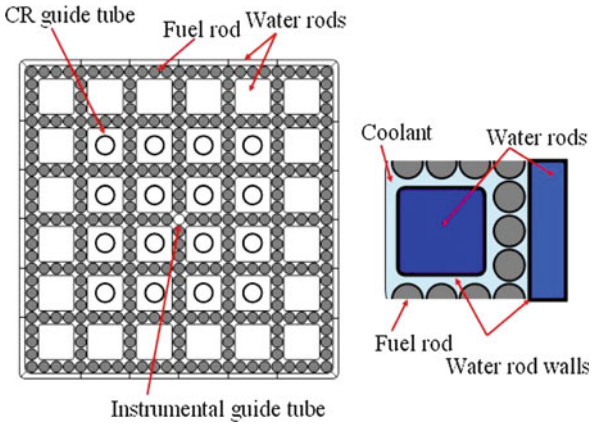


Fig. 2.15 Super LWR fuel assembly (horizontal cross section). (Taken from doctoral thesis of A. Yamaji, the University of Tokyo (2005) [9])

may consist of a single rod, surrounded by the coolant in a concentric circle geometry; the equivalent diameters are determined by taking into account the fuel to coolant volume ratio.

The lattice structure of the Super LWR fuel assembly is rather different from lattice structures of BWRs or PWRs. The fuel rods are aligned in a cruciform-like lattice around the square water rods. The moderator flowing through the water rods occupies a relatively large area in the fuel assembly and the moderator density is relatively high compared with the coolant density. The neutron moderation is mainly provided by the moderator flowing through the water rods. Therefore, the unit fuel cell of the Super LWR fuel assembly should consist of not only one fuel rod and the surrounding coolant, but also the adjacent water rods. The cell burnup calculation geometry for the "normal fuel rod" is shown in Fig. 2.16 [9]. The term "normal fuel rod" is used to distinguish the fuel rods without gadolinia from the fuel rods with gadolinia mixed into the pellets. The fuel pellet and the gap between the pellet and the fuel rod cladding are smeared into the homogeneous fuel section. This fuel section is surrounded by the cladding. The cladding is surrounded by the coolant, the water rod walls, and the moderator. Each constituent is converted into a concentric circle. The reflective boundary condition is adopted, assuming that the unit fuel cells are aligned endlessly in an infinitely large space. For the fuel assembly burnup calculation, the fuel pellet, cladding, and the coolant regions are homogenized into one region, and the water rod is separately treated.

For the cell burnup calculations, a total of 107 (61 fast and 47 thermal) energy groups based on the JENDL3.3 nuclear data library are used. These energy groups are collapsed into ten (five fast and five thermal) energy groups. The NR approximation is used for evaluation of the effective resonance cross sections. The burnup steps are gradually increased from 100 MWD/t at the beginning of life (BOL) to 1,000–10,000 MWd/t near the end of life (EOL) of the fuel. The small burnup step at the BOL is primarily for accurately considering the initial build ups of xenon.

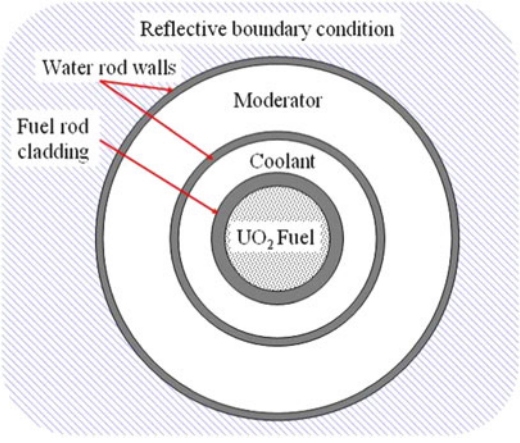


Fig. 2.16 Cell burnup calculation geometry for a normal fuel rod. (Taken from doctoral thesis of A. Yamaji, the University of Tokyo (2005) [9])

2.3.1.3 Cell Burnup Calculations of Fuel Rods with Gadolinia

Gadolinia (Gd_2O_3) is mixed into the pellets of some of the fuel rods for burnup reactivity compensation. To distinguish it from the normal fuel rod, the term "gadolinia rod" is used here. In the cell burnup calculations of the gadolinia rod, the gadolinia is assumed to be homogenously mixed into the pellets. The single-cell burnup calculation geometry used for the normal fuel rod calculation is not appropriate for modeling the gadolinia rod burnup. Using the same geometry would lead to the assumption that all fuel rods in the fuel assembly are gadolinia rods. In reality, only some of the fuel rods in the assembly are gadolinia rods. The geometry shown in Fig. 2.17 [9] is used to model the burnup of a gadolinia rod surrounded by six normal fuel rods. Gadolinia has a very large self-shielding effect due to the large neutron absorption cross section. Hence, most of the neutrons are initially absorbed at a pellet surface and the burnup gradually proceeds from the outer pellet surface to the inside. To model this, the pellet is divided into ten or more calculation meshes.

2.3.1.4 Assembly Burnup Calculations

The ASMBURN assembly burnup calculation code is based on the neutron flux calculation by the collision probability method and the burnup calculation by interpolations of macro-cross sections [14]. As the burnup proceeds, the compositions of the fuel rods in the assembly start to differ from each other depending on the spatial distribution of the neutron flux. Therefore, a precise modeling would require production and decay calculations for each fuel rod constituting the fuel assembly. However, when the fuel rods are aligned in a regular lattice, the differences in the

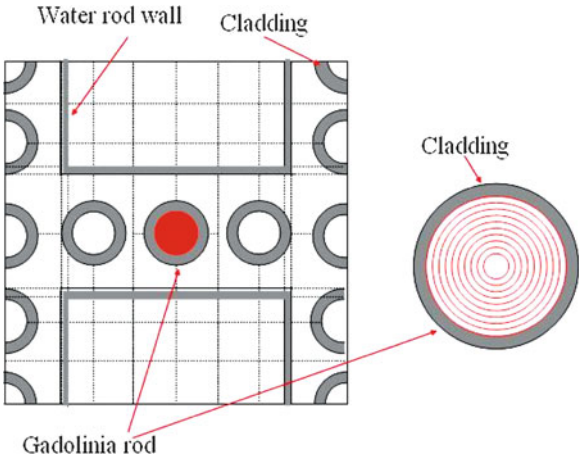


Fig. 2.17 Cell burnup calculation geometry for a gadolinia rod. (Taken from doctoral thesis of A. Yamaji, the University of Tokyo (2005) [9])

macro-cross sections between the rods can be approximated by the differences in the burnups.

ASMBURN uses the macro-cross section sets of the fuel cells, which are prepared by the cell burnup calculations in advance as described above. Those cell burnup calculations assume that one fuel cell is surrounded by the same fuel cells. Therefore, the ASMBURN modeling is not applicable when different types of fuel rods are aligned in large irregularities. ASMBURN first interpolates the macro-cross section of each fuel cell by the burnup as shown in Fig. 2.18 [9]. Then the neutron flux distribution is calculated and normalized by the thermal power of the fuel assembly at each burnup step. The burnup increase of each fuel cell is calculated by multiplying the relative power distribution by the time exposure at each burnup step, and the calculation proceeds to the next burnup step.

The ASMBURN calculation geometry of the Super LWR fuel assembly is shown in Fig. 2.19 [9]. The 1/4 symmetric geometry is adopted with perfect reflection boundary conditions along the symmetry lines. The boundary conditions for the sides of the fuel assembly are white reflections. The macro-cross section sets of the normal fuel rods and gadolinia rods are placed in the corresponding positions (the arrangement is an example). The nonburnable materials such as the water rod walls and moderators are treated heterogeneously. Inside the control rod guide tubes, the macro-cross section of either the moderator or boron carbide (B_4C) is

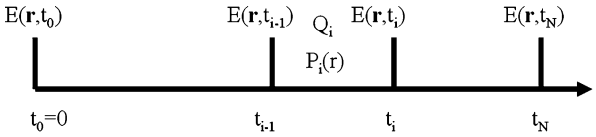


Fig. 2.18 Macro-cross section set interpolations by burnups. (Taken from doctoral thesis of A. Yamaji, the University of Tokyo (2005) [9])

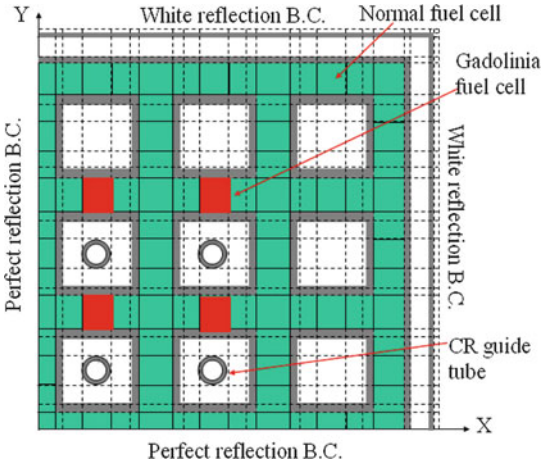


Fig. 2.19 ASMBURN calculation geometry (1/4 symmetric fuel assembly). (Taken from doctoral thesis of A. Yamaji, the University of Tokyo (2005) [9])

allocated to model the insertion and withdrawal of the control rods. The assembly burnup calculations are carried out with the ten (five fast and five thermal) energy groups, and the macro-cross section sets of the fuel assembly are prepared by collapsing down to two (one fast and one thermal) energy groups for the core burnup calculations.

2.3.1.5 Core Burnup Calculations

As is briefly mentioned above, COREBN is based on the macro-cross section interpolations by burnups and the finite difference diffusion method for the neutron flux calculations. The macro-cross section sets for each fuel assembly type are prepared by ASMBURN as described above. COREBN linearly interpolates the macro-cross section sets tabulated for the three parameters, namely, the burnup, fuel temperature, and the moderator temperature. The burnup process of COREBN is similar to that of ASMBURN. Since COREBN is not equipped with a coupling function to the thermal-hydraulic calculations, the user has to give the input data of fuel temperature and moderator temperature for the calculations.

The core burnup calculations are also carried out in a 1/4 symmetric core geometry as shown in Fig. 2.20 [9]. The macro-cross section sets of the fuel assemblies are allocated according to the cycle number of the fuel assemblies (first cycle, second cycle, and third cycle), insertion or withdrawal of the control rods, and coolant and moderator densities. These fuel assemblies are surrounded by light water with some stainless steel smeared to model the reflectors. The macro-cross section sets are allocated for each fuel element volume and renewed as the burnup proceeds. Each fuel element is further divided into calculation meshes to evaluate neutron flux distributions. The three-dimensional core power distribution is obtained by evaluating the power density for each calculation mesh. This means

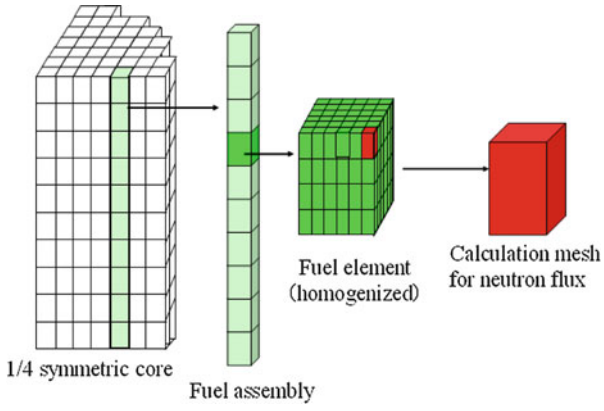


Fig. 2.20 COREBN calculation geometry (1/4 symmetric core). (Taken from doctoral thesis of A. Yamaji, the University of Tokyo (2005) [9])

that detailed pin-wise power distributions cannot be obtained with the method described here. The method for obtaining such detailed power distributions is explained in Sect. 2.7. The energy groups handled by the core burnup calculations correspond to those of the macro-cross section sets of the fuel assemblies, which have been prepared by the assembly burnup calculations. Thus, in this case, the two energy groups (one fast and one thermal) are used for the core burnup calculations. The precisions of the core burnup calculations may be increased by increasing the number of energy groups to be handled by the calculations.

2.3.1.6 Handling of Control Rods in ASMBURN and COREBN

The control rods of the Super LWR are similar to those of PWRs. They are cluster type control rods, located at the top of the core for insertion into the fuel assemblies. In the COREBN calculation, the fuel regions have to be allocated by homogenized macro-cross sections, which are prepared by SRAC and ASMBURN beforehand. Therefore, the homogenized cross section of the fuel element has to be prepared for two cases: the case with the control rods inserted into the fuel assembly and the case without the control rods.

The main roles of the control rods during normal operation are to make fine adjustments of the core reactivity and power distributions. Hence, most of the control rods are withdrawn from the core during the operation. The macro-cross section sets for such fuel elements should be prepared first, by calculating the nuclide compositions of the fuel assemblies without control rods present, and then, by evaluating the macro-cross section sets at each burnup step with them present. The normal burnup calculations by SRAC or ASMBURN are not capable of performing such calculations. Hence, the "branching burnup calculation" function of the codes will be used to model the insertion of control rods. The concept of this calculation is explained later in this section.

The insertion and withdrawal of control rods in COREBN are modeled by selecting appropriate macro-cross section sets as described in Fig. 2.21 [9]. In the COREBN calculations, the control rods inserted into the fuel assembly are assumed to be smeared into the fuel assembly and homogenized.

2.3.1.7 Branching Burnup Calculation

The core average coolant outlet temperature of the Super LWR is kept constant at 500°C throughout the operation. The coolant temperature is 280°C at the inlet and rises to the average outlet temperature of 500°C. Although most of the fuel assemblies are burnt in the environment close to this core average condition, some of the fuel assemblies may temporarily experience conditions that are deviated from the core average condition. Such deviations may occur due to, for example, the local insertion of control rods. Since the Super LWR is a thermal spectrum reactor and the coolant undergoes large density changes in the core, such local or temporary

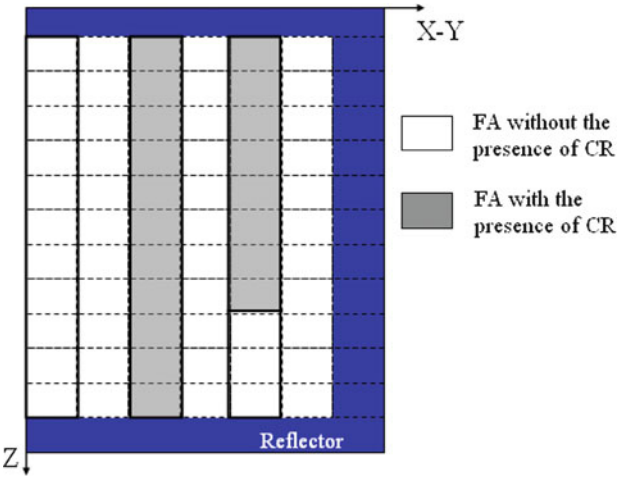


Fig. 2.21 Control rod models in COREBN. (Taken from doctoral thesis of A. Yamaji, the University of Tokyo (2005) [9])

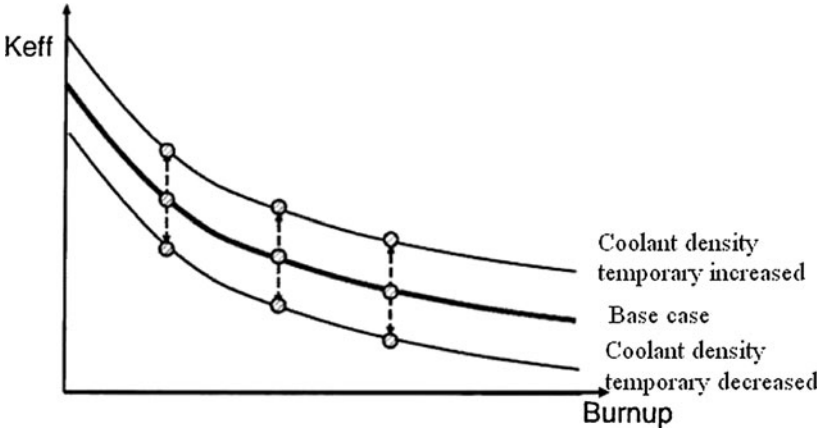


Fig. 2.22 Concept of the branching burnup calculation. (Taken from doctoral thesis of A. Yamaji, the University of Tokyo (2005) [9])

deviations in the coolant and moderator densities need to be accurately modeled in the calculations.

The branching burnup calculation modes of SRAC and ASMBURN allow the modeling of temporary changes in the coolant and moderator densities [14]. The branching burnup modes calculate the collapsed macro-cross sections when the coolant (moderator) density or fuel temperature is instantaneously changed from the base case. This concept is described in Fig. 2.22 [9]. The thick line in the figure represents the base case (coolant density ρ_0). For example, the dependence of the coolant density reactivity coefficient on the burnup can be evaluated as follows:

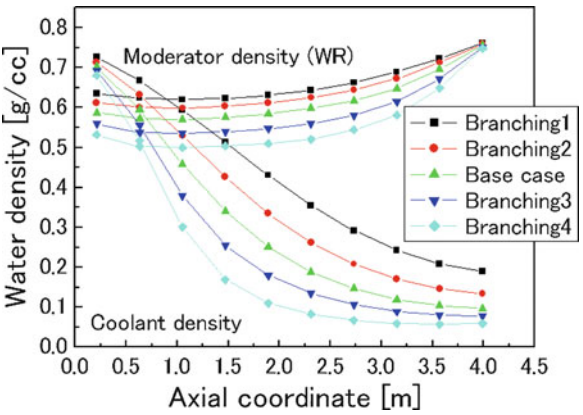


Fig. 2.23 Water density distributions considered for the core design (Example 1). (Taken from doctoral thesis of A. Yamaji, the University of Tokyo (2005) [9])

First, the burnup calculation proceeds until the target burnup is at the coolant density of ρ_0, then at the target burnup, the coolant density is instantaneously changed to $\rho_0 + \Delta\rho$ or $\rho_0 - \Delta\rho$. The descriptive term "branching" came from the way this calculation branches off from the base case at a particular burnup step. This calculation differs from the calculation when the normal burnup calculation is carried out at the coolant density of $\rho_0 + \Delta\rho$ or $\rho_0 - \Delta\rho$. The latter calculation simply represents the change of normal operating conditions and does not represent the effect of burnup on the coolant density reactivity coefficient.

In order to model the burnup history of various fuels with respect to coolant density changes, the macro-cross section sets need to be prepared for various density distributions which may be expected in the core. Such calculations are possible with the branching burnup calculations. Figures 2.23 [9] and 2.24 [9] show examples of water density distributions considered for the core designs. Depending on the core designs, especially the coolant flow scheme in the core, the density distributions to be considered for the core design vary. Figure 2.23 [9] shows that while the coolant density changes greatly from the bottom to the top of the core, the moderator density (flowing through water rods) is kept high. Figure 2.24 [9] shows the fuel assembly average water density, which is the average density of the coolant and the moderator. The distributions are for designing a core where outer regions of the core (outer fuel assemblies) are cooled by descending coolant flow from the top to the bottom of the core (the details of the design are explained in Sect. 2.4). The coolant densities around the outer core region of such designs vary greatly from the inner core. Hence, macro-cross section sets need to be prepared for the inner and outer fuel assemblies.

2.3.1.8 Summary of the Neutronic Calculations

The neutronic calculations are described by Fig. 2.25 [9]. In the example there the core is divided into three different enrichment sections. Within each of the three

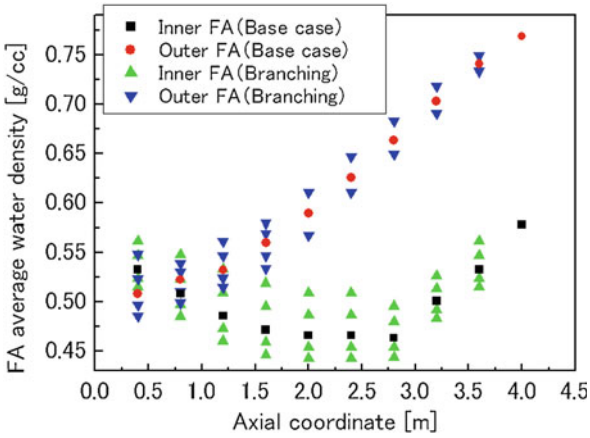


Fig. 2.24 Water density distributions considered for the core design (Example 2). (Taken from doctoral thesis of A. Yamaji, the University of Tokyo (2005) [9])

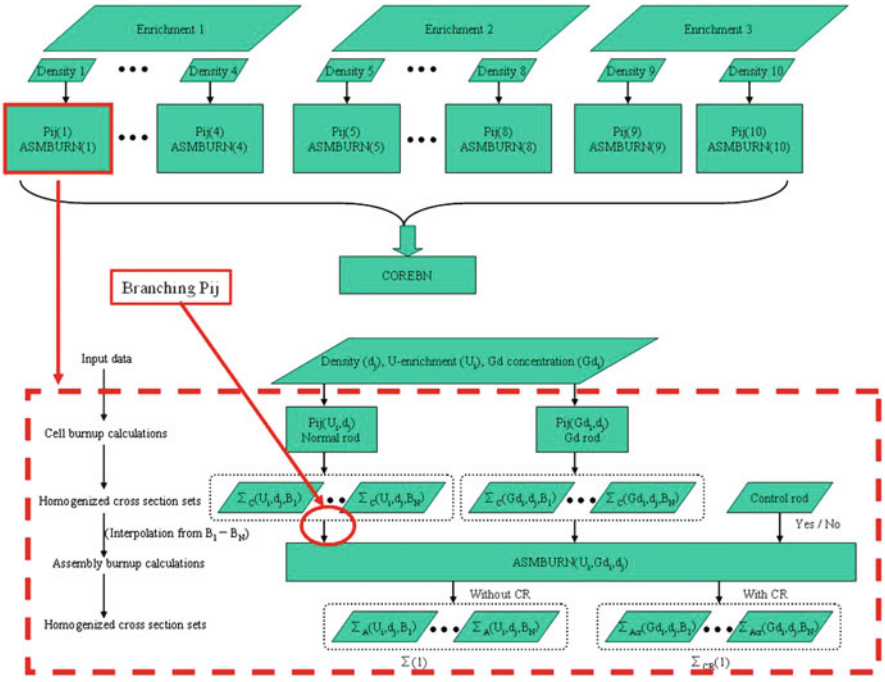


Fig. 2.25 Schematic summarizing the neutronic calculations. (Taken from doctoral thesis of A. Yamaji, the University of Tokyo (2005) [9])

axial regions, the coolant and moderator densities change along the core height. Therefore, each region is further divided into a number of segments. The macro-cross section sets of the fuel segment are obtained for each fuel segment with corresponding coolant and moderator densities by SRAC and ASMBURN. The branching burnup calculations are carried out to model the burnup history of each fuel segment. These calculations are carried out for the cases with and without the control rods to model the insertions and withdrawals of control rods.

Figure 2.26 [9] outlines the cell burnup calculations (SRAC) and assembly burnup calculations (ASMBURN). The input parameters for these calculations are the basic fuel information such as the fuel enrichment, gadolinia concentration, coolant density, and moderator density. The normal burnup calculations are first carried out with the base density distributions. After that, the branching burnup calculations are carried out to consider the density changes on insertion and withdrawal of control rods.

2.3.2 *Thermal-Hydraulic Calculations*

The thermal-hydraulic calculations are important for designing the Super LWR core, since the fission reactions by thermal neutrons are greatly affected by the

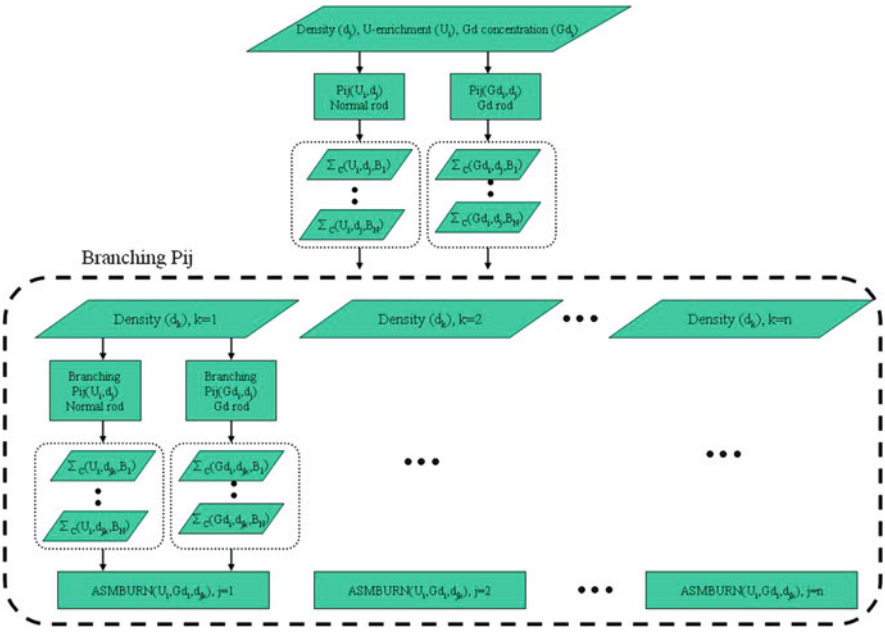


Fig. 2.26 Outline of the cell burnup calculations and assembly burnup calculations. (Taken from doctoral thesis of A. Yamaji, the University of Tokyo (2005) [9])

coolant and moderator density distributions in the core. The thermal-hydraulic calculations are also required to evaluate the basic thermal-hydraulic characteristics of the core, such as the average coolant outlet temperature, and to verify that all fuel rods are efficiently cooled.

Due to the constraints in the neutronic calculation models used for the core design, the fuel assemblies are axially divided into a number of fuel elements, and within each fuel element, the fuel assembly is homogenized. For the purposes of evaluating the thermal-hydraulic feedback to the neutronic calculations and evaluating the basic thermal-hydraulic characteristics of the core, detailed calculations involving the modeling of each fuel rod are not necessary. There are three fundamental thermal-hydraulic parameters required for the core design calculations:

1. Average coolant density (and temperature) of the fuel element for the neutronic calculations
2. Average moderator density (and temperature) of the fuel element for the neutronic calculations
3. Estimated peak cladding temperature for roughly considering the effective cooling of fuel rods

Among these three parameters, the coolant and moderator densities are necessary for the neutronic calculations. The estimated cladding temperatures are also necessary, because the peak cladding temperature is the primal thermal limit when designing a high temperature core. Hence, the estimated peak cladding temperature is used in the core design to determine appropriate design parameters such as the fuel loading patterns, control rod patterns, and the coolant flow rate adjustments by inlet orifices for the fuel assemblies.

Generally, there are three types of thermal-hydraulic calculation methods for core design purposes: single-channel analysis, subchannel analysis, and three-dimensional computational fluid dynamics (CFD). The single channel analysis is based on the simplest model for obtaining the first estimation while the CFD is based on the most fundamental physical model. The subchannel analysis is an intermediate method. The computational power requirements for these calculations depend on the level of precisions in their models. For the core design of the Super LWR, the single channel analysis model is used to determine the basic core characteristics first, and then the subchannel analyses are carried out to evaluate the peak cladding temperature.

Figure 2.27 [9] describes the single channel analysis model used in the SPROD code, which is the thermal-hydraulic calculation code developed by researchers at the University of Tokyo for designing the Super LWR core. The geometry of the model consists of the pellet, gap, cladding, coolant, water rod wall, and the moderator. Each fuel channel is axially divided into 40 layers and the radial heat conductions and transfers within each layer are calculated. After these calculations, the axial heat transport by the coolant and the moderator are calculated. In these calculations, the axial heat conduction is neglected. This assumption is applicable because the radial temperature gradient in the fuel pellet is much greater than that in the axial direction.

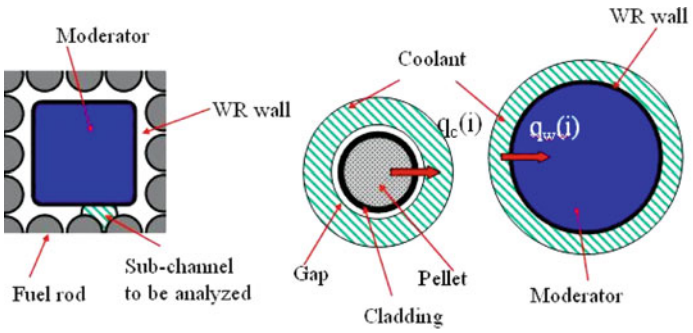


Fig. 2.27 Single channel thermal-hydraulic analysis model. (Taken from doctoral thesis of A. Yamaji, the University of Tokyo (2005) [9])

2.3.2.1 Radial Heat Conductions and Transfers

The radial heat conductions and transfers are considered from the pellet to the gap, cladding, coolant, water rod wall, and the moderator.

1. Fuel pellet

The heat equation of the heat conduction from the pellet center to the surface can be expressed as follows:

$$\frac{1}{r}\cdot\frac{d}{dr}\cdot k_{\text{fuel}}\cdot r\cdot\frac{dT}{dr}=-q''',$$

$$k_{\text{fuel}}=\frac{3,824}{T+129.4}+6.13\times10^{-11}\cdot T^3, \tag{2.2}$$

where r_{fuel} is the pellet radius and k_{fuel} is the pellet thermal conductivity.

From the above equations, the temperature drop can be expressed as follows:

$$\Delta T_{\text{fuel}}=\frac{q'''\cdot r^2{}_{\text{fuel}}}{4\bar{k}_{\text{fuel}}}=\frac{q'}{4\pi\bar{k}_{\text{fuel}}}, \tag{2.3}$$

where $\bar{k}_{\text{fuel}}$ is the average thermal conductivity of the pellet.

The temperature drop depends only on the linear heat rate and the thermal conductivity of the pellet and it does not depend on the pellet radius. This implies that in order to keep the fuel temperature below a certain limit, the linear heat generation rate needs to be limited.

2. Gap

There is initially a gap of about 0.1 mm between the pellet and the cladding at the beginning of exposure. This gap is initially filled with helium and gradually the fission product (FP) gasses start to accumulate as the burnup proceeds. Although the

gap size is very small, the temperature drop in this gap is large because of the low thermal conductivities of these gasses.

Since there is no source of heat at the gap, the right hand side of (2.2) becomes zero as shown below.

$$\frac{1}{r} \cdot \frac{d}{dr} \cdot k_{\text{gap}} \cdot r \cdot \frac{dT}{dr} = 0. \tag{2.4}$$

Therefore, the following relationships can be obtained:

$$\Delta T_{\text{gap}} = \frac{q'}{2\ \pi \left(\frac{k_{\text{gap}}}{t_{\text{gap}}}\right) r_{\text{fuel}}} = \frac{q'}{2\ \pi h_{\text{gap}} r_{\text{fuel}}}, \tag{2.5}$$

where k_{gap} is the thermal conductivity of the gas, t_{gap} is the gap size, and h_{gap} is the gap conductance.

3. Cladding

There is no source of heat at the cladding, so the heat equation becomes as follows:

$$\frac{1}{r} \cdot \frac{d}{dr} \cdot k_{\text{cladding}} \cdot r \cdot \frac{dT}{dr} = 0, \tag{2.6}$$

where k_{cladding} is the thermal conductivity of the cladding.

Therefore the temperature drop in the cladding can be expressed as follows:

$$\Delta T_{\text{cladding}} = \frac{q'}{2\ \pi \left(\frac{k_{\text{cladding}}}{t_{\text{cladding}}}\right) r_{\text{fuel}}}, \tag{2.7}$$

where t_{cladding} is the thickness of the cladding.

The thermal conductivity of the cladding is relatively high, so the temperature drop in the cladding is small.

4. Coolant

The ratio of the number of fuel rods to the number of water rods (N_{fw}) is considered and the hydraulic diameter of the fuel channel is determined. The total area occupied by the coolant and the moderator for a unit cell can be expressed as follows:

$$S = S_{\text{coolant}} + \frac{S_{\text{waterrod}}}{N_{\text{fw}}}, \tag{2.8}$$

$$N_{\text{fw}} = \frac{N_{\text{fuelrod}}}{N_{\text{waterrod}}}. \tag{2.9}$$

The hydraulic diameter of the coolant can be expressed as follows:

$$D_{\mathrm{h}} = \frac{4s}{\pi\left(D_{\mathrm{fuel}} + \dfrac{D_{\mathrm{waterrod}}}{N_{\mathrm{fw}}}\right)}. \tag{2.10}$$

Thus,

$$T_n^{\mathrm{surface}} - T_n^{\mathrm{coolant}} = \frac{q_n^{\mathrm{fuel}'}}{\pi h_s^{\mathrm{coolant}} D_{\mathrm{h}}}, \tag{2.11}$$

$$h_s^{\mathrm{coolant}} = \frac{Nu_{\mathrm{coolant}} k_{\mathrm{coolant}}}{D_{\mathrm{h}}}, \tag{2.12}$$

where h_s^{coolant} is the heat conductance to the coolant, Nu_{coolant} is Nusselt number of the coolant, k_{coolant} is the thermal conductivity of the coolant, T_n^{coolant} is the coolant temperature at the nth mesh, and $q_n^{\mathrm{fuel}'}$ is the linear heat generation rate of the fuel rod at the nth mesh.

To evaluate the Nusselt number, the Oka–Koshizuka correlation [7] is used.

5. Moderator

The heat transfer from the coolant to the moderator is similar to that from the cladding to the coolant. It can be expressed as follows:

$$\begin{aligned} T_n^{\mathrm{coolant}} - T_n^{\mathrm{waterrod}} = q_n^{\mathrm{coolant}} \Bigg[& \frac{1}{\pi h_s^{\mathrm{waterrod}} (D_{\mathrm{waterrod}} - 2t_{\mathrm{cladding}})} \\ & + \frac{1}{\pi h_s^{\mathrm{waterrod}} (D_{\mathrm{waterrod}} - 2t_{\mathrm{cladding}})} \\ & + \frac{R_{\mathrm{cool}}}{\pi\left(\frac{k_{\mathrm{hedge}} \bar{N}u}{t_{\mathrm{cladding}}}\right)(D_{\mathrm{hedge}} - t_{\mathrm{hedge}})} + \frac{R_{\mathrm{build}}}{\pi\left(\frac{k_{\mathrm{cladding}}}{t_{\mathrm{hedge}}}\right)(D_{\mathrm{hedge}} - t_{\mathrm{hedge}})} \Bigg]. \\ & + \frac{1}{\pi\left(\frac{k_{\mathrm{cladding}}}{t_{\mathrm{cladding}}}\right)(D_{\mathrm{waterrod}} - 2t_{\mathrm{cladding}})} \\ & + \frac{1}{\pi\left(\frac{k_{\mathrm{cladding}}}{t_{\mathrm{cladding}}}\right)(D_{\mathrm{hedge}} - 2t_{\mathrm{cladding}})} \end{aligned} \tag{2.13}$$

The first term of the right hand side of (2.13) denotes the heat transfer of the moderator, the second term is the heat transfer of the coolant, and the third term is the heat conduction of the water rod wall.

The radial temperature drops obtained by these equations are shown in Fig. 2.28 [9].

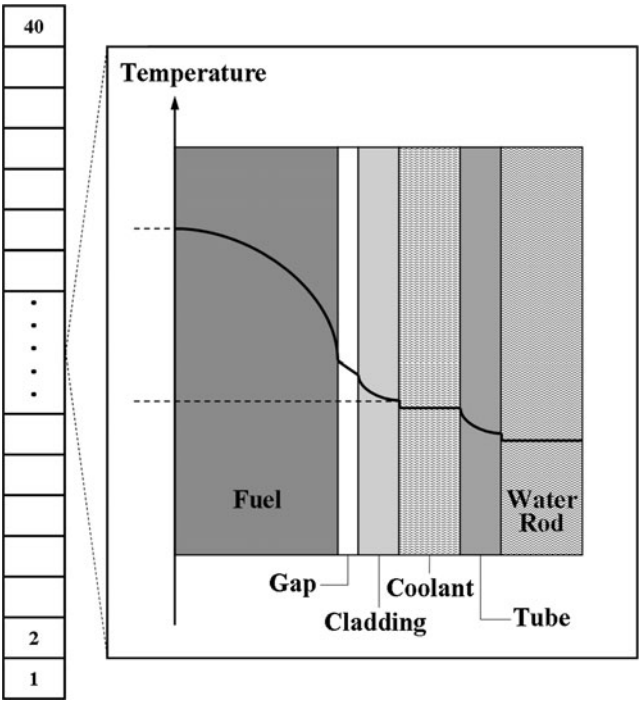


Fig. 2.28 Radial temperature drops predicted by the single channel analysis model. (Taken from doctoral thesis of A. Yamaji, the University of Tokyo (2005) [9])

2.3.2.2 Heat Transfer Correlation for Supercritical Water Cooling

Generally, the heat transfer rate can be expressed by the Nusselt number, the thermal conductivity, and the hydraulic diameter as follows:

$$H_s = \frac{Nu \cdot \lambda}{D_h}, \tag{2.14}$$

where H_s is the heat transfer rate, Nu is Nusselt number, λ is the thermal conductivity, and D_h is the hydraulic diameter.

The Nusselt number is calculated by the Oka–Koshizuka correlation [7] as described in (2.1). This correlation can be easily applied to the thermal-hydraulic calculations for the core design because it does not require the wall temperature.

2.3.2.3 Axial Heat Transport

The single channel analysis model for the core thermal-hydraulic calculations does not consider the pressure drops and only takes into account the conservations of

energy and mass. In the actual core design, the coolant inlet flow rate to each fuel assembly is assumed to be adjusted by the inlet orifice attached to it. However, for the simplicity of calculations, the pressure drops are not evaluated and the coolant flow rate is given as assumed by the design. The pressure drops and the conservation of momentum are considered in the subchannel analyses, which are explained later in Sect. 2.5. Here, first, the axial heat transport by the coolant and moderator are considered. The conservation of energy is expressed as follows:

$$q_n{}' \cdot \Delta h = w_n \cdot H(P_n, T_n) - w_{n-1} \cdot H(P_{n-1}, T_{n-1}), \tag{2.15}$$

where Δh is the mesh height, $q_n{}'$ is the linear heat rate of the fuel rod at the nth mesh, H is the enthalpy, w_n is the coolant flow rate (mass flux) at the nth mesh, P_n is the coolant pressure at the nth mesh, and T_n is the coolant temperature at the nth mesh.

Here, the conservation of mass is expressed as follows:

$$w = w_n = w_{n-1}. \tag{2.16}$$

By neglecting the pressure drops, (2.17) is obtained.

$$P = P_n = P_{n-1}. \tag{2.17}$$

Thus the conservation of energy can be expressed as follows:

$$q_n{}' \cdot \Delta h = w \cdot H(P, T_n) - w \cdot H(P, T_{n-1}). \tag{2.18}$$

The axial heat transport is calculated by (2.18). Similar expressions can be obtained for the moderator in the water rod. Hence, the conservation of energy for the coolant and moderator can be expressed as follows:

$$\left(q_n{}^{\text{fuel}'} - q_n{}^{\text{coolant}'}\right) \cdot \Delta h = w_{\text{coolant}} \cdot H\left(P, T_n{}^{\text{coolant}}\right) - w_{\text{coolant}} \cdot H\left(P, T_{n-1}{}^{\text{coolant}}\right), \tag{2.19}$$

$$q_n{}^{\text{coolant}} \cdot N_{\text{fw}} \cdot \Delta h = w_{\text{waterrod}} \cdot H\left(P, T_n{}^{\text{waterrod}}\right) - w_{\text{waterrod}} \cdot H\left(P, T_{n-1}{}^{\text{waterrod}}\right), \tag{2.20}$$

where w_{coolant} is the coolant flow rate, $w_{\text{water rod}}$ is the moderator flow rate, $T_n{}^{\text{coolant}}$ is the coolant temperature at the nth mesh, and $T_n{}^{\text{waterrod}}$ is the moderator temperature at the nth mesh.

2.3.2.4 Outline of the Single Channel Thermal-Hydraulic Analysis

The analysis explained so far can be summarized as follows:

1. Input geometrical parameters and inlet coolant temperature and flow rate.
2. Read the axial heat flux distribution from the core calculation.

3. Determine an adequate inlet flow rate tentatively.
4. Determine an adequate coolant temperature and moderator temperature tentatively.
5. Evaluate the radial heat conduction and transfer from the tentatively determined temperature distribution in step 4, assuming that the heat flux from the fuel rod is kept constant.
6. Evaluate the axial heat transport from the coolant to moderator heat flux obtained in step 5 and the fuel rod heat flux, and determine the new coolant and moderator temperatures.
7. Repeat steps 4–6 until the coolant and moderator temperatures are converged.
8. Evaluate the coolant and moderator temperature distributions and the cladding temperature.

2.3.2.5 Applying the Single Channel Model to Core Thermal-Hydraulic Calculations

The core thermal-hydraulic calculations are based on the single channel analysis model. On the other hand, the three-dimensional core power distribution is obtained by COREBN for the calculation mesh described in Fig. 2.20 [9]. In the core thermal-hydraulic calculations, the neutron flux calculation mesh of the COREBN is assumed to compose a "fuel channel group." The fuel channels in this fuel channel group are assumed to be identical.

Figure 2.29 [9] shows the core thermal-hydraulic calculations by the single channel model. Each fuel assembly is assumed to be composed of 36 fuel channel

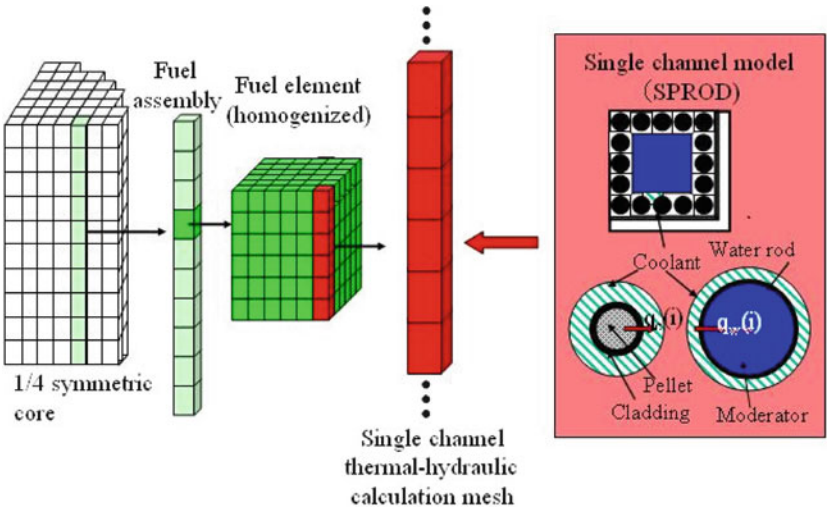


Fig. 2.29 Core thermal-hydraulic calculations by the single channel model. (Taken from doctoral thesis of A. Yamaji, the University of Tokyo (2005) [9])

groups. Within each fuel channel group, the fuel channels are assumed to be identical to each other. Since it is based on the single channel model, the energy and mass transports between the adjacent subchannels are neglected. The pressure drops and the transports of energy, mass and momentum between the subchannels are considered by the subchannel analyses described in Sect. 2.5.

2.3.3 Equilibrium Core Calculations

2.3.3.1 Two- and Three-Dimensional Core Calculation Models

The R-Z two-dimensional core calculation model, as described by Fig. 2.30, may be a good first approximation to calculate a fast reactor core with a relatively simple loading pattern of hexagonal fuel assemblies (a tight fuel lattice). In such a configuration, the spatial dependence of the fast neutron flux is small and the rough estimation by the R-Z two-dimensional model may be applicable.

However, when calculating a thermal-spectrum core with large heterogeneities, the R-Z two-dimensional model is inadequate for design purposes. In a thermal-spectrum core, the spatial dependence of the thermal neutron flux is large. The fuel assemblies are loaded with a relatively complex pattern to flatten the neutron flux distributions. Hence, the calculation of such a core requires the modeling of each fuel assembly with a three-dimensional model as shown in Fig. 2.31. To conserve computational power, symmetric boundary conditions can be applied.

In the case of the Super LWR core, design, the X-Y-Z three-dimensional core calculation model is essential. It is a thermal-spectrum core with large heterogeneities. Not only the neutron flux but also the special dependences of the coolant temperature and density are large. These parameters may also be largely affected by the local insertions of control rods. The core characteristics also depend on the burnup distributions, which ultimately depend on the core power distributions, control rod patterns and fuel replacement patterns. In order to consider these parameters in the design, the three-dimensional core calculation model is required.

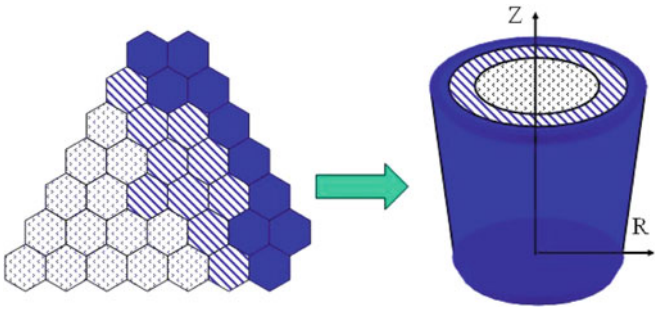


Fig. 2.30 R-Z two-dimensional core calculation model

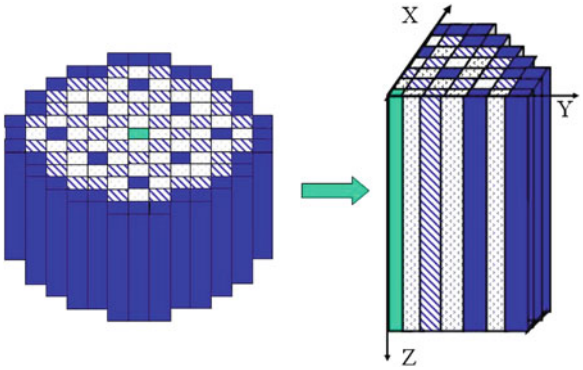


Fig. 2.31 X-Y-Z three-dimensional core calculation model (1/4 symmetric core)

2.3.3.2 Coupling of Neutronic and Thermal-Hydraulic Calculations

The coupling of neutronic and thermal-hydraulic calculations is especially important for designing the Super LWR core. The density change of the coolant (and moderator) is large and sensitive to the enthalpy rise of the coolant as it flows from the core inlet to the outlet. On the other hand, the core neutronic characteristics strongly depend on the coolant and moderator density distributions.

The COREBN code does not have the coupling function. Hence, the burnup calculations for one cycle of the core operation is divided into a number of burnup steps. Within each burnup step, the neutronic and thermal-hydraulic calculations are coupled by the core power and density distributions (within each burnup step, the coolant density distribution is assumed to be constant). These calculations are repeated until the core power distribution and the density distributions are converged. Once the convergence is obtained, the burnup step proceeds to the next step. For the coupling calculations, the macro-cross section sets of the fuel assemblies are prepared for different coolant and moderator densities and these are interpolated by burnups.

2.3.3.3 Equilibrium Core Calculations

Normally, a thermal spectrum core requires several different types of fuel assemblies in appropriate loading positions to flatten the radial power distributions. When a reactor first starts operation (i.e., burning the initial core), all fuel assemblies in the core are fresh but not identical. Fuel assemblies with different average enrichments are used to flatten the radial power distributions. After one cycle of operation, the reactor is shutdown and low reactivity fuel assemblies are removed from the core and new fresh fuel assemblies are introduced into the core (depending on the core, about 1/4 to 1/3 of the fuel assemblies are replaced). During the fuel replacement, the loading positions of the newly introduced fresh fuel assemblies and the

rest of the irradiated fuel assemblies are shuffled. The shuffling patterns are determined from the viewpoint of the neutron economy and also to achieve flat core power distributions. At the end of each operational cycle, such fuel replacements take place before starting the operation of the next cycle.

By repeating the sequence of operation followed by fuel replacements, the core gradually reaches the equilibrium state where the Nth cycle of the operation is identical to the $(N + 1)$th cycle of the operation. Such a core is called the "equilibrium core." In some designs, the Nth cycle is identical to the $(N + 2)$th cycle. Such a core is also regarded as an equilibrium core. Here, the core design of the Super LWR implies the equilibrium core design unless stated otherwise. The characteristics of the equilibrium core are considered to be representative and it is considered to be appropriate to develop the new design concepts with the equilibrium core design.

In a strict sense, the designing of an equilibrium core requires the designing of the initial core and the subsequent transition cores to reach the equilibrium state. However, it is not an efficient way to develop the new core concepts. Instead, the equilibrium core can also be designed in the following way. First, some adequate initial burnup distribution of the equilibrium core is determined at the begin of cycle (BOC). Then, core calculations of one cycle are carried out with some suitable control rod patterns and then some suitable fuel reload patterns. Next, the initial core burnup distribution at the BOC of the next cycle is renewed from the results obtained by the core calculations of the previous cycle and the fuel reload patterns. The control rod patterns and the fuel reload patterns are fixed and these calculations are repeated until the initial burnup distributions are converged. When the convergence is obtained, the core can be regarded to be an equilibrium core. Once the equilibrium core is obtained, the parameters subject to the design margins, such as the maximum cladding temperature or the MLHGR, are evaluated. The design parameters such as the control rod patterns or the fuel reload patterns can be reconsidered, if necessary, to increase the design margins or to improve the design. Such an equilibrium core design is shown in Fig. 2.32 [9].

2.4 Core Designs

This section describes the basic design concepts of the Super LWR core including the fuel rod and fuel assembly designs. The core thermal-hydraulic characteristics are unique and strongly coupled with the neutronic characteristics of the core.

2.4.1 Fuel Rod Designs

The basic fuel rod design concept of the Super LWR is described in the following. Some of the design parameters are tentatively determined for the purpose of

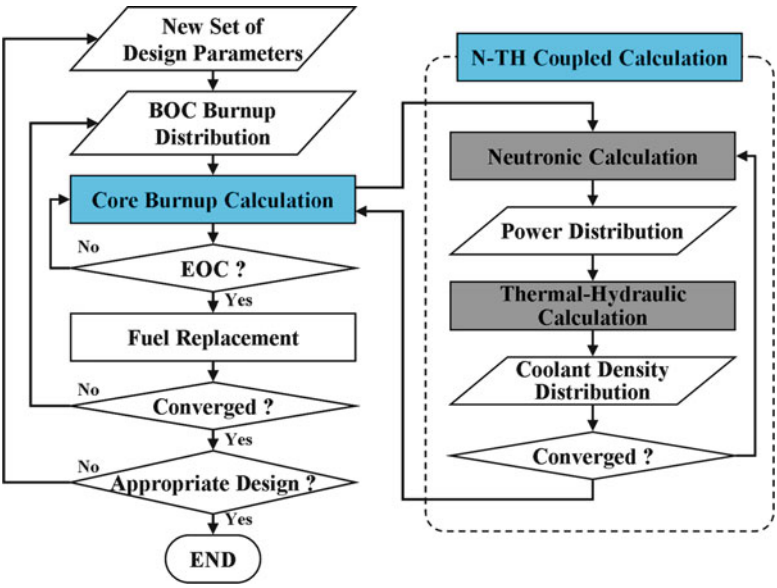


Fig. 2.32 Outline of the equilibrium core calculations. (Taken from doctoral thesis of A. Yamaji, the University of Tokyo (2005) [9])

designing the core. These parameters are reconsidered with respect to the fuel integrity under the fuel rod analyses in Sects. 2.7 and 2.8.

2.4.1.1 Fuel Rod Heated Length

As described in Sect. 2.2.3, the heated length (i.e., the active core height) of the fuel rod is determined from the considerations made in determining the core size. Thus, the heated length of the fuel rod is 4.20 m. This is a little longer than in BWRs or PWRs (about 3.70 m), but the manufacturing of such fuel rods is expected to be readily attainable with current technologies.

The entire length of the fuel rod can be approximated by the sum of the heated length and the plenum length. The fuel rod length ultimately affects the height of the reactor pressure vessel (RPV). If the plenum to fuel volume ratio of the fuel rod is around 10% (which is about the same as that of the PWR fuel rod), then the RPV height of the Super LWR will be roughly the same as that of PWRs.

2.4.1.2 Fuel Rod Diameter

A thin fuel rod is desirable from the viewpoint of gaining the necessary core power density. However, the manufacturability of thin rods needs to be considered. Also, especially in the case of a fast reactor with MOX fuel, the pellet diameter has a large

influence on the plutonium conversion ratio of the core. For current LWRs, the fuel rod diameters are about 12.0 mm for BWRs and 9.5 mm for PWRs. Historically, their fuel rod diameters have been decreasing predominantly to lower the MLHGR. By considering these points, the fuel rod diameter of the Super LWR is tentatively determined as 10.2 mm.

2.4.1.3 Fuel Rod Cladding Materials

Due to the high pressure and temperature, the Zircaloy claddings, which have been extensively used in BWRs and PWRs, cannot be used in the Super LWR. Research and development for new cladding materials is currently proceeding in various organizations. The candidate materials include stainless steels (austenitic and ferrite), ODS steels (ODS: oxide dispersion strengthened), nickel alloys, and many other alloys, which have high strength at elevated temperatures.

Regarding stainless steels, type 304 stainless steel was used in early PWRs and type 316L has been used in LMFBRs. Stainless steels also have been extensively used as ex-core structural materials for nuclear reactors. Stress corrosion cracking (SCC) may become a problem when stainless steels are used as cladding materials. This problem should be carefully considered in the Super LWR. On the other hand, from the long experience of supercritical FPP operations, SCC has not been a problem.

As for nickel alloys, type 625 and type 800 alloys have been considered for the steam cooled FBR concept by B&W, GE, and WH [16]. Table 2.1 [9] shows an example composition of a nickel alloy and neutron absorption cross sections of each nuclide. From the viewpoint of neutron economy, materials with low thermal neutron absorption cross sections are more desirable for the cladding. It can be easily seen from Table 2.1 [9] that nickel has the dominant contribution to the neutron absorptions of the alloy. Chromium and iron also have relatively large contributions. Although boron has an especially large thermal neutron absorption cross section, since its content is very small, its influence is expected to be negligible on the neutron economy.

Table 2.1 Example composition of a nickel alloy. (Taken from doctoral thesis of A. Yamaji, the University of Tokyo (2005) [9])

Nuclide	composition (wt%)	Thermal neutron absorption cross section (isotope average) (barn)	Nuclide	Composition (wt%)	Thermal neutron absorption cross section (isotope average) (barn)
B	0.003	759	Fe	18.366	2.55
Mn	0.175	13.3	Nb	5.125	1.15
Ti	0.90	6.1	S	0.008	0.520
Ni	52.5	4.43	Al	0.50	0.230
Cu	0.15	3.79	P	0.008	0.180
Cr	19.0	3.1	Si	0.175	0.16
Mo	3.05	2.65	C	0.04	0.0034

2.4.1.4 Evaluating Method and Limits for Cladding Stress

For a given fuel rod diameter, changing the cladding thickness has various neutronic and mechanical influences. From the viewpoint of the neutronics, the moderator to fuel volume ratio varies and the neutron absorption by the cladding changes. Mechanically, the thermal stress and mechanical stress on the cladding vary. Therefore, the effects are not simple and need to be considered comprehensively. In PWRs, due to the high coolant pressure and temperature, buckling collapse of the cladding is considered in designing the cladding thickness. The coolant pressure and temperature of the Super LWR are even higher than those of PWRs. Therefore, consideration of buckling collapse is important in designing the Super LWR fuel rod. In this section, the cladding thickness is first determined with rough and conservative estimations. This fuel rod design is used for the core design to evaluate basic core characteristics. Then, the fuel rod integrity is considered through fuel rod analyses in Sects. 2.7 and 2.8 based on the operating conditions obtained by the core design.

The cladding thickness is conservatively determined to prevent mechanical failure of the cladding during abnormal transients. In this process, detailed fuel rod behaviors such as FP gas release or PCMI are not considered. Instead, the following rough estimation method is used. This method is also used in BWR fuel rod design for the first estimation. The stresses acting on the cladding are classified and evaluated according to the basic concept of the ASME Boiler and Pressure Vessel Code Section III-NB. This code was developed based on the maximum shearing stress theory.

Another method is based on the theory given by Von Mises. This method generally describes the experimental results better than the maximum shearing stress theory. However, it requires detailed stress analyses.

The simple method based on the maximum shearing stress theory is enough for determining the first trial design of the Super LWR fuel rod. The evaluated cladding stresses are compared with the stress limit ratios shown in Table 2.2 [9]. Generally, the cladding materials have good ductility and high yield strength. Among the stress limits, the limit for the primary membrane stress is most limiting. Hence, the stress limits for the cladding effectively limit the primary membrane stress to a value below half of the tensile strength of the cladding during abnormal transients.

Table 2.2 Stress limit ratios [9]. (Taken from doctoral thesis of A. Yamaji, the University of Tokyo (2005) [9])

	Stress limit ratios			
	Normal operation		Transients	
	Against the yield strength	Against the tensile strength	Against the yield strength	Against the tensile strength
Primary membrane stress	2/3	1/2	2/3	1/2
Primary membrane + bending stresses	1	1/2	1	3/4
Primary membrane + bending + secondary stresses	2	1	2	3/2

2.4.1.5 Design Conditions

The cladding should not mechanically fail during normal operations, nor should it fail during abnormal transients. Therefore the abnormal transient conditions are conservatively determined for assessing the cladding thickness required. The maximum operating pressure of the RPV is assumed to be 27.5 MPa (1.1 times the normal operating pressure of 25 MPa). Further pressurization of up to 28.9 MPa (1.05 times the maximum operating pressure) is assumed during abnormal transients (see Chap. 6 on safety designs). By further assuming the minimum fuel rod internal pressure to be 10 MPa, the maximum pressure difference on the cladding becomes 18.9 MPa.

The cladding mechanical strength gradually decreases with increasing temperature. As described so far, the outlet coolant temperature may become locally much higher than the average temperature of 500°C. Further temperature rise is inevitable during abnormal transients. Cladding mechanical failures should be prevented under such elevated temperature conditions. Hence, a conservative temperature of 850°C is assumed for determining the cladding thickness.

2.4.1.6 Stress Evaluations and Determination of the Cladding Thickness

When the fuel rod internal pressure is lower than the external pressure (i.e., the coolant pressure), the pressure difference acts on the cladding. When the radial compressive stress on the cladding exceeds the elastic limit of the cladding, buckling collapse occurs. That is to say, the buckling collapse pressure can be expressed by a function of the modulus of elasticity (Young's modulus) as follows:

$$P_{\text{collapse}} = \frac{1}{3} \times 2.2E\left(\frac{t}{D-t}\right)^3, \tag{2.21}$$

where E is Young's modulus, t is the cladding thickness, and D is the cladding outer diameter. This equation is based on the equation for a hollow cylinder. The factor 1/3 preserves conservatism in the evaluation; it is necessary because even a little difference from the perfect cylinder due to manufacturing error may cause a substantial decrease in the buckling collapse pressure.

Generally, Young's modulus of stainless steels and nickel alloys gradually decreases with increasing temperature, but temperature dependences are not large and not much different between materials. On the other hand, as can be seen from (2.21), the buckling collapse pressure depends strongly on the cladding thickness. When the cladding outer diameter is much larger than the thickness, the buckling collapse pressure is almost proportional to t^3. Hence, the cladding thickness needs to be large enough even assuming various engineering uncertainties such as manufacturing errors and reduction of thickness due to corrosion during operation. The pressure difference between inside and outside fuel rod cladding usually takes the

maximum value near the BOL of the fuel when almost no FP gasses have been released.

The primary membrane stress on the cladding can be estimated by the following equation.

$$\sigma_\theta = \frac{(r_1{}^2 P_1 + r_2{}^2 P_1 - 2r_2{}^2 P_2)}{(r_2{}^2 - r_1{}^2)}. \tag{2.22}$$

Here, r_1 denotes the cladding inner radius, r_2 denotes the cladding outer radius, P_1 denotes the fuel rod internal pressure, and P_2 denotes the fuel rod external pressure (coolant pressure). The evaluated stress should not exceed the limits defined in Table 2.2 [9]. It should also not exceed the creep rupture strength of the cladding for the expected operating period. It should be noted that the primary membrane stress evaluated by (2.22) does not take PCMI into account. In reality, the contribution of PCMI to the cladding stress is expected to be relatively large. However, PCMI depends on details of the fuel rod designs (e.g., gap size) and irradiated conditions, and the fuel rod behavior with progression of burnup (e.g., pellet swelling) needs to be evaluated by fuel rod analyses.

While the cladding thickness is very sensitive to the buckling collapse, it is not as sensitive to the primary membrane stress. Buckling collapse is most limiting for fresh fuel, but the primary membrane stress usually becomes larger towards the EOL of the fuel and depends on the irradiated conditions. The material parameter relevant to the buckling collapse (i.e., Young's modulus) is not much different between cladding candidate materials, while the tensile strength or creep strength do differ between materials. Hence, for the design purpose, the cladding thickness is determined based on the viewpoint of preventing buckling collapse. The fuel integrity is considered with the fuel rod analyses in Sects. 2.7 and 2.8.

Young's modulus of a stainless steel or a nickel alloy is about 1.4×10^{11} Pa at around 850°C. The maximum pressure difference is assumed to be 18.9 MPa. Substituting these conditions into (2.21) gives the condition t/D (ratio of cladding thickness to outer diameter) is equal to or greater than 0.057. When the cladding outer diameter is 10.2 mm, this condition corresponds to the minimum cladding thickness of 0.58 mm. This minimum thickness already takes into account a safety factor of 3. However, a further safety margin of about 10% is taken and the final design value of the cladding thickness is determined as 0.63 mm.

2.4.1.7 Initial Gap Size

The thermal conductivity of the gas between the pellet and the cladding is low. This is the cause of the low gap conductance and the large temperature drop from the pellet to the cladding. A lower pellet temperature is desirable from the viewpoint of maintaining safety margins during the operation. Moreover, a higher pellet temperature would cause more FP gasses to be released to the plenum volume of the fuel

rod and that would increase the rod internal pressure. On the other hand, the pellet volume increases with the burnup (i.e., swelling) and cladding creepdown progresses. Hence, the initial gap between the pellet and the cladding gradually closes and PCMI starts.

In BWRs or PWRs, PCMI is one of the major causes of fuel rod failures. This is partly due to the high coolant pressure (i.e., cladding creepdown) and partly due to the low thermal expansion coefficient of the cladding (lower than that of the UO_2 pellet). The PCMI is also sensitive to the pellet swelling, which primarily depends on the initial pellet density, the linear heat generation rate, and the burnup. As for these aspects, the high coolant pressure of the Super LWR may cause a severer PCMI compared with BWRs or PWRs. On the other hand, the relatively large thermal expansion coefficients of the cladding candidate materials may contribute to PCMI reduction.

A larger initial gap size may leave more space for the pellet swelling to close the gap, but it would lead to a higher pellet temperature, which may cause large pellet volume expansions and more release of FP gasses. The thermal and mechanical interactions between the pellet and the cladding are complicated and difficult to predict without doing detailed fuel rod analyses. For a typical BWR fuel rod, the initial diameter gap size is about 0.20 mm (for fuel rod diameter of 12.3 mm and cladding thickness of 0.86 mm) and for a typical PWR fuel rod, it is about 0.17 mm (for the fuel rod diameter of 9.5 mm and cladding thickness of 0.57 mm). By referring to these design examples and the above mentioned characteristics of the Super LWR fuel rod, the initial diameter gap size is tentatively determined as 0.17 mm.

2.4.1.8 Initial Pellet Density

A higher initial pellet density is desirable from the viewpoint of increasing the pellet thermal conductivity to reduce the pellet temperature (this also leads to a lower FP gas release rate). If the initial pellet density is low, densification near the BOL becomes large and may cause substantial pellet deformation. Higher initial pellet density is also advantageous from the viewpoint of dehydrating the pellet and preventing the propagation of cladding corrosion from the pellet side.

The initial pellet density is limited mainly by manufacturing capabilities. For recent PWR or BWR pellets, it is about 95–97% of the theoretical density. Hence, an initial pellet density of 97% of the theoretical density is expected for the Super LWR fuel pellet.

2.4.2 Fuel Assembly Designs

2.4.2.1 Requirements for the Fuel Assembly Design

The plant system of the Super LWR is a once-through direct cycle without recirculation in the core. The core flow rate is much lower than that of current

LWRs (about 1/8 of that of a BWR with the same thermal output). The coolant enthalpy rise in the core is large and the coolant temperature and density changes are large. For inlet coolant temperature of 280°C and density of 0.8 g/cm^3, the average outlet coolant temperature is 500°C and density is less than 0.1 g/cm^3. Hence, fuel assembly design should be such that both the fuel rod cooling and neutron moderations are effectively achieved.

From the viewpoint of effectively cooling the fuel rods with low coolant flow rate, the gap size between the fuel rods needs to be minimized to gain sufficient coolant flow velocity to increase the heat transfer coefficient. The minimum gap size is essentially limited by manufacturing capabilities of the spacers. Recently, thermal-hydraulic experiments under BWR conditions were carried out with a fuel rod gap size of around 1.0 mm [17]. Hence, the rod gap size of 1.0 mm is expected to be possible for the Super LWR fuel assembly.

Another important design issue for effectively cooling the fuel rods is to design the fuel assembly such that the enthalpy rise of the coolant is uniform across the assembly. This is equivalent to achieving a uniform coolant temperature distribution across the assembly outlet. For uniform cooling of the fuel rods across the fuel assembly, the heat generation and removal need to be uniform. Therefore, reducing the local power peaking and removing the heat with uniform subchannels are important design issues.

2.4.2.2 Hexagonal Fuel Assembly

The hexagonal fuel assembly with a tight triangular fuel rod lattice, shown in Fig. 2.33 [18], is one of the design options. The fuel assembly is surrounded by a hexagonal channel box. It is one of the early design ideas that was intended to maximize the coolant flow velocity with the tight fuel rod bundle lattice so that the heat transfer rate to the coolant can be maximized. It is also suitable for gaining the desired core power density. Such an approach is similar to that of LMFBRs. In the hexagonal fuel assembly of the Super LWR, there are many hexagonal water rods to provide neutron moderation. Cluster type control rods are designed to be inserted from the top of the core into some of the water rods.

The drawbacks of the hexagonal fuel assembly are that the local power peaking tends to be relatively high and the subchannels are not as uniform as desired. Figure 2.34 [18] shows an example of the local power distribution of the hexagonal fuel assembly. Although three different types of fuel rods with different fuel enrichments are used, the local power peaking factor is 1.16 without the considerations of gadolinia rods or control rods. The high local peaking is predominantly due to the localized thermal neutron flux around the water rods. The local power distribution is strongly affected by the relative positions of the fuel rods and the water rods. The fuel rods close to the water rods tend to have relatively high powers whereas those fuel rods away from the water rods tend to have lower powers. Especially, the fuel rods facing the channel box have low powers due to the lack of neutron moderations. The subchannel analyses of the hexagonal fuel assembly

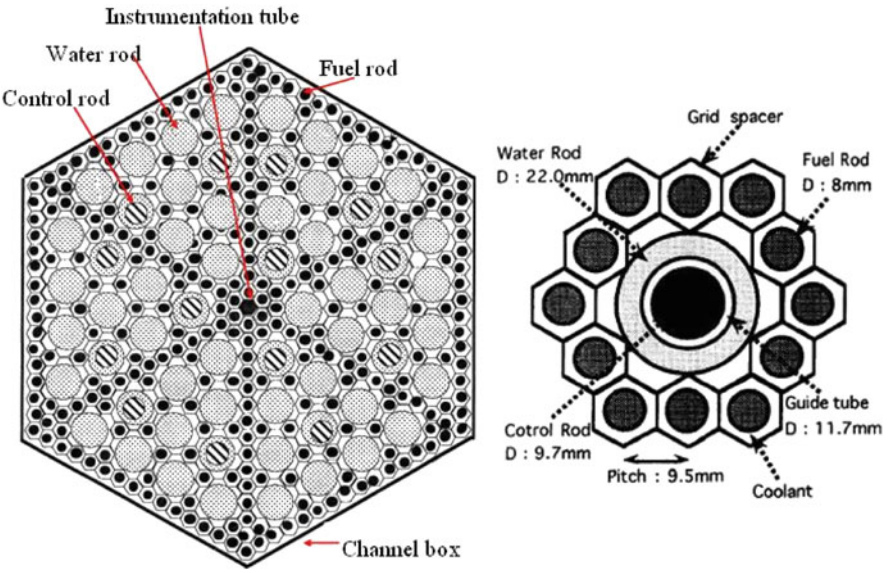


Fig. 2.33 Hexagonal fuel assembly. (Taken from doctoral thesis of K. Dobashi, the University of Tokyo (1998) [18])

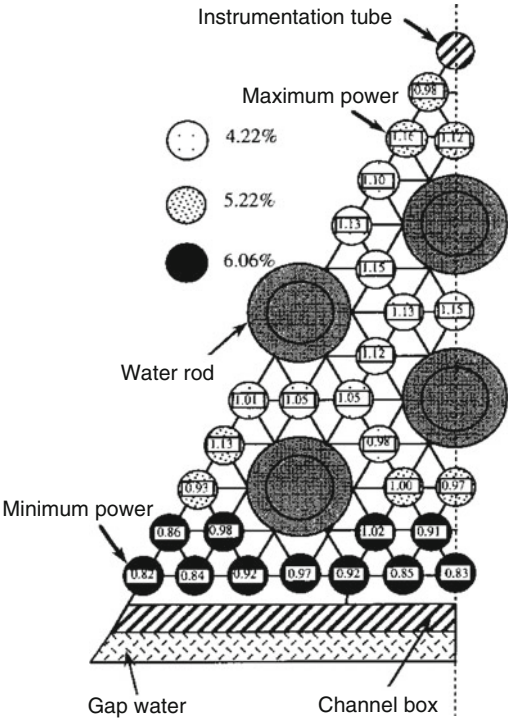


Fig. 2.34 Example of a local power distribution of the hexagonal fuel assembly. (Taken from doctoral thesis of K. Dobashi, the University of Tokyo (1998) [18])

show that the hexagonal fuel assembly design is not suitable for designing a core with a high average core outlet temperature.

The hexagonal fuel assembly design also needs to be revised to improve the neutron economy. The neutron moderation provided by the water rods is not sufficient and the core designed with this fuel assembly is under-moderated.

2.4.2.3 Square Fuel Assembly

The square fuel assembly shown in Fig. 2.35 [9] is designed to overcome the problems encountered with the hexagonal fuel assembly. The design is intended to flatten the coolant outlet temperature distribution at the outlet of the assembly by using uniform subchannels and a lower local power peaking. The area of the water rods is also increased from the hexagonal fuel assembly to gain neutron moderations.

The square fuel assembly consists of 300 fuel rods, 36 square water rods within the fuel rod array (inner water rods), and 24 rectangular water rods surrounding the fuel rods (outer water rods). The outer water rods provide the neutron moderation for the fuel rods near the outer region of the assembly, which was lacking in the hexagonal assembly design. They also serve as a channel box by enclosing the fuel rods and separating the coolant from the interassembly coolant. Among the 36 inner water rods, 16 water rods are equipped with control rod guide tubes, which allow a cluster type control rod unit to be inserted from the top of the core. Compared with the insertion of *Y* shaped control rods in between the adjacent fuel assemblies, the

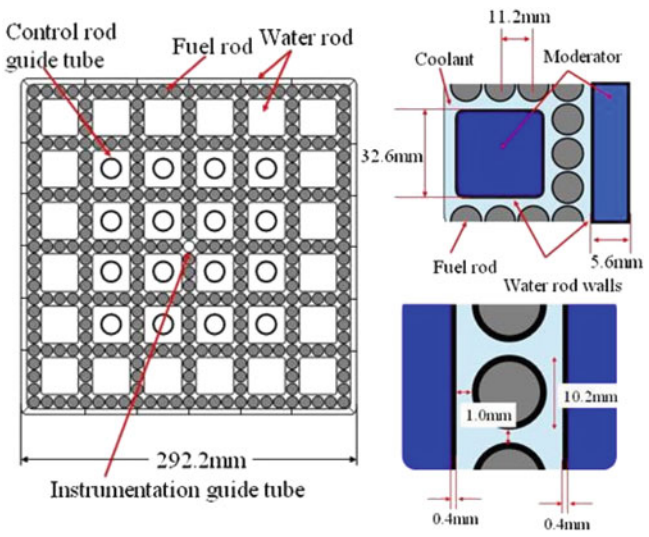


Fig. 2.35 Square fuel assembly. (Taken from doctoral thesis of A. Yamaji, the University of Tokyo (2005) [9])

insertion of cluster type control rods into the assembly is desirable from the viewpoint of reducing local power peaking. Except for the fuel rods at the corners of the square water rods, all fuel rods are located between the water rods. The fuel rod bundle lattice may be described as a cruciform lattice. This feature allows the square assembly to provide uniform and sufficient neutron moderation and fuel rod cooling. There is an instrumentation guide tube at the center of the fuel assembly.

A schematic drawing of the top structure of the square fuel assembly is shown in Fig. 2.36 [9]. At the top, the control rod cluster guide tube branches off to the water rods. The coolant flows through the gap between the outer water rods to the outlet of the core. Such a structure should distribute the moderator to each fuel assembly and allow the insertion of the cluster type control rods into the assembly from the top of the core.

In the case of the BWR fuel assembly, fuel rods with different fuel enrichments are used to reduce the local power peaking. Such enrichment adjustments are unnecessary for the square Super LWR fuel assembly, since uniform neutron moderation is achieved with uniformly arranged water rods. The local power peaking can be easily reduced by designing an appropriate gap size between the fuel assemblies. Figure 2.37 [9] shows the assembly burnup (ASMBURN) calculation geometry with 1/4 symmetric boundary conditions for determining an appropriate inter-assembly gap size. The calculations are carried out under typical core average conditions (coolant density of 0.3 g/cm^3, moderator density of 0.6 g/cm^3).

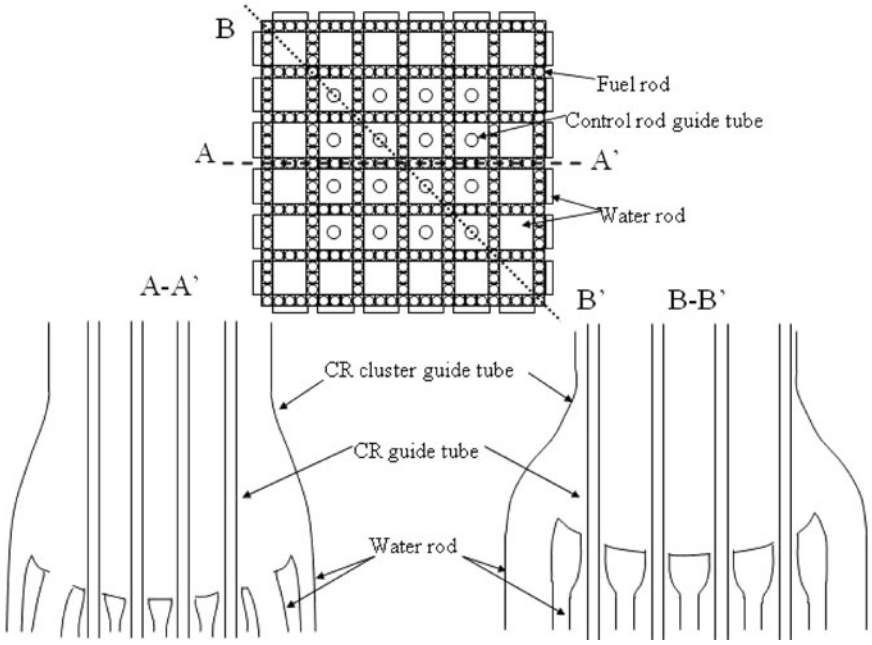


Fig. 2.36 Top structure of the square fuel assembly (schematic). (Taken from doctoral thesis of A. Yamaji, the University of Tokyo (2005) [9])

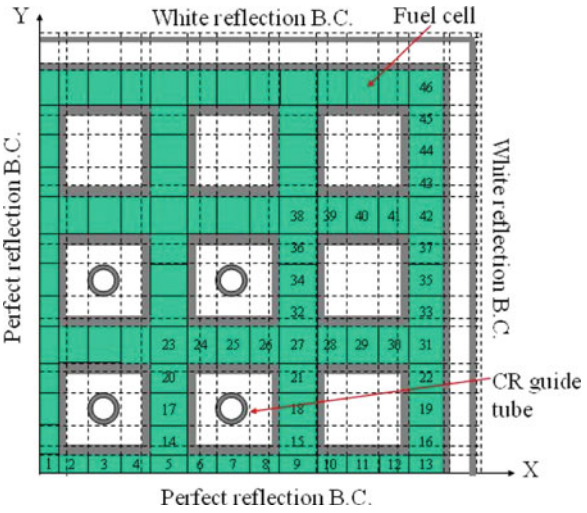


Fig. 2.37 ASMBURN calculation geometry with pin numbers (*BC* boundary condition). (Taken from doctoral thesis of A. Yamaji, the University of Tokyo (2005) [9])

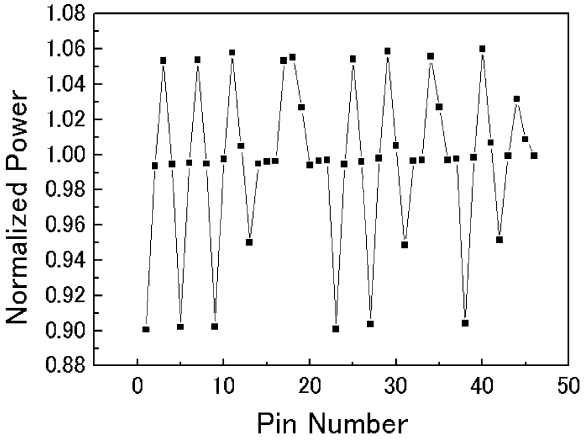


Fig. 2.38 Relative fuel rod power distribution. (Taken from doctoral thesis of A. Yamaji, the University of Tokyo (2005) [9])

From these calculations, the interfuel assembly gap size is determined to be 4.0 mm. In this case, the local power peaking factor takes the lowest value of 1.06 without fuel rod enrichment controls. The relative fuel rod power distribution for the case with inter-fuel assembly gap size of 4.0 mm is shown in Fig. 2.38 [9]. The pin number (from 1 to 46) on the x axis of this figure corresponds to the pin number position shown in Fig. 2.37 [9]. Although the pin powers tend to be relatively high near the middle of the water rods, and relatively low at the corners of the water rods, the overall power distribution is flat.

The burnup reactivity compensation is mainly done by gadolinia (Gd_2O_3) as used in BWRs. Among the 300 fuel rods in the fuel assembly, a number of fuel rods contain pellets, which are a mixture of UO_2 and Gd_2O_3. Since gadolinia has a large self-shielding effect due to its large thermal neutron absorption cross section, most neutrons are absorbed at the surface of the gadolinia rod. The burnup of the gadolinia rod gradually proceeds from its outer surface toward its center and the neutron absorption by the gadolinia rod decreases accordingly. Hence, the degree of the initial reactivity suppression by gadolinia can be changed by altering the number of gadolinia rods in the fuel assembly. In contrast, the duration of the reactivity suppression by the gadolinia rod can be controlled by adjusting the initial gadolinia concentration in the pellets.

As is briefly introduced in Sect. 2.2.4, the flattening of the core outlet temperature is one of the most important design issues of the Super LWR core. For this purpose, each fuel assembly is equipped with an inlet orifice to keep an appropriate coolant flow rate for the power generation of the fuel assembly. In order to effectively adjust the power to the flow rate ratio for each fuel assembly, flattening of the radial core power and also reducing the changes in the radial core power distribution are important during the operation. In BWRs, the burnup reactivity compensation by the gadolinia rods is designed such that the infinite multiplication factor (K_{inf}) of the fuel gradually increases from the first exposure cycle and reaches the maximum at the second exposure cycle. Such a design does not suit well with the Super LWR core design aimed at minimizing the radial core power distribution fluctuations during operation. In order to minimize the radial core power fluctuations with burnup, the burnup reactivity compensations by the gadolinia rods should be such that the infinite multiplication factor of the fuel assembly monotonously decreases from the BOL to the EOL. The burnup changes of infinite multiplication factors of the Super LWR fuel are shown in Fig. 2.39 [9]. In this case, 24 fuel rods

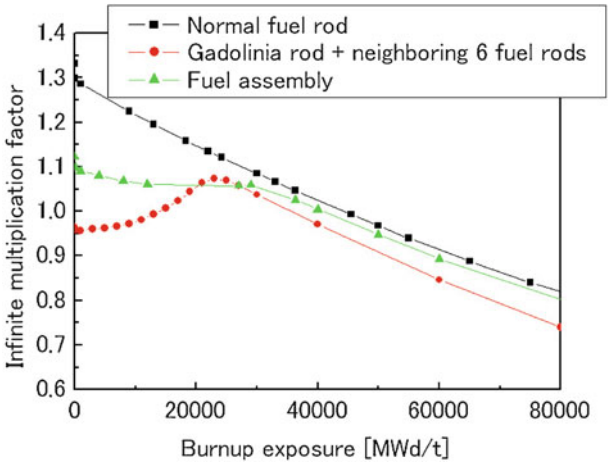


Fig. 2.39 Burnup changes of infinite multiplication factors of the fuel. (Taken from doctoral thesis of A. Yamaji, the University of Tokyo (2005) [9])

are gadolinia rods containing 10 wt% of gadolinia. The "normal fuel rod" denotes the infinite multiplication factor of the normal fuel rod containing only the UO_2 pellet with 6.6 wt% enrichment. The "gadolinia rod with six neighboring fuel rods" denotes the unit fuel cell for calculating gadolinia burnups as described in Fig. 2.17 [9]. The resultant infinite multiplication factor with respect to the burnup is denoted by the "fuel assembly" as shown in Fig. 2.39 [9]. The infinite multiplication factor of the fuel assembly is monotonously decreasing with respect to the burnup. As is described later in this section, the design restriction of this monotonous decrease in the infinite multiplication factor of the fuel assembly can be removed by adopting a downward coolant flow in the outer region of the core. The details of this concept are described in Sect. 2.4.6.

To flatten the axial power distribution, the fuel assembly is axially divided into three regions. The size and fuel enrichment in each of these regions are determined from the core average axial water density distribution as shown in Fig. 2.40 [9]. The coolant flow scheme is explained later in this section. The axial density change of the coolant is large as it decreases from about 0.8 g/cm^3 at the bottom of the core to less than 0.1 g/cm^3 at the top of the core (the density change is more than ten times from the bottom to the top of the core). While the moderator density is high at the top of the core and decreases toward its center, the density change is relatively small (only about 25% of the initial density at the top of the core). In the Super LWR fuel assembly design, the contribution of the coolant is relatively small compared with that of the moderator for the neutronics. The averaged axial water density (average of the coolant and moderator) distribution is relatively flat. The maximum density change is only about 30% of the inlet density (this is smaller than the corresponding value of about 50% for BWRs due to void generations). Figure 2.41 [9] shows an example of the axial fuel assembly design. The fuel assembly is axially divided into three regions with the height ratio of 4:4:2. The U-235 fuel enrichments for these

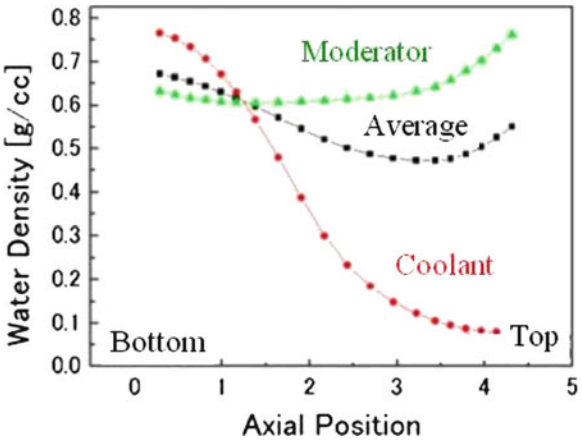


Fig. 2.40 Core average axial water density distributions. (Taken from doctoral thesis of A. Yamaji, the University of Tokyo (2005) [9])

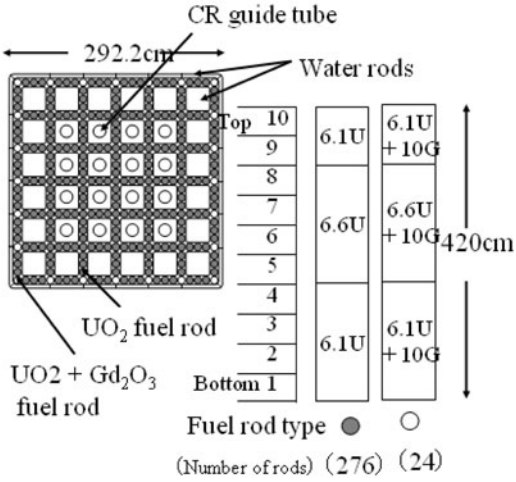


Fig. 2.41 Axial design of the fuel assembly. (Taken from doctoral thesis of A. Yamaji, the University of Tokyo (2005) [9])

regions are 6.1, 6.6, and 6.1 wt% from the bottom to the top, respectively. The fuel enrichment of the middle region is higher to account for the relatively low average water density in this region. In this case, the average fuel enrichment of the fuel assembly becomes 6.3 wt%.

When a fresh PWR fuel assembly is submerged in cold water, the effective multiplication factor (K_{eff}) of the fuel is higher than when a fresh BWR fuel assembly is submerged. No fuel assembly should become critical outside the core. In this sense, the fresh PWR fuel assembly has a smaller safety margin compared with the fresh BWR fuel assembly for two reasons: the PWR fuel assembly is about four times larger than the BWR fuel assembly and the fresh PWR fuel assembly has much higher initial reactivity than the fresh BWR fuel assembly, as the former does not normally contain significant amounts of burnable poisons, whereas the latter normally does. (In PWRs, chemical shim is primarily used for burnup reactivity compensation.) The calculation geometry shown in Fig. 2.42 [9] is used to evaluate the effective multiplication factor of the Super LWR fuel assembly when submerged in cold water and the factor obtained is about 0.91. This is sufficiently below the critical value and it is lower than *K*-eff of the PWR fuel assembly.

2.4.2.4 Other Designs (Solid Moderator and Water Rods)

Although the main design concept of the Super LWR is being developed with the square fuel assembly explained above, several different designs have been considered. As already explained so far, the key design concerns are achieving both efficient cooling of fuel rods and neutron moderation.

One of the earliest designs adopted zirconium-hydride rods as solid moderators [19]. In this design, the fuel rod pitch to diameter ratio (P/D) can be reduced to

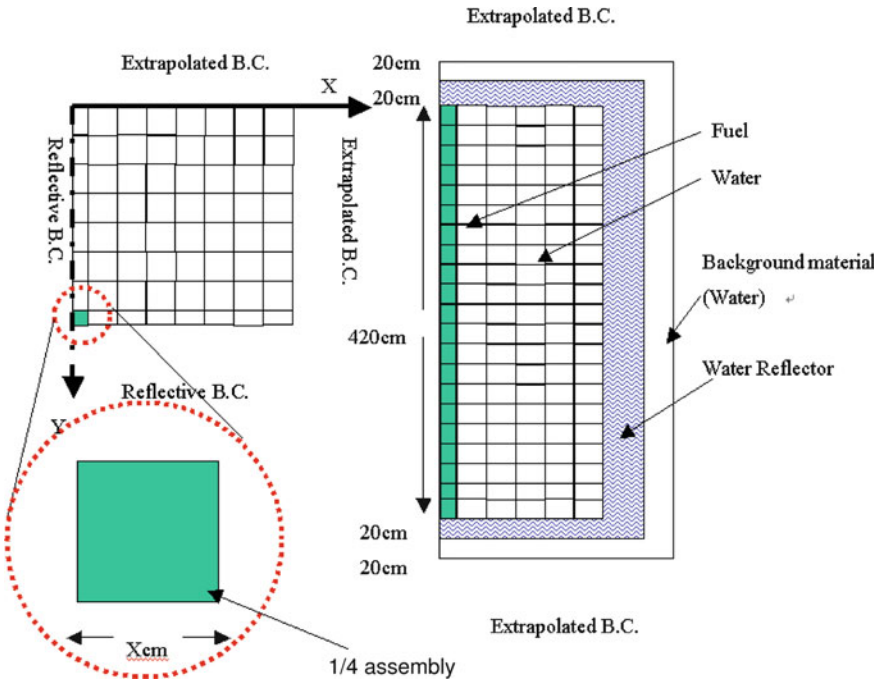


Fig. 2.42 Calculation geometry for evaluating K_{eff} of the fuel assembly. (Taken from doctoral thesis of A. Yamaji, the University of Tokyo (2005) [9])

enhance the heat transfer to the coolant, while attaining sufficient neutron moderation by the zirconium-hydride rods. However, the neutron absorptions by the zirconium reduced the neutron economy. Also, the use of zirconium-hydride rods raised the problem of increasing the amount of radioactive waste after exposure.

Water rods were then considered for the moderator from the viewpoints of reducing the radioactive waste and improving the reliabilities since they have a long history of use in current LWRs. Three types of water rods were initially considered: the single tube type, the semidouble tube type, and the double tube type [20]. Both the hexagonal and square fuel assembly designs have adopted the single tube type water rods. The double and semidouble tube types were dropped from further consideration as they involved structural complexities.

Breeding is possible when MOX fuel is used with a tight lattice without any water rods or solid moderators. The design concepts of fast and fast breeder reactors are presented in Chap. 7.

2.4.3 Coolant Flow Scheme

All core design concepts described here are based on the coolant flow scheme in Fig. 2.43. This unique flow scheme achieves effective cooling of fuel rods and

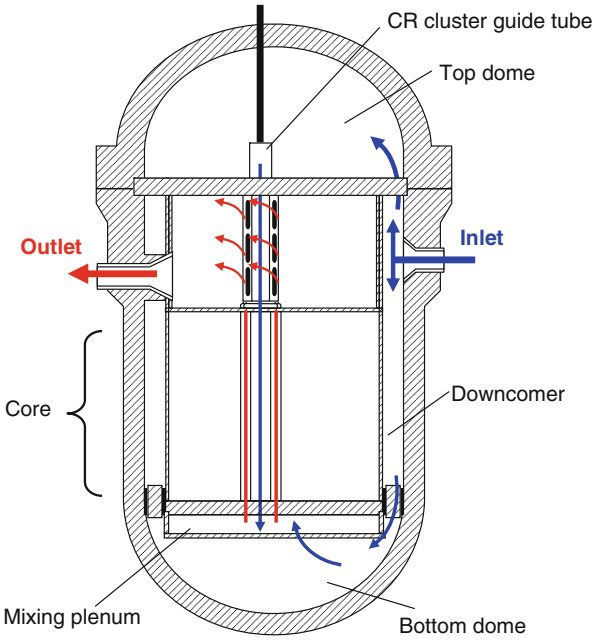


Fig. 2.43 Core coolant flow scheme

neutron moderations. In the figure, only one fuel assembly is schematically presented for a simple description of this concept.

Part of the inlet coolant is led to the top dome and the rest flows to the bottom dome via the downcomer. The coolant in the top dome then flows down to the mixing plenum through the water rods via the control rod cluster guide tube. At the mixing plenum, the coolant from the downcomer and the water rods are mixed and the mixture rises up the coolant channels in the fuel assemblies. This flow scheme is to be achieved by designing appropriate pressure drop coefficients at various places of the core. The designing of orifices with appropriate pressure drop coefficients is one of the design issues for developing the Super LWR. For example, the nonlinear change of the coolant flow distributions during abnormal transients or during the plant startup need to be considered.

The coolant flow scheme may be characterized by the "downward flow water rods." In this flow scheme, while the coolant flow direction is upward as in other types of reactors, the moderator flow direction in the water rods is downward. One of the reasons for adopting downward flow in the water rods is to prevent the mixing of a relatively cold moderator and a relatively hot coolant near the core outlet. Such mixing would not only reduce the core average outlet temperature, but also cause a thermal fatigue of the structural materials (e.g., control rod cluster guide tubes). Another reason is to flatten the axial water density distribution (average of the coolant and moderator). By making the coolant and moderator flow directions opposite each other, the axial density changes tend to cancel each other. The

resultant average density distribution is relatively flat as shown in Fig. 2.40 [9]. The flow scheme is also important to reduce the material development requirements for the RPV. By guiding part of the inlet coolant to the top dome, the pressure boundary and the temperature boundary can be separated. The RPV facing the coolant pressure boundary of 25 MPa is always cooled by the inlet coolant temperature of 280°C, whereas the hot regions near the top of the core do not face any pressure boundaries. Hence, it is expected that not much research and development work is necessary for RPV fabrication. The coolant flow scheme is one of the most important design parameters of the Super LWR core. The downward flow in the water rods increases the average core outlet temperature, which is one of the most important core parameters of the Super LWR. The core average outlet temperature can be further increased by adopting downward flow cooling in the core outer region. Details of that design are described in Sect. 2.4.6.

An example of the fuel assembly top structure is shown with the coolant and moderator flow directions indicated in Fig. 2.44 [9]. The control rod cluster guide tube is connected to the water rod structures at the top of the fuel assembly and the moderator is distributed into the water rods by downward flow. On the other hand, the coolant, having risen from the mixing plenum, flows through the gap space between the water rods at the top of the fuel assembly and flows to the core outlet.

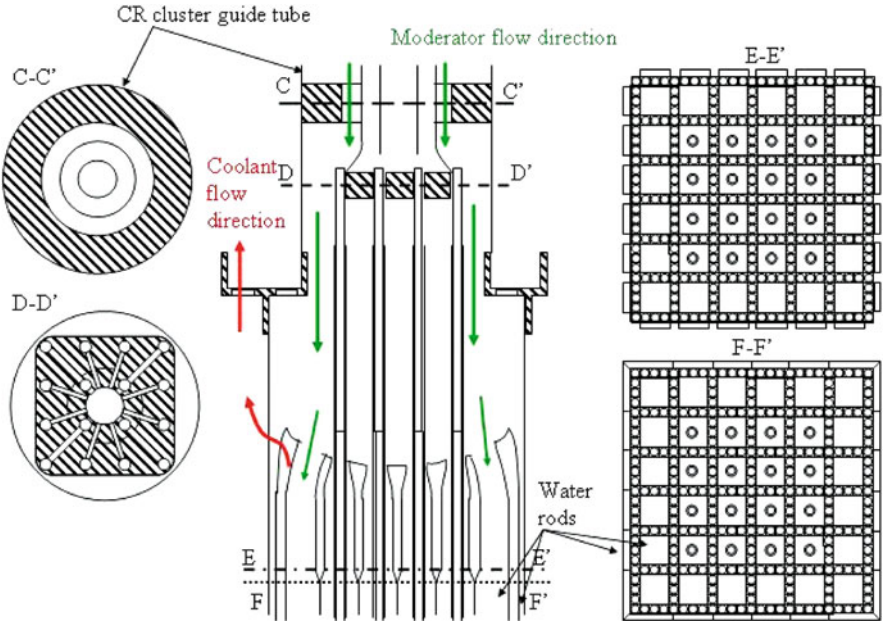


Fig. 2.44 Fuel assembly top structure with flow directions. (Taken from doctoral thesis of A. Yamaji, the University of Tokyo (2005) [9])

2.4.4 *Low Temperature Core Design with R-Z Two-Dimensional Core Calculations*

An example of the low temperature design concept (critical heat flux-dependent design concept) is shown in this section with the hexagonal fuel assembly and by using R-Z two-dimensional core calculations. It is one of the early design concepts. Although this design concept shows some advantages over the current LWR designs, the potential ability of the Super LWR to achieve high outlet temperature is limited due to the critical heat flux design criterion. The basic core characteristics can be roughly evaluated with the R-Z two-dimensional core calculations, but the X-Y-Z three-dimensional core calculations are necessary for quantitatively clarifying the design issues and further developing the concept.

2.4.4.1 Design Criteria

The following design criteria are tentatively considered in this design. The actual values of these criteria need to be revised with further analyses and experiments.

1. The maximum linear heat generation rate (MLHGR) of the fuel rod is equal to or below 40 kW/m.
2. The stainless steel cladding surface temperature is equal to or below 450°C.
3. The minimum deterioration heat flux ratio (MDHFR) is above 1.30.
4. Coolant density reactivity coefficient is positive.

The MLHGR criterion keeps the fuel centerline temperature below about 1,900°C to prevent centerline melting during abnormal transients. The linear heat generation rate is relatively low compared with those of BWRs or PWRs. This is mainly due to the high coolant temperature of the Super LWR. The maximum cladding surface temperature (MCST) design criterion is intended to prevent excess corrosion of the cladding surface. The cladding temperature also needs to be limited from the viewpoint of assuring cladding mechanical integrity both during normal operation and abnormal transients. The MDHFR criterion is set to prevent heat transfer deterioration during abnormal transients. The positive coolant (and moderator) density coefficient corresponds to the negative void reactivity coefficient of BWRs or PWRs. This is essential for retaining the inherent safety of the core, but since the Super LWR is a thermal-spectrum reactor, this criterion is met without any specific considerations unless the core is over moderated. The core shutdown margin design criterion is omitted in this design consideration since the evaluation of the control rod worth is not accurate enough with the R-Z two dimensional core calculation model.

2.4.4.2 Fuel Design

The fuel is enriched uranium dioxide with 95% T.D. The fuel rods are arranged in the tight triangular lattice with grid spacers (Fig. 2.33 [18]). The fuel rod

diameter is 8.0 mm and the pitch is 9.5 mm. The stainless steel cladding is 0.46 mm thick. For simplicity, only the cell burnup calculations are carried out to model the fuel. Structural materials such as the channel box and control rod guide tubes are neglected in the core calculations.

2.4.4.3 Core Characteristics Evaluations with R-Z Two-Dimensional Core Calculations

The fuel loading pattern is shown in Fig. 2.45 for the 1/6 symmetric core geometry. The core consists of the three-cycle fuel with an out-in refueling pattern, which means that fresh fuel is loaded near the outer region of the core and the fuel is reloaded towards the inner core at the end of each cycle. Such a loading pattern is advantageous for flattening the radial core power distributions, but it is undesirable from the viewpoint of the neutron economy. In this design, the flattening of the core radial power distribution is given priority for roughly evaluating the core average outlet temperature under the MDHFR design criterion with the hexagonal fuel assembly.

As stated in Sect. 2.3.3, the R-Z two dimensional core calculation model assumes the core consists of concentric cylinders. Then, the fuel loading pattern described by Fig. 2.45 is modeled by the four cylindrical regions of the figure. The burnup of the fuel in each region is assumed to be represented by the average of the fuel in the region and the actual burnup for each fuel assembly is not considered for calculational simplicity. The burnups during the cycle are assumed to be uniform for all four regions. Different coolant flow rates, as shown in Fig. 2.46, are determined for each region to model the coolant flow adjustments by the inlet orifices attached to the fuel assemblies. The minimum coolant flow rate, which satisfies the MDHFR criterion, is determined for each region to maximize the core average outlet temperature. In evaluating MDHFR, the core axial power distribution is

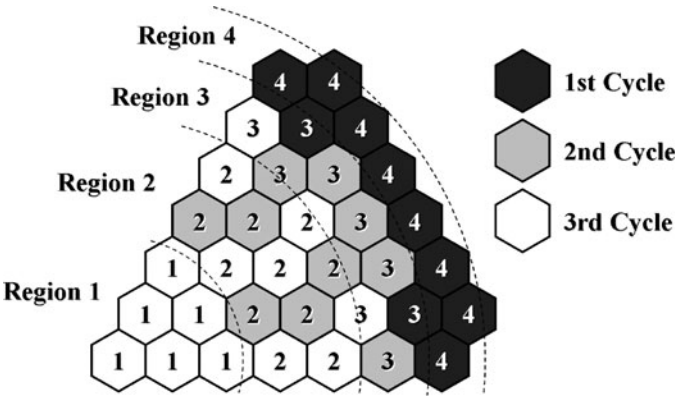


Fig. 2.45 Fuel loading pattern (1/6 symmetric core)

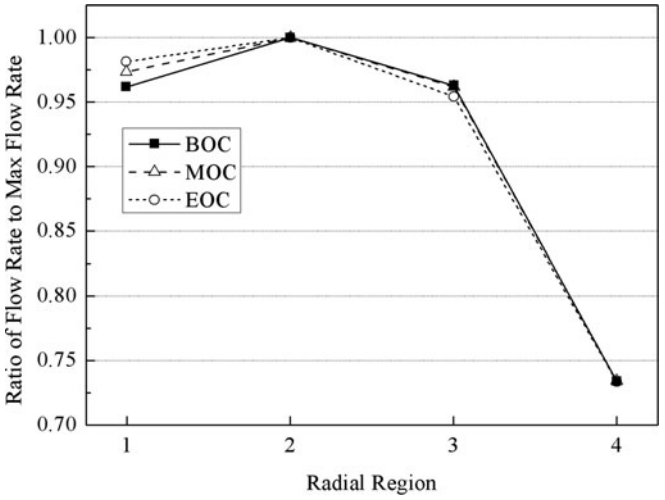


Fig. 2.46 Relative coolant flow rates to the radial regions

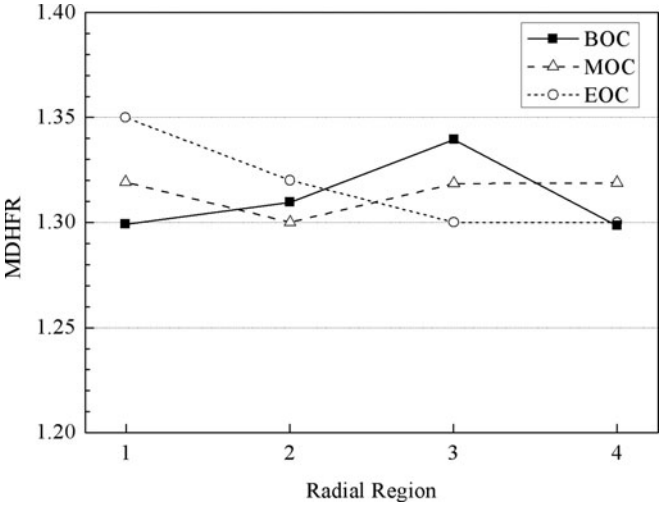


Fig. 2.47 MDHFR for the radial regions

assumed to be a cosine distribution and the results are shown in Fig. 2.47 for each of the four radial regions. Under the given burnup distributions and coolant flow rate conditions, the core neutronic calculations and thermal-hydraulic calculations are coupled to evaluate the radial power distributions and coolant density distributions. Figure 2.48 shows that the radial core power distribution of the Super LWR may become flat when an appropriate fuel loading pattern is designed and the core power distribution is evaluated by taking into account the density feedback effects

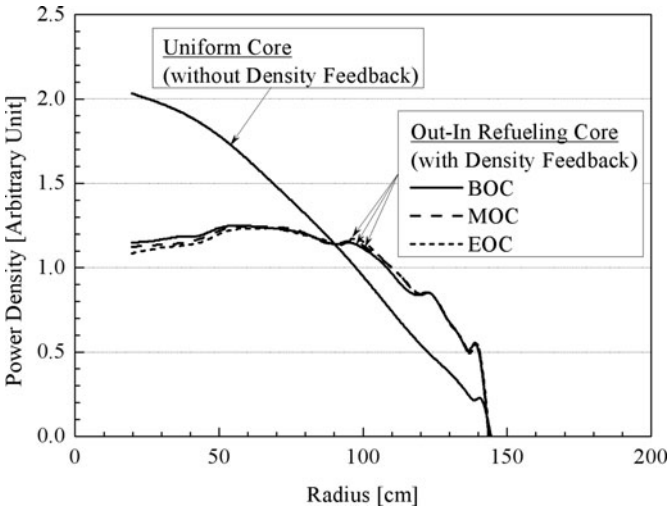


Fig. 2.48 Radial core power distributions

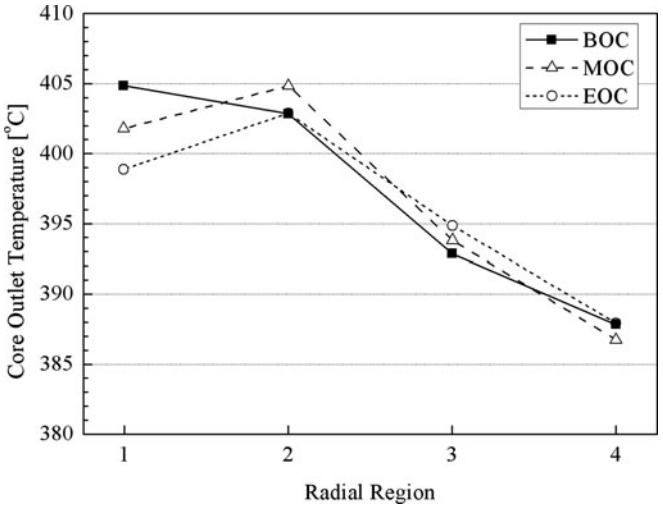


Fig. 2.49 Coolant outlet temperature from the radial regions

of the coolant. The coolant outlet temperatures from the radial regions are shown in Fig. 2.49. The core average outlet temperature is about 397°C, which is only about 12°C higher than the pseudocritical temperature of the coolant at 25 MPa. There may be a further need to reduce the core outlet temperature (i.e., increase the core flow rate) to meet the MDHFR criterion when the local power peaking inside the fuel assembly is considered. The core outlet temperature is essentially limited by the MDHFR criterion.

The characteristics of the CHF dependent core design with the hexagonal fuel assemblies are summarized in Table 2.3 [18]. The core parameters listed there should be regarded as the first rough estimations, since their evaluations by R-Z two-dimensional core calculations included numerous simplifications and assumptions. However, the following design issue may be identified from these results. That is, although the plant thermal efficiency of 40.7% is much higher than that of current LWRs (about 35%), it is not as high as expected from the potential ability of the Super LWR. This is mainly due to the low core outlet temperature, which is limited by the critical heat flux design criterion (MDHFR). In order to increase the core outlet temperature, the MDHFR criterion needs to be excluded from the design criteria and the excess heat up of the fuel rod cladding needs to be directly evaluated from the cladding temperature calculations. As the coolant temperature becomes significantly higher than the pseudo-critical temperature, its specific enthalpy decreases and more accuracy would be required in the calculations. Hence, three-dimensional core calculations with full coupling of the neutronic and thermal-hydraulic calculations would be necessary. Uniform neutron moderations with uniform cooling are required for effective fuel rod cooling.

Table 2.3 Characteristics of the CHF dependent core design with a hexagonal fuel assembly. (Taken from doctoral thesis of K. Dobashi, the University of Tokyo (1998) [18]

Thermal/electric power (MW)	2,490/1,013
Thermal efficiency (%)	40.7
Pressure (MPa)	25
Fuel assembly	
Fuel/fuel rod dia./pitch (cm)	UO_2/0.80/0.95
Cladding/thickness (cm)	SS/0.046
Number of fuel/water/control rods	258/30/9
Uranium enrichment, upper/middle/lower (%)	6.41/5.22/4.66
Number of fuel rods containing gadolinia	31
Gadolinia concentration, upper/middle/lower (wt%)	2.1/3.1/4.3
Number of fuel assemblies	163
Average power density (MW/m^3)	106
Discharge burnup (GW d/t)	45
Refueling period (days)	400
Feedwater flow rate (kg/s)	2,314
Coolant inlet/outlet temperature (°C)	324/397
Core height/dia. (m)	3.70/2.84
Reactor pressure vessel thickness (cm)	32.2
Total peaking factor (for design)	2.50
Calculated total/axial/radial/local peaking factors	2.31/1.58/1.26/1.16
Doppler coefficient at HFP (pcm/K)	−2.4
Coolant density coefficient ($dk/k/(g/cm^3)$)	0.45

2.4.5 *High Temperature Core Design with Three-Dimensional Core Calculations*

The high temperature design concept is developed using the three-dimensional core calculations based on the target outlet temperature of 500°C. In order to achieve such high temperature with a low core flow rate, the critical heat flux design criterion (MDHFR) is replaced by the maximum cladding surface temperature (MCST) evaluations and the newly designed square fuel assembly is used for uniform moderation and cooling. This design may be considered to be the "first trial design" of the high temperature core with three-dimensional neutronic and thermal-hydraulic coupled core calculations.

2.4.5.1 Core Size

The average linear heat generation rate (ALHGR) is determined to be 18 kW/m, which is about the same as that of current LWRs. There are 300 fuel rods in one fuel assembly and the fuel assembly pitch is 296.2 mm for the square fuel assembly design (Sect. 2.4.2. Therefore, the core power density is 61.5 W/cm^3. The average power generation of the fuel assembly with an active height of 4.20 m is about 22.68 MW.

The target electric output is determined to be about 1,000–1,200 MW. With the plant thermal efficiency of about 43.8% (corresponding to the respective inlet and outlet temperatures of 280 and 500°C), the target thermal output is 2,280–2,740 MW. Therefore, the required number of fuel assemblies is about 100–121. Considering the three-batch core with $(12N + 1)$ fuel assemblies, the number of fuel assemblies becomes either 109 or 121. The fuel assembly arrangements under these restrictions are relatively limited. Some of the possible arrangements are shown in Fig. 2.50. Among them, the arrangement with 121 fuel assemblies is relatively close to a circular shape and compatible with the RPV; thus, it is chosen for the core design. This core has an equivalent diameter of 3.68 m, the plant thermal output is 2,744 MW, and the electric output with 43.8% thermal efficiency is 1,202 MW.

2.4.5.2 Fuel Loading and Reloading Patterns

The fuel loading and reloading patterns are shown in Fig. 2.51 [9] for the 1/4 symmetric core. The core consists of 120 fuel assemblies of first to the third cycle fuel (3×40) and one assembly with fourth cycle fuel at the center of the core. The out-in reload pattern is adopted with a design priority to reduce the radial core power peaking and achieve the high core outlet temperature. While the initial fuel loading pattern is 1/8 symmetric, the degree of symmetry of the reloading pattern is less with 1/4 symmetry. However, this small asymmetry does not have a large

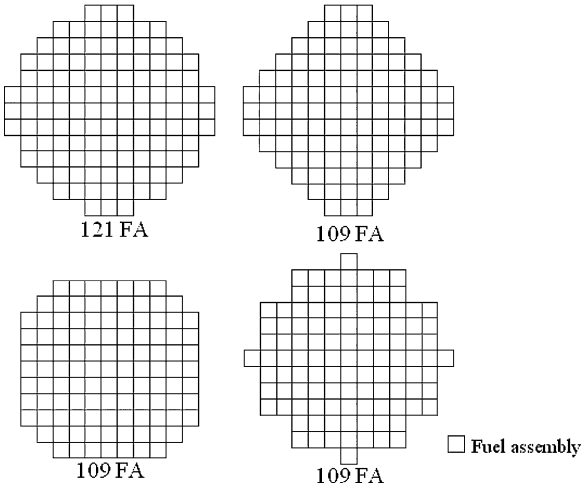


Fig. 2.50 Examples of fuel assembly arrangements

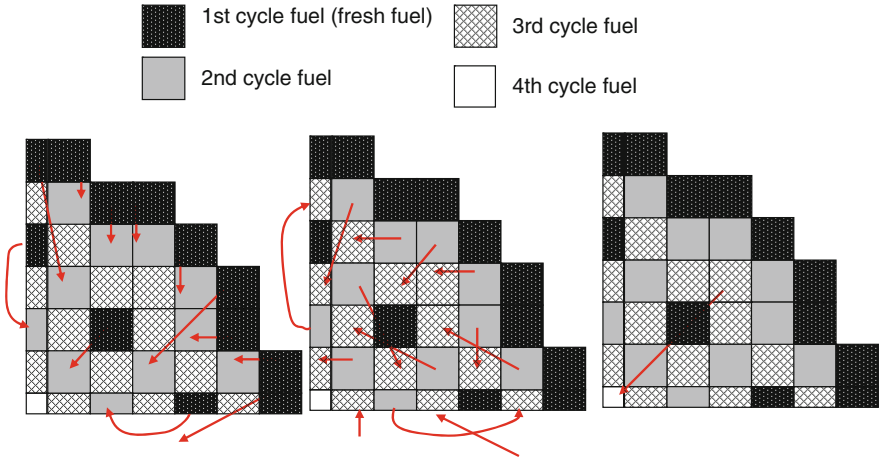


Fig. 2.51 Fuel loading and reloading patterns (1/4 symmetric core). (Taken from doctoral thesis of A. Yamaji, the University of Tokyo (2005) [9])

influence on the core characteristics such as the radial core power distribution and the core may be regarded as almost 1/8 symmetric.

2.4.5.3 Coolant Flow Distributions

The basic coolant flow scheme is explained in Sect. 2.4.3 (see also Fig. 2.43). In this design, 30% of the inlet coolant is led to the top dome. The coolant then flows down

to the mixing plenum through the control rod cluster guide tubes and water rods before mixing with the rest of the coolant and flowing up the fuel channels.

Since the core thermal output is determined to be 2,744 MW, the core flow rate required to attain the average outlet temperature of 500°C with the inlet temperature of 280°C is 1,420 kg/s. (This is easily determined from the simple relationship of $QW\Delta H$, where Q is the thermal output, W is the core flow rate, and ΔH is the enthalpy rise of the coolant in the core.)

When designing the core with an average outlet temperature significantly higher than the pseudocritical temperature, the change of the coolant temperature with respect to its enthalpy becomes large (i.e., the coolant specific heat capacity becomes small). Therefore, in order to effectively cool the fuel, the inlet coolant flow rate to each fuel assembly needs to be adjusted using an inlet orifice to keep the power to flow ratio in an appropriate range. This is similar to the core design of LMFBRs.

Adjusting the power to flow rate ratio is difficult for the fuel assemblies loaded in the outer region of the core (outer fuel assemblies). This is due to the large radial power gradient inside them. The mismatch between the fuel rod power generation and the coolant flow rate arises within the outer fuel assemblies depending on the positions of the fuel rod within the fuel assembly. It is found that even with the flow adjustment for each fuel assembly, the coolant outlet temperature from the outer fuel assemblies cannot be raised high enough and achieving the average core outlet temperature of 500°C is difficult. Hence, the coolant flow rate is determined for each quarter of the fuel assembly with the inlet orifices and flow separation plates. This is essentially the same as reducing the fuel assembly size to 1/4 of the original size. The relative coolant flow distributions by the inlet orifices are shown in Fig. 2.52 [9] for the 1/4 symmetric core. The relative coolant flow rate for each

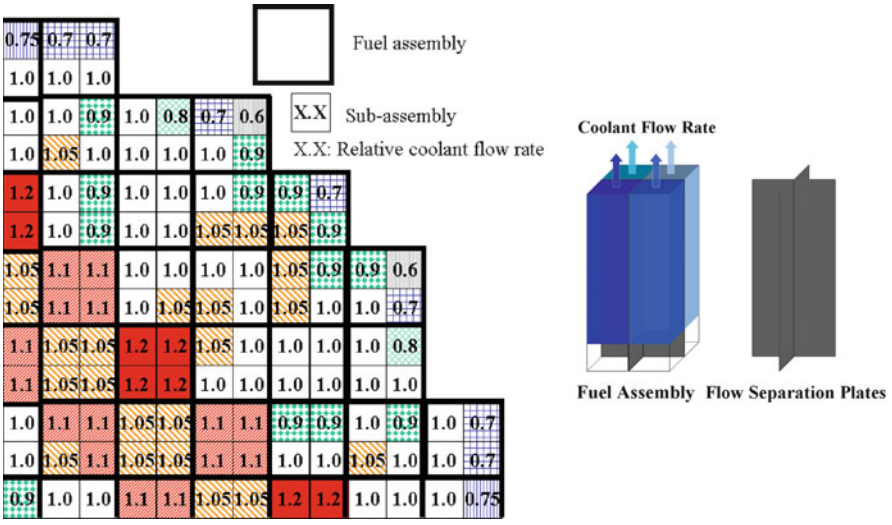


Fig. 2.52 Relative coolant flow distributions by inlet orifices (1/4 symmetric core). (Taken from doctoral thesis of A. Yamaji, the University of Tokyo (2005) [9])

subassembly, bounded by the flow separation plates, is shown. Relatively large coolant flow rate is determined for the fresh fuel assemblies and low flow rates are determined for the third and fourth cycle fuel assemblies and for the outer fuel assemblies. The separation of the fuel assembly into four subassemblies can increase the core average outlet temperature by about 40–50°C.

2.4.5.4 Control Rod Design and Control Rod Patterns

Cluster type control rods are designed to control the excess reactivity as well as to control the core power distributions during operation. The control rods should also be capable of bringing the core to a cold shutdown state with a sufficient margin. The shutdown margin of the core is evaluated after designing the equilibrium core and all design parameters are determined.

Natural boron carbide (B_4C) with 70% T.D. is used for the control rods. Boron carbide has long been used for BWR control rods. Although the coolant temperature may exceed 500°C, the operating temperature of the control rods is expected to be within the feasible range. The control rods are to be used below the pseudocritical temperature of supercritical water (i.e., below 385°C at 25 MPa) since they are used inside the water rods.

Boron carbide has a large self-shielding effect due to its large thermal neutron absorption cross section. Hence, most neutrons are absorbed at the surface of the control rods. This implies that the control rod worth can be altered by changing the surface area of the control rods. In this design, the number of "fingers" of the cluster type control rod is 16 and these control rods are inserted into the 16 inner water rods of the fuel assembly. The control rod diameter is determined to be 12.4 mm. The control rod diameter needs to be revised in relation with the reactivity controls as well as the core shutdown margin criterion (greater than or equal to 1%dk/k). The macro-cross sections of the fuel assembly with and without the control rods are shown in Fig. 2.53. The calculation for the case with the control rods inserted is done by the branching burnup calculations explained in Sect. 2.3.1.

The control rod patterns are determined for each of the 15 burnup steps of the equilibrium cycle (cycle burnup exposure of 0–14.8 GWd/t). Figure 2.54 [9] shows the control rod patterns for the equilibrium core (1/4 core symmetry). Each box represents a fuel assembly and the value in the box represents the control rod withdrawn rate out of 40. A blank box represents a fuel assembly with control rods completely withdrawn. While the control rod patterns are adjusted at every 1.1 GW/t throughout most of the cycle, the fine adjustment of the control rod pattern at a cycle burnup of 0.22 GWd/t is necessary to compensate for a rapid drop of BOC excess reactivity. The excess reactivity drop is relatively fast with respect to the burnup at BOC because of the initial build up of xenon gas and other fission products. The concentration of xenon reaches equilibrium shortly after operation commences and from there, the rate of the excess reactivity drop becomes lower and almost constant. The control rod patterns are determined by considering control of the core power distributions while keeping the core critical. The radial core

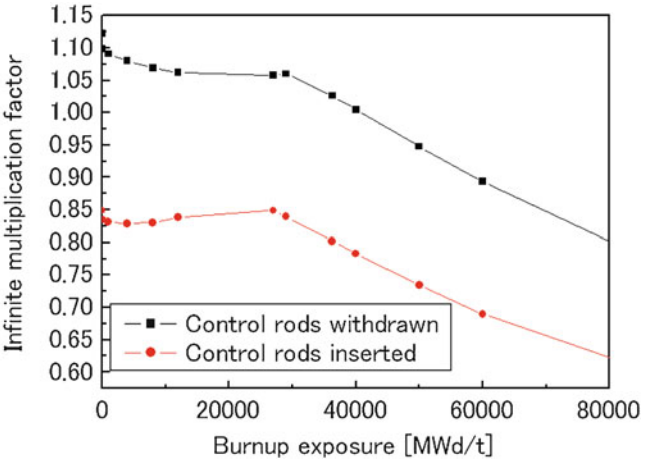


Fig. 2.53 Infinite multiplication factor of the fuel assembly (CRs inserted and withdrawn cases)

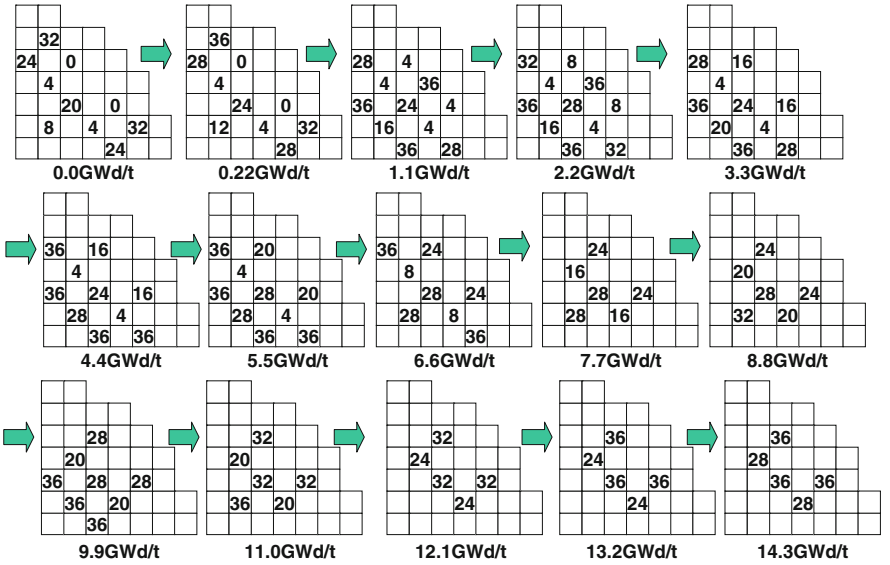


Fig. 2.54 Control rod patterns (1/4 symmetric). (Taken from doctoral thesis of A. Yamaji, the University of Tokyo (2005) [9])

power distributions are controlled so they match the coolant flow rate distributions for effective cooling of the fuel rods. The axial power distributions are controlled and large power peaks near the top of the core are prevented. The coolant temperature is high around the top of the core and large power peaks near the top lead to

high cladding surface temperatures. In this design, some control rods remain inserted at shallow positions for this purpose. However, such use of control rods is not desirable from the viewpoint of neutron economy. The shallow insertion of control rods is not necessary if the fuel axial design is optimized.

Control rods are also required for plant control to allow power maneuvering and give operating flexibility, and some control rods must be inserted throughout a cycle for these purposes. These are described in more detail in Chap. 4.

2.4.5.5 Radial Core Power Distributions and Radial Core Power Peaking Factor

The axially averaged radial core power distributions at BOC, MOC, and EOC of the equilibrium cycle are shown in Fig. 2.55 [9] for the 1/4 core symmetry. The radial power tends to be high around the fresh fuel but the overall radial power distribution is kept flat and relatively stable without large fluctuations during the cycle. The radial core power distribution is similar to the relative coolant flow rate distributions determined by the inlet orifices as shown in Fig. 2.52 [9]. Keeping the power to flow rate ratio constant is important for effectively cooling the fuel rods and raising the average core outlet temperature. The radial power peaking factor is defined as the ratio of the maximum fuel assembly power to the average fuel assembly power in the core. The radial power peaking factors at BOC, MOC, and EOC are 1.19, 1.22, and 1.23 respectively.

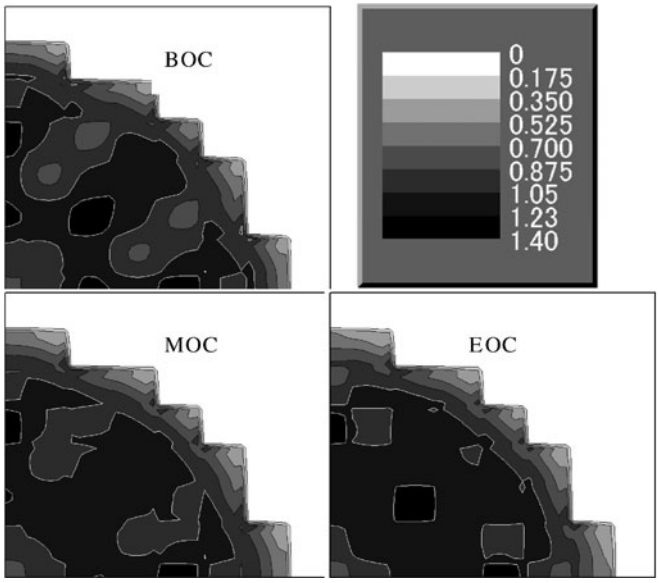


Fig. 2.55 Radial core power distributions (1/4 symmetric core). (Taken from doctoral thesis of A. Yamaji, the University of Tokyo (2005) [9])

These calculated results imply that with an appropriate core design, suitable radial core power distributions to achieve a high outlet temperature can be obtained. The design parameters of main concern here are the fuel loading patterns, the coolant flow rate distributions (orifice designs), and the control rod patterns.

2.4.5.6 Axial Core Power Distributions and Axial Core Power Peaking Factor

The horizontally averaged axial power distributions at BOC, MOC, and EOC of the equilibrium cycle are shown in Fig. 2.56 [9]. As the cycle burnup increases and the control rods are gradually withdrawn, the power distribution shifts from a bottom peak to a top peak. However the peak near the top of the core near EOC is kept small by the insertion of shallow control rods to prevent excess heat up of the fuel rod cladding. The axial power peaking factor is defined as the ratio of the maximum planar power to the average planar power in the maximum power fuel assembly. It has a relatively high value of 1.60 at the BOC. This should not be a big concern for fuel rod cooling, because the peak power plane appears near the bottom of the core where the coolant temperature is low. After that, the axial core power peaking factor is kept relatively low at around 1.25–1.40.

The calculated results imply that although the coolant axial density change is large in the Super LWR core, the axial core power distribution can be kept flat by adopting downward flow water rods, axially dividing the fuel enrichment zones, and using appropriate control rod patterns. The shallow insertions of some of the control rods at the EOC are shown to be effective for preventing large power peaks near the top of the core. The control rods of the Super LWR are inserted from the top of the core the same as in PWRs. The insertion of control rods from the bottom

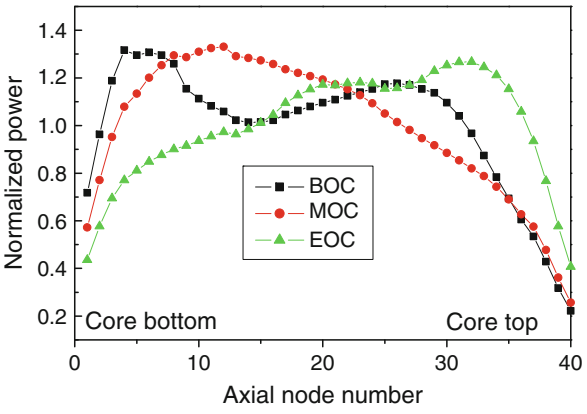


Fig. 2.56 Axial core power distributions. (Taken from doctoral thesis of A. Yamaji, the University of Tokyo (2005) [9])

of the core, as in BWRs, is not desirable as it would cause large power peaks near the top of the core, which may lead to excess heat up of the fuel rod cladding.

2.4.5.7 Local Power Distributions for a Homogenized Fuel Assembly

The usual definition of the local power peaking factor is the ratio of the maximum fuel rod power to the average fuel rod power at the maximum power plane of the maximum power fuel assembly. However, as explained in Sect. 2.3, this cannot be directly evaluated with the three-dimensional core calculations when the macro-cross section sets of the fuels are homogenized. The core calculations used in this design can only evaluate the volume averaged power density for each calculation mesh dividing the fuel assembly into 36 regions in the horizontal plane and 40 regions in the axial direction. The power distributions inside the fuel assembly of a particular plane arise from the heterogeneity of the core in the horizontal plane (e.g., fuel loading patterns, control rod patterns).

The relative fuel rod power inside the fuel assembly can be evaluated by combining the fuel assembly burnup calculations (ASMBURN, explained in Sect. 2.3.1) with the subchannel analyses (explained in Sect. 2.5). However, in such evaluations, the fuel assembly is assumed to be isolated in an infinitely large space with reflective boundary conditions. The effects of the fuel loading patterns or control rod patterns cannot be taken into account in these calculations.

The true local power distribution may be evaluated by combining the homogenized fuel assembly power distribution (which is obtained by the three-dimensional core calculations) with the relative fuel rod power distribution of an isolated fuel assembly (which is obtained by coupling the assembly burnup calculations and subchannel analyses). The former distribution is referred to as the "homogenized local power distribution" and the latter is referred to as the "isolated local power distribution" to distinguish them in this chapter. Similarly, the corresponding local power peaking factors are referred to as the "homogenized local power peaking factor" and the "isolated local power peaking factor." The homogenized local power peaking factor is obtained by the three-dimensional core calculations as about 1.05–1.10 during the equilibrium cycle.

2.4.5.8 Total Power Peaking Factor and MLHGR

The total power peaking factor is defined as follows:

$$\begin{aligned}\text{Total power peaking factor} = &\,(\text{radial power peaking factor})\\ &\times (\text{axial power peaking factor})\\ &\times (\text{local power peaking factor}).\end{aligned}$$

By using the total power peaking factor, MLHGR can be evaluated as follows:

$$\text{MLHGR} = (\text{total power peaking factor}) \times \text{ALHGR}.$$

The above relationships assume that the maximum power point always appears in the maximum power fuel assembly. Such an assumption may be acceptable when the core power distribution is relatively smooth, and it seems to be acceptable for the Super LWR core design as far as the three-dimensional core calculation results are concerned.

As noted previously, the local power peaking factor cannot be determined with the three-dimensional core calculations without further coupling calculations of the assembly burnup calculations and subchannel analyses. Nevertheless, the MLHGR can be roughly evaluated with the assumption that the fuel assembly is completely homogenized in the horizontal plane (i.e., the homogeneous model). Considering the relatively small local power distributions evaluated by the ASMBURN in Sect. 2.4.2 (1.06 for the fuel assembly without burnable poisons and control rods), this rough evaluation may be acceptable at this stage.

The burnup profiles of the power peaking factors and the MLHGR are shown in Fig. 2.57 [9]. The local power peaking factors are evaluated with the homogenized fuel assembly model. The total power peaking factor takes the maximum value of 2.05 at the cycle burnup of about 2 GWd/t, which corresponds to the MLHGR of 36.9 kW/m. While the radial and local power peaking factors are relatively constant throughout the cycle, the fluctuations in the axial power peaking factors are relatively large. The axial power peaking factor may also be reduced by improving the axial fuel designs and control rod patterns.

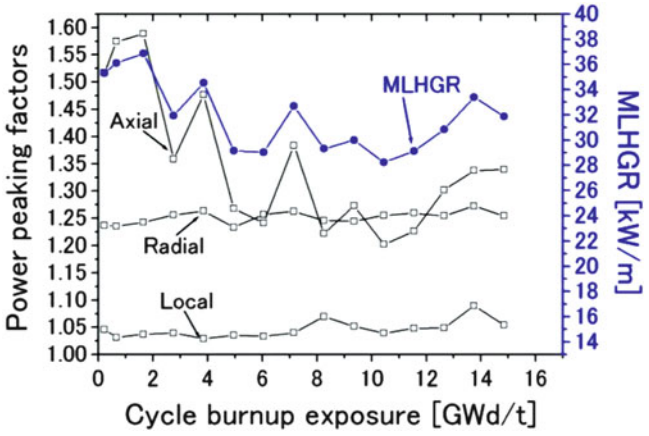


Fig. 2.57 Burnup profiles of power peaking factors and MLHGR. (Taken from doctoral thesis of A. Yamaji, the University of Tokyo (2005) [9])

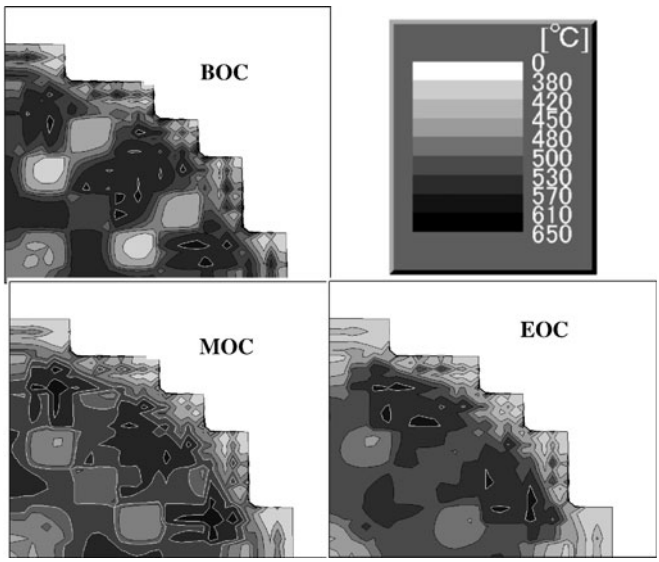


Fig. 2.58 Coolant outlet temperature distributions (1/4 symmetric core). (Taken from doctoral thesis of A. Yamaji, the University of Tokyo (2005) [9])

2.4.5.9 Coolant Outlet Temperature Distribution

The coolant outlet temperature distributions at BOC, MOC, and EOC are shown in Fig. 2.58 [9] for 1/4 core symmetry. These thermal-hydraulic calculations are also based on the homogenized fuel assembly model and use the single channel analysis model as explained in Sect. 2.3.2. The detailed subchannel analysis results are explained in Sect. 2.5.

For the average core outlet temperature of 500°C, the coolant outlet temperature ranges from about 385 to 602°C. Most of the relatively cold outlet coolant comes from the outer regions of the core. This is due to the power to flow rate mismatches in the outer fuel assemblies which are caused by the large power gradient within the horizontal plane of the outer fuel assemblies.

2.4.5.10 Maximum Cladding Surface Temperature Distribution

The MCST is defined as the maximum surface temperature of the cladding along the axial direction at a particular burnup. The MCST is shown for each "fuel channel group" at BOC, MOC, and EOC in Fig. 2.59 [9] for 1/4 core symmetry (for an explanation of fuel channel group see Sect. 2.3.2). The evaluations are based on the same methods as already explained so far (homogenized fuel assembly model with a single channel thermal-hydraulic analysis model).

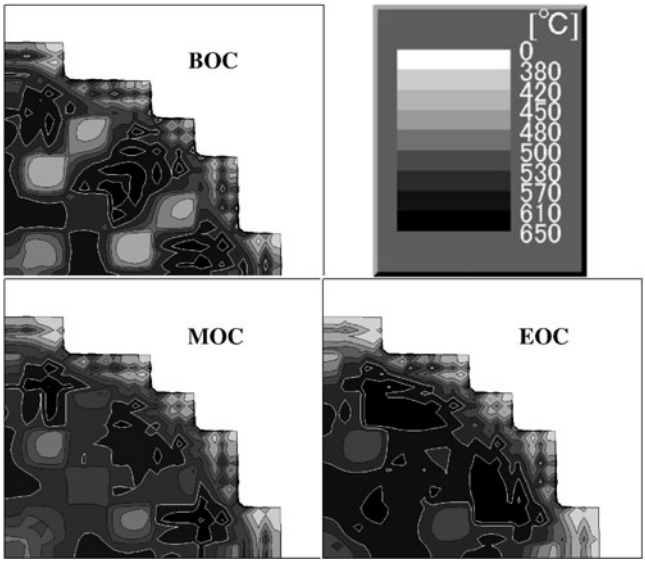


Fig. 2.59 MCST distributions (1/4 symmetric core). (Taken from doctoral thesis of A. Yamaji, the University of Tokyo (2005) [9])

The MCST of the fuel channel groups range from about 390 to 650°C. The hot region with MCST greater than 570°C is relatively limited at BOC or MOC, but spreads to a greater part of the core toward the EOC. This is related to the gradual shift of the core axial power distribution from the bottom peak to the top peak due to control rod withdrawals.

2.4.5.11 Water Density Reactivity Coefficient

The water density reactivity coefficient corresponds to the void reactivity coefficient of BWRs or PWRs and it is an important index parameter when judging the inherent safety characteristics of the Super LWR. The density reactivity coefficient for a typical fuel is shown with respect to the water density (average of the coolant and moderator densities) in Fig. 2.60 [9]. The coefficients are derived from the change in the infinite multiplication factor of the fuel when the average density is instantaneously changed at a particular burnup using the branching burnup calculations (Sect. 2.3.1).

The density reactivity coefficients tend to increase with burnup. This is due to plutonium buildup in the fuel; Pu has a larger thermal neutron absorption cross section, fission cross section, and the resonance absorption cross section than U. Although the density reactivity coefficient decreases with increasing water density, it is kept positive for all density region (i.e., the void reactivity coefficient is negative). Hence, the core can secure the inherent safety characteristics.

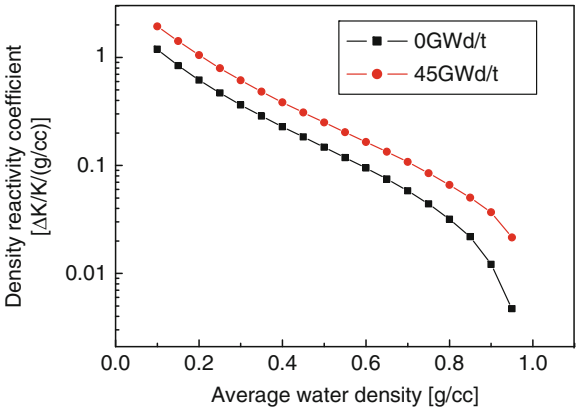


Fig. 2.60 Density reactivity coefficients for a typical fuel. (Taken from doctoral thesis of A. Yamaji, the University of Tokyo (2005) [9])

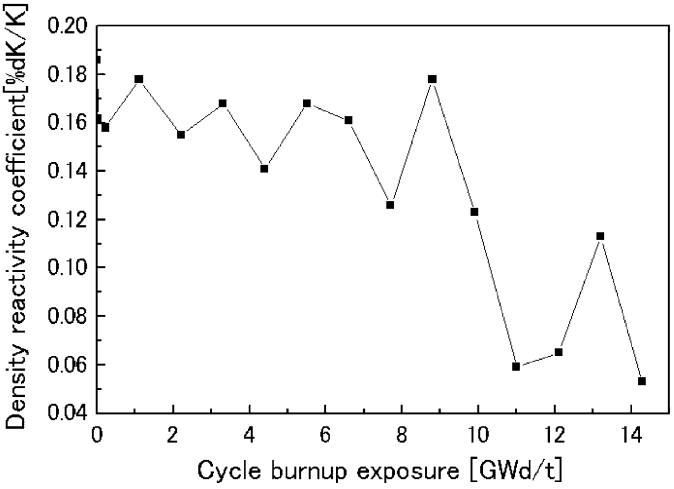


Fig. 2.61 Burnup profile of the density reactivity coefficient of the equilibrium core. (Taken from doctoral thesis of A. Yamaji, the University of Tokyo (2005) [9])

The burnup profile of the density reactivity coefficient of the equilibrium core is shown in Fig. 2.61 [9]. Although the calculation methods used in this chapter are not accurate enough to state the precise density coefficient values, the tendency of the density reactivity coefficient to decrease with the cycle burnup exposure can be seen. This decreasing trend is due to the increase in the core average density with the burnup from about 0.50 g/cm^3 at the BOC to about 0.57 g/cm^3 at the EOC. The gradual increase of the core average water density can be explained by the gradual shift of the axial core power distribution from the bottom peak to the top peak towards the EOC. As the axial power distribution shifts to the top peak, the axial

position where the coolant passes the pseudocritical temperature moves to the upper region of the core. The axial shift of this pseudocritical temperature point changes the volumetric ratio of the high density cold region to the low density hot region in the core. Thus, the core average water density gradually decreases with the cycle burnup. In BWRs or PWRs, the void reactivity coefficient tends to become more negative (i.e., density reactivity tends to increase) with the burnup due to the plutonium buildup. However, in this design, the density reactivity coefficient tends to decrease with the burnup because of the increase in the core average density.

2.4.5.12 Doppler Reactivity Coefficient

Figure 2.62 [9] plots the Doppler reactivity coefficient for a typical fuel. The evaluation is also based on the branching burnup calculations as used in the evaluations of the density reactivity coefficient. The Doppler reactivity coefficient tends to become more negative with the burnup, but the sensitivity is not very large. The temperature dependence of the Doppler reactivity coefficient is also not very large and it is kept negative for the temperature range of 150–2,000°C.

2.4.5.13 Core Shutdown Margin

The core shutdown margin is evaluated with the assumption that one cluster of control rods with the maximum worth is stuck at its operating position. The evaluation is done with the conservative xenon-free condition at the BOC. All coolant and moderator temperatures are assumed to be 30°C with a density of 1.0 g/cm^3.

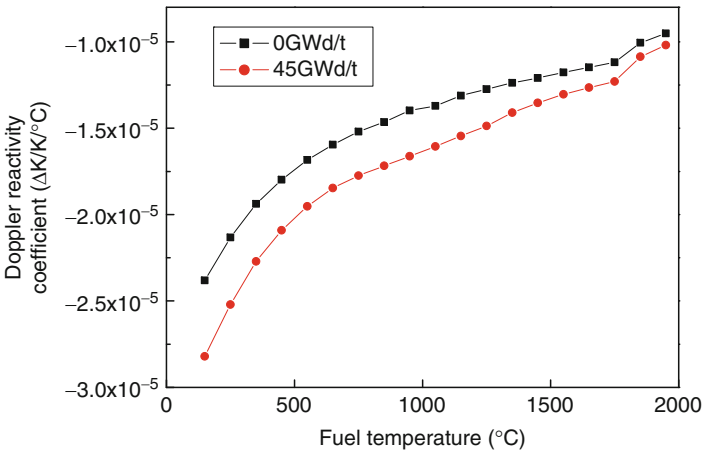


Fig. 2.62 Doppler reactivity coefficients for a typical fuel. (Taken from doctoral thesis of A. Yamaji, the University of Tokyo (2005) [9])



Fig. 2.63 Shutdown margin evaluation geometry (1/2 symmetric core). (Taken from doctoral thesis of A. Yamaji, the University of Tokyo (2005) [9])

The evaluation is carried out with the 1/2 symmetric core calculation model (Fig. 2.63 [9]). The one cluster of control rods with the maximum worth is assumed to be stuck and fails to be inserted into the core with the scram.

When the hot operating condition is brought to a cold standby condition, a positive reactivity is inserted due to the increased water density. This reactivity insertion is evaluated as about 6.9%dk/k for the xenon-free condition and about 5.7%dk/k for the xenon equilibrium condition. The core shutdown margin is evaluated as about 0.9%dk/k, which is not enough to satisfy the design criterion (1%dk/k). However, the design criterion can be satisfied by increasing the rod diameter from the current 12.4 to 13.0 mm (then the core shutdown margin is about 1.3%dk/k).

The maximum cluster worth is about 7.5%dk/k (equivalent to about $12). This cluster worth is about 39% of the worth of all the clusters that can be inserted into the core (about 19.0%dk/k). It is higher than the maximum worth of BWRs (about 30% of the total worth). This is because in BWRs, the cruciform type control rods are inserted into the control cell, which consists of four fuel assemblies with different burnup cycles. The volume averaged reactivity of the BWR control cell is lower than that of the fresh fuel assembly of the Super LWR.

2.4.5.14 Scram Reactivity Curve

The scram reactivity insertion, in this design, is defined to be the reactivity inserted into the core by the scram relative to the operating condition. The scram control rod insertion rate is defined as the insertion rate of the control rod which is at the complete withdrawal position before the scram initiation. Hence, the scram control rod insertion rate is 0% at the operating condition. The control rod positions during normal operation are shown in Fig. 2.54 [9]. The scram reactivity curve is shown in Fig. 2.64 [9]. It is assumed that all control rods are simultaneously inserted at the same rate except for the maximum worth cluster. The density and temperature feedbacks to the scram are ignored. This scram reactivity curve may be used in the

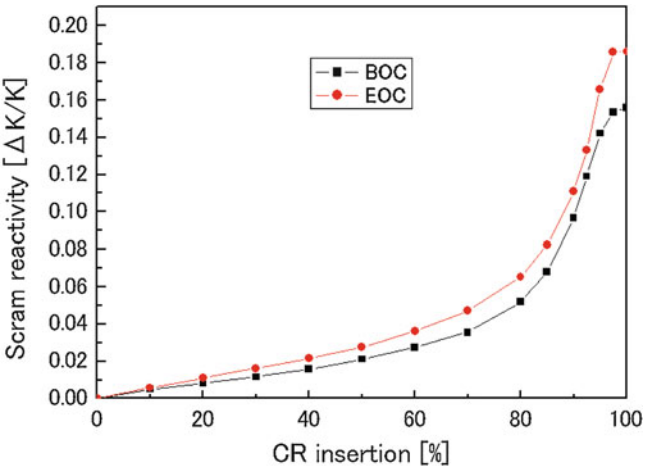


Fig. 2.64 Scram reactivity curve. (Taken from doctoral thesis of A. Yamaji, the University of Tokyo (2005) [9])

plant safety analyses to characterize the behavior of the plant system during reactivity insertion events.

In BWRs, the reactivity insertion by scram is especially important for the first two seconds of the abnormal events. During this period, about 50% of the control rods are inserted into the core and about 2–3%dk/k of negative reactivity is inserted. The scram reactivity insertion is more effective at the BOC than EOC. This is because at the BOC, there are a number of relatively deeply inserted control rods and there are relatively large power peaks just above their upper edges.

As for the Super LWR, the negative reactivity inserted with 50% insertion rate is about 2–3%, which is about the same level as that in BWRs. The difference is that in the Super LWR, the scram reactivity insertion is more effective at the EOC than BOC. There may be two reasons for the difference. First, this particular design is such that the control rod insertion rate at the BOC operating condition is significantly higher than that at the EOC. The use of too many control rods is not desirable from the viewpoint of neutron economy. The use of control rods at BOC can be reduced by revising the fuel design and optimizing the excess reactivity controls. The second reason is that in the case of the present design, there are relatively large power peaks just below the edges of the control rods at the EOC.

2.4.5.15 Alternative Shutdown System

In the unlikely event whereby all control rods fail to be inserted into the core, the reactor should be equipped with an alternative shutdown system to safely bring the core to a cold shutdown state. For BWRs, the borated water injection system is used. This system is expected to be equally effective for the Super LWR.

Hence, the required boron concentration for the core shutdown is evaluated assuming all injected borated water is uniformly diluted in the core. All coolant and moderator are assumed to be at a temperature of 30°C with a density of 1 g/cm^3. The boron concentration is defined as the number of boron atoms relative to the number of hydrogen atoms (in the coolant). The required boron concentration is evaluated as about 1,200 ppm (parts per million) to achieve the core effective multiplication factor of less than 0.95.

2.4.5.16 Summary and Design Issues of the "First Trial Design"

For the "first trial design" of the high temperature Super LWR core the equilibrium core is designed with an out-in refueling pattern of 121 three-batch fuel assemblies (including one assembly with fourth cycle fuel). The thermal output of the core is 2,744 MW with an ALHGR of 18 kW/m (corresponding to power density of 62 W/cm^3), active core height of 4.2 m, and equivalent core diameter of 3.68 m (fuel assembly pitch of 296.2 mm). Assuming a plant thermal efficiency of 43.8%, the electric output of the plant is 1,202 MW. The thermal-hydraulic design of the core can be characterized by the coolant pressure of 25 MPa (supercritical pressure), inlet temperature of 280°C, and average outlet temperature of 500°C. Thirty percent of the inlet coolant is led to the top dome of the RPV and it flows down the water rods as a moderator (downward flow moderation), and coolant flow rate is adjusted by the inlet orifices to achieve a high outlet temperature. The cluster type control rod is designed and the control rod patterns are determined to show that appropriate distributions can be achieved throughout the cycle for achieving the high outlet temperature. Thus, a reasonable set of design parameters is derived to achieve an average outlet temperature of 500°C.

The reference core characteristics of the Super LWR are summarized and compared with those of one typical Japanese BWR (Hamaoka-4) and one PWR (Ohi-3) in Table 2.4 [9]. The core pressure of the Super LWR is about 3.6 times larger than that of the BWR and about 1.6 times larger than that of the PWR. For the Super LWR, the inlet temperature is about the same as those of the BWR and PWR, but the enthalpy rise of the core is high and the average outlet temperature of 500°C is much higher than the 286°C of the BWR and 325°C of the PWR. The core flow rate per unit electric output of the Super LWR is about 1/10 of those of the BWR and PWR and close to that of supercritical FPPs (about 0.8 kg/s/MW).

The main issue encountered in the first trial design is the relatively cold outlet coolant from the outer region of the core. The cold coolant from the outer fuel assemblies is effectively limiting the average outlet temperature. Flow separation plates should be inserted into the fuel assemblies for coolant flow rate adjustments to account for the large power gradients in the horizontal plane of the outer fuel assemblies. The insertion of the flow separation plates is effectively the same as dividing the fuel assembly into smaller four subassemblies, but plate insertion would cause structural complications. The flow separation plates may also deteriorate the neutron economy by absorbing neutrons (this effect is not evaluated in the

Table 2.4 Core characteristics. (Taken from doctoral thesis of A. Yamaji, the University of Tokyo (2005) [9])

	Super LWR (Reference design)	BWR (Hamaoka-4)	PWR (Ohi-3)
Primary coolant pressure (MPa)	25.0	7.03	15.4
Inlet/outlet temperature (°C)	280/500	216/286	289/325
Core flow rate (kg/s)	1,420	13,400	16,700
Thermal/electric output (MW)	2,740/1,200	3,293/1,137	3,411/1,180
(Core flow rate per electric output) (kg/s/MW)	1.18	11.8	14.2
Plant thermal efficiency (%)	43.8	34.5	34.6
Active core height/equivalent diameter (m)	4.20/3.68	3.7/4.8	3.7/3.4
ALHGR (W/cm)/Power density (W/cm^3)	180/62	180/50	179/100
Fuel rod outer diameter/cladding thickness (mm) (clad material)	10.2/0.63 (Ni alloy)	12.0/0.9 (Zircaloy 2)	9.5/0.64 (Zircaloy 4)
Average discharge burnup (GWd/t)	45.0	33.0	32.0
Average U-235 enrichment (wt%)	6.3	3.0	3.5

first trial design). Without the use of the flow separation plates, the average outlet temperature is expected to decrease by about 40–50°C.

Another design issue is the relatively high U-235 enrichment for the target discharge burnup. It is partly due to the excess use of burnable poison, which still remains in the core at the EOC. The neutron economy can also be improved by revising the fuel loading patterns for low neutron leakages. Normally, the in–out refueling patterns are adopted to reduce the neutron leakages, but there is a tradeoff relationship between the neutron economy and flattening of the core power distributions. The first trial design has the characteristic that the average outlet temperature decreases with increasing radial power peaking factor. This is because as the radial power peaking factor increases, mismatching between the power to flow rate increases. Hence, the improvement of the neutron economy is also strongly related to the thermal-hydraulic design of the core. The relatively large neutron absorption cross section of the nickel alloy (cladding material) also raises the U-235 fuel enrichment requirement. The use of an alternative material, such as certain stainless steels may improve the neutron economy.

2.4.6 Design Improvements

The core average coolant outlet temperature may be greatly increased by improving the core thermal-hydraulic design. A new coolant flow scheme is designed, which allows the high temperature core design without the difficulties faced by the first trial design presented in the previous section. The new coolant flow scheme is characterized by downward flow cooling in the outer region of the core. This flow scheme is able to increase not only the average outlet temperature but also the

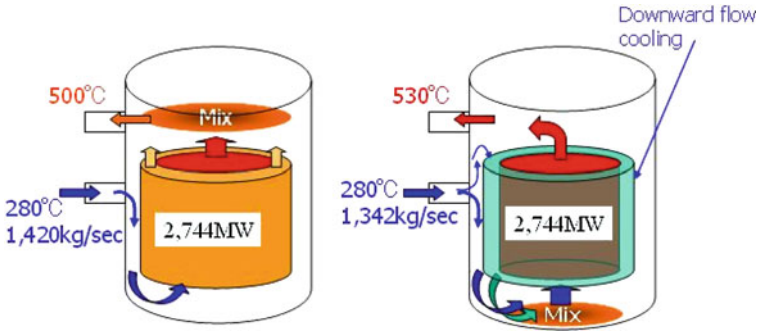


Fig. 2.65 Concept of the outer core downward flow cooling. (Taken from doctoral thesis of A. Yamaji, the University of Tokyo (2005) [9])

degrees of freedom in the neutronic designs to improve the neutron economy. Below, the effects of adopting the new coolant flow scheme are verified through two designs, which are based on the first trial design.

2.4.6.1 Coolant Flow Scheme: Outer Core Downward Flow Cooling

The concept of the outer core downward flow cooling is described by Fig. 2.65 [9]. When this flow scheme is adopted, the relatively cold outlet coolant from the outer region of the core mixes with the rest of the coolant at the mixing plenum; hence, their mixing does not occur at the core outlet. When designing a high temperature core with this flow scheme, the outlet temperature of the outer core region does not have to be raised to a high temperature. The outer core downward flow cooling is suitable for achieving a high average outlet temperature with a once-through direct cycle.

In the following design, the thermal output of the core is the same as in the first trial design at 2,744 MW. However, the core flow rate is reduced by 5.5% to 1,342 kg/s to increase the average outlet temperature to 530°C. All other design parameters (including the fuel design and fuel loading patterns) are basically the same as those of the first trial design except for the control rod patterns, which need slight adjustments. To distinguishing the two core designs presented here, they are called the "out-in refueling core with outer core downward flow cooling" and the "in–out refueling core."

The flow scheme of the out-in refueling core is described by Fig. 2.66 [9]. Among the 121 fuel assemblies, 89 inner fuel assemblies are cooled by upward flow of the coolant, while the 32 outer fuel assemblies are cooled by coolant downward flow. The core pressure is 25 MPa and the inlet coolant temperature is 280°C. Most of the inlet coolant (76.7%) is guided to the top dome and distributed to the water rods of the inner fuel assemblies (30.0% of the inlet coolant), water rods of the outer fuel assemblies (10.8% of the inlet coolant), and the fuel channels

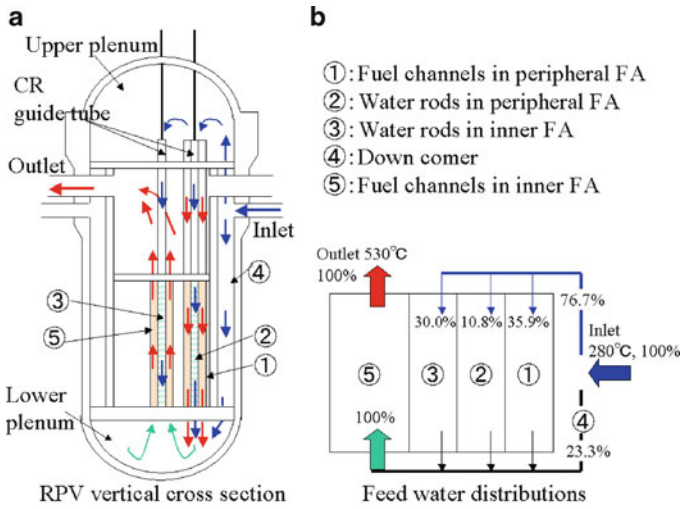


Fig. 2.66 Flow scheme of the outer core downward flow cooling core. (Taken from doctoral thesis of A. Yamaji, the University of Tokyo (2005) [9])

of the outer fuel assemblies (35.0% of the inlet coolant). The rest (23.3% of the inlet coolant) of the coolant flows down the downcomer and mixes with the outlet coolant from the outer fuel assemblies. The mixed coolant finally rises in the core through the fuel channels of the inner fuel assemblies. The inlet coolant temperature of the inner fuel assemblies ranges from about 377 to 384°C depending on the radial core power distributions. The core outlet temperature is kept constant at 530°C throughout the cycle since the core thermal output and the core flow rate are fixed.

Figure 2.67 [9] schematically shows the top structure of the outer fuel assembly. The control rod cluster guide tube has a double-tube structure and the coolant flow in the outer and inner tubes are separated. The coolant flowing down the outer tube is guided to the fuel channels of the outer fuel assembly and flows down to the mixing plenum while removing the heat from the fuel rods. The coolant flow in the inner tube is guided to the water rods of the outer fuel assembly and flows down to the mixing plenum as a moderator. The flow rate of the downward flowing coolant and moderator are determined by the orifices attached to the outer and inner tubes.

The flow separation plates were introduced in the first trial design mainly to increase the coolant outlet temperature from the outer region of the core. However, such separations are not necessary when the outer core downward flow cooling scheme is adopted.

Figure 2.68 [9] shows the relative coolant flow rate. The distribution is determined by the inlet orifice attached to each fuel assembly for the 1/4 symmetric core (the flow rate is not normalized, and the average is 0.99). The outer (or peripheral) fuel assemblies are cooled by downward flow. A relatively large flow rate can be distributed to the outer fuel assemblies compared with the expected power generation because the outlet coolant temperature does not need to be high. By eliminating

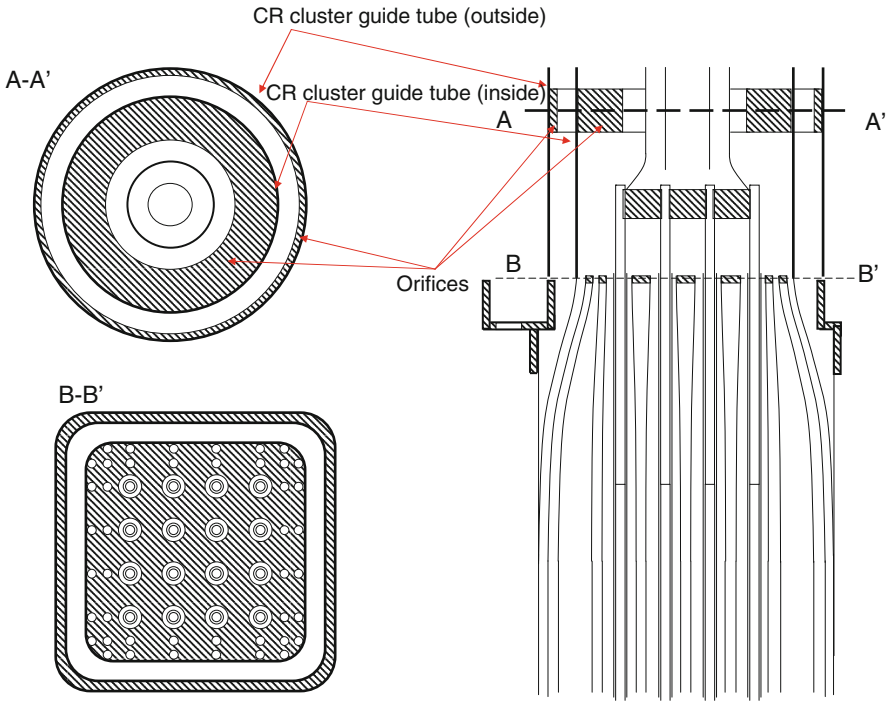


Fig. 2.67 Top structure of the outer fuel assembly (outer core downward flow cooling). (Taken from doctoral thesis of A. Yamaji, the University of Tokyo (2005) [9])

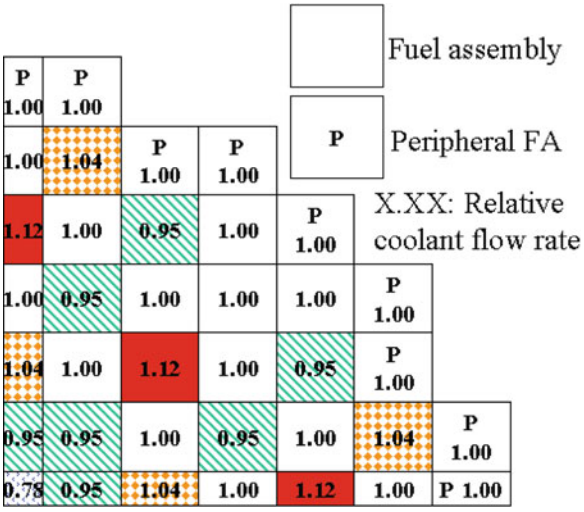


Fig. 2.68 Relative coolant flow rate by the inlet orifices (outer core downward flow cooling). (Taken from doctoral thesis of A. Yamaji, the University of Tokyo (2005) [9])

the flow separation plates, the number of orifice types is reduced from nine of the first trial design to five.

2.4.6.2 Power Distributions and MLHGR

The control rod patterns are slightly adjusted from the first trial core design to match the outer core downward cooling. The axially averaged radial core power distributions at BOC, MOC, and EOC are shown in Fig. 2.69 [9] for 1/4 core symmetry. The radial power distribution is flat and stable throughout the cycle. The radial power peaking factors range from 1.19 to 1.23. The radial power peaking factors are lower than those of the first trial core design (1.25–1.27). When the downward flow cooling is adopted for the outer core with a relatively high flow rate, the average water density in the outer core region is higher than that of the first trial core. This is the reason for the reduced radial power peaking factor. The core axial power distributions are similar to those of the first trial core and the axial core power peaking factors range from 1.20 to 1.60. The homogenized local power peaking factors range from 1.03 to 1.08. Their slight reduction compared with the first trial core is simply due to the lower core radial power peaking factor (i.e., flatter radial core power distributions).

When the outer core downward flow cooling is adopted for the out-in refueling core, the maximum power fuel rod may not belong to the maximum power fuel assembly. As can be seen from the radial core power distributions in Fig. 2.69 [9],

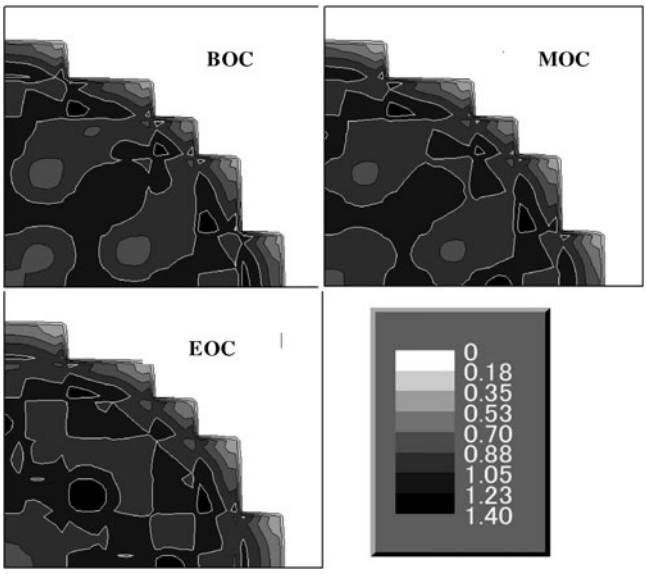


Fig. 2.69 Radial power distributions of the outer core downward flow cooling core (1/4 symmetric core). (Taken from doctoral thesis of A. Yamaji, the University of Tokyo (2005) [9])

large power peaks can be seen at the inner sides (facing the inner core) of the outer fuel assemblies. This is due to the combination of the relatively high coolant density in the outer core regions and the high reactivity of the fresh fuel loaded in the outer core region. Therefore, the total power peaking factor cannot be evaluated by multiples of the radial, axial, and local power peaking factors. Instead, the total power peaking factor is directly evaluated from the three-dimensional core calculation results by finding the maximum power mesh. The MLHGR can then be evaluated by the product of the ALHGR and the total power peaking factor. Burnup profiles of the total power peaking factor and the MLHGR are shown in Fig. 2.70 [9]. The MLHGR is slightly higher than that of the first trial core, but the difference is small. In this design, the MLHGR appears in the outer core region where the flow rate of the downward flowing coolant is relatively high. Hence, the slightly higher MLHGR is not a concern as the fuel temperature is expected to be relatively low.

2.4.6.3 Coolant Outlet Temperature Distribution

The coolant outlet temperature distributions at BOC, MOC, and EOC are shown in Fig. 2.71 [9] for 1/4 core symmetry. The outlet coolant temperature in the outer core region represents that of the coolant flowing down to the mixing plenum. The outlet temperature of the outer core region ranges from about 360 to 470°C. After coolant mixing at the mixing plenum, the inlet coolant temperature for the fuel channels of the inner core ranges from about 377 to 384°C (complete mixing is assumed at the mixing plenum). The inlet temperature fluctuates depending on the relative heat generations of the inner and outer core regions.

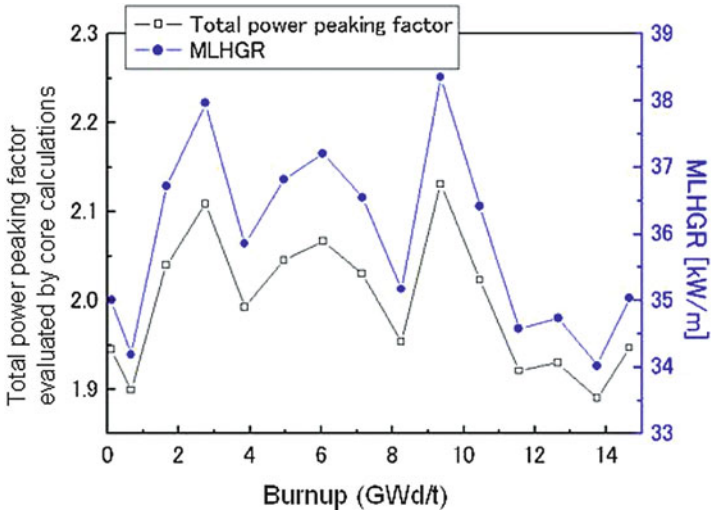


Fig. 2.70 Burnup profiles of the total power peaking factor and the MLHGR (outer core downward flow cooling). (Taken from doctoral thesis of A. Yamaji, the University of Tokyo (2005) [9])

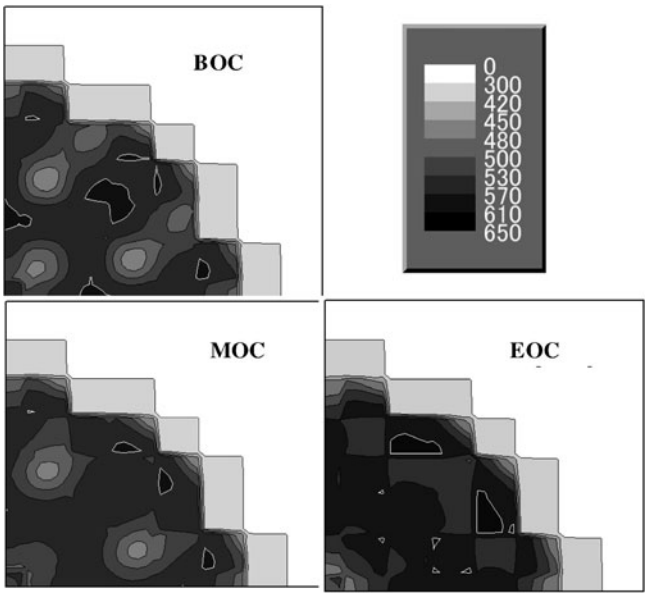


Fig. 2.71 Coolant outlet temperature distributions (outer core downward flow cooling). (Taken from doctoral thesis of A. Yamaji, the University of Tokyo (2005) [9])

The average coolant core outlet temperature is kept at 530°C throughout the cycle since the core thermal output and the core total flow rate are fixed. To maintain this average of 530°C, the outlet coolant temperature from the inner core region ranges from about 440 to 584°C. This temperature range is reduced from that of the first trial core (which ranged from 385 to 602°C). This demonstrates the significance of adopting the outer core downward flow cooling to achieve high average outlet temperature with a once-through direct cycle plant system.

The MCST is evaluated with three-dimensional core calculations using the homogenized fuel assembly model and the single channel thermal-hydraulic analysis model as before. The peak value of the MCST is about 650°C, which is the same as that of the first trial core. As noted above, the removal of the flow separation plates for the first trial core decreases the core outlet temperature by about 40–50°C. Taking this reduction into account, the outer core downward flow cooling can effectively raise the average outlet temperature by about 70–80°C, which may have a great impact on the plant economy.

2.4.6.4 Improvements of the Neutron Economy

When the outer core downward flow cooling is adopted, the average core outlet temperature becomes insensitive to the radial core power distributions. Hence, there

is more flexibility for the neutronic design, which in turn allows a core design with an improved neutron economy.

For the neutronic design of the fuel assembly, the monotonous decrease of the infinite multiplication factor of the fuel (Fig. 2.39 [9]) is suitable for reducing fluctuations in the radial core power distribution during the operation cycle. However, in order to reduce the excess reactivity at the BOC, highly concentrated burnable poison, which still remains at the EOC, needs to be introduced. This design restriction can be removed by cooling the outer core region by the downward flow. Hence, the concentration of the burnable poison can be reduced so that it does not remain at the end of the first cycle of exposure as shown in Fig. 2.72.

As for the fuel loading pattern, the low leakage loading pattern (LLLP) as shown in Fig. 2.73 [21] with the in–out refueling scheme of Fig. 2.74 [22] can be adopted with the outer core downward flow cooling. When these design options are chosen, the neutron economy becomes better compared with the out-in loading patterns

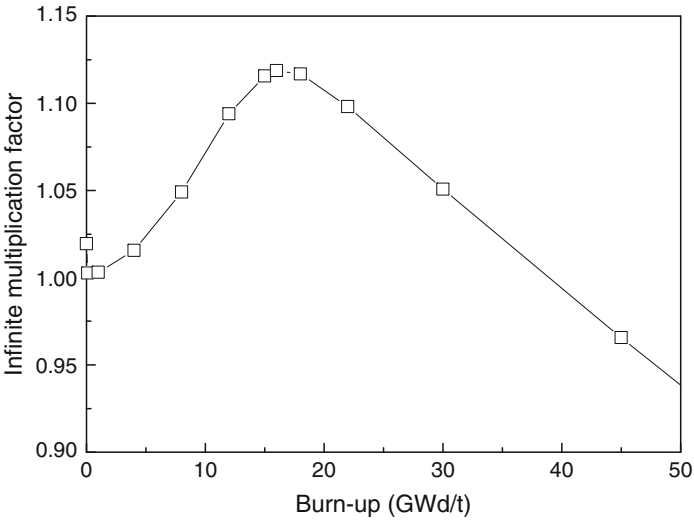


Fig. 2.72 Burnup profile of K_{inf} of the fuel assembly for improved neutron economy

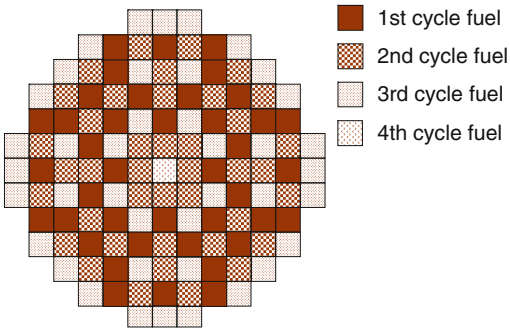


Fig. 2.73 Low neutron leakage fuel loading pattern. (Taken from [21])

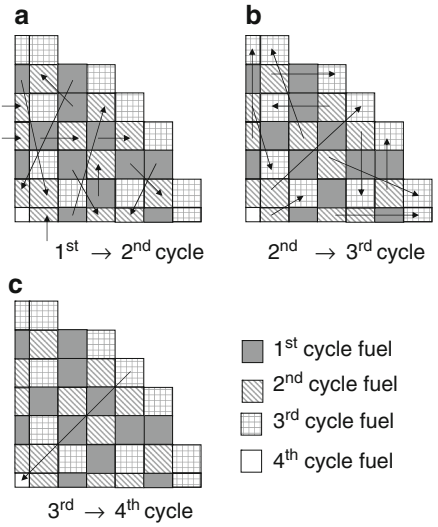


Fig. 2.74 In–out refueling scheme. (Taken from [22] and used with permission from Atomic Energy Society of Japan)

(Fig. 2.51 [9]) because the fuel with high reactivity is loaded in the inner region of the core, where the neutron flux is high, and the fuel with low reactivity is loaded in the outer region of the core, where the neutron flux is low. Thus, fewer neutrons leak out of the core and the neutrons are more effectively used for the fission reactions. The radial core power peaking tends to increase when the loading pattern is changed from the out–in to the in–out. However, the outer core downward flow cooling can tolerate a reasonable radial core power peaking without the need to reduce the average core outlet temperature. The relative coolant flow rate due to the inlet orifices for the outer core downward flow cooling with LLLP is shown in Fig. 2.75 [21]. The thermal-hydraulic design tolerance to the radial core power peaking factor increases with the increasing number of fuel assemblies with the downward flow cooling. The optimization of the burnable poison design together with the LLLP can conserve the U-235 fuel enrichment by about 0.9 wt% (absolute value) for the same average discharge burnup of 45 GWd/t.

The fuel rod cladding and water rod walls are the main neutron absorbers in the core (apart from the fuel). Hence, the choice of materials for the cladding and the water rod wall is important from the viewpoint of the neutron economy. Rough evaluation shows that replacing the nickel alloy cladding and water rod walls with stainless steels can conserve the U-235 enrichment by about 0.7 wt% (absolute value). Thus, the maximum of 1.6 wt% (absolute) reduction in the U-235 fuel enrichment may be possible by changing the neutronic designs from the first trial core.

Due to the large coolant temperature rise in the core, a cosine distribution may not be the ideal axial power distribution for the Super LWR. From the viewpoint of reducing the fuel temperature and effectively cooling the fuel rods, a bottom peak distribution may be more suitable than the cosine distribution. A bottom peak power distribution can be attained by dividing the fuel into two axial enrichment zones as shown in Fig. 2.76. Compared with the middle peak design (for the cosine power

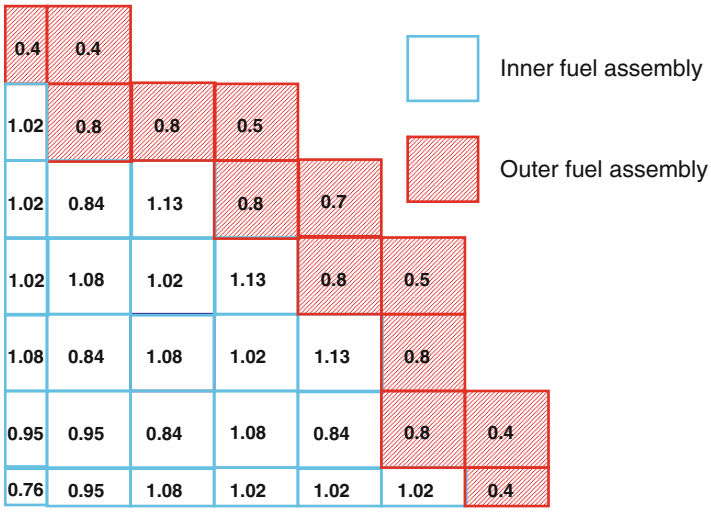


Fig. 2.75 Relative coolant flow rate (for outer core downward flow cooling). (Taken from [21])

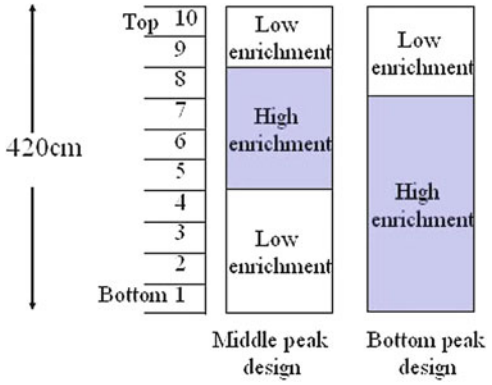


Fig. 2.76 Axial fuel enrichment designs

distribution), the number of fuel enrichment zones is reduced, and this is also an advantage from the viewpoint of fuel manufacturing costs. The burnup profiles of the power peaking factors of the core are shown in Fig. 2.77 [22]. The power peaking factors can be kept at sufficiently low levels with the outer core downward flow cooling.

2.4.7 Summary

The fuel rod design parameters were tentatively determined for the purpose of core designs, but with the expectations that its integrity was sustained at the worst

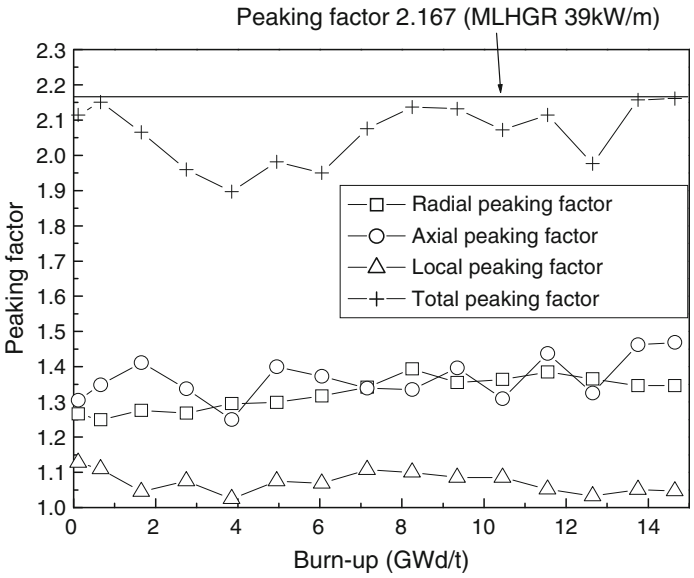


Fig. 2.77 Power peaking factors (outer core downward flow cooling). (Taken from [22] and used with permission from Atomic Energy Society of Japan)

transient event. The fuel rod diameter and heated length were determined by considering the core size and power density for the target output (about 1,000–1,200 MWe). The fuel cladding material was yet to be determined until sufficient results were obtained from experiments. For developing the core design concepts, a nickel alloy and stainless steel were tentatively used as the representative materials that possess high mechanical strengths at elevated temperatures. The cladding thickness was tentatively determined with simple but conservative assumptions. It should be able to withstand the largest coolant pressure expected during the design transients (preventing buckling collapse) at an elevated temperature of 850°C with a safety factor of 3 in the evaluation of the buckling collapse pressure and an assumption of 10% cladding thickness reduction by corrosions.

The fuel assemblies were designed with a tight fuel rod pitch (1.0 mm gap) to achieve high average core outlet coolant temperature and many water rods to attain sufficient neutron moderations. The hexagonal fuel assembly design with a tight triangular fuel rod lattice is adequate for acquiring heat transfer to the coolant by increasing the coolant velocity for a given mass flow rate. However, the high local power peaking and the irregularities in the subchannel and water rod arrangements are not suitable for achieving a high average outlet temperature. Hence, the square fuel assembly was designed for uniform cooling and neutron moderation. In this design, the fuel enrichment zoning in the horizontal plane of the fuel assembly (i.e., the use of different enrichments of fuel rods in the assembly) is not necessary to reduce the local power peaking. Among the 36 square water rods, the 24 central water rods are equipped with control rod guide tubes for the cluster type control

rods to be inserted from the top of the core. Among the 300 fuel rods in the square assembly, some fuel rods contain gadolinia (Gd_2O_3) as a burnable poison.

The core coolant flow scheme can be characterized by the downward flow in the water rods. This flow scheme is intended to:

1. Separate the pressure boundaries and the temperature boundaries in the core
2. Achieve high average core outlet coolant temperature
3. Reduce axial water density distribution

The low temperature core design concept was preliminarily developed with a CHF design criterion (MDHFR $>$ 1.3) using the hexagonal fuel assembly and R-Z two-dimensional core calculations. Each fuel assembly is equipped with an inlet orifice at the bottom to have a safety margin against heat transfer deterioration. The MDHFR criterion limits the average core outlet temperature to around 397°C, which is just above the pseudocritical temperature of the coolant (385°C).

The high temperature core design concept was developed by removing the critical heat flux design criterion and evaluating the maximum cladding temperature. The major core design parameters (e.g., refueling patterns, control rod patterns, coolant flow rate to each fuel assembly, etc.,) were considered and the basic core characteristics (e.g., coolant outlet temperature distributions, core power distributions, water density reactivity coefficients, etc.,) were revealed with three-dimensional core calculations (neutronic and thermal-hydraulic calculations are coupled). The designs and analyses showed that cooling the outer region of the core with a downward flow was effective in raising the average core outlet temperature to 500°C. It was also shown that this flow scheme enabled flexibilities in the core neutronic designs to achieve a high neutron economy. The comparison of the thermal-hydraulic characteristics of the Super LWR core designs are summarized in Table 2.5. From the early design concept (low temperature design), the average core outlet coolant temperature was increased by about 100°C to reach 500°C by removing the MDHFR design criterion and adopting downward flow cooling

Table 2.5 Thermal-hydraulic characteristics of the super LWR

	Low temperature design	High temperature designs	
Inlet/average outlet temperatures (°C)	324/397	280/450	280/500
Limit for the outlet temperature	Heat transfer deterioration	Peak cladding temperature	Peak cladding temperature
Fuel assembly type	Hexagonal	Square	Square
Moderator flow direction	Downward	Downward	Downward
Coolant flow direction	Upward	Upward	Upward/downward
ALHGR (W/cm)/Power density (W/cm^3)	160/106	180/62	180/62
Thermal power (MW)	2,490	2,740	2,740
Coolant pressure (MPa)	25	25	25

in the core outer region. The outlet temperature of the high temperature design is essentially limited by the peak cladding temperature, and it needs to be accurately determined. This evaluation requires accurate modeling of the coolant flows and property changes in the subchannels of the fuel assembly and it is described in detail in the next section.

The average U-235 fuel enrichment required for the average discharge burnup of 45 GWd/t is about 5–6 wt% depending on the cladding material and the neutronic designs. Changing the cladding material and water rod wall material from a nickel alloy to a stainless steel may reduce the average enrichment by about 0.7 wt% (absolute). The combination of optimized burnable poison design with LLLP and the outer core downward flow cooling may potentially reduce the enrichment by about 0.9 wt% (absolute).

2.5 Subchannel Analysis

Since supercritical pressure water is single phase over all operation temperatures, there are no phenomena associated with burnout or dry-out along the fuel rods, unlike in current LWRs. For this reason, MCST has been a crucial design criterion rather than DNB or CPR to avoid cladding overheating over the fuel lifetime.

Single channel analysis has been widely used for thermal-hydraulic coupled core design procedures by reason of its low calculation cost and it is known to be conservative in current LWR fuel assembly design when there is a large fuel rod gap clearance. However, it is not well known if such conservatism of single channel analysis can be kept in the supercritical pressure operating condition with small fuel rod gap clearance.

A subchannel analysis code at supercritical pressure was developed at the University of Tokyo [23, 24]. It has been applied to thermal-hydraulic fuel assembly design and has been used to evaluate PCST at supercritical pressure. The subchannnel analysis model and some results obtained by it for the Super LWR fuel assembly design are described in this section.

2.5.1 Subchannel Analysis Code

2.5.1.1 Governing Equations

Subchannel analysis is based on a control volume approach. A coolant flow channel is treated as a control volume which interacts with an adjacent control volume through gaps between the fuel pins. The subchannel analysis method consists of following four governing equations at the steady state:

1. The mass continuity equation

$$\frac{\partial}{\partial z}(\rho_{\mathrm{i}} u_{\mathrm{i}} A_{\mathrm{i}}) + \sum_j (\rho' v_{\mathrm{ij}}) S_{\mathrm{ij}} = 0. \tag{2.23}$$

The first term in (2.23) represents axial mass flow change and the second term denotes mass transfer from adjacent subchannels, j.

2. The axial momentum conservation equation

$$\frac{\partial}{\partial z}(\rho_i u_i^2 A_i) + \sum_j (\rho' u' v_{ij}) S_{ij} = -A_i \frac{\partial P_i}{\partial z} - \frac{1}{2}\left(\frac{f}{D_h} + \frac{k}{\Delta z}\right)(\rho_i u_i^2) A_i - A_i \rho_i g \cos\theta - \sum_j C_T w'(u_i - u_j). \tag{2.24}$$

The left-hand side of (2.24) represents the change of axial force. The first term on the right-hand side denotes the axial change of pressure force and the second term is a pressure loss term by frictional and form loss. The third term represents gravitational force and the last gives axial momentum exchange between adjacent channels.

3. Transverse momentum conservation equation

$$\frac{\partial}{\partial z}(\rho_i u' v_{ij} S_{ij}) + C_s \sum_k \frac{\rho' v_k^2}{l_{ij}} \cos\beta_k S_{ij} = \frac{P_i - P_j}{l_{ij}} S_{ij} - \frac{1}{2} K_g \frac{\rho' v_{ij}^2}{l_{ij}} S_{ij} - \rho_i g \sin\theta \cos\gamma \cdot S_{ij}. \tag{2.25}$$

The transverse momentum equation represents the momentum exchange in the transverse direction by cross-flow. The first term of the left-hand side represents the transverse momentum change coming from the axial direction and the second term is the transverse momentum coming from adjacent channels. The first term of right-hand side is the pressure force between adjacent channels, the second is the frictional loss by cross-flow and the last is the gravitational force.

4. Energy conservation equation

$$\frac{\partial}{\partial z}(\rho_i u_i h_i A_i) + \sum_j (\rho' h' V_{ij}) S_{ij} = \sum_l q' p_h \Delta z + \frac{\partial}{\partial z}\left(A_i k \frac{\partial T}{\partial z}\right) - \sum_j Ck \frac{T_i - T_j}{l_{ij}} - \sum_j w'_{ij}(h_i - h_j). \tag{2.26}$$

The first term of the left-hand side is energy transfer of the axial and transverse directions. The terms of the right-hand side are, respectively, heat from a fuel rod by convection, axial heat conduction, heat conduction from adjacent channels, and heat transfer by flow mixing with an adjacent channel.

The coolant velocity and properties at the boundary,u',ρ',h', with adjacent channels are expressed as the average values of two adjacent channels:

$$\rho' = \frac{\rho_i + \rho_j}{2}. \tag{2.27}$$

The turbulent flow mixing between channels is evaluated as the product of axial mass flux and mixing coefficient as

$$w'_{ij} = \beta \cdot G \cdot s_{ij}, \tag{2.28}$$

where $S_{ij}$is the fuel rod gap clearance. Turbulent mixing coefficient β of 0.015 is used in the analysis considering microscopic turbulent dispersion and macroscopic convective transfer between tight lattice arrangements for the single phase flow.

Frictional pressure drop is evaluated by

$$\Delta P_{\mathrm{f}} = f \frac{L}{D_{\mathrm{h}}} \frac{\rho}{2} u^2, \tag{2.29}$$

where the frictional loss coefficient f is calculated by the Blasius equation, (2.30).

$$f = 0.3164 Re^{-0.25}. \tag{2.30}$$

The pressure loss by the grid spacer is evaluated with (2.31):

$$\Delta P_G = K_{\mathrm{g}} \frac{\rho}{2} u^2, \tag{2.31}$$

where loss coefficient for a grid spacer is calculated as

$$K_{\mathrm{g}} = C_{\mathrm{v}} \varepsilon^2, \tag{2.32}$$

in which C_{v} is a revised friction coefficient and ε is $A_{\mathrm{projected}}/A_{\mathrm{channel}}$.

2.5.1.2 Iterative Procedure

The iterative procedure to solve the above equations is schematically shown in Fig. 2.78 [24] and has four steps.

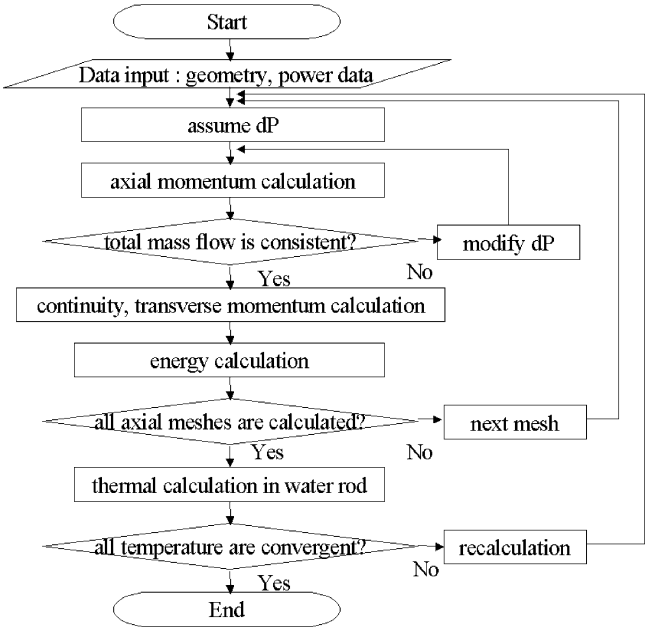


Fig. 2.78 Flow diagram of subchannel analysis code. (Taken from [24])

1. For given coolant channel geometries and power distribution, axial pressure loss of ΔP is assumed to be the same throughout all coolant channels because the transverse pressure difference between adjacent channels is considered to be much smaller than the axial pressure difference. The axial momentum equation (2.24) is solved to obtain the axial coolant velocity while adjusting the axial pressure loss. This is repeated until the total mass flow rate is converged.
2. Mass continuity and transverse momentum equations are solved to obtain transverse velocities and pressures until transverse pressure distributions are converged.
3. The energy conservation equation is solved to calculate enthalpy distribution for each node.
4. Steps from 1 to 3 are repeated for all axial nodes.

2.5.1.3 Heat Transfer Coefficient

The Oka–Koshizuka heat transfer correlation [7] and Watts–Chou correlation [25] are used to evaluate the cladding surface temperature for upward and downward flow regions, respectively, which is consistent with those in thermal-hydraulic coupled nuclear calculations. Heat transfer improvement by the grid spacer is not considered for conservatism.

2.5.2 Subchannel Analysis of the Super LWR

2.5.2.1 Computational Conditions

In the subchannel analysis, 1/8 symmetry of the assembly is used. The geometry and designations of the various areas are shown in Fig. 2.79 [24]. The 1/8 assembly is divided into 70 subchannels (lower right drawing: numbered 1–70 white areas) and includes 46 fuel rods (numbered 1–46 black circles), six water rods inside the assembly (numbered areas 1–6 in white squares or partial squares) and one water rod outside the assembly (numbered area 7). Three kinds of subchannels, A, B, and C, are used (upper left drawing). Subchannels A surround each corner of the six water rods inside the assembly. Subchannels C surround each corner of the assembly and they are surrounded by the water rod outside the assembly. Subchannels B

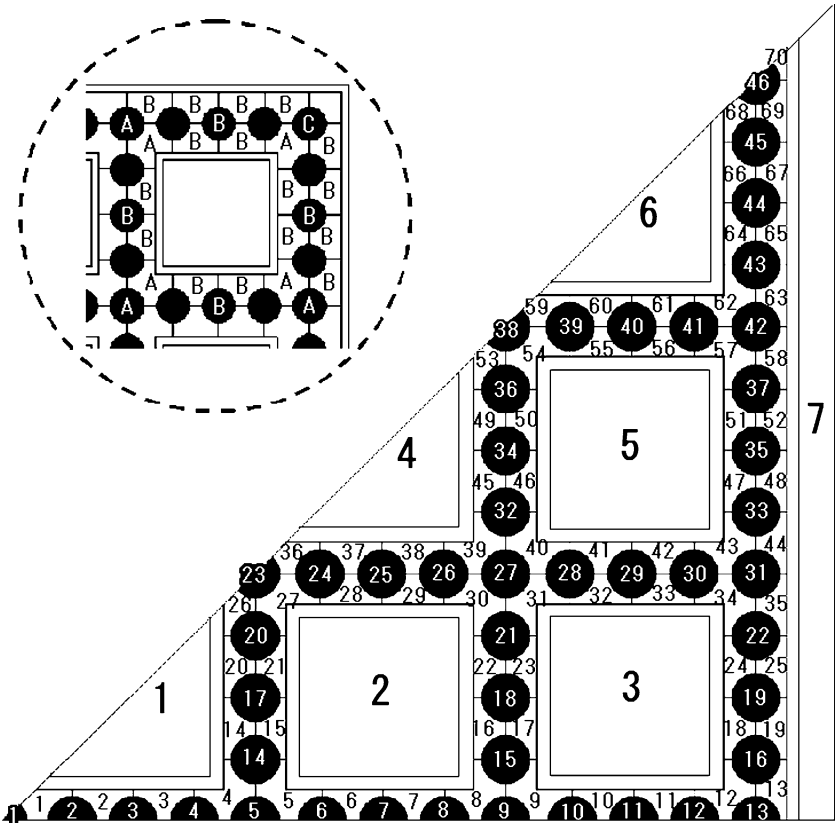


Fig. 2.79 Computational model of the fuel assembly of the Super LWR (Numbers/letters in black circles are fuel rods; numbers/letters in small white spaces are subchannel designations; numbers 1–7 in large white areas are water rods). (Taken from [24])

Table 2.6 Computational conditions. (Taken from [24])

Average linear heat rate	18.0 kW/m
Axial power distribution	Cosine
Number of fuel rods	300
Neutron heating rate	0.025
Flow rate of assembly	13.59 kg/s
Flow rate fraction of water rod	0.4
Coolant inlet temperature of assembly	379.4°C
Coolant inlet temperature of water rod	280.0°C
Coolant flow direction in fuel subchannel	Upward
Coolant flow direction in water rod	Downward

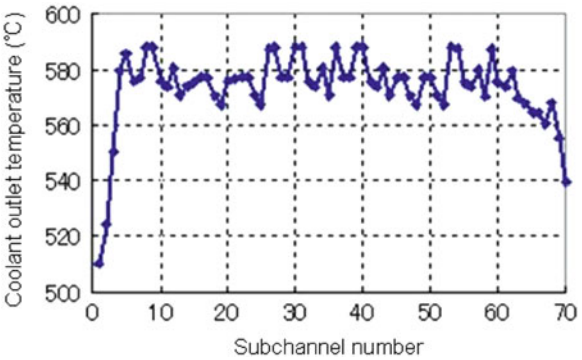


Fig. 2.80 Coolant outlet temperature distribution. (Taken from [24])

refer to all remaining subchannels. Table 2.6 [24] gives some basic computational conditions of subchannel analysis.

2.5.2.2 Subchannel Analysis

1. Coolant outlet temperature distribution.
   Figure 2.80 [3] plots a coolant outlet temperature distribution for the 70 subchannels of Fig. 2.79 [24] with flat power distribution. Although the same powers are used, the coolant temperatures of these subchannels are different due to the difference in subchannel type. For Subchannels A, the coolant temperature is 10°C higher than the average outlet coolant temperature. The coolant temperature of Subchannels B is a little higher than that of Subchannels C. The subchannel with the lowest coolant temperature is in the center of the assembly and is B type. The coolant temperature is affected by the channel area, the wetted perimeter of the fuel rod and the wetted perimeter of the water rod as shown in Table 2.7 [24]. Subchannel A has the biggest channel area, while the

Table 2.7 Parameters of the three subchannel types. (Taken from [24])

Subchannel	Channel area S	Wetted perimeter of fuel rod Lf	Lf/S	Wetted perimeter of water rod Lw	Lw/S
A	3.81E−05	0.0240	630.0	0.0102	267.4
B	2.75E−05	0.0160	583.4	0.0112	407.8
C	1.68E−05	0.0080	477.4	0.0122	727.0

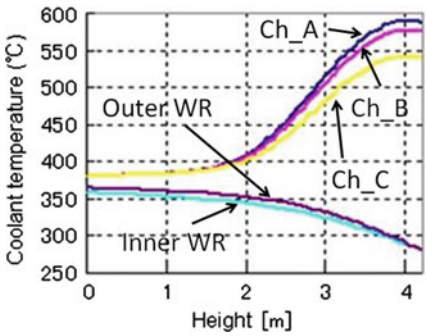


Fig. 2.81 Coolant temperature distributions in the axial direction. (Taken from [24])

Table 2.8 Channel area and heated perimeter parameters of the water rods. (Taken from [24])

	Channel area S	Heated perimeter Lf	Lf/S
Water rods inside the assembly	7.73E−04	0.111	143.9
Water rod outside the assembly	5.82E−03	1.143	196.6

channel area of Subchannel C is smallest. Bigger Lf/S values and smaller Lw/S values mean a better heating effect and a poorer moderating effect, respectively. So Subchannels A have the biggest coolant temperature.

2. Axial coolant temperature distribution
   The coolant temperatures in the axial direction of the three types of subchannels are shown in Fig. 2.81 [24]. The coolant flows down through the water rod and is at 280°C. After heating, the average coolant outlet temperature is 358°C. The inlet and outlet temperatures of the upward flow in the fuel subchannels are 380 and 575°C, respectively.
   For Subchannels A, the coolant temperature is higher than those of Subchannels B and C. Table 2.8 [24] gives parameters of the water rods. The coolant temperature for the water rod outside the assembly is 8°C higher than that of water rods inside the assembly.
3. Distribution of coolant flow rate

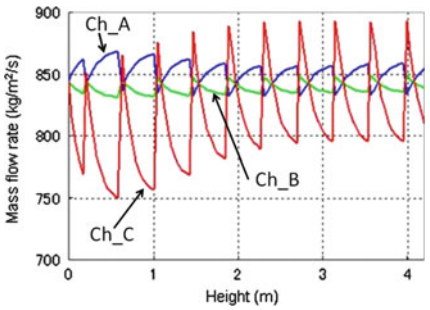


Fig. 2.82 Distribution of coolant mass flow rate. (Taken from [24])

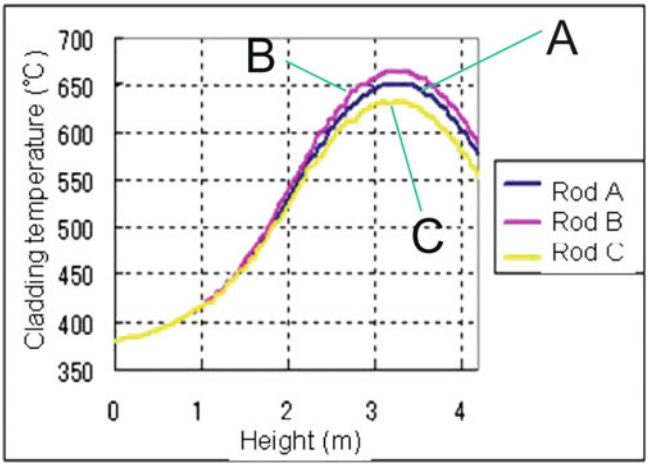


Fig. 2.83 Temperature distribution of cladding in the axial direction. (Taken from [24])

The coolant mass flow rates of Subchannels A, B and C are shown in Fig. 2.82 [24]. As Table 2.7 [24] indicates, the equivalent diameters are different. According to (2.29), the coolant flow rate of Subchannels A is higher due to bigger equivalent diameter than Subchannel C.

4. Temperature distribution of cladding

The temperature distribution of cladding in the axial direction matches the cosine curve and is shown in Fig. 2.83 [24]. The highest temperature is at 3.1 m in the axial direction. Figure 2.84 [24] gives the temperatures of cladding in the assembly. The temperature of cladding belonging to Subchannels A (Rod A; Fig. 2.79 [24] for this and the other rods) is higher than those of Subchannels B (Rods B) and C (Rod C) due to the different flow rate. The highest temperature of single channel analysis is 650°C which is increased by 16°C in the subchannel analysis. This difference can be explained by the heat transfer in the assembly.

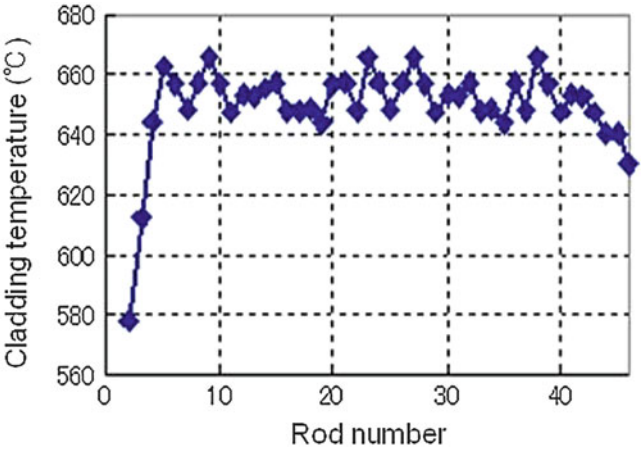


Fig. 2.84 Temperature distribution of cladding in the assembly. (Taken from [24])

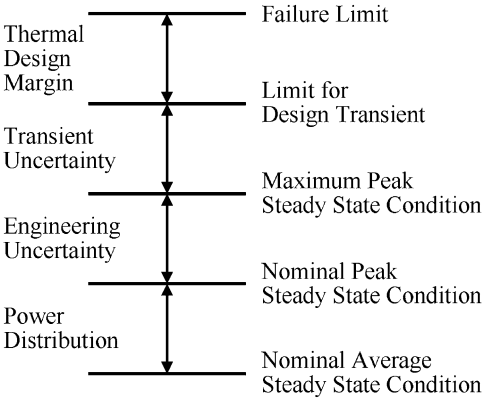


Fig. 2.85 Thermal design nomenclature

2.6 Statistical Thermal Design

The goal of the Super LWR is to achieve safe, reliable, and economical operation. Since the coolant temperature and its density change greatly within the Super LWR fuel assemblies, it is important to effectively evaluate the thermal-hydraulic performance and all associated uncertainties, given that this performance is a critical component of the overall core design.

The impact of various thermal conditions for a typical core is shown in Fig. 2.85. The design tasks can be divided into three main parts: consideration of the power distribution, the engineering uncertainty, and the transient uncertainty [26]. The power distribution considers the effects of the radial, axial and, local heat flux distributions. The transient uncertainty takes into account the uncertainties in

design transient response. The engineering uncertainties of the Super LWR are the main topic of this section. Nominal results have to be corrected to account for such effects as calculation approximations, measurement errors, instrumentation accuracy, manufacturing and fabrication tolerances, correlation uncertainties, and so on.

Various methods have been developed and utilized successfully to evaluate and combine the engineering uncertainties for most types of nuclear reactors other than the Super LWR. These methods treat the uncertainties by using values directly or by using dimensionless factors and they combine all the uncertainties by different methods, including the deterministic, semistatistical, and statistical methods.

Here, a statistical thermal design procedure is established for the Super LWR in order to develop an effective method to evaluate the extent to which the actual Super LWR performance may depart from the nominal performance due to various engineering uncertainties. This procedure is referred to as the Monte Carlo Statistical Thermal Design Procedure for Super LWR (MCSTDP) [27]. The uncertainties of several important core system parameters, the nuclear hot factors, the engineering hot spot factors, and the heat transfer correlation are all considered in this procedure. Moreover, different burnups and different types of probability distributions of the random samples are also taken into account. The engineering uncertainties for the thermal design of the Super LWR are evaluated by the MCSTDP to get an approximate quantification. The results are compared with those of the Revised Thermal Design Procedure (RTDP) [28, 29].

2.6.1 Comparison of Thermal Design Methods

Thermal design methods that address engineering uncertainties can be divided into two types: the first uses the random values of the parameters directly and the second uses dimensionless factors, which are known as engineering hot spot factors.

The thermal design methods can also be divided into deterministic, semistatistical, and statistical methods according to the different ways they combine various uncertainties. The direct deterministic method uses values of random parameters directly to account for engineering uncertainties. It is usually employed during the preliminary stage of the core design. All the parameters are taken at their worst values and are assumed to occur at the same time and at the same location. Such a cumulative approach is highly conservative.

Considering the engineering uncertainties by using the engineering hot spot factors is widely employed for PWR core design. All the engineering uncertainties are expressed as dimensionless engineering hot spot subfactors. Then these dimensionless engineering hot spot subfactors are combined into engineering hot spot factors. The mathematical product of these factors and the nominal value of the concerned quantity is actually used in the design and safety analyses. The simplest way to combine the subfactors is to multiply all of them directly into a cumulative factor, which is very conservative. This is known as the deterministic method. Since most of the subfactors are independent, they can be combined statistically.

Therefore, it is reasonable to introduce a statistical method to deal with engineering uncertainties. An intermediate approach, so-called semistatistical methods, is also widely used as a compromise between the deterministic and statistical methods. In the semistatistical method, the subfactors are divided into two groups of cumulative contributors and statistical contributors and then two different approaches can be taken: the semistatistical vertical approach and the semistatistical horizontal approach, based on different combination schemes [30].

The deterministic method is very conservative while the statistical and semistatistical methods are more realistic in treating the various uncertainties affecting the thermal performance of a reactor core. A comparison of different combination schemes is shown in Fig. 2.86 [27]. In this figure, (1) shows a deterministic method. The deterministic uncertainties are added to the nominal value of the crucial design criteria directly. The engineering uncertainty is large and the most conservative. (2) shows a semistatistical method, in which the uncertainties include deterministic and statistical parts. As a result, the engineering uncertainty will decrease. (3) shows a statistical method, which uses a fully statistical combination, and the uncertainties are all combined statistically. In general, the statistical engineering uncertainty decreases.

Hot spot factors consider the effects of the uncertainties separately. This means that each subfactor is evaluated in an independent manner, relative only to a specific uncertainty and without respect to other uncertainties. However, different types of

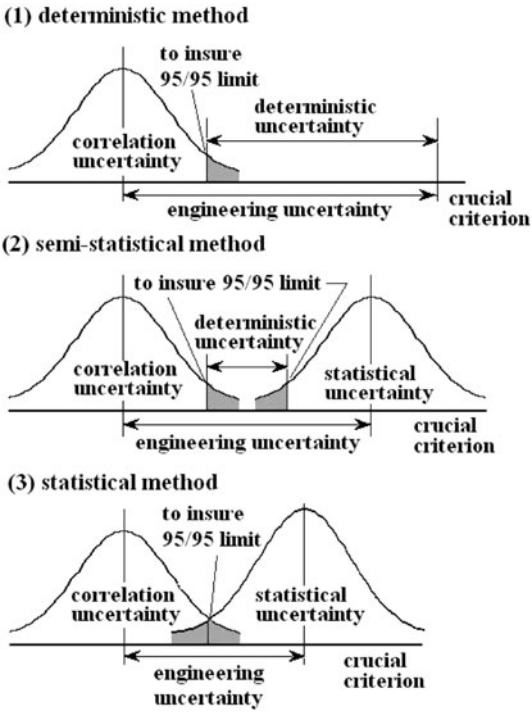


Fig. 2.86 Comparison of methods considering uncertainties. (Taken from [27] and used with permission from Atomic Energy Society of Japan)

uncertainties, especially the uncertainties of system parameters that are the most important in the core design, affect the considered quantity altogether in nature. Although all the uncertainties can be combined statistically, a more refined treatment should be developed. For current reactor core designs, especially for PWRs, more and more fully statistical methods are becoming employed, and the uncertainties are treated in a purely statistical way by using the values of the core system parameters randomly. These methods fall into two categories: (1) methods based on the Root Sum Square (RSS) technique and (2) methods based on the Monte Carlo technique. The Improved Thermal Design Procedure (Westinghouse) (ITDP), the Revised Thermal Design Procedure (Westinghouse) (RTDP), and the Statistical Thermal Design Procedure (Belgium) (STDP) [31] are some examples of the RSS technique. The General Statistical Method (Framatome) (MGS) [32], and the Optimized Monte Carlo Thermal Design Process (Belgium) (MTDP) [33] are some application examples of the Monte Carlo technique. In PWR core designs, both types of methods are used effectively, treating the core system parameters and the hot factors as random values with certain statistical distributions, and employing different combination schemes. Some studies show that the Monte Carlo technique gives a slightly incremental thermal design margin.

2.6.2 Description of MCSTDP

2.6.2.1 Design Criteria

The core design criteria of the Super LWR are significantly different from those of PWRs; there is no criterion like the minimum departure from nucleate boiling ratio (DNBR) and the heat transfer deterioration at supercritical pressure is not such a violent phenomenon as DNB at subcritical pressure.

The most important thermal design criterion recently applied in the core design of the Super LWR is that the maximum cladding surface temperature MCST must be less than a limited value. The MCST is restricted in order to avoid oxidation corrosion of the cladding and ensure the fuel integrity. The MCST is the main parameter to be evaluated in the core design of the Super LWR, and it must not exceed the design limit at any core location during normal operation and during postulated accidents. The MCST is used as the crucial criterion in the Super LWR to evaluate cladding overheating.

Similar to the 95/95 limit in PWR core design, a special requirement is defined to specify the acceptable criteria for the evaluation of fuel design limits for the Super LWR. This is to ensure that there is at least a 95% probability at a 95% confidence level that the MCST of the reactor core does not exceed the design limit. This is referred to as the 95/95 limit of the Super LWR. Thus, all the uncertainties should be treated with at least 95% probability at a 95% confidence level to assess the engineering uncertainty for the Super LWR.

2.6.2.2 Philosophy of the Design Procedure

For the MCSTDP [24], all the uncertainties are sampled according to certain distributions, and the calculated distribution of the result is analyzed to evaluate the engineering uncertainty. Figure 2.87 [27] illustrates how the statistical thermal design procedure of the Super LWR is done. The right-hand distribution is the uncertainty distribution of the heat transfer correlation used to evaluate the supercritical water heat transfer coefficient at the cladding surface. The left-hand distribution indicates the statistical uncertainty of the MCST due to different engineering uncertainties such as system parameter uncertainties, nuclear hot factor uncertainties, and engineering hot spot factors uncertainties. The statistical distribution and the correlation uncertainty distribution coincide at their 95/95 limit values by way of the root mean square. These two distributions are combined to get the distribution of the total uncertainty. Therefore, the engineering uncertainty is evaluated from the distribution of the total uncertainty for the Super LWR.

The MCSTDP is different from a method that uses only the hot spot factors. The MCSTDP has a natural way of combining the uncertainties of the system parameters. For the MCSTDP, these parameters are sampled and used directly in the calculation. When using only hot spot factors, all the uncertainties can only be evaluated individually and then must be combined statistically. The MCSTDP also uses the nuclear and engineering hot spot factors to consider the other uncertainties because it is impossible to sample all the uncertainties in the Monte Carlo technique. The uncertainties evaluated by the hot spot factors are those that are less

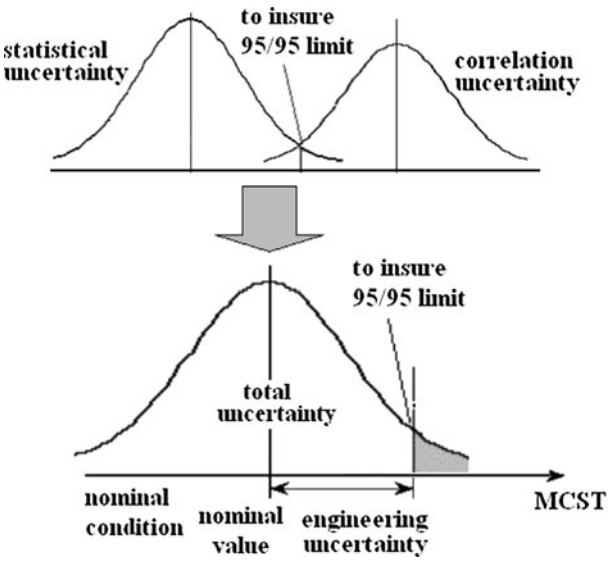


Fig. 2.87 Statistical thermal design procedure for the Super LWR. (Taken from [27] and used with permission from Atomic Energy Society of Japan)

important than the system parameters, those that are not easily sampled in the Monte Carlo technique, and those that can be sampled but may have a huge sample size, etc. Although these uncertainties are evaluated separately, they are combined statistically. When using only the hot spot factors, the $k\sigma$ values of the combined factors are usually used in the thermal analysis and the calculated result of the criterion is treated as the $k\sigma$value of this criterion. The MCSTDP samples these factors randomly according to their distributions and the distribution of the results is analyzed to get the $k\sigma$ value of the criterion.

2.6.2.3 Uncertainties Considered

Table 2.9 [27] lists the uncertainties considered in the MCSTDP. In general, the normal distribution is the most commonly used distribution for parameter uncertainties; the uniform distribution is also frequently used, but more conservative. Both of them are utilized as random distributions of the system parameters in comprehensive evaluations.

The uncertainties of system parameters and hot factors are sampled directly in the Monte Carlo technique. The standard deviation of the calculated distribution of MCST due to the uncertainties of the system parameters and factors is defined as σ_{PF}.

1. System parameter uncertainties

The uncertainties of the system parameters are induced by measurement errors, instrumentation accuracy, and random variation during the operation and control. The determination of the total engineering uncertainty is sensitive to these system parameter uncertainties, and these uncertainties are considered by using their random values directly and statistically.

Core power level: The uncertainty of the core power level represents the calibration error in core power measurements and the control system dead band. A typical error of 2% of the nominal value is used to determine the maximum and minimum bounds, and this error is usually taken as 2σ for a normal distribution and $\sqrt{3}\sigma$ for a uniform distribution. Therefore, the standard deviation σ is 1% of the

Table 2.9 Uncertainties considered in the MCSTDP. (Taken from [27] and used with permission from atomic energy society of Japan)

(1) System parameter uncertainties of the core	Coolant inlet temperature uncertainty
	Power uncertainty
	Coolant flow rate uncertainty
	Pressure uncertainty
	Uncertainty of the ratio of flow rate in water rods to the total flow rate
(2) Hot factor uncertainties	Nuclear hot factor uncertainties
	Engineering hot spot factors
(3) Correlation uncertainties	

nominal value for the normal distribution and 1.15% for the uniform distribution. In the statistical design procedure for the Super LWR, the uncertainty of the average linear power is used to represent that of the core power with a nominal value of 18 kW/m.

Core coolant inlet temperature: The nominal design value of the core coolant inlet temperature in the Super LWR is 280°C and the typical error due to temperature measurement is about 2.2°C, which is used to determine the maximum and minimum bounds. The standard deviation is 1.1°C for the normal distribution and 1.27°C for the uniform distribution.

Core coolant flow rate: The nominal design value of the core coolant flow rate is 1,420 kg/s, and the typical measurement error of 2% of the nominal value is used. The standard deviation is 1% for the normal distribution and 1.15% for the uniform distribution.

Core pressure: The nominal operating pressure is 25 MPa, and the typical control error is taken as 200 kPa with the standard deviation of 100 kPa for the normal distribution and 115 kPa for the uniform distribution.

Ratio of the water rods flow rate to the core flow rate: This ratio is designed as 30% at the nominal condition, which is important in deciding the mixed coolant temperature in the mixing plenum. The control and measurement error of this ratio is taken as 6% of the nominal value to determine the maximum and minimum bounds, while the standard deviation is 3% of the nominal value for the normal distribution and 3.46% for the uniform distribution.

2. Hot factor uncertainties

Nuclear hot factors are employed in the calculation to consider the effects of the power distribution in the core, including the radial nuclear hot assembly factor $f_{\mathrm{R}}^{\mathrm{n}}$, the axial nuclear hot assembly factor $f_{\mathrm{z}}^{\mathrm{n}}$ and the linear heat flux nuclear hot spot factor $f_{\mathrm{P}}^{\mathrm{n}}$. The factor $f_{\mathrm{R}}^{\mathrm{n}}$ is defined as the ratio of the hot assembly power to the core average assembly power and is used to determine the power level of the hot assembly. The factor $f_{\mathrm{z}}^{\mathrm{n}}$ is defined as the ratio of the maximum planar power to the average planar power in the hot assembly and is used to describe the axial power distribution in the hot assembly. The factor $f_{\mathrm{P}}^{\mathrm{n}}$ is defined as the ratio of the maximum linear heat flux to the core average linear heat flux and is used to determine the power distribution of the hot channel and the power of the hot spot of the core.

The uncertainties of the nuclear hot factors are considered in the statistical design procedure. Normal distributions are assumed to be the probability distributions for these nuclear hot factors with a calculation error of 2% of the nominal values and a standard deviation of 1%.

The engineering hot spot factors are also utilized in the MCST calculation to take into account various engineering uncertainties. There are two engineering factors associated with the MCST calculation. One is the coolant temperature rise engineering hot spot factor $f_{\mathrm{l}}^{\mathrm{e}}$, and the other is the cladding surface temperature rise engineering hot spot factor $f_{\mathrm{cs}}^{\mathrm{e}}$.

Table 2.10 Engineering subfactors. (Taken from [27] and used with permission from atomic energy society of Japan)

Subfactors	Uncertainties explained by subfactors
Nuclear data	Nuclear properties of the fuel rods
Power distribution	Hot assembly power distribution
Fissile fuel content tolerance	Enrichment and amount of fissile material
Inlet flow maldistribution	Assembly hydraulic resistance and orifice uncertainties
Flow distribution calculation	Intra-assembly flow maldistribution
Subchannel flow area	Geometric tolerances of fuel rod diameter and pitch on the subchannel flow area
Pellet-cladding eccentricity	Eccentric position of the fuel pellet within the cladding
Coolant properties	Coolant properties data
Cladding properties	Thickness and thermal conductivity of the cladding
Gap properties	Conductivity of the gap between the fuel and cladding

The engineering hot spot factors are the statistical combinations of the subfactors. The subfactors and the engineering uncertainties explained by the corresponding subfactors are listed in Table 2.10 [27]. The engineering hot spot factors are applied statistically in the calculation of MCST in the statistical design procedure with the nominal values of 1.0 and 3σ normal distributions.

3. Correlation uncertainty

The Oka–Koshizuka correlation [7] is used to calculate the heat transfer coefficient at the cladding surface.

$$\begin{aligned} Nu &= 0.015 \times Re^{0.85} \times Pr^{0.69-81000/qs+fc\times q}, \\ qs &= 200 \times G^{1.2} \end{aligned} \tag{2.33}$$

$$fc = \begin{cases} 2.9 \times 10^{-8} + \dfrac{0.11}{qs} \\ h < 1.5 \text{ MJ/kg} \\ -8.7 \times 10^{-8} - \dfrac{0.65}{qs} \\ 1.5 \text{ MJ/kg} \leqslant \text{h} \leqslant 3.3 \text{ MJ/kg} \\ -9.7 \times 10^{-7} + \dfrac{1.30}{qs} \\ 3.3 \text{ MJ/kg} \leqslant \text{h} \leqslant 4.0 \text{ MJ/kg} \end{cases}.$$

Here G is the flow flux, h is the bulk enthalpy and q is the heat flux.

The value calculated by this correlation should be compared with experimental results. This uncertainty can be treated in two ways. One is to use a corresponding engineering hot spot subfactor and the other is to combine this uncertainty with other uncertainties directly. The latter is applied here to consider the correlation uncertainty because of its importance. The standard deviation of the distribution of MCST due to the correlation uncertainty is defined as σ_C.

2.6.2.4 Details of the Design Procedure

The evaluation of the engineering uncertainty by the MCSTDP can be summarized in the following steps:

Step 1: All the uncertainties of system parameters, nuclear hot factors, and engineering hot spot factors are sampled according to their distributions. The samples are generated by a random process and are combined into groups used as the input data to calculate MCST.

Two cases of the probability distribution are considered in the calculation. The normal distribution is used in case 1 and the uniform distribution is used in case 2 to consider the uncertainties of system parameters. In each case, different core power distributions at the typical burnups, BOC, MOC, and EOC, are considered by using the corresponding nuclear hot factors and the axial power distributions.

Step 2: For each probability distribution case and for each burnup, many groups of system parameters and hot factors are sampled randomly. For each group of samples, a subchannel analysis is carried out to calculate the MCST of the core. The resulting distribution of MCST is then determined.

Step 3: The distribution of MCST is analyzed to obtain the value of σ_{PF} which is the maximum value among different cases and different burnups. The correlation uncertainty σ_C is also evaluated. The total uncertainty is evaluated by the root mean square method:

$$\sigma_T^2 = \sigma_{PF}^2 + \sigma_C^2. \tag{2.34}$$

Step 4: According to the central limit theorem of statistics, the probability distribution of MCST is an approximate normal distribution. The peak error of this distribution at a one-sided 95% confidence level is evaluated by (2.35), which is the engineering uncertainty of the Super LWR:

$$\text{Engineering uncertainty} = k\sigma_T = k\sqrt{\sigma_{PF}^2 + \sigma_C^2}. \tag{2.35}$$

Here k, which is taken as 1.645, is the coefficient to ensure the 95/95 limit. Figure 2.88 [27] illustrates the determination of the peak error and the k value.

The fuel assemblies in the Super LWR are a closed type, so the analysis on a single fuel assembly is possible and reasonable especially for the thermal hydraulic

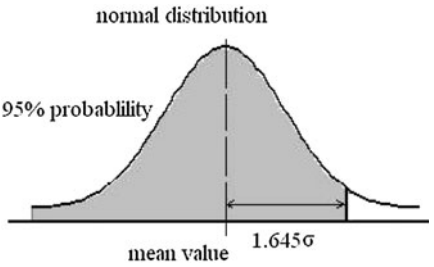


Fig. 2.88 Determination of value. (Taken from [27] and used with permission from Atomic Energy Society of Japan)

analysis. A subchannel code, which was verified and effectively applied in the thermal analysis, is employed to analyze the single fuel assembly for the Super LWR.

In the Monte Carlo sampling Step 1, the calculations have to be carried out with many groups of input data samples to obtain the statistical distribution of MCST. In order to reduce the required computing time and to ensure accuracy, a subchannel procedure, which is applied in a conservative manner, is adopted for this study. The subchannel analysis for the hot assembly in the core is performed for each group of samples. The hot channel and the hot spot are assumed to be in the hot assembly. Therefore, this closed hot assembly not only has the maximum assembly power, but also has the worst thermal condition in the core. Some results of the three-dimensional core design are used to determine the nominal power distribution and other parameters in the hot assembly.

2.6.3 Application of MCSTDP

2.6.3.1 Statistical Characteristics of Uncertainties

The statistical characteristics of the system parameters used as input data are shown in Table 2.11 [27]. The nominal values, standard deviation values, and one-sided width values of the distribution for the core system parameters are given. In case 1, all the uncertainties of the system parameters are assumed to follow normal distributions, while in case 2, all the system parameter uncertainties are assumed to follow uniform distributions.

The nominal values of the nuclear hot factors at different burnups, BOC, MOC, and EOC, are taken from the results of the three-dimensional design of the Super LWR and are listed in Table 2.12 [27]. The axial power distributions in the hot assembly at BOC, MOC, and EOC under the nominal condition are shown in Fig. 2.89 [27].

The distributions are assumed to be cosine distributions, with the ratio of the maximum value to the average value equal to the value of the axial hot assembly factor f_z^n. The same assumption is applied for all calculations with randomly

Table 2.11 Statistical characteristics of the system parameters. (Taken from [27] and used with permission from Atomic Energy Society of Japan)

		Case 1	Case 2
Core inlet temperature (°C)	Distribution type	Normal	Uniform
	Nominal value (E)	280	280
	Standard deviation	1.1	1.27
	One-sided width	2.2	2.2
Core inlet flow rate (kg/s)	Distribution type	Normal	Uniform
	Nominal value (E)	1,420	1,420
	Standard deviation	1%E	1.15%E
	One-sided width	2%E	2%E
Average linear power (kw/m)	Distribution type	Normal	Uniform
	Nominal value (E)	18	18
	Standard deviation	1%E	1.15%E
	One-sided width	2%E	2%E
Flow rate ratio of water rods to total	Distribution type	Normal	Uniform
	Nominal value (E)	0.3	0.3
	Standard deviation	3%E	3.46%E
	One-sided width	6%E	6%E
Pressure (MPa)	Distribution type	Normal	Uniform
	Nominal value (E)	25	25
	Standard deviation	0.1	0.115
	One-sided width	0.2	0.2

Table 2.12 Nominal values of nuclear hot factors of different burnups. (Taken from [27] and used with permission from Atomic Energy Society of Japan)

Factors	BOC	MOC	EOC
f_R^n	1.23	1.26	1.27
f_z^n	1.57	1.38	1.33
f_P^n	2.00	1.83	1.72

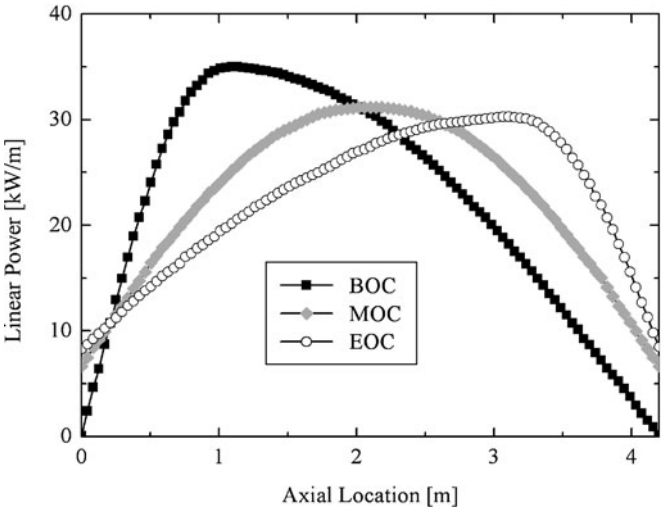


Fig. 2.89 Axial power distributions of different burnups

Table 2.13 Determination of the engineering hot spot factors. (Taken from [27] and used with permission from atomic energy society of Japan)

Temperature rise statistical factors (3σ)	Coolant	Cladding surface
Nuclear data	1.02	1.02
Power distribution	1.01	1.01
Fissile fuel content tolerance	1.025	1.025
Inlet flow maldistribution	1.03	1.0
Flow distribution calculation	1.03	1.0
Subchannel flow area	1.07	1.05
Pellet-cladding eccentricity	1.0	1.10
Coolant properties	1.017	1.0
Cladding properties	1.0	1.0
Gap properties	1.0	1.0
Combined value of hot factors	1.090	1.116
Standard deviation of hot factor	0.030	0.039

sampled f_z^n. The errors of these approximate distributions are considered in the engineering subfactors.

The values of the engineering hot spot factors and all the subfactors for the coolant temperature rise and the cladding surface temperature rise are shown in Table 2.13 [27]. The subfactors are treated as 3σ statistical factors and most of them are evaluated from the typical data of the preliminary work as well as other designs. Some of the values of these subfactors of the Super LWR are different from those of the past preliminary work for the high-temperature supercritical-pressure fast reactor (SCFR-H), such as the subfactors of nuclear data, fissile content, and subchannel area. Among all the subfactors, the subchannel area subfactor is the most important and most sensitive one, and it is evaluated using a Monte Carlo technique and a subchannel analysis. This is discussed later.

The engineering hot spot factors are combined statistically as shown below.

$$f^e = 1 + \sqrt{\sum (f_i^e - 1)^2}. \tag{2.36}$$

The subfactor data and (2.36) are used and the factors f_l^e and f_{cs}^e are calculated as 1.090 and 1.116, respectively. These results are the worst values (3σ values) of the distributions of f_l^e and f_{cs}^e. Since the distributions are normal distributions with the same nominal values of 1.0, the standard deviations can be calculated by (2.37).

$$\begin{aligned} \sigma(f_l^e) &= (1.090 - 1.0)/3.0 = 0.030, \\ \sigma(f_{cs}^e) &= (1.116 - 1.0)/3.0 = 0.039. \end{aligned} \tag{2.37}$$

The statistical characteristics of the nuclear hot factors and engineering hot spot factors used in the calculations are summarized in Table 2.14 [27], with their nominal values, standard deviation values and one-sided width values of the distributions. The values of the hot factors are the same for case 1 and case 2, since the normal distribution is assumed for all the hot factors in both cases.

Table 2.14 Statistical characteristics of nuclear and engineering factors. (Taken from [27] and used with permission from atomic energy society of Japan)

f_z^n	Standard deviation	1%E
	One-sided width	2σ
f_R^n	Standard deviation	1%E
	One-sided width	2σ
f_P^n	Standard deviation	1%E
	One-sided width	2σ
f_l^e	Nominal value	1.0
	Standard deviation	0.030
	One-sided width	3σ
f_{cs}^e	Nominal value	1.0
	Standard deviation	0.039
	One-sided width	3σ

2.6.3.2 Subfactor of Subchannel Area

In designing the Super LWR, the gap size between two adjacent fuel rods or between the fuel rod and its neighboring water rod is only 1 mm, so a small change in the subchannel area may cause a large change in the thermal performance. The determination of the engineering hot spot subfactor for the subchannel area is thus important in the thermal design of Super LWR. Since the movements of the fuel rods are restricted by the water rods and the displacement of fuel rods is very small in the fuel assembly, the value of this subfactor is different from those of other types of reactors such as PWRs and FBRs. Here, a Monte Carlo process with the subchannel analysis is designed to statistically evaluate the uncertainty of the subchannel area.

The uncertainty of the subchannel area is caused by the displacement uncertainties of the fuel rods during fabrication and the manufacturing tolerance of the fuel rod diameter. In the Monte Carlo technique, the direction and the distance of the displacement, and the diameter of every fuel rod in the hot assembly are sampled randomly and simultaneously according to certain distributions. As shown in Fig. 2.90 [27], only four directions are considered as the displacement directions, and the displacement directions are sampled using the uniform distribution. The displacement distance and the diameter of the fuel rod are assumed to be normal distributions with the maximum bounds (3σ values) of 0.1 mm, which is 10% of the gap size between two adjacent fuel rods or between the fuel rod and its neighboring water rod. Five thousand groups of combined samples of all the fuel rods in 1/8 fuel assembly are utilized.

For each sample combination of the fuel rod locations and the fuel rod diameters, the values of MCST and the coolant temperature at hot spots are calculated. The calculated distributions of the cladding surface temperature rise ΔT_{cs} and the coolant temperature rise ΔT_l at hot spots are utilized to evaluate the cladding surface temperature rise hot spot subfactor f'_{cs} and the coolant temperature rise hot spot subfactor f'_l. The coolant temperature rise at the hot spot is defined as the difference between the coolant temperature at the hot spot and the corresponding inlet coolant temperature. The cladding surface temperature rise at the hot spot is

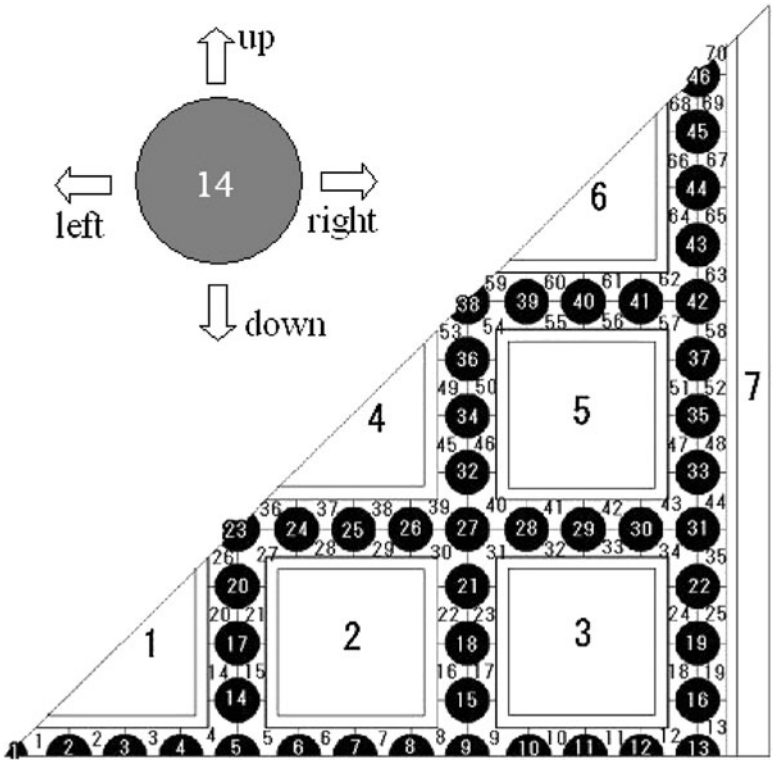


Fig. 2.90 Channels and fuel rods of 1/8 fuel assembly. (Taken from [27] and used with permission from atomic energy society of Japan)

Table 2.15 Calculation conditions. (Taken from [27] and used with permission from atomic energy society of Japan)

Location change size		Diameter		Sampled fuel rods	Sample size
Nominal	3σ value	Nominal	3σ value		
0.0	0.1 mm	10.2 mm	0.1 mm	All fuel rods of 1/8 fuel assembly	5,000

defined as the difference between the cladding surface temperature and the coolant temperature at the hot spot.

The calculation conditions and results are listed in Tables 2.15 [27] and 2.16 [27], respectively. The calculated distributions of temperature rises are shown in Fig. 2.91 [27]. These distributions are approximated as normal distributions. The values of f_l' and f_{cs}' are calculated as 1.07 and 1.05 by using the following equations:

$$f_l' = 1.0 + \frac{3\sigma \text{ value of } \Delta T_l}{\text{mean value of } \Delta T_l}, \tag{2.38}$$

Table 2.16 Calculation results. (Taken from [27] and used with permission from atomic energy society of Japan)

ΔT_{cs} (°C)	Mean value	83.91
	σ	1.42
	3σ	4.26
Value of f'_{cs}		1.05
ΔT_l (°C)	Mean value	272.51
	σ	6.22
	3σ	18.66
Value of f_l'		1.07

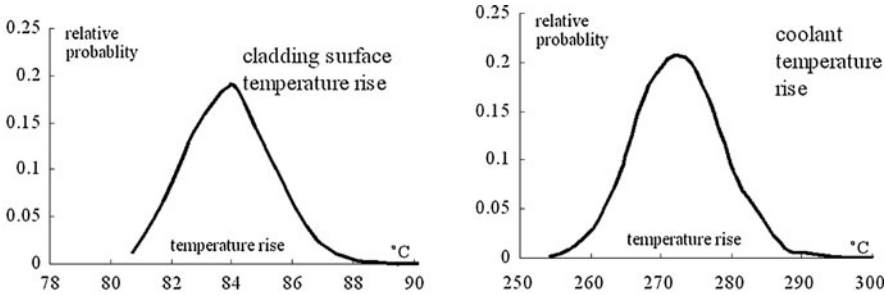


Fig. 2.91 Distribution of ΔT_{cs} and ΔT_l. (Taken from [27] and used with permission from atomic energy society of Japan)

$$f'_{cs} = 1.0 + \frac{3\sigma \text{ value of } \Delta T_{cs}}{\text{mean value of } \Delta T_{cs}}. \tag{2.39}$$

2.6.3.3 Results and Discussion

For each probability distribution and each burnup, 3,000 groups of random system parameters and factors are sampled. Altogether, 18,000 groups of data are calculated. MCST is calculated for each group of the samples. The calculated MCST distributions of case 1 and case 2 for BOC, MOC and EOC are represented in Fig. 2.92 [27]. The evaluated statistical characteristics of the MCST distributions are summarized in Table 2.17 [27].

The standard deviation of the parameter and factor uncertainties σ_{PF}, taken from the maximum value of both cases of probability distributions and all burnups, is 18.32°C.

The convergence curves of the mean value and the standard deviation of the MCST distributions are obtained. As an example, Fig. 2.93 [27] shows the convergence curves for case 2. These figures demonstrate that the sample size of the Monte Carlo technique is large enough to get converged results.

The standard deviation of the uncertainty of the heat transfer correlation σ_C is 6.33°C, after comparing the results of the Oka–Koshizuka correlation [7] with the

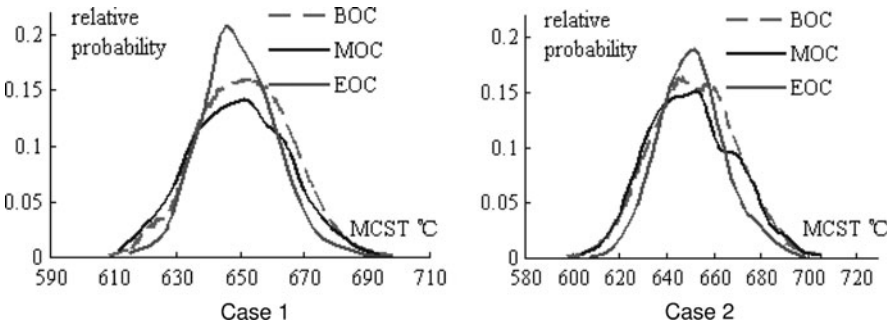


Fig. 2.92 Distributions of MCST of different burnups. (Taken from [27] and used with permission from atomic energy society of Japan)

Table 2.17 Statistical characteristics of MCST. (Taken from [27] and used with permission from atomic energy society of Japan)

	MCST (°C)	Case 1	Case 2
BOC	Mean value	651.64	651.63
	Standard deviation	14.91	17.81
	Maximum value	702.88	710.38
MOC	Mean value	649.65	650.51
	Standard deviation	15.54	18.32
	Maximum value	696.43	708.70
EOC	Mean value	649.73	650.91
	Standard deviation	12.01	14.51
	Maximum value	700.96	693.26
Maximum standard deviation		15.54	18.32
σ_{PF}		18.32	

experimental data and other correlation results. Figure 2.94 [27] shows the results of the Oka–Koshizuka correlation [7] and experimental data in the low coolant enthalpy region. Figure 2.95 [27] shows the results of the Oka–Koshizuka correlation [7] and the Dittus–Boelter correlation in the high coolant enthalpy region. The data are analyzed statistically with two assumptions: (1) the bulk coolant enthalpy is sampled uniformly and (2) the differences of the values between the correlations or between the correlation and the experimental data are assumed to satisfy normal distributions. The standard deviation of the correlation uncertainty is 4.71°C in the low bulk enthalpy region and 6.33°C in the high bulk enthalpy region. The latter is taken as the correlation uncertainty because this value is larger and the hot spot is always in the high bulk enthalpy region. As a result, the engineering uncertainty of the Super LWR is 31.88°C and it is calculated as follows:

$$1.645\sqrt{\sigma_{PF}^2 + \sigma_C^2} = 31.88°C. \tag{2.40}$$

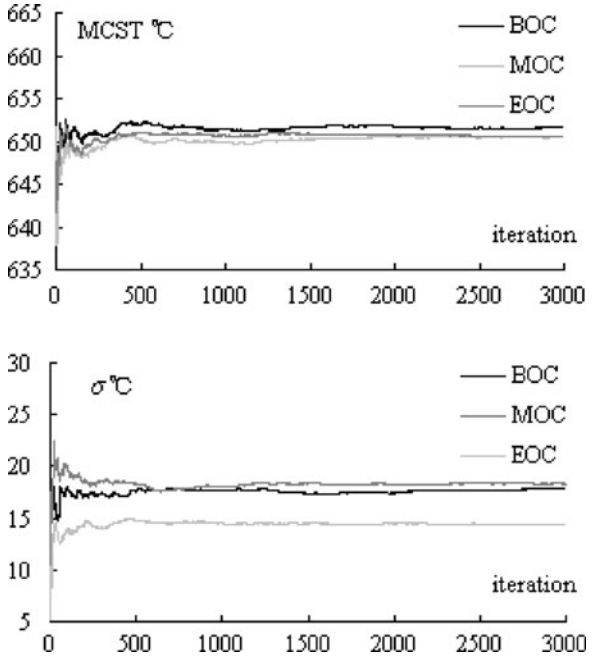


Fig. 2.93 Convergence curves of the results. (Taken from [27] and used with permission from atomic energy society of Japan)

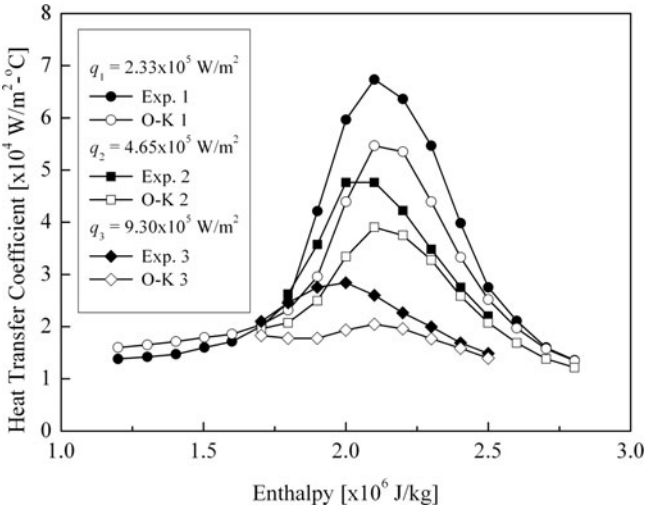


Fig. 2.94 Comparison of the heat transfer coefficient in the low enthalpy area. (Taken from [27] and used with permission from atomic energy society of Japan)

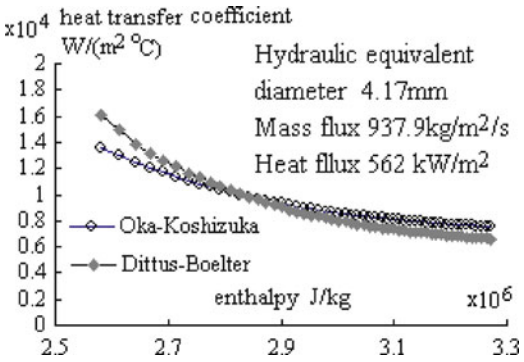


Fig. 2.95 Comparison of the heat transfer coefficient in the high enthalpy area. (Taken from [27] and used with permission from atomic energy society of Japan)

Table 2.18 Parameters used in RTDP. (Taken from [27] and used with permission from atomic energy society of Japan)

	Nominal value	σ of case 1	σ of case 2
Inlet temperature (K)	553.15	1.1	1.27
Flow rate (kg/s)	1,420	$1\%\mu$	$1.15\%\mu$
Power (kW/m)	18	$1\%\mu$	$1.15\%\mu$
Flux ratio	0.3	$3\%\mu$	$3.46\%\mu$
Pressure (MPa)	25	0.1	0.115
f_z^n	1.26	$1\%\mu$	$1\%\mu$
f_R^n	1.38	$1\%\mu$	$1\%\mu$
f_P^n	1.83	$1\%\mu$	$1\%\mu$
f_I^e	1.0	0.030	0.030
f_{cs}^e	1.0	0.039	0.039

2.6.4 Comparison with RTDP

2.6.4.1 Introduction of RTDP

The Revised Thermal Design Procedure (RTDP) is also used to calculate the engineering uncertainty as a comparison. The following approximated equation is utilized to calculate σ_{PF}:

$$\left(\frac{\sigma_{PF}}{\mu_{MCST}}\right)^2 = S_{Tin}^2\left(\frac{\sigma_{Tin}}{\mu_{Tin}}\right)^2 + S_{flux}^2\left(\frac{\sigma_{flux}}{\mu_{flux}}\right)^2 + S_{power}^2\left(\frac{\sigma_{power}}{\mu_{power}}\right)^2 \cdots \tag{2.41}$$

where μ is the nominal value of each system parameter or factor and S is the sensitivity factor. Some values used in (2.41) are listed in Table 2.18 [27]. S can be evaluated using the following approximate equation (x represents any of the system parameters or factors).

$$\begin{aligned} S_x &= (\partial \mathrm{MCST}/\partial x)(\partial x/\partial \mathrm{MCST}) \\ &= (\Delta \mathrm{MCST}/\Delta x)(\Delta x/\Delta \mathrm{MCST}). \end{aligned} \tag{2.42}$$

2.6.4.2 Results and Comparison

The MCST is calculated with the values close to the nominal values of the system parameters or factors using the subchannel code to obtain the approximate slope $\Delta \mathrm{MCST}/\Delta x$ for each uncertainty. The slope of the uncertainty of the system pressure is very small compared with other system parameters and factors. The sensitivity factors are calculated by (2.42) and their results are listed in Table 2.19 [27].

It can be seen that the inlet coolant temperature, the inlet coolant flow rate, and the core power are the most sensitive parameters toward MCST. The inlet coolant temperature and the core power have a direct effect on the value of MCST. If the inlet coolant temperature and the core power fluctuate around their nominal value, the temperature distributions of the core will change greatly. The inlet coolant flow rate is also a very sensitive parameter to the cladding surface temperatures and the MCST results because the difference between the inlet and the outlet coolant flow velocities is large and the subchannel area is small in the Super LWR. When the inlet coolant flow rate decreases, the flow velocity near the outlet drops substantially, resulting in a large decrease in the heat transfer coefficient and a corresponding increase in the cladding surface temperature.

The value of σ_{PF} is calculated by (2.41) with the values in Tables 2.18 [27] and 2.19 [27]. The RTDP results are shown in Table 2.20 [27], where σ_{PF} is 18.80°C. This value is 2.6% larger than the value determined by the Monte Carlo technique. The conclusion is similar to that for PWRs.

Table 2.19 Sensitivity factor results. (Taken from [27] and used with permission from atomic energy society of Japan)

	Sensitivity factor
Inlet temperature (K)	1.038727
Flow rate (kg/s)	1.01491
Power (kW/m)	1.000386
Flux ratio	0.030643
Pressure (MPa)	0.00
$f_{\mathrm{z}}^{\mathrm{n}}$	0.701845
$f_{\mathrm{R}}^{\mathrm{n}}$	0.13658
$f_{\mathrm{P}}^{\mathrm{n}}$	0.293824
$f_{\mathrm{l}}^{\mathrm{e}}$	0.268926
$f_{\mathrm{cs}}^{\mathrm{e}}$	0.097482

Table 2.20 RTDP results. (Taken from [27] and used with permission from atomic energy society of Japan)

MCST (°C)	Case 1	Case 2
Standard deviation	17.21	18.80
Max. standard deviation	18.80	

2.6.5 Summary

The statistical thermal design procedure for the Super LWR was developed by using a purely statistical Monte Carlo method to effectively evaluate the engineering uncertainty of the Super LWR.

The engineering uncertainty of the Super LWR was evaluated as 31.88°C based on the MCSTDP. The engineering uncertainty was also evaluated by the RTDP and found to be slightly larger than that evaluated by the MCSTDP.

2.7 Fuel Rod Behaviors During Normal Operations

The concepts for the design criteria of the Super LWR need to be developed with an accurate evaluation of the peak fuel rod cladding temperature, using three-dimensional core calculations, subchannel analyses, and the statistical thermal design method for the normal operating condition. The fuel rod analyses with this maximum peak steady state condition can evaluate the behaviors of the fuel rod and mechanical strength requirement for the fuel rod cladding. The peak fuel rod cladding temperature should be accurately evaluated.

2.7.1 Evaluation of the Maximum Peak Cladding Temperature

In accordance with the method described in Fig. 2.13 [9], the maximum peak cladding temperature of the reference core, the characteristics of which are summarized in Table 2.4 [9], can be obtained as summarized in Table 2.21 [34].

The results show that, for the average coolant core outlet temperature of 500°C, the maximum peak cladding surface temperature can be as high as 740°C with 95% confidence and 95% probability. However, optimizing the design and improving the fabrication qualities can reduce the maximum peak cladding surface temperature. Meanwhile the heat transfer improvement by the grid spacers in the evaluation of the cladding temperature should be taken into account.

The relatively large temperature rises calculated by the subchannel analyses and statistical thermal design shown that these analyses are essential in determining the maximum peak cladding temperature of the Super LWR core.

Table 2.21 Peak cladding surface temperature [34]. (Taken from [34] and used with permission from atomic energy society of Japan)

Analysis	Results
Core calculation	650°C
Subchannel analysis	+58°C from core calculation result (nominal peak)
Statistical thermal design	+32°C from the nominal peak
Maximum peak cladding surface temperature (with 95% confidence and 95% probability)	740°C

2.7.2 *Fuel Rod Analysis*

2.7.2.1 Calculation Code

The Light Water Reactor Fuel Analysis Code FEMAXI-6 developed by researchers at JAEA is used for the fuel rod analysis [35]. It is capable of obtaining a complete coupled solution of the thermal analysis and mechanical analysis, enabling an accurate prediction of pellet-clad gap size and pellet-clad mechanical interaction (PCMI) in high burnup fuel rods not only in normal operation but also in transient conditions. It is based on a deterministic method and the main features of its calculation models are as follows:

The code considers a single fuel rod and surrounding coolant in an axis-symmetric cylindrical geometry (Fig. 2.96 [34]) and carries out both thermal and mechanical calculations. The fuel pellet stack is modeled by 36 iso-volume ring elements, and cladding by eight iso-thickness ring elements. The burnup histories of rod average linear heat generation rates, axial power distributions along the fuel stack, and radial power density distributions inside the pellets are given as input.

At each time step, the calculations start by using the results of the last time step as initial conditions. First, heat generations, conductions, and removals are calculated to determine tentative temperature distributions. Then, these temperature distributions are used to evaluate fission gas diffusions, releases, and internal pressure changes. The one-dimensional mechanical calculations are carried out based on these evaluated temperature and pressure conditions for each axial segment and the gap size is renewed. This gap size is fed to the thermal analysis again. Thus, thermal and mechanical calculations are iterated. When convergences are obtained, the calculations proceed to the next time step.

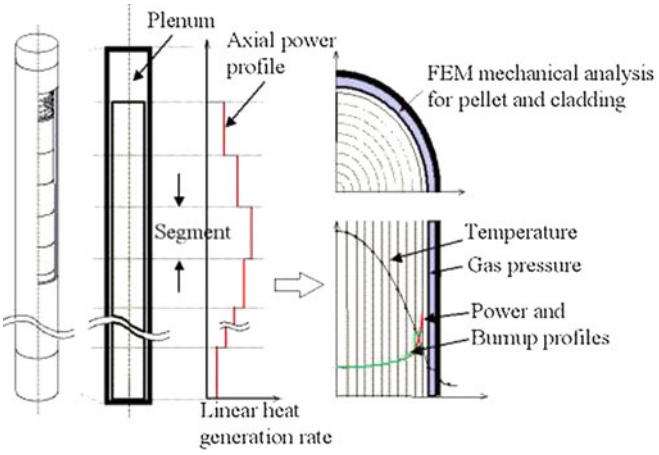


Fig. 2.96 FEMAXI-6 calculation model. (Taken from [34] and used with permission from atomic energy society of Japan)

2.7.2.2 Irradiation History of the Fuel Rod

The linear heat generation rate affects the fuel centerline temperature strongly. The average linear heat generation rate and the average coolant core outlet temperature are assumed to be 170 W/cm and 500°C, respectively. All other core characteristics are assumed to be the same as the reference core design summarized in Table 2.4 [9].

The irradiation history of the fuel rod is conservatively determined so that essentially, all fuel rods in the core are taken into account.

The maximum cladding surface temperature of the fuel rod is assumed to be 740°C from the BOL to the EOL of the fuel rod. The fuel rod is axially divided into segments (from segment number 1 at the bottom to segment number 10 at the top). The axial cladding surface temperature profile of the fuel rod is assumed to be as described by Fig. 2.97 [34].

The gas plenum of the fuel rod may be placed in the upper part of the fuel rod or the lower part of the fuel rod. If the gas plenum is placed in the upper part of the fuel rod, its temperature is assumed to be equal to that of the outlet coolant, which is assumed to vary from 400 to 600°C. If the gas plenum is placed in the lower part of the fuel rod, its temperature is assumed to be equal to that of the inlet coolant (280°C). For the core average discharge burnup of 45,000 MWd/t, the fuel rod subject to the analysis is assumed to have a burnup of 62,800 MWd/t (fuel rod average) with peak pellet burnup of 71,700 MWd/t. The core is assumed to have fuel of three cycles with operation periods of 500 days/cycle. The average linear heat generation rates of the fuel rod in the first, second, and third cycles are assumed to be 285.6, 249.3, and 176.7 W/cm, respectively, as shown in Fig. 2.98 [34].

While the average linear heat generation rate of the fuel rod is assumed to be constant during each cycle, the axial power distribution is assumed to vary from the

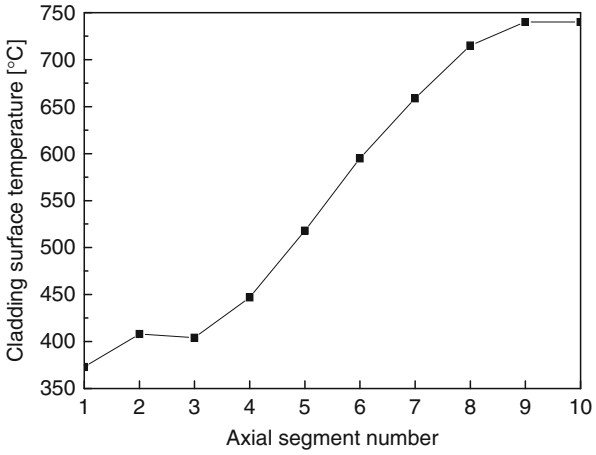


Fig. 2.97 Axial cladding surface temperature profile of the fuel rod. (Taken from [34] and used with permission from atomic energy society of Japan)

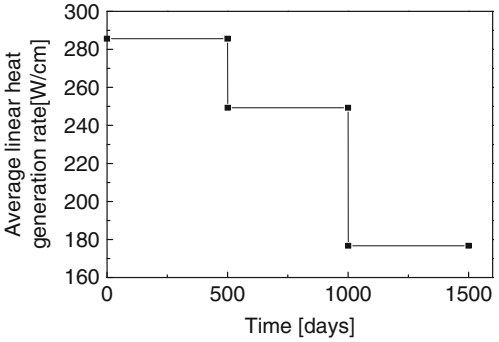


Fig. 2.98 Average linear heat generation rate profile of the fuel rod. (Taken from [34] and used with permission from atomic energy society of Japan)

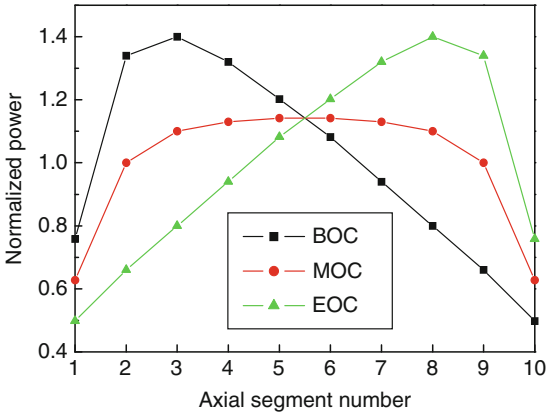


Fig. 2.99 Axial power distribution profile of the fuel rod. (Taken from [34] and used with permission from atomic energy society of Japan)

bottom peak at the BOC to the top peak at the EOC as shown in Fig. 2.99 [34]. The maximum linear heat generation rate of the fuel rod reaches 400 W/cm at the BOC and the EOC of the first cycle.

2.7.2.3 Basic Fuel Rod Behaviors

Toward the EOC of each cycle, the axial power distribution shifts to the upper part of the fuel rod, where the cladding temperature is high. This affects the burnup profile of the fuel pellet centerline temperature. As is shown in Fig. 2.100 [34], the pellet centerline temperatures increase toward the EOC in the upper part of the fuel rod (segment numbers 9 and 10).

Figure 2.101 [34] shows the burnup profile of the average FP gas release rate and gas plenum pressure of the fuel rod. The FP gas release rate of the fuel rod rapidly increases until the average burnup of about 25 GWd/t, and thereafter, it remains almost constant.

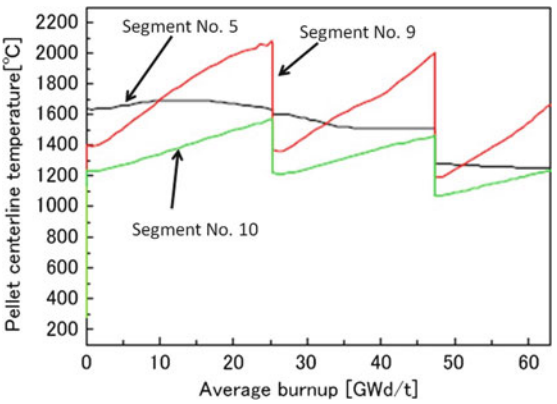


Fig. 2.100 Burnup profile of the peak pellet centerline temperature. (Taken from [34] and used with permission from atomic energy society of Japan)

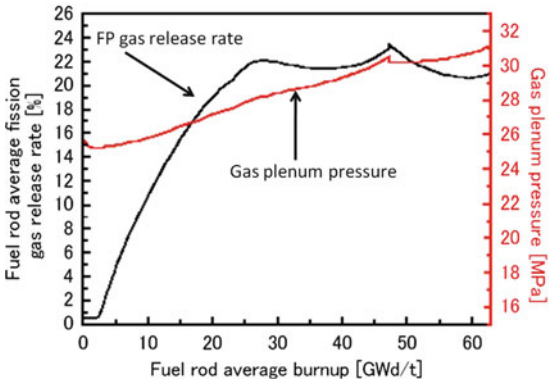


Fig. 2.101 Burnup profiles of the fuel rod average FP gas release rate and gas plenum pressure. (Taken from [34] and used with permission from atomic energy society of Japan)

The primary membrane stress (hoop stress) on the cladding is a good index for the mechanical strength requirement for the fuel rod cladding. Figure 2.102 [34] shows the burnup profile of the hoop stress on the cladding.

At the BOL hot standby, a large compressive stress is exerted on the cladding due to the high core pressure. As the core starts up, the fuel rod internal pressure increases rapidly due to the fuel rod heat up and the compressive stress is reduced accordingly. Here, the reactor shutdowns at the end of second and third cycles for fuel replacements are neglected.

After the startup of the core, the fuel pellets start to release FP gasses into the gas plenum volume. The internal pressure starts to rise and the compressive stress on the cladding gradually decreases accordingly. As the burnup proceeds, the fuel pellet starts to swell and PCMI starts. The PCMI causes a large tensile stress on the cladding toward the EOL. Thus, the hoop stress on the cladding is compressive at the BOC due to the large core pressure and becomes tensile towards the EOC due to the FP gas release and PCMI. From the viewpoint of evaluating the mechanical

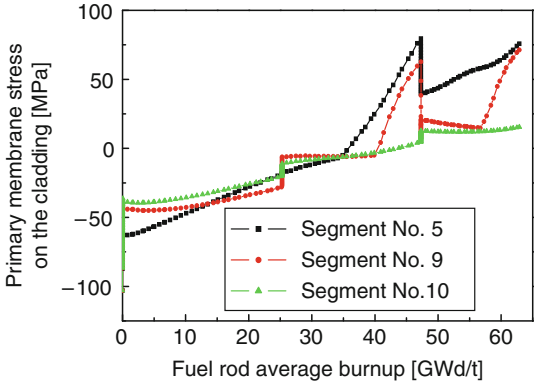


Fig. 2.102 Burnup profile of the hoop stress on the cladding. (Taken from [34] and used with permission from atomic energy society of Japan)

strength requirement for the cladding, the stress on the cladding in the upper part of the fuel rod, where the cladding temperature is high, is important. Since the stress acts on the cladding throughout the lifetime of the fuel rod, the creep rupture strength of the cladding material is important.

2.7.3 Fuel Rod Design

After the basic behaviors of the fuel rod are analyzed in the sensitivity study, requirements with respect to the cladding should be considered.

2.7.3.1 Sensitivity Study

In designing the fuel rod for the Super LWR, the initial internal pressurization of the fuel rod, the release of the FP gases, and the PCMI behavior of the fuel rod are the important factors. These factors are related to each other and the FP gas release is particularly closely related to the PCMI behavior of the fuel rod.

As described by Fig. 2.103 [34], increasing the initial pellet grain size can reduce the internal pressure increase of the fuel rod due to the FP gas release. In PWRs, a grain size of up to 50 μm is being tested for development of high burnup fuels.

However, as can be seen in Fig. 2.104 [34], increasing the initial pellet grain size has the effect of causing a higher PCMI pressure at the EOL. This is due to the larger swelling of the pellet. Increasing the initial pellet-cladding gap size can reduce the PCMI pressure, but it has the effect of increasing the pellet temperature, which also leads to a higher FP gas release rate.

Thus, generally, designing efforts in reducing the FP gas release and PCMI are in a tradeoff. That, in turn, implies that the designing efforts in reducing the compressive stress on the cladding at the BOL and the tensile stress at the EOL are also in a tradeoff.

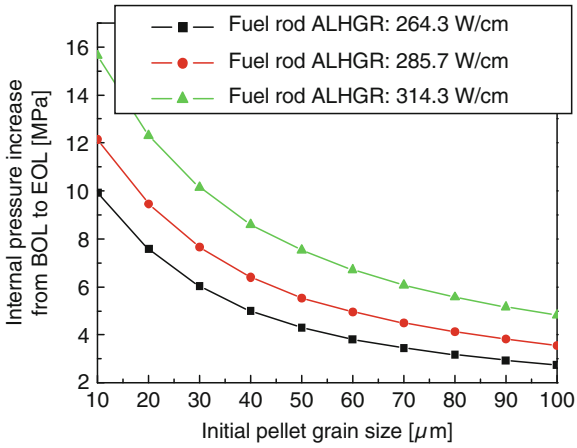


Fig. 2.103 Effect of initial pellet grain size on FP gas release. (Taken from [34] and used with permission from atomic energy society of Japan)

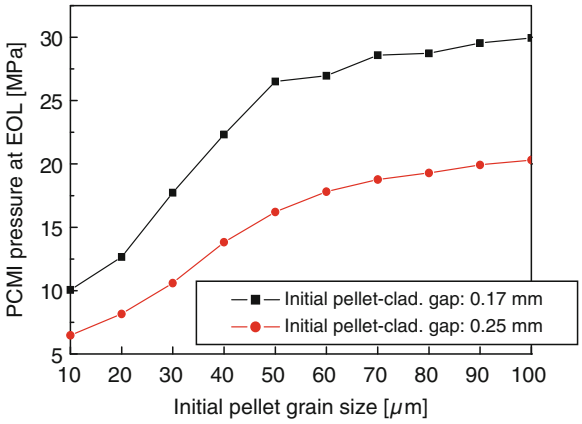


Fig. 2.104 Effect of initial pellet grain size on PCMI. (Taken from [34] and used with permission from atomic energy society of Japan)

From the viewpoint of the core design, Fig. 2.103 [34] implies that increasing the core average linear heat generation rate (ALHGR) leads to larger FP gas release in the fuel rod.

Figure 2.105 [34] shows the linear relationship between the peak pellet centerline temperature and the maximum linear heat generation rate. The peak pellet centerline temperature is higher than those of BWRs or PWRs for the same maximum linear heat generation rate, because the coolant temperature in the Super LWR is higher. The design criterion of the maximum linear heat generation rate should be determined so that the pellet centerline temperature does not reach its melting point during all abnormal transients.

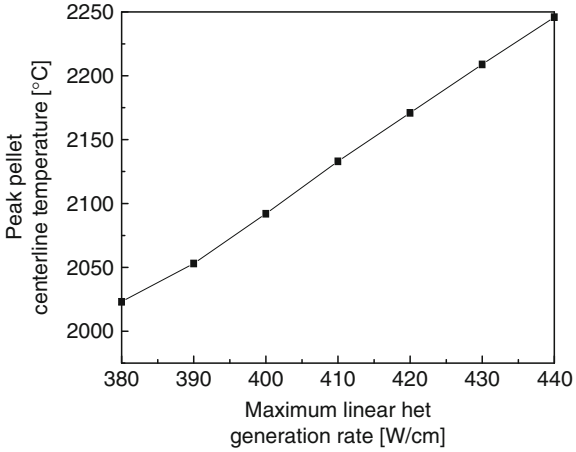


Fig. 2.105 Relationship between the peak pellet centerline temperature and the maximum linear heat generation rate. (Taken from [34] and used with permission from atomic energy society of Japan)

2.7.3.2 Mechanical Strength Requirement of Cladding

Eight fuel rods are designed under different conditions. Among the eight fuel rods, four fuel rods are designed with a constraint that the fuel rod internal pressure is kept below the coolant pressure of 25 MPa throughout their lifetimes and the other four fuel rods are designed without the constraint on the internal pressure. For both cases, fuel rods are designed with different gas plenums. The position (upper/lower) and size of the gas plenums are altered.

Table 2.22 [34] summarizes the cladding hoop stresses for the eight fuel rods designed. Negative stress implies a compressive stress and positive stress implies a tensile stress. The range of the stresses covers all fuel rods (fresh fuel rod at hot standby to the high burnup, high temperature fuel rod) in the core from the BOL to the EOL.

For each fuel rod design, the initial internal pressurization of the fuel rod, the initial pellet grain size, and the pellet-cladding gap size are designed to reduce the hoop stress on the cladding. The hoop stresses are compared at segment number 9, where the cladding temperature becomes the highest. In this segment, the peak cladding centerline temperature is about 757°C.

As can be seen from Table 2.22 [34], placing the gas plenum in the lower part of the fuel rod is effective in reducing the stress on the cladding. When the gas plenum is placed in the upper part of the fuel rod, roughly five times larger gas plenum volume is required to achieve the same stress level as achieved by placing the gas plenum in the lower part of the fuel rod. There are mainly two reasons for this.

First, for the same amount of FP gasses released into the gas plenum volume, placing the gas plenum at the lower part of the fuel rod can reduce the increase in

Table 2.22 Comparison of the cladding hoop stresses for different fuel rod designs. (Taken from [34] and used with permission from atomic energy society of Japan)

Internal pressure	Gas plenum position	Plenum/fuel volume ratio	Cladding hoop stress (MPa)
Lower than coolant pressure	Upper	0.1	−140 to +129
		0.5	−118 to +100
	Lower	0.1	−96 to +100
		0.5	−75 to +59
No constraints	Upper	0.1	−93 to +97
		0.5	−66 to +68
	Lower	0.1	−64 to +71
		0.5	−34 to +36

the internal pressure of the fuel rod, because the plenum temperature is lower in the lower part of the fuel rod than in its upper part.

Secondly, and more essentially, placing the gas plenum in the lower part of the fuel rod makes the initial internal pressurization of the fuel rod more effective in reducing the stress on the cladding. In the case where the gas plenum is placed in the upper part of the fuel rod, the internal pressure of the fuel rods may vary by about 20–30% among the fuel rods located in different places of the core, due to the coolant outlet temperature distribution. Since the core pressure is high in the Super LWR, such fraction of the fluctuation in the internal pressure of the fuel rod may lead to a large stress change on the cladding. In the case where the gas plenum is placed in the lower part of the fuel rod, such fluctuation of the internal pressure does not occur.

One of the fuel rod designs is summarized in Table 2.23 [34] and compared with those of a typical BWR and PWR. In the case of this design, the cladding material needs to withstand the stress of −64 to +71 MPa at a temperature of 757°C for the period of 36,000–48,000 h (500 days multiplied by 3–4 cycles). Some advanced austenitic stainless steels, such as PNC1520 of the former Japan Nuclear Cycle Development Institute (JNC) may be able to meet such requirement.

2.8 Development of Transient Criteria

The criteria for abnormal transients to ensure the fuel integrity are very important. They limit the maximum allowable coolant temperature and the choice of the fuel cladding material to be used at high temperature. So, to maximize the economical potential of the Super LWR, and minimize the research and development efforts, the criteria need to be rationalized based on detailed fuel rod analyses.

In the following, the FEMAXI-6 code [35], described in Sect. 2.7.2 is used with the same models for the fuel rod analyses.

Table 2.23 Comparison of the fuel rod designs. (Taken from [34] and used with permission from atomic energy society of Japan)

		Super LWR	BWR (8 by 8)	PWR (17 by 17)
Primary coolant pressure (MPa)		25.0	7.03	15.4
Average coolant outlet temperature (°C)		500	286	325
Pellet	Diameter (mm)	8.77	10.38	8.19
	length (mm)	10.0	10.0	10.0
	Initial pellet density (% theoretical density)	97	97	95
	Initial pellet grain size (μm)	30	10–15	10–15
Cladding	Material	Stainless steel	Zircaloy 2	Zircaloy 4
	Diameter (mm)	10.2	12.3	9.5
	Thickness (mm)	0.63	0.86	0.57
	Gap (mm)	0.25	0.20	0.17
Fuel rod	Active height (mm)	4,200	3,710	3,660
	Average/maximum LHGR (W/cm)	170/400	180/440	179/431
	Gas plenum to fuel volume ratio	0.10	0.10	0.10
	Gas plenum position	Lower	Upper	Upper
	Initial internal pressurization (MPa)	9.6	0.5	3.0

2.8.1 Selection of Fuel Rods for Analyses

In order to ensure the fuel integrities for all fuel rods in a core, the fuel analysis needs to be carried out for all fuel rods in the core, but in practice this is too time-consuming. Here, ten different fuel rods (one containing fresh fuel and nine containing irradiated fuel of different burnups) are selected for fuel analyses, so that essentially, all fuel rods in the core are covered in evaluating the fuel integrity.

The Super LWR core is designed from three-cycle fuel. Hence, the fuel rods to be analyzed need to represent fuel in each of the three cycles as well as fresh fuel. For this purpose, the fuel rods to be analyzed are categorized into four groups: the fresh fuel, the first cycle fuel, the second cycle fuel, and the third cycle fuel. To represent each category of irradiated fuel, three different fuel rods are selected, the high-power fuel, midpower fuel, and the low-power fuel rods.

It is assumed that all fuel rods are exposed at constant power with an axially top peak power distribution (peaking factor of 1.50) during normal operation with operation period of 470 days per cycle. Hence, the combination of the maximum linear heat generation rate and the peak pellet burnup defines the fuel rod to be selected. The fuel rods to be selected are described in Fig. 2.106 as a function of the maximum linear heat generation and the peak pellet burnup. The notations in the figure describe the power levels (high, mid, low) corresponding to the fuel rod to be selected. For example, the fuel "H" for EO1C describes the high-power first cycle fuel rod, having been irradiated in the core at maximum linear heat generation rate of 390 W/cm for 470 days. The irradiation history of the axial power distributions and the cladding surface temperature distributions are conservatively determined so

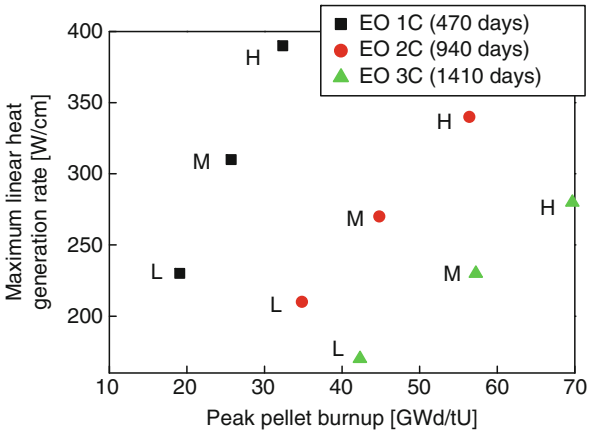


Fig. 2.106 Fuel rods to be analyzed

that the axial position of the peak power pellet coincides with that of the hottest cladding.

2.8.2 Principle of Rationalizing the Criteria for Abnormal Transients

2.8.2.1 Principle of Ensuring the Fuel Integrity at Abnormal Transients

Abnormal transients are defined as events that will lead to the situation in which the nuclear plant cannot maintain the normal operation due to an external disturbing factor that may occur during the life span of the nuclear plant under the operational conditions including single failure or malfunction of the devices or single operational errors by operators, and to the abnormal situation in which the nuclear plant is not planned to operate and that may occur with the same probability as the former. A set of abnormal transients and accidents as standard safety analysis of the current LWRs is studied for the Super LWR, including the loss of coolant accident (LOCA) and the anticipated transients without scram (ATWS) (see Chap. 6 for details).

The requirements for the Super LWR are same as those of LWRs:

1. No systematic fuel rod damage
2. No fuel pellet damage
3. No reactor pressure vessel (RPV) damage

The above three requirements are not directly related to parameters that can be easily obtained in the plant safety analyses. Instead of directly examining satisfaction of these requirements, the following criteria had been typically adopted in the safety analyses of the Super LWR. To meet requirement 1, the criterion of the peak

cladding temperature (PCT) is set to 800°C for Ni alloy cladding (19Cr–3Mo–18-Fe–5Nb–Ni) and the criterion of the plastic deformation is 1.0%. To meet requirement 2, the criterion of the fuel enthalpy at reactivity transients is 270 J/g, the same as current LWRs. To meet requirement 3, the criterion of the system pressure is 28.9 MPa (105% of the maximum pressure for normal operation).

Among the criteria, the criterion for the peak cladding temperature had been estimated by simple but conservative calculations. However, it is expected to depend on the material of the cladding and the fuel rod design. Based on the above requirements, the following four principles are adopted to derive rationalized new criteria for abnormal transients.

- The fuel rod buckling collapse should not occur when the fuel rod cooling is deteriorated.
- The fuel rod mechanical failure should not occur.
- The fuel enthalpy should be below the limit.
- The primary coolant pressure boundary should not fail.

The above principles can be rewritten quantitatively as in the case for LWRs. For example, the same or similar values that have been used for LWRs may be directly adopted as follows: the pressure difference on the cladding should be less than 1/3 of the collapse pressure of the cladding, the average plastic strain of the cladding in the radial direction should be less than 1%, the fuel enthalpy is less than 170 cal/gUO_2, and the system pressure does not exceed 28.9 MPa (105% of the maximum pressure for normal operation).

Since there have not been any experiments for Super LWR fuel to confirm its integrity, some further conservatism may be necessary at this stage of the conceptual development. Here, the following criteria are determined.

- The pressure difference on the cladding should be less than 1/3 of the collapse pressure of the cladding.
- The strain level on the cladding should not exceed the elastic limit (i.e., no plastic strain on the cladding).
- The fuel pellet centerline temperature should be less than its melting point.
- The system pressure should not exceed 28.9 MPa (105% of the maximum pressure for normal operation).
- The internal pressure of the fuel rod should not become excessively high (less than the coolant pressure during normal operation).

In reality, the cladding mechanical failure occurs at some point in the plastic strain region. In the case of Zircaloy claddings of BWRs or PWRs, experimental results have shown that the cladding failures can be prevented as long as the cladding plastic strain level is less than 1%. Such experiments need to be conducted for the Super LWR fuel claddings in the future. In the meantime, the elastic strain limit is conservatively determined for the conceptual development.

Similarly, it is commonly known that the centerline melting criterion is conservative. The pellet centerline melting may lead to excessive fuel volume expansions or FP gas releases, which may cause pellet cladding interaction (PCI) or excessive

increase of the fuel rod internal pressure. These phenomena may lead to the cladding failures.

2.8.2.2 Classification of Abnormal Transients and Modeling

As is the case for most reactors, the abnormal transients of Super LWR can be classified into two events, namely, "overheating events" and the "overpower events." These events are modeled as described in Fig. 2.107. In both overheating and overpower events, the fuel integrity is examined for three different MCSTs of 750, 800 and 850°C.

In overheating events, such as the "partial loss of the reactor coolant flow" transient, heat removal from the fuel rod cladding surface decreases and its temperature rises, while the reactor power decreases mainly due to the coolant density feedback effect and the reactor scram. In such an event, the fuel integrity is limited by the cladding collapse criterion, which depends on the cladding surface temperature and the pressure difference on the cladding.

The model for overheating events is determined such that the pressure difference on the cladding is higher than the actual value expected. The coolant pressure is assumed to increase to 30 MPa, which is much higher than the criterion of 28.9 MPa. The fuel rod power is assumed to linearly decrease to 1% of the normal operating power in 0.1 s.

In overpower events, such as the "control rod withdrawal at normal operation," the fuel rod heat generation increases and the cladding temperature increases accordingly. In such an event, the fuel integrity is limited by the pellet centerline temperature criterion and the cladding elastic strain limit criterion, which depends on the cladding temperature and the pellet expansion (i.e., limited by PCMI).

The model for overpower events is determined such that the pellet centerline temperature and the PCMI are greater than the expectations for the event. The coolant pressure is assumed to decrease to 20 MPa, the fuel rod power is assumed to

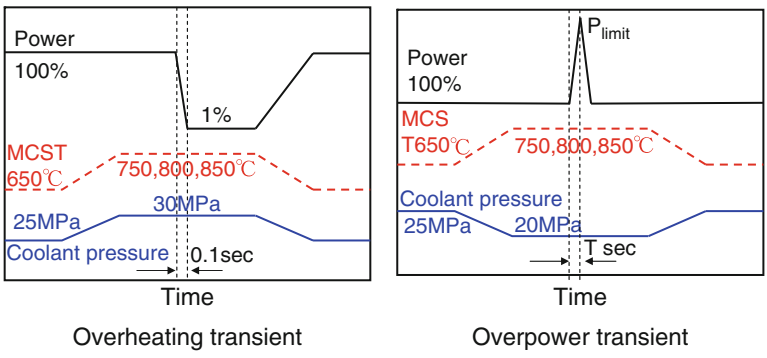


Fig. 2.107 Models for overheating and overpower events

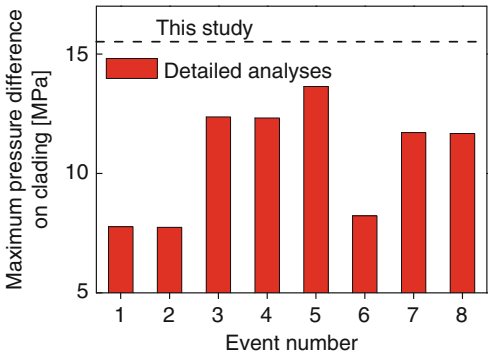
linearly increase until the pellet centerline temperature exceeds its melting point, or the fuel rod cladding strain reaches the elastic limit.

The covering of all major abnormal transients by these proposed models are confirmed by comparing the results obtained by them with results obtained from detailed fuel rod analyses modeling each abnormal transient event. The following eight abnormal transient events are analyzed for confirmation: inadvertent startup of the auxiliary feedwater system (AFS);loss of feedwater heating; loss of load without turbine bypass; withdrawal of control rods at normal operation; main coolant flow control system failure; pressure control system failure; partial loss of reactor coolant flow; and loss of offsite power.

Figure 2.108 shows the maximum pressure difference on the cladding. The line indicated by "this study" is obtained by using the model for the overheating events proposed here. Each bar shows the maximum pressure difference on the cladding corresponding to each abnormal transient event. Similarly, the results are compared for the maximum cladding circum strain in Fig. 2.109 and for the maximum pellet centerline temperature in Fig. 2.110. For all cases, the results obtained using the models proposed here show more conservative results.

2.8.2.3 Evaluations of Allowable Maximum Cladding Temperature and Fuel Rod Power

In the actual operation of the plant, the fuel integrity cannot be monitored. Even in the plant safety analysis, it is too time consuming to perform detailed fuel analysis for each transient event.



1: Inadvertent startup of AFS
2: Loss of feedwater heating
3: Loss of turbine load without turbine bypass
4: Uncontrolled CR withdrawal at normal operation
5: Reactor coolant flow control system failure
6: Pressure control system failure
8: Partial loss of reactor coolant flow
9: Loss of offsite power

Fig. 2.108 Maximum pressure differences on the cladding

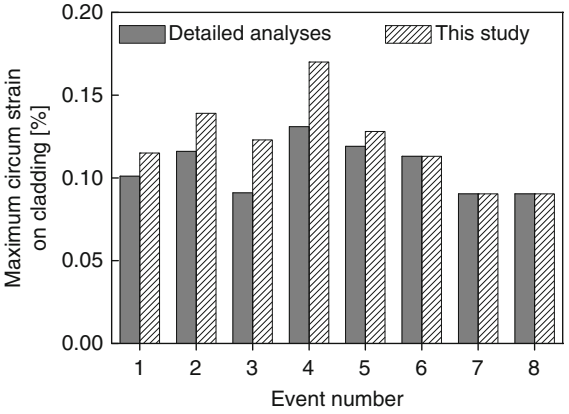


Fig. 2.109 Maximum cladding circumstance strains

1: Inadvertent startup of AFS
2: Loss of feedwater heating
3: Loss of turbine load without turbine bypass
4: Uncontrolled CR withdrawal at normal operation
5: Reactor coolant flow control system failure
6: Pressure control system failure
8: Partial loss of reactor coolant flow
9: Loss of offsite power

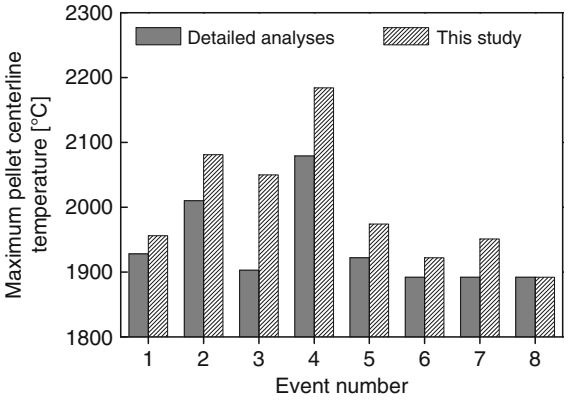


Fig. 2.110 Maximum pellet centerline temperature

1: Inadvertent startup of AFS
2: Loss of feedwater heating
3: Loss of turbine load without turbine bypass
4: Uncontrolled CR withdrawal at normal operation
5: Reactor coolant flow control system failure
6: Pressure control system failure
8: Partial loss of reactor coolant flow
9: Loss of offsite power

By using the fuel analysis code with the models explained in the previous section, the allowable maximum cladding temperature and power can be determined, so that as long as the cladding temperature and the fuel rod power are below the limits, the fuel integrity can be assured. These limits are considered to be useful in the plant safety analysis for confirming the fuel integrity during abnormal transient events. It may also be used in the operating plant for assisting the plant operators.

The allowable maximum cladding temperature can be determined from the cladding collapse criterion for overheating events; in this case, the fresh fuel rod is limiting. The collapse pressure of the cladding is conservatively determined by the equation for an infinite length cylinder, (2.21).

As can be seen from the equation, the allowable maximum cladding temperature depends sensitively on the cladding thickness, t, and it also depends on the initial internal pressure of the fuel rod (i.e., the pressure difference on the cladding with respect to the collapse pressure, P_{collapse}).

Figure 2.111 shows the limit for the maximum cladding temperature as a function of the cladding thickness reduction for three different initial internal pressures. Currently, the corrosion behavior of the cladding material in supercritical water is not clear. Here, assuming about 10% reduction of the cladding thickness (0.063 mm), the limit for the cladding temperature can be evaluated as about 950°C. However, material properties at such high temperature are not well known and the validity of the model describing the modulus of elasticity needs to be considered. Hence, a margin of 100°C is taken and the allowable maximum cladding temperature is determined as 850°C.

The new criterion of allowable maximum cladding temperature of 850°C is 50°C higher than the past criterion of 800°C. The criterion has been rationalized by detailed fuel analysis, assuring the fuel integrity in all abnormal transient events.

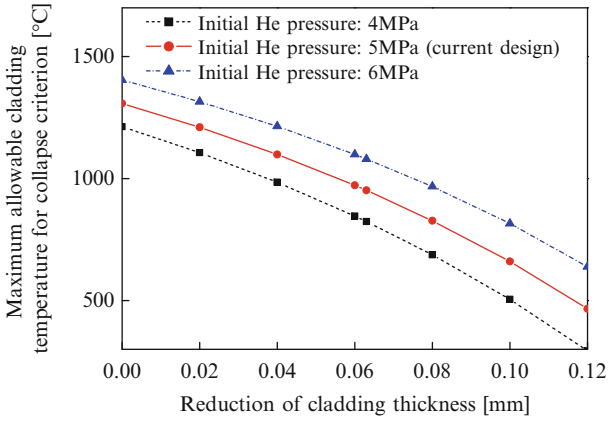


Fig. 2.111 Maximum allowable cladding temperature

The allowable maximum fuel rod power can be determined from the pellet centerline temperature and the cladding strain criteria for overpower events. Unlike overheating events, the limiting fuel is not necessarily the fresh fuel or any other particular fuel. The fuel integrity is mainly determined by the pellet centerline temperature criterion and the PCMI behavior of the fuel rod, which depends on the fuel rod power, power rise rate, and the burnup of the pellet.

Figure 2.112 shows an example of the relationship between the allowable maximum power, maximum linear heat generation rate at normal operation, and the peak pellet burnup. It is obtained for a power rise rate of 1% P_0/s (P_0: peak power at normal operation). It shows that the allowable power is lower for high power fuel with high peak pellet burnup than low power fuel with low peak pellet burnup.

Here, the allowable maximum power is determined for each fuel rod selected for evaluations as described in Sect. 2.8.1, and the allowable maximum power are summarized for three different power rise rate as shown in Table 2.24. All overpower events with power rise rate greater than 0.1% P_0/s are covered. For any slower event, the criterion for normal operation should be adopted. The new criterion for the overpower events allows the reactor power to reach up to 182%, depending on the power rise rate.

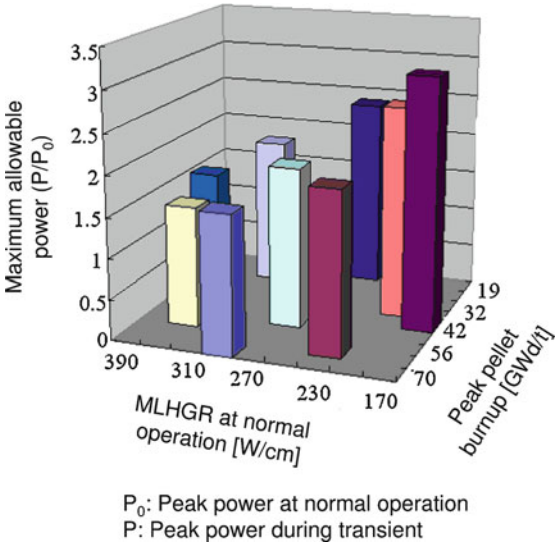


Fig. 2.112 Example of maximum allowable powers

Table 2.24 Allowable maximum power

Power rise rate X (% P_0/s)	Allowable max. power (% P_0)
$0.1 \leq X < 1$	124
$0.1 \leq X < 10$	136
$10 \leq X$	182

Here the power limit for the Super LWR is derived from direct evaluation of the fuel integrity. The determinations of the temperature and power limits for normal operation are to be considered in the future studies. When the power limits for normal operation and abnormal transient events are determined, these limits may be used for determining the set point of the reactor scram.

2.9 Summary

This chapter described the design concepts of the Super LWR core, including the fuel rod and fuel assembly designs. Considerations of the design margins, criteria, boundary conditions, and target were made and the core design scope of the Super LWR was roughly defined.

The core calculations were also introduced, including the neutronic and thermal-hydraulic parts. The core thermal-hydraulic characteristics are unique and strongly coupled with the neutronic characteristics of the core.

Subchannel analyses were carried out for the Super LWR. Coolant outlet temperature distribution, axial coolant temperature distribution, flow rate distribution of coolant, and temperature distribution of cladding were analyzed.

Statistical thermal design uncertainty was evaluated by a Monte Carlo sampling technique combined with the subchannel analysis code. The engineering uncertainty of the Super LWR is evaluated as 31.88°C based on the Monte Carlo Statistical Thermal Design Procedure.

After evaluating the maximum peak cladding temperature, the basic fuel rod behavior was analyzed. Then, the sensitivity study about fuel rod design was developed. The mechanical strength requirements for the fuel rod cladding under different design constraints and conditions were obtained for the development of the cladding material and the core concept.

The principle of rationalization of the criteria for abnormal transients of the Super LWR was developed. Detailed fuel analyses showed that allowable limits to the maximum fuel rod power and maximum cladding temperature can be determined to ensure the fuel integrity for abnormal transients of the Super LWR.

Glossary

AFS	Auxiliary feedwater system
ATWS	Anticipated transients without scram
ALHGR	Average linear heat generation rate
BOC	Beginning of cycle
BOP	Balance of plant
BOL	Beginning of life
BWR	Boiling water reactor

CFD	Computational fluid dynamics
CHF	Critical heat flux
DNB	Departure from nucleate boiling
DNBR	Departure from nucleate boiling ratio
EOL	End of life
FR	Fast reactor
FBR	Fast breeder reactor
FCMI	Fuel cladding mechanical interaction
FPP	Fossil fired power plant
FP	Fission product
HTD	Heat transfer deterioration
LMFBR	Liquid metal fast breeder reactor
ITDP	Improved Thermal Design Procedure
LLLP	Low leakage loading pattern
LOCA	Loss of coolant accident
LWR	Light water reactor
MCST	Maximum cladding surface temperature
MCSTDP	Monte Carlo Statistical Thermal Design Procedure
MDHFR	Minimum deterioration heat flux ratio
MTDP	Optimized Monte Carlo Thermal Design Process
MGS	General Statistical Method
MLHGR	Maximum linear heat generation rate
ODS	Oxide dispersion strengthened
PCMI	Pellet-cladding mechanical interaction
PCI	Pellet cladding interaction
PIJ	Collision probability calculation module
PWR	Pressurized water reactor
RIA	Reactivity insertion accident
RPV	Reactor pressure vessel
RTDP	Revised Thermal Design Procedure
RSS	Root Sum Square
SCC	Stress corrosion cracking
STDP	Statistical thermal design procedure

References

1. H. S. Swenson, J. R. Carver and C. R. Kakarala, “Heat transfer to supercritical water in smooth-bore tubes,” *Journal of Heat Transfer*, Vol. 87, 477–484 (1965)
2. B. S. Shiralkar and P. Griffith, “Deterioration in heat transfer to fluids at supercritical pressure and high heat fluxes,” *Journal of Heat Transfer*, Vol. 91, 27–36 (1969)
3. E. Stewart, P. Stewart and A. Watson, “Thermo-acoustic oscillations in forced convection heat transfer to supercritical pressure water,” *International Journal of Heat and Mass Transfer*, Vol. 16, 257–270 (1973)

4. J. D. Jackson and W. B. Hall, Forced convection heat transfer to fluids at supercritical pressure. In *Turbulent Forced Convection in Channels and Bundles*, Vol. 2, 563–611. Hemisphere, New York (1979).
5. S. Koshizuka, N. Takano and Y. Oka, "Numerical analysis of deterioration phenomena in heat transfer to supercritical water," *International Journal of Heat and Mass Transfer*, Vol. 38(16), 3077–3084 (1995)
6. S. Koshizuka and Y. Oka, "Computational Analysis of Deterioration Phenomena and Thermal-Hydraulic Design of SCR," *Proc. SCR2000*, Tokyo, November 6–8 (2000)
7. K. Kitoh, S. Koshizuka and Y. Oka, "Pressure and flow-induced accident and transient analyses of a direct-cycle, supercritical-pressure, light-water-cooled fast reactor," *Nuclear Technology*, Vol. 123, 233–244 (1998)
8. K. Yamagata, K. Nishikawa, S. Hasegawa, T. Fujii and S. Yoshida, "Forced convection heat transfer to supercritical water flowing in tubes," *International Journal of Heat and Mass Transfer*, Vol. 15, 2575–2593 (1972)
9. A. Yamaji, "Fuel and Core Design of Super LWR," Doctoral thesis, the University of Tokyo (2005) (in Japanese)
10. I. L. Pioro and R. B. Duffey, "Experimental heat transfer in supercritical water flowing inside channels (survey)," *Nuclear Engineering and Design*, Vol. 235, 2407–2430 (2005)
11. H. Mori, S. Yoshida, et al., "Heat Transfer Study Under Supercritical Pressure Conditions for Single Rod Test Section," *Proc. ICAPP'05*, Seoul, Korea, May 15–19, 2005, Paper 5303 (2005)
12. Y. Oka and S. Koshizuka, "Supercritical-pressure, once-through cycle light water cooled reactor concept," *Journal of Nuclear Science and Technology*, Vol. 38(12), 1081–1089 (2001)
13. Y. Oka, S. Koshizuka, Y. Ishiwatari, et al., "Overview of Design Studies of High Temperature Reactor Cooled by Supercritical Light Water at the University of Tokyo," *Proc. GENES4/ANP2003*, Kyoto, Japan, September 15–19, Paper 1068 (2003)
14. K. Okumura, T. Kugo, K. Kaneko and K. Tsuchihashi "SRAC (Ver.2002); The comprehensive neutronics calculation code system," Japan Atomic Energy Research Institute (JAERI) Tokai-mura, Naka-gun, Ibaraki-ken, 319-1195, Japan
15. K. Shibata, T. Kawano, T. Nakagawa, et al., "Japanese Evaluated Nuclear Data Library Version 3 Revision-3: JENDL-3.3," *Journal of Nuclear Science and Technology*, Vol. 39 (11), 1125–1136 (2002)
16. "An evaluation of steam-cooled fast breeder reactors," *WASH-1088*, 1969
17. M. Kureta, H. Tamai, A. Ohnuki, T. Sato, W. Liu and H. Akimito, "Critical power experiment with a Tight-Lattice 37-Rod Bundle," *Journal of Nuclear Science and Technology*, Vol. 43(2), 198–205 (2006)
18. K. Dobashi, "Conceptual Design of Supercritical-pressure Light Water Cooled and Moderated Reactor," Doctoral thesis, the University of Tokyo (1998) (in Japanese)
19. Y. Oka, S. Koshizuka and T. Yamasaki, "Direct cycle light water reactor operating at supercritical pressure," *Journal of Nuclear Science and Technology*, Vol. 29(6), 585–588 (1992)
20. Y. Okano, S. Koshizuka and Y. Oka, "Core design of a direct-cycle, supercritical pressure, light water reactor with double tube water rods," *Journal of Nuclear Science and Technology*, Vol. 33(4), 365–373 (1996)
21. K. Kamei, "Core design of Super LWR and its safety analysis at subcritical-pressure," Master's thesis, the University of Tokyo (2006) (in Japanese)
22. K. Kamei, Y. Yamaji, Y. Ishiwatari, et al., "Fuel and core design of super light water reactor with low leakage fuel loading pattern," *Journal of Nuclear Science and Technology*, Vol. 43 (2), 129–139 (2006)
23. T. Tanabe, S. Koshizuka and Y. Oka, "A Subchannel Analysis Code for Supercritical-Pressure LWR with Downward-Flowing Water Rods," *Proc. ICAPP'04*, Pittsburgh, PA, June 13–17, 2004, Paper 4333 (2004)

24. T. Tanabe, "Subchannel Analysis of Super Light Water Reactor," M.S. Thesis, University of Tokyo (2005) (In Japanese)
25. M. J. Watts and C. T. Chou, "Mixed Convection Heat Transfer to Supercritical Pressure Water," *Proc. 7th Int. Heat Transfer Conf.*, Munich, W. Germany, September 6–10, 1982, 495–500 (1982)
26. N. E. Todreas, and M. S. Kazimi, "Nuclear Systems I; Thermal Hydraulic Fundamentals," Taylor & Francis, New York (1990)
27. J. Yang, Y. Oka, J. Liu, Y. Ishiwatari and A. Yamaji, "Development on statistical thermal design procedure to evaluate engineering uncertainty of super LWR," *Journal of Nuclear Science and Technology*, Vol. 43(1), 32–42 (2006)
28. S. Ray, A. J. Friedland and E. H. Novendstern, "Westinghouse Advanced Statistical DNB Methodology – The Revised Thermal Design Procedure," *Proc. NUTHOS-3*, Seoul, Korea, November, 1988, A5-261 (1988)
29. L. S. Tong and J. Weisman, "Thermal Analysis of Pressurized Water Reactors 3rd Edition," *America Nuclear Society*, 582 (1996)
30. N. E. Todreas and M. S. Kazimi, "Nuclear Systems II; Elements of Thermal Hydraulic Design," Hemisphere Publ. Corp., New York (1990)
31. J. Robeyns, F. Parmentier and G. Peeters, "Application of a Statistical Thermal Design Procedure to Evaluate the PWR DNBR Safety Analysis Limits," *Proc. ICONE 9*, Nice, France, April 8–12, 2001, ICONE-9091 (2001)
32. J. P. Bourteele, J. Greige and M. Missaglia, "The Framatome Generalized Statistical DNBR Method (MSG)," *Proc. NURETH-6*, Grenoble, France, October 5–8, 1993, v.1-355 (1993)
33. K. L. Eeckhout and J. J. Robeyns, "MTDP – An Optimized MONTE CARLO Method for Evaluation of the PWR Core Thermal Design Margin," *Proc. NURETH-8*, Kyoto, Japan, September 30–October 4, 1997, v.1-421 (1997)
34. A. Yamaji, Y. Oka, J. Yang, J. Liu, Y. Ishiwatari and S. Koshizuka, "Design and Integrity Analyses of the Super LWR Fuel Rod," *Proc. Global 2005*, Tsukuba, Japan, October 9–13, 2005 Paper 556 (2005)
35. M. Suzuki and H. Saitou, Light Water Reactor Fuel Analysis Code FEMAXI-6(Ver.1), *JAEA Data/Code 2005-003* (2005)

Chapter 3
Plant System Design

3.1 Introduction

Basically, the same plant system is possible for the Super LWR and Super FR. This chapter gives a brief description of the plant system design of Super LWRs as an example. The heat balance of the plant in evaluating the thermal efficiency of the Super LWRs is also discussed.

The Super LWRs employ the supercritical steam cycle, and it is designed based on past experiences in FPPs and LWRs. The major components of the Super LWRs are used within the pressure and temperature ranges based on these past experiences. Schematic diagrams of plant systems for the Super LWR, PWR, BWR, and FPP are shown in Fig. 3.1. Because the coolant system is a once-through direct cycle, all the coolant is directly fed to the turbines and hence, unlike for PWRs, steam generators are unnecessary for the Super LWRs. Water does not undergo a change of phase above the critical pressure of 22.1 MPa. There is no boiling phenomenon in the supercritical pressure region. Hence, unlike for BWRs, the in-vessel steam-water separators, dryer and recirculation system are not necessary for the Super LWRs. The reactor pressure vessel (RPV) of the Super LWRs is similar to that of PWRs.

From studies performed worldwide on the potential characteristics of the Super LWR concept, the following major advantages of the Super LWR Nuclear Power Plant (NPP) system can be recognized over conventional LWRs:

1. Simple plant system due to the once-through direct steam cycle
2. Compact plant system due to elimination of steam-water separators, steam dryer, recirculation system, and steam generators
3. High thermal efficiency due to high pressure and high temperature steam conditions
4. Low coolant flow rate and small coolant inventory due to high coolant enthalpy rise
5. Small plant size due to compactness of the once-through system

Y. Oka et al., *Super Light Water Reactors and Super Fast Reactors*,
DOI 10.1007/978-1-4419-6035-1_3, © Springer Science+Business Media, LLC 2010

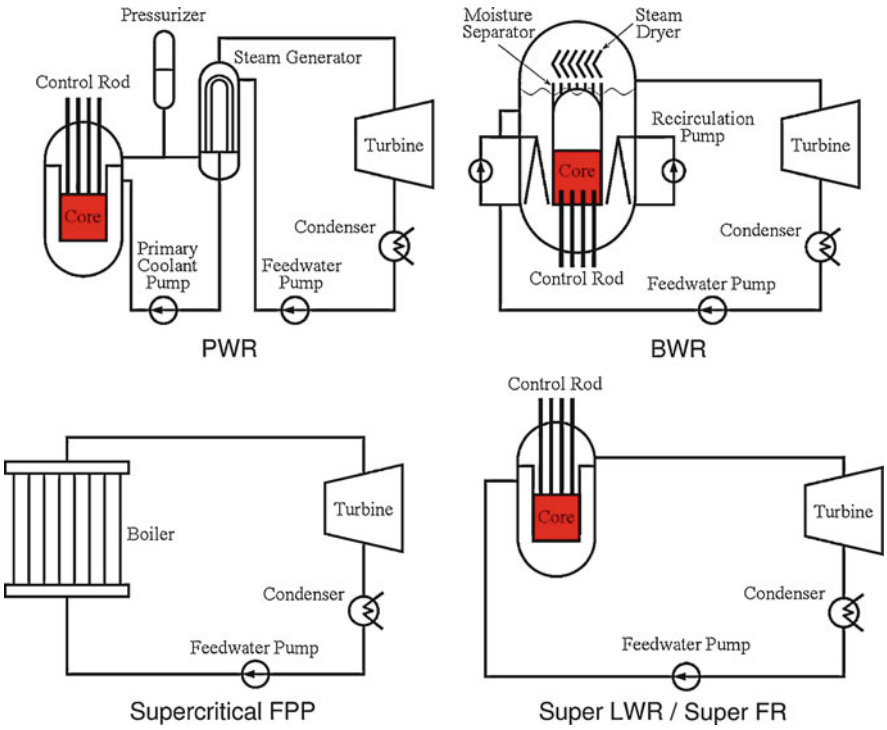


Fig. 3.1 Schematic diagrams of plant systems

6. Potential cost reductions due to small material expenditure, short construction period, and effective use of nuclear fuel

3.2 System Components and Configuration

The main components of a Super LWR NPP system include the RPV, containment vessel and internals, supercritical steam turbine system and safety systems. The main specifications of a 1700MWe level Super LWR plant system and the improvements from a 1350MWe-class advanced BWR (ABWR) are listed in Table 3.1 [1].

A layout for the Super LWR NPP is drawn in Fig. 3.2 [2]. It is a two-loop system. The supercritical steam flows into the turbine system through the outlet nozzles of the RPV and the main steam lines. The water is pumped out of the condenser by a series of pumps and back to the reactor through the inlet nozzles. A series of low pressure and high pressure feedwater heaters are placed upstream and downstream from the main feedwater pumps, respectively, to preheat the cold water before it flows into the reactor. The safety system design and characteristics are discussed in Chap. 6 in detail.

Table 3.1 Main specifications of 1700MWe-class Super LWR plant system and 1350MWe-class ABWR. (Taken from [1] and used with permission from Atomic Energy Society of Japan)

	Super LWR	ABWR	Improvement (%)
Thermal efficiency, %	44.0	34.5	28
RPV weight, *t*	750	910	18
CV volume, m^3	7,900	17,000	54
Steam line number	2	4	50
Turbine speed, rpm	3,000[a]	1,500[b]	50
Condenser	2	3	33

[a]3,600 rpm in western Japan
[b]1,800 rpm in western Japan

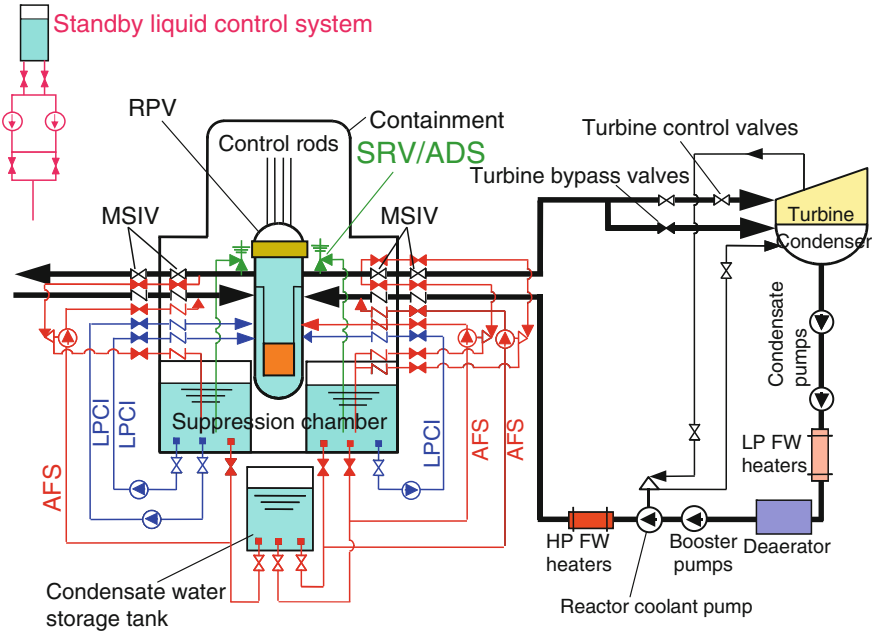


Fig. 3.2 Schematic drawing of a Super LWR NPP. (Taken from [2] and used with permission from Korean Nuclear Society)

3.3 Main Components Characteristics

The main design principle and characteristics of each Super LWR NPP component is presented in this section. Attention is focused on the design characteristics of the pressure containment and RPV which are fundamentally different from existing FPPs and LWRs. As for the supercritical turbine, the feedwater heaters and the feedwater pumps, the design principle is similar to that of FPPs. Their fabrication technologies are mature with full of operating experience.

3.3.1 Containment

Both dry and pressure suppression type containment vessels are feasible for Super LWR and Super FR. The containment of the Super LWRs in the early designs is a pressure suppression type with a condensation pool for pressure suppression under loss of coolant accident conditions (essentially the same design as modern ABWRs) as illustrated in Fig. 3.3a. It supplies support for the floor slabs of the reactor building (secondary containment) and the refueling pools, more importantly, it serves as the final radiation shielding layer and mitigates the accidental sequence in case of a severe accident. The primary containment consists of several major components, many of which can be seen in Fig. 3.3a. The upper pool is designed for refueling and storage of spent fuel from the viewpoint of convenient mechanical operation. The drywell is a cylindrical, reinforced concrete structure with a

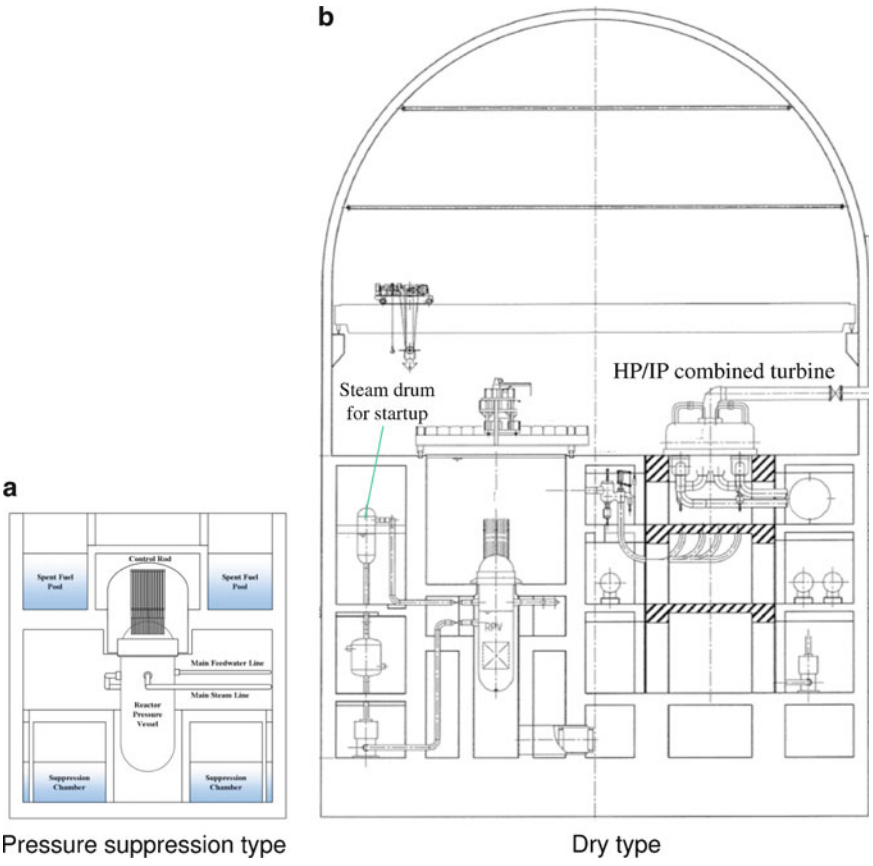


Fig. 3.3 Examples of the containment of Super LWR

removable head. The drywell is designed to withstand and confine steam generated during a pipe rupture inside the containment and to channel the released steam into the suppression pool. The suppression pool contains a large volume of water for rapidly condensing steam directed to it. A leak tight, cylindrical, steel containment vessel surrounds the drywell and the suppression pool to prevent gaseous and particulate fission products from escaping to the environment following a pipe break inside the containment.

The containment is designed to condense steam and to contain fission products released at a loss of coolant accident (LOCA) so that offsite radiation doses do not exceed the specified criteria and to provide a heat sink and water source for certain safety related equipment.

As schematically shown in Fig. 3.4 [1], the pressure suppression type containment of the Super LWR can be more compact compared to the containments of typical PWRs and ABWRs. That is because the primary system of the Super LWR contains smaller coolant inventories and energy due to no steam generator, no recirculation system, and a smaller RPV than that of BWRs.

A dry type containment like that of PWRs is also considered for the Super LWR as illustrated in Fig. 3.3b. As the Super LWR has no steam generator, a high pressure and intermediate pressure combined turbine and a startup system (see Sect. 5.7) are installed inside the containment in this example to effectively utilize the space in the containment and therefore make the turbine building more compact.

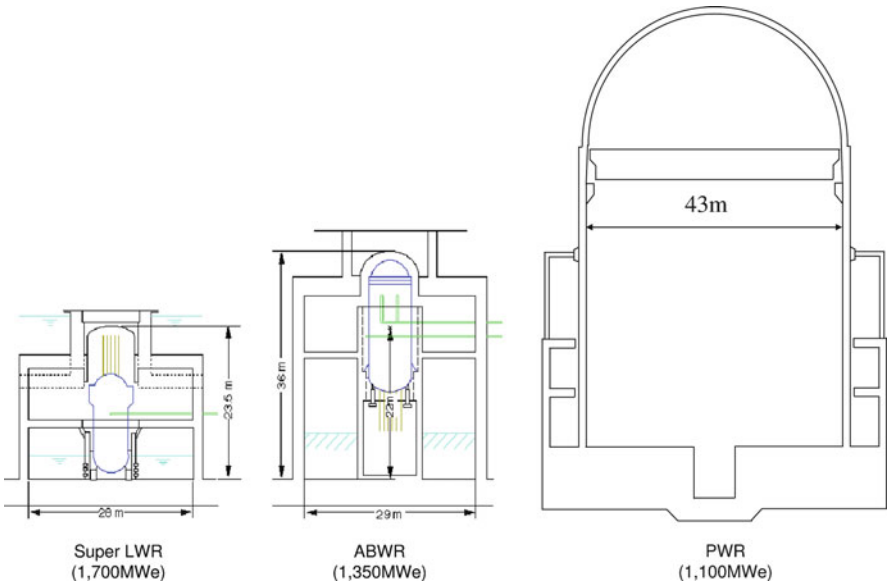


Fig. 3.4 Comparison of containment sizes. (Taken from [1] and used with permission from Atomic Energy Society of Japan)

3.3.2 Reactor Pressure Vessel

Although the primary coolant system of the Super LWRs and Super FRs is a direct-cycle which is similar to that of BWRs, the RPV design is quite similar to that of PWRs. The major functions of the Super LWR RPV assembly are the following.

1. House the reactor core
2. Serve as part of the reactor coolant pressure boundary
3. Support and align the fuel and control rods
4. Provide a flow path for circulation of coolant past the fuel

The RPV of a Super FR is illustrated in Fig. 3.5 [3]. The RPV of the Super LWR is similar to that of the Super FR. Like a typical RPV in PWRs, it has no major penetrations through the lower head. Control rods are inserted from the top of the core because there are no steam separators or dryers. All the internal walls are cooled by the inlet coolant. Only the outlet nozzles are exposed to the hot outlet coolant; consequently, they may require a thermal sleeve. This limited exposure avoids thermal creep of the structural steel at the elevated temperature so the conventional steel of the PWR vessel can be used. There are only two inlet and outlet nozzles because the coolant or steam flow rate per electric power is smaller than that of LWRs.

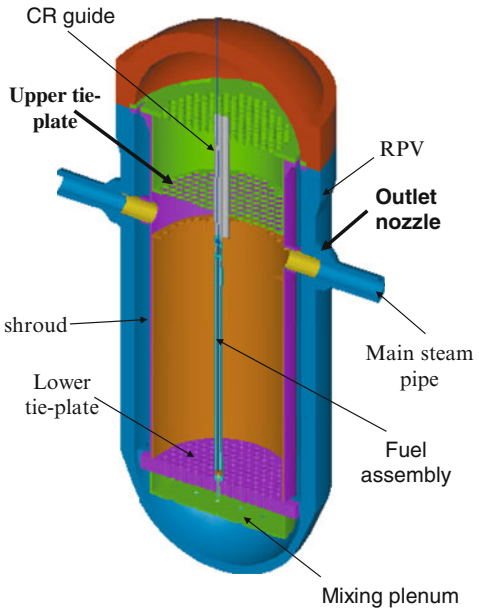


Fig. 3.5 Reactor pressure vessel and core internals of a Super FR. (Taken from [3] and used with permission from Atomic Energy Society of Japan)

The expected radiation damage to the vessel over a 60-year lifetime is within a typical PWR range due to a similar downcomer width and somewhat lower power density. Nevertheless, radiation embrittlement issues will be minimized by controlling the use of sensitizing elements (Cu, P) in the weld regions and by forging a single ring for the active core region to avoid the need for circumferential welds in that region. Also, a surveillance program will be implemented to monitor changes in the thick sections of the vessel wall. It has already been confirmed by one-dimensional transport calculations that the fast neutron irradiation damage of the vessel shell would be within the limit in a 100-year period [4]. Detailed three-dimensional numerical analyses, including the effects of penetrations, vessel weight, and thermal stresses, should be further conducted to evaluate the reliability of the vessel. The vessel is expected to be fabricated by forging in Japan Steel Works (JSW).

Further investigations on the Super LWR RPV should be carried out to achieve the following.

1. Effective thermal insulation of outlet nozzles through choice of a suitable thermal sleeve design
2. Formal confirmation of manufacturing capabilities
3. Maintenance of mechanical and chemical properties during fabrication
4. Monitoring flaw density in the very thick shell

3.3.3 Internals

The important RPV internals can be seen in Fig. 3.5 [3]. All the RPV internals will be designed for periodic replacement so that very high fluence loadings will not need to be considered. Some of these components, including the lower tie-plate and the control rod guide tubes in the upper head, will be subjected to normal PWR coolant temperature conditions and will be similar to the components typically used in PWRs. However, some of the RPV internals, including the upper tie-plate, the control rod guide tubes in the hot plenum and the RPV hot nozzle sleeve, will be in contact with coolant at the inlet temperature of 280°C on one side and the hot outlet coolant at a temperature of about 500°C on the other side. Possible insulating materials for the vessel internals will need to be explored further.

As for the available materials recommended for vessel internals, three factors will affect the properties and choice of the structural materials for the fabrication of RPV internals. These factors are the effects of irradiation, high temperature exposure, and interactions with both the subcritical and supercritical water environment to which they are exposed. An extensive testing and evaluation program will be required to assess the effects that these factors have on the properties of the potential materials for Super LWR construction to enable a preliminary selection of the most promising materials to be made and to then qualify those selected for the service conditions required.

3.3.4 Turbine

For the Super LWRs, the coolant is heated to above 500°C and delivered to a power conversion cycle, which blends LWR and supercritical FPP technology; high, intermediate and low pressure (HP, IP, and LP) turbines are employed with two reheating cycles. The Super LWR thermal recycle characteristic is presented in Sect. 3.4.

The Super LWRs can utilize the existing mature technology of the supercritical turbine from supercritical water cooled FPPs, so significant research in this area is not needed. Table 3.2 summarizes the worldwide distribution of fossil-fired supercritical plants. Most new coal-fired power plants are supercritical. Design and developments of supercritical FPPs are introduced in Appendix A of this book.

The physical boundaries on improving the turbine internal efficiency by optimizing the flow characteristics of the blades and other components have almost been reached. Large-scale conversion to innovative sealing technologies, such as brush-type glands or the use of abrasive coatings, will contribute only marginally to further enhancing overall efficiency.

A further increase in steam temperature, on the other hand, still holds promise of worthwhile improvements in efficiency, and for this reason it will be one of the main thrusts in the ongoing developments of steam turbine technology in the coming years. The efforts being made by manufacturers and operators regarding the power plant initiative maximum efficiency are geared toward supercritical steam parameters with temperatures up to 700°C. Progress made in materials technology and in casting and forging techniques has led to the development of steels for rotors, casings and turbine blades capable of operating reliably at these steam conditions.

The temperature of 700°C goes beyond the present application ranges of ferritic and austenitic steels used until now and calls for innovative material developments and novel constructions using nickel-based materials. The areas exposed to the highest temperatures in the HP turbine are made of suitably temperature-resistant materials [5]. Intelligent cooling approaches will have to be devised to make it technically possible to cope with these high temperatures, while at the same time keeping the cost to a reasonable level in fabrication. Even the introduction of thermal barrier coatings, as used in gas turbine design, may catch on. In this context,

Table 3.2 Coal-fired SC plants worldwide

Country/region	Number of units	Installed capacity (GWe)
USA	149	106
Japan	108	68
Eastern Europe	123	52
Western Europe	53	29
Other countries	29	14
Total	462	269

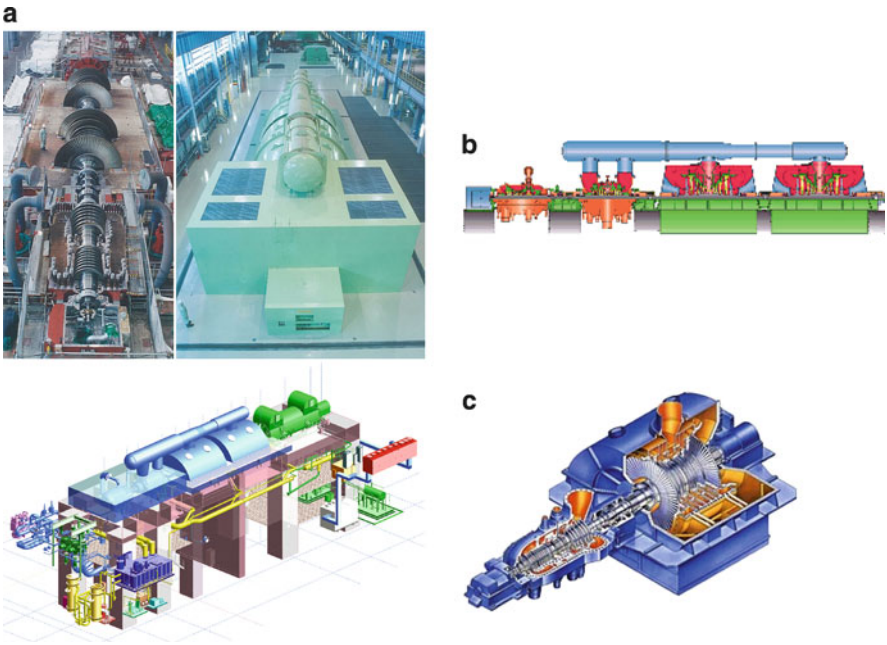


Fig. 3.6 Supercritical steam turbines of main venders in Japan. (**a**) Supercritical steam turbines of Hitachi, Ltd (Taken from http://www.power-hitachi.com/products/ffp/st/fortpp.html and used with permission from Hitachi, Ltd). (**b**) Supercritical steam turbines of Toshiba Corporation (Taken from http://www3.toshiba.co.jp/power/english/thermal/index.htm and used with permission from Toshiba Corporation). (**c**) Supercritical steam turbines of Mitsubishi Heavy Industries, Ltd (Taken from http://www.mhi.co.jp/en/products/category/steam_turbine.html and used with permission from Mitsubishi Heavy Industries, Ltd)

besides the challenge of how to manufacture the large components involved, there is also the challenge of how to make it possible to weld these high temperature materials together. Figure 3.6a–c show the supercritical steam turbines which have been manufactured by the major venders in Japan.

The pumps adopted in Super LWR plant systems include the condensate, booster, and main feedwater pumps. The main feedwater pumps will be low flow and high head pumps located on the feedwater lines between the LP heater and HP heater outside the containment, and they are expected to operate at approximately 190°C. The purpose of the feedwater pumps (reactor coolant pumps) is to provide forced primary coolant flow to remove the heat generated by the fission process. The material candidates for the pump casing are a forged low alloy steel and candidates for pump internals are high strength casting alloy. An austenitic cladding with controlled delta ferrite content would be required if a low alloy steel is selected. Alternatively, an austenitic stainless steel such as SA-336 Gr F304 could be considered.

3.3.5 Steam Lines and Candidate Materials

Due to the higher steam density, only two small steam lines are needed for the large size Super LWRs compared with four lines for LWRs of comparable power, which further reduces the capital cost of the Super LWRs.

As for the material selection for steam piping lines, the experiences with supercritical FPPs can be referred and some development of this issue can be found in Appendix A of this book.

3.4 Plant Heat Balance

3.4.1 Super LWR Steam Cycle Characteristics

A conceptual study of the power conversion cycle for the Super LWRs is necessary to identify an optimal configuration for the goals of thermal efficiency and electric power output maximization and capital cost minimization. Particular attention is also given to ensure that all components are either commercially available or within current design capabilities.

As mentioned in the previous section, the Super LWR system has a power conversion cycle that is very similar to that of a supercritical coal-fired plant, with the boiler replaced by the nuclear reactor. At the same time, the Super LWR plant system is also similar to an ABWR. So the design of the Super LWR power conversion cycle is the combination of that of the ABWR and FPP to some degree. Figure 3.7 shows the Balance of Plant (BOP) system configuration for an ABWR, FPP, and Super LWR. The HP, IP, and LP turbines are used like the supercritical pressure FPPs. Compared with the ABWR, one IP turbine takes the place of one LP turbine. The Super LWR steam cycle designed here is a two-stage reheating and eight-stage regenerative system. Steam has to be reheated by the main steam in the Super LWR like ABWR, while steam is reheated by returning it to the boiler in the FPP. Thus, the moisture separator reheater is installed between the IP and LP turbines.

In the Super LWR plant, the main steam from the core is fed to the HP turbine. At the HP turbine, regenerative steam is extracted from two points to be led to the first and second HP feedwater heaters. Before entering the HP turbine, part of the main steam is also extracted for the second reheater. Then, the steam exhausted from the HP turbine enters the IP turbine, where regenerative steam is extracted from two points to be led to the third and fourth HP feedwater heaters. The steam out of the IP turbine is fed to the moisture separator reheater, where its wetness is separated and then reheated twice to be superheated steam. Finally, the steam enters the LP turbines, where regenerative steam is extracted from four points and led to four LP feedwater heaters. The steam out of the LP turbines is condensed to water in the condenser. The water is pressurized by the LP condensate pumps and mixed

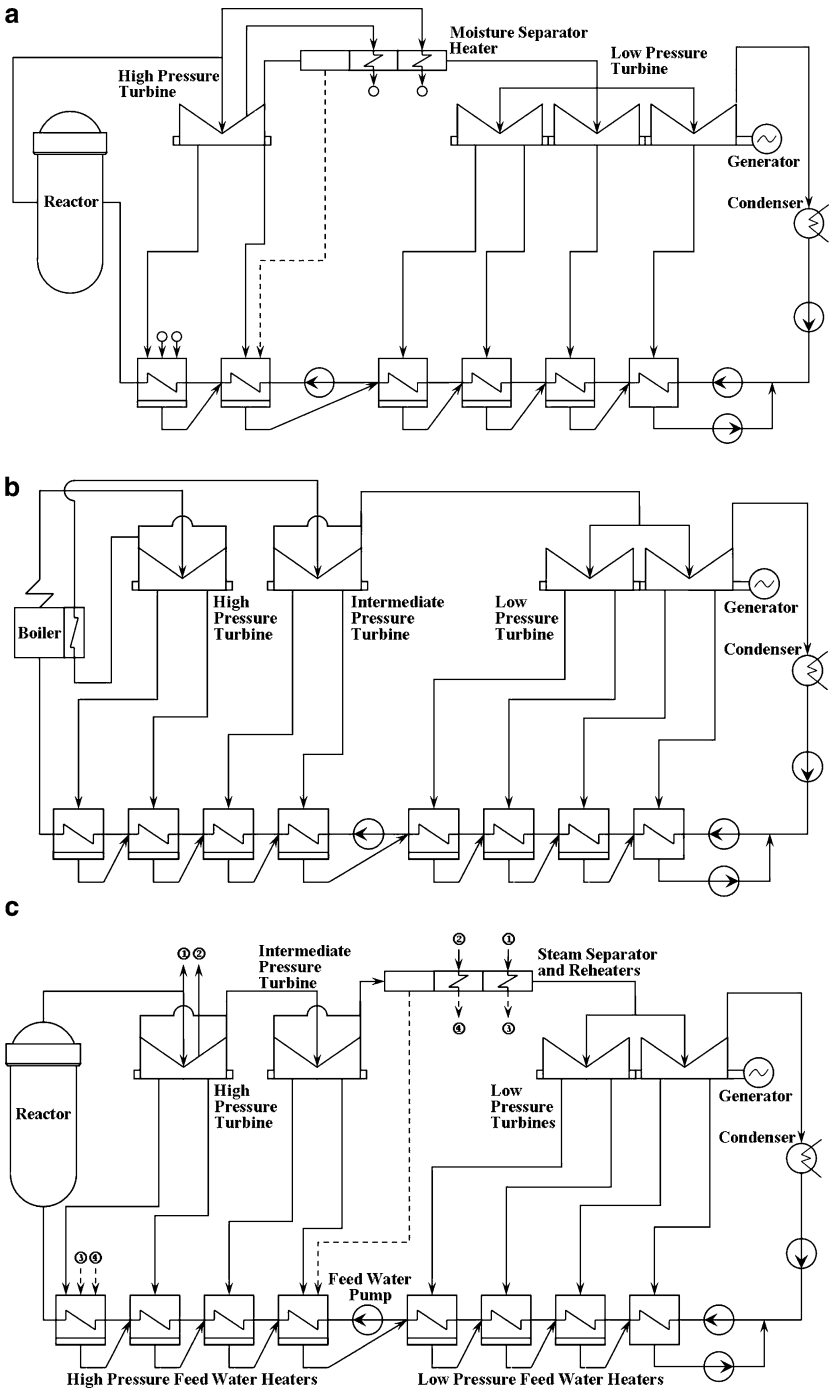


Fig. 3.7 BOP system configuration for ABWR, FPP, and Super LWR plants. (**a**) ABWR, (**b**) FPP, and (**c**) Super LWR

with regenerative steam. Then, the feedwater is pressurized by the HP condensate pumps and heated by the four LP feedwater heaters. The feedwater is pressurized again by the booster and main feedwater pumps and heated by four HP feedwater heaters before entering the reactor vessel. The eight extraction points in total are selected from turbine stages to achieve the highest thermal efficiency. There are one HP turbine casing, one IP turbine casing, and two LP turbine casings. Each turbine has a two-flow system.

Overall, the main steam cycle characteristics of the Super LWR can be summarized as the following.

1. Reduced rotation speed, 1,500 or 1,800 rpm, single-shaft turbine-generator
2. One HP turbine, one IP turbine, and two LP turbines
3. A moisture separator reheater with two reheating stages, between the IP and LP turbines
4. Eight feedwater heaters (four HP and four LP) raising feedwater temperature to 280°C
5. Two turbine-driven feedwater pumps operating at about 190°C

3.4.2 Thermal Efficiency Evaluation

The evaluation procedure for thermal efficiency is shown in Fig. 3.8 [3]. The core outlet temperature is given from the core design. Eight extraction points are selected in HP, IP, and LP turbine stages. Then, the steam conditions in each part of the steam cycle are calculated considering the efficiencies of the turbine, the moisture separator reheaters, condenser, pumps, feedwater heaters, and so on. The heat balance and the mass flow rate are calculated in each part of the steam cycle as well. The exhaust loss is also calculated. The steam with a high velocity of about 300 m/s at the last stage in the LP turbines is exhausted to the condenser. This exhaust loss reduces steam work in the LP turbines and decreases the thermal efficiency. Finally, thermal efficiency is calculated from steam conditions and mass flow rates in all parts of the steam cycle. The extraction points are decided to give the highest thermal efficiency.

An example of the heat balance diagram and corresponding T-S chart of the Super LWR steam cycle are depicted in Fig. 3.9 [3]. According to the engineering thermodynamic knowledge, the thermal efficiency of the Super LWR steam cycle depicted in Fig. 3.10 [3] can be finally calculated by (3.1).

$$\begin{aligned}\eta = {} & ((m_0 - m_{r_1})(H_{1'} - H_{x_4}) - (m_1 + m_{r_1})(H_{x_1} - H_{x_4}) - m_2(H_{x_2} - H_{x_4}) \\ & - m_3(H_{x_3} - H_{x_4}) + (m_0 - m_1 - m_2 - m_3 - m_4 - m_s - m_{r_1} - m_{r_2}) \\ & \times (H_{r_2} - H_2) - m_5(H_{x_5} - H_2) - m_6(H_{x_6} - H_2) - m_7(H_{x_7} - H_2) \\ & - m_8(H_{x_8} - H_2) - m_0(H_4 - H_{w_5}) - m_c(H_{4'} - H_3) \\ & - m_0(H_{4'''} - H_{4''}))/m_0(H_1 - H_{w_1}).\end{aligned} \tag{3.1}$$

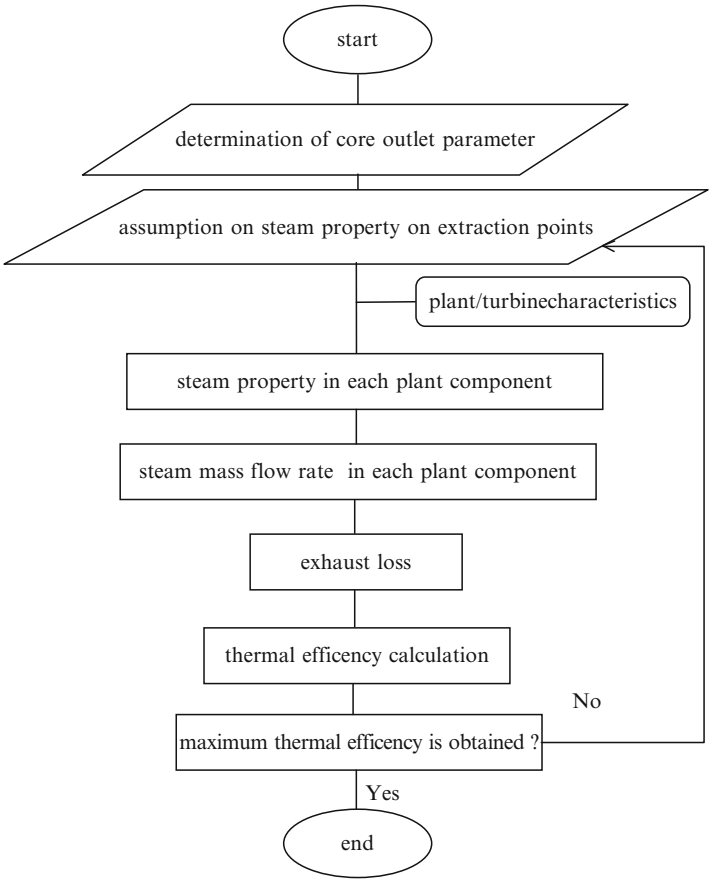


Fig. 3.8 Calculation procedure for thermal efficiency of Super LWR. (Taken from [4])

Figure 3.10 [5] shows an example of the detailed heat balance characteristics of a 1000MWe class Super LWR. Steam conditions and mass flow rates in all parts of the steam cycle are provided in the figure. According to (3.1), the gross plant thermal efficiency of a low temperature Super LWR steam cycle with core outlet temperature of 397°C is 40.7%, which is 18% higher than that of the ABWR efficiency of 34.5%.

In other studies, another simple calculation method for thermal efficiency has also been used. First, thermal efficiencies of Carnot and Rankine cycles were calculated with the given steam conditions. Second, an averaged value between these efficiencies was obtained and a factor was calculated so that the thermal efficiency of the current BWR was correctly estimated by this method. If the core outlet temperature is given as 400°C, the thermal efficiencies obtained by the

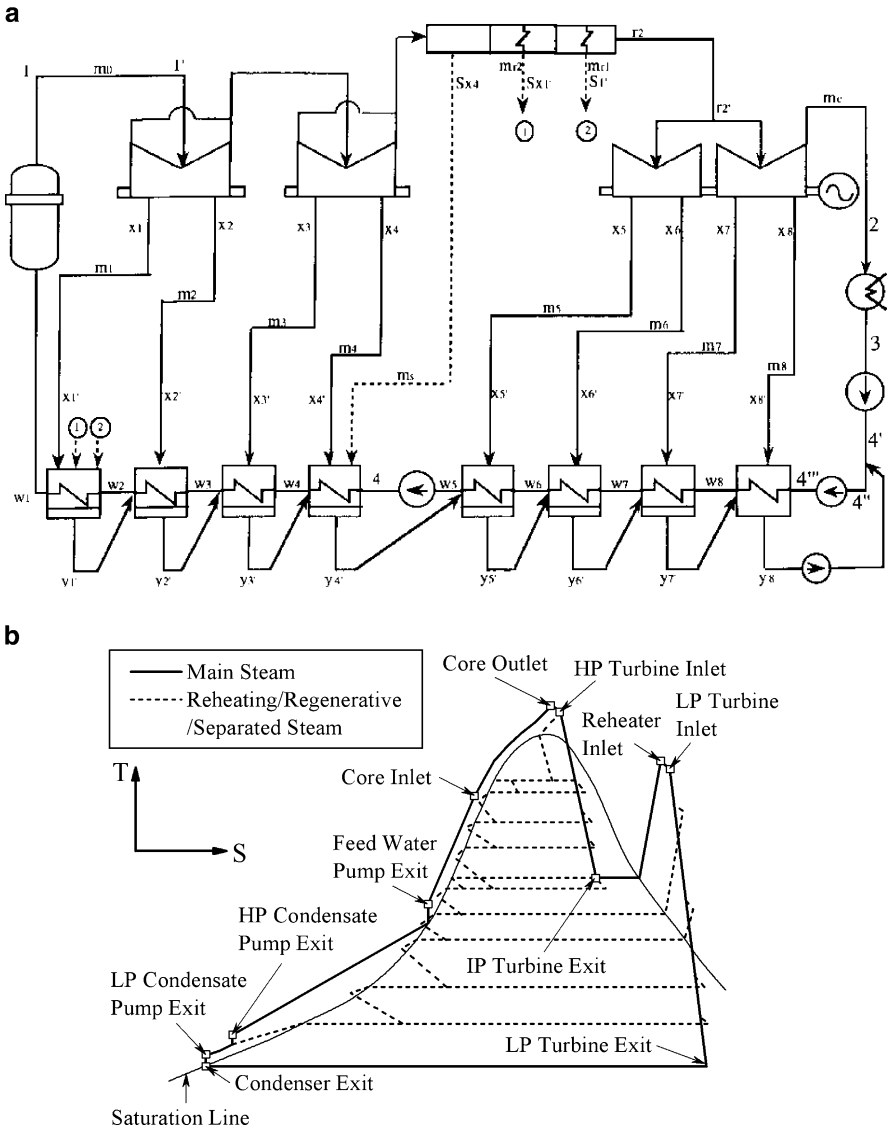


Fig. 3.9 Super LWR heat balance diagram and an example of corresponding T-S chart. (Taken from [4].) (**a**) Heat balance diagram and (**b**) T-S chart

simple and the present accurate calculations are 40.2 and 41.0%, respectively [6]. If the core outlet temperature is given as 600°C, the thermal efficiencies obtained by the simple and the present accurate calculations are 45.7 and 45.1%, respectively [6]. There is no large deviation between their results.

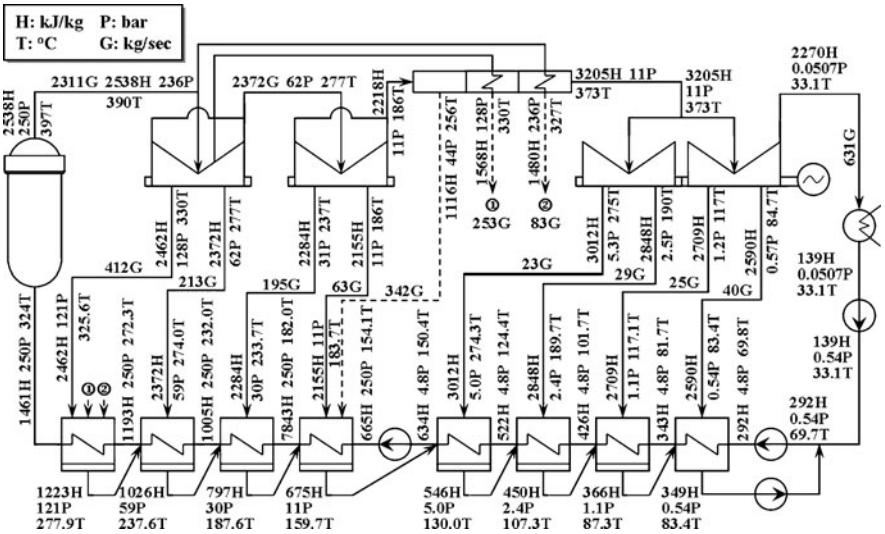


Fig. 3.10 Heat balance characteristics of a low temperature Super LWR steam cycle. (Taken from [4])

3.4.3 Factors Influencing Thermal Efficiency

3.4.3.1 Core Outlet Temperature

Increase in thermal efficiency with the core outlet temperature is shown in Fig. 3.11. The thermal efficiency is about 41% in the Super LWR plant with the core outlet temperature of 400°C. It is about 45% when the core outlet temperature is 566°C, the same outlet temperature as the supercritical FPP. The present design criteria require the outlet temperature be higher than 500°C, which corresponds to a thermal efficiency higher than 43.8%.

Given that the extraction points are decided to give the highest thermal efficiency, the relationship between the reheating steam flow rate in the moisture separator and the core outlet temperature is shown in Fig. 3.12a. It can be found that, with the core outlet temperature increasing from 400 to 600°C, the second extracted reheating steam flow rate increases from 5 to 15% of the total steam flow rate, however, the first extracted reheating steam flow rate slightly decreases. Thus, the total extracted reheating steam flow rate increases from 15 to 23% corresponding to the core outlet temperature varying from 400 to 600°C. The relationship between the core outlet temperature and the ratio of regenerating steam mass flow rate to the total flow rate is shown in Fig. 3.12b. The extracted regenerating steam mass flow rate from the HP turbine and the IP turbine obviously decreases with the increased core outlet temperature. The regenerating steam extracted from the LP turbine is nearly invariable.

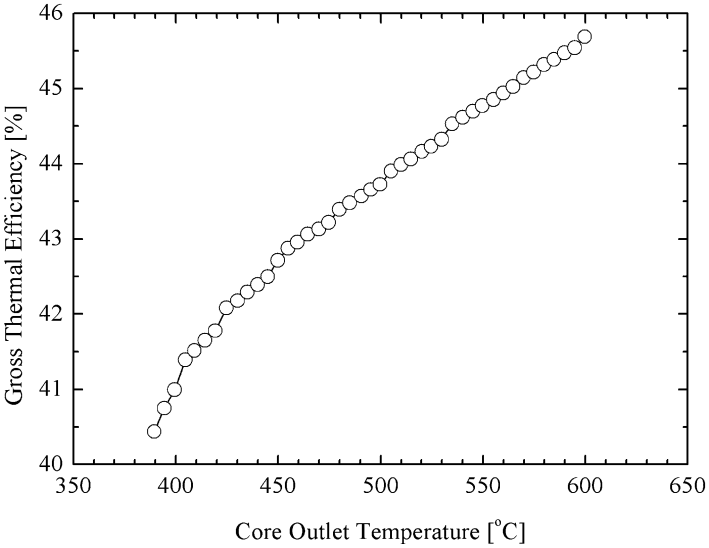


Fig. 3.11 Increase in thermal efficiency with core outlet temperature

At the same time, the ratio of extracted steam flow rate from the moisture separator to the fourth HP feedwater heater (S_{x4} in Fig. 3.9a [4]) should be greatly reduced when enhancing the core outlet temperature. As shown in Fig. 3.12c, when the core outlet temperature is set at 400°C, S_{x4} is about 20% of the total flow rate, while S_{x4} is nearly 0 when the core outlet temperature is raised to 600°C. Again, it should be remembered that the extraction points are decided to obtain the highest thermal efficiency.

As shown in Fig. 3.12d, the steam flow rate through the condensers increases with the core outlet temperature.

The relationship between the overall branch steam flow rate and the core outlet temperature is shown in Fig. 3.12e.

3.4.3.2 Core Inlet Temperature

If the core outlet temperature is given and the extraction points are selected to achieve the highest thermal efficiency, the core inlet temperature is decided from the first HP feedwater heater. In general, if the core inlet temperature is high while keeping the core outlet temperature constant, the heat absorption of the steam cycle decreases. This makes thermal efficiency high. However, the work of the steam cycle also decreases because more steam is extracted from upper stages of the turbine. The highest thermal efficiency is obtained when these effects are balanced. Changes of thermal efficiency with the core inlet temperature, where the core outlet temperature is constant, are shown in Fig. 3.13. Regardless of the core outlet temperature, the best core inlet temperature for obtaining the highest thermal

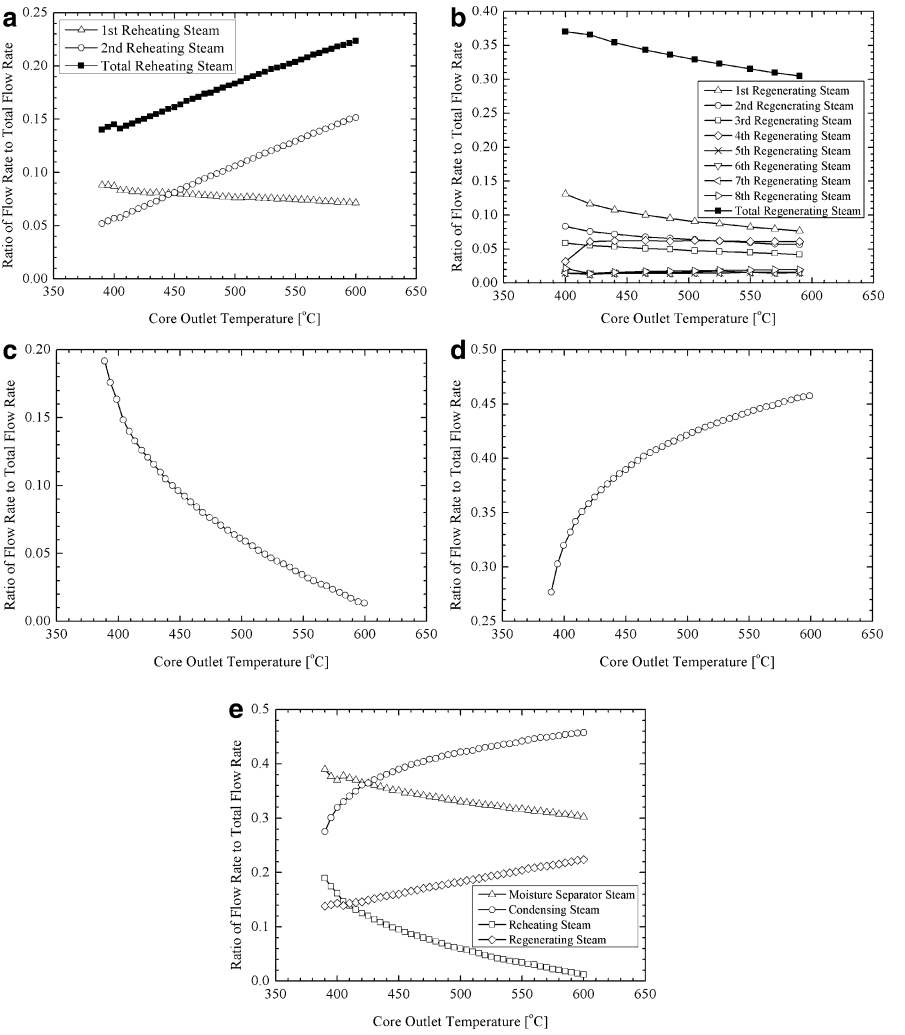


Fig. 3.12 Relationships between steam flow rate ratios and core outlet temperature. (**a**) Reheating steam flow rate vs. core outlet temperature. (**b**) Regenerating steam flow rate vs. core outlet temperature. (**c**) Extracted steam flow rate from moisture separator vs. core outlet temperature. (**d**) Steam flow rate in condensers vs. core outlet temperature. (**e**) Overall branch steam flow rate vs. core outlet temperature

efficiency is about 295°C. However, the variation of thermal efficiency is not so large around 295°C, especially when the core outlet temperature is 600°C. Here, the core inlet coolant temperature is not continuous because extraction points are selected among turbine stages. For the case of the TC4F-52 type turbine, there are five turbine stages in the HP turbine, four in the IP turbine, and seven in the LP turbines. In reality, if there are many turbine stages, the best core inlet temperature

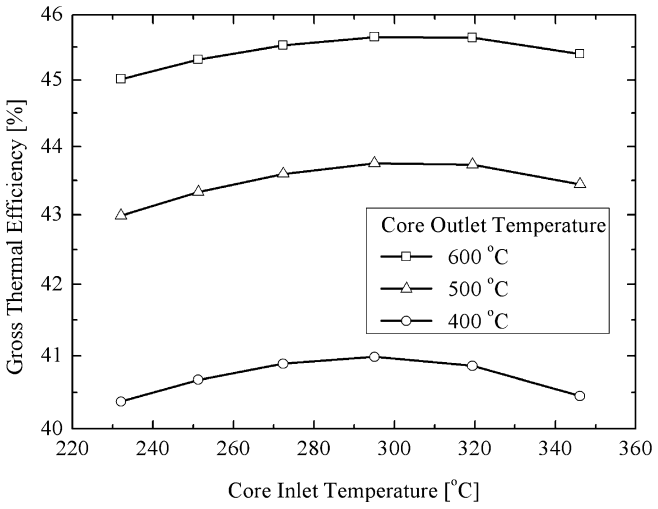


Fig. 3.13 Relationship between thermal efficiency and core inlet temperature

obtaining the highest thermal efficiency may be higher as the core outlet temperature is higher.

The feedwater temperature can be gradually decreased by removing the HP feedwater heaters [6]. When the feedwater temperature is 280°C, the BOP requires four HP and four LP low pressure feedwater heaters. When it is 210°C, the cycle has two HP and four LP feedwater heaters. There are only four LP feedwater heaters in the case of 150°C.

In supercritical FPPs, high thermal efficiency is favorable because the fuel cost occupies a large fraction in the total power cost. Fuel cost fraction, however, is a relatively small part of the NPP cost. Lowering the feedwater temperature reduces the number of feedwater heaters. This decreases the size of the BOP. The decrease in the coolant flow rate per electric output will be more effective in decreasing the capital cost than increasing the thermal efficiency in the Super LWR. The flow rate of the Super LWR with the outlet temperature around 500°C decreases by 31% when the feedwater temperature is 210°C and by 35% when it is 150°C, compared with that of the ABWR [7]. The size of the turbines and the capacities of the pumps will decrease with the feedwater flow rate.

3.5 Summary

The main characteristics of Super LWR plant components were briefly introduced with comparison with conventional PWRs, BWRs, and FPPs. The plant system is compact and greatly simplified from those of LWRs which will contribute to the reduction of plant capital cost. The relatively higher thermal efficiency also ensures high economic performance.

References

1. Y. Oka, S. Koshizuka, Y. Ishiwatari and A. Yamaji, "Overview of Design Studies of High Temperature Reactor Cooled by Supercritical Light Water at the University of Tokyo," *Proc. Int. Conf. Global Environment and Advanced Nuclear Power Plants (GENES4/ANP2003)*, Kyoto, Japan, September 15–19, 2003, Paper-1168 (2003)
2. Y. Ishiwatari, Y. Oka and S. Koshizuka, "Safety of the Super LWR," *Nuclear Engineering and Technology*, Vol. 39(4), 257–272 (2007)
3. Y. Ishiwatari, Y. Yamakawa, et al., "Research and Development of a Super Fast Reactor (1) Overview and High-Temperature Structural Design," *Proc. 16th PBNC*, Aomori, Japan, October 13–18, 2008, P16P1290 (2008)
4. K. Dobashi, "Conceptual design of supercritical light water cooled and moderated reactor," Doctoral Thesis, The University of Tokyo (1998) (in Japanese)
5. U. Wilfried, "The Situation in Steam Turbine Construction and Current Development. Steam Turbine Development Trends," *Power Plant: Operation Maintenance and Materials Issues*, Vol. 2(3) (2003)
6. K. Dobashi, Y. Oka and S. Koshizuka, "Core and Plant Design of the Power Reactor Cooled and Moderated by Supercritical Light Water with Single Tube Water Rods," *Annals of Nuclear Energy*, Vol. 24(16), 1281–1300 (1997)
7. K. Dobashi, Y. Oka and S. Koshizuka, "Conceptual Design of a High Temperature Power Reactor Cooled and Moderated by Supercritical Light Water," *Proc. ICONE-6*, San Diego, CA, May 10–15, 1998, ICONE-6232 (1998)

Chapter 4
Plant Dynamics and Control

4.1 Introduction

The Super LWR adopts the once-through coolant cycle as the supercritical fossil fuel-fired power plants (FPPs) do. The Super LWR has no steam generator, pressurizer, steam-water separator, steam dryer, or recirculation system. Its plant dynamics differ from those of conventional LWRs. The core outlet temperature and therefore the main steam temperature change with the power to flow rate ratio in the core while they are equal to the saturation temperature of the corresponding pressures in BWRs. In contrast to FPPs, reactivity feedbacks from fuel temperature and coolant density exist in the Super LWR. In this chapter, the plant dynamics of the Super LWR are explained by analyzing its responses against various perturbations using a plant transient analysis code SPRAT-DOWN. Based on the plant dynamics, the plant control system of the Super LWR is designed. The controllability of the Super LWR is assessed by the plant stability analyses with the designed control system as done in LWRs.

4.2 Analysis Method for Plant Dynamics

From the beginning of the conceptual study on supercritical water cooled reactors, several plant transient analysis codes have been developed, modified, and applied to them [1–9]. The general name of these codes is Supercritical Pressure Reactor Accident and Transient analysis code (SPRAT). SPRAT mainly calculates mass and energy conservations, fuel rod heat conduction, and point kinetics. The relation among these calculations is shown in Fig. 4.1. SPRAT can deal with flow, pressure, and reactivity induced transients and accidents at supercritical pressure. The flow chart is shown in Fig. 4.2.

As mentioned in Chap. 2, the fuel assemblies of the Super LWR contain many water rods for neutron moderation. The water rods are cooled by downward flow.

Y. Oka et al., *Super Light Water Reactors and Super Fast Reactors*,
DOI 10.1007/978-1-4419-6035-1_4, © Springer Science+Business Media, LLC 2010

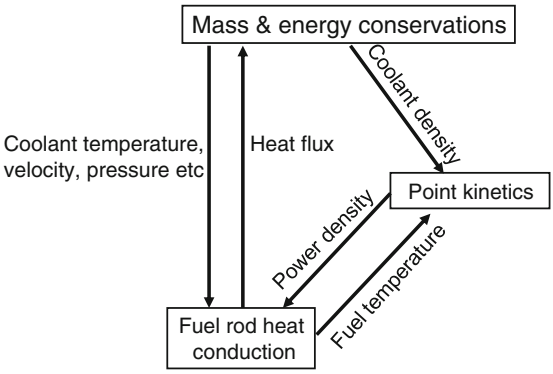


Fig. 4.1 Basic structure of SPRAT

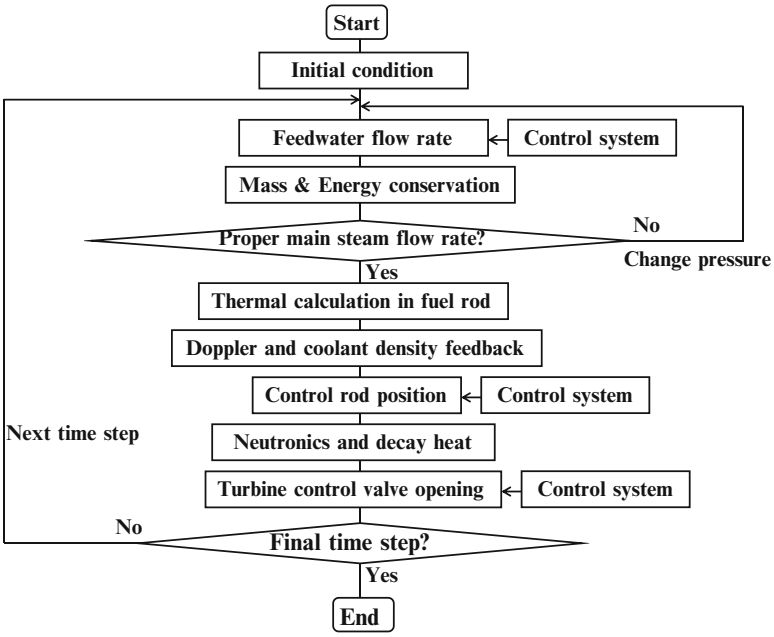


Fig. 4.2 Flow chart of SPRAT

The basic SPRAT was modified to deal with water rods cooled by downward flow [6]. It is called SPRAT-DOWN [7–9]. The coolant flow scheme is shown in Fig. 4.3. The fuel channel and the water rod channel are modeled as single channels with 20 meshes. At normal operation, 30% of the feedwater is led to the water rod channel through the upper dome and the control rod guide tube. The lower plenum, including the downcomer, is divided into 20 meshes. The upper plenum, including the main steam line, is also divided into 20 nodes. The main feedwater line and the

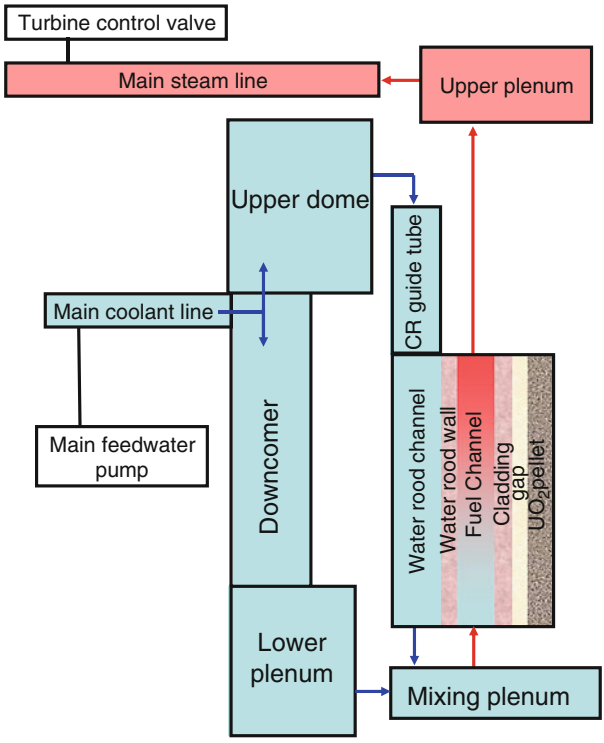


Fig. 4.3 Coolant flow scheme in SPRAT-DOWN

upper dome are each divided into ten nodes. Governing equations of mass and energy conservations are shown below.

$$\frac{\partial \rho(z,t)}{\partial t} + \frac{\partial G(z,t)}{\partial z} = 0, \tag{4.1}$$

$$\frac{\partial \{\rho(z,t)h(z,t)\}}{\partial t} + \frac{\partial G(z,t)h(z,t)}{\partial z} = \frac{1}{A_\mathrm{f}}\{l_\mathrm{f} Q''(z,t) - l_\mathrm{w} Q''_\mathrm{w}(z,t)\}, \tag{4.2}$$

$$\frac{\partial \{\rho(z,t)h(z,t)\}}{\partial t} + \frac{\partial G(z,t)h(z,t)}{\partial z} = \frac{1}{A_\mathrm{w}}\, l_\mathrm{w} Q''_\mathrm{w}(z,t), \tag{4.3}$$

$$\frac{\partial \{\rho(z,t)h(z,t)\}}{\partial t} + \frac{\partial G(z,t)h(z,t)}{\partial z} = 0, \tag{4.4}$$

where z is the position (m), t is the time (s), $\rho(z,t)$ is the density (kg/m^3), $G(z,t)$ is the mass flux (kg/m^2/s), $h(z,t)$ is the specific enthalpy (J/kg), $Q''(z,t)$ is the heat flux on fuel rod surface (W/m^2), $Q''_\mathrm{w}(z,t)$ is the heat flux between coolant and moderator (W/m^2), l_f is the wetted perimeter of fuel rod (m), l_w is the average wetted perimeter

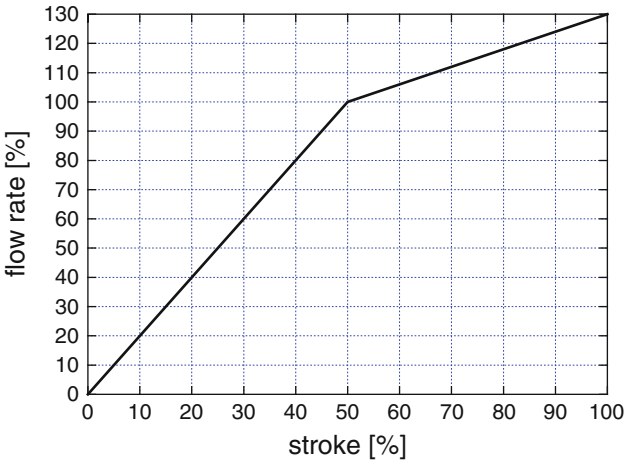


Fig. 4.4 Change of steam flow rate with turbine control valve stroke. (Taken from [6] and used with permission from Atomic Energy Society of Japan)

of water rod inner/outer surfaces (m), A_f is the flow area of fuel rod channel (m), and A_w is the flow area of water rod channel (m).

Equations (4.2), (4.3), and (4.4) are for the fuel channel, water rod channel, and outside core, respectively. The governing equations are discretized using the upwind difference scheme and the full implicit scheme. The boundary conditions are the feedwater flow rate, the feedwater temperature, and the turbine inlet flow rate. The characteristic of the turbine control valve, expressed as the change of steam flow rate, is shown in Fig. 4.4 [6]. The feedwater flow rate changes with the core pressure as shown in Fig. 4.5 [6].

The radial heat transfer model is shown in Fig. 4.6. The fuel pellet is divided into several rings and heat balance is calculated among them.

$$\rho V_i C_p \frac{T_i^{k+1} - T_i^k}{\Delta t} = 2\pi \Delta z \left(r_{i-1} Q''^k_{i-1} - r_i Q''^k_i \right) + Q'''^k V_i, \tag{4.5}$$

where k is the time step, Δt is the time step size (s) (10^{-2} s in general), Δz is the axial mesh size (m) (0.1–0.2 m in general), i is the radial ring number, T_i^k is the average temperature of ith ring (K), Q''^k_i is the heat flux on outer surface of ith ring (W/m^2), r_i is the outer diameter of ith ring (m), V_i is the volume of ith ring (m^3), ρ is the density of fuel pellet (kg/m^3), and C_p is the specific heat of fuel pellet (J/K/kg).

The power density of the fuel pellet at nth axial mesh is calculated as

$$Q'''^k_n = \frac{Q'_{\max}}{\pi {r_4}^2} \cos\left(\pi \frac{0.5N_z - (n - 1/2)}{1.06N_z} \right) \frac{N}{N^0}, \tag{4.6}$$

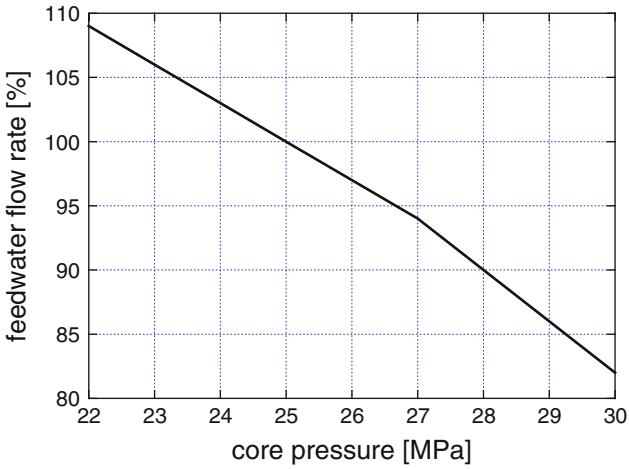


Fig. 4.5 Change of feedwater flow rate with core pressure. (Taken from [6] and used with permission from Atomic Energy Society of Japan)

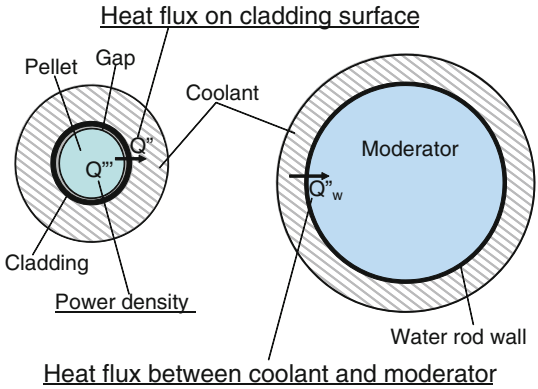


Fig. 4.6 Radial heat transfer model

where N_z is the number of axial meshes (m) (20–40 in general), $Q'_{\max}$ is the peak linear heat generation rate (W/m), and N/N^0 is the ratio of neutron number to initial value (equal to relative power).

The heat flux on the outer surface of the ith ring is calculated as

$$Q''^k_i = \frac{2\pi\Delta z K_f \left(\frac{T_i^{k-1}+T_{i+1}^{k-1}}{2}\right)}{\ln(r_{i+1}/r_i)}(T_i^{k-1} - T_{i+1}^{k-1}), \tag{4.7}$$

where K_f is the thermal conductivity of fuel pellet (W/m K).

Gap heat transfer and heat conduction in the cladding are also calculated. The heat flux on the cladding surface is calculated using the cladding temperature, coolant temperature, and the heat transfer coefficient. The heat flux between the coolant and moderator is calculated as

Table 4.1 Parameters of reactor dynamics of Super LWR

$\Lambda = 4.3 \times 10^{-5}$ s		
$\sum_{i=1}^{6} \beta_i = 0.064$		
i	$\frac{\beta_i}{\sum_{i=1}^{6} \beta_i}$	λ_i (s^{-1})
1	0.038	0.0127
2	0.213	0.0317
3	0.188	0.1155
4	0.407	0.3108
5	0.128	1.3975
6	0.026	3.8723

$$Q''^{k}_{n,\mathrm{w}} = \frac{2\pi(T^{k}_{n} - T^{k}_{n,\mathrm{w}})}{\frac{1}{h_{\mathrm{sw1}}{}^{k}_{n} r_{\mathrm{wout}}} + \frac{\ln(r_{\mathrm{wout}}/r_{\mathrm{win}})}{K_{\mathrm{cw}}} + \frac{1}{h_{\mathrm{sw2}}{}^{k}_{n} r_{\mathrm{win}}}}, \tag{4.8}$$

where T^{k}_{n} is the coolant temperature (K), $T^{k}_{n,\mathrm{w}}$ is the moderator temperature (K), $h_{\mathrm{sw1}}{}^{k}_{n}$ is the heat transfer coefficient for water rod outer surface (W/m^2 K), $h_{\mathrm{sw2}}{}^{k}_{n}$ is the heat transfer coefficient for water rod inner surface (W/m^2 K), K_{c} is the thermal conductivity of water rod wall (W/m K), r_{cin} is the inner diameter of water rod converted to equivalent circle (m), and r_{cout} is the outer diameter of water rod converted to equivalent circle (m).

The heat transfer coefficient is calculated using the Oka–Koshizuka correlation [5] that was described in Sect. 2.3.2.1.

The point kinetics model is used. The dynamic parameters are shown in Table 4.1. They are similar to those of typical LWRs. Since the Super LWR is a water-cooled thermal reactor just like LWRs, where coolant density and fuel temperature dominate the reactivity feedback, only these effects are considered. The space effect on reactivity feedback is considered by calculating the "average" coolant density and the "average" pellet temperature at each time step. The contribution of each mesh to the "average" value is proportional to the square of the linear power density (cosine distribution). Since supercritical pressure fluid has no phase change and the relation between temperature and density is not linear, using the moderator temperature coefficient or the void reactivity coefficient is not suitable for the Super LWR. The density coefficient is used. It is a function of the average coolant density as shown in Fig. 4.7. It was determined based on the 3-D core design. The Doppler coefficient as a function of the "average" pellet temperature is shown in Fig. 4.8. It is also obtained from the 3-D core design.

4.3 Plant Dynamics Without a Control System

It is necessary to analyze the responses of the plant against stepwise perturbations in the components used for plant control. In BWRs, these components are the control rods, the recirculation pumps, the feedwater pumps and the turbine control valves.

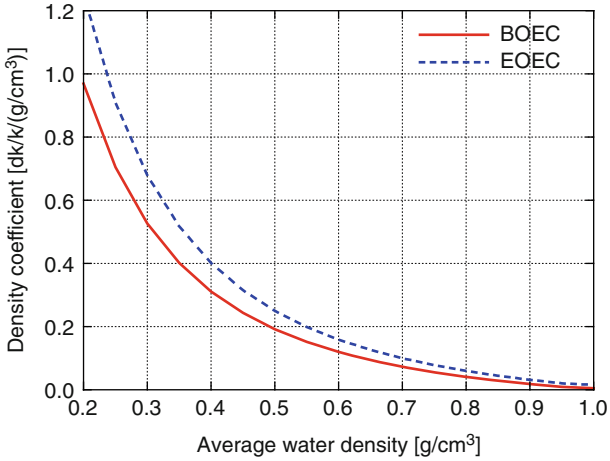


Fig. 4.7 Density coefficient used for plant transient analysis

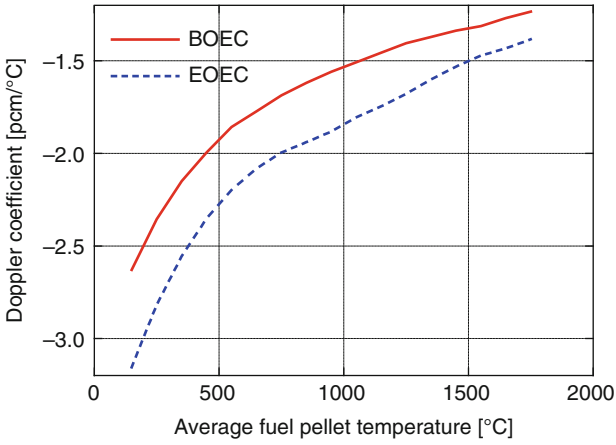


Fig. 4.8 Doppler coefficient used for plant transient analysis

Since the Super LWR is a plant with a direct-steam cycle like BWRs, those components are selected by referring to BWRs. The control rods, the feedwater pumps and the turbine control valves are to be used for plant control of the Super LWR. It is noted that the Super LWR has no recirculation pumps.

Major perturbations are as follows [7].

1. Increase in the reactivity by \$0.1 resulting from withdrawal of a control rod cluster.
2. Decrease in the feedwater flow rate by 5%.
3. Decrease in the main steam flow rate by 5% resulting from closure of the turbine control valves.

Table 4.2 Characteristics of the Super LWR for plant dynamics analysis

Core	
Equivalent diameter/height (m)	3.6/4.2
Number of fuel assemblies	96
Feedwater/average outlet temperature (°C)	280/500
Average/maximum linear heat generation rate (kW/m)	18/39
Reactor pressure vessel, main piping	
RPV inner diameter/thickness/height (m)	4.34/0.35/15
Volume of top dome/upper plenum/lower plenum/downcomer (m^3)	55/24/21/26
Inner diameter of main feedwater lines/main steam line (m)	0.27/0.46
Fuel assembly	
Fuel rod diameter/fuel rod pitch/cladding thickness (mm)	10.2/11.2/0.63
Number of fuel rods/water rods in a fuel assembly	300/36
Plant	
Core pressure/turbine inlet pressure (MPa)	25.0/24.5
Thermal power/electric power (MW)	2,300/1,000
Feedwater flow rate (kg/s) (= main steam line flow rate)	1,190

The responses to these three perturbations are analyzed without a control system. In this chapter, the 1,200 MWe class Super LWR described in Sect. 2.4.5 is scaled down to a 1,000 MWe class plant. Its characteristics are shown in Table 4.2.

4.3.1 Withdrawal of a Control Rod Cluster

A positive reactivity of \$0.1 is inserted stepwise as a reactivity perturbation. The feedwater flow rate and the turbine control valve opening are kept constant. The results are shown in Figs. 4.9 and 4.10. The power quickly increases to 111% of the initial value. It is consistent with the analytical solution of "prompt jump." Then, the power decreases due to reactivity feedbacks from Doppler and coolant density. The main steam temperature changes by following the power. The main steam pressure and the core pressure increase due to increases in the temperature and hence the volume flow rate of the main steam. The fuel channel inlet flow rate changes with the core pressure due to the relation between the feedwater flow rate and the core pressure shown in Fig. 4.4. The plant almost reaches a new steady state in 40 s.

4.3.2 Decrease in Feedwater Flow Rate

The feedwater flow rate decreases stepwise to 95% of the initial value. The control rod position and the turbine control valve opening are kept constant. The results are shown in Figs. 4.11 and 4.12. Due to the once-through coolant cycle, a decrease in the feedwater flow rate directly leads to a decrease in the core coolant flow rate. The main steam temperature increases. The core and main steam pressures

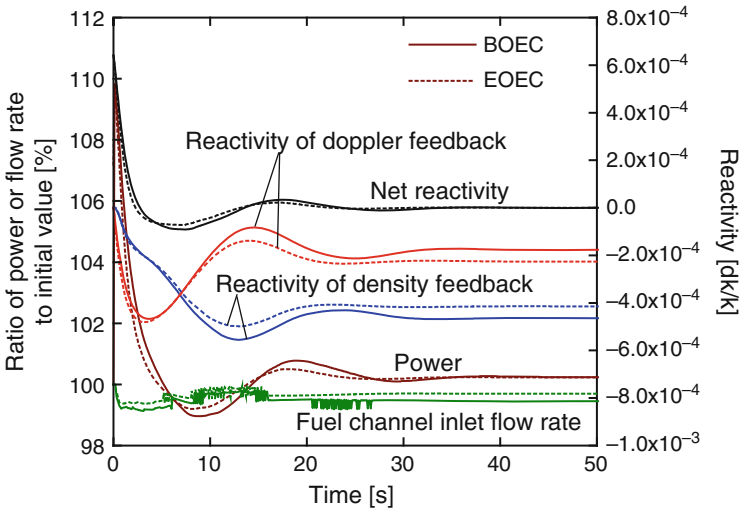


Fig. 4.9 Response to stepwise reactivity insertion (1)

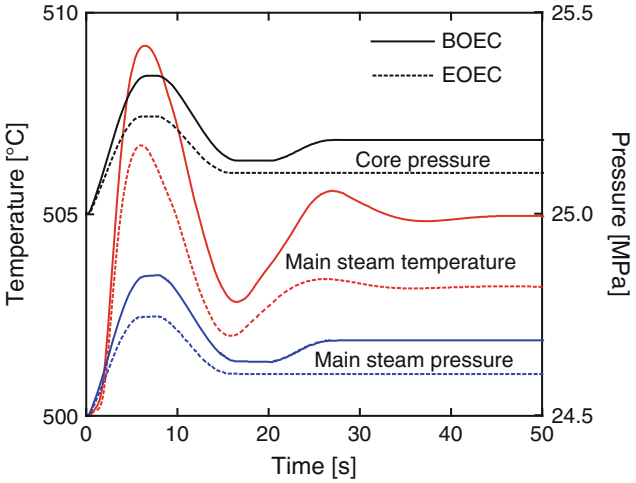


Fig. 4.10 Response to stepwise reactivity insertion (2)

decrease. These responses are different from those of BWRs. The change in the densities is shown in Fig. 4.13. Since the heat transfer is small between the fuel channels and the water rod channels, the change in the moderator density is much smaller than the change in the coolant density. The volume fractions of the moderator and coolant are about 70 and 30%, respectively. The change in the average density and hence the density feedback are small. It is a characteristic of

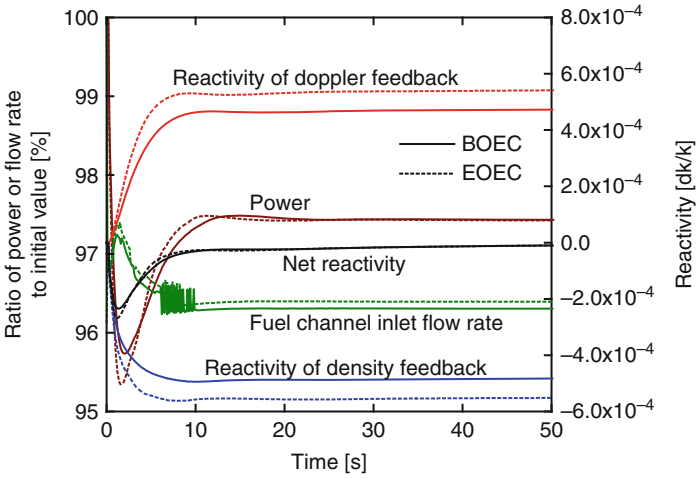


Fig. 4.11 Response to stepwise decrease in feedwater flow rate (1)

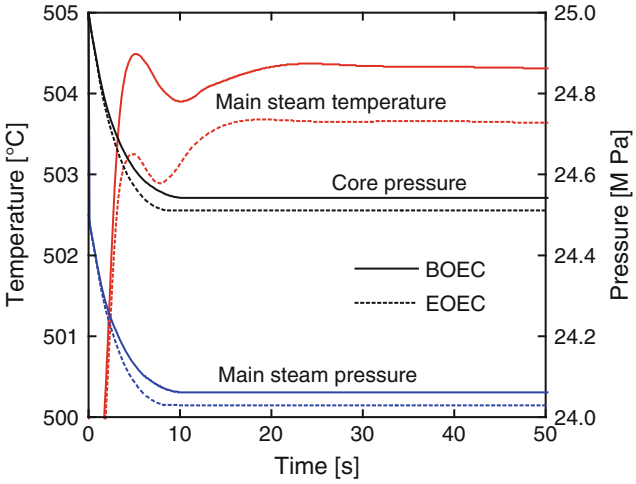


Fig. 4.12 Response to stepwise decrease in feedwater flow rate (2)

the Super LWR that its many water rods make the power rather insensitive to the flow rate. The plant almost reaches a new steady state in 30 s.

4.3.3 Decrease in Turbine Control Valve Opening

The turbine control valve opening decreases stepwise to 95% of the initial value. The control rod position and the feedwater flow rate are kept constant. The results

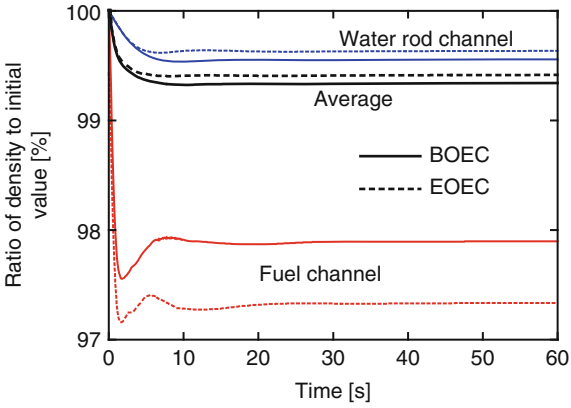


Fig. 4.13 Response to stepwise decrease in feedwater flow rate (3)

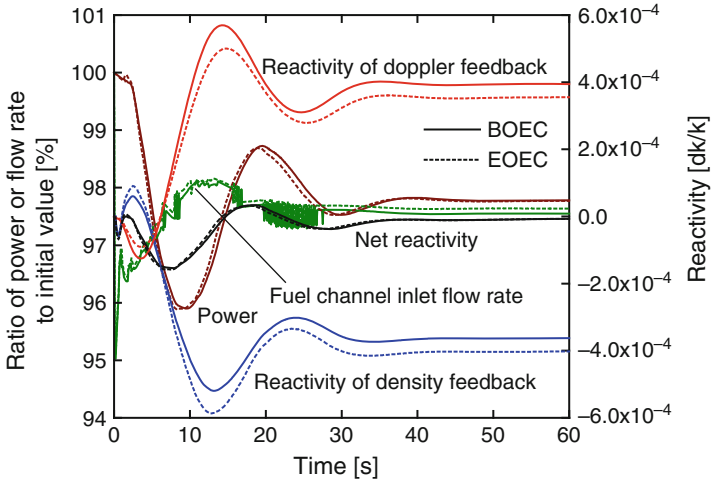


Fig. 4.14 Response to stepwise decrease in turbine control valve opening (1)

are shown in Figs. 4.14 and 4.15. The core and main steam pressures increase due to the valve closure. Since the difference of density between "water" and "steam" is small at supercritical pressure compared to subcritical pressure, the average density of the Super LWR core is less sensitive to the pressure than that of BWRs. Since the closure of the outlet valves leads to a decrease in the coolant flow rate in the core, negative reactivity is inserted due to an increase in the coolant temperature. The influence of the increase in the temperature to the reactivity is larger than that of the pressurization so that the power does not increase but decreases against the valve closure. It is noted that the power of the Super LWR core shows an opposite response to outlet valve closure compared to BWRs where pressurization leads to an increase in the power due to void collapse in the core. The plant almost reaches a new steady state in 40 s.

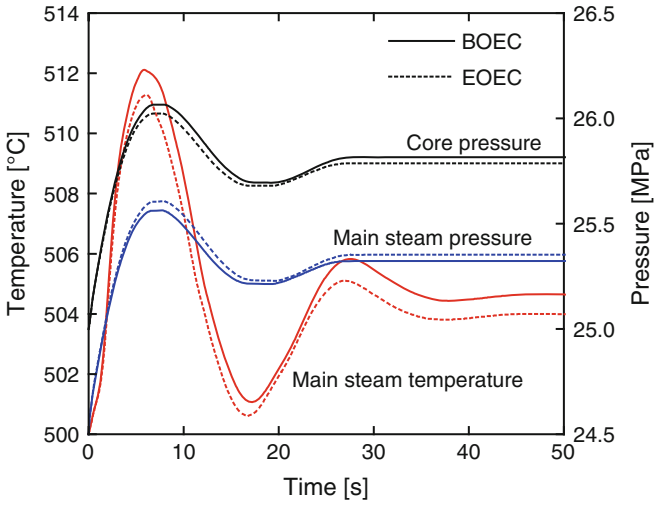


Fig. 4.15 Response to stepwise decrease in turbine control valve opening (2)

4.4 Control System Design

There are two types of plant control strategies for steam cycle power stations. One is the boiler (reactor)-following-turbine control. Electric power is adjusted to turbine load by regulating turbine inlet flow rate. Then, main steam pressure is indirectly adjusted by regulating boiler or reactor power. PWRs use this mode because the reactor power naturally follows the electric power or the turbine inlet flow rate through heat removal at the steam generators. The other is the turbine-following-boiler (reactor) control. Boiler or reactor power is adjusted to turbine load first. Then, electric power is indirectly adjusted to boiler or reactor power by regulating turbine inlet flow rate and main steam pressure. BWRs use this mode due to the reverse response of the reactor power to the electric power of the turbine inlet flow rate through void reactivity feedback in the core. FPPs use boiler-turbine-coordinated control where both electric power and pressure are controlled by a combination of turbine control valves and boiler input.

As described in Sect. 4.3.3, the reactor power of the Super LWR follows the turbine inlet flow rate through the reactivity feedback from the coolant temperature, rather than the pressure. Just as for PWRs, the reactor-following-turbine control may be applicable to the Super LWR; however, the turbine-following-reactor control is applied here like in BWRs from the following reasons.

- Too much fluctuation of the turbine inlet flow rate and temperature is not good from the viewpoint of thermal fatigue.
- The Super LWR adopts a direct steam cycle like BWRs do.

- The primary purpose of control system design in the conceptual stage is to control the Super LWR plant stably, rather than to show the capability of load following operation.

Figure 4.15 shows that the main steam pressure is sensitive to the turbine control valve opening. Thus, the main steam pressure is regulated by the turbine control valves like in BWRs. The reactor power is controlled by the control rods. Even though Fig. 4.12 shows that the reactor power is also sensitive to the flow rate, control of the reactor power by regulating the core coolant flow rate as is done in BWRs is not suitable for the Super LWR because:

- The Super LWR has no recirculation pumps
- The reactor power of the Super LWR is not very sensitive to the core coolant flow rate as described in Sect. 4.3.2
- The core coolant flow rate is the primary safety requirement as described in Sect. 6.2

Since the Super LWR does not use saturated steam, the main steam temperature changes with the power to flow rate ratio in the core. It needs to be kept constant in order to avoid too much thermal stress or thermal fatigue on the structures. Since the Super LWR has no superheaters that are utilized to control the main steam temperature as in FPPs, another method is needed. The analysis results described in Sect. 4.3.2 show that the main steam temperature is sensitive to the feedwater flow rate. Thus, the main steam temperature is controlled by regulating the feedwater flow rate. It is also suitable from the viewpoint of the safety principle of the Super LWR, i.e., keeping the core coolant flow rate (described in Sect. 6.2) because the feedwater flow rate indirectly follows the reactor power in this control method. The plant control system employed for the Super LWR is shown in Fig. 4.16. The plant control strategies of the Super LWR, PWRs, BWRs, and FPPs are compared in Table 4.3.

The control system should be designed so that it does not generate divergent or continuous oscillations that exceed the permissible range. To do that, the parameters of the three control systems are tuned in the following sections.

4.4.1 Pressure Control System

The pressure at the turbine inlet is kept constant by regulating the opening of the turbine control valves. The same logic as used in BWRs is adopted. It is shown in Fig. 4.17. The opening is proportional to the deviation of the pressure from the setpoint with lead-lag compensation. The turbine control valve opening ratio is calculated from the following equations.

$$V_s(t) = V_0 - \frac{P(t) - P_{set}}{K}, \tag{4.9}$$

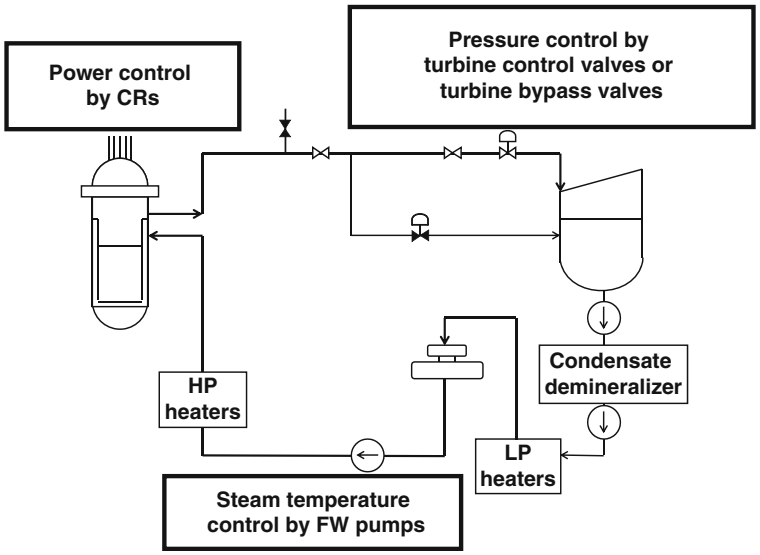


Fig. 4.16 Control system of Super LWR plant

Table 4.3 Comparison of control strategies

	Control strategy	Control method		
		Electric power	Steam pressure	Reactor or boiler power
Super LWR	Turbine following reactor	Reactor power	Turbine control valves	Control rods
BWR				Control rods, recirculation pumps
PWR	Reactor following turbine	Turbine control valves	Reactor power	Control rods, Chemical and volume control system
FPP	Boiler turbine coordinated	Turbine control valves, boiler input		

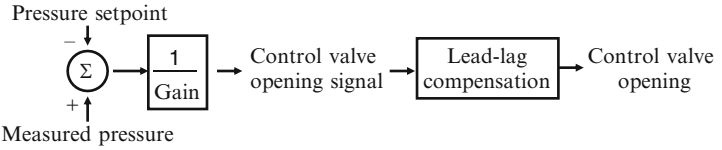


Fig. 4.17 Pressure control system

$$V(t) = V_s(t) + T_1 \frac{dP}{dt} - T_2 \frac{dV}{dt}, \tag{4.10}$$

where V_0 is the rated value of turbine control valve opening (= 100 (%)), $V_s(t)$ is the signal of turbine control valve opening (%) (relative to V_0), $V(t)$ is the turbine control

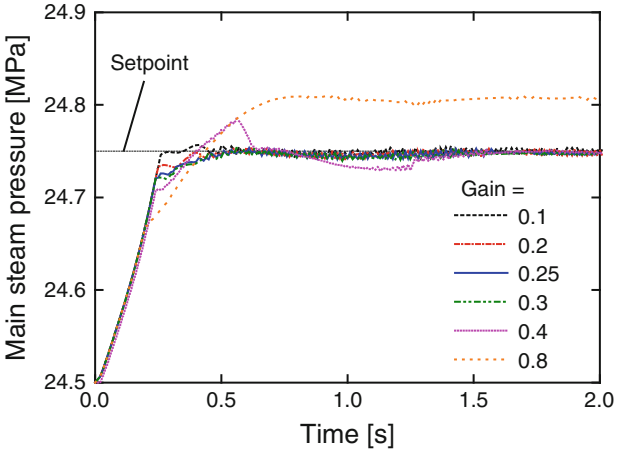


Fig. 4.18 Calculation results for tuning gain in the pressure control system

valve opening (%) (relative to V_0), $P(t)$ is the main steam pressure (MPa), P_{set} is the setpoint of main steam pressure (MPa), T_1 is the lead time (s), T_2 is the lag time (s), and K is the gain converting deviation of pressure into valve opening signal (MPa).

The maximum speed of the valve stroke is limited to 100%/3.5 s, taken from that of BWRs. The values of T_1 and T_2 are 2 and 5 s, respectively, and also taken from BWRs.

Sensitivity analysis is carried out with various K to minimize overshoot of the pressure when the setpoint of the main steam pressure increases stepwise by approximately 1% (from 24.5 to 24.75 MPa). The results are shown in Fig. 4.18 and K is determined to be 0.25 MPa.

4.4.2 Main Steam Temperature Control System

The main steam temperature is kept constant by regulating the feedwater flow rate. The logic is shown in Fig. 4.19. A PI controller is used. The feedwater flow rate is calculated based on the following equations.

$$u(t) = K_{\text{P}} e(t) + K_I \int_0^t e(t)dt, \tag{4.11}$$

$$e(t) = \frac{T_{\text{lead-lag}} - T_{\text{set}}}{T_{\text{set}}} \times 100, \tag{4.12}$$

$$T_{\text{lead-lag}} = T_{\text{meas}} + T_1 \frac{dT_{\text{meas}}}{dt}, \tag{4.13}$$

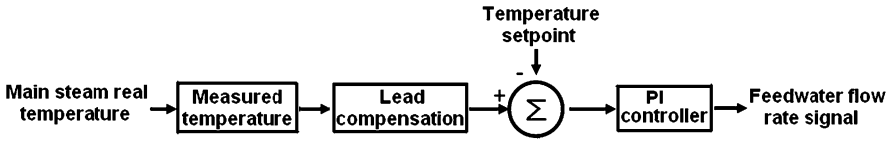


Fig. 4.19 Main steam temperature control system

$$T_{\text{meas}} = T_{\text{steam}} - T_2 \frac{\mathrm{d}T_{\text{meas}}}{\mathrm{d}t}, \tag{4.14}$$

where $u(t)$ is the feedwater flow rate signal (%), $e(t)$ is the deviation of main steam temperature from setpoint (%), T_{steam} is the actual main steam temperature (°C), T_{meas} is the main steam temperature measured by thermometer (°C), $T_{\text{lead-lag}}$ is the main steam temperature measured by thermometer with lead compensation (°C), T_{set} is the setpoint of main steam temperature (°C), T_1 is the lead time (s), T_2 is the lag time (time constant of thermometer) (s), K_P is the proportional gain, and K_I is the integral gain.

T_2 is set to 20 s based on a lag time for general thermometers. T_1 is also set to 20 s in order to avoid instability.

Sensitivity analysis is carried out with various K_P and K_I when the setpoint of the main steam temperature increases stepwise by 4°C. Operation of the pressure control system tuned in the previous section is considered. The criteria for selecting these values are as follows.

- Overshoot of temperature is within 5% of setpoint change.
- Settling time is the shortest. It is defined as the time by which the change of the temperature from the initial condition settles into the range of 95–105% of the setpoint change.

The influence of K_P without using the integral controller is shown in Fig. 4.20. From these results, 0.5 is selected as K_P. The influence of K_I with fixed K_P of 0.5 is shown in Fig. 4.21. From these results, it is seen that the integral controller makes the Super LWR less stable. Thus, only the proportional controller with the gain of 0.5 is selected for the main steam temperature control system.

4.4.3 Reactor Power Control System

The reactor power is controlled by the control rods. The control logic is based on what is widely used in nuclear reactors, including LWRs, and it is shown in Fig. 4.22. The speed of the control rod drive is calculated as (4.15).

$$v = \begin{cases} v_{\max} e/b & (e < b) \\ v_{\max} & (e \geqslant b) \end{cases}, \tag{4.15}$$

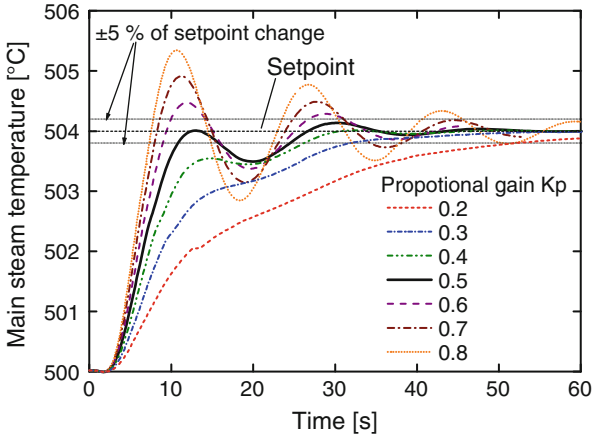


Fig. 4.20 Calculation results for tuning proportional gain in main steam temperature control system

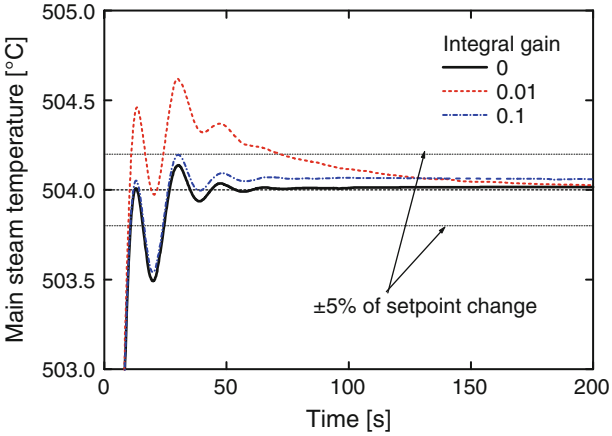


Fig. 4.21 Calculation results for tuning integral gain in main steam temperature control system

where v is the control rod drive speed (cm/s), v_{max} is the maximum speed (cm), e is the deviation of power from setpoint (%), and b is the maximum deviation for proportional control (%).

As shown in Fig. 4.23, the speed of the control rod drive is proportional to the deviation of the power from the setpoint if the deviation is below a certain value b while the control rods keep the maximum speed v_{max} with larger deviation from the viewpoint of safety. The maximum speed is 1.9 cm/s taken from PWRs.

Sensitivity analysis is carried out with various b when the setpoint of the reactor power decreases stepwise by 5%. Operation of the pressure control system and the

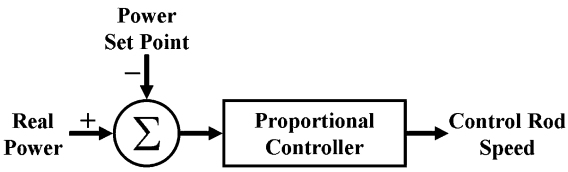


Fig. 4.22 Reactor power control system

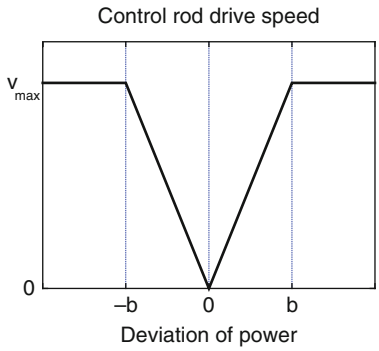


Fig. 4.23 Control rod drive speed vs. deviation of power

main steam temperatures tuned in the previous sections are considered. The criteria for selecting *b* are as follows.

- Undershoot of power is within 5% of the setpoint change.
- Fluctuation of main steam temperature is within 5% of that which has been achieved in FPPs.
- Settling time is the shortest. It is defined as the time by which the change of the power from its initial condition settles into the range of 95–105% of the setpoint change and also the change of the main steam temperature from initial condition is within 0.2°C.

The influence of *b* is shown in Fig. 4.24 and 25% is selected as *b*.

4.5 Plant Dynamics with Control System

For BWR design, five types of stabilities are considered: thermal-hydraulic stability, coupled neutronic thermal-hydraulic stability, regional stability, plant stability, and xenon stability. Plant stability is assessed by analyzing plant dynamics with a control system. There are two criteria for evaluating the plant stability. One is the limiting criterion where the oscillation of parameters must be within the decay ratio of 1.0 for all operating conditions. The other is the operational goal, which is not a criterion for licensing, where the decay ratio should be below 0.25.

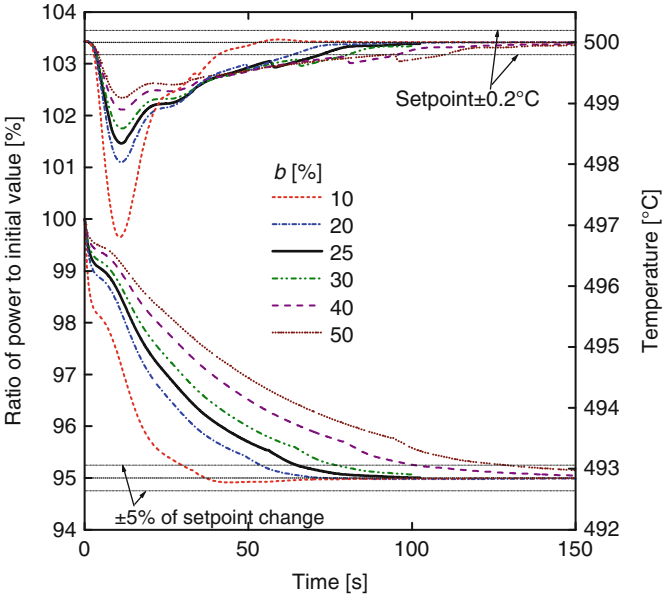


Fig. 4.24 Calculation results for tuning maximum deviation for proportional control in reactor power control system

In this section, the plant stability of the Super LWR is checked by analyzing the response to the following perturbations with the control system designed and tuned in Sect. 4.4.

- Stepwise increase in the pressure setpoint by approximately 1%.
- Stepwise increase in the setpoint of the main steam temperature by 4°C.
- Stepwise decrease in the setpoint of the reactor power by 10%.
- Impulsive increase in the feedwater flow rate by 5%.
- Stepwise decrease in the feedwater temperature by 10°C.

The same operational goal as used in BWRs is applied here. Thermal-hydraulic stability and coupled neutronic thermal-hydraulic stability of the Super LWR are described in Chap. 5.

4.5.1 Stepwise Increase in Pressure Setpoint

The setpoint of the main steam pressure increases stepwise from 24.5 to 24.75 MPa. The results are shown in Figs. 4.25 and 4.26. The turbine control valves are rapidly closed by the pressure control system. At the beginning, the feedwater flow rate decreases because of the increase in the core pressure. Thus, the main steam

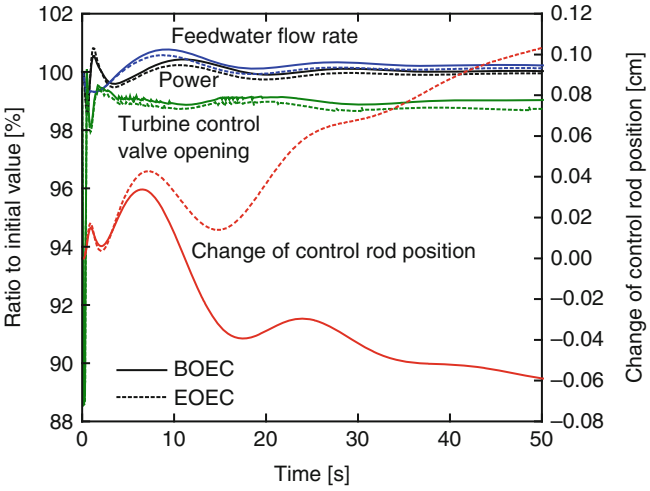


Fig. 4.25 Response to stepwise change in pressure setpoint from 24.5 to 24.75 MPa with control system (1)

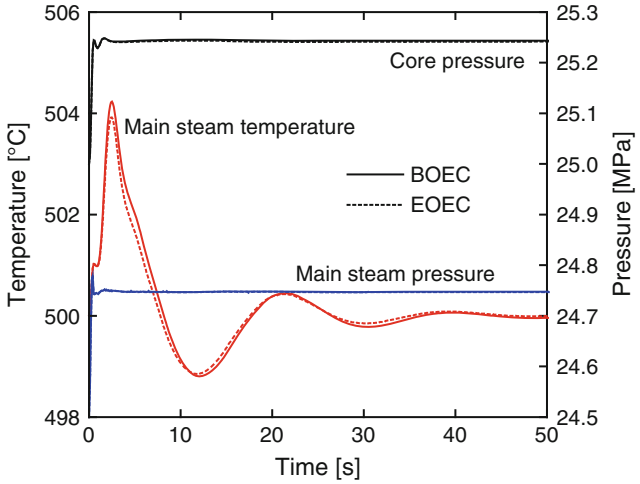


Fig. 4.26 Response to stepwise change in pressure setpoint from 24.5 to 24.75 MPa with control system (2)

temperature increases. Successively, the control system increases the feedwater flow rate by detecting the change of the main steam temperature. The power is kept almost constant by the control rods. After 30 s, the plant is settled at a new steady state. Although some parameters oscillate, the decay ratio is well below 0.25. The variations of the main steam temperature and the reactor power are below 5°C and 0.3%, respectively.

4.5.2 *Stepwise Increase in Temperature Setpoint*

The setpoint of the main steam temperature increases stepwise from 500 to 504°C. The results are shown in Figs. 4.27 and 4.28. The feedwater flow rate is decreased so as to increase the main steam temperature. Although the power decreases by the coolant density feedback, it is only about 2%, and then, the power returns to the

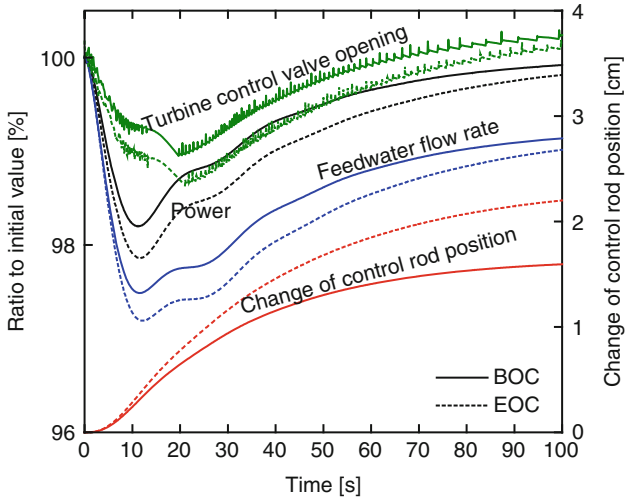


Fig. 4.27 Response to stepwise change in temperature setpoint from 500 to 504°C with control system (1)

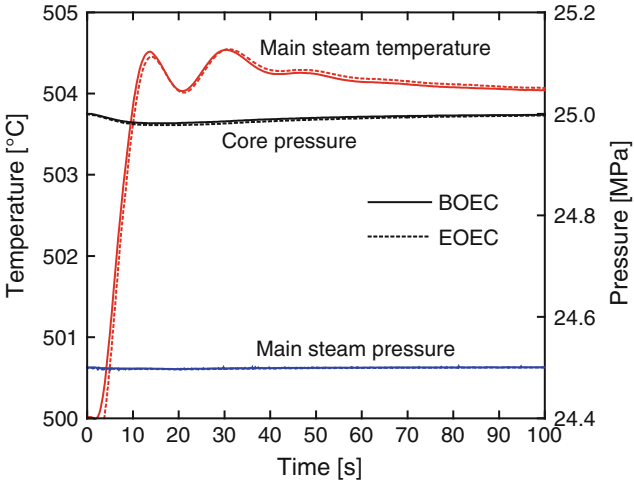


Fig. 4.28 Response to stepwise change in temperature setpoint from 500 to 504°C with control system (2)

initial value by withdrawal of the control rods. The pressure is kept almost constant. After 60 s, the plant is settled.

4.5.3 Stepwise Decrease in Power Setpoint

The power setpoint decreases stepwise from 100 to 90%. The results are shown in Figs. 4.29 and 4.30. The control rods are inserted so as to decrease the power. The power reaches the new setpoint without oscillation. The main steam temperature decreases with the power. The feedwater flow rate is gradually decreased to 90% of the initial value so as to keep the main steam temperature 500°C. The main steam pressure is kept constant by the turbine control valves. The pressure loss in the main steam lines decreases because of the decrease in the main steam flow rate. As a result, the core pressure decreases by about 0.1 MPa. After 80 s, the plant is settled at a new steady state. The variation of the main steam temperature is around 3°C.

4.5.4 Impulsive Decrease in Feedwater Flow Rate

The feedwater flow rate drops stepwise from 100 to 95%. The results are shown in Figs. 4.31 and 4.32. The main steam temperature increases and then returns to the initial value as the feedwater flow rate is recovered by the main steam temperature control system. Although the main steam temperature oscillates, the decay ratio is

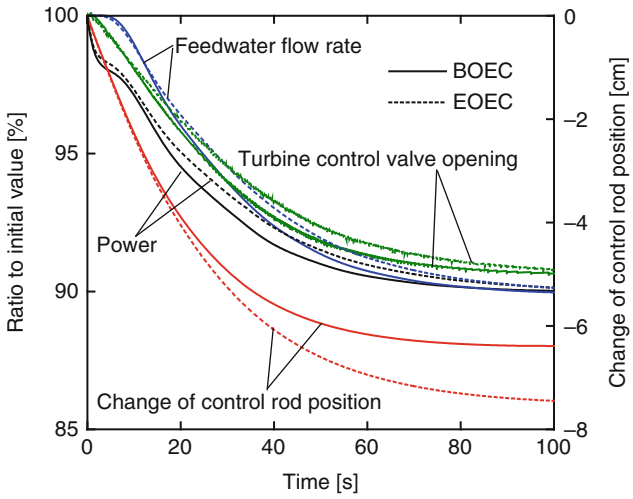


Fig. 4.29 Response to stepwise change in power setpoint from 100 to 90% of rated power with control system (1)

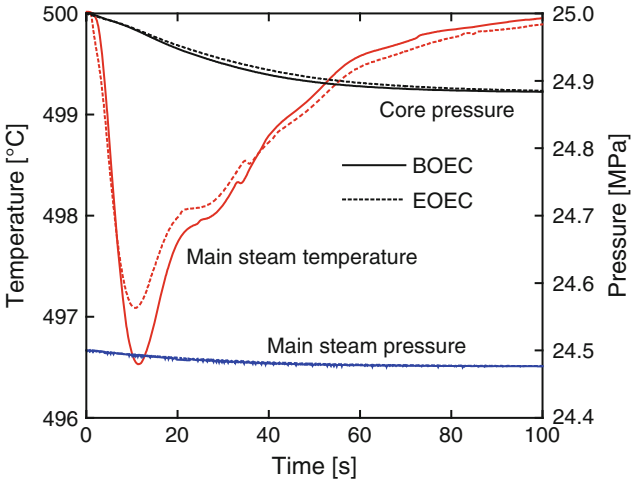


Fig. 4.30 Response to stepwise change in temperature setpoint from 500 to 504°C with control system (2)

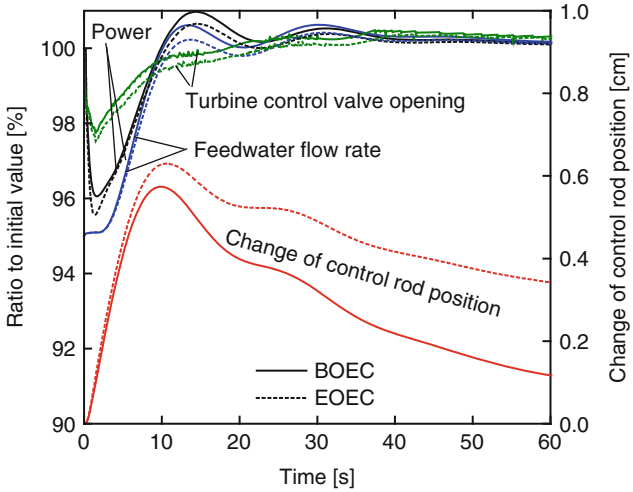


Fig. 4.31 Response to impulsive decrease in feedwater flow rate with control system (1)

below 0.25. The reactor power decreases by about 4% due to density feedback and then returns to the initial value as the control rods are withdrawn by the power control system. The pressure and the power decrease. The feedwater flow rate returns to 100% by detecting the increase in the main steam temperature. The pressure fluctuation is within 0.04 MPa. After 60 s, the plant returns to the initial condition. The Super LWR is stable against flow perturbations although it adopts the once-through coolant cycle without recirculation.

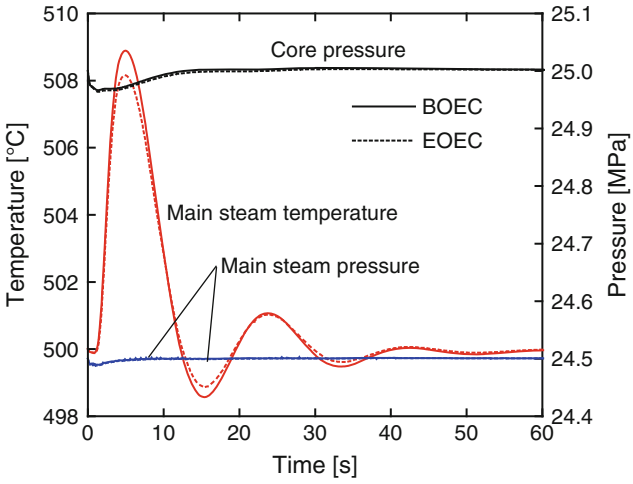


Fig. 4.32 Response to impulsive decrease in feedwater flow rate with control system (2)

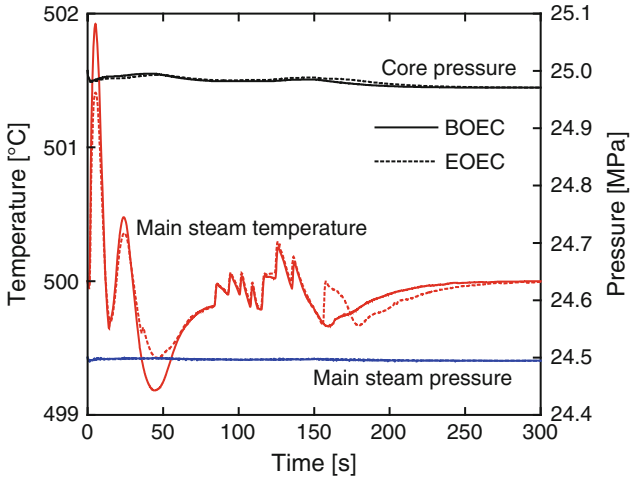


Fig. 4.33 Response to stepwise decrease in feedwater temperature with control system (1)

4.5.5 Decrease in Feedwater Temperature

The feedwater temperature decreases stepwise from 280 to 270°C. The results are shown in Figs. 4.33 and 4.34. At the beginning, the "volume" flow rate at the reactor vessel inlet decreases because the density of feedwater increases. It temporarily decreases the flow rate at the fuel channel inlet, and hence the main steam temperature increases and the power decreases. This behavior is one of the characteristics of the Super LWR with the once-through coolant cycle which differs

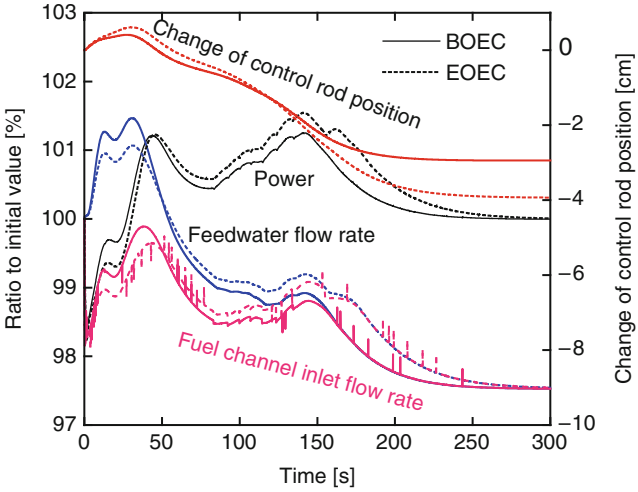


Fig. 4.34 Response to stepwise decrease in feedwater temperature with control system (2)

from BWRs with recirculation. Then, the power begins to increase as the main steam temperature control system increases the feedwater flow rate and also the low temperature coolant enters the water rods. The power control system suppresses the power peak around 101% of the rated value. The pressure fluctuation is small. It takes 200 s, the longest time among the five perturbations analyzed here, to stabilize the plant. The main reason is that the core inlet temperature is strongly affected by the feedwater temperature in the once-through cycle without recirculation.

4.5.6 Discussion

The perturbation of the feedwater flow rate is not so influential on the system behavior because the existence of many water rods makes the water density and the reactivity less sensitive to the feedwater flow rate. Compared to the flow rate, the perturbation of the feedwater temperature takes a longer time to be settled because the density of water in the water rods directly depends on the feedwater temperature, where over 70% of the water rod volume is filled with water.

The controllers of the feedwater pumps and the main steam temperature have longer time constants than the turbine control valves have. Thus, the power and the main steam temperature settle more slowly than the pressure at all the perturbations.

The coolant density coefficient depends on the core design, while the Doppler coefficient is almost constant as long as low-enriched UO_2 fuel is used. Sensitivity analysis is carried out in order to look at the robustness of the plant dynamics of the Super LWR plant against the density coefficient. The impulsive decrease in the feedwater flow rate analyzed in Sect. 4.5.4 is selected as the perturbation. The

Table 4.4 Influence of coolant density coefficient on plant response to impulsive decrease in feedwater flow rate

Coolant density coefficient at initial condition (dk/k/(g/cm^3))	0.01	0.05	0.11 (BOEC)[a]	0.15 (EOEC)[a]	0.2	0.4	0.8
Fluctuation of power (%)	1.5	2.4	3.9	4.4	6.0	10.3	17.1
Fluctuation of main steam temperature (°C)	11.7	10.4	8.9	8.2	7.5	5.5	3.7
Settling time (s)[b]	51	46	38	37	39	78	140

[a]Taken from Fig. 4.7

[b]Time at which power stays within 0.5% of the initial value and the main steam temperature stays within 0.2°C of the initial value

fluctuations of the power and main steam temperature and the settling time are summarized in Table 4.4. As the density coefficient gets larger, the fluctuation of power becomes higher, and hence its stabilization time becomes longer. As the density coefficient gets smaller, the fluctuation of main steam temperature becomes larger, and hence its stabilization time becomes longer. The plant stabilization time is the smallest when the stabilization times of power and main steam temperature are equal.

4.6 Summary

The plant dynamics of the Super LWR were understood by plant transient analyses. Although the Super LWR is a thermal spectrum reactor, the reactor power is not very sensitive to the flow rate because the water rods with large volume fraction mitigate fluctuation of the average water density. Based on the plant transient analyses and also referring to LWRs and FPPs, the plant control system of the Super LWR was designed and tuned. Finally, the adequacy of the control system was assessed by plant stability analyses.

References

1. Y. Okano, S. Koshizuka, K. Kitoh and Y. Oka, "Flow-Induced Accident and Transient Analyses of a Direct-Cycle, Light Water-Cooled Fast Breeder Reactor Operating at Supercritical Pressure," *Journal of Nuclear Science and Technology*, Vol. 33(4), 307–315 (1996)
2. Y. Okano, S. Koshizuka and Y. Oka, "Safety Analysis of a Supercritical Pressure, Light Water Cooled and Moderated Reactor with Double Tube Water Rods," *Annuals of Nuclear Energy*, Vol. 24, 1447–1456 (1997)
3. T. Nakatsuka, Y. Oka and S. Koshizuka, "Control of a Fast Reactor Cooled by Supercritical Light Water," *Nuclear Technology*, Vol. 121, 81–92 (1998)
4. K. Kitoh, S. Koshizuka and Y. Oka, "Pressure and Flow-Induced Accident and Transient Analyses of a Direct-Cycle, Supercritical-Pressure, Light-Water-Cooled Fast Reactor," *Nuclear Technology*, Vol. 123, 233–244 (1998)

5. K. Kitou, S. Koshizuka and Y. Oka, "Refinement of Transient Criteria and Safety Analysis for a High-Temperature Reactor Cooled by Supercritical Water," *Nuclear Technology*, Vol. 135, 252–284 (2001)
6. Y. Ishiwatari, Y. Oka and S. Koshizuka, "Control of a High Temperature Supercritical Pressure Light Water Cooled and Moderated Reactor with Water Rods," *Journal of Nuclear Science and Technology*, Vol. 40(5), 298–306 (2003)
7. Y. Ishiwatari, Y. Oka, S. Koshizuka, A. Yamaji and J. Liu, "Safety of Super LWR, (II) Safety Analysis at Supercritical Pressure," *Journal of Nuclear Science and Technology*, Vol. 42(11), 935–948 (2005)
8. Y. Ishiwatari, Y. Oka, S. Koshizuka and J. Liu, "ATWS Characteristics of Super LWR with/Without Alternative Action," *Journal of Nuclear Science and Technology*, Vol. 44(4), 572–580 (2007)
9. Y. Ishiwatari, Y. Oka and S. Koshizuka, "Safety of the Super LWR," *Nuclear Engineering and Technology*, Vol. 39(4), 257–272 (2007)

Chapter 5
Plant Startup and Stability

5.1 Introduction

In this chapter, the startup and stability of the Super LWR plant are described. Since the plant system of the Super LWR differs from those of LWRs, the startup scheme that is suitable for the Super LWR plant needs to be proposed. The reason why the plant startup and stability are described in the same chapter is that the stability is one of the design limitations for the startup procedure.

In Sect. 5.2, two startup schemes for the Super LWR plant are proposed referring to those of fossil-fuel fired power plants (FPPs). The required sizes and weights of the equipment for these startup schemes are calculated.

In Sect. 5.3, the operating region of the reactor power and feedwater flow rate for satisfying the thermal criteria is identified with thermal analyses. It includes both supercritical and subcritical pressure conditions. Based on the results, the startup curves are designed.

Although the coolant flow in the Super LWR is single-phase, the coolant enthalpy and therefore the density change substantially in the core because the coolant flow rate per thermal power in the Super LWR core is less than one eighth of LWR cores. Thus, the Super LWR can be susceptible to flow oscillations as the BWRs are. In Sect. 5.4, thermal hydraulic stability of the Super LWR is analyzed with the frequency domain approach. The analysis includes both supercritical and subcritical pressure conditions.

Power oscillations may also occur like BWRs because there is a time delay from the change in the thermal power (or neutron flux) to the change in the coolant or moderator density through heat conduction and heat transfer. In Sect. 5.5, coupled neutronic thermal-hydraulic stability of the Super LWR is analyzed with the frequency domain approach. The analysis includes both supercritical and subcritical pressure conditions.

In Sect. 5.6, the startup curve, based only on thermal considerations, is redesigned based on both thermal and stability considerations. The limiting constraint is identified for each process of plant startup.

Y. Oka et al., *Super Light Water Reactors and Super Fast Reactors*,
DOI 10.1007/978-1-4419-6035-1_5, © Springer Science+Business Media, LLC 2010

Table 5.1 Characteristics of the 1,000 MWe class Super LWR

Core thermal power (MW)	2,300
Electric power (MW)	1,000
Thermal efficiency (%)	43.5
Core pressure (MPa)	25
Core diameter/height (m)	3.6/4.2
Number of fuel assemblies	96
Core inlet/outlet coolant temperature (°C)	280/500
Core inlet/outlet coolant density (kg/m^3)	770/90
Feedwater flow rate (kg/s)	1,190
Average power density (MW/m^3)	62
Maximum linear power generation rate (kW/m)	39
Doppler coefficient at normal operating condition (dk/k/°C)	-1.2×10^{-5}
Density coefficient at normal operating condition (dk/k/(g/cm^3))	0.2
Number of fuel rods/water rods per fuel assembly	300/36
Fraction of mass flow rate ratio led to water rods (%)	30
Mass flux in fuel channels/water rods (kg/m^{2}s) (hot channel)	1,160/45
Fuel pellet diameter (mm)	8.74
Cladding thickness (mm)	0.63
Fuel rod outer diameter (mm)	10.2
Fuel rod lattice pitch (mm)	11.2
Number of feedwater lines/steam lines	2/2
Inner diameter of main feedwater line/main steam line (m)	0.27/0.46

The pressure is a given parameter in the thermal and stability analyses above. It is also important how to pressurize the system during startup. In Sect. 5.7, system pressurization by nuclear heating and the equipment to do that are proposed with reference to experiences in BWRs and FPPs. The feasibility of this concept is assessed by system transient analyses.

In this chapter, the 1,200 MWe class Super LWR described in Sect. 2.4.5 is scaled down to a 1,000 MWe class plant. Its characteristics are summarized in Table 5.1. The analyses and design are based on this plant.

5.2 Design of Startup Systems

5.2.1 Introduction to Startup Schemes of FPPs

There are two kinds of startup schemes currently used in FPPs [1]. One is the constant pressure startup scheme, in which the boiler operates at constant supercritical pressure after the coolant is pressurized to this point. The other is the sliding pressure startup scheme, in which the boiler operates with variable pressures and the pressure increases with the generation output.

5.2.1.1 Constant Pressure Supercritical Boiler

The original supercritical boiler units were designed for constant pressure operation. They were developed for base load and load cycling operations. The water conditions in the boiler remain at a constant supercritical pressure throughout the entire load change during startup. For startup of constant pressure once-through boilers, a startup bypass system is required to maintain the minimum flow in the furnace for adequate cooling.

The plant system of the constant pressure supercritical fossil-fired boiler is shown in Fig. 5.1. The startup bypass system includes a flash tank, pressure-reducing valves, and bypass valves. First, a minimum feedwater flow is established in the furnace prior to the firing of the boiler to prevent overheating of the tube walls. During the cold cleanup mode of operation, the flow is bypassed from the inlet of the primary superheater to the flash tank, until the water chemistry is brought to a predetermined level and the boiler firing starts.

After this firing is initiated, and the temperature of the steam leaving the primary superheater reaches about 300°C, the steam from the flash tank is led to the condenser. When the flash tank pressure becomes high, the saturated steam from the flash tank can be used to roll the turbine. After this, the turbine is ramped to about 7% load. At about 20% unit load, the startup bypass operation is shifted to once-through operation. When the temperatures become stabilized, the feedwater flow and the turbine load are increased slowly to 100% of full load value.

The system configuration of the constant pressure supercritical boiler is complicated and pressure ramp-up operation is required. The startup valves experience a

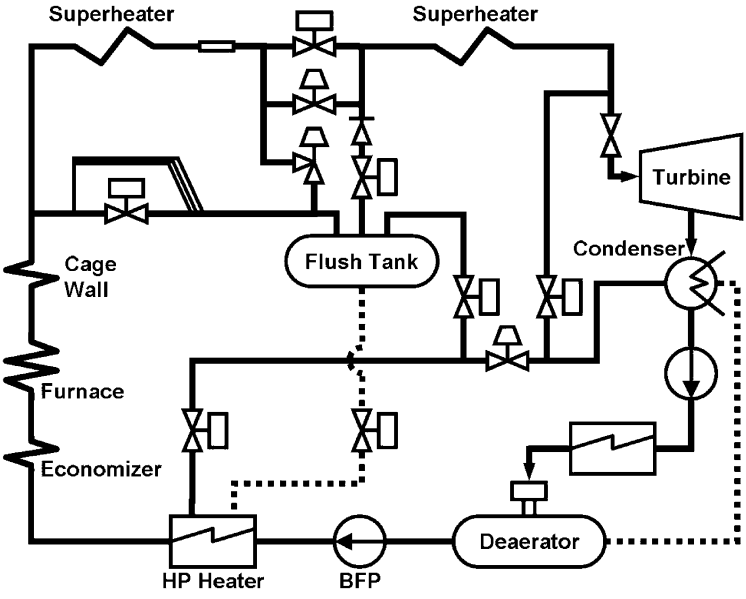


Fig. 5.1 Plant system of constant pressure FPP

large pressure difference during bypass operation, causing faster erosion, which in turn requires frequent valve maintenance.

5.2.1.2 Sliding Pressure Supercritical Boiler

Sliding pressure supercritical boiler units were introduced to meet the requirements of frequent load cycling and to solve the problems encountered in the earlier installed constant pressure supercritical boiler units. The boiler firing is started at a subcritical pressure and the pressure increases in proportion to the generation output. For the startup of the sliding pressure once-through boilers, a bypass system (turbine bypass and superheater bypass) and a low load recirculation system are required. The turbine bypass system serves to control the main steam temperature and pressure before turbine rolling, while the recirculation system serves to route the water, which is not evaporated in the furnace back to the economizer inlet, recovering the heat loss during startup.

The plant system of the sliding pressure supercritical fossil-fired boiler is shown in Fig. 5.2. It requires a steam-water separator, a separator drain tank, drain valves, and recirculation pumps. A minimum flow rate is maintained through the furnace walls by using a recirculation pump to add a recirculating flow to that provided by a boiler feedwater pump. The water leaving the furnace is passed to the steam-water separators. The water from the separators is collected in the drain tank and routed back to the economizer inlet via the boiler recirculation pump.

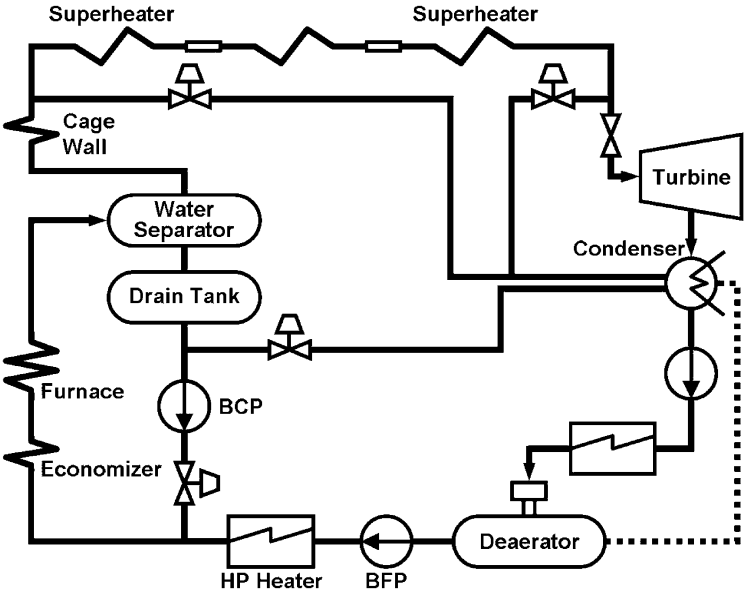


Fig. 5.2 Plant system for sliding pressure FPP

During the initial startup phase, the steam from the separator flows through the superheater circuit and turbine bypass valves to the condensers. After the steam pressure becomes high enough, the steam from the separator is used to roll the turbines. The turbine is then ramped to about 7% load. Once the minimum load is achieved, the startup system operation is shifted to once-through operation. The pressure is increased in proportion to the output load. The main steam temperature can be kept almost constant during the load change by sliding pressure operation.

Faster ramp rates are possible in sliding pressure operation, as the thermal stress in the turbine during the load change is reduced. Plant thermal efficiency is much improved in partial load operations. Turbine life expenditure per cycle can also be reduced by ramping pressure with load.

5.2.2 *Constant Pressure Startup System of the Super LWR*

The constant pressure startup is proposed with reference to that of FPPs. Nuclear heating starts at supercritical pressure, and the pressure is kept constant during load change. Because the reactor operates at a constant supercritical pressure, the coolant in the fuel channels is single phase and steam-water separation is not necessary. The constant pressure startup system for the Super LWR is shown in Fig. 5.3 [2]. It is required to establish a sufficient flow rate to prevent the

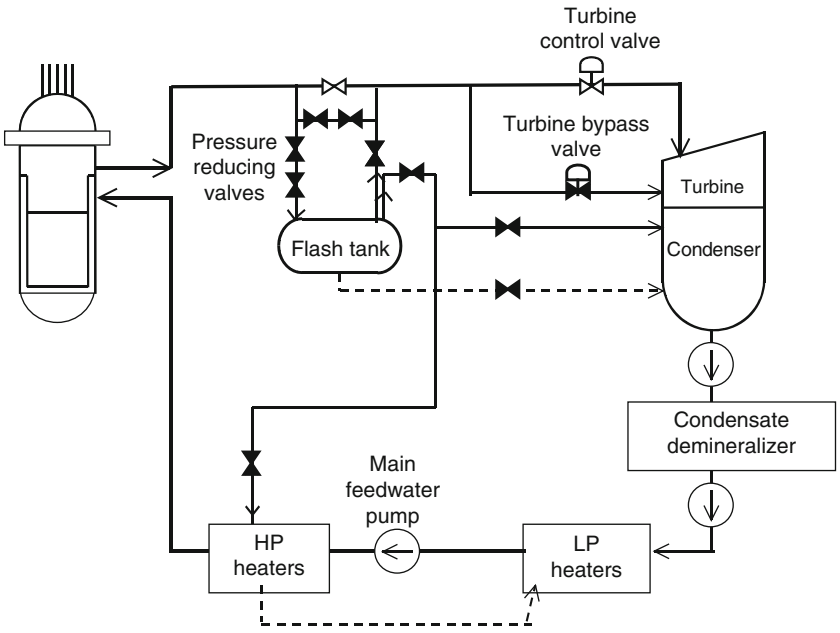


Fig. 5.3 Constant pressure startup system for Super LWR

overheating of fuel cladding and ensure adequate core cooling during initial operation. A startup bypass system, which is comprised of a flash tank and pressure-reducing valves, is used so that the minimum required flow rate can be maintained at startup. This startup bypass system will also serve to reduce the pressure and temperature of the core outlet coolant to conditions that are suitable for the flash tank, condensate system, and feedwater system. During initial startup, the steam from the flash tank can be routed back to the feedwater heaters to recover the heat loss.

The constant pressure startup system can be classified into five phases, which are briefly described below.

(a) *Pressurization to a supercritical pressure*. The reactor is first pressurized to a supercritical pressure by feedwater pumps. A minimum flow rate must be established prior to the nuclear heating to prevent overheating of the fuel cladding during initial startup. The required minimum feedwater flow rate is assumed to be 25%, which is the same as that of constant pressure supercritical boilers.

(b) *Start of nuclear heating*. Nuclear heating starts at the supercritical pressure of 25 MPa. The core outlet coolant is depressurized by pressure-reducing valves and flows into the flash tank. Steam is separated from water in the flash tank. Saturated steam from the flash tank goes to the high pressure feedwater heaters. The extra steam will be led to the condenser through the turbine bypass valves. The core inlet coolant temperature is increased to 280°C by nuclear heating.

(c) *Startup of turbines*. When the pressure of the flash tank reaches about 6.9 MPa (the same as that of the supercritical FPPs), the saturated steam from the flash tank flows through the main steam line to the turbines until the enthalpy at the core outlet becomes sufficiently high. The core outlet coolant temperature is kept about 420°C, lower than the design core outlet temperature (500°C), by setting the reactor core power to about 20%. The main steam temperature at turbine startup is about 284°C.

(d) *Switch from startup bypass operation to once-through operation*. After turbine startup, the source of the main steam is shifted from the flash tank to the reactor core outlet, and the main steam pressure then increases to 25 MPa. When the core outlet coolant enthalpy becomes higher than that of the flash tank steam, the startup bypass operation mode is changed to the once-through normal operation mode.

The core outlet coolant enthalpy must be greater than that of the saturated steam from the flash tank to prevent the main steam temperature from decreasing through the line switching. The relation between the required core outlet temperature and the flash tank pressure is shown in Fig. 5.4 [3]. If the flash tank pressure is taken to be 6.9 MPa (the same as that of supercritical FPPs), the coolant temperature at the core outlet must be greater than 420°C. This core outlet temperature is readily achievable in the present design (1,000 MWe class) of the Super LWR.

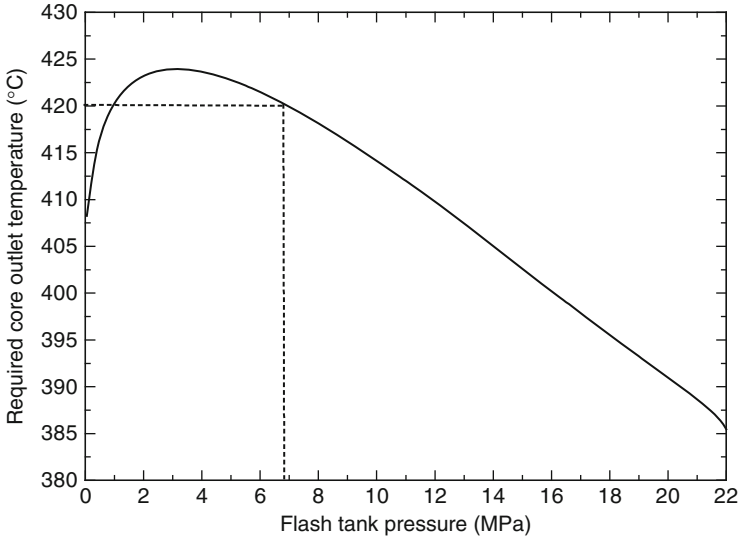


Fig. 5.4 Relation between required core outlet temperature and flash tank pressure (Pressure = 25 MPa) (taken from ref. [3] and used with permission from Atomic Energy Society of Japan)

(e) Power increase. After switching of lines, the core outlet temperature and main steam temperature increase to 500°C by increasing the core power from 20 to 25%. The reactor power is then increased with the feedwater flow rate.

The flash tank and pressure reducing valves are necessary initially during constant pressure startup of the Super LWR. The flash tank is designed such that the moisture content in the steam at turbine inlet is less than 0.1%. The dimensions of the flash tank required for startup are determined by using the correlations for the droplet entrainment and carryover from a boiling pool by a streaming gas, developed by Kataoka and Ishii [4].

Figure 5.5 shows the dependence of the amount of droplet entrainment on the height from the boiling surface. There are three regions of entrainment depending on the height above the pool surface: the near surface, momentum controlled, and deposition controlled regions.

The near surface region is defined as

$$h^* < h_1 = 1.038 \times 10^3 j_g^* N_{\mu g}^{0.5} D_H^{*\,0.42} \left(\frac{\rho_g}{\Delta\rho} \right)^{0.23}. \tag{5.1}$$

In this region, the entrainment is independent of height and gas velocity. It consists of all the droplets entrained at the pool surface and is given by

$$E_{fg}(h, j_g) = 4.84 \times 10^{-3} \left(\frac{\rho_g}{\Delta\rho} \right)^{-1.0}. \tag{5.2}$$

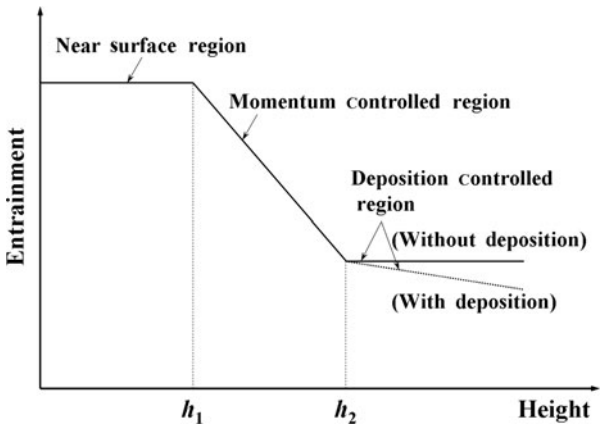


Fig. 5.5 Effect of height from the boiling surface on the droplet entrainment amount

The momentum controlled region is defined as

$$h_1 < h^* < h_2 = 1.97 \times 10^3 N_{\mu g}^{0.33} D_H^{*\,0.42} \left(\frac{\rho_g}{\Delta\rho}\right)^{0.23}. \tag{5.3}$$

In this region, the amount of entrainment decreases with increasing height from the pool surface and increases with increasing gas velocity. The entrainment consists partly of the droplets which attain height h due to the initial momentum and partly of droplets whose terminal velocity is less than the gas velocity. This second region is divided into three subregions depending on the gas velocity. The first, the low gas flux subregion, is defined as

$$j_g^* < 6.39 \times 10^{-4} h^*. \tag{5.4}$$

Its entrainment is given by

$$E_{fg}(h, j_g) = 2.21 \left(\frac{j_g^*}{h^*}\right) N_{\mu g}^{1.5} D_H^{*\,1.25} \left(\frac{\rho_g}{\Delta\rho}\right)^{-0.31}. \tag{5.5}$$

The second, the intermediate gas flux subregion, is defined as

$$6.39 \times 10^{-4} h^* \leqslant j_g^* \leqslant 5.7 \times 10^{-4} N_{\mu g}^{-0.5} D_H^{*\,-0.42} h^* \left(\frac{\rho_g}{\Delta\rho}\right)^{0.1}. \tag{5.6}$$

Its entrainment is given by

$$E_{fg}(h, j_g) = 5.42 \times 10^6 \left(\frac{j_g^*}{h^*}\right)^3 N_{\mu g}^{1.5} D_H^{*\,1.25} \left(\frac{\rho_g}{\Delta\rho}\right)^{-0.31}. \tag{5.7}$$

The third, the high gas flux subregion, is defined as

$$j_{\mathrm{g}}^{*} > 5.7 \times 10^{-4} N_{\mu \mathrm{g}}^{-0.5} D_{\mathrm{H}}^{*\,-0.42} h^{*} \left(\frac{\rho_{\mathrm{g}}}{\Delta \rho} \right)^{0.1}. \tag{5.8}$$

Its entrainment is given by

$$E_{\mathrm{fg}}(h, j_{\mathrm{g}}) \propto \left(\frac{j_{\mathrm{g}}^{*}}{h^{*}} \right)^{7-20}. \tag{5.9}$$

The deposition controlled region is defined as

$$h^{*} > h_2 = 1.97 \times 10^{3} N_{\mu \mathrm{g}}^{0.33} D_{\mathrm{H}}^{*\,0.42} \left(\frac{\rho_{\mathrm{g}}}{\Delta \rho} \right)^{0.23}. \tag{5.10}$$

In this region, the amount of entrainment is mainly determined by the deposition of droplets. The entrainment consists of droplets whose terminal velocity is less than the gas velocity. The entrainment decreases with increasing height due to deposition and given by:

$$E_{\mathrm{fg}}(h, j_{\mathrm{g}}) = 7.13 \times 10^{-4} j_{\mathrm{g}}^{*3} N_{\mu \mathrm{g}}^{0.5} \left(\frac{\rho_{\mathrm{g}}}{\Delta \rho} \right)^{-1.0} \exp[-0.205(h/D_{\mathrm{H}})]. \tag{5.11}$$

The dimensionless gas velocity j_{g}^{*}, dimensionless height above the pool surface h^{*}, gas viscosity number $N_{\mu \mathrm{g}}$, and dimensionless hydraulic diameter of the vessel D_{H}^{*} are defined below.

$$j_{\mathrm{g}}^{*} = \frac{j_{\mathrm{g}}}{(\sigma g\ \Delta \rho / \rho_{\mathrm{g}}^{2})^{1/4}}. \tag{5.12}$$

$$h^{*} = \frac{h}{\sqrt{\sigma / (g\ \Delta \rho)}}. \tag{5.13}$$

$$N_{\mu \mathrm{g}} = \frac{\mu_{\mathrm{g}}}{\left(\rho_{\mathrm{g}} \sigma \sqrt{\sigma / (g\ \Delta \rho)} \right)^{1/2}}. \tag{5.14}$$

$$D_{\mathrm{H}}^{*} = \frac{D_{\mathrm{H}}}{\sqrt{\sigma / (g\ \Delta \rho)}}, \tag{5.15}$$

where j_g is the superficial gas velocity, h is the height above the pool surface, μ_{g} is the gas viscosity, D_{H} is the hydraulic diameter of vessel, σ is the surface tension, G is the acceleration due to gravity, ρ_{g} is the density of gas, and $\Delta \rho$ is the density difference between gas and liquid.

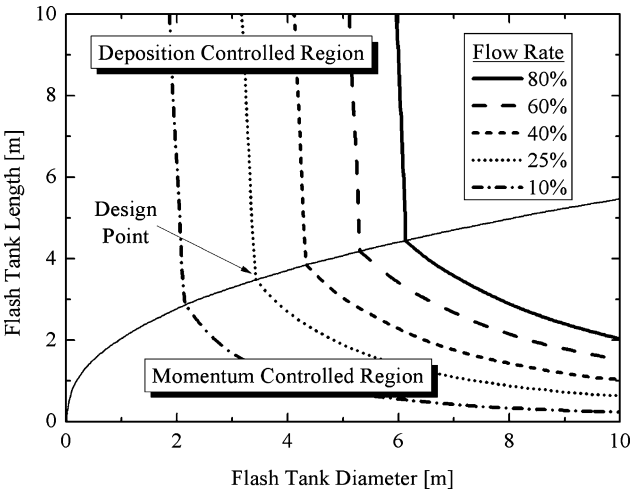


Fig. 5.6 Relation between flash tank length and flash tank diameter (Pressure = 6.9 MPa) (taken from ref. [3] and used with permission from Atomic Energy Society of Japan)

The flash tank is designed for the conditions in the deposition controlled region as the droplet entrainment amount changes only gradually with height in this region. The dimensions of the flash tank required for constant pressure startup of the Super LWR are determined for various pressures and various flow rates. The relationship between the shell height and the inner diameter of the required flash tank for 6.9 MPa (design pressure: 7.6 MPa) for various flow rates is shown in Fig. 5.6 [3]. The diameter to height ratio of the required flash tank increases as the flow rate increases.

If the feedwater flow rate is assumed to be 25% (which is the same as that of constant pressure FPPs), the flash tank length should be greater than 3.6 m while the flash tank diameter should be about 3.4 m. The shell thickness t is calculated from the maximum allowable pressure P and the maximum allowable stress S by the following formula:

$$t = \left(\sqrt{\frac{SE + P}{SE - P}} - 1 \right) R. \tag{5.16}$$

The dome thickness d is calculated by using the formula for a pressure vessel given by

$$d = \frac{P}{2S - 0.2P} R, \tag{5.17}$$

where R is inner radius of the shell and the efficiency E is taken as 100%.

Table 5.2 Calculated dimensions and weight of the flash tank required for constant pressure startup of the Super LWR for various flash tank pressures (taken from ref. [3] and used with permission from Atomic Energy Society of Japan)

Material	SBV2			
Applicable thickness	6–150 mm			
Allowable stress	13.8 kg/mm^2 (135.2 MPa)			
Density	8.7 g/cm^3			
Feedwater flow rate	25% (297.5 kg/s)			
Flash tank pressure (MPa)	3	6.9	10	14
Design pressure (MPa)	3.3	7.6	11	15.4
Design temperature (°C)	239	291	318	344
Inner diameter (m)	4.6	3.4	3.0	2.7
Shell length (m)	4.0	4.0	4.1	4.4
Shell thickness (m)	0.057	0.10	0.128	0.164
Dome thickness (m)	0.028	0.048	0.062	0.078
Height (m)	8.656	7.496	7.224	7.256
Weight (kg)	44,900	52,300	58,300	68,800

The calculated dimensions and weights of the required flash tanks are shown in Table 5.2 [3] if SBV2 is used as the tank material and different flash tank pressures are used as a parameter. The diameter to height ratio of the required flash tank decreases with increasing flash tank pressure. If the flash tank pressure is increased, the required flash tank diameter and size decrease, but as the required shell thickness increases, the required flash tank weight increases. From the viewpoint of the required flash tank size and weight, it is deemed appropriate to take the operating pressure of the flash tank as 6.9 MPa, which is the same as that of the constant pressure FPPs. Then, the design pressure of the flash tank is taken as 7.6 MPa (1.1 times 6.9 MPa) and the design temperature as 291°C (the saturation temperature of 7.6 MPa).

5.2.3 Sliding Pressure Startup System of the Super LWR

Nuclear heating starts at a subcritical pressure. The startup bypass system, which consists of a steam-water separator, a drain tank, and drain valves, is required for two-phase flow at subcritical pressures. In FPPs, the heat from the saturated water in the drain tank can be recovered by either using a high temperature recirculation pump or setting up an additional heater. Installation of a circulation pump or an additional heater in the Super LWR will be cost-effective since it will reduce the startup heat losses. During initial startup, this startup bypass system serves to separate the steam-water mixture leaving the reactor, sending the steam to the condenser, and routing the water back to the reactor through the recirculation pumps or additional heaters, providing adequate core cooling. The plant system for sliding pressure startup of the Super LWR is shown in Figs. 5.7 and 5.8 [2].

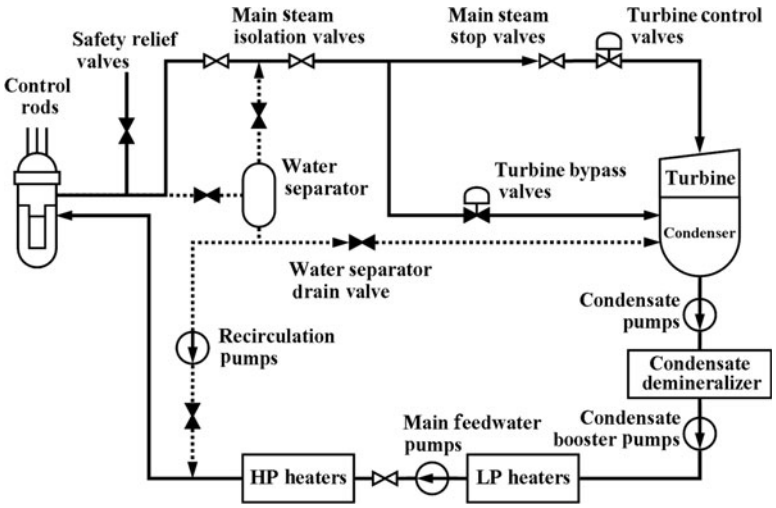


Fig. 5.7 Sliding pressure startup system of Super LWR with recirculation pumps (taken from ref. [2] and used with permission from American Nuclear Society)

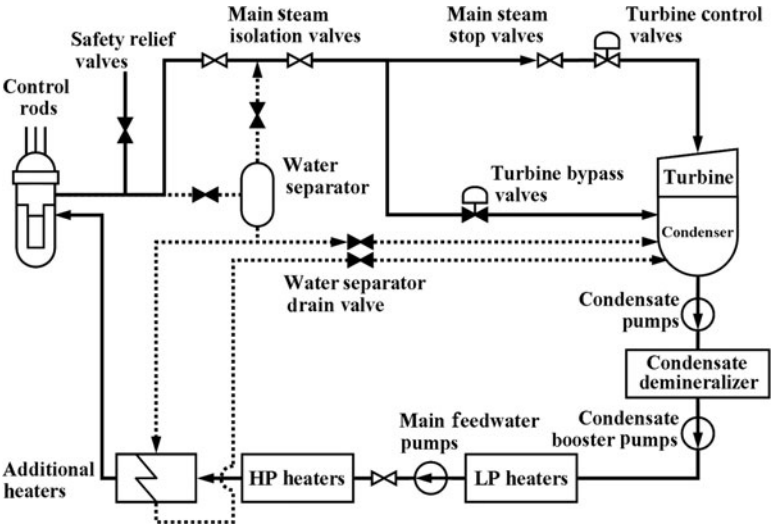


Fig. 5.8 Sliding pressure startup system of the Super LWR with additional heaters (taken from ref. [2] and used with permission from American Nuclear Society)

The sliding pressure startup system can be differentiated into six phases described below.

(a) *Start of nuclear heating at subcritical pressure*. Nuclear heating starts after the reactor is pressurized to an adequate subcritical pressure by feedwater pumps, and the feedwater flow rate is set to 35%. The feedwater temperature must be low enough at subcritical pressures to prevent boiling in the water rods, where the water enthalpy may be high. The initial feedwater temperature is kept about

120°C. The core outlet coolant flows to the water separator in the bypass line. The saturated steam from the separator goes to the condenser through the turbine bypass valves. The saturated water from the separator is led to additional heaters and the condenser.

(b) *Startup of turbines*. When the reactor power becomes high enough, saturated steam from the separator flows through the main steam line to the turbines. The minimum pressure required for turbine startup is assumed to be 8.3 MPa, which is the same as that of the sliding pressure supercritical FPPs. As the core pressure is increased to 8.3 MPa, the main steam temperature increases to 298°C. The feedwater temperature is increased to 280°C by nuclear heating. The reactor pressure remains constant at 8.3 MPa until the reactor power reaches 20%.

(c) *Pressurization to supercritical pressure*. After turbine startup, the reactor is pressurized from 8.3 MPa to a supercritical pressure of 25 MPa with a core power of 20% and a flow rate of 35%. When the core pressure is subcritical, the main steam temperature is equal to the saturation temperature at that pressure because the core outlet coolant is a two-phase mixture. When the reactor pressure reaches 25 MPa, the main steam temperature becomes about 388°C.

(d) *Switch from startup bypass operation to once-through operation*. When the reactor pressure becomes 25 MPa, the plant is shifted from the startup bypass operation mode to the once-through normal operation mode.

(e) *Temperature increase*. After line switching, the core outlet temperature and the main steam temperature increase until they become 500°C.

(f) *Power increase*. When the main steam temperature reaches 500°C, the core power is increased to 100%. The core inlet and outlet temperatures are kept constant.

During subcritical pressure operation in the sliding pressure startup of the Super LWR, a steam-water separator is required to separate the steam and water such that the water can be recirculated to the reactor inlet by recirculation pumps or by additional heaters, in order to maintain adequate core cooling. The size and weight of the steam-water separator are determined by referring to those of sliding pressure supercritical FFPs. The characteristics of the reference 700 MW supercritical boiler and the properties of its steam-water separators are given in Table 5.3.

The dimensions and weight of the separator required for the Super LWR startup are calculated by comparing the flow rates of Super LWR and the reference boiler.

Table 5.3 Characteristics of the steam-water separator of the reference supercritical boiler (taken from ref. [3] and used with permission from Atomic Energy Society of Japan)

Electrical output of boiler (MW)	700
Feedwater flow rate (tons/h)	2,300
Design pressure (MPa)	24.6
Design temperature (°C)	425
Shell length (m)	3.9
Outer diameter (m)	1.2
Shell thickness (m)	0.13
Inner diameter (m)	0.94
Dome thickness (m)	0.06
Separator volume (m^3)	3.15
Cross-sectional area (m^2)	0.694
Number of separators	4
Total cross-sectional area (m^2)	2.776

Feedwater flow rate of Super LWR = 4,284 tons/h (1,190 kg/s)
Feedwater flow rate of supercritical boiler = 2,300 tons/h

$$\frac{\text{flow rate of Super LWR}}{\text{flow rate of reference boiler}} = \frac{4{,}284}{2{,}300} = 1.863.$$

The cross-sectional area of the water separator required is proportional to the flow rate of the coolant passing through the separator. Thus, the required cross-sectional area of the separator for the Super LWR should be 1.863 times that of the supercritical boiler if the separator is placed in the main steam line, and the flow rate passing through the separator is 100%. The design temperature of the separator placed in the main line should be the same as the main steam temperature (500°C).

The size and weight of the separator are determined within the applicable thickness range of the present standards for the pressure vessel material. The separator shell length (3.9 m) is set as similar to that of the boiler. The maximum shell thickness t is determined so that it is within the applicable thickness of the separator material. The maximum radius of the separator is calculated from shell thickness t, allowable stress S and separator pressure P by (5.16). The total number of the separators required is obtained from the biggest possible cross-sectional area of one separator and the total required cross-sectional area of all of them.

If SCMV4 (2.25Cr – 1Mo alloy steel plate commonly used for boilers and pressure vessels and suitable for high temperature use) is used as the separator material, the maximum shell thickness is taken as 0.28 m and the number of the separators required is 4. The design pressure of the separator is 27.5 MPa (1.1 times 25 MPa). The total weight of the separators required is about 162 tons.

If a separator is placed in the bypass line, the required cross-sectional area of the separator will be 0.652 times that of the boiler, as the flow rate through the separator is only 35% (which is the minimum required feedwater flow rate for sliding pressure startup). For this separator in the bypass line, the separator design temperature can be lowered to about 400°C and its pressure is 27.5 MPa. The number of the separators required is also reduced, as the allowable stress is larger and the flow rate is smaller. The total weight of the separator(s) required will be about 34 tons if SBV2 is used (one separator), and 43.3 tons if SCMV4 is used (two separators). The calculated dimensions and weights of the separators required for sliding pressure startup of the Super LWR are shown in Table 5.4 [3].

5.3 Thermal Considerations

5.3.1 Startup Thermal Analysis Code

The plant analysis code developed at the University of Tokyo for the Super LWR with downward flow type water rods is used here. The thermal hydraulic analyses are carried out by using the one-dimensional single-channel model of the fuel

Table 5.4 Dimensions and weight of water separators required for sliding pressure startup of the Super LWR (taken from ref. [3] and used with permission from Atomic Energy Society of Japan)

	Main line	Bypass line	
Design pressure (MPa)	27.5	27.5	27.5
Design temperature (°C)	500	400	400
Material	SCMV4	SBV2	SCMV4
Applicable thickness (mm)	6–300	6–150	6–300
Allowable stress (kg/mm^2)	8.7	13.8	11.9
Shell length (m)	3.9	3.9	3.9
Shell thickness (m)	0.26	0.13	0.22
Inner diameter (m)	1.283	1.08	1.56
Dome thickness (m)	0.11	0.06	0.10
Height (m)	5.4	5.1	5.66
Cross-sectional area (m^2)	1.293	0.91	1.91
Number of separators required	4	2	1
Unit weight (kg)	40,500	17,000	43,300
Total weight (kg)	162,000	34,000	43,300

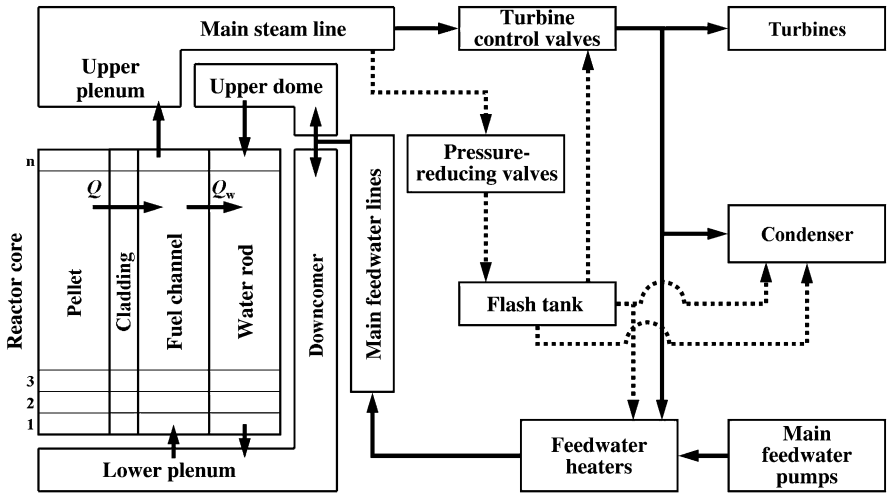


Fig. 5.9 Calculation model for constant pressure startup scheme (taken from ref. [3] and used with permission from Atomic Energy Society of Japan)

assembly. The reactor system is divided into five parts: the reactor core, main feedwater lines, upper dome, lower plenum, and upper plenum. The calculation models for constant pressure startup and sliding pressure startup are shown in Figs. 5.9 and 5.10 [3], respectively. The balance of plant system and the startup bypass system are also shown in the figures. The reactor core and the upper and lower plena are modeled as a single channel. The coolant channel and the fuel are divided axially into 20 nodes in the constant pressure startup analysis. They are divided axially into 40 nodes in the sliding pressure startup analysis, as it is necessary to determine the thermal-hydraulic parameters more exactly at subcritical pressure. Finer axial meshes are used when the local heat flux exceeds the critical

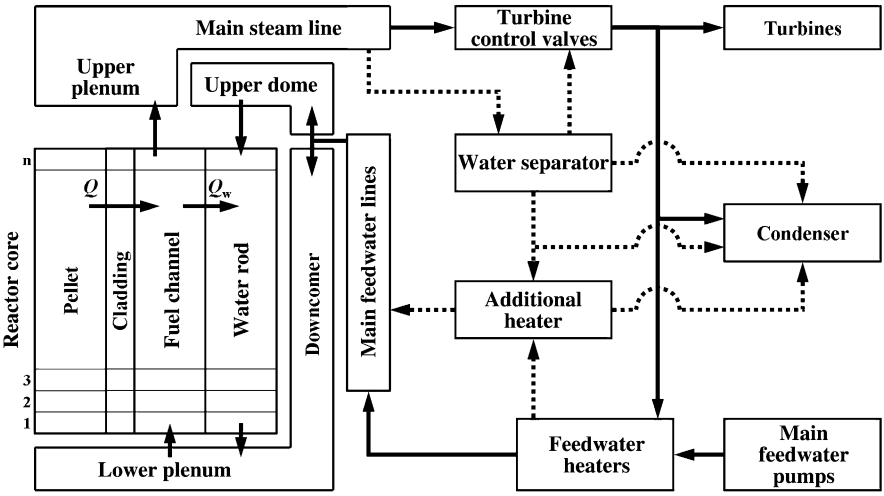


Fig. 5.10 Calculation model for sliding pressure startup scheme (taken from ref. [3] and used with permission from Atomic Energy Society of Japan)

heat flux and dry out occurs. The lower plenum includes the downcomer and the upper plenum includes the main steam line. The lower plenum, the upper plenum, the main feedwater lines, and the upper dome are divided into 20, 20, 10, and 10 nodes, respectively. The thermodynamic properties of the coolant and the moderator are assumed to be spatially uniform within each node.

The thermal calculations are carried out from the core inlet to the core outlet. The inlet coolant temperature and mass flow rate are used as boundary conditions. The temperatures of the coolant in fuel channels and those of the moderator water in the water rods are calculated from the mass and energy conservation equations. The axial power is assumed to follow a cosine distribution. The radial power distribution in the fuel assembly is not considered. The steady-state temperature distributions are assumed in the fuel pellet, fuel cladding, and the gap. The thermal power generated in the reactor is to be consumed among the turbines, the condenser, and the feedwater heaters. The calculations are carried out iteratively until the solutions are convergent to steady-state values.

From the coolant and moderator temperature distributions, the fuel and cladding temperatures are calculated using one-dimensional heat transfer equations. The heat transfer between the fuel channel and the water rod and the heat transfer between the fuel pellet and the coolant are considered.

5.3.1.1 Heat Transfer Correlations

For supercritical pressures, the heat transfer coefficients are calculated by using the Oka–Koshizuka correlation (see Sect. 2.3.2.2).

Table 5.5 Heat transfer correlations used for different heat transfer types

Mode	Heat transfer type	Heat transfer correlation
1	Forced convection in subcooled liquid	Dittus–Boelter correlation
2	Nucleate boiling	Thom correlation
3	Forced convective vaporization	Schrock–Grossman correlation
4	Forced convection in superheated vapor	Dittus–Boelter correlation
5	Transition boiling	McDonough, Milich and King correlation
6	Stable film boiling	Groeneveld correlation
7	Pool film boiling	Modified Bromley correlation
8	Low pressure flow film boiling	Dougall and Rohsenow correlation

For subcritical pressures, the heat transfer coefficients are calculated by employing the correlations used in RELAP-4 [5]. Heat transfer correlations used for different heat transfer types are shown in Table 5.5.

The correlations for pre-CHF (critical heat flux) conditions are listed below.

1. Forced convection in subcooled liquid (Dittus–Boelter correlation)

$$h = 0.023\left(\frac{k_\mathrm{f}}{D_\mathrm{e}}\right)(\mathrm{Pr}_\mathrm{f})^{0.4}\left(\frac{GD_\mathrm{e}}{\mu_\mathrm{f}}\right)^{0.8}. \tag{5.18}$$

2. Nucleate boiling (Thom correlation)

$$h = \frac{10^6}{\mathrm{d}T}\left(\frac{\Delta T_\mathrm{sat}\mathrm{e}^{P/8.7}}{22.7}\right)^2, \tag{5.19}$$

where P is in MPa.

3. Forced convective vaporization (Schrock–Grossman correlation)

$$h = (2.50)(0.023)\left(\frac{k_\mathrm{f}}{D_\mathrm{e}}\right)(\mathrm{Pr}_\mathrm{f})^{0.4}\left[\frac{GD_\mathrm{e}(1-X)}{\mu_\mathrm{f}}\right]^{0.8}\left(\frac{1}{X_\mathrm{tt}}\right)^{0.75}, \tag{5.20}$$

$$\frac{1}{X_\mathrm{tt}} = \left(\frac{X}{1-X}\right)^{0.9}\left(\frac{\rho_\mathrm{f}}{\rho_\mathrm{g}}\right)^{0.5}\left(\frac{\mu_\mathrm{g}}{\mu_\mathrm{f}}\right)^{0.1}. \tag{5.21}$$

4. Forced convection in superheated vapor (Dittus–Boelter correlation)

$$h = 0.023\left(\frac{k_\mathrm{g}}{D_\mathrm{e}}\right)(\mathrm{Pr}_\mathrm{g})^{0.4}\left(\frac{GD_\mathrm{e}}{\mu_\mathrm{g}}\right)^{0.8}. \tag{5.22}$$

The choice of which pre-CHF heat transfer correlation to use depends on the value of void fraction, as shown in Table 5.6.

Table 5.6 Selection of pre-CHF heat transfer correlations

Void fraction	Heat transfer mode
$\infty \leq 0$	Mode 1
$0.0 < \alpha < 0.8$	Mode 2
$0.8 \leq \alpha < 0.9$	Intermediate between mode 2 and mode 3
$0.9 \leq \alpha < 0.95$	Mode 3
$0.95 \leq \alpha < 1.0$	Intermediate between mode 3 and mode 4
$\alpha \geq 1.0$	Mode 4

The correlations for post-CHF conditions are listed below.

1. Transition boiling (McDonough, Milich and King correlation)

$$h = \frac{q_{\mathrm{CHF}} - \mathrm{const}(T_{\mathrm{w}} - T_{\mathrm{w,CHF}})}{\mathrm{d}T}. \tag{5.23}$$

2. Stable film boiling (Groeneveld correlation)

$$h = 0.00327\left(\frac{k_{\mathrm{g}}}{D_{\mathrm{e}}}\right)(\mathrm{Pr}_{\mathrm{v,w}})^{1.32}\left[\left(\frac{GD_{\mathrm{e}}}{\mu_{\mathrm{g}}}\right)\left(X + \frac{\rho_{\mathrm{g}}}{\rho_{\mathrm{f}}}(1-X)\right)\right]^{0.901} Y^{-1.50}, \tag{5.24}$$

$$Y = \max\left[1 - 0.1(1-X)^{0.4}\left(\frac{\rho_{\mathrm{f}}}{\rho_{\mathrm{g}}} - 1\right)^{0.4} 0.1\right]. \tag{5.25}$$

3. Pool film boiling (Modified Bromley correlation (Berenson))

$$h = 0.425\left[\frac{k_{\mathrm{g}}^3 \rho_{\mathrm{g}}(\rho_{\mathrm{f}} - \rho_{\mathrm{g}}) g H_{\mathrm{fg}}}{\mu_{\mathrm{g}}\ \Delta T_{\mathrm{sat}} \frac{\lambda_{\mathrm{c}}}{2\pi}}\right], \tag{5.26}$$

where

$$\frac{\lambda_{\mathrm{c}}}{2\pi} = \left(\frac{g_0 \sigma}{g(\rho_{\mathrm{f}} - \rho_{\mathrm{g}})}\right)^{1/2},$$

λ_{c} is the minimum critical hydrodynamic wave length and H_{fg} is a correction to the heat of vaporization, h_{fg}, which includes the energy absorbed by the vapor surrounding the tube.

$$H_{\mathrm{fg}} = h_{\mathrm{fg}} + 0.5 C_{\mathrm{pg}}\ \Delta T_{\mathrm{sat}}. \tag{5.27}$$

4. Low pressure flow film boiling (Dougall and Rohsenow correlation)

$$h = 0.023\left(\frac{k_{\mathrm{g}}}{D_{\mathrm{e}}}\right)(\mathrm{Pr}_{\mathrm{g}})^{0.4}\left[\left(\frac{GD_{\mathrm{e}}}{\mu_{\mathrm{g}}}\right)\left(X + \frac{\rho_{\mathrm{g}}}{\rho_{\mathrm{f}}}(1-X)\right)\right]^{0.8}. \tag{5.28}$$

Table 5.7 Selection of post-CHF heat transfer correlations

$P \leq 500$ psia	$G \geq 2 \times 10^5$ lbm/ft^{2}h	h = max [mode 5, min
($P \leq 34.475$ bar)	(or) $G \geq 271.26$ kg/m^{2}s	(mode 6, mode 8)]
	$G < 2 \times 10^5$ lbm/ft^{2}h	h = max [mode 5, mode 7, min
	(or) $G < 271.26$ kg/m^{2}s	(mode 6, mode 8)]
$P > 500$ psia	$G \geq 2 \times 10^5$ lbm/ft^{2}h	h = max (mode 5, mode 6)
($P > 34.475$ bar)	(or) $G \geq 271.26$ kg/m^{2}s	
	$G < 2 \times 10^5$ lbm/ft^{2}h	h = max (mode 5, mode 6, mode 7)
	(or) $G < 271.26$ kg/m^{2}s	

The choice of which post-CHF heat transfer correlation to use depends on the values of pressure and mass flux, as shown in Table 5.7.

5.3.1.2 Determination of Critical Heat Fluxes

The CHFs are determined by using the 1995 lookup table for CHF in tubes which was developed by Groeneveld et al. [6–8]. The 1995 lookup table was chosen because of its wider range of application and better prediction accuracy, with a root-mean-square error of 7.82% and an average error of 0.69%, compared with other correlations. The CHF lookup table is based on the tube data normalized to a tube inside diameter of 8 mm and provides CHF values at discrete values of pressure, mass flux, and equilibrium quality. It covers the ranges 0.1–20.0 MPa, 0.0–8,000.0 kg/m^{2}s, and equilibrium steam quality values of -0.5 to $+1.0$. Correction factors can be employed to extend the use of the table to tubes with diameter other than 8 mm and for rod bundles.

The CHF value for a given pressure, mass flux, and quality is determined by interpolating between the eight table values. The CHF value obtained from the table by interpolation is then multiplied by the following correction factors. The grid spacer factor is not considered in the present calculation.

1. Tube diameter factor

$$\begin{aligned} k_1 &= (0.008/D_\mathrm{h})^{1/2} \quad (D_\mathrm{h}<25\,\mathrm{mm}) \\ k_1 &= 0.57 \qquad\qquad\quad (D_\mathrm{h}<25\,\mathrm{mm}) \end{aligned} \tag{5.29}$$

2. Bundle factor

$$k_2 = \min\left[0.8, 0.8\exp(-0.5X^{0.33})\right] \quad \text{(for rod bundles).} \tag{5.30}$$

3. Heated length factor

$$k_3 = \exp\left\{\frac{D_\mathrm{h}}{L}e^{2\alpha}\right\}. \tag{5.31}$$

4. Axial power factor

$$\begin{aligned} k_4 &= 1.0 \quad \text{for } X \leqslant 0, \\ k_4 &= \frac{q_{\text{local}}}{q_{\text{bla}}} \quad \text{for } X > 0. \end{aligned} \tag{5.32}$$

5. Radial flux distribution factor

$$\begin{aligned} k_5 &= 1.0 \quad \text{for } X \leqslant 0, \\ k_5 &= \frac{q(z)_{\text{avg}}}{q(z)_{\text{max}}} \text{ for } X > 0. \end{aligned} \tag{5.33}$$

6. Horizontal factor

$$\begin{aligned} k_6 &= 1 \quad \text{if vertical flow,} \\ k_6 &= 1 \quad \text{if horizontal high flow,} \\ k_6 &= 0 \quad \text{if horizontal stratified flow.} \end{aligned} \tag{5.34}$$

$$\text{CHF} = \text{CHF}_{\text{table}} \bullet k_1 k_2 k_3 k_4 k_5 k_6. \tag{5.35}$$

5.3.2 Thermal Criteria for Plant Startup

In the Super LWR, a design criterion is set on the maximum cladding surface temperature (MCST) in order to maintain fuel rod integrity and prevent cladding failures. MCST is limited to not greater than 620°C as an example for the following discussion [9].

Beyond the critical pressure and temperature, there is no actual distinction between liquid phase and vapor phase. The moisture content in the main steam is not a limiting factor during normal operation of the Super LWR (i.e., at 25 MPa pressure and 500°C temperature) because the turbine inlet steam is superheated steam. However, during Super LWR startup at subcritical pressure, the moisture content in the steam becomes a limiting factor as the turbine inlet steam is saturated steam. The moisture content in the steam is limited to not greater than 0.1% so that turbine blade damage can be prevented. This criterion is consistent with that of current BWRs.

Since the Super LWR plant system does not have a superheater, the main steam conditions need to be adjusted during startup and low power operations. The enthalpy of the core outlet coolant must be high enough to provide the required turbine inlet steam enthalpy. At subcritical pressure operation in the sliding pressure startup scheme, boiling and dry out in the descending moderator water rods are undesirable and should be prevented because they affect the inlet subcooling.

Thus, the following criteria are set to be satisfied at startup of the Super LWR.

1. The MCST must not exceed the rated value of 620°C.
2. The moisture content in the turbine inlet steam must be less than 0.1%.

3. The enthalpy of the core outlet coolant must be high enough to provide the required turbine inlet steam enthalpy.
4. Boiling should be prevented in the water rods.

5.3.3 Thermal Analyses

It is assumed that MCST occurs in the maximum power channel where the maximum linear power generation rate is 39 kW/m. Using the Super LWR plant analysis code, the maximum power channel is analyzed to calculate MCST and to determine whether it satisfies the criterion or not.

5.3.3.1 Power Increase Phase in Constant Pressure Startup or Sliding Pressure Startup

There is no difference between the pressurization phases of the constant pressure startup and sliding pressure startup schemes because the pressurization phase appears after the line switching to the once-through mode. It is assumed that the core inlet and outlet temperatures are kept equal to their respective values in the normal operating condition. While the reactor core power is increased, the feedwater flow rate is also increased proportionally. MCSTs are calculated for various core powers from 30 to 100% at intervals of 10%, and the calculated results are shown in Fig. 5.11. It is found that MCST satisfies the criterion of 620°C throughout the power increase phase.

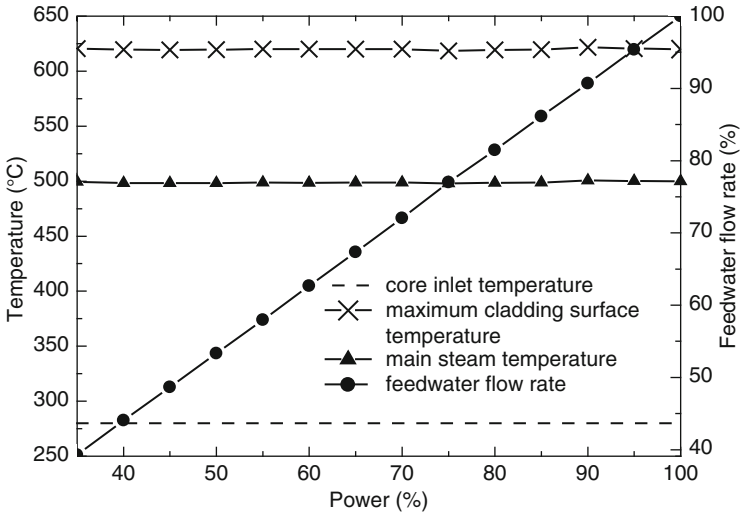


Fig. 5.11 Plant parameters during power increase phase of the Super LWR

5.3.3.2 Pressurization Phase in Sliding Pressure Startup

The power to flow rate ratio must be low enough to keep MCST below the criterion and to prevent boiling in the water rods. The maximum allowable powers are calculated with various feedwater flow rates and various feedwater temperatures. Figs. 5.12 and 5.13 [3] show the results at two pressures of 10 and 20 MPa, respectively. The maximum allowable power increases with increasing flow rate, or decreasing feedwater temperature. Figure 5.14 [3] shows the maximum allowable powers as a function of the pressure. The maximum allowable powers for various flow rates during pressurization from 8 to 25 MPa with constant feedwater temperature of 280°C are shown in Fig. 5.15.

Unlike FPPs, the Super LWR has no superheater. Thus, the main steam conditions during startup of the Super LWR need to be adjusted so that they are suitable for steam turbines. The enthalpy of the core outlet coolant must be high enough to provide the required turbine inlet steam enthalpy. Herein, it is assumed that 5% of the rated power is necessary for turbine startup. The minimum required powers are calculated with various feedwater flow rates and feedwater temperatures. The calculated results at 10 MPa are shown in Fig. 5.16 and those at 20 MPa are shown in Fig. 5.17. It is found that the minimum required power decreases with decreasing flow rate or increasing the feedwater temperature. Figure 5.18 [3] shows the minimum required powers as function of the pressure.

It is desirable to pressurize the reactor with low flow rate and low power in order to minimize the size of the steam-water separator. The minimum flow rate required

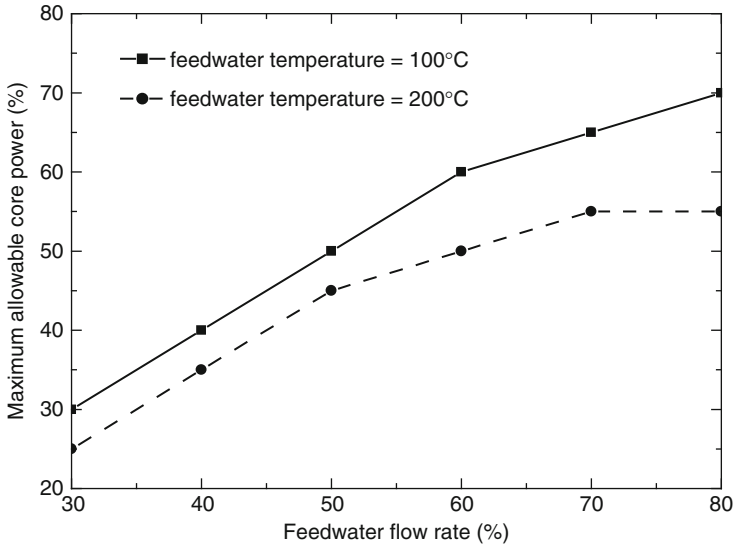


Fig. 5.12 Maximum allowable powers at 10 MPa (taken from ref. [3] and used with permission from Atomic Energy Society of Japan)

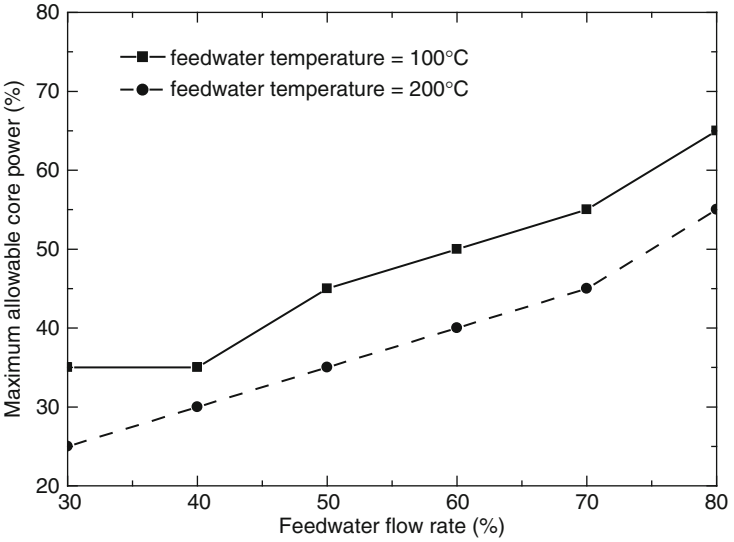


Fig. 5.13 Maximum allowable powers at 20 MPa (taken from ref. [3] and used with permission from Atomic Energy Society of Japan)

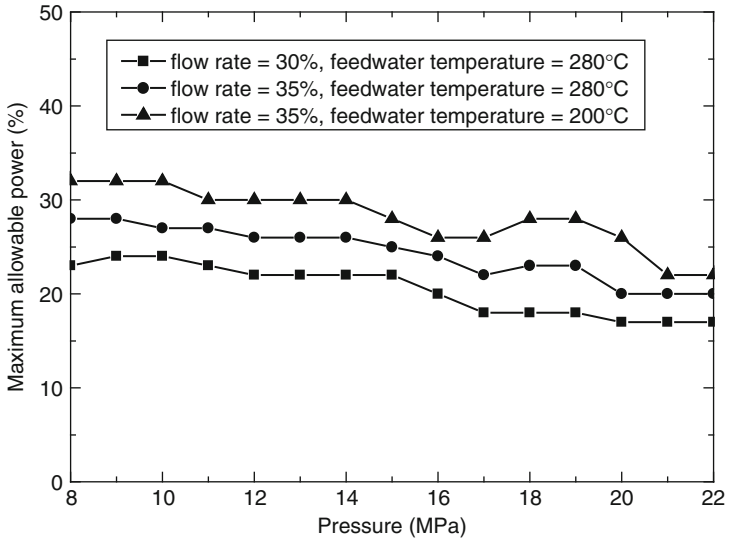


Fig. 5.14 Maximum allowable powers during pressurization phase while keeping feedwater temperature at 280°C (taken from ref. [3] and used with permission from Atomic Energy Society of Japan)

for sliding pressure startup is 28% of the rated value in typical FPPs. However, in the present design of the Super LWR, it is found that 28% flow rate is not enough to prevent boiling in the water rods. Thus, it is determined that the feedwater flow rate

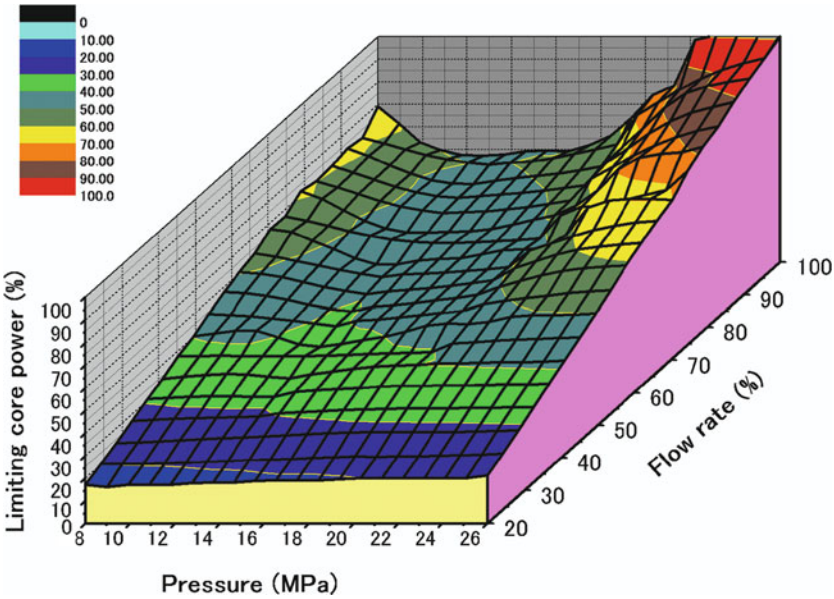


Fig. 5.15 Three-dimensional representation of the maximum allowable powers during pressurization phase while keeping feedwater temperature at 280°C

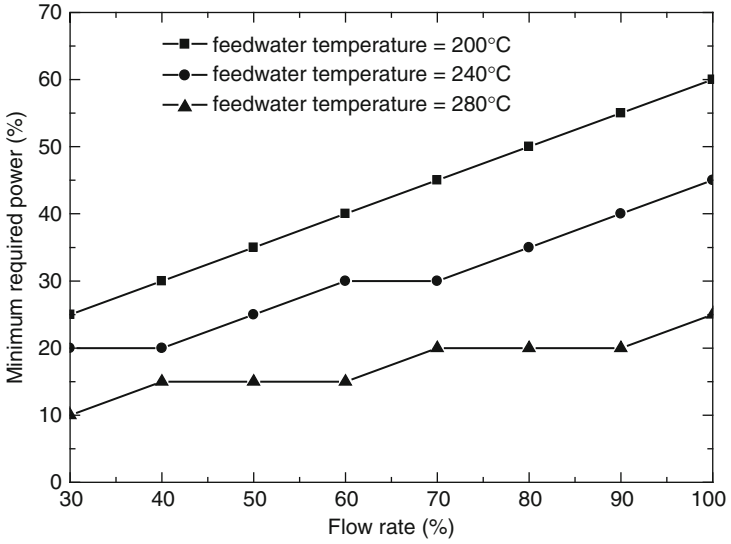


Fig. 5.16 Minimum required powers at 10 MPa

should be kept at 35% of the rated value in the pressurization phase. The feedwater temperature is also kept constant (280°C). The available region of the power is calculated as shown in Fig. 5.19 with these conditions. Because the CHF and post-CHF

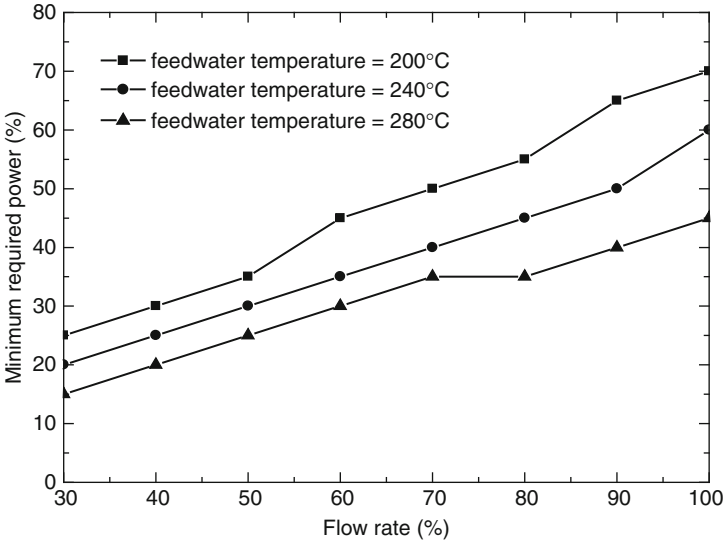


Fig. 5.17 Minimum required powers at 20 MPa

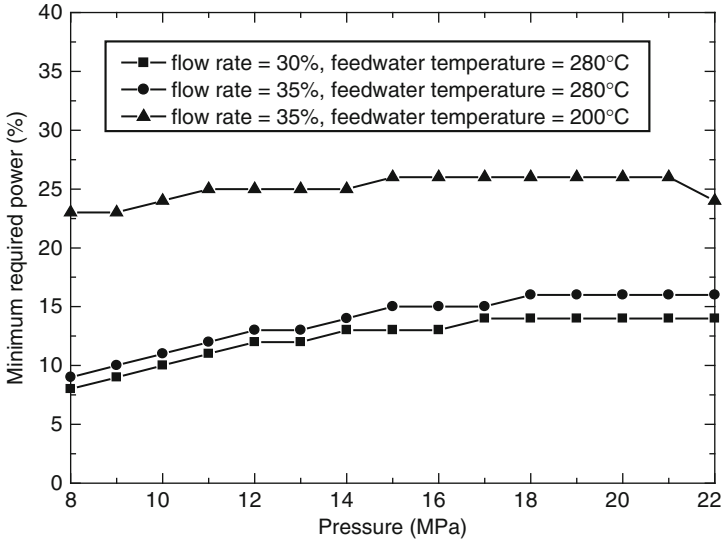


Fig. 5.18 Minimum required powers during pressurization phase (taken from ref. [3] and used with permission from Atomic Energy Society of Japan)

heat transfer coefficients are relatively small just below the critical pressure, the maximum allowable power and hence the available region are small.

Based on the available region, it is determined that the core power is kept as 20% of the rated value during pressurization. The plant parameters in the pressurization phase are shown in Fig. 5.20 [3, 10].

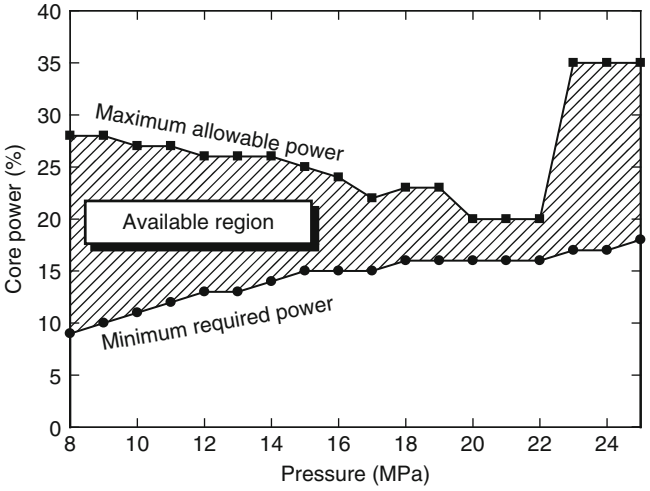


Fig. 5.19 Available region of core power in pressurization phase with feedwater flow rate of 35% and feedwater temperature of 280°C

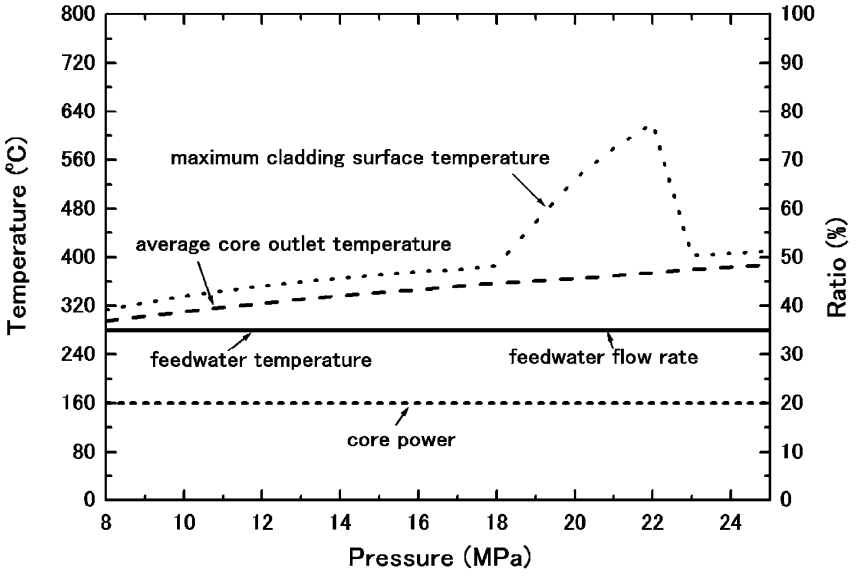


Fig. 5.20 Plant parameters in pressurization phase (taken from ref. [3] and used with permission from Atomic Energy Society of Japan)

5.3.3.3 Temperature Increasing Phase in Sliding Pressure Startup

After the pressurization phase, the coolant cycle is switched from the bypass mode to the once-through mode while keeping the feedwater flow rate, feedwater

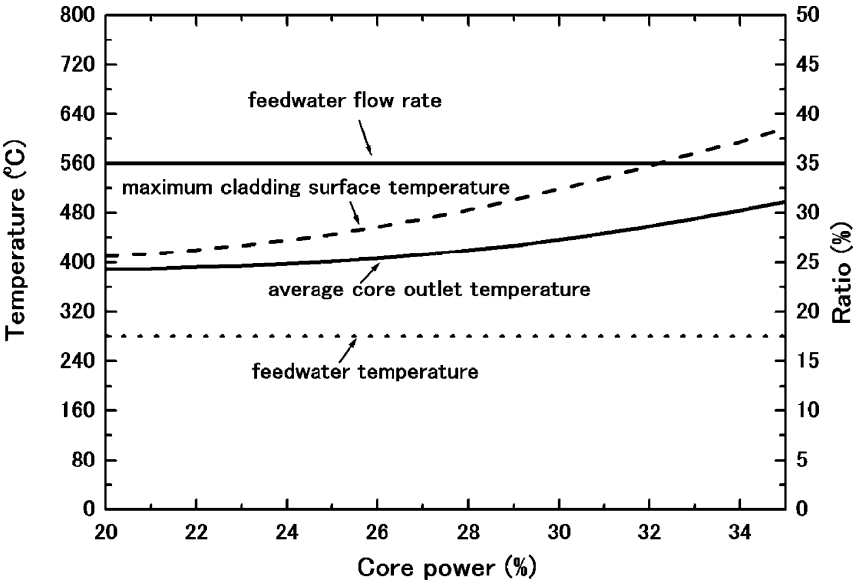


Fig. 5.21 Plant parameters in temperature increase phase (taken from ref. [3] and used with permission from Atomic Energy Society of Japan)

temperature, core power, and pressure unchanged from the end state of the pressurization phase. Next comes the temperature increase phase. The core outlet temperature is raised to 500°C by increasing the core power from 28 to 35% of the rated value. The plant parameters in the temperature increase phase are shown in Fig. 5.21 [3]. The MCST is kept below the criterion.

5.3.3.4 Design of Startup Curves Based on Thermal Considerations

Based on the thermal considerations above, the general startup curves for the constant pressure startup scheme of the Super LWR are designed as shown in Fig. 5.22 [3]. Those for the sliding pressure startup scheme are designed as shown in Fig. 5.23 [3].

5.4 Thermal-Hydraulic Stability Considerations

5.4.1 Mechanism of Thermal-Hydraulic Instability

Fundamentally, the thermal-hydraulic instability is caused by the lag introduced into the thermal-hydraulic system by the finite speed of propagation of density perturbations. As described in the previous section, as the coolant flows from the

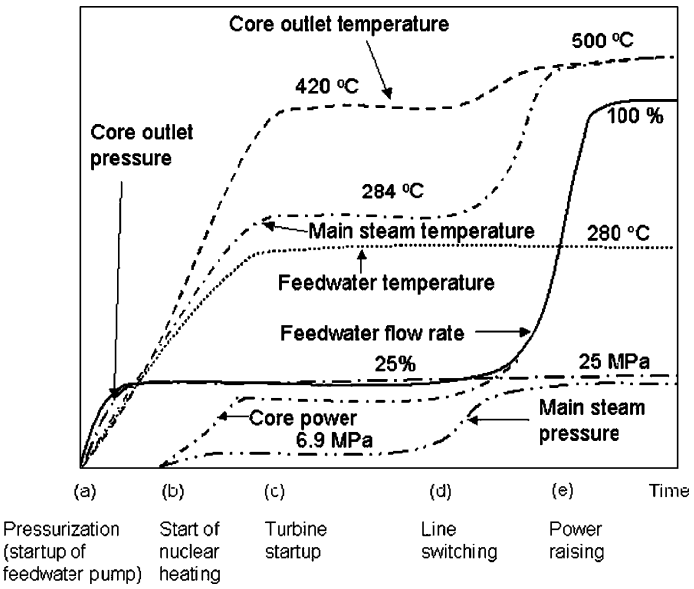


Fig. 5.22 Constant pressure startup curves for the Super LWR (taken from ref. [3] and used with permission from Atomic Energy Society of Japan)

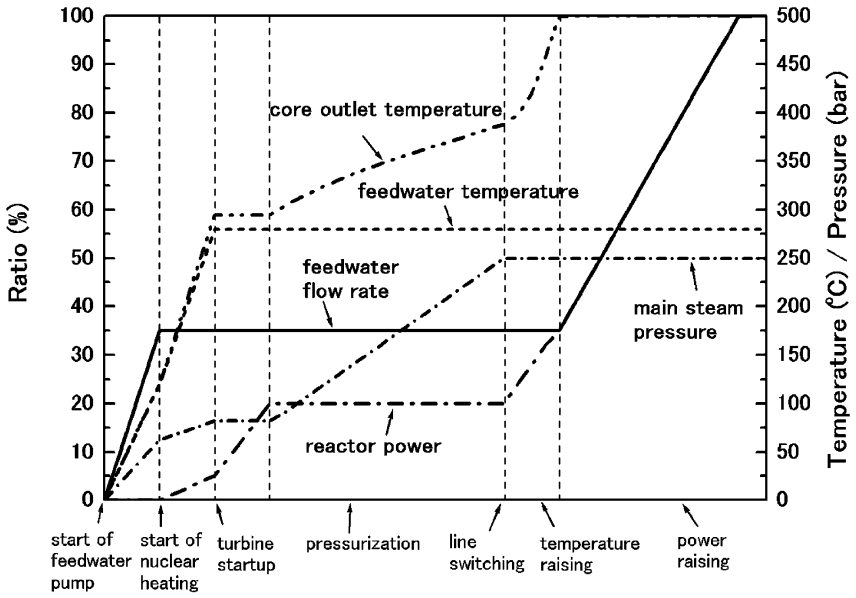


Fig. 5.23 Sliding pressure startup curves for the Super LWR (taken from ref. [3] and used with permission from Atomic Energy Society of Japan)

fuel channel inlet to the fuel channel outlet in the Super LWR, the coolant temperature passes through the pseudocritical temperature of 385°C, at which the water density changes drastically. So there is a large difference in coolant density between the core inlet and core outlet. The coolant in the fuel channels of the Super LWR flows in the upward direction through the core. As the variations in the coolant density travel upwards with the coolant flow, it causes a change in the local pressure drop at each axial position, which is delayed axially by the time taken by the coolant to travel upwards through the core. The sum of all these local pressure drops causes a change in the total pressure drop and a significant lag results between the channel outlet pressure drop perturbations and the inlet velocity perturbations. The thermal-hydraulic instability occurs if the channel pressure drop perturbations become out-of-phase with the inlet flow perturbations. The physical mechanism causing the thermal-hydraulic instability is shown in Fig. 5.24.

5.4.2 Selection of Analysis Method

There are two types of approaches used in stability analyses: a time domain approach and a frequency domain approach.

In the time domain approach, the purpose is to simulate the transient behavior of the reactor plant system. The governing equations, which describe the physical phenomena of the reactor dynamics system, are integrated in the time domain. This approach permits the considerations of detailed physical mechanisms, including nonlinear features. It does not need simplified assumptions and can provide information on the behavior of the reactor system beyond the stability threshold. However, a much longer time is necessary to calculate the extensive number of time steps than the frequency domain approach.

It is well-recognized that instability is a highly nonlinear phenomenon. However, the dynamic behavior of nuclear reactors can be assumed to be linear for small

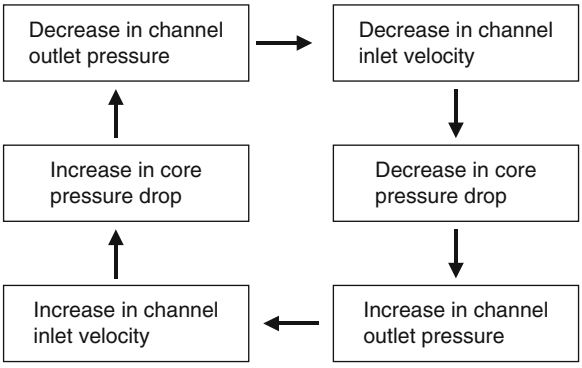


Fig. 5.24 Physical mechanism causing thermal-hydraulic instability

perturbations around steady-state conditions. This makes it possible to study the reactor stability and predict the threshold of instability in nuclear reactors by the frequency domain approach. Unlike the time domain approach, it is based on linearization of governing equations and analyzing them in the frequency domain. As a consequence, the analysis is much faster as it does not involve the full set of differential equations. This approach can be used to predict the stability margin of operating conditions under small perturbations. Since nonlinear effects are not taken into account, this approach cannot predict the behavior of the reactor system beyond the stability threshold.

For the purpose of preliminary conceptual design of the Super LWR, first, it is important to determine whether the instability will be a problem, and how it can be avoided if it occurs. Thus, the first aim is to investigate what may cause the instability and when it can occur in the Super LWR. To achieve that aim, the approach is to use a simple model which can explain the essential features of the physical phenomena of the system without the requirement of much computing effort. Hence, the simple frequency domain linear stability analysis method is employed to investigate the onset of instability in the Super LWR.

5.4.3 Thermal-Hydraulic Stability Analysis Method

5.4.3.1 Mathematical Model

The one-dimensional single-channel single-phase conservation equations of mass, energy and momentum, and the state equation for the coolant channel are written below.

Mass conservation:

$$\frac{\partial \rho}{\partial t} + \frac{\partial (\rho u)}{\partial z} = 0. \tag{5.36}$$

Energy conservation:

$$\frac{\partial (\rho h)}{\partial t} + \frac{\partial (\rho u h)}{\partial z} = \frac{P_{\mathrm{e}}}{A} q'' - \frac{N_{\mathrm{f}}}{N_{\mathrm{w}} A_{\mathrm{w}}} Q_{\mathrm{w}}. \tag{5.37}$$

Momentum conservation:

$$-\frac{\partial P}{\partial z} = \frac{\partial (\rho u)}{\partial t} + \frac{\partial (\rho u^2)}{\partial z} + \rho g \cos\theta + \frac{2f}{D_h} \rho u^2. \tag{5.38}$$

State equation:

$$\rho = \rho(P, h), \tag{5.39}$$

where P_e, A, q'', N_f, N_w, A_w, and Q_w are the heated perimeter, cross-sectional area of the fuel channel, heat flux at the cladding surface, number of fuel rods, number of water rods, cross-sectional area of each water rod, and linear heat transfer rate between the fuel channel and the water rod, respectively.

The same equations are used for single-phase and two-phase regions. For single-phase regions, the thermophysical properties are those of subcooled liquid or superheated vapor. For two-phase regions, the thermophysical properties are mass-averaged or volume-averaged values for two-phase homogeneous mixture. The compressibility of the fluid is taken into consideration. The friction pressure drop coefficient f is determined from the Blasius equation.

Single-phase region:

$$f_{SP} = 0.079\left(\frac{GD_h}{\mu}\right)^{-1/4} = f_{fo}. \tag{5.40}$$

Two-phase region:

$$f_{TP} = 0.079\left(\frac{GD_h}{\bar{\mu}}\right)^{-1/4} = f_{fo}\left[1 + x\left(\frac{\mu_{fg}}{\mu_g}\right)\right]^{-1/4}. \tag{5.41}$$

The mean two-phase viscosity is evaluated as

$$\frac{1}{\bar{\mu}} = \frac{x}{\mu_g} + \frac{(1-x)}{\mu_f}. \tag{5.42}$$

The conservation equations are numerically discretized along the axial direction by the forward finite difference method. The discretization or nodalization is done by dividing the coolant channel and the water rods into nodes of equal length and by approximating the time-dependent thermal-hydraulic variables as spatially uniform within these nodes. Equations (5.36)–(5.39) are expressed as follows for each axial node i.

$$\frac{\partial \rho_i}{\partial t} + \frac{\rho_i u_i - \rho_{i-1} u_{i-1}}{\Delta z} = 0. \tag{5.43}$$

$$\frac{\partial(\rho_i h_i)}{\partial t} + \frac{\rho_i u_i h_i - \rho_{i-1} u_{i-1} h_{i-1}}{\Delta z} = \frac{P_e}{A} q_i'' - \frac{N_f}{N_w A_w} Q_{w\,i}. \tag{5.44}$$

$$\frac{P_{i-1} - P_i}{\Delta z} = \frac{\partial(\rho_i u_i)}{\partial t} + \frac{\rho_i u_i^2 - \rho_{i-1} u_{i-1}^2}{\Delta z} + \rho_i g \cos\theta + \frac{2 f_i}{D_h} \rho_i u_{i-1}^2. \tag{5.45}$$

$$\rho_i = \rho_i(P_i, h_i). \tag{5.46}$$

These equations are perturbed, linearized, and Laplace-transformed from the time domain to the frequency domain to evaluate the transfer functions between various thermal-hydraulic parameters. The Laplace-transformed equations are solved simultaneously by means of a matrix equation.

For the single-phase region, the state equation becomes

$$\delta\hat{\rho}_i = \left(\frac{\partial\rho_i}{\partial P_i}\right)\delta\hat{P}_i + \left(\frac{\partial\rho_i}{\partial h_i}\right)\delta\hat{h}_i. \tag{5.47}$$

For the two-phase region, the state equation is given as

$$\delta\hat{\rho}_i = \left(\frac{\partial\rho_i}{\partial\alpha_i}\right)\left(\frac{\partial\alpha_i}{\partial x_i}\right)\left(\frac{\partial x_i}{\partial h_i}\right)\delta\hat{h}_i + \left(\frac{\partial\rho_i}{\partial P_i}\right)\delta\hat{P}_i. \tag{5.48}$$

The mixture density and the mixture specific enthalpy are defined as

$$\rho_i = \alpha\rho_{\mathrm{g}} + (1-\alpha)\rho_{\mathrm{f}}, \tag{5.49}$$

and

$$h_i = xh_{\mathrm{g}} + (1-x)h_{\mathrm{f}}. \tag{5.50}$$

The homogeneous fluid specific volume is defined by

$$v = xv_{\mathrm{g}} + (1-x)v_{\mathrm{f}} = 1/\rho. \tag{5.51}$$

The slip ratio is assumed to be one. The void fraction and the steam quality are related as

$$\alpha = \frac{x\rho_{\mathrm{f}}}{x\rho_{\mathrm{f}} + (1-x)\rho_{\mathrm{g}}}. \tag{5.52}$$

The properties of supercritical water are determined by utilizing the JSME 1980 Steam Table in SI units. The thermal-hydraulic properties at the outlet of one node are used to determine the corresponding properties at the inlet of the next downstream node. As for the boundary conditions, the channel inlet coolant enthalpy and flow rate are specified from the water rod outlet enthalpy and water rod outlet flow rate.

The axial core power is assumed to follow a cosine distribution for simplicity. The variation of the axial power distribution with fuel burnup is not considered here. It should be noted that the actual distribution of the axial core power may be top-peak, bottom-peak or chopped cosine, depending on the fuel burnup during the cycle. Also, the effect of the axial power distribution on thermal-hydraulic stability is not taken into account here.

The conservation equations of mass, energy, and momentum and the state equation in the downward flowing water rod may be written similarly to (5.36)–(5.39).

Mass conservation:

$$\frac{\partial \rho_{\mathrm{w}}}{\partial t} + \frac{\partial (\rho_{\mathrm{w}} u_{\mathrm{w}})}{\partial z} = 0. \tag{5.53}$$

Energy conservation:

$$\frac{\partial (\rho_{\mathrm{w}} h_{\mathrm{w}})}{\partial t} + \frac{\partial (h_{\mathrm{w}} \rho_{\mathrm{w}} u_{\mathrm{w}})}{\partial z} = \frac{N_{\mathrm{f}}}{N_{\mathrm{w}} A_{\mathrm{w}}} Q_{\mathrm{w}}. \tag{5.54}$$

Momentum conservation:

$$-\frac{\partial P_{\mathrm{w}}}{\partial z} = \frac{\partial (\rho_{\mathrm{w}} u_{\mathrm{w}})}{\partial t} + \frac{\partial (\rho_{\mathrm{w}} u_{\mathrm{w}}^2)}{\partial z} + \rho_{\mathrm{w}} g \cos\theta + \frac{2 f_{\mathrm{w}}}{D_{\mathrm{h}}} \rho_{\mathrm{w}} u_{\mathrm{w}}^2. \tag{5.55}$$

State equation:

$$\rho_{\mathrm{w}} = \rho_{\mathrm{w}}(P_{\mathrm{w}}, h_{\mathrm{w}}). \tag{5.56}$$

These equations are axially discretized, perturbed, linearized, and Laplace-transformed to evaluate the transfer functions between various thermal-hydraulic parameters in the water rods.

An orifice is designed at the inlet of the fuel assembly to enhance the flow stability. Thus, the orifice pressure drop coefficient is modeled by the following equation.

$$\Delta p = \zeta \frac{\rho u^2}{2}. \tag{5.57}$$

Perturbing and Laplace-transformation of this equation gives

$$\delta\, \Delta \hat{p} = \zeta \rho u \delta \hat{u}. \tag{5.58}$$

5.4.3.2 Steady-State Calculation

In the linear approach, the steady-state parameters are required as initial conditions for the evaluation of system stability, and they are calculated by the plant analysis code developed for the Super LWR, considering the effects of water rods on the coolant channels. The fuel channel is axially discretized into meshes of equal length, and the fuel and coolant properties are assumed uniform within each mesh. The one-dimensional single-channel single-phase conservation equations are solved for each axial mesh in the fuel channel and in each water rod, starting from the core inlet to the core outlet. The core inlet coolant temperature and mass

flow rate are used as boundary conditions. The axial core power is assumed to follow a cosine distribution. All the heat generated in the fuel is assumed to be transferred to the coolant.

The axial distributions of the enthalpy, temperature, density, and velocity of the coolant and the moderator are determined for a given core power, feedwater temperature, feedwater flow rate, and the pressure. The calculation is carried out iteratively until the temperature distributions are convergent to steady-state values. The fuel and cladding temperatures are calculated for each axial mesh with one-dimensional radial heat transfer equations using the coolant and moderator temperature distribution. Steady-state temperature distributions are assumed in the fuel pellet, fuel cladding, and the gap. The heat transfer between fuel pellet and the coolant, as well as the heat transfer between the fuel channel and the water rods is considered. The heat transfer coefficients are calculated by the Oka–Koshizuka correlation, which was developed by using the Jones-Launder k–ε turbulence model.

5.4.3.3 Frequency Domain Analysis

The linearized and Laplace-transformed equations of the models described above are used to evaluate the various system transfer functions as functions of the Laplace variables $s = \sigma + j\omega$, where σ is the real part and ω is the imaginary part of the complex variable s. σ refers to the damping constant (or damped exponential frequency) and ω refers to the resonant oscillation frequency of the system.

If the forward transfer function and feedback transfer function of the system are represented by $G(s)$ and $H(s)$ respectively, then the closed loop transfer function is expressed by

$$\frac{G(s)}{1 + G(s)H(s)}. \tag{5.59}$$

The poles of the closed loop transfer function are determined by solving the characteristic equation.

$$1 + G(s)H(s) = 0. \tag{5.60}$$

The poles of the closed loop system transfer function may be real and/or complex conjugate pairs. For systems with more than one pole, the pole which has the slowest response is dominant over other poles after some time. For stable systems, the dominant pole is the pole nearest to the imaginary axis (the pole with largest value of $\sigma/|\omega|$), and it is used to determine the stability of the system. The stability of the system depends on the value of σ. For the system to be stable, all the poles of the closed loop transfer function must have negative real parts ($\sigma < 0$). The system becomes unstable if a pole crosses the imaginary axis and enters into the

right half of the s-plane ($\sigma > 0$). The system will be on the margin of stability and will sustain an oscillation without damping if the pole lies on the imaginary axis ($\sigma = 0$). The farther the pole is from the imaginary axis on the complex s-plane, the faster the system responds, and the more stable it is. On the other hand, the farther the pole is from the real axis on the complex s-plane, the faster is the oscillation and the more unstable the system is.

5.4.3.4 Decay Ratio

The system stability is described by the decay ratio, which is defined as the ratio of two consecutive peaks of the impulse response of the oscillating variable as shown in Fig. 5.25 [11]. For the complex pole $s = \sigma + j\omega$, the impulse response of the system is represented by $Ke^{\sigma t}(\cos \omega t + j \sin \omega t)$ where K is a constant. Hence, if we know the position of the complex poles of the closed loop transfer function, the decay ratio (DR) can be calculated by using (5.61).

$$\text{Decay ratio} = \text{DR} = \frac{y_2}{y_1} = \frac{|Ke^{\sigma t_2}(\cos \omega t_2 + j \sin \omega t_2)|}{|Ke^{\sigma t_1}(\cos \omega t_1 + j \sin \omega t_1)|} = e^{\sigma(t_2 - t_1)} = e^{2\pi\sigma/\omega}. \tag{5.61}$$

The axial mesh size is found to have a significant effect on DR and the frequency response. DR generally increases as the axial mesh size decreases as shown in Fig. 5.26 [11]. Thus, DR is determined by extrapolation to zero mesh size using the method of least squares.

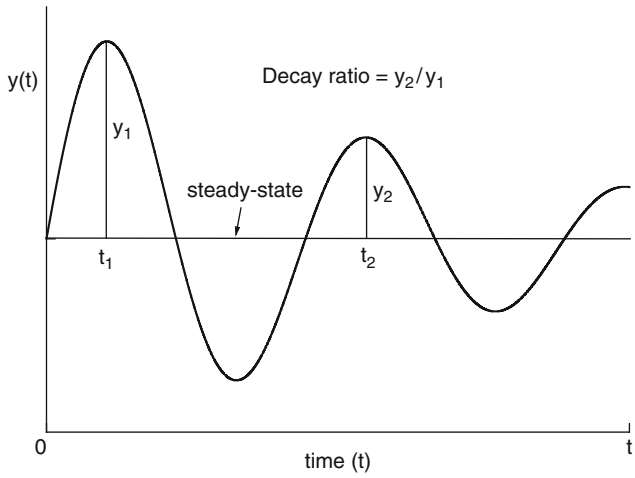


Fig. 5.25 Definition of decay ratio (taken from ref. [11] and used with permission from Atomic Energy Society of Japan)

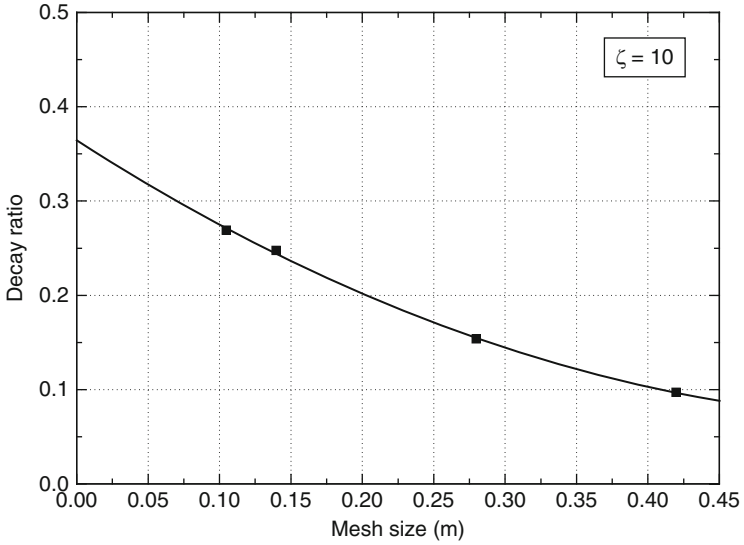


Fig. 5.26 Effect of axial mesh size on decay ratio (taken from ref. [11] and used with permission from Atomic Energy Society of Japan)

5.4.3.5 Stability Criterion

The following stability criteria of decay ratio for thermal-hydraulic stability are imposed on the Super LWR to guarantee the safety and stability of the reactor. These criteria are taken from those of BWRs.

(a) DR $\leq$ 0.5 (damping ratio $\sigma \geq 0.11$) for normal operating conditions
(b) DR $\leq$ 1.0 (damping ratio $\sigma \geq 0$) for all operating conditions

It should be mentioned that the calculation uncertainty has not been considered yet in the stability criteria of the $DR = 1.0$ for transient conditions. This does not affect the analysis results obtained here, as this chapter essentially deals with normal operating conditions, rather than with transient conditions.

5.4.4 Thermal-Hydraulic Stability Analyses

The fuel channel thermal-hydraulics model and the channel inlet orifice model are used in the thermal-hydraulic stability analyses. The axial power distribution is taken as a cosine distribution. The power generation in the fuel is assumed to be constant and only flow feedback is considered. The block diagram for thermal-hydraulic stability is shown in Fig. 5.27 [10, 11]. The forward transfer function is evaluated from the channel inlet orifice model. The feedback transfer function is

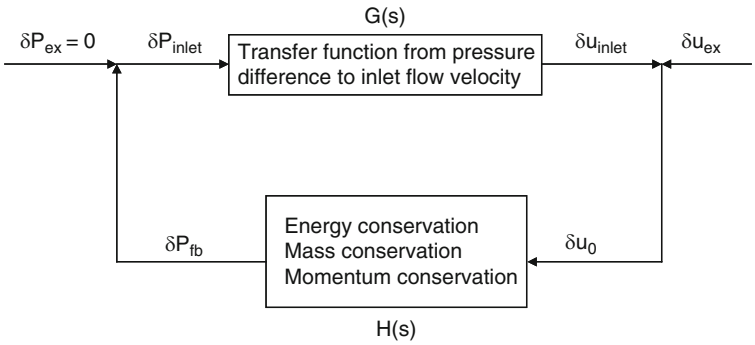


Fig. 5.27 Block diagram for thermal-hydraulic stability analysis (taken from ref. [11] and used with permission from Atomic Energy Society of Japan)

Table 5.8 Calculation conditions for thermal-hydraulic stability analyses of the Super LWR (taken from ref. [11] and used with permission from Atomic Energy Society of Japan)

	Maximum channel	Average channel
Linear power generation rate (kW/m)	39	24.6
Coolant mass flux (kg/m^{2}s)	1,160	822
Channel inlet temperature (°C)	302	299.5
Channel outlet temperature (°C)	575	500
Water rod flow ratio	30%	30%
Water rod mass flow rate (kg/s)	357	253
Inlet/outlet coolant density(kg/m^3)	740/75	744/90
Inlet/outlet coolant velocity (m/s)	1.6/15.5	1.1/9.2

determined from the thermal-hydraulics model. The closed loop transfer function is given as

$$\frac{\delta \hat{u}_{\text{in}}}{\delta \hat{P}_{\text{in}}} = \frac{G(s)}{1 + G(s)H(s)}. \tag{5.62}$$

Herein, both the maximum power channel and the average power channel are analyzed to investigate the thermal-hydraulic stability. For the maximum power channel, the maximum linear heat generation rate in the axial direction is 39 kW/m and the core outlet temperature is 575°C. For the average power channel, the maximum linear heat generation rate in the axial direction is 24.6 kW/m and the core outlet temperature is 500°C. The calculation conditions used for the thermal-hydraulic analyses of maximum power channel and average power channel are shown in Table 5.8 [11].

The present stability code is checked by the characteristics of the frequency response of the transfer functions at the steady state by using Bode plots. For instance, the frequency response of the inlet velocity to outlet pressure transfer function shows that at low frequency the phase lag of the outlet pressure to that of

inlet velocity is 180°. This confirms the fact that when the inlet velocity increases, the outlet pressure decreases due to an increase in channel pressure drop.

The frequency response of the closed loop transfer function of thermal-hydraulic stability for the average power channel of the Super LWR at 100% power operation with different mesh sizes (assuming an orifice pressure drop coefficient of 10) is shown in Figs. 5.28 and 5.29. A resonant peak is observed at the frequency of about 2.5 rad/s due to the flow feedback effect. A similar resonant peak is observed at the frequency of about 4 rad/s for the 100% maximum power channel as shown in Figs. 5.30 and 5.31. These resonant frequencies are consistent with the corresponding coolant transit time (about 1.6 s for the average power channel and about 1.0 s for the maximum power one).

5.4.4.1 Thermal-Hydraulic Stability at Full Power Normal Operation

The decay ratios for thermal-hydraulic stability are calculated for the maximum power channel as well as the average power channel for the Super LWR at 100% power and 100% flow rate at constant pressure. The calculation is carried out with different mesh sizes and with various orifice pressure drop coefficients. The relation between the decay ratios (obtained by extrapolation to the zero mesh size) and orifice pressure drop coefficients is shown in Fig. 5.32 [11]. The reactor is found to become more stable when the orifice pressure drop coefficient increases. It can be seen that the thermal-hydraulic stability criterion is satisfied in the Super LWR at

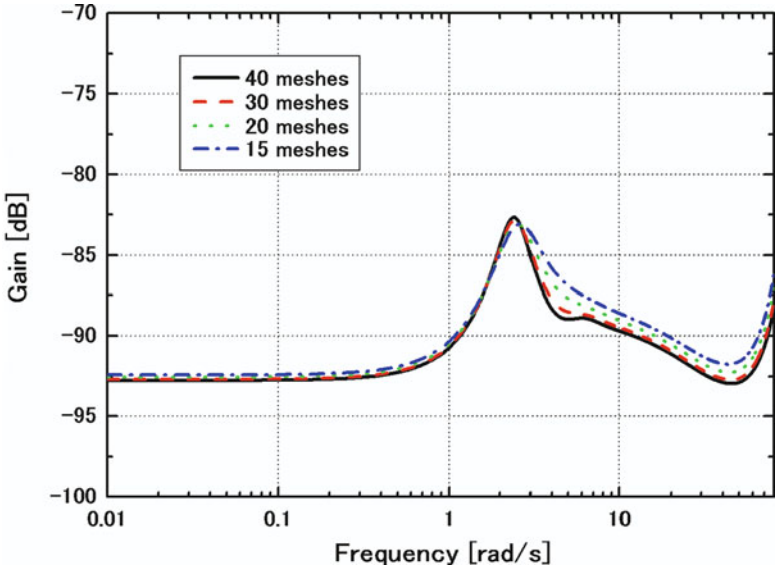


Fig. 5.28 Gain response of closed loop transfer function of thermal-hydraulic stability in average power channel at full power operation ($\zeta = 10$)

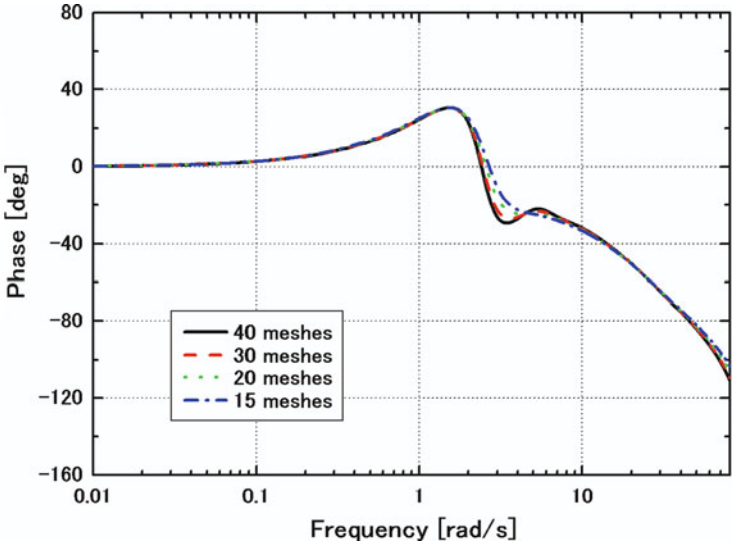


Fig. 5.29 Phase response of closed loop transfer function of thermal-hydraulic stability in average power channel at full power operation ($\zeta = 10$)

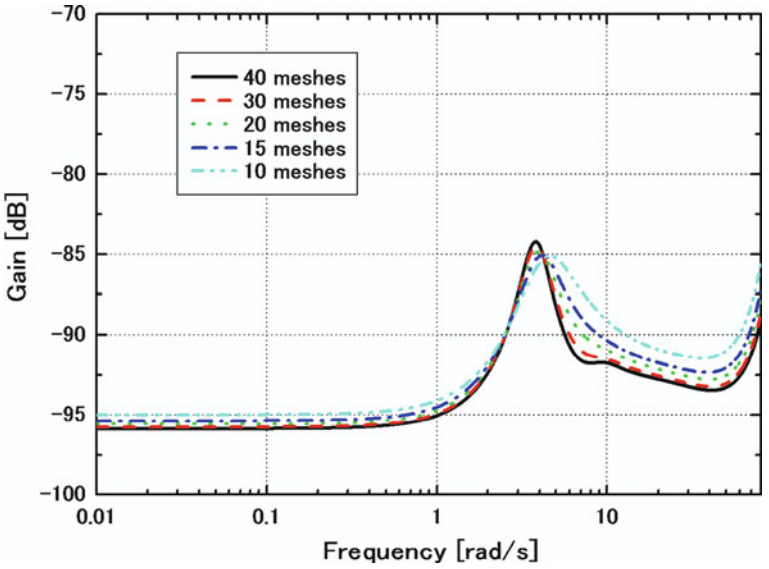


Fig. 5.30 Gain response of closed loop transfer function of thermal-hydraulic stability in maximum power channel at full power operation ($\zeta = 10$)

full power normal operation for the average power channel. The maximum power channel can be stabilized by applying a proper orifice pressure drop coefficient. The minimum orifice pressure drop coefficient required for thermal-hydraulic stability

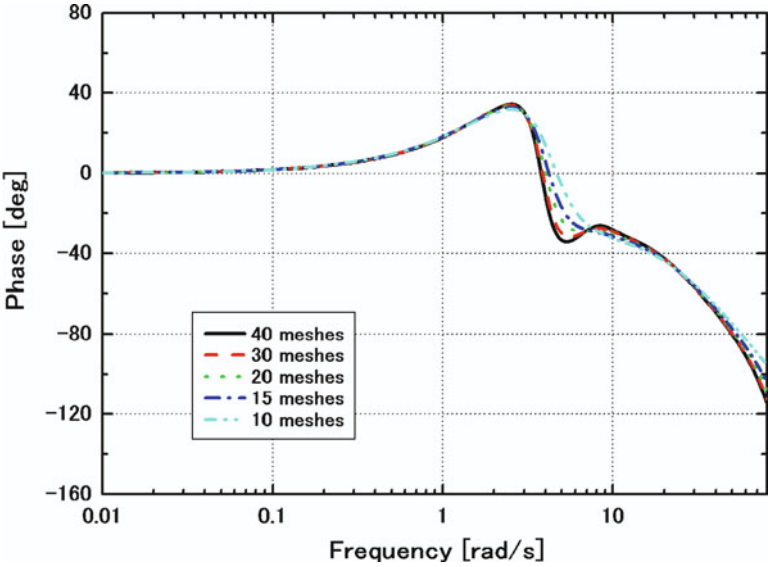


Fig. 5.31 Phase response of closed loop transfer function of thermal-hydraulic stability in maximum power channel at full power operation ($\zeta = 10$)

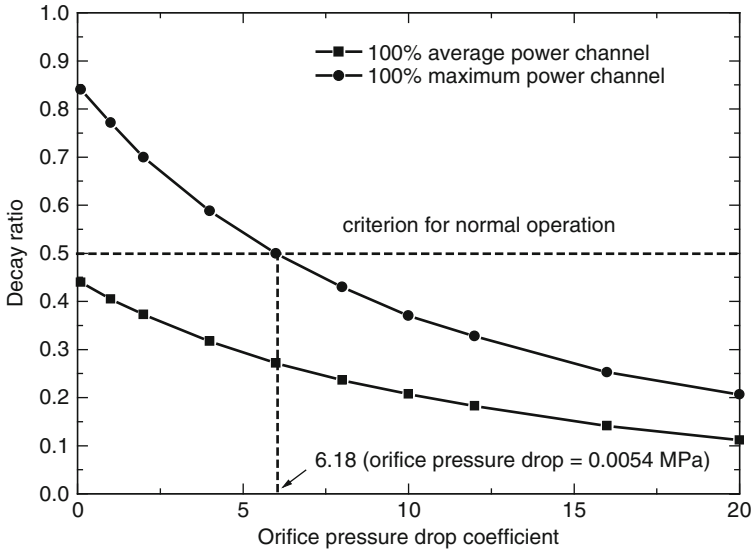


Fig. 5.32 Orifice pressure drop coefficient versus decay ratio of thermal-hydraulic stability at full power operation (taken from ref. [11] and used with permission from Atomic Energy Society of Japan)

at full power operation is found to be 6.18, which corresponds to a pressure drop of 0.0054 MPa. The total core pressure drop, including the inlet orifice at full power operation, is about 0.133 MPa. Thus, the required orifice pressure drop is not large compared with the total core pressure drop. The analysis results of thermal-hydraulic stability with the orifice pressure drop coefficient of 6.18 are summarized in Table 5.9 [11].

5.4.4.2 Thermal-Hydraulic Stability at Partial Power Operations at 25 MPa

Next, the decay ratios are calculated in the maximum power channel with various powers and orifice pressure drop coefficients while keeping the power to flow rate ratio constant. The results are shown in Fig. 5.33. With relatively large orifice pressure drop coefficients, the decay ratio increases as the core power decreases.

Table 5.9 Calculated results for thermal-hydraulic stability analyses of the Super LWR (taken from ref. [11] and used with permission from Atomic Energy Society of Japan)

	Maximum channel	Average channel
Orifice pressure drop coefficient	6.18	6.18
Core pressure drop (MPa)	0.133	0.076
Orifice pressure drop (MPa)	0.0054	0.0027
Resonant frequency (rad/s)	4.0	2.5
Oscillation frequency (Hz)	0.58	0.33
Damping ratio	0.11	0.2
Decay ratio	0.5	0.27

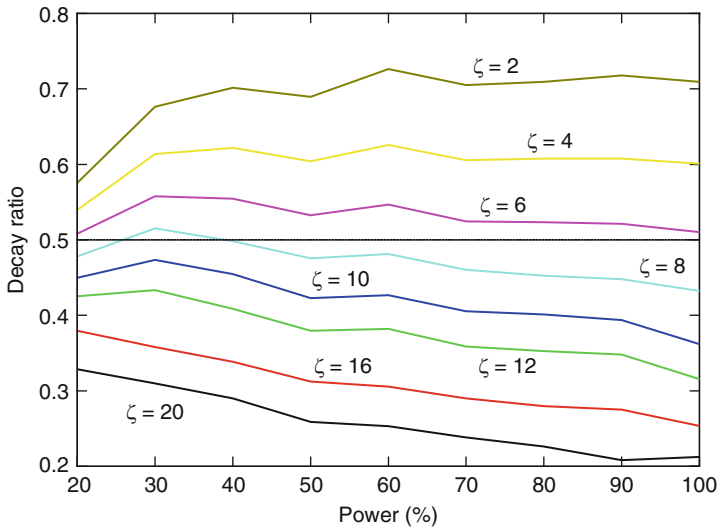


Fig. 5.33 Decay ratios of thermal-hydraulic stability in maximum power channel at partial power operations

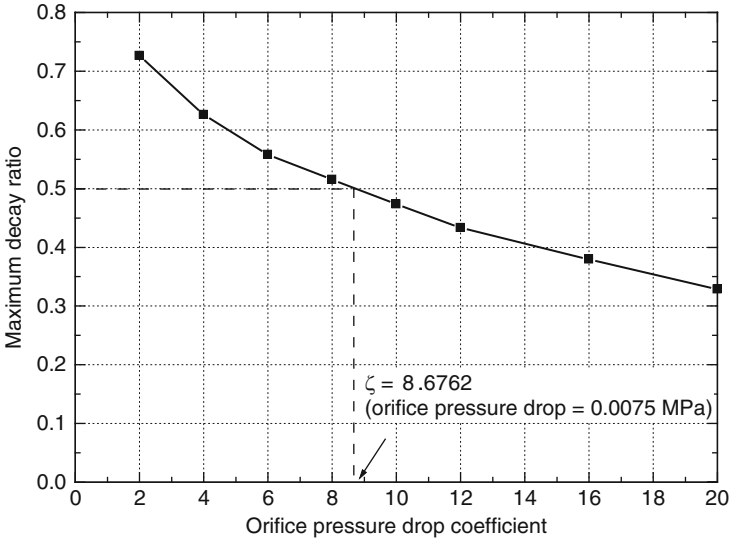


Fig. 5.34 Orifice pressure drop coefficient versus maximum decay ratio of thermal-hydraulic stability in maximum power channel at partial power operations

On the other hand, the decay ratio decreases with the core power when the orifice pressure drop coefficient is relatively small. The maximum decay ratios determined from Fig. 5.33 are plotted in Fig. 5.34. The minimum orifice pressure drop coefficient required to satisfy the stability criteria is found to be 8.68. Even with higher pressure drop coefficients (20 or 30), the fraction of the orifice pressure drop in the total core pressure drop is still considerably small as shown in Fig. 5.35. The orifice pressure drop is still much lower than the total core pressure drop.

The dependence of decay ratio of thermal-hydraulic stability on the power to flow ratio is also investigated. The decay ratios are calculated for various values of power and flow rate in the maximum power channel of the Super LWR assuming the orifice pressure drop coefficient is 20 and the mesh size is 0.105 m. They are shown in Fig. 5.36. Generally, the decay ratio increases, and hence, the channel becomes less stable as the power to flow ratio increases.

When the power to flow rate ratio is unity, the decay ratio is much lower than 0.5. This implies that the criterion for thermal-hydraulic stability can be made less limiting than the MCST at the power increasing phase by having a reasonable pressure drop at the inlet orifice.

5.4.4.3 Thermal-Hydraulic Stability at Pressurization Phase

From the thermal considerations in Sect. 5.3.3.2, the core power, feedwater flow rate, and feedwater temperature are designed as 20 and 35% of the rated values and 280°C, respectively. With these conditions, the decay ratios of thermal-hydraulic

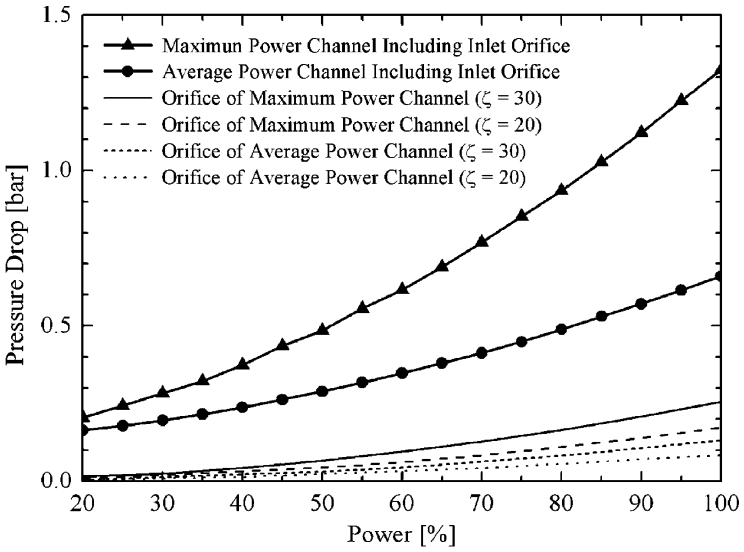


Fig. 5.35 Core power versus pressure drop

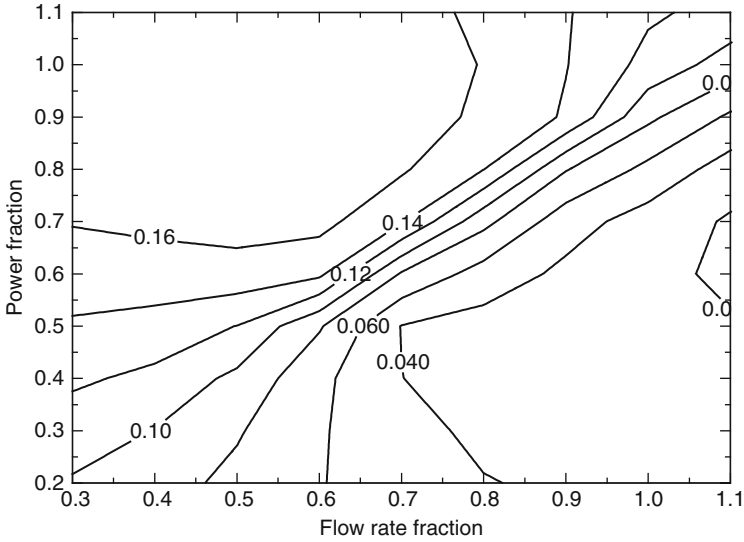


Fig. 5.36 Decay ratio map of thermal-hydraulic stability for maximum power channel (axial mesh size = 0.105 m, $\zeta = 20$)

stability are calculated with the orifice pressure drop coefficient as 30. The results are shown in Fig. 5.37. It is found that the stability criterion is satisfied with sufficient margin during pressurization. The pressure drop in the maximum power channel, including the orifice pressure drop, ranges from 0.027 to 0.037 MPa during

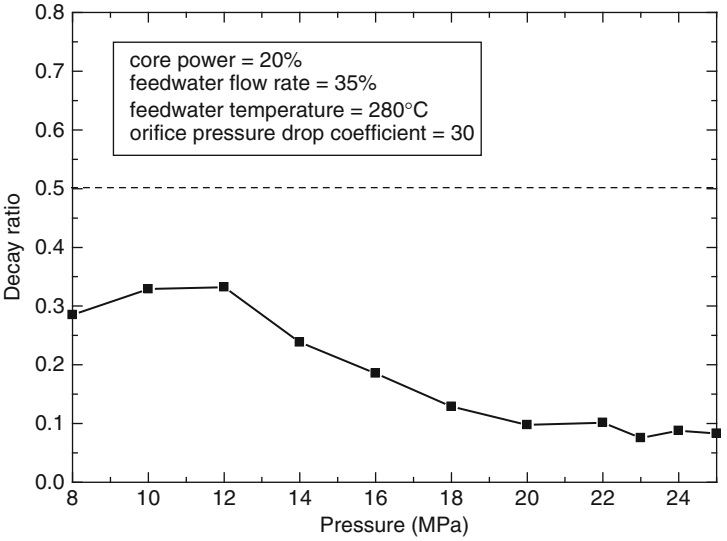


Fig. 5.37 Thermal-hydraulic stability of the Super LWR during pressurization phase

the pressurization phase, while the orifice pressure drop is only 0.0034 MPa. This implies that the criterion for thermal-hydraulic stability can be made less limiting than the MCST at the pressurization phase by having a reasonable pressure drop at the inlet orifice. The orifice pressure drop coefficient of 30 does not cause a large pressure drop during the power increase phase, either, as shown in Fig. 5.35.

5.4.4.4 Parametric Studies of Thermal-Hydraulic Stability

The thermal-hydraulic stability of the Super LWR may be sensitive to various operating conditions and design parameters. Because the present design is just an example, parametric studies are important in order to know the influences of various parameters and the robustness of the Super LWR.

Because the Super LWR is a forced convection system, increasing the inlet pressure drop increases the pressure head to force the coolant through the fuel channel. It enforces damping and hence makes the system more stable as shown in Figs. 5.32–5.34 although it does not affect the oscillation frequency of the system, as shown in Fig. 5.38.

The density ratio between the channel inlet and outlet gets larger as the power to flow rate ratio increases. This makes the channel less stable as shown in Fig. 5.36 and also increases the oscillation frequency as shown in Figs. 5.39–5.40 [11].

In the present design of the Super LWR, the operating pressure is 25 MPa. The effect of this pressure is investigated while keeping the feedwater flow rate, core power, and inlet and outlet coolant enthalpies constant. The relation between the decay ratio and the pressure is shown in Fig. 5.41 [11]. The reason why the decay

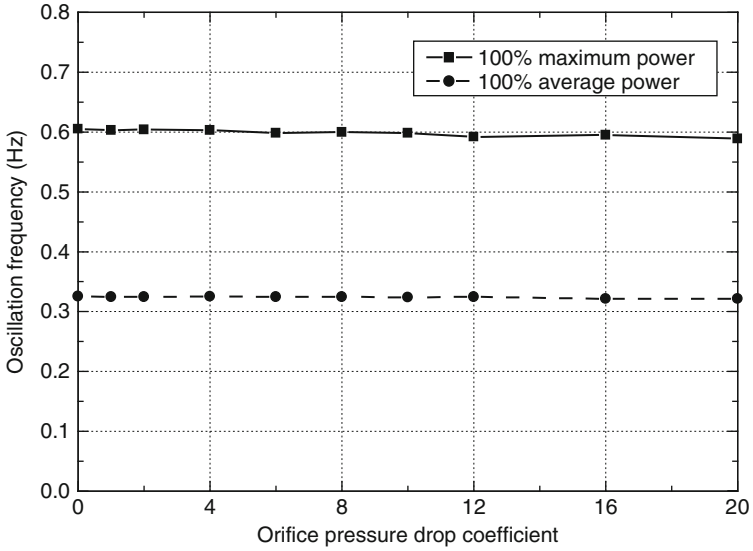


Fig. 5.38 Effect of orifice pressure drop coefficient on oscillation frequency of thermal-hydraulic stability

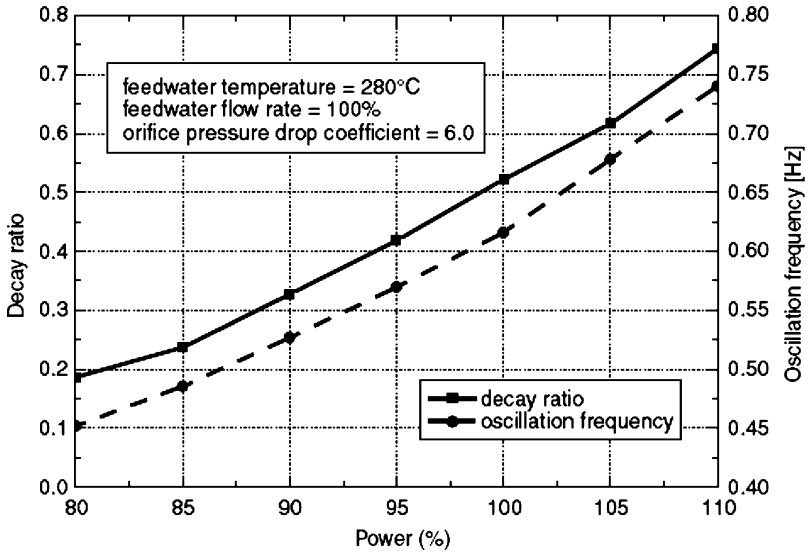


Fig. 5.39 Effect of core power on decay ratio and oscillation frequency of thermal-hydraulic stability with constant flow rate (taken from ref. [11] and used with permission from Atomic Energy Society of Japan)

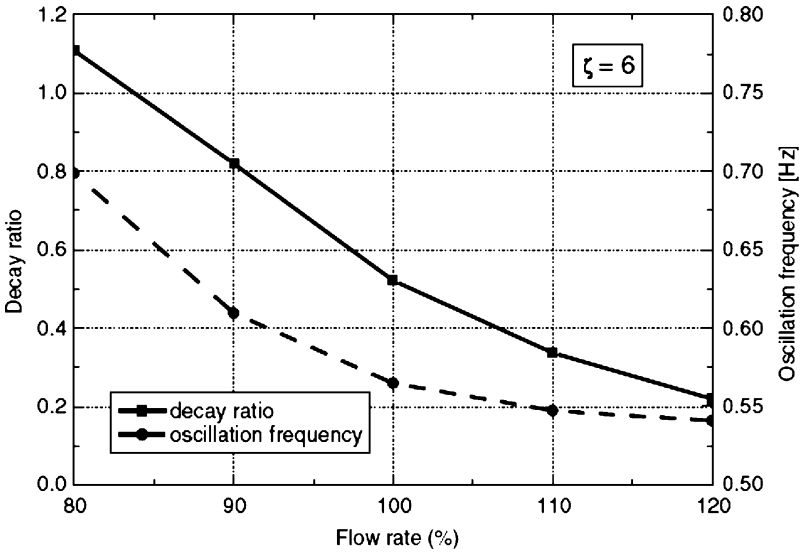


Fig. 5.40 Effect of feedwater flow rate on decay ratio and oscillation frequency of thermal-hydraulic stability with constant core power (taken from ref. [11] and used with permission from Atomic Energy Society of Japan)

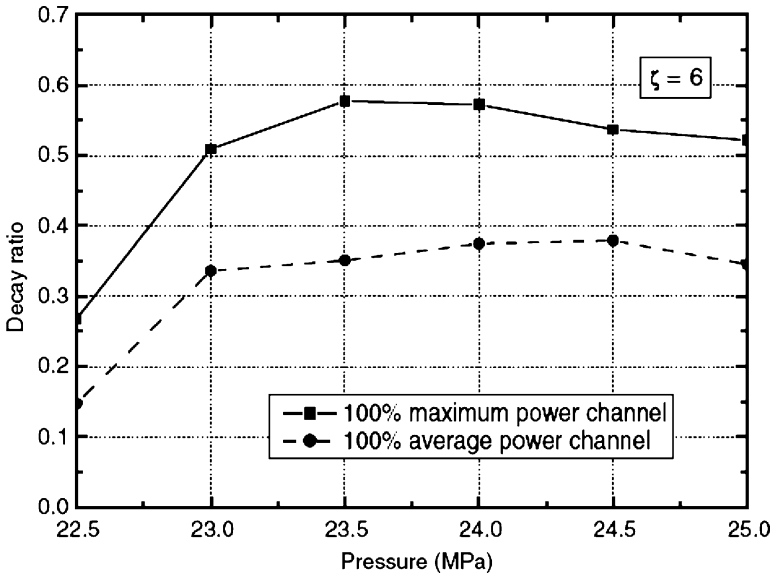


Fig. 5.41 Effect of pressure on decay ratio of thermal-hydraulic stability (taken from ref. [11] and used with permission from Atomic Energy Society of Japan)

ratio does not change monotonously but shows a peak value can be explained by the two coexisting opposite effects stated below.

1. When the pressure decreases, the density ratio between the core inlet and outlet gets larger. This makes the system less stable.
2. When the pressure decreases, the average coolant density in the core decreases, and hence the average coolant velocity increases. This makes the system more stable.

The core inlet temperature affects the temperature and velocity distributions in the core. When it is lower, the coolant temperatures and density ratio between the core inlet and outlet become smaller which has a stabilizing effect. On the other hand, it also leads to lower coolant flow velocity and core pressure drop, resulting in a longer time delay which destabilizes the system. The net effect depends on the individual operating conditions. Here, the core power and flow rate are kept constant and the effect of inlet feedwater temperature on stability is investigated. As shown in Fig. 5.42 [11], under the operating conditions of the present parametric study, decreasing the inlet temperature leads to lower oscillation frequency and decay ratio which stabilizes the reactor.

In the present design of the Super LWR, the ratio of the mass flow rate that passes through the water rods is 30% of the total feedwater flow rate. The effect of this parameter is investigated next. When the ratio of the mass flow rate that passes through the water rods increases, the oscillation frequency and the decay ratio increase as shown in Fig. 5.43. When the mass flow ratio and therefore the moderator mass flux increase, heat transfer from the coolant to moderator also increases so that

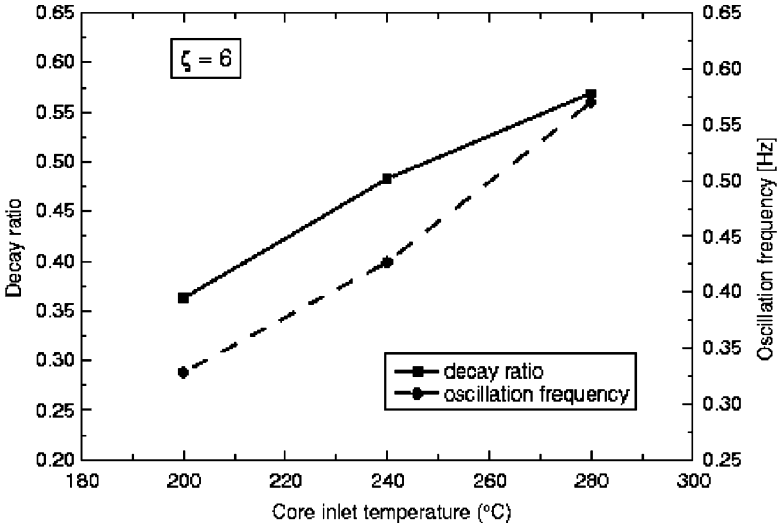


Fig. 5.42 Effect of core inlet temperature on decay ratio and oscillation frequency of thermal-hydraulic stability (taken from ref. [11] and used with permission from Atomic Energy Society of Japan)

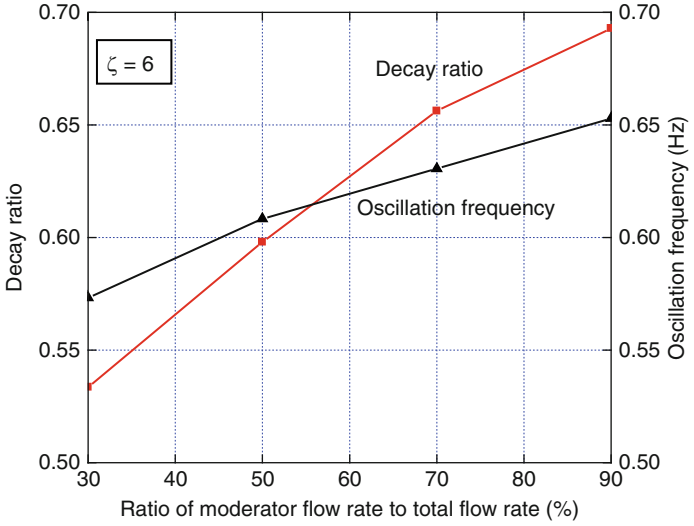


Fig. 5.43 Effect of water rod mass flow ratio on decay ratio and oscillation frequency of thermal-hydraulic stability

the inlet temperature of the fuel channel gets higher. This leads to an increase in the average coolant velocity and hence a pressure drop in the fuel channel, while the pressure drop in the inlet orifice is kept constant. As a result, the fraction of the orifice pressure drop in the total pressure drop decreases and the system is less stable.

5.5 Coupled Neutronic Thermal-Hydraulic Stability Considerations

5.5.1 Mechanism of Coupled Neutronic Thermal-Hydraulic Instability

The interaction between thermal-hydraulics and neutronics may bring about instability in the Super LWR and this instability also needs to be considered in the Super LWR design. These two processes are coupled through the heat transfer from the fuel rod to the coolant and moderator and through the reactivity feedback effects due to changes in temperature and changes in density of the coolant and the moderator.

Since the power generation is affected by the reactivity feedback, it depends on the average fuel temperature and average water density in the core. In the forward loop, when a small reactivity oscillation occurs in the reactor system, the reactor power oscillates, and it leads to average fuel temperature perturbations and average water density perturbations through the fuel dynamics and channel thermal-hydraulics. In the feedback loop, as a consequence of these average fuel

temperature oscillations and average water density oscillations which are established in the reactor core after some time delay, the reactivity and thus the reactor power oscillate according to the neutronic feedback effect.

The neutronic feedback involves the neutron kinetics, the fuel dynamics, the core thermal-hydraulics, and the reactivity feedback dynamics. The neutron kinetics affects and is affected by the power generation in the fuel, and is directly responsible for the power perturbations. The fuel dynamics affects and is affected by the fuel surface heat flux, and is responsible for the time delays between power production and the response of coolant flow heating. The core thermal-hydraulics affects the power production and the response of the water density perturbations to fuel surface heat flux perturbations. Finally, the reactivity feedback dynamics is responsible for the feedback reactivity due to water density perturbations and fuel temperature perturbations, and is affected by neutron kinetics.

In most cases, the reactivity feedback dynamics, which is characterized by the magnitude of the reactivity coefficients and the time delay of the feedback process, is responsible for exciting power oscillation in the reactor system. If the feedback reactivity magnitude is smaller than the magnitude of the initial reactivity perturbations, the reactivity oscillations decay and the reactor system is stable. If the feedback reactivity magnitude is larger than the magnitude of initial perturbations, the oscillations will diverge, making the reactor unstable. The physical mechanism involved in coupled neutronic thermal-hydraulic instability is shown in Fig. 5.44.

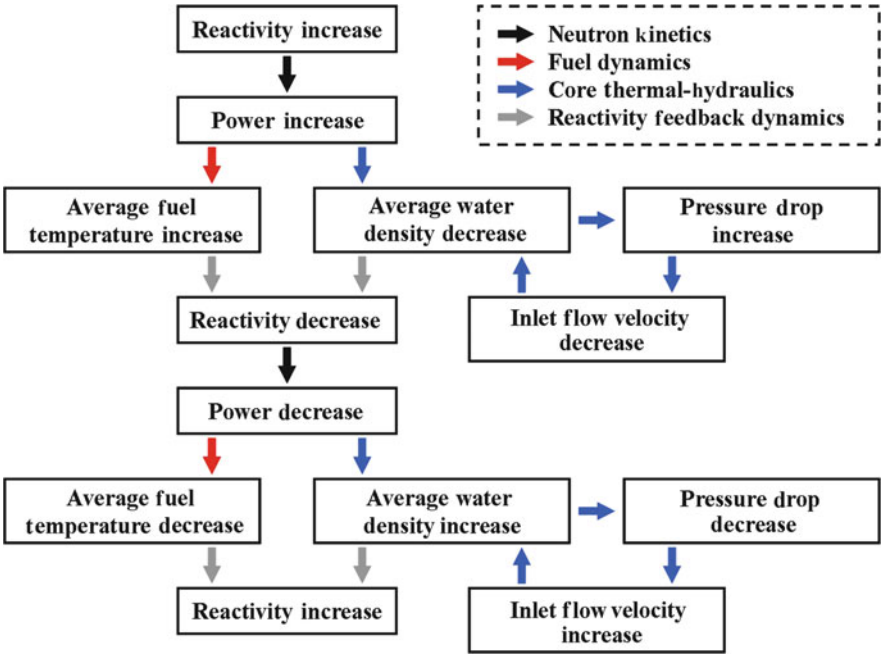


Fig. 5.44 Physical mechanism causing coupled neutronic thermal-hydraulic instability

The time delay of the heat transfer to the coolant and moderator water is an important factor in the mechanism of coupled neutronic thermal-hydraulic instability. The Super LWR is a reactor system with a positive density coefficient of reactivity and a large time-delay constant. If there is no time delay, a decrease in density would cause a decrease in power generation, which suppresses further decrease in density, stabilizing the system. However, if there is a large time delay, it causes a decrease in the gain of the density-reactivity transfer function and reduces the effect of density reactivity feedback, making the system less stable.

The Super LWR employs separate large square water rods as neutron moderators. The time delay of the heat transfer to the water rod is much larger than that of the heat transfer to the coolant. Thus, the reactor system becomes less stable when a water rod model is included than when no water rod model is used. The descending water rods will have a significant effect on the coupled neutronic thermal-hydraulic stability because of the moderator density reactivity feedback from the large square water rods, and it needs to be considered in stability analysis of the Super LWR.

5.5.2 Coupled Neutronic Thermal-Hydraulic Stability Analysis Method

Like in the thermal-hydraulic stability analyses, the frequency domain analysis method is used here, too. The mathematical model contains six submodels – the neutron kinetics model, the fuel rod heat transfer model, water rod heat transfer model, fuel channel thermal-hydraulic model, water rod thermal-hydraulic model, and the excore circulation system model. The fuel channel thermal-hydraulic model and water rod thermal-hydraulic model are the same as the thermal-hydraulic stability analysis model described in Sect. 5.4.3.

5.5.2.1 Neutron Kinetics Model

Point neutron kinetics equations with six delayed neutron precursor groups are employed to calculate the transfer function from reactivity to core power.

$$\frac{\partial n(t)}{\partial t} = \frac{\Delta\rho - \beta}{\Lambda} n(t) + \sum_{i=1}^{6} \lambda_i C_i(t). \tag{5.63}$$

$$\frac{\partial C_i(t)}{\partial t} = \frac{\beta_i}{\Lambda} n(t) - \lambda_i C_i(t). \tag{5.64}$$

$$\beta = \sum_{i=1}^{6} \beta_i. \tag{5.65}$$

Table 5.10 Delayed neutron data for thermal fission of U-235 in the Super LWR

Group	Effective delayed neutron decay constant (λ_i) (s^{-1})	Effective delayed neutron fraction (β_i)
1	0.01271596	0.0002432
2	0.03173751	0.0013632
3	0.11552453	0.0012032
4	0.3108028	0.0026048
5	1.39747415	0.0008192
6	3.87233068	0.0001664
Total delayed neutron fraction		0.0064
Prompt neutron generation time		0.000043 s

Here β is the effective delayed neutron fraction. The delayed neutron data for the Super LWR are given in Table 5.10.

The relationship between power perturbation and reactivity perturbation is given by using a perturbation in the vicinity of the steady-state conditions, Laplace-transforming (5.63) and (5.64), and eliminating $\delta\hat{C}_i$.

$$\frac{\delta\hat{n}}{\delta\hat{\Delta}\rho} = \frac{N_0}{s\left\{\Lambda + \sum_{i=1}^{6} \frac{\beta_i}{s+\lambda_i}\right\}}. \tag{5.66}$$

$N_0 = n(0)$ is the steady-state initial neutron density. The Doppler coefficient of reactivity and the density coefficient of reactivity are considered for the reactivity feedback. The reactivity distribution in the axial direction is assumed to follow the square of the cosine distribution.

$$\Delta\rho = \Delta\rho(T_{\mathrm{f}}^{\mathrm{ave}}, \rho). \tag{5.67}$$

$$\delta\hat{\Delta}\rho = \frac{\partial\Delta\rho}{\partial T_{\mathrm{f}}^{\mathrm{ave}}}\delta\hat{T}_{\mathrm{f}}^{\mathrm{ave}} + \frac{\partial\Delta\rho}{\partial\rho}\delta\hat{\rho}. \tag{5.68}$$

$$\delta\hat{\Delta}\rho = \frac{\sum_{i=1}^{N} \delta\hat{\Delta}\rho_i(\cos^2 z)_i}{\sum_{i=1}^{N} (\cos^2 z)_i}. \tag{5.69}$$

The reactivity in point kinetics equations depends on time-dependent average fuel temperature and time-dependent distributions of coolant and moderator density, and hence this model couples reactor neutronics with thermal-hydraulics. This model receives the fuel temperature distribution from the fuel rod heat transfer model and the coolant density distribution and moderator density distribution from the two thermal-hydraulic models. Then, it generates the power distribution to the fuel rod heat transfer model.

5.5.2.2 Fuel Rod Heat Transfer Model

The lumped parameter model is employed for the fuel dynamics. No significant temperature gradients are assumed to exist in the fuel pellet, and the volumetric heat generation across it is assumed to be uniform. The one-dimensional radial heat conduction equation is used and the axial and azimuthal heat conduction within the fuel is neglected. The gamma energy deposition in the pellet-clad gap and the fuel cladding is not considered. The equation for the temperature distribution within the fuel rod is given by:

$$\frac{\partial}{\partial t}(\rho_{\mathrm{f}} C_{\mathrm{p}} T_{\mathrm{f}}) = \frac{1}{r}\frac{\partial}{\partial r}\left(r k_{\mathrm{f}} \frac{\partial T_{\mathrm{f}}}{\partial r}\right) + q'''. \tag{5.70}$$

The fuel average temperature $T_{\mathrm{f}}^{\mathrm{ave}}$ is defined by

$$T_{\mathrm{f}}^{\mathrm{ave}} = \frac{\int_0^{r_{\mathrm{f}}} 2\pi r T_{\mathrm{f}} \mathrm{d}r}{\int_0^{r_{\mathrm{f}}} 2\pi r \mathrm{d}r} = \frac{\int_0^{r_{\mathrm{f}}} 2\pi r T_{\mathrm{f}} \mathrm{d}r}{\pi r_{\mathrm{f}}^2}. \tag{5.71}$$

The boundary conditions are given by the symmetry condition at the fuel pellet center as described in (5.72) and the interface condition at the fuel pellet surface as described in (5.73).

$$\left.\frac{\partial T_{\mathrm{f}}}{\partial r}\right|_{r=0} = 0. \tag{5.72}$$

$$q''(r_{\mathrm{f}}, t) = -k_{\mathrm{f}}(T_{\mathrm{f}}) \left.\frac{\partial T_{\mathrm{f}}}{\partial r}\right|_{r=r_{\mathrm{f}}}. \tag{5.73}$$

Integrating (5.70) from $r = 0$ to r_{f} and using (5.72) and (5.73) gives

$$\rho_{\mathrm{f}} C_{\mathrm{p}} \pi r_{\mathrm{f}}^2 \frac{\partial}{\partial t} T_{\mathrm{f}}^{\mathrm{ave}} = -2\pi r_{\mathrm{c}} q''(r_{\mathrm{c}}, t) + \pi r_{\mathrm{f}}^2 q'''. \tag{5.74}$$

The thermal conductivity of the fuel k_{f} is calculated from the fuel average temperature $T_{\mathrm{f}}^{\mathrm{ave}}$ by the following formula, which is commonly used in combustion engineering problems [12].

$$k_{\mathrm{f}} = \frac{3,824}{402.4 + T_{\mathrm{f}}^{\mathrm{ave}}} + 6.1256 \times 10^{-11} (T_{\mathrm{f}}^{\mathrm{ave}} + 273)^3. \tag{5.75}$$

The density and the specific heat capacity of the fuel pellet are assumed constant. The heat transfer equation from the fuel cladding surface to the coolant is given as

$$q''(r_{\mathrm{c}}, t) = h_{\mathrm{c}}[T_{\mathrm{s}} - T]. \tag{5.76}$$

The heat transfer coefficients at supercritical pressures are calculated by the Oka–Koshizuka correlation.

Assuming steady-state heat conduction in the gap and in the fuel cladding, the relation between the average fuel temperature and cladding surface temperature can be given by:

$$T_{\mathrm{f}}^{\mathrm{ave}} - T_{\mathrm{s}} = \left(\frac{r_{\mathrm{f}} + t_{\mathrm{c}}}{r_{\mathrm{f}}}\right)\left[\frac{r_{\mathrm{f}}}{4k_{\mathrm{f}}} + \frac{1}{h_{\mathrm{g}}} + \frac{t_{\mathrm{c}}}{k_{\mathrm{c}}}\right] q''. \tag{5.77}$$

The pellet-clad gap conductance h_{g} and the thermal conductivity of the fuel cladding k_{c} are assumed constant. The values of the gap conductance and cladding thermal conductivity used in the present analysis are 8,000 W/m^{2}K and 20.4 W/mK, respectively.

Perturbing at the steady-state conditions and Laplace-transforming (5.74), (5.76), and (5.77) give the following equations.

$$(\rho_{\mathrm{f}} C_{\mathrm{p}} \pi r_{\mathrm{f}}^2 s)\delta\hat{T}_{\mathrm{f}}^{\mathrm{ave}} = -2\pi r_{\mathrm{c}}\delta\hat{q}'' + \pi r_{\mathrm{f}}^2 \delta\hat{q}'''. \tag{5.78}$$

$$\delta\hat{q}'' = h_{\mathrm{c}}^0(\delta\hat{T}_{\mathrm{s}} - \delta\hat{T}) + (T_{\mathrm{s}} - T)\delta\hat{h}_{\mathrm{c}}. \tag{5.79}$$

$$\delta\hat{T}_{\mathrm{f}}^{\mathrm{ave}} - \delta\hat{T}_{\mathrm{s}} = \left(\frac{r_{\mathrm{f}} + t_{\mathrm{c}}}{r_{\mathrm{f}}}\right)\left[\frac{r_{\mathrm{f}}}{4k_{\mathrm{f}}} + \frac{1}{h_{\mathrm{g}}} + \frac{t_{\mathrm{c}}}{k_{\mathrm{c}}}\right]\delta\hat{q}''. \tag{5.80}$$

For single-phase flow, the heat transfer equation from the fuel cladding surface to the coolant is given by

$$q''(r_{\mathrm{c}}, t) = h_{\mathrm{c}}[T_{\mathrm{s}} - T]. \tag{5.81}$$

The Dittus–Boelter equation is used to calculate single-phase heat transfer coefficient. The single-phase heat transfer coefficient is evaluated as a function of flow velocity, pressure, and fluid bulk temperature. Perturbing about the steady-state values and Laplace-transforming (5.81) give

$$\delta\hat{q}'' = h_{\mathrm{c}}^0(\delta\hat{T}_{\mathrm{s}} - \delta\hat{T}) + (T_{\mathrm{s}} - T)\delta\hat{h}_{\mathrm{c}} \tag{5.82}$$

where $\delta\hat{h}_{\mathrm{c}}$ and $\delta\hat{T}$ are given by

$$\delta\hat{h}_{\mathrm{c}} = \frac{\partial h_{\mathrm{c}}}{\partial u}\delta\hat{u} + \frac{\partial h_{\mathrm{c}}}{\partial P}\delta\hat{P} + \frac{\partial h_{\mathrm{c}}}{\partial T}\delta\hat{T}, \tag{5.83}$$

and

$$\delta\hat{T} = \frac{\partial T}{\partial P}\delta\hat{P} + \frac{\partial T}{\partial h}\delta\hat{h}. \tag{5.84}$$

For nucleate boiling in two-phase flow, the heat transfer from the fuel cladding surface to the coolant is given by Thom's equation

$$q'' = 10^6 \times \left(\frac{e^{P/8.7}}{22.7}\right)^2 (T_s - T_{sat})^2, \tag{5.85}$$

where P is in MPa. Perturbing and Laplace-transforming give

$$\delta\hat{q}'' = 2 \times 10^6 \times \left(\frac{e^{P/8.7}}{22.7}\right)^2 (T_s - T_{sat})\delta\hat{T}_s. \tag{5.86}$$

The boiling heat transfer coefficient is given by

$$h_c = 10^6 \times \left(\frac{e^{P/8.7}}{22.7}\right)^2 (T_s - T_{sat}). \tag{5.87}$$

The nucleate boiling heat transfer coefficient is independent of flow velocity. It is sensitive to pressure and the surface wall temperature.

Similarly, for forced convective vaporization in the two-phase region, the Schrock–Grossman correlation is used to calculate heat transfer coefficient, and the perturbed surface heat flux and the heat transfer coefficient are given by (5.88) and (5.89), respectively.

$$\delta\hat{q}'' = h_c^0(\delta\hat{T}_s - \delta\hat{T}_{sat}) + (T_s - T_{sat})\delta\hat{h}_c. \tag{5.88}$$

$$\delta\hat{h}_c = \frac{\partial h_c}{\partial u}\delta\hat{u} + \frac{\partial h_c}{\partial P}\delta\hat{P} + \frac{\partial h_c}{\partial X}\delta\hat{X}. \tag{5.89}$$

For the post-dry out region, the Groeneveld correlation is used to determine film boiling heat transfer coefficient, and the perturbed surface heat flux and heat transfer coefficient are given in the same way by (5.88) and (5.89).

In the present analysis, the axial core power is assumed to follow a cosine distribution for calculation simplicity. The variation of the axial power distribution with fuel burnup is not considered in the present analysis. It should be noted that the actual distribution of the axial core power may be top-peak, bottom-peak, or chopped cosine, depending on the fuel burnup during the fuel cycle.

The fuel rod heat transfer model receives the power generation rate from the neutron kinetics model and supplies the heat flux distribution to the fuel channel thermal-hydraulics model. Using the coolant temperature distribution and heat transfer coefficients from the fuel channel thermal-hydraulic model, it feeds the fuel average temperature distribution back to the neutron kinetics model (Doppler feedback effect).

5.5.2.3 Water Rod Heat Transfer Model

In this model, the heat transfer between fuel channel coolant and water rod moderator through the water rod wall structure is considered. Axial heat conduction in the water rod is assumed to be negligible. Since the water rod wall structure is relatively thin, heat conduction in the water rod structure is also neglected. The governing equations for this model are given below.

$$T_{\mathrm{ws}} = T - \frac{N_{\mathrm{f}} Q_{\mathrm{w}}}{N_{\mathrm{w}} \pi D_{\mathrm{w}} h_{\mathrm{s}_1}}. \tag{5.90}$$

$$T_{\mathrm{w}} = T_{\mathrm{ws}} - \frac{N_{\mathrm{f}} Q_{\mathrm{w}}}{N_{\mathrm{w}} \pi (D_{\mathrm{w}} - 2t_{\mathrm{ws}}) h_{s_2}}. \tag{5.91}$$

Thus,

$$T - T_{\mathrm{w}} = \frac{N_{\mathrm{f}}}{N_{\mathrm{w}}} Q_{\mathrm{w}} \left[\frac{1}{\pi D_{\mathrm{w}} h_{s_1}} + \frac{1}{\pi (D_{\mathrm{w}} - 2t_{\mathrm{ws}}) h_{s_2}} \right], \tag{5.92}$$

where T, T_{w}, and T_{ws} are water temperature in the fuel channel, water temperature in the water rod, and temperature of the water rod structure, respectively.

The coolant temperature distribution, the moderator temperature distribution, and the heat transfer coefficients between fuel channels and water rods are used in this model to generate the rate of heat transfer between fuel channel coolant and water rod moderator to the two thermal-hydraulics models.

5.5.2.4 Excore Circulation Model

This model includes an orifice at the inlet of the fuel assembly, a feedwater pump, a feedwater pipe, and an exit valve. The coolant density and coolant temperature in the feedwater pipe are assumed to be uniform. The coolant density in the feedwater pipe is also assumed to be time-independent. The momentum loss in the feedwater line is assumed to be negligible. The mathematical models used are described below.

Channel inlet orifice model and exit valve model:

$$\Delta p = \zeta \frac{\rho u^2}{2}. \tag{5.93}$$

Feedwater pump model:

$$\delta \hat{P} = C_{\mathrm{pump}} \delta \hat{u}. \tag{5.94}$$

Feedwater pipe model:

$$-\frac{\mathrm{d}P}{\mathrm{d}x}=\frac{\mathrm{d}}{\mathrm{d}t}\rho u+\frac{\mathrm{d}}{\mathrm{d}x}\rho u^2+\left(\frac{2f}{D}\right)\rho u^2. \tag{5.95}$$

Linearization and Laplace-transformation of (5.93) and (5.95) give the next equations.

$$\delta\Delta\hat{p}=\zeta\rho u\delta\hat{u}. \tag{5.96}$$

$$\delta\hat{u}=\frac{\left(-\frac{1}{L\rho}\right)}{s+\left(\frac{4f}{D}u\right)}\delta\hat{P}. \tag{5.97}$$

Equations (5.94), (5.96), and (5.97) are used to obtain the transfer functions from pressure drop to flow velocity.

5.5.2.5 Stability Criteria

The same stability criteria for the decay ratio as those used for BWRs are imposed on the Super LWR to provide reactor safety and stability. The margin for uncertainty has not been taken into consideration in the decay ratio criterion of 1.0 for transient conditions. However, that does not affect the analysis results obtained here, as Chap. 5 deals essentially with normal operating conditions.

(a) The decay ratio should be less than 0.25 for normal operating conditions. (damping ratio $\geq$0.22)
(b) The decay ratio must be less than 1.0 for all operating conditions. (damping ratio $\geq$0.0)

5.5.3 Coupled Neutronic Thermal-Hydraulic Stability Analyses

The average power channel is analyzed to study coupled neutronic thermal-hydraulic stability of the Super LWR. A block diagram is shown in Fig. 5.45 [10, 13]. The neutronic model is used to find the forward transfer function $G(s)$, i.e., the transfer function from the reactivity perturbations to the power perturbations. The thermal-hydraulic, heat transfer, and excore models are used to determine the feedback transfer function $H(s)$ which is the transfer function from the power perturbations to the feedback reactivity perturbations through the neutronic effect.

The Doppler reactivity coefficient and the density reactivity coefficient of the present design of the Super LWR are shown in Figs. 5.46 and 5.47. Under normal operation, the Doppler coefficient and density coefficient are -1.2×10^{-5}dk/k/°C and 0.2 dk/k/(g/cm^3), respectively. Compared to other LWRs, the Doppler

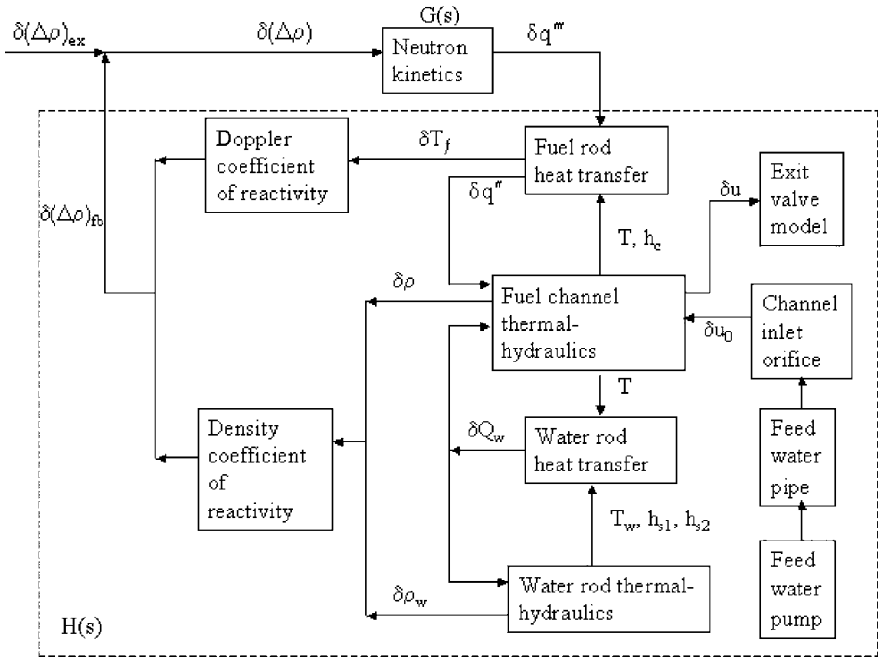


Fig. 5.45 Block diagram for coupled neutronic thermal-hydraulic stability of the Super LWR (taken from ref. [13] and used with permission from Atomic Energy Society of Japan)

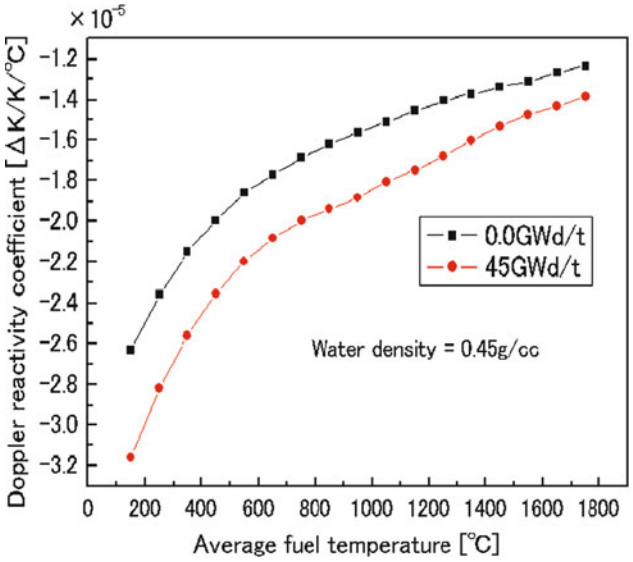


Fig. 5.46 Doppler coefficient of the Super LWR

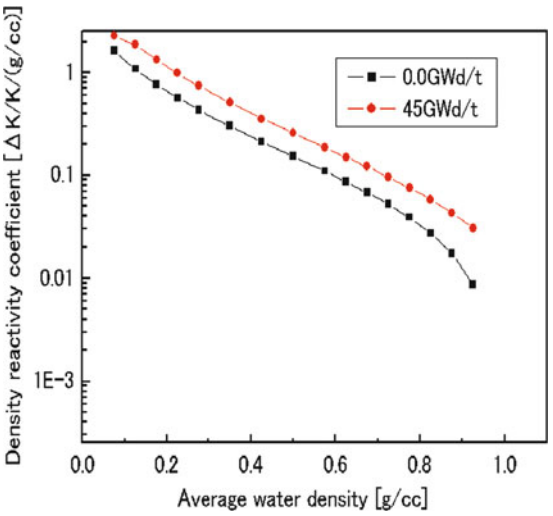


Fig. 5.47 Density coefficient of the Super LWR

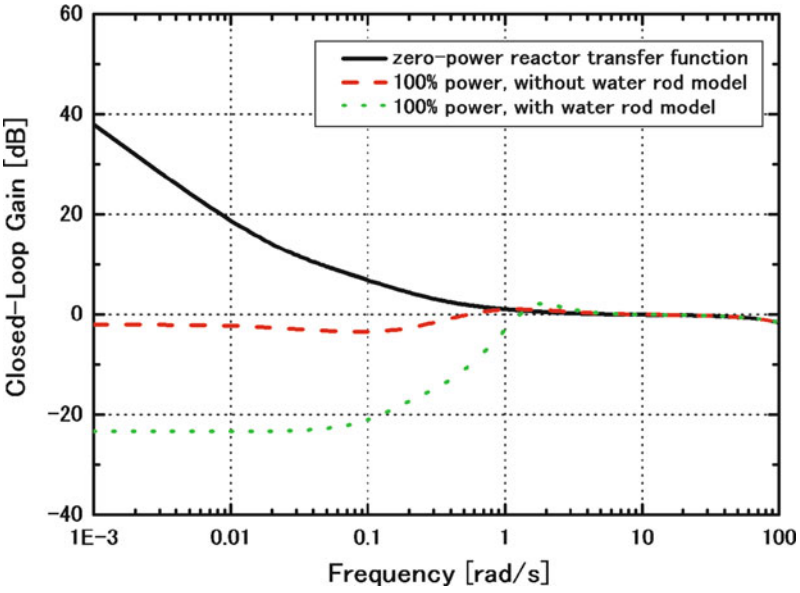


Fig. 5.48 Gain response of closed loop transfer function of coupled neutronic thermal-hydraulic stability

coefficient of the Super LWR is a little smaller due to higher fuel enrichment. The density coefficient of the Super LWR is the same order of magnitude as that of BWRs.

The frequency response of the closed loop transfer function for coupled neutronic thermal-hydraulic stability of the Super LWR for the 100% average power channel is shown in Figs. 5.48 and 5.49. It can be observed that the presence of

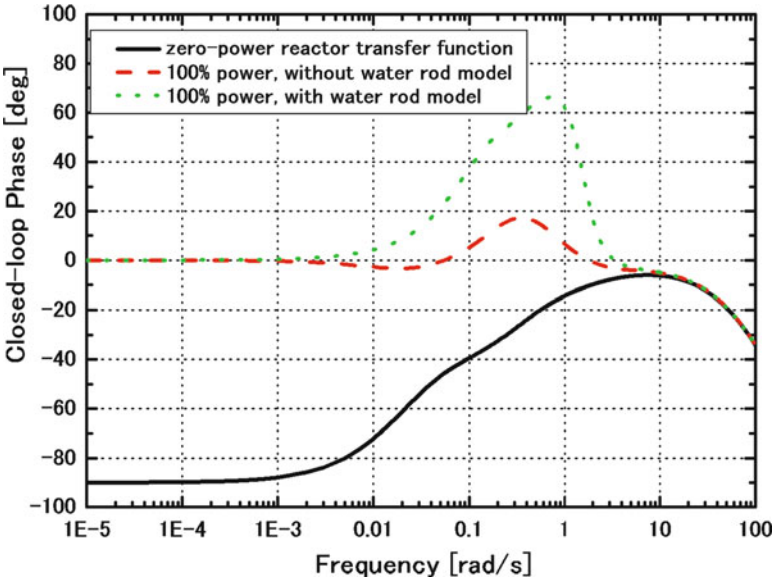


Fig. 5.49 Phase response of closed loop transfer function of coupled neutronic thermal-hydraulic stability

water rods increases the resonant peak and the phase lag of the closed loop transfer function, due to the time lag between the changes in the coolant and moderator temperatures.

5.5.3.1 Coupled Neutronic Thermal-Hydraulic Stability at Full Power Normal Operation

The decay ratios are calculated in the average power channel at 25 MPa for 100% power and 100% flow conditions. The decay ratio is calculated as 0.185 by extrapolation in Fig. 5.50 to the zero mesh size. The oscillation frequency is about 0.3 Hz, which is typical for density wave oscillation. The stability criterion is satisfied.

5.5.3.2 Coupled Neutronic Thermal-Hydraulic Stability at Partial Power Operations at 25 MPa

Partial power operating conditions are also analyzed to investigate the stability during the power increase phase. The calculated decay ratios at 40% core power with various flow rates are shown in Fig. 5.51 and those at 50% core power are shown in Fig. 5.52. The decay ratio map is shown in Fig. 5.53. Unstable conditions arise when the power to flow rate ratio is high, especially at low power operation. Figure 5.54 shows the flow rate required to satisfy the criterion of coupled neutronic

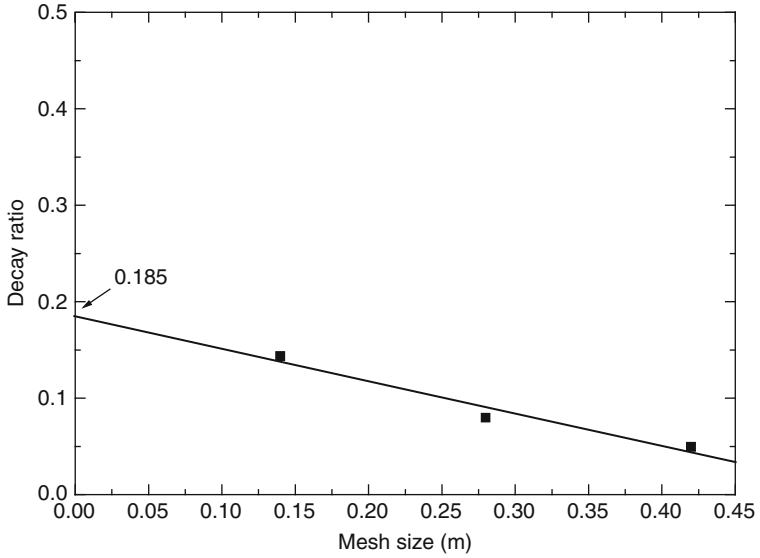


Fig. 5.50 Decay ratio of coupled neutronic thermal-hydraulic stability at full power

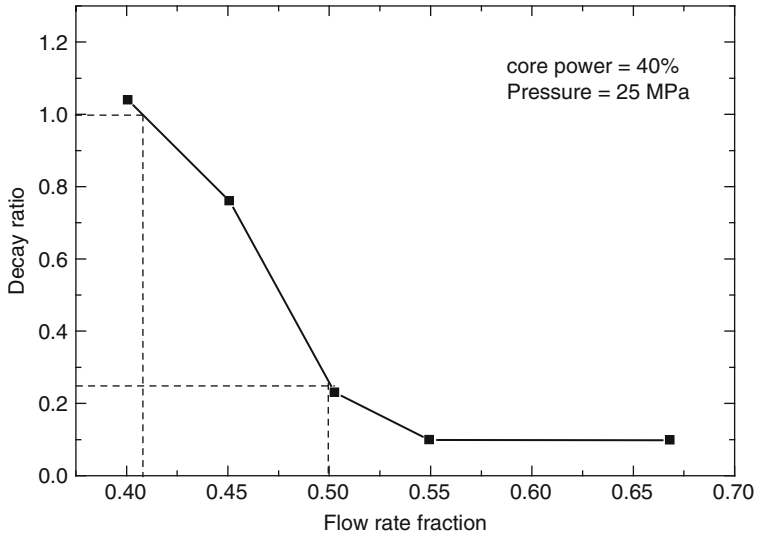


Fig. 5.51 Effect of flow rate on coupled neutronic thermal-hydraulic stability at 40% power

thermal-hydraulic stability at the power increase phase. The flow rate required for coupled neutronic-thermal hydraulic stability is higher than those for MCST or thermal-hydraulic stability when the power is below 90% of the rated value. This implies that coupled neutronic thermal-hydraulic stability is the most limiting at the power increase phase.

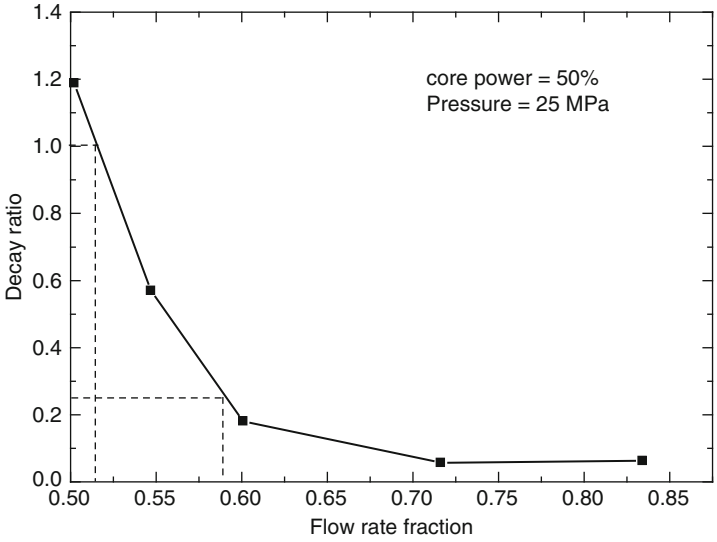


Fig. 5.52 Effect of flow rate on coupled neutronic thermal-hydraulic stability at 50% power

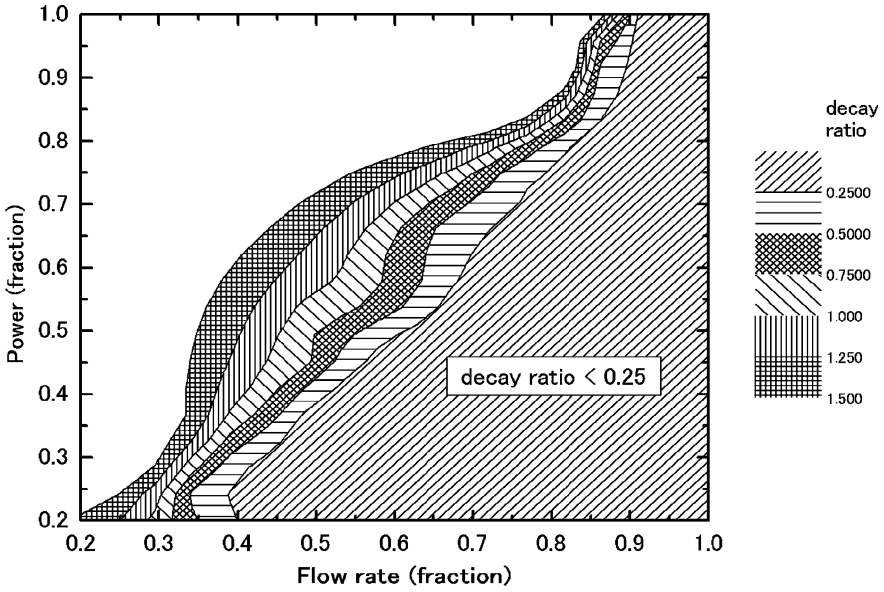


Fig. 5.53 Decay ratio map for coupled neutronic and thermal-hydraulic stability of the Super LWR

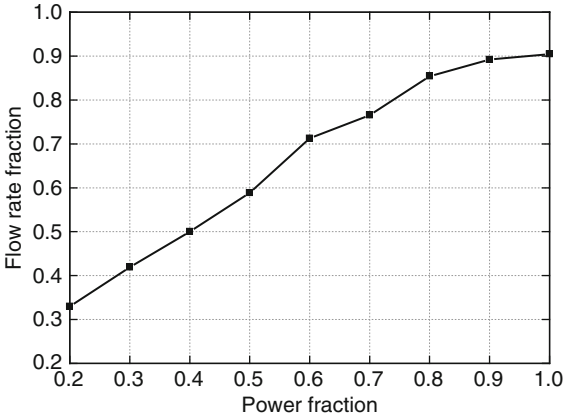


Fig. 5.54 Coolant flow rate required to satisfy stability criterion at power increase phase

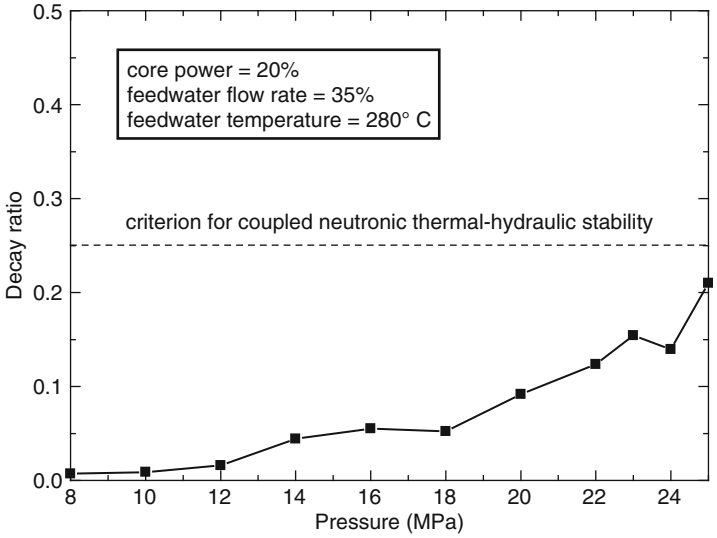


Fig. 5.55 Coupled neutronic thermal-hydraulic stability at pressurization phase (Taken from ref. [10] and used with permission from Atomic Energy Society of Japan)

5.5.3.3 Coupled Neutronic Thermal-Hydraulic Stability at Pressurization Phase

From the thermal considerations in Sect. 5.3.3.2, the core power, feedwater flow rate and feedwater temperature are designed as 20 and 35% of the rated values and 280°C, respectively. The decay ratios of coupled neutronic thermal-hydraulic stability are then calculated with these conditions. The results are shown in Fig. 5.55 [10]. The stability criterion is satisfied with sufficient margin during

pressurization. This implies that the criterion for the coupled neutronic thermal-hydraulic stability is less limiting than the MCST at the pressurization phase.

5.5.3.4 Parametric Studies of Coupled Neutronic Thermal-Hydraulic Stability

The coupled neutronic thermal-hydraulic stability of the Super LWR is also sensitive to various operating conditions and design parameters. Sensitivity analyses are carried out in order to predict the influences of parameter changes on the stability of the Super LWR. Here, the effects of the density coefficient, core power, mass flow rate, system pressure, core inlet temperature, and water rod flow ratio on coupled neutronic thermal-hydraulic stability of the Super LWR are investigated.

The effect of the coolant density coefficient is shown in Fig. 5.56 [13]. The oscillation frequency and the decay ratio increase as the density coefficient increases. The decay ratio is still below 1.0 even when the density coefficient is five times higher than the reference value.

The effect of the core power with constant flow rate is shown in Fig. 5.57 [13]. The oscillation frequency and the decay ratio increase with the power. As the power increases, the density changes increase in the coolant channels and the water rods. This results in a destabilizing effect due to the density reactivity feedbacks from the coolant and the moderator. However, this effect is not as large as that of thermal-hydraulic stability. Conversely, when the flow rate increases while keeping the core power constant, the decay ratio and oscillation frequency decrease as shown in Fig. 5.58 [13]. When the flow rate increases, the coolant temperature decreases.

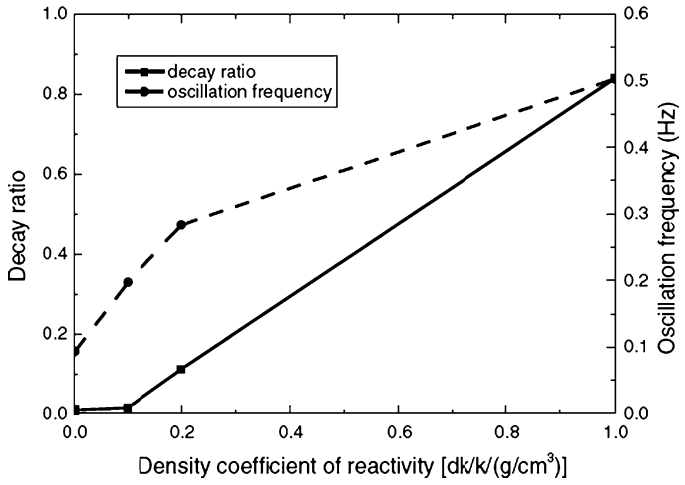


Fig. 5.56 Effect of density coefficient on coupled neutronic thermal-hydraulic stability (taken from ref. [13] and used with permission from Atomic Energy Society of Japan)

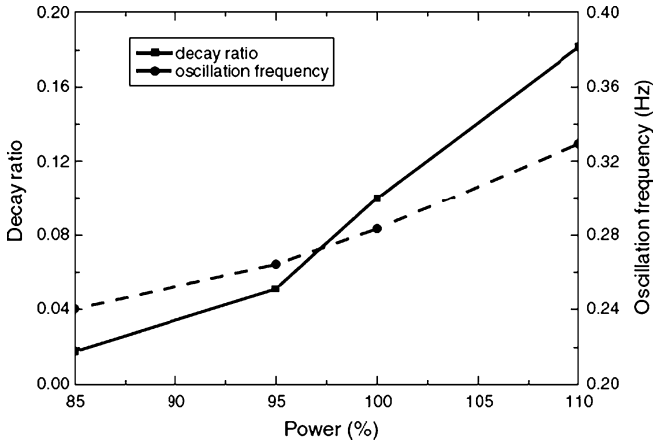


Fig. 5.57 Effect of core power on coupled neutronic thermal-hydraulic stability with constant flow rate (taken from ref. [13] and used with permission from Atomic Energy Society of Japan)

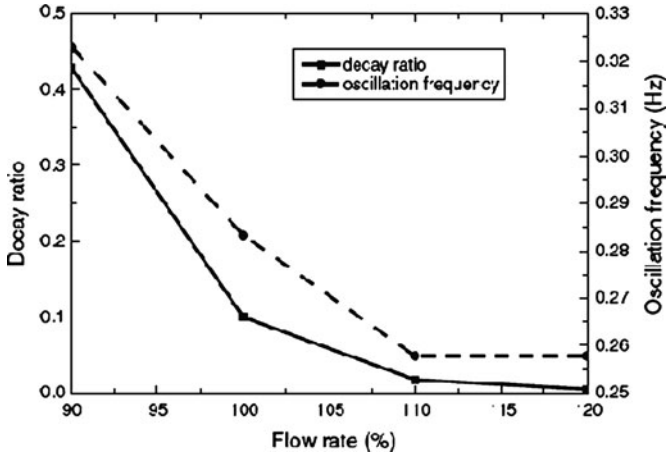


Fig. 5.58 Effect of flow rate on coupled neutronic thermal-hydraulic stability with constant power (taken from ref. [13] and used with permission from Atomic Energy Society of Japan)

Figures 5.57 and 5.58 [13] imply that the coupled neutronic thermal-hydraulic stability gets worse when the power to flow rate ratio increases. The effect of the core power (or flow rate) on the constant power to flow rate ratio is also investigated. The result is shown in Fig. 5.59 [13]. The stability becomes worse as the power or flow rate become lower. This is because of the destabilizing effect of the decreases in the flow rate and moderator density feedback. The sensitivity of the coupled neutronic thermal-hydraulic stability is more than that of the thermal-hydraulic stability.

The effect of the pressure (supercritical region) is shown in Fig. 5.60 [13]. The core inlet temperature, core power, and flow rate are kept constant. When the

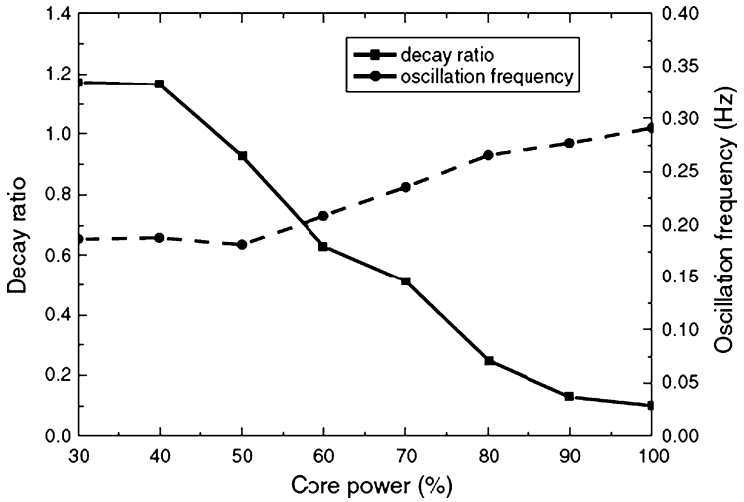


Fig. 5.59 Effect of core power on coupled neutronic thermal-hydraulic stability with constant power to flow rate ratio (taken from ref. [13] and used with permission from Atomic Energy Society of Japan)

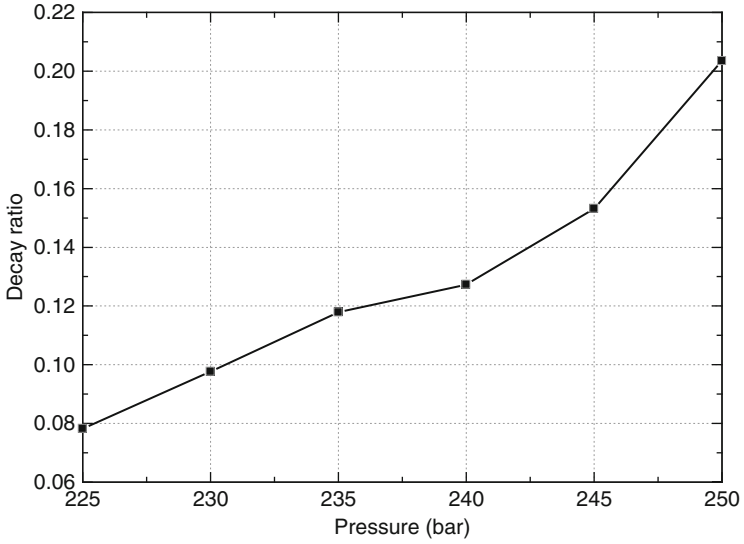


Fig. 5.60 Effect of pressure on coupled neutronic thermal-hydraulic stability (taken from ref. [13] and used with permission from Atomic Energy Society of Japan)

system pressure decreases, both the temperature and density of the outlet coolant decrease. Thus, the coolant velocity increases and the system becomes more stable especially when the pressure approaches the critical pressure. In this case, the sensitivity is smaller than that of the thermal-hydraulic stability.

The lower core inlet temperature has two effects.

1. Since the coolant temperature and hence the density ratio decrease, the density feedback effect is reduced and the stability is improved (neutronic feedback).
2. Since the coolant flow velocity and hence core pressure drop decrease, the time delay is longer and flow feedback is larger, destabilizing the reactor (hydraulic feedback).

The net effect on the stability depends on the balance between the above two effects. In the present analysis, the neutronic feedback effect is found to be dominant over the hydraulic feedback effect. Here, the core power and flow rate are kept constant and the decay ratios are calculated with various feedwater temperatures. The decay ratio is found to decrease when the core inlet temperature decreases as shown in Fig. 5.61.

When the flow fraction to the water rods is higher, the heat transfer between the coolant and moderator is enhanced. It has two opposite effects.

1. The density change of the coolant is decreased by the "heat sink" effect of the water rods, stabilizing the reactor.
2. The density change of the moderator is increased by the larger heat transfer from the coolant, destabilizing the reactor.

The total effect on the stability depends on the dominant one of the above effects. Due to the time delay associated with the heat transfer to the water rod and larger volume fraction of the moderator, it is found that the second effect is stronger. Figure 5.62 shows the relation between the flow fraction and the decay ratio. It can be observed that the decay ratio increases with the flow ratio.

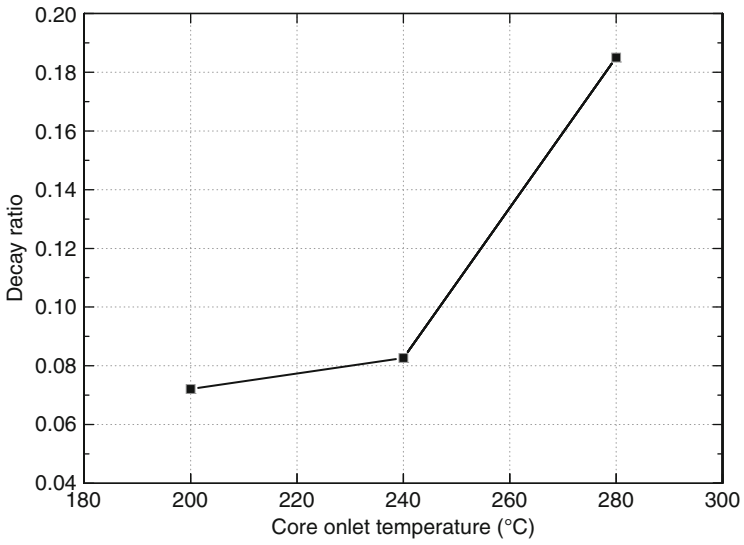


Fig. 5.61 Effect of inlet temperature on coupled neutronic thermal-hydraulic stability

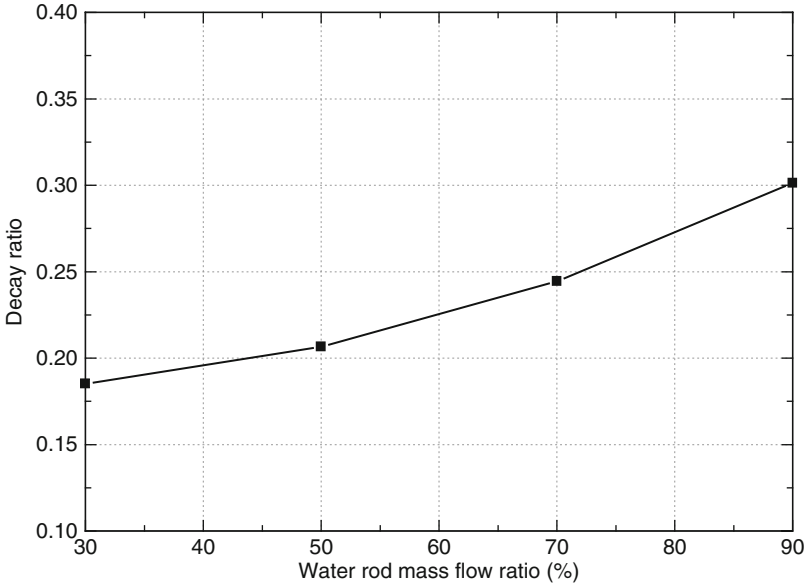


Fig. 5.62 Effect of water rod mass flow ratio on coupled neutronic thermal-hydraulic stability

5.6 Design of Startup Procedures with Both Thermal and Stability Considerations

The startup curve for the sliding pressure startup scheme that is designed based on only the thermal considerations (Fig. 5.23) is redrawn taking the stability considerations into account as well. The constant pressure startup is not discussed here because the partial power operating conditions in the constant pressure startup are covered by the temperature increase phase and power increase phase of the sliding pressure startup.

It is found that the thermal criterion (i.e., the MCST) is more limiting than the stability criteria, and hence, it dominates the available range of the power and flow rate at the pressurization phase. When the feedwater temperature and flow rate are kept as 280°C and 35% of the rated value, respectively, the available range of the core power is identified as shown in Fig. 5.19. The core power is also fixed as 20% of the rated value during pressurization that is within the available range. Both the thermal and stability criteria are satisfied as shown in Figs. 5.20, 5.37, and 5.54. The startup curve in the pressurization phase is not changed from that of Fig. 5.23.

The partial power operating conditions at 25 MPa after the line switching are divided into the temperature increase phase and the power increase phase with only the thermal considerations as shown in Fig. 5.23. In the temperature increase phase, the power is gradually increased from 20 to 35% of the rated value, while the flow rate is fixed at 35% of the rated flow so that the core outlet temperature reaches the normal operating point (500°C). Then, both the power and flow rate are increased

together from 35 to 100% of the rated values while keeping the core outlet temperature 500°C. However, the core outlet temperature cannot reach 500°C at the power level below 90% of the rated value because the required flow rate fraction is higher than the corresponding power fraction from the coupled neutronic thermal-hydraulic stability consideration as shown in Fig. 5.53. The temperature increase phase is merged into the power increase phase where the power, flow rate, and outlet temperature are increased at the same time. The line for elevating the flow rate is determined as shown in Fig. 5.63. Both the thermal and stability criteria are satisfied as shown in Figs. 5.64–5.66. The pressure drop at the inlet orifice does not occupy a large fraction of the total pressure drop as shown in Fig. 5.67.

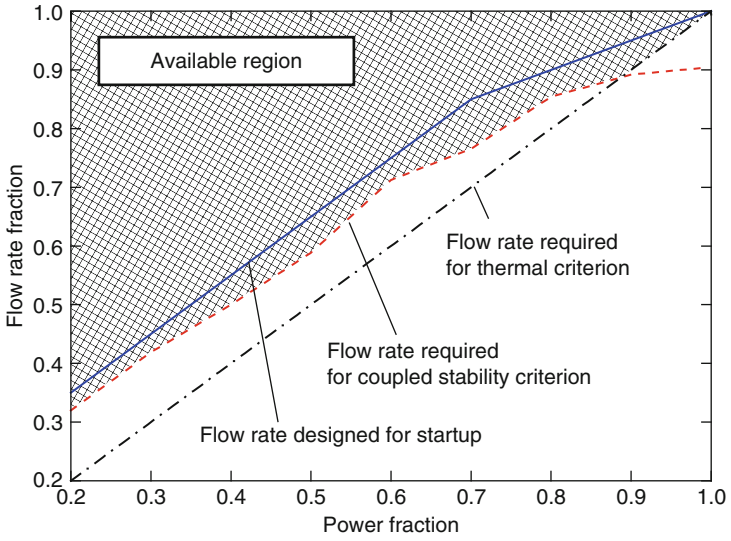


Fig. 5.63 Available region and design of power and flow rate at power increase phase

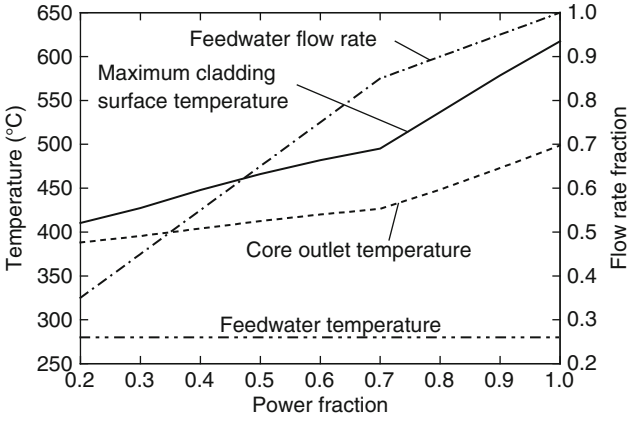


Fig. 5.64 Thermal hydraulic analysis result at power increase phase

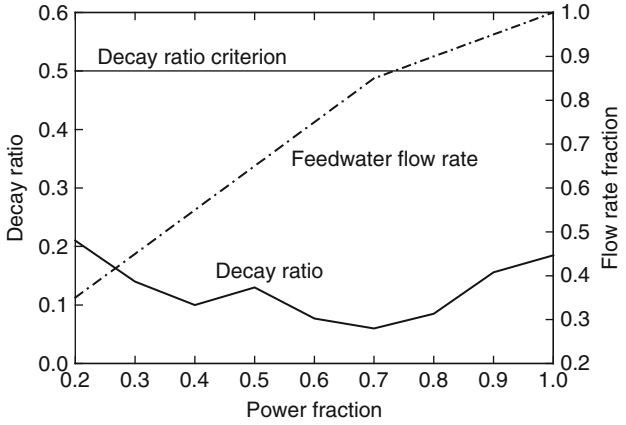


Fig. 5.65 Thermal hydraulic stability analysis result at power increase phase

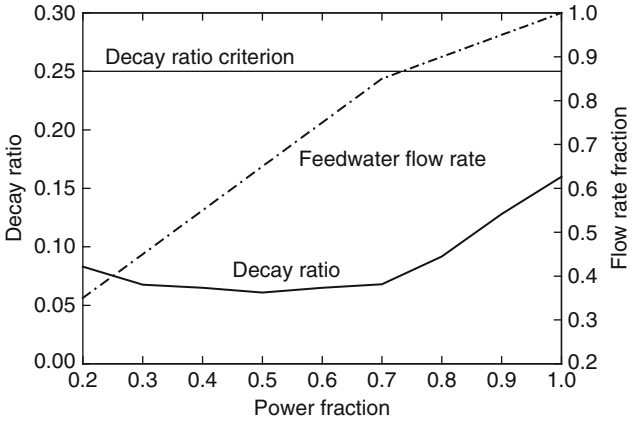


Fig. 5.66 Coupled neutronic thermal-hydraulic stability analysis result at power increase phase

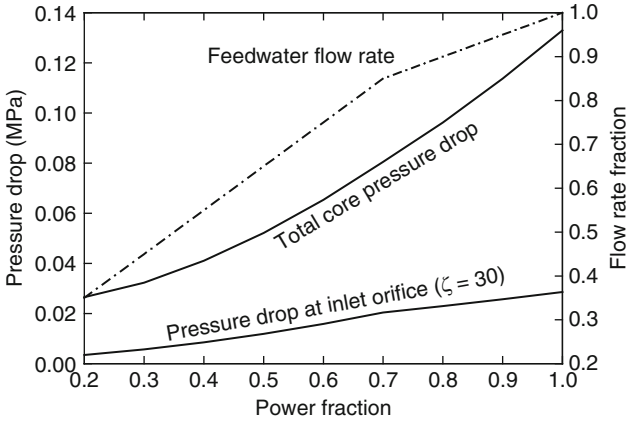


Fig. 5.67 Pressure drops in maximum power channel at power-raising phase

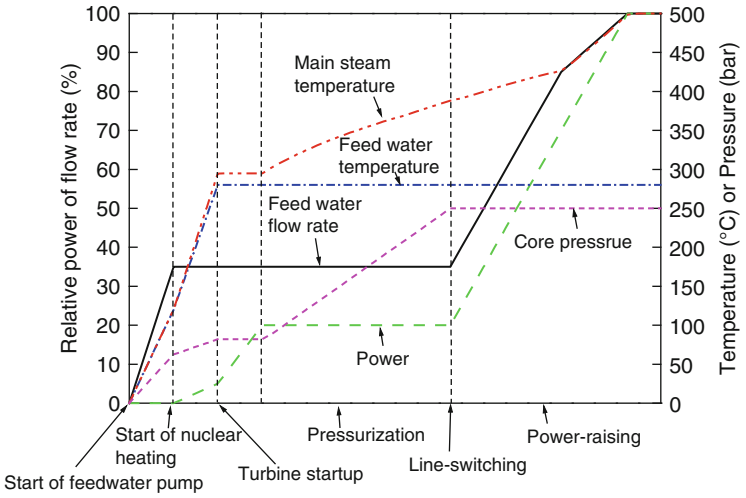


Fig. 5.68 Sliding pressure startup curve with thermal and stability considerations

Table 5.11 Comparison of three constraints in plant startup of Super LWR

	Pressurization phase (subcritical pressure)	Power increase phase (supercritical pressure)
Maximum cladding surface temperature	Limiting	Not limiting
Thermal-hydraulic stability	Not limiting with reasonable pressure drop at inlet orifice	
Coupled neutronic thermal-hydraulic stability	Not limiting	Limiting

The startup curve for the sliding pressure startup scheme of the Super LWR is redrawn as shown in Fig. 5.68. Compared to Fig. 5.23, the temperature increase phase is merged into the power increase phase, and the feedwater flow rate is higher, and hence the main steam temperature is lower at the power increase phase. The limiting constraints in the pressurization phase and the power increase phase are summarized in Table 5.11.

5.7 Design and Analysis of Procedures for System Pressurization and Line Switching in Sliding Pressure Startup Scheme

5.7.1 Motivation and Purpose

In the sliding pressure startup scheme, the system pressure of the Super LWR is assumed to be raised by nuclear heating the same as in BWRs. In the thermal and stability considerations for the sliding pressure startup introduced in Sects. 5.3–5.6,

the change in the system pressure is given with an assumption that the system pressure can be raised independently from the power. This might be a too simplified assumption.

In sliding pressure FPPs, the turbines are warmed and started using superheated steam that is generated by the superheaters. On the other hand, the turbines of the Super LWR are warmed and started using saturated steam from the water separator in the sliding startup system introduced in Sect. 5.2. There is a concern that saturated steam cannot be used for warming and starting the supercritical turbines. The Super LWR has no superheater, and it is difficult to generate superheated steam in the core due to a concern about fuel damage by boiling transition at subcritical pressure. As another option, a boiler or an electric heater acting as a superheater could be suggested, but they would worsen the economic competitiveness of the Super LWR.

From these two background facts, the purposes of this section are to revise the design of the sliding pressure startup scheme, propose its detailed procedures, and assess their feasibility by a system transient analysis. This section covers just the procedures before the power raising phase because the power raising phase itself would not be changed.

5.7.2 *Redesign of Sliding Pressure Startup System*

The redesigned system is schematically described in Fig. 5.69. The startup bypass system in the original design is replaced by the separate recirculation system that consists of a steam drum, a heat exchanger, a circulation pump, and pipes. Neither the inlet nor outlet of the recirculation system are connected to the main lines, rather they are directly connected to the reactor vessel in order to form a closed space for pressurization like the recirculation system of BWRs.

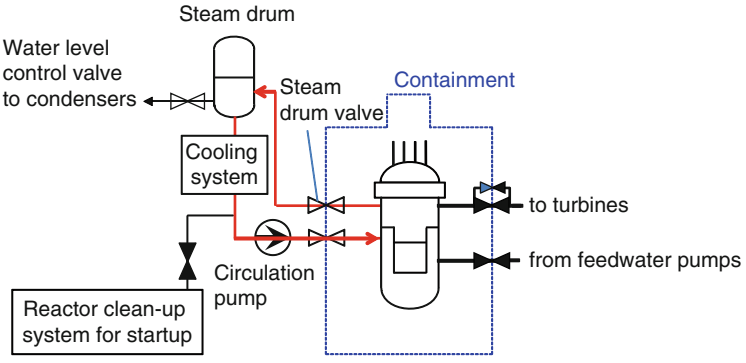


Fig. 5.69 Redesigned system for sliding pressure startup scheme

The role of the steam drum is to provide a water level and form a gas phase that consists of saturated steam. The pressure and hence saturated temperature increase with the amount of steam generated in the core like BWRs. There is no line from the gas phase of the steam drum to the main steam line because the saturated steam is not used for warming and starting the turbines. In the redesigned system, the system is pressurized to the operating point (25 MPa) first, and then the supercritical steam (thermo-physically similar to superheated steam) is sent to the turbines through the reactor vessel outlet nozzles and the main steam line.

The circulation pump keeps the coolant flow rate in the loop. The water level in the steam drum is controlled for stable pressurization. This is done by opening a water level control valve and dumping water from the steam drum into the condensers.

The system needs to be pressurized at pressures from atmospheric to supercritical level in the recirculation system. The saturation temperature increases to 374°C (critical temperature) during the pressurization. In order to keep the reactor vessel inlet temperature from exceeding the feedwater temperature at normal operation (280°C), the water is cooled by the heat exchanger before entering the circulation pump. This heat exchanged is similar to the heat exchanger of the Component Cooling Water System of LWRs. It should be noted that 280°C is below the operating temperature of the circulation pumps used in FPPs.

5.7.3 *Redesign of Sliding Pressure Startup Procedures*

The startup procedures are redesigned in detail, referring to LWRs and FPPs. The coolant flow paths during these procedures are schematically described in Figs. 5.70–5.74 as red lines.

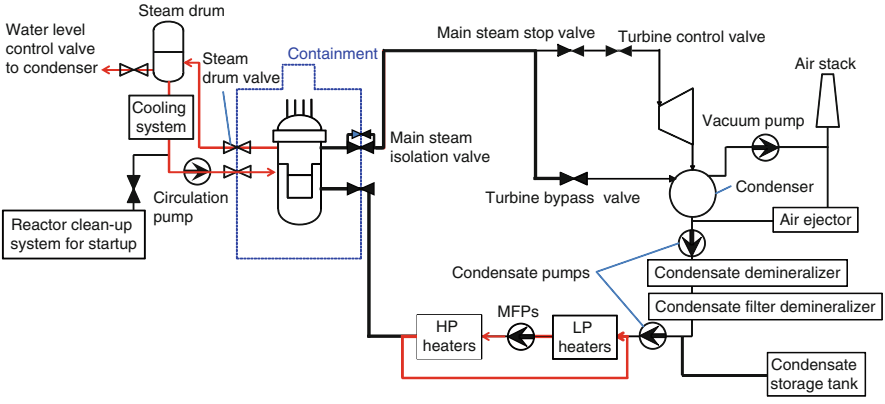


Fig. 5.70 Coolant flow during system pressurization and warming of feedwater system

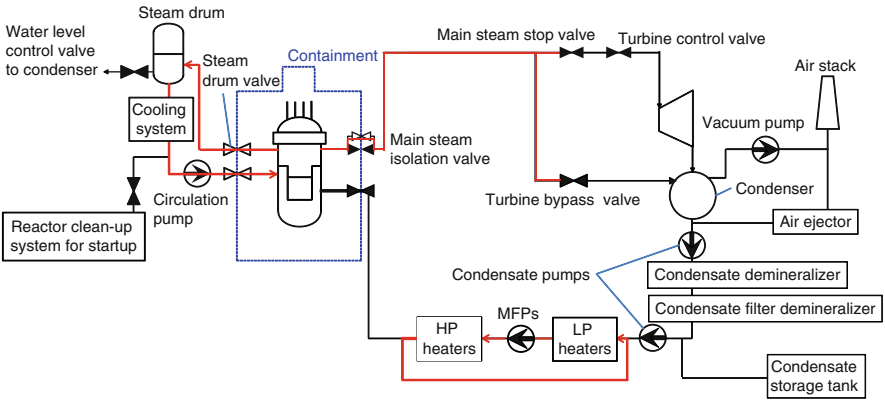


Fig. 5.71 Coolant flow during warming of main steam line and feedwater system

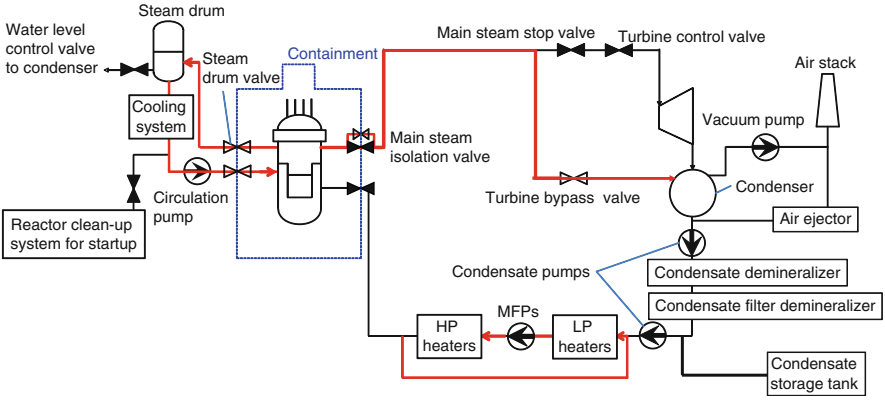


Fig. 5.72 Coolant flow during warming of turbine bypass line and feedwater system

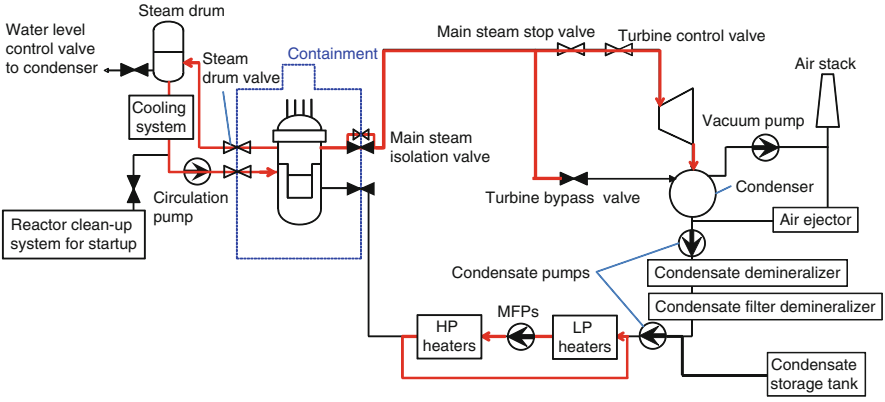


Fig. 5.73 Coolant flow during warming of turbines and feedwater system

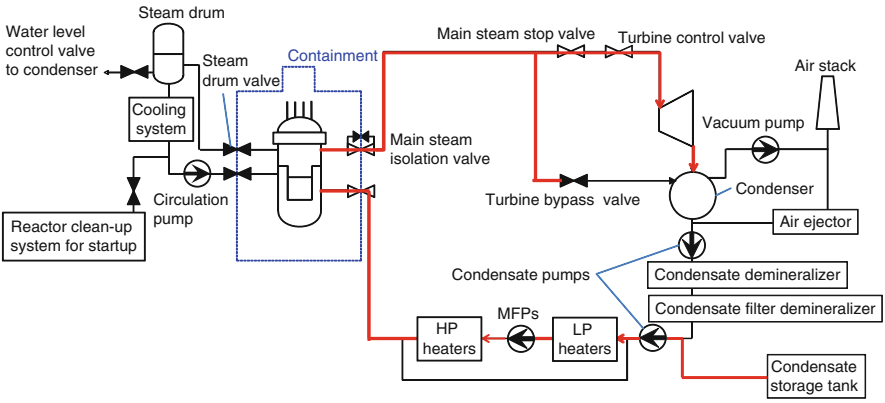


Fig. 5.74 Coolant flow after isolating recirculation system

5.7.3.1 Procedures Before Nuclear Heating

The condensate demineralizer and condensate filter demineralizer clean the condensate system and feedwater system (called the main coolant system in safety design). The reactor is also cleaned with the reactor clean-up system. It should be mentioned that the reactor cleanup system is used for only the startup, and the coolant is purified in the condensate system during the once-through operation as done in FPPs. Also, as in BWRs, the condenser is vacuumized in order to prepare it for start up.

The recirculation system, including the steam drum, is initially fully filled with water. The water level is generated by dumping part of the water into the condensers. The space above the water level is almost a vacuum. By using this procedure, the recirculation system is filled with only water. Noncondensable gas is not needed to generate a gas phase. Then, starting the circulation pump begins circulation of the coolant in the loop.

5.7.3.2 Start of Nuclear Heating and Feedwater Warming

The control rods are carefully withdrawn to start nuclear heating and raise the power. The power rise is kept slow in order to satisfy the limit of temperature rise (55°C/h) as is also applied in LWRs. At the same time, the motor-driven feedwater pumps are started, and the water circulates in the "feedwater loop," which is provided to warm the feedwater system during startup. This procedure is necessary to avoid cold shock on the reactor vessel inlet nozzles when the recirculation mode is switched to the once-through mode.

When the saturation temperature reaches 80°C, the reactor is temporarily kept subcritical. The MSIVs and the turbine bypass valves are opened. The condensers are put under vacuum and the reactor is deaerated. The purpose of this procedure is to avoid corrosion of the reactor internals and pipes.

5.7.3.3 System Pressurization to the Operating Point

After the deaeration, nuclear heating is restarted. First, the reactor power is kept constant at a low level. When the saturation temperature reaches 280°C, the heat exchanger starts. The reactor power is kept constant until the system attains a steady state. Then, the reactor power is raised again while keeping the pump inlet temperature constant (280°C) using the heat exchanger. When the pressure approaches the critical point (22.1 MPa), the physical properties of saturated water and steam get closer, and hence it is difficult to control the water level. The water level control valve is kept closed above 20 MPa.

5.7.3.4 Switch to Once-Through Mode

When the pressure reaches the operating point (25 MPa), the system is gradually switched from the recirculation to the once-through mode. First, the small valves that are in parallel to the MSIVs are opened for warming the main steam line. Then, the turbine bypass valves are opened for warming the turbine bypass line. From this moment, the system pressure is controlled by regulating the turbine bypass valves as in the pressure control system introduced in Chap. 4. During these procedures, the reactor power continues to rise in order to raise the reactor temperature to an appropriate level for warming the turbines. When the main steam temperature is high enough for turbine warming, the MSIVs, the main steam stop valves and the turbine control valves are opened. Then, the feedwater heaters are started using the steam extracted from the turbines. The recirculation system is isolated from the reactor. Instead of the circulation pump, the coolant flow in the core is kept by the reactor core isolation cooling (RCIC) system which is also called the auxiliary feedwater system (AFS) in the safety design (see Chap. 6). When the feedwater temperature is high enough, the reactor is connected to the feedwater system and the RCIC system is stopped.

5.7.4 System Transient Analysis

The system pressurization and line switching are analyzed using a system transient analysis code. Since the startup system and procedures are the same between the Super LWR and Super FR, the Super FR is analyzed as an example. The Super FR has higher power density and smaller heat capacity compared to the Super LWR so that the analysis of the Super FR covers that of the Super LWR from the viewpoint of the criteria of the MCST and the rate of increase in the coolant temperature.

The calculation model is shown in Fig. 5.75. The governing equations, empirical correlations, and algorithm are almost the same as those of the SPRAT-DOWNSUB code (a safety analysis code for the Super LWR during subcritical pressure

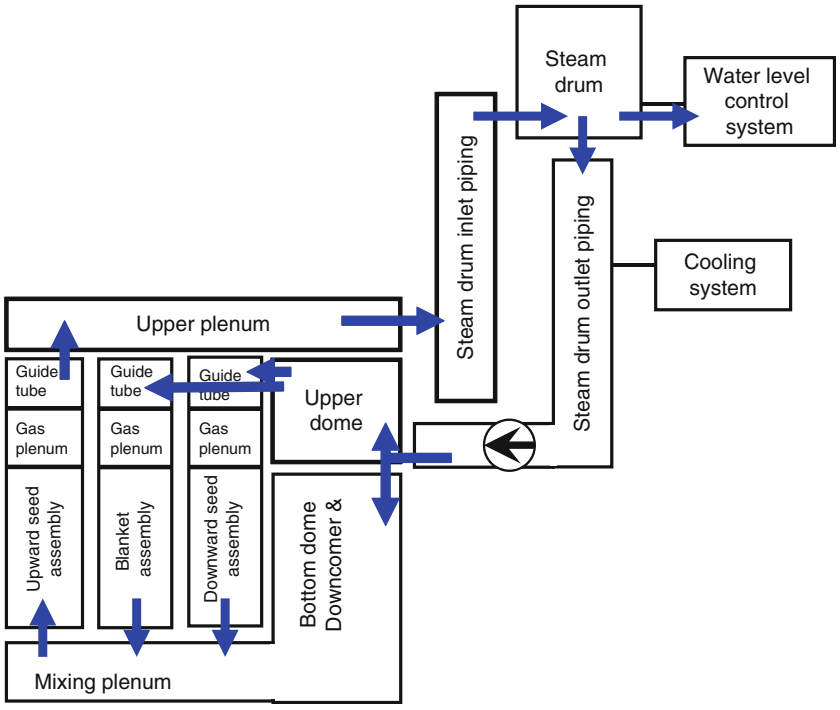


Fig. 5.75 System transient analysis model during recirculation mode

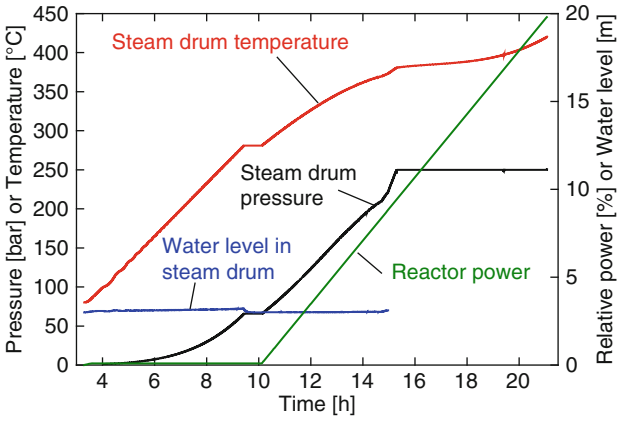


Fig. 5.76 Results of system transient analysis

operation) introduced in Sect. 6.6.2. The node assignment scheme in the reactor vessel is the same as that of the SPRAT-F introduced later in Sect. 7.11.

The results of the system transient analysis after the deaeration (see Sect. 5.7.3.2) are shown in Fig. 5.76. The reactor power is raised to 0.1% of the rated value and

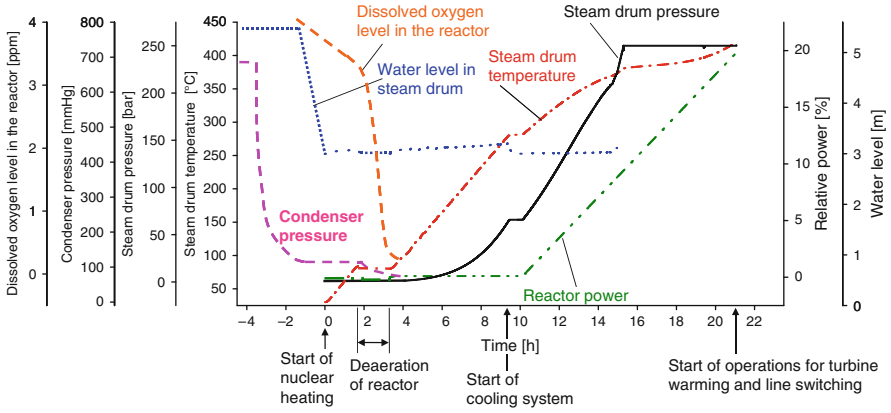


Fig. 5.77 Redesigned curves of sliding pressure startup before the power raising phase

kept constant. When the saturation temperature reaches about 100°C, the coolant starts boiling and the pressure calculation starts. Then, the temperature and pressure continue to rise. When the temperature reaches 280°C, the heat exchanger is started. A steady state is obtained shortly after the startup of the heat exchanger because the heat input by the fuel rods and the heat removal by the heat exchanger balance. Then, the reactor power is raised further and the pressure and temperature rise again. When the system is pressurized to supercritical pressure, the water level disappears and the steam drum is filled with supercritical steam. The line switching procedure starts at 25 MPa. When the small valves located in parallel to the MSIVs are opened first, the pressure decreases slightly due to a small release of the steam from the recirculation system. Then, the turbine bypass valves are opened, and the pressure is controlled as constant by these valves. After the steam temperature exceeds 400°C, turbine warming is started.

The startup curves based on the results of the analysis are shown in Fig. 5.77. The condenser pressure and dissolved oxygen level in the reactor are plotted by referring to the startup curves of BWRs. In the system transient analysis, the MCST is also calculated in order to consider the fuel rod integrity during the startup. The MCSTs in the three hot channels are shown in Fig. 5.78. They do not exceed 650°C which is the criterion for the three-dimensional core design (see Chap. 7).

5.8 Summary

In this chapter, the plant startup and stability were introduced. Both constant pressure and sliding pressure startup schemes are designed by referring to FPPs. The constant pressure startup system requires a startup bypass system consisting of a flash tank and pressure-reducing valves. The sliding pressure startup scheme

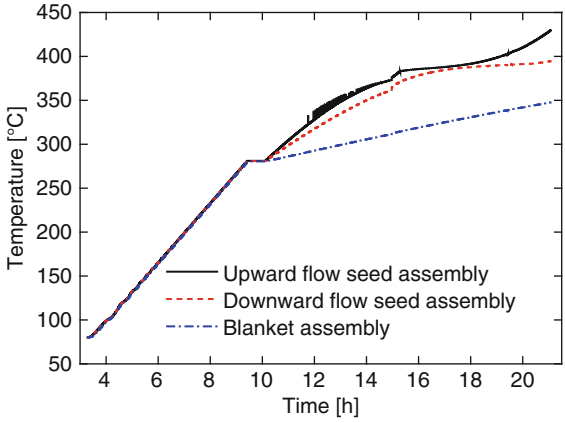


Fig. 5.78 Maximum cladding surface temperatures during system pressurization and line switching

needs a bypass system with a steam-water separator, a drain tank, and some drain valves. An additional heater can be installed to recover the startup heat from the saturated water in the drain tank. The sliding pressure startup scheme uses smaller component weight, and has smaller material expenditure and simpler system configuration requirements.

Based on a typical example of the Super LWR, the startup systems and startup procedures were investigated by thermal-hydraulic analyses, thermal-hydraulic stability analyses, and coupled neutronic thermal-hydraulic stability analyses. The thermal criterion (i.e., the MCST) is more limiting than the stability criteria of the decay ratio, and hence it dominates the available range of the power and flow rate at the pressurization phase in the sliding pressure startup. The coupled neutronic thermal-hydraulic stability criterion of the decay ratio is more limiting than the thermal criterion and the thermal-hydraulic stability criterion of the decay ratio, and hence it dominates the available range of the power and flow rate at the power-raising phase in both the constant pressure and sliding pressure startups. In spite of much smaller coolant flow rate compared to BWRs, the thermal-hydraulic instability of the Super LWR is not the limiting constraint as long as an adequate orifice pressure drop exists in the fuel assembly inlet. This is because the ratio of the coolant densities at the core inlet and outlet is smaller than that in BWRs. The coupled neutronic thermal hydraulic stability is affected by the water rods due to the moderator density feedback. The presence of the water rods increases the resonant peak and the phase lag. This increases the decay ratio and makes the system less stable.

Especially for the sliding pressure startup scheme, system pressurization and line switching from recirculation to once-through mode were investigated in detail. The feasibility of the system and procedures for them were assessed by a system transient analysis.

References

1. J. Matsuda, N. Shimono and K. Tamura, "Supercritical fossil fired power plants design and developments," *Proc. SCR 2000*, Tokyo, November 6–9, 2000, 79–89 (2000)
2. T. Nakatsuka, Y. Oka and S. Koshizuka, "Startup thermal considerations for supercritical-pressure light water cooled reactors," Nuclear Technology, Vol. 134(6), 221–230 (2001)
3. T. T. Yi, Y. Ishiwatari, S. Koshizuka and Y. Oka, "Startup thermal analysis of a high-temperature supercritical-pressure light water reactor," Journal of Nuclear Science and Technology, Vol. 41(8), 790–801 (2004)
4. I. Kataoka and M. Ishii, "Mechanistic modeling of pool entrainment phenomenon," International Journal of Heat and Mass Transfer, Vol. 27(11), 1999–2014 (1984)
5. K. V. Moore and W. H. Rettig, "RELAP-4: A computer program for transient thermal-hydraulic analysis," ANCR-1127, Aerojet Nuclear Company (1973)
6. D. C. Groeneveld, L. K. H. Leung, et al., "The 1995 look-up table for critical heat flux in tubes," Nuclear Engineering and Design, Vol. 163, 1–23 (1996)
7. "Thermohydraulic relationships for advanced water cooled reactors," IAEA-TECDOC-1203, April 2001 (2001)
8. "RELAP5/MOD3 code manual, volume V: Models and correlations," Scientech Inc., March 1998 (1998)
9. A. Yamaji, Y. Oka and S. Koshizuka, "Three-dimensional core design of Super LWR with neutronic and thermal-hydraulic coupling," *Proc. GLOBAL 2003*, New Orleans, LA, November 16–20, 2003, Paper 87845 (2003)
10. T. T. Yi, Y. Ishiwatari, J. Liu, S. Koshizuka and Y. Oka, "Thermal and stability considerations of super LWR during sliding pressure startup," Journal of Nuclear Science and Technology, Vol. 42(6), 537–548 (2005)
11. T. T. Yi, S. Koshizuka and Y. Oka, "A linear stability analysis of supercritical water reactors, (I) Thermal-hydraulic stability," Journal of Nuclear Science and Technology, Vol. 41(12), 1166–1175 (2004)
12. N. E. Todreas and M. S. Kazimi, "Nuclear systems I: Thermal hydraulic fundamentals," Hemisphere Publishing Co. (1990)
13. T. T. Yi, S. Koshizuka and Y. Oka, "A linear stability analysis of supercritical water reactors, (II) Coupled neutronic thermal-hydraulic stability," Journal of Nuclear Science and Technology, Vol. 41(12) 1176–1186 (2004)

Chapter 6
Safety

6.1 Introduction

Although the Super LWR plant evolves from conventional LWR plants, it has several safety characteristics that are unique to its design. This chapter comprehensively describes safety of the Super LWR.

The safety principle and safety system design are described in Sects. 6.2 and 6.3, respectively. Then, the deterministic approach to the Super LWR safety is described in Sects. 6.4–6.7; these describe safety analysis methods, selection and classification of abnormal events, the criteria for safety analyses, and the results of safety analyses. In addition, development of a transient subchannel analysis code and its application to the flow decreasing events are described in Sect. 6.8. Based on the safety system design and the deterministic safety analyses, level-1 probabilistic safety assessment (PSA), which is also called level-1 probabilistic risk assessment (PRA), is presented.

6.2 Safety Principle

The coolant cycle of the Super LWR is compared with those of LWRs in Fig. 6.1 [1]. LWRs have a coolant circulation system, i.e., the primary system of PWRs and the recirculation system of BWRs. The fundamental safety requirement for LWRs is keeping sufficient coolant inventory in the circulation system so as to maintain core flooding and heat removal by either forced or natural circulation. The coolant inventory is maintained by monitoring the water level in the reactor vessel of BWRs or the pressurizer of PWRs.

Since the Super LWR is cooled by single-phase flow, there is no water level in the reactor vessel. Also, the Super LWR is not equipped with a pressurizer. It is difficult to monitor the coolant inventory inside the pressure boundary. However, the coolant inventory is not the fundamental safety requirement for the Super LWR because the once-through coolant cycle is not a circulation system. The inlet and outlet of coolant are separated. The coolant enters the pressure boundary of the

Y. Oka et al., *Super Light Water Reactors and Super Fast Reactors*,
DOI 10.1007/978-1-4419-6035-1_6, © Springer Science+Business Media, LLC 2010

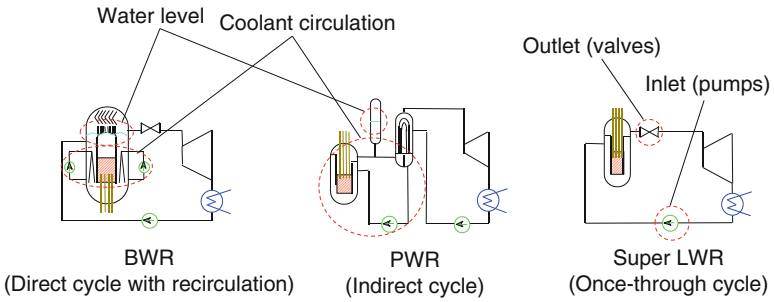


Fig. 6.1 Comparison of coolant cycles. (Taken from ref. [1] and used with permission from Korean Nuclear Society)

Table 6.1 Comparison of safety principles

	PWR	BWR	Super LWR
Requirement	Primary coolant inventory	Coolant inventory in the reactor vessel	Coolant flow rate in the core
Monitored parameter	Water level in the pressurizer	Water level in the reactor vessel	Main coolant flow rate, turbine inlet pressure

once-through coolant cycle from the inlet pumps and goes out through the outlet valves. In consideration of these design features, the safety principle of the Super LWR must be to "maintain the core coolant flow" [2]. This is accomplished by maintaining the supply of coolant from the cold-leg while also maintaining the discharge of coolant at the hot-leg. The safety principles are compared in Table 6.1.

"Loss of feedwater flow" is the same as "loss of reactor coolant flow" for the Super LWR. BWRs have the recirculation system and large coolant inventory in the reactor vessel. PWRs have the secondary system. Therefore, the feedwater of the Super LWR is more important for its safety than that of LWRs. In this chapter, "feedwater flow," "feedwater system," and "feedwater pump" of the Super LWR are called "main coolant flow," "main coolant system," and "reactor coolant pump (RCP)", respectively, to distinguish them from those of LWRs. The main coolant flow rate is equal to the core coolant flow rate and the main steam flow rate at the steady-state.

6.3 Safety System Design

6.3.1 Equipment

The safety system of the Super LWR has previously been schematically described in Figs. 1.3.38 and 3.2.1 [2]. The emergency core cooling system (ECCS) of the Super LWR consists of the auxiliary feedwater system (AFS), low pressure core

injection system (LPCI), and automatic depressurization system (ADS). A simplistic configuration of the AFS and LPCI is shown in Fig. 6.2. It is based on that of ABWRs. The equipment of the safety system is introduced below.

6.3.1.1 Reactor Shutdown System

For reactor shutdown, the reactor scram system and the standby liquid control system (SLCS) are prepared in the same manner as in BWRs. The scram reactivity curve is shown in Fig. 6.3 [2]. The same shape is taken as the curve for PWRs since the control rod drive mechanism is similar to that of PWRs, where the control rods are inserted from the reactor vessel top. In the safety analyses, the signal delay is assumed as 0.55 s, which is equal to the longest one in ABWR design, excluding the signal delay for "water level low" (remember that the Super LWR has no water level). The influence of this parameter on the reactor safety is investigated in Sect. 6.7. The reactivity inserted through the reactor scram is conservatively assumed as −10%dk/k in the safety analyses while it is estimated as −15.4 and −18.6%dk/k in the three-dimensional core design (see Fig. 2.4.32). The reactivity curves are compared in Fig. 6.4 [3]. Since the absolute value of the inserted reactivity until 70% of the rod stroke, which dominates the response of reactor power, is smaller in the assumption for safety analysis, this assumption is conservative. The SLCS is provided for backup shutdown. The required tank volume and

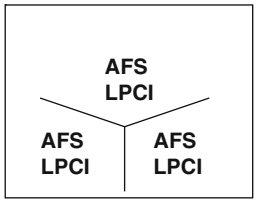


Fig. 6.2 ECCS configuration

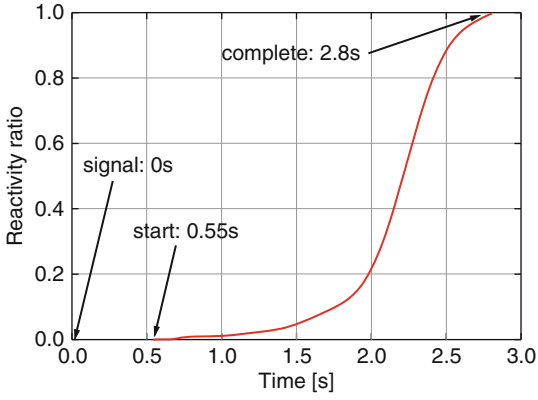


Fig. 6.3 Scram reactivity curve for safety analysis. (Taken from ref. [2] and used with permission from Atomic Energy Society of Japan)

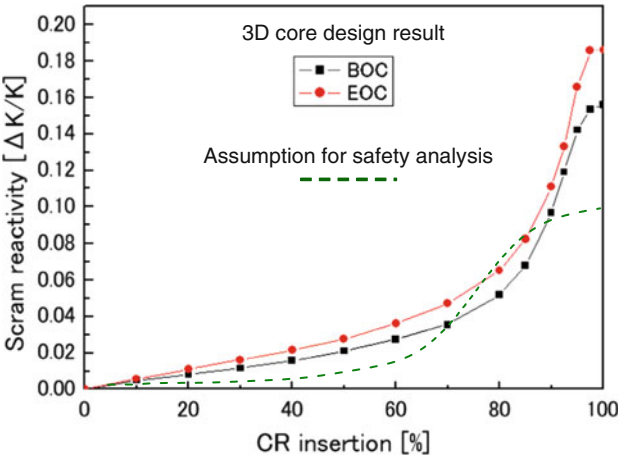


Fig. 6.4 Comparison of scram reactivity curve. (Taken from ref. [3])

boron concentration for cold shutdown are estimated as almost the same as those of ABWRs [3].

6.3.1.2 Coolant Supply System

The Super LWR has two main coolant lines. Two turbine-driven RCPs are provided for normal operation. For plant startup and backup of the turbine-driven RCPs, two motor-driven RCPs with half the capacity of that of the turbine-driven RCPs are provided as in BWRs.

Three trains of the AFS are provided for the backup of these RCPs. It should be noted that the motor-driven RCPs are not credited in the safety analyses just as they are not credited in BWRs. The capacity of a single train is 4% of the rated flow; this is determined on the basis of removing the decay heat up to 6% of the rated power by two trains considering a single failure. The AFS also plays the role of reactor core isolation cooling (RCIC) because the main steam is extracted upstream from the main steam isolation valves (MSIVs). The start time of the AFS is determined by reference to the turbine-driven RCIC of ABWRs. The start-up curve to be used in safety analysis is shown in Fig. 6.5 [2]. The influence of its start time on the reactor safety is investigated in Sect. 6.7.

Three trains of the LPCI are provided for the backup of the AFS and mitigation of loss of coolant accident (LOCA). The LPCI is one of the functions of the residual heat removal (RHR) system. The capacity of the single train is 12% of the rated flow that is determined to keep the peak cladding temperature (PCT) well below the safety criterion even with single failure. The emergency diesel generators supply electric power to the LPCI even if the offsite power is lost. In that case, 30 s is assumed as the start time of the emergency diesel generators.

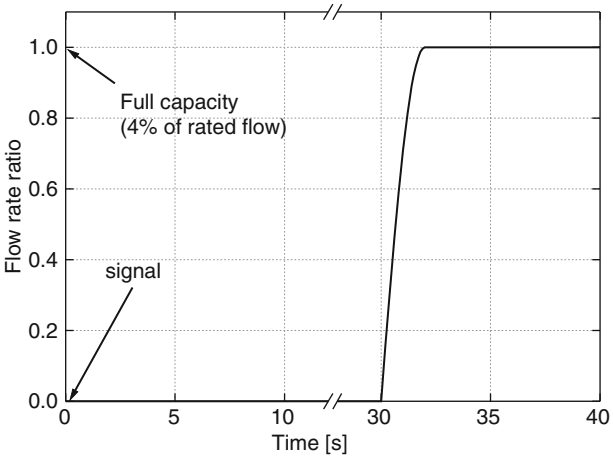


Fig. 6.5 Startup curve of AFS. (Taken from ref. [2] and used with permission from Atomic Energy Society of Japan)

6.3.1.3 Valves for Coolant Discharge and Isolation

For the discharge of coolant, safety relief valves (SRVs) are prepared in case of a turbine trip without bypass or MSIV closure. The SRVs also have the function of acting as the ADS, as in BWRs.

One of the advantages of the once-through coolant cycle is that depressurization cools the core effectively. The ADS lends unique behavior to the Super LWR [1–4]. Reactor depressurization by opening 8 ADS valves has been analyzed using the SPRAT-DOWN-DP code, introduced in Sect. 6.4. Coolant flow during reactor depressurization is shown in Fig. 6.6 [1]. The supply of coolant from the cold-leg is assumed to stop in 5 s. The analysis results are shown in Fig. 6.7 [1]. Initiating the ADS induces strong core coolant flow in the core. This safety characteristic derives from the once-through coolant cycle. During depressurization, the top dome passively supplies its coolant inventory to the fuel channels in a manner similar to an "in-vessel accumulator". This is a key advantage of the two-path core with downward-flow channels, including the water rods, because the downward-flow channels are not a bypass flow path from the top dome to the hot-leg. The core coolant flow rate is maintained even when the supply of coolant from the cold-leg has stopped. Also, depressurization decreases the reactivity because the Super LWR has a negative void reactivity coefficient. Due to these thermal-hydraulic and neutronic effects of reactor depressurization, the hottest cladding temperature does not exceed the initial value. Discharge of the coolant inventory does not threaten safety because maintaining the coolant inventory is not the fundamental safety requirement as long as the core coolant flow is maintained. After depressurization, the core is cooled by the LPCI. Although maintenance of the supply of coolant from the cold-leg and discharge of coolant at the hot-leg are required for decay heat removal on a long time scale, the core can be cooled by reactor

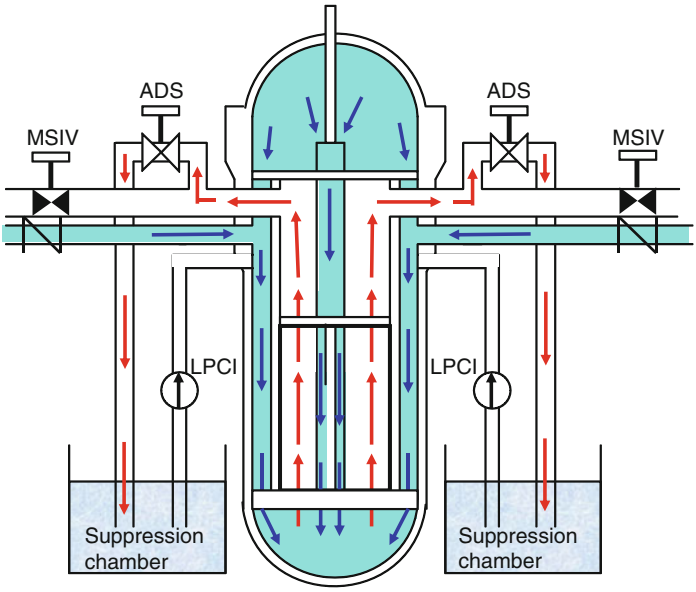


Fig. 6.6 Coolant flow during reactor depressurization. (Taken from ref. [1] and used with permission from Korean Nuclear Society)

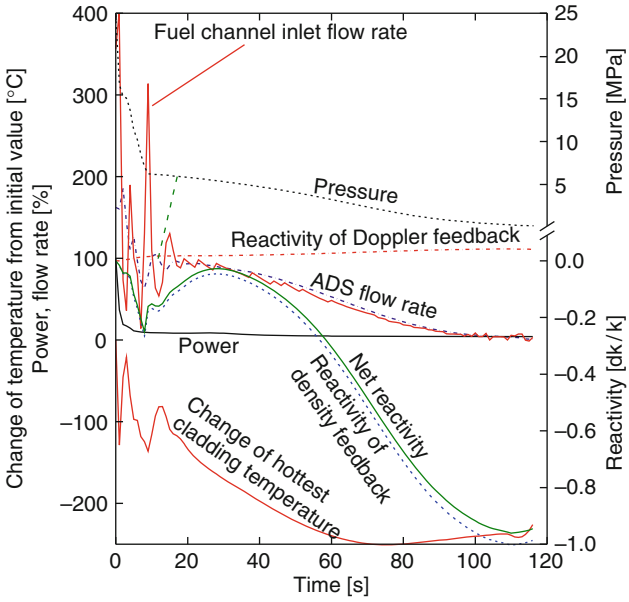


Fig. 6.7 Behavior during reactor depressurization. (Taken from ref. [1] and used with permission from Korean Nuclear Society)

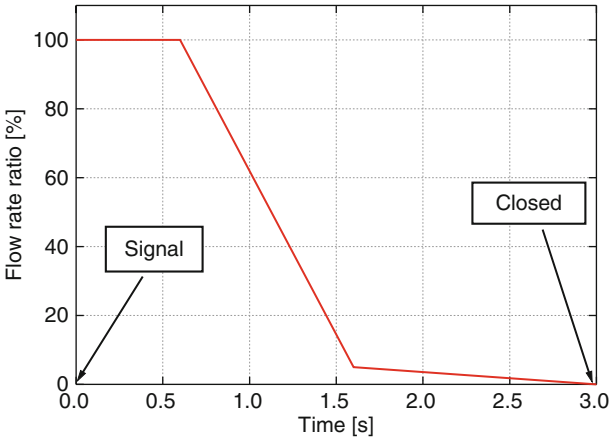


Fig. 6.8 Characteristic of closing MSIV. (Taken from ref. [2] and used with permission from Atomic Energy Society of Japan)

depressurization for short times up to 1–2 min according to the reactor vessel size without the supply of coolant from the cold-leg. This allows the emergency diesel generators for the LPCI or the RHR to have a realistic start time similar to the 30-s time in LWRs.

The function of the MSIVs in the Super LWR is to avoid the release of radioactivity outside of the containment as in BWRs. The MSIV characteristic is determined to be the same as that of ABWRs as shown in Fig. 6.8 [2].

6.3.2 Actuation Conditions of the Safety System

The principle for safety system actuation is summarized in Table 6.2 [2]. Abnormalities in supplying coolant from the cold-leg are detected as "flow rate low" levels, while abnormalities in discharging coolant at the hot-leg are detected as "pressure high" levels. When the decay heat cannot be removed at supercritical pressure, which corresponds to a low level 3 flow rate, the reactor is depressurized, as illustrated in Figs. 6.2 and 6.3, and then cooled by the LPCI. When the pressure decreases from the supercritical to subcritical region, boiling transition will occur on the fuel rod surface, leading to a rapid increase in the cladding temperature. It is known that the minimum heat transfer coefficient is especially small just below the critical pressure. Therefore, the pressure should not stay at or decrease slowly around the critical pressure. So, the reactor is depressurized at a low level 2 pressure, which is 106% of the critical pressure.

The safety system design and actuation conditions are summarized in Table 6.3. The actuation conditions are determined by reference to LWRs and also considering the uniqueness of the Super LWR [2].

Table 6.2 Principle of safety system actuation

Flow rate low (feedwater or main steam)	
Level 1 (90%)[a]	Reactor scram
Level 2 (20%)[a]	AFS
Level 3 (6%)[a]	ADS/LPCI system
Pressure high	
Level 1 (26.0 MPa)	Reactor scram
Level 2 (26.2 MPa)	SRV
Pressure low	
Level 1 (24.0 MPa)	Reactor scram
Level 2 (23.5 MPa)	ADS/LPCI system

Taken from ref. [2] and used with permission from Atomic Energy Society of Japan
AFS auxiliary feedwater system, *ADS* automatic depressurization system, *LPCI* low pressure core injection system
[a]100% corresponds to normal operation

Table 6.3 Summary of safety system design

Safety system	Actuation conditions				
Reactor scram system	Pressure high (level 1)		Main coolant flow rate low (level 1)		
	Pressure low (level 1)		Reactor power high (120%)		
	MSIV closure (90%)		Turbine control valve quickly closed		
	ECCS start-up		Main stop valve closure		
	Drywell pressure high		Earthquake acceleration large		
	Reactor period short (10 s)		Loss of offsite power		
	Reactor coolant pump trip		Condensate pump trip		
AFS (4% capacity × 3 units) (Turbine-driven)	Reactor coolant pump trip		Main coolant flow rate low (level 2)		
	Loss of offsite power		Turbine control valves quickly closed		
	Condensate pump trip		Main stop valves closure		
			MSIV closure (90%)		
SRV (20% capacity × 8 units)	Relief valve function			Safety valve function	
	Open (MPa)	Close (MPa)	Number	Open (MPa)	Number
	26.2	25.2	1	27.0	2
	26.4	25.4	1	27.2	3
	26.6	25.6	3	27.4	3
	26.8	25.8	3		
ADS (20% capacity × 8 units)	Pressure low (level 2)				
MSIV	Main coolant flow rate low (level 3)				
LPCI (12% capacity × 3 units) (Motor-driven)	Drywell pressure high				

A "2-out-of-4" logic using four independent detectors is taken for each scram signal as in LWRs. Most of the signals are taken from those of LWRs. Those which are used in both BWRs and PWRs are "pressure high," "reactor power high," and "earthquake acceleration large." "Reactor period short," "turbine control valves quickly closed," "drywell pressure high," "MSIV closure," and "main stop valves

closure" are taken from BWRs. "Main coolant flow rate low," "pressure low," and "ECCS start-up" are taken from PWRs. Since the main coolant flow rate is important for the Super LWR, other abnormalities that cause a trip of the RCPs are also taken as the scram signals. They are "condensate pump trip," "loss of offsite power," and "turbine control valves quickly closed." "Reactor coolant pump trip" itself is also taken as one of the scram signals.

Since the function of the AFS is to keep the main coolant flow rate in the event of the unavailability of the RCPs, its actuation signals should be released by detecting an abnormality in the RCPs or a decrease in the main coolant flow rate. "Reactor coolant pump trip" and "main coolant flow rate low" are taken as the AFS signals. "Loss of offsite power," "condensate pump trip," "turbine control valves quickly closed," "main stop valves closure," and "MSIV closure" are also taken as the AFS signals because these abnormalities cause a trip of the RCPs.

The SRVs are actuated by two mechanisms just like BWRs. Functioning as relief valves, they are opened and closed by external force. The lowest setpoint for opening several valves corresponds to level 2 of high pressure. Functioning as safety valves, they are opened when the system pressure is large enough to compress the spring and closed again when the system pressure decreases. The safety valves are backups for the relief valves.

The function of the ADS in BWRs is to decrease the system pressure so as to enable operation of the low pressure ECCS. "Water level low" and "drywell pressure high" are taken as the ADS signals using "and" logic so as to prevent inadvertent actuations. The ADS are actuated 30 s after the signal for the start of the low pressure ECCS. For the Super LWR, meanwhile, the function of the ADS is to induce the coolant flow during depressurization and to keep the coolant outlet open during core reflooding by the LPCI or long-term cooling by the RHR. The actuation signals are "main coolant flow rate low (level 3)," "pressure low (level 2)," or "drywell pressure high". If the MSIVs are closed and the ADS is not opened in case of a cold-leg break LOCA, significant core heat-up would occur due to closure of the coolant outlet at the hot-leg. That is why "or" logic is used for the ADS signal without any delay time unlike the situation in BWRs. The function of the LPCI is to keep the coolant supply after depressurization. Therefore, the actuation signals should be the same as those of the ADS. Therefore, the MSIVs, ADS, and LPCI share the actuation signals.

6.4 Selection and Classification of Abnormal Events

Abnormalities of LWRs are categorized as several types. Since the Super LWR is also a light water cooled reactor and the components are similar to those of LWRs, its abnormalities are taken from those of PWRs and BWRs. Reference is also made to sodium cooled reactors. Although many of the abnormalities in sodium cooled reactors are also considered in LWRs, there are some abnormalities that are not considered. However, these abnormalities are not possible in the Super LWR. Gas cooled reactors are also considered; however, there are no abnormalities which are

special for gas cooled reactors and are of concern in the Super LWR. The abnormal events of the Super LWR are summarized in Table 6.4 together with those of LWRs [1]. All the events are taken from either PWRs or BWRs. Those abnormalities related to the secondary system of PWRs are not taken into consideration.

6.4.1 Reactor Coolant Flow Abnormality

The abnormal events related to a "decrease in core coolant flow rate" are the most important for the Super LWR because the core coolant flow rate is the fundamental safety requirement, as described in Sect. 6.2. Since the coolant cycle of the Super LWR is different from those of both PWRs and BWRs, the events need to be carefully selected and classified.

The "loss of all feedwater flow" of LWRs is classified as an abnormal transient. In PWRs, it occurs in the secondary system, and there is a large water inventory in the steam generators. BWRs have the recirculation system, and there is a large water inventory in the RPV. Therefore, the "total loss of feedwater" does not immediately lead to a low-of-flow in the core. The "total loss of reactor coolant flow" corresponds to a trip of all the primary coolant pumps of PWRs and a trip of all the recirculation pumps of BWRs. It is classified as an accident.

The once-through coolant cycle of the Super LWR is schematically illustrated in Fig. 6.9 [1]. The feedwater pump is the same as the RCP. The "loss of all feedwater flow" and the "total loss of reactor coolant flow" are the same incidents. Classification of this event depends on the frequency. Also, the guidelines for Japanese LWRs are followed. A simultaneous sudden trip of all pumps that have been directly maintaining the core coolant flow rate must be classified as a "total loss of reactor coolant flow" accident. These pumps correspond to the primary pumps of PWRs and the recirculation pumps of BWRs. Since the RCPs of the Super LWR also maintain the core coolant flow rate, a simultaneous sudden trip of the RCPs is classified as the "total loss of reactor coolant flow" accident, assuming that its frequency will be less than 10^{-3} per year by system separation and high reliability.

Loss of supply of coolant to the deaerator would also cause a trip of the RCPs because the inlet pressure of the RCPs decreases with the water level in the deaerator. This abnormality is represented by the "loss of offsite power" transient where the motor-driven condensate pumps stop. Since there is a large amount of water in the deaerator, the RCPs are expected not to stop for some period after the trip of the condensate pumps. The capacity of the deaerator has not yet been determined. If it is 140 m^3, which corresponds with the typical design of 1,000 MWe class FPPs, the water level in the deaerator would decrease by only 7% in 10 s after the trip of the condensate pumps. In the safety analysis, it is conservatively assumed that the trip of the RCPs occurs 10 s after the condensate pump trip [5]. This transient is less severe than a "total loss of reactor coolant flow" accident because a reactor scram is possible before the trip of the RCPs. In the safety analysis, the reactor scram by the signal of "loss of offsite power," "condensate pump trip," or "turbine control valves quickly closed" is credited.

Table 6.4 Comparison of abnormal events – *Open circle*: transient; *Filled diamond*: accident. (Some events are listed more than once.)

Type of abnormality	Event	PWR	BWR	Super LWR
Abnormality in reactivity and power distribution	Uncontrolled CR withdrawal	○	○	○
	CR assembly misalignment and drop	○		○
	CR ejection	◆		◆
	CR drop		◆	
	Boron dilution	○		
	Startup of an inactive reactor coolant loop	○	○	[a]
	Loss of feedwater heating		○	○
	Reactor coolant flow control system failure		○	○
	Feedwater control system failure		○	
	Inadvertent startup of AFS			○
Decrease in core coolant flow rate	Partial loss of reactor coolant flow	○	○	○
	Total loss of reactor coolant flow	◆[b]	◆	◆
	Loss of offsite power	○	○	○
	Loss of turbine load			○
	Isolation of main steam line			○
	Reactor coolant pump seizure	◆	◆	◆
Abnormality in reactor pressure and coolant inventory	Loss of offsite power		○	○
	Loss of turbine load		○	○
	Isolation of main steam line		○	○
	Depressurization of reactor coolant system	○		○
	Inadvertent start-up of ECCS	○	○	
	Pressure control system failure		○	○
	Inadvertent SRV opening		○	○
	Loss of all feedwater flow		○	[c]
	LOCA	◆	◆	◆
	Main steam line break	◆	[d]	[d]
	Main feedwater pipe rupture	◆	[d]	[d]
Abnormality in secondary system	Loss of turbine load	○		
	Load increase	○		
	Depressurization	○		
	Loss of all feedwater flow	○		
	Feedwater system malfunction	○		
Abnormality in containment	LOCA	◆	◆	◆
	Generation of H_2 gas	◆	◆	◆
	Dynamic load to containment		◆	◆
Radioactive release	Waste gas decay tank rupture	◆	◆	◆
	Improper fuel assembly insertion or drop	◆	◆	◆
	Main steam line break outside containment		◆	◆
	SG tube rupture	◆		
	LOCA	◆	◆	◆
	CR ejection	◆		◆
	CR drop		◆	

Taken from ref. [1] and used with permission from Korean Nuclear Society

[a]Not possible for the Super LWR due to the two-loop configuration

[b]Classified as an accident for Japanese PWRs

[c]The same as "total loss of reactor coolant flow" due to the absence of the recirculation or secondary system

[d]Covered by LOCA due to the absence of the secondary system

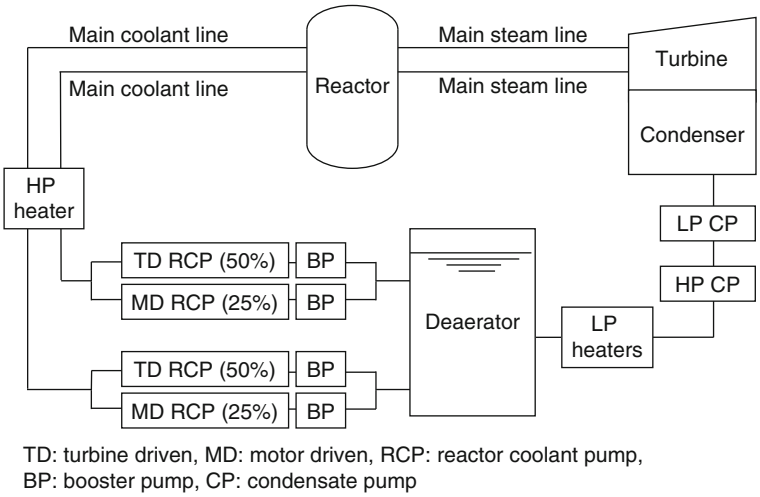


Fig. 6.9 Once-through coolant cycle of Super LWR. (Taken from ref. [1] and used with permission from Korean Nuclear Society)

Loss of the supply of steam to the turbine-driven RCPs would also cause a trip of the RCPs. The "loss of turbine load" transient and the "isolation of main steam line" transient are followed by this situation. The RCPs are assumed not to stop for some period because there is residual steam in the main steam lines and turbines, similar to BWRs. In the safety analyses, the trip of the RCPs is assumed to occur 10 s after the initiation of the transients. A reactor scram by the signal of "turbine control valves quickly closed" or "MSIV closure" is credited before the trip of the RCPs.

6.4.2 Other Abnormalities

In the other types of abnormalities, the event classification follows those of LWRs because the components such as the valves and the control rod drives are expected to be similar to those of PWRs or BWRs. In the category of the "reactivity abnormality," the incidents related to the control rods are taken from those of PWRs. The "loss of feedwater heating" is taken like BWRs. Most of the incidents of the "pressure abnormality" are taken from BWRs because the Super LWR also adopts the direct steam cycle. The "reactor depressurization" is taken from PWRs. The abnormalities categorized into the "inadvertent start or malfunction of core cooling system" are taken from those of PWRs or BWRs. The "inadvertent startup of AFS" of the Super LWR corresponds to the "inadvertent startup of ECCS" of PWRs. The "core coolant flow control system failure" is the same as the "feedwater control system failure" for the Super LWR while the two incidents are different in BWRs due to the recirculation system. All the accidents categorized into the "loss

of reactor coolant inventory" and "others" are taken from PWRs or BWRs except those relating to the secondary system of PWRs.

6.4.3 Event Selection for Safety Analysis

For the safety analysis, the abnormal transients and accidents are taken from each category as the "reactivity abnormality," "pressure abnormality," "reactor coolant flow abnormality," and "inadvertent start or malfunction of core cooling system" in Table 6.4 except the "CR assembly misalignment and drop" transient, and the "depressurization of core cooling system" transient. They are shown in Table 6.5.

The "CR assembly misalignment and drop" is representative of the radial power distribution abnormality. However, it cannot be analyzed because only the single channel model and point kinetics are used here. The change of the radial power distribution is expected to affect the cladding temperature distribution as it affects the departure from nucleate boiling ratio distribution of PWRs. The "depressurization of core cooling system" transient is not analyzed because it will be almost the same as the "pressure control system failure" transient. It should be remembered that reactor depressurization does not threaten the Super LWR safety as is described in Sect. 6.3.

The "waste gas decay tank rupture" accident and the "improper fuel assembly insertion or drop" accident are not considered in this book.

Table 6.5 Abnormal events in safety analysis

Abnormal transients
Decrease in core coolant flow rate
Partial loss of reactor coolant flow
Loss of offsite power
Abnormality in reactor pressure
Loss of turbine load
Isolation of main steam line
Pressure control system failure
Abnormality in reactivity
Loss of feedwater heating
Inadvertent startup of AFS
Reactor coolant flow control system failure
Uncontrolled CR withdrawal at normal operation
Uncontrolled CR withdrawal at startup
Accidents
Decrease in core coolant flow rate
Total loss of reactor coolant flow
Reactor coolant pump seizure
Abnormality in reactivity
CR ejection at full power
CR ejection at hot standby
LOCA
Large LOCA
Small LOCA

6.4.4 Uniqueness in the LOCA of the Super LWR

There are mainly two differences in blowdown phenomena at LOCA between the Super LWR and LWRs. The first one is that blowdown of the Super LWR starts at supercritical pressure. The second one is that a double-ended break does not occur in the Super LWR. Figure 6.10 shows a comparison of the blowdown phenomena among a PWR, a BWR, and the Super LWR [6]. Since PWRs and BWRs have circulation loops in the primary cooling system, i.e., the primary system of PWRs and the recirculation system of BWRs, two flow paths are generated to both sides of the break. In the Super LWR, only one break flow path is generated because the once-through coolant cycle has both the coolant inlet and outlet. It is a single-ended break. However, in the design and analysis of the containment (a future subject), a double-ended break must be considered due to the coolant discharge from the balance of plant. The reflooding phase of the Super LWR is similar to that of PWRs rather than BWRs. Figure 6.11 shows a comparison of the reflooding phenomena between a PWR and the Super LWR [6]. Since the Super LWR adopts the pressure-suppression

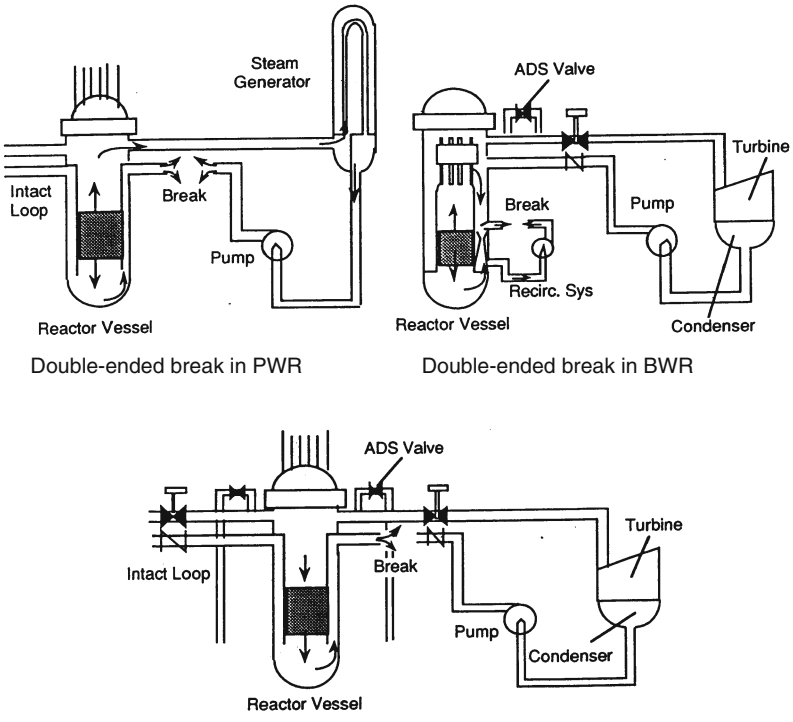


Fig. 6.10 Comparison of blowdown phenomena. (Taken from ref. [6] and used with permission from Atomic Energy Society of Japan)

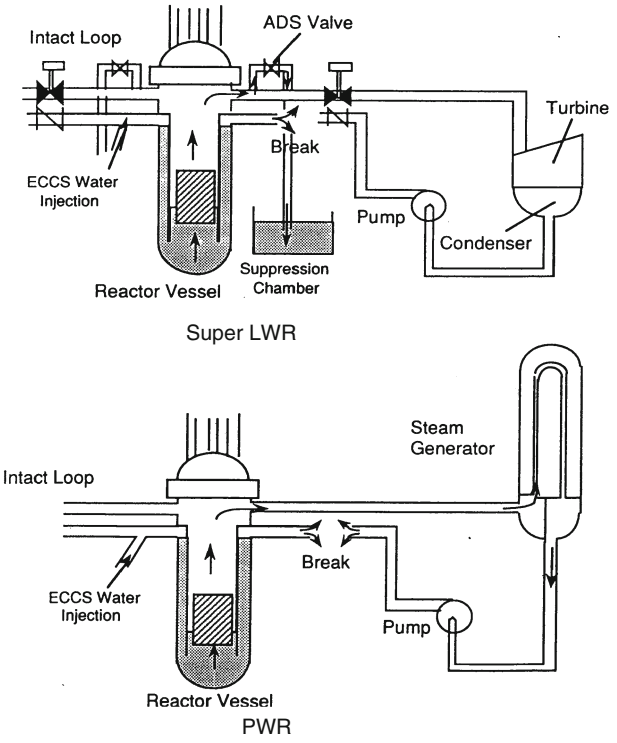


Fig. 6.11 Comparison of reflooding phenomena. (Taken from ref. [6] and used with permission from Atomic Energy Society of Japan)

type containment like BWRs, the steam generated in the core is released through the ADS lines to the suppression chamber, while it is released through the steam generators and the break point to the dry type containment in PWRs.

6.5 Safety Criteria

Since the Super LWR is presently in the concept development phase, the safety criteria cannot be determined based on experiments. The principle for the safety criteria and tentative values for the safety analyses have been determined [4–6]. The requirements for abnormal transients are the same as those of LWRs: no systematic fuel rod damage and no pressure boundary damage. The requirements for accidents are no excessive core damage and no pressure boundary damage, which also correspond with LWRs. The safety criteria described below are determined for concept development. Experiments will be necessary for assessing their validity.

6.5.1 Criteria for Fuel Rod Integrity

The fuel rod cladding material of the Super LWR is being developed and tested. For fuel rod design of the Super LWR in the concept development phase, typical austenitic stainless steels or Ni-alloys are applied as described in Chap. 2. The principle of the safety criteria for fuel rod integrity is shown in Table 6.6. Since heat transfer deterioration is a much milder phenomenon than boiling transition, the minimum deterioration heat flux ratio was eliminated from the transient criterion related to fuel rod heat-up [7]. The types of abnormalities are separated into "loss of cooling" and "overpower".

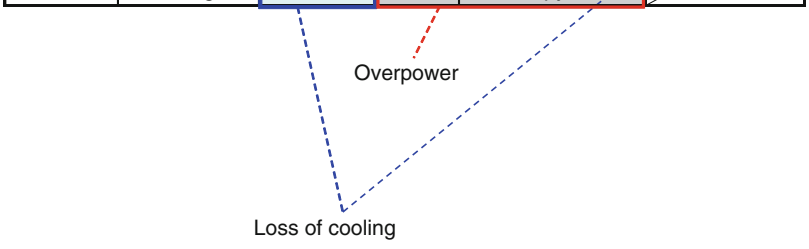
For the "loss of cooling" type transients, the limiting failure mode is expected to be buckling collapse of the cladding due to a decrease in the Young's modulus at the elevated temperature. The maximum allowable temperature of the cladding is determined as 850°C in Chap. 2, taking several conservatisms, so that the pressure difference on the cladding is less than one-third of the collapse pressure.

For the "loss of cooling" type accidents, the requirement is to maintain a coolable geometry, as in LWRs. The limiting failure mode is expected to be oxidation of the cladding. The criterion of the cladding temperature is set at 1,260°C for stainless steels, taken from the criterion for LOCA of early US PWRs with stainless steel cladding [8]. The criterion for Ni-alloys is also set at 1,260°C because the oxidation behavior of Ni-alloys is expected to be similar to that of stainless steels.

For the "overpower" type transients, the limiting failure mode is expected to be burst or pellet cladding mechanical interaction (PCMI). The maximum allowable powers listed in Table 2.8.1 are determined through the fuel rod thermal and mechanical analyses in Chap. 2, taking several conservatisms so as to prevent melting of the pellet centerline and keep the circumferential strain on the cladding

Table 6.6 Principle of safety criteria for fuel rod integrity

Category	Requirement	Mechanical failure			Heat-up
		Buckling	Burst	PCI	
Accident	No excessive damage			Enthalpy < Limit (RIA)	Oxidation<Limit MSCT<Limit
Transient	No systematic damage	ΔP on clad. < Limit	Plastic strain < Limit	Pellet temp.<Limit Plastic strain<Limit Enthalpy<Limit	



within the elastic region. A transient with reactivity insertion over $1 is not expected in the Super LWR because the reactor is tripped before a CR cluster is fully withdrawn. Thus, the maximum allowable fuel enthalpy is not taken as a criterion for abnormal transients.

For the "overpower" type accidents, such as the CR ejections, the maximum allowable fuel enthalpy needs to be determined, as in LWRs. The same criterion as that of LWRs (230 cal/g) is taken. The validity should be assessed by experiments in the future.

6.5.2 Criteria for Pressure Boundary Integrity

The relative pressure change in the Super LWR is smaller than that in LWRs due to the once-through coolant cycle and the high operating pressure [4, 5]. The maximum allowable pressures for abnormal transients and accidents are set at 105% and 110% of the maximum pressure of normal operation (27.5 MPa), respectively, while those of LWRs are 110% and 120%. Since the average core outlet temperature is high, similar to the temperature for sodium cooled reactors, thermal creep of the main steam lines should be considered for both normal and abnormal conditions in future designs. It might be reasonable to limit the duration of high temperature conditions by considering the cumulative damage fraction (CDF), as is done for sodium cooled reactors. A material used for the main steam lines in FPPs, such as 9Cr-1Mo, has high creep strength and is a promising candidate material because the operating temperature and pressure of the Super LWR are within those of recently constructed FPPs.

6.5.3 Criteria for ATWS

An anticipated transient without scram (ATWS) is defined as an abnormal transient followed by failure of a reactor scram. Since the Super LWR is a simplified LWR, the probability of an ATWS is expected to be on the same order as that of LWRs. An ATWS of the Super LWR is classified as a "beyond design basis event" (BDBE). A deterministic evaluation of an ATWS is a global requirement because it is a potential safety issue that may lead to core damage under postulated conditions. Also, it is expected that inherent safety characteristics of nuclear reactors, not only reactivity feedback but also reactor system dynamics, can be clearly identified at ATWS conditions due to a scram failure. Therefore, deterministic ATWS analyses are carried out for the Super LWR in Sect. 6.7 as well as the abnormal transients and accidents.

Despite the significantly low probability of an ATWS compared to other accidents, the same criteria as those of accidents are applied, as in LWRs. It should be noted that release of fission product gases to the coolant does not bring about an

issue of positive reactivity insertion because the Super LWR has a negative void reactivity coefficient, as in LWRs.

6.6 Safety Analysis Methods

In this section, four computer codes with a 1-D model for deterministic safety analyses of the Super LWR are introduced. They are summarized in Table 6.7.

6.6.1 Safety Analysis Code for Supercritical Pressure Condition

The plant transient analysis code SPRAT-DOWN, described in Sect. 4.2, is extended for the analyses of abnormal transients and accidents. The calculation model is shown in Fig. 6.12. The models of the equipment, i.e., the AFS, SRV, MSIVs, and turbine bypass valves, are added for safety analyses. A hot channel, where the linear heat generation late and maximum cladding surface temperature are the highest in the core, is modeled as well as the average channel in order to calculate the highest values of cladding temperature and pellet enthalpy. The flow chart is shown in Fig. 6.13.

The coolant entering the RPV is divided into the downcomer flow (70%) and the water rod flow (30%) at the normal operating conditions. The pressure drops of those two paths are balanced by means of orifices. At abnormal conditions, flow-redistribution would occur between those two paths due to the loss of pressure balance. The flow-redistribution is considered along with calculation of the pressure drop balance and momentum conservation. The pressure drops of each flow path are calculated as follows.

Friction:

$$\Delta P_{\mathrm{fri}} = \sum_i 2\left(\frac{\Delta z}{D_h}\right)\rho_i v_i{}^2 f_i \tag{6.1}$$

Table 6.7 Codes for safety analyses of Super LWR

Code	Initial condition	Analyzed events
SPRAT-DOWN	Steady-state at supercritical pressure	Abnormal transients or accidents, including small LOCA without depressurization
SPRAT-DOWN-SUB	Steady-state at subcritical pressure	Abnormal transients or accidents
SPRAT-DOWN-DP	Steady-state at supercritical pressure	Blowdown at large LOCA or reactor depressurization
SCRELA reflood module	End stage of blowdown	Core reflooding after blowdown

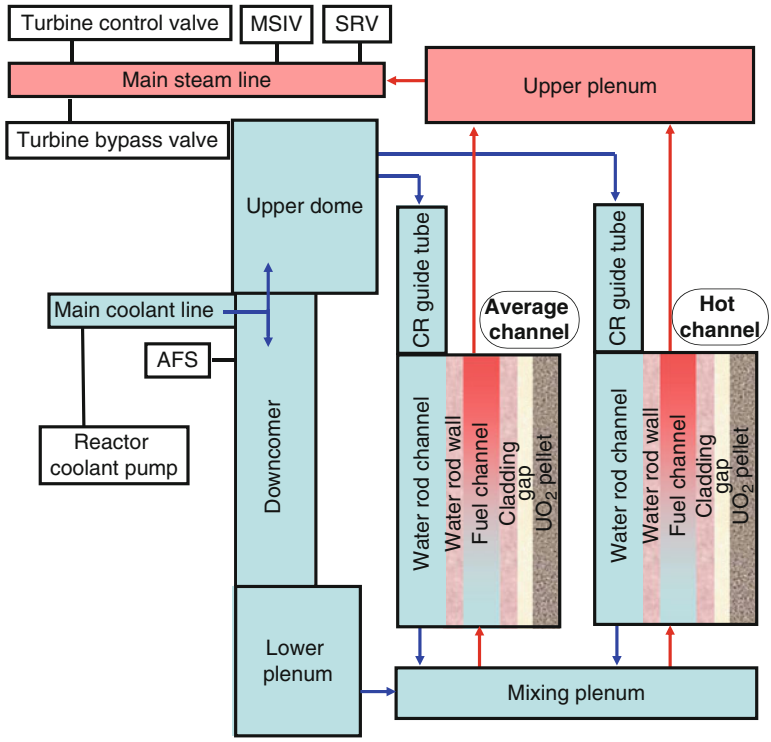


Fig. 6.12 Calculation model of SPRAT-DOWN for safety analyses

$$f_i = 0.0791\mathrm{Re}_i^{-0.25} \quad \text{(Blagius correlation)} \tag{6.2}$$

Acceleration:

$$\Delta P_{\mathrm{acc}} = \sum_i \left(\frac{\rho_i v_i^2}{2} - \frac{\rho_{i-1} v_{i-1}^2}{2} \right) \tag{6.3}$$

Buoyancy:

$$\Delta P_{\mathrm{buo}} = \rho_0 g \Delta z N - \sum_i \rho_i g \Delta z \quad \text{(calculated downward)} \tag{6.4}$$

Orifice:

$$\Delta P_{\mathrm{ori}} = \sum_i K_{\mathrm{ori}} \rho_i \frac{v_i^2}{2} \tag{6.5}$$

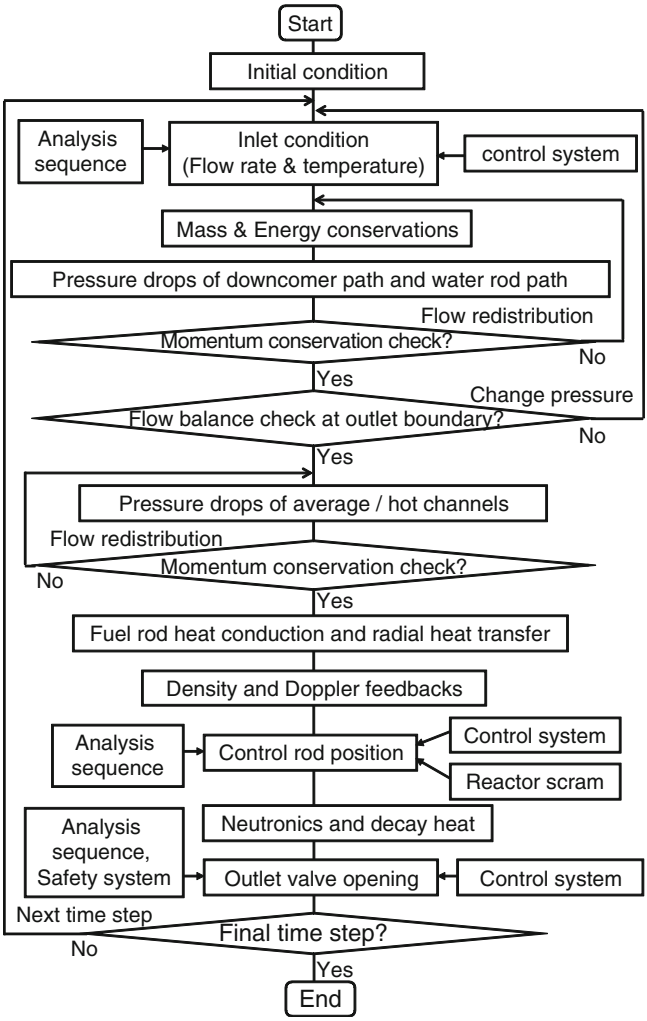


Fig. 6.13 Flow chart of SPRAT-DOWN for safety analyses

Total:

$$\Delta P_{\text{tot}} = \Delta P_{\text{fri}} + \Delta P_{\text{acc}} + \Delta P_{\text{buo}} + \Delta P_{\text{ori}} \tag{6.6}$$

D_h: Hydraulic diameter
f: Friction pressure drop coefficient
g: Gravity
h: Specific enthalpy
K: Resistance coefficient
ΔP: Pressure drop
Re: Reynolds number

v: Velocity
Δz: Mesh size
ρ: Density

Subscripts
acc: Acceleration
buo: Buoyancy
fri: Friction
i: Mesh number
ori: Orifice
tot: Total

At the normal operating conditions, the total pressure drop of each path is 0.019 MPa. The flow rate ratio between the first meshes of the two flow paths is iteratively changed to satisfy the momentum conservation.

$$\frac{\mathrm{Mom}_{\mathrm{round}}^{k} - \mathrm{Mom}_{\mathrm{round}}^{k-1}}{\Delta t}\ [\mathrm{kg/m^2 s^2}] = \frac{\Delta P_{\mathrm{tot-WR}} - \Delta P_{\mathrm{tot-DC}}}{l_{\mathrm{round}}}\ [\mathrm{kg/m^2 s^2}] \tag{6.7}$$

l: Length
Mom: Momentum per unit volume
Δt: Time step interval

Subscripts
DC: Downcomer path
k: Time step
round: Round path
WR: Water rod path

The left side is the rate of change in the average momentum per unit volume of the "round" flow path, and the right side is the average pressure drop of the "round" flow path per unit length. The "round" flow path is from/to the first mesh of the downcomer through the bottom dome, the water rod (upward), the CR guide (upward), and the top dome in that order.

Flow-redistribution between the average and hot channels is also considered by calculating the pressure drop balance and momentum conservation. The pressure drops of the average and hot channels are calculated as follows.

Friction: the same as (6.1) and (6.2)
Acceleration: the same as (6.3)
Grid spacer:

$$\Delta P_{\mathrm{grid}} = \sum_{j=1}^{10} K_{\mathrm{grid}} \rho_{4j-2} \frac{v_{4j-2}^2}{2} \quad (K_{\mathrm{grid}} \text{ is assumed as } 1.2) \tag{6.8}$$

Buoyancy:

$$\Delta P_{\mathrm{buo}} = \sum_{i=1} \rho_i g \Delta z - \rho_0 g \Delta z N \quad (\text{calculated upward}) \tag{6.9}$$

Inlet orifice:

$$\Delta P_{\mathrm{ori}} = \sum_i K_{\mathrm{ori}} \rho_i \frac{{v_i}^2}{2} \tag{6.10}$$

Total:

$$\Delta P_{\mathrm{tot}} = \Delta P_{\mathrm{fri}} + \Delta P_{\mathrm{acc}} + \Delta P_{\mathrm{grid}} + \Delta P_{\mathrm{buo}} + \Delta P_{\mathrm{ori}} \tag{6.11}$$

Subscript
ave: Average channel
grid: Grid spacer
hot: Hot channel

The resistance coefficient of the grid spacer K_{grid} is provisionally taken as 1.2 by referring to the typical grid spacer experiment under the subcooled water condition [9]. An example of the pressure drop at the normal operating conditions is shown in Table 6.8. The total pressure drop in the fuel channel is 0.282 MPa. The flow rate in the average channel is calculated from mass and energy conservations as described in Sect. 4.2. The inlet flow rate of the hot channel is iteratively changed until the momentum conservation is satisfied.

$$\frac{\mathrm{Mom}_{\mathrm{hot}}^{k} - \mathrm{Mom}_{\mathrm{hot}}^{k-1}}{\Delta t} = \frac{\Delta P_{\mathrm{tot,ave}} - \Delta P_{\mathrm{tot,hot}}}{N \Delta z} \tag{6.12}$$

The left side is the rate of change in the average momentum per unit volume in the hot channel. The right side is the difference in the pressure drops between the average and hot channels per unit length.

Since the system pressure is kept supercritical at small LOCA (see Sect. 6.7), the small LOCA is also analyzed using SPRAT-DOWN. The break flow is calculated by the correlations used in the blowdown analysis described in Sect. 6.6.3 and given as the boundary conditions.

As described in Sect. 6.5, the PCT is limited for fuel rod integrity at abnormal transients and accidents and ATWSs. The heat transfer coefficient under the limiting condition is important from the safety viewpoint. Loss of flow events, including small LOCA, gives the highest PCTs for each category. These PCTs appear under the thermal-hydraulic condition of high bulk temperature (above

Table 6.8 Pressure drops at normal operating conditions (in MPa)

	Average channel	Hot channel
Inlet orifice	0.208	0.139
Friction	0.058	0.101
Grid spacer	0.029	0.052
Acceleration	0.004	0.008
Buoyancy	−0.017	−0.018
Total	0.282	0.282

600°C for transients and above 800°C for accidents and ATWSs) and low mass flux (below 600 kg/m^{2}s for transients and below 200 kg/m^{2}s for accidents and ATWSs). The Dittus–Boelter correlation [10] is a good benchmark at such high bulk temperatures. The Oka–Koshizuka correlation [7] gives slightly lower heat transfer coefficients than the Dittus–Boelter correlation under the highest PCT conditions mentioned above. Unlike the steady-state thermal-hydraulic design, the safety analysis does not strictly require accuracy of the heat transfer coefficient because there is a margin between the highest PCTs and the criteria. The Oka–Koshizuka correlation is conservatively applied to SPRAT-DOWN. Sensitivity of the heat transfer coefficient in the case of the highest PCTs is investigated in Sect. 6.7.

The point-kinetics model is a good approximation to analyze the transient behavior as long as the reactivity does not change locally and the space effect on the reactivity feedback is considered. It is still a good approximation even for localized CR withdrawal events as long as the power changes slowly over a longer time scale relative to the effective neutron lifetime. Since the Super LWR is a water-cooled thermal spectrum reactor, like LWRs, where the coolant density feedback and Doppler feedback are dominant, only these feedbacks are considered. The space effect on reactivity feedback is considered by calculating the "average" values of the coolant density and pellet temperature at each time step. Contribution of each mesh to the "average" values is proportional to the square of the linear power density (chopped-cosine distribution). Decay heat is calculated with a two-group approximation of the "ANS+20%" model [11] which is presently known as a very conservative model.

6.6.2 Safety Analysis Code for Subcritical Pressure Condition

As described in Chap. 5, the sliding pressure startup is one of the candidate startup schemes. It is necessary to understand the reactor behavior in case of abnormal transients and accidents during the pressurization phase. To do that, SPRAT-DOWN is extended to the SPRAT-DOWN-SUB which can be applied to the transients and accidents during subcritical pressure operation [12].

In the calculation meshes with the two-phase condition, the homogeneous equilibrium model (HEM) is applied to the mass, momentum, and energy conservation equations. The following heat transfer correlations are used by referring to RELAP4 [13].

- Forced convection of single phase flow: Dittus–Boelter 1930
- Nucleate boiling: Thom [14] or Schrock and Grossman [15]
- Transition boiling: McDonough, Milich and King [16]

Furthermore, Groeneveld's 2002 look-up table is used for the stable film boiling heat transfer [17]. Groeneveld's 1995 look-up table is used for the critical heat flux [18]. The critical heat flux and stable film boiling heat transfer are the most important from the viewpoint of safety. When the pressure is below 20 MPa,

these look-up tables are applicable. However, the look-up tables may overestimate the critical heat flux and the heat transfer coefficient of stable film boiling at pressures between 20 MPa and the critical point. It is known that they are extraordinarily low at this region. In the safety analyses, the heat transfer coefficient of stable film boiling calculated by the look-up table is reduced by 34%, which is determined by comparing with an experiment for sliding pressure FPPs [12]. The pressure drop of two-phase flow is calculated using the physical property of the saturated water at the corresponding pressure and the multiplier proposed in ref. [19].

6.6.3 Blowdown Analysis Code

The blowdown analysis code is developed based on SPRAT-DOWN [6]. It is called SPRAT-DOWN-DP. The calculation domain is described in Fig. 6.14 [6]. The nodalization is the same as that of SPRAT-DOWN. At an early stage of SCWR studies in the University of Tokyo, a simple code for blowdown analysis, the SCRELA blowdown module which does not model the two-path flow scheme or water rods, was developed [20, 21]. The SPRAT-DOWN-DP adopts the models of heat transfer coefficient and break flow used in the SCRELA module.

In the mass and energy conservation calculations, the HEM is applied to two-phase meshes like the SPRAT-DOWN-SUB. Flow-redistribution between parallel paths is not calculated in contrast with SPRAT-DOWN. Instead, flow boundary conditions are used as shown in Fig. 6.15 [6]. The effect of the flow boundary condition on the PCT was investigated in ref. [4]. Since there is no fuel rod in the

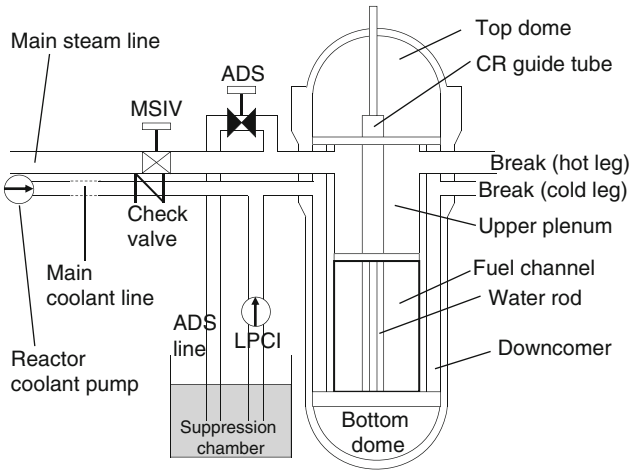


Fig. 6.14 Calculation domain of SPRAT-DOWN-DP. (Taken from ref. [6] and used with permission from Atomic Energy Society of Japan)

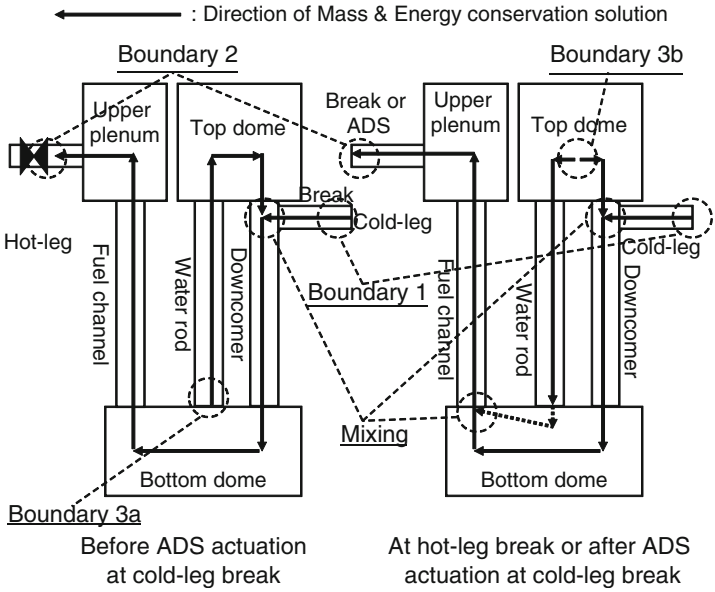


Fig. 6.15 Boundaries and directions of mass and energy conservation solution. (Taken from ref. [6] and used with permission from Atomic Energy Society of Japan)

water rod path or the downcomer path, the flow-redistribution between these paths does not influence the PCT. The hot and average channels are not distinguished, unlike in SPRAT-DOWN. The influence of the flow rate ratio between the hot and average channels was also investigated in ref. [4]. Even when the hot channel flow rate is conservatively assumed to be half of the average channel flow rate, the increase in the PCT is about 300°C, which is sufficiently smaller than the safety margin.

The radial heat transfer model is the same as that of SPRAT-DOWN. During depressurization, the PCT appears at a superheated-steam condition. The heat transfer coefficient of this condition is important. The Dittus–Boelter correlation [10], which is widely used for LWRs, is applied. The heat transfer coefficient at the two-phase condition is less important because the cladding temperature during blowdown is always lower than the hottest cladding temperature at the normal operating conditions. The Dougal–Rhosenow film boiling correlation is conservatively applied to both preCHF and postCHF conditions. Radiation hat transfer is considered at superheated steam condition using Hottel's correlation.

Since the pressure drop in the main coolant lines and the RPV is negligibly compared with the pressure drop at the break or in the ADS lines, the pressure is assumed to be uniform in the main coolant lines and the RPV. Decrease in the pressure is governed by the break flow rate. Since the break flow rate cannot be calculated by SPRAT-DOWN-DP, it is calculated using correlations and given as the boundary conditions. The correlations selected and used in the LOCA analysis

code are detailed in refs. [20, 21]. At subcritical pressure, three correlations of the break flow are used. In the superheated steam region, isentropic ideal gas is assumed. The mass flux and pressure at the critical flow condition are calculated as shown in the following equations [22].

Mass flux:

$$G = \rho_0 \sqrt{2C_p T_0 \left[\left(\frac{P_{cv}}{P_0} \right)^{2/\gamma} - \left(\frac{P_{cv}}{P_0} \right)^{(1+\gamma)/\gamma} \right]} \tag{6.13}$$

Critical pressure:

$$P_{cr} = P_0 \left(\frac{2}{1+\gamma} \right)^{\gamma/(\gamma-1)} \tag{6.14}$$

ρ_0: Density at break point (kg/m^3)
C_p: Specific heat under constant pressure at break point (J/K/kg)
T_0: Temperature at break point (K)
P_0: Core pressure (MPa)
P_{cv}: Drywell pressure (MPa)
γ: Ratio of specific heat coefficients

When the critical pressure is higher than the drywell pressure, the mass flux is determined regardless of the critical pressure.

Two phase critical flow is calculated based on Moody's HEM.

Critical mass flux:

$$G_{cr} = \left[\frac{\chi}{\rho_g} + \frac{1-\chi}{\rho_f} \right]^{-1} \sqrt{2\left[h_0 - \chi h_g - (1-\chi) h_f \right]} \tag{6.15}$$

$$\chi = \frac{s_0 - s_f}{s_g - s_f} \tag{6.16}$$

h: Specific enthalpy (J/kg)
ρ: Density (kg/m^3)
s: Specific entropy (J/K/kg)

Subscripts
0: Two phase
g: Saturated steam
f: Saturated water

This model is known to be accurate above 2 MPa [22].
In the subcooled region, Zauloudeck's correlation is used [23].
Mass flux:

$$G = \sqrt{2 \times 1.0133 \times 10^5 \rho_0 (P_0 - P_{cv})} \quad (P_{cv} > P_{sat}) \tag{6.17}$$

Critical mass flux:

$$G_{cr} = 0.95\sqrt{2 \times 1.0133 \times 10^5 \rho_{sat}(P_0 - P_{sat})} \quad (P_{cv} \leqslant P_{sat}) \tag{6.18}$$

P_0, P_{cv}, ρ_0: The same as (6.13)
P_{sat}: Saturation pressure under isentropic process (MPa)
ρ_{sat}: Density of saturated water at P_{sat} (kg/m^3)

The correlations in the subcritical pressure are also applied to the supercritical pressure region. If the stagnation temperature is below or equal to the pseudo-critical point, the subcooled water region is assumed. If the temperature is higher than the pseudo-critical point, the superheated steam region is assumed. Figure 6.16 shows the critical mass fluxes at various pressures. Influence of the break flow on the PCT is investigated by changing the break area in the sensitivity analysis (see Sect. 6.7).

The SCRELA blowdown module was validated by comparing with REFLA-TRAC, a best estimation code developed by the Japan Atomic Energy Agency (JAEA) [20, 21]. The modified SPRAT-DOWN-DP is also compared with these two codes. The calculations of SPRAT-DOWN-DP and SCRELA start at 25 MPa while the REFLA-TRAC calculation starts at 17 MPa because REFLA-TRAC cannot calculate at the supercritical pressure condition. However, the influence of this difference is small because the period in which supercritical pressure exists is within 1s. Figure 6.17 compares the pressures at the 100% cold-leg break. The SPRAT-DOWN-DP code with the water rod model gives a different result from other codes [6]. It cannot be directly compared with other codes especially

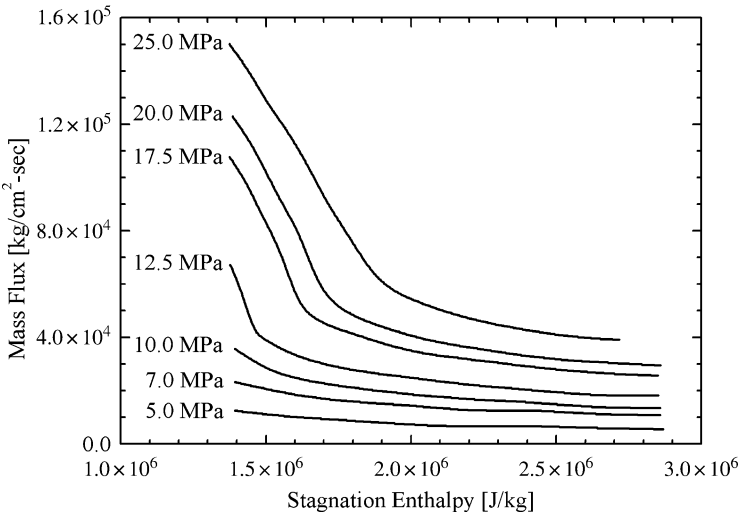


Fig. 6.16 Critical mass flux as a function of stagnation enthalpy and pressure

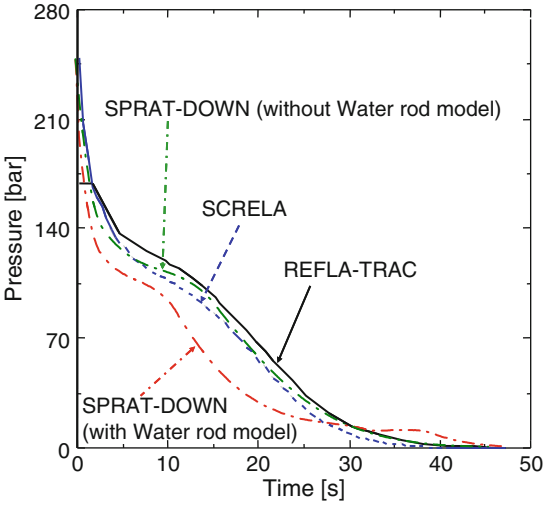


Fig. 6.17 Comparison of pressure trends in cold-leg break blowdown

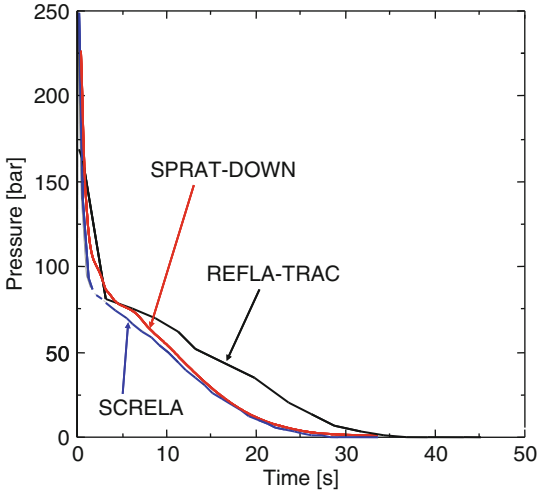


Fig. 6.18 Comparison of pressure trends in hot-leg break blowdown

at the cold-leg break calculation because the water rod, which has the coolant with a relatively higher temperature than the feedwater, would affect the break flow at the cold-leg. When the water rod model is eliminated, the result agrees well with the other codes. Figure 6.18 compares the pressures at the 100% hot-leg break. The SPRAT-DOWN-DP and SCRELA codes exhibit slightly faster blowdown compared with REFLA-TRAC. This is due to the approximation by the HEM model because the HEM model leads to a higher flow velocity than the two fluid models. However, these three codes qualitatively agree and it should be noted that the hot-leg break is much less important than the cold-leg break from the viewpoint of the

PCT because the cladding temperature does not exceed its initial value as described in Sect. 6.7.

6.6.4 *Reflooding Analysis Code*

The water rods are neglected which is conservative from the viewpoint of their role as a heat sink. The effect of the water rods on the quench front velocity should be assessed in a future study. The SCRELA reflood module is used in the calculation for which the flow chart is shown in Fig. 6.19. This module, also developed at the early stage of SCWR studies in the University of Tokyo like the SCRELA blowdown module, was based on the REFLA of JAEA [20, 21]. The flow chart of the calculation is shown in Fig. 6.19. The SCRELA reflood module includes the "system momentum calculation," the "thermal equilibrium relative velocity correlation," and the "quench front velocity correlation".

The system momentum calculation is modeled by coupling a reactor vessel part and an ADS line part as described in Fig. 6.20. The reactor vessel part is represented by momentum balance between the downcomer and the core water levels. The equation is described in terms of acceleration, pressure difference between the

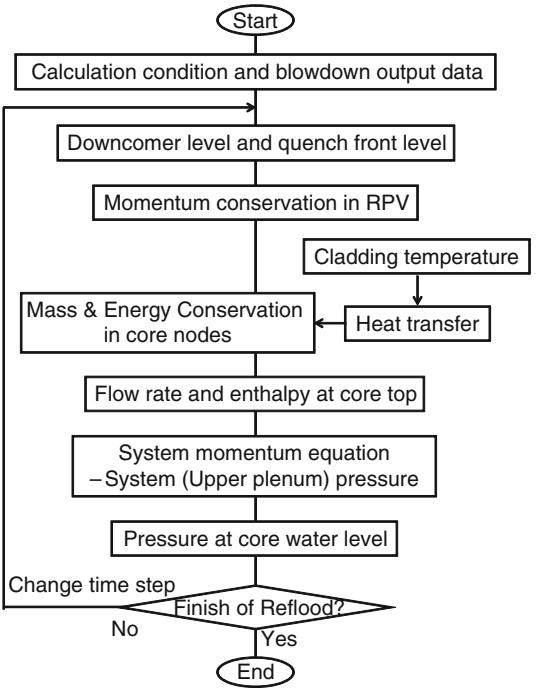


Fig. 6.19 Flow chart of SCRELA reflood module. (Taken from ref. [6] and used with permission from Atomic Energy Society of Japan)

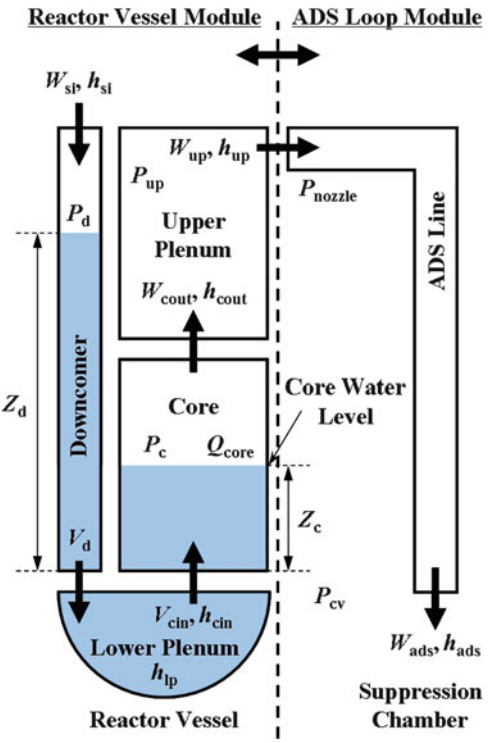


Fig. 6.20 Momentum calculation model in SCRELA reflood module

downcomer and the core water levels, static pressure head due to the water level difference, and inertia.

$$\frac{\mathrm{d}V_d}{\mathrm{d}t}\cdot A_d\left[\frac{Z_d}{A_d}+\frac{Z_c}{A_c}+\frac{\mathrm{Vol_{lp}}}{A_{\mathrm{lp}}^2}\right]=\frac{P_d-P_c}{\rho_l}+g_c(Z_d-Z_c)-V_d|V_d|\cdot A_d^2\left(\frac{1}{A_c}-\frac{1}{A_d}\right)\left(\frac{1}{A_{\mathrm{lp}}}+\frac{1}{2A_c}+\frac{1}{2A_d}\right) \tag{6.19}$$

$$P_c=P_{\mathrm{up}}+G_c^2\left(\frac{K_c}{2\rho_c}+\frac{1}{\rho_c}-\frac{1}{\rho_l}\right) \tag{6.20}$$

V: Velocity
A: Flow area
Z: Height
Vol: Volume
P: Pressure
g: Gravity
ρ: Density

Subscripts
d: Downcomer
c: Core

lp: Lower plenum
l: Liquid

The pumping head of the LPCI and the friction loss are neglected. The boundary conditions are the water levels and pressures in the downcomer and the core. As described in (6.20), the pressure at the core water level is obtained as the addition of the pressure in the upper plenum, the friction loss from the core water level to the upper plenum.

The system pressure, defined as the upper plenum pressure, is calculated by adding the pressure loss to the drywell pressure. The pressure drop consists of friction, nozzle, acceleration, and head loss in the suppression pool. The depth of the suppression pool and the submergence of the quencher will be determined from the containment design. It is presently assumed as 2.0 m, which means that the head loss is 0.02 MPa. The sensitivity of this parameter is investigated in Sect. 6.7.

The core water level is calculated from a detailed core thermal-hydraulic calculation. The quench front is calculated by a theoretical correlation proposed by Yamanouchi, et al. [24]. The heat transfer coefficient sharply changes by about 2 orders of magnitude in the vicinity of the quench front. In order to prevent the numerical instability caused by the abrupt change in the heat transfer coefficient, the neighboring nodes of the quench front are more finely divided into a size 1/100 of the thickness of the normal node as shown in Fig. 6.21. The flow regimes assumed in the reflood analysis are described in Fig. 6.22. Various heat transfer correlations are prepared according to the flow conditions. Table 6.9 [21] summarizes them.

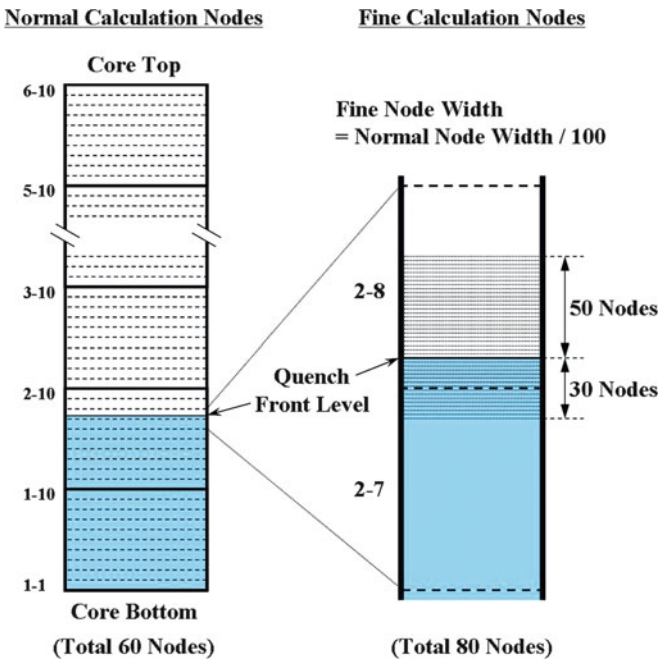


Fig. 6.21 Noding near quench front in SCRELA reflood module

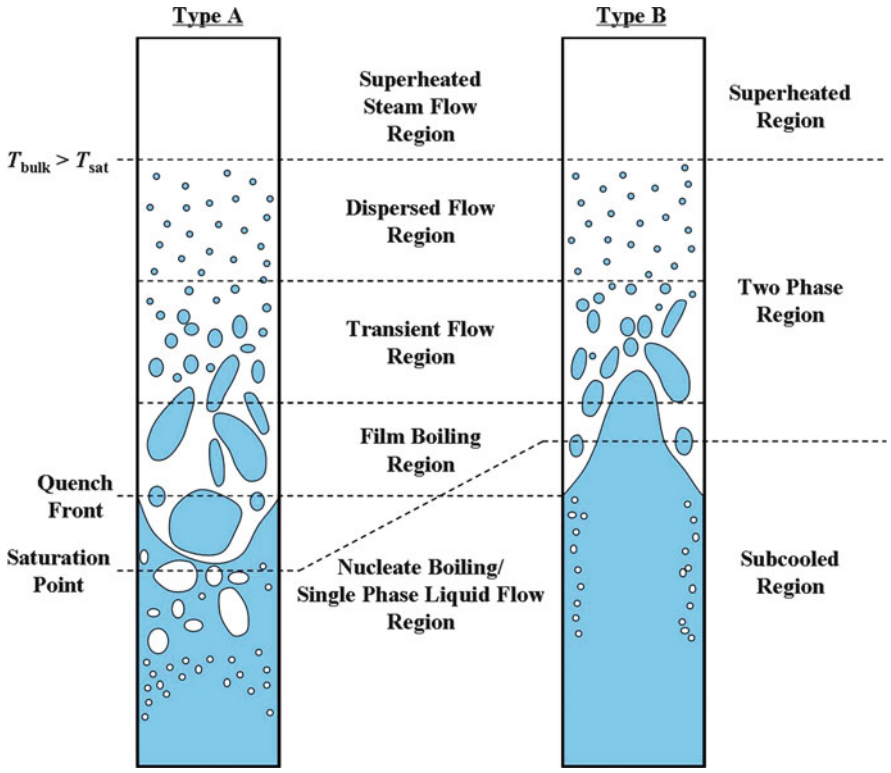


Fig. 6.22 Heat transfer regime during reflooding

The SCRELA reflood module was validated by comparing with the REFLA code in the geometry where the pitch to diameter ratio (P/D) is 1.4 [20, 21]. Since the Super LWR analyzed in this study has tight lattice bundles where P/D is about 1.1, an additional validation is carried out by comparing with the NEPTUN LWHCR test (P/D = 1.13) which was also used to assess the applicability of the REFLA code for tight lattice bundles [25]. The results by the SCRELA reflood module are compared with those of experiments and the REFLA calculation in Figs. 6.23 and 6.24 [6]. This SCRELA module predicts the quench front propagation of the NEPTUN LWHCR test qualitatively well like the REFLA code. The cladding temperature is slightly overestimated and the reflooding speed is slightly underestimated by the SCRELA reflood module, which is conservative.

6.7 Safety Analyses

The same plant characteristics as in Chap. 4 are used for the safety analyses. The initial conditions are shown in Table 6.10. The hottest cladding temperature of 650°C is the same as the criterion applied in the three-dimensional core design

Table 6.9 Flow regimes and heat transfer correlations used in SCRELA reflood module

Position	Heat transfer regime	Heat transfer correlation
Below quench front level	Single liquid phase/subcooled nucleate boiling flow	Tom's correlation $q'' = \exp(2P/8.7)(T_w - T_{sat})^2/22.7^2$
	Saturated two-phase flow	The same as case (1)
	Subcooled film boiling flow	Murao and Sugimoto's correlation $h = h_{sub} + h_R$ $h_{sub} = h_{sat}[1.0 + 0.025(T_{sat} - T_l)]$ $h_R = E\varepsilon(T_W^4 - T_{sat}^4)/(T_w - T_{sat})$
	Film boiling/transient boiling flow	Murao and Sugimoto's correlation $h = h_{sat} + h_R$ $h_{sat} = 0.94\left[\lambda_g^3 \rho g \rho l h_{fg} g / L_q \mu_g (T_w - T_{sat})\right]^{1/4}$ $h_R = E\varepsilon(T_w^4 - T_{sat}^4)/(T_W - T_{sat})(1-\alpha)^{0.5}$
Above quench front level	Dispersed flow	Compensated Murao and Sugimoto's correlation $h = h_{sat,comp} + h_R$ $h_{sat,comp} = F_{cp} \times h_{sat}$, F_{cp}: compensation factor $h_R = E\varepsilon(T_w^4 - T_{sat}^4)/(T_w - T_{sat})(1-\alpha)^{0.5}$
	Superheated steam flow	Dittus–Boelter's correlation $h = 0.023\,(k/D_h)Re^{0.8}Pr^{0.4}$

Taken from ref. [21]

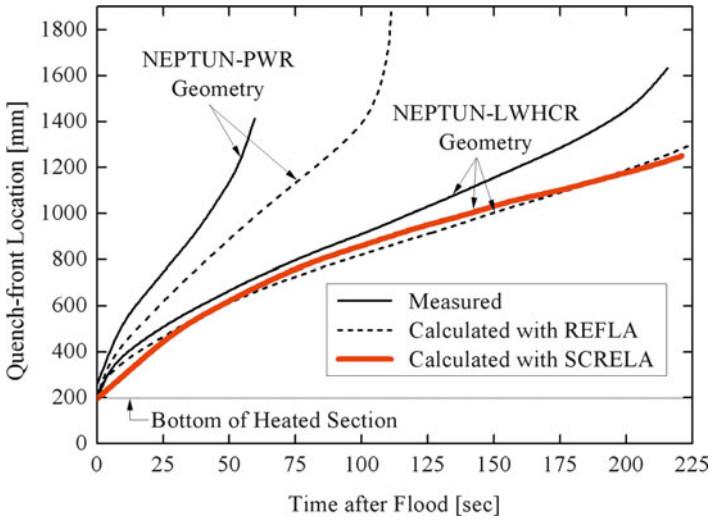


Fig. 6.23 Comparison of quench front propagations. (Taken from ref. [6] and used with permission from Atomic Energy Society of Japan)

where single-channel thermal-hydraulic analyses are carried out for homogenized fuel assemblies. However, the maximum cladding surface temperature is evaluated as 740°C considering the pin-by-pin power distribution, cross flow in the fuel assemblies, and the engineering uncertainties as described in Chap. 2. Therefore, the allowable increase in the hottest cladding temperature from the initial conditions

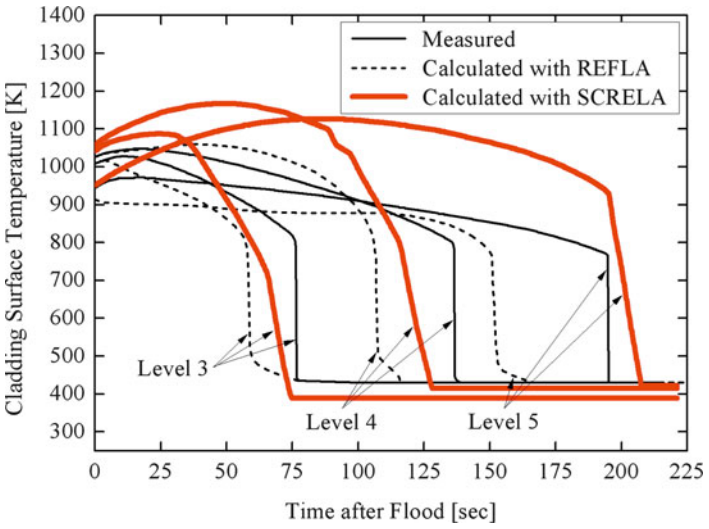


Fig. 6.24 Comparison of cladding surface temperatures. (Taken from ref. [6] and used with permission from Atomic Energy Society of Japan)

Table 6.10 Initial conditions for safety analyses

Fuel channel	Average	Hot
Maximum linear power (kW/m)	28	39
Mass flux (kg/s/m^2)	945	1,159
Coolant inlet/outlet temperature (°C)	305/500	305/573
Hottest cladding temperature (°C)	–	650
Water rod channel	Average	Hot
Mass flux (kg/s/m^2)	94	113
Coolant inlet/outlet temperature (°C)	280/366	280/348

Taken from ref. [1] and used with permission from Korean Nuclear Society

is set to 110°C (850–740°C) for the abnormal transients, and 520°C (1,260–740°C) for the accidents and ATWS.

Both beginning-of-equilibrium-cycle (BOEC) and end-of-equilibrium-cycle (EOEC) are analyzed. For each event, either the result of BOEC or EOEC having a smaller margin to the criteria is shown as a figure and/or a table. Operation of the plant control system is considered to be as in BWRs since the Super LWR also adopts a direct steam cycle while PWRs neglect the plant control system.

6.7.1 Abnormal Transient Analyses at Supercritical Pressure

6.7.1.1 Partial Loss of Reactor Coolant Flow

One of the RCPs is assumed to trip. The coast-down time is 5 s in consideration of the inertia of the pump and driving turbine. The analysis results are shown in

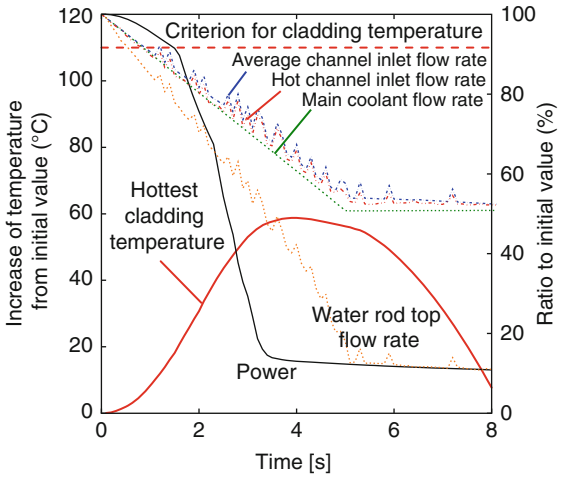


Fig. 6.25 Calculated results for "partial loss of reactor coolant flow"

Table 6.11 Sensitivity analysis for "partial loss of reactor coolant flow"

RCP coast-down time (s)/ΔMCST (°C)				
1/140	2/120	3/100	4/80	**5/60**
Scram delay (s)/ΔMCST (°C)				
0.55/60	1/70	3/130	>5/150	
Ratio of density coefficient to reference case/ΔMCST (°C)				
0.25/70	0.5/70	**1/60**	2/50	

Bold characters reference case, *ΔMCST* increase in maximum cladding surface temperature

Fig. 6.25. The main coolant flow rate decreases linearly to 50% of the rated flow. Flow rate low level 1 is detected and the scram signal is released at 1 s. Although the trip of the RCP itself would release the scram signal, it is conservatively neglected. The cladding temperature increases until 3.6 s due to the decrease in the flow rate and then decreases due to the decrease in the power. The increase in the hottest cladding temperature is 60°C which is the highest among the abnormal transients. It is sensitive to the coast-down time and the scram delay as shown in Table 6.11.

6.7.1.2 Loss of Offsite Power

This is the typical transient where both RCPs trip. However, its sequence is different from a "total loss of reactor coolant flow" accident as described in Sect. 6.4. In the "loss of offsite power," the motor-driven condensate pumps are assumed to trip instantaneously. The turbine control valves are quickly closed due to a turbine trip. The turbine bypass valves open immediately after that. A scram signal and AFS signal are released by detecting the "loss of offsite power" or "turbine control valves quickly closed" or "condensate pump trip." Both RCPs are assumed to trip at 10 s

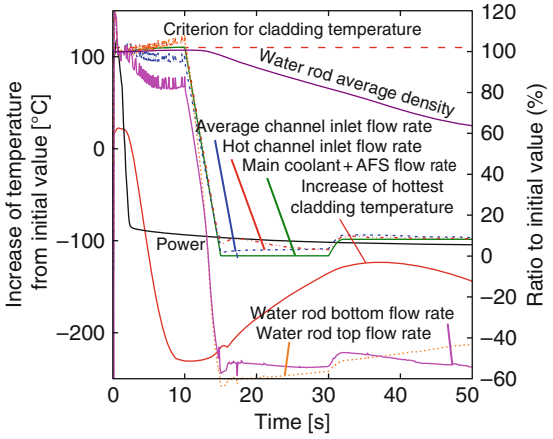


Fig. 6.26 Calculated results for "loss of offsite power"

Table 6.12 Sensitivity analysis for "loss of offsite power"

RCP trip delay (s)/ΔMCST (°C)			
3/150[b]	5/110[b]	**10/20**[a]	
AFS signal delay (s)/ΔMCST (°C)			
30/20[a]	45/40[b]	60/110[b]	
AFS capacity (%/unit)/ΔMCST (°C)			
1/150[b]	2/120[b]	3/20[a]	**4/20**[a]

Bold characters reference case, *ΔMCST* increase in maximum cladding surface temperature
[a]First peak
[b]Second peak

due to a decrease of the water level in the deaerator and loss of steam sent to the turbine-driven RCPs. Two-out-of-three AFS units are assumed to start at 30 s. The calculation results are shown in Fig. 6.26. At the beginning, the cladding temperature and the pressure increase due to the closure of the turbine control valves. Then, the cladding temperature decreases due to the turbine bypass and the reactor scram. After the trip of the RCPs, the cladding temperature increases again. After two-out-of-three AFS units start up, the cladding temperature decreases again.

There are two peaks in the cladding temperature curve. The first one appears within 1 s and is caused by the turbine trip; it is higher than the initial (steady-state) value by 20°C. The second one appears after the trip of the RCPs, and it is lower than the initial value. The increase in the pressure is only 0.6 MPa due to the successful opening of turbine bypass valves. The second peak height of the cladding temperature is sensitive to the delay of the pump trip, the delay of the AFS start, and the capacity of the AFS as shown in Table 6.12.

6.7.1.3 Loss of Turbine Load

In the safety analysis of BWRs, both cases with and without turbine bypass are analyzed. When the turbine bypass is credited, the analysis scenario is the same as

that of the "loss of offsite power." Thus, only the case without the turbine bypass is analyzed. This event is a typical pressurization transient. The reactor behavior before the trip of the RCPs is shown in Fig. 6.27. Since the turbine bypass fails, the pressure quickly increases. But the increase in the reactor power is only 4%, which is much lower than that in BWRs. One reason is that the density difference between supercritical "water" and supercritical "steam" is much lower than that between saturated water and steam at the BWR operating pressure. The other reason is that flow stagnation occurs in the core due to the closure of the turbine control valves. This stagnation causes an increase in the coolant temperature which mitigates the increase in the coolant density caused pressurization. When opening the SRVs, the pressure and reactor power begin to decrease.

The reactor behavior is similar to that of at the "loss of offsite power" after the trip of the RCPs at 10 s. The maximum pressure is about 26.8 MPa, the highest among the abnormal transients but is low enough compared to the criterion (28.9 MPa). The hottest cladding temperature increases by about 50°C from the initial value during the flow stagnation caused by the closure of the coolant outlet.

Since the peaks of pressure, power, and temperature appear in a very short time scale within 1 s, only the SRVs are effective to mitigate them. The reactor scram starts after the peaks come. The results of sensitivity analysis are shown in Table 6.13. The maximum pressure depends on the SRV setpoint. The maximum power is not sensitive to the density coefficient because the increase in the coolant density itself is small. The increase in the cladding temperature is not sensitive to either parameter.

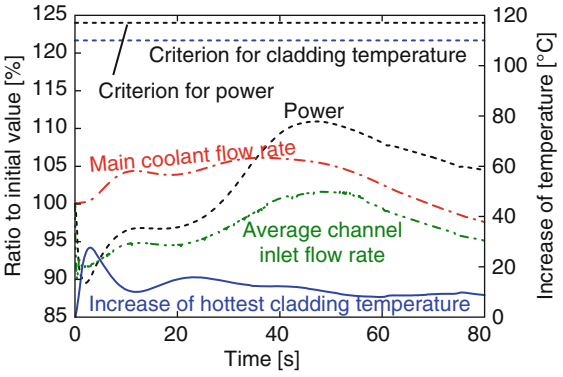


Fig. 6.27 Calculated results for "loss of feedwater heating"

Table 6.13 Sensitivity analysis for "loss of turbine load without turbine bypass"

	SRV setpoint (MPa)				Ratio of density coefficient to reference case			
	26.0	**26.2**	26.5	27.0	0.5	**1**	2	4
Maximum pressure (MPa)	26.6	**26.8**	27.1	27.6	26.8	**26.8**	26.8	26.8
Maximum power (%)	103	**104**	105	105	**102**	**104**	110	123
ΔMCST (°C)	50	**50**	60	70	**50**	**50**	50	60

Bold characters reference case, *ΔMCST* increase in maximum cladding surface temperature

6.7.1.4 Isolation of Main Steam Line

All of the MSIVs are assumed to be closed with the characteristics previously shown in Fig. 6.8. The calculation results before the trip of the RCPs are shown in Fig. 6.28. The reactor behavior is similar to that of "loss of turbine load without turbine bypass". Since the closure of the MSIVs is much slower than that of the turbine control valves at the turbine trip, the increases in the pressure and cladding temperature are slightly smaller than those at "loss of turbine load without turbine bypass". The reactor power does not increase from the initial value.

6.7.1.5 Pressure Control System Failure

This is a typical pressure decreasing transient. The maximum turbine control valve opening is assumed and it is 130% of the rated value. The cladding temperature is always below the initial temperature because the main steam flow rate and therefore the core coolant flow rate increase. A scram signal is released when the pressure reaches the low level 1 (24.0 MPa). A depressurization signal is released when the pressure reaches the low level 2 (23.5 MPa). After opening the ADS, the reactor behavior is similar to that shown in Fig. 6.7 [1].

6.7.1.6 Loss of Feedwater Heating

Loss of one stage of the feedwater heating will cause a 35°C drop of the feedwater temperature. In the safety analysis, it is conservatively assumed as 55°C as is done in the safety analysis of ABWRs. The result is shown in Fig. 6.29. At the beginning of the transient, the fuel channel inlet flow rate decreases because the coolant density increases, and hence the volume flow rate decreases upstream from the fuel channel. This is one of the characteristics of the once-through coolant cycle without recirculation. The cladding temperature increases and the reactor power

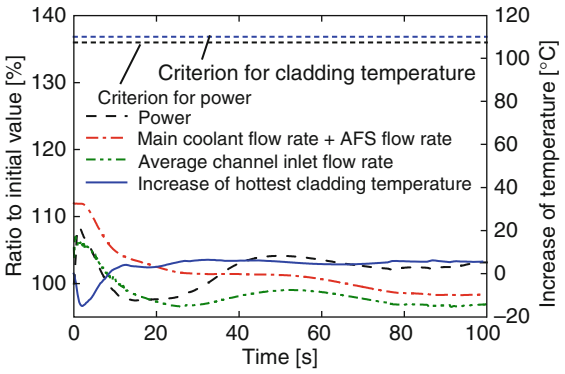


Fig. 6.28 Calculated results for "inadvertent startup of AFS"

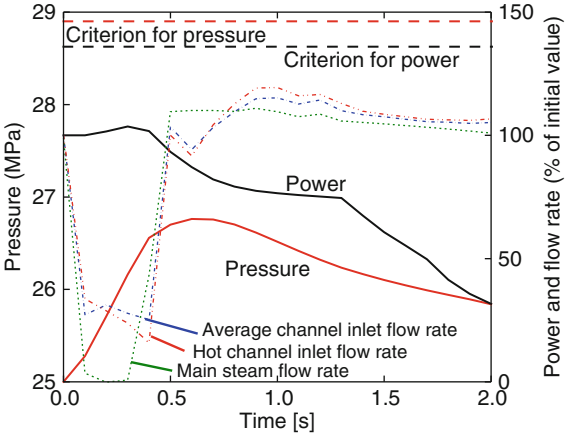


Fig. 6.29 Calculated results for "loss of turbine load without turbine bypass"

Table 6.14 Sensitivity analysis for "loss of feedwater heating"

Reduction of feedwater temperature reduction (°C)/ΔMCST (°C)					
55/30		80/40		100/50	
Ratio of lower plenum volume to reference case/ΔMCST (°C)					
0.25/30	0.5/30	**1/30**	2/30		4/30
Ratio of density coefficient to reference case/ΔMCST (°C)					
0.25/40		0.5/40	**1/30**	2/20	

Bold characters reference case, *ΔMCST* increase in maximum cladding surface temperature

decreases due to the decrease in the fuel channel inlet flow rate. The control rods are withdrawn by the control system to keep the reactor power as the rated value. The main coolant flow rate is increased by the control system to keep the main steam temperature as the initial value. After the fuel channel inlet flow rate is recovered, the reactor power begins to increase. But it does not reach the scram setpoint because the control rods are inserted by the control system. The maximum increase in the hottest cladding temperature is below 30°C. Sensitivity analyses are summarized in Table 6.14. No parameter has a large influence on the increase in cladding temperature.

6.7.1.7 Inadvertent Startup of AFS

Three units of the AFS are assumed to start. The AFS flow (12% of rated value, 30°C) is added stepwise to the main coolant flow at 0 s. The results are shown in Fig. 6.30. The main coolant flow rate and the fuel channel inlet flow rate increase due to the AFS startup. At the beginning, the fuel channel inlet flow rate is lower than the main coolant flow rate because the feedwater temperature, which is the same as the "loss of feedwater heating" transient described above, decreases. The

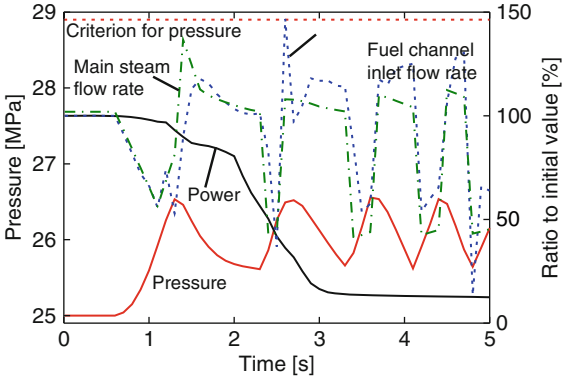


Fig. 6.30 Calculated results for "isolation of main steam line"

reactor power increases due to the density feedback. Then, the main coolant flow rate is decreased by the control system to keep the main steam temperature as the initial value. The reactor power is decreased by the density feedback and the control rods inserted by the power control system. This transient is also mitigated without a reactor scram. The increase in cladding temperature is not sensitive to such parameters as the AFS capacity and the density feedback coefficient [3].

6.7.1.8 Reactor Coolant Flow Control System Failure

This is a typical flow increasing transient. The demand of the main coolant flow rate is assumed to rise stepwise up to 138% of the rated flow as is assumed in the "feedwater control system failure" of Japanese ABWRs. Since increase in the core coolant flow rate is mild in ABWRs due to the large recirculation flow, the feedwater flow rate is assumed to increase stepwise. This assumption is too conservative for the Super LWR. The main coolant flow rate is gradually increased by the control system in the safety analysis. The calculation results are shown in Fig. 6.31. The reactor power increases with the flow rate due to water density feedback. A scram signal is released when the reactor power reaches 120% of the rated power. The maximum power is 124% while the criterion is 182%. The increase in the pressure is small. The sensitivity analysis is summarized in Table 6.15.

6.7.1.9 Uncontrolled CR Withdrawals

The maximum reactivity worth of a CR cluster depends on the loading pattern of the fuel assemblies and the CR pattern. Any limitation of the loading pattern or any interlock of the CR pattern, like the rod worth minimizer of BWRs, is not considered conservatively. From core neutronics analyses, the highest reactivity worth of a CR cluster under all the considerable loading patterns and CR patterns is estimated as 1.05%dk/k at the normal operating condition and 2.8%dk/k at the hot

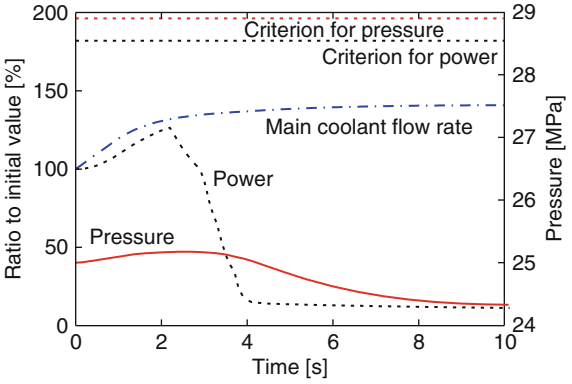


Fig. 6.31 Calculated results for "reactor coolant flow control system failure"

Table 6.15 Sensitivity analysis for "reactor coolant flow control system failure"

	Flow rate demand (%)		Ratio of density coefficient to reference case			Scram delay (s)		
	138	150	**1**	2	4	**0.55**	1	>3
Maximum pressure (MPa)	**25.2**	25.2	**25.2**	25.20	25.3	**25.2**	25.3	25.4
Maximum power (%)	**126**	131	**126**	140	164	**126**	128	132

Bold characters reference case

standby condition (pressure: 25 MPa, temperature: 280°C) [3]. Since the CR drive is supposed to be similar to that of PWRs, CR ejection at the cold shutdown condition is not considered as is not considered in PWRs.

"Control rod withdrawal at normal operation" is analyzed. The reactivity worth of the withdrawn CR cluster is conservatively assumed as 1.3%dk/k. The same withdrawal speed as of PWRs (114 cm/min) is taken. The CR cluster is withdrawn until the reactor power reaches the scram setpoint (120% of rated power). The inserted reactivity is \$0.69. The calculation results are shown in Fig. 6.32. The power increasing rate is small due to the reactivity feedbacks from the water density and fuel temperature. The cladding temperature increases by only 10°C because the main coolant flow rate is increased by the control system so as to keep the main steam temperature. If the control system is not considered, the increase in the temperature is about 110°C. The influence of the CR worth is small because the inserted reactivity before the reactor scram is almost the same [5].

The "CR withdrawal at startup" is analyzed. The initial condition is the hot standby where k_{eff} is 1.0, the reactor power is 1.0×10^{-6} of the rated power, and the main coolant flow rate is 20% of the rated flow. The analysis is made assuming adoption of the constant pressure startup scheme described in Chap. 5. The similar analysis for the sliding pressure startup scheme is described in Sect. 6.7.2. The reactivity worth of the withdrawn CR cluster is 2.8%dk/k. The same withdrawal speed as of PWRs is taken. The CR cluster is withdrawn until the reactor period decreases to the scram setpoint (10 s). The inserted reactivity is \$0.39.

6.7.1.10 Summary

The peak values are summarized in Figs. 6.33–6.35. All the criteria are satisfied with considerable margins. The Super LWR has mild response to the abnormal transients. Even in the case of the trip of both RCPs, the cladding temperature is kept low by actuating the reactor scram in advance. The key characteristic at pressurization type transients is that the power rise is very mild, because the average coolant density is not sensitive to the pressure at supercritical pressure where the difference in density is small between "steam" and "water", and because closing the outlet of the once-through coolant cycle causes flow stagnation in the core, which suppresses an increase in the coolant density. The relative change in the pressure is smaller than those in LWRs due to the high steam density and the mild power response. The duration of the

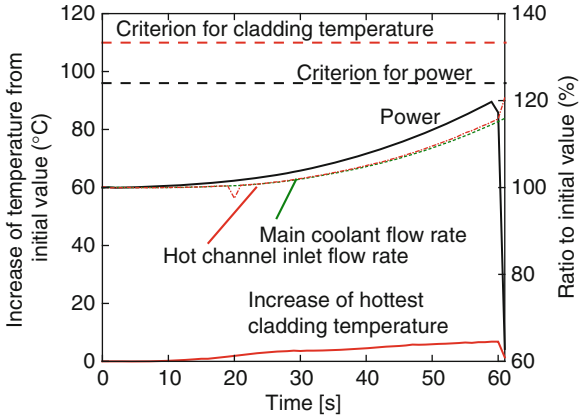


Fig. 6.32 Calculated results for "CR withdrawal at normal operation"

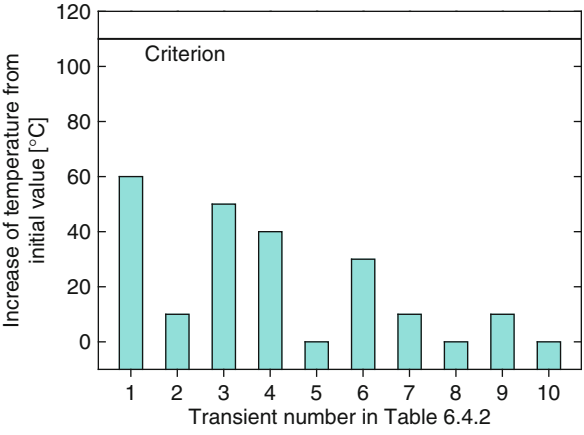


Fig. 6.33 Summary of increases in hottest cladding temperature at abnormal transients

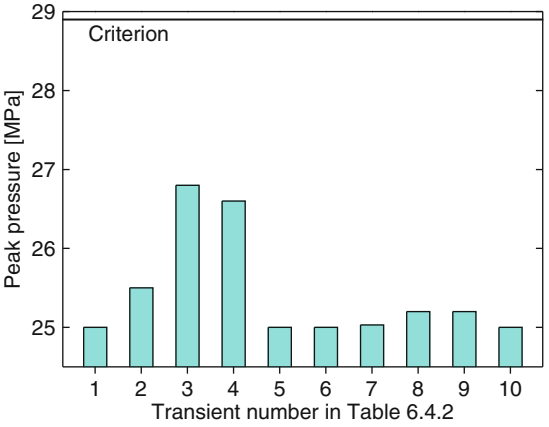


Fig. 6.34 Summary of peak pressures at abnormal transients

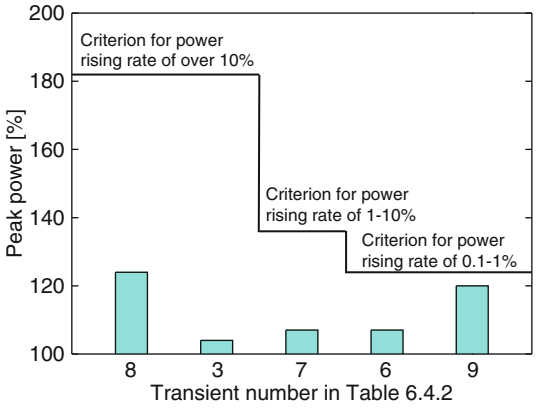


Fig. 6.35 Summary of peak powers at abnormal transients

high temperature of cladding is short as summarized in Table 6.16. This provides the basis for rationalizing the criteria for fuel integrity from time-independent stress-based criteria to time-dependent strain-based ones described in Chap. 2.

6.7.2 Accident Analyses at Supercritical Pressure

6.7.2.1 Total Loss of Reactor Coolant Flow

This accident is defined as a simultaneous sudden trip of both RCPs, including an inadvertent "zero flow" signal from the two independent control systems. The main coolant flow rate decreases linearly to zero in 5 s. The scram signal is released by detecting "flow rate low level 1" at 0.5 s. Although the trip of the RCPs itself would release the scram signal, it is conservatively neglected. The AFS signal is released at 0 s and the actuation of the AFS is assumed to start at 30 s.

Table 6.16 Durations of high cladding temperature at abnormal transients

Abnormal transients	Duration of high cladding temperature (s)	
	>Initial value + 20°C	>initial value + 40°C
Partial loss of reactor coolant flow	4.9	2.5
Loss of turbine load (without bypass)	1.2	0.1
Isolation of main steam line	0.8	0.1
Loss of feedwater heating	6.3	–

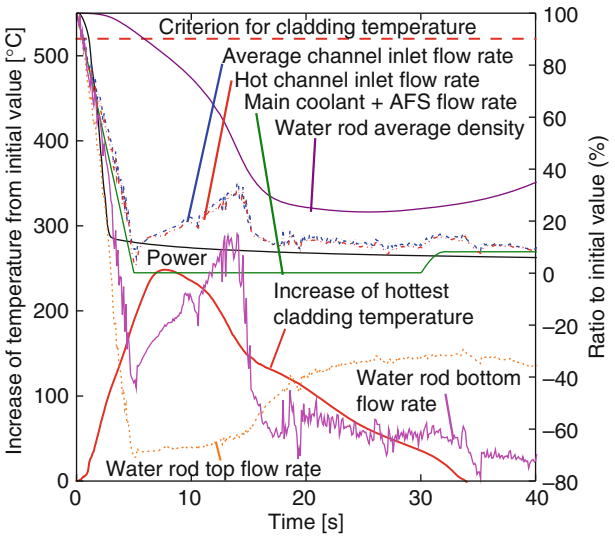


Fig. 6.36 Calculated results for "total loss of reactor coolant flow"

The calculation results are shown in Fig. 6.36. The power decreases to the decay heat level due to the reactivity feedback and reactor scram. Reverse flow occurs in the water rod channel because the buoyancy pressure drop dominates the pressure drop balance. Heat conduction to the water rods increases when the coolant temperature in the fuel channel increases. This implies that the water rods serve as a "heat sink". As the coolant expands in the water rods due to heat-up, there is an increase in the flow rate downstream from the water rods, including the fuel channel inlet. Consequently, the fuel channel flow rate is maintained even though the coolant supply from the cold-leg has stopped. This is called the "water source" effect of the water rods. The "heat sink" and "water source" effects mitigate heat-up of the fuel rod cladding, and hence enable the AFS to have a realistic delay time. The hottest cladding temperature begins to decrease before the initiation of the AFS. The increase in the hottest cladding temperature is about 250°C while the criterion is 520°C.

The results of sensitivity analyses are summarized in Table 6.17. The influence of the coast-down time of the RCPs is not significant because the peak temperature appears at least 5 s after the coast-down has been completed. The influence of the scram delay is not significant because the reactor power is also decreased by the reactivity feedback. It should be noted that the peak temperature does not depend on the capacity or delay of the AFS because the peak temperature appears before the initiation of the AFS.

6.7.2.2 Reactor Coolant Pump Seizure

Coolant flow from one of the two RCPs is assumed to suddenly stop. The calculation results are shown in Fig. 6.37. The increase in the cladding temperature is below half of that in the "total loss of reactor coolant flow" because one of the RCPs is available.

6.7.2.3 CR Ejections

The CR cluster having the maximum reactivity worth is assumed to eject from the core with the velocity of 9,500 m/s as is assumed in PWRs. Reactivity feedback

Table 6.17 Sensitivity analysis for "total loss of reactor coolant flow"

RCP coast-down time (s)/ΔMCST (°C)				
1/310	2/300	3/280	4/270	**5/250**
Scram delay (s)/ΔMCST (°C)				
0.55/250	1/260	3/280	>7/310	
Ratio of density coefficient to reference case/ΔMCST (°C)				
0.25/250	0.5/250	**1/250**	2/240	

Bold characters reference case, *ΔMCST* increase in maximum cladding surface temperature

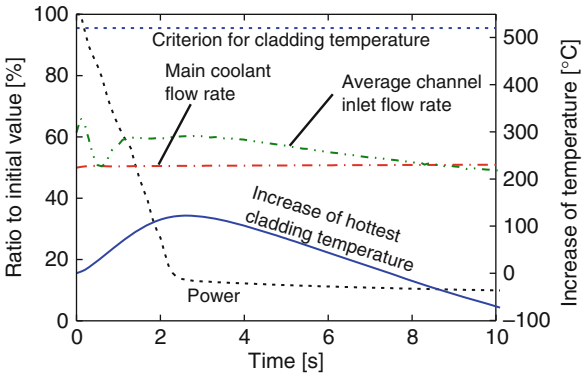


Fig. 6.37 Calculation results for "reactor coolant pump seizure"

from the coolant density is conservatively neglected. Only the Doppler feedback is considered.

In the analysis of "CR ejection at full power," the inserted reactivity is set as 1.3%dk/k. The calculation results are shown in Figs. 6.38 and 6.39. The peak value of the maximum fuel enthalpy is below 160 cal/g while the criterion is 230 cal/g. The pressure increases up to 26.4 MPa and then oscillates due to the opening and closing of the SRVs. The cladding temperature increases by about 250°C. These peak values are sensitive to the inserted reactivity and the Doppler coefficient as shown in Table 6.18. However, it should be mentioned that the inserted reactivity is already conservative and the Doppler coefficient does not significantly change as long as oxide fuel is used.

In the analysis of "CR ejection at hot standby", the inserted reactivity is set as 2.8%dk/k. The peak fuel enthalpy is below 150 cal/g. The increase in the pressure is more extensive compared to the full power case. The active initiation of the SRVs (in their relief valve function) is not credited. The SRVs are assumed to open passively as the safety valve function. The peak pressure is 27.2 MPa.

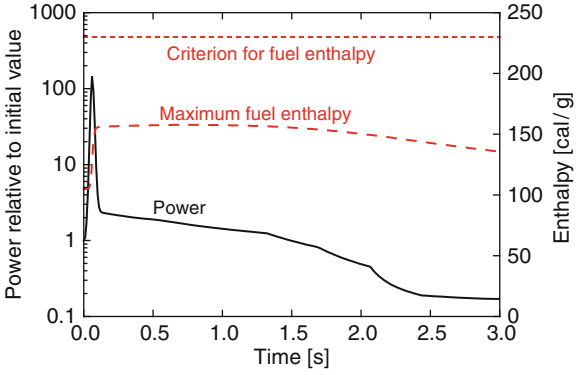


Fig. 6.38 Calculated results for "CR ejection at full power" (1)

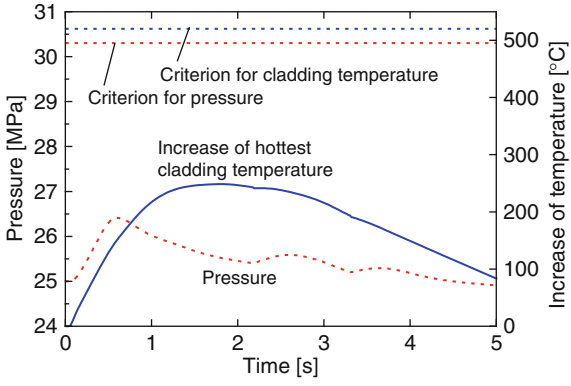


Fig. 6.39 Calculated results for "CR ejection at full power" (2)

Table 6.18 Sensitivity analysis for "CR ejection at normal operation" accident

	Inserted reactivity in %dk/k and $			Ratio of Doppler coefficient to reference case		
	1.3/2.0	1.5/2.3	2.0/3.1	0.5	**1**	1.5
ΔMCST (°C)	**250**	330	500	590	**250**	170
Peak fuel enthalpy (cal/g)	**158**	172	216	218	**158**	139

Bold characters reference case, *ΔMCST* increase in maximum cladding surface temperature

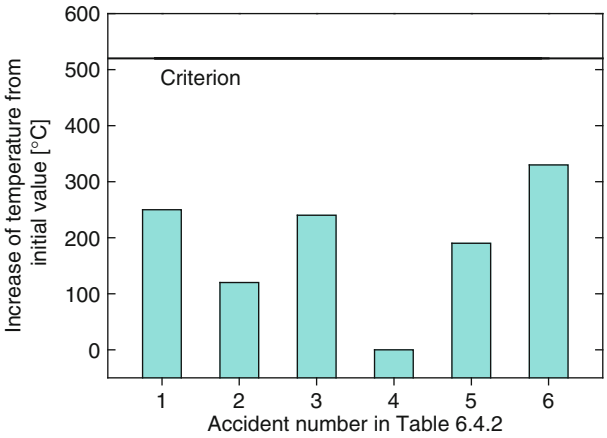


Fig. 6.40 Summary of increases in hottest cladding temperature at accidents

6.7.2.4 Summary

All the criteria are satisfied with considerable margins. The increases in the hottest cladding temperature are summarized in Fig. 6.40, including the LOCA events described in Sect. 6.7.3. The safety margin in the "total loss of reactor coolant flow" is owned to the "heat sink" and "water source" effects of the downward-flow water rods. The highest values of the pressure and fuel enthalpy are 27.2 MPa and below 160 cal/g, respectively, while the criteria are 30.3 MPa and 230 cal/g. The Super LWR has enough margins at design basis accidents at supercritical pressure.

6.7.3 Loss of Coolant Accident Analyses

6.7.3.1 Large LOCA

The "large LOCA" is defined as a pipe break followed by a decrease in the pressure down to the depressurization setpoint (23.5 MPa) even if the RCPs and the pressure control system are assumed to operate. In the present design and break flow

correlations, if the break area is over 15% of the cold-leg pipe or 34% of the hot-leg pipe, it is a large LOCA. These thresholds will change when the design of pipe diameters or the break flow correlations are changed.

In the LOCA analysis, the reactor scram, the MSIVs, the ADS, and the LPCIs are considered. The actuation conditions were summarized in Table 6.3. Since the drywell pressure is not analyzed, the safety actuations by "drywell pressure high" signal are not credited. Furthermore, since the offsite power is assumed to be lost as is assumed in LWRs, a delay of 30 s is assumed for starting the LPCIs due to the start time of the emergency diesel generators. A single failure of the LPCI or the emergency diesel generators are assumed because they give the largest impact on the peak temperature compared to other safety systems. Although the design pressure of the LPCIs is 1.0 MPa, they conservatively start operation when the core pressure decreases below 0.8 MPa. The RCPs are assumed not to trip until the ADS signal is released because operation of the RCPs delays the decrease in the pressure and hence gives a higher peak temperature. Also, operation of the pressure control system is assumed until the ADS signal is released for the same reason.

The 100% break is presented here as an example. The time sequence is shown in Table 6.19 [6]. The calculation results of the blowdown phase are shown in Fig. 6.41. The pressure and break flow rate quickly decrease when the quality of the break point is zero (until 6 s), and then they decrease more slowly after boiling starts in the top/bottom domes and downcomer.

The coolant flow during blowdown at a cold-leg large break LOCA is described in Fig. 6.42 [6]. Before the ADS actuation, the cladding temperature increases because flow stagnation occurs at the upper part of the core. After the ADS actuation, the core coolant flow recovers and the cladding temperature decreases. The large water inventory in the top dome and the water rods are used for core cooling like an "in-vessel accumulator". The reactor power rapidly decreases before the reactor scram due to the decrease in the coolant density. The LPCIs are actuated at 0.8 MPa. When the coolant from the LPCIs fills the bottom dome at 78 s, the blowdown calculation is finished. The increase in the cladding temperature is about 70°C.

Table 6.19 Time sequence of 100% cold-leg break LOCA

Time (s)	Event or action
0	Break
0.1	Pressure low level 1 (24.0 MPa)
	Pressure low level 2 (23.5 MPa)
0.2	ADS actuation
0.65	Scram start
2.85	Scram complete
3.1	MSIV closed
42	LPCI actuation
78	Reflooding start
500	Reflooding complete

Taken from ref. [6] and used with permission from Atomic Energy Society of Japan

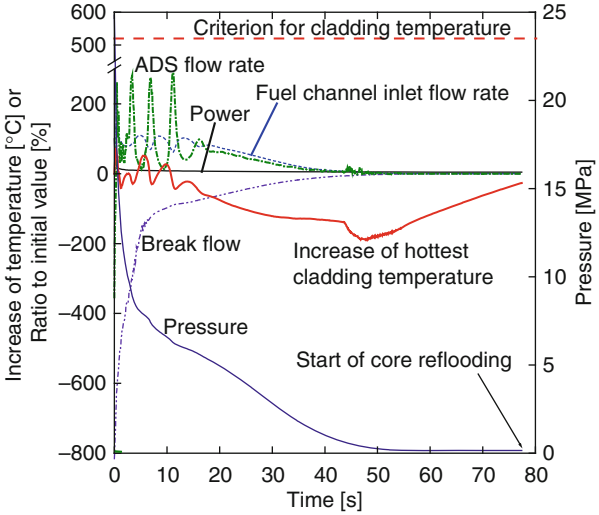


Fig. 6.41 Blowdown phase of 100% cold-leg break LOCA

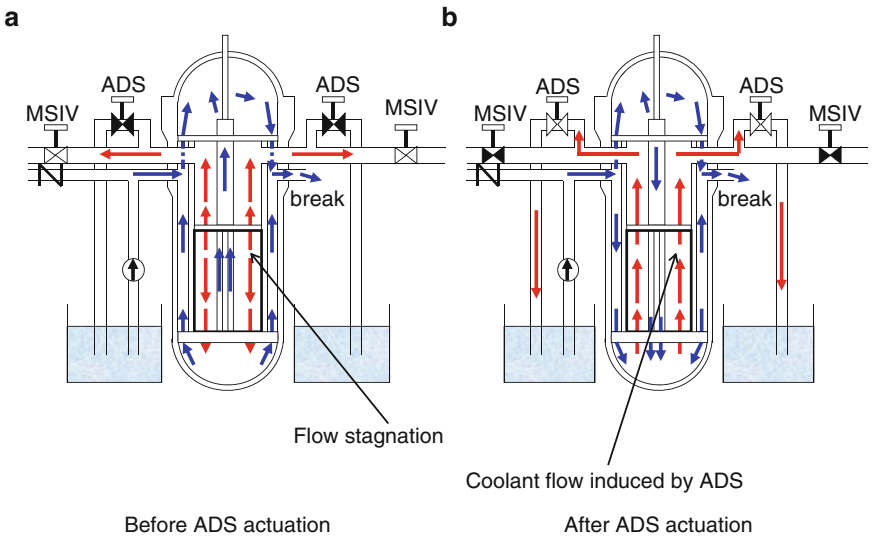


Fig. 6.42 Coolant flow during blowdown at a cold-leg large break LOCA. (Taken from ref. [6] and used with permission from Atomic Energy Society of Japan)

Sensitivity analyses for the blowdown phase of the cold-leg break large LOCAs are summarized in Table 6.20. The peak temperature is not sensitive to the break area, which means that the peak temperature is not sensitive to the break flow rate. It is sensitive to the ADS parameters such as the delay from the signal and the number

Table 6.20 Sensitivity analysis for blowdown phase of cold-leg break large LOCAs

Break size (%)/ΔMCST (°C)			
15/140	30/60	70/80	**100/70**
ADS delay/ΔMCST (°C)			
0.1/ 70	1/230	3/350	10/490
Number of ADS valves opened/ΔMCST (°C)			
3/300	5/150	**8/70**	

Bold characters reference case, *ΔMCST* increase in maximum cladding surface temperature

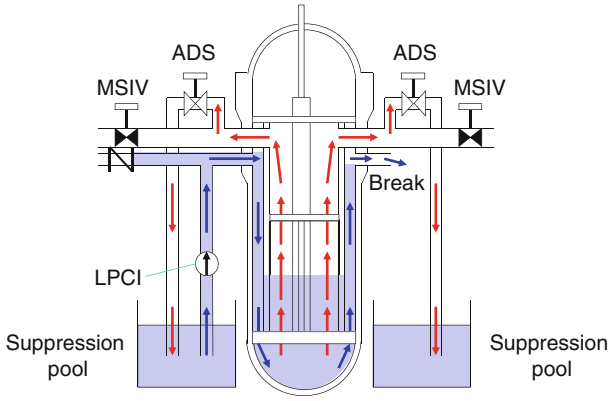


Fig. 6.43 Coolant flow during reflooding at a cold-leg large break LOCA. (Taken from ref. [6] and used with permission from Atomic Energy Society of Japan)

of valves opened. The ADS is more important for the Super LWR than it is for BWRs because it generates coolant flow in the core which is the fundamental safety requirement. Even if the heat transfer coefficient is assumed to be half, the peak temperature increases by only 50°C.

The reflooding phase of the 100% cold-leg break LOCA starts at 78 s. The coolant flow during reflooding at a cold-leg large break LOCA is described in Fig. 6.43. The calculation results are shown in Fig. 6.44. The downcomer is filled with the coolant supplied by the LPCIs at 112 s. The quench flow goes up gradually and reaches the core top at about 500 s. The increase in the cladding temperature is about 190°C. The results of the sensitivity analyses are shown in Table 6.21. If the capacity of the LPCIs is smaller, the start of reflooding and also quench front propagation take more time. However, the impact on the peak temperature is not large. If the axial power shape is the top peak, the quench front propagation is slower and the peak temperature is higher. However, the sensitivity is not large. The submergence of the quenchers in the suppression pool is tentatively set as 2.0 m according to the Mark-I containment of BWRs. How much submergence is needed will be assessed by containment design and related experiments or simulations. The influence of this parameter on the reflooding behavior is investigated as shown in Fig. 6.45. The deeper submergence gives a higher pressure drop to the steam flow

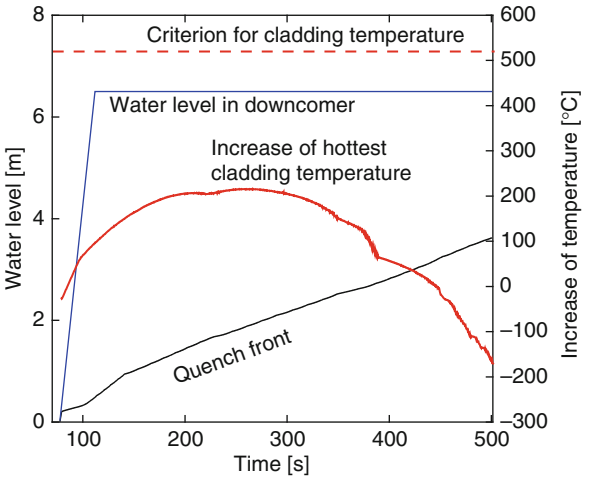


Fig. 6.44 Reflooding phase of 100% cold-leg break LOCA

Table 6.21 Sensitivity analysis for reflooding phase of 100% cold-leg break LOCA

LPCI capacity (%)/Start time of reflooding (s)/ΔMCST (°C)		
8/150/390	12/113/300	**24/78/190**
Axial power distribution/End time of reflooding (s)/ΔMCST (°C)		
Cosine/500/190	Top peak/670/280 (Power peak at 80% of core height)	

Bold characters reference case, *ΔMCST* increase in maximum cladding surface temperature

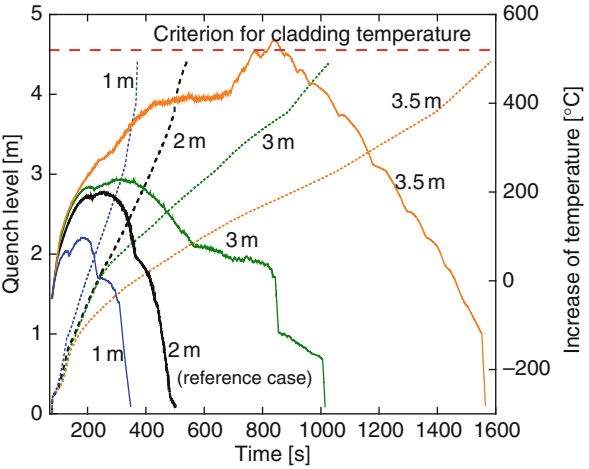


Fig. 6.45 Influence of submergence of quencher in suppression pool

path and hence slower reflooding and higher peak temperature. Its sensitivity becomes large when the submergence is over 3 m. This parameter should be carefully determined in the containment design.

In contrast to the cold-leg break, a hot-leg break is less important for the Super LWR. This is because the core coolant flow rate naturally increases during blowdown (cf. Fig. 6.7 [1]), and because forced flooding by the LPCIs is expected after the blowdown.

6.7.3.2 Small LOCA

The small LOCAs include breaks where the pipe break area is smaller than that defined as large LOCAs. The small LOCAs are represented by cases with a cold-leg break because the cladding temperature does not increase in the case of a hot-leg break. Several cases of different break areas of the cold-leg are analyzed. Operation of the RCPs and pressure control system are assumed in order to give higher cladding temperatures. The SPRAT-DOWN code, developed for the supercritical pressure condition, is used because the pressure is kept supercritical. The results are shown in Figs. 6.46 and 6.47. The peak temperature increases with the break area because the reduction of the core coolant flow rate also increases. The 15% break, which is the upper limit of the small LOCA, gives the highest temperature. If the critical mass flux is changed as a result of future experiments, the break area of the upper limit of the small LOCA will also be changed. However, the peak temperature will not change significantly because the break flow rate at the upper limit of the small LOCA will not significantly change. Even if the heat transfer coefficient is assumed to be half, the peak temperature increases by only 50°C. If the "drywell pressure high" signal is assumed to be detected, the ADS is actuated and hence the peak temperature is lower [6].

6.7.3.3 Summary

As shown in Fig. 6.40, the small break LOCA gives the highest temperature among all the accidents which is the same tendency as demonstrated by PWRs. This is

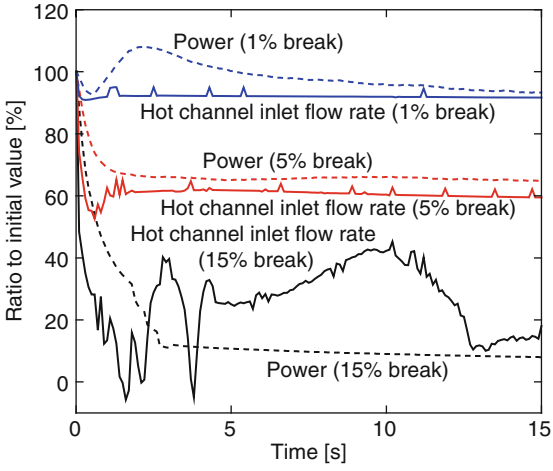


Fig. 6.46 Cold-leg small break LOCAs (1)

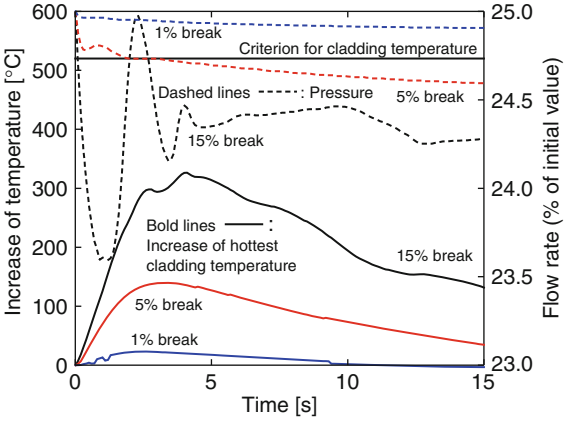


Fig. 6.47 Cold-leg small break LOCAs (2)

mainly because the small LOCA has the severest power to flow rate ratio. It is noted, as described in Sect. 6.7.3.2, that the peak temperature can be decreased by crediting an initiation of the ADS by taking the signal of "drywell pressure high". The large break LOCA gives relatively lower peak temperature compared to the small LOCA. The peak temperature appears during the reflooding, not during the blowdown.

6.7.4 ATWS Analysis

As described in Sec. 6.7.2, eight transients are accompanied by a reactor scram. These transients make up the ATWS events of the Super LWR. The same analysis sequences as used in the abnormal transient analyses are applied with the exception of the reactor scram occurrence.

Since the limiting condition and the safety characteristics appear before the reactor reaches a "high-temperature stable condition," where all the parameters are stable, the analyses are carried out until the high temperature stable condition is obtained. An operation of the "existing" active safety system is considered in the same manner as LWRs [26–29]. The existing safety systems should be "designed to perform their function in a reliable manner and independent (from sensor output to the final actuation device) from the existing reactor trip system" (see 10CFR50.62 of the US-NRC). A single failure is not considered due to the extremely low probability of the ATWS events. Although the backup rod insertion system and the standby liquid control system are actuated manually or automatically for the final shutdown, they are not credited in the analyses.

Alternative actions for the ATWS mitigation are credited in the analyses of LWRs [27–39]. PWRs need the ATWS Mitigating System Actuation Circuitry (AMSAC) to initiate a turbine trip and the AFS function as alternative actions so as to satisfy the pressure limit [29]. Opening the ADS induces strong coolant flow

and decreases reactivity as shown in Fig. 6.7 [1]. Opening the ADS has the potential to be an effective alternative action for the ATWS mitigation. It is initiated by detecting one of the scram signals and "reactor power ATWS permissive (20% of rated power) for 5 s" as an alternative action of the ADS [4]. The scram conditions are assumed to be detected by sensors independent from the existing reactor trip system. The power level and the duration for the "ATWS permissive" are provisional. They are design parameters that should be optimized. It should be noted that the ADS is not intended for the ATWS mitigation but is one of the functions of the "existing" SRV configuration just like in BWRs. The ATWS events are analyzed with and without alternative action of the ADS in order to understand its necessity and effectiveness.

6.7.4.1 ATWS Analysis with Alternative Action

Until the ADS is initiated, the reactor behavior is analyzed with SPRAT-DOWN. After that, the blowdown is analyzed with SPRAT-DOWN-DP. Since SPRAT-DOWN-DP does not distinguish between the hot and average channels, only the hot channel parameters are transferred. After initiating the ADS, the reactor behavior for all the ATWS events is similar to the behavior described in Fig. 6.7 [1] because the depressurization is an intense phenomenon that is not influenced by the condition before it. The ATWS events having relatively fast responses before initiating the ADS are important here. Representative results are shown below.

Only the "partial loss of reactor coolant flow" is accompanied by a decrease in the main coolant flow rate before initiating the ADS. The ADS is actuated at 5 s by the ATWS signal which is "reactor coolant pump trip" and "reactor power ATWS permissive for 5 s". The calculation results are shown in Fig. 6.48. A decrease in the flow rate leads to an increase in the coolant temperature due to the power and flow mismatch. The cladding temperature increases due to the coolant heat-up and a decrease in the heat transfer coefficient. The net reactivity and the reactor power decrease due to coolant density feedback. The increase in the cladding temperature is about 120°C, which is the highest value of all the ATWS events with the alternative action.

The "loss of turbine load" is a typical pressurization event. The turbine bypass is not credited. The ADS is initiated at 5 s by the ATWS signal of the "turbine control valve quickly closed" and "reactor power ATWS permissive for 5 s." The calculation results are shown in Fig. 6.49. The pressure increases due to the closure of the turbine control valves. As described in Sect. 6.7.1.3, the inherent characteristics of the Super LWR design make the reactivity insertion and the power increase very small. The peak power is only 104% of the initial value. When the SRVs open, the pressure begins to decrease. After initiating the ADS as the alternative action, the pressure, power, and cladding temperature decrease. The increase in the cladding temperature is about 50°C and the peak pressure is about 26.8 MPa. They are exactly the same as those obtained in the abnormal transient analysis with a reactor scram (see Sect. 6.7.1.3).

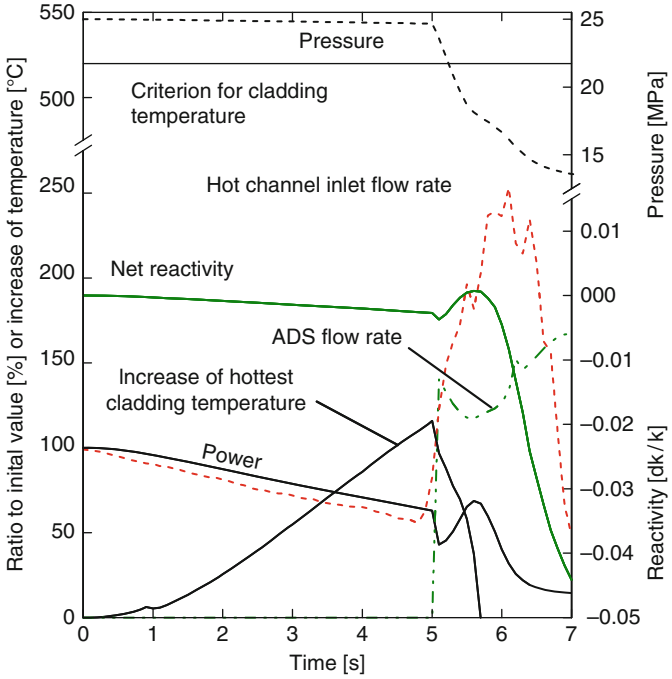


Fig. 6.48 Calculation results for "partial loss of reactor coolant flow" (ATWS) with alternative action

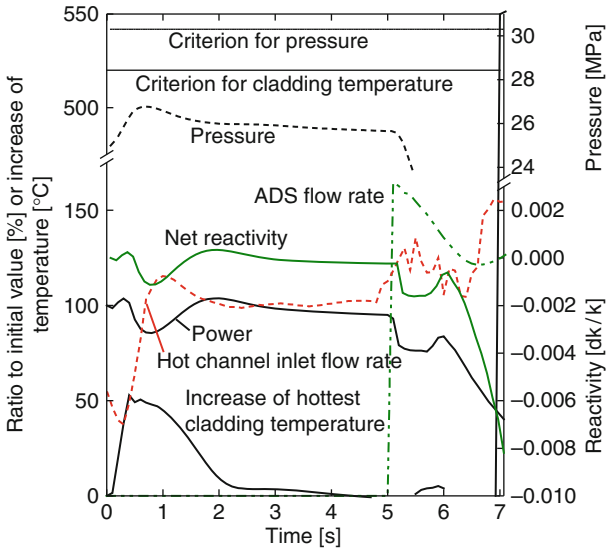


Fig. 6.49 Calculation results for "loss of turbine load without turbine bypass" (ATWS) with alternative action

6.7.4.2 ATWS Analysis Without Alternative Action

Since the pressure is kept supercritical due to no depressurization, only SPRAT-DOWN is used. The reactor behavior is analyzed until a high temperature stable condition is obtained.

The calculation results of the "partial loss of reactor coolant flow" are shown in Fig. 6.50. The reactor response is exactly the same as that with the alternative action (Fig. 6.48) until 5 s. The hottest cladding temperature begins to decrease at 7 s due to a decrease in the reactor power by coolant density feedback. Reverse flow occurs in the water rods at 12 s. For a few hundred seconds after that, the reactivity of density feedback gradually increases because upward flow in the water rods causes an increase in the average coolant density [4]. The reactor power and the cladding temperature gradually increase with the net reactivity. However, the second peak of the cladding temperature does not exceed the first one. When the coolant that has flowed out of the water rods returns to the water rods through the CR guide, the top dome, the downcomer, and the bottom dome at around 290 s, the reactivity of density feedback decreases again due to an increase in the water rod inlet temperature. The reactor has almost reached a high temperature stable condition at 500 s. The increase in the cladding temperature is about 140°C.

The "loss of offsite power" is the typical loss of flow event. Both of the turbine-driven RCPs are assumed to trip at 10 s. The AFS signal caused by "loss of offsite power" is given at time zero and three units of the AFS start at 30 s. The coolant temperature from the AFS is assumed as 30°C. The calculation results are shown in Fig. 6.51. Basically, the features of the reactor response are the same as the "partial

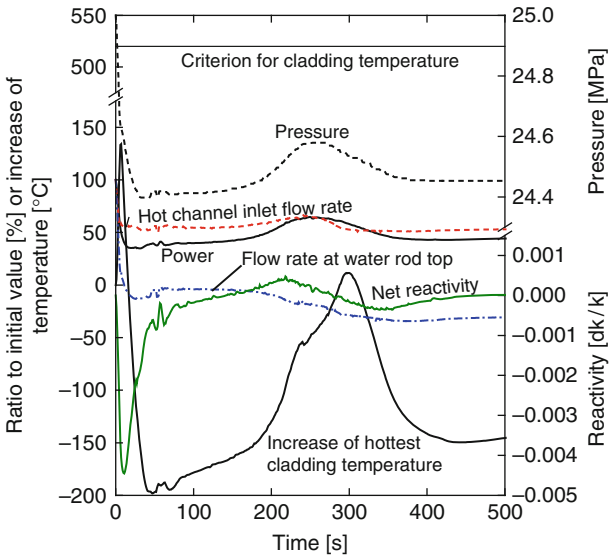


Fig. 6.50 Calculation results for "partial loss of reactor coolant flow" (ATWS) without alternative action

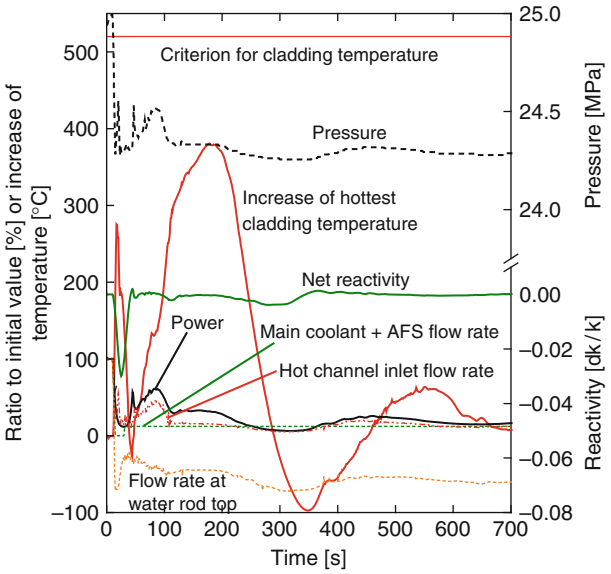


Fig. 6.51 Calculation results for "loss of offsite power" (ATWS) without alternative action

loss of reactor coolant flow" described above. After the trip of the RCPs at 10 s, the decrease in the flow rate causes an increase in the cladding temperature. The reactivity and the power decrease. Reverse flow occurs in the water rods. The coolant flow in the fuel channels is still maintained after the coast-down of the RCPs has finished at 15 s. This is due to the "water source" effect of the water rods as described in Sect. 6.7.2.1. The cladding temperature begins to decrease at 17 s because the power becomes relatively smaller than the flow rate. The average coolant density and the reactivity of density feedback shift and increase at 25 s. Start of the AFS supplying low temperature coolant also increases the average coolant density. After the core returns to criticality, the net reactivity is kept around zero by the coolant density and Doppler feedbacks. The power stays higher than the decay heat level. After 43 s, the cladding temperature increases again and keeps increasing until 177 s. During this period, the power to flow rate ratio is at its worst levels. The second peak of the hottest cladding temperature is higher than the first peak, unlike for the "partial loss of reactor coolant flow". The reactor has almost reached a high temperature stable condition at 700 s. The increase in the cladding temperature is about 380°C, which is the highest value of all the ATWS events. However, it is still well below the criterion even though no alternative action is credited.

The "uncontrolled CR withdrawal" is a typical reactivity insertion event. Although the CR withdrawal itself would be stopped at a certain power level by an interlock system independent from the reactor trip system, the CR having the maximum reactivity worth is conservatively assumed to be fully withdrawn. The calculation results starting from the normal operating condition are shown

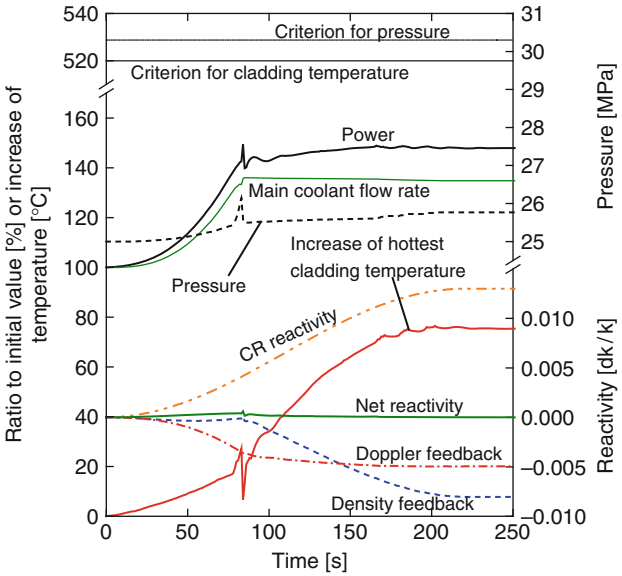


Fig. 6.52 Calculation results for "uncontrolled CR withdrawal" at normal operation (ATWS) without alternative action

in Fig. 6.52 The rate of increase in the power is small because of reactivity feedback. The main coolant flow rate increases with the reactor power due to the operation of the main steam temperature control system. The maximum value of the main coolant flow rate is assumed as 138% of the rated value. When the main coolant flow rate exceeds 130% of the rated value, the pressure quickly increases because the upper limit of the turbine control valve opening is assumed as 130% of the initial value. The increase in the pressure is suppressed by the SRVs. The reactor has almost settled to a high temperature stable condition by 250 s. The peak values of the temperature increase, the fuel enthalpy, and the pressure are about 70°C, 146 cal/g, and 26.2 MPa, respectively. They are well below the criteria. When the main steam temperature control system is not considered, the power and flow mismatch gets worse. It causes a higher cladding temperature and a stronger density feedback. The peak temperature is higher and the peak fuel enthalpy is lower than the reference case by 140°C and 21 cal/g, respectively. They are also well below the criteria.

The "loss of turbine load without bypass" is a typical pressurization event over a short duration. It is also a typical loss of flow event over a long time scale because both of the turbine-driven RCPs are assumed to trip due to the shutdown of the steam supply to the turbines. Since the difference of the analysis sequences between this event and the "loss of offsite power" is only the success or failure of the turbine bypass, the long-term reactor behavior is similar to the behavior shown in Fig. 6.51. The behavior in the "isolation of main steam line" is almost the same as that in the "loss of turbine load without bypass." At "uncontrolled CR withdrawal at startup,"

the reactor power settles at 10% of the rated power and the peak value of the fuel enthalpy is about 37 cal/g due to Doppler and density feedbacks. The "core coolant flow control system failure" is a typical flow-increasing event. The reactor power increases due to the positive reactivity of density feedback. It is mitigated by Doppler feedback. Since the power to flow rate ratio is always below unity, the cladding temperature is always below the initial value. The pressure increase is small. The "pressure control system failure" is a typical pressure-decreasing event. Since an increase in the turbine control valve opening leads to an increase in the core coolant flow rate, the cladding temperature decreases from the outset. When the pressure decreases to the ADS setpoint of 23.5 MPa, the reactor is depressurized. It should be noted that this ADS actuation is not the alternative action.

6.7.4.3 Sensitivity Analyses in ATWS Events

The density coefficient changes with the average density and the burnup. At the initial condition of the ATWS analysis, the average density is 0.52 g/cm^3, which results in 0.16 dk/k/(g/cm^3) for BOEC and 0.21 dk/k/(g/cm^3) for EOEC. The 3D core design study gives the range of the average coolant density of 0.50–0.57 g/cm^3 for the normal operating condition. For the sensitivity analysis, a wider range of 0.45–0.65 g/cm^3 is assumed in consideration of an operating margin for the power distribution, design change of the pitch to diameter ratio (P/D), water rod size, and inlet and outlet temperatures, etc., as well as the calculation uncertainty of the coolant density itself. This density range corresponds to the range of the density coefficient, 0.09–0.31 dk/k/(g/cm^3). Furthermore, uncertainties in the nuclear data, the neutronics calculation model, etc., are taken into account when establishing the ±20% error band of the density coefficient. Consequently, the sensitivity analysis is carried out with a range of 0.07–0.38 dk/k/(g/cm^3) at the initial condition. The results are summarized in Table 6.22. The increase in the temperature at the loss of

Table 6.22 Sensitivity analysis on coolant density coefficient

Abnormality type	Loss of flow	Pressurization	Reactivity insertion	Flow increase
Typical ATWS event	Loss of offsite power[a]	Loss of turbine load without bypass[b]	Uncontrolled CR withdrawal[a]	Main coolant flow control system failure[a]
Density coefficient (dk/k/(g/cm^3))	ΔMCST (°C)	Peak pressure (MPa)/peak power (%)	Peak fuel enthalpy (cal/g)	Peak power (%)
0.07	420	26.8/101	155	132
0.16 (BOEC)	**380**	**26.8/103**	**146**	**143**
0.21 (EOEC)	**380**	**26.8/104**	**146**	**147**
0.38	360	26.8/107	143	169

Bold characters reference case, *ΔMCST* increase in maximum cladding surface temperature
[a]Without alternative action
[b]Regardless of the use or nonuse of alternative action due to fast responses

flow events without the alternative action does not change significantly with the density coefficient because the peak temperature appears at the second peak of the cladding temperature when the reactivity of density feedback is almost zero. This means that the highest temperature of the ATWS events is not sensitive to the density coefficient. The variation of the density coefficient influences the initial power peak at the pressurization events because it is caused by the density increase. However, the power peak does not change significantly with the density coefficient because the density change itself is small. Influence of this parameter on the peak pressure is also small. For the reactivity insertion events without the alternative action, the maximum fuel enthalpy is not sensitive to the density coefficient because Doppler feedback is more dominant. For the flow increasing events with the alternative action, the peak power is sensitive to the density coefficient. However, the power settles to a stable condition in all the cases because of negative reactivity insertion by Doppler feedback. The influence of the density coefficient on depressurization behavior is also checked within the range of 0.07–0.38 dk/k/(g/cm^3). In spite of the large variation of the density coefficients, the differences in reactor behavior are not significant as shown in Fig. 6.53. The sensitivity analysis shows that the wide range variation of the density coefficients does not significantly influence the safety margin for the ATWS events, which will allow flexible core design and operation.

It is expected that the Doppler coefficient does not change significantly as long as the Super LWR is a light water cooled thermal reactor with UO_2 fuel. It changes with the average fuel temperature and the burnup. The average fuel temperature is 920°C at the initial condition. For the sensitivity analysis, a wide variation of ±200°C is assumed in consideration of an operating margin and uncertainties. This corresponds to a Doppler coefficient range from −1.47 to −2.00 pcm/K.

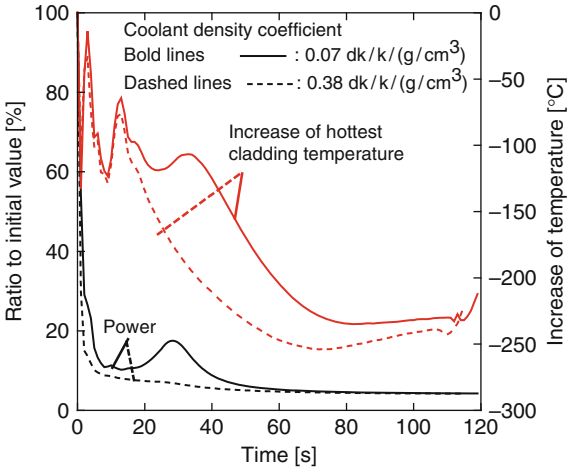


Fig. 6.53 Comparison of reactor depressurization behaviors with large and small density coefficients

As noted above, uncertainties in the nuclear data, the calculation model, etc., are taken into account when establishing an error band of ±20% of the Doppler coefficient. The range of −1.17 to −2.40 pcm/K is assumed for the sensitivity analysis. Even if the Doppler coefficient is −1.17 pcm/K, the maximum fuel enthalpy of the reactivity insertion events without the alternative action is 148 cal/g, which is higher than that of the reference case by only 1% because the contribution of coolant density feedback becomes higher. The peak power of the flow increasing events without the alternative action is 154% of the rated power with a Doppler coefficient of −1.17 pcm/K. It is higher than the reference case but other parameters, i.e., peak temperature and peak pressure, are almost the same.

The bulk temperature is over 800°C at the highest PCT condition. Because the temperature is much higher than the pseudo-critical point, the Dittus–Boelter correlation would work well. The Dittus–Boelter correlation gives a higher heat transfer coefficient than the Oka–Koshizuka correlation under this condition. The peak temperature obtained with the Dittus–Boelter correlation is lower than that with the Oka–Koshizuka correlation by about 20°C. The effect of the fuel assembly geometry, such as the subchannel shape, the water rod wall, and the grid spacers, is not taken into account in the existing correlations. Also, the flow transient effect against the steady-state is not considered. The sensitivity analysis shows that a 1% change of the heat transfer coefficient produces about a 2°C change of the highest temperature.

The coast-down time of the turbine-driven RCPs was calculated as 5 s considering the inertia of the pump itself and the driving-turbine [30]. If the inertia is changed with the pump design, the coast-down time will also change. The peak temperatures of the abnormal transients and the accidents are influenced by the coast-down time as described in Sects. 6.7.1 and 6.7.2. However, the highest temperature of the ATWS events that is obtained at the "loss of offsite power" does not change because it appears at the second peak, much later than the pump trip (see Fig. 6.51).

The AFS delay after detecting one of the actuation conditions is taken from that of the turbine driven RCIC system of BWRs. Its influence on the peak temperature for the "loss of offsite power" event is checked. Due to the "water source" effect of the water rods, the core coolability is not influenced by the AFS delay. On the other hand, the net reactivity tends to increase with the shorter AFS delay because the AFS supplies cold coolant to the core. The peak temperature is higher with the shorter AFS delay. The increase in the cladding temperature is about 450°C for a delay time of 15 s and 330°C for 100 s. In spite of the wide variation of the AFS delay that would cover the actual design point, the degree of the temperature variation is well below that of the safety margin to the criterion.

The SRVs mitigate the pressurization events. Their setpoint is a design matter that must consider various uncertainties. The sensitivity analysis shows that the difference between the peak pressure and the first SRV setpoint is always about 0.6 MPa regardless of the setpoint itself. This is useful information for the actual SRV design considering the pressure limit and uncertainties.

6.7.4.4 Summary

The increases in the hottest cladding temperature and the peak pressures are well below the criteria as summarized in Figs. 6.54 and 6.55, respectively. Also, the peak fuel enthalpy at reactivity insertion events is well below the criterion. Even if the alternative action is not credited, the Super LWR has considerable safety margins at the ATWS events. The alternative action is especially effective in reducing the peak temperature at the loss of flow events.

The limiting ATWS events differ among PWRs, BWRs, and the Super LWR due to their design differences. Loss of the heat sink at the secondary system is the most important event for PWRs because it is accompanied by an increase in the coolant temperature and then rapid pressurization at the primary system. Pressurization is the most important event for BWRs because it is accompanied by considerable increases in the reactivity and power caused by void collapse. Loss of flow is the

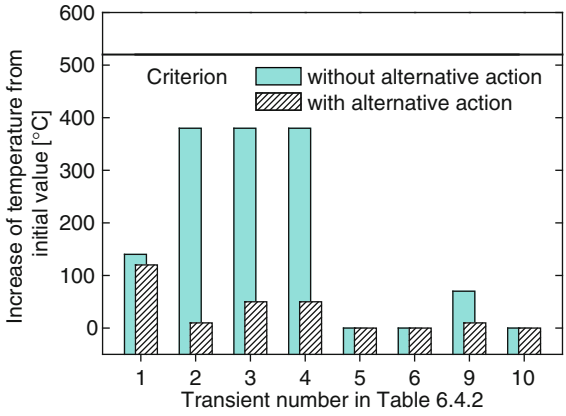


Fig. 6.54 Summary of increases in hottest cladding temperature at ATWS

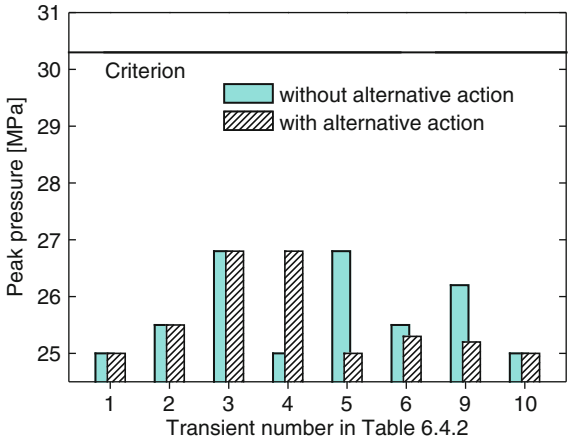


Fig. 6.55 Summary of peak pressures at ATWS

most important event for the Super LWR because natural circulation cannot be used for decay heat removal in the once-through coolant cycle. It should be mentioned that there is a possibility to utilize the recirculation loop, prepared for plant startup (see Chap. 5), as a natural circulation path for decay heat removal.

An increase in the fuel channel temperature leads to an increase in the heat conduction to the water rods, which is referred to as the "heat sink" effect. It is a key safety advantage of the large water rods in the Super LWR. Next, the coolant expands in the water rods due to heat-up, which increases the downstream flow rate regardless of the water rod flow direction. Consequently, the fuel channel flow is maintained for the loss of flow events, which is referred to as the "water source" effect. It is a safety advantage of the downward-flow water rods placed upstream from the fuel channels, compared to upward-flow water rods and solid moderators. Although the Super LWR does not have a natural circulation path, unlike LWRs, the "water source" effect gives the Super LWR extra time to start the active coolant supply.

The average coolant density is less sensitive to the pressure than that of BWRs because of no void collapse and a smaller density difference between "steam" and "water". It is one of the essential characteristics of supercritical pressure water cooling. Closure of the coolant outlet of the once-through cooling system causes flow stagnation in the core, which leads to an increase in the coolant temperature due to the power and flow mismatch. This means that the pressurization events of the once-through cooling system naturally behave in a manner similar to the recirculation pump trip of BWRs. Due to these characteristics, the pressurization events of the Super LWR are essentially milder than BWRs. The density change and the power increase are much smaller than those of BWRs even though the recirculation pump trip as an alternative action is considered for BWRs.

The relative pressure change is smaller than that of BWRs due to the higher main steam density and the much milder power change at the pressurization events. Since an "all solid" condition does not occur in the once-through coolant cycle where compressive fluid flows, the relative pressure change is also smaller than that of PWRs.

The Super LWR has self-controllability of the reactor power against loss of flow and reactivity insertion, like LWRs, due to coolant density and Doppler feedbacks although reverse-flow in the downward-flow water rods slightly complicates the behavior of density feedback. The wide-range sensitivity analyses show that variation of the feedback coefficients does not significantly influence the self-controllability or the safety margin.

Reactor depressurization by opening the ADS increases the core coolant flow rate. Discharge of the coolant inventory does not threaten safety because maintaining the coolant inventory is not the fundamental safety requirement for the once-through coolant cycle as long as the core coolant flow is maintained. During depressurization, the top dome passively supplies its coolant inventory to the fuel channels like an "in-vessel accumulator". It is a key advantage of a core with downward-flow water rods because these rods are not a bypass flow path. Also, depressurization decreases the reactivity because the moderator is discharged from

the core, which is a general characteristic of water cooled thermal reactors. Due to the good behavior of reactor depressurization, opening the ADS would be an effective alternative action to increase the safety margin at the ATWS events.

Gas-cooled reactors also have good ATWS characteristics without any alternative action. But the power rating and the core dimensions are limited so as not to release fission gas from the coated particle fuels at accidents. On the other hand, the good ATWS characteristics of the Super LWR are achieved with a high core power rating. Therefore, it is an advantage in the reactor design.

6.7.5 *Abnormal Transient and Accident Analyses at Subcritical Pressure*

The abnormal transients and design basis accidents, except some the reactivity events, start from the normal operating condition in the licensing reports of LWRs and other reactors. There are mainly two reasons. One is that the probability of abnormal incidents is the highest at the normal operating condition due to its being the state in which the reactor is the longest. The other is that the abnormal incidents during the normal operating condition give a smaller safety margin. Although the present safety analyses of the Super LWR are not for licensing, it is important to check whether the abnormal transients and accidents at the normal operating condition are the representative (most important) incidents for the Super LWR safety. Herein, the abnormal transients and accidents occurring at the pressurization phase in the sliding-pressure startup, described in Chap. 5, are analyzed using SPART-DOWN-SUB.

The core designed by Kamei et al. [31] is analyzed here. During the pressurization from 8 MPa to 22 MPa, the feedwater temperature is raised from 150°C to 280°C linearly with the pressure. The reactor power and the feedwater flow rate are kept at 20% and 40% of the rated value, respectively. These conditions are slightly different from those described in Chap. 5 due to the difference in the core characteristics.

The pressure control system and the power control system designed in Chap. 4 are used. However, the main steam temperature control system cannot be used because the core outlet temperature is the saturation temperature. Therefore, a feedwater controller for subcritical pressure operating conditions is needed. During subcritical pressure operation, the feedwater flow rate is regulated in order to keep the water level in the steam water separator, instead of regulating the main steam temperature. A combined proportional and derivative controller (PD controller) is found to be suitable for that purpose [12].

The transients and accidents shown in Table 6.5, excluding LOCA events, are analyzed. As representative cases, the initial conditions at 8.3 MPa, 15 MPa, and 21 MPa are selected. The same criteria as described in Sect. 6.5 are applied. The MCST during the pressurization phase is lower than that of the normal operating condition by 350°C at 8.3 MPa, 310°C at 15 MPa and 30°C at 21 MPa. These differences of the MCST are added to the allowable increases in the cladding

temperature for abnormal transients (110°C) and accidents (520°C) that are applied for the safety analyses starting from the normal operating condition. The allowable increases in the temperature at abnormal transients and accidents are 440°C and 870°C at 8.3 MPa, 420°C and 830°C at 15 MPa, and 140°C and 550°C at 21 MPa, respectively.

The calculation results of the "total loss of reactor coolant flow" at 15 MPa are shown in Fig. 6.56 as an example of the loss of flow events. Due to the coast-down and hence the decrease in the core coolant flow rate, departure-from-nucleate-boiling (DNB) occurs at 3 s and the cladding temperature quickly increases. However, the peak value is much lower than the criterion. Although the "water source" effect of the water rods is small at subcritical pressure, the core coolant flow can be kept by natural circulation in the recirculation loop before the start of the AFSs.

Although two phase flow exists in the core at pressurization phase, the increase in the power is very small at pressurization events unlike BWRs. It is because the quality or void fraction is very small during the pressurization phase, and hence the increase in the coolant density by void collapse is also small.

The calculation results of the "uncontrolled CR withdrawal" at 15 MPa, an example of reactivity insertion events, are shown in Fig. 6.57. As the power increases, the minimum DNB ratio (MDNBR) decreases and then reaches 1.0. The cladding temperature quickly increases when DNB occurs. However, the criterion is well satisfied. The peak fuel enthalpy at the CR ejection accidents are determined by the inserted reactivity and the Doppler coefficient, like the results of normal operating condition (see Table 6.18).

The increases in the hottest cladding temperature are summarized in Figs. 6.58 and 6.59. All the criteria are satisfied. The reactivity events (uncontrolled CR

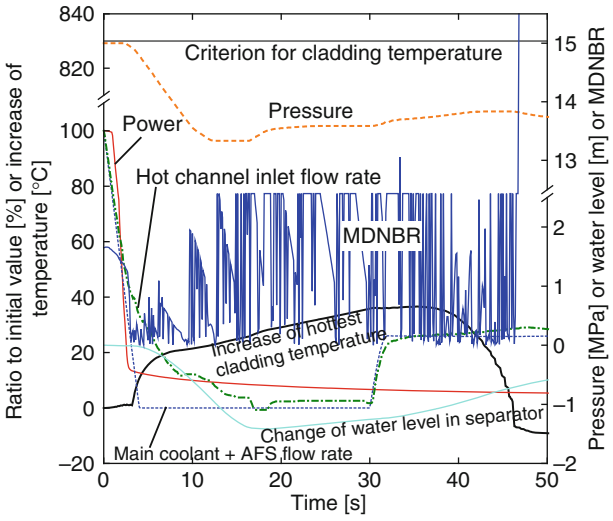


Fig. 6.56 Calculation results for "total loss of reactor coolant flow" starting at 15MPa

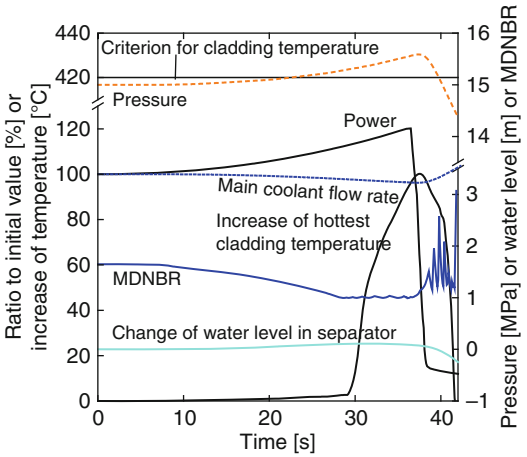


Fig. 6.57 Calculation results for "uncontrolled CR withdrawal" starting at 15MPa

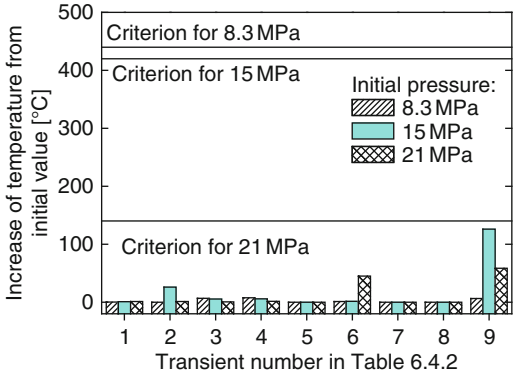


Fig. 6.58 Summary of increases in the hottest cladding temperature at abnormal transients during pressurization phase

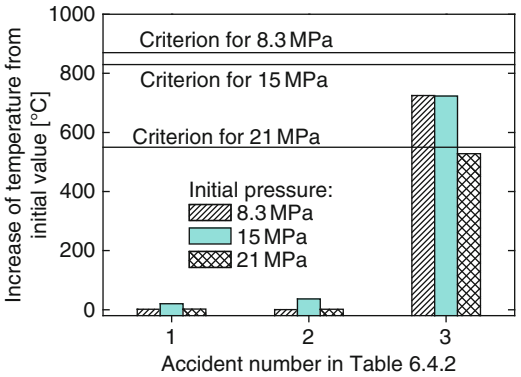


Fig. 6.59 Summary of increases in hottest cladding temperature at accidents during pressurization phase

withdrawals and CR ejections) give the smallest margins to the criteria. Even though DNB occurs at several events, the increase in the cladding temperature is not significant due to the small power (20%). The relative increase in the pressure and power are the same degree as those of the safety analysis results at supercritical pressure. The fuel enthalpy at the CR ejection accidents can be kept well below the criterion by adequately designing the control rod worth and Doppler coefficient.

6.8 Development of a Transient Subchannel Analysis Code and Application to Flow Decreasing Events

The cross flow between subchannels is considered in the steady-state thermal hydraulic design using the steady-state subchannel analysis code as described in Chap. 2. On the other hand, the deterministic safety analyses are performed using the single channel code in Sect. 6.7 with an assumption that the relative mass flux distribution in a fuel assembly at abnormal conditions is the same as that at a steady-state condition. There is a concern that the distribution may change at abnormal conditions, especially flow decreasing conditions, due to the change in the pressure drop distribution. In this section, a transient subchannel analysis code is introduced and applied to representative flow decreasing events, an abnormal transient and an accident, in order to estimate whether and how much the safety margins to the criteria of the cladding temperature change from the results obtained in Sect. 6.7.

6.8.1 A Transient Subchannel Analysis Code

The geometry and mesh arrangement in the fluid region are exactly the same as those of the steady-state subchannel analysis code. Figure 6.60 shows the entire algorithm. The momentum conservation equations for three directions and a mass conservation equation are solved with the Simplified Marker And Cell (SMAC) method [32]. In the SMAC method, a temporary velocity field is calculated, the Poison equation is solved, and then the velocity and pressure fields are calculated as shown in Fig. 6.61. The Successive Over-Relaxation (SOR) method is used to solve a matrix.

The radial heat transfer model is almost the same as that of SPRAT-DOWN (see Fig. 4.2.6). The coolant enthalpy is calculated by solving an energy conservation equation. The heat fluxes on the fuel rods and the water rod walls that have been calculated at the previous time step are utilized the same as in SPRAT-DOWN. This does not cause a problem by keeping the time step reasonably short.

The semi-implicit scheme is chosen to solve the mass and momentum conservation equations where only the pressure is implicitly solved. The Runge–Kutta

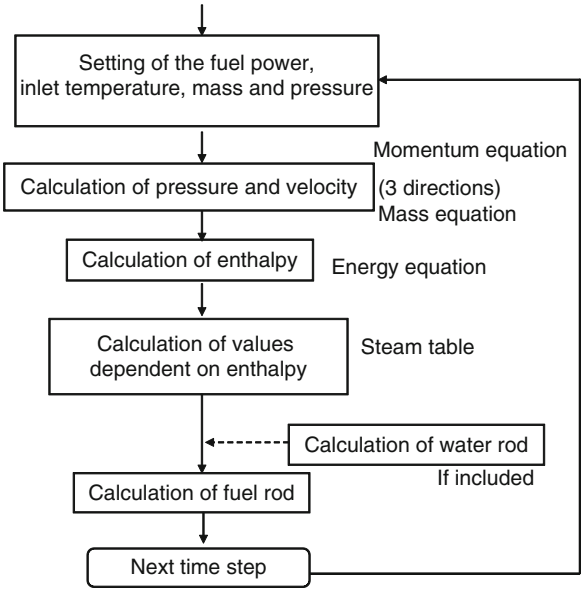


Fig. 6.60 Algorithm of transient subchannel analysis code

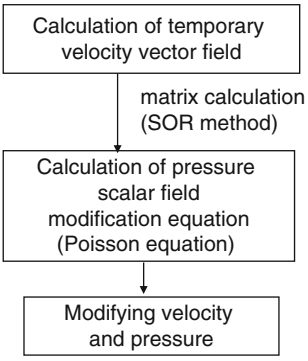


Fig. 6.61 SMAC method

scheme is used to solve the energy conservation equation. The up-wind difference scheme is used to avoid numerical oscillations. Table 6.23 shows the combinations of the boundary conditions of the velocity and pressure at the inlet and outlet.

The advection of coolant in a time step is limited below one-third of the mesh size, which means that the Courant number is below one-third. The diffusion in a time step is limited below one-third of the mesh size, which means that the diffusion number is below one-third.

For the verification of this code, three typical steady-states are calculated and compared to the results by the steady-state subchannel analysis code. Table 6.24 summarizes the three steady-state cases. Figure 6.62 shows the pin power distributions in those cases. The steady-state conditions are obtained using the transient

Table 6.23 Boundary conditions

	Inlet		Outlet	
	Velocity	Pressure	Velocity	Pressure
Neumann condition (values fixed)	○			
Dirichlet condition (gradients fixed)		○	○	○

Open circle: Used in the subchannel analysis code

Table 6.24 Steady-state conditions

	Case 1	Case 2	Case 3
Radial power distribution	Flat	Typical one with control rods inserted	Typical one after control rods withdrawn
Axial power distribution	Cosine	Cosine	Top peak
Average linear heat rate (kW/m)	18	18 × 0.7	18
Inlet mass flux (kg/s/m^2)	739	739	739 × 1.3

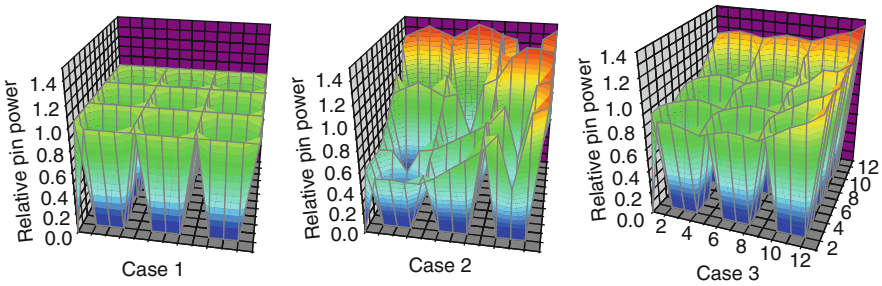


Fig. 6.62 Pin power distributions (1/4 assembly)

code by making all the parameters converge after a sufficiently long enough calculation time. For each case, the distributions of the cladding surface temperature the axial position having the highest temperature are compared between the steady-state and transient codes. They agree very well. The comparison in Case 2 is shown in Fig. 6.63 as an example.

6.8.2 Analyses of Flow Decreasing Events

As representative flow decreasing events, the "partial loss of reactor coolant flow" and the "total loss of reactor coolant flow" are analyzed. The former gives the highest increase in the cladding temperature among the flow decreasing transients analyzed by the single channel code. The latter gives the highest increase in the cladding temperature among the flow decreasing accidents, excluding the small LOCA, analyzed by the single channel code.

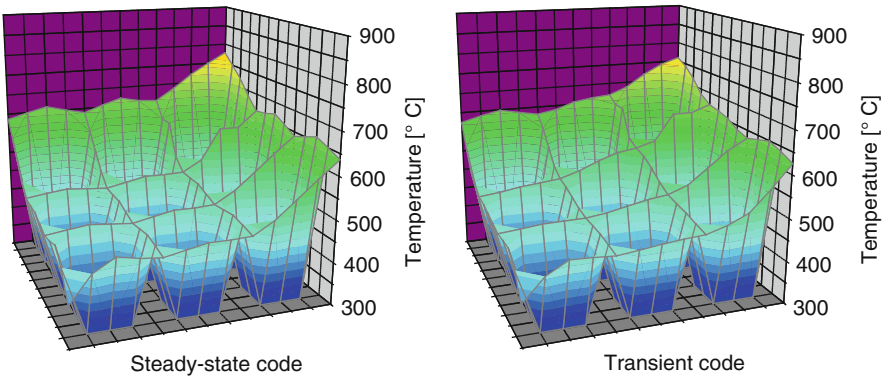


Fig. 6.63 Comparison of cladding surface temperature distribution in Case 3

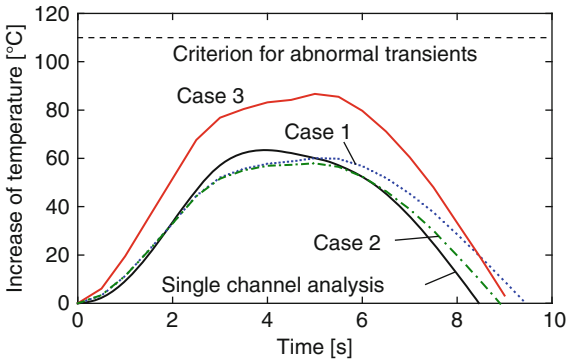


Fig. 6.64 Profiles of the ΔMCSTs at partial loss of reactor coolant flow

Since the transient subchannel analysis code does not have the functions prepared in typical system analysis codes, several parameters are taken from the calculation results by the single channel safety analyses performed in Sect. 6.7. These parameters are the flow rate, temperature and pressure at the inlet of the hot fuel assembly, and the relative power. The radial and axial power distributions are assumed not to change with time. This is reasonable because the reactivity is not locally changed at the flow decreasing events.

6.8.2.1 Partial Loss of Reactor Coolant Flow

The time profiles of the increase in the maximum cladding surface temperature (ΔMCST) are shown in Fig. 6.64. The peak values of Cases 1 and 2 are almost equal to that calculated by the single channel code while that of Case 3 is higher than the result by the single channel code by about 25°C.

The distributions of the cladding surface temperature at the axial position of the highest temperature are compared between the steady-state and the moment of

the highest ΔMCST in Figs. 6.65–6.67. For Case 1, the distributions are almost the same between the steady-state and transient conditions. That is why the ΔMCST is almost equal to that calculated by the single channel code.

For Case 2, the temperature distribution is expanded at the transient condition. In the subchannels surrounded by the fuel rods with relatively high power, the coolant density decreases earlier and hence the pressure drop caused by acceleration, friction, and grid spacers increases earlier, then the coolant escapes to the surrounding subchannels as cross flow. This phenomenon is called "flow-redistribution". For Case 2, the difference between the highest and lowest temperatures in the fuel

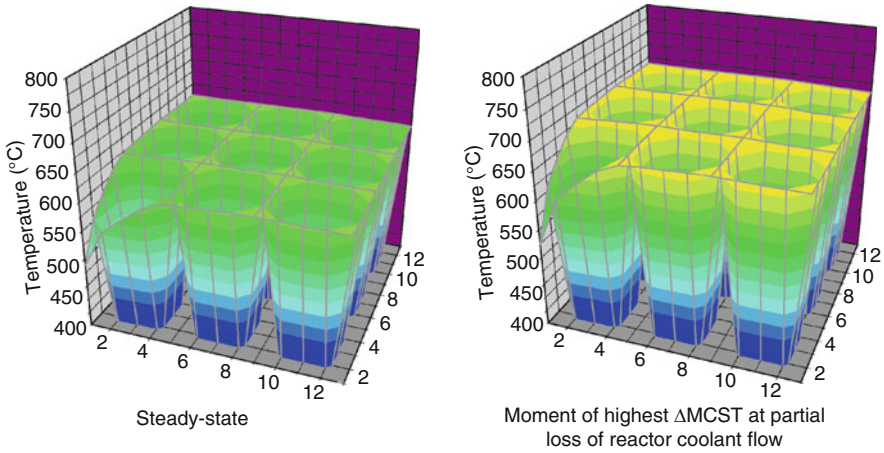


Fig. 6.65 Cladding surface temperature distributions in Case 1 (1)

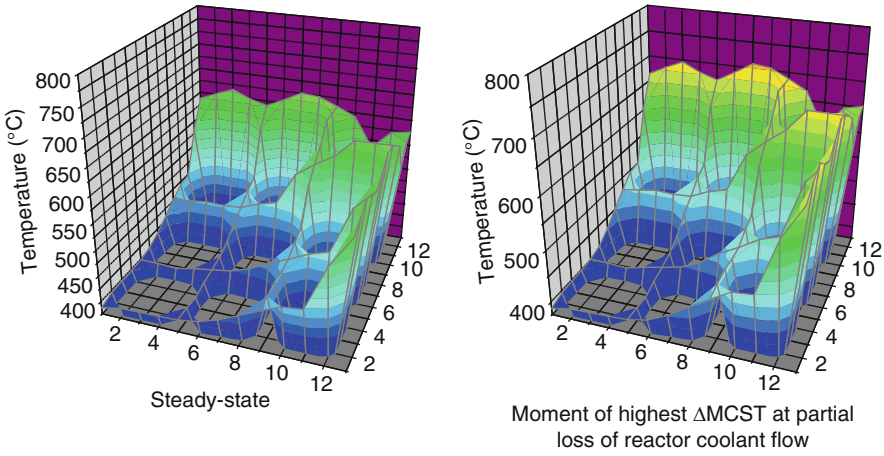


Fig. 6.66 Cladding surface temperature distributions in Case 2 (1)

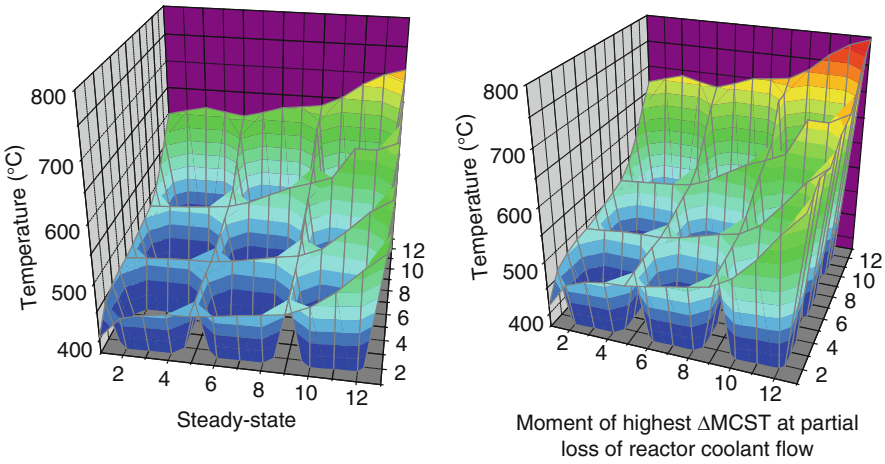


Fig. 6.67 Cladding surface temperature distributions in Case 3 (1)

assembly increases at the transient condition from the steady-state by about 50°C. The reason why the highest ΔMCST is almost equal to that calculated by the single channel code is that the coolant outlet temperature is relatively low, and hence the specific heat is relatively high due to the lower power to flow rate ratio (see Table 6.24).

For Case 3, the difference between the highest and lowest temperatures in the fuel assembly increases at the transient condition from the steady-state by about 75°C due to the strong flow-redistribution and the top peak power distribution. It should be mentioned, however, that the Super LWR still has a margin to the limitation of the ΔMCST although it decreases from 50°C to 25°C by considering the cross flow.

6.8.2.2 Total Loss of Reactor Coolant Flow

The time profiles of the ΔMCST are shown in Fig. 6.68. The distributions of the cladding surface temperature at the axial position of the highest temperature are compared between the steady-state and the moment of the highest ΔMCST in Figs. 6.69–6.71.

The same tendency as in the "partial loss of reactor coolant flow" is obtained although both the ΔMCST and the temperature difference in the fuel assembly are higher for this accident. The highest ΔMCSTs for Cases 1 and 2 are almost equal to that calculated by the single channel analysis while that for Case 3 is higher than the single channel result by about 140°C. The difference between the highest and lowest temperatures in the fuel assembly increases from the steady-state to the accident condition by about 120, 180, and 280°C for Cases 1–3, respectively.

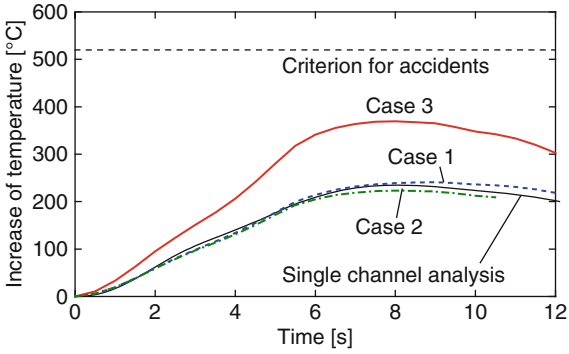


Fig. 6.68 Profiles of the ΔMCSTs at total loss of reactor coolant flow

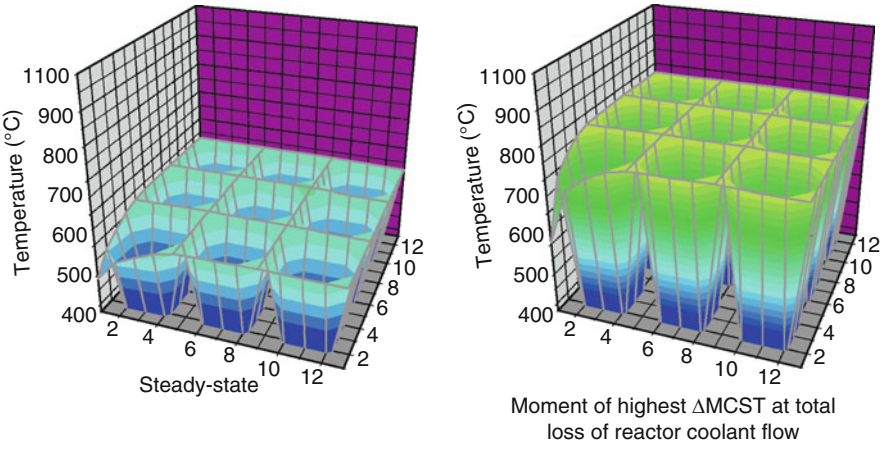


Fig. 6.69 Cladding surface temperature distributions in Case 1 (2)

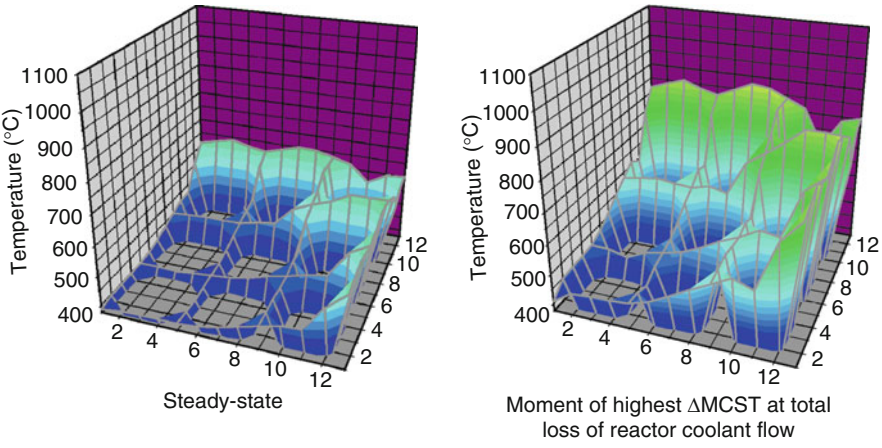


Fig. 6.70 Cladding surface temperature distributions in Case 2 (2)

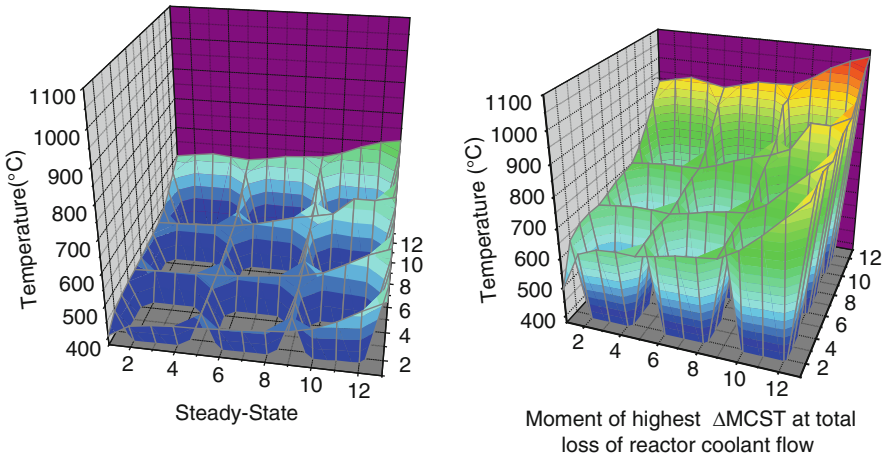


Fig. 6.71 Cladding surface temperature distributions in Case 3 (2)

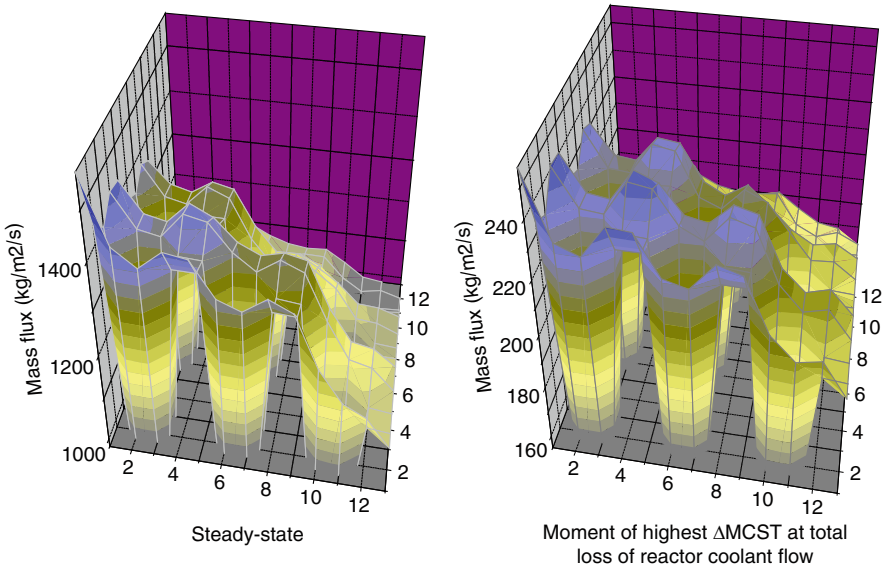


Fig. 6.72 Mass flux distributions in Case 3

The most significant flow-redistribution is recognized for Case 3. The mass flux distributions at the axial position of the highest temperature are compared between the steady-state and the moment of the highest ΔMCST in Fig. 6.72. It should be mentioned that the Super LWR still has a margin to the limitation of the ΔMCST although it decreases from 290°C to 150°C by considering the cross flow.

6.8.3 Summary

A transient subchannel analysis code for the Super LWR was introduced. Through the application of this code to the representative flow decreasing events, it was found that the temperature distribution in the fuel assembly became more significant at flow decreasing events due to the relative increase in the cross flow from high temperature subchannels to low temperature subchannels (flow-redistribution) when the pin-by-pin power distribution was strong. This increased the ΔMCST compared to the single channel safety analyses. The calculated ΔMCSTs by the transient subchannel analysis code were higher than those by the single channel model by about 25°C and 140°C, respectively, although the Super LWR still had a margin to each criterion.

6.9 Simplified Level-1 Probabilistic Safety Assessment

Both deterministic and probabilistic approaches are important and useful for clarifying the safety characteristics of new reactors concepts. In this section, simplified level-1 PSA (probabilistic safety assessment) of the Super LWR is introduced. Information from preliminary PSA studies on the SCWR [21, 33] and PSA documents for US LWRs [34–37] and for Japanese LWRs [38–41] is mainly referred to in this section.

6.9.1 Preparation of Event Trees

Five events are selected after referring to event trees used for BWRs [39, 41].

- Large LOCA
- Small LOCA
- Loss of offsite power (LOSP)
- Transients with power conversion system (PCS) available at the initial stage (T-PCS)
- Transients with PCS unavailable at the initial stage (T-nPCS)

The large LOCA is defined as a pipe break that leads to core damage unless the ADS is initiated. The small LOCA is defined as a pipe break that can avoid core damage while maintaining the supercritical pressure if the RCPs are intact. The classification of large, intermediate, and small LOCAs used in LWRs is not suitable for the Super LWR. The frequency of the large LOCAs in the Super LWR is given as a sum of the frequencies of the large and intermediate LOCAs in PWRs. The designation "PCS available" means that the condenser works as the final heat sink. Here, the transients with PCS unavailable at the initial stage are regarded as the "isolation of main steam line" and the "loss of turbine load" (without turbine bypass). The transients with PCS available are regarded as all other transients,

including the "loss of turbine load" (with turbine bypass). Interface LOCA and manual shutdown are not considered here.

The mitigation systems and actions for the Super LWR are selected by reference to LWRs. They are summarized in Table 6.25. The functions of these systems and actions can be categorized into several groups.

The event trees for the Super LWR are prepared using the initiating events and the mitigation systems and actions described above. A core damage sequence (CD) is assumed if one of the following conditions is satisfied.

- The fuel cladding temperature is expected to exceed the criterion for accidents due to a failure of core cooling.
- Heat removal from containment finally fails.
- The reactor finally cannot be kept subcritical.
- All the DC and AC power supplies are lost (total station blackout).

The event tree of the large LOCA is shown in Fig. 6.73. The normal sequence is: (1) reactor depressurization by the ADS; (2) negative reactivity insertion by the RPS; (3) core cooling by the LPCI; and (4) containment cooling by the RHR. A failure of the ADS is regarded as causing immediate core damage and written as the core damage sequence "AX1" in the event tree. During the core reflooding after the successful depressurization, the reactor might return to criticality or become supercritical if both the RPS and the SLCS fail, which might lead to a core damage sequence ("AC1C2" in the event tree). Even if the depressurization and negative reactivity insertion are both successful, a failure of the core cooling by the LPCI

Table 6.25 Mitigation systems and actions used in PSA of the Super LWR

Function	Mitigation system or action	Abbreviation in PSA	Symbol in text figures
Negative reactivity insertion	Reactor protection system	RPS	C1
	Standby liquid control system	SLCS	C2
	Manual depressurization for initiating SLCS	DEP	X2
Core cooling	Reactor coolant pumps (both turbine-driven and motor-driven)	RCP	R
	Auxiliary feedwater system	AFS	U
	Safety relief valves reclose		
	1 valve	SRVc1	P1
	2 valves	SRVc2	P2
	3 valves	SRVc3	P3
	Automatic depressurization system	ADS	X1
	Low pressure core injection system	LPCI	V
Containment cooling	Power conversion system	PCS	W1
	Residual heat removal system	RHR	W2
	Containment vent	CV	Y
Electricity	Emergency diesel generators	E/G	B
	Recovery of offsite power		
	in 0.5 h	ROSP 0.5 h	O1
	in 8 h	ROSP 8 h	O2

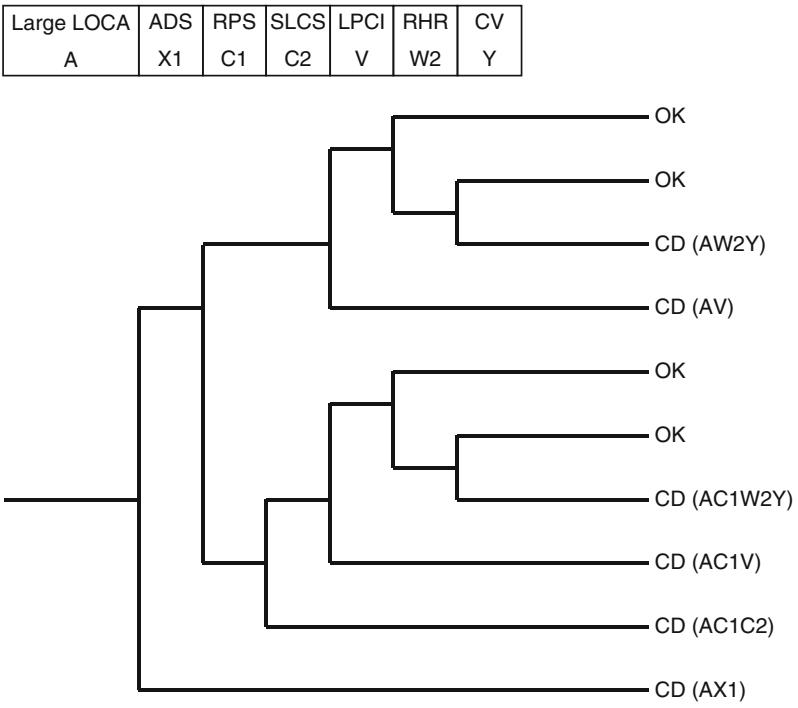


Fig. 6.73 Event tree of large LOCA (OK = "okay", CD = "core damage")

leads to two other core damage sequences ("AV" and "AC1V"). After the successful core cooling, containment cooling by the RHR or the CV is needed. If both fail, the core will be damaged ("AW2Y" and "AC1W2Y").

The event tree of the small LOCA is shown in Fig. 6.74. If the RPS operation is successful and the RCPs are intact, the core is expected to avoid a core damage sequence. Even if the RPS fails, it does not immediately cause core damage because the core power naturally decreases by the reactivity feedback as shown before in Fig. 6.45. However, negative reactivity needs to be inserted for final shutdown. To do that by the SLCS, the core needs to be manually depressurized (DEP). Thus, a failure of the manual depressurization or the SLCS after the failure of the RPS is regarded as two core damage sequences ("SC1X2" or "SC1C2"). If the RCPs are not intact, the core needs to be depressurized by the ADS and cooled by the LPCI, and then the containment needs to be cooled by the RHR or CV. The core damage sequences related to these systems are written as "SRX1," "SRV,", and "SRW2Y" in the event tree.

The event tree of the loss of offsite power (LOSP) is shown in Fig. 6.75. The turbine-driven RCPs are not available due to the turbine trip. The motor-driven RCPs are conservatively assumed to be always unavailable. If the RPS operation is

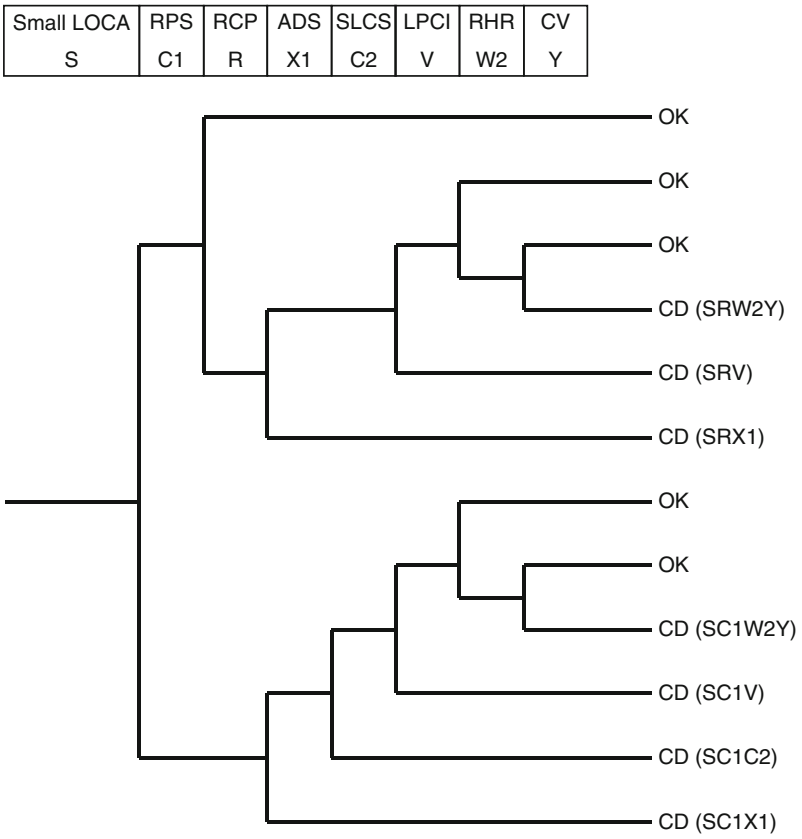


Fig. 6.74 Event tree of small LOCA (OK = "okay", CD = "core damage")

successful, core damage can be avoided without depressurization by maintaining core cooling at supercritical pressure. The core cooling at supercritical pressure is possible using the AFS. Since the AFS is turbine-driven, the core cooling should be maintained without electricity for at least 8 h. If both recovery of the E/G and recovery of the offsite power are not successfully obtained in 8 h, core damage is assumed because the decay heat cannot be removed by the LPCI after the AFS is no longer available. Thus, the failed supply of electricity during 8 h is regarded as a core damage sequence and it is written as "TeBO1O2" in the event tree. If the AFS fails, the reactor needs immediate depressurization by the ADS, then core cooling by the LPCI, followed finally by the containment cooling. The core damage sequence "TeUB" corresponds to a failure of supplying electricity from the E/G to the LPCI. It should be mentioned that a failure of the RPS does not immediately lead to core damage as long as the AFS is available (see Fig. 6.50). If the E/G is initiated or the offsite power is recovered, it is assumed that core damage can be

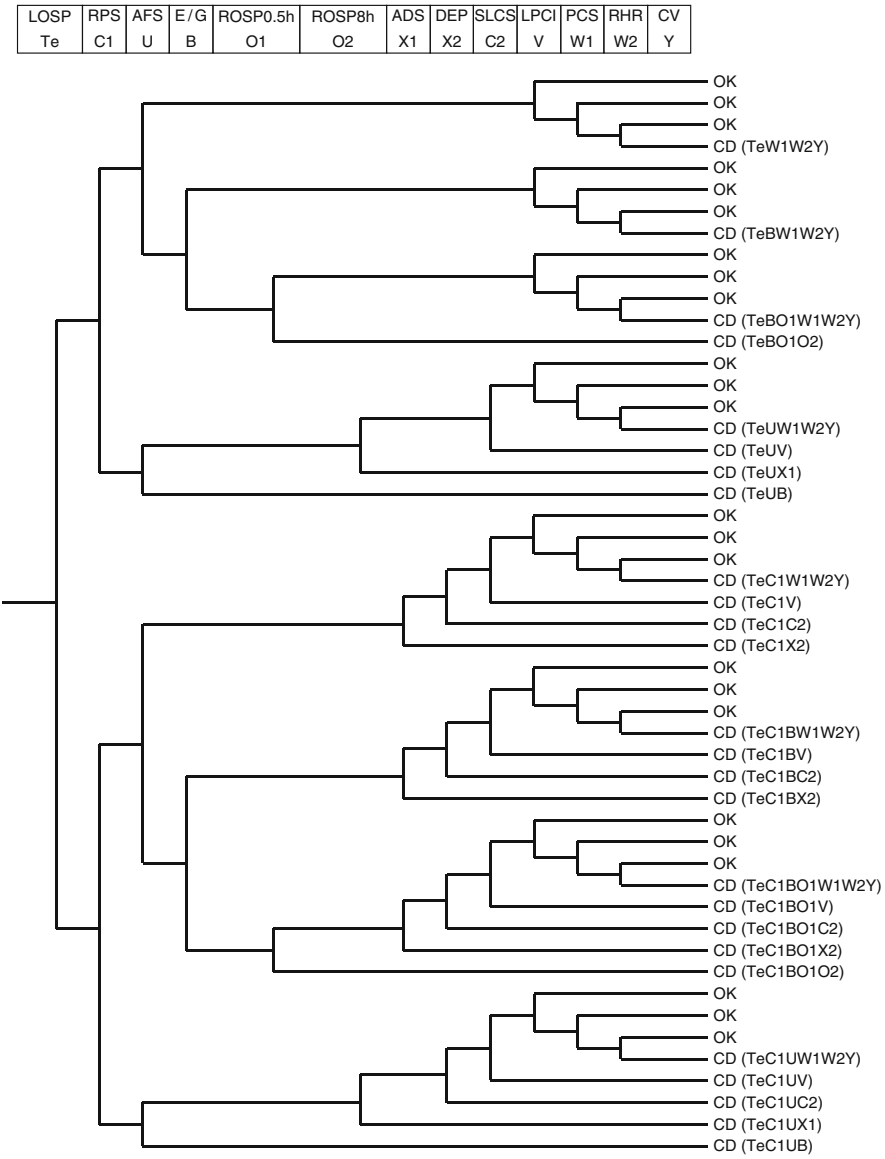


Fig. 6.75 Event tree of loss of offsite power (OK = "okay", CD = "core damage")

finally avoided by the manual depressurization, SLCS, LPCI, and containment cooling. If both the RPS and AFS fail, the reactor needs to be immediately depressurized by the ADS. In summary, the core damage sequences of the LOSP can be categorized as belonging to four groups: failures of core cooling (ending with "X1" or "V"), failures of containment cooling (ending with "Y"), failures to

supply electricity (ending with "B," "O1," or "O2"), and failures to keep the reactor subcritical (ending with "X2" or "C2").

The event tree of the transients with PCS available at the initial stage is shown in Fig. 6.76. Since the PCS is intact initially, which means that the steam can be discharged from the core to the condensers through the turbine control valves or the turbine bypass valves, the SRVs are not needed. However, the turbine-driven RCPs are assumed to be unavailable at all times because a turbine trip is taken into account. If both the RPS operation and initiation of the motor-driven RCPs are successful, it is assumed that the core can avoid core damage based on scenarios of BWRs [41]. Even if the motor-driven RCPs fail, core damage can be avoided by the successful function of the AFS and containment cooling. If the AFS fails, the

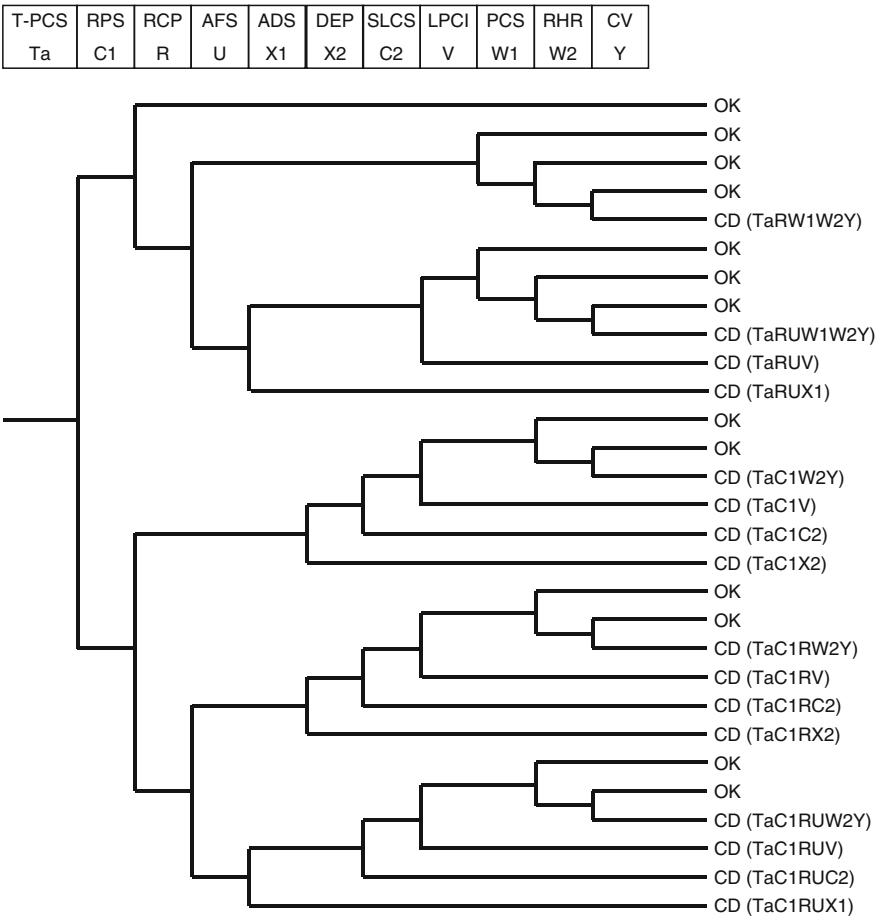


Fig. 6.76 Event tree of transients with power conversion system available at the initial stage (OK = "okay", CD = "core damage")

immediate depressurization by the ADS, then core cooling by the LPCI, and finally the containment cooling are necessary. If the RPS fails, it is necessary to automatically or manually depressurize the reactor, initiate the SLCS and finally cool the containment. In summary, the core damage sequences for this initiating event can be categorized as belonging to three groups: failures of core cooling (ending with "X1" or "V"), failures of containment cooling (ending with "Y"), and failures to keep the reactor subcritical (ending with "X2" or "C2").

The event tree of the transients with PCS available at the initial stage is shown in Figs. 6.77 and 6.78. It is assumed that the steam cannot be discharged from the core to the condenser due to the closure of the MSIVs or the turbine trip without turbine bypass. Thus, the SRVs need to be opened in order to protect the pressure boundary and also keep the coolant flow in the core. Since the safety valve function of the SRVs (see Sect. 6.3) is passively actuated, their failure to open is not considered for

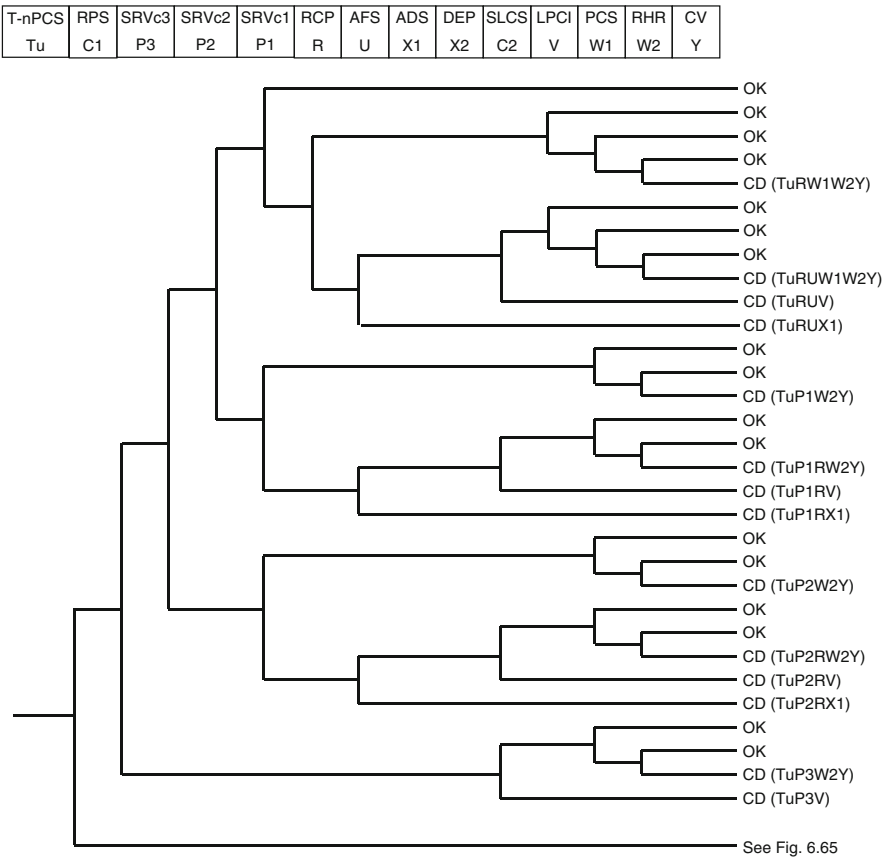


Fig. 6.77 Event tree of transients with power conversion system unavailable at the initial stage (1/2) (OK = "okay", CD = "core damage")

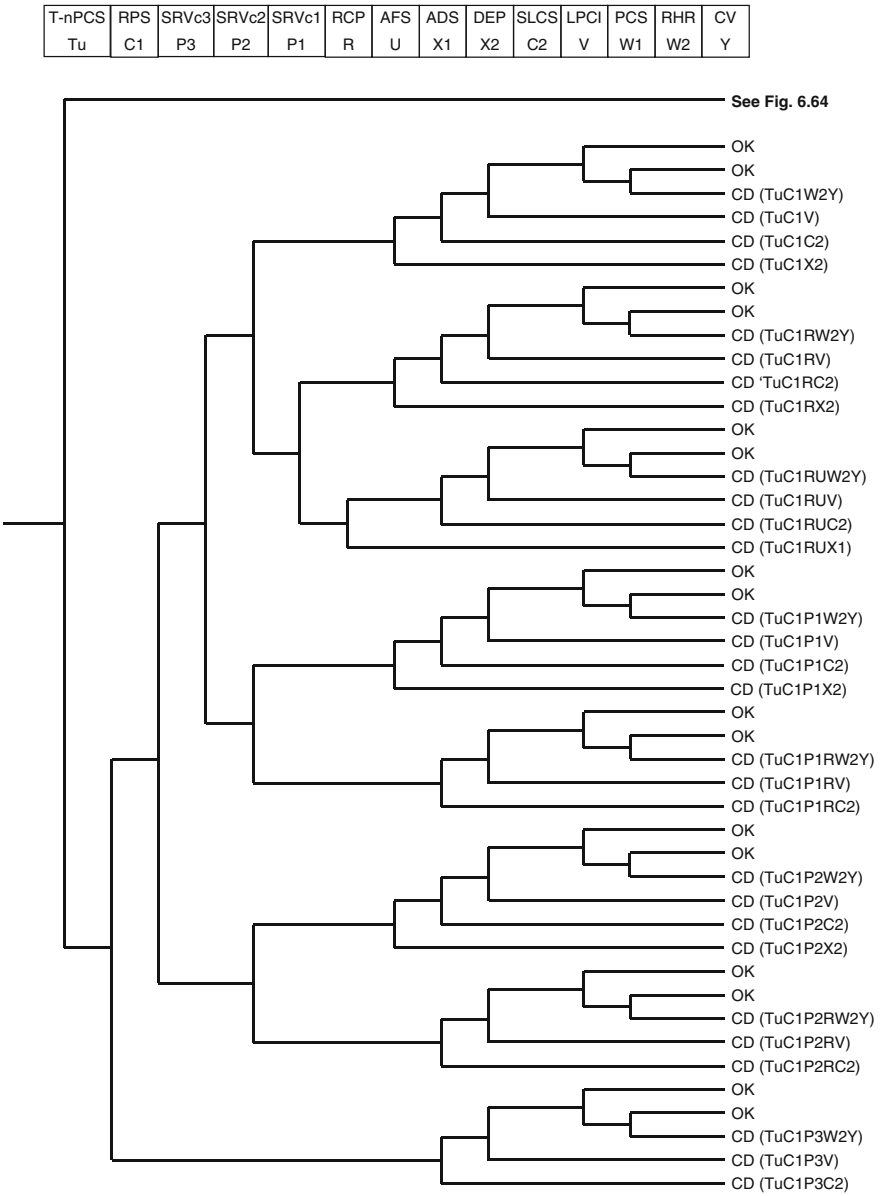


Fig. 6.78 Event tree of transients with power conversion system unavailable at the initial stage (2/2) (OK = "okay", CD = "core damage")

BWRs [41]. However, failures of the SRVs to reclose should be considered. The event tree of this initiating event is prepared by adding the failures of the SRVs to reclose ("SRVc3," "SRVc2," and "SRVc1") to the event tree of the transients with

PCS available at the initial stage (between the "RPS" and "RCP"). If all the SRVs are successfully reclosed after both the success and failure of the RPS, the event tree is the same as that of the transients with PCS available at the initial stage. If only one or two valves fail to reclose and the motor-driven RPCs are successfully initiated, it is assumed that the core can be cooled at supercritical pressure because the steam flow rate through the SRV(s) is up to 40% of the rated value while the capacity of the motor-driven RCPs is 50% of the rated value in total. If three SRVs fail to reclose, the pressure inevitably decreases like in the large LOCA, so that the core needs to be cooled by the LPCI. In the cases with failure of the SRV(s) to reclose, the containment needs to be cooled by the RHR or CV, not by the PCS. If the RPS fails, manual or automatic depressurization and initiation of the SLCS are finally needed. In summary, the core damage sequences for this initiating event can also be categorized into three groups like the transients with PCS available at the initial stage.

6.9.2 Initiating Event Frequency and Mitigation System Unavailability

As the Super LWR has never been constructed, it is impossible to prepare the database for PSA. However, taking suitable data from the available PSA database of LWRs helps to roughly estimate the core damage frequency (CDF) and to identify the dominant sequences for the CDF.

The frequencies of the initiating events used for the PSA of the Super LWR are summarized in Table 6.26. Since the reactor vessel is similar to those of PWRs, the frequencies of the LOCAs are taken from PWRs [40]. Since most of the abnormal transients of the Super LWR are taken from those of BWRs as shown in Table 6.4 [1], the frequencies of the three transients are taken from those of BWRs [41]. The unavailabilities of the mitigation systems are also taken from those of LWRs as summarized in Table 6.27. Since the control rods of the Super LWR are inserted from the core top like PWRs, the unavailability of the reactor protection system is taken from PWRs [40]. Since other safety systems, the containment system, and power conversion system are similar to those of BWRs, the unavailabilities of these systems are taken from those of BWRs [41].

Table 6.26 Initiating event frequencies

Abbreviation	Symbol	Frequency (year^{-1})	References
Large LOCA	A	6.2E-05[a]	PWR [40]
Small LOCA	S	1.5E-04	PWR [40]
LOSP	Te	3.9E-03	BWR [41]
T-PCS	Ta	2.4E-01	BWR [41]
T-nPCS	Tu	3.4E-02	BWR [41]

[a]Sum of large LOCAs (1.5E-05) and intermediate LOCAs (4.7E-05) of PWRs [40]

Table 6.27 Unavailabilities of mitigation systems

Mitigation system	Unavailability (demand^{-1})	References	Remark
RPS	1.26E-06	PWR [40]	
SLCS	2.7E-01	BWR [41]	1/2
RCP	At T-nPCS: 1.0E-01 At other events: 1.0E-02	BWR [41]	Feedwater system of BWRs
SRVc1	2.7E-02	BWR [41]	
SRVc2	1.3E-03	BWR [41]	
SRVc3	2.1E-04	BWR [41]	
ADS	At large LOCA: 6.2E-03 At other events: 1.7E-04	BWR [41]	
DEP	2.9E-03	BWR [41]	
AFS	4.2E-03	BWR [41]	1/3[a]
LPCI	At LOSP: 2.4E-03 At other events: 2.1E-03	BWR [41]	1/3
PCS	1.86E-02	BWR [41]	
RHR	At LOCAs: 4.44E-04 At T-PCS or T-nPCS: 4.33E-04 At LOSP: 4.34E-04 After failure of RPS: 8.05E-03	BWR [41]	1/2[b]
CV	3.7E-02	BWR [41]	
E/G	2.5E-02	BWR [41]	1/2[b]
ROSP 0.5 h	1.1E-01	BWR[41]	
ROSP 8 h	2.1E-02	BWR [41]	

[a]Unavailability of the RCIC of the BWR (4.2E-3) [41] multiplied by a factor to account for 3 HPIs (high pressure injections) of the PWR (0.1) [40]
[b]Conservatively using data of two trains despite having three trains in the Super LWR design

6.9.3 Results and Considerations

The CDF of the Super LWR is estimated and the total CDF is calculated as 1.0E-06. It is not very meaningful to compare this value with existing LWRs because the PSAs of LWRs are based on detailed plant designs and huge volumes of testing and operating data while the PSA here is based on a simple, conceptual design using LWR data. What is more important is to understand the safety characteristics of the Super LWR from considerations of the dominant sequences and the important mitigation systems and to compare them with LWRs.

The fundamental safety requirement is maintaining the core cooling flow even at LOCAs. The AFSs are designed for mitigating the loss of flow events, and their capacity is too small to maintain the core coolant flow at cold-leg break LOCAs. Thus, the core coolant flow must be maintained by the reactor depressurization and a failure of only the ADS leads to a core damage sequence at the large LOCA. The "AX1" is the most dominant core damage sequence occupying nearly 40% of the total CDF as shown in Fig. 6.79. Also, failure of only the LPCI at the large LOCA ("AV") is the third most dominant sequence in the Super LWR. As a result, the large LOCA gives the largest CDF among the five initiating events as shown in Fig. 6.80. On the other hand, failures of at least two systems among the accumulator, high and low pressure injection systems, and spray injection system are

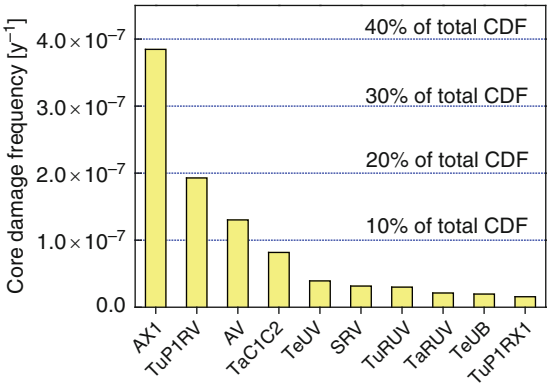


Fig. 6.79 Ten sequences with high CDF

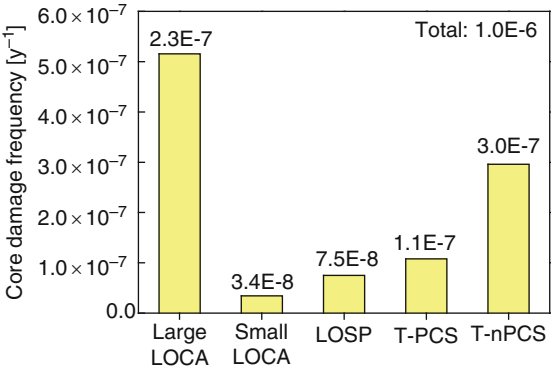


Fig. 6.80 CDFs from each initiating event

necessary to cause core damage at the large or intermediate LOCAs of PWRs. Also, failures of at least two systems among the high and low pressure injection systems and ADS are necessary to cause core damage at the large or intermediate LOCAs of BWRs.

Although the frequency of the small LOCA is more than twice of that of the large LOCA in the Super LWR, the CFD from the small LOCA is much smaller than that of the large LOCA. This is because the reactor depressurization is not necessary to avoid core damage as long as the RPS and RCPs work. Also, the unavailability of the ADS at the small LOCA is much lower than that at the large LOCA as shown in Table 6.27. The most dominant sequence in the small LOCA is "SRV" where the RCPs fail, then the ADS is successfully initiated but the LPCI fails to cool the core at low pressure. It is the sixth most dominant in the total CDF ranking and occupies less than 3% of the total CDF as shown in Fig. 6.79.

At LOSP, T-PCS, and T-nPCS, the turbine-driven RCPs which supply coolant to the core at the normal operating condition are assumed to be unavailable. The most dominant core damage sequence at those three transients is "TuP1RV" where one of the SRVs fails to close and also the motor-driven RCPs fail to start, then the automatic depressurization is successful but the LPCI fails. It is the second most

dominant sequence in the total CDF ranking and occupies nearly 20% of the total CDF as shown in Fig. 6.79. Although it is rare that both of the negative reactivity insertion systems (RPS and SLCS) fail, the "TaC1C2" occupies nearly 10% of the total CDF. This is because the frequency of the T-PCS is much higher than those of other initiating events as shown in Table 6.26. The transients related to "loss of flow" (LOSP, T-PCS and T-nPCS) give smaller CDFs than the large LOCA. One reason is that the motor-driven RCPs, AFS, and LPCI form a good "defense-in-depth" condition for supplying coolant.

The core damage sequences are finally caused by the failure of one of the safety functions described in Table 6.25. They are classified as several groups according to which function finally fails. The function of "core cooling" is divided into "supplying coolant to core" and "automatic depressurization". The contributions of the failures of each function are summarized and compared to LWRs in Fig. 6.81. The failure of "supplying coolant to core" occupies 46% in the Super LWR. It should be mentioned that six of the top 10 dominant sequences end with the failure of the LPCI ("V") as shown in Fig 6.79. The failure of "automatic depressurization" occupies 40% of the total CDF in the Super LWR and it comes mostly from "AX1" (the most dominant sequence) as mentioned above (Fig. 6.79). The contribution of "negative reactivity insertion" is below 10% in the Super LWR while it is about one fourth in BWRs. Also, it is not significantly larger than that in PWRs

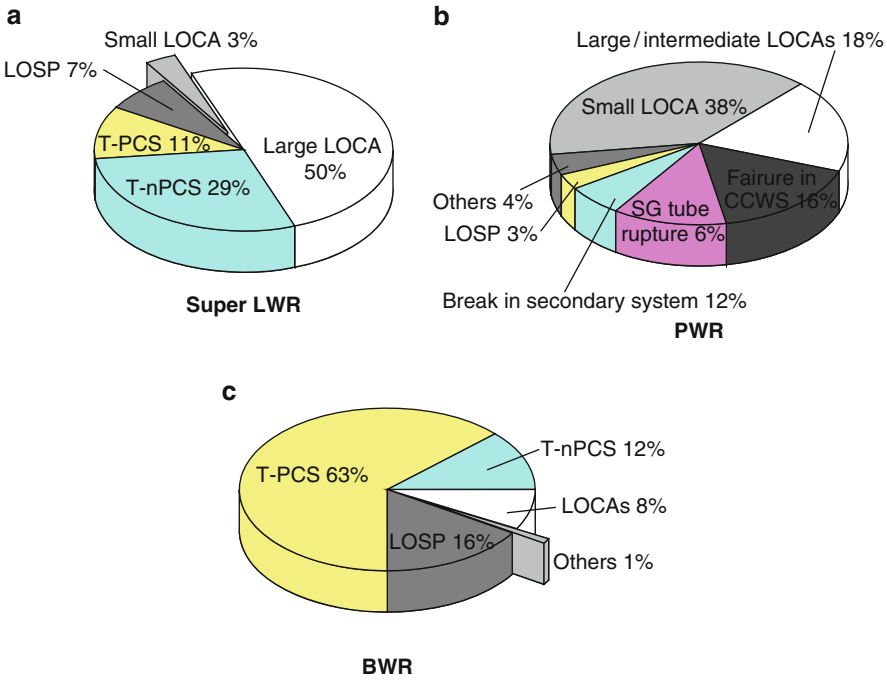


Fig. 6.81 Contributions of initiating events to total CDF in the Super LWR and LWRs

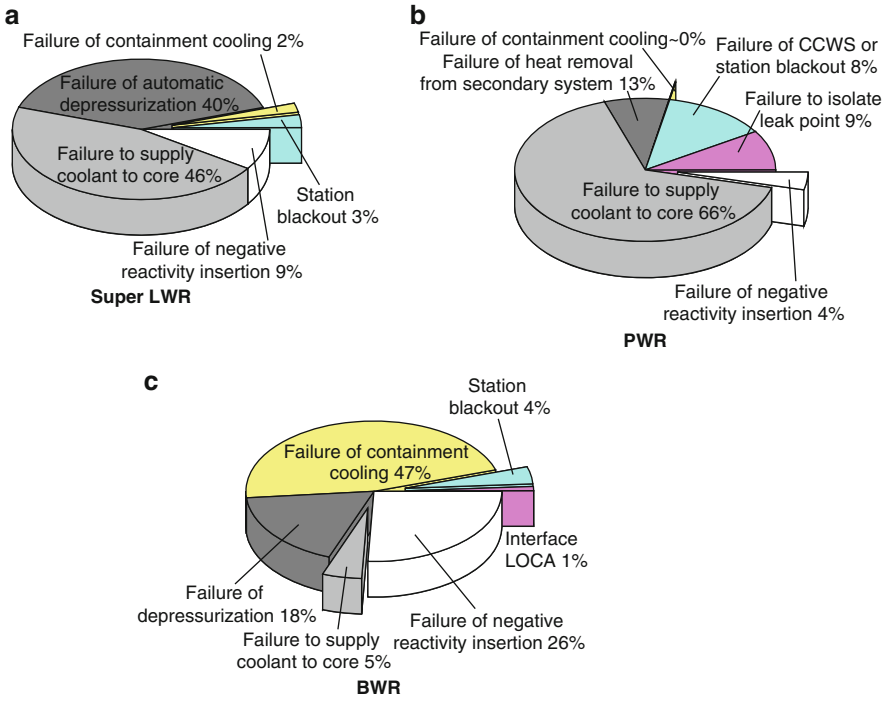


Fig. 6.82 Contributions of each function to the total CDF in the Super LWR and LWRs

although a diverse scram system is not credited in the Super LWR. As found out by the deterministic ATWS analyses in Sect. 6.7, the Super LWR can avoid core damage at the initial stage of the ATWS conditions as long as the core coolant flow is maintained at supercritical pressure or the automatic depressurization is successful. The failure of "containment cooling" is not dominant in the Super LWR and PWRs, while it occupies nearly half of the total CDF in BWRs. The station blackout is not dominant in any of the three reactors.

6.9.4 Summary

Based on the plant system design, the safety system design and the deterministic safety analyses described in Chap. 3, Sects. 6.3 and 6.7, respectively, the simplified level-1 PSA is performed. Although the event trees are simple and all the data are taken from those of LWRs, the PSA results allow a rough understanding of the safety characteristics of the Super LWR. The large LOCA occupies the largest fraction among the total CDF because failure of only the ADS or LPCI leads to core damage. It is expected to be reduced by improving the reliability of the ADS and LPCI or using an accumulator like PWRs do. All the transients, including the loss of

offsite power are assumed to be followed by the trip of the turbine-driven RCPs, and hence the CDF is mainly dominated by the failures of the systems supplying coolant to the core. Thus, the CDF from the transients will be reduced by improving the reliability of these systems. Also, utilizing forced or natural circulation of the coolant along with the heat exchanger in the recirculation system for the plant startup (see Sect. 5.7) might be an efficient accident management approach that reduces the CDF from the failure of "core cooling".

6.10 Summary

Safety studies on the Super LWR are summarized in this chapter. In contrast with LWRs, the appropriate safety principle for the Super LWR is not the inventory control but the flow rate control. It is the starting point for understanding the safety of the Super LWR. The safety system of the Super LWR is designed by referring to LWRs, especially BWRs, and at the same time taking the single safety principle of the Super LWR into account.

Safety analysis codes are prepared for the deterministic approach to the Super LWR safety. The possible abnormal transients and accidents in the Super LWR are selected from those of LWRs and analyzed using these codes. There are several key safety characteristics of the Super LWR that are inherent in the design features and their benefits have been identified through systematic safety analyses. In the case of loss of flow type accidents, fuel rod heat-up is mitigated by the "heat sink" and "water source" effects of the water rods. The response of the reactor power against the pressurization events is mild due to the small sensitivity of the average coolant density to the pressure and the flow stagnation of the once-through coolant cycle. The relative pressure change is also small due to the high steam density and the mild power response. The duration of the high cladding temperature is very short at the abnormal transients. Opening the ADS valves provides effective heat removal from the fuel rod. The "in-vessel accumulator" effect of the reactor vessel top dome enhances the fuel rod cooling. A large LOCA is mitigated by the ADS. The most important inherent safety characteristic is that the Super LWR does not need alternative actions to satisfy the safety criteria for ATWS events. It is also confirmed that the Super LWR has enough safety margin when the abnormal transients and accidents occur during the pressurization phase of the plant startup.

In order to investigate the influence of cross flow in the fuel assemblies on the safety margin, a transient subchannel analysis code for the Super LWR is prepared. It is found that the safety margin decreases at the flow decreasing events by considering the cross flow but the Super LWR still has a considerable safety margin.

For the probabilistic approach to the Super LWR safety, level-1 PSA is performed. The large LOCA is the largest fraction among the total CDF. All the transients, including the loss of offsite power, are assumed to be followed by the trip of the turbine-driven RCPs, and hence the CDF is mainly dominated by the failures of the systems supplying coolant to the core.

Glossary

ABWR	advanced boiling water reactor
ADS	automatic depressurization system
AFS	auxiliary feedwater system
ATWS	anticipated transient without scram
BDBE	beyond design basis event
BWR	boiling water reactor
CDF	core damage frequency/cumulative damage fraction
ECCS	emergency core cooling system
E/G	emergency diesel generator
FPP	fossil-fired power plant
HEM	homogeneous equilibrium model
LOCA	loss of coolant accident
LOSP	loss of offsite power
LPCI	low pressure core injection
LWR	light water reactor
MSIV	main steam isolation valve
PCMI	pellet cladding mechanical interaction
PCS	power conversion system
PCT	peak cladding temperature
PSA	probabilistic safety assessment
PWR	pressurized water reactor
RCIC	reactor core isolation cooling
RCP	reactor coolant pump
RHR	residual heat removal
ROSP	recovery of offsite power
RPS	reactor protection system
RPV	reactor pressure vessel
SCWR	supercritical pressure water cooled reactor
SG	steam generator
SLCS	standby liquid control system
SRV	safety relief valve
Super LWR	high temperature thermal reactor version of SCWR

References

1. Y. Ishiwatari, Y. Oka and S. Koshizuka, “Safety of the Super LWR,” Nuclear Engineering and Technology, Vol. 39(4), 257–272 (2007)
2. Y. Ishiwatari, Y. Oka, S. Koshizuka, A. Yamaji and J. Liu, “Safety of Super LWR, (I) Safety System Design,” Journal of Nuclear Science and Technology, Vol. 42(11), 927–934 (2005)
3. Y. Ishiwatari, “Safety of Super LWR,” Doctoral thesis, the University of Tokyo (2006) (in Japanese)

4. Y. Ishiwatari, Y. Oka, S. Koshizuka and J. Liu, "ATWS Characteristics of Super LWR with/without Alternative Action," Journal of Nuclear Science and Technology, Vol. 44(4), 572–580 (2007)
5. Y. Ishiwatari, Y. Oka, S. Koshizuka, A. Yamaji and J. Liu, "Safety of Super LWR, (II) Safety Analysis at Supercritical Pressure," Journal of Nuclear Science and Technology, Vol. 42(11), 935–948 (2005)
6. Y. Ishiwatari, Y. Oka, S. Koshizuka and J. Liu, "LOCA Analysis of Super LWR," Journal of Nuclear Science and Technology, Vol. 43(3), 231–241 (2006)
7. K. Kitoh, S. Koshizuka and Y. Oka, "Refinement of Transient Criteria and Safety Analysis for a High-temperature Reactor Cooled by Supercritical Water," Nuclear Technology, Vol. 135, 252–264 (2001)
8. F. D. Coffman, Jr., "LOCA Temperature Criterion for Stainless Steel Clad Fuel," NUREG-0065, (1976)
9. Y. F. Shen, Z. D. Cao and Q. G. Lu, "An Investigation of Cross Flow Mixing Effect Caused by Grid Spacer with Mixing Blades in Rod Bundle," Nuclear Engineering and Design, Vol. 125 (2), 111–119 (1991)
10. F. W. Dittus and L. M. K. Boelter, "Heat Transfer in Automobile Radiators of the Tubular Type," University of California Publications in English, Berkeley, Vol. 2, 443–461 (1930)
11. Proposed standard ANS-5.1 – 1971, American Nuclear Society (1971)
12. K. Kamei, "Core Design of Super LWR and Its Safety Analysis at Subcritical-pressure," Master's thesis, the University of Tokyo (2006) (in Japanese)
13. K. V. Moore and W. H. Rettig, "RELAP-4: A Computer Program for Transient Thermal-hydraulic Analysis," ANCR-1127, Aerojet Nuclear Company (1973)
14. J. R. S. Thom, W. M. Walker, T. A. Fallon and G. F. S. Reising, "Boiling in Subcooled Water During Flow Up Heated Tubes or Annuli," Proc. Inst. Mech. Eng. 180 (Part 3C) (1966)
15. V. E. Schrock and I. N. Grossman, "Forced Convection Boiling Studies, Final Report on Forced Convection Vaporization Project," TID-14632 (1959)
16. J. B. McDonough, W. Milich and E. C. King, "Partial Film Boiling with Water at 2000 psig in a Round Vertical Tube," MSA Research Corp., Technical Report 62 (1958) (NP-6976)
17. D. C. Groeneveld, L. K. H. Leung, A. Z. Vasic, Y. J. Guo and S. C. Cheng, "A Look up Table for Fully Developed Film Boiling Heat Transfer," Nuclear Engineering and Design, Vol. 225, 83–97 (2003)
18. D. C. Groeneveld, L. K. H. Leung, P. L. Kirillov, V. P. Bobkov, I. P. Smogalev, V. N. Vinogradov, X. C. Huang and E. Royer, "The 1995 Look-up Table for Critical Heat Flux in Tubes," Nuclear Engineering and Design, Vol. 163, 1–23 (1996)
19. R. C. Martinelli and D. B. Nelson, "Prediction of Pressure Drop During Forced-circulation Boiling of Water," Transactions of ASME, Vol. 71, 695–702 (1948)
20. J. H. Lee, S. Koshizuka and Y. Oka, "Development of a LOCA Analysis Code for the Supercritical-pressure Light Water Cooled Reactors," Annals of Nuclear Energy, Vol. 25 (16), 1341–1361 (1998)
21. J. H. Lee, "LOCA Analysis and Safety System Consideration for the Supercritical-Water Cooled Reactor," Doctoral thesis, the University of Tokyo (1996)
22. N. E. Todreas and M. S. Kazimi, "Nuclear Systems I – Thermal Hydraulic Fundamentals," Hemisphere Publishing Corporation, ISBN 0-89116-935-0 (1990)
23. F. M. Bordelon, et al., "SATAN IV Program: Comprehensive Space-time Dependent Analysis of Loss of Coolant," WCAP-8302 (1974)
24. A. Yamanouchi, "Effect of Core Spray Cooling in Transient Stat After Loss of Coolant Accident," Journal of Nuclear Science and Technology, Vol. 5(11), 547–558 (1968)
25. Y. Murao and T. Hojo, "Numerical Simulation of Reflooding Behavior in Tight-Lattice Rod Bundles," Nuclear Technology, Vol. 80, 83 (1998)
26. Anticipated Transients Without Scram for Light Water Reactors, NUREG-0460, US-NRC (1978)
27. Preliminary Safety Analysis Report Lungmen Nuclear Power Station Units 1 & 2, GE Nuclear Energy (1997)

28. ABWR Standard Safety Analysis Report, 23A6100 Rev. 1, GE Nuclear Energy (1993)
29. D. Y. Oh, S. H. Ahn and I. G. Kim, "Sensitivity Study on the Safety Parameters During ATWS with/without AMSAC," Proc. ICAPP'03, Cordoba, Spain, May 4–7, 2003, Paper 3149 (2003)
30. Y. Okano, S. Koshizuka, K. Kitoh and Y. Oka, "Flow-induced Accident and Transient Analyses of a Direct-cycle, Light-water Cooled, Fast Breeder Reactor Operating at Supercritical Pressure," Journal of Nuclear Science and Technology, Vol. 33(4), 307–315 (1996)
31. K. Kamei, A. Yamaji, Y. Ishiwatari, Y. Oka and J. Liu, "Fuel and Core Design of Super Light Water Reactor with Low Leakage Fuel Loading Pattern," Journal of Nuclear Science and Technology, Vol. 43(2), 129–139 (2006)
32. A. A. Amsden and F. H. Harlow, "The SMAC Method: A Numerical Technique for Calculating Incompressible Fluid Flows," Los Alamos Scientific Laboratory, Report LA-4370 (1970)
33. J. H. Lee, Y. Oka and S. Koshizuka, "Safety System Consideration of a Supercritical-water Cooled Fast Breeder Reactor with Simplified PSA," Reliability Engineering & System Safety, Vol. 64, 327–338 (1999)
34. Reactor Safety Study, An Assessment of Accident Risks in US Commercial Nuclear Power Plants, WASH-1400, Appendix-I, US Nuclear Regulatory Commission (1974)
35. Reactor Safety Study, An Assessment of Accident Risks in US Commercial Nuclear Power Plants, WASH-1400, Appendix-II, US Nuclear Regulatory Commission (1974)
36. Analysis of Core Damage Frequency from Internal Events: Peach Bottom Unit 2. Science Applications International Corp, NUREG/CR-4550, Vol. 4, US Nuclear Regulatory Commission (1986)
37. Severe Accident Risks: An Assessment for Five US Nuclear Power Plants, NUREG-1150, Vol. 1, US Nuclear Regulatory Commission (1990)
38. Level-1 PSA of 1,100 MWe-class PWRs: Annual Report of FY1997, Nuclear Power Engineering Corporation (NUPEC), INS/M97-04 (1998) (in Japanese)
39. Development of Level-1 PSA Methods for BWR Plants: Annual Report of FY1999, Nuclear Power Engineering Corporation (NUPEC), INS/M99-15 (2001) (in Japanese)
40. Development of Level-1 PSA Methods for PWR Plants at Power: Annual Report of FY2000, Nuclear Power Engineering Corporation (NUPEC), INS/M00-04 (2001) (in Japanese)
41. Development of Level-1 PSA Methods for BWR Plants: Annual Report of FY2000, Nuclear Power Engineering Corporation (NUPEC), INS/M00-09 (2001) (in Japanese)

Chapter 7
Fast Reactor Design

7.1 Introduction

A fast spectrum option of the SCWR is expected to be possible with the same plant system as the Super LWR. The fast spectrum SCWR studied at the University of Tokyo is called the Super Fast Reactor (Super FR). The Super FR produces a higher power rating than the thermal reactor with the same RPV size because moderator is not necessary, so the unit capital cost will be reduced further. In addition to the economical potential, the Super FR also offers more flexible fuel cycle options. This chapter aims to briefly describe the design, control, startup and stability, and safety of the Super FR.

7.2 Design Goals, Criteria, and Overall Procedure

7.2.1 Design Goals and Criteria

In order to provide economical competitiveness for the Super FR, the following design goals are established [1].

1. 1,000 or 700 MWe class intermediate scale reactor
2. Core average power density over 100 W/cm^3 including blanket region
3. Core average outlet temperature over 500°C
4. Core average linear heat rate around 17 kW/m
5. Average fuel assembly discharge burnup around 70 MWd/kgHM
6. Nonflat core in which active core height is similar to or larger than core equivalent diameter

Among them, the high power density is of most interest because it allows for reducing the size of the RPV, containment, and reactor building. Core average power densities of PWRs, BWRs, and the Super LWR are about 100, 50, and 60 W/cm^3, respectively. The average fuel assembly discharge burnup of

Y. Oka et al., *Super Light Water Reactors and Super Fast Reactors*,
DOI 10.1007/978-1-4419-6035-1_7, © Springer Science+Business Media, LLC 2010

70 MWd/kgHM is determined as the target, which is the same as that of typical FRs using MOX fuel [2]. The flat core concept has been known to be beneficial for reducing coolant void reactivity by increasing neutron leakage, but it increases the core equivalent diameter and consequent RPV wall thickness.

The following principle thermal design criteria are used in the Super FR design for assuring fuel and cladding integrities. They are taken from the Super LWR design, as described in Chap. 2.

1. Nominal value of the maximum linear heat generation rate (MLHGR) is less than 39 kW/m.
2. Nominal value of the maximum cladding surface temperature (MCST) is less than 650°C.

Figure 7.1 [1] shows the thermal design bases for the Super FR. It is similar to Fig. 2.13 for the Super LWR. The most bottom state denotes the core average condition with the outlet temperature of 500°C as a target value and with the average linear heat rate of 17 kW/m.

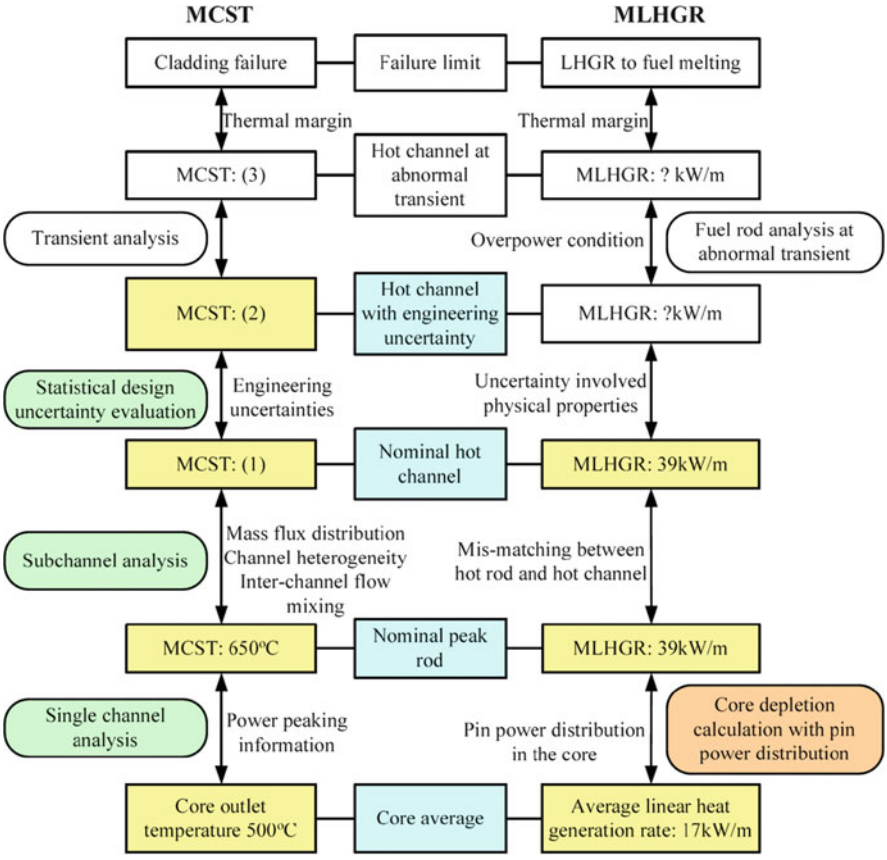


Fig. 7.1 Thermal design bases for the Super FR. (Taken from [1])

The nominal peak rod is defined as the fuel rod with the highest linear heat rate during normal operation. The highest linear heat rate is limited by the nominal design criterion of the MLHGR (39 kW/m), with which the cladding surface temperature is calculated by a single channel analysis and also limited by the nominal MCST of 650°C. The nominal peak rod is determined by the thermal hydraulic coupled neutronic depletion calculation introduced in Sect. 7.4.

The nominal hot channel is defined as a coolant channel location having the highest cladding surface temperature. The results of single channel analysis with the peak fuel rod are known to be more conservative than those from subchannel analysis in current LWRs having a large fuel rod gap clearance. Mass and energy of coolant at the hot channel are mixed with mass and energy of relatively cold coolant channels neighboring the hot channel, and coolant channel heterogeneity of the rectangular fuel pin arrangement is substantially smaller compared to the hexagonal arrangement. However, axial flow velocity and consequent axial momentum are much higher than those in the transverse direction because of the small fuel rod gap clearance (about 1.0 mm). For this reason, it is not well known if such conservatism of the single channel analysis can be kept in the Super FR design or not. Also, the location of the hot channel and hot rod might not be same, which would result from coolant channel heterogeneity and deflection of mass flux and coolant enthalpy by inter-channel mass and energy transfer. Subchannel analysis is used to determine the limiting thermal condition denoted as (1) in Fig. 7.1 [1].

"Nominal" means that all the actual operating conditions are the same as those of the design parameters. However, the actual individual operating condition (temperature, pressure, flow rate, etc.) must vary within a certain range around the nominal condition. Those uncertainties mainly come from measurement, calculation, fabrication, and data processing errors, which should be covered by the limiting thermal condition.

The local peaking factor is considered in the three-dimensional core depletion calculation of the Super FR, while it is separately considered by the assembly burnup analyses coupled with the subchannel analyses in the Super LWR (see Chap. 2). The reason is that the local power peaking is mainly caused by the zirconium hydride ($ZrH_{1.7}$) layers located in the blanket assemblies, introduced in Sect. 7.3. The local power peaking must be calculated along with the radial power distribution considering the arrangement of both the seed and blanket assemblies in the whole core, while it instead depends on the control rods and burnable poisons inside a fuel assembly in the Super LWR.

7.2.2 Overall Design Procedure

The overall core design procedure consists of three parts: (1) fuel rod design, (2) neutronic core design coupled with single channel analysis (TH coupled nuclear design), and (3) thermal hydraulic fuel assembly design by subchannel analysis. The overall diagram and interrelationships between the parts are depicted in

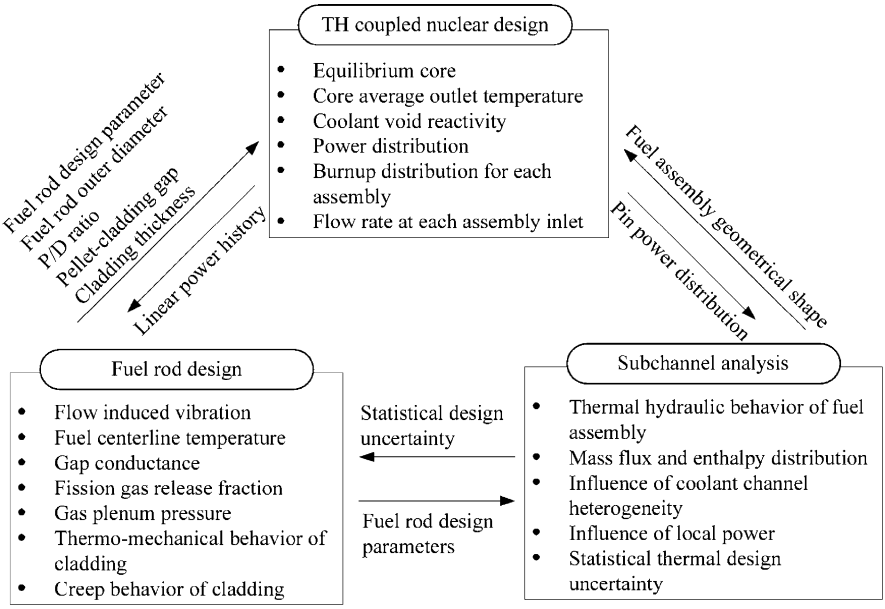


Fig. 7.2 Overall design procedure and interrelationships. (Taken from [1])

Fig. 7.2 [1]. All three parts are concatenated to other parts. Several iterations are conducted among them.

The fuel rod outer diameter and its pitch-to-diameter (P/D) ratio are determined in the fuel rod design part. The fuel rod design is divided into two areas. The former covers determining the fuel rod diameter and P/D so as not to violate the design goal and criteria. The latter covers determining the pellet-cladding gap and available design range in terms of the length, location, and initial pressure of the gas plenum. Cumulative damage fraction (CDF) of the cladding by creep is investigated by thermo-mechanical analysis.

The geometrical structure of the fuel assemblies and its influence on the cladding surface temperature are investigated by subchannel analysis, which provides an appropriate fuel assembly design to the TH coupled nuclear design part. Subchannel analysis also gives statistical design uncertainty associated with the MCST. This uncertainty is used as an input value for the thermo-mechanical behavior analysis of the fuel rod cladding.

The overall core design procedure provides the core-wide thermo-nuclear parameters. The core average outlet temperature, coolant void reactivity, power distribution, and flow rate distribution are calculated from the TH coupled nuclear design part. Most of the design goals are confirmed in this part. All the parameters related to the design goals and criteria are calculated in equilibrium states. The TH coupled nuclear design part also offers the pin power distribution as the input of both the fuel rod analysis and subchannel analysis.

7.3 Concept of Blanket Assembly with Zirconium Hydride Layer

Negative void reactivity is more necessary for water cooled reactors than liquid metal fast breeder reactors (LMFBRs) because the former are operated at high pressure, and hence a loss of coolant accident (LOCA) is one of the most important events. A great number of studies on various ways of reducing the void reactivity of FRs (both water and liquid metal cooled) have been aimed at developing the reactor concept with low void worth or eventually negative void worth. The ways that have been studied can be sorted into two basic approaches: the first is based on an increase in neutron leakage from the core, and the second, on the mitigation of neutron spectrum hardening. The design options to realize them are flattening core geometry (pancake cores), implementing various types of heterogeneous cores (axially heterogeneous or modular cores), and introducing moderating materials in the core [1]. Flattening the core enhances the neutron leakage at coolant voiding, thus reducing the void reactivity. The big disadvantage of such a design is an increase in capital cost due to the greatly enlarged diameter of the core. The mitigation of neutron spectrum hardening obtained by adding moderator (such as BeO) into the core is not very significant for reducing the void reactivity, while it has the disadvantage of causing significant degradation of the conversion ratio.

A new method was devised in the early study of the Super FR [3]. It utilizes neutron moderation through a fixed hydrogenous layer that is placed between the seed and blanket fuel regions. The effect was extensively analyzed in succeeding studies [4–11]. $ZrH_{1.7}$ is selected as the hydrogenous moderator layer material. It is a metal compound on or in which the hydrogen atoms are absorbed, and it contains more hydrogen atoms than water does. $ZrH_{1.7}$ has been used as the moderator of the driver core in the German KNK-II, an experimental liquid metal cooled fast reactor. The $ZrH_{1.7}$ pins were placed in the outer driver assemblies. Also, $ZrH_{1.7}$ was used in combination with steel inside the reflector assemblies. Experiences proved the suitable use of $ZrH_{1.7}$ under the temperature and radiation conditions in liquid metal fast reactor cores.

In this section, the effectiveness of the hydrogenous moderator layer in reducing the coolant void reactivity is explained. Its influence on breeding capability is also studied. The neutron spectra with and without the layer are analyzed and compared. Two different coolants, steam (water) and liquid sodium, are considered. The hydrogen leakage from the layer during normal operation and accidental conditions are also studied.

7.3.1 Effect of Zirconium Hydride Layer on Void Reactivity

Homogeneous cores (in the seed fuel region) of the Super FR and a LMFBR were adopted to study the effect of a $ZrH_{1.7}$ layer [12]. The calculation models of the cores are shown in Fig.7.3. Both cores are high enough that the transverse leakage

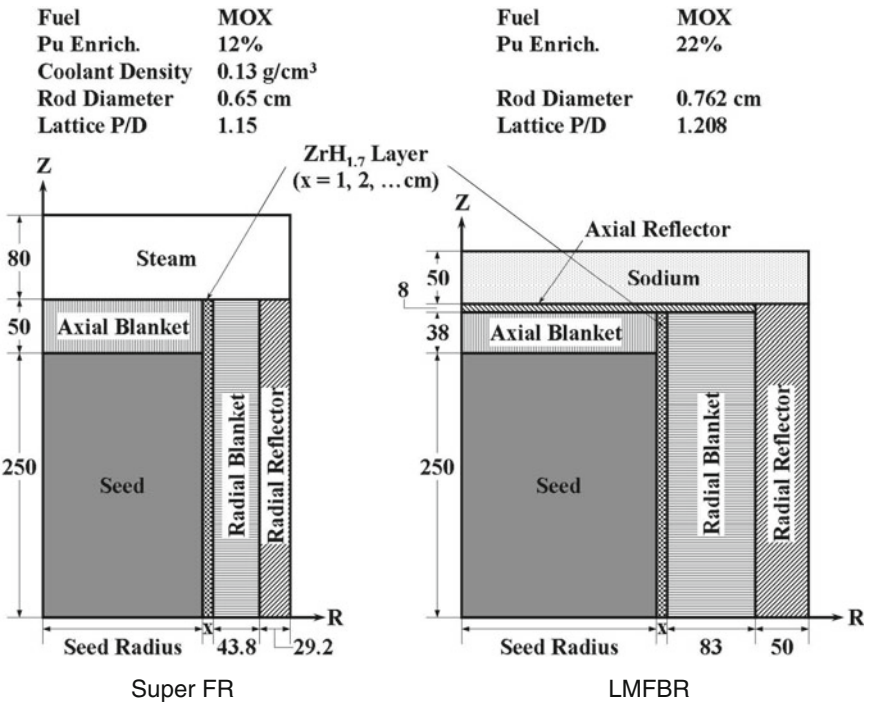


Fig. 7.3 Two-dimensional calculation models of the homogeneous cores (1/4 core) (in centimeters)

influence on void reactivity reduction can be neglected. The $ZrH_{1.7}$ layer is placed between the seed and radial blanket. Since the LOCA is the design basis accident of the Super FR, the complete void reactivity is considered. For the LMFBR, the seed sodium void reactivity is considered since it shows a higher value than the complete void reactivity. In both cases, for calculating the void reactivity, the coolant is placed above the core for conservatively estimating the leakage.

The multi-group diffusion code, CITATION, was used for the neutronic calculation adopting a two-dimensional model of the cores. The 3-group cross section sets were collapsed by the one-dimensional cell burnup calculations using the SRAC code system. The collision probability method with 107 group cross sections (61 fast and 46 thermal) was used for a multi-region unit cell calculation. The one-dimensional cylinder cell represents the fuel element divided into several concentric regions. The SRAC code system includes a burnup calculation. This process produces tabulated sets of cross sections prepared for the required ranges of burnup, material temperatures, and various cell compositions, and they are used later for the core calculation by the CITATION code. The burnup calculation assumes 3-batch core refueling, and the residence time of the radial blanket is a 3-core cycle. It is further assumed that the burnup proceeds linearly with time. The void reactivity

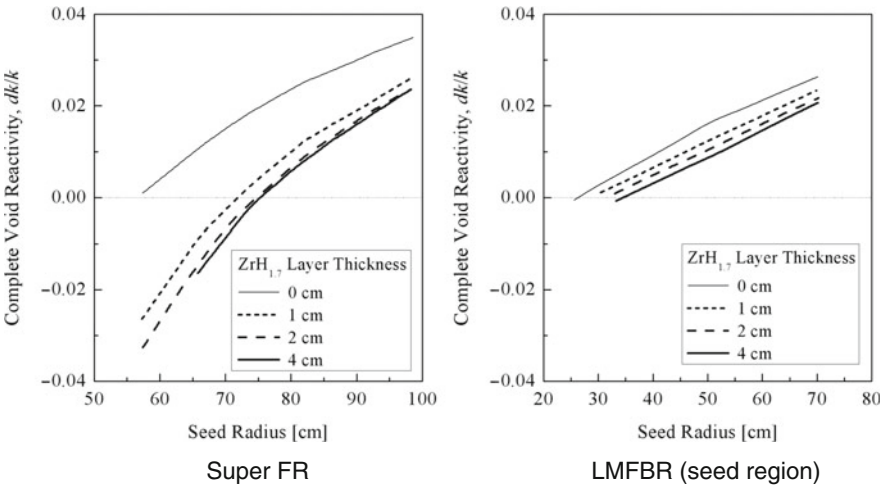


Fig. 7.4 Changes of void reactivity as a function of seed radius and $ZrH_{1.7}$ layer thickness in homogeneous cores

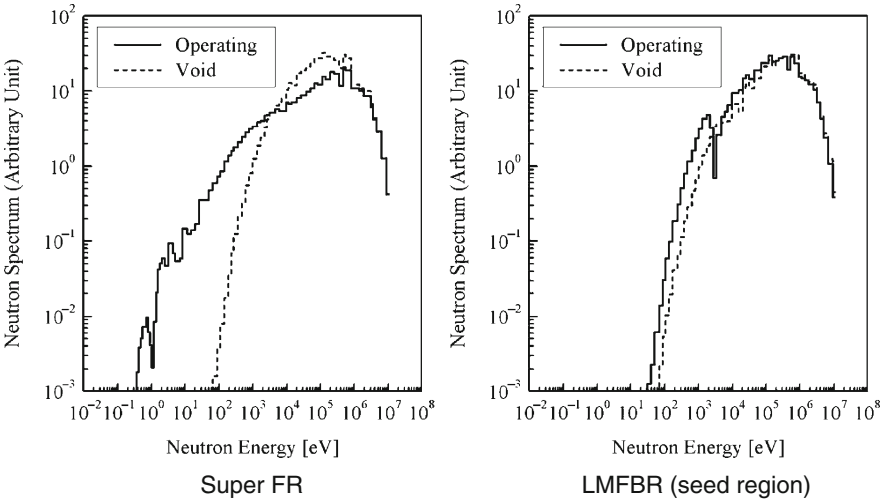


Fig. 7.5 Neutron spectra at complete void and normal operating conditions in homogeneous cores

results are based on the direct eigenvalue calculations with the cross sections prepared for each core zone at the voided state.

The changes of the void reactivity as a function of the seed fuel region radius and $ZrH_{1.7}$ thickness are shown in Fig. 7.4. In the case of the Super FR, using a 1-cm thick $ZrH_{1.7}$ layer has an equivalent effect to decreasing the radius of the seed fuel region by 35%. When the layer thickness is above 2 cm, the effect is saturated.

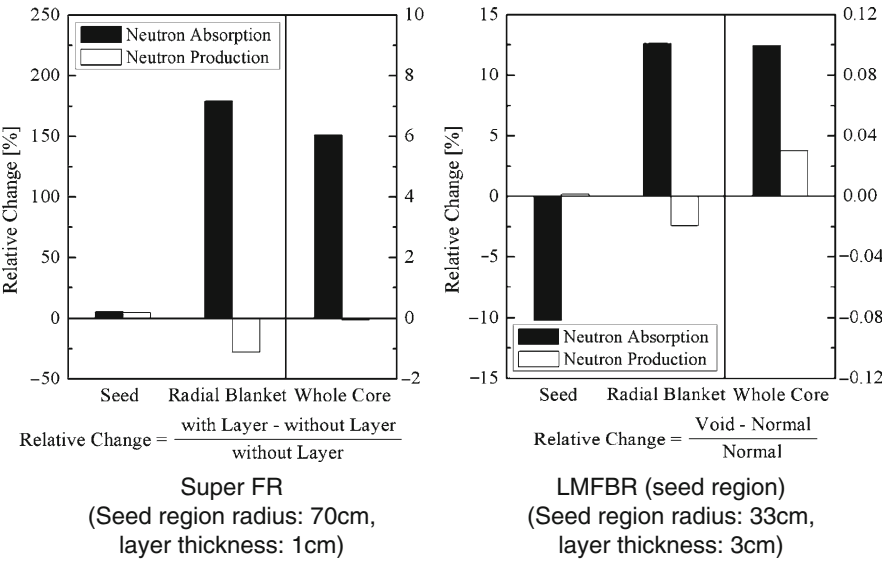


Fig. 7.6 Relative changes in neutron production and absorption in homogeneous cores with and without $ZrH_{1.7}$ layer at complete void condition

In the case of the LMFBR, where the neutron spectrum is much harder (see Fig. 7.5), 2–3 cm thicknesses of the layer are needed.

Both neutron production and neutron absorption change between the normal and complete void conditions, as shown in Fig. 7.6. It can be observed that the absorption significantly increases in the radial blanket of the Super FR, while the production decreases there. The blanket region dominates the reactivity change in the whole core. In the LMFBR also, the neutron absorption increases and neutron production decreases in the blanket region, while the opposite situation occurs in the seed region. The neutron absorption and neutron production in the whole core are dominated by the blanket region and seed fuel region, respectively.

The mechanism of reducing the void reactivity by the $ZrH_{1.7}$ layer is described as follows. At the void condition, both fast fission and neutron leakage increase. If the layer is placed facing the direction of the dominant neutron leakage, fast neutrons are slowed down in the layer due to scattering by hydrogen. Thus, the neutrons incoming to the blanket have reduced energy. Keeping in mind the threshold behavior of the fission cross section of ^{238}U (the main isotope in the blanket region) and an increase in its capture cross section at the low neutron energy region, the slowed down neutrons incoming to the blanket would produce fewer fast fissions and would have a better chance for absorption. Also, the capture to fission ratio for ^{239}Pu produced in the blanket region increases with decreasing energy. As a result, the neutron balance in the whole core becomes negative at the void condition. This realizes the negative coolant void reactivity.

The slowing down of neutrons in the layer plays an essential role in realizing negative void reactivity. The physical process of reducing void reactivity differs

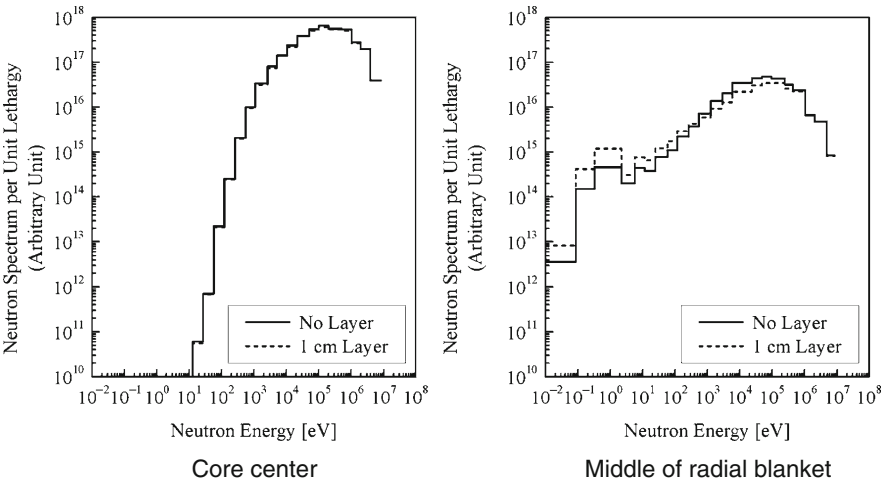


Fig. 7.7 Neutron spectra of homogeneous Super FR core at complete void condition (1)

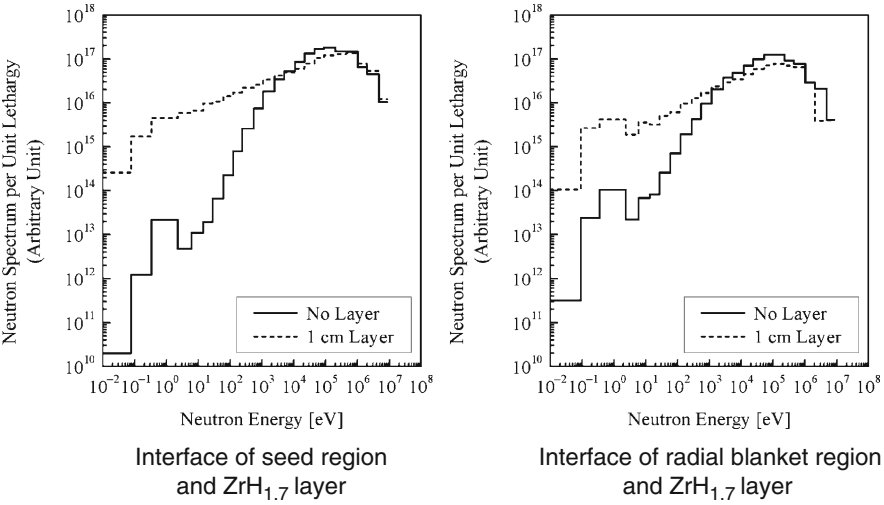


Fig. 7.8 Neutron spectra of homogeneous Super FR core at complete void condition (2)

from that of the conventional homogeneous introduction of moderator in a seed region where the main role of the moderator is mitigation of neutron spectrum hardening in the whole core region. When the hydrogenous moderator layer is used, the neutron spectrum is softened locally, not in the whole core. To illustrate this, the neutron spectra are compared between the core with and without a 1-cm thick layer at the void condition. The calculation is carried out by the one-dimensional CITATION code using 23 group cross sections. The spectrum is not affected far

from the layer, as shown in Fig. 7.7. It is, however, much softened by the layer at the interface of the layer and the seed or blanket region, as shown in Fig. 7.8.

7.3.2 *Effect of Zirconium Hydride Layer on Breeding Capability*

Since any introduction of moderator in fast breeder reactors causes a negative effect on their breeding capability, the effect of a fixed hydrogenous layer on breeding is analyzed in comparison with the homogeneous introduction of the same moderator in the seed region. The breeding capability is expressed through the surviving ratio, which is defined as the ratio of fissile atoms at the end to that at the beginning of the fuel cycle. The core configurations are the same as those given in Fig. 7.3, but the core characteristics are different. In the homogeneous Super FR, the fuel enrichment is selected as 15%, and the average coolant density is 0.13 g/cm^3 during operation. The core radius is 75 cm. The height of the seed fuel region is 110 cm, and axial blanket thickness is 5 cm. In the homogeneous LMFBR, the plutonium enrichment is 34%. The rod diameter is 0.882 cm, and the P/D is 1.306. The height and radius of the seed fuel region are 200 and 35 cm, respectively. The thickness of the radial blanket and radial reflector are 83.5 and 62.6 cm, respectively. The upper and lower axial blankets are 15 cm thick, while the thickness of the axial reflector is 8 cm. The absolute values of void reactivity and surviving ratio are compared in Table 7.1 for the Super FR and in Table 7.2 for the LMFBR. In both cases, the effect of the $ZrH_{1.7}$ layer on the surviving ratio is not significant, while the void reactivity is significantly reduced. On the other hand, the homogeneous mixture does not significantly reduce the void reactivity, and it gives a lower surviving ratio compared to the layer.

At the operating condition with existence of coolant, the neutron spectrum in the whole core is not much affected by the presence of the hydrogenous moderator

Table 7.1 Effect of $ZrH_{1.7}$ on complete void reactivity and surviving ratio of Super FR

Addition of $ZrH_{1.7}$	Complete void reactivity (%)	Surviving ratio
None	+1.575	1.11
Layer with 2 cm thickness	−0.004	1.09
1.1% Homogeneous mixture in seed fuel	+0.763	1.02

Table 7.2 Effect of $ZrH_{1.7}$ on complete void reactivity and surviving ratio of LMFBR

Addition of $ZrH_{1.7}$	Void reactivity (%) (complete void at seed region)	Surviving ratio
None	+0.67	1.510
Layer with 1.9 cm thickness	−0.04	1.461
3% Homogeneous mixture in seed fuel	+0.31	1.430

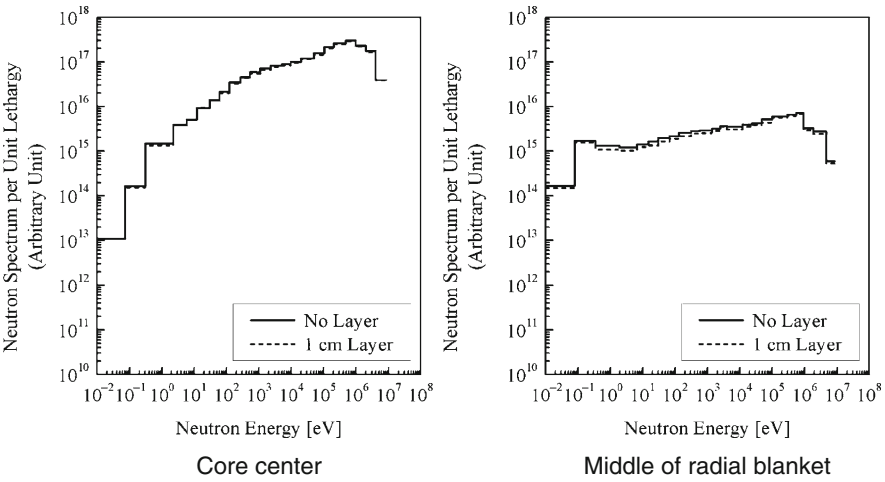


Fig. 7.9 Neutron spectra of homogeneous Super FR core at normal operating conditions

layer, as can be seen in Fig. 7.9. This is the reason why the breeding capability is not deteriorated so much. Compared to the cases with no $ZrH_{1.7}$, the surviving ratio is more reduced by the $ZrH_{1.7}$ layer in the LMFBR than in the Super FR. This is because the smaller radius of the seed region of the LMFBR makes the region relatively larger in which the spectrum is softened by the layer.

7.3.3 *Effect of Hydrogen Loss from Zirconium Hydride Layers on Void Reactivity*

The residence time of the $ZrH_{1.7}$ layer would be the same as that of the blanket fuel, that is, three fuel cycles in the inner blanket or six fuel cycles in the radial blanket. During that time, hydrogen from $ZrH_{1.7}$ will permeate through the stainless steel layers, which wrap the $ZrH_{1.7}$. The permeation rate is estimated assuming that the chemical equilibrium of zirconium and hydrogen in ZrH_x is achieved. The hydrogen pressure P is determined from the following relationship [13]:

$$\log P = -1.95 \times 10^4 \left(\frac{1}{T + 273} - \frac{1}{923} \right) + 11.962x^2 - 26.556x + 19.966, \quad (7.1)$$

where T is the maximum operating coolant temperature (°C) and x is the hydrogen content in ZrH_x.

The hydrogen permeability, p, is given by

$$p = 4.7 \times 10^{-6} \exp\left[-\frac{81.5 \times 10^3}{R(T + 273.5)}\right]. \tag{7.2}$$

The permeation rate, ϕ, depends on the thickness of the stainless steel layer d.

$$\phi = p \times \sqrt{P}/d. \tag{7.3}$$

The long-term permeation rate of hydrogen from the $ZrH_{1.7}$ layer is calculated. The permeation rate of hydrogen from the $ZrH_{1.7}$ layer depends on the temperature, cladding material, cladding thickness, and layer thickness. Figure 7.10 shows the hydrogen permeation rate for several different temperatures. It can be observed that the hydrogen permeation rate increases with temperature and time. The increase due to the temperature rise is caused by the increase in hydrogen pressure, as understood by (7.1). For a 3-year period, it is seen that the hydrogen content remains high even at 550°C. The hydrogen content will be kept high by increasing the layer thickness and cladding thickness.

The short-term permeation rate of hydrogen from the $ZrH_{1.7}$ layer at an accident is also calculated. The hypothetical scenario in which the temperature of the $ZrH_{1.7}$ layer is suddenly increased to 1,260°C (the criterion of the cladding surface temperature at the LOCA is created, and the void reactivity is analyzed). The results are shown in Fig. 7.11. It can be seen that several hours are needed to lose one third of the hydrogen from the layer. That is much longer than the time required for the control rod insertion and borated water injection. Therefore, the hydrogen loss does not impose any severe problem for reactor safety.

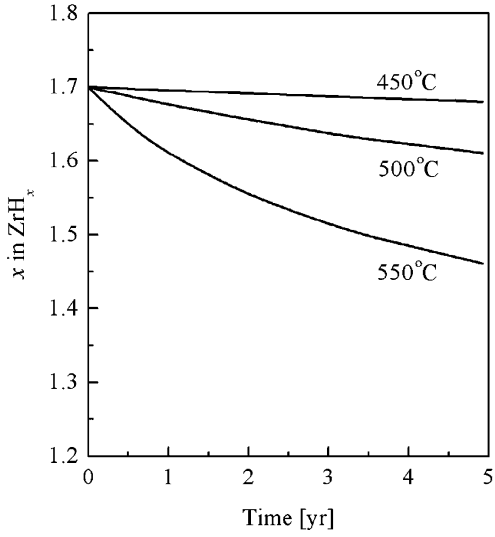


Fig. 7.10 Long-term, steady-state permeation rate of hydrogen from $ZrH_{1.7}$ layer as a function of layer temperature (Layer thickness, 0.9 cm; cladding thickness, 0.376 cm)

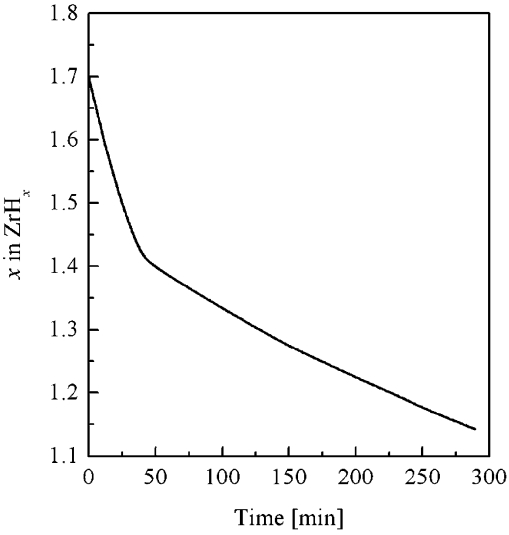


Fig. 7.11 Short-term permeation rate of hydrogen from the ZrH_x layer at 1,260°C. (Layer thickness, 0.9 cm; cladding thickness, 0.376 cm)

7.4 Fuel Rod Design

7.4.1 Introduction

Mixed-oxide fuel (MOX: $PuO_2 + UO_2$) has been used as fuel material for the fuel design of the Super FR. The plutonium nuclide amounts used in this study are shown in Table 7.3 [1]. Fissile plutonium (^{239}Pu and ^{241}Pu) occupies about 57.8 wt%. The plutonium enrichment is controlled by adjusting the weight fraction of plutonium oxide and uranium oxide. In general, depleted uranium having ^{235}U content of 0.2% is used for making MOX fuel.

The fuel cladding of the Super FR fuel cladding is subjected to high compressive stress because of the large pressure difference between internal pressure and coolant pressure at the beginning of lifetime (BOL). The compressive stress on the fuel cladding of the Super FR is about 1.2 times larger than that of PWRs. In addition to the high coolant pressure, the maximum cladding temperature of the Super FR is much higher than those of current LWRs. Furthermore, burning MOX fuel produces large releases of fission gases and swelling; both impose high hoop stress on the fuel cladding at the end of lifetime (EOL). At present, stainless steels have been regarded as the most promising candidate for the cladding material owing to their many irradiation experiences in nuclear reactors.

The operating conditions involved in the fuel rod design of the Super FR fuel rod design at BOL are similar to those of PWRs where compressive stress on the fuel cladding is important, while those at EOL is similar to those of LMFBRs where tensile stress on the cladding from fission gas release and pellet swelling is important. Compressive stress or cladding collapse is not a concern in LMFBR

Table 7.3 Plutonium nuclide amounts in fresh MOX fuel of the Super FR. (Taken from [1])

Nuclides	Weight percent (wt%)
Pu-238	0.4
Pu-239	51.3
Pu-240	37.8
Pu-241	6.5
Pu-242	4

fuel design because LMFBRs are operated at nearly atmospheric pressure, but creep rupture of cladding at EOL is a major concern. In this context, it has been a basic design issue if fuel and cladding integrities can be kept throughout the whole fuel lifetime under the operating conditions of the Super FR with currently available cladding materials or candidate materials. In order to investigate those potentials and applicabilities, the failure modes of the fuel and cladding and the requirements to prevent them need be quantitatively clarified.

7.4.2 Failure Modes of Fuel Cladding

In order to establish the fuel rod design criteria, it is necessary to investigate, which modes of the fuel rods might be limiting under the Super FR operating conditions. For this purpose, it is helpful to examine what kinds of fuel rod failure modes have been considered in LWRs and LMFBRs. Brief summaries of the fuel rod failure modes that have been considered in LWRs and LMFBRs and that might also be limiting in the Super FR are given below.

7.4.2.1 Melting of Fuel Pellets

Melting of fuel pellets has been traditionally considered as leading to cladding failure. It is assumed that a fuel rod fails if misalignment of the fuel centerline takes place because of high temperature melting. For normal operation and anticipated operational occurrences, misalignment of the fuel centerline due to melting is not permitted. The melting temperature of MOX is 2,740°C in the ideal, unirradiated case, which is slightly lower than that of UO_2 (2,805°C) for the unirradiated case. Taking the fabrication uncertainty in the oxygen-to-metal ratio in fuel pellets into consideration, 2,650°C was used as the design criterion in MOX fuel design for the MONJU reactor. Both the fuel centerline temperature and MLHGR have been used as the design criteria. Table 7.4 [1] shows the design criteria that have been used in several LMFBR designs. The MLHGR directly corresponds to the fuel centerline temperature with given pellet-cladding gap and initial gas pressure regardless of the fuel pellet diameter, as stated in Chap. 2. The fuel centerline temperature should be estimated with the MLHGR over the fuel lifetime, including the available over-power margin for abnormal transients, hot spot factors, and uncertainties.

Table 7.4 Fuel rod design criteria for LMFBRs. (Taken from [1])

Failure	Design criteria	CRBRP	MONJU	SNR-2
Overheating of fuel pellets	Fuel centerline temperature (°C)			
	Normal	2,350	2,350	2,200
	Anticipated transient	–	2,600	–
	Peak linear heat rate (kW/m)	42	36	42
Overheating of cladding	Cladding mid-wall temperature (°C)			
	Normal	700 (675)	675 (700)	650
	Anticipated transient	788	830	–
	Unlikely event	871	830	–

Numbers in parentheses indicate values for blanket fuel rods

7.4.2.2 Overheating of Cladding

Overheating of cladding has also been considered as leading to cladding failure if the thermal criteria, MDNBR for PWRs and MCPR for BWRs, are not satisfied. In LMFBRs, the maximum cladding mid-wall temperature has been limited. The design criteria for cladding overheating of several LMFBRs are shown in Table 7.4 [1].

7.4.2.3 Cladding Collapse

Cladding collapse failure can be classified into two phenomena. One is the time independent failure due to densification of fuel pellets under a high outer pressure of fuel rod. The other is the time dependent failure due to elastic instability arising from initial deviation from cladding ovality. Collapse failures have been eliminated in modern fuel rod designs of LWRs by the fabrication process of high density sintered pellets. If the cladding collapses, it closes the gap between pellet and cladding. This decreases the fuel centerline temperature due to an increase in the gap conductance. Even though the cladding is collapsed in the fuel region, fuel pellets support it. In contrast, if cladding in the gas plenum region is collapsed and is not supported by any internal structure such as the support spring, the gas plenum volume will be significantly reduced, which leads to high hoop stress because of an increase in the gas plenum pressure.

Collapse failures have not been a concern in LMFBRs due to the low coolant pressure. Rather, rupture of cladding has been a greater concern in LMFBRs than collapse. Rod internal pressure is always higher than coolant pressure. Only hoop tensile stress is a consideration.

7.4.2.4 Rod Overpressure

Rod overpressure has been considered as a hypothetical cladding failure in LWR fuel rod designs. If rod internal pressure becomes larger than coolant pressure, outward creep of fuel cladding may start. If outward creep rate exceeds the fuel

swelling rate, the pellet-cladding gap may increase. This phenomenon is called "liftoff." The liftoff of fuel cladding may decrease gap conductance, and that in turn, will increase fission gas release because of an increase in pellet temperature. Thus, such a positive feedback effect between gap conductance and pellet temperature may cause a quick increase in fuel centerline temperature and may finally lead to fuel failure. This is the reason why rod overpressure is avoided in PWRs and BWRs.

Rod overpressure has not been considered as a cause of cladding failure in LMFBRs using MOX fuel because swelling rate of MOX fuel is larger than that of UO_2 fuel. To ensure the cladding mechanical integrity under high internal pressure, LMFBRs use the design criterion of creep rupture rather than internal gas pressure itself.

7.4.2.5 Pellet Cladding Interaction

Pellet cladding interaction (PCI) may result in cladding failure during rapid power ramp due to large tensile stress and iodine-assisted stress corrosion cracking. Two kinds of design criteria have been applied in the LWR fuel rod design. One is to limit the uniform inelastic hoop strain below 1%. The other is to avoid fuel melting, which is also mentioned in Sect. 7.4.2.1. Large volume expansion resulting from fuel melting might cause high tensile stress on fuel cladding. Even now, the design criterion against PCI phenomenon in LWRs is still a design issue.

7.4.2.6 Other Failure Modes

Fretting of the fuel rods has been considered a failure mode. It results from erosion by debris collecting at the interference between the fuel rods and grid spacers or flow induced vibration (FIV) of the fuel rods and grid spacers. Corrosion, hydriding and embrittlement of cladding at LOCA have also been regarded as fuel failure modes in LWRs.

7.4.3 Fuel Rod Design Criteria

The fuel rod design criteria of the Super FR for each failure mode are summarized in Table 7.5 [1]. Each criterion is explained below.

7.4.3.1 Thermal Design Criteria

As one thermal design criterion to prevent overheating of the fuel pellet, melting of the pellet centerline should be avoided even considering various uncertainties. The fuel centerline temperature of 1,900°C and the MLHGR of 39 kW/m are used as

Table 7.5 Fuel rod design criteria of the Super FR. (Taken from [1])

Thermal design criteria	
Fuel centerline temperature	<1,900°C
Maximum linear heat rate	<39 kW/m
Maximum cladding surface temperature	<650°C
Hydrodynamic design criteria	
Flow dynamic design consideration	<0.02 MPa
Thermo-mechanical design criteria	
Pressure difference	<1/3 Buckling collapse pressure
Inelastic strain	<0.2%
Compressive to yield strength ratio	<0.2
Cumulative damage fraction	<1

the design criteria (with the melting temperature of unirradiated MOX being 2,650°C). The cladding surface temperature is limited to 650°C at the nominal condition.

7.4.3.2 Hydrodynamic Design Criterion

The coolant flow velocity, which is usually determined by flow experiments, has been limited in LMFBR designs in order to prevent excessive vibration of the fuel rods. Smaller fuel rod diameters are advantageous for a high power density concept with fixed average linear heat rate, but this concept requires more mass flux to keep the cladding surface temperature below the limit. High mass flux, that is, high flow velocity, raises a concern of FIV.

Several experimental correlations have been suggested for evaluating FIV for single phase water since the 1950s. For a rough evaluation, a simplified correlation form is used for the Super FR [1].

$$\left(\frac{\delta}{D}\right) \propto \left(\frac{1}{2}\rho V^2\right)^{1.16} Re^{0.25} \quad \text{or} \quad \left(\frac{\delta}{D}\right) \propto \frac{1}{2}\rho V^2, \tag{7.4}$$

where δ is the maximum rod displacement, D is the cladding outer diameter, ρ is the coolant density, V is the coolant velocity, and Re is the Reynolds number.

The fractional rod displacement is assumed to be proportional to flow dynamic pressure and Reynolds number, that is, kinetic energy and degree of turbulence, respectively.

In order to establish the limiting criterion of FIV, a future comprehensive flow experiment will be essential. For the present, the same degree of fractional rod displacement with past liquid metal reactors is taken as the design criterion. $((1/2)\rho V^2)^{1.16} Re^{0.25}$ and $(1/2)\rho V^2$ of a typical LMFBR (the Clinch River Breeder Reactor Project, CRBRP) are 2.17 and 0.0238 MPa, respectively, and the criteria for the Super FR are set as 2 and 0.02 MPa, respectively. Table 7.6 [1] compares the

Table 7.6 Comparison of coolant conditions from viewpoint of flow induced vibration. (Taken from [1])

	CRBRP	Super Fast Reactor
Coolant material	Na	Water
Inlet temperature (°C)	388	280
Outlet temperature (°C)	538	500
Outlet coolant density (kg/m^3)	824	89.9
Maximum flow velocity (m/s)	7.6	19.88
Viscosity (kg/s m)	2.3E−04	3.1E−05
Reynolds number	1.1E+05	1.9E+05
Fuel rod diameter (mm)	5.8	7.6
Dynamic pressure (Pa)	2.38E+04	1.78E+04
$\left(\frac{1}{2}\rho V^2\right)^{1.16} Re^{0.25}$	2.17E+06	1.78E+06

calculated right hand side values of (7.4) for an example fuel rod design with those of the CRBRP. Both values are lower than those of the CRBPR. It should be mentioned that these values of the Super FR are calculated for the hot channel having the highest flow rate and temperature, while those of the CRBRP are for the core average condition.

7.4.3.3 Thermo-Mechanical Design Criteria

Cladding collapse has been excluded in LWR fuel rod design. However, in the Super FR, pressure difference between internal gas and coolant is higher than that of PWRs. Collapse of cladding is kept as one possible cladding failure mode in the Super FR design. The pressure difference is limited by the buckling collapse pressure with a safety factor of 3 as in the Super LWR (see Chap. 2).

Evaluating creep collapse behavior of fuel cladding under high external pressure needs comprehensive mechanical analysis with respect to initial deviation from ovality. For the present design, the compressive to yield stress ratio is used to assess this behavior to avoid time dependent creep collapse resulting from elastic instability. The ratio is limited below that of PWRs and compared with PWR conditions, a compressive to yield stress ratio of 0.2 is expected to be conservative.

Strain controlled limit has been applied in LMFBRs rather than load controlled limit. Inelastic or creep strain have been used as design criteria in LMFBRs. In the Fast Flux Test Facility or CRBRP fuel rod designs, inelastic hoop strain was limited to 0.1% on average and 0.2% as the peak for normal operation conditions, 0.3% at an anticipated transient, and 0.7% at an unlikely event [14]. Inelastic strain limit was an earlier approach used for a failure criterion and is a straightforward concept.

Cladding strain prior to cladding rupture strongly depends on temperature, neutron fluence, and strain rate. A more sophisticated failure criterion including environmental factors is the cumulative damage fraction (CDF), which is based on linear lifetime fraction rule. The CDF is the sum of the steady-state component and the fatigue component. The steady-state component is based on a cumulative rule of time-to-rupture. During its lifetime, the fuel rod might experience a series of

different stresses and temperatures, where the damage fraction is assumed to accumulate linearly. Fatigue is also treated in the same fashion. The method for fatigue determines the number of thermal cycles to failure. The CDF is calculated and limited as (7.5).

$$\mathrm{CDF} = \sum_i \frac{\delta t_i}{t_{r,i}} + \sum_j \frac{N_j}{N_{f,j}} < 1, \tag{7.5}$$

where δt_i is the lifetime at ith condition, $t_{r,i}$ is the time to rupture at ith condition, N_j is the number of thermal cycles at jth condition, and $N_{f,j}$ is the number of thermal cycles to failure at jth condition.

The time to rupture and cycles to failure are entirely empirical and depend on cladding material. The fatigue component will not be limiting if only base load operation is considered for the Super FR without load following operation or other such kinds of load maneuvering.

As stated in Sect. 7.4.3, the rod internal pressure has been limited to coolant pressure to avoid rod overpressure in PWRs. However, that criterion has not been used in LMFBRs, where rod internal pressure is always higher than the coolant pressure. Rod internal pressure is not limited unless cladding creep strain exceeds the limiting value. MOX fuel tends to swell more than UO_2 fuel, and then the pellet-cladding gap is closed at an early fuel cycle. Herein, the rod overpressure failure is not considered as a limiting design criterion as in LMFBRs as long as cladding integrity is ensured against creep rupture by CDF.

7.4.4 Fuel Rod Design Method

The fuel rod design criteria except those of collapse and creep collapse are investigated with single channel thermal hydraulic analysis and fuel rod thermo-mechanical analysis. Design criteria are assessed by the FEMAXI-6 code as is also used for the Super LWR (see Chap. 2). Figure 7.12 shows the interaction of the fuel

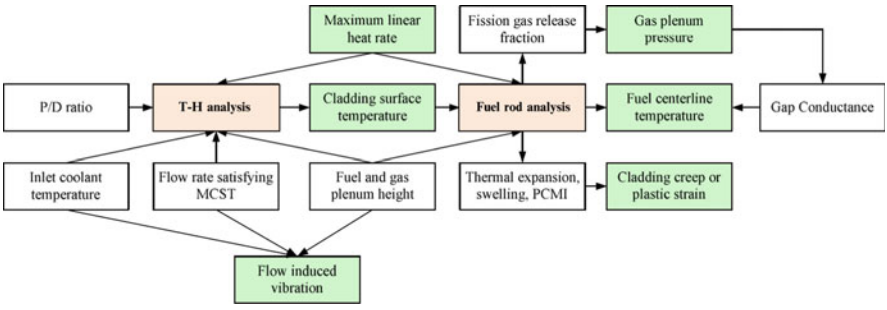


Fig. 7.12 Interaction of fuel rod design parameters, analyses and phenomena

rod design parameters and the phenomena associated with the analyses. FEMAXI-6 can treat MOX fuel as well as UO_2 fuel. SUS304 is assumed as the cladding material because it can be treated by FEMAXI-6. The axial distribution of the cladding surface temperature, calculated by the thermal hydraulic analysis, is given as the boundary condition.

The Baron model [15], which assumes considerable degradation of thermal conductivity by burnup, is used for the thermal conductivity of MOX fuel. It has been known to be more conservative than MATPRO-11 model [16] in most aspects of the fuel rod thermal behavior such as fuel centerline temperature and fission gas release [17]. The amount of fission gas generation in MOX fuel is assumed to be the same as that in UO_2 fuel. Fission gas release is predicted by the White and Tucker-Speight model [18, 19]. The Studsvik model [20] is adopted as it is a representative fuel pellet swelling model. Other material properties are taken from the MATPRO-11 model.

If MOX fuel containing a large portion of transuranium (TRU) nuclides is used, helium gas produced by alpha particle decays of TRU nuclides is not negligible in evaluating the gas plenum pressure and additional stress on the fuel cladding. Because FEMAXI-6 cannot treat those helium productions and releases, the contribution of helium gas release to gas plenum pressure and additional hoop stress is evaluated separately as the ratio of relative accumulated helium production to gaseous fission products (Xe and Kr). Relative production of helium is calculated by the unit cell depletion calculation in the SRAC system with average linear heat rate of 17 kW/m. Figure 7.13 [1] shows the results of relative helium production and gaseous fission products. At the end of fuel lifetime with peak discharge burnup

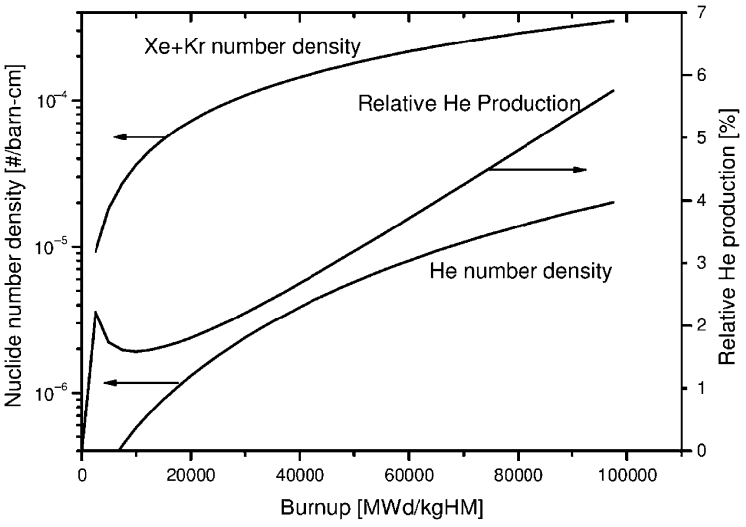


Fig. 7.13 Helium gas production relative to gaseous fission products. (Taken from [1])

of 100 MWd/kgHM, the relative helium production to fission gas is evaluated as about 6%.

The contributions of helium to gas plenum pressure and fission gas release fraction at EOL are calculated by (7.6), where complete release of helium is conservatively assumed by reason of the high diffusivity of helium gas in fuel pellets.

$$F_{\mathrm{g}} = \left(\frac{F_{\mathrm{He}} + F_0}{1 + F_{\mathrm{He}}}\right), \quad P_{\mathrm{g}} = P_0\left(1 + \frac{F_{\mathrm{He}}}{F_0}\right), \tag{7.6}$$

where F_{g} is the revised fission gas release fraction, F_{He} is the helium production relative to fission gas release, F_0 is the fission gas release fraction without consideration of helium, P_{g} is the revised gas plenum pressure, and P_0 is the gas plenum pressure without consideration of helium.

Contribution of the helium gas to the gas plenum pressure might also increase hoop tensile stress on the fuel cladding. As shown in Fig. 7.13 [1], the relative helium production is almost linear with respect to the burnup except for early in the irradiation time. The additional stress resulting from the helium production and release is calculated by (7.7) because stress is additive.

$$\sigma_{\mathrm{He}} = (P_{\mathrm{g}} - P_{\mathrm{o}})\frac{\bar{R}}{t}, \tag{7.7}$$

where t is the cladding thickness and $\bar{R}$ is the mean radius of cladding.

The buckling collapse pressure for a given pressure difference is calculated by an infinite cylinder model.

$$P_{\mathrm{collapse}} = 2.2E\left(\frac{t}{D - t}\right)^3, \tag{7.8}$$

where E is the Young's modulus and D is the cladding outer diameter.

When the required cladding thickness against buckling collapse is calculated, the safety factor of 1/3 is applied and 110% of the system pressure of 27.5 MPa and the cladding temperature of 800°C are considered.

The CDF is evaluated with a time-to-rupture correlation for the creep rupture term and a fatigue cycle to failure for the fatigue term in (7.5). The time-to-rupture correlation is usually expressed as the Larson–Miller Parameter (LMP), and there are corresponding correlations that can be used for stainless steels [21]. In general, creep damage and fatigue damage are treated separately with a linear summation, based on an assumption that creep fatigue interaction is not significant. In the creep damage evaluation, only the duration and the absolute value of stress corresponding to given strain is a concern, while the number of cycles and the total strain range is a concern in fatigue damage.

7.4.5 Fuel Rod Design and Analysis

Three candidates for fuel rod design are selected to find the design area where the MLHGR of 39 kW/m and cosine shape of axial power distribution are assumed and they do not change throughout the fuel rod lifetime. The candidates are summarized in Table 7.7 [1], Assuming the MLHGR of 39 kW/m over the fuel rod lifetime is expected to be very conservative. The MCST of 650°C is also assumed. The distribution of the cladding temperature is calculated by single channel analysis with the given MLHGR and axial power distribution.

The cladding thickness is calculated to avoid buckling collapse by (7.8), where the internal pressure is assumed as 6 MPa. The pellet-cladding gap size and gas plenum length are determined to keep the fuel centerline temperature below the design criterion according to several active core heights. The fission gas release fraction, consequent gas plenum pressure, and creep strain of the fuel cladding are evaluated by the FEMAXI-6 calculation. The preliminary results are summarized in Table 7.7 [1].

The most important parameters of fuel rod design for the high power density core are the fuel rod diameter and P/D. Higher power density and more compact core size can be realized as the fuel rod diameter gets smaller and rods are arranged more tightly. Then, the fuel rod design studies described below are used to determine the rod diameter and P/D without violation of the design criteria and other design concerns.

Table 7.7 Preliminary results of fuel rod analysis for candidate fuel rod designs. (Taken from [1])

Case	1			2			3		
Fuel rod diameter (mm)	6.7			7.6			8.8		
Fuel pellet diameter (mm)	5.84			6.65			7.64		
Cladding thickness (mm)	0.38			0.43			0.50		
Initial gas pressure (MPa)	6			6			6		
MLHGR (kW/m)	39			39			39		
Active core height (cm)	260	280	300	260	280	300	260	280	300
Gas plenum length (cm)	160	170	180	155	165	180	165	175	185
Maximum fuel temperature (ºC)	1,869	1,889	1,889	1,898	1,900	1,900	1,897	1,903	1,901
Fission gas release fraction (%)	44.5	44.3	44.1	47.8	47.6	48.2	51.8	51.4	52.4
Gas plenum pressure at EOL (MPa)	24.8	24.8	24.9	24.9	24.9	24.8	24.8	24.8	24.9
Creep strain (%)									
Circum.	−0.07	−0.07	−0.07	−0.07	−0.07	−0.06	−0.10	−0.11	−0.01
Axial	0.07	0.06	0.07	0.06	0.06	0.07	0.06	0.06	0.07
Radial	0.01	0.01	0.01	0	0	−0.01	0.04	0.04	0.04
Equivalent	0.08	0.08	0.08	0.07	0.08	0.08	0.1	0.11	0.11

7.4.5.1 Admissible Design Area

Smaller fuel rod diameter, smaller P/D and longer heated length of the fuel rods require higher mass flux and flow velocity in order not to violate the criterion of the MCST. Such higher flow velocity might cause excessive hydrodynamic excitation along the fuel rods. FIV limits the lower bound of the fuel rod diameter, P/D, and heated length.

The limiting flow velocities for each diameter and P/D are determined so that the cladding surface temperature reaches the limiting value with given MLHGR of 39 kW/m. Then, degree of FIV is evaluated from those flow velocities. All the evaluations are conducted by single channel analyses.

The admissible design area can be depicted in Fig. 7.14 [1] as a function of fuel rod diameter, P/D and heated length based on the aforementioned design criteria. In the figure, the area below the line of the maximum admissible height denotes the allowable design area for each fuel rod diameter and P/D. The limitation of core height means the limit in the core thermal power because the heated length is increased as the total core power gets larger and the active core height should be the same or larger than the core equivalent diameter as one of the design goals (see Sect. 7.2). For a 1,000 MWe class core with 40% thermal efficiency as a minimum, the lowest fuel rod design parameter satisfying all the design criteria and design goals can be determined as: fuel rod diameter ≧7.0 mm and P/D ≧1.14.

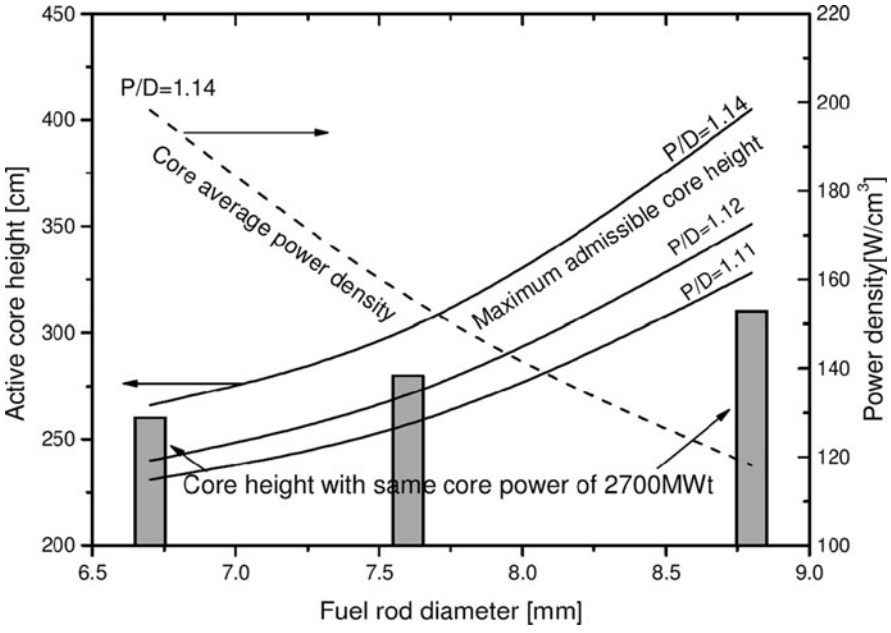


Fig. 7.14 Allowable fuel rod design area. (Taken from [1])

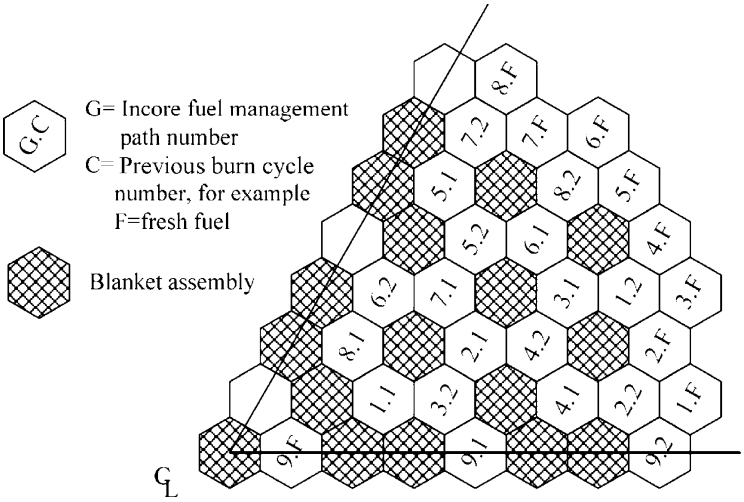


Fig. 7.15 Core arrangement used in nuclear performance analysis. (Taken from [1])

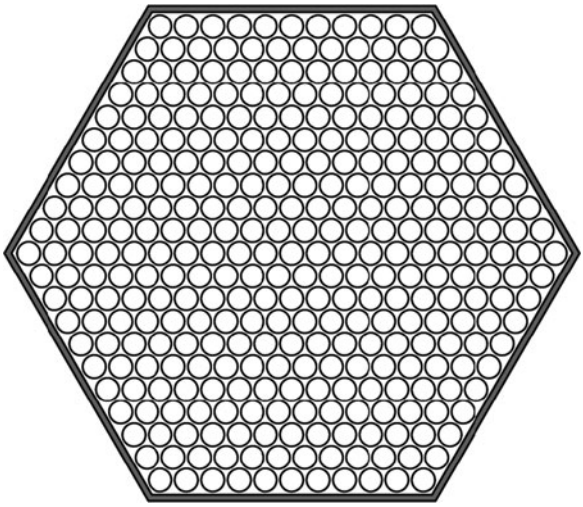


Fig. 7.16 Fuel assembly for nuclear performance evaluation of candidate fuel rod designs. (Taken from [1])

7.4.5.2 Nuclear Performance of Candidate Fuel Rod Designs

The nuclear performance is evaluated by the SRAC system with the core arrangement illustrated in Fig. 7.15 [1] and the fuel assembly configuration illustrated in Fig. 7.16 [1], where the total number of the fuel rods in the seed assembly, wrapper

Table 7.8 Summary of nuclear performance for candidate fuel rod designs. (Taken from [1])

Case	1	2	3
Fuel rod diameter (cm)	0.67	0.76	0.88
Thermal power (MWt)	2,088	2,358	2,721
Core equivalent diameter (cm)	236	267	308
Core height (cm)	240	270	310
Pu fissile enrichment (%)	23.67	21.94	20.78
Total Pu fissile inventory (ton)	6.7	9.0	13.0
Total fissile inventory/thermal power (kg/MWt)	3.21	3.82	4.76
Cycle length (FPD)	345	450	580
Burnup reactivity swing (%Δk/k)	2.00	2.19	3.40
Average assembly discharge burnup (MWd/kg)	69.6	70.04	68.4
Peak discharge burnup (MWd/kg)	95.3	94.1	99.8
Coolant void reactivity (%Δk/k)			
BOEC	−0.78	−0.70	−1.20
EOEC	0.58	1.11	1.15
Fuel volume fraction	0.463	0.468	0.472
Moderator to fuel volume ratio	0.757	0.750	0.743

tube thickness, and assembly gap are fixed in all cases to 331, 2, and 2 mm, respectively. The loading pattern and shuffling scheme of the fuel assemblies are also fixed to evaluate only the influence of the fuel rod diameter. The cycle length is adjusted so that the candidate cores have similar average discharge burnup of 70 MWd/kgHM. The core arrangement used in this evaluation is different from those in the core design in Sect. 7.5. The influence of the core arrangements on the coolant void reactivity is discussed in Sect. 7.5 with a detailed description of the core calculation procedure.

The parameters of nuclear performance for each candidate fuel rod design are shown in Table 7.8 [1] and Fig. 7.17. Using small diameter fuel rods is predicted to be beneficial for most nuclear performance values, that is, fissile plutonium inventory per unit thermal power, burnup reactivity swing and core power density, but not fissile plutonium enrichment. However, the fissile plutonium enrichment itself does not increase fuel cycle cost for MOX fuel. Plutonium enrichment can be controlled by adjusting the mixing fraction of PuO_2 with depleted UO_2, which does not require an additional separate working unit (SWU) cost. Accordingly, the total plutonium inventory is a more significant parameter affecting the fuel cycle cost.

7.4.6 Summary of Fuel Rod Design

The fuel rod design parameters were determined with consideration of the limiting criteria. Table 7.9 [1] summarizes the final fuel rod design parameters. The P/D was restricted to less than 1.2 for high core outlet temperature while keeping the cladding surface temperature below 650°C. The fuel rod diameter and P/D were limited to avoid excessive fuel rod vibration that might arise from excessively high

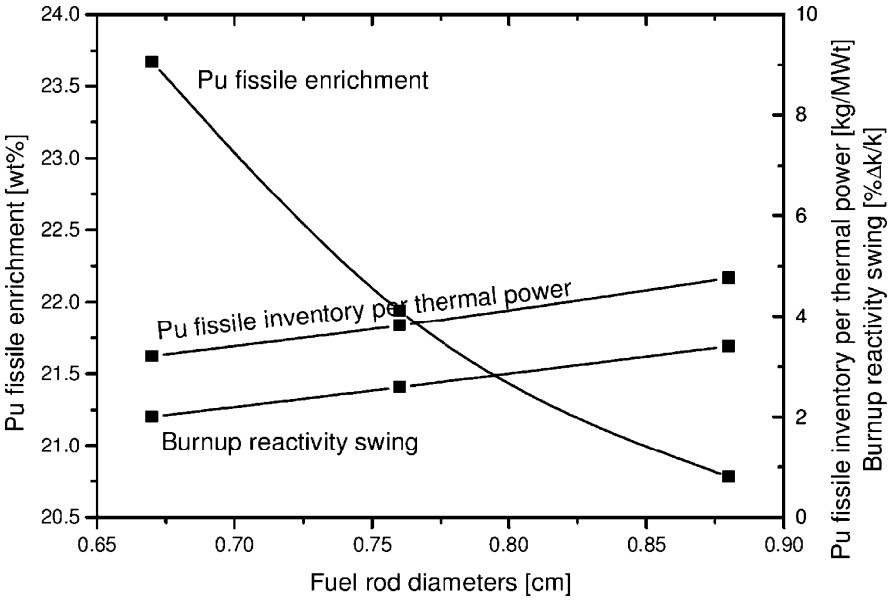


Fig. 7.17 Nuclear performances of each candidate fuel rod design

Table 7.9 Final fuel rod design parameters. (Taken from [1])

Fuel material	MOX
Fuel density	95% TD
Fuel pin outer diameter (mm)	7.6
P/D	1.14
Cladding thickness (mm)	0.43
Cladding material	Stainless steel
Diametral pellet cladding gap (mm)	0.1
Gas plenum location	Upper
Initial gas pressure (MPa)	7
Average linear heat rate (kW/m)	17
Equivalent fission gas plenum length (cm)	160
Fission gas release fraction (%)	45

flow velocity. The cladding thickness was determined to avoid instantaneous buckling collapse. The pellet-cladding gap was a little smaller than gaps of LMFBRs. High coolant pressure of 25 MPa played a positive role against PCI and gas pressure loading; it allowed a smaller gap design and was beneficial for reducing the fuel centerline temperature. In addition to the determination of the fuel rod design parameters to be used in core design (Sect. 7.5) and thermal-hydraulic design of the fuel assembly (Sect. 7.6), the fuel rod failure modes and associated fuel rod design criteria were established.

7.5 Core Design Method and 1,000 MWe Class Core Design

In this section, the core design method for the Super FR is introduced, and then an example of a 1,000 MWe core is designed based on the fuel rod design introduced in Sect. 7.4.

7.5.1 Discussion of Neutronic Calculation Methods

The neutron diffusion equation has long been used to provide neutronic solutions for nuclear core designs of both thermal and fast nuclear reactors. Its most popular solutions are the finite difference method (FDM) and nodal method. In order to treat wide ranges of neutron energy and space, a reactor design method is based on staged spatial homogenization and neutron energy group collapse, in which finer descriptions of space and neutron energy groups are used with a solution of the neutron transport calculation, for example, the SN transport method, collision probability method (CPM), or method of characteristics (MOC).

The FDM is a numerical method in use since the early days of nuclear reactors; it solves the multi-group neutron diffusion equation with a homogenized fine mesh structure. Owing to its simplicity, flexibility in geometrical description, and reasonable calculation time cost, the FDM is still being used today for conceptual design of various core types.

Modern nuclear design methods for commercial LWRs have been based on nodal methods: the nodal expansion method (NEM), analytic nodal method (ANM), and analytic function expansion nodal method (AFEN). The nodal method treats a fuel assembly as a node, and an intra-node neutron flux is expressed as a synthesis of a polynomial expansion (NEM) or an analytic solution for each direction (ANM), or its combined expansion (AFEN), which provides very fast solutions for core design.

Owing to rapid growth of computing system ability, whole core neutron transport calculations have been tried in order to treat complicated core design features of innovative reactors by either the integral neutron transport method or Monte Carlo neutron transport method. The geometrical description in the calculation model is less restricted in the integral neutron transport method and not under restriction in the Monte Carlo neutron transport method. Those methods have been used for reference calculations of the FDM and nodal method and they are being developed by coupling with thermal-hydraulic calculations and by adding depletion calculation abilities. However, they are not yet suitable for the nuclear core design phase in which a number of core calculations are required.

Since the core-wide nuclear performance parameters and local power distribution within a fuel assembly depend highly on the moderator condition in LWRs, thermal-hydraulic coupled calculations have been regarded as essential in the core design procedure for thermal neutron spectrum cores. As the thermal-hydraulic

calculation module, single channel analysis has been widely used for calculating the changes in the coolant density and temperature.

In LMFBR core design, there is no drastic change of the coolant density along the fuel rod. The axial coolant density distribution significantly affects neither the core-wide nor the local nuclear parameters. Since the fuel rods of LMFBRs are arranged more tightly, neutronic coupling between the fuel rods is tighter, and hence, the local power distribution within an assembly is flatter than that of LWRs. For these reasons, thermal-hydraulic coupling has been regarded as not essential as long as the average coolant properties are well defined.

The Super FR also has a tight lattice arrangement of the fuel rods. The core-wide neutronic performance would not be significantly affected by the axial distribution of the coolant density. However, the core thermal performance depends highly on the power to flow ratio. Furthermore, the coolant density changes drastically from the assembly inlet to outlet, which causes axial power peaking even in the fast spectrum core. In order to evaluate the core outlet temperature with an appropriate flow rate distribution and to consider changes in the local parameters arising from coolant properties, thermal-hydraulic coupling is essential for the Super FR design.

The SRAC system is used for core design analysis of the Super FR just as it was used for the Super LWR core design (see Chap. 2). It contains many kinds of calculation modules based on integral or differential neutron transport and FDM solutions. However, the SRAC system does not contain a thermal-hydraulic calculation module for coupling. The thermal-hydraulic calculation module is coupled with the original SRAC system.

7.5.2 Core Design Method

The core design procedure consists of two parts, nuclear design and thermal-hydraulic analysis. The former is based on the fine-mesh multi-group neutron diffusion solution. The latter is based on single channel analyses for the average and hot channels of all the fuel assemblies. This approach is the same as that in the Super LWR design.

Figure 7.18 [1] shows the overall design procedure for the Super FR core design. The procedure to determine the "fuel rod design parameters" appears in Sect. 7.4. The neutronic and thermal-hydraulic solutions are coupled to each other like those of the Super LWR. The nuclear design part transfers the linear heat rate distribution in the core to single channel analyses, in which axial coolant density distributions are evaluated for given coolant channels representing each fuel assembly with the flow rate satisfying the criterion of the MCST and those are transferred to the nuclear part.

The nuclear design limits and the nuclear performance are examined in the nuclear design part, while the core outlet temperature and MCST are examined in the single channel analyses. Detailed descriptions for each part are discussed below.

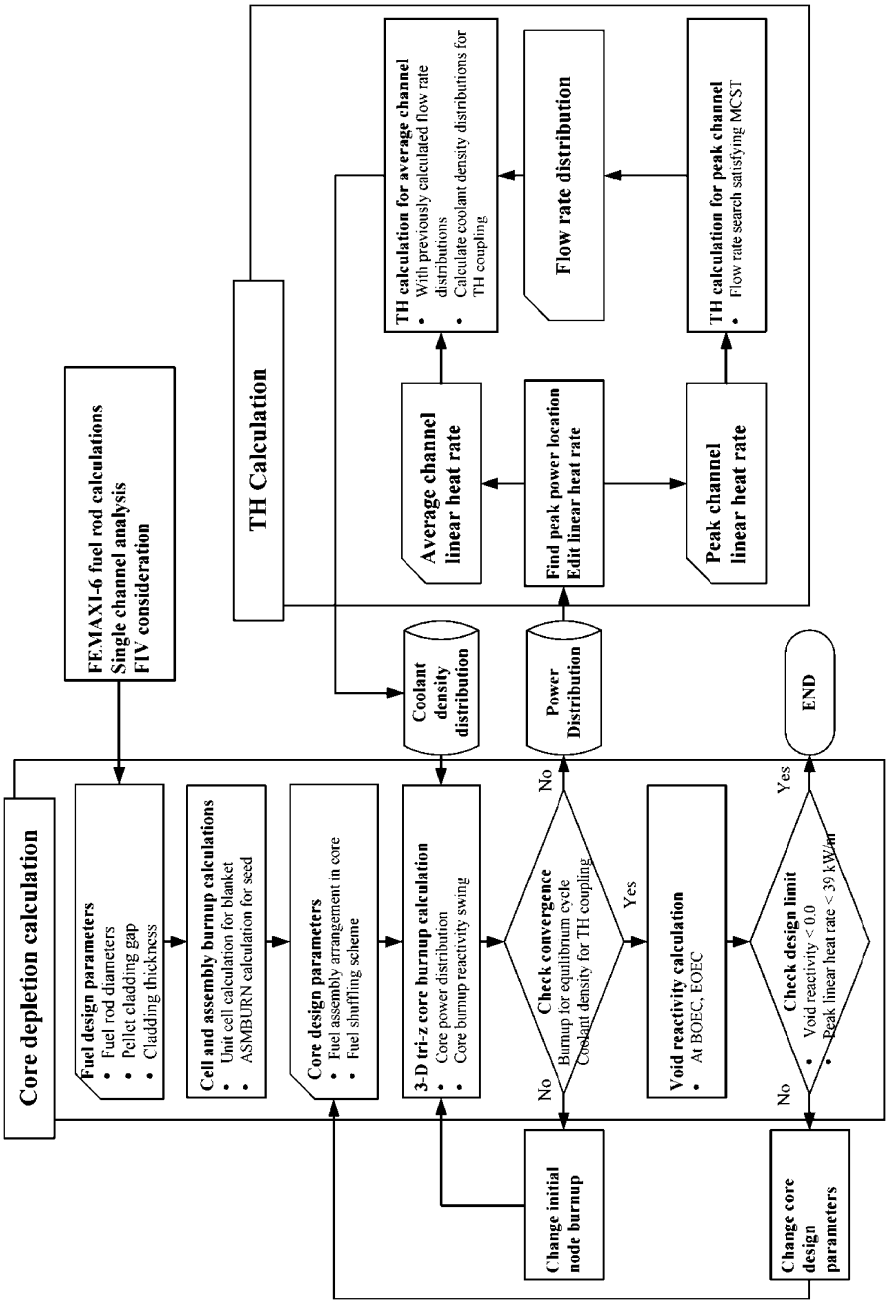


Fig. 7.18 Overall design procedure for Super FR core design. (Taken from [1])

7.5.2.1 Nuclear Design Method

The nuclear design method is based on the Tri-Z fine mesh finite difference solution of the neutron diffusion equation with multi-neutron energy groups. SRAC2002 is used here. It includes the major neutron data library JENDL-3.3, which contains 107 group neutron cross sections for more than 300 nuclides.

In order to effectively treat the complicated core geometry of the Super FR, the core analysis is conducted with homogenized macroscopic cross sections for each fuel assembly, which are provided by a staged homogenized procedure from the unit cell to the fuel assembly while preserving the neutron reaction rate in a given geometry. The staged homogenized procedure is depicted in Fig. 7.19 [1].

The unit cell depletion calculation reflects spatial and neutron energy group self shielding effects coming from the spatial distribution of group neutron flux and change of neutron spectrum. At first, one representative cell containing a fuel rod

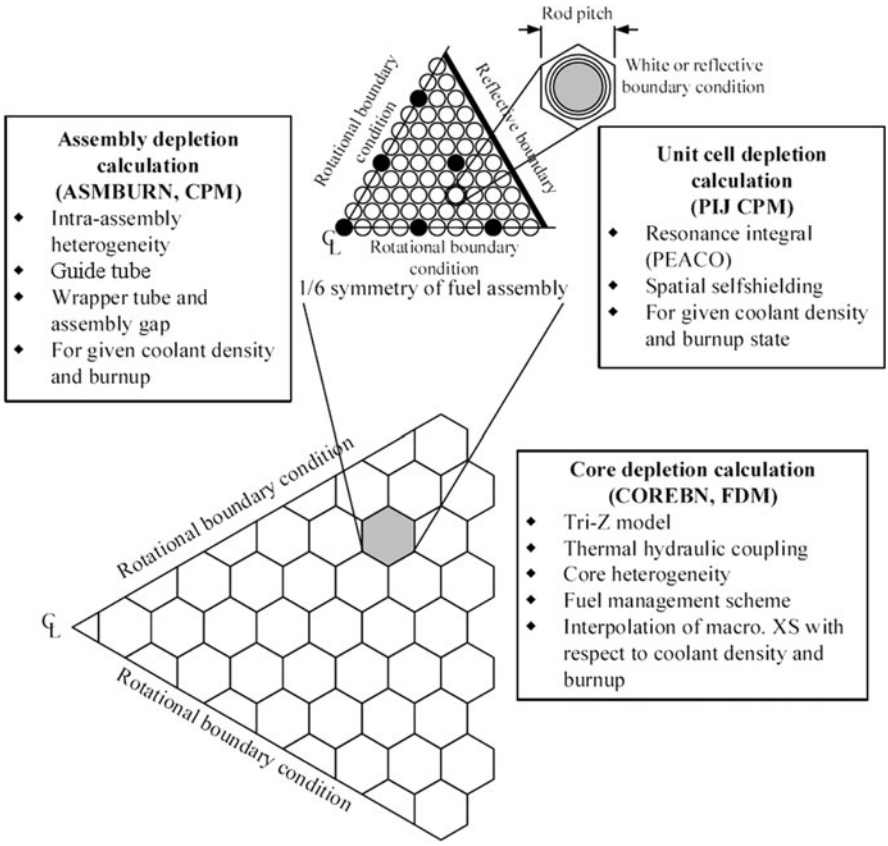


Fig. 7.19 Schematic diagram of staged homogenized procedure. (Taken from [1])

and surrounding coolant is established from the fuel rod design data, which is called a unit cell. The spatial distribution of the group neutron flux and effective resonance cross sections are calculated for the unit cell with white or reflective boundary conditions. The PIJ module provides three kinds of resonance integral methods, narrow resonance (NR) approximation, intermediate resonance (IR) approximation, and direct calculation with hyper-fine neutron energy group (PEACO). The PEACO routine is used to calculate the effective resonance cross section here.

For the thermal-hydraulic coupled core depletion calculation, the macroscopic cross sections for various states of coolant densities and burnup are calculated by a branch calculation. A reference depletion calculation is made first with the core average coolant density, in which the nuclide concentrations for each given burnup states are calculated with the reference neutron spectrum. Then, the branch calculation is conducted with the same nuclide concentrations but different coolant densities over the burnup, whose cross sections are to be interpolated in the core depletion calculation for given burnup states and coolant densities. The macroscopic cross sections are prepared at eight different coolant densities from 0.001 to 0.8 g/cc and at 11 burnup states up to 150 MWd/kgHM to cover all the operation ranges of the coolant density and burnup.

Two depletion methods are available in the PIJ module. One is by a constant linear heat rate. The other is by a constant neutron flux. The former is used for the seed fuel rods and the latter is for the blanket fuel rods because their linear heat rate changes significantly with the burnup.

The assembly depletion calculation is intended to reflect intra-assembly heterogeneities due to the presence of the control rod guide tubes, wrapper ducts, and fuel assembly gap regions, where the self-shielded macroscopic cross sections produced from the unit cell depletion calculations are used for given coolant densities and burnup states. Eighteen group neutron cross sections collapsed through the unit cell calculations are used in the assembly depletion calculation. An assembly depletion calculation produces nine group cross sections again that are homogenized over the fuel assembly geometry. They are used in the core depletion calculation.

A fuel assembly is described by the 1/6 symmetric model as shown in Fig. 7.19 [1]. The assembly calculations are conducted for the same coolant densities and burnup state by the branch calculation as in the unit cell depletion calculation. Figure 7.20 [1] shows the concept of the branch calculation for the coolant densities. ASMBURN implemented in the SRAC system is used for the assembly depletion calculations. ASMBURN is also based on the integral neutron transport calculation of CPM.

The core depletion calculation is based on the fine mesh Tri-Z finite difference neutron diffusion solution of the CITATION module. The core is described as the 1/6 symmetric Tri-Z fine mesh structure as shown in Fig. 7.21 [1], in which a black boundary condition and a rotational boundary condition are applied to the outer radial direction and symmetric line, respectively. The radial water reflector is placed in the outer region of the core, and it denotes the downcomer. The axial reflectors are placed in the bottom and top of the core and denote the lower and upper plenums.

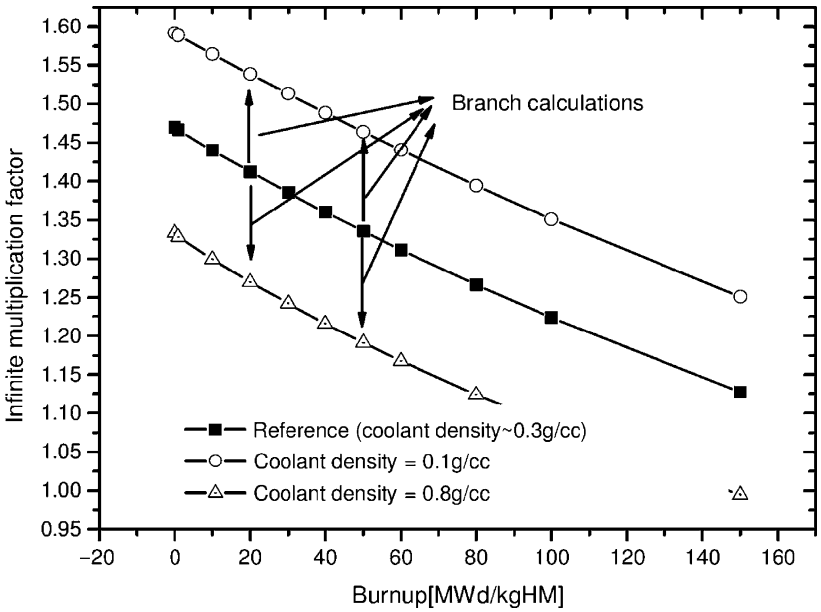


Fig. 7.20 Concept of branch calculations for coolant densities. (Taken from [1])

A fuel assembly is divided into 96 triangular meshes and 20 axial meshes, where the FDS of the neutron diffusion equation solves the neutron flux distribution for each mesh interval. The burnup and coolant density distributions are evaluated assembly-wise for a given axial interval to be consistent with the assembly burnup calculation. The $ZrH_{1.7}$ layer is described in the Tri-Z meshes as explicitly as possible. Since the thickness of the $ZrH_{1.7}$ layer (about 1 cm) does not exactly fit into the triangular mesh interval, structural material surrounding the layer is homogenized with the layer by volume weighting.

The COREBN module implemented in the SRAC system provides linear interpolation of a macroscopic cross section as a function of burnup state. It also offers two additional variables reserved for additional neutronic coupling. One of those parameters is used for the thermal-hydraulic coupling with the coolant density. The macroscopic cross sections are provided for the coupled calculation for several given states of the coolant densities. Eight coolant densities from 0.001 to 0.8 g/cc are used for the thermal-hydraulic coupling to cover the whole core. The COREBN module, then, linearly interpolates the macroscopic cross sections with respect to both burnup and coolant density.

The original SRAC system does not include the capability for pin power reconstruction. It only provides the neutron fluxes and power distributions for the homogenized mesh structure. If the intra-assembly heterogeneity is not significant, the fluxes and power distributions for homogenized regions must be similar to those of local ones. On the other hand, the local power distribution in a fuel assembly may

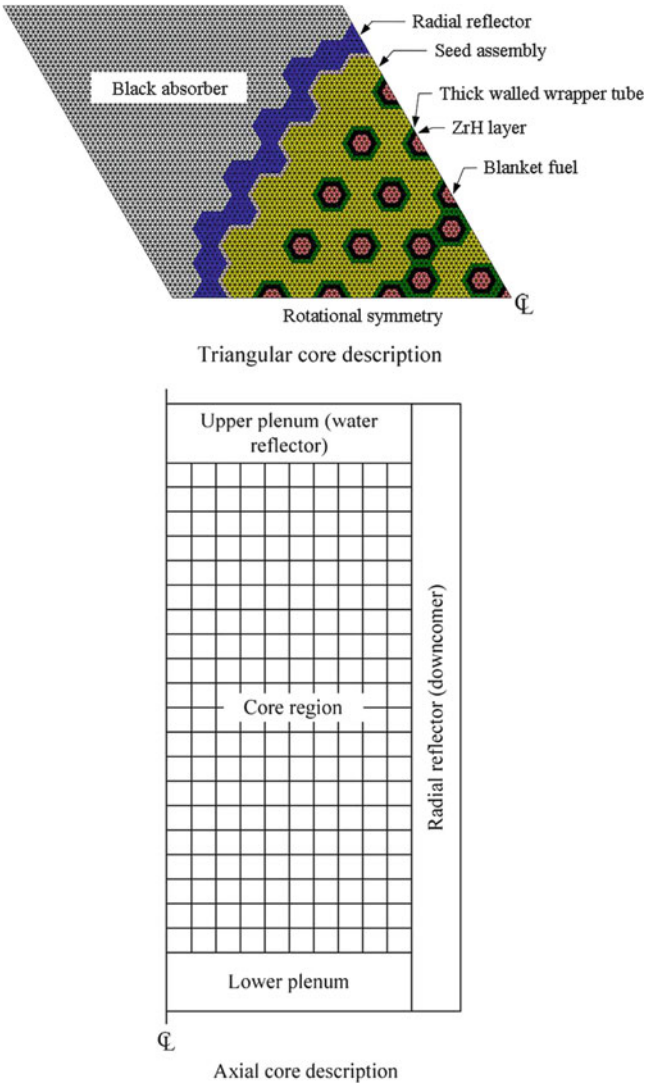


Fig. 7.21 Tri-Z description for core depletion calculation. (Taken from [1])

significantly differ from those for the homogenized regions if heterogeneity within a fuel assembly is significant. Figure 7.22 [1] shows the local power peaking factors of a fuel assembly with single Pu enrichment of 35 wt% with respect to the coolant densities. The local power peaking factor tends to increase as the coolant density increases. The local power peaking factor in a fuel assembly mainly results from the control rod guide tube, wide gaps between the peripheral fuel rods and wrapper tube, and the assembly gap. Even though the local power peaking at the average

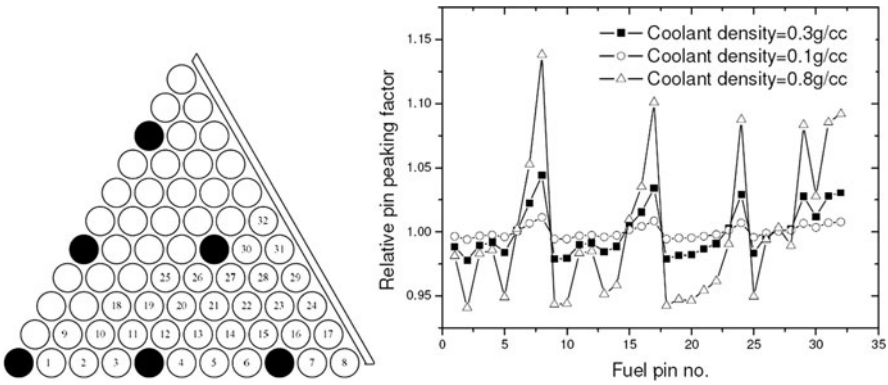


Fig. 7.22 Local peaking factors with respect to coolant density. (Taken from [1])

coolant density up to 0.3 g/cc is relatively small, this, at high coolant density is not negligible. Furthermore, if multiple fuel enrichment is used in a fuel assembly, the amplitude of the local power peaking will get larger. For these reasons, pin power reconstruction is required, which reflects the influence of the intra-assembly heterogeneity.

The pin power reconstruction has been widely used in the nodal code system for LWRs. The pin power reconstruction process involves a fundamental assumption that detailed pin-by-pin distributions within an assembly can be estimated by the product of a global intra-nodal distribution and a local heterogeneous form factor (HFF). The HFF accounts for the assembly heterogeneities caused by the control rod guide tubes, gaps between peripheral fuel rods and wrapper tube, fuel enrichment zonings, etc. It is generated for each fuel assembly type by a lattice physics code at the same time when the homogenized cross sections are generated. The assumption of separability of the global intra-nodal flux and the local form factor is commonly adopted in various pin power reconstruction methods that have been extensively researched in the past two decades [22, 23].

A general description of HFF is defined by (7.9).

$$f_{\mathrm{g}}(x,y) = \frac{\kappa \sum_{f_{\mathrm{g}}}(x,y) \cdot \phi_{\mathrm{g}}^{\mathrm{hetero}}(x,y)}{\kappa \bar{\sum}_{f_{\mathrm{g}}} \bar{\phi}_{\mathrm{g}}}. \tag{7.9}$$

By using the HFFs and homogeneous intra-nodal neutron flux, the pin power at a given position is defined as (7.10).

$$p(x,y) = \sum_{\mathrm{g}} \kappa \bar{\sum_{f_{\mathrm{g}}}} \phi_{\mathrm{g}}^{\mathrm{homo}}(x,y) f_{\mathrm{g}}(x,y). \tag{7.10}$$

The HFFs are produced from a lattice physics calculation of ASMBURN with respect to the coolant density and burnup the same as in producing the macroscopic

cross sections and they are interpolated in the core calculation for a given coolant density and burnup. If the one-group HFF is considered, the final pin power for axial node k is defined as (7.11).

$$p_k(x, y) = HP_k(x, y) \cdot \mathrm{HFF}(x, y, \rho, BU) \cdot p_{\mathrm{avg}}. \tag{7.11}$$

The Method of Successive Smoothing with Analytic Solution (MSS-AS) has been employed in the nodal code system to produce a smooth intra-nodal neutron flux distribution for homogenized fuel assemblies. However, there is abundant intra-nodal information in the fine mesh neutron diffusion solution. The intra-assembly homogeneous neutron flux distribution is evaluated by bilinear triangular interpolation with the neutron flux of the nearest three triangular meshes. Figure 7.23 [1] shows conceptual diagrams obtained by the pin power reconstruction procedure. The upper left figure accounts for the intra-assembly power distribution in the triangular meshes. The upper right figure is an example of the HFF evaluated

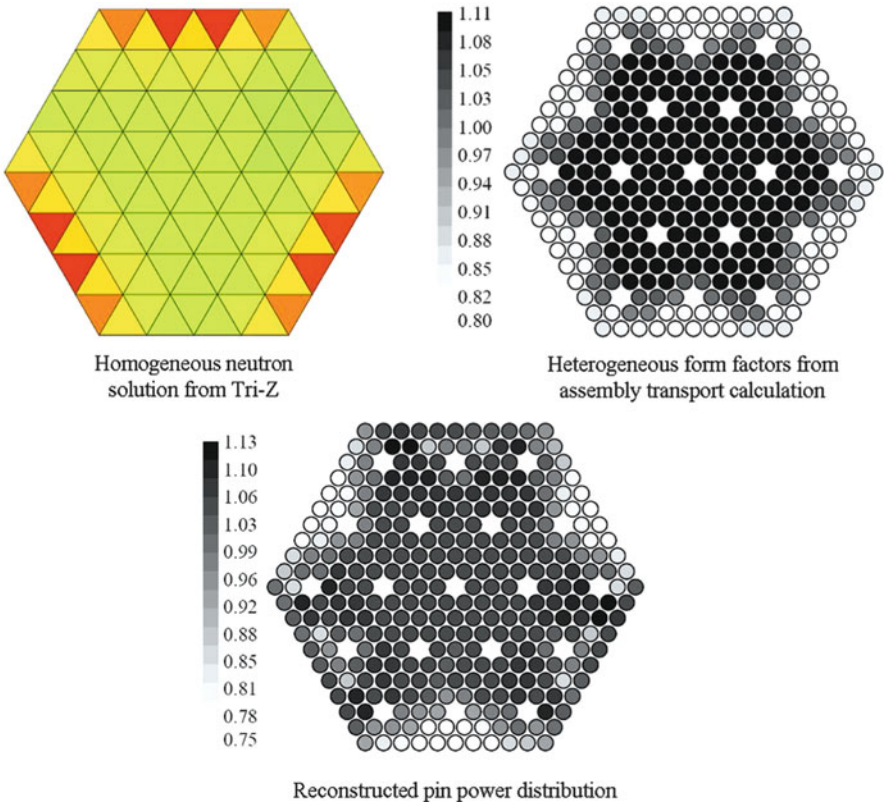


Fig. 7.23 Example of pin power reconstruction. (Taken from [1])

Table 7.10 Comparison of k_{eff} between SRAC and MCNP4C with respect to neutron energy. (Taken from [1])

Model	k_{eff}	σ
MCNP4C with ENDF/B-VI	1.04177	0.00027
SRAC/COREBN with JENDL3.3	k_{eff}	Diff
107 g (61 + 46)	1.04234	–
23 g (20 + 3)	1.04149	−0.00085
21 g (20 + 1)	1.03032	−0.01201
9 g (6 + 3)	1.04092	−0.00141
7 g (6 + 1)	1.02994	−0.01239

from the assembly transport calculation. Those two distributions are multiplied together to produce the final pin power distribution shown in the bottom figure.

For validating the methods introduced above, the results of the SRAC system are compared with that of the typical Monte Carlo code, MCNP4C. Since there is no available critical experiment with the $ZrH_{1.7}$ layer in a supercritical pressure water, the results of the Monte Carlo calculation are used as the reference. Since the Monte Carlo method treats a continuous neutron energy structure without restrictions of geometric description, it has been widely used for reference calculations to validate neutron transport or diffusion solutions. The calculations are made with a fixed coolant density distribution and single fuel enrichment. The MCNP4C calculation is done with the ENDF/BVI neutron library, while the JENDL-3.3 library is used for the SRAC system. The difference between these libraries is known to be below 0.2%dk in the Super FR design [24]. As shown in Table 7.10 [1], the results of the SRAC system are in good agreement with the MCNP4C results within 0.053%dk even considering the error arising from the difference between the cross section libraries. The comparisons are conducted with various combinations of the neutron energy groups, that is, fast and thermal energy groups. Three thermal neutron energy groups are required as the minimum number of thermal neutron energy groups, while six fast neutron energy groups provide satisfactory accuracy. Therefore, nine groups (six fast and three thermal) are used for the core depletion calculation.

7.5.2.2 Thermal-Hydraulic Design Method

The thermal-hydraulic calculation is based on single channel analyses for multi coolant channels. A fuel assembly is expressed as two representative coolant channels. One is the average channel, and the other is the peak power channel. Both channels have the same thermal-hydraulic parameters, and only the linear heat rate distributions are different from each other.

The peak fuel rod is defined as a fuel rod having the peak linear heat rate within an assembly, and it is used to evaluate the MCST within an assembly. The average channel is represented by the average linear heat rate over a fuel assembly, which is used for evaluating the average coolant density distribution to be utilized in the nuclear calculations.

The total flow rate can be determined by the total core thermal power and enthalpy rise. The cladding surface temperatures and coolant densities are evaluated with a given relative flow rate distribution and linear heat rate distribution. It is examined whether the criterion of the MCST is satisfied or not. Conversely, the core mass flow rate can be defined as the sum of the individual assembly flow rates satisfying the criterion of the MCST. The core outlet temperature is evaluated with those flow rates and the average linear heat rate. The latter approach is more effective to find the appropriate flow rate distribution iteratively. The single channel analysis code used here has the feature of an automatic flow rate search in the multi coolant channels. If the feedwater is fed directly into all the coolant channels, that is, the assembly inlet temperature is always the same as the feedwater temperature in all the fuel assemblies, the flow rate distribution can be directly searched throughout all the burnup states without iteration. However, if the feedwater is divided into two parts and several fuel assemblies have downward flow, the thermal condition at the assembly inlet varies with how much of the power share is from the assemblies with downward flow. The flow rate should be determined iteratively until the inlet temperature of the upward flow fuel assemblies converges. The iterative procedure is described in Fig. 7.24 [1]. The heat transfer coefficient is calculated using the Oka–Koshizuka correlation in the upward flow conditions and using the Watts–Chou correlation in the downward flow conditions.

7.5.2.3 Neutronic Thermal-Hydraulic Coupled Equilibrium Core Calculation Method

The neutron calculations and thermal-hydraulic calculations stated in Sects. 7.5.2.1 and 7.5.2.2 are all implemented into an automatic calculation scheme written in Perl and Awk script languages. The macroscopic cross section sets and HFFs are prepared for given coolant densities and burnup states by the staged homogenization of the unit cell and the assembly transport calculation. The auxiliary mesh generation module produces the Tri-Z mesh structure to be used in COREBN and CITATION.

The main control module automatically prepares the inputs required for both neutronic and thermal-hydraulic calculations. It also produces the pin power distribution and burnup distribution, and then prepares the peak and average channels for each fuel assembly. The neutronic and thermal-hydraulic calculations are executed by the main control module internally and coupled to each other by pin power and coolant density distributions.

The automatic scheme has a feature for equilibrium cycle search. The equilibrium cycle is defined as a core state in which all nuclear parameters are the same as in the previous cycle. All the nuclear performance values are evaluated in the equilibrium core. As a principle parameter to decide the equilibrium core, the initial node burnup distribution is compared with the previous one. Once the fuel shuffling schemes are given as the input parameter of the main control module, the initial burnup distribution of the non-fresh fuel assemblies is automatically taken from the

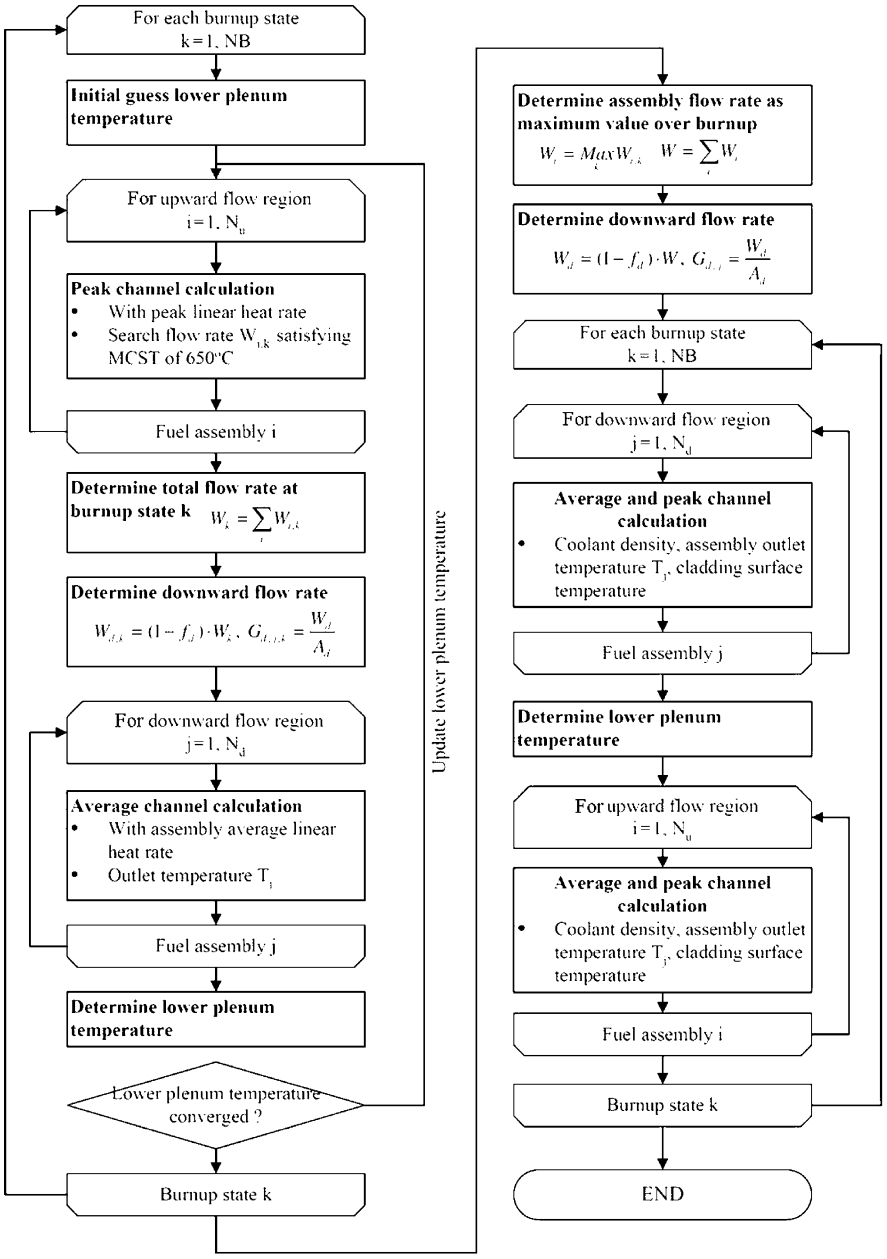


Fig. 7.24 Thermal hydraulic single channel analysis procedure for multi-assembly channel. (Taken from [1])

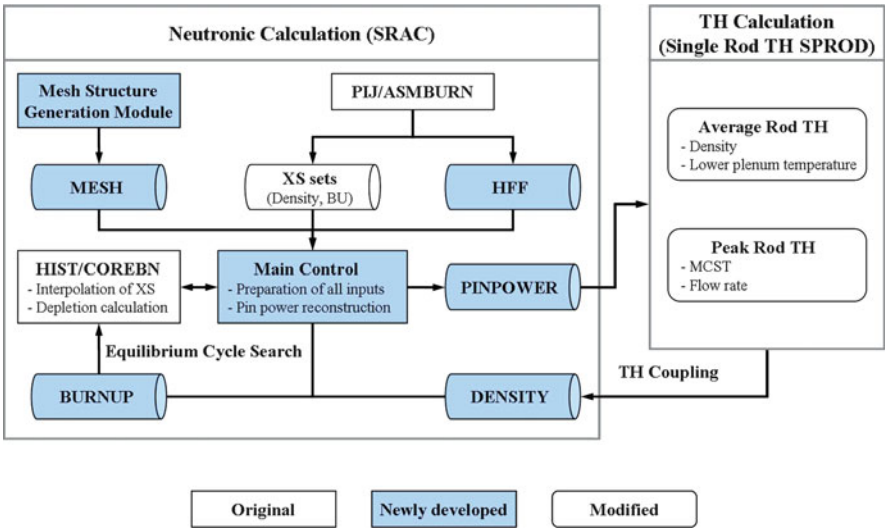


Fig. 7.25 Schematic diagram for thermal hydraulic coupling and equilibrium cycle search. (Taken from [1])

burnup at the end of previous cycle. The core depletion calculation is continued until the initial burnup distributions in all the nodes are converged.

The thermal-hydraulic coupling is not conducted at the individual burnup states, but after the core depletion calculation is finished; this reduces overall calculation time. Figure 7.25 [1] shows the schematic diagram for the thermal-hydraulic coupling and equilibrium cycle search. The white boxes in the figure mean the original SRAC system. The shaded boxes represent the newly developed modules here. The cylindrical boxes are modified from the previous design method based on a two-dimensional R-Z model.

7.5.3 Materials Used in Core Design

The fuel rod design summarized in Table 7.9 [1] is used. A fuel rod consists of fuel pellets and the surrounding fuel cladding. MOX fuel reprocessed from LWR spent fuel is used. Its theoretical density (TD) is assumed as 95% of 11.06 g/cm^3. The plutonium nuclide percentages used here are shown in Table 7.3 [1].

Stainless steel cladding is considered as the cladding material due to its high mechanical strength and abundant experiences in nuclear reactors. There are a variety of stainless steels. The most popular stainless steels in nuclear uses are SUS304 and SUS316. Although their mechanical properties are quite different, influences of the properties on nuclear performance are similar if a strong neutron

Table 7.11 Elemental composition of SUS304. (Taken from [1])

Nuclide	Composition (wt%)	Nuclide number density (#/barn-cm)
Mn-55	1.71	1.4801E−03
Ni	13.22	1.0714E−02
Mo	2.21	1.0969E−03
Cr	16.37	1.4977E−02
Fe	65.74	5.6000E−02
S	0.01	1.4918E−05
P-31	0.03	4.3240E−05
Si	0.63	1.0730E−03
C-12	0.08	3.1889E−04

absorber is not used. SUS304 is selected as the cladding material here. Its density is about 7.9 g/cm^3 and the elemental composition is listed in Table 7.11 [1]. SUS304 is also used as the wrapper duct material and other in-vessel structure materials. Materials development and testing remain for future study.

The $ZrH_{1.7}$ layer is made by gaseous diffusion of hydrogen into a zirconium metal lattice at high temperature. Hydrogen atoms exist as interstitials in the zirconium metal lattice structure. The density of $ZrH_{1.7}$ varies according to its hydrogen contents x in ZrH_x [25].

$$\begin{aligned} \rho_{ZrH} &= \frac{1}{0.1541+0.0145\cdot x}\ \text{g/cm}^3, \quad \text{for } x < 1.6, \\ \rho_{ZrH} &= \frac{1}{0.1706+0.0042\cdot x}\ \text{g/cm}^3, \quad \text{for } x \geqslant 1.6. \end{aligned} \tag{7.12}$$

After $ZrH_{1.7}$ fabrication, however, hydrogen atoms are dissociated from zirconium metal lattice at high temperature, which degrades its moderating ability. To prevent this, the $ZrH_{1.7}$ layer is enveloped by a dense metal cladding such as stainless steel.

7.5.4 *Fuel Assembly Design*

An example of the seed fuel assembly is shown in Fig. 7.26 [1]. It has 312 fuel rods and 18 control rod guide tubes and one instrumentation tube in a hexagonal arrangement. The seed fuel assembly has a very similar configuration to that of typical LMFBRs.

The existence of $ZrH_{1.7}$ layers in the blanket assembly disturbs the radial power distribution, particularly in the neighborhood of the seed-blanket interface. The high power peak at the periphery of the seed assembly results from thermal neutrons gathered after slowing down through the $ZrH_{1.7}$ layer. For this reason, the $ZrH_{1.7}$ layer needs to be located at a slightly inner position from the boundary of the blanket assembly. However, direct exposure of a large portion of the blanket fuel, that is, at a more inner position of the $ZrH_{1.7}$ layer in the blanket assembly, increases fast fission in the exposed blanket fuel at voiding, which results in more positive void reactivity.

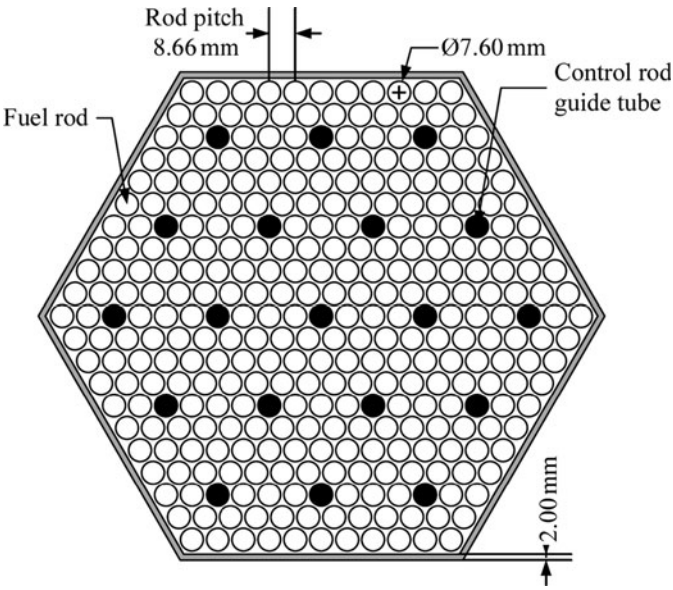


Fig. 7.26 Seed fuel assembly design. (Taken from [1])

As a countermeasure, the exposed blanket fuel rods can be replaced by a thick walled duct tube as shown in Fig. 7.27 [1]. The thick walled duct tube acts like an internal reflector between the seed assembly and $ZrH_{1.7}$ layer. The fast neutrons coming from the seed region are also slowed down through the stainless steel tube but are less thermalized while the effect of the $ZrH_{1.7}$ layer on the void reactivity remains the same. Since there is no blanket fuel directly exposed to the seed region, the fast fission in the blanket region is reduced, which also contributes to more negative void reactivity.

Figure 7.28 [1] compares radial power distributions with ordinary blanket fuel rods or thick walled duct tubes in the outer region of blanket assemblies. Simplified R-Z calculations for radial heterogeneous cores are used to clarify the effect of the duct tubes. The relative power peak near the seed and blanket interface is significantly reduced by replacing the blanket fuel rods with the duct tubes.

7.5.5 Core Arrangement

7.5.5.1 In-Vessel Flow Path

The flow rate at each fuel assembly inlet is controlled by an orifice and is not changeable during the operation, while the power share of the blanket assemblies gets larger as burnup proceeds. Flow rate that is large enough to cool the blanket

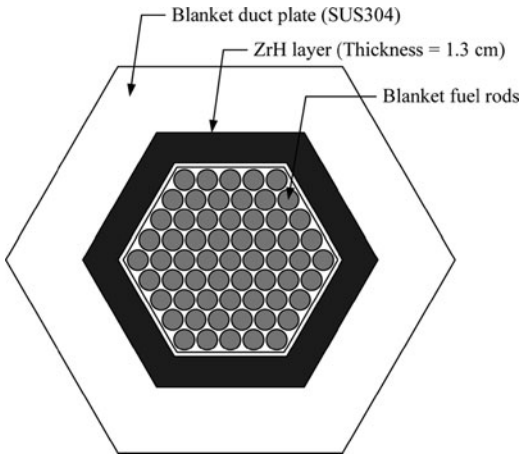


Fig. 7.27 Blanket fuel assembly design. (Taken from [1])

fuel assemblies at the end of equilibrium cycle (EOEC) is provided to them and kept constant over the cycle. If all the seed and blanket assemblies are cooled by upward flow (one-path design), the average outlet temperature is degraded because the power to flow ratios in the blanket assemblies are small. In order to keep the average outlet temperature high, two-pass design is adopted like the Super LWR with the downward flow water rods (see Chap. 2).

7.5.5.2 Fuel Loading Pattern for Negative Void Reactivity

The void reactivity depends on the shape, loading pattern, and neutronic coupling (with seed assemblies) of the $ZrH_{1.7}$ layer. The three-dimensional design method provides flexibility in the core arrangement. Several types of core arrangement are used to calculate the void reactivity. The total number of the fuel assemblies and the fraction of the blanket assemblies are kept constant. Five types, (a) radial heterogeneous, (b) fully scattered, (c) petal, (d) composite 1, and (e) composite 2, are considered as shown in Fig. 7.29. The void reactivities with each core arrangement are evaluated for fresh cores with fixed coolant density in order to assess only the effect of the core arrangement.

Table 7.12 summarizes the results. The composite type arrangements have the most negative void reactivity. This can be simply explained in terms of the degree of neutronic coupling. The neutronic coupling can be expressed by the number of surfaces that a seed assembly faces on neighboring seed fuel assemblies. This number in the composite type arrangements is less than 3, while it is more than 4 in the radial heterogeneous type, more than 3 in the petal type, and 3 in the fully scattered type except for the outermost fuel assemblies, where neutron leakage is more dominant than neutronic coupling at voiding. Although the composite 1 type has more negative void reactivity than the composite 2 type, the fuel management

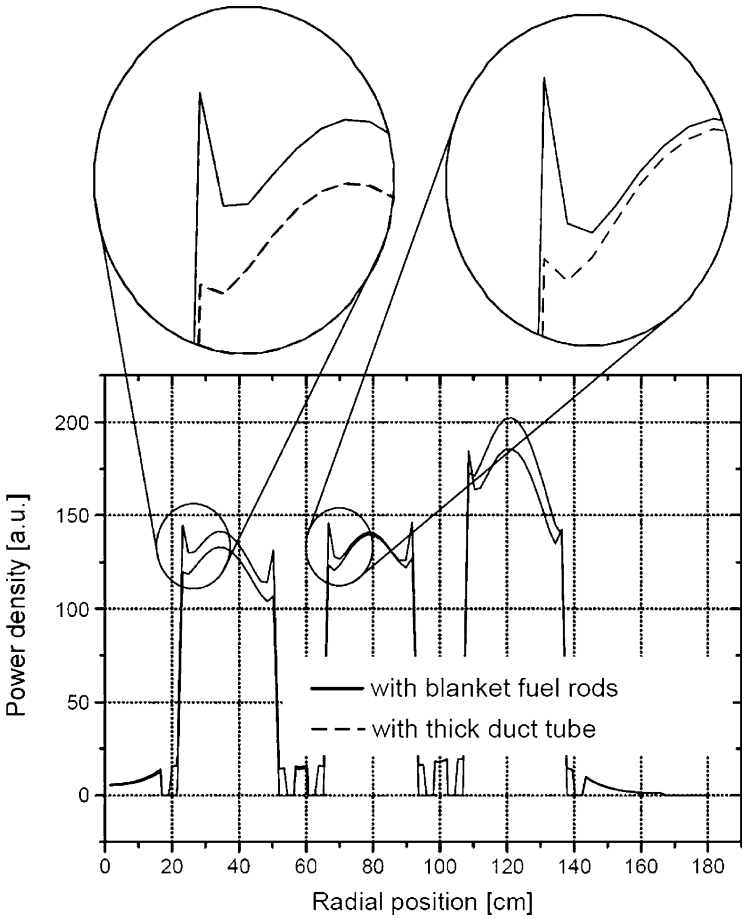


Fig. 7.28 Change of radial power distribution with thick walled duct tube. (Taken from [1])

scheme for the former is restricted because the power distribution cannot be well controlled with fewer blanket assemblies in the core central region. The composite 2 type is selected as the final core arrangement.

Figure 7.30 shows an example of the core arrangement and fuel management scheme in the equilibrium core of a 1,000 MWe class Super FR. A typical out-in fuel management scheme is used.

7.5.6 Design of 1,000 MWe Class Core

The fuel enrichment in the seed assemblies is axially zoned to avoid excessive power peaking at the bottom part of the core where the coolant density is high.

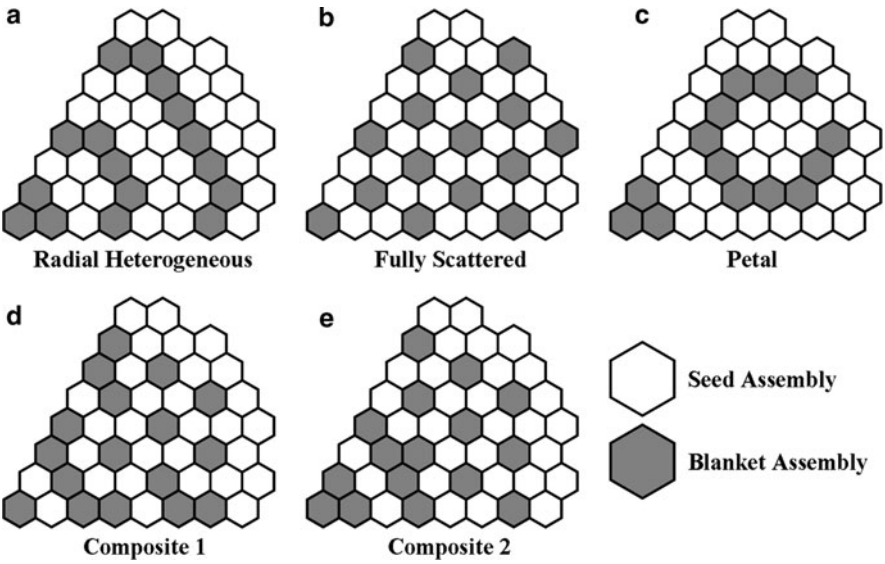


Fig. 7.29 Core arrangements for void reactivity calculations

Table 7.12 Coolant void reactivities with various core arrangements

Type of core arrangement	Void reactivity (%dk/k)	
	BOEC	EOEC
(a) Radial heterogeneous	−0.52	1.15
(b) Fully scattered	2.59	2.68
(c) Petal	−0.84	0.74
(d) Composite 1	−1.79	−0.64
(e) Composite 2	−1.43	−0.50

The average fissile Pu enrichments are 20.2, 19.6, 20.8, 21.3 wt% from the bottom to top regions of the core for the division shown in Fig. 7.31 [1]. The preliminary design parameters are summarized in Table 7.13. All the design criteria and goals are satisfied except for the average core outlet temperature, which is far from the design goal of 500°C. The main reason for the low outlet temperature is the high local power peaking factor of the seed assemblies. Although the thick walled duct tube surrounding the $ZrH_{1.7}$ layer is effective for reducing the local power peak in the peripheral seed fuel rods as stated in Sect. 7.5.4, the local power peaking factor is still large and reaches 1.4. Large flow rate is needed for cooling the peripheral fuel rods in the seed assemblies, which results in low average outlet temperature. However, the high local power peaking only appears within a few rows from the boundary of the seed fuel assemblies as can be seen in Fig. 7.32. This is because the diffusion length of thermalized neutrons through the $ZrH_{1.7}$ layer is a few centimeters in the seed fuel assembly.

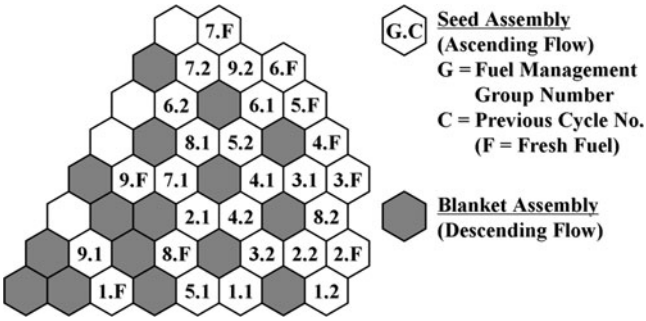
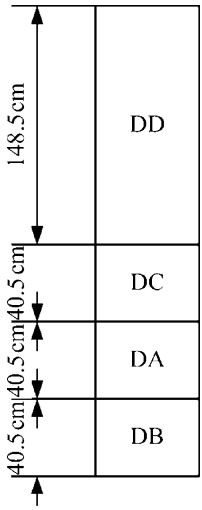


Fig. 7.30 Example of core arrangement and fuel management scheme for 1,000 MWe class Super FR

Fig. 7.31 Axial division of core for enrichment zoning. (Taken from [1])



Three approaches are proposed to improve the core outlet temperature. One is radial fuel enrichment zoning. High local power of the seed fuel rods near the boundary of the seed assembly can be controlled by placing low enriched fuel rods there. The Pu fissile enrichment is zoned as shown in Fig. 7.33 [1]. The enrichment zoning has a 1/6 symmetric pattern. Low enriched fuel rods are placed at the center of the outermost layer having the highest local power. The enrichment gradually increases as the fuel rod position gets closer to the fuel assembly center. The inner part of the seed fuel assembly has a constant enrichment. The second approach is to separately control the flow rate between the inner and outer regions of the seed fuel assembly. The inner region has relatively low power density and the power distribution is rather flat. In most seed assemblies, high power peaking appears in the

Table 7.13 Preliminary design parameters for 1,000 MWe class Super FR

Thermal power (MW)	2,358
Active core height/equivalent core diameter (m)	2.70/2.67
Average fissile Pu enrichment (%)	20.8
Average power density (MW/m^3)	156
Average/maximum linear heat generation rate (kW/m)	17/38.9
Coolant inlet/average outlet temperature (°C)	280/431
Core coolant flow rate (kg/s)	1,438
Coolant void reactivity at BOEC/EOEC (%dk/k)	−1.85/−1.0
Average discharge burnup (GWD/tHM)	68.3

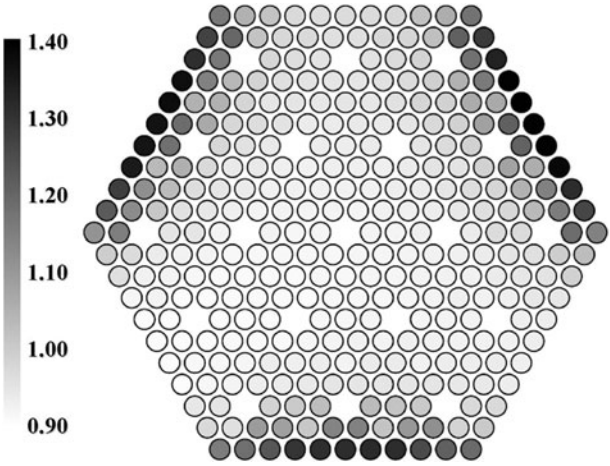


Fig. 7.32 Pin power distribution in typical seed assembly

outer region. The separated flow control can be achieved by placing the flow separation plate between the high and low power regions as shown in Fig. 7.34 [1]. The third approach is to employ downward flow in some of the seed assemblies as well as the blanket assemblies. The local power distribution in the inner seed assemblies can be well controlled by just radial enrichment zoning, while that in the peripheral seed assemblies has a very steep gradient. This cannot be easily controlled by the radial enrichment zoning or separated flow rate control. Downward flow is employed in the peripheral and innermost seed assemblies as shown in Figs. 7.35 and 7.36.

The average core outlet temperatures obtained by each approach are summarized in Table 7.14. The radial enrichment zoning and separated flow control are effective for improving the temperature but have a limitation for the peripheral seed assemblies, which have a steep power gradient. This limitation is solved by applying downward flow, and a high outlet temperature of over 500°C is achieved. Downward flow cooling of peripheral seed fuel assemblies is also advantageous for coolant void reactivity. Coolant densities of those assemblies are a little higher than in the upward flow assemblies. Neutron leakage from peripheral seed assemblies gets

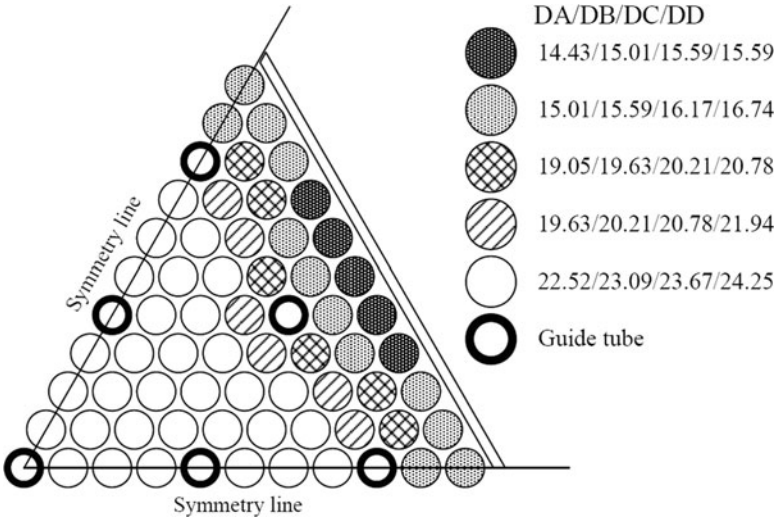


Fig. 7.33 Example of radial zoning of Pu fissile enrichment for 1,000 MWe class Super FR (unit: wt%). (Taken from [1])

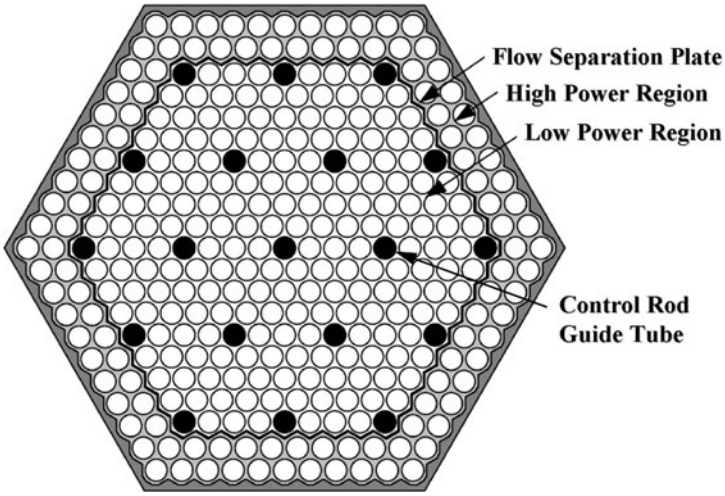


Fig. 7.34 Fuel assembly design for separated flow rate control

more dominant at voiding. Other nuclear parameters are not significantly changed since the average Pu fissile enrichment is kept constant for all the cases. Thus, a combination of the first (radial enrichment zoning) and the third (downward flow in some seed assemblies) approaches is chosen.

An example of the final core design is summarized in Table 7.15. All the design criteria and goals including the average core outlet temperature are satisfied.

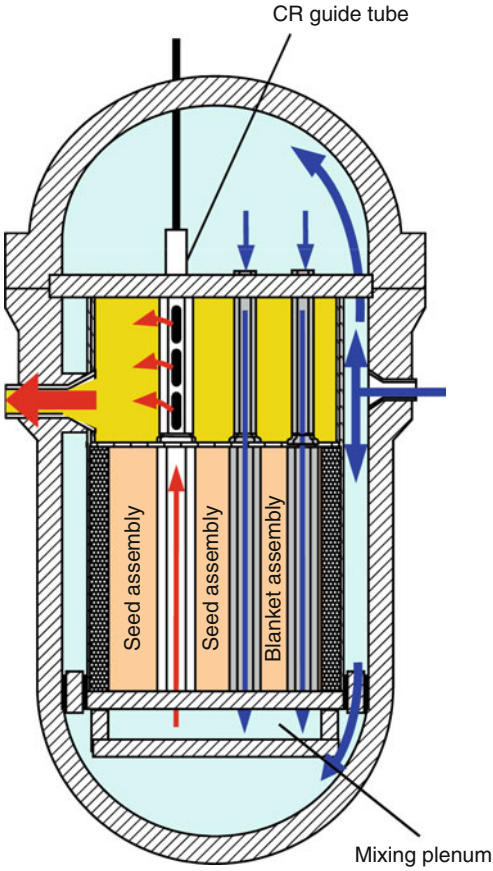


Fig. 7.35 Two-pass flow scheme with downward flow in blanket assemblies and part of the seed assemblies

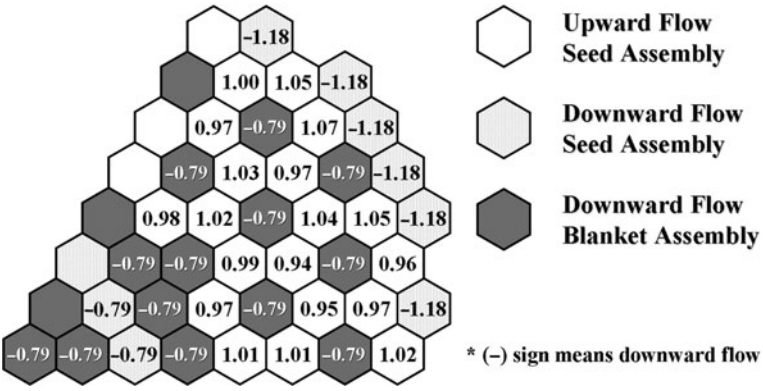


Fig. 7.36 Example of flow distribution design for 1,000 MWe class Super FR

The maximum linear generation heat rate over the equilibrium cycle is 38.9 kW/m. The linear heat generation rate tends to decrease as burnup proceeds as shown in Fig. 7.37 because the power share of the seed fuel assemblies gets smaller. Figure 7.38 shows the assembly power peaking factors at BOEC and EOEC. Since the fresh seed fuel assemblies are loaded in the core peripheral regions, the peak power appears in the outer region at BOEC and moves to the core central region toward EOEC.

The local power peaking factor for each fuel assembly is shown in Fig. 7.39. The local power peaking factors in an assembly range from 1.08 to 1.25 in the upward flow regions and those in the peripheral seed assemblies are relatively large. A small local power peaking factor in the upward flow region is essential for high average outlet temperature and is achieved by the radial enrichment zoning in the seed assemblies.

The coolant outlet temperatures at each fuel assembly are shown in Fig. 7.40. They vary from 446 to 541°C and directly correspond to the local power peaking factors. A small local power peaking factor yields high assembly outlet temperature. Maximum change of the assembly outlet temperature is about 8.5% (in ^{o}C) over the cycle. The mixing plenum temperature also varies because the power share of the downward flow region gets larger towards EOEC. The maximum

Table 7.14 Average core outlet temperature obtained by three approaches

	Core coolant flow rate (kg/s)	Average outlet temperature (°C)
Enrichment zoning only	1,278	476
Enrichment zoning and separated flow control	1,244	488
Enrichment zoning and downward flow in part of the seed assemblies	1,210	503

Table 7.15 Example of core design result of 1,000 MWe class Super FR

Thermal/electric power (MW)	2,358/1,033
Active core height/equivalent core diameter (m)	2.70/2.67
Fuel rod length including gas plenum (m)	4.3
Number of seed/blanket/total fuel assemblies	162/73/235
Cycle length (FPD)/number of batches	45/3
Average fissile Pu enrichment (wt%)	20.8
Fissile Pu inventory (ton)	8.44
Average power density (MW/m^3)	156
Average/maximum linear heat generation rate (kW/m)	17/38.9
Average discharge burnup (GWD/tHM)	68.3
Coolant inlet/average outlet temperature (°C)	280/503
Maximum cladding surface temperature (°C)	643
Mixing plenum temperature at BOEC/EOEC (°C)	368/373
Coolant void reactivity at BOEC/EOEC	−1.9/−1.8

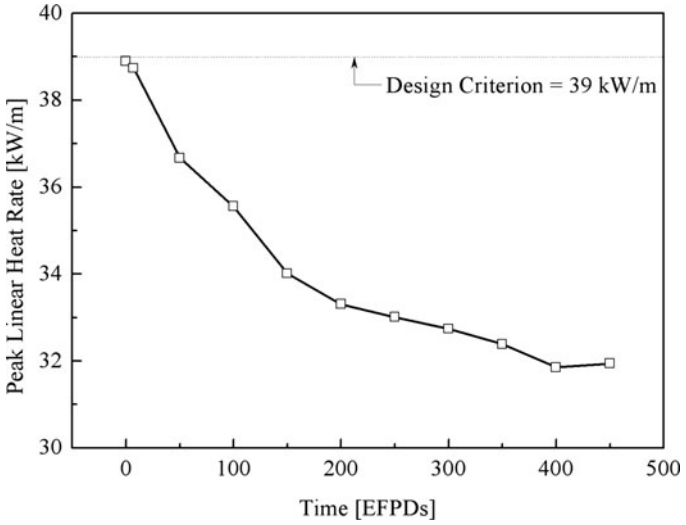


Fig. 7.37 Example of peak linear heat rate of 1,000 MWe class Super FR

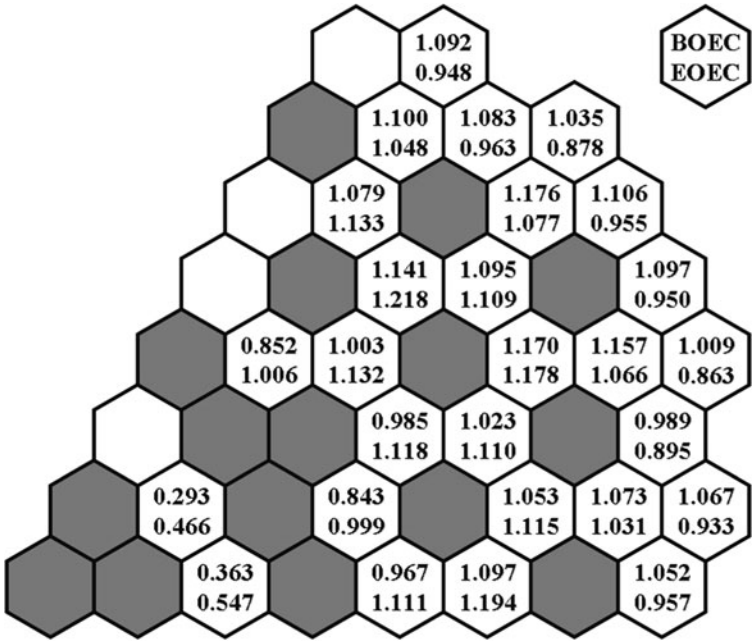


Fig. 7.38 Example of assembly power peaking factors of 1,000 MWe class Super FR

temperature is about 373°C, which is slightly lower than the pseudo-critical temperature of 384°C at 25 MPa.

The peak values of the cladding surface temperatures in each seed assembly are shown in Fig. 7.41. The MCST throughout the equilibrium cycle, calculated by the single channel analyses, is 643°C. The local power distribution within an assembly is taken into account, but heterogeneity of the subchannels is not considered. The maximum cladding surface temperature is calculated again by subchannel analyses in Sect. 7.6.

7.6 Subchannel Analysis

7.6.1 Introduction

The heterogeneities of the subchannels and turbulent mixing among the subchannels in the hexagonal fuel assembly of the Super FR are different from those in the square fuel assembly of the Super LWR. The many water rods of the Super LWR tend to disturb the flow mixing, while the heterogeneity of the subchannels in the square fuel assembly is substantially smaller than that in the hexagonal fuel assembly. In the Super LWR design (see Chap. 2), the local power distribution

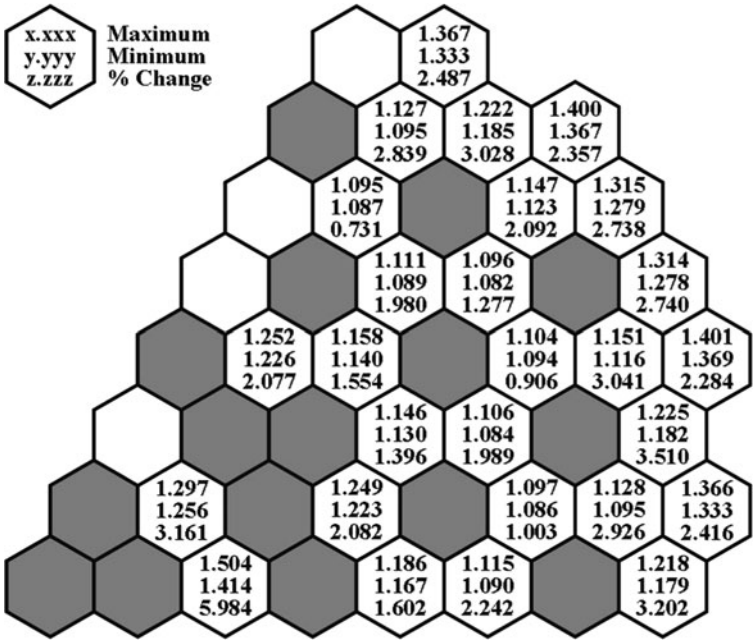


Fig. 7.39 Example of local power peaking factors of 1,000 MWe class Super FR

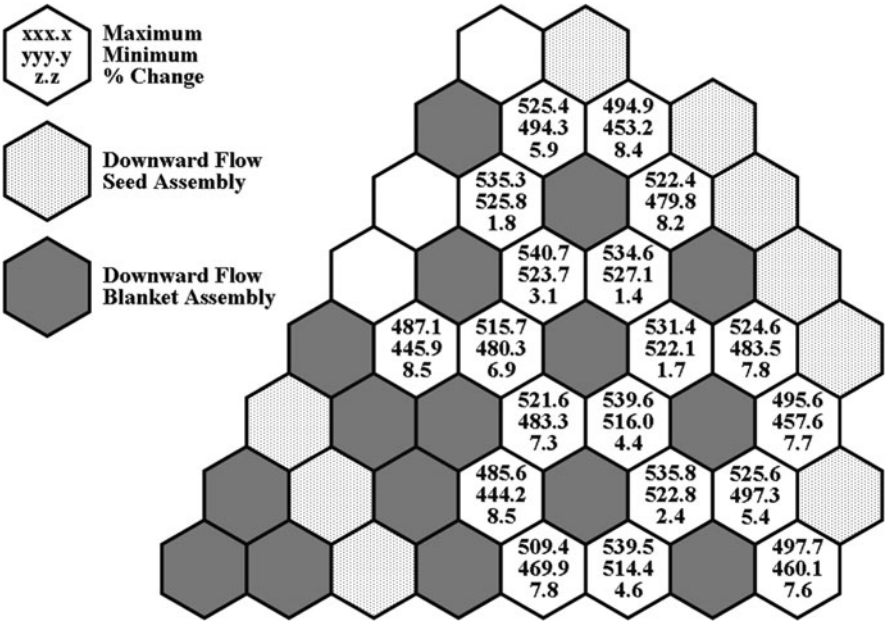


Fig. 7.40 Example of assembly outlet temperatures of 1,000 MWe class Super FR

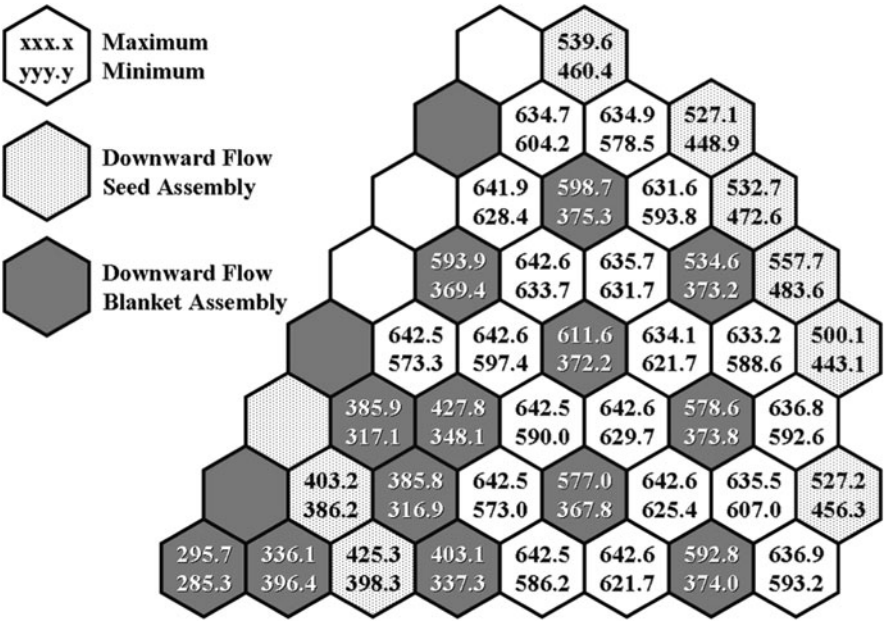


Fig. 7.41 Example of peak cladding surface temperatures of 1,000 MWe class Super FR

within the fuel assembly is treated separately from the thermal-hydraulic coupled core calculation in evaluating the MCST. That results in the large temperature rise of the MCST (about 58°C). In the Super FR design, however, the local power distribution within an assembly is already treated in the single channel analyses coupled with the nuclear calculation as stated in Sect. 7.5.

This section describes the deviation of cladding surface temperature arising from the subchannel heterogeneity in the hexagonal fuel assembly and how it can be controlled by modification of the fuel assembly design. Several local power distributions taken from the core depletion calculation are used to evaluate the MCST. The influence of the local power on flow deflection and consequent cladding surface temperature deviation are also evaluated based on the results of the subchannel analysis. Several thermal design considerations are made in terms of the subchannel heterogeneity and local power peaking factor as well as the MCST.

7.6.2 Temperature Difference Arising from Subchannel Heterogeneity

7.6.2.1 Introduction of Fuel Assembly and Subchannel Parameters

A fuel assembly has 312 fuel rods, 18 control rod guide tubes and one instrumentation tube. The fuel rods are arranged as a triangular lattice structure with the P/D of 1.14 as shown in Fig. 7.26 [1]. The heated length of a fuel rod is 2.7 m and five grid spacers are assumed to be placed equi-distant along the fuel rods. Placing more grid spacers will enhance mechanical stability and improve the turbulent mixing and heat transfer. The assumption of five grid spacers as the minimum number will yield more conservative results from the viewpoint of thermal design.

There are four different subchannels, (a) ordinary, (b) edge, (c) corner, and (d) near guide tube as shown in Fig 7.42 [1]. Main heterogeneities come from the near guide tube and edge subchannels, which are a considerable portion of a fuel assembly. The channel parameters for each subchannel type are summarized in Table 7.16 [1]. The heated perimeter over the channel is an index of how much heat is transferred through the fuel cladding surface to neighboring coolant and is a key parameter to determine the subchannel heterogeneity.

7.6.2.2 Rise of Maximum Cladding Surface Temperature by Subchannel Heterogeneity

In order to evaluate the influence of the subchannel heterogeneity, the pin power distribution is set as uniform and the axial power distribution is set as cosine with the maximum linear heat generation rate of 39 kW/m. Figure 7.43 [1] shows the mass flux distribution at the assembly outlet. Due to a relatively large hydraulic

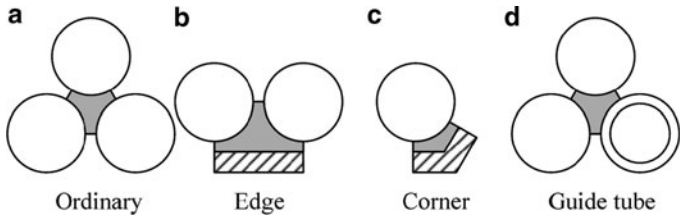


Fig. 7.42 Subchannel shapes. (Taken from [1])

Table 7.16 Thermal hydraulic parameters of subchannels. (Taken from [1])

	Ordinary	Edge	Corner	Guide
Channel area, A (mm^2)	9.82	19.46	6.10	9.82
Wetted perimeter, P_w (mm)	11.94	20.60	9.60	11.94
Heated perimeter, P_h (mm)	11.94	11.94	3.98	7.96
Hydraulic diameter, D_h (mm)	3.29	3.78	2.54	3.29
P_h/A (mm^{-1})	1.22	0.61	0.65	0.81
Number of channels	486	60	6	114

diameter, and hence smaller friction pressure drop, relatively high mass flux is obtained in the edge subchannels. The mass flux is relatively low in the ordinary subchannels. Figure 7.44 [1] shows the relative distributions of the coolant outlet temperature and peak cladding surface temperature along the fuel rod. All the peak cladding surface temperatures appear near the axial position 90% from the bottom (based on heated length).

The central ordinary subchannels have larger coolant temperature rise than the others. This results in higher peak cladding surface temperature. The peak to average ratio of the cladding surface temperature is about 1.27 (in °C). This is because the ratio of the heated perimeter to channel area (P_h/A) of the ordinary subchannel is about twice that of the ratios of the edge and corner subchannels and there is the relatively low mass flux as mentioned above. The P_h/A can be controlled by adjusting the P/D. It becomes more uniform as the P/D gets larger as shown in Fig. 7.45 [1]. However, a tight fuel rod arrangement is essential for both a hard fast spectrum and high coolant outlet temperature. Increasing the P/D ratio results in softer neutron spectrum and hence requires more fissile Pu enrichment. Reducing the gap between the fuel rod and duct wall raises fabrication concerns.

The subchannel heterogeneity is controlled by altering the subchannel shapes except for the ordinary subchannels as shown in Fig. 7.46 [1] while keeping the fuel rod gap clearance over 1 mm at any location. The edge subchannel shape is modified by introducing the protrusion to the wrapper duct tube. The corner subchannel shape is modified by rounding the corner of the wrapper duct tube. The guide tube subchannel shape can be modified by enlarging the diameter of the guide tube or inserting dummy rods near the guide tube. If the guide tube diameter is enlarged, the gap clearance between the fuel rod and guide tube gets smaller, and it might raise fabrication concerns. Thus, this approach is not taken and the dummy

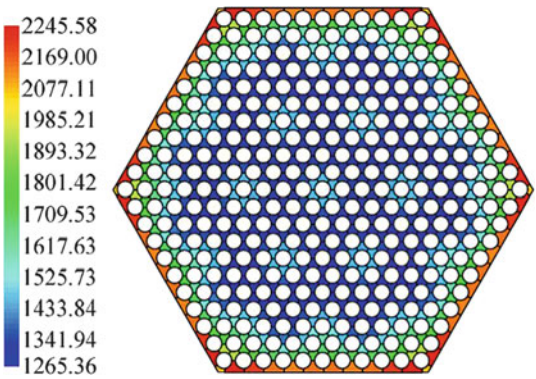


Fig. 7.43 Mass flux distribution in seed fuel assembly under uniform pin power distribution (unit: kg/m^{2}s). (Taken from [1])

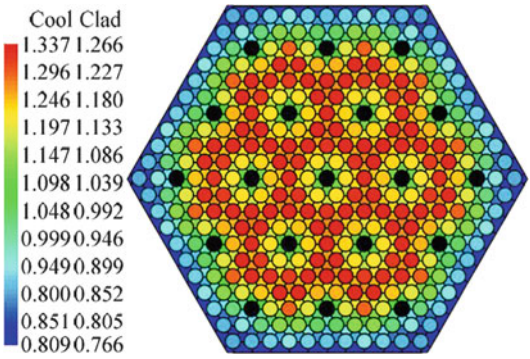


Fig. 7.44 Relative distribution of outlet coolant and peak cladding temperatures in seed fuel assembly under uniform pin power distribution. (Taken from [1])

rod is chosen here. The modified channel parameters are shown in Table 7.17 [1]. The subchannel heterogeneity is mitigated.

Table 7.18 [1] shows the MCSTs and their difference from 650°C with respect to several combinations of the modifications. The coolant outlet and peak cladding surface temperature distributions and the mass flux distributions in each case are shown in Figs. 7.47–7.49 [1]. These calculations are carried out with the flow rate providing the MCST of 650°C in single channel analysis. The increase in the MCST from 650°C can be kept smaller in the Super FR than in the Super LWR.

7.6.3 Evaluation of MCST over Equilibrium Cycle

Generally, the local power peaking factor in a fuel assembly of conventional LMFBRs is small due to the longer mean free path of neutrons and better neutronic coupling. However, the local power peaking factor of the Super FR is rather high.

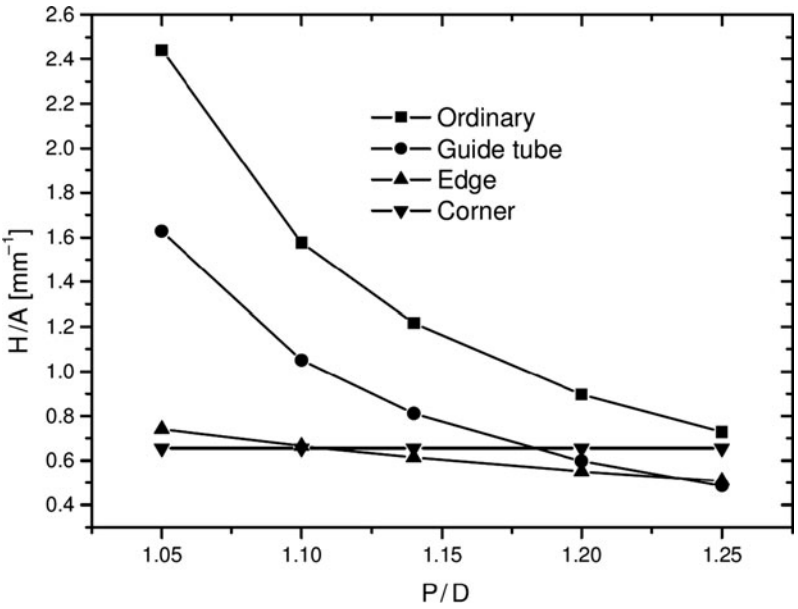


Fig. 7.45 Change of P_h/A as a function of P/D. (Taken from [1])

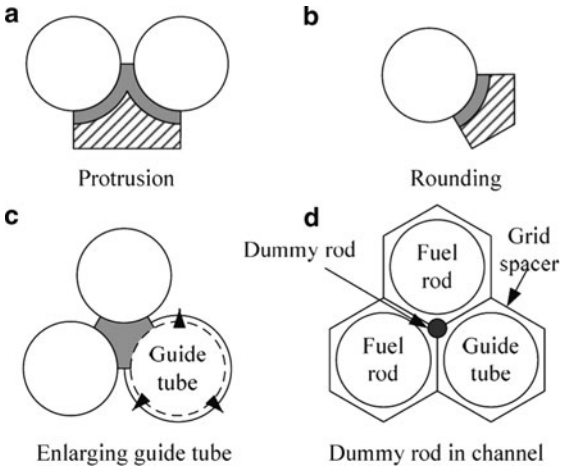


Fig. 7.46 Modifications of subchannel shapes. (Taken from [1])

This is mainly because of the existence of the $ZrH_{1.7}$ layer for negative void reactivity. So as to reduce the local power peaking factors, the radial enrichment zoning is used as described in Sect 7.5.

There are two competitive phenomena associated with the MCST calculation. One is the subchannel heterogeneity as discussed above. The other is the flow mixing among the subchannels, which mitigates the flow and coolant enthalpy

Table 7.17 Modified subchannel parameters. (Taken from [1])

Type	Channel area (mm^2)	Wetted perimeter (mm)	Heated perimeter (mm)	D_h (mm)	H/A (1/mm)	Original H/A
Ordinary	9.82	11.94	11.94	3.29	1.22	1.22
Edge	12.89	22.63	11.94	2.28	0.93	0.61
Corner	4.83	9.07	3.98	2.13	0.82	0.65
Near guide tube						0.81
1.0-mm dummy rod	9.04	15.08	7.96	2.40	0.88	
1.5-mm dummy rod	8.05	16.65	7.96	1.93	0.99	

Table 7.18 MCSTs with respect to modification of subchannel shapes. (Taken from [1])

Case	Calculation condition	MCST (°C)	Relative change (°C)
–	Single channel analysis	650	–
1	Protrusion in wrapper tube Rounded corner of wrapper duct tube	680.2	30.2
2	Protrusion in wrapper tube Rounded corner of wrapper duct tube Dummy rod with 1.0 mm diameter	668.5	18.5
3	Protrusion in wrapper tube Rounded corner of wrapper duct tube Dummy rod with 1.5 mm diameter	666.1	16.1

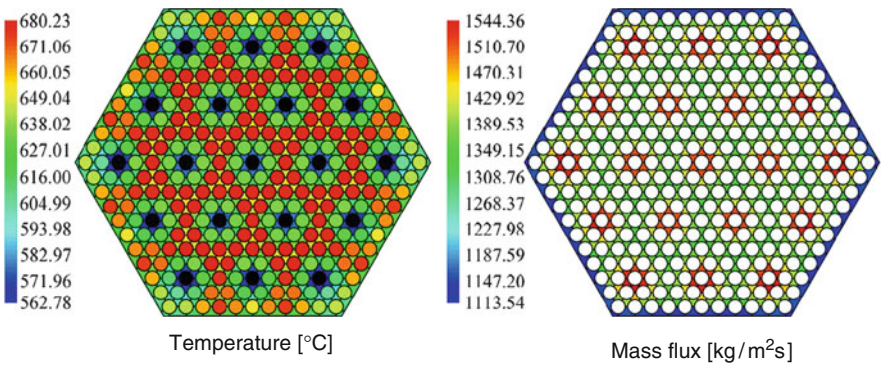


Fig. 7.47 Subchannel analysis results in Case 1 of Table 7.18. (Taken from [1])

deviations arising from the subchannel heterogeneity and local power peaking. The differences of the MCSTs between the single and subchannel analyses are determined by which effect is more dominant. Evaluating such differences between the single and subchannel analyses is important to clarify whether the single channel analysis is conservative regarding the core design or not.

Based on the two fuel assembly designs (Cases 2 and 3 in Table 7.18 [1]), subchannel analysis is carried out with the pin power distributions taken from the thermal-hydraulic coupled neutronic calculation in order to evaluate the MCST

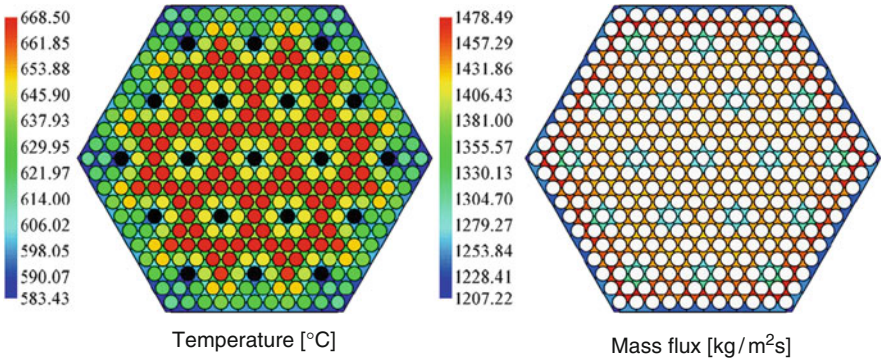


Fig. 7.48 Subchannel analysis results in Case 2 of Table 7.18. (Taken from [1])

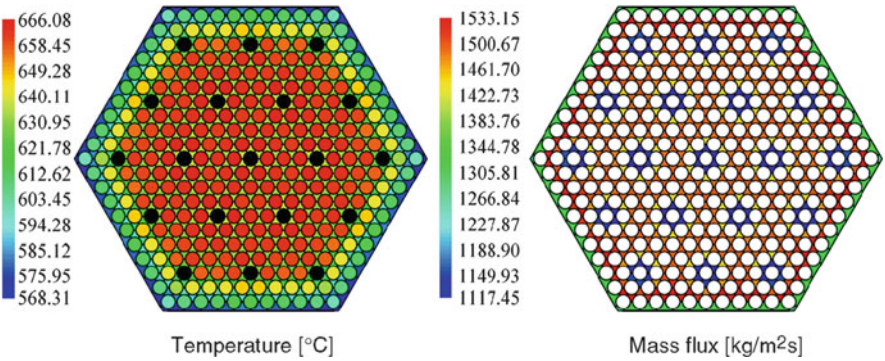


Fig. 7.49 Subchannel analysis results in Case 3 of Table 7.18. (Taken from [1])

over the equilibrium cycle and compared with those from the single channel analysis. Figures 7.50 [1] and 7.51 [1] show the MCSTs over the cycle. The highest value is 645.3°C calculated by the subchannel analysis, which is little larger than that calculated by the single channel analysis and below the design criterion of 650°C.

Figure 7.52 shows the differences in the MVSTs between single and subchannel analyses as a function of the local power peaking factors. The single channel analysis provides the higher MCST, which means that the flow mixing is more dominant, unless the local power peaking factor exceeds a certain value depending on the subchannel heterogeneity. Based on these results, it is found out that the local power peaking should be kept below 1.2 for the upward flow seed assemblies in order to avoid excessive deviation of the cladding surface temperature and to keep the single channel analysis conservative. The maximum difference of the MCSTs in the downward flow region is 85°C but the MCST is still below the criterion due to relatively smaller power to flow ratio. The downward flow cooling of the seed

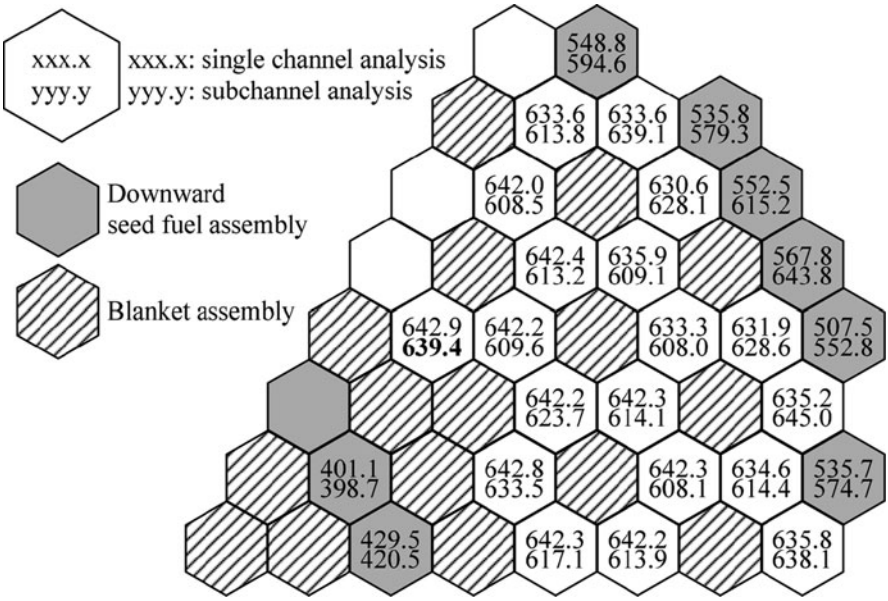


Fig. 7.50 Comparison of MCSTs between single and subchannel analyses in Case 2 of Table 7.18. (Taken from [1])

assemblies having relatively high local power peaking factor is effective for keeping the MCST below the criterion.

7.7 Evaluation of Maximum Cladding Surface Temperature with Engineering Uncertainties

In order to investigate fuel rod integrity during normal operation and abnormal conditions, the MCST is evaluated in consideration of the engineering uncertainties by using an approach similar to the Monte Carlo Statistical Thermal Design Procedure (MCSTDP) introduced in Chap. 2.

7.7.1 Treatment of Downward Flow

The MCSTDP for the Super LWR is improved to treat the seed assemblies with downward flow. Even though the hot spot is located at the upward flow region, the downward flow region is also affected by the uncertainties of the system parameters. The improved MCSTDP consists of two parts. One is for the upward flow

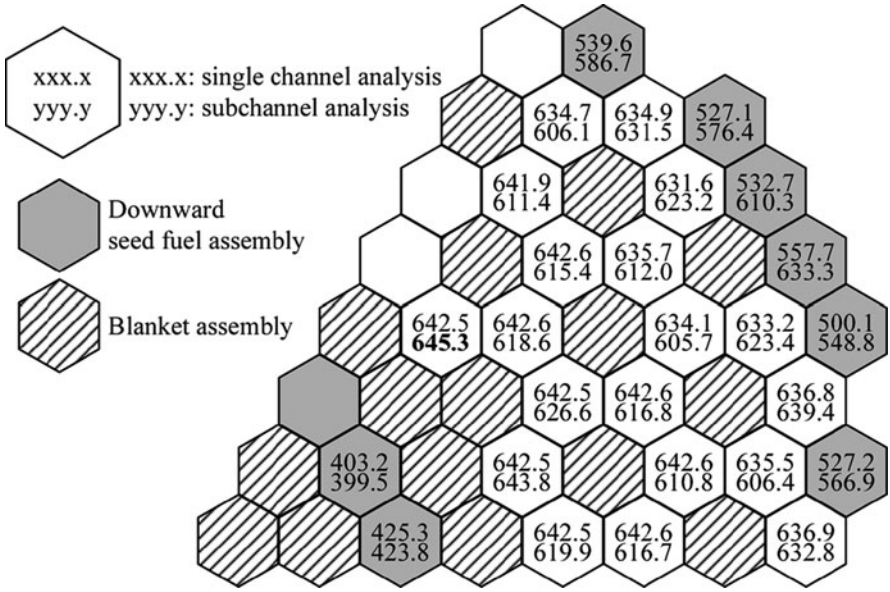


Fig. 7.51 Comparison of MCSTs between single and subchannel analyses in Case 3 of Table 7.18. (Taken from [1])

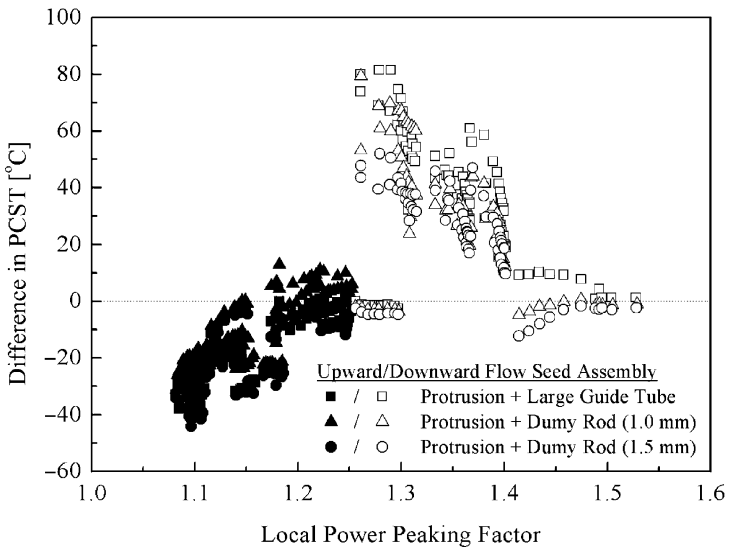


Fig. 7.52 Difference in MCSTs between subchannel and single channel analyses with respect to local power peaking factor. (ΔMCST is negative when the single channel analysis provides a higher MCST.)

region, and the other is for the downward flow region. The MCST in the upward flow region is calculated by subchannel analysis, while single channel analysis is used for evaluating the mixing plenum temperature. Only the system parameter uncertainties are taken into account in the single channel analysis for the downward flow region, while all the design uncertainties are considered in the subchannel analysis of the hot assembly. The overall calculation procedure and associated uncertainties are depicted in Fig. 7.53 [1]. The calculation conditions are summarized in Table 7.19 [1].

7.7.2 Nominal Conditions and Uncertainties

The MCSTs are evaluated for three burnup states, BOEC, MOEC (middle of equilibrium cycle) and EOEC. The nominal conditions at these burnup states are shown in Table 7.20 [1]. The nominal MCST over the cycle appears at EOEC and is 645.3°C.

The system parameter uncertainties taken into account here are listed in Table 7.21 [1]. Calibration errors associated with measurement of the feedwater temperature are typically in the range of ±2.22°C. The standard deviation for this calibration error is 1.27°C in a uniform distribution. The typical measurement error of the feedwater flow rate is 2% of the nominal value. The standard deviation of 2% error is 1.15%, of the nominal value for the uniform distribution. The uncertainty of the core power level is caused by the calibration error of core total power measurement and control system dead band. A typical error (2% of the nominal value) is considered. Then, the standard deviation of the total power level is 1.15% considering the uniform distribution. The system pressure uncertainty of 200 kPa is considered. The standard deviation of the system pressure is 115 kPa, considering the uniform distribution.

The nuclear hot factors are used to consider the power distribution in the core. It consists of three hot factors, radial, local, and axial nuclear. The radial nuclear enthalpy rise hot factor is defined as the ratio of the hot assembly power to the average assembly power. The local nuclear enthalpy rise hot factor is defined as the ratio of the hot fuel rod power to the hot assembly average power. Finally, the axial nuclear enthalpy rise hot factor is defined as the ratio of the maximum axial plane power to the average plane power. In the full statistical treatment, the nuclear enthalpy rise hot factor is not an absolute value. It also varies around the nominal value with given tolerance. The uncertainty of the nuclear enthalpy rise hot factor is mainly induced by neutronic calculation errors. A typical error of 2% for each component of the hot factors is considered. If the normal distribution is assumed, the standard deviation of each hot factor is 1% of the nominal value. Table 7.22 [1] shows the uncertainties of the nuclear enthalpy rise hot factors considered here.

The engineering temperature rise hot channel factors account for flow conditions and tolerances of the hot coolant channel. They arise from the tolerances of dimensions, fissile contents, data processing, and so on. The engineering factors consist of two parts. One is the coolant temperature rise hot channel factor. The other is the film temperature rise hot channel factor. The engineering temperature

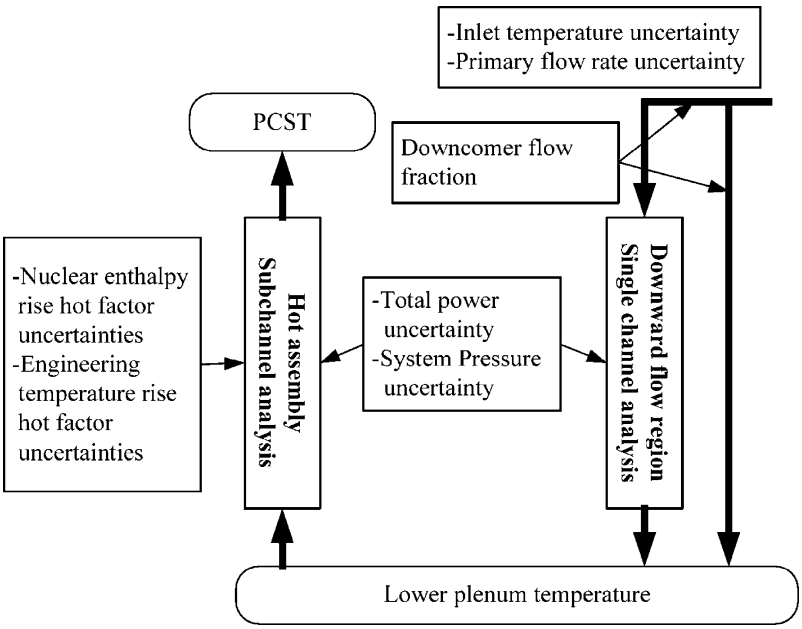


Fig. 7.53 Flow diagram of statistical thermal design procedure for the Super FR. (Taken from [1])

Table 7.19 Calculation conditions of hot assembly and downward flow region in statistical thermal design procedure for the Super FR. (Taken from [1])

	Hot assembly	Downward flow region
Method	Subchannel analysis	Single channel analysis
Linear heat rate	MLHGR	ALHGR
Uncertainties to be considered	System parameter Nuclear enthalpy rise Engineering temperature rise	System parameter
Kind of result	Peak cladding surface temperature	Lower plenum temperature

MLHGR maximum liner heat generation rate; *ALHGR* average linear heat generation rate

Table 7.20 Nominal conditions of hot assemblies in statistical thermal design procedure of the Super FR

	BOEC	MOEC	EOEC
Feedwater temperature (°C)	280		
Mixing plenum temperature (°C)	368.0	370.6	372.7
MCST (°C)	623.2	624.8	645.3
Mass flux (kg/m^{2}s)	1,708.4	1,558.3	1,558.3

Table 7.21 System parameter uncertainties assumed for the Super FR

Feedwater temperature	Distribution type	Uniform
	Nominal value (°C)	280
	Standard deviation (°C)	1.27
	One side width (°C)	2.2
Feedwater flow rate	Distribution type	Uniform
	Nominal value (kg/s)	1,209.7
	Standard deviation (%)	1.15
	One side width (%)	2
Total core power	Distribution type	Uniform
	Nominal value (MWt)	2,352
	Standard deviation (%)	1.15
	One side width (%)	2
System pressure	Distribution type	Uniform
	Nominal value (MPa)	25
	Standard deviation (MPa)	0.115
	One side width (MPa)	0.2

Table 7.22 Uncertainties of nuclear enthalpy rise hot factors assumed for the Super FR

Radial nuclear enthalpy rise hot factor $\left(F^{\mathrm{N}}_{\Delta H,\mathrm{r}}\right)$	Distribution type	Normal
	Nominal (E)	1
	Standard deviation	1%E
	One side width	2%E
Local nuclear enthalpy rise hot factor $\left(F^{\mathrm{N}}_{\Delta H,\mathrm{l}}\right)$	Distribution type	Normal
	Nominal (E)	1
	Standard deviation	1%E
	One side width	2%E
Axial nuclear enthalpy rise hot factor $\left(F^{\mathrm{N}}_{\Delta H,\mathrm{z}}\right)$	Distribution type	Normal
	Nominal (E)	1
	Standard deviation	1%E
	One side width	2%E

hot sub-factors are explained in Table 7.23 [1]. The typical values that have been used in statistical thermal designs of PWRs and the LMFBRs and assumed for the Super FR are listed in Table 7.24 [1] in comparison with those of the Super LWR. The engineering temperature rise hot factors of the Super FR are a little larger than those of the Super LWR. This is mainly due to the use of MOX fuel, since nuclear data files for transuranium nuclides have been less well evaluated than those for uranium. This causes large uncertainties to nuclear data and hence power distribution. The fissile content of MOX fuel is controlled by adjusting the mixing ratio between PuO_2 and UO_2, for which a larger uncertainty of fissile content is involved. The total engineering temperature rise hot factors can be summed over all individual hot sub-factors for the coolant temperature rise and film temperature rise hot factors.

$$F^{\mathrm{E}}_{\Delta H} = 1 + \sqrt{\sum_i \left(f^{\mathrm{e}}_i - 1\right)^2}, \tag{7.13}$$

where $F^{\mathrm{E}}_{\Delta H}$ is the engineering temperature rise hot factor and f^{e}_i is the engineering temperature hot sub-factor.

Table 7.23 Engineering temperature hot sub-factors. (Taken from [1])

Hot sub-factors	Involved uncertainty
Nuclear data	Evaluated nuclear data used in reactor physics calculation
Power distribution	Mismatch of calculated power distribution
Fissile fuel content tolerances	Uncertainty of fissile content in fuel
Inlet flow mal-distribution	Assembly hydraulic resistance and orifice uncertainty
Flow distribution calculation	Intra-assembly flow mal-distribution
Subchannel flow area	Geometrical tolerances of fuel rod displacement or expansion on coolant channel flow area
Pellet-cladding eccentricity	Eccentric position of fuel pellet within the cladding
Coolant properties	Uncertainties from coolant properties

Table 7.24 Uncertainties of engineering temperature rise hot sub-factors assumed for the Super FR. (Taken from [1])

Engineering temperature rise hot sub-factors	BOEC		MOEC		EOEC		Super LWR	
	f_l	f_{cs}	f_l	f_{cs}	f_l	f_{cs}	f_l	f_{cs}
Nuclear data	1.050	1.050	1.050	1.050	1.050	1.050	1.020	1.020
Power distribution	1.020	1.020	1.020	1.020	1.020	1.020	1.010	1.010
Fissile fuel content tolerances	1.052	1.052	1.052	1.052	1.052	1.052	1.025	1.025
Inlet flow mal-distribution	1.039	1.000	1.039	1.000	1.039	1.000	1.030	1.000
Intra-assembly flow mal-distribution	1.055	1.000	1.055	1.000	1.055	1.000	1.030	1.000
Subchannel flow area	1.080	1.030	1.090	1.070	1.080	1.070	1.070	1.050
Pellet-cladding eccentricity	1.000	1.150	1.000	1.150	1.000	1.150	1.000	1.100
Coolant properties	1.017	1.000	1.017	1.000	1.017	1.000	1.017	1.000
Total	1.130	1.170	1.136	1.182	1.130	1.182	1.136	1.182
Standard deviation of hot factors	0.043	0.057	0.045	0.061	0.043	0.061	0.045	0.061

They are treated as 3σ in normal distribution, where standard deviation σ of each hot factor is

$$\sigma = \frac{1}{3}(F_{\Delta H}^{\mathrm{E}} - 1). \tag{7.14}$$

In Table 7.24 [1], the engineering hot sub-factors for the change in the subchannel flow area are calculated by the MCSTDP combined with subchannel analysis. Both displacement and expansion variations of the fuel rod of 0.1 mm are taken into account as the 3σ value and the variations are sampled in the normal distribution. The directions of fuel rod displacement are also equally sampled within the range of -180 to 180°. The calculation conditions are summarized in Table 7.25 [1] and the model for fuel rod displacement and expansion is depicted in Fig. 7.54 [1]. Once the fuel rod displacement and the diameter change are sampled for all the fuel rods in a fuel assembly, the parameters of the subchannel geometry are changed. Subchannel analyses are conducted in three representative burnup states, BOEC, MOEC, and EOEC. Two cases are calculated in each burnup step. Case 1 is for radial flat power distribution with cosine shape of axial power distribution. Case 2 is for the three-dimensional power distribution of the hot assembly taken from the core calculation. Table 7.26 [1] shows the results of the

Table 7.25 Calculation conditions of engineering hot factors for change of subchannel area. (Taken from [1])

Total number of sample groups		4,000
Fuel rod diameter (mm)	Nominal	7.6
	3σ	0.1
Location of fuel rod (mm)	Nominal	0.0
	3σ	0.1
Direction of fuel rod displacement (rad)	Nominal	0.0
	Range	$-\pi$ to π
Number of sampled fuel rod		312

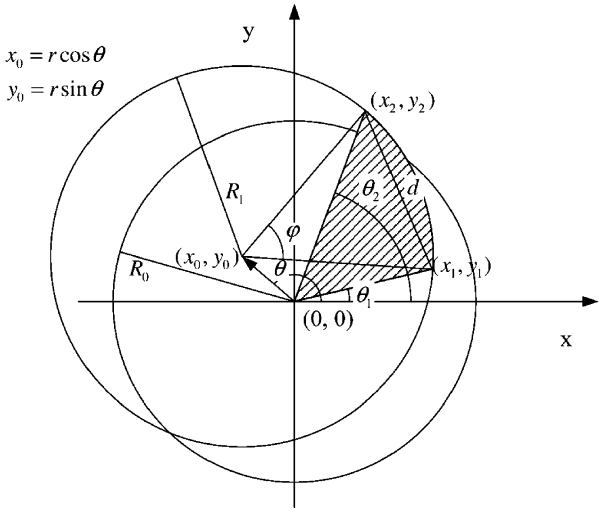


Fig. 7.54 Model for fuel rod displacement and expansion. (Taken from [1])

engineering temperature rise hot factors for the change of subchannel area. The resultant hot factors are slightly larger than those of the Super LWR.

The uncertainty of heat transfer correlation can be treated in two ways; one is to use a corresponding engineering hot channel factor, the other is to treat this uncertainty separately with parametric uncertainties. The latter is applied to this study as is done for the Super LWR in Chap. 2. The uncertainty of the heat transfer correlation is evaluated by comparing with the Oka–Koshizuka correlation and the Dittus–Boelter correlation in the high coolant enthalpy region. The uncertainty is evaluated as 6.33°C. It is taken as the correlation uncertainty because the hot spot is always in the high coolant enthalpy region.

7.7.3 Statistical Thermal Design of the Super FR

The results of the design uncertainty associated with the MCST are shown in Table 7.27 [1]. The MCST ensuring 95/95 limit is evaluated as 31°C with a

Table 7.26 Results of engineering temperature rise hot factors for change of subchannel area. (Taken from [1])

		Case 1	Case 2			Super LWR
			BOEC	MOEC	EOEC	
ΔT_{cs} (°C)	Mean value	52.80	54.37	59.53	71.78	83.91
	σ	0.60	0.52	1.35	1.58	1.42
	3σ	1.79	1.56	4.04	4.73	4.26
	f_{cs}	1.03	1.03	1.07	1.07	1.05
ΔT_l (°C)	Mean value	360.30	225.71	223.78	238.07	272.51
	σ	10.34	6.30	7.06	6.54	6.22
	3σ	31.03	18.90	21.18	19.61	18.66
	f_l	1.09	1.08	1.09	1.08	1.07

statistical combination of heat transfer correlation uncertainty. It does not significantly vary through the burnup states. The design uncertainty of 31°C in Super FR is almost the same as that of the Super LWR. The distributions of the MCST are shown in Fig. 7.55 [1].

As can be seen in Table 7.27 [1], the results of Monte Carlo procedure are in good agreement with those by the Revised Thermal Design Procedure (RTDP) (see Chap. 2) throughout the burnup states. Since all the uncertainties are merged into one sampling group in the Monte Carlo procedure, it is difficult to know the parametric contribution of an individual uncertainty to the total thermal design uncertainty. The RTDP method is very useful in assessing the parametric contribution of an individual uncertainty to the overall design uncertainty. The sensitivity factors for the Super FR are shown in Table 7.28 [1] and compared with those of the Super LWR. Most of the sensitivity factors of the Super FR except for the radial peaking factor are smaller than those of the Super LWR. Small sensitivity factors for other parametric variations are owing to better thermal hydraulic coupling between the coolant channels than the coupling in the Super LWR.

7.7.4 Comprehensive Evaluation of Maximum Cladding Surface Temperature at Normal Operation

Based on the subchannel analyses in Sect. 7.6 and the statistical thermal design in Sect. 7.7.3, the comprehensive evaluation of the MCST for the Super FR at normal operation can be drawn as Fig. 7.56 [1]. The MCST including the engineering uncertainties is predicted to be 681°C (650°C as limitation of nominal value + 31°C as engineering uncertainty), which ensures 95/95 limit. The reason is that the nominal MCST is directly evaluated by subchannel analysis in the Super FR without significant increase in the MCST compared to the single channel analysis due to the flatter pin power distribution and the better coolant mixing in the fuel assembly while the single channel analysis and subchannel analysis are separately

Table 7.27 Results of statistical thermal design and comparison with RTDP results. (Taken from [1])

		BOEC	MOEC	EOEC
Monte Carlo	Number of sampling groups	1,461	2,431	3,998
	Mean MCST (°C)	623.57	624.68	648.09
	Standard deviation of MCST (°C)	17.65	17.66	17.22
	Uncertainty in MCST (°C)	30.84	30.85	30.18
RTDP	Standard deviation of MCST (°C)	17.60	18.28	18.93
	Uncertainty in MCST (°C)	30.77	31.82	32.83

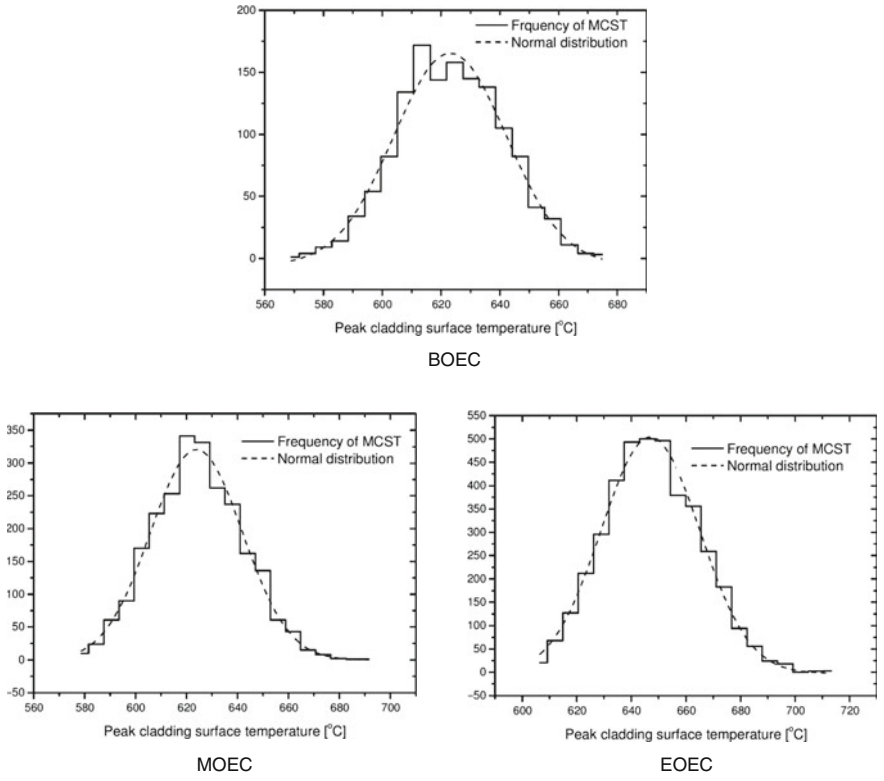


Fig. 7.55 Distributions of MCST. (Taken from [1])

conducted in the Super LWR (see Fig. 2.13 and Table 2.21) due to the larger local power peaking and the smaller coolant mixing. As a result, the MCST of the Super FR is lower than that of the Super LWR by about 60°C.

Based on the result here, the hot channel, which is treated in the thermal and stability analyses in Sect. 7.10 and the Safety analysis in Sect. 7.11, has the MCST of 681°C.

Table 7.28 Comparison of sensitivity factors between the Super FR and Super LWR. (Taken from [1])

	Super FR	Super LWR
Inlet temperature (K)	0.976	1.039
Mass flow rate	0.950	1.015
Power	0.964	1.000
Radial peaking factor	0.753	0.702
Local peaking factor	0.261	0.294
Axial peaking factor	0.081	0.137
Coolant temperature rise sub-factor	0.218	0.269
Cladding surface temperature rise sub-factor	0.079	0.097

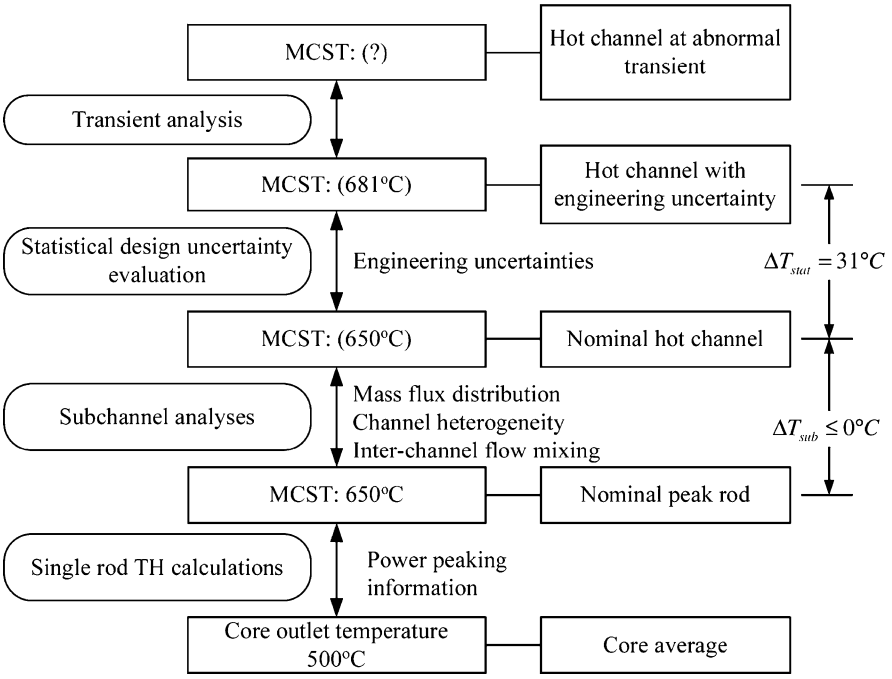


Fig. 7.56 Flow chart describing comprehensive MCST evaluation of the Super FR at normal operation. (Taken from [1])

7.8 Design and Improvements of 700 MWe Class Core

In this section, principles for core design improvements of the Super FR are introduced, and three cores, a reference core and two improved cores, with 700 MWe class power are designed as examples.

Table 7.29 Fuel rod design results of reference 700 MWe class Super FR. (Taken from [26] and used with permission from Atomic Energy Society of Japan)

Fuel material	MOX
Fuel density	95% TD
Fuel rod outer diameter (mm)	7.0
P/D	1.16
Cladding material	SUS304
Cladding thickness (mm)	0.43
Active core height (cm)	300
Average linear heat generation rate (kW/m)	17
Initial gas plenum pressure (MPa)	7.5

7.8.1 Design of Reference Fuel Rod and Core

First, the fuel and core of a 700 MWe class Super FR are designed as the starting point of improvements. The design goals, criteria, and methods are the same as those for the 1,000 MWe class Super FR described earlier in this chapter.

Table 7.29 [26] shows the fuel rod design results. The fuel rod diameter and P/D are 7.0 mm and 1.16, respectively. The rod arrangements in the seed and blanket assemblies are the same as those of the 1,000 MWe class design as shown in Fig. 7.57 [26]. The fuel loading pattern and flow distribution design are shown in Fig. 7.58 [26]. The distributions of the MCST calculated by single channel analyses and subchannel analyses are shown in Fig. 7.59 [26]. The highest value is kept well below the criterion of 650°C by modifying the subchannel shapes as introduced in Sect. 7.6. The core design results are summarized in Table 7.30 [26]. Based on the reference core design, two important performances are improved in Sects. 7.8.2 and 7.8.3.

7.8.2 Core Design Improvement for Negative Local Void Reactivity

The coolant void reactivity calculated for the reference core is the "overall" void reactivity. Its definition is the change of reactivity when the coolant disappears from all the fuel assemblies. The Super FRs are designed with closed fuel assemblies. No cross flow exists among the fuel assemblies. The local void reactivity, which is defined as the reactivity change when the coolant of one assembly disappears, needs to be kept negative throughout the cycle because there is possibility of a decrease in the coolant density in a particular fuel assembly.

The mechanism of the local void reactivity is more complex than the overall void reactivity. Fuel assembly configurations and core configurations influence the distribution of the local void reactivity. The effects of those configurations on the local void reactivity of the Super FR are quantitatively investigated here. An example of the 700 MWe class core is designed, which has negative local void reactivity for all the seed assemblies throughout the cycle.

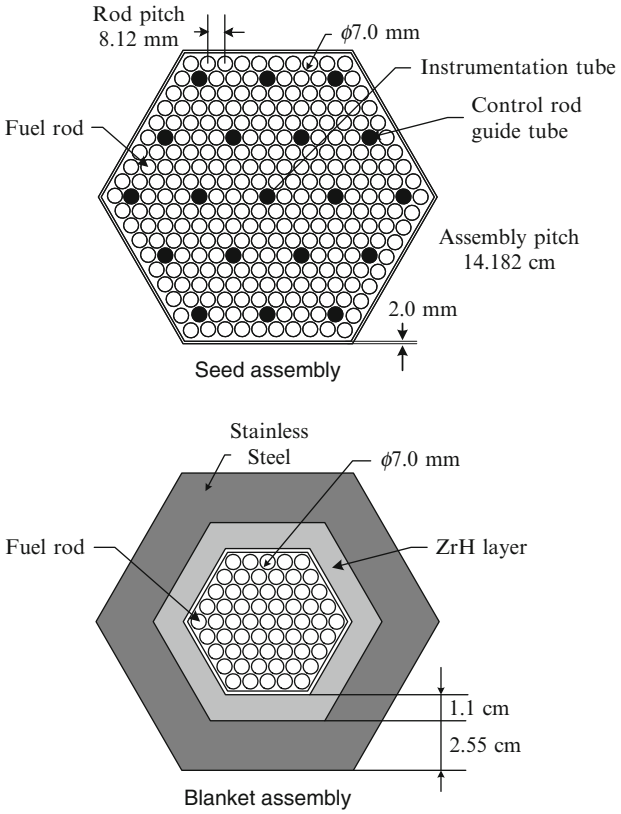


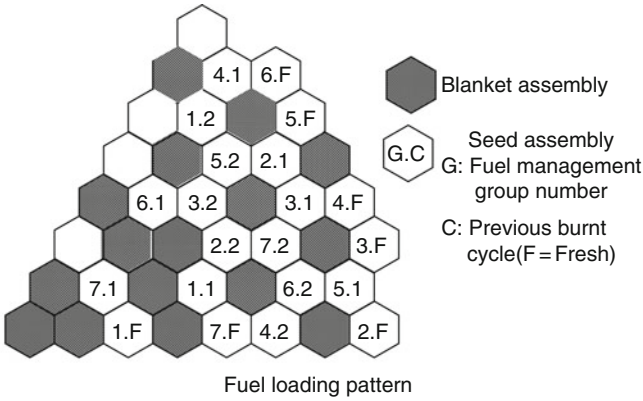
Fig. 7.57 Fuel assemblies of reference 700 MWe class Super FR. (Taken from [26] and used with permission from Atomic Energy Society of Japan)

7.8.2.1 Principles for Reducing Local Void Reactivity

The main concern arising from coolant voiding is the hardening of the neutron spectrum, which increases fast fission in both seed and blanket fuel regions, and also increases neutron leakage at the same time. Then, coolant void reactivity is determined by a change in neutron balance coming from those opposing effects. The void reactivity can be quantitatively analyzed by considering the neutron balance. The general equation for neutron balance is the diffusion equation.

$$\frac{\mathrm{d}n}{\mathrm{d}t} = -D\nabla^2\phi - \sum_{\mathrm{a}}\phi + S, \tag{7.15}$$

where n is the number of neutrons, D is the diffusion coefficient, ϕ is the neutron flux, $\sum_{\mathrm{a}}$ is the macroscopic absorption cross section, and S is the neutron production.



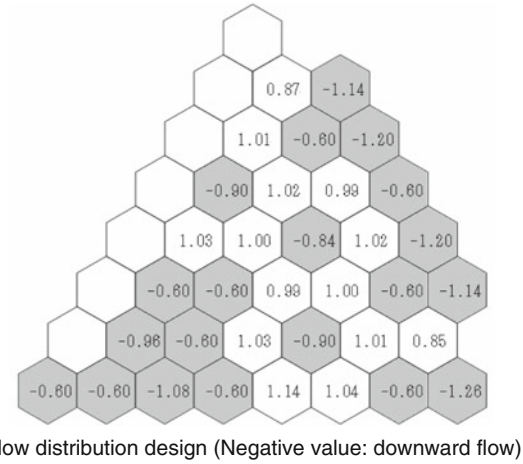


Fig. 7.58 Fuel loading pattern and flow distribution design of reference 700 MWe class Super FR. (Taken from [26] and used with permission from Atomic Energy Society of Japan)

When a neutron chain reaction is in the equilibrium state, the above equation becomes

$$S = D\nabla^2\phi + \sum_{a}\phi \tag{7.16}$$

Which means that the production is equal to the sum of leakage and absorption.

The effective multiplication factor is the ratio of the number of neutrons of a given generation to the number of neutrons of the immediately preceding generation. It can be expressed as

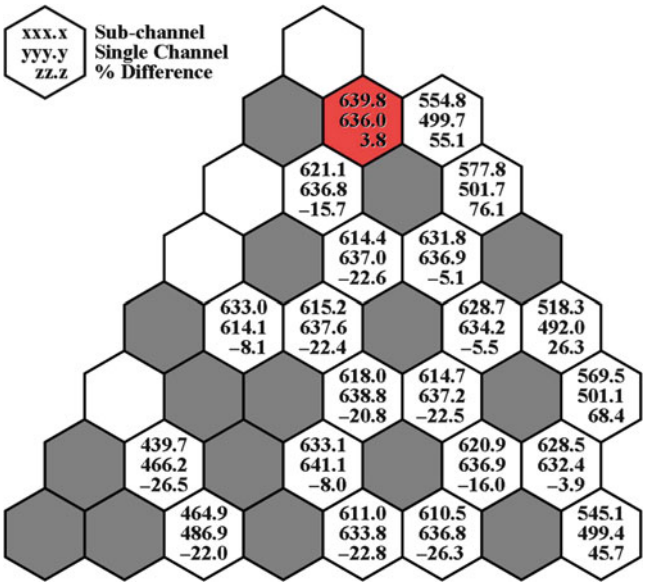


Fig. 7.59 MCST distribution in reference 700 MWe class Super FR. (Taken from [26] and used with permission from Atomic Energy Society of Japan)

Table 7.30 Core design results of reference 700 MWe class Super FR. (Taken from [26] and used with permission from Atomic Energy Society of Japan)

Core thermal power (MWt)	1,650
Core electrical power (MWe)	723
Core height (cm)	300
Equivalent diameter (cm)	210
Number of seed assemblies	126
Number of blanket assemblies	73
Number of seed assemblies with downward flow	42
Fissile Pu enrichment (wt%)	24.87
Fissile Pu inventory (ton)	6.571
Heavy metal inventory (ton)	26.42
Coolant outlet temperature (°C)	503.7
Maximum cladding surface temperature (°C)	639.8
Cycle length (EFPD)	380
Average power density (W/cm^3)	158.8
Average linear heat rate (kW/m)	17.3
Maximum linear heat rate (kW/m)	35.9
Flow rate (kg/s)	850.0
Average discharge burnup (MWd/kgHM)	69.3
Coolant void reactivity (%dk/k)	
BOEC	−1.23
EOEC	−2.07

$$k_{\text{eff}} = \frac{\text{production}}{\text{absorption} + \text{leakage}}. \tag{7.17}$$

The void reactivity is defined as

$$\Delta\rho = \rho_{\text{void}} - \rho_{\text{normal}} = \frac{k_{\text{eff}}^{\text{void}} - 1}{k_{\text{eff}}^{\text{void}}} - \frac{k_{\text{eff}}^{\text{normal}} - 1}{k_{\text{eff}}^{\text{normal}}} = \frac{k_{\text{eff}}^{\text{void}} - k_{\text{eff}}^{\text{normal}}}{k_{\text{eff}}^{\text{void}} k_{\text{eff}}^{\text{normal}}}. \tag{7.18}$$

So, the negative void reactivity requires

$$\frac{P_{\text{v}}}{P_{\text{n}}} < \frac{A_{\text{v}}}{A_{\text{n}} + L_{\text{n}}} + \frac{L_{\text{v}}}{A_{\text{n}} + L_{\text{n}}}, \tag{7.19}$$

where P_{v} is the neutron production at void condition, P_{n} is the neutron production at normal condition, A_{v} is the neutron absorption at void condition, A_{n} is the neutron absorption at normal condition, L_{v} is the neutron leakage at void condition, and L_{n} is the neutron leakage at normal condition.

For convenience, f_{p}, f_{a} and f_{l} are defined as

$$f_{\text{p}} = \frac{P_{\text{v}}}{P_{\text{n}}}, \quad f_{\text{a}} = \frac{A_{\text{v}}}{A_{\text{n}} + L_{\text{n}}}, \quad f_{\text{l}} = \frac{L_{\text{v}}}{A_{\text{n}} + L_{\text{n}}}. \tag{7.20}$$

Using these definitions, (7.19) can be written as

$$f_{\text{p}} < f_{\text{a}} + f_{\text{l}}. \tag{7.21}$$

Then, the void reactivity can be approximately expressed as

$$\Delta\rho \approx f_{\text{p}} - f_{\text{a}} - f_{\text{l}}. \tag{7.22}$$

The local void reactivity is defined as the reactivity change caused by the loss of the coolant inside one assembly. Similarly, it can be written as

$$\Delta\rho_i \approx f_{\text{p},i} - f_{\text{a},i} - f_{\text{l},i}, \tag{7.23}$$

where i is the index of fuel assembly.

This equation shows that there are three options for reducing the local void reactivity of a seed assembly: decreasing the fission rate, increasing the neutron leakage rate, or increasing the neutron absorption at the void condition. Two of them are realized by inserting the $ZrH_{1.7}$ layer between the seed and blanket assemblies. This layer slows down the fast neutrons leaked from the seed assemblies at void condition and decreases the fast fission at blanket assemblies. More neutrons moderated by the layer will be absorbed in blanket assemblies; this increases the neutron absorption at the void condition. Therefore, the fuel assembly

configurations, including the thickness of the $ZrH_{1.7}$ layer and the layout of the seed assembly, will affect both the overall and local void relativities.

If one seed assembly, which is surrounded by several blanket assemblies, is focused on, those neutrons generated in this seed assembly and absorbed in its neighboring blanket assemblies can be seen as the neutron leakage of this seed assembly. Increasing the number of interfaces between seed and blanket assemblies can decrease the local void reactivity of this seed assembly. Therefore, the core arrangement and the loading pattern will affect the distribution of the local void reactivity.

7.8.2.2 Sensitivity Analyses for Negative Local Void Reactivity

In order to quantitatively evaluate the effect of those core design parameters, that is, the thickness of the $ZrH_{1.7}$ layer, the fuel layout in a seed assembly, the core arrangement, and the loading pattern, on the local void reactivity, sensitivities of those configurations are analyzed here. The reference core designed in Sect. 7.8.1 is used for the sensitivity analyses.

When the coolant in the seed assembly disappears, more neutrons would flow from the voided seed assembly through the $ZrH_{1.7}$ layer to the neighboring blanket assemblies. They are slowed down in the $ZrH_{1.7}$ layer and then absorbed by the blanket fuel. Because the depleted UO_2 contains a large amount of ^{238}U, which has a large thermal absorption cross section and a small thermal fission cross section, thermal neutrons will be absorbed and cause no fission. Because of the role of the $ZrH_{1.7}$ layer, the void reactivity is very sensitive to its thickness. A thicker layer has higher moderating capability, but too much thickness will prevent thermal neutrons from penetrating the layer and thus reduce the absorption rate. It is necessary to optimize the thickness to pursue the most negative local void reactivity. In order to optimize the thickness, the local void reactivity is calculated with different $ZrH_{1.7}$ layer thicknesses, 1.109, 1.143, 1.160, 1.193, and 1.243 cm, which are labeled as Cases 1.1–1.5, respectively. The local void reactivity of all the seed assemblies at BOEC and EOEC are calculated. There are seven seed assemblies, which are located at the middle region of the core and have very small negative or large positive local void reactivity. Since the aim of this study is to ensure negative local void reactivity for all of the seed assemblies, those seven assemblies are focused on. The summation of the local void reactivity of those seven assemblies and the maximum value among them are plotted with respect to the thickness of the $ZrH_{1.7}$ layer in Fig. 7.60 [27]. It can be found that the local void reactivity does not monotonously decrease with increasing $ZrH_{1.7}$ layer thickness. It can be roughly concluded that the layer thickness of 1.15 cm is the optimized value for the local void reactivity. The following analyses are done with the layer thickness fixed as 1.15 cm.

In order to depress the power peaking caused by the existence of the $ZrH_{1.7}$ layer, the seed assembly is designed with the Pu enrichment zoning as described in Sect. 7.5. The layout of seed assembly will affect the amount of fast neutrons

penetrating the $ZrH_{1.7}$ layer. Numerical results show that higher Pu enrichment in the fuel rods at the periphery of the assembly induces higher neutron leakage and hence increases $f_{1,i}$ of (7.23) [28]. Therefore, a larger number of highly enriched fuel rods are located at the peripheral region of the seed assembly in the following analyses. It is also shown that the position of the control rod guide tubes does not obviously affect the void reactivity [28]. According to the high temperature mechanical analyses of the in core structures conducted at the University of Tokyo, it is better to place the control rod guide tubes at the central region of the fuel assembly as much as possible in order to decrease the size of the hole on the upper tie plate (see Fig. 7.61 [29]) and hence reduce the thermal stress on the regiment. Therefore, the layout of the control rod guide tubes are modified as illustrated in Fig. 7.62 [30].

The seed assemblies located in the peripheral region of the core have sufficiently negative local void reactivity. This is due to the large neutron leakage. But the seed assemblies located at the inner region have less negative or positive local void reactivity. The local void reactivity in this region must be focused on. The core arrangement, namely, the location of the seed and blanket assemblies, has an essential effect on the distribution of local void reactivity. As the suitable thickness of the $ZrH_{1.7}$ layer can reduce the local void reactivity of its neighboring seed assemblies, more blanket assemblies can be put at the inner region of the core in order to reduce the local void reactivity there. A new core arrangement is proposed. The calculated distribution of local void reactivity is shown in Fig. 7.63 [27]. From the original arrangement shown in Fig. 7.58 [26], the fraction of the blanket assemblies in the middle region is increased by moving the peripheral blanket assemblies and some inner region blanket assemblies to it. In this arrangement,

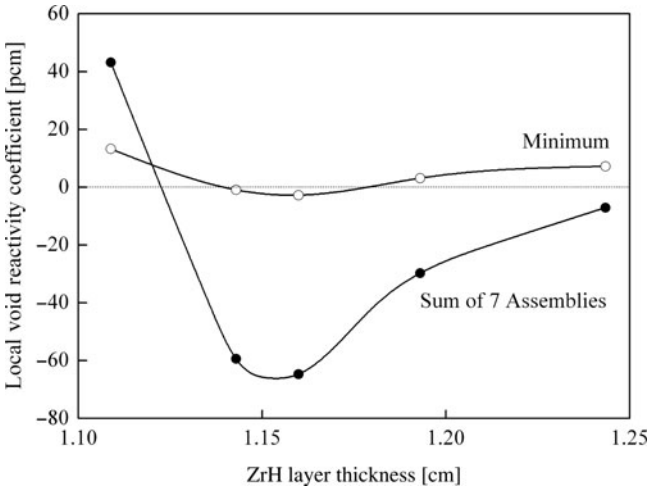


Fig. 7.60 Local void reactivity with respect to thickness of $ZrH_{1.7}$ layer. (Taken from [27] and used with permission from Atomic Energy Society of Japan)

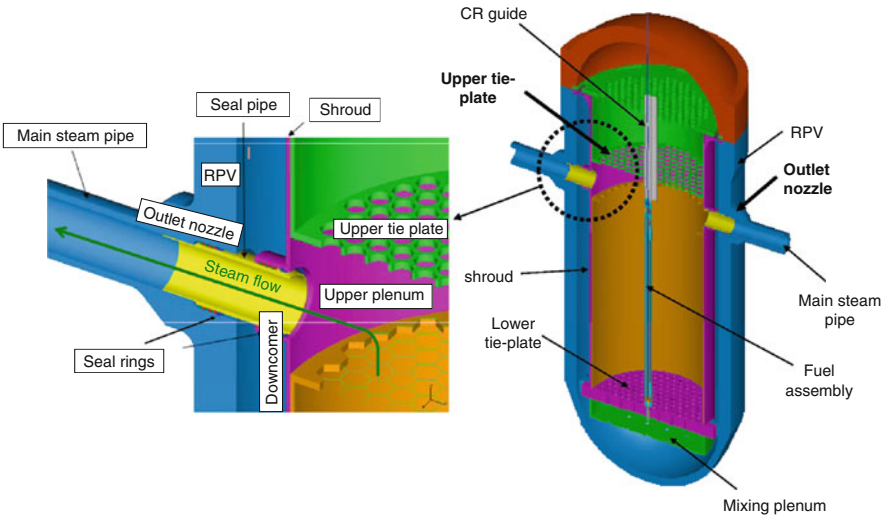


Fig. 7.61 Example of in-core structure of Super FR. (Taken from [29] and used with permission from Atomic Energy Society of Japan)

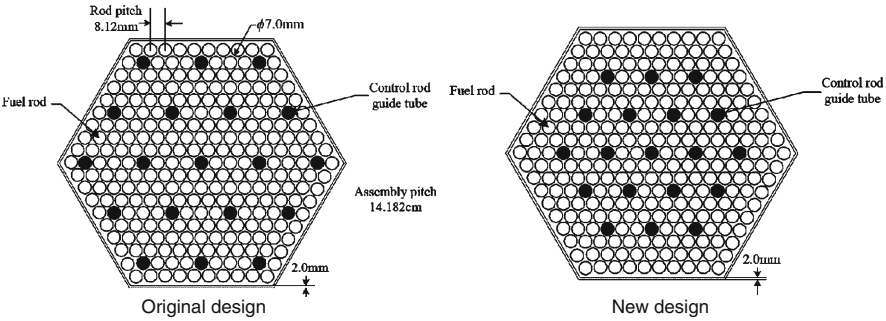


Fig. 7.62 Change of CR guide tube position in seed fuel assembly. (Taken from [30] and used with permission from Atomic Energy Society of Japan)

all the seed assemblies have negative local void reactivity throughout the cycle. The larger negative local void reactivity of the peripheral assemblies is due to the larger neutron leakage rate and that of the inner assemblies is due to the larger fraction of the neighboring blanket assemblies.

Even though the negative local void reactivity of all the seed assemblies is achieved above, its distribution is not uniform. The peripheral assemblies have relatively strong negative local void reactivities, while some of the inner assemblies have values very close to zero. It is better to keep all the local void reactivities below −30 pcm in consideration of uncertainties from nuclear data, design methods, etc. In the reference design, the typical "out-in" reloading pattern for the seed

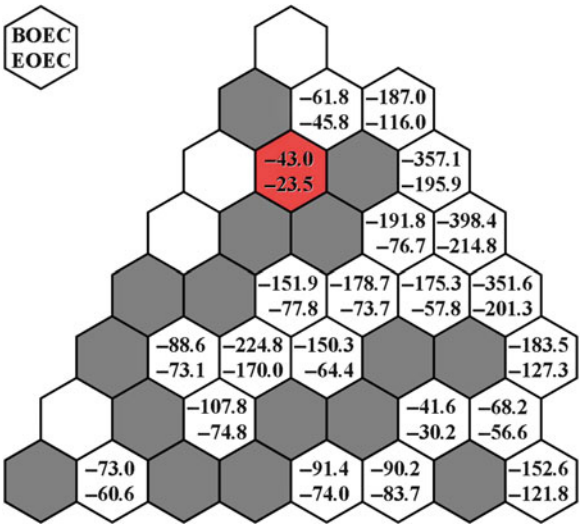


Fig. 7.63 New core arrangement and local void reactivity. (Taken from [27] and used with permission from Atomic Energy Society of Japan)

assemblies is employed as can be seen in Fig. 7.58 [26] in order to reduce the power peaking. In the new arrangement, some blanket assemblies are moved to the inner region, which makes the relative power at the inner region lower. So, the power peaking is a smaller concern here. On the other hand, compared to the used fuel, the fresh fuel has a larger portion of fast fissions, which means the $f_{a,i}$ of (7.23) is higher for the void condition. It is effective to use the $ZrH_{1.7}$ layer to reduce the local void reactivity in the core inner region. The typical in-out reloading pattern is employed here. Some fresh fuel assemblies are loaded at the middle region of the core and some used fuel assemblies are loaded at the periphery of the core. It was confirmed that the in-out reloading pattern has a flatter distribution of local void reactivity [28]. Also, the in-out reloading pattern leads to lower neutron fluence on the pressure vessel due to lower leakage of fast neutrons from the core periphery.

7.8.2.3 Example of Improved Core with Negative Local Void Reactivity

Considering the above sensitivity analyses, an example improved core is designed, which satisfies the negative local void reactivity as well as all the design goals. It is called the "Improved Super FR (1)" here. Table 7.31 [27] summarizes the main parameters and calculated results. All the design goals and criteria are satisfied. The local void reactivity distributions are given in Fig. 7.64 [27]. The highest values are −52.6 and −42.0 pcm at BOEC and EOEC, respectively. They are more negative than −30 pcm.

Table 7.31 Core design results of Improved Super FR (1). (Taken from [27] and used with permission from Atomic Energy Society of Japan)

Core thermal power (MWt)	1,650
Core height (cm)	300
Equivalent diameter (cm)	210
Number of seed assemblies	126
Number of blanket assemblies	73
ZrH layer thickness (cm)	1.15
Coolant outlet temperature (°C)	509.7
MCST (°C)	637.8
Cycle length (EFPD)	380
Maximum linear heat rate (kW/m)	38.9
Average discharge burnup (GWd/tHM)	69.4
Average fissile Pu enrichment	25.62
Coolant flow rate (kg/s)	837.2
Overall void reactivity (%dk/k) at BOEC/EOEC	−3.0/−2.9

7.8.3 Core Design Improvement for Higher Power Density

The 1,000 MWe class Super FR and two 700 MWe class Super FRs have the average power density (including the blanket region) below 160 MW/m^3 while those of typical LMFBRs are around 300 MW/m^3 or higher. The power density directly affects the reactor vessel size and hence the containment and reactor building sizes. In order to pursue the economic advantage of the Super FR, the principles for improving the power density are discussed and an example of the high power density core is designed here.

7.8.3.1 Principle of Improving Power Density

The most limiting restriction of increasing the power density is the criterion of the maximum linear heat generation rate (MLHGR), which is 39 kW/m. The MLHGR always appears at BOEC and the power generated in the blanket region is almost negligible at BOEC. Thus, the discussion in this section mainly focuses on the seed assemblies at BOEC.

The power density is calculated by (7.24).

$$q = \frac{P_{\text{tot}}}{V_{\text{tot}}} = \frac{P_{\text{tot}}}{N_{\text{pin}} S_{\text{cell}} H \frac{N_{\text{tot_assem}}}{N_{\text{seed_assem}}}}, \tag{7.24}$$

where P_{tot} is the total thermal power, V_{tot} total core volume, N_{pin} total fuel pin number, S_{cell} area of each cell $(= (\sqrt{3}/2)P^2$, P, fuel rod pitch), H core active height, $N_{\text{tot_assem}}$ total assembly number, and $N_{\text{seed_assem}}$ total seed assembly number.

The total power can be described using the average linear heat rate q_{l}.

$$P_{\text{tot}} = N_{\text{pin}} \times q_{\text{l}} \times H. \tag{7.25}$$

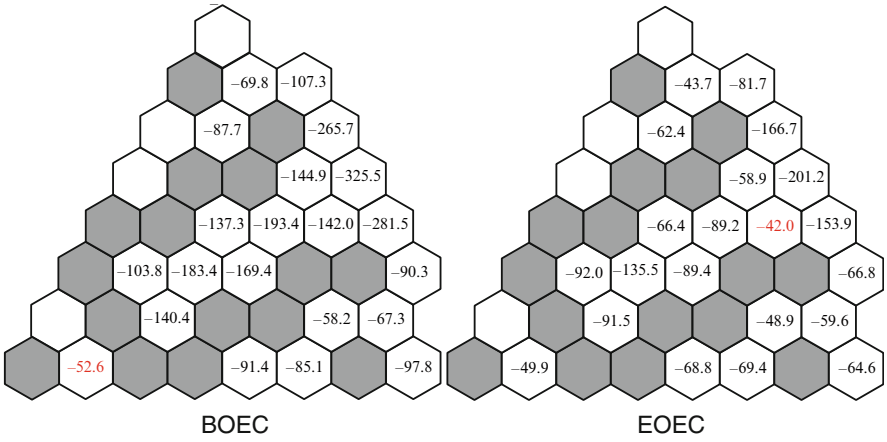


Fig. 7.64 Local void reactivity distributions of improved 700 MWe class Super FR. (Taken from [27] and used with permission from Atomic Energy Society of Japan)

Substituting the above two equations, the power density is described as (7.26).

$$q = \frac{q_{\mathrm{l}}}{S_{\mathrm{cell}} \frac{N_{\mathrm{tot_assem}}}{N_{\mathrm{seed_assem}}}} = \frac{q_{\mathrm{l}}}{\frac{\sqrt{3}}{2} P^2 \frac{N_{\mathrm{tot_assem}}}{N_{\mathrm{seed_assem}}}} = \frac{q_{\mathrm{l}}}{\frac{\sqrt{3}}{2} (P/D \times D)^2 \frac{N_{\mathrm{tot_assem}}}{N_{\mathrm{seed_assem}}}}, \tag{7.26}$$

where D is the fuel rod diameter and P is the fuel rod pitch.

It is obvious that the power density is inversely proportional to $(P/D \times D)^2$. Decreasing the fuel rod diameter or P/D is the most effective way to increase the average power density. The power density is also proportional to q_{l} and $N_{\mathrm{tot_assem}}/N_{\mathrm{seed_assem}}$, which indicates that increasing the average linear heat generation rate (ALHGR) by flattening the power distribution and increasing the fraction of the seed assemblies are two other possible ways.

7.8.3.2 Sensitivity Analyses for Higher Power Density

Decreasing the fuel rod diameter and P/D is very effective for improving the power density. However, there are limitations because the gap clearance between the fuel rods should be large enough from thermal hydraulic and mechanical considerations. The minimum gap clearance is kept larger than 1 mm here. In the meanwhile, the P/D ratio has the upper boundary for achieving high coolant outlet temperature by keeping sufficient mass flux. The coolant outlet temperature will decrease rapidly if the P/D exceeds 1.2 with the fuel rod diameter around 7 mm [26]. Considering the above limitations, the available design range of the diameter and P/D are drawn in Fig. 7.65 [30]. Case 1 in this figure corresponds to the design for the 1,000 MWe class Super FR described in Sect. 7.4. Case 2 corresponds to the reference Super FR

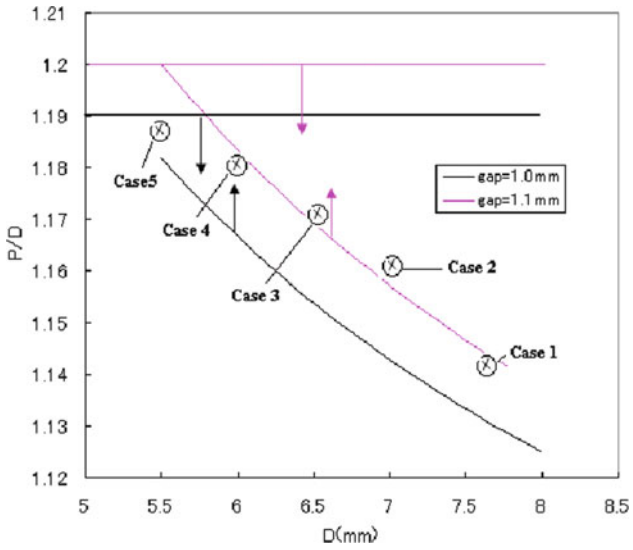


Fig. 7.65 Available design range of fuel rod geometry and examples of design points. (Taken from [30] and used with permission from Atomic Energy Society of Japan)

or the Improved Super FR (1) described in Sects. 7.8.1 and 7.8.2. Cases 3–5 are chosen as the candidates for other improved cores. The fuel rod dimensions and the fuel assembly designs for the five cases are summarized in Tables 7.32 and 7.33 [30], respectively. The fuel rod diameter in Case 5 is 5.5 mm, which is equal to the diameter of the driver fuel rods in the existing Japanese experimental LMFBR, JOYO. The rod configurations in the seed assemblies in Case 1, Case 2, and the other cases are illustrated in Figs. 7.26 [1], 7.57 [26] (left), and 7.62 [30] (right), respectively.

The core design parameters are compared among the five cases in Table 7.34 [30]. As the active height is limited by the FIV constriction (see Sect. 7.4), it needs to be decreased in the cases with smaller fuel rod diameter. The numbers of seed assemblies are increased from 126 in Case 2 to 162 in Cases 3–5. This is good for increasing the fraction of the seed assemblies to the total fuel assemblies. The ALHGR is increased from around 17 kW/m in Cases 1 and 2 to around 20 kW/m in Cases 3–5 by flattening the power distribution. Naturally, when the fuel rod diameter is smaller, the total volume and fuel inventory is consequently reduced continuously from Case 1 to 5. As the smaller core has the higher neutron leakage, the Pu enrichment has to be higher to keep the discharged burnup.

The performances of those five cases are summarized in Table 7.35 [30]. The average power densities are plotted in Fig. 7.66 [30]. Although Case 5 has an outlet temperature slightly below the design goal of 500°C, it has the highest power density. The core design of Case 5 is taken as a base for the high power density core design, called the "Improved Super FR (2)" in the next section.

Table 7.32 Comparison of fuel rod dimensions. (Taken from [30] and used with permission from Atomic Energy Society of Japan)

	Case 1	Case 2	Case 3	Case 4	Case 5
Diameter (cm)/P/D	0.76/1.14	0.70/1.16	0.65/1.17	0.60/1.18	0.55/1.19
Gap clearance (mm)	1.064	1.120	1.105	1.080	1.045
Cladding thickness (cm)	0.043	0.043	0.42	0.41	0.040
Pellet cladding gap (cm)	0.010	0.004	0.003	0.003	0.003
Heated length (cm)	270	300	240	230	220

Table 7.33 Comparison of fuel assembly designs. (Taken from [30] and used with permission from Atomic Energy Society of Japan)

		Case 1	Case 2	Case 3	Case 4	Case 5
Seed	Number of rods (total/fuel/CR tube)	331/312/19	271/252/19	271/252/19	271/252/19	271/252/19
	Assembly pitch	16.58	14.182	13.3	12.45	11.56
	Assembly gap (cm)	0.2	0.2	0.2	0.2	0.2
	Duct thickness (cm)	0.2	0.2	0.2	0.2	0.2
Blanket	Number of fuel rods	91	61	61	61	61
	$ZrH_{1.7}$ layer thickness (cm)	1.3	1.2	0.9	0.83	0.77
	Duct thickness (cm)	2.4	2.1	2.0	1.92	1.74
	Assembly gap (cm)	0.2	0.2	0.2	0.2	0.2

Table 7.34 Comparison of core design parameters. (Taken from [30] and used with permission from Atomic Energy Society of Japan)

	Case 1	Case 2	Case 3	Case 4	Case 5
Thermal power (MWt)	2,358	1,650	1,960	2,010	1,800
Active height (cm)	270	300	240	230	220
Equivalent diameter (cm)	267	210	230	200	186
Number of seed assemblies	162	126	162	162	162
Number of blanket assemblies	73	73	73	73	73
Fissile Pu enrichment (wt%)	20.8	24.87	25.9	27.7	28.7
Fissile Pu inventory (ton)	8.44	6.571	5.61	5.56	3.63
Heavy metal inventory (ton)	40.58	26.42	24.4	20.1	14.9

7.8.3.3 Example of Improved Core with Higher Power Density

Since the coolant outlet temperature in Case 5 is below 500°C, the flow pattern and loading scheme are adjusted to meet this design goal. Also, the core height is reduced to 200 cm in order to adjust the expected electric power to the 700 MWe level. After those modifications, the Improved Super FR (2) with an average power density of 294.8 W/cm^3 is designed. This power density is competitive with that of typical LMFBRs. Table 7.36 [30] summarizes the main parameters and calculated results of the final core design. All the design goals including the coolant outlet temperature and the design criteria are satisfied. In this core, the local void reactivity is also kept negative throughout the cycle.

Table 7.35 Comparison of core design results. (Taken from [30] and used with permission from Atomic Energy Society of Japan)

	Case 1	Case 2	Case 3	Case 4	Case 5
Coolant outlet temperature (°C)	503	501.5	502.96	501.84	497.58
Maximum cladding surface temperature (°C)	642.6	641.1	642.4	642.4	644.3
Cycle length (EFPD)	450	380	320	280	220
Average power density (W/cm^3)	156	158.8	226.0	265.5	301
Average linear heat rate (kW/m)	17	17.3	20	20.5	20
Maximum linear heat rate (kW/m)	38.9	35.9	38.5	38.6	38.9
Flow rate (kg/s)	1,210	850.0	847.7	850.3	856.4
Average discharge burnup (GWd/tHM)	68.3	69.3	68.9	69.3	69.8
Coolant void reactivity (%dk/k) at BOEC	−1.9	−1.23	−1.5	−0.23	−0.35
Coolant void reactivity (%dk/k) at EOEC	−1.8	−2.07	−1.2	−1.25	−1.39

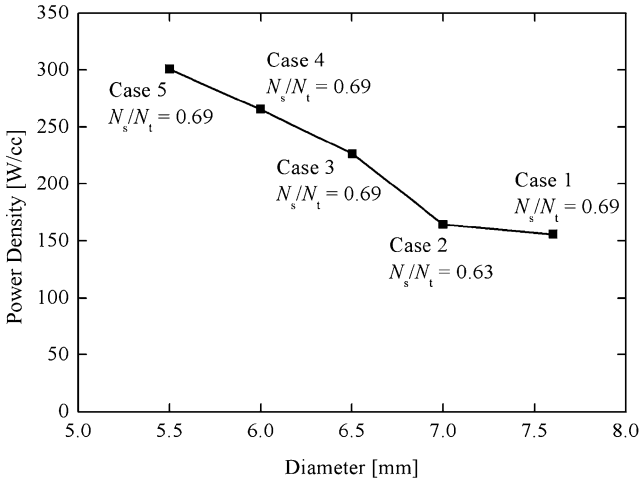


Fig. 7.66 Average power densities. (Taken from [30] and used with permission from Atomic Energy Society of Japan)

In summary, it was confirmed in Sect. 7.8.3 that the power density of the Super FR could be increased by decreasing the fuel rod diameter, increasing the ALHGR (flattening power distribution) and increasing the fraction of seed fuel assemblies while satisfying all the design goals and criteria.

7.9 Plant Control

In the control systems of the Super LWR designed in Chap. 4, the main steam temperature is simply controlled by the feedwater pumps. Since the moderator in the large water rods mitigates the change in the coolant temperature in the Super LWR, the change in the main steam temperature is not very large (within 8°C). The

Table 7.36 Fuel and core design results of Improved Super FR (2). (Taken from [30] and used with permission from Atomic Energy Society of Japan)

Fuel rod diameter (mm)	5.5
P/D	1.19
Gap clearance (mm)	1.045
Cladding thickness (mm)	0.4
Pellet cladding gap (mm)	0.03
Heated length (cm)	200
Assembly pitch (cm)	11.561
Number of rods in a seed assembly (total/fuel/CR tube)	271/252/19
Core thermal power (MWt)	1,602
Equivalent diameter (cm)	186
Number of seed assemblies	162
Number of blanket assemblies	73
Coolant outlet temperature (°C)	504.6
MCST calculated by subchannel analysis (°C)	628.5
Average power density (W/cm^3)	294.8
Coolant void reactivity (%dk/k) at BOEC/EOEC	−0.839/−1.712

Super FR has almost the same enthalpy rise as that in the Super LWR but it has a smaller heat capacity due to no water rods being used. The change in the main steam temperature against various perturbations and operations is expected to be larger in the Super FR. In this section, several concepts for improving the feedwater controller are introduced in order to suppress the fluctuation of main steam temperature of the Super FR against perturbations. The reference Super FR designed in Sect. 7.8.1 is treated here as an example.

7.9.1 Plant Transient Analysis Code for the Super FR

The plant transient analysis code for the Super FR is called SPRAT-F. It is based on the 1-D node junction model with radial heat transfer and point kinetics models such as SPRAT-DOWN for the Super LWR (see Chaps. 4 and 6). The nodalization is shown in Fig. 7.67. The models used in SPRAT-F are the same as those in SPRAT-DOWN. The turbine control valve regulates the main steam pressure by changing the main steam flow rate as in BWRs and the Super LWR. The relation between its stroke and the steam flow rate is the same as that of the Super LWR (Fig. 4.4). The relation between the core pressure and the feedwater flow rate (with constant pump speed) is also the same as that in the Super LWR (Fig. 4.5).

7.9.2 Basic Plant Dynamics of the Super FR

The plant dynamics of the Super FR toward perturbations as assumed in Chap. 4 are analyzed first without a control system in order to understand the basic

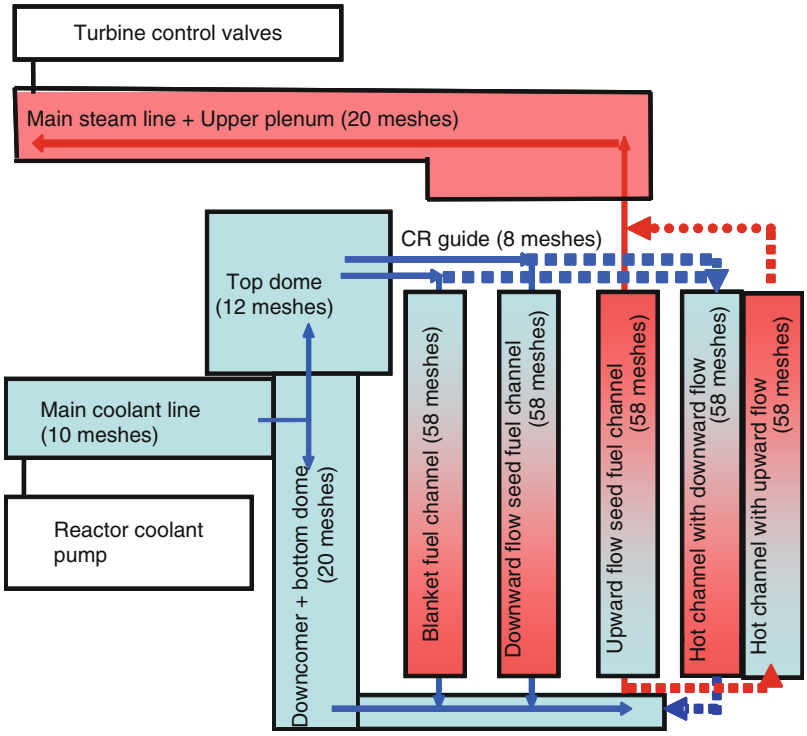


Fig. 7.67 Nodalization of SPRAT-F

characteristics of the plant dynamics. Each perturbation is caused by one of the three control devices: control rods (CRs), turbine control valves or feedwater pumps.

A positive reactivity (\$0.1) is inserted stepwise by withdrawing the CRs. The feedwater pump speed and the turbine control valve stroke are kept constant. The results are shown in Fig. 7.68 [31]. The reactor power increases about 10% almost stepwise due to the prompt jump and then gradually decreases due to the reactivity feedbacks from the fuel temperature and coolant density. This behavior implies that the Super FR also has inherent self controllability of the reactor power despite the much smaller density reactivity coefficient compared to that of the Super LWR. The main steam temperature increases, which leads to an increase in the main steam and core pressures because the specific volume of the main steam increases. The increase in the core pressure leads to a decrease in the feedwater and core flow rates, which increases the main steam temperature further. As a result, the maximum increase in the main steam temperature is nearly 40°C while that in the Super LWR is only 9°C (see Fig. 4.10).

The turbine control valve s close slightly, and the main steam flow rate decreases by 5%. The CR position and the feedwater pump speed are kept constant.

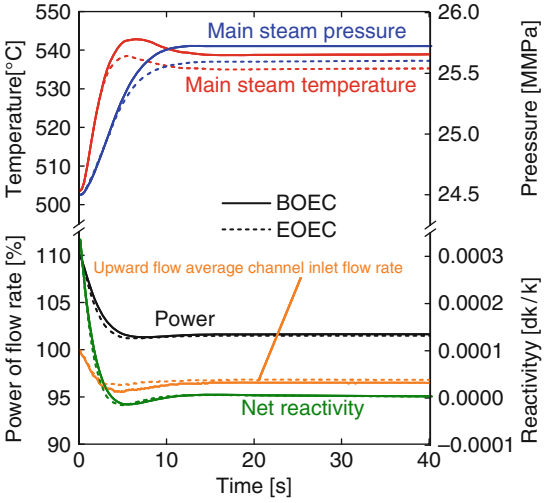


Fig. 7.68 Response of the Super FR to stepwise reactivity insertion. (Taken from [31] and used with permission from Atomic Energy Society of Japan)

The results are shown in Fig. 7.69 [31]. The main steam pressure increases. The core coolant flow rate decreases with the main steam flow rate, which increases the main steam temperature. The increase in the main steam temperature is nearly 20°C while that in the Super LWR is 12°C.

The feedwater flow rate decreases by 5%. The CR position and the turbine control valve stroke are kept constant. The results are shown in Fig. 7.70 [31]. The main steam pressure increases. The core coolant flow rate decreases with the main steam flow rate, which increases the main steam temperature. The increase in the main steam temperature is nearly 20°C while that in the Super LWR is below 5°C.

7.9.3 Design of Reference Control System

The analyses in the previous section show that the Super FR qualitatively has the same basic plant dynamics as the Super LWR although the change in the main steam temperature is larger. Thus, the same plant control system as that of the Super LWR is designed and tuned here as the basis of improvements.

The gain K in the pressure control system, described as (4.9) and (4.10), is tuned as 0.396 so that the overshoot is minimized against the 1% stepwise increase in the pressure setpoint. The main steam temperature is controlled by regulating the feedwater flow rate. The equation for the feedwater controller is written again because it is the basis for the improvement in the next section.

$$\frac{\mathrm{d}u}{\mathrm{d}t} = K_{\mathrm{P1}} \frac{T - T_{\mathrm{set}}}{T_{\mathrm{set}}} + K_I \int_0^t \frac{T - T_{\mathrm{set}}}{T_{\mathrm{set}}} \mathrm{d}t, \tag{7.27}$$

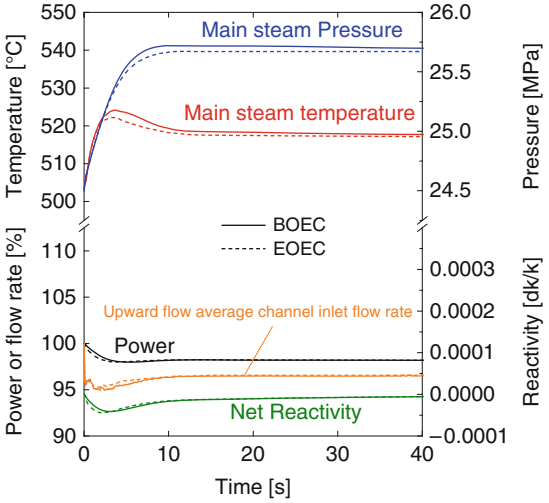


Fig. 7.69 Response of the Super FR to stepwise decrease in turbine control valve opening. (Taken from [31] and used with permission from Atomic Energy Society of Japan)

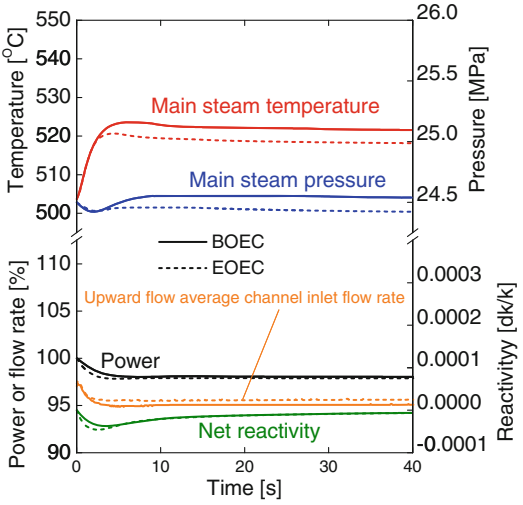


Fig. 7.70 Response of the Super FR to stepwise decrease in feedwater flow rate. (Taken from [31] and used with permission from Atomic Energy Society of Japan)

where u is the feedwater signal (%), T is the measured main steam temperature with lead compensation (°C), T_{set} is the setpoint of main steam temperature (°C), K_{P1} is the proportional gain converting deviation of main steam temperature to feedwater signal, and K_I is the integral gain.

The rate of change in u is limited to 20%/s. The proportional gain and the integral gain are determined as 13.5 and 0.0, respectively, so that the overshoot is minimized against the stepwise increase in setpoint of the main steam temperature by 4°C.

The reactor power is controlled by the CRs. The speed of the CRs is in proportion to the deviation of the reactor power from the setpoint when the deviation is below a certain value b. When the deviation is larger than b, the CRs keep the maximum speed 1.9 cm/s; this is the same as for PWRs. The value of b is determined as 0.7 so that the settling time and the undershoots of both the reactor power and main steam temperature are reasonable against the 5% stepwise decrease in the setpoint of the reactor power.

In order to clarify the characteristics of the reference control system, the plant dynamics is analyzed with the designed control system against the 10% stepwise decrease in the setpoint of the reactor power. The results are shown in Fig. 7.71 [31]. The pressure control system and the power control system work well. However, the change in the main steam temperature is still considerable.

7.9.4 Improvement of Feedwater Controller

The coolant outlet temperature and hence the main steam temperature are determined by the power to flow rate ratio in the core with constant inlet temperature. Thus, the change in the main steam temperature can be kept small by keeping the power to flow rate ratio constant. As shown in Fig. 7.72 [31], three feedback signals for the feedwater controller are proposed and added to (7.27) for that purpose. In this section, only the plant dynamics at BOEC is analyzed because there are almost no differences in plant dynamics between BOEC and EOEC.

7.9.4.1 Feedback from Power to Flow Rate Ratio

The first idea is that the deviation of the power to flow rate ratio itself is fed back to the feedwater controller.

$$\frac{\mathrm{d}u}{\mathrm{d}t} = 0.135\frac{T - T_{\mathrm{set}}}{T_{\mathrm{set}}} + K_{\mathrm{P2a}}\frac{q/w - q_0/w_0}{q_0/w_0}, \tag{7.28}$$

where q is the relative power (%), q_0 is the rated power (%) (=100), w is the relative feedwater flow rate (%), w_0 is the rated feedwater flow rate (%) (=100), and K_{P2a} is the proportional gain converting deviation of power to flow rate ratio to feedwater signal.

The improved control system with the feedwater controller described as (7.28) is designated Control system (A). The gain K_{P2a} is tuned by analyzing the plant dynamics against the 10% stepwise decrease in the setpoint of the reactor power. The results are shown in Fig. 7.73 [31]. The changes in the power to flow rate ratio and the main steam temperature can be decreased from the case with the reference control system. 0.4 is chosen as K_{P2a} so that these changes are minimized.

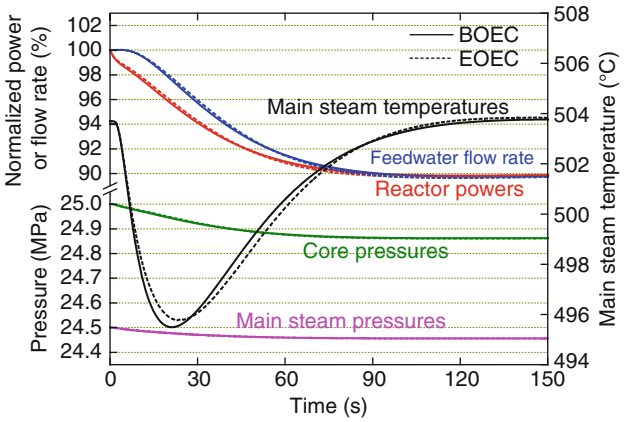


Fig. 7.71 Response to 10% stepwise decrease in power setpoint with reference control system. (Taken from [31] and used with permission from Atomic Energy Society of Japan)

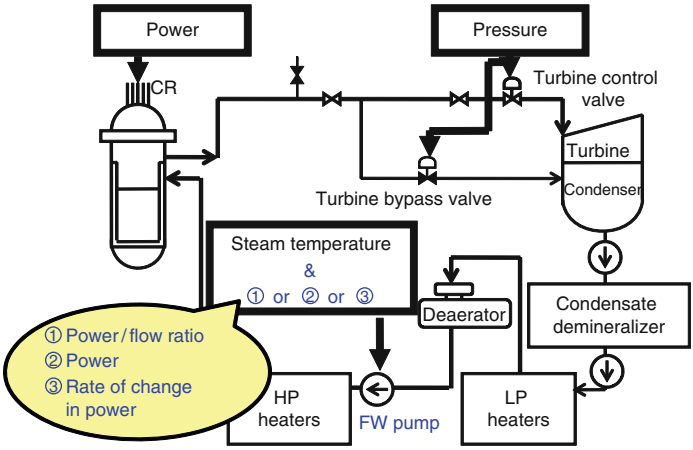


Fig. 7.72 Additional feedback signals for feedwater controller. (Taken from [31] and used with permission from Atomic Energy Society of Japan)

7.9.4.2 Feedback from Reactor Power

When the reactor power is higher than the rated value, the CRs are inserted and then the power will decrease. The opposite case is also expected. The second idea is that the deviation of the power is fed back to the feedwater controller too in order to make the flow rate follow the power.

$$\frac{\mathrm{d}u}{\mathrm{d}t} = 0.135\frac{T - T_{\mathrm{set}}}{T_{\mathrm{set}}} + K_{\mathrm{P2b}}\frac{q_{\mathrm{set}} - q}{q_{\mathrm{set}}}, \tag{7.29}$$

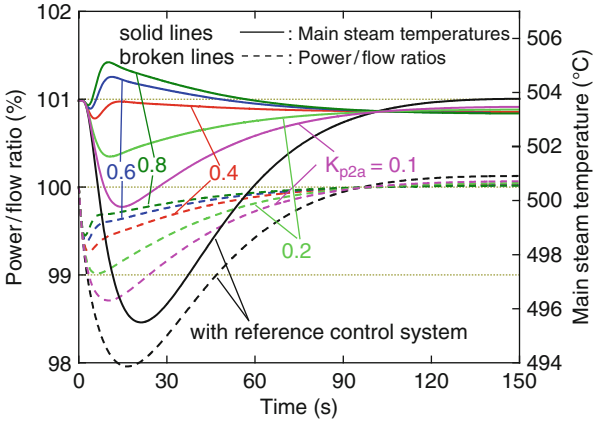


Fig. 7.73 Responses to 10% decrease in power setpoint with Control system (A). (Taken from [31] and used with permission from Atomic Energy Society of Japan)

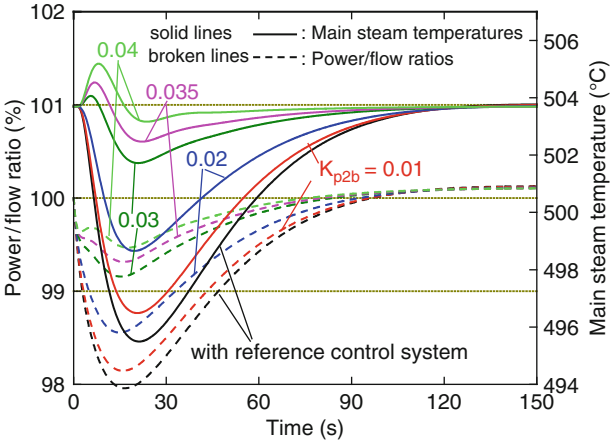


Fig. 7.74 Responses to 10% decrease in power setpoint with Control system (B). (Taken from [31] and used with permission from Atomic Energy Society of Japan)

where q_{set} is the setpoint of rated power (%) and K_{P2a} is the proportional gain converting deviation of power to feedwater signal.

The improved control system with the feedwater controller described as (7.29) is designated Control system (B). The gain K_{P2b} is also tuned by analyzing the plant dynamics against the same perturbation. The results are shown in Fig. 7.74 [31]. This control system also works better than the reference control system. 0.35 is chosen as K_{P2b}.

7.9.4.3 Feedback from Derivative of Power

The third idea is that the derivative of the power is fed back to the feedwater controller, which also helps make the flow rate follow the power.

$$\frac{\mathrm{d}u}{\mathrm{d}t} = 0.135\frac{T - T_{\mathrm{set}}}{T_{\mathrm{set}}} + K_{\mathrm{D}}\frac{\mathrm{d}q}{\mathrm{d}t}, \tag{7.30}$$

where K_{D} is the derivative gain.

The improved control system with the feedwater controller described as (7.30) is designated Control system (C). The derivative gain K_{D} is also tuned by analyzing the plant dynamics against the same perturbation. The results are shown in Fig. 7.75 [31]. This control system also works better than the reference control system. 0.9 is chosen as K_{D}.

7.9.5 Plant Stability Analyses

The improved control systems are characterized against the reference control system by plant stability analyses. The same perturbations as analyzed for the Super LWR in Chap. 4 are chosen. In this section, the results at BOEC are introduced. Those at EOEC are very similar [31].

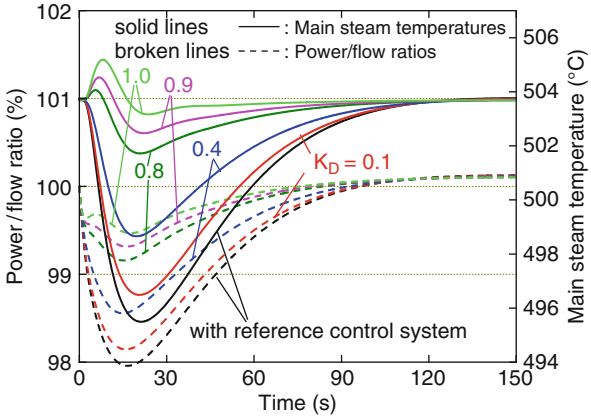


Fig. 7.75 Responses to 10% decrease in power setpoint with Control system (C). (Taken from [31] and used with permission from Atomic Energy Society of Japan)

7.9.5.1 10% Decrease in Power Setpoint

The same event is analyzed in Sects. 7.9.3 and 7.9.4. The results are shown in Fig. 7.76 [31]. The reactor power settles to the new setpoint at around 100 s with all the control systems. Since the feedwater flow rate follows the reactor power more closely with the improved control systems than the reference case, the changes in the main steam temperature are kept smaller.

7.9.5.2 1% Increase in Pressure Setpoint

The results are shown in Fig. 7.77 [31]. With all the control systems, the pressure quickly settles to the new setpoint by regulating the turbine control valves. Since the plant response to the valve action is too fast to be affected by the feedwater controller, the peak value of the main steam temperature is almost the same for all the cases.

The second term of (7.28) in Control system (A) tries to keep the enthalpy rise in the core equal to that in the initial condition. Since the core outlet temperature increases with the pressure when the outlet coolant enthalpy is kept constant, the main steam temperature settles to a slightly higher value than the initial one in this event. However, the difference is 0.7°C, and it does not seem to be a problem in practice.

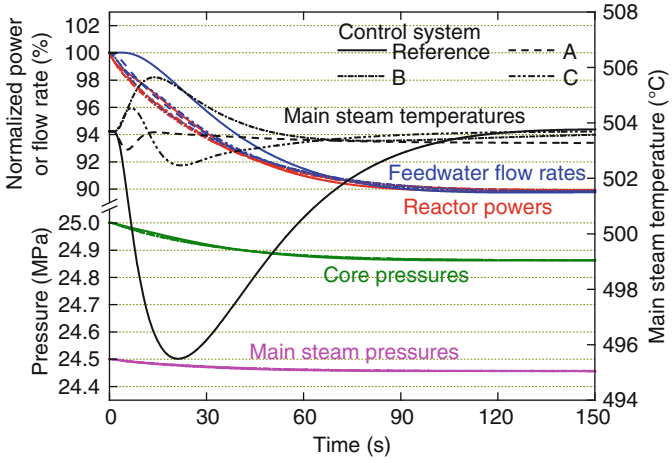


Fig. 7.76 Responses to 10% decrease in power setpoint with four control systems. (Taken from [31] and used with permission from Atomic Energy Society of Japan)

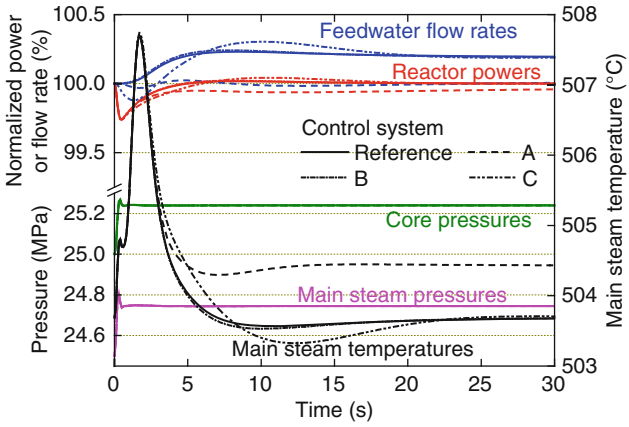


Fig. 7.77 Responses to 1% increase in pressure setpoint with four control systems. (Taken from [31] and used with permission from Atomic Energy Society of Japan)

7.9.5.3 4°C increase in Steam Temperature Setpoint

The results are shown in Fig. 7.78 [31]. In order to increase the main steam temperature, the power to flow rate ratio needs to be increased by decreasing the feedwater flow rate. The main steam temperature does not reach the new setpoint with control system (A) because the second term of (7.28) tries to make the flow rate follow the power. With other control systems, the main steam temperature settles to the new setpoint.

Since the reactor power temporarily decreases due to the coolant density feedback in this event, the change in the feedwater flow rate is slowed down by the second term of (7.29), so that the main steam temperature reaches the new setpoint without overshoot with Control system (B). On the other hand, the change in the feedwater flow rate is accelerated by the second term of (7.30), so that the settling time is shorter with Control system (C) than that with the reference control system.

7.9.5.4 Impulsive Decrease in Feedwater Flow Rate by 5%

In this event, the feedwater flow rate decreases stepwise by 5% and then is recovered by the feedwater controller. The results are shown in Fig. 7.79 [31].

With Control system (A), the recovery of the flow rate is faster, and hence the change in the main steam temperature is smaller than the reference case. This is because the power to flow rate ratio itself is fed back to the feedwater controller.

With Control system (B), the plant response is almost the same as the reference case. This is because the reactor power does not change significantly due to the small reactivity feedback from the coolant density and hence the second term of (7.29) has almost no effect compared to the first term.

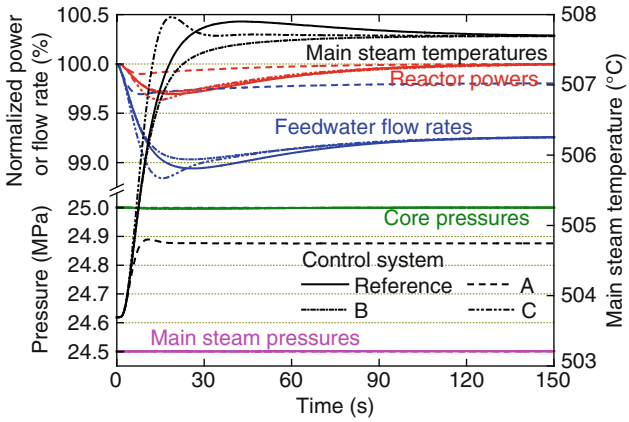


Fig. 7.78 Responses to 4°C increase in steam temperature setpoint with four control systems. (Taken from [31] and used with permission from Atomic Energy Society of Japan)

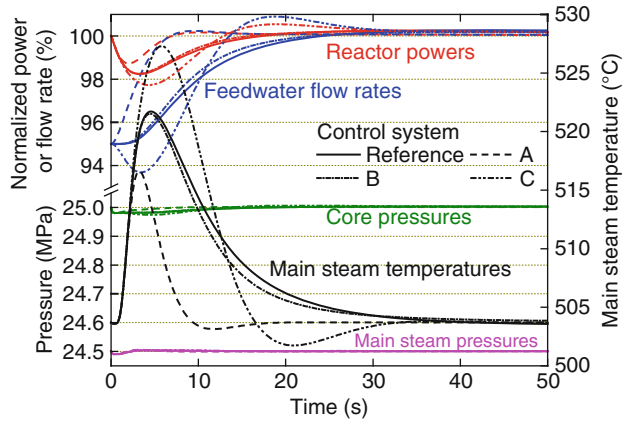


Fig. 7.79 Responses to 5% impulsive decrease in feedwater flow rate with four control systems. (Taken from [31] and used with permission from Atomic Energy Society of Japan)

With Control system (C), the feedwater flow rate decreases further at the beginning and hence the change in the main steam temperature is larger than the reference case. This is because the derivative control term of (7.30) decreases the feedwater flow rate by detecting the initial decrease in the reactor power.

7.9.5.5 10°C Decrease in Feedwater Temperature

In this event, the feedwater temperature decreases stepwise by 10°C and does not recover. In the beginning, the main steam temperature increases and the reactor

power decreases because the decrease in the volume flow rate from the feedwater pumps leads to the decrease in the core inlet flow rate. This is a common characteristic of the Super LWR and Super FR due to no recirculation. Then, the main steam temperature decreases, and the reactor power increases after the cold feedwater begins to enter the core. The results are shown in Fig. 7.80 [31].

In order to settle the main steam temperature to the initial value for lower feedwater temperature, the enthalpy rise in the core needs to be kept larger than that in the initial condition by decreasing the feedwater flow rate. With Control system (A), the main steam temperature settles to a value that is lower by about 10°C because the flow rate is settled to nearly the rated value by the second term of (7.28). With other control systems, the main steam temperature returns to the initial value.

With the reference control system, all the parameters return to the initial values within 2 min. With Control system (B), the fluctuation of the main steam temperature is slightly mitigated because the second term of (7.29) tends to assist the first term in this event. On the other hand, the fluctuation is larger with Control system (C) because the second term of (7.30) tends to cancel the first term.

7.9.6 Comparison of Improved Feedwater Controllers

The reactor power is not sensitive to the flow rate because the Super FR is a fast reactor with small reactivity feedback from coolant density. The reactor power is mainly regulated by the CRs. Therefore, the responses of the reactor power do not significantly differ with the four control systems including the reference one. Since the responses of the core and main steam pressures are very fast and determined by only the turbine control valves, they are almost the same with the four control systems. The changes in the main steam temperature obtained by the plant stability analyses are summarized in Table 7.37 [31]. The advantages and the issues of each control system are discussed below.

Control system (A), where the power to flow rate ratio is fed back to the feedwater controller, keeps the main steam temperature more stable than the reference control system against the perturbations of the reactor power and the flow rate as evinced in Figs. 7.76 [31] and 7.79 [31]. On the other hand, the main steam temperature does not settle to the setpoint when the setpoint itself or the feedwater temperature changes, and hence the required power to flow rate ratio is not equal to the initial value as in Figs. 7.78 [31] and 7.80 [31]. This problem might be solved by changing the target of the power to flow ratio according to the required enthalpy rise in the core.

Control system (B), where the reactor power is fed back to the feedwater controller, keeps the main steam temperature more stable than the reference control system when the power level is changed by the CRs as in Fig. 7.76 [31]. However, this control system gives similar plant dynamics to those with the reference control system unless the reactor power is significantly changed by the CRs. This is because the reactor power is less sensitive to the flow rate and mainly influenced by CRs.

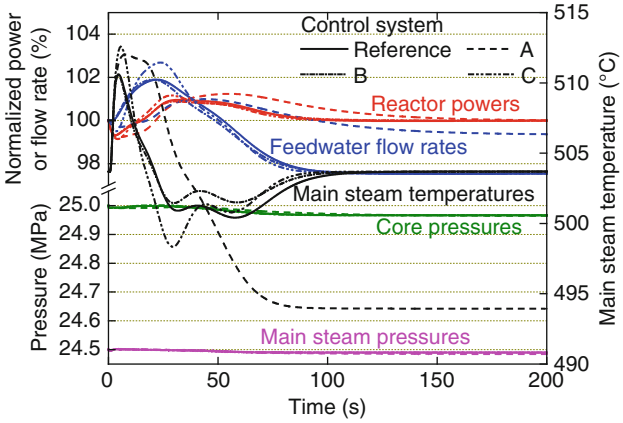


Fig. 7.80 Responses to 10°C decrease in feedwater temperature setpoint with four control systems. (Taken from [31] and used with permission from Atomic Energy Society of Japan)

The feedwater controller of Control system (C) also makes the flow rate follow the reactor power. When the change in the power is caused by CRs, this control system works better than the reference control system as evinced in Fig. 7.76 [31]. When it is caused by the reactivity feedback from the coolant density, the change in the main steam temperature is larger than the reference cases as in Figs. 7.79 [31] and 7.80 [31].

7.9.7 Summary of Improvement of Feedwater Controller

It was found that the main steam temperature of the Super FR changes more sensitively than that of the Super LWR because there is no moderator with a large heat capacity. In order to suppress the fluctuation of the main steam temperature by keeping the power to flow rate ratio constant, three types of feedback methods were proposed and added to the original feedwater controller that took only the deviation of the main steam temperature into consideration.

Control system (A), taking the power to flow rate ratio into the feedwater controller, worked best against the perturbations of the power or flow rate. However, it had a problem that the main steam temperature did not settle to the setpoint when the setpoint or the feedwater temperature was changed. Control system (B), taking the deviation of the power in the feedwater controller, worked better or at least not worse than the original control system against all the perturbations. Control system (C), taking the derivative of the power in the feedwater controller, worked better than the original control system when the power was changed by the CRs, but did not when the power was changed by the coolant density feedback.

Table 7.37 Changes in main steam temperature from initial condition. (Taken from [31] and used with permission from Atomic Energy Society of Japan)

Event	Reference control system	Improved control system		
		A	B	C
10% decrease in power setpoint	−8.2 to +0	−0.7 to +0	−0.3 to +1.9	−1.2 to +0.8
1% increase in pressure setpoint	−0.1 to +4.1	0 to +4.1	−0.1 to +4.1	−0.4 to +4.2
4°C increase in steam temperature setpoint	0 to +4.3	0 to +1.0[a]	0 to +4.0	0 to +4.3
Impulsive decrease in feedwater flow rate by 5%	0 to +18.0	−0.6 to +13.0	0 to +17.8	−2.0 to +24.9
10°C decrease in feedwater temperature	−3.6 to +6.9	−9.7 to +8.3[b]	−2.2 to +6.8	−5.4 to +9.3

[a]The main steam temperature does not reach the new setpoint
[b]The main steam temperature settles to a value lower than the initial value by about 10°C

7.10 Thermal and Stability Considerations During Power Raising Phase of Plant Startup

7.10.1 Introduction

The startup system and startup procedure of the Super FR are basically the same as those of the Super LWR introduced in Chap. 5. Both the sliding pressure startup and the constant pressure startup schemes include the power raising phase where the core power and feedwater flow rate gradually increase to the rated values after the once-through coolant cycle is achieved with the operating pressure of 25 MPa. The available ranges of the core power and feedwater flow rate need to be obtained for the power raising phase of the Super FR as they were for the Super LWR in Chap. 5. The issues during this phase are fuel rod heat-up and thermal-hydraulic instability caused by an improper power to flow rate ratio. Coupled neutronics thermal-hydraulic instability is less important than the thermal-hydraulic instability because the Super LWR is a fast reactor with very small reactivity feedback from the coolant density.

In the Super LWR analyzed in Chap. 5, the coolant channels of all the fuel assemblies are cooled by upward flow, so that only one hot channel is treated in the thermal analysis and thermal hydraulic stability analysis. On the other hand, the coolant flow scheme in the reactor pressure vessel of the Super FR is the so-called two-pass scheme where part of the seed fuel assemblies and all the blanket fuel assemblies are cooled by downward flow as shown in Fig. 7.35. The fractions of the downward flow rate in the seed assemblies, blanket assemblies, and downcomer at the normal operating condition are determined in the core design as shown in Figs. 7.36 and 7.58 [26]. The flow distribution among those downward flow paths would change during the power raising phase so as to balance the pressure drops.

In the rest of Sect. 7.10, the flow distribution among the downward flow paths is calculated first with respect to the core power and feedwater flow rate. Based on the

flow distribution, thermal analyses and thermal-hydraulic stability analyses are conducted for the three hot channels in the upward flow seed assemblies, downward flow seed assemblies, and downward flow blanket assemblies, respectively. Then, the available ranges of the core power and feedwater flow rate are obtained for the Super FR. As an example, the 1,000 MWe class design introduced in Sect. 7.5 is analyzed.

7.10.2 Calculation of Flow Distribution

The plant transient analysis code SPRAT-F, introduced in Sect. 7.9, is used to calculate the flow distribution and the MCST in the three hot channels with respect to the core power and feedwater flow rate. The nodalization is shown again in Fig. 7.81 [32]. Since the core power and feedwater flow rate are raised very slowly at the power raising phase, the reactor can be practically treated as in a steady state

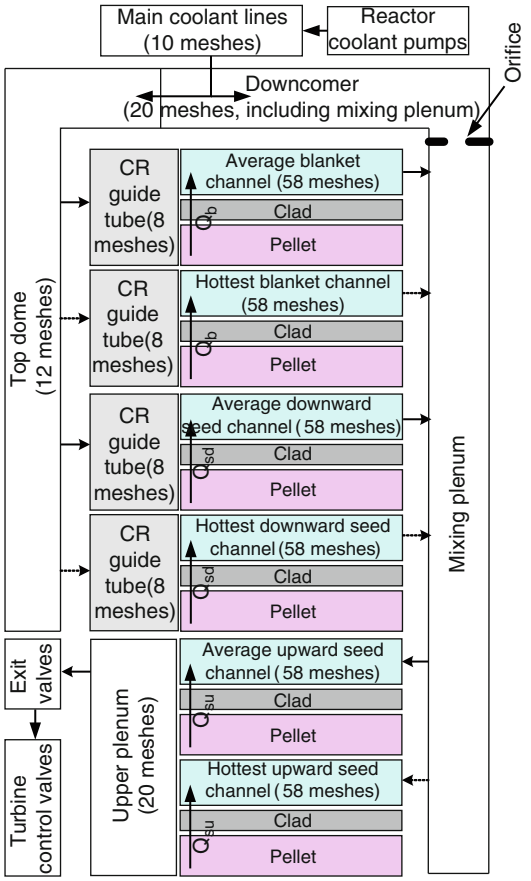


Fig. 7.81 Nodalization of SPRAT-F which calculates flow distribution and MCST. (Taken from [32] and used with permission from Atomic Energy Society of Japan)

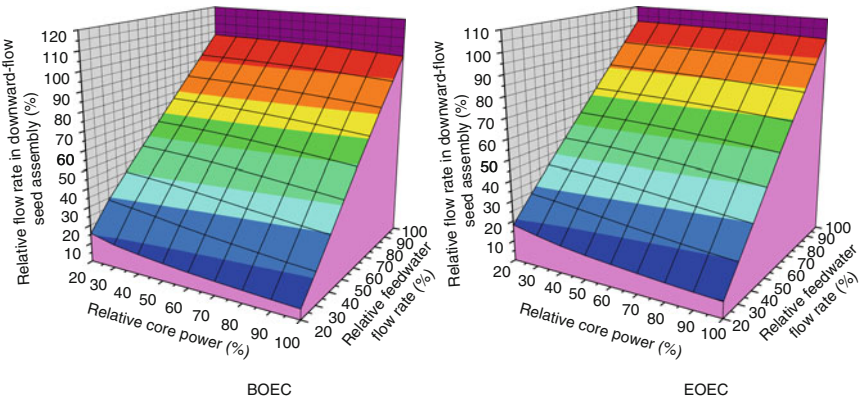


Fig. 7.82 Relative downward flow rate in average seed channel. (Taken from [32] and used with permission from Atomic Energy Society of Japan)

as is also assumed in LWRs. Thus, the flow distribution at a certain power and feedwater flow rate is calculated by obtaining a steady state. The orifice pressure drop coefficients at the inlet of each average channel are determined so that the flow distribution is consistent with that in the core design. The orifice pressure drop coefficients at the inlet of each hot channel are determined so that the MCST for the upward flow seed channel is 681°C, which is evaluated with consideration of engineering uncertainties in Sect. 7.7, and the MCSTs in the downward flow seed and blanket channels are higher than those evaluated by subchannel analyses in Sect. 7.6 by 31°C.

The flow fractions to the seed and blanket assemblies with downward flow are calculated for various core powers (20–100%) and feedwater flow rates (20–100%) at intervals of 10%. The relative flow rates in the average channels as functions of the core power and feedwater flow rate are plotted in Figs. 7.82 and 7.83 [32]. They are also shown in Fig. 7.84 [32] with fixed feedwater flow rate. In these figures, "100% of the relative flow rate" corresponds to each value at the normal operating condition with rated power and rated feedwater flow rate. It should be noted that "100%" does not mean the rated value of the feedwater flow rate in these figures. With a fixed feedwater flow rate, the downward flow rate in the average seed channel decreases as the power increases due to an increase in the buoyancy pressure drop. This, in the average blanket channel, exhibits the same tendency at EOEC. On the other hand, the blanket flow rate shows the opposite behavior at BOEC because the blanket assemblies have very small power at BOEC, and hence the fraction of buoyancy pressure drop is very small. It should be mentioned that the flow rate in the average seed channel cooled by upward flow is in proportion to the feedwater flow rate regardless of the core power.

Thermal and stability considerations should be done for the hot channels because the hot channels are expected to give the limiting conditions. The ratios of the hot channel flow rate to the average channel flow rate are shown in Figs. 7.85–7.87 [32].

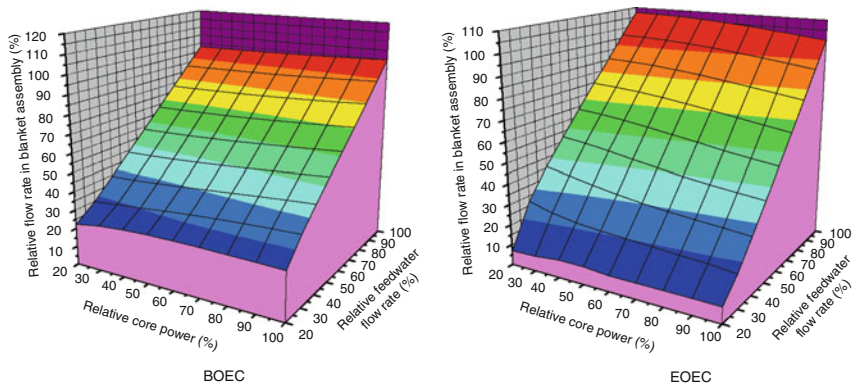


Fig. 7.83 Relative downward flow rate in average blanket channel. (Taken from [32] and used with permission from Atomic Energy Society of Japan)

The hot-to-average flow rate ratios decrease with the ratio of core power to feedwater flow rate increases because the pressure drop by volume expansion (flow acceleration) increases with the power to flow rate ratio more rapidly in the hot channels than in the average channels. The buoyancy pressure drop has the same tendency in the downward flow channels, which can explain the reason why the hot to average flow rate ratios decrease more significantly for the downward flow conditions compared to the upward flow condition.

Based on those results, the database of the flow rates in the three hot channels as functions of the core power and feedwater flow rate is prepared. It is used for the thermal and stability considerations introduced next.

7.10.3 Thermal and Thermal-Hydraulic Stability Considerations

The thermal criterion is that the MCST must be below that at the normal operating condition as is applied for the Super LWR in Chap. 5. The MCSTs at the hot channels are calculated under various powers and feedwater flow rates using SPRAT-F. The contour maps of the MCST for the hot channels are drawn in Figs. 7.88–7.90. The MCST is kept almost the same as that at the normal operating condition in the upward flow seed channel by keeping the power to flow rate ratio as unity. This is because the flow rate at the upward flow average seed channel is in proportion to the feedwater flow rate regardless of the power and that the hot to average flow rate ratio among the upward flow seed channels is almost constant as long as the ratio of power to feedwater flow rate is kept as unity (see Fig. 7.85 [32]). The ratio of power to feedwater flow rate must be lower than unity at low power region in order to satisfy the thermal criterion in the downward flow seed channel at BOEC and the blanket channel at EOEC because the linear heat generation rate is relatively high and hence a relatively low flow rate is distributed to these channels.

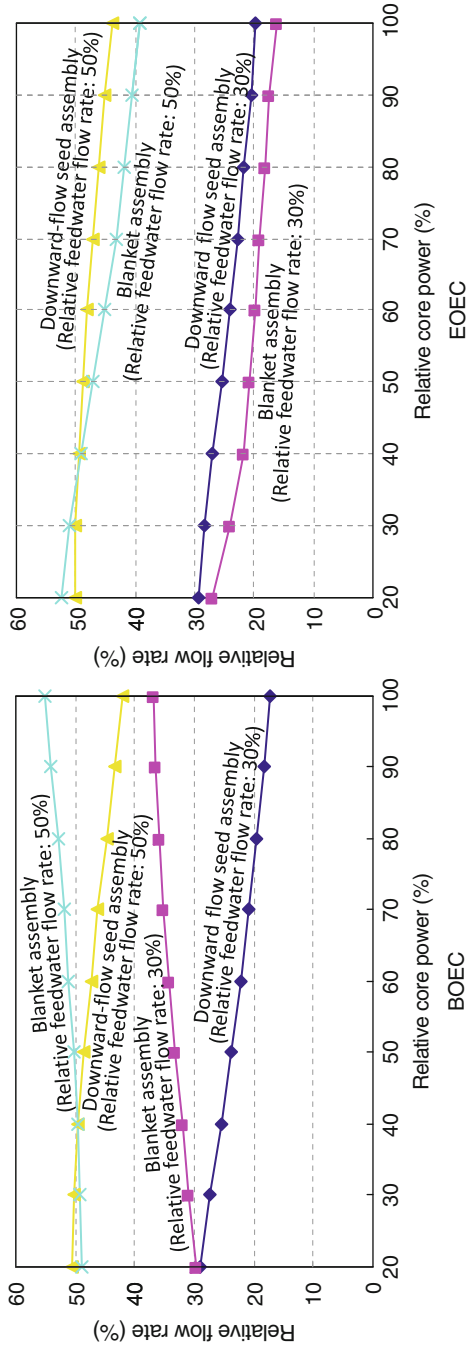


Fig. 7.84 Relative downward flow rates in average seed and blanket channels. (Taken from [32] and used with permission from Atomic Energy Society of Japan)

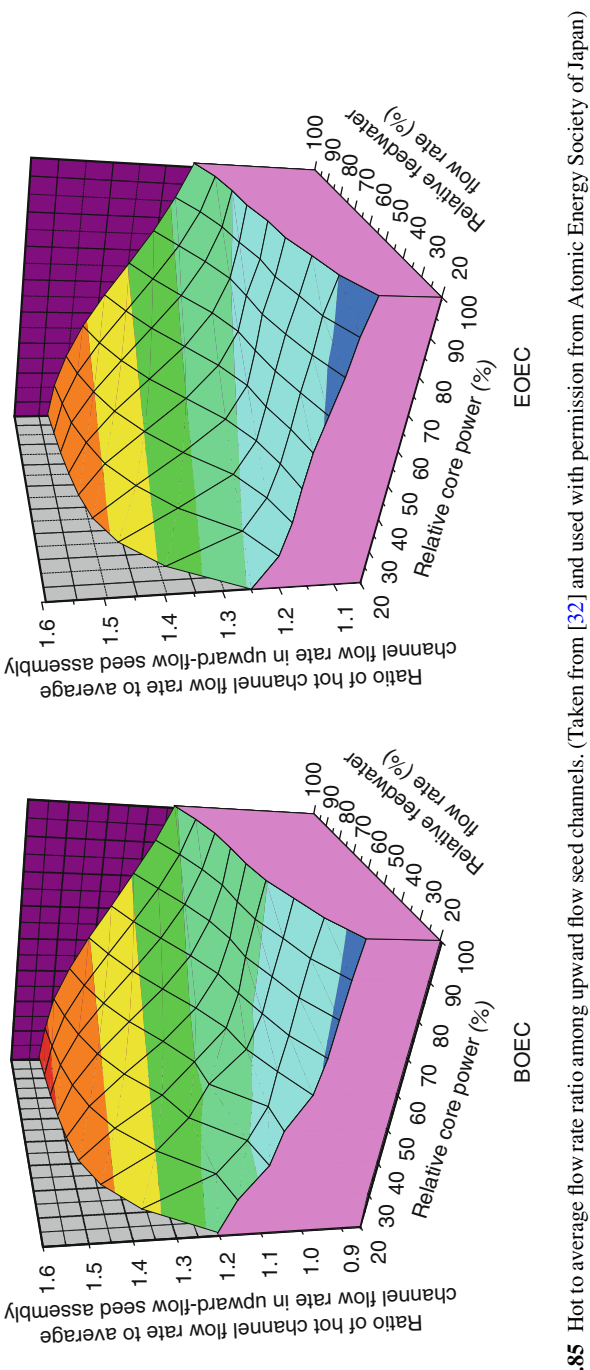


Fig. 7.85 Hot to average flow rate ratio among upward flow seed channels. (Taken from [32] and used with permission from Atomic Energy Society of Japan)

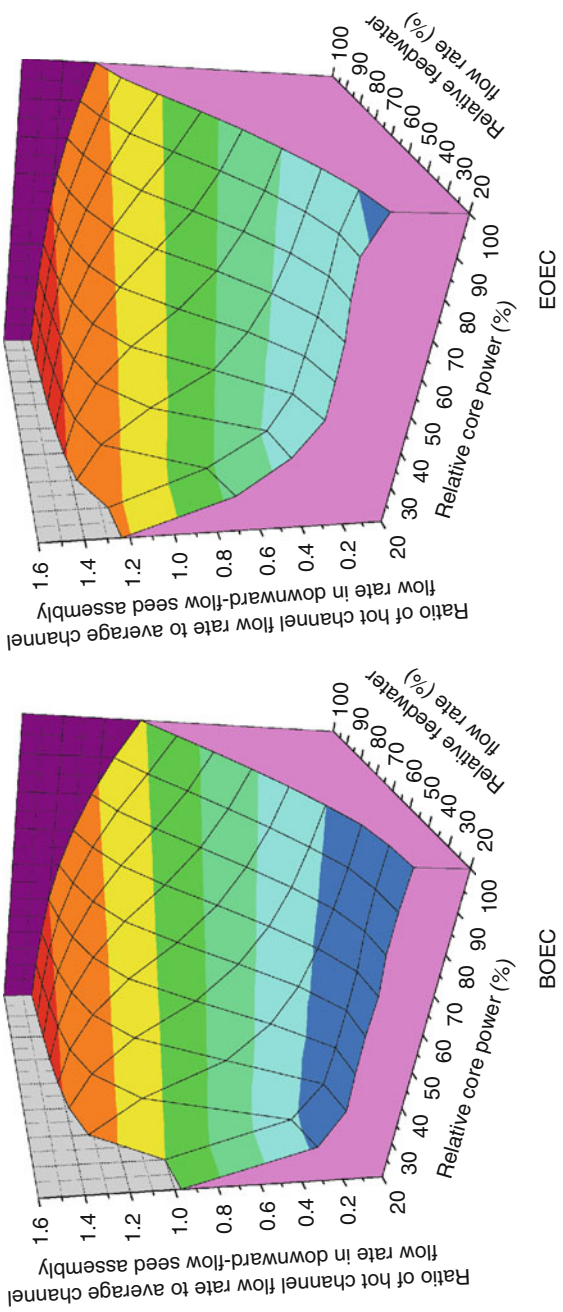


Fig. 7.86 Hot to average flow rate ratio among downward flow seed channels. (Taken from [32] and used with permission from Atomic Energy Society of Japan)

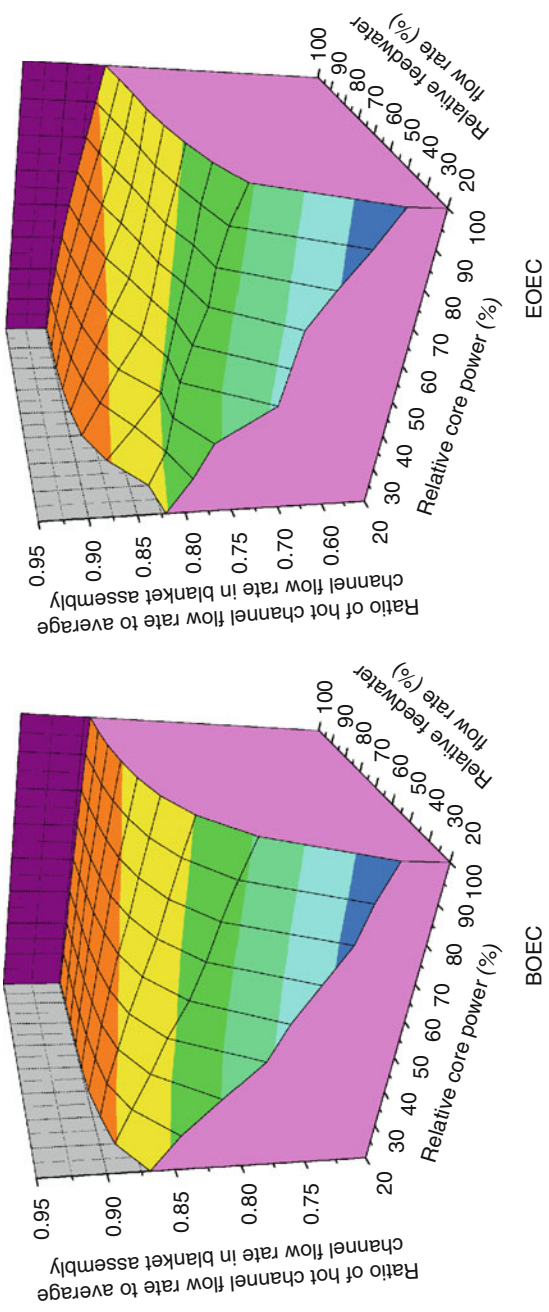


Fig. 7.87 Hot to average flow rate ratio among blanket channels. (Taken from [32] and used with permission from Atomic Energy Society of Japan)

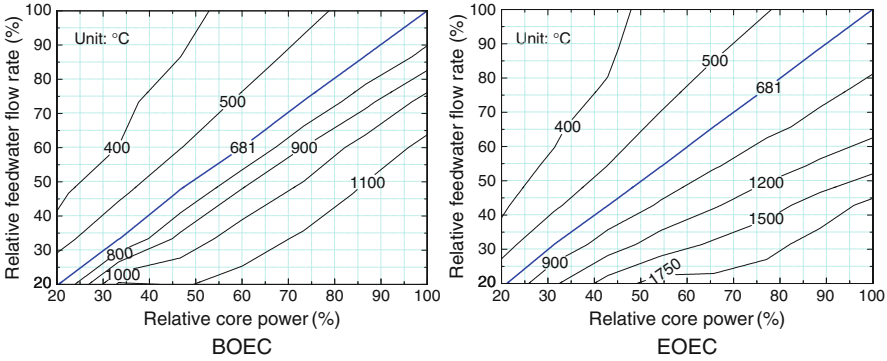


Fig. 7.88 Contour maps of MCST for hot seed channel with upward flow

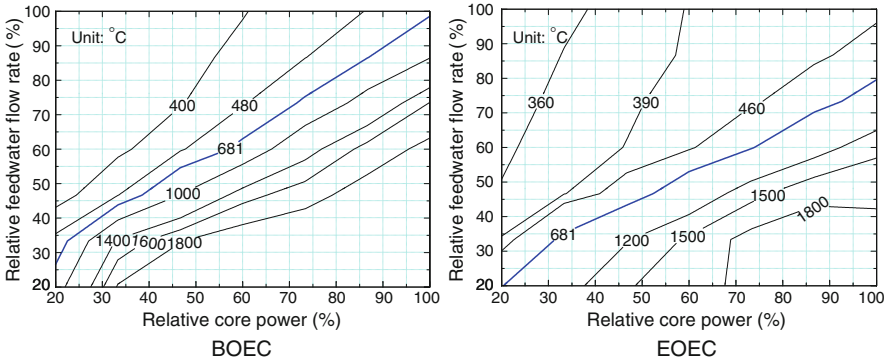


Fig. 7.89 Contour maps of MCST for hot seed channel with downward flow

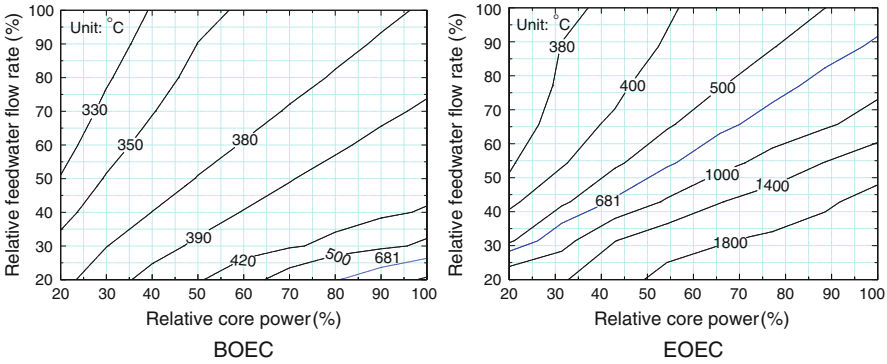


Fig. 7.90 Contour maps of MCST for hot blanket channel

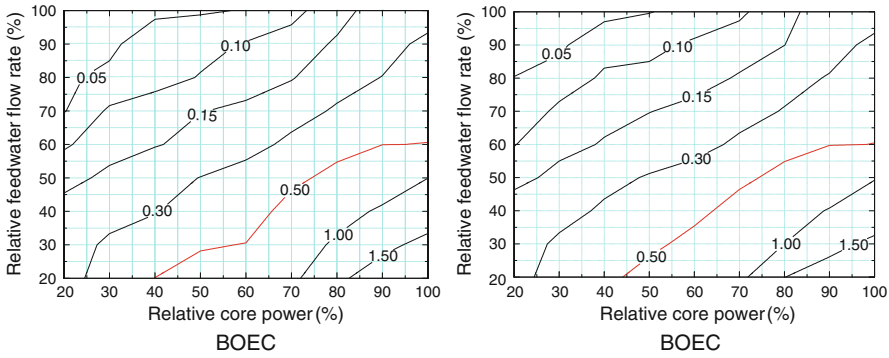


Fig. 7.91 Contour maps of decay ratio of thermal-hydraulic stability for hot seed channel with upward flow

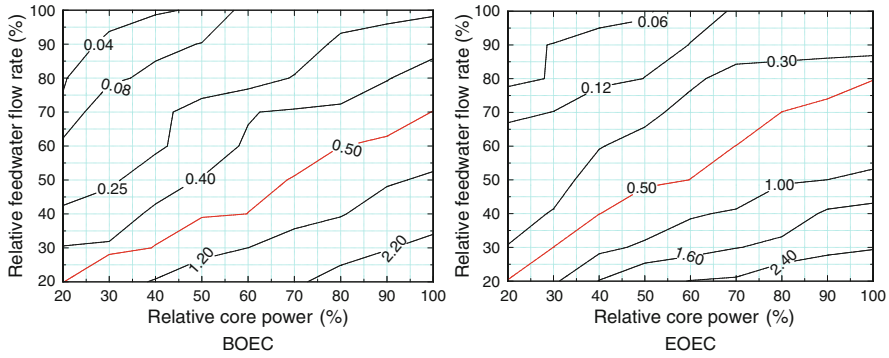


Fig. 7.92 Contour maps of decay ratio of thermal-hydraulic stability for hot seed channel with downward flow

On the other hand, it can be higher than unity in the downward flow seed channel at EOEC and the blanket channel at BOEC for the opposite reason.

The criterion of the thermal-hydraulic stability is that the decay ratio must be below 0.5 as is applied for the Super LWR in Chap. 5. The decay ratios at the hot channels are calculated under various powers and feedwater flow rates by the frequency domain approach introduced in Chap. 5. The orifice pressure drop coefficient is conservatively given as 30 at the inlet of each hot channel while the designed values are over 30. It should be mentioned that a smaller orifice pressure drop gives a higher decay ratio. The contour maps of the decay ratio for the hot channels are drawn in Figs. 7.91–7.93. For the blanket channel at EOEC, the constant power to flow ratio is not enough to satisfy the criterion because a relatively low flow rate is distributed to this channel at EOEC. For other channels including the blanket channel at BOEC, the power to flow rate ratio can be above unity.

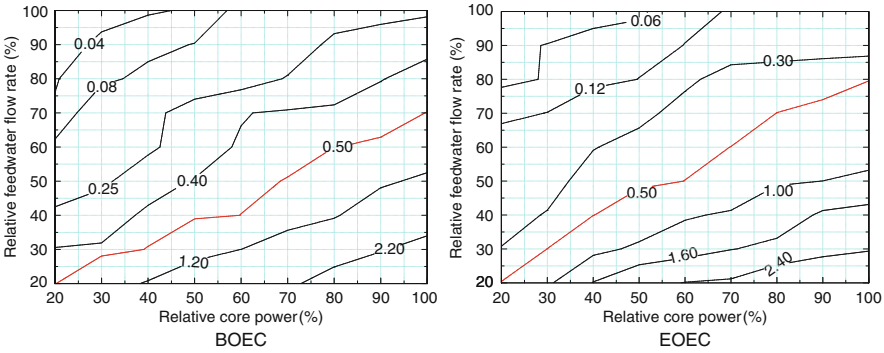


Fig. 7.93 Contour maps of decay ratio of thermal-hydraulic stability for hot blanket channel

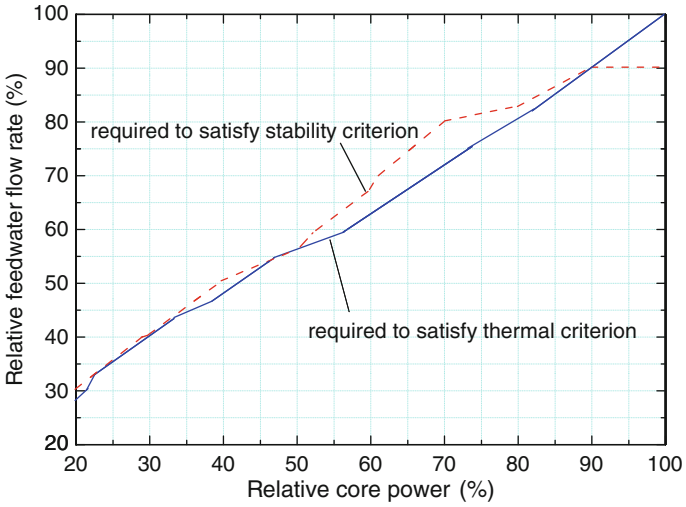


Fig. 7.94 Feedwater flow rates required to satisfy respective thermal and stability criteria. (Taken from [32] and used with permission from Atomic Energy Society of Japan)

Based on the results of thermal and stability analyses, the flow rates required for satisfying the respective thermal and stability criteria in all the channels at both BOEC and EOEC are shown in Fig. 7.94 [32]. The higher relative feedwater flow rate compared to the relative power is required for both criteria at the relative power level below about 80%.

Finally, the curve for raising the feedwater flow rate is determined in the available region as shown in Fig. 7.95 [32]. With the designed flow rates, the MCSTs are calculated again and shown in Fig. 7.96 [32] along with other parameters. Since the power to flow rate ratio is kept below unity, the core outlet

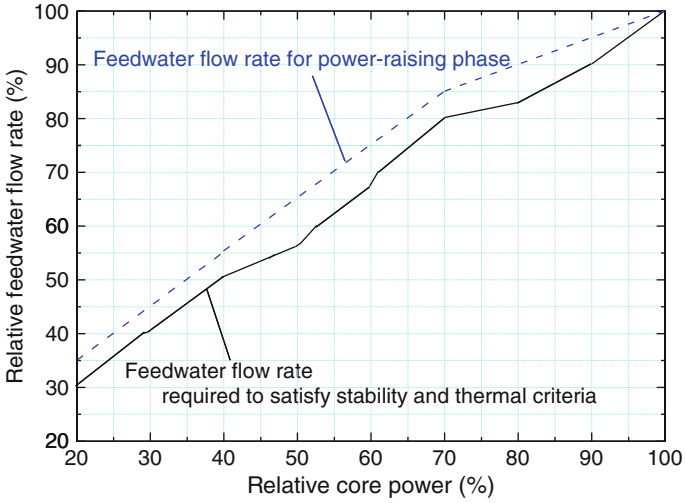


Fig. 7.95 Designed feedwater flow rate for power raising phase of 1,000 MWe class Super FR. (Taken from [32] and used with permission from Atomic Energy Society of Japan)

temperature is kept below that calculated by the core design in Sect. 6.5 until full power condition is reached. The decay ratios of thermal-hydraulic stability are calculated again and shown in Fig. 7.97 [32]. They are kept well below the criterion throughout the power raising phase.

7.10.4 Sensitivity Analyses

Four typical correlations of heat transfer coefficient are applied to SPRAT-F in order to investigate the influence of heat transfer correlations on the MCST. The results are summarized in Table 7.38. The correlation proposed by Watts and Chou [33] gives the highest MCST in all the channels at both BOEC and EOEC.

The influence of axial power shape on the MCSTs is investigated. The results are summarized in Table 7.39. The MCST in the upward flow seed channel is relatively high with the typical top peak because the heat flux is relatively high at the position where the MCST appears. The MCSTs in the downward flow seed and blanket channels are relatively high with the typical bottom peak for the same reason. The downward flow seed channel at BOEC is influenced the most where the MCST with the typical bottom peak is higher than that in the reference case by 76°C. This shows considerably high sensitivity.

The influence of axial power shape on the decay ratios of the thermal-hydraulic stability is investigated. The results are summarized in Table 7.40. The decay ratio in the upward flow seed channel is relatively high with the typical top peak because the heat flux and hence the flow acceleration are relatively high near the channel

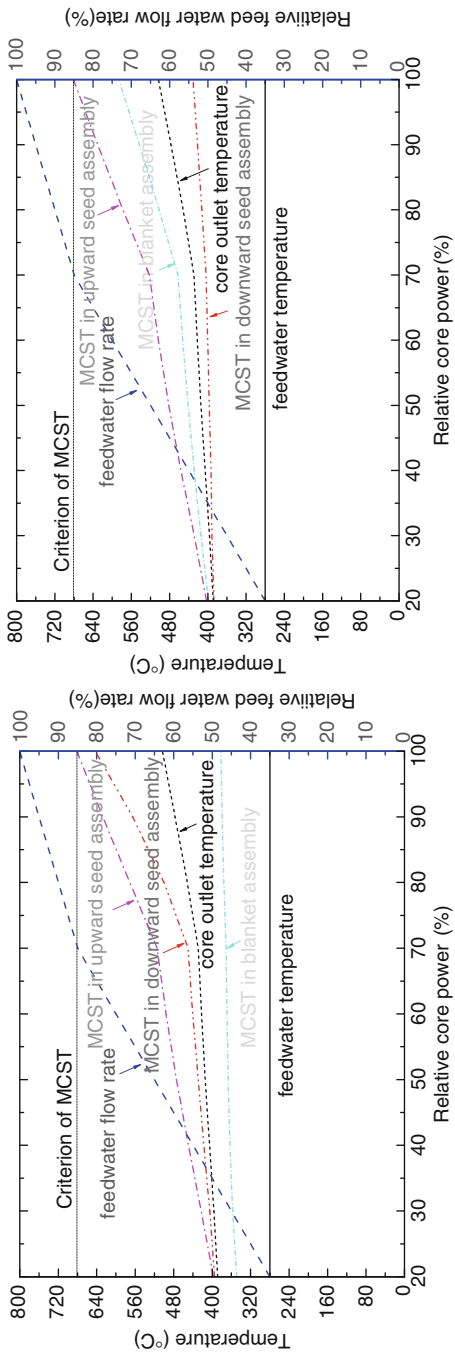


Fig. 7.96 Parameters during power raising phase of 1,000 MWe class Super FR. (Taken from [32] and used with permission from Atomic Energy Society of Japan)

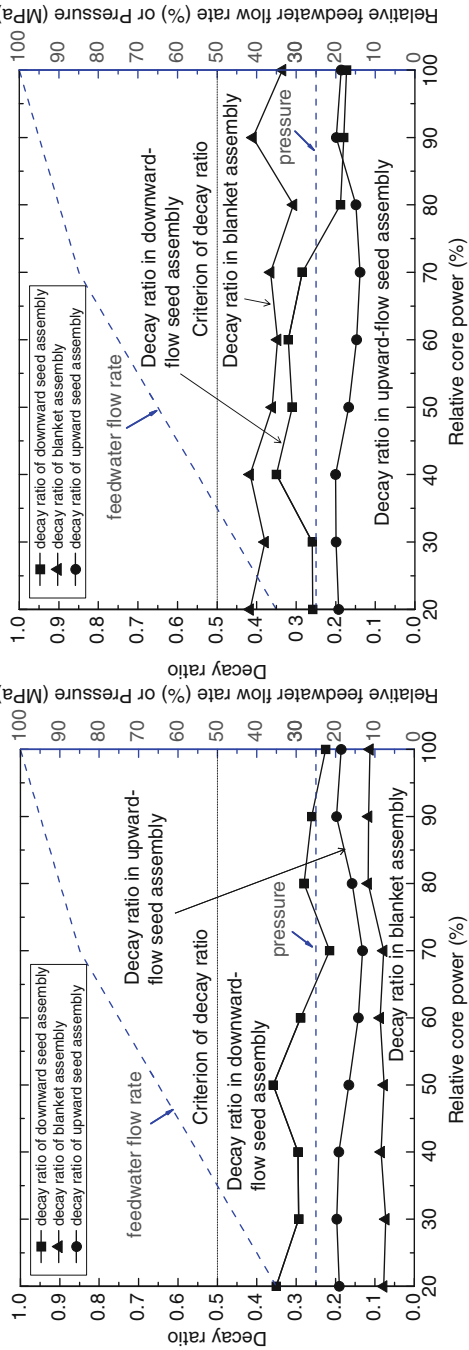


Fig. 7.97 Decay ratios of thermal-hydraulic stability during power raising phase of 1,000 MWe class Super FR. (Taken from [32] and used with permission from Atomic Energy Society of Japan)

Table 7.38 Highest values of MCSTs during power raising phase with various heat transfer correlations at BOEC/EOEC (unit: °C)

Correlation	Upward seed	Downward seed	Blanket
Watts and Chou[a] [33]	681/681	643/431	382/586
Oka–Koshizuka [34]	652/641	606/425	382/575
Bishop [35]	654/644	610/414	382/577
Dittus–Boelter [36]	665/658	619/420	382/580

[a]Reference case

Table 7.39 Highest values of MCSTs during power raising phase with various axial power shapes at BOEC/EOEC (unit: °C)

Axial power shape	Upward seed	Downward seed	Blanket
Taken from core design[a]	681/681	643/431	382/586
Cosine	689/680	645/431	381/594
Typical bottom peak	680/675	719/442	387/627
Typical top peak	714/715	625/430	381/609

[a]Reference case

Table 7.40 Highest decay ratios of thermal-hydraulic instability during power raising phase with various axial power shapes at BOEC/EOEC

Axial power shape	Upward seed	Downward seed	Blanket
Taken from core design[a]	0.186/0.187	0.225/0.173	0.113/0.335
Cosine	0.186/0.186	0.226/0.173	0.112/0.336
Typical bottom peak	0.186/0.186	0.231/0.174	0.113/0.339
Typical top peak	0.190/0.190	0.224/0.174	0.112/0.328

[a]Reference case

outlet. The decay ratios in the downward flow seed and blanket channels are relatively high with the typical bottom peak for the same reason. However, the sensitivity is very low. This implies that the thermal-hydraulic stability of the Super FR is sufficiently robust against the axial power shape.

7.11 Safety

7.11.1 Introduction

Safety of the Super FR is basically the same as that of the Super LWR. However, there are three important characteristics of the Super FR compared to the Super LWR. One is that the Super FR has a higher power density and hence a smaller heat capacity than those of the Super LWR. Mismatch of heat generation and heat removal would thus be more significant under loss of flow and LOCA conditions. The second is that the Super FR has a much smaller reactivity feedback from the

coolant density than the Super LWR has, which would make the ATWS events of the Super FR severer. The third is the complicated coolant flow and change in the flow distribution under abnormal conditions in the two-pass flow scheme.

In the rest part of this chapter, the basic safety characteristics of the Super FR are investigated and compared to those of the Super LWR by analyzing the abnormal transients, accidents and ATWS events of the 1,000 MWe class Super FR as an example. The same safety system design as that of the Super LWR summarized in Table 6.2 is used. The same safety criteria as those of the Super LWR described in Sect. 6.5 are applied. The same events as those of the Super LWR summarized in Table 6.4 are analyzed. The same control system as designed for the Super LWR in Chap. 4 or designed for the Super FR in Sect. 7.9 (the reference control system) is used.

7.11.2 *Analyses of Abnormal Transients and Accidents at Supercritical Pressure*

Ten abnormal transients and four accidents are analyzed using the SPRAT-F code introduced in Sects. 7.9 and 7.10. Six fuel channels are modeled: average and hot channels for each of the upward flow seed assemblies, downward flow seed assemblies, and blanket assemblies. The initial conditions of these channels are summarized in Tables 7.41 and 7.42. The orifice pressure drop coefficients at the

Table 7.41 Initial conditions of 1,000 MWe class Super FR at BOEC for safety analyses

	Upward flow seed channel		Downward flow seed channel		Blanket channel	
	Average	Hot	Average	Hot	Average	Hot
Peak linear heat rate (kW/m)	21.7	39	21.9	32.6	4.3	6.4
Mass flux (kg/s/m^2)	1,581	2,105	1,497	1,413	934	920
Coolant inlet/outlet temperature (°C)	374/503	374/620	280/406	280/549	20/358	280/379
Hottest cladding temperature (°C)	536	681	437	599	360	384

Table 7.42 Initial conditions of 1,000 MWe class Super FR at EOEC for safety analyses

	Upward flow seed channel		Downward flow seed channel		Blanket channel	
	Average	Hot	Average	Hot	Average	Hot
Peak linear heat rate (kW/m)	22.3	37	19.6	28.8	15.3	22.5
Mass flux (kg/s/m^2)	1,581	2,208	1,497	1,571	934	818
Coolant inlet/outlet temperature (°C)	376/503	376/594	208/391	280/418	280/417	280/601
Hottest cladding temperature (°C)	551	681	402	436	430	630

inlet of each average channel are determined so that the flow distribution is consistent with that in the core design. The orifice pressure drop coefficients at the inlet of each hot channel are determined so that the MCST for the upward flow seed channel is 681°C, which is evaluated with consideration of engineering uncertainties in Sect. 7.7. The allowable increases in the MCST (ΔMCST) at the abnormal transients and accidents are 169°C (850–681°C) and 579°C (1,260–681°C), respectively, in the upward flow seed channel. They are higher than those for the Super LWR (110 and 520°C) by about 60°C, each, owing to the lower nominal MCST realized by the smaller local peaking and larger coolant mixing among the subchannels as introduced in Sect. 7.6. The MCSTs in the downward flow seed and blanket channels are higher than those evaluated by subchannel analyses in Sect. 7.6 by 31°C. Typical results are introduced below whereby comparisons of the characteristics of the Super FR to the Super LWR are readily apparent.

The analysis results of the "partial loss of reactor coolant flow" (transient) are shown in Fig. 7.98. The inlet flow rates of the three hot channels similarly decrease with the main coolant flow rate. The highest cladding temperature appears in the upward flow seed channel due to its higher value initially. The ΔMCST in the upward flow seed channel is about 80°C, which is higher than that in the Super LWR by 20°C. This is because the Super FR has a smaller heat capacity and also because the smaller reactivity feedback from the coolant density makes the decrease in the power slower before initiating the reactor scram. However, there is still a margin of over 60°C to the criterion.

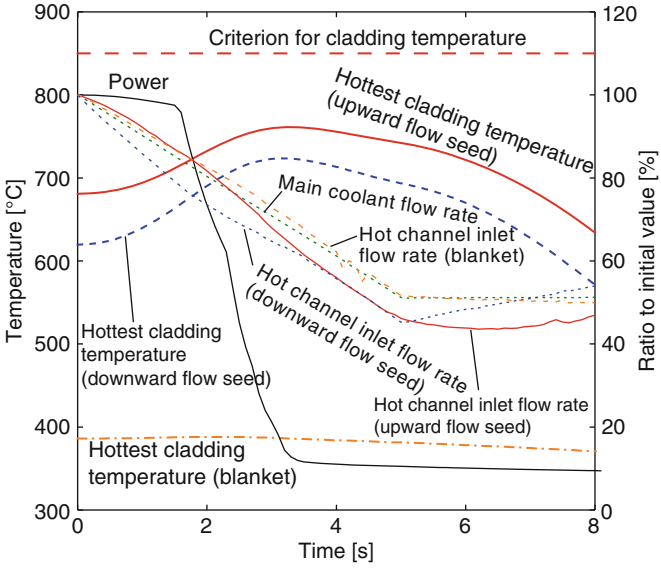


Fig. 7.98 Calculated results for "partial loss of reactor coolant flow" (BOEC)

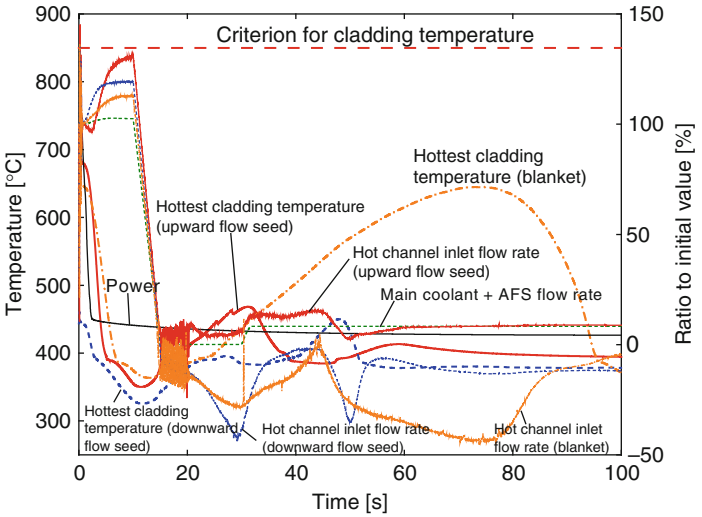


Fig. 7.99 Calculated results for "loss of offsite power" (EOEC)

The analysis results of the "loss of offsite power" (transient) are shown in Fig. 7.99. A relative increase in the buoyancy pressure drop after the trip of the RCPs leads to inverse flow in the downward flow channels. Since the absolute mass flux in the blanket channel is small, the cladding temperature increases more rapidly than it does in the seed channels after the trip of the RCPs. However, its peak value does not exceed the first peak in the upward flow seed channel, which is caused by the initial turbine trip, and is the highest throughout this transient.

The analysis results of the "reactor coolant flow control system failure" (transient) are shown in Fig. 7.100. Since the reactivity feedback from the coolant density is smaller than that in the Super LWR, the increase in the power is smaller and hence the reactor is not tripped.

The analysis results of the "total loss of reactor coolant flow" (accident) are shown in Fig. 7.101. The coolant in the blanket channels expands and flows into the upward flow seed channels, which is similar to the "water source" effect of the water rods in the Super LWR. However, the increase in the cladding temperature is larger than that in the Super LWR by about 180°C due to the smaller heat capacity. Furthermore, a strong buoyancy pressure drop in the downward flow seed channel induces reverse flow there and the absolute flow rate is kept small. This leads to a large increase in the cladding temperature in the downward flow seed channel.

The peak cladding temperatures and peak pressures at the abnormal transients are summarized in Figs. 7.102 and 7.103. Although the largest ΔMCST is larger in the Super FR than the Super LWR, the absolute peak temperature is smaller due to the lower initial temperature. The highest pressure is almost the same as that in the Super LWR. All the criteria including the allowable peak power are satisfied with considerable margins.

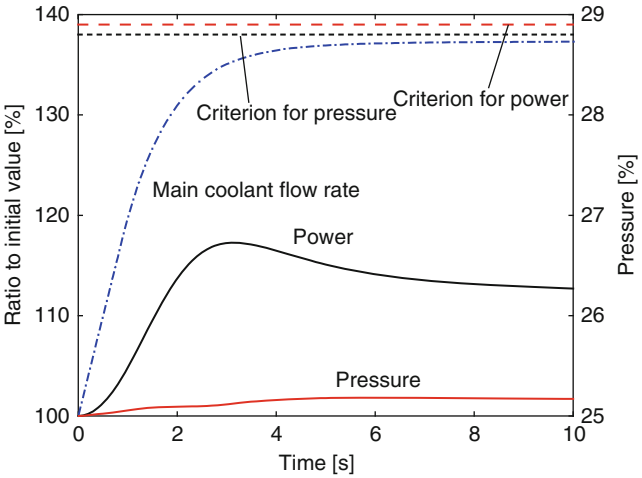


Fig. 7.100 Calculated results for "reactor coolant flow control system failure" (EOEC)

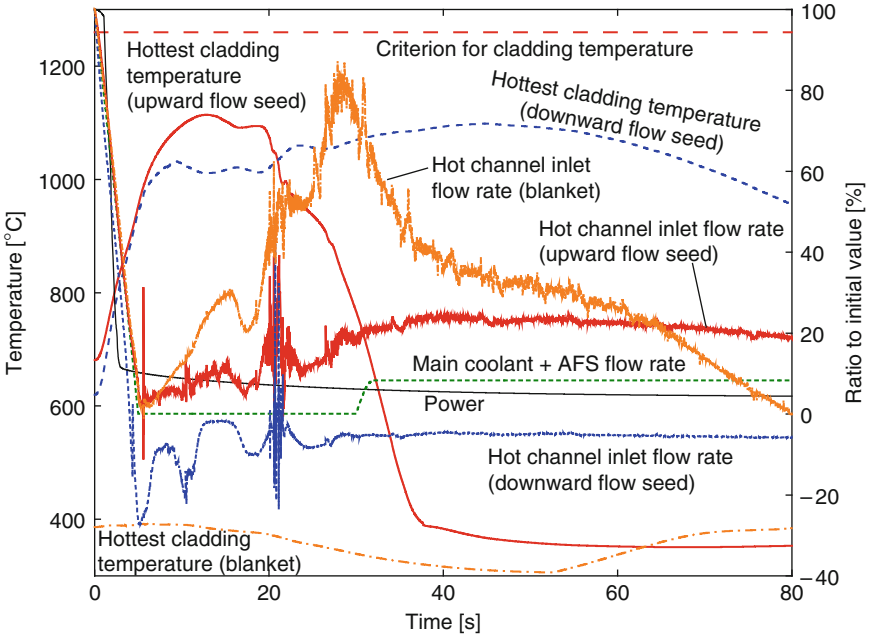


Fig. 7.101 Calculated results for "total loss of reactor coolant flow" (BOEC)

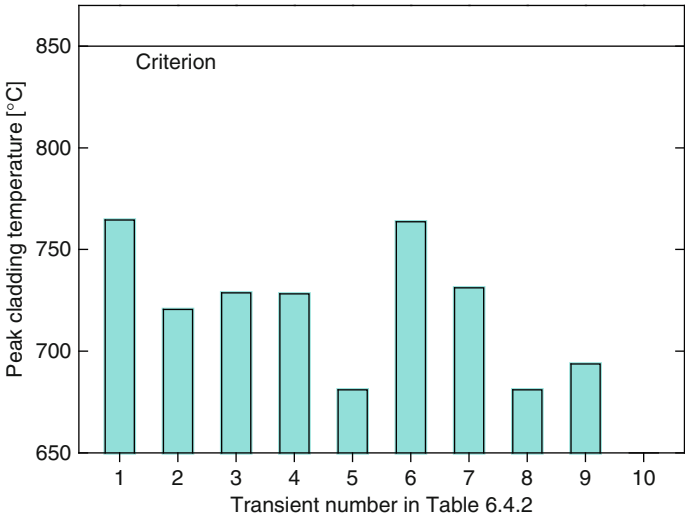


Fig. 7.102 Summary of peak cladding temperatures at abnormal transients

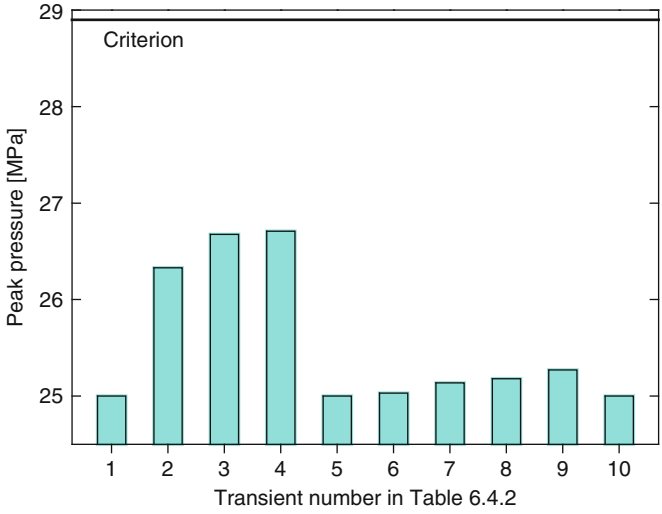


Fig. 7.103 Summary of peak pressures at abnormal transients

The peak cladding temperatures at the accidents, including LOCA events described in the next section, are summarized in Fig. 7.104. The criterion is satisfied although the margin is much smaller in the "total loss of reactor coolant flow" than that in the Super LWR mainly due to the higher power density and smaller heat capacity. Other criteria for the pressure and fuel enthalpy are satisfied with large enough margins.

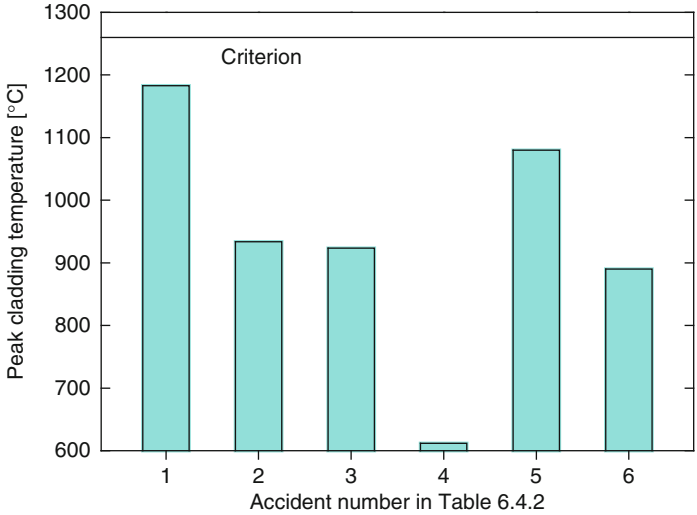


Fig. 7.104 Summary of peak cladding temperatures at accidents

7.11.3 Analyses of Loss of Coolant Accidents

During blowdown, the coolant flow in the reactor vessel of the Super FR is more complicated than that of the Super LWR due to the two-pass flow scheme. The coolant flow schemes are illustrated in Fig. 7.105 [37]. In order to analyze the blowdown of the two-pass core, the SPRAT-F is modified to the SPRAT-F-DP [37]. Flow redistribution among the downward flow seed channels, blanket channels, and downcomer are calculated in this code. The initial conditions for the LOCA analyses are the same as those for the safety analyses at supercritical pressure.

The analysis results of the blowdown phase after the 100% cold-leg break are shown in Fig. 7.106 [37]. The increase in the cladding temperature at the upward flow seed channel is below 200°C, and the hottest cladding temperature decreases down to around 400°C because the top dome serves as the "in-vessel accumulator" as in the Super LWR. However, the flow rate in the downward flow seed channel is kept significantly low due to an unfavorable flow distribution, and hence, the hottest cladding temperature at the downward flow seed channel remains over 1,100°C until the reflooding phase starts. It can be easily expected that the criterion of 1,260°C is not satisfied during the reflooding phase when the reflooding starts with such a high cladding temperature. In the core design of the Super FR, the flow rate distribution is determined without consideration of safety. Herein, the desirable flow distribution is proposed in order to improve the LOCA behavior. The flow fraction to the downcomer is decreased from 50 to 10% of the feedwater flow rate. The flow fractions to the downward flow seed assemblies and blanket assemblies are increased from 40% and 10% to 60% and 30% of the feedwater flow rate, respectively. After this modification, the initial values of the hottest cladding

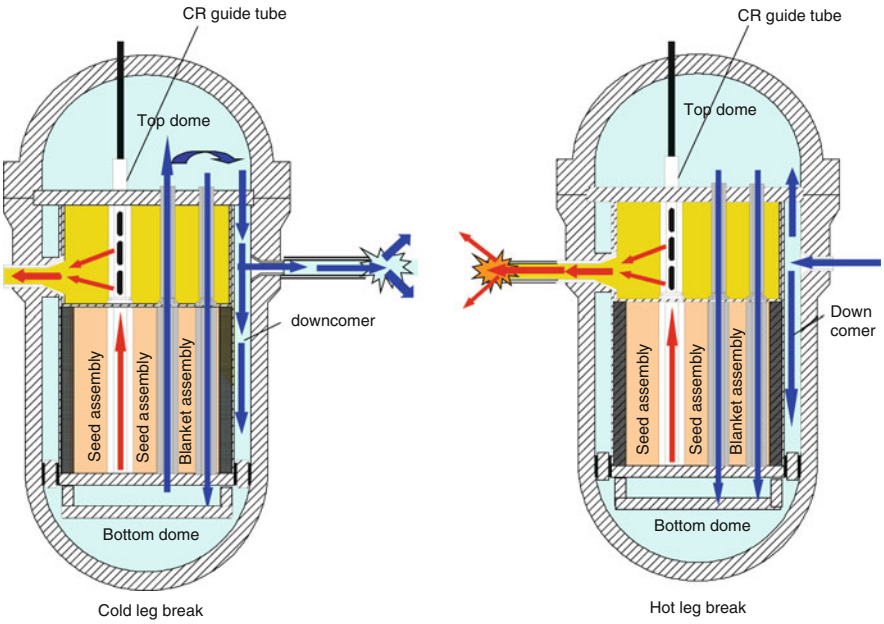


Fig. 7.105 Coolant flow during blowdown or small LOCA of the Super FR. (Taken from [37] and used with permission from Atomic Energy Society of Japan)

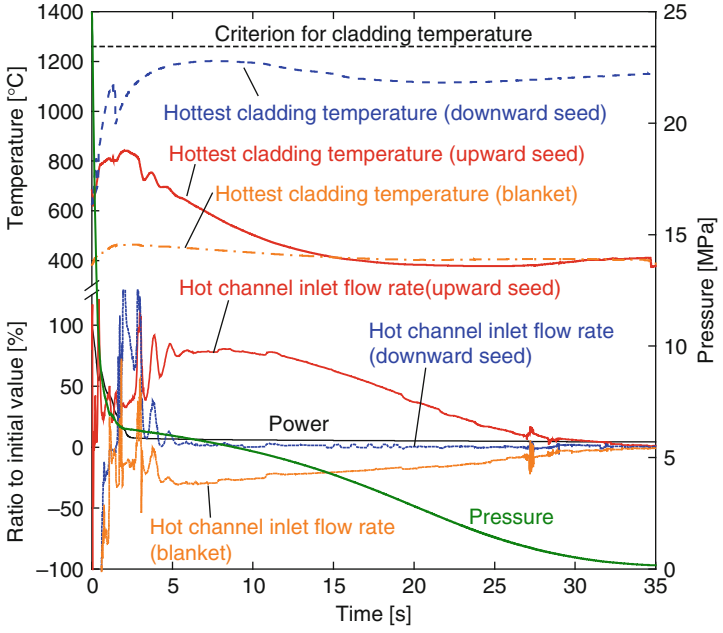


Fig. 7.106 Calculated results for blowdown phase of 100% cold-leg break LOCA (BOEC)

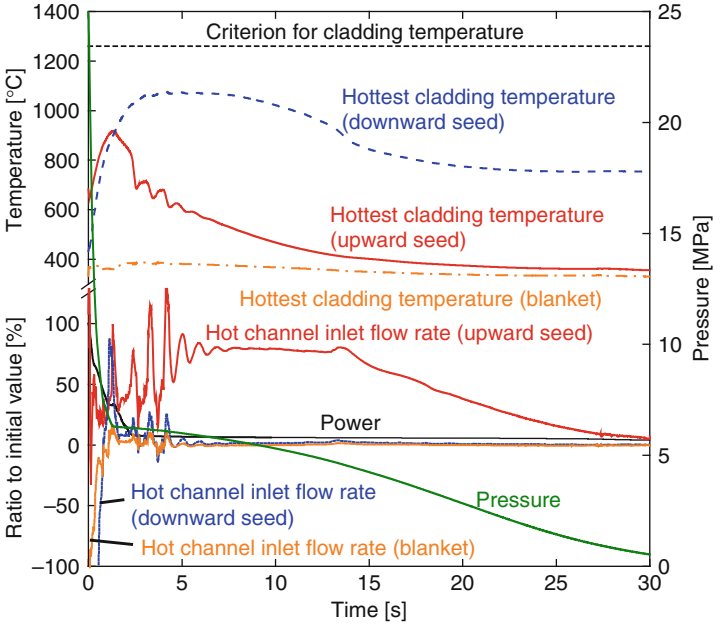


Fig. 7.107 Calculated results for blowdown phase of 100% cold-leg break LOCA (BOEC) with modification of initial flow distribution

temperature at the downward flow channels are lower than the original values and also more coolant tends to flow into these channels instead of being the bypass flow through the downcomer. The analysis results with the modified flow distribution are shown in Fig. 7.107 [37]. The hottest cladding temperature at the peak point and the end of the blowdown are both decreased from the original results, respectively.

The analysis results of the blowdown phase after the 100% hot-leg break are shown in Fig. 7.108 [37]. The cladding temperatures are kept lower than those in the cold-leg break because all the coolant flows to the break point or the ADS through the core, which is the same tendency as that of the Super LWR.

During reflooding, the coolant flow in the reactor vessel of the Super FR is also more complicated than that of the Super LWR due to the two-pass flow scheme. The coolant flow schemes are illustrated in Fig. 7.109 [37]. In order to analyze the reflooding of the two-pass core, the SCRELA reflood module is modified to the SCRELA-M [37]. The main modification is for the momentum conservation as illustrated in Fig. 7.110 [37] because two different channels are separately reflooded in the SCRELA-M. The coolant flow entering the core is distributed to these two channels while satisfying the momentum conservation [37].

The analysis results of the reflooding phase following the end stage of Fig. 7.107 [37] are shown in Fig. 7.111 [37]. The changes of the quench front and hottest cladding temperature in the upward flow seed channel are quite similarly to those of the Super LWR. The peak temperature is much lower than the criterion of 1,260°C.

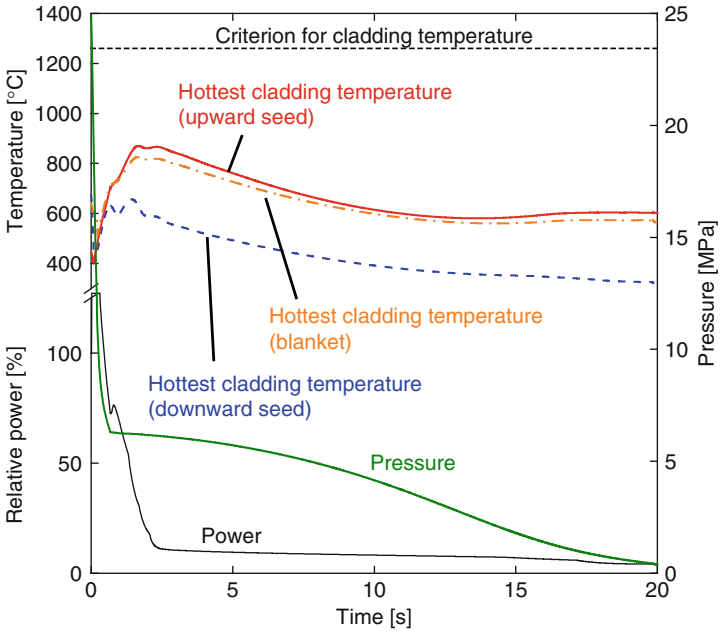


Fig. 7.108 Calculated results for blowdown phase of 100% hot-leg break LOCA (EOEC)

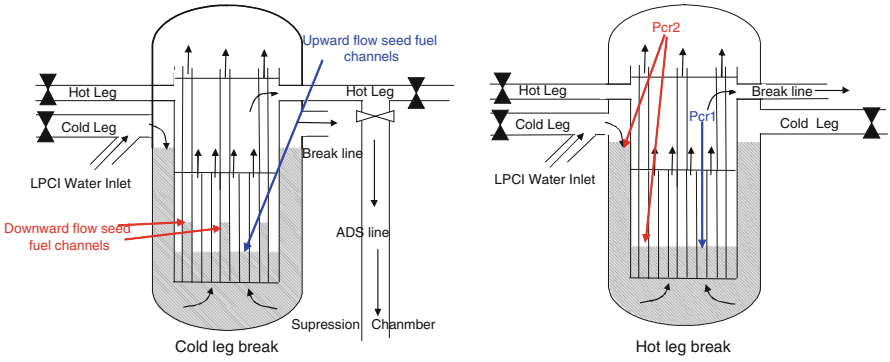


Fig. 7.109 Coolant flow during reflooding of the Super FR. (Taken from [37] and used with permission from Atomic Energy Society of Japan)

On the other hand, the quench front propagates much faster, and hence, the increase in the hottest cladding temperature is almost zero in the downward flow seed channel. This is because the pressure drop from the quench front in the downward flow seed channel to the steam discharge point (break) is much smaller than that from the quench front in the upward flow seed channel to another steam discharge point (the quencher in the suppression pool).

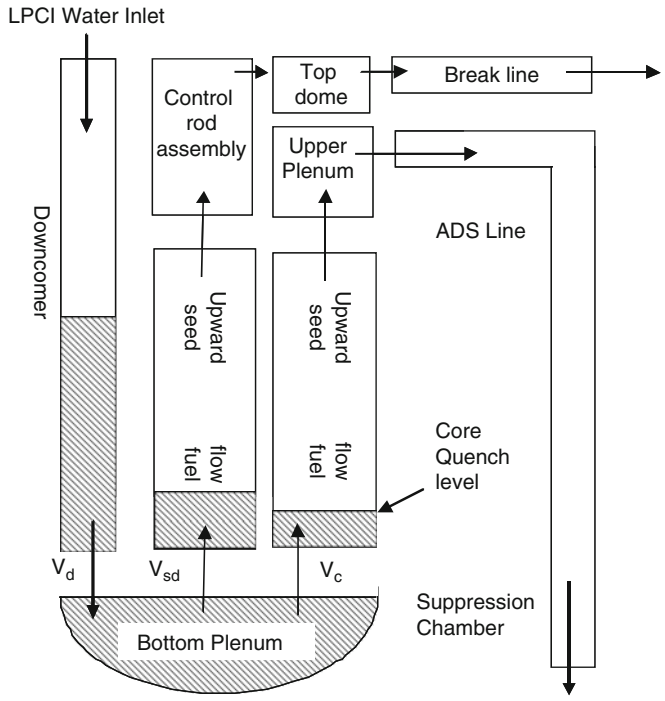


Fig. 7.110 Coolant flow in momentum conservation calculation at the reflooding phase (for the cold-leg break as an example). (Taken from [37] and used with permission from Atomic Energy Society of Japan)

In the hot-leg break, the steam generated in the downward flow channels is expected to accumulate in the closed space, which includes the top dome, CR guide tubes, downcomer, and cold-leg pipes because there is no path for discharging steam to the containment as shown in Fig. 7.109 [37] (right). Although forced reflooding by the LPCIs is expected at the hot-leg break, the quench front propagation is significantly slow in the downward flow seed channel because the steam pressure keeps increasing above the quench front. It should be mentioned that steam condensation on the reactor vessel inner walls and in-core structures is neglected in the analysis. Herein, putting small core sprays in the top dome is proposed for condensing the steam, and hence, enabling fast reflooding in the downward flow channels. This idea is illustrated in Fig. 7.112. With the spray capacity of 400 kg/s, the reflooding phase is made sufficiently fast enough as shown in Fig. 7.113.

The small LOCA of the Super FR is distinguished from the large LOCA in the same manner as that of the Super LWR (see Sect. 6.7). As the severest case, 12% cold-leg break is introduced here. The analysis results are shown in Fig. 7.114. All the conditions for actuating the reactor scram and ADS are assumed not to be reached in the small LOCA, so that the reactor power decreases by only the reactivity feedback and the pressure is kept supercritical. Due to the small heat

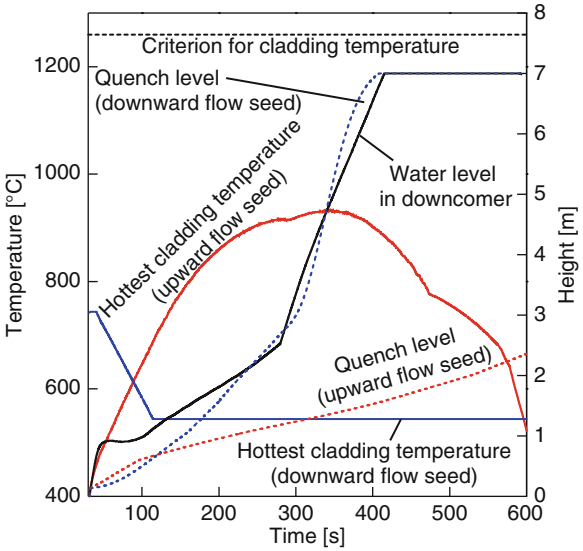


Fig. 7.111 Calculated results for reflooding phase of 100% cold-leg break LOCA (BOEC) with modification of initial flow distribution

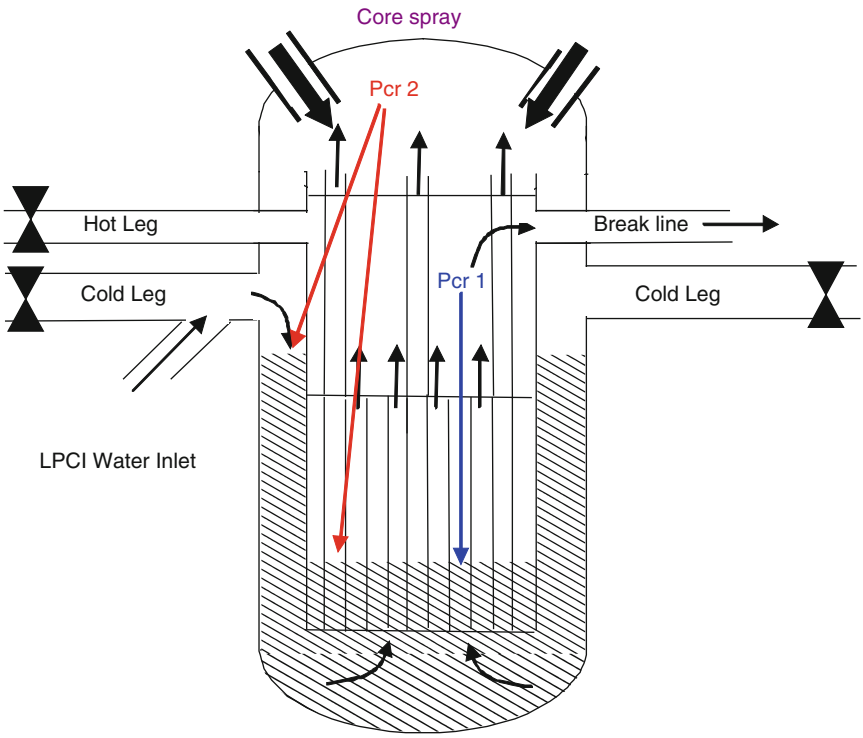


Fig. 7.112 Concept of core sprays in top dome

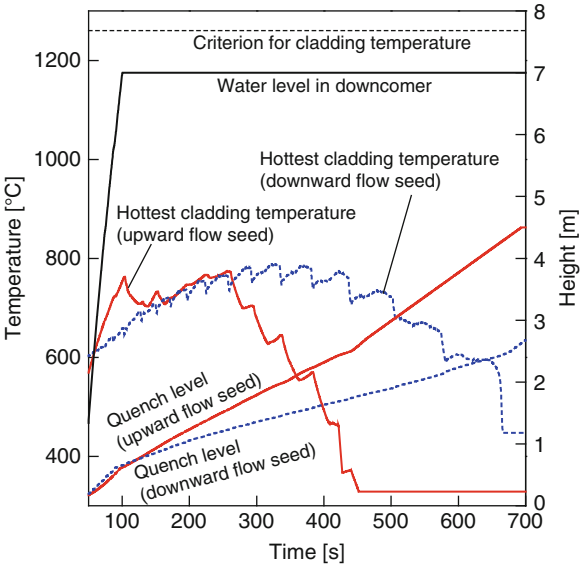


Fig. 7.113 Calculated results for reflooding phase of 100% hot-leg break LOCA (EOEC) with core sprays

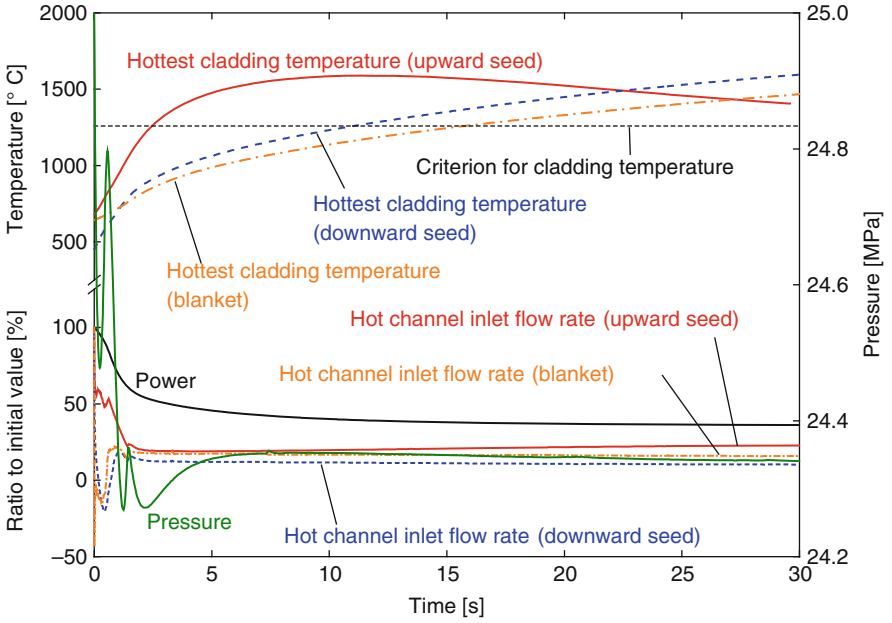


Fig. 7.114 Calculated results for 12% cold-leg break LOCA (EOEC) without depressurization

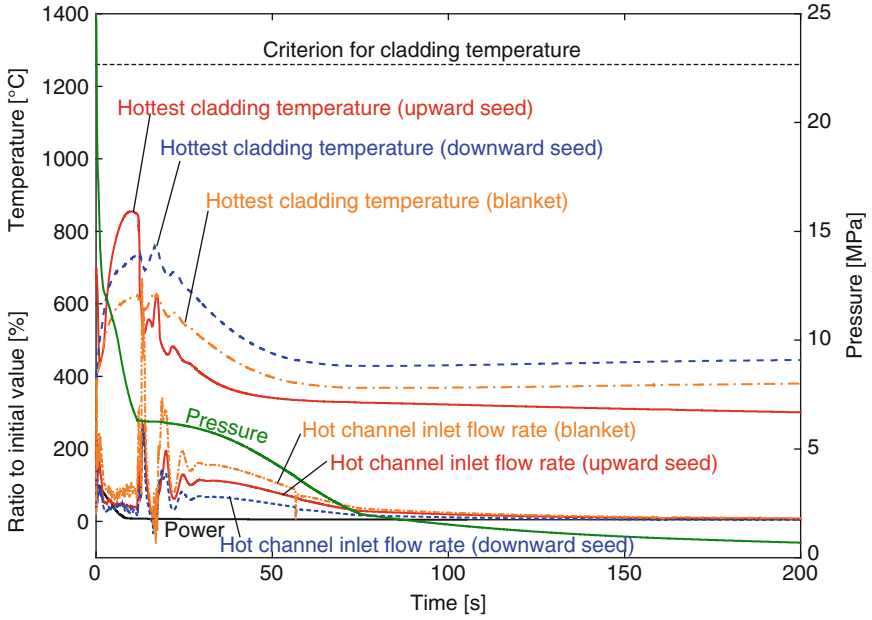


Fig. 7.115 Calculated results for 12% cold-leg break LOCA (EOEC) with depressurization

capacity and slow decrease in the power caused by weak reactivity feedback, the power/flow mismatch at the small LOCA is much severer than that in the Super LWR. The criterion is not satisfied. Early actuation of the ADS is a rational and efficient way to improve safety of the Super FR at the small LOCA. To do that, detecting abnormally large values of the drywell pressure, drywell radioactivity, or mismatch between main coolant flow rate and main steam flow rate is newly added to the original actuation conditions for the ADS. The analysis results when actuating the ADS at 1 s are shown in Fig. 7.115. The cladding temperatures begin to decrease by opening the ADS and the criterion is satisfied.

Finally, the peak cladding temperatures at large and small LOCAs are about 1,080 and 890°C, respectively, as summarized in Fig. 7.104. Despite the high power density of the Super FR, they are considerably below the criterion of 1,260°C.

7.11.4 Analyses of Anticipated Transient Without Scram Events

The most important (severest) ATWS events for the Super FR are the "loss of flow" type ones, the same as in the Super LWR. As an example, the "loss of offsite power" is analyzed here without a reactor scram. The analysis results without the alternative action of the ADS are shown in Fig. 7.116. Due to the small heat

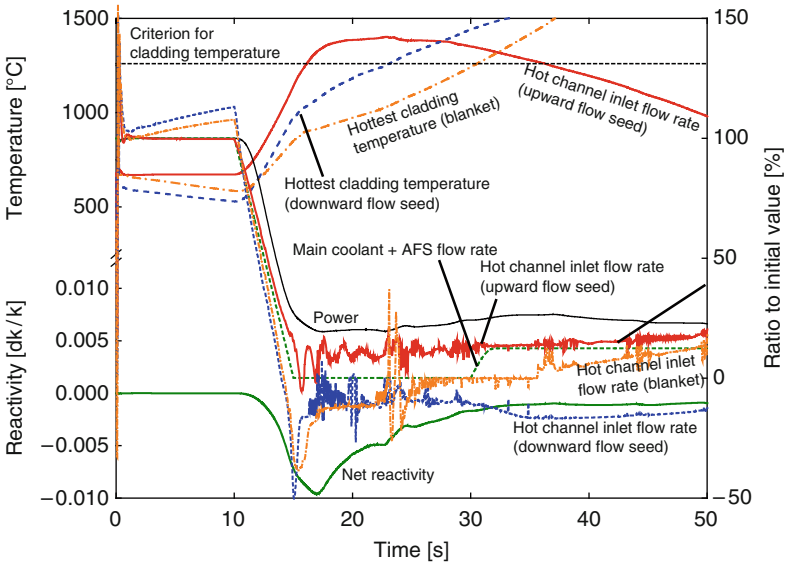


Fig. 7.116 Calculation results for "loss of offsite power" (ATWS) without alternative action

capacity and weak reactivity feedback, the relative flow rate in each hot channel is always smaller than the relative power. The cladding temperatures in all the three hot channels exceed the criterion. The analysis results with the alternative action of the ADS at 5 s are shown in Fig. 7.117. After opening the ADS valves, a high enough flow rate is kept compared to the power in each hot channel. The criterion of the cladding temperature is well satisfied.

Besides the high power density, the small reactivity feedback from the coolant density makes the ATWS behavior of the Super FR severer than that of the Super LWR. However, the ATWS events of the Super FR can be mitigated by effective alternative action(s) as those of LWRs are.

7.12 Summary

The Super FR has higher power density than the Super LWR due to no moderator, so that the Super FR has the potential to reduce the plant capital cost further compared to the Super LWR. The studies on the design, control, startup and stability, and safety of the Super FR were introduced in this chapter.

Fuel rod failure modes and associated fuel rod design criteria were established. As an example of the fuel rod design, the parameters were determined with those criteria including thermo-hydrodynamic and thermo-mechanical considerations.

The hydrogenous moderator layers in the blanket assemblies were shown to be effective in reducing the coolant void reactivity. The fuel rod design method and an

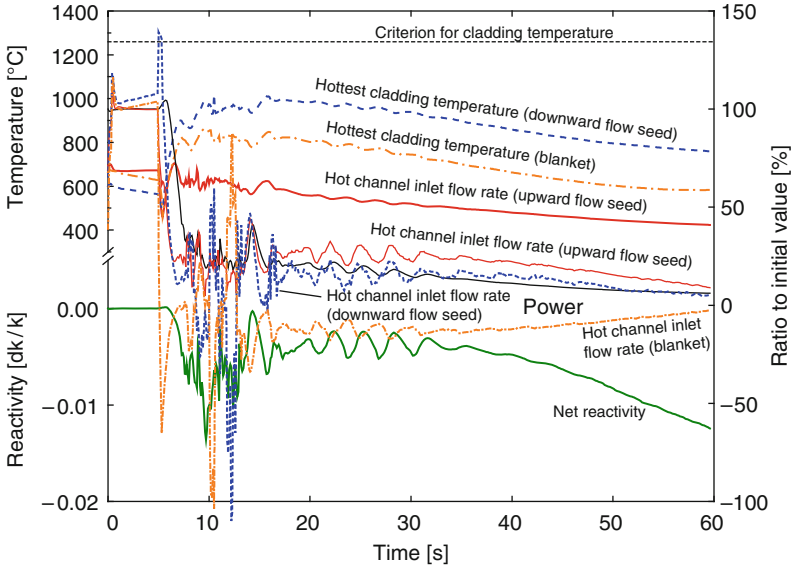


Fig. 7.117 Calculation results for "loss of offsite power" (ATWS) with alternative action

example of the fuel rod design were introduced. Three-dimensional nuclear core design procedure fully coupled with thermal hydraulic calculation was developed. The core arrangement for negative void reactivity was proposed. An example 1,000 MWe class Super FR core was designed.

The nominal value of the MCST was estimated by subchannel analysis. Large subchannel heterogeneity in the hexagonal type fuel assembly could be controlled by altering the subchannel geometry rather than adjusting the P/D. It was found that the single channel analysis could be more conservative than the subchannel analysis as long as the local power peaking in the upward flow fuel assemblies was kept below 1.2. The nominal MCST of the Super FR could be below 650°C, keeping the same coolant outlet temperature as that of the Super LWR, while the nominal MCST of the Super LWR calculated by subchannel analysis is around 700°C. That is because the local power peaking is smaller and coolant mixing among the subchannels is stronger in the Super FR. Statistical thermal design uncertainty associated with the MCST was evaluated as 31°C by Monte-Carlo sampling technique combined with the subchannel analysis code. In summary, the MCST of the Super FR at the normal operating condition was 681°C, which is used for the initial condition of the safety analyses.

Methods to achieve negative local void reactivity and increase the power density were introduced. Based on them, examples of the 700 MWe class middle size cores were designed with negative local void reactivity throughout the cycle and increased power density comparable to typical LMFBRs.

The main steam temperature of the Super FR changes more sensitively than that of the Super LWR due to smaller heat capacity. In order to suppress the fluctuation of the main steam temperature by keeping the power to flow rate ratio constant, three types of feedback methods were proposed and added to the original feedwater controller designed for the Super LWR in Chap. 4.

The power raising phase in the plant startup was designed in consideration of the thermal and thermal-hydraulic stability criteria. Due to the two-pass flow scheme, the power to flow rate ratio became locally large in the downward flow channels during certain power and flow conditions. Thus, the flow rate required to satisfy those criteria was determined by the MCST and the decay ratio of thermal-hydraulic stability in the downward flow channels.

Safety of the Super FR was found to be severer than that of the Super LWR due to the higher power density, smaller reactivity feedback and the complicated two-pass flow scheme. The safety analyses for the 1,000 MWe class Super FR showed that (1) a larger flow rate should be given to the fuel assemblies cooled by downward flow in the core design in order to avoid a very small flow rate in the downward flow channels at the cold-leg break large LOCA, (2) the steam generated in the downward flow channels at the reflooding phase in the hot-leg break LOCA should be condensed by core sprays in the top dome, and (3) the reactor should be depressurized at the cold-leg break small LOCA and the loss of flow type ATWS events in order to avoid strong power/flow mismatch. By making these improvements, the same criteria as used in the Super LWR were satisfied.

Glossary

ADS	Automatic depressurization system
AFEN	Analytic function expansion nodal method
ALHGR	Average linear heat generation rate
ANM	Analytic nodal method
ATWS	Anticipated transient without scram
BOEC	Beginning of equilibrium cycle
BOL	Beginning of fuel lifetime
BWR	Boiling water reactor
CDF	Cumulative damage fraction
CPM	Collision probability method
CR	Control rod
CRBRP	Clinch River Breeder Reactor Project
EOEC	End of equilibrium cycle
EOL	End of fuel lifetime
FDM	Finite difference method
FDS	Finite difference scheme
FIV	Flow induced vibration
FR	Fast reactor

HFF	Heterogeneous form factor
IR	Intermediate resonance
LMFBR	Liquid-metal-cooled fast breeder reactor
LMP	Larson–Miller Parameter
LOCA	Loss of coolant accident
LPCI	Low-pressure core injection
LWR	Light water reactor
MCPR	Minimal critical power ratio
MCST	Maximum cladding surface temperature
MCSTDP	Monte Carlo Statistical Thermal Design Procedure
MDNBR	Minimum departure from nucleate boiling ratio
MLHGR	Maximum linear heat generation rate
MOC	Method of characteristic
MOEC	Middle of equilibrium cycle
MOX	Mixed oxide
MSS-AS	Method of successive smoothing with analytic solution
NEM	Nodal expansion method
NR	Narrow resonance
PCI	Pellet cladding interaction
P/D	Pitch-to-diameter
PWR	Pressure water reactor
RCP	Reactor coolant pump
RPV	Reactor pressure vessel
RTDP	Revised thermal design procedure
SCWR	Supercritical Water-Cooled Reactor
SWU	Separate working unit
TD	Theoretical density
TH	Thermal hydraulic
TRU	Transuranium
ZRH	Zirconium hydride

References

1. J. Yoo, "Three-Dimensional Core Design of Large Scale Supercritical Light Water-Cooled Fast Reactor," Doctoral thesis, the University of Tokyo (2006)
2. A. E. Waltar and A. B. Reynolds, "Fast Breeder Reactors," Pergamon Press (1980)
3. Y. Oka and K. Kataoka, "Conceptual Design of a Fast Breeder Reactor Cooled by Supercritical Steam," *Annals of Nuclear Energy*, Vol. 19, 243–247 (1992)
4. T. Jevremovic, Y. Oka and S. Koshizuka, "Effect of Zirconium-Hydride Layers on Reducing Coolant Void Reactivity of Steam Cooled Fast Breeder Reactors," *Journal of Nuclear Science and Technology*, Vol. 30(6), 497–504 (1993)
5. T. Jevremovic, Y. Oka and S. Koshizuka, "Design of an Indirect-Cycle Fast Breeder Reactor Cooled by Supercritical Steam," *Nuclear Engineering and Design*, Vol. 144, 337–344 (1993)
6. T. Jevremovic, Y. Oka and S. Koshizuka, "Conceptual Design of an Indirect-Cycle, Supercritical Steam Cooled Fast Breeder Reactor with Negative Coolant Void Reactivity Characteristics," *Annals of Nuclear Energy*, Vol. 20, 305–313 (1993)

7. Y. Oka, S. Koshizuka, T. Jevremovic and Y. Okano, "Design Concept of a Supercritical-Water-Cooled Fast Breeder Reactor," *Proc. 9th KAIF/KNS Annual Conference*, Seoul, Korea, April 6–8, 1994, 183–194 (1994)
8. Y. Oka, T. Jevremovic and S. Koshizuka, "Negative Void Reactivity in a Large Liquid-Metal Fast Breeder Reactor with Hydrogeneous Moderator (ZrH1.7) Layers," *Nuclear Technology*, Vol. 107, 15–22 (1994)
9. T. Jevremovic, Y. Oka and S. Koshizuka, "Core Design of a Direct-Cycle, Supercritical-Water-Cooled Fast Breeder Reactor," *Nuclear Technology*, Vol. 108, 24–32 (1994)
10. Y. Oka, T. Jevremovic and S. Koshizuka, "Negative Coolant Void Reactivity in Large FBRs with Hydrogeneous Moderator Layers," *Proc. ANS Topical Meeting on Advances in Reactor Physics*, Knoxville, TN, USA, April 11–15, 1994, 419–428 (1994)
11. Y. Oka, S. Koshizuka, T. Jevremovic and Y. Okano, "Systems Design of Direct-Cycle, Supercritical-Water-Cooled Reactors," *Transactions of ENC'94, Int. Nucl. Congress*, Lyon, France, October 2–6, 1994, 473–477 (1994)
12. Y. Oka and T. Jevremovic, "Negative Void Reactivity in Large Fast Breeder Reactors with Hydrogeneous Moderator Layer," *Annals of Nuclear Energy*, Vol. 23, 1105–1115 (1996)
13. T. Namba, M. Yamawaki and S. Kanno, "Surface Processes of Hydrogen Transport in Fusion Reactor Materials," *Journal of Nuclear Materials*, Vols. 128–129, 646–651 (1984)
14. M. Suzuki and H. Saitou, "Light Water Reactor Fuel Analysis Code FEMAXI-6 (Ver.1)," JAEA-Data/Code 2005-003, JAEA (2005)
15. D. Baron and J. C. Couty, "A Proposal for Unified Fuel Thermal Conductivity Model Available for UO_2, $(U\text{-}Pu)O_2$, and UO_2-Gd_2O_3 PWR Fuel," *Proc. the IAEA TCM on Water Reactor Fuel Element Modeling at High Burnup and Its Experimental Support*, Windermere, UK (1994)
16. M. Suzuki, H. Saitou and T. Iwamura, "Analysis of MOX Fuel Behavior in Reduced Moderation Water Reactor by Fuel Performance Code FEMAXI-RM," *Nuclear Engineering and Design*, Vol. 227, 19–27 (2004)
17. R. J. White and M. O. Tucker, "A New Fission Gas Release Model," *Journal of Nuclear Materials*, Vol. 118, 1–38 (1983)
18. M. V. Speight, "A Calculation on the Migration of Fission Gas in Material Exhibiting Precipitation and Re-solution of Gas Atoms Under Irradiation," *Nuclear Science and Engineering*, Vol. 37, 180–185 (1969)
19. D. Schrire, A. Kindlund and P. Ekberg, "Solid Swelling of LWR UO_2 Fuel," *Proc. Enlarged HPG Meeting*, Lillehammer, Norway, HPR-349/22 (1998)
20. D. L. Hagrman and G. A. Reyman, "MATPRO-Version 11. A Handbook of Materials Properties for Use in the Analysis of Light Water Reactor Fuel Rod Behavior," NUREG/CR-0497, TREE-1280, Rev. 3, US-NRC (1979)
21. T. Kaito, T. Mizuno and S. Ukai, "An Evaluation of Creep Rupture Strength of Advanced Austenitic Stainless Steel (PNC1520)," JNC-TN-9400-99-036, JNC (1999) (In Japanese)
22. K. Rempe, K. Smith and A. Henry, "SIMULATE-3 Pin Power Reconstruction: Methodology and Benchmarking," *Proc. Int. Reactor Phys. Conf.*, Jackson Hole, Wyoming, September 18–22, 1988, Vol. III, 19 (1988)
23. R. Boer and H. Finnemann, "Fast Analytical Flux Reconstruction Method for Nodal Space–Time Nuclear Reactor Analysis," *Annals of Nuclear Energy*, Vol. 19, 617–628 (1992)
24. M. Mori, "Core Design Analysis of the Supercritical Water Fast Reactor," Doctoral thesis, Institut fur Kernenergetik und Energiesysteme der Universitat Stuttgart (2005)
25. Uranium-Zirconium Hydride Fuels for TRIGA Reactors, General Atomics Report, UZR-28, General Atomics (1997)
26. L. Cao, Y. Oka, Y. Ishiwatati and Z. Shang, "Fuel, Core Design and Subchannel Analysis of a Super Fast Reactor," *Journal of Nuclear Science and Technology*, Vol. 45(2), 1–11 (2008)
27. L. Cao, H. Ju, Y. Ishiwatari, et al., "Research and Development of a Super Fast Reactor (2) Core Design Improvement on Local Void Reactivity," *Proc. 16th PBNC*, Aomori, Japan, October 13–18, 2008, P16P1291 (2008)

28. L. Cao, Y. Oka, Y. Ishiwatari and S. Ikejiri, "Three-Dimensional Core Analysis on a Super Fast Reactor with Negative Local Void Reactivity," *Nuclear Engineering and Design*, Vol. 239, 408–417 (2009)
29. Y. Ishiwatari, M. Yamakawa, Y. Oka and S. Ikejiri, "Research and Development of a Super Fast Reactor (1) Overview and High-Temperature Structural Design," *Proc. 16th PBNC*, Aomori, Japan, October 13–18, 2008, P16P1290 (2008)
30. H. Ju, L. Cao, Y. Ishiwatari, et al., "Core Design and Fuel Rod Analyses of a Super Fast Reactor with High Power Density," *Proc. ICAPP'09*, Tokyo, Japan, May 10–14, 2009, Paper 9264 (2009)
31. Y. Ishiwatari, C. Peng, T. Sawada, et al., "Design and Improvement of Plant Control System for a Super Fast Reactor," *Proc. ICAPP'09*, Tokyo, Japan, May 10–14, 2009, Paper 9261 (2009)
32. J. Cai, Y. Ishiwatari, S. Ikejiri and Y. Oka, "Thermal and Stability Considerations for a Supercritical Water-Cooled Fast Reactor During Power-Raising Phase of Plant Startup," *Proc. ICAPP'09*, Tokyo, Japan, May 10–14, 2009, Paper 9265 (2009)
33. M. J. Watts and C. T. Chou, "Mixed Convection Heat Transfer to Supercritical Pressure Water," *Proc. 7th Int. Heat Transfer Conf.*, Munich, W. Germany, September 6–10, 1982, 495–500 (1982)
34. K. Kitoh, S. Koshizuka, and Y. Oka, "Refinement of Transient Criteria and Safety Analysis for a High-Temperature Reactor Cooled by Supercritical Water," *Nuclear Technology*, Vol. 135, 252–284 (2001)
35. A. A. Bishop, R. O. Sandberg and L. S. Tong, "Forced Convection Heat Transfer to Water at Near-Critical Temperatures and Supercritical Pressures," *WCAP-2056*, Part IV, Westinghouse Electric Corp. (1964)
36. F. W. Dittus and L. M. K. Boelter, "Heat Transfer in Automobile Radiators of the Tubular Type," University of California Publications in English, Berkeley, Vol. 2, 443–461 (1930)
37. S. Ikejiri, Y. Ishiwatari and Y. Oka, "Loss of Coolant Accident Analysis of a Supercritical-Pressure Water-Cooled Fast Reactor with Downward Flow Channels," *Proc. ICAPP'09*, Tokyo, Japan, May 10–14, 2009, Paper 9257 (2009)

Chapter 8
Research and Development

8.1 Japan

There have been extensive research and development (R&D) activities on the Super Light Water Reactor (Super LWR), the Super Fast Reactor (Super FR), and other supercritical water-cooled reactors (SCWR, SCPR) in Japan. The major ones are listed this section.

8.1.1 Concept Development

Conceptual studies of a pressure-vessel type SCWR, Super LWR, and Super FR were started at the University of Tokyo in 1989. To date, the conceptual studies have covered almost all aspects of conceptual design for both thermal and fast options as introduced in Chaps. 1–7. New ideas have been characterized and quantified by various analyses that included developing computer codes and methodologies. The pressure-vessel type SCWR concept in the Generation-IV International Forum (GIF) is based on what had been developed at the University of Tokyo. The conceptual design studies at the University of Tokyo are well summarized in Sect. 8.1.3. The R&D project on the Super FR led by the University of Tokyo has been introduced in references [1–3]. In addition to the research subjects introduced in Chap. 7, several other subjects were studied in this project. The fuel rod behavior under the normal operating condition was analyzed with the FEMAXI-VI code to understand the basic fuel rod behavior and to obtain the available parameter ranges of the fuel rods [4, 5]. The fuel rod behavior under an abnormal transient was also analyzed to understand the basic fuel rod behavior under abnormal conditions and to assess the validity and conservativeness of the safety criteria used in the safety analyses. The nuclear transmutation capability of minor actinides and long-lived fission products by the Super FR has been estimated [6, 7]. Along with the transmutation study, the expected backend risk and the

Y. Oka et al., *Super Light Water Reactors and Super Fast Reactors*,
DOI 10.1007/978-1-4419-6035-1_8, © Springer Science+Business Media, LLC 2010

possibility of its reduction were studied by the research group on waste disposal at the University of Tokyo. The nonuniform geometry of the subchannels in tight-lattice arrangement leads to a circumferential temperature distribution on the fuel rod cladding surface. In order to quantify and prepare the database for this temperature distribution, several types of subchannels have been analyzed using computational fluid dynamics [8, 9]. The temperature difference between the reactor inlet and outlet is over 200°C, and in-core structural design, considering such a large temperature difference, is a key point. The outlet nozzles, upper tie plate, and shroud were selected as the most important parts for analyzing stress levels under steady-state and transient conditions, and mechanical analyses were conducted for these parts [2]. In case of a loss of coolant accident (LOCA) or opening of depressurization valves, high temperature and high pressure steam need to be condensed inside the containment just like in boiling water reactors (BWRs). An innovative simulation method using a typical particle method has been developed to treat condensation phenomena of high temperature and high pressure fluids, including supercritical fluids [10].

The Japan Atomic Energy Agency (JAEA) has contributed to the conceptual design studies at the University of Tokyo by providing the neutronic design code SRAC, the nuclear transmutation analysis code SWAT, and the fuel rod thermal/mechanical analysis code FEMAXI-IV. The database needed for applying the SWAT code to the Super FR has been prepared by the reactor physics group in JAEA.

Industries have also been working on the concept development in collaboration with the University of Tokyo. A feasibility study of the "low temperature design concept, SCLWR" of the University of Tokyo was led by Tokyo Electric Power Company (TEPCO) in 1994 and 1995 together with the three LWR manufacturers in Japan: Toshiba Corporation, Hitachi Ltd., and Mitsubishi Heavy Industry Ltd. (MHI) [11]. It included considerations of fuel, core, reactor vessel, internal structures, and whole plant system. Dimensions of the reactor building and turbine building, as well as the configurations of the components inside the buildings, were determined as an example. The capital cost and the construction cost were roughly estimated. The main conclusions of this study are that the concept is technically feasible. But, the economical feasibility remained for future study. One of the reasons was that the SCLWR design adopted critical heat flux (CHF) criterion for the core design, and the coolant flow rate was very large. TEPCO joined the R&D project on the Super FR in 2005. Desirable characteristics for the Super FR have been considered from the utility's viewpoint [12, 13]. Safety and plant characteristics were also discussed in this project.

Following these joint studies, the two Japanese BWR manufacturers, Toshiba Corporation, and Hitachi Ltd., have been developing the plant concept for a pressure-vessel type thermal spectrum SCWR, called SCPR [3, 14–16]. This concept is based on their many experiences in the development, construction, and operation of BWRs in Japan. A cut-away view of a plant utilizing the concept is shown in Fig. 8.1 [16]. The target design specifications are set to maximize the economic advantage of the SCWRs and to minimize the technology challenges.

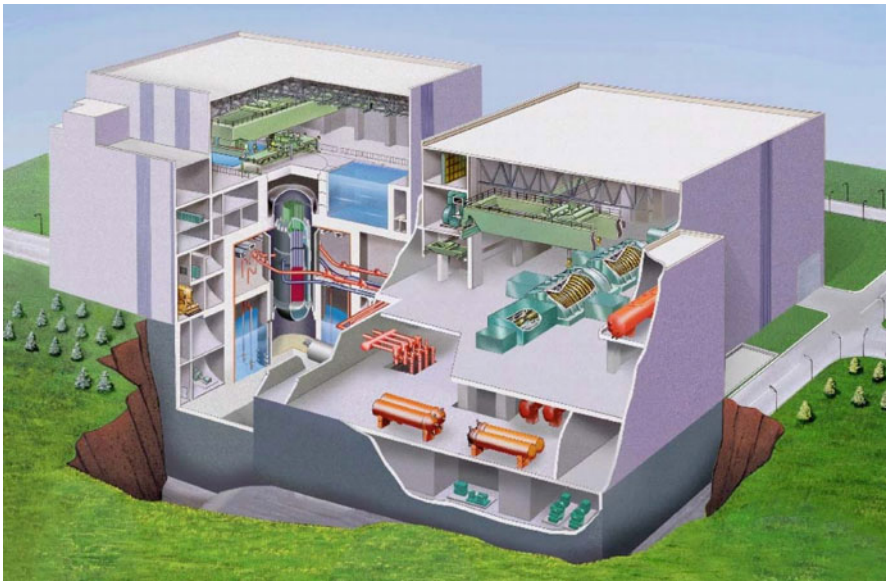


Fig. 8.1 Cut-away view of the SCPR plant using the concept developed by Japanese industries (taken from ref. [16])

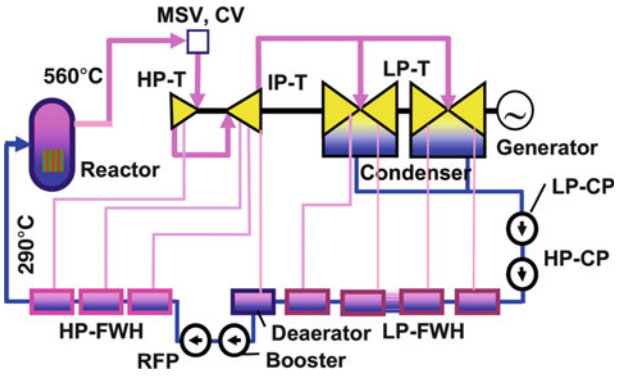


Fig. 8.2 An example of BOP design by Japanese industries (taken from ref. [16])

The target of the core outlet temperature is 560°C in order to make the turbine system simpler and more compact by applying a combined high pressure and intermediate pressure turbine and full speed low pressure turbines without a moisture separator or moisture separator reheater. An example of the balance of plant (BOP) system design is shown in Fig. 8.2 [16]. The targeted average power density is 100 MW/m^3 which is comparable with pressure water reactors (PWRs). Fuel rods were designed and their burnup behavior was analyzed using the fuel rod thermal/mechanical analysis code PAPIRUS developed by Nippon Nuclear Fuel

Development (NFD), Hitachi Ltd., and Toshiba Corporation for fast reactors and LWRs [17, 18]. The fuel rod design procedure is schematically described in Fig. 8.3 [17]. The three-dimensional neutronic thermal/hydraulic coupled core simulator for BWRs of Toshiba Cooperation is modified for the SCPR cores. Core designs were performed using this simulator [17, 19–22]. Examples of the fuel assembly design and core configuration are shown in Figs. 8.4 and 8.5 [17]. The steady-state subchannel analysis code SILFEED for BWRs of Hitachi Ltd. is modified for the SCPR cores. Subchannel analyses were performed using this code [23]. The R&D activities have also included sizing and arrangement of components and buildings and cost estimation based on ABWRs.

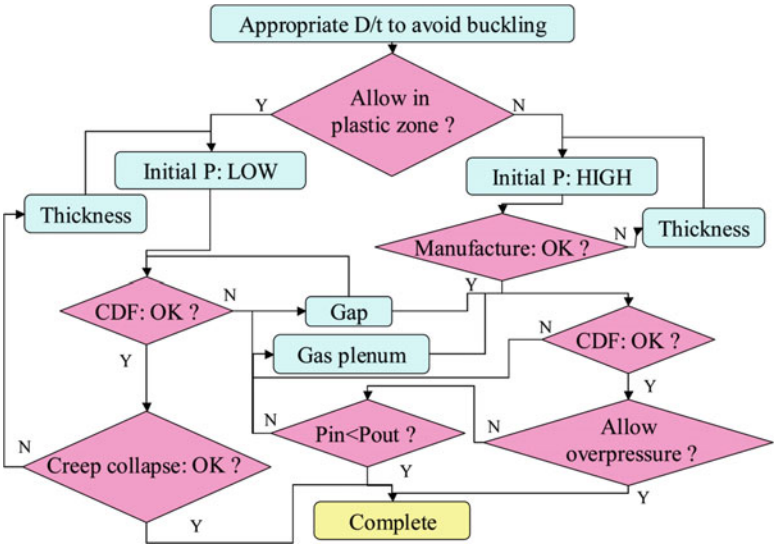


Fig. 8.3 Fuel rod design procedure (taken from ref. [17] and used with permission from French Nuclear Energy Society)

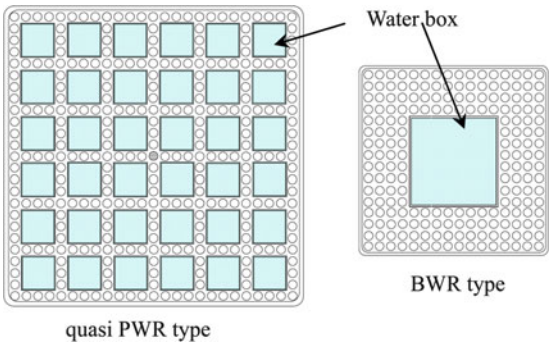


Fig. 8.4 Examples of fuel assembly design (taken from ref. [17] and used with permission from French Nuclear Energy Society)

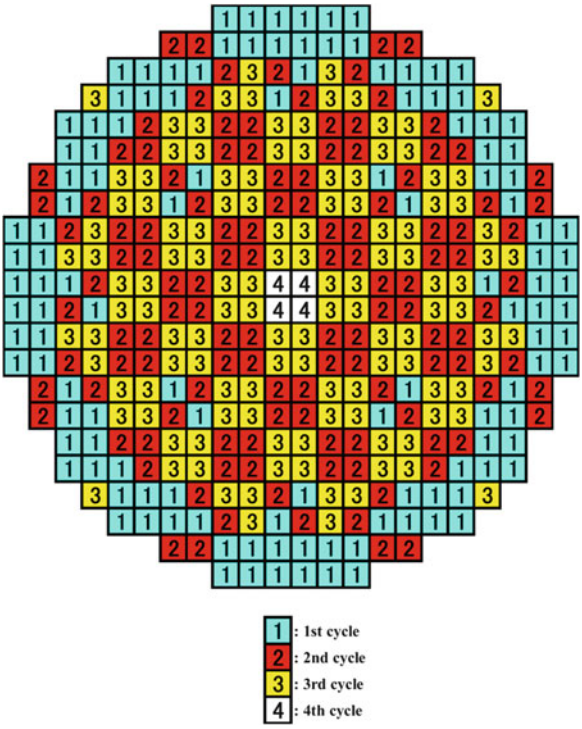


Fig. 8.5 An example of a fuel loading pattern (taken from ref. [17] and used with permission from French Nuclear Energy Society)

8.1.2 Thermal Hydraulics

A strong and active group has been studying thermal hydraulics of supercritical fluids at Kyushu University. Members have been performing various experiments related to the Super FR and Super LWR and SCPR using a loop with a hydrochlorofluorocarbon gas (Freon-22, HCFC22) in collaboration with industrial partners and the University of Tokyo [24–28] (see Fig. 1.63). The geometry of the test section has been changed step by step: a single tube, an annulus with a single rod, a three-rod bundle, and a seven-rod bundle. The test sections of the single tube and seven-rod bundle are shown in Fig. 8.6 [28]. The flow direction is both vertically upward and downward. A wide range of mass fluxes, heat fluxes, and inlet temperatures were tested. Mainly, the heat transfer coefficient and pressure drop under steady-state conditions at supercritical pressure were measured. Flow transient conditions were also tested. Effects of grid spacers on the heat transfer coefficient and pressure drop were investigated by changing the shape and axial pitch of the grid spacers.

The thermal hydraulics group in the Naka Fusion Institute of JAEA has a test loop of supercritical pressure water (see Fig. 1.64). An annular flow test section with a heater rod and a seven-rod bundle test section are installed into the test loop

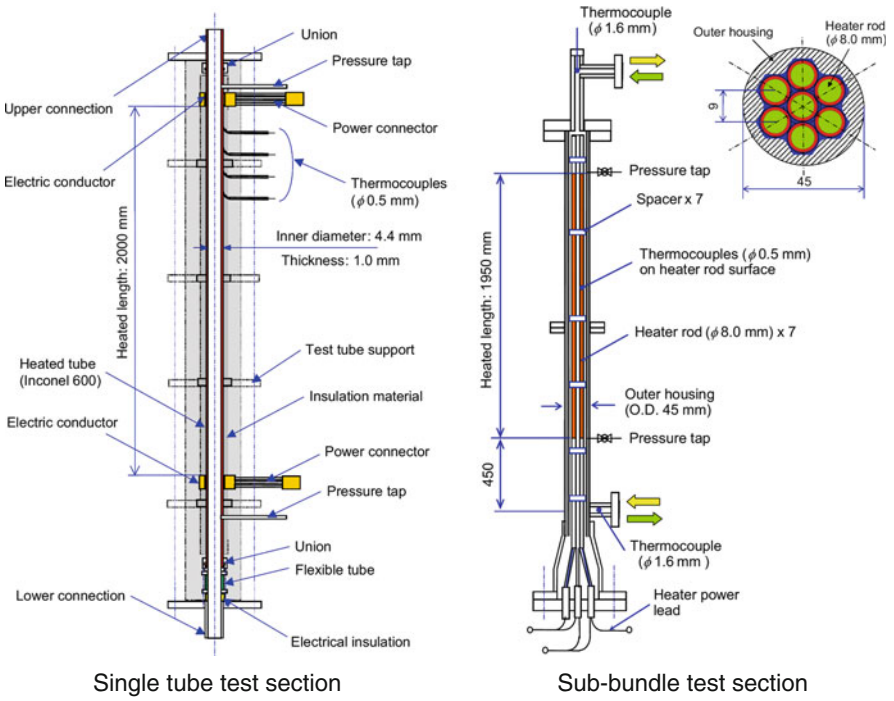


Fig. 8.6 Test sections at Kyushu University for thermal hydraulic experiments using HCFC22 (taken from ref. [28] and used with permission from Atomic Energy Society of Japan)

for the R&D of the Super FR and Super LWR (see Fig. 1.64). Heat transfer coefficient and pressure drop in these test sections were measured at the steady state in order to validate the experiments using HCFC22 done at Kyushu University and to provide benchmark data for validation of computational fluid dynamics (CFD) codes [29–31].

To potentially replace the need for large scale experiments to develop fuel bundles in future R&D work, the three-dimensional CFD code ACE-3D, developed by JAEA based on the two-fluid model for BWR conditions, was modified to handle supercritical pressure fluid in the fuel bundle geometries. The heat transfer experiments by Kyushu University with HCFC22 and by JAEA with water were analyzed for its validation [31–36]. Also the three-dimensional model of this code for the fuel bundles was combined with the one-dimensional model for future applications to plant system analyses.

The Super LWR and Super FR may be operated at subcritical pressure during startup if the sliding pressure startup scheme is chosen. Also, the pressure decreases from supercritical to subcritical at depressurization events such as a LOCA. The CHF and the post boiling transition (post-BT) heat transfer are important, especially just below the critical pressure because the CHF, the enthalpy of the CHF condition and the post-BT heat transfer coefficient are all substantially smaller than those at a

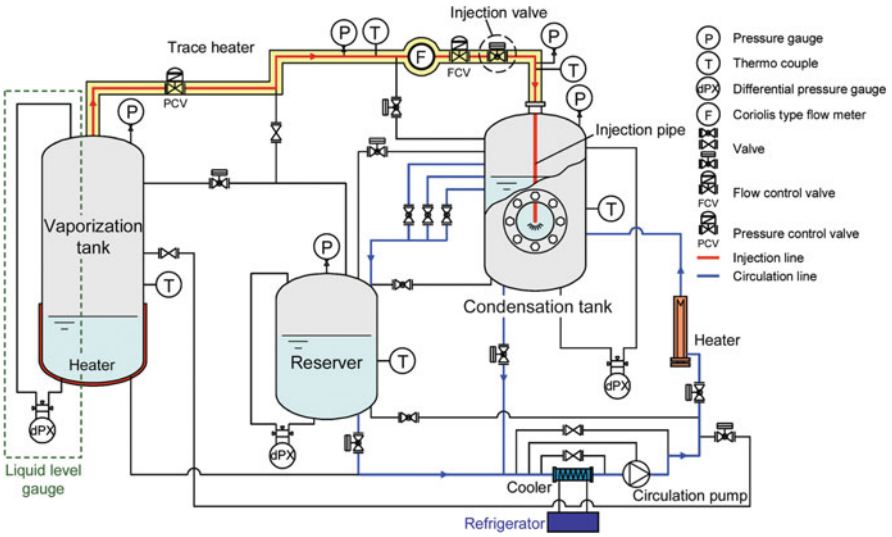


Fig. 8.7 Experimental apparatus at Kyushu University for a condensation experiment with high temperature vapor in a subcooled liquid pool (taken from ref. [38] and used with permission from Atomic Energy Society of Japan)

lower pressure region. They were investigated at both steady state and pressure increasing or decreasing transient conditions using the same experimental loop and fluid at Kyushu University as described above [37].

The critical flow from supercritical pressure fluid is not well known, and there is no correlation or database. Critical flow tests were done by Kyushu University using another typical Freon gas, HCFC123.

The pressure suppression type containment like that of BWRs is a candidate for the containment of the Super LWR and Super FR. The steam temperature and pressure discharged into the suppression pool through the vent pipes or safety relief valve (SRV) pipes will be higher than those in BWRs. Especially from the SRV pipes, superheated steam or supercritical steam may be discharged. The characteristics of its condensation in the subcooled water at low pressure (containment pressure) need to be well understood. Kyushu University researchers carried out a unique experiment to observe condensation behavior with a high speed camera and to measure pressure oscillation of vapor discharge into a subcooled liquid pool [38]. HCFC123 was used in this experiment and the experimental apparatus is shown in Fig. 8.7 [38].

8.1.3 Materials and Water Chemistry

Developments and tests of candidate materials for fuel cladding and in-core structures of the SCPR, Super FR, and Super LWR are mainly performed in joint projects among universities, research institutes, and industries.

Principally, to find Zircaloy alternatives for fuel cladding of the thermal spectrum SCWR, SCPR screening tests were performed jointly among Hitachi Ltd., Toshiba Corporation, and Hokkaido University workers. As the first step, commercially available materials were tested to select promising candidates for the next step tests [14, 15]. The tested materials, austenitic stainless steels, ferritic–martensitic steels, nickel alloys, and titanium alloys are summarized in Table 8.1 [14]. The screening tests included general corrosion tests [39–41], stress corrosion cracking (SCC) tests [42, 43], mechanical strength tests, and simulated irradiation tests.

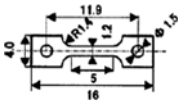
Based on the screening tests, several candidate materials were selected and tested further by researchers at Tohoku University, Toshiba Cooperation, Hitachi Ltd., and the University of Tokyo [44]. Testing methods included high temperature tensile tests, creep tests, helium embrittlement tests, general corrosion tests, SCC tests, and neutron irradiation tests along with post irradiation examinations (PIEs). Improved stainless steels such as fine grain stainless steels and stainless steels with added over-sized elemental particles were tested as well as commercial stainless steels and nickel-based alloys that had been found to have better properties through the screening tests. Oxide dispersion strengthening (ODS) steels were also tested. The neutron irradiation tests were performed in the Japan Material Test Reactor (JMTR) and the experimental fast reactor JOYO that are operated by JAEA. The PIEs were conducted for microstructure, mechanical strength, hardness, and creep deformation as summarized in Table 8.2 [44]. As a result of this joint work, one of the improved stainless steels, SUS310S+Zr, was considered as a candidate material for the fuel cladding material of the thermal spectrum SCWR, SCPR because it has high temperature strength, low creep, general corrosion resistance, and good irradiation resistance [45].

Based on the advanced austenitic stainless steel (PNC1520) with high creep strength developed by JAEA for sodium cooled fast reactors [46], the candidate

Table 8.1 Materials for screening tests (taken from ref. [14] and used with permission from Atomic Energy Society of Japan)

Stainless steel	Austenitic	SS304H
		SS310
		SS316
		SS316L
	Ferritic	12Cr-1Mo1WVNb
		Mod. 12Cr-1 Mo
Nickel alloy		Alloy690
		Alloy718
		Alloy800H
		Alloy825
		Hastelloy C22
		Hastelloy C276
		Alloy600
		Alloy625
Titanium alloy		Ti-3Al-2.5V
		Ti-6Al-4V
		Ti-15V-3Al-3Sn-3Cr
		Ti-15Mo-5Zr-3Al

Table 8.2 PIE evaluation items and irradiation conditions (taken from ref. [44] and used with permission from French Nuclear Energy Society)

PIE	Evaluation item	Specimen	Irradiation condition (n/cm^2)
TEM analysis	Void swelling Grain boundary segregation Phase transformation	3 mm-diameter disk	JMTR: 600°C(He[a])/ 4.0–4.4 × 10^{20}
Tensile test	Mechanical property change He embrittlement		JOYO: 500°C(He)/4.3 × 10^{21} JOYO: 600°C(He)/1.2 × 10^{22} JOYO: 600°C(Na[b])/9 × 10^{21}
Hardness	Mechanical property change	Thickness: 0.25 mm	JOYO: 700°C(Na)/9 × 10^{21}
Pressurized tube test	Irradiation assisted creep	 4.57 mmOD 30 mmL 0.285 mmT	JOYO: 600°C(Na)/9 × 10^{21} JOYO: 700°C(Na)/9 × 10^{21}

[a]He-bond capsule
[b]Na-bond capsule
All dimensions in mm

materials for the fuel cladding of the Super FR were manufactured and tested. Not only typical specimens, but also tubes with a geometry (i.e., diameter, thickness, etc.) consistent with the typical Super FR design were manufactured and tested. Tensile tests up to 750°C and creep tests up to 700°C were conducted at JAEA. Corrosion tests in supercritical water up to 600°C were conducted at JAEA and the University of Tokyo [47, 48]. System steering committee (SSC) tests were conducted at JAEA. The high fluence irradiation facility (HIT) at the University of Tokyo [49] has been used to imitate the reactor core irradiation environment and high temperature irradiation tests up to 500°C have been conducted.

In the Super LWR and the Super FR, a large temperature difference exists between one side and another of structures such as the water rods, channel boxes, control rod guide tubes, shroud, upper tie plate, etc. Thermal insulation will be necessary to mitigate thermal stress and thermal fatigue on these structures. The requirements for the thermal insulator are low heat conductivity, low neutron absorption, and good thermal shock resistance and dimensional stabilities. Candidate materials were surveyed from an existing database. Porous 8 mol% yttria-stabilized zirconia (8YSZ) or porous 3 mol% yttria-stabilized zirconia (3YSZ) were selected. Specimens of these materials were fabricated and tested and very low thermal conductivity was achieved as shown in Fig. 8.8 for 8YSZ [50].

Supercritical water exhibits unique properties. Its chemistry and radiolysis have been studied by the research group on radiation chemistry at the University of Tokyo in collaboration with research institutes and industries. The R&D items of supercritical water chemistry under a radiation field are described in Fig. 8.9 [51]. Fundamental studies on radiolysis of supercritical water were conducted at the

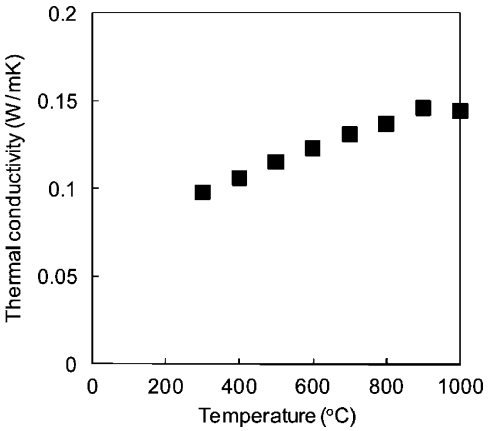


Fig. 8.8 Thermal conductivity of sintered porous 8YSZ (taken from ref. [50] and used with permission from Atomic Energy Society of Japan)

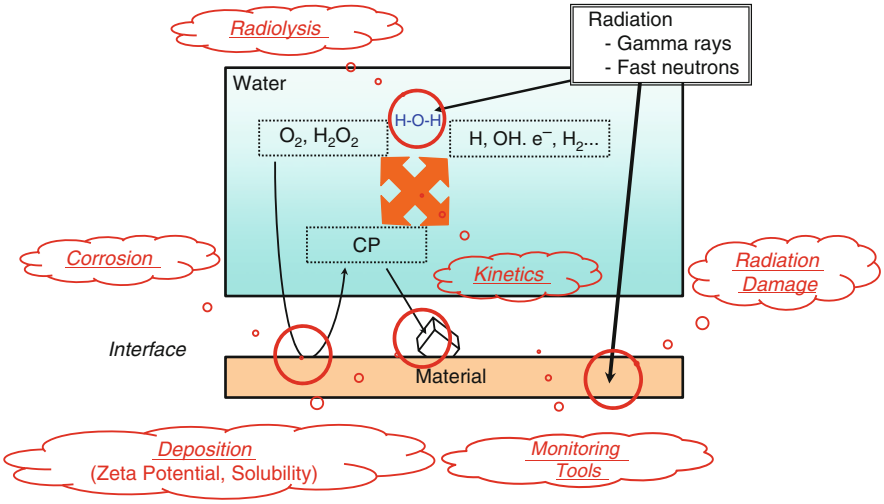


Fig. 8.9 R&D items of supercritical water chemistry under radiation field (taken from ref. [57] and used with permission from Prof. Y. Katsumura)

University of Tokyo under the support by Japan Society for the Promotion of Science (JSPS) [52–57]. Then, the chemistry of supercritical pressure water under a radiation field was studied under a joint project by the University of Tokyo, JAEA, Central Research Institute of Electric Power Industry (CRIEPI), Hitachi Ltd., and Toshiba Corporation supported by the Ministry of Education, Culture, Sports, Science and Technology (MEXT) of Japan [51, 58–62].

It is very important to understand the elution characteristic of stainless steel materials in supercritical pressure water in order to manage turbine contamination. A new approach to evaluate it has been developed at the University of Tokyo.

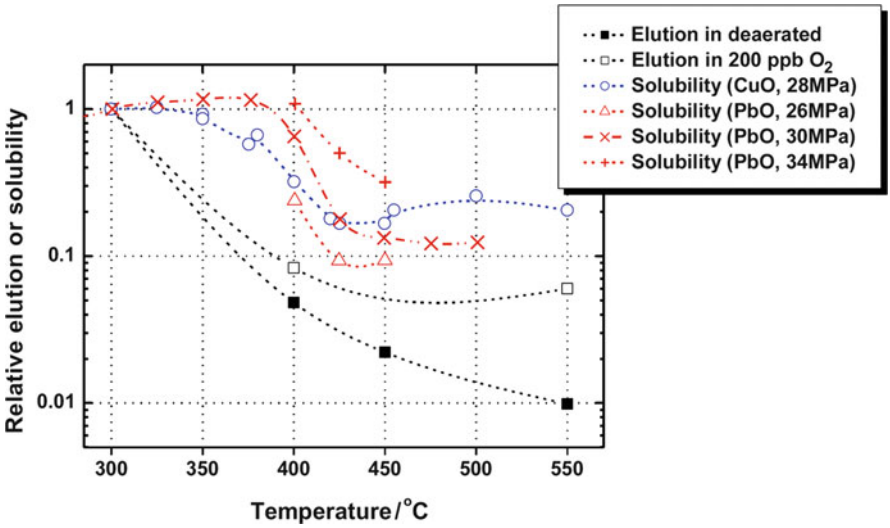


Fig. 8.10 Comparisons between elution and solubility of some metal oxide in sub- and supercritical water (taken from ref. [64] and used with permission from Dr. Y. Muroya)

Radioactivated specimens of SUS304 with a known radioactivity were set in an autoclave vessel installed in a supercritical water loop system. By measuring gamma-rays emitted from the eluted material, the elution can be quantified with high sensitivity. The test conditions were from 300 to 550°C, 25 MPa and dissolved O_2 concentrations were from 0 to 200 ppb [63, 64]. The elution efficiency at 550°C becomes much lower than that at 300°C as shown in Fig. 8.10 [64], although the corrosion rate increases with temperature.

8.2 Other Countries

8.2.1 Europe

In Europe, R&D on the SCWR has been performed as the high performance light water reactor (HPLWR) projects. The HPLWR is the designation of the pressure vessel type, thermal spectrum SCWR.

8.2.1.1 HPLWR-I Project

The HPLWR-I project, from 2000 to 2002, was part of the fifth Framework Program of the European Commission [65–67]. This project was conducted by a consortium of research institutes and industries in Europe and coordinated by Forschungszentrum Karlsruhe (FZK) of Germany. The University of Tokyo also

joined. The results of the design studies by the University of Tokyo were employed as the reference design and the starting point of the HPLWR project-I. The feasibility of the HPLWR was studied to determine whether LWRs operating under supercritical steam conditions could be feasible considering the European Utility Requirements (EUR) and the Generation-IV technology goals, to estimate their economic potential, and to understand their safety features compared with existing LWRs. The results showed the HPLWR was a promising concept [67]. The major conclusion of the first phase was that the HPLWR concept had technical merit and potential to be economically feasible in comparison with other nuclear or fossil-fueled power plants. An initial economic target for the HPLWR was set at 1,000 €/kWe and 3–4 cent/kWh levelized generation cost. A list of open questions and research needs to be addressed in future HPLWR projects was outlined in a roadmap [68].

8.2.1.2 HPLWR-II Project

The HPLWR-II project started in September 2006 with a planned duration of 42 months (running until 2009) as part of the sixth Framework Program of the European Commission [69–72]. It was also coordinated by FZK. This consortium consists of ten organizations from eight European countries: seven research centers, two universities, and one industrial company. In September 2008, the mid-term assessment took place [71].

The main differences of the HPLWR design compared to the Super LWR studied by the University of Tokyo and the thermal spectrum SCWR developed by Japanese industries are the three-pass core and the wire wrapped fuel assembly. The first coupled neutronic and thermal-hydraulic analyses of the core were performed for full load, steady-state conditions. They showed that the envisaged power profile and coolant density distribution are feasible. CFD analyses of coolant mixing inside assemblies as well as in the mixing chambers above and below the core predicted an acceptable temperature distribution at the inlet of each heat up step. Stress and deformation analyses of the reactor pressure vessel, the major reactor internals, and of the assembly boxes indicated areas for design optimization which are going to be addressed with the next design iteration.

The physics of deterioration of heat transfer of the flow of supercritical water with low mass flux through a tube with high heat flux has been studied with CFD. A numerical study of turbulence enhancement by ribs on the heated wall indicated that this measure is appropriate to avoid deterioration of heat transfer. A first design proposal of a containment for the HPLWR has been worked out. First transient analyses of design basis accidents have been started. Stability analyses of coolant flow through the core have been completed: like with BWRs, inlet orifices can avoid density wave oscillations in the core.

Corrosion tests have been performed with supercritical water at temperatures up to 650°C with two ferritic–martensitic steels, four austenitic stainless steels, three ODS (oxide dispersion strengthened) steels, and one Ni-based alloy. The first SCC

experiments have also been conducted. An experimental, supercritical in-pile loop has been constructed by the Nuclear Research Institute in the Czech Republic. The loop is ready for out-of-pile commissioning and testing prior to its installation into the research reactor of this institute.

8.2.2 Canada

Canada has been considering the development of the CANDU type SCWR (CANDU-SCWR) as the natural evolution of existing CANDU technologies [73, 74]. In 2006, Natural Resources Canada (NRCan) established a national program (Generation-IV National Program) to support Generation-IV R&D specifically relevant to Canada and to meet Canada's commitments to GIF [73, 74]. The CANDU-SCWR is one of the two concepts that the program is focusing on developing.

The fuel is contained in a large number of pressure tubes that form the pressure boundary of the primary heat transport system [73]. This concept avoids the use of a large pressure vessel, and makes it possible to use a separate moderator around the fuel channels that does not have to operate at the same conditions as the primary coolant. Detailed considerations on the fuel channel design can be found in reference [75]. The role of the moderator as a passive heat sink can be significantly enhanced by optimizing the heat transfer characteristics of the fuel channel [76].

A major focus of Canadian SCWR R&D is directed toward obtaining the data needed for material selection and evaluation. This includes identification of suitable materials for in-core components (e.g., fuel cladding, and the ceramic insulator and metal liner used in the insulated fuel channel concept) as well as for critical out-of-core components. Work underway includes measurements of the corrosion resistance in high and low density water as a function of exposure time and temperature [77], SCC susceptibility, high temperature creep resistance, and long-term microstructural stability at the designed operating temperature. Ongoing work includes surface alloying of ferritic–martensitic steels with chromium metal and oxide (zirconia) coating of steels. Other ongoing work on materials includes fabrication of insulation materials, modeling of microstructural damage by radiation, and trial production of high-Cr alloys for corrosion studies and for further processing into ODS alloys.

Computer simulations using a combination of molecular dynamics and Monte Carlo simulations have been a major part of the Canadian SCWR program to date with regard to water radiolysis and chemistry. An experimental program is currently being established to measure some of the key parameters (e.g., reaction rate constants of radiation-induced species) needed in order to improve the models.

Test facilities are being constructed for heat-transfer experiments using CO_2, Refrigerant-134a, and water as coolant in tubes, annuli, and small bundle subassemblies [78]. Analytical models have been developed for predicting the onset of dynamic instability with in-phase one-dimensional oscillations and out-of-phase

two-dimensional, and three-dimensional oscillations [79]. A separate test facility is being constructed to measure critical flow of water at supercritical conditions.

8.2.3 Korea

SCWR research in Korea has been mainly promoted by the Korea Atomic Energy Research Institute (KAERI) and Korea Electric Power Research Institute (KEPRI). The work has consisted of a feasibility study, a core conceptual study, experiments for supercritical heat transfer, and an investigation of the corrosion and radiation effects on candidate materials [80–84].

The feasibility study from economic and strategic viewpoints has been jointly proceeded by KAERI and KEPRI [84]. The interim results revealed that the SCWR development in Korea would be expected to be sufficiently feasible considering various future environments and would provide great economical advantage in the total capital cost of construction. The results of the feasibility study will be used for policy-making in Korea regarding future SCWR development.

A conceptual design of a 1,400 MWe reactor core with a solid moderator, ZrH_2, has shown reasonable results [80–83, 85–87]. The idea of a solid moderator was introduced since it was believed to simplify the coolant passage in the reactor upper dome. A conceptual design study for a 1,700 MWe core has been also started with a sensitivity study [87].

Heat transfer experiments have been performed with CO_2 using the test facility, SPHINX [88–93]. The test sections of tubes, a concentric annulus, and an eccentric annulus have been used. Steady-state conditions have been mainly investigated. The flow direction is both vertically upward and downward. In addition to the experiments without turbulence promoters, influence of the turbulence promoter on the heat transfer has been investigated using a tube type text section where a helical wire is inserted [93].

A range of candidate materials for the SCWR, which includes ferritic–martensitics, Ni-based alloys, and ODS alloys, is being taken into account. Corrosion and radiation effects are getting special attention and several ion accelerators are being used.

8.2.4 China

In 2005, Shanghai Jiao Tong University (SJTU) started the first Chinese SCWR R&D activities focusing on feasibility studies and basic technologies with these main purposes: to promote the national working group and gain support of the Chinese nuclear community, to provide a starting point for Chinese SCWR conceptual design, and to follow progress in international activities and enhance international exchanges. The activities of SJTU have resonated strongly within the Chinese nuclear community. At the beginning of 2006, the Chinese SCWR Technical Working Group (CSTWG) was founded under the leadership of SJTU

with seven partners. The main tasks of the CSTWG are: to give advice to the government for preparing a long-term strategic development program of nuclear power, to make suggestions of a suitable R&D roadmap for the SCWR in China, to coordinate and organize SCWR R&D activities of Chinese research institutions, to answer "Calls for Proposals" and coordinate project applications, and to establish a platform for scientific exchanges within the international SCWR community. Through the efforts of the CSTWG, the first SCWR large-scale national key project (973 project) was started in July 2007 [94].

Preliminary reactor core concepts have been proposed at various institutions. Among them, the concept with mixed neutron spectrum proposed by SJTU [95, 96] has achieved the special attention of Chinese researchers. The mixed spectrum SCWR core combines the merits of both thermal and fast spectra as far as possible. The basic idea is to divide the reactor core into two zones with different neutron spectra. In the outer zone, the neutron energy spectrum is similar to that of PWRs. To assess the performance of the reactor core, a coupled neutron-physics and thermal-hydraulics analysis was conducted [96].

Research activities on flow-induced material corrosion and thermal hydraulic behavior in water at supercritical pressure are key parts of the 973 project. A supercritical water multi-purpose test loop, named SWAMUP, has been designed and is currently being constructed at SJTU. SWAMUP will serve as an experimental facility for material corrosion and thermal hydraulic tests in supercritical water. The design pressure and test section outlet temperature are 30 MPa and 550°C, respectively. Material irradiation tests are planned. Based on an extensive review of the capabilities of existing irradiation facilities (domestic and international) and an assessment of budget and time schedule, it was decided to carry out high energy (20 MeV) proton irradiation tests. In addition, extensive theoretical and numerical investigations in all fundamental aspects, especially in thermal-hydraulics, are ongoing.

Since the CSTWG was founded, the SCWR concept has attracted interest from more and more Chinese vendors and utilities. In March 2009, several institutions within the Chinese nuclear community expressed their strong desire, to construct an experimental SCWR reactor [94]. In September 2009, China Guangdong Nuclear Power Group (CGNPG) announced the plan of starting the construction of an experimental SCWR in 2016.

8.2.5 USA

The USA operated several R&D programs on the SCWR from 1999 to around 2006. Overviews can be found in the literature [97, 98]. The US SCWR Generation-IV program was initiated in 2003 and led by the Idaho National Laboratory (INL) [99]. National laboratories, universities, and industries joined this program. The Super LWR concept with the downward-flow water rods developed by the University of Tokyo was selected as the reference design. Nuclear Energy Research Initiative (NERI) programs and International Nuclear Energy Initiative (I-NERI) programs

with Korea and Japan were operated. Unfortunately, all the programs on the SCWR R&D were finished by 2006, and there is no support from the US government until 2009. However, important results were produced through those programs. The universities, especially, contributed fundamental research studies. Representative ones are summarized below.

The University of Wisconsin–Madison (UW–Madison) was researching the fields of thermal hydraulics [100–105], material science [106–120], water radiolysis [121–124], and core design [125–128]. A series of integral heat transfer measurements were performed using the supercritical water heat transfer test facility at UW–Madison [97]. The uniqueness of the heat transfer studies in UW–Madison is that mean and turbulent velocities were measured with a two-component laser Doppler velocimetry system (LDV) for validation of the CFD codes and explanation of the heat transfer deterioration. Critical flow of Supercritical CO_2 was measured for numerous stagnation thermodynamic conditions, geometry, and outlet tube roughness [104]. It was found that a one-dimensional homogeneous equilibrium model was capable of relatively good (less than 10% error) prediction of the test data. The corrosion performance of the potential candidate alloys for the fuel cladding were evaluated using the corrosion loop at UW–Madison [97]. Ferritic–martensitic steels, including ODS, austenitic alloys, and Ni-based alloys were tested. Surface treatment and grain boundary engineering were also studied experimentally to improve protective oxidation behavior. The concentration of radiolytic species in supercritical water under neutron irradiation was directly measured using the supercritical water loop inside the experimental reactor at UW–Madison [97]. Also, measures to suppress radiolysis such as hydrogen injection were investigated. The extended system analysis method for the US reference SCWR with downward-flow water rods (very similar to the Super LWR) was established by coupling the three-dimensional steady-state and transient neutronics code PARCS and the system analysis code RELAP5. Using this method, the behaviors of the US reference SCWR under not only steady-state, including burnup, but also typical flow transient conditions were analyzed.

The University of Michigan has contributed to the fundamental understanding of corrosion, SCC, and irradiation effects on the candidate materials through wide testing of ferritic–martensitic steels, austenitic alloys, and Ni-based alloys [129–142]. Grain boundary engineering was also applied.

Thermal-hydraulic and neutronic thermal-hydraulic coupled instabilities were analytically investigated for the US reference SCWR with downward-flow water rods (very similar to the Super LWR) at Massachusetts Institute of Technology [143–146]. The main conclusions were consistent with those of the preceding studies at the University of Tokyo introduced in Chap. 5.

Notre Dame University also contributed to the radiolysis studies in collaboration with UW–Madison and argonne national laboratory (ANL). Iowa State University, the University of Maryland, and Pennsylvania State University, as well as INL, joined collaborative research on advanced computational thermal fluid physics.

8.3 International Activities

8.3.1 Generation-IV International Forum

The term "Generation-IV" was first proposed in a meeting of the American Nuclear Society in June, 1999. In January 2000, an intergovernmental workshop on the GIF was held. The GIF was chartered in July 2001 to lead the collaborative efforts of the world's leading nuclear technology nations to develop next generation nuclear energy systems to meet the world's future energy needs. The nine GIF founding members (Argentina, Brazil, Canada, France, Japan, Korea, South Africa, the UK, and the US) were joined by Switzerland in 2002, Euratom in 2003, and by China and Russia at the end of 2006. The technology roadmap for the six reactor concepts was opened to the public in December 2002 (available on the GIF website [147]). This unique international effort reached a major milestone in 2005 when five of the forum's member countries (Canada, France, Japan, Korea, and the US) signed the world's first agreement aimed at the international development of advanced nuclear energy systems.

In May 2002, the SCWR was selected as one of the six reactor concepts. Among them only the SCWR is a water cooled reactor concept. The first information exchange meeting (IEM) was held and informal collaborative R&D started in November 2002. The IEMs have been held one or two times a year. The first informal meeting of the SSC was held in April 2003. The system research plan (SRP) was prepared in 2003 and revised in 2004 according to the comments from the group of experts. After the system agreement (SA) was concluded by Canada and Euratom in November 2006 and then joined by Japan in February 2007, the SSC became a formal committee. The formal SSC meetings have been held two or three times a year from 2007. As of 2009, Canada (chair), Euratom, and Japan are its formal members. China, France, and Korea are observers. The main task of the SCC is to promote collaborative R&D by controlling the project management boards (PMBs), mentioned below.

Three PMBs on system integration and assessment (SI&A), thermal hydraulics and safety (TH&S), and materials and chemistry (M&C) were provisionally established in November 2003. A PMB on fuel qualification (FQ) was additionally established in 2008. The tasks of the PMBs are to propose concrete collaborative R&D, prepare the project plan, and exchange information among the member and observer countries. The project agreements (PAs) and the concrete project plan for each PMB are currently being prepared.

8.3.2 IAEA-Coordinated Research Program

One of the key roles of the International Atomic Energy Agency (IAEA) is to foster collaboration among Member States on the development of advances in technology

for advanced nuclear power plants. There is high international interest, both in developing and industrialized countries, in the SCWR, primarily because such concepts will achieve high thermal efficiencies (44–45%) and promise improved economic competitiveness utilizing and building upon the recent developments for highly efficient fusion power plants (FPPs). Following the advice of the IAEA Nuclear Energy Department's Technical Working Groups on Advanced Technologies for LWRs and HWRs (the TWG-LWR & TWG-HWR), with feedback from the Gen-IV SCWR Steering Committee, and in coordination with the OECD–NEA, IAEA has started a Coordinated Research Program (CRP) in the areas of heat transfer behavior and testing of thermo-hydraulic computer methods for the SCWR. The first Research Coordination Meeting (RCM) of the CRP was held at the IAEA Headquarters, in Vienna, Austria in July 2008. Universities, research institutes, and industries from nine countries joined and 16 activities have been proposed: ten for "heat transfer, pressure drop and flow behavior," four for "thermo-hydraulic code testing" and two for "documentation of results" [148].

8.3.3 International Symposiums

In order to promote information exchange and international collaborations, international symposiums on the SCWR have been held. The first symposium (SCR-2000) was held at the University of Tokyo in November 2000. Thirty-three papers were presented from various fields, including FPP design and developments (introduced in Appendix A of this book) and review of high temperature water and steam cooled reactor concepts (introduced in Appendix B of this book). The second one (SCR-2003) was also again held at the University of Tokyo in September 2003. It focused on the radiation effects on water chemistry and 18 papers were presented by specialists. The third one was held at SJTU, China, in March 2007. Over 60 papers were presented from widely diverse fields. The fourth one was held at Heidelberg, Germany in March 2009 and over 80 papers were presented. The fifth one is planned by the Canadian SCWR community.

Glossary

3YSZ	3 mol% yttria-stabilized zirconia
8YSZ	8 mol% yttria-stabilized zirconia
ANL	argonne national laboratory
BOP	balance of plant
BWR	boiling water reactor
CANDU	CANada Deuterium Uranium
CFD	computational fluid dynamics
CHF	critical heat flux

CRIEPI	Central Research Institute of Electric Power Industry
CRP	Coordinated Research Program
CSTWG	Chinese SCWR Technical Working Group
EUR	European Utility Requirement
FQ	fuel qualification
FPP	fusion power plant
FZK	Forschungszentrum Karlsruhe
GIF	Generation-IV International Forum
HIT	High fluence irradiation facility
HPLWR	High performance light water reactor
IAEA	International Atomic Energy Agency
IEM	information exchange meeting
I-NERI	International Nuclear Energy Initiative
INL	Idaho National Laboratory
JAEA	Japan Atomic Energy Agency
JMTR	Japan Material Test Reactor
JSPS	Japan Society for the Promotion of Science
KAERI	Korea Atomic Energy Research Institute
KEPRI	Korea Electric Power Research Institute
LDV	laser Doppler velocimetry
LOCA	loss of coolant accident
LWR	light water reactor
M&C	materials and chemistry
MEXT	Ministry of Education, Culture, Sports, Science and Technology
MHI	Mitsubishi Heavy Industry Ltd.
NERI	Nuclear Energy Research Initiative
NFD	Nuclear Fuel Development
NRCan	Natural Resources Canada
ODS	Oxide dispersion strengthening
PA	project agreement
PIE	post irradiation examination
PMB	project management board
PWR	pressure water reactor
R&D	research and development
RCM	Research Coordination Meeting
SA	system agreement
SCC	stress corrosion cracking
SCWR	supercritical water cooled reactor
SI&A	system integration and assessment
SJTU	Shanghai Jiao Tong University
SRP	system research plan
SRV	safety relief valve
SSC	system steering committee
SWAMUP	supercritical water multi-purpose test loop

TEPCO	Tokyo Electric Power Company
TH&S	thermal hydraulics and safety
TWG-LWR	Technical Working Groups on Advanced Technologies for LWR

References

1. Y. Oka, Y. Ishiwatari, et al., "Research Program on Super Fast Reactor," *Proc. ICAPP'06*, Reno, NV, June 4–8, 2006, Paper No. 6353 (2006)
2. Y. Ishiwatari, Y. Yamakawa, et al., "Research and Development of a Super Fast Reactor (1) Overview and High-Temperature Structural Design," *Proc. 16th PBNC*, Aomori, Japan, October 13–18, 2008, P16P1290 (2008)
3. Y. Ishiwatari, Y. Oka and K. Yamada, "Japanese R&D Projects on Pressure-Vessel Type SCWR," *Proc. 4th Int. Symp. on SCWR*, Heidelberg, Germany, March 8–11, 2009, Paper No. 73 (2009)
4. H. Ju and L. Cao, "Research and Development of a Super Fast Reactor (3) Fuel Rod Analyses Under Normal Operating Condition," *Proc. 16th PBNC*, Aomori, Japan, October 13–18, 2008, P16P1292 (2008)
5. H. Ju, L. Cao, et al., "Core Design and Fuel Rod Analyses of a Super Fast Reactor with High Power Density," *Proc. ICAPP'09*, Tokyo, Japan, May 10–14, 2009, Paper No. 9264 (2009)
6. L. Cao, H. Lu, et al., "Research and Development of a Super Fast Reactor (4) Transmutation Analyses of Minor Actinides and Transuranium Elements," *Proc. 16PBNC*, Aomori, Japan, October 13–18, 2008, P16P1293 (2008)
7. H. Lu, Y. Ishiwatari, et al., "Evaluation of Transmutation Performance of Long-Lived Fission Products with a Super Fast Reactor," *Proc. ICAPP'09*, Tokyo, Japan, May 10–14, 2009, Paper No. 9263 (2009)
8. J. Gou, Y. Ishiwatari, et al., "Research and Development of a Super Fast Reactor (5) Thermal Hydraulic Analyses of Tight-Lattice Subchannels," *Proc. 16th PBNC*, Aomori, Japan, October 13–18, 2008, P16P1294 (2008)
9. J. Gou, Y. Ishiwatari, et al., "CFD Analyses in Tight-Lattice Subchannels and Seven-Rods Bundle Geometries of a Super Fast Reactor," *Proc. ICAPP'09*, Tokyo, Japan, May 10–14, 2009, Paper No. 9262 (2009)
10. W. Tian, Y. Ishiwatari, et al., "Numerical Computation on Thermally Controlled Steam Bubble Condensation Using MPS-MAFL," *Proc. 4th Int. Symp. on SCWR*, Heidelberg, Germany, March 8–11, 2009, Paper No. 05 (2009)
11. S. Tanaka, Y. Shirai, et al., "Plant Concept of Supercritical Pressure Light Water Reactor," *Proc. ICONE-5*, Nice, France, May 26–30, 1997, ICONE-5-2346 (1997)
12. S. Goto, Y. Ishiwatari and Y. Oka, "Considerations for the Reactor Characteristics of Super Fast Reactor," *Transactions of ANS/ENS 2007 Int. Conf. on Making the Renaissance Real*, Washington, DC, November 7–15, 2007, 869–870 (2007)
13. S. Goto, Y. Ishiwatari and Y. Oka "Research and Development of a Super Fast Reactor (12) Considerations for the Reactor Characteristics," *Proc. 16th PBNC*, Aomori, Japan, October 13–18, 2008, P16P1276 (2008)
14. A. Shioiri, K. Moriya, et al., "Development of Supercritical-Water Cooled Power Reactor Conducted by a Japanese Joint Team," *Proc. GENES4/ANP2003*, Kyoto, Japan, September 15–19, 2003, Paper No. 1121 (2003)
15. Y. Oka and K. Yamada, "Research and Development of High Temperature Light Water Cooled Reactor Operating at Supercritical-Pressure in Japan," *Proc. ICAPP'04*, Pittsburgh, PA, June 13–17, 2004, Paper No. 4233 (2004)
16. K. Yamada, M. Ookawa, et al., "Recent Activities and Future Plan of Thermal-Spectrum SCWR Development in Japan," *Proc. 3rd Int. Symp. on SCWR*, Shanghai, China, March 12–15, 2007, Paper No. SCWR2007-P054 (2007)

17. S. Higuchi, S. Sakurai and T. Ishida, "A Study of Fuel Behavior in an SCWR Core with High Power Density," *Proc. ICAPP'07*, Nice, France, May 13–18, 2007, Paper No. 7206 (2007)
18. S. Higuchi and S. Sakurai, "A Study on Thermo-Mechanical Behavior of Typical Fuel Rods in an SCWR Core," *Proc. 4th Int. Symp. on SCWR*, Heidelberg, Germany, March 8–11, 2009, Paper No. 72 (2009)
19. S. Sakurai, N. Yoshida, et al., "Development of Supercritical-Water Cooled Power Reactor Core Design Study with 3-D Core Simulator," *Proc. GENES4/ANP2003*, Kyoto, Japan, September 15–19, 2003, Paper No. 1115 (2003)
20. S. Sakurai, S. Higuchi and A. Shioiri, "Development of SCPR Fuel Design Criteria and Core Design Study," *Proc. Global 2003*, New Orleans, LA, November 16–20, 2003, 1746–1753 (2003)
21. M. Ookawa, S. Sakurai and K. Yamada, "Optimization Method for Design of the Supercritical-Water-Cooled Reactor Fuel Assembly," *Proc. ICAPP'05*, Seoul, Korea, May 15–19, 2005, Paper No. 5216 (2005)
22. S. Sakurai, "SCWR Fuel and Core Design Study," *Proc. Global 2009*, Paris, France, September 6–11, Paper No. 9373 (2009)
23. K. Kitou, K. Nishida, et al., "Investigation of Fuel Assembly by Using Subchannel Analysis for Supercritical-Water Cooled Power Reactor," *Proc. GENES4/ANP2003*, Kyoto, Japan, September 15–19, 2003, Paper No. 1100 (2003)
24. S. Yoshida and H. Mori, "Heat Transfer to Supercritical Pressure Fluids Flowing in Tubes," *Proc. 1st Int. Symp. on SCWR*, Tokyo, Japan, November 6–8, 2000, Paper No. 106 (2000)
25. T. Yamashita, S. Yoshida, et al., "Heat Transfer Study Under Supercritical Pressure Conditions," *Proc. GENES4/ANP2003*, Kyoto, Japan, September 15–19, 2003, Paper No. 1119 (2003)
26. H. Komita, S. Morooka, et al., Study on the Heat Transfer to the Supercritical Pressure Fluid for Supercritical Water Cooled Power Reactor Development," *Proc. NURETH-10*, Seoul, Korea, October 5–9, 2003, 1–11 (2003)
27. H. Mori, S. Yoshida, et al., "Heat Transfer Study Under Supercritical Pressure Conditions for Single Rod Test Section," *Proc. ICAPP'05*, Seoul, Korea, May 15–19, 2005, Paper No. 5303 (2005)
28. H. Mori, M. Ohno, et al., "Research and Development of a Super Fast Reactor (7) Heat Transfer to a Supercritical Pressure Fluid Flowing in a Sub-bundle Channel," *Proc. 16th PBNC*, Aomori, Japan, October 13–18, 2008, P16P1297 (2008)
29. K. Ezato, M. Akiba, et al., "Research and Development of a Super Fast Reactor (8) Heat Transfer Experiments Around a Simulated Fuel Rod with Supercritical Pressure Water," *Proc. 16th PBNC*, Aomori, Japan, October 13–18, 2008, P16P1240 (2008)
30. K. Ezato, Y. Seki, et al., "Heat Transfer in a Seven-Rod Test Bundle with Supercritical Pressure Water (1) Experiments," *Proc ICAPP'09*, Tokyo, Japan, May 10–14, 2009, Paper No. 9464 (2009)
31. T. Misawa, T. Nakatsuka, et al., "Numerical Analysis of Heat Transfer Experiment of Supercritical Pressure Water in Seven-Rod Test Bundle," *Proc. NURETH-13*, Kanazawa, Japan, September 27–October 2, 2009 (2009)
32. T. Misawa, H. Yoshida, et al., "Numerical Analysis of Heat Transfer Test of Supercritical Water in a Tube Using the Three-Dimensional Two-Fluid Model Code," *Proc. ICONE16*, Orlando, FL, May 11–15, 2008, ICONE16-48690 (2008)
33. T. Misawa, T. Nakatsuka, et al., "Research and Development of a Super Fast Reactor (9) Numerical Analysis of Heat Transfer Experiment of Supercritical Pressure Water and Freon in a Rod Bundle," *Proc. 16th PBNC*, Aomori, Japan, October 13–18, 2008, P16P1065 (2008)
34. H. Yoshida, T. Nakatsuka and T. Suzuki, "Numerical Simulation of Heat Transfer Test of Forced Convection Supercritical Water in a Circular Pipe," *Proc. NTHAS6,* Okinawa, Japan, November 24–27, 2008, N6P1082 (2008)

35. T. Nakatsuka, T. Misawa, et al., "Numerical Simulation of Heat Transfer Experiment of Supercritical Water by Two-Fluid Model Code ACE-3D," *Proc. 4th Int. Symp. on SCWR*, Heidelberg, Germany, March 8–11, 2009, Paper No. 31 (2009)
36. T. Nakatsuka, T. Misawa, et al., "Numerical Simulation on Thermal-Hydraulic Characteristics in Fuel Assemblies of Supercritical Water Cooled Reactors Using Two-Fluid Model Analysis Code ACE-3D," *Proc. Global 2009*, Paris, France, September 6–11, Paper No. 9486 (2009)
37. H. Mori, M. Ohno and Y. Hamamoto, "Experimental Study for Research and Development of a Super Fast Reactor (1) Critical Heat Flux in the Near-Critical Pressure Region," *Proc. ICAPP'09*, Tokyo, Japan, May 10–14, 2009, Paper No. 9368 (2009)
38. H. Mori, Y. Hamamoto and Y. Ohno, "Experimental Study for Research and Development of a Super Fast Reactor (2) Oscillatory Condensation of High Temperature Vapor Directly Discharged into Sub-cooled Liquid Pool," *Proc. ICAPP'09*, Tokyo, Japan, May 10–14, 2009, Paper No. 9369 (2009)
39. S. Kasahara, J. Kuniya, et al., "General Corrosion of Iron, Nickel and Titanium Alloys as Candidate Materials for the Fuel Claddings of the Supercritical-Water Cooled Power Reactor," *Proc. GENES4/ANP2003*, Kyoto, Japan, September 15–19, 2003, Paper No. 1132 (2003)
40. J. Kaneda, S. Kasahara, et al., "Corrosion Film Properties of the Candidate Materials for the Fuel Claddings of the Supercritical-Water Reactor," *Proc. ICAPP'05*, Seoul, Korea, May 15–19, 2005, Paper No. 5594 (2005)
41. J. Kaneda, S. Kasahara, et al., "General Corrosion Properties of Titanium Based Alloys for the Fuel Claddings in the Supercritical Water-Cooled Reactors," *Proc. 12th Int. Conf. on Environmental Degradation of Materials in Nuclear Systems-Water Reactors*, Salt Lake City, UT, August 14–18, 2005 (2005)
42. Y. Tuchiya, F. Kano, et al., "SCC and Irradiation Properties of Metals Under Supercritical-Water Cooled Power Reactor Conditions," *Proc. GENES4/ANP2003*, Kyoto, Japan, September 15–19, 2003, Paper No. 1096 (2003)
43. Y. Tsuchiya, F. Kano, et al., "SCC Properties of Metals Under Supercritical-Water Cooled Power Reactor Conditions," *Proc. Corrosion 2004*, New Orleans, LA, March 28–April 1, 2004, Paper No. 4485 (2004)
44. H. Matusi, Y. Sato, et al., "Material Development for Supercritical Water-Cooled Reactors," *Proc. ICAPP'07*, Nice, France, May 13–18, 2007, Paper No. 7447 (2007)
45. J. Kaneda, S. Kasahara, et al., "Material Properties of Stainless Steels Modified with Addition of Zirconium for Supercritical Water-Cooled Reactor," *Proc. ICAPP'07*, Nice, France, May 13–18, 2007, Paper No. 7500 (2007)
46. M. Katsuragawa, H. Kashihara and M. Akebi, "Status of Liquid Metal Fast Breeder Reactor Fuel Development in Japan," *Journal of Nuclear Materials*, Vol. 204, 14–22 (1993)
47. Y. Nakazono, T. Iwai and H. Abe, "Corrosion Properties of PNC1520 Austenitic Stainless Steel in Supercritical Water as a Fuel Cladding Candidate Material for Supercritical Water Reactor," *Proc. 4th Int. Symp. on SCWR*, Heidelberg, Germany, March 8–11, 2009, Paper No. 59 (2009)
48. Y. Nakazono, T. Iwai and H. Abe, "Corrosion Properties of Modified PNC1520 Austenitic Stainless Steel in Supercritical Water as a Fuel Cladding Candidate Material for Supercritical Water Reactor," *Proc. ICAPP'09,* Tokyo, Japan, May 10–14, 2009, Paper No. 9456 (2009)
49. http://www.nuclear.jp/~hit/index_e.html
50. K. Sasaki, T. Kubo, et al., "Research and Development of a Super Fast Reactor (10) Fabrication and Characterization of Durable Thermal Shielding Material," *Proc. 16th PBNC*, Aomori, Japan, October 13–18, 2008, P16P1427 (2008)
51. G. Wu, Y. Katsumura, et al., "Pulse Radiolysis of High Temperature and Supercritical Water: Experimental Setup and e^-_{aq}-Observation," *Radiation Physics and Chemistry*, Vol. 60, 395–398 (2001)

52. G. Wu, Y. Katsumura et al., "Temperature Dependence of $(SCN)_2^{\bullet-}$ in Water at 25–400°C: Absorption Spectrum, Equilibrium Constant, and Decay," *Journal of Physical Chemistry A*, Vol. 105, 4933–4939 (2001)
53. G. Wu, Y. Katsumura, et al., "Temperature Dependence of Carbonate Radical in $NaHCO_3$ and Na_2CO_3 Solutions: Is the Radical a Single Anion?," *Journal of Physical Chemistry A*, Vol. 106, 2430–2437 (2002)
54. M. Mostafavi, M. Lin, et al., "Pulse Radiolysis Study of Absorption Spectra of Ag^0 and Ag_2^+ in Water from Room Temperature up to 380°C," *Journal of Physical Chemistry A*, Vol. 106, 3123–3127 (2002)
55. G. Wu, Y. Katsumura, et al., "Temperature Dependence of Ketyl Radical in Aqueous Benzophenone Solutions up to 400°C: A Pulse Radiolysis Study," *Physical Chemistry Chemical Physics*, Vol. 4, 3980–3988 (2002)
56. M. Lin, Y. Katsumura, et al., "Pulse Radiolysis Study on the Estimation of Radiolytic Yields of Water Decomposition Products in High-Temperature and Supercritical Water: Use of Methyl Viologen as a Scavenger," *Journal of Physical Chemistry A*, Vol. 109, 8287–8295 (2004)
57. Y. Katsumura, K. Kiuchi, et al., "Fundamental R&D Program on Water Chemistry of Supercritical Pressure Water Under Radiation Field," *Proc. 2nd Int. Symp. on SCWR (SCR-2003)*, Tokyo, Japan, September 18–19, 2003, 1–6 (2003)
58. Y. Katsumura, K. Kiuchi, et al., "Research Program on Water Chemistry of Supercritical Pressure Water Under Radiation Field," *Proc. 14th Int. Conf. on the Properties of Water and Steam*, Kyoto, Japan, August 29–September 3, 2004, 545–550 (2004)
59. T. Miyazaki, Y. Katsumura, et al., "Gamma-Radiolysis of Benzophenone Aqueous Solution at Elevated Temperatures up to Supercritical Condition," *Radiation Physics and Chemistry*, Vol. 75, 218–228 (2006)
60. N. Saito, Y. Tsuchiya, et al., "Chemical Thermodynamics Consideration on Corrosion Products in Supercritical-Water-Cooled Reactor Coolant," *Nuclear Technology*, Vol. 155, 105–113 (2006)
61. T. Miyazaki, Y. Katsumura, et al., "Radiolysis of Phenol in Aqueous Solution at Elevated Temperatures," *Radiation Physics and Chemistry*, Vol. 75, 408–415 (2006)
62. Z. Han, Y. Katsumura, et al., "Effect of Temperature on the Absorption Spectra of the Solvated Electron in 1-Propanol and 2-Propanol: Pulse Radiolysis and Laser Photolysis Studies at Temperatures up to Supercritical Condition," *Radiation Physics and Chemistry*, Vol. 77, 409–415 (2008)
63. Z. Han and Y. Muroya, "Research and Development of a Super Fast Reactor (11) An Approach to Evaluate the Elution Characteristic of Stainless Materials in Subcritical and Supercritical Water," *Proc. 16th PBNC*, Aomori, Japan, October 13–18, 2008, P16P1315 (2008)
64. Z. Han and Y. Muroya, "Development of a New Method to Study Elution Properties of Stainless Materials in Subcritical and Supercritical Water," *Proc. 4th Int. Symp. on SCWR*, Heidelberg, Germany, March 8–11, 2009, Paper No. 75 (2009)
65. G. Heusener, U. Muller, T. Schulenberg and D. Square, "A European Development Program for a High Performance Light Water Reactor (HPLWR)," *Proc. 1st Int. Symp. on Supercritical Water-Cooled Reactors*, Tokyo, Japan, November 6–9, 2000, Paper No. 102 (2000)
66. D. Squarer, D. Bittermann, et al., "Overview of the HPLWR Project and Future Direction," *Proc. ICAPP'03*, Cordoba, Spain, May 4–7, 2003, Paper No. 3137 (2003)
67. D. Squarer, T. Schulenberg, et al., "High Performance Light Water Reactor," *Nuclear Engineering and Design*, Vol. 221, 167–180 (2003)
68. J. Starflinger, N. Aksan, et al., "Roadmap for Supercritical Water-Cooled Reactor R&D in Europe," *Proc. Global 2003*, New Orleans, LA, November 16–20, 2003, 1137–1142 (2003)
69. J. Starflinger, T. Schulenberg, et al., "European Research Activities within the Project: High Performance Light Water Reactor Phase 2," *Proc. ICAPP'07*, Nice, France, May 13–18, 2007, Paper No. 7416 (2007)

70. T. Schulenberg and J. Starflinger, "European Research Project on the High Performance Light Water Reactor," *Proc. 4th Int. Symp. on SCWR*, Heidelberg, Germany, March 8–11, 2009, Paper No. 54 (2009)
71. J. Starflinger, T. Schulenberg, et al., "Results of the Mid-Term Assessment of the High Performance Light Water Reactor 2 Project," *Proc. ICAPP'09*, Tokyo, Japan, May 10–14, 2009, Paper No. 9268 (2009)
72. T. Schulenberg, C. Maraczy, J. Heinecke and W. Bernnat, "Design and Analysis of a Thermal Core for a HPLWR – a State of the Art Review," *Proc. NURETH-13*, Kanazawa, Japan, September 27–October 2, 2009, Paper N13P1039 (2009)
73. D. Brady, D. Duttey, et al., "Generation IV Reactor Development in Canada," *Proc. 3rd Int. Symp. on SCWR*, Shanghai, China, March 12–15, 2007, SCR2007-P057 (2007)
74. D. Boyle, D. Brady, et al., "Canada's Generation IV National Program – Overview," *Proc. 4th Int. Symp. on SCWR*, Heidelberg, Germany, March 8–11, 2009, Paper No. 74 (2009)
75. C. K. Chow and H. F. Khartabil, "Conceptual Fuel Channel Designs for CANDU-SCWR," *Nuclear Engineering and Technology*, Vol. 40(2), 139–146 (2008)
76. H. F. Khartabil, "Review and Status of the Gen-IV CANDU-SCWR Passive Moderator Core Cooling System," *Proc. ICONE-16*, Orlando, FL, May 11–15, 2008, ICONE16-48741 (2008)
77. D. Guzonas, et al., "Corrosion of Candidate Materials for Use in a Supercritical Water CANDU Reactor," *Proc. 13th Int. Conf. on Environmental Degradation of Materials in Nuclear Power Systems – Water Reactors*, Whistler, BC (2007)
78. D. C. Groeneveld, S. Tavoularis, et al., "Analytical and Experimental Program of Supercritical Heat Transfer Research at the University of Ottawa," *Nuclear Engineering and Technology*, Vol. 40(2), 107–116 (2008)
79. V. Chatoorgoon, V. Shah, et al., "Linear Predictions of Supercritical Flow Stability in Parallel Channels," *Proc. 3rd Int. Symp. on SCWR*, Shanghai, China, March 12–15, 2007, SCR2007-P097 (2007)
80. Y. Y. Bae, K. M. Bae, et al., "R&D on a Supercritical Pressure Water Cooled Reactor in Korea," *Proc. ICAPP'06*, Reno, NV, June 4–8, 2006, Paper No. 6022 (2006)
81. Y. Y. Bae, K. M. Bae, et al., "SCWR Research in Korea," *Proc. 3rd Int. Symp. on SCWR*, Shanghai, China, March 12–15, 2007, SCR2007-P006 (2007)
82. Y. Y. Bae, G. Jang, et al., "Research Activities on a Supercritical Pressure Water Reactor in Korea," *Nuclear Engineering and Technology*, Vol. 39(4), 273–286 (2007)
83. Y. Y. Bae, H. Y. Kim, et al., "Update on the SCWR Research in Korea," *Proc. 4th Int. Symp. on SCWR*, Heidelberg, Germany, March 8–11, 2009, Paper No. 52 (2009)
84. S. Y. Hong, K. Lee, et al., "Interim Results of SCWR Development Feasibility Study in Korea," *Proc. 4th Int. Symp. on SCWR*, Heidelberg, Germany, March 8–11, 2009, Paper No. 50 (2009)
85. H. K. Joo, J. W. Yoo and J. M. Noh, "A Conceptual Design for a Rectangular Fuel Assembly for the Thermal SCWR System," *Proc. Global 2003*, New Orleans, LA, November 16–20, 2003, 1149–1154 (2003)
86. K. M. Bae, H. K. Joo and Y. Y. Bae, "Conceptual Design of a 1,400 MWe Supercritical Water Cooled Reactor Core with a Cruciform Type U/Zr Solid Moderator," *Proc. ICAPP'07*, Nice, France, May 13–18, 2007, Paper No. 7502 (2007)
87. Y. B. Kim, S. M. Bae, et al., "Sensitivity Study of SCWR Core Design Concepts in Korea," *Proc. 16th PBNC*, Aomori, Japan, October 13–18, 2008, P16P1132 (2008)
88. H. Y. Kim, H. Kim, et al., "Heat Transfer Test in a Vertical Tube Using CO_2 at Supercritical Pressures," *Journal of Nuclear Science and Technology*, Vol. 44(3), 1–9 (2007)
89. H. Y. Kim, H. Kim, et al., "Experimental Investigations on Heat Transfer to CO_2 Flowing Upward in a Narrow Annulus at Supercritical Pressures," *Nuclear Engineering and Technology*, Vol. 40(2), 155–162 (2008)

90. H. Kim, H. Y. Kim, et al., "Heat Transfer to Supercritical Pressure Carbon Dioxide Flowing Upward Through Tubes and a Narrow Annulus Passage," *Progress in Nuclear Energy*, Vol. 50, 518–525 (2008)
91. H. Kim, Y. Y. Bae, et al., "Experimental Investigations on Heat Transfer Characteristics in Upward Flow of Supercritical Carbon Dioxide," *Nuclear Technology*, Vol. 164, 119–129 (2008)
92. Y. Y. Bae and H. Y. Kim, "Convective Heat Transfer to CO_2 at a Supercritical Pressure Flowing Vertically Upward in Tubes and an Annular Channel," *Experimental Thermal and Fluid Science*, Vol. 33(2), 329–339 (2009)
93. Y. Y. Bae, H. Y. Kim and T. Yoo, "Heat Transfer Experiments in a Wire-Inserted Tube at Supercritical Conditions," *Proc. 4th Int. Symp. on SCWR*, Heidelberg, Germany, March 8–11, 2009, Paper No. 27 (2009)
94. X. Cheng, "R&D Activities on SCWR in China," *Proc. 4th Int. Symp. on SCWR*, Heidelberg, Germany, March 8–11, 2009, Paper No. 53 (2009)
95. X. Cheng, X. J. Liu, et al., "A Mixed Core for Supercritical Water-Cooled Reactors, *Nuclear Engineering and Technology*, Vol. 40(1), 1–10 (2008)
96. X. J. Liu and X. Cheng, "Coupled Thermal-Hydraulics and Neutron-Physics Analysis of SCWR with Mixed Spectrum Core," *Proc. 4th Int. Symp. on SCWR*, Heidelberg, Germany, March 8–11, 2009, Paper No. 44 (2009)
97. J. Buongiorno, "The Supercritical Water Cooled Reactor: Ongoing Research and Development in the US," *Proc. ICAPP'04*, Pittsburgh, PA, June 13–17, 2004, Paper No. 4229 (2004)
98. S. M. Modro, "The Supercritical Water Cooled Reactor Research and Development in the US," *Proc. ICAPP'05*, Seoul, Korea, May 15–19, 2005, Paper No. 5694 (2005)
99. J. Buongiorno and P. Macdonald, "Supercritical Water Reactor (SCWR), Progress Report for the FY03 Generation-IV R&D Activities for the Development of the SCWR in the US," *INEEL/EXT03-03-01210, Idaho National Engineering and Environmental Laboratory* (2003)
100. J. Licht, M. Anderson and M. Corradini, "Heat Transfer to Water at Supercritical Pressures," *Proc. ICAPP'07*, Nice, France, May 13–18, 2007, Paper No. 7223 (2007)
101. J. Licht, M. Anderson and M. Corradini, "Heat Transfer to Water at Supercritical Pressures in Circular and Square Annular Flow Geometry," *International Journal of Heat and Fluid Flow*, Vol. 29, 156–166 (2008)
102. J. Licht, M. Anderson and M. Corradini, "Deterioration of Heat Transfer in Upward Flowing Supercritical Pressure Water," *Proc. ICAPP'09*, Tokyo, Japan, May 10–14, 2009, Paper No. 9391 (2009)
103. G. Mignot, M. Anderson and M. Corradini, "Critical Flow Experiment and Analysis for Supercritical Fluid," *Nuclear Engineering and Technology*, Vol. 40(2), 133–138 (2008)
104. G. Mignot and M. Anderson, "Experimental Study of Supercritical CO_2 depressurization," *Proc. International Workshop on Thermal-Hydraulics of Innovative Reactor and Transmutation Systems –THIRS*, Karlsruhe, Germany, April 14–16, 2008, SC1 (2008)
105. G. Mignot, M. Anderson and M. Corradini, "Measurement of Supercritical CO_2 Critical Flow: Effects of L/D and Surface Roughness," *Nuclear Engineering and Design*, Vol. 239, 949–955 (2009)
106. K. Sridharan, A. Zillmer, et al., "Corrosion Behavior of Candidate Alloys for Supercritical Water Reactors," *Proc. ICAPP'04*, Pittsburgh, PA, USA, June 13–17, 2004, Paper No. 4136 (2004)
107. T. Allen, L. Tan, et al., "Corrosion and Radiation Response of Advanced Ferritic–Martensitic Steels for Generation IV Application," *Proc. Global 2005*, Tsukuba, Japan, October 9–13, 2005, Paper No. IL001 (2005)
108. T. Allen, L. Tan, et al., "Corrosion of Ferritic–Martensitic Alloys in Supercritical Water for GenIV Application," *Proc. Global 2005*, Tsukuba, Japan, October 9–13, 2005, Paper No. 419 (2005)
109. T. Allen, G. Was, et al., "Radiation Resistance of Advanced Ferritic–Martensitic Steel HCM12A," *Journal of ASTM international*, Vol. 2(8), Paper ID JAI12382 (2005)

110. Y. Chen, K. Sridharan and T. Allen, "Corrosion Behavior of Ferritic/Martensitic Steel T91 in Supercritical Water," *Corrosion Science*, Vol. 48(9), 2843–2854 (2006)
111. L. Tan, Y. Yang and T. Allen. "Oxidation Behavior of Alloy HCM12A Exposed in Supercritical Water," *Corrosion Science*, 48, 4234–4242 (2006)
112. L. Tan, Y. Yang and Y. Allen, "Porosity Prediction in Supercritical Water Exposed Ferritic/Martensitic Steel HCM12A," *Corrosion Science*, 48, 3123–3138 (2006)
113. L. Tan, K. Sridharan and T. Allen, "The Effect of Grain Boundary Engineering on the Oxidation Behavior of INCOLOY Alloy 800H in Supercritical Water," *Journal of Nuclear Materials*, Vol. 348, 263–271 (2006)
114. X. Ren, K. Sridharan and T. Allen, "Corrosion of Ferritic–Martensitic Steel HT9 in Supercritical Water," *Journal of Nuclear Materials*, Vol. 358, 227–234 (2006)
115. Y. Chen, K. Sridharan, et al., "Microstructural Examination of Oxide Layers Formed on an Oxide Dispersion Strengthened Ferritic Steel Exposed to Supercritical Water," *Journal of Nuclear Materials*, Vol. 359, 50–28 (2006)
116. Y. Chen, K. Sridharan, et al., "Oxidation of 9Cr Oxide Dispersion Strengthened Steel Exposed in Supercritical Water," *Journal of Nuclear Materials*, Vol. 371, 118–128 (2007)
117. X. Ren, K. Sridharan and T. Allen, "Corrosion Behavior of Alloys 625 and 718 in Supercritical Water," *Corrosion*, Vol. 63(7), 603–612 (2007)
118. L. Tan, X. Ren, et al., "Effect of Shot-peening on the Oxidation of Alloy 800H exposed to Supercritical Water and Cyclic Oxidation," *Corrosion Science*, 50, 2040–2046 (2008)
119. L. Tan, X. Ren, et al., "Corrosion Behavior of Ni-base Alloys for Advanced High Temperature Water-Cooled Nuclear Plants," *Corrosion Science*, 50, 3056–3062 (2008)
120. T. Allen, K. Sridharan, et al., "Materials Development and Selection for Corrosion Resistance: A Critical Issue in Supercritical Water Reactors," *Proc. 16th PBNC*, Aomori, Japan, October 13–18, 2008, P16P1032 (2008)
121. E. Edwards, D. Bartels, et al., "Radiation Chemical Yields of Water in Neutron and Gamma Radiation," *Transactions of ANS*, 92, 125–126 (2005)
122. P. Humrickhouse, P. Wilson, et al., "Gamma Shield Design for the Supercritical Water Neutron Radiolysis Experiment," *Transactions of ANS*, 92, 161–162 (2005)
123. E. Edwards, P. Wilson, et al., "University of Wisconsin Supercritical Water Loop Radiation Energy Deposition Calibration," *Transactions of ANS*, 94, 533–534 (2006)
124. E. Edwards, P. Wilson, et al., "Radiation Chemistry Results from the Supercritical Water Loop at UW-Madison," *Transactions of ANS*, 95, 939–940 (2006)
125. P. Wilson and P. Hu, "Accounting for Moderator Heating in Supercritical Water Reactor Analysis," *Transactions of ANS*, 92, 520–521 (2005)
126. P. Wilson and P. Hu, "Reactor Analysis for Counter-flowing Moderator and Coolant in a Supercritical Water Reactor," *Proc. ICONE-14*, July 17–20, 2006, Miami, FL, ICONE14-89392 (2006)
127. P. Hu and P. Wilson, "Core Flow Distribution from Coupled Supercritical Water Reactor Analysis," *Proc. 3rd Int. Symp. on SCWR*, Shanghai, China, March 12–15, 2007, Paper No. SCWR2007-P058 (2007)
128. P. Hu and P. Wilson, "Supercritical Water Reactor Steady State, Burnup and Transient Analysis with Extended PARCS/RELAP5," *Proc. 4th Int. Symp. on SCWR*, Heidelberg, Germany, March 8–11, 2009, Paper No. 13 (2009)
129. J. McKinley, S. Teysseyre, et al., "Corrosion and Stress Corrosion Cracking of Austenitic Alloys in Supercritical Water," *Proc. GENES4/ANP2003*, Kyoto, Japan, September 15–19, 2003, Paper No. 1027 (2003)
130. G. Was, S. Teysseyre and J. McKinley, "Corrosion and Stress Corrosion Cracking of Iron- and Nickel-base Austenitic Alloys in Supercritical Water," *Proc. NACE's Annual Conference, Corrosion 2004*, New-Orleans, LA, USA, March 28–April 1, 2004, Paper No. 04492 (2004)
131. P. Ampornrat, C. Bahn and G. Was, "Corrosion and Stress Corrosion Cracking of Ferritic–Martensitic Alloys in Supercritical Water," *Proc. 12th Int. Conf. on Environmental*

Degradation of Materials in Nuclear Systems-Water Reactors, Salt Lake City, UT, August 14–18, 2005 (2005)
132. G. Was and S. Teysseyre, "Challenges and Recent Progress in Corrosion and Stress Corrosion Cracking of alloys for Supercritical Water Reactor Core Components," *Proc. 12th Int. Conf. on Environmental Degradation of Materials in Nuclear Systems-Water Reactors*, Salt Lake City, UT, August 14–18, 2005 (2005)
133. G. Gupta and G. Was, "Effect of Proton Irradiation and GBE on SCC of F-M Alloys in SCW," *Proc. 12th Int. Conf. on Environmental Degradation of Materials in Nuclear Systems-Water Reactors*, Salt Lake City, UT, August 14–18, 2005 (2005)
134. G. Was, S. Teysseyre, et al., "Corrosion of Austenitic Alloys in Supercritical Water," *Proc. NACE's Annual Conference, Corrosion 2005*, Houston TX, April 3–7, 2005, Paper No. 05397 (2005)
135. G. Gupta and G. Was, "The Role of Grain Boundary Engineering on the High Temperature Creep of Ferritic–Martensitic Alloy T91," *Journal of ASTM international*, Vol. 2(3), Paper ID JAI12355 (2005)
136. G. Was, S. Teysseyre and Z. Jiao, "Corrosion of Austenitic Alloys in Supercritical Water," *Corrosion*, Vol. 62(11), 989–1005 (2006)
137. S. Teysseyre and G. Was, "Stress Corrosion Cracking of Austenitic Alloys in Supercritical Water," *Corrosion*, Vol. 62(12), 1100–1116 (2006)
138. G. Gupta, G. Was, et al., "Role of Grain Boundary Engineering in Mitigating Stress Corrosion Cracking of HT-9 in Supercritical Water," *Journal of Nuclear Materials*, Vol. 361, 160–173 (2007)
139. P. Ampornrat and G. Was, "Oxidation of Ferritic–Martensitic Alloys T91, HCM12A and HT-9 in Supercritical Water," *Journal of Nuclear Materials*, Vol. 371, 1–17 (2007)
140. S. Teysseyre, Q. Peng, et al., "Facility for Stress Corrosion Cracking of Irradiated Specimens in Supercritical Water," *Journal of Nuclear Materials*, Vol. 371, 98–106 (2007)
141. S. Teysseyre, Z. Jiao, et al., "Effect of Irradiation on Stress Corrosion Cracking In Supercritical Water," *Journal of Nuclear Materials*, Vol. 371, 107–117 (2007)
142. G. Was, P. Ampornrat, et al., "Corrosion and Stress Corrosion Cracking in Supercritical Water," *Journal of Nuclear Materials*, Vol. 371, 176–201 (2007)
143. J. Zhao, P. Saha and M. Kazimi, "Stability of Supercritical Water-Cooled Reactor During Steady-State and Sliding Pressure Start-up," *Proc. NURETH-11*, Avignon, France, October 2–6, 2005, Paper No. 106 (2005)
144. J. Zhao, P. Saha and M. Kazimi, "Coupled Neutronic and Thermal-Hydraulic Out-of-Phase Stability of Supercritical Water Cooled Reactors," *Proc. ICAPP'06*, Reno, NV, June 4–8, 2006, Paper No. 6424 (2006)
145. J. Zhao, P. Saha and M. Kazimi, "Hot Channel Stability of Supercritical Water-Cooled Reactors (Part I): Steady State and Sliding Pressure Startup," *Nuclear Technology*, Vol. 158, 158–173 (2007)
146. J. Zhao, P. Saha and M. Kazimi, "Hot Channel Stability of Supercritical Water-Cooled Reactors (Part II): Effect of Water Rods Heating and Comparison with BWR Stability," *Nuclear Technology*, Vol. 158, 174–190 (2007)
147. http://www.gen-4.org/PDFs/GenIVRoadmap.pdf
148. S. León and N. Aksan, "IAEA Coordinated Research Programme on Heat Transfer Behavior and Thermo-Hydraulics Code Testing for Super Critical Water Cooled Reactors," *Proc. ICAPP'09*, Tokyo, Japan, May 10–14, 2009, Paper No. 9482 (2009)

Appendix A: Supercritical Fossil Fired Power Plants – Design and Developments

Introduction

In the 1950s, in Japan, the number of large capacity supercritical pressure fossil fuel-fired power plants increased, making good use of rich deposits and cheaply priced imported oil by measure of its scale merit in facility costs, as an alternative to former smaller capacity subcritical pressure fossil fuel-fired plants using domestic coal for fuel.

In the early 1970s, energy dependence of imported oil reached approximately 80%.

Oil shocks occurred twice, in 1973 and 1978, giving a terrible blow to the electric power generation industry, which triggered moves for fuel diversification and energy saving. Consequently, the demand for liquid natural gas increased as the most immediate effective substitute fuel.

After the 1980s, imported coal was the main energy resource in coping with a stable supply and the mixing of electric power resources.

With the increase of nuclear power plants for base load operations at the same time and wide variations of electric load demands, most newly planned power units tended to be designed for cyclic duties.

Figure A.1 [1] shows the general trends of utility boilers supplied by Babcock Hitachi K.K. (BHK) of Japan in the last half century.

Improvement of Steam Conditions

Higher steam conditions were initiated through global environmental issues, for example, to reduce air pollutants, especially CO_2 emissions by improving plant efficiency. Figure A.2 [1] shows a record of steam parameter improvements established by BHK in Japan. The first "USC" plant in Japan was built in 1989 employing gas fired boilers with steam conditions of 31 MPa/566°C/566°C/566°C.

Y. Oka et al., *Super Light Water Reactors and Super Fast Reactors*,
DOI 10.1007/978-1-4419-6035-1, © Springer Science+Business Media, LLC 2010

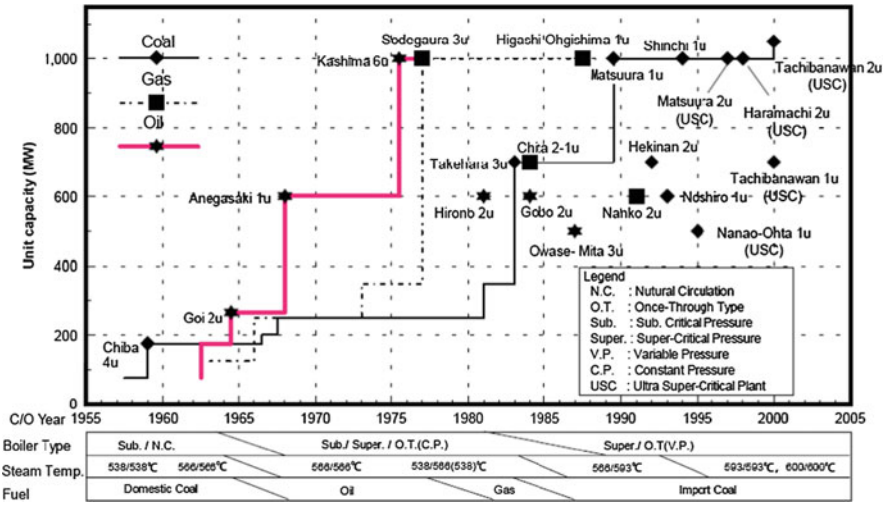


Fig. A.1 General trends of utility boilers supplied by BHK in Japan (Taken from ref. [1])

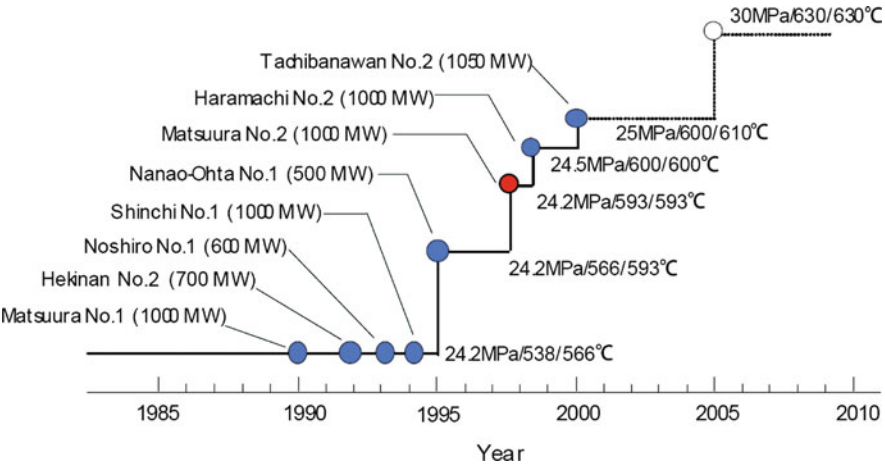


Fig. A.2 Improvement of steam conditions in Japan (Taken from ref. [1])

Then, the newly installed coal fired plants had a typical live steam pressure of 24.1 MPa, though steam temperatures improved gradually. The most advanced steam condition currently in commercial operation is 24.1 MPa/566°C/593°C, which was applied to Nanao-Ohta No. 1 boiler of Hokuriku Electric Power Company supplied by BHK in 1995. This trend continues with Matsuura No. 2 Unit, the steam parameters of which were 24.1 MPa/593°C/593°C in 1997.

Furthermore, subsequent units with planned completions after 1997 are expected to have slightly higher steam conditions as shown in Fig. A.2 [1]. Power plants

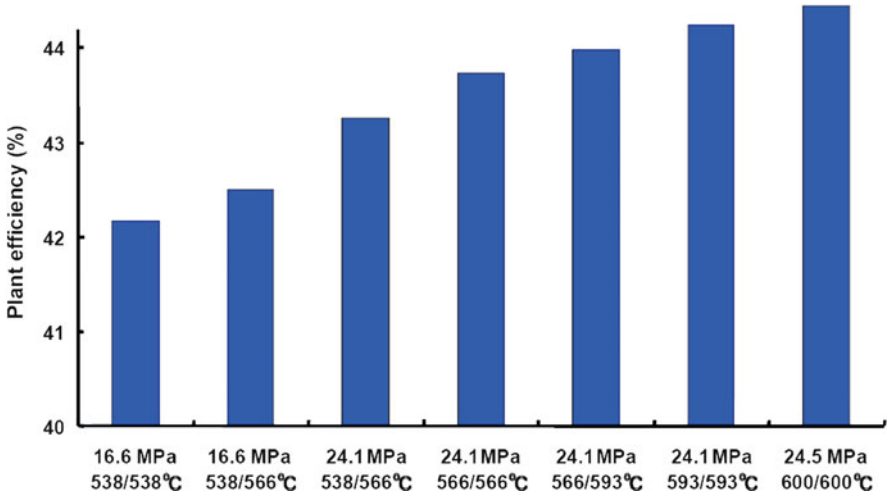


Fig. A.3 Improvement of plant efficiency (Taken from ref. [1])

of the next generation are expected to have more advanced steam conditions. Figure A.3 [1] shows typical efficiency improvements by applying advanced steam conditions.

Boiler Design Features

Table A.1 [1] shows a comparison of boiler types.

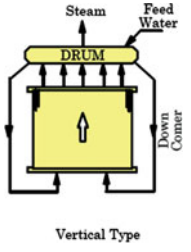
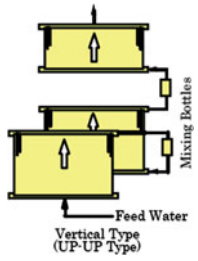
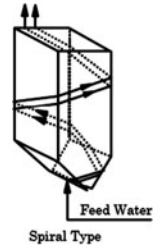
Natural Circulation Boilers

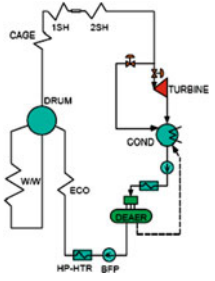
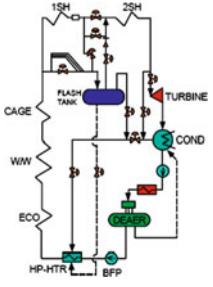
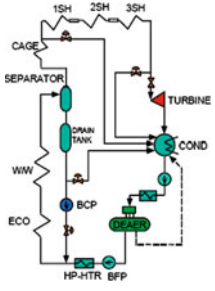
In natural circulation, the gravity acting on the density difference between the subcooled water in the downcomer and the steam-water mixture in the furnace water wall tubes produces the driving force for the circulation flow. Natural circulation is limited in its application to a pressure smaller than around 180 bar in the drum.

Once-Through Boilers (UP: Universal Pressure Boiler for Constant Pressure Operation)

The water pumped into the boiler as subcooled water passes sequentially through all the pressure part heating surfaces, where it is converted to superheated steam as it absorbs heat. There is no recirculation of water within the unit and, for this reason,

Table A.1 Boiler types and furnace construction (Taken from ref. [1])

	NC boiler	UP boiler	Benson boiler
Furnace construction			
Operating pressure	Subcritical (constant or sliding)	Subcritical or supercritical (constant pressure)	Subcritical to supercritical region (sliding pressure)
Mixing bottles	Mixing bottles are not necessary	Mixing bottles are necessary to reduce effect of heat flux unbalance	Mixing bottles are not necessary by spiral type water wall
Applicable steam pressure	Subcritical	Supercritical & subcritical	Supercritical & subcritical
Through furnace	Self balance	Base	Much better
Enclosure tubes	Better	Base	Much better
Fluid stability	Approx. 13%	100%	100%
Temperature uniformity	Yes	No	Wide range
Mass flow rate Variable pressure?			
Allowable min. load (%)	15	35–34	25–35 (OT Mode) 15 (Circ. Mode)
Load change rate	Base	Slightly higher	Higher
Startup time (min.) (hot start)	120–150 with TB by pass	250	120–150 with TB by pass

Furnace enclosure	Vertical	Vertical	Spiral
Construction	57.0–63.5	22.5–31.8	31.8–38.1
Tube O/D (mm)			
Max. unit capacity in operation (MW)	800	1,300	1,000
Furnace construction			
Startup bypass system	• Not installed • Operation of drain valves and vent valves in necessary	• Main valve is installed in the main steam line • Shift operation of startup valves in necessary • Operation of drain valves and vent valves is necessary	• Simplified startup bypass system • Shift operation of startup valves is not necessary • Operation of drain valves and vent valves is necessary
Heat loss during startup	• Continuous blowing (in case of bad water quality)	• Warming of startup bypass system	• Warming of startup bypass system • Heat recovery of circulated water by BCP

NC natural circulation, *OT* once through, *Circ* circulation, *O/D* outside diameter

a conventional drum is not required to separate water from steam. Firing rate, feedwater flow, superheater division valves, and turbine throttle valves are coordinated to control steam flow and pressure. Superheater steam temperature is controlled by coordinating firing and pumping rate.

This boiler is designed to maintain a minimum flow inside the furnace water wall tubes to prevent tube overheating during all operating conditions. This flow must be established before startup of the boiler. A bypass system, integral with the boiler, turbine, condensate, and feedwater system, is provided.

Once-Through Boilers (Benson Boilers for Sliding Pressure Operation)

Benson type boilers have been developed and designed for variable pressure operation plants of high efficiency at all loads, which is suitable for both base and middle load operations. The startup system consists of a steam/water separator, a boiler circulation pump, and associated piping, which ensures a smooth startup and shutdown of the plant and easy operability.

A spirally wound water wall construction is applied to the furnace to have sufficient mass flow velocity in the water wall tubes under variable loads to prevent departure from nucleate boiling (DNB) and to achieve uniform water temperature distribution at the furnace outlet when operating below critical pressure and without pseudo DNB when operating above critical pressure. All heated water walls will be arranged to have upward fluid flows.

Sliding Pressure Operation

The sliding pressure operation is a control system in which the main steam is controlled by sliding pressure in proportion to the generation output as shown in Fig. A.4 [1]. Steam quality at the turbine inlet can be changed at constant volume flows while keeping the turbine governing valve open.

By the sliding pressure, thermal efficiency of the turbine is improved in partial operating loads though with decreasing thermodynamic efficiency, as follows, in comparison with constant pressure operation.

1. A smaller governing value loss enables improvement of high pressure turbine internal efficiency.
2. Decrease of feedwater pump input.
3. Boiler reheat steam temperature can be maintained at higher levels because of higher temperatures in high pressure turbine exhaust steam.

For a supercritical sliding pressure operation boiler, flow stability through tubes and pipes against various changes in flow characteristics between supercritical and subcritical pressure are important factors.

In addition, combusted flue gas characteristics are necessary to meet environmental requirements.

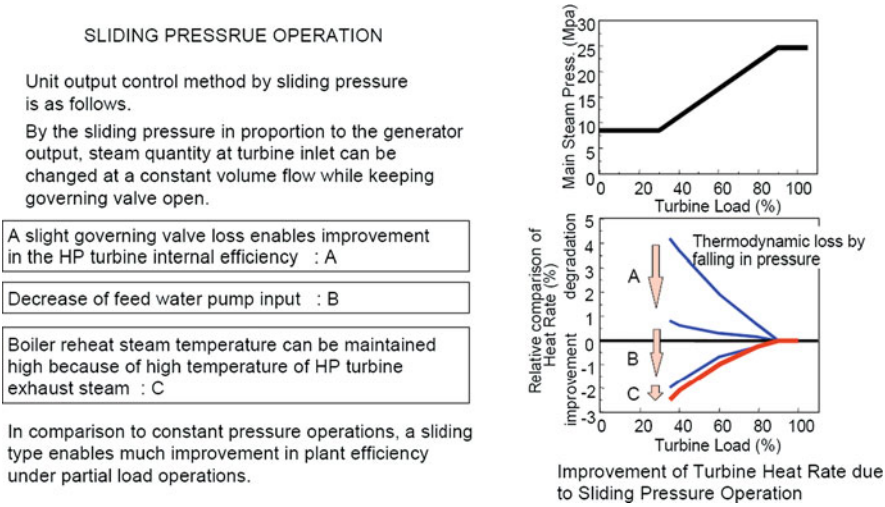


Fig. A.4 Features of coal firing supercritical sliding pressure operation boiler (Taken from ref. [1])

Typical Arrangement of a Benson Boiler

Figure A.5 [1] shows a typical arrangement of the latest large capacity supercritical coal fired Benson boiler. The design features are the following.

(a) The best feature of this Benson type boiler is the spirally wound water wall arrangement at the lower furnace wall. This design, together with an opposed firing system, will result in a very uniform metal temperature profile at the water wall outlet, which makes it possible to carry out reliable operations.
(b) The boiler and furnace walls are suspended from overhead steel work so that the whole expansion of pressure parts is in a downward direction and there is no relative expansion between the furnace walls. The furnace walls are of all-welded membrane construction, which ensures complete gas tightness and saves erection time at the site.
(c) The combusted gas flows upward from the furnace, then turns into the pendant convection passage where pendant superheaters and reheaters are located to absorb the heat from hot gas efficiently. Then the gas flows down through the rear horizontal convection passages.
(d) The primary superheaters and reheaters are located in parallel and horizontal convection passages as along with economizers, giving a sufficient amount of reheater heating surface in this zone to allow quick responses for steam temperature control by a gas biasing system.
(e) Steam/water separator is positioned at the front side of the boiler. This system is used during startup and shutdown and at loads lower than the minimum once-through load for smooth and reliable operation.

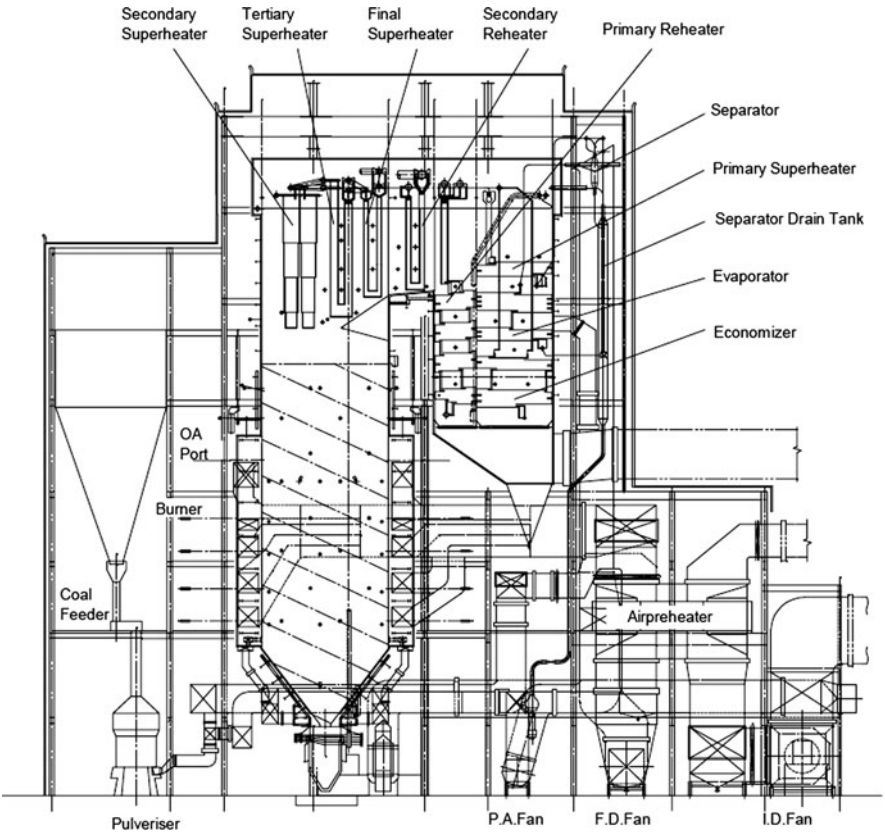


Fig. A.5 Typical arrangement of latest large capacity supercritical coal fired Benson boiler (Taken from ref. [1])

Water Chemistry Guidelines

Characteristics of Water Chemistry in Boilers

Boilers which are applied in thermal power plants are classified roughly into natural circulation type boilers and once-through type boilers.

In natural circulation type boilers, the water system and steam system are divided by a steam drum. Boiler feedwater is preheated at the economizer and fed into a steam drum, then evaporated at the water wall (Evaporator) connected to the steam drum, before coming back to the steam drum as water-steam mixture. Water and steam are separated at the steam drum, then steam is led into superheaters and water is led into the water wall (Evaporator) again. Therefore, impurities of silica, etc., contained in boiler feedwater concentrates during boiler operation. The drum has a blow-down line to avoid concentration with a continuous blow-down to the

boiler exterior. Moreover, sodium phosphate is injected into the drum water to avoid scale adhesion and corrosion. (Some boiler plants have no chemical injection by applying All Volatile Treatment (AVT)).

On the other hand, in a once-through type boiler, boiler feedwater is fed once-through and preheated at the economizer, evaporated water wall and evaporator, superheated at superheater and led to the steam turbine. Therefore, impurities contained within boiler feedwater will deposit inside the evaporator or be carried into the steam turbine. Consequently, once-through type boilers require more severe water quality control than natural circulation type boilers. AVT has been applied as feedwater treatment for all once-through type boiler plants for many years, but Combined Water Treatment (CWT); Oxygen Treatment has been used with good results since about 10 years ago. Since then, water treatment in once-through type boilers has been switched from AVT to CWT in sequence.

Table A.2 [1] shows Hitachi's recommendations on high pressure natural circulation boilers and once-though type boilers.

Application of Low pH Coordinated Phosphate Treatment for Natural Circulation Boilers

Hitachi recommends applying low pH coordinated phosphate treatment for natural circulation boilers as Hitachi's standard for the following reasons. Hitachi has experienced water wall tube explosions that originated in hard zinc scale adhesion. It was thought that zinc dissociated from condensation tubes of copper alloy and deposited on water wall tubes.

Water Treatment Methods in Actual Circumstances

Effects from different water treatment in both kinds of boilers were investigated. Some boilers had accidents due to deposition of hard zinc scale, while other heavy oil burning boilers had no accidents despite having almost the same design. Table A.3 [1] shows the steam pressure and fuel of these boilers and their water treatment methods. Boilers A and B experienced accidents while boiler C had no accidents. In these three boilers, water was treated with volatile matter or the equivalent, but boiler D, using low phosphate treatment, showed no abnormal behavior. Zinc deposition was found in boilers A, B, and C and not in boiler D. Boiler C, particularly, had a large amount of zinc scale. The different effects can be thought of as a key to solving problems of water treatment in boilers.

Chemical Analysis Results of the Scale

Table A.4 [1] shows the analysis results of scale withdrawn from the tubes after a tube explosion of Boiler A (described in Table A.3 [1]). The main component was zinc, approximately 30%; copper and nickel were also contained at nearly 10% each.

Table A.2 Comparison of water treatment methods for boiler plants (Hitachi standard) (Taken from ref. [1])

Item	Treatment	Phosphate treatment	Volatile treatment	Oxygen treatment
	Application	150–200 bar natural circulating boiler Hitachi standard	Once through super critical boiler Hitachi standard	Once through super critical boiler Hitachi standard
Injected chemical	Feed water	N_2H_4	NH_3 & N_2H_4	O_2, NH_3
	Boiler water	Na_2HPO_4 (in case pH is not raised, Na_3PO_4 is also added)	–	–
Water conditioning				
Feed water	pH (at 25°C)	Target 9.4–9.5 (in case all heater tube material is carbon steel)	Target 9.4–9.5 (in case all heater tube material is Carbon steel)	8.0–9.0
	Dissolved oxygen (DO) (ppb)	< 7	< 7	50–150
	Iron Fe (ppb)	< 20	< 10	< 10
	Copper Cu (ppb)	< 5	< 2	< 2
	Hydrazine N_2H_4 (ppb)	10–30	< 10–30	–
	(Cation conductivity (μS/cm at 25°C)	< 0.3	< 0.25	< 0.2 (Target 0.1)
	Silica (SiO_2) (ppm)	–	< 20	< 20
Boiler water	pH (at 25°C)	9.0–9.5	–	–
	Total solid (ppm)	< 10	–	–
	Specific conductivity (μS/cm at 25°C)	< 25	–	–
	Phosphate ion (PO_4^{3-}) (ppm)	1–3	–	–
	Silica (SiO_2) (ppm)	< 0.2	–	–
Remarks		Including PO_4^{3-} in blow down water	1. NH_3 type condensate polishing plant mandatory required 2. Causing pressure drop rise due to wave shape scale	H-OH type condensate polishing plant operation is recommended

Table A.3 Tested boilers (Taken from ref. [1])

Boilers tested	Kind of boilers		Water treatment	Remarks
	S/H outlet press. (MPa)	Burning		
A	17.0	Heavy oil only	Volatile	Tube explosion
B	17.1	Heavy oil only	Volatile or equivalent[a]	Tube explosion
C	17.1	Heavy oil only	Volatile or equivalent[a]	No accident lots of zinc scale
D	17.1	Heavy oil only	Low phosphate	No accident

[a]Low phosphate was said to be used, but in reality it was the same as volatile treatment

Table A.4 Analysis results of boiler a scale (%) (Taken from ref. [1])

Fe	Cu	Ni	Zn	Si	Mn
9	9.5	9.1	30.8	2.6	2.2

Table A.5 Products in pure water and Ammonia water (pH 9.5) after heating Zinc compounds at 350°C for 100 h (Taken from ref. [1])

Initial Composition solution	Zn	ZnO	Zn $(OH)_2$	Zn^{2+}
Pure water	ZnO	ZnO	ZnO	Zn^{2+}
pH 9.5 NH_4OH	ZnO	ZnO	ZnO	ZnO

Zinc Compounds in Ammonia Water

Zinc, zinc oxide, zinc hydroxide, and zinc ions (added as $ZnSO_4$) were treated at 350°C in pure water or in ammonia water (pH 9.5) for 100 h. The reaction products in these experiments were identified by X-ray diffraction patterns and the results are shown in Table A.5 [1]. The reaction products were zinc oxide in every case except for the case of zinc ions in pure water; therefore, the zinc brought into the boiler water must be obtained as zinc oxide in all cases of volatile treatment. This agreed with the fact that in the volatile treatment mentioned in Sect. A.4.2.2, zinc in the scale was mainly present as zinc oxide (a scant portion was present as zinc silicate).

Reaction of Zinc Compounds in Sodium Phosphate Solution

Zinc, zinc oxide, zinc hydroxide, and zinc ions were treated at 350°C for 100 h in sodium phosphate solution (0.5 mol/l concentration). The Na/PO_4 molar ratio was varied from 0 to 3.0. Laboratory experiments gave the following results.

(1) Zinc compounds in high temperature water formed zinc phosphate in sodium phosphate solutions of Na/PO_4 molar ratio <2.0 and zinc oxide in sodium phosphate solutions of molar ratio 2.5 and 3.0.

(2) In the experimental range of 100–350°C, more zinc phosphate was formed at higher temperatures.
(3) In the case of the boiler scale containing zinc, a decrease in the scale by means of low phosphate treatment occurred.

Research Conclusions

For boilers susceptible to zinc deposition, low phosphate treatment using disodium phosphate should be adopted for boiler water treatment rather than volatile matter and trisodium phosphate. As the experiments showed, zinc deposition was not only prevented but also zinc scale already deposited was removed from the tube. Consequently, Hitachi recommended the low-pH coordinated phosphate treatment using disodium phosphate ($Na_2HPO_4 \cdot 12H_2O$).

Doing CWT on Once-Through Type Boilers

In Japan, AVT has been applied as the feedwater treatment for all once-through boiler plants for the last 10 years. In some plants, AVT has been accompanied by problems such as an increased pressure drop in the boiler and scale fouling in the preboiler system. To resolve these problems, CWT was used in the once-through boilers beginning about 10 years ago.

The AVT and CWT are compared in Table A.6 [1].

Observation of Pressure Drop in Boiler

The change of pressure drop in one boiler after CWT was observed and results are shown in Fig. A.6 [1]. Three points were clear.

- Pressure drop increased by 8 bar for 1.5 months with AVT only.
- Pressure drop began to decrease by switching to CWT 1 month later.
- Pressure drop decreased by 8 bar during 10.5 months of operation using CWT.

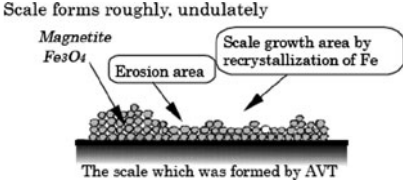
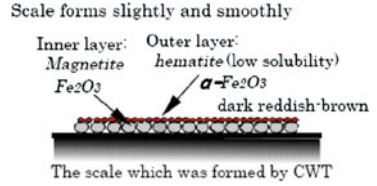
CWT gave satisfactory results, and consequently, water treatment in once-through type boilers has been changed from AVT to CWT in Japan.

Pressure Parts Materials

Materials for Conventional Super Critical Boilers

Table A.7 [1] lists typical materials used for conventional super critical boilers with steam conditions of 24.1 MPa/538°C/566°C and Fig. A.7 [1] shows allowable stresses of the boiler materials. Whether materials for boiler pressure parts are appropriate and economical depends on a number of factors such as material

Table A.6 Comparison of AVT and CWT (Taken from ref. [1])

	AVT	CWT
Outline of method	pH of feed water is raised, and the dissolved oxygen density is brought close to zero. (forming magnetite (Fe_3O_4) scale)	Dissolved oxygen is kept a fixed value and forming coat of low solubility. (forming hematite (Fe_2O_3) scale)
Formation of scale		
Injected chemical	Hydrazine, Ammonia	Oxygen gas, Ammonia
Feed water quality		
pH (at 25°C)	9.4–9.5	8.0–9.0
Dissolved oxygen (ppb)	<7	50–150
Electric conductivity (μS/cm at 25°C)	<0.25	<0.2 (target; <0.1)

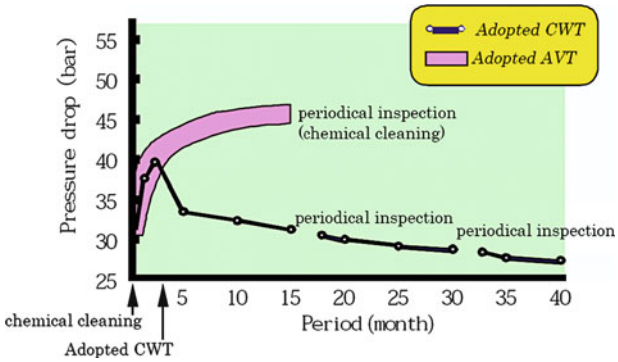


Fig. A.6 Pressure drop change in boiler after CWT was done (Taken from ref. [1])

Table A.7 Typical materials for conventional supercritical boiler (Taken from ref. [1])

Pressure part		Steam conditions: 24.1 MPa/538°C/566°C	
		Metal temperature (°C)	Materials
Tubing	Economizer	300–350	Carbon steel (STB510)
	Furnace wall	350–500	0.5Mo (STBA13) 0.5Cr0.5Mo (STBA20) 1Cr0.5Mo (STBA22)
	Superheater	450–590	0.5Mo (STBA13) 0.5Cr0.5Mo (STBA20) 1Cr0.5Mo (STBA22) 2.25Cr1Mo (STBA24) 18Cr10NiTi (SUS321HTB)
	Reheater	350–610	Carbon steel (STB340) 0.5Mo (STBA13) 1Cr0.5Mo (STBA22) 2.25Cr1Mo (STBA24) 18Cr10NiTi (SUS321HTB)
Header piping	Superheater header Main steam pipe	550	2.25Cr1Mo (STPA24)
	Reheater header hot reheat pipe	570	2.25Cr1Mo (STPA24, SCMV4)

strength properties, corrosion resistance, and metallurgical stability. Therefore, it is necessary to choose the optimum steel, considering these factors at anticipated metal temperatures.

As data of Fig. A.7 [1] show, carbon steel (STB510) has a tendency to undergo graphitization (seen as a drop in allowable stress) at temperatures over 426°C, and it is safe and prudent to restrict its service use to a temperature limit of this value. Consequently, at these higher temperatures, molybdenum steels are commonly used for tubing and piping. For greater resistance to graphitization under prolonged usage, the best material is chromium-molybdenum steel.

Dry steam is delivered to the superheater from the furnace wall at temperatures ranging up to about 450°C. As the steam passes through the tubes, it may be

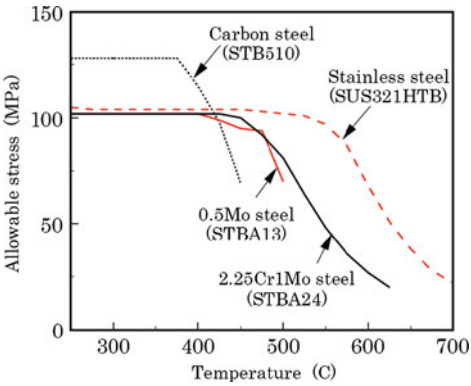


Fig. A.7 Allowable stresses of boiler materials (Taken from ref. [1])

superheated to the final temperature of about 590°C. To assure long life required for satisfactory superheater design, the steel used must meet such requirements as resistance to creep rupture and resistance to corrosion by steam and flue gas, at the anticipated operating temperatures.

To establish an adequate margin of safety and length of service life, these characteristics of the steel must be given due consideration in design. Economy dictates that the lowest cost alloy with properties suitable to the conditions should be used, stepping up from carbon steel to molybdenum steel and to chromium-molybdenum steel as temperatures increase. For metal temperatures approaching about 550°C, lower alloy ferritic steels up to and including 2.25% chromium are usually adequate. Stainless steels are used at higher temperatures, where conditions require an increase in resistance to corrosion and oxidation. Stainless steel tubes have a higher carbon content in order to increase creep rupture strength. In spite of the sensitization due to the higher carbon content during use in elevated temperature service, no stress corrosion cracking has been experienced in the stainless steel tubes. This may be related to the fact that the inside surface of the tubes contacts with dry steam.

The steam headers and pipes connecting the boiler and turbine are highly important components of the power plant. Such piping should be properly designed and installed to absorb thermal expansion and vibratory stresses. Stainless steel pipes had been used in power plants and serious cracking problems, which were caused by high thermal stresses due to higher thermal expansion coefficients of the materials, were experienced under service conditions. Therefore, these thick-walled components should be fabricated using ferritic steel whose thermal expansion coefficient is relatively low.

Materials for the Advanced Super Critical Boiler

There are strong environmental and economic demands to increase the thermal efficiency of coal fired power plants. This has led to a steady increase in steam temperatures and pressures resulting in advanced super critical plants. To meet the

requirements of such plants, it is necessary to develop suitable materials for high temperature components. Research and development of high temperature materials has been carried out in Japan, Germany, the UK, and the USA. Development progress on ferritic chromium-molybdenum steel pipes and austenitic stainless steel tubes is shown in Figs. A.8 [1] and A.9 [1].

Figure A.10 [1] shows a comparison of allowable stresses between conventional and advanced chromium-molybdenum steel pipes. For high temperature headers and pipes of superheaters and reheaters, STPA28 (Mod.9Cr1Mo) developed by Oak Ridge National Laboratories is suitable because of its high temperature strength and

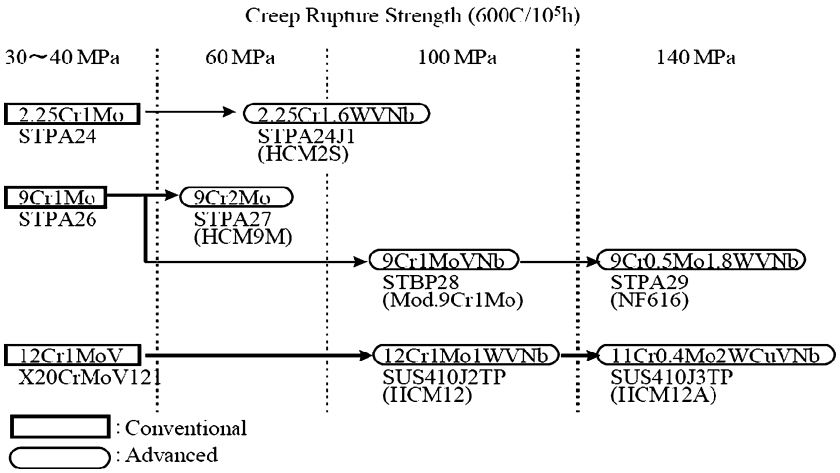


Fig. A.8 Development progress of Ferritic CrMo steel pipes (Taken from ref. [1])

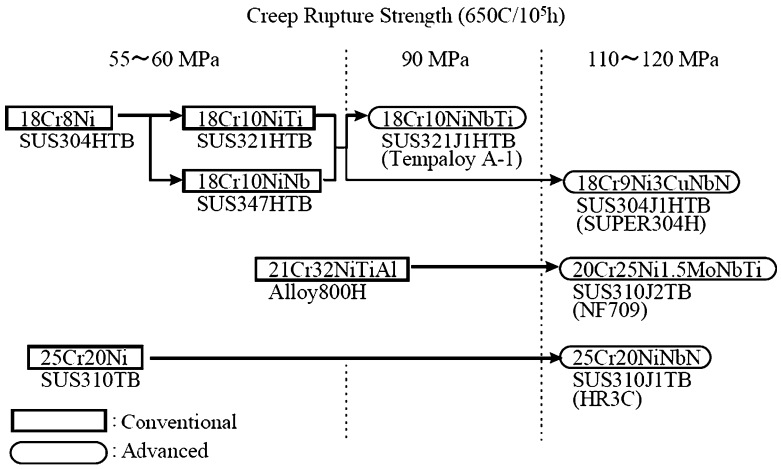


Fig. A.9 Development progress of Austenitic stainless steel tubes (Taken from ref. [1])

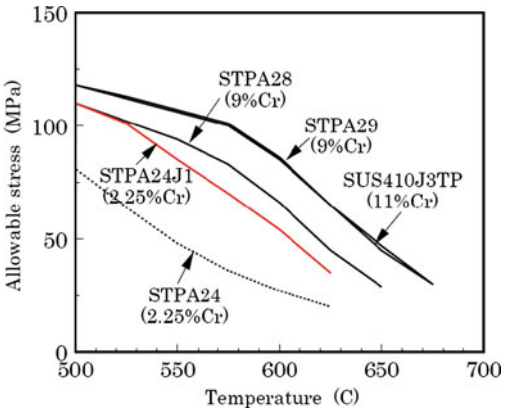


Fig. A.10 Comparison of allowable stresses between conventional and advanced CrMo steel pipes (Taken from ref. [1])

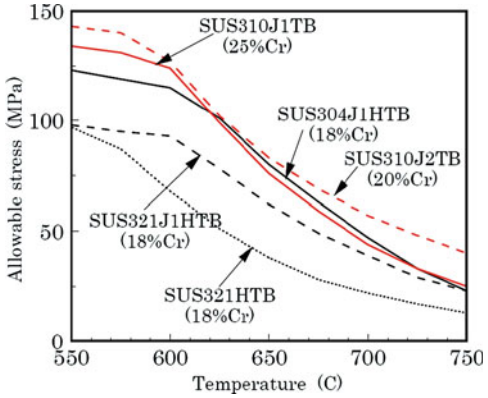


Fig. A.11 Comparison of allowable stresses between conventional and advanced stainless steel tubes (Taken from ref. [1])

excellent resistance to oxidation. Since the late 1980s, this steel has been widely used in Japan and Europe for advanced power plants with the steam conditions of about 25 MPa/600°C/600°C. STPA29 (NF616) developed by Nippon Steel and SUS410J3TP (HCM12A) developed by Sumitomo Metal have higher creep strengths than that of STPA28, and these steels have been used for advanced power plants with steam conditions of 25MPa/600°C/610°C.

Figure A.11 [1] shows a comparison of allowable stresses between conventional and advanced stainless steel tubes. Newly developed austenitic stainless steels such as SUS304J1HTB (SUPER304H) developed by Sumitomo Metal and SUS310J2TB (NF709) developed by Nippon Steel have extremely high creep rupture strength and the allowable stresses are twice as high compared to SUS321HTB at 650°C. These steels have been applied to high temperature superheater tubes. For severe corrosion loads SUS310J3TB (HR3C) developed by Sumitomo Metal can be used because of its higher chromium content.

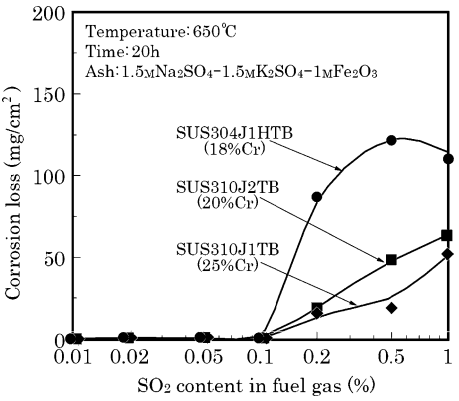


Fig. A.12 Effect of SO_2 content on coal ash corrosion loss of stainless steel tubes (Taken from ref. [1])

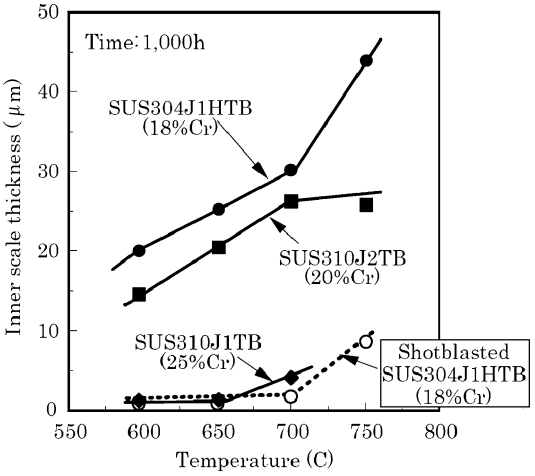


Fig. A.13 Effect of temperature on steam Oxide scale of stainless steel tubes (Taken from ref. [1])

Another problem to take into consideration when selecting materials for high temperature tubing is the resistance to coal ash corrosion caused by sulfur in coal. Figure A.12 [1] shows the effect of SO_2 content on corrosion loss. At SO_2 content of 0.1% (corresponding to about 1% sulfur in coal) or less, corrosion loss is negligible for austenitic stainless steels containing 18% chromium. When the sulfur content of coal is around 5% (corresponding to about 5% SO_2 in fuel gas), it is necessary to use a high-chromium austenitic stainless steel such as SUS310J1TB (HR3C).

Figure A.13 [1] shows the effect of steam temperatures on steam oxide scale thickness. With increasing steam temperatures, materials with an improved steam oxidation resistance have to be used for superheater and reheater tubes. Spalled steam oxide scales have the potential to plug steam flows and erode turbine components. Using high chromium content or fine grained stainless steel tubes is

effective to minimize steam oxidation problems. Figure A.13 [1] also shows that shot-blasted stainless steel tube containing 18% chromium has the same resistance to steam oxidation as high chromium stainless steel at temperatures up to 700°C.

The welding procedures for these advanced tubing and piping materials have been established. Figure A.14 [1] shows macro structures of tungsten inert gas (TIG) welds of tube materials. Figure A.15 [1] shows the macro structures of

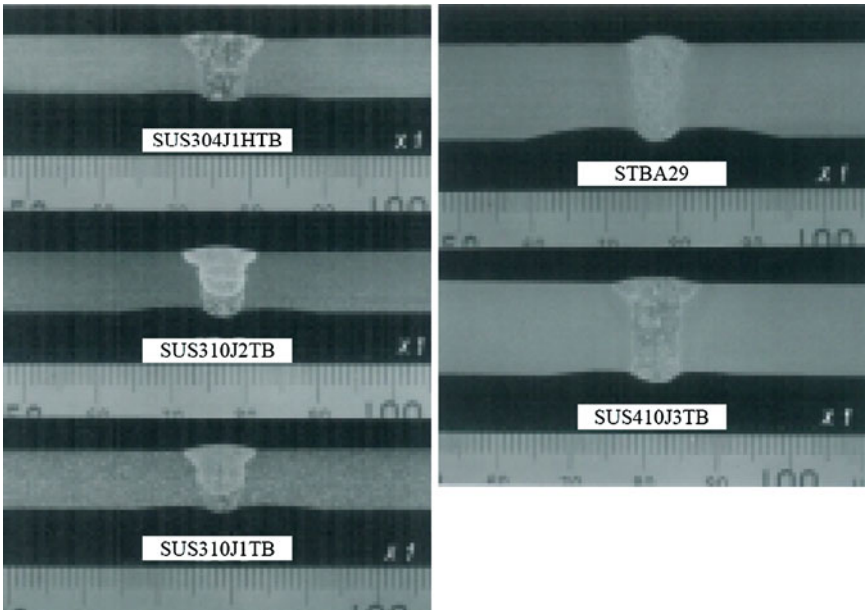


Fig. A.14 Macro structures of TIG weld of tube materials (Taken from ref. [1])

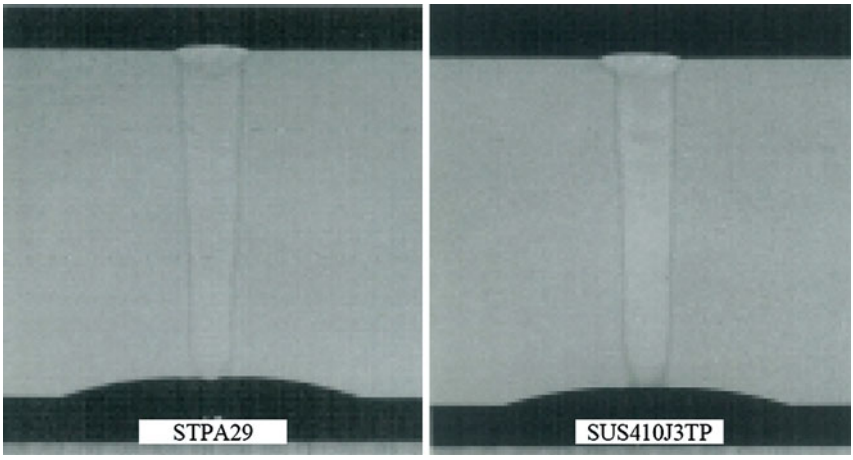


Fig. A.15 Macro structures of narrow gap TIG weld of pipe materials (Taken from ref. [1])

narrow gap TIG welds of thick walled pipe materials. Narrow gap TIG welding process, which was developed by Babcock-Hitachi K.K., is suitable for welding 9–10% chromium thick-walled steel pipes.

Summary

Advances in the steam conditions that are used in plants have played a key role in meeting increased electricity demands while reducing pollutant emissions and keeping up with global trends for improved efficiency of power plants.

Appendix A is based on Ref. [1].

References

1 J. Matsuda, N. Shimono and K. Tamura, "Supercritical Fossil Fired Power Plants-Design and Developments," *Proc. 1st Int. Symp. on SCWR,* Tokyo, Japan, November 6–8, 2000, Paper 107 (2000)
2 J. Matsuda and K. Saito "Low grade coal firing super critical sliding pressure operation boiler," *Proc. 2nd Int. Sym. on Clean Coal Technology*, November 8–10, 1999
3 K. Sakai and S. Morita, "The design of a 1000MW coal-fired boiler with the advanced steam conditions of 593°C/593°C," *Transactions of IMechE*, Vol. 1997-2, 155–167 (1997)
4 STEAM its q and use: Babcock & Wilcox Company
5 ASME Boiler & Pressure Vessel Code, Part D Properties (1998)
6 T.C. McGough, J.V. Pigford, P.A. Lafferty, S. Tomasevich, et al., "Selection and Fabrication of Replacement Main Steam Piping for the Eddystone No. 1 Supercritical Pressure Unit," *Welding Journal*, Vol. 64(1), 29–36 (1985)
7 K. Miyashita, "Overview of advanced steam plant development in Japan," *Transactions of IMechE*, Vol. 1997-2, 17–30 (1997)
8 K. Muramatsu, "Development of Ultra-Super Critical Plant in Japan," *Advance Heat Resistant Steels for Power Generation*, EPRI Conference Pre-Print, April 27–29, 1998 (1998)

Appendix B: Review of High Temperature Water and Steam Cooled Reactor Concepts

Introduction

High temperature water and steam cooled reactors were studied in the 1950s and 1960s as one of a variety of reactor concepts. After being ignored in the 1970s and 1980s, new supercritical-pressure reactor concepts emerged in the 1990s from Japan, Russia, and Canada as innovative water cooled reactors. There is no difference between water and steam at supercritical pressure, but low density water above a pseudo-critical temperature is called "steam." A steam cooled reactor is defined as having steam, not water, as the core inlet coolant. It requires steam blowers and huge heating of the feedwater.

In this appendix, a brief summary is provided on the design concepts of supercritical pressure reactors (SCRs), which are cooled either by water or "steam," nuclear superheaters, and steam cooled fast reactors from the 1950s to the mid 1990s.

The high temperature water and steam cooled reactor concepts are summarized under the following groupings. Some views and comments on the past concepts are also included.

1. Supercritical pressure reactors
2. Nuclear superheaters
3. Steam cooled fast reactors

Supercritical Pressure Reactors

The following reactor concepts are found in the literature.

WH:

- Water moderated, supercritical steam cooled reactor (1957)
- Once-through, graphite moderated, supercritical light water cooled pressure-tube-type SCOTT-R (1962)

- Indirect cycle, supercritical light water cooled and moderated SC-PWR (1966)

GE:

- Once-through, heavy water moderated, supercritical-pressure light water cooled pressure-tube-type reactor (1959)

The University of Tokyo:

- Once-through supercritical-pressure light water cooled (moderated) reactors with reactor pressure-vessel (RPV), SCLWR, and SCFR (early version of Super LWR and Super FR) (1992)

Kurchatov Institute:

- Natural circulation, integrated SC-PWR, B-500SKDI (1992)

AECL:

- Supercritical pressure CANDU, CANDU-X (1998)

Both WH and GE studied the concepts of SCRs in the late 1950s [1]. The concepts were reviewed by Argonne National Laboratory (ANL) in 1960 [2].

Water Moderated, Supercritical Steam Cooled Reactor (WH, 1957)

The basic fuel assembly of the WH concepts is shown in Fig. B.1 [3]. It consists of seven close-packed rods surrounded by a double tube shroud. Each fuel rod consists

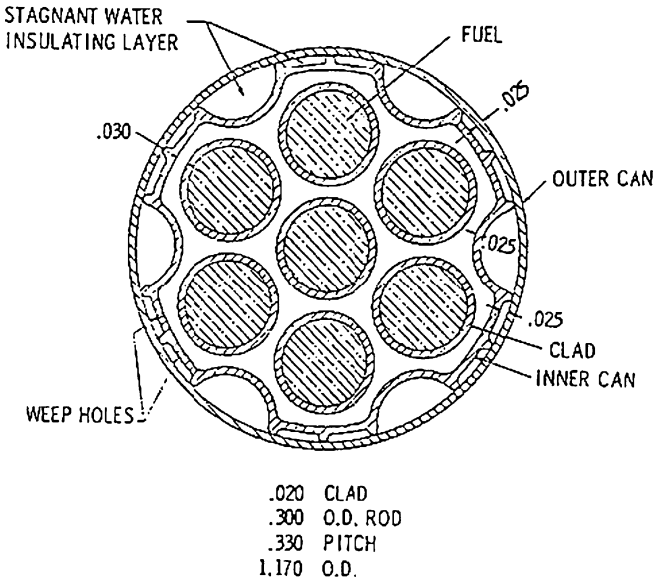


Fig. B.1 Fuel assembly of supercritical steam cooled reactor (WH) (Taken from ref. [3])

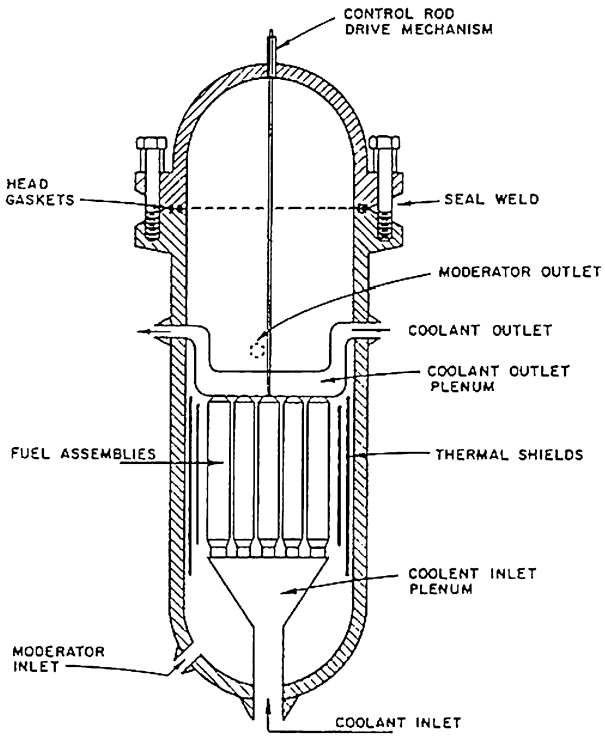


Fig. B.2 Pressure vessel and core of supercritical steam cooled reactor (WH) (Taken from ref. [3])

of uranium oxide pellets clad in stainless steel. The reactor core and vessel arrangement envisioned are shown in Fig. B.2 [3]. There are two flows within the reactor vessel. Low temperature (260°C) high density water is used for moderator. High temperature supercritical steam cools the fuel assemblies in the tubes. The direct cycle, the throttled direct cycle (Fig. B.3 [3]), and indirect cycle (Fig. B.4 [3]) were all considered in the study. Because of the rapid change of physical properties with temperatures, the designers decided to avoid having the coolant water pass through the critical point in the reactor. This was based on the fear that this would promote instabilities in flow, heat transfer, and reactivity. This decision led to undue complications in all cycles. The review by ANL concluded that the concern about instability was overestimated by the designers, since BWRs had already demonstrated stable operation under conditions considerably worse than property changes of supercritical water. Because of the fear of radioactivity deposition in the secondary system of a direct cycle plant, an indirect cycle was chosen for the plant by WH. The reactor power is substantially smaller, 21.1 MWe than in current ones as seen in Table B.1 [3]. The thermal efficiency is low, 30.3% due to the indirect cycle. The reactor internals are very complex for the indirect cycle design because of many tubes in the RPV.

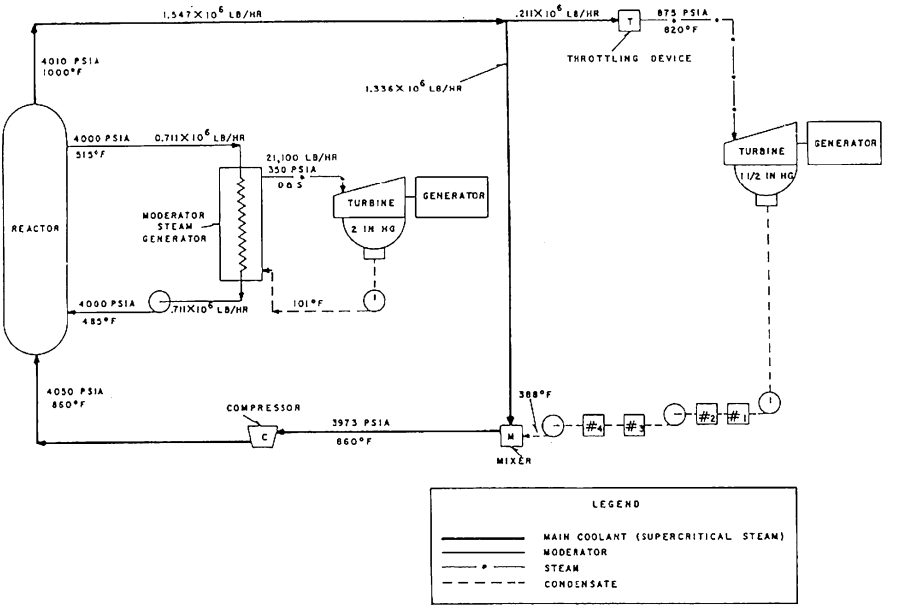


Fig. B.3 Schematic flow diagram of supercritical steam cooled reactor, throttled direct cycle (WH) (Taken from ref. [3])

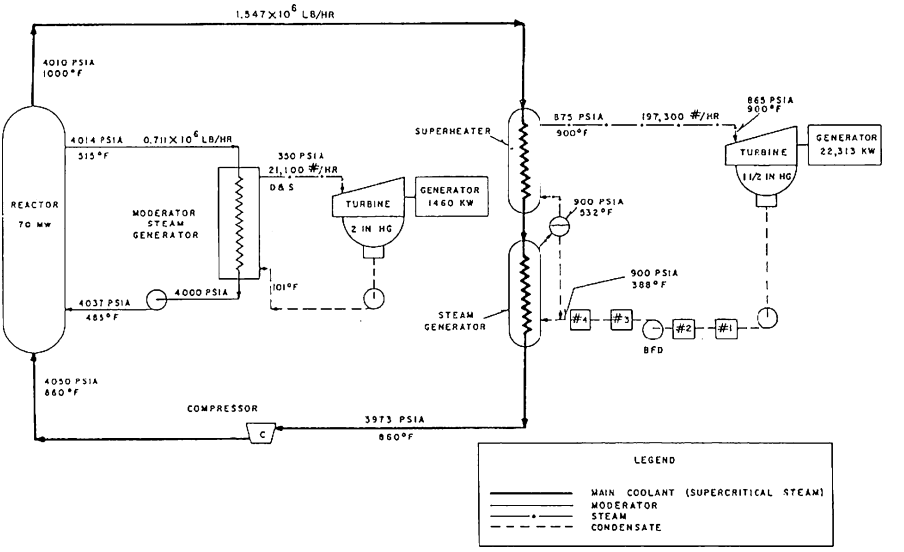


Fig. B.4 Schematic flow diagram of supercritical steam cooled reactor, indirect-cycle (WH) (Taken from ref. [3])

Table B.1 Characteristics of supercritical pressure reactors (Taken from ref. [3])

Reactor type	WH thermal	GE thermal	SCOTT-R thermal	B-500SKDI thermal
System pressure (MPa)	27.6	37.9	24.1	23.5
Reactor power (thermal/electric) (MW)	70/21.2	300/–	2,297/1,010	1,350/515
Thermal efficiency (%)	30.3	~40	43.5	38.1
Coolant temperature (at outlet) (°C)	538	621	566	~380
Primary coolant flow rate (kg/s)	195	850	979	~2,700
Core height/diameter (m)	1.52/1.06	3.97/4.58	6.1/9.0	4.2/2.61
Fuel material	UO_2	UO_2	UO_2	UO_2
Cladding material	SS	Inconel-X	SS	Zr-alloy or SS
Fuel rod diameter/pitch (cm)	0.762/ 0.8382	10.3/–	10.5/–	0.91 or 0.85/1.35
Cladding thickness (cm)	0.051	–	–	~0.069 or ~0.039
Moderator	H_2O	D_2O	Graphite	H_2O

SS stainless steel

Under current LWR design standards, bottom mounted inlet coolant pipes are not allowed from LOCA considerations. The inlet coolant compressors are necessary. These are larger in capacity and power consumption than feedwater pumps of LWRs, because of the low density of the high temperature supercritical steam. These factors finally led to a loss of interest in developing the water moderated, supercritical steam cooled reactor.

Heavy Water Moderated, Light Water Cooled, Once-Through Pressure-Tube Type Reactor (GE Hanford, 1959)

A conceptual design of a heavy water moderated once-through pressure-tube type reactor was described in a US Atomic Energy Commission (AEC) report from Hanford Laboratories carrying the name of GE [1]. An artist's conception of the plant is shown in Fig. B.5 [3]. The reactor consists of a cylindrical tank. It contains 300 vertically suspended fuel element thimbles. The reactor tank serves as a container for the heavy water moderator and reflector. The flow system arrangement for the reactor and auxiliaries is shown in Fig. B.6 [3]. The light water primary coolant passes through the reactor four times during each cycle through the flow system. In two passes through the reactor, the fluid is heated to 621°C and 37.9 MP and is then fed into a steam-reheat heat exchanger. The coolant enters a second steam reheat exchanger following a third reactor pass. After a fourth pass through the reactor, water enters the supercritical turbine. The high operating conditions of coolant temperature and pressure were chosen on the basis of their use in the Philo Unit 6 supercritical pressure fossil fuel-fired power plant, which started operation in

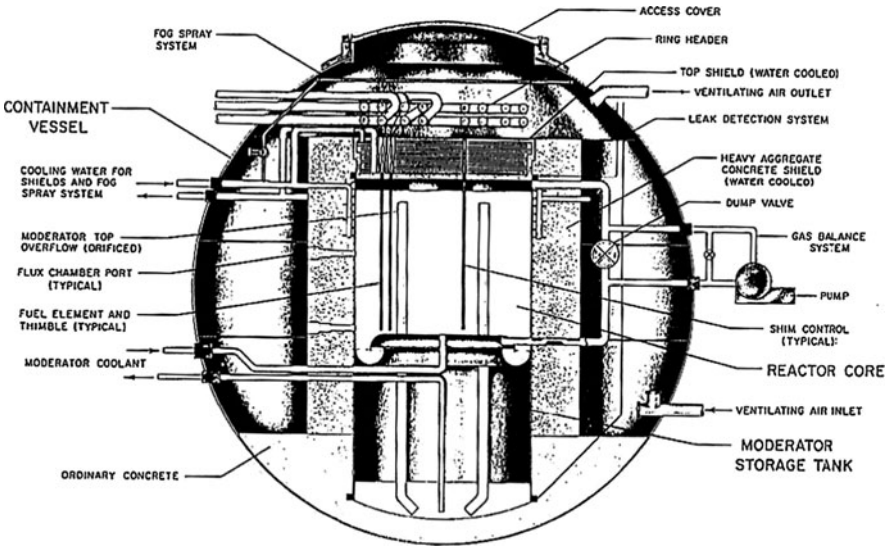


Fig. B.5 Supercritical pressure power reactor (GE) (Taken from ref. [3])

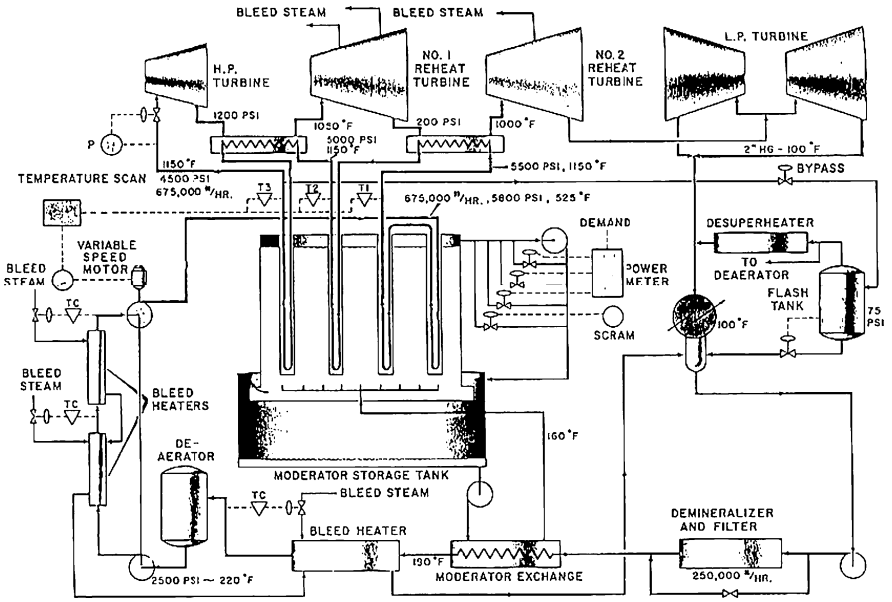


Fig. B.6 Flow and system arrangement of supercritical pressure power plant (GE) (Taken ref. [3])

the 1950s. The fuel element assemblies are internally cooled UO_2 elements. The fuel element arrangement is shown in Fig. B.7 [3]. Each element contains 12 axial coolant channels. The coolant flows downward in six of the tubes and returns in the

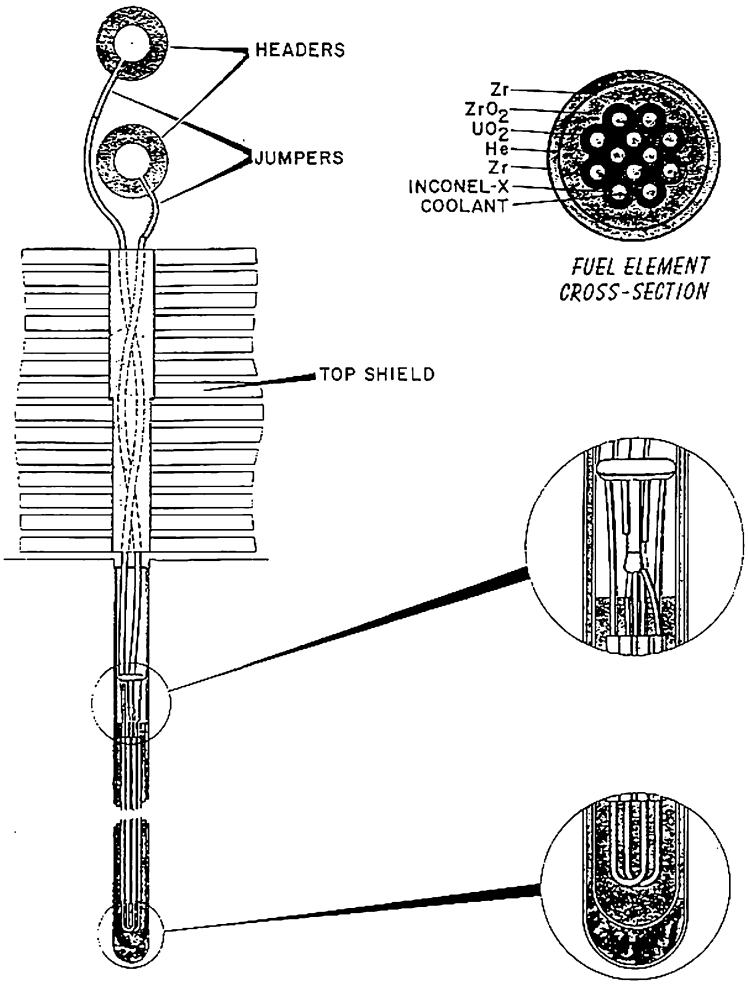


Fig. B.7 Fuel element arrangement (GE) (Taken from ref. [3])

other six. To restrict the heat transfer from the fuel to moderator, zirconia is provided between the fuel elements and an outer Zircaloy can. Inconel-X tubing was used for the internal jacket. Refueling is accomplished by lifting circular header and attached fuel elements as a single assembly from the reactor and moving them into a storage basin. The ANL review described that operation of the supercritical water reactor on the direct cycle offered the highest probability for achieving economic power generation and that the major gap in supercritical water technology pertaining to a reactor system was the lack of information on the magnitude of the problems of radioactivity deposition in the external system and of the buildup of internal crud under irradiation. Eddystone and Philo were the first supercritical boilers in USA. They operated at higher pressure and temperature than current ones.

SCOTT-R, Once-Through, Graphite Moderated, Light Water Cooled Tube Reactor (WH, 1962)

In 1963, WH completed a design study for a 1,000 MWe central station plant under AEC contract. A series of reports (WCAP-2042, 2056, 2120, 2222, 2240, 2647, 2703, 3374) were published between 1962 and 1968 from WH. The concept selected was the Supercritical Once-Through Tube Reactor (SCOTT-R), a direct cycle, pressure tube, thermal reactor with graphite moderator. Figure B.8 [3] shows an artist's conception of the reactor. A schematic flow diagram is shown in Fig. B.9 [3]. It is equipped with several hundred vertical pressure tubes, containing fuel and coolant and penetrating the moderator block. The graphite moderator-pressure tube complex is contained in a low pressure tank, which maintains a helium environment. It is cooled separately by circulating helium. The reactor is fueled with UO_2 clad with austenitic stainless steel. The heat transfer system is of the once-through type where feedwater is introduced into the core and is heated continuously until it emerges as 1,150°F (556°C) steam. The coolant is collected in heads and then taken directly to the turbine. The fuel may be in the form of either annular rings or rod bundles. The SCOTT-R design employs the former ring fuel assembly with coolant flow progressing in four consecutive passes from outside to the center of the fuel

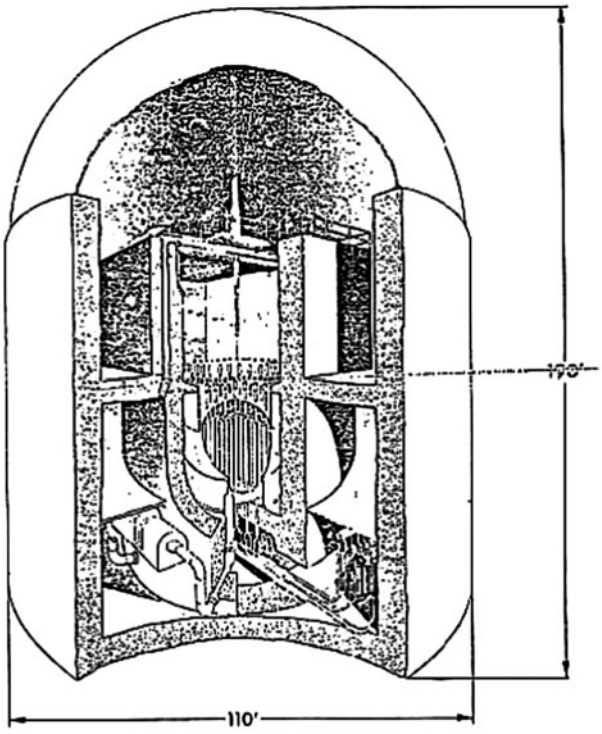


Fig. B.8 1,000 MWe SCOTT-R (WH) (Taken from ref. [3])

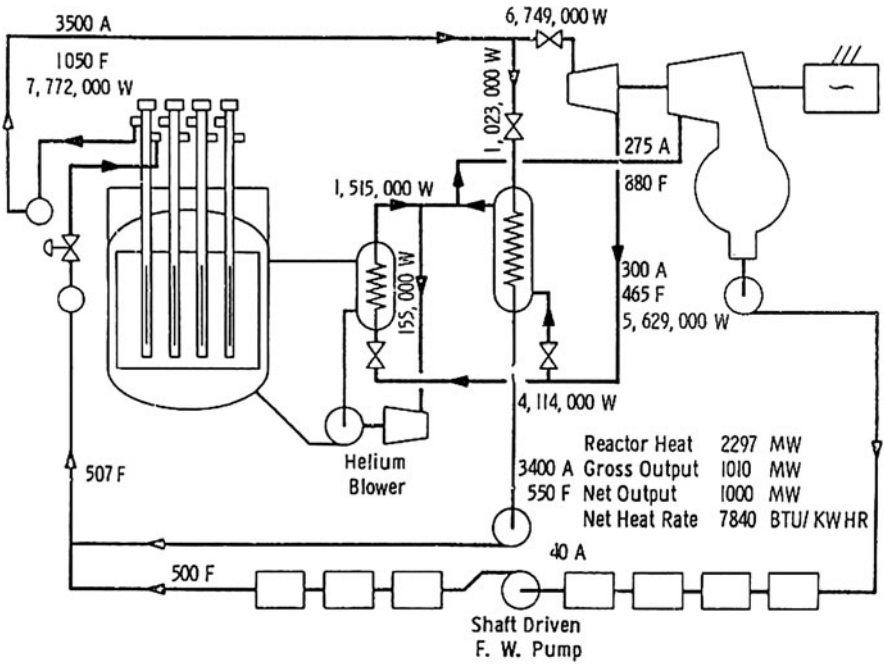


Fig. B.9 Schematic flow diagram of SCOTT-R (Taken from ref. [3])

assembly. This arrangement, which is shown in Figs. B.10 [3] and B.11 [3], provides the high mass flow rate necessary for good heat transfer performance and meets the requirements of maintaining the pressure tube operation temperature at a satisfactory level. The collapsed cladding is provided on each surface of UO_2 fuel. The reactor characteristics are seen in Table B.1 [3]. The reactor electric power is 1,010 MW. The dimensions of the core are large due to the low power density of the graphite moderated core. The research program of supercritical water cooled reactor technology by WH was funded by the USAEC for several years in the 1960s. A supercritical water cooled in-pile fuel testing loop was constructed in the Saxton Reactor for irradiating collapsed clad fuel elements in a reactor environment. But the program was suspended in April 1965, just 3 weeks after shakedown of the loop [4]. WH was also studying the feasibility of the 1,000 MWe PWR at that time with financial support from AEC. WH decided to pursue a way to increase the power of PWRs by standardization for commercialization.

SC-PWR: Indirect-Cycle, Supercritical-Pressure PWR (WH)

The concept of SC-PWR, an indirect cycle supercritical light water cooled and moderated reactor with a reactor pressure vessel is described briefly in reference [5]. It is an 800 MWe two-loop supercritical pressure PWR as shown in Fig. B.12 [3].

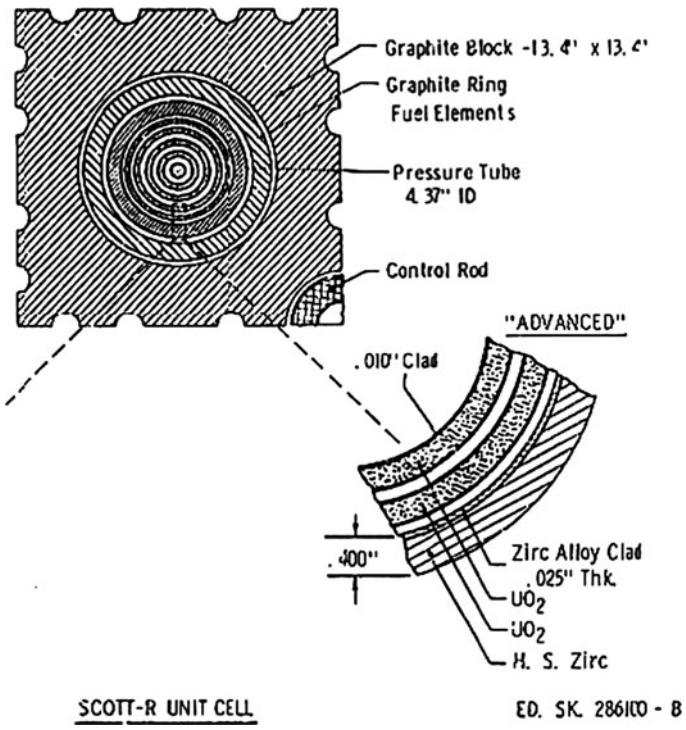


Fig. B.10 SCOTT-R unit fuel cell (Taken from ref. [3])

It is similar to the present day PWRs. It incorporates an open lattice, single-pass core operating in a thermal neutron spectrum. An inert gas pressurizer is provided to accommodate large volume change of supercritical water with temperature.

SCLWR and SCFR: Light Water Cooled (Moderated) Once-Through Reactor with RPV (the University of Tokyo, 1992)

Design concept of light water cooled reactors operating at supercritical pressure with once-through cycle was developed at the University of Tokyo [6,7]. Both the thermal reactor, SCLWR and the fast reactor, SCFR and their high temperature versions SCLWR-H and SCFRH were developed. Many water rods are introduced in the fuel assembly of the thermal reactor for moderation. The reactor and plant system are shown in Fig. B.13 [3]. Roughly speaking, the reactor pressure vessel (RPV) and control rods are similar to those of PWRs, the containment and engineered safety features are similar to those of BWRs and the balance of plant is similar to supercritical fossil fuel-fired power plants. The RPV wall is cooled by inlet coolant (280°C) as in PWRs. This is an advantage for RPV strength in spite of

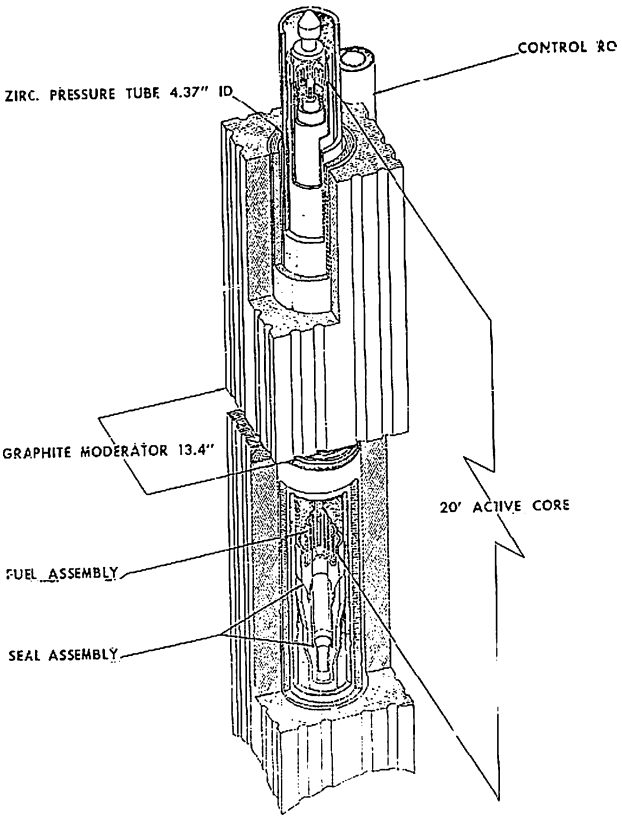


Fig. B.11 SCOTT-R fuel assembly (Taken from ref. [3])

the high outlet coolant temperature. The safety requirement of the once-through reactor was developed and was to monitor the "coolant flow rate" instead of the "water level" as in LWRs. Safety criteria were developed referring to those of LWRs.

The coolant flow rate of the once-through reactor is inevitably small because of no recirculation coolant. That gave rise to a difficulty in optimizing between thermal hydraulic and neutronic core designs when taking similar criteria such as the MCHFR of LWRs for transients. The coolant flow velocity in the fuel assembly was too low to remove heat effectively in the normal fuel lattice. It was not possible to take high enthalpy rise and low flow rate in the design. But the method and the database of heat transfer coefficients were developed to evaluate the cladding temperature directly during transients when heat transfer deterioration occurs. This made it possible to utilize the advantage of high enthalpy rise of the once-through SCR. High temperature reactors, SCLWR-H, SCFR-H, were designed based on this improvement. The core coolant flow rate of the supercritical once-through cycle is approximately one-eighth that of LWRs due to the high enthalpy

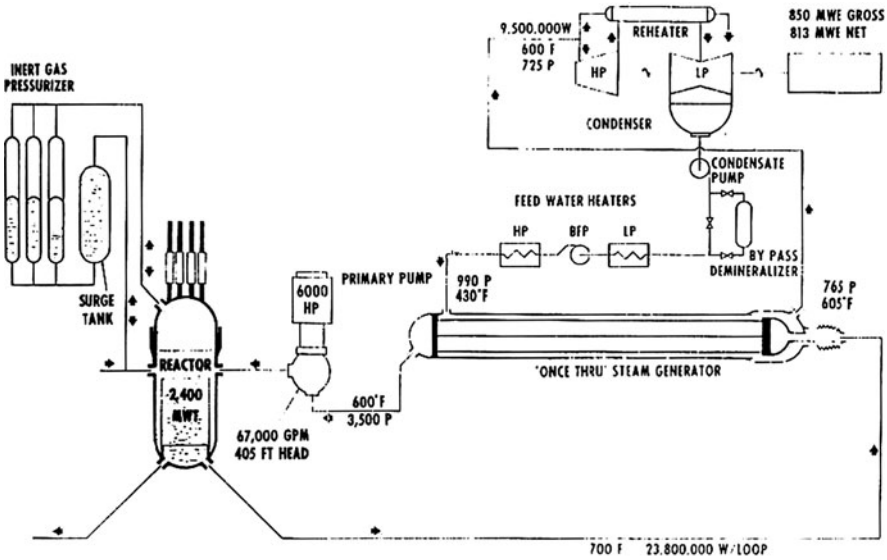


Fig. B.12 800 MWe two-loop SC-PWR (WH) (Taken from ref. [3])

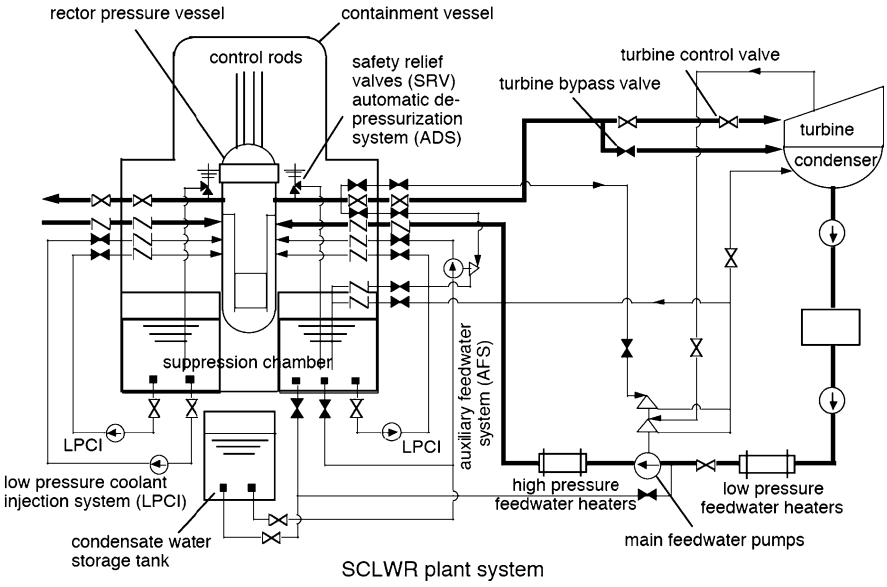


Fig. B.13 SCLWR plant and safety system (Taken from ref. [3])

rise in the core. The whole coolant enthalpy inside the containment is one-fourth of that of an ABWR because of the smaller vessel of the SCLWR-H or SCFR-H that eliminates recirculation and steam-water separation systems. The comparison of containment vessels is shown in Fig. B.14 [3]. The plant characteristics are compared with ABWR, PWR and supercritical fossil fuel-fired power plants in Table B.2 [3].

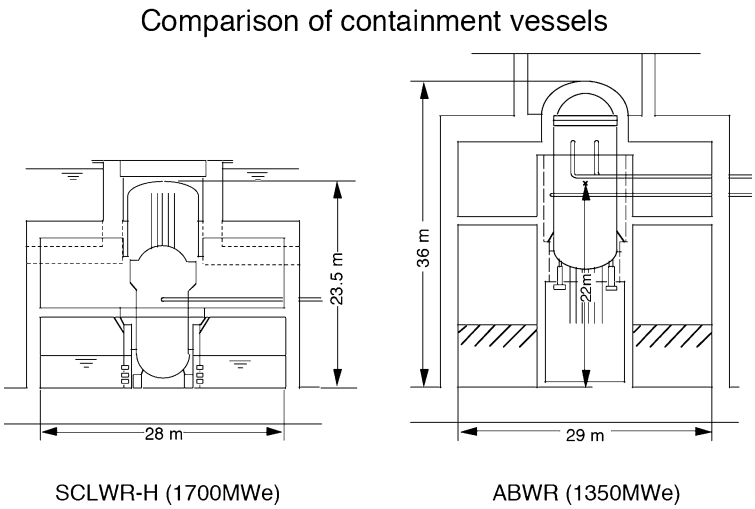


Fig. B.14 Comparison of containment vessels (Taken from ref. [3])

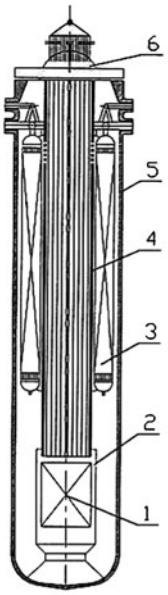
Table B.2 Comparison of plant characteristics (Taken from ref. [3])

	ABWR	PWR	Supercritical fossil-fired power plant	Supercritical watercooled reactor SCLWR-H
Coolant system	Direct-cycle with recirculation	Indirect-cycle	Once-through direct-cycle	Once-through direct-cycle
Electric power (MW)	1,350	1,150	1,000	1,700
Thermal efficiency (%)	34.5	34.4	41.8	44.0
Primary pressure (MPa)	7.2	15.5	24.1	25
Inlet/outlet temperature (°C)	269/286	289/325	289/538	280/508
Coolant flow rate (t/s)	14.4	16.7	0.821	1.97
Coolant flow rate/power (kg/s/MWe)	10.6	14.5	0.821	1.19

The fast reactor, SCFR adopted a tight fuel lattice with light water cooling. The supercritical once-through cycle is more compatible with a tight lattice core than LWRs due to the small core coolant flow rate, pumping power, and stability. The negative reactivity at coolant loss was achieved by inventing the zirconium-hydride layer concept, according to which a thin zirconium hydride layer between the seed and blanket was placed. Fast neutrons at voiding are moderated through the layer and absorbed in the blanket. The neutron balance of the reactor becomes negative at voiding. The plant system of the fast reactor is the same as that of the thermal reactor. The power density of SCFR is higher than that of SCLWR. This means that the fast reactor will be more economical than the thermal reactor when MOX fuel is available at reasonable cost. The features of the research, although only conceptual, have covered almost all aspects of the feasibility assessment in nearly 20 years of study. Those are safety design, accident and transient analysis, LOCA analysis, probabilistic safety assessment, plant heat balance, control and startup, coupled core neutronic and thermal hydraulics, subchannel analysis, and stability. They were done by developing computer codes for this purpose. The concepts are based on experiences of LWR design and safety. Simplicity and compactness are the characteristics of the concepts. Although design optimization and experimental verification remain for future studies, methods and fundamental guidelines in designing the once-through supercritical reactor were developed.

B500SKDI, Natural Circulation Integrated SCPWR (Kurchatov, Institute 1992)

The concept of B500SKDI was presented by Russian researchers in 1992 [8]. The B500SKDI is an integral PWR in which the core and SGs (steam generators) are contained within the steel pressure vessel (Fig. B.15 [3]). The core is cooled by natural circulation. The pressurizer is located apart from the pressure vessel. The guard tube block shroud separates the riser and downcomer parts of the coolant circulation path. The hot coolant moves from the core through the riser and upper shroud windows into the steam generators located in the downcomer. The coolant moves due to the difference in coolant densities in the downcomer and riser. The SG is a once-through vertical heat exchanging apparatus arranged in an annular space between the RPV and guard tube block shroud. Each SG consists of 18 modules, which are joined into six sections. Each of the sections has an individual steam header and feedwater header, inserted through the RPV nozzles. The core design is based on the VVER technology. It has 121 shroud-less fuel assemblies with either Zr alloy or stainless steel cladding. The main technical parameters are listed in Table B.3 [3]. The electric power is 515 MWe. The coolant outlet temperature is approximately 380°C. It is substantially lower than other supercritical pressure reactors. Gross thermal efficiency is 38.1%. The general layout of the containment vessel arrangements is shown in Fig. B.16 [3]. The main equipment weights for VVER-1000 and B-500SKDI are presented in Table B.4 [3]. Main circulation pumps, primary pipings, and accumulators and outside SG are eliminated.

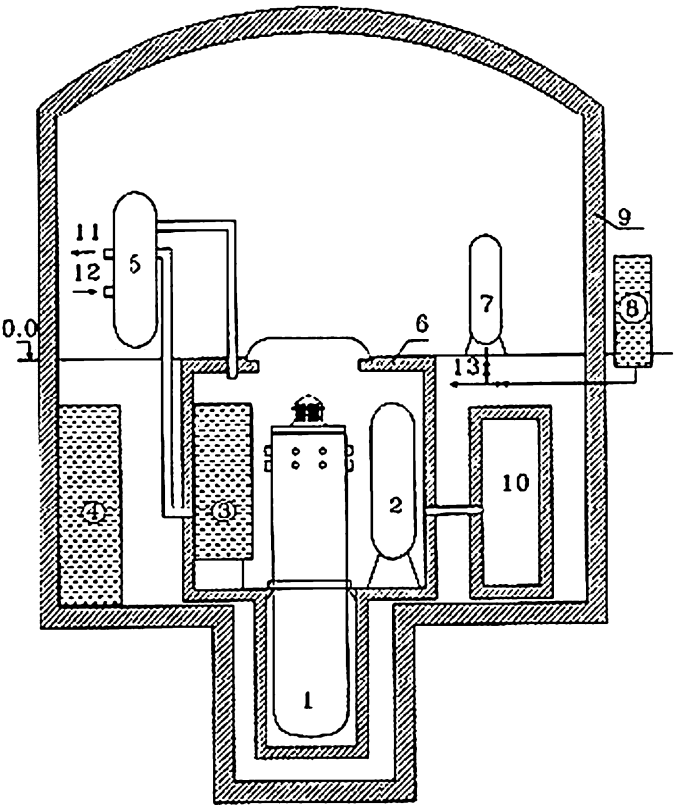


1. Reactor core
2. Core berrel
3. Steem generators
4. Guard tube block shroud
5. Reactor pressure vesseel
6. Reactor closure head

Fig. B.15 B-500 SKDI reactor (Taken from ref. [3])

Table B.3 Main characteristics of B-500SKDI (Taken from ref. [3])

Name (size)	Beginning of fuel lifetime/end of fuel lifetime
Thermal power (MW)	1,350/1,350
Electric power (MW)	515/515
Operation pressure at the core outlet (MPa)	235/23.5
Coolant temperature (°C)	
Core inlet	365/345
Core outlet	381.1/378.8
Core coolant flow (kg/s)	2,470/2,880
Time period between refuelings (rated power) (year)	2
Fuel lifetime (year)	6
SG steam pressure (MPa)	10.0
SG capacity (t/h)	2,320/2,400
Feedwater temperature (°C)	252/240
Generated steam temperature (°C)	379/375
Number of steamgenerator modules	18
Heat exchange tube material	Ti alloy
Tube diameter/thickness (mm)	12/1.3
Number of tubes per module	698
Pitch of SG tube bundle (mm)	21
Calculated effective length of heat exchange tube (m)	10.8
Full heat transfer area (m^2)	5,120



1. Reactor
2. Pressurizer
3. Hydrotank
4. Spent fuel pool
5. Bubble-condenser
6. Guard vessel
7. Hydro-accomulator
8. Water storage tank
9. Containment

Fig. B.16 General layout of the containment vessel arrangement (Taken from ref. [3])

The B-500SKDI RPV weight is heavier than that of the VVER-1000, but the specific metal expenditures are close to those for VVER-1000. Titanium alley is used for the SG tubes. It was described in reference [8] that the large amount of heat transfer experimental data at supercritical pressure water flow in large bundles were obtained in Kurchatov Institute, and that there was no heat transfer deterioration in the experiments with multi rod bundles within the same test parameters range at which heat transfer deterioration occurred in tubes. It is said that the B500-SKDI concept

Table B.4 Main equipment weights (Taken from ref. [3])

Name (size)	B-500 SKDI	VVER-1000
Vessel (t)	930	330
Upper block (t)	150	158
In-vessel equipment (t)	175	170
Steamgenerators (t)	55	1,288
Pressurizer (t)	260	214
Main circulation pumps (t)	–	520
Main circulation pipelines (t)	–	232
Safety tanks (t)	–	340
Total mass (t)	1,570	3,250
Specific metal expenditures per MW(e) (t/MW)	3.25	3.45

Table B.5 CANDU-X design characteristics. (Taken from *Proc. 1st Int. Symp. on SCWR*, Paper 104 (2000) [3])

	CANDU-X mark 1	CANDU-X NC	CANDUal-X1	CANDUal-X2
Thermal power (MW)	2,280	930	2,340	2,536
Electric power (MW)	910	370	950	1,143
EFF. (%)[a]	41	40	40.6	45
Press. (MPa)	25	25	25	25
Inlet temp (°C)	380	350	312	353
Outlet temp (°C)	430	400	450	625
Inlet density (g/ml)	0.451	0.624	0.720	0.615
Outlet density (g/ml)	0.122	0.167	0.109	0.068
Core flow (kg/s)	2,530	976	1,504	1,321
Number of channels	380	232	~300	~300
Ave. channel power (MW)	6	4	7.8	8.5

[a]Estimated

was developed to meet reactor design demands after the Chernobyl accident. Safety considerations are found in reference [8].

CANDU-X, Supercritical-Pressure CANDU (AECL, 1998)

AECL studies advanced reactor concepts with the aim of significant cost reduction through improved thermodynamic efficiency and plant simplification [9]. The program, generically called CANDU-X, also incorporates enhanced safety features, and flexible, proliferation-resistant fuel cycles while retaining the fundamental design characteristics of the CANDU: Neutron Moderator that provides a passive heat sink. Table B.5 [3] shows the CANDU-X design numbers. The cycles of four CANDU-X concepts are shown in Fig. B.17 [3]. The reactor concepts range in output from ~375 to 1,150 MWe. Each concept uses supercritical water as the coolant at a nominal pressure of 25 MPa. Core outlet temperatures range from ~400 to 625°C, resulting in substantial improvements in thermodynamic efficiencies compared to current nuclear stations. The CANDU-X Mark I concept is an

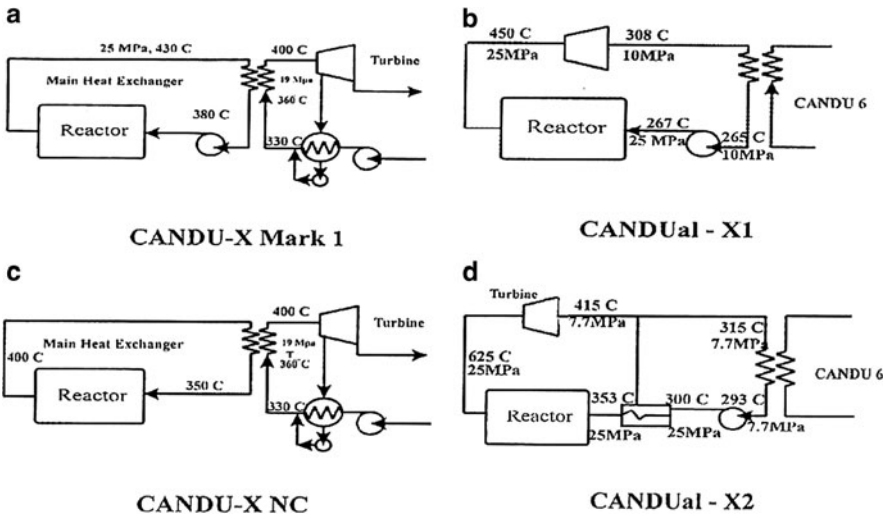


Fig. B.17 Cycles of four CANDU-type reactors cooled by supercritical water (Taken from ref. [3])

extension of the present CANDU design. An indirect cycle is employed, but efficiency is increased due to higher coolant temperature, and changes to the secondary side; as well, the size and number of pumps and steam generators are reduced. Safety is enhanced through facilitation of thermo-siphoning of decay heat by increasing the temperature of the moderator. The CANDU-X NC concept is also based on an indirect cycle, but natural convection is used to circulate the primary coolant. This approach enhances cycle efficiency and safety, and is viable for reactors operating near the pseudo-critical temperature of water because of large changes in heat capacity and thermal expansion in that region.

In the third concept of CANDUal-X, a dual cycle is employed. Supercritical water exits the core and feeds directly into a very high pressure (VHP) turbine in a topping cycle. The exhaust from the turbine is subsequently fed into a steam generator that is the heat source for an indirect cycle, similar to the secondary side in the existing CANDU design. Alternately, the concept could use the exhaust from the VHP turbine to drive a cogeneration system, such as for desalination or H_2 production. Enabling technologies that are generic to each of the reactor concepts include development of a CANTHERM fuel channel, SCW thermal-hydraulics and chemistry, and materials compatibility.

Nuclear Superheaters (GE, 1950s–1960s)

Nuclear superheaters were one of the three BWR designs that GE pursued for the commercialization of BWRs under the “Operation Sunrise” program in the 1950s and 1960s [10]. Nuclear superheaters had two versions, the integral-superheater

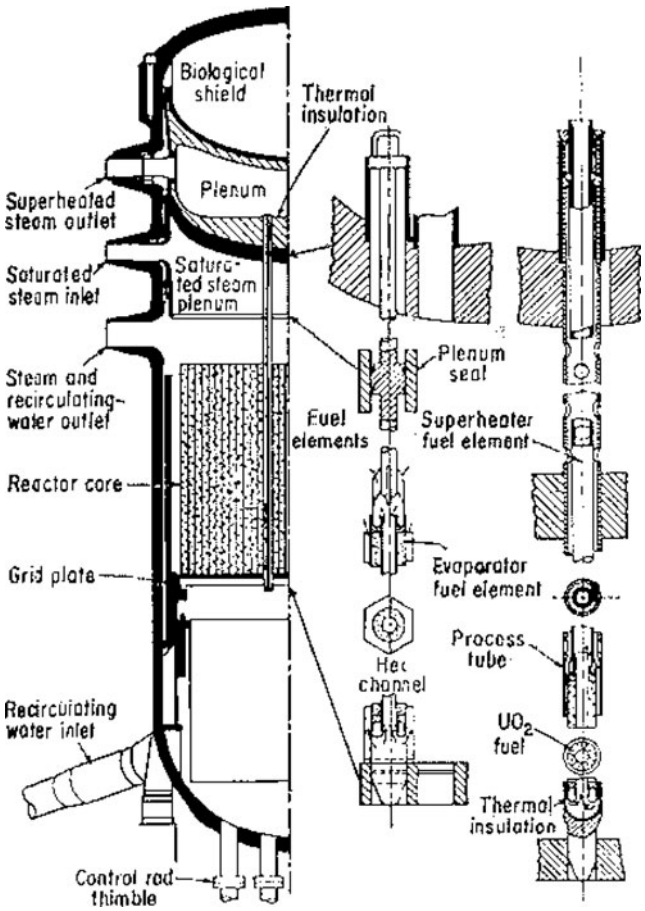


Fig. B.18 Core and vessel design for ISH-1 reactor in integral-superheater series (Taken from ref. [3])

(Fig. B.18 [3]) and the separate-superheater (Fig. B.19 [3]) series. Both operate at subcritical pressure. In the integral-superheater, there is a two-pass core with boiling and superheating regions. In the separate-superheater, a separate reactor, which is water moderated and steam cooled, superheats the steam produced in a boiling reactor. All three reactor design approaches in "Operation Sunrise" share the same technology with respect to reactor design, reactor core physics, fuel and structural materials, and plant layout and control. Ferrous alloys rather than zirconium are required as fuel cladding in the superheated steam region. It is said that the nuclear superheater did not take the main line of BWR development due to the poor integrity of fuel cladding, which experienced stress corrosion cracking, low power density, and only marginal economic improvement.

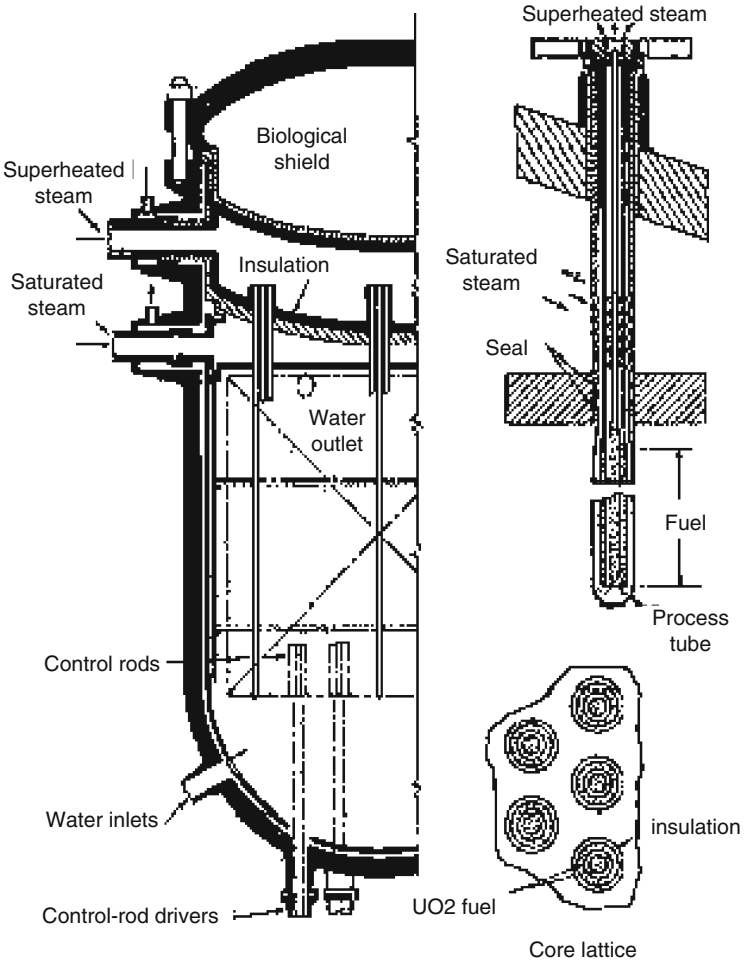


Fig. B.19 Core and vessel design for SSH-2 in separate-superheater series (Taken from ref. [3])

Steam Cooled Fast Breeder Reactors

Steam cooled fast breeders were studied as an alternative to liquid metal cooled ones in the 1950s and 1960s. The concepts are summarized below.

- Subcritical pressure steam cooled FBR by GE (1950–1960s), KFK (1966) and B&W (1967).
- Supercritical pressure steam cooled FBR by B&W (1967).
- Subcritical pressure steam cooled high converter by Edlund & Schultz (1985, USA).
- Subcritical pressure water-steam cooled FBR by Alekseev and coworkers (1989, Russia).

Table B.6 Characteristics of steam cooled fast reactors (Taken from ref. [3])

	Low-pressure system (B&W)	Intermediate-pressure system (KFK)	High-pressure system (B&W)
Reactor power (thermal/electric) (MW)	2,900/1,012	2,519/1,000	2,326/980
Thermal efficiency (%)/system pressure (MPa)	34.9/8.6	39.7/18.4	42.2/25.3
Coolant temperature (at outlet) (°C)	496	541	538
Coolant flow rate (kg/s)	4,649	3,169	3,214
Core volume (l)	7,437	8,190	4,160
Core height to diameter ratio	0.206	0.574	0.64 annular
Fuel material	MOX	MOX	MOX
Cladding material	Inconel 625	Inconel 625	19-9DL SS
Fuel rod diameter/pitch (cm)	0.89/1.016	0.70/0.879	0.584/0.732
Cladding thickness (cm)	0.030	0.038	0.0254
Pumping power (MW)	101	67	46
Breeding ratio	1.38	1.14	1.11
Average core power density (kw/l)	353	286	447
Maximum linear heat rating (kw/m)	59.7	40.3	54.8

The subcritical pressure steam cooled FBRs were studied by GE, KFK [11] and B&W [12]. The supercritical pressure steam cooled FBR was studied by B&W [13]. The subcritical and supercritical reactor concepts by B&W and KFK were evaluated by Oak Ridge National Laboratory [14]. They were called low pressure, high pressure, and intermediate pressure systems in the report, respectively. The characteristics of the reactors are summarized in Table B.6 [3]. All these concepts operate on a direct cycle Loeffler type boiler principle in which a portion of the superheated steam from the outlet of the reactor is sent to the turbine generators to produce power and the remainder of the steam is mixed with feedwater to produce steam, which is circulated to the inlet of the reactor. The schematic flow diagram for the low pressure steam cooled FBR, shown in Fig. B.20 [3], illustrates a so-called "integral" design in which steam is recirculated inside the primary reactor vessel. The direct contact boiler is located at the bottom of the primary reactor vessel, where feedwater is sprayed so that it makes direct contact with the superheated steam from the bottom of the core. In the other designs, the boiler and circulators are located external to the reactor vessel, as shown in Figs. B.21 [3] and B.22 [3]. For these designs, more piping is required to convey the large volume of recirculated steam. However, the boiler and the circulator are more accessible for maintenance. In the design illustrated in Fig. B.20 [3], the only steam leaving the primary vessel is that required to operate the turbines that drive the electric generator and the circulators.

The steam cooled FBR resembles BWRs in that it employs a direct cycle, with the steam from the reactor being used to drive the turbine. When reheat is necessary, steam-to-steam surface heat exchangers are used, as shown in Figs. B.21 [3]

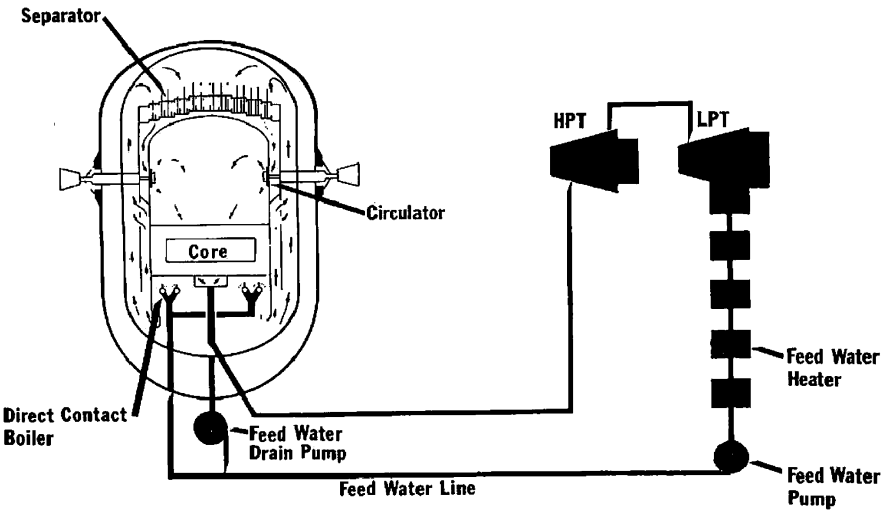


Fig. B.20 Simplified flow diagram of low pressure steam cooled FBR (B&W) (Taken from ref. [3])

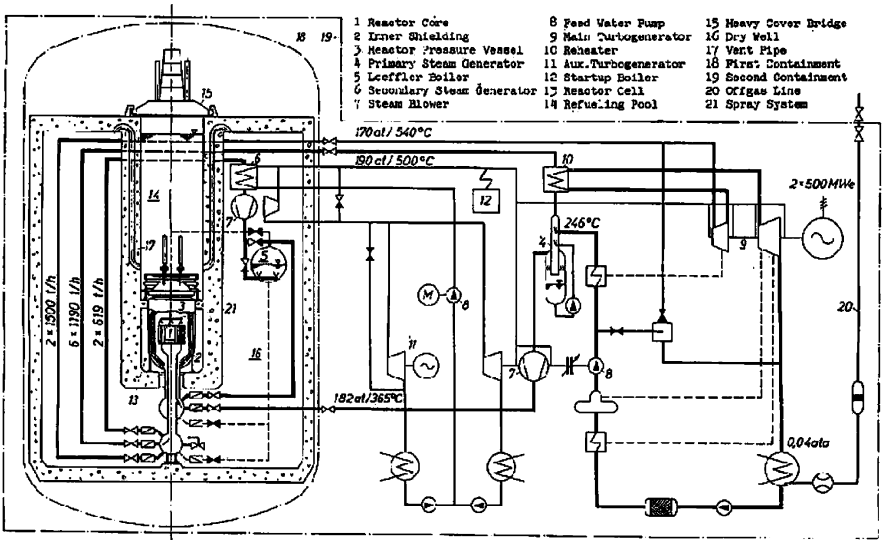


Fig. B.21 Simplified flow diagram and containment system of steam cooled FBR (KFK) (Taken from ref. [3])

and B.22 [3]. The major components of the concepts for the 1,000 MWe FBRs are the reactor vessel, steam generators, circulators, containment vessel, and shutdown and emergency core cooling systems.

Common safety concerns of the steam cooled breeders are the reactivity insertion at loss of coolant and coolant voiding. The reactivity is also inserted at core

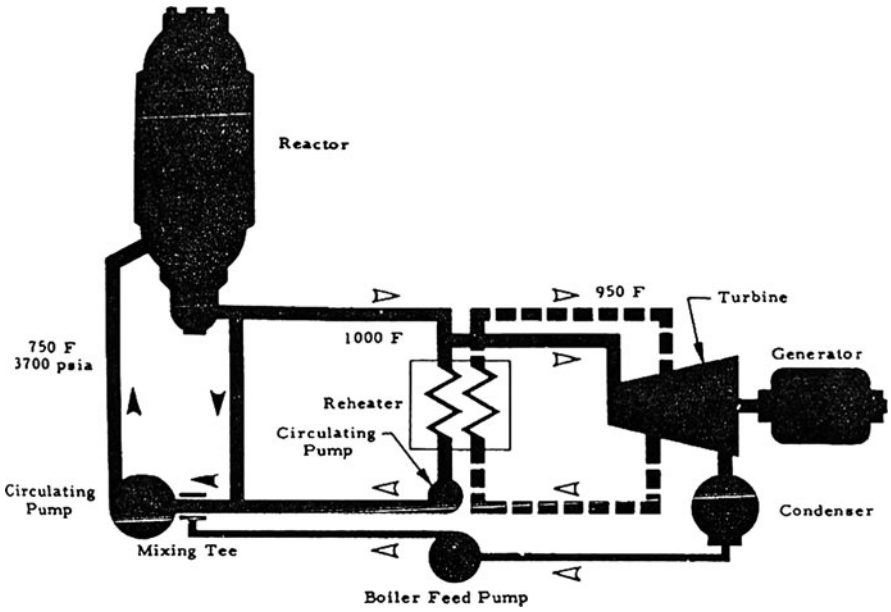


Fig. B.22 Simplified flow diagram of high pressure FBR (B&W) (Taken from ref. [3])

flooding. This is the extreme case of loss of feedwater heating of water cooled reactors. The fuel will heat up at a rate four to five times as fast as that in water cooled reactors if it is not cooled. The time margin for starting emergency cooling will be much shorter. The steam circulators are necessary besides the feedwater pumps. The experiences of high pressure large capacity circulators are far fewer than the experiences of pumps.

The intermediate pressure design produced at KFK appears conservative to prevent centerline melting of the fuel, as contrasted with the two designs by B&W, which would probably have melting in some parts of the fuel, because of the higher heat rating of the fuel rods.

In 1985, Schultz and Edlund [15] published a paper that proposed a new steam cooled reactor. A schematic flow diagram of the reactor is shown in Fig. B.23 [3]. The reactor is installed in the "PIUS" type vessel, which is filled with water. The density lock at the diffuser connected to the steam outlet pipe will automatically shut the reactor down and cool it. The other characteristic is that it is designed to operate at one fixed steam density. The reactivity becomes the maximum at that density to avoid reactivity insertion in both voiding and flooding of the core. The plant operates at low pressure, 6.9 MPa. The thermal efficiency is estimated as 35%. It should be pointed out that the reactivity change with density is always kept positive (negative in void coefficient) in BWR design to avoid the problem associated with the positive void coefficient during startup. This means that the reactivity should not increase automatically during startup when the coolant density changes from high to low.

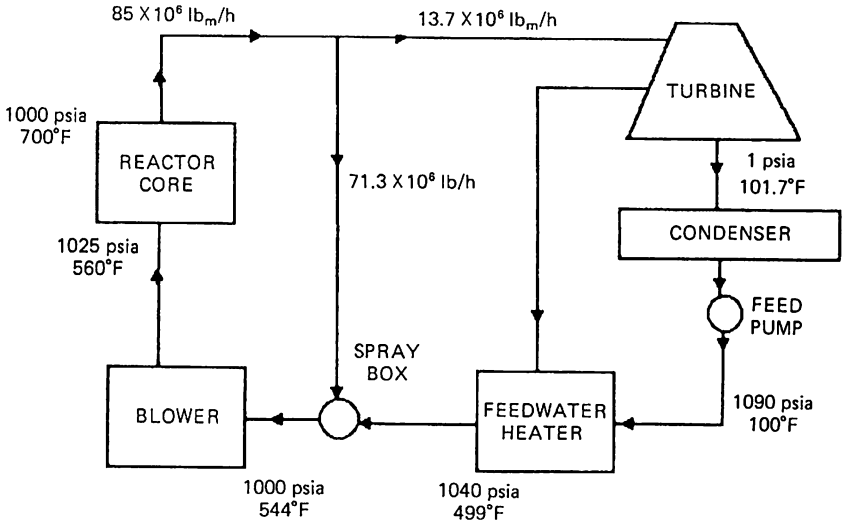


Fig. B.23 Steam flow cycle of the new steam cooled reactor (Edlund & Schultz) (Taken from ref. [3])

In 1989, the steam-water power reactor concept was presented by Alekseev and colleagues working in the former USSR [16]. The use of steam-water mixture for the reactor cooling is a key feature of the concept. There are two versions of the steam-water mixture preparation and distribution system. In one, the steam is supplied externally by steam blowers to the RPV and it mixes with feedwater in the special nozzle mixers set at the fuel assembly inlet. In the other, the steam is circulated in the RPV by jet pumps. The steam-water mixture is prepared in the jet pumps. The diagram of the steam-water power reactor is shown in Fig. B.24 [3]. There is no description on the feasibility of steam-water mixture generation. The plant system is indirect cycle. The primary pressure is 16.0 MPa. The core inlet and outlet temperatures are 347 and 360°C, respectively. The core inlet quality is 40%. The average void fraction of the core is estimated to be 93%. The core average coolant density is estimated to be 0.14 g/cm^3. It should be pointed out that the technical and safety problems will be similar to those of the steam cooled FBR.

Summary

Supercritical pressure reactor concepts and nuclear superheaters were studied as reactor concepts by WH and GE in the 1950s and 1960s when LWR design and safety had not yet been established. New supercritical pressure reactor concepts emerged in the 1990s from Japan, Russia, and Canada as innovative water cooled reactors. Steam cooled FBRs were studied in the 1950s and 1960s as an alternative to liquid metal fast breeder reactors. These steam cooled FBRs require a

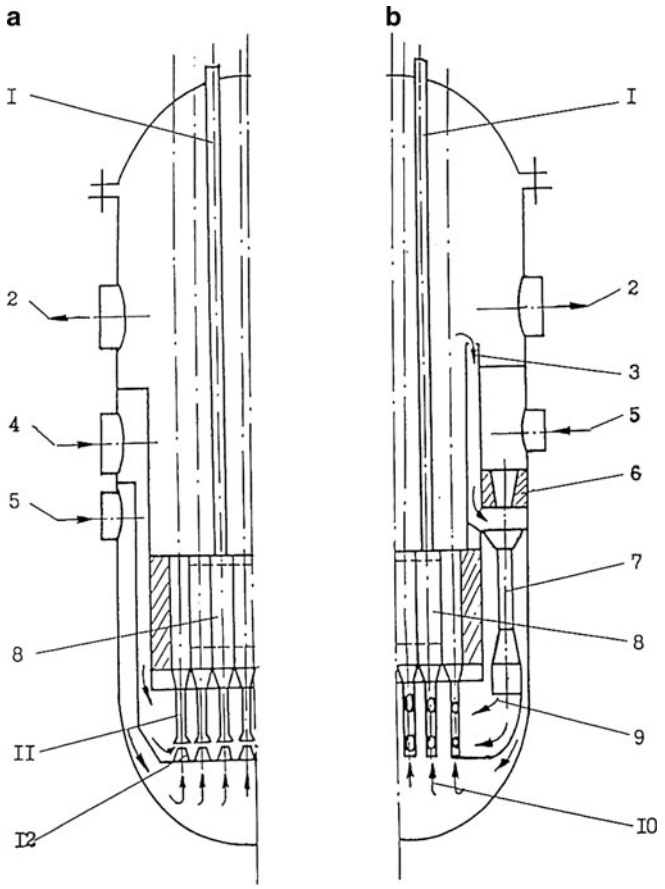


Fig. B.24 Diagram of SWPR for the versions with steam circulation by steam blowers (**a**) and by jet pumps (**b**) (Taken from ref. [3])

Loeffler-type boiler for generating inlet steam. Steam blowers are required rather than feedwater pumps. Short time margin for emergency core cooling due to high power density and positive reactivity coefficient is an engineering drawback.

Appendix B is based on Ref. [3].

References

1. HW-59684, "Supercritical pressure power reactor, a conceptual design," Hanford Laboratories, General Electric (1959)
2. J. F. Marchaterre and M. Petrick, "Review of the Status of Supercritical Water Reactor Technology," Atomic Energy Commission Research and Development report, ANL-6202, Argonne National Laboratory (1960)

3. Y. Oka, "Review of high temperature water and steam cooled reactor concepts," *Proc. 1st Int. Symp. on SCWR,* Tokyo, Japan, November 6–8, 2000, Paper 104 (2000)
4. J. F. Patterson, "Supercritical Technology Program, Final Report," WCAP-3394-8 (1968)
5. (5) J. H. Wright and J. F. Patterson "Status and Application of Supercritical-Water Reactor Coolant," *Proc. of American Power Conference*, Vol. 28, 139–149 (1966)
6. Y. Oka and S. Koshizuka, "Conceptual design of a Supercritical-pressure Direct-cycle Light water reactor," *Proc. ANP'92*, Tokyo, Japan, October 25–29, 1992, Vol. 1, Session 4.1, 1–7 (1992)
7. Y. Oka, S. Koshizuka, Y. Okano, et al., "Design Concepts of Light Water Cooled Reactors Operating at Supercritical Pressure for Technology Innovation," *Proc. 10th PBNC*, Kobe, Japan, October 20–25, 1996, 779–786 (1996)
8. V. A. Slin, V. A. Voznessensky and A. M. Afrov, "The Light Water Integral Reactor with Natural Circulation of the Coolant at Supercritical Pressure B-500 SKDI," *Proc. ANP'92*, Tokyo, Japan, October 25–29, 1992, Vol. 1, Session 4.6, 1–7 (1992)
9. S.J. Bushby, G. R. Dimmick, R. B. Duffery, et al., "Conceptual Designs for Advanced, High-Temperature CANDU Reactors," *Proc. ICONE-8*, Baltimore, MD, April 2–6, 2000, ICONE-8470 (2000)
10. K. Cohen and E. Zebroski, "Operation Sunrise," *Nucleonics*, 63–71 (1959)
11. R. A. Mueller, F. Hofmann, E. Kiefhaber and D. Schmidt, "Design and Evaluation of a Steam Cooled Fast Breeder Reactor of 1000MW(e)," *Proc. London Conference on Fast Breeder Reactors*, British Nuclear Energy Society, May, 1966, 79 (1966)
12. BAW-1318, "1000MWe, 1250 psi Steam Cooled Breeder Reactor Design, Final Report" (1967)
13. BAW-1309 "1000MWe, 3600psi Steam Cooled Breeder Reactor Design" (1967)
14. WASH 1088, "An Evaluation of Steam-Cooled Fast Breeder Reactors," Oak Ridge National Laboratory
15. M. A. Schultz and M. C. Edlund, "A New Steam-Cooled Reactor," *Nuclear Science and Engineering*, Vol. 90, 391–399 (1985)
16. P. N. Alekseev, E. I. Grishman and Y. A. Zverkev ,"Steam-Water Power Reactor Concept," Soviet-Japanese Seminar on Theoretical, *Computational and Experimental Study of Physical Problems in Designing of Fast Reactors*, July 1989

Glossary

DNB	Departure from nucleate boiling
AVT	All Volatile Treatment
CWT	Combined Water Treatment
TIG	Tungsten Inert Gas
SCOTT-R	Supercritical Once-Through Tube Reactor
ABWR	Advanced Boiling Water Reactor
SCLWR	Super Critical Light Water Reactor
SCFR	Super Critical Fast Reactor
RPV	Rector Pressure Vessel

Index

A
Abnormal condition, 551, 571
Abnormal transients, 10, 17, 18, 40–43, 45, 46, 384, 401, 409, 454, 551, 553, 554, 571
Accidents, 44, 46, 358, 360, 361, 383, 391, 392, 394, 395, 398, 399, 409, 412
Accumulators, 396, 411, 632
Assembly, 56, 441, 443, 444, 464, 466–468, 470–478, 480–482, 484–487, 489–492, 495, 497–499, 501, 502, 504, 506, 509, 513–515, 520, 523, 565
Auxiliary safety system, 222
Axial power, 13, 19, 462, 468, 493

B
Base load, 271
Blowdown, 396
Boiler, 599, 601, 604–607, 609, 610, 613, 625, 639
Boiling, 3, 6, 9, 26, 27, 37, 63
Boiling phenomenon, 9
Bottom dome, 37, 386, 396, 404
Boundary condition, 244, 460, 471
Brunup, 443
Buckling collapse, 17, 41, 42, 458, 461, 462, 466
Bulk temperature, 409
Burnup, 446, 460, 461, 465, 471, 472, 474, 477, 481, 486, 489, 501, 504, 506, 512, 518, 520, 522, 573, 586
Bypass system, 604

C
Calculation models, 407, 409
Calculation uncertainty, 304
Capital cost, 230, 445, 572, 584
Centerline temperature, 454, 456, 460, 462, 466
Cladding, 442–444, 452–463, 465, 479, 480, 491–495, 498, 572, 577–579, 583, 586
Cladding collapse, 453
Cladding failure, 458
Cladding ovality, 455
Cladding temperatures, 10, 12, 14–16, 18, 22, 25–27, 37, 40, 41, 44, 49, 55
Cladding thickness, 18
Coated particle fuels, 412
Cold-leg break, 396, 398
Collision probability, 446, 467
Compressive stress, 453
Conceptual stage, 253
Condensate pumps, 357, 383
Condensate pump trip, 357, 383
Condensate system, 274, 342
Condensation pool, 224
Condenser, 230, 232, 236, 271, 273, 279, 281, 284, 340, 342, 345
Constant pressure, 4, 22, 25
Constant pressure startup, 270, 273–275, 278, 279, 283, 289, 295, 335, 345, 536
Construction cost, 572
Construction period, 222
Containment, 1, 8, 48, 224, 225, 229, 441, 518, 560, 572, 577, 582, 628, 631, 632, 634, 640
Control rod (CR), 1, 8, 9, 13, 14, 19, 21, 226, 242, 246–248, 250, 253, 256, 257, 260, 262, 263, 265, 443, 452, 471, 473, 474, 480, 493, 515, 524, 579, 628

Control rod drives, 360
Control rod guide tube, 242
Control rod withdrawals, 389
Control system, 19–22, 43, 57, 241, 246, 248, 253–266, 501, 522, 523, 525, 527–529, 531–536, 551, 553, 554
Coolant density, 450, 468, 471–474, 476, 477, 482, 509, 524, 532, 534–536, 551–553, 564, 582
Coolant density feedback, 402, 404, 409
Coolant enthalpy, 443, 496
Coolant flow rate, 221, 222, 238
Coolant inventory, 221, 361, 411
Coolant pressure, 17, 18, 30, 453, 455, 459
Coolant system, 221, 226
Coolant velocity, 11, 15
Core arrangement, 464, 465, 482–485, 514, 515, 517, 565
Core coolant flow rates, 248, 253, 386, 388, 396, 400, 407, 411
Core damage frequency (CDF), 50, 53
Core design, 443, 444, 465–469, 487, 489, 497, 508, 509, 514, 520–522, 536, 538, 547, 550, 556, 565, 566
Core inlet temperature, 236
Core outlet temperature, 232, 233, 235–238
Core power, 463, 465, 501, 503, 536–539
Corner subchannel, 494
Cosine distribution, 284, 300, 302, 304, 319, 322
Coupled neutronic thermal-hydraulic stability, 258
Creep rupture, 17, 454, 456, 461, 613, 615
Creep rupture strength, 613, 615
Creep strain, 458, 459, 462
Creep strength, 615
Critical point, 621
Critical pressure, 221, 230
Cross section, 446, 448, 449, 470–472, 474–477, 510, 514
Cumulative damage fraction (CDF), 458

D
Deaerator, 357, 384
Decay heat, 37, 39, 405
Decay ratio, 30–32, 34, 35, 258, 260, 262, 303, 304, 306, 309, 310, 312–316, 324, 327, 330, 331, 334, 346, 545–547, 550, 566
Delayed, 319
Delayed neutron, 318, 319
Density coefficient, 34
Density lock, 641
Deposition, 275, 277, 278, 320
Depressurization, 37, 354, 361, 395, 408, 411
Depressurization setpoint, 395
Design basis accident, 446
Design criteria, 10, 442, 443, 454–459, 462, 463, 466, 484, 498
Diesel generators, 396
Direct cycle, 620, 621, 625–627, 636, 639, 642
Discharge burnup, 441, 460, 465
Doppler coefficient, 246, 247, 265
Doppler feedbacks, 394, 405, 407–409, 411
Downcomer, 14, 19, 37, 227, 242, 284, 386, 396, 404, 601, 632
Downward flow, 16, 37, 55, 57, 62, 63, 477, 482, 486, 488, 489, 498, 499, 502, 512, 536, 538–540, 542, 544, 545, 547, 550, 551, 553, 556, 559, 560, 566
Drain tank, 272, 279, 346
Dryout, 10, 11, 25–28, 35, 40, 284, 288, 322
Drywell, 224
Drywell pressure, 356, 396, 400
Duct tube, 481, 483, 484
Dummy rod, 494

E
Economizer, 605–607
Effective multiplication factor, 60, 61, 511
Eigenvalue, 447
Electric power, 230
Energy group, 467, 470, 476
Entrainment, 275–278
Equilibrium quality, 287
Equivalent diameter, 441, 442, 463

F
Failure mode, 454–456, 466
Fast neutron, 227, 448, 476, 481, 513, 514, 517
Fast reactors, 9, 10, 54, 56, 58–64, 74
Fast spectrum, 468, 494
Feedback transfer function, 302, 304, 324
Feedwater, 27, 269–272, 274, 275, 278, 280–284, 289–292, 294, 302, 310, 312, 314, 315, 323, 330, 334, 335, 338, 340–342
Feedwater controller, 523, 525, 527–532, 534, 535, 566
Feedwater control system failure, 360
Feedwater flow, 358, 388
Feedwater flow rate, 21, 244, 245, 247, 248, 250, 253, 255, 259, 261–266, 274, 302, 526
Feedwater heater, 274

Feedwater pump, 1, 9, 19, 21, 38, 50, 57, 222, 223, 229, 232, 246, 265, 522, 524, 534, 604, 623, 641, 643
Feedwater temperature, 27, 232, 237, 238, 244, 259, 264, 265, 280, 290, 292, 294–295, 310, 330, 343, 386, 387, 477, 501, 533–536
Film boiling, 286
Fission gas release, 12, 17, 55, 456, 460–462
Fission product, 225
Fission rate, 513
Flash tank, 271, 274, 275, 278, 279, 345
Flow mixing, 491, 496, 498
Flow rate, 443, 444, 458, 468, 477, 481, 484–487, 495, 501, 503, 518, 523–525, 527–539, 541–543, 545–547, 552, 553, 556, 563, 564, 566
Flow rate control system, 389
Flow rates, 6, 8–11, 15, 18, 19, 21, 22, 25–27, 34–40, 43, 49, 54, 57
Flow stagnation, 385, 396, 411
Flow velocity, 10, 30, 443, 457, 463, 466
Forced circulation, 38
Forward finite difference, 299
Frequency domain approach, 269, 297, 298
Fresh fuel, 14, 477, 517
Friction pressure drop coefficient, 299
Fuel assembly, 14, 18, 620, 626, 628, 629, 642
Fuel assembly gap, 471
Fuel bundle, 576
Fuel centerline temperature, 12, 17
Fuel cycle, 450, 451, 459, 465
Fuel enrichment, 14, 19, 450, 474, 476, 485
Fuel lattice, 9, 54
Fuel lifetime, 454, 460
Fuel loading, 13, 14
Fuel load patterns, 388
Fuel rod, 11, 13–19, 40–42, 55, 56, 62, 64, 67, 443, 444, 453–460, 462–468, 470, 471, 473, 476, 479–481, 484, 485, 493, 494, 499, 501, 504, 505, 509, 515, 519–522, 536, 564, 571–573
Fuel swelling, 456
Full implicit scheme, 244
Furnace, 601, 604, 605, 612

G
Gap clearance, 443, 494, 519
Gap conductance, 321, 455, 456
Gas cooled reactors, 358
Gas plenum, 17, 444, 455, 460, 461
Generator, 222, 232
Grid spacer, 16, 62–64, 409, 456, 493, 575
Guide tube, 471, 473, 474, 480, 493, 494

H
Heat balance, 13, 62, 221, 230, 232–235
Heat capacity, 523, 535, 550, 552, 553, 555, 560–564, 566
Heat conduction, 241, 245
Heat conductivity, 579
Heated length, 463
Heat flux, 10, 11, 13, 27, 41, 63, 547, 575, 576, 582
Heat sink, 44, 225, 411, 635
Heat source, 636
Heat transfer, 3, 10, 11, 16, 27, 31, 34, 35, 44, 62–65, 477, 493, 505, 506, 523, 547, 550, 575, 576, 582–584, 586, 588
Heat transfer coefficients, 398, 400, 402, 409
Heat transfer deterioration, 629, 634
Heavy water, 620, 623
Heterogeneous core, 445, 481
Heterogeneous form factor (HFF), 474
Hoop stress, 453, 455, 460
Hot channel, 443, 458, 468, 501, 505, 507, 536–539, 545, 551, 552, 564
Hot channel factors, 14
Hot spot, 454, 499, 505
Hydraulic feedback, 334
Hydraulic vibrations, 17
Hydrogenous moderator layer, 445, 450–451

I
Improved, 334
Indirect cycle, 621, 636
Inelastic strain, 458
Inert gas, 617, 628
Initial conditions, 389, 402, 407, 408
Inlet nozzle, 222
Inlet temperature, 63, 477, 575
Instrumentation tube, 480, 493
Integral controller, 256
Interlock systems, 405
Internal, 222, 227–229
Internal pressure, 18

J
Jet pump, 642, 643

L
Lag time, 255, 256
Lead-lag compensation, 253
Lead time, 255, 256
Least square, 303

Linear heat rate, 441–443, 457, 460, 471, 476, 477, 489
Loading pattern, 465, 482, 509, 511, 514, 516
Loss of coolant, 224, 225
Loss of coolant accident (LOCA), 13, 445
Loss of turbine load, 406
Lower plenum, 242

M
Main coolant flow, 357, 383, 387–389, 391, 402, 406
Main coolant flow control system failure, 388
Main feedwater line, 242, 248
Main steam, 270, 272–275, 281, 282, 284, 288, 290, 338, 340, 341, 343
Main steam line, 242, 262, 406
Main steam pressure, 248, 251–253, 255, 256, 259, 262
Main steam temperature, 241, 248, 253, 255, 256, 258–262, 264–266, 274, 281, 282, 343, 526
Main stop valves, 356
Mass flow rate, 232, 233, 235
Mass flux, 10, 19, 44, 287, 305, 315, 443, 457, 463, 493–495, 519, 553, 575, 582
Maximum cladding surface temperature (MCST), 56, 442–444, 462, 463, 468, 476, 477, 491, 493, 495–502, 504–509, 512, 518, 523, 537, 539, 544, 546, 547, 550, 552, 553, 565, 566
Maximum linear heat generation rate (MLHGR), 442, 443, 454, 456, 462, 463
MCST. *See* Maximum cladding surface temperature
Melting temperature, 454, 457
Mesh, 242, 244–246
Mixed-oxide fuel (MOX), 442, 453, 454, 456, 457, 459, 460, 465, 479, 503, 509
MLHGR. *See* Maximum linear heat generation rate
Moderator, 621, 623, 626, 636
Moderator temperature coefficient, 246
Moisture content, 275, 288
MOX. *See* Mixed-oxide fuel

N
Natural circulation, 3, 38, 50, 53, 411, 601, 606, 607, 632
Natural convection, 636
Negative reactivity, 45, 58, 60
Neutron absorption, 448, 513, 579
Neutron balance, 448, 510
Neutron density, 319
Neutron diffusion, 467, 468, 470–472, 475
Neutron flux, 467, 470–472, 474, 475
Neutronic calculation, 446, 497
Neutronic coupling, 468, 472, 482
Neutronic feedback, 317, 334
Neutron irradiation, 578, 586
Neutron kinetics, 317, 318, 322
Neutron leakage, 442, 445, 448, 482, 486, 510, 513–515, 520
Neutron library, 476
Neutron moderation, 241
Neutron production, 448
Neutron spectrum, 56, 58, 60, 445, 448–450, 467, 470, 471, 494, 510, 585
Neutron transport, 467, 468, 471, 476
Nominal condition, 443, 457, 501
Normal condition, 499, 513
Normal operation, 443, 445, 454, 458, 499, 506, 508
NPP. *See* Nuclear power plant
Nuclear data, 503, 516
Nuclear design, 444, 467, 468, 470
Nuclear enthalpy, 501, 503
Nuclear heating, 274, 279, 281, 338, 342, 343
Nuclear power plant (NPP), 221–223
Nuclear transmutation, 571, 572
Nucleate boiling, 322

O
Offsite power, 357, 383–385, 404, 406, 409
Once-through, 1, 9, 11, 12, 25, 28, 36–38, 47, 50, 53, 54, 61, 63, 221
Once-through operation, 271, 273, 274, 281, 342
Orifice, 481
Outlet coolant temperature, 572
Outlet nozzle, 222, 226, 227
Outlet temperature, 9, 55, 56, 441, 442, 444, 465, 468, 477, 482, 484–487, 489, 492, 494, 512, 518–523, 527, 531, 546–547, 551, 565

P
Partial power operation, 309, 310
Peaking factors, 14
Pellet temperature, 246
Permeation rate, 451, 452
Pin power distribution, 475, 495, 497, 506
Pin power reconstruction, 472, 474, 475
Pin-wise power distribution, 14, 15
Pitch to diameter ratio, 10
Plant control system, 382
Plant dynamics, 241–246, 248, 258, 265, 266

Plant stability, 241, 258, 259, 266
Plant system, 221–223, 229, 230, 572, 576
Plenum temperature, 489, 501, 502
Plutonium inventory, 465
Point kinetics, 241, 246
Power control system, 388
Power cost, 238
Power density, 54, 56, 441, 457, 462, 465, 485, 486, 489, 512, 518–523, 550, 555, 563–566, 573
Power distribution, 444, 462, 467, 468, 472, 475, 477, 480, 481, 483, 486, 491, 493, 497
Power gradient, 486
Power peaking, 443, 468, 473, 484, 485, 489–491, 493, 495, 497–500, 507, 514, 517, 565
Power plants, 1, 3–5, 7, 9, 22, 582
Power raising phase, 339, 345
Pressure abnormality, 360, 361
Pressure containment, 222, 223
Pressure containment vessel, 222
Pressure control system, 361, 395, 396, 407
Pressure control system failure, 361, 386, 407
Pressure drop, 9, 31, 32, 34–36, 54, 56, 494, 536, 538, 539, 545, 551, 553, 559, 575, 576, 588
Pressure tube, 626
Pressure-vessel, 571, 572, 581–583
Pressurization transient, 385
Pressurizer, 241, 628, 632
Primary coolant, 8, 9, 37
Primary coolant loops, 8, 9
Primary coolant pumps, 358
Primary loop, 12, 21
Proportional controller, 256
Pump, 222, 229, 230, 232, 238

R
Rated power, 290
Reaction rate, 470
Reactivity abnormality, 360, 361
Reactivity coefficient, 13, 61
Reactivity feedback, 241, 246, 252, 316–319, 331, 389, 406, 524, 534–536, 550, 552, 553, 560, 564, 566
Reactivity insertion, 389, 402, 405, 408, 411
Reactivity worth, 388, 389, 394
Reactor building, 572
Reactor coolant flow abnormality, 361
Reactor depressurization, 360, 361, 412
Reactor electric power, 627
Reactor internal, 621
Reactor pressure vessel (RPV), 1, 6, 222, 223, 226, 227, 536, 627, 628
Reactor scram, 384, 385, 388, 389, 393, 396, 401
Reactor trip system, 401, 405
Reactor vessel, 572
Recirculation, 241, 246, 253, 263, 265
Recirculation pump, 246, 253, 272, 279–281, 358
Recirculation system, 221, 241, 358, 360
Reflector, 445, 450, 471, 481, 623
Reflooding, 398
Refueling pool, 224
Regional stability, 258
Reheater, 605, 614, 616
Residence time, 446, 451
Resonant oscillation frequency, 302
Riser, 632
RPV. *See* Reactor pressure vessel

S
Safety analysis, 361, 383, 386, 388, 391
Safety criteria, 571
Saturated steam, 253, 271, 274, 281, 288, 339, 340
Scram delay, 383, 393
Scram failure, 401
Scram setpoint, 387, 389
Scram signal, 383, 391
Secondary system, 358, 361
Sensitivity analysis, 385, 393, 398, 407–409
Separator, 221, 226, 230, 232, 235–237, 604, 605
Setpoint, 253, 255–263
Shuffling, 477
Shutdown margin, 13
Single channel, 13, 15, 61, 443, 459, 462, 463, 468, 476–478, 491, 493, 495, 497, 498, 500, 501, 506, 509, 565
Single-phase flow, 321
Sliding pressure, 3, 4, 22, 25–29, 35
Sliding pressure operation, 604
Sliding pressure startup, 25, 28, 270, 279, 281–284, 288, 289, 291, 295, 335, 338, 339, 345, 346, 536, 576
Small reactivity, 532
Specific heat, 6
Specific heat capacity, 320
Spent fuel, 5, 9, 479
Stability, 32–34, 36, 269, 295, 297, 300–318, 324–338, 345, 346
Stability margin, 298

Stainless steel, 229, 451–453, 461, 479–481, 578, 580, 582, 613–616, 621, 626
Startup bypass operation, 271, 274, 281
Startup bypass system, 271, 274, 279, 283, 339, 345
Startup scheme, 269, 270, 345
Steady state, 250, 251, 260, 262
Steam, 221, 222, 225, 226, 228–230, 232, 233, 235–237
Steam blower, 619, 642, 643
Steam circulator, 641
Steam drum, 606
Steam dryer, 241
Steam flow rate, 235
Steam generator, 5, 8, 21, 38, 48, 221, 241, 252, 358, 632, 636, 640
Steam line, 222, 230
Steam pressure, 523, 525, 534, 560
Steam temperature, 3, 21, 57, 522, 524–527, 531–536, 566, 577
Steam turbines, 1, 4, 5, 8
Steam-water separator, 6, 8, 22, 25, 241, 272, 279, 281, 290, 346
Stepwise perturbation, 246
Stress corrosion cracking, 613, 637
Stress rupture, 17, 41
Subchannel, 14, 15, 46, 55, 56, 62, 443, 444, 491–501, 504–506, 509, 523, 538, 552, 565, 572, 574
Subcooled water, 601
Supercritical, 221, 222, 228–230, 235, 238
Supercritical pressure reactor, 619, 623, 632, 642
Supercritical pressure reactor accident and transient analysis code, 241
Superheated steam, 601, 637, 639
Superheater, 253, 271, 272, 288, 290, 339, 604–607, 612, 614–616, 619, 636–638, 642
Suppression pool, 224, 225
System pressure, 461, 501

T
Theoretical density (TD), 479
Thermal conductivity, 320, 321
Thermal damage, 41
Thermal efficiency, 3–5, 9, 13, 22, 54, 221, 230, 232, 233, 235, 236, 238, 463, 604, 613, 621, 632, 641
Thermal expansion, 3, 17, 613, 636
Thermal fatigue, 252, 253
Thermal hydraulic(s), 13, 65, 443, 459, 466–468, 471, 472, 476–479, 493, 497, 506, 519, 536, 537, 545–547, 549, 550, 565, 566, 575–577, 582, 585, 586
Thermal-hydraulic stability, 258, 259, 304, 306, 312, 318, 328, 331, 332, 346
Thermal power, 463, 465
Thermal reactors, 9, 10, 54, 62
Thermal spectrum, 266, 572, 578, 581, 582
Thermal stress, 26, 65, 253, 613
Time-delay, 357
Time domain approach, 297, 298
Top dome, 19, 37, 49, 386, 396, 404, 411
Transfer function, 33, 34, 300–308, 318, 324, 326, 327
Transient analysis code, 241
Transient criterion, 10
Transients, 44, 46, 358, 361, 383–388, 390, 394, 409
Tube explosion, 607
Turbine, 221–223, 228–230, 232, 235, 236, 238, 271–275, 281, 284, 288–290, 339–343, 345, 572, 573, 580, 604, 607, 613, 616, 623, 636, 639
Turbine building, 572
Turbine bypass valves, 383
Turbine control, 251, 252
Turbine control valve(s), 21, 244, 246–248, 250–254, 259, 262, 265, 356, 357, 383–386, 406, 407, 523–526, 531, 534
Turbine exhaust steam, 604
Turbine internal efficiency, 604
Turbine stage, 232, 237
Turbine trip, 383, 385

U
Upper dome, 242
Upper plenum, 242
Upward flow, 14, 16, 477, 482, 486, 489, 498, 499, 536–539, 541, 544, 545, 547, 551–553, 556, 558, 565
Upwind difference scheme, 244
Used fuel, 517

V
Valve, 271–275, 279, 281, 323, 340, 342, 343, 345
Valves, 360, 383, 402
Vessel, 225–227
Vibratory stress, 613
Void collapse, 251, 385, 411
Void condition, 448, 449, 513, 517
Void fraction, 21

Void reactivity, 56, 442, 444–453, 465, 481–484, 486, 489, 496, 509, 510, 512–519, 521–523, 564
Void reactivity coefficient, 246

W
Waste gas decay tank rupture, 361
Water inventory, 358, 396
Water rod(s), 12, 13, 19, 21, 25, 32, 34, 35, 37, 44, 48, 49, 61, 62, 65, 579, 585, 586, 628
Wrapper duct, 471, 480, 494
Wrapper tube, 464–465, 473, 474

X
Xenon stability, 258

Z
Zirconium hydride layer, 55, 56, 59, 60, 632
ZrH layer, 445–452, 472, 476, 480–482, 484, 496, 513–515, 517, 521